PhD-FSTC-2019-40
The Faculty of Sciences, Technology and Communication

DISSERTATION

Defence held on 19/06/2019 in Luxembourg
to obtain the degree of

DOCTEUR DE L'UNIVERSITÉ DU LUXEMBOURG

EN SCIENCES DE L'INGÉNIEUR

by

Maciej Piotr CHRZANOWSKI
Born on 4th November 1988 in Pułtusk, (Poland)

SHEAR TRANSFER IN HEAVY STEEL-CONCRETE COMPOSITE COLUMNS WITH MULTIPLE ENCASED STEEL PROFILES

Dissertation defence committee

A-Prof. Dr.-Ing. Danièle Waldmann-Diederich, Chairman
Associate Professor, Université du Luxembourg, Faculté des Sciences, de la Technologie et de la Communication

Prof. Dr.-Ing. Hervé Degée, Vice-chairman
Professor, Universiteit Hasselt, Faculteit Industriële Ingenieurswetenschappen

Prof. Dr.-Ing. Christoph Odenbreit, dissertation supervisor
Professor, Université du Luxembourg, Faculté des Sciences, de la Technologie et de la Communication

Dr.-Ing. Teodora Bogdan
Senior Research Engineer, ArcelorMittal Global R&D, Luxembourg

Prof. Dr.-Ing. Dennis Lam
Professor, University of Bradford, Faculty of Engineering & Informatics

Preface

This Thesis was realised during my time as a Doctoral Researcher at the University of Luxembourg in the Faculty of Sciences, Technology and Communication, in the Research Unit of Engineering Sciences and as a member of the ArcelorMittal Chair of Steel and Façade Engineering. The industrial project partner ArcelorMittal Global R&D in the framework of the common research project "MultiCoSteel" supported the conducted research from the very beginning. The conducted research was funded by the Luxembourgish National Research Fund (FNR).

Many great people supported the performed research work, inspired me, encouraged me and shared with me their opinions. Even, if they were not fully aware about it. I strongly believe that without their contribution, the accomplishment of this thesis would be much harder and my time spent on the research would be not so interesting and fruitful. It would be extremely hard to list all the people that I would like to thank but at this place, I would like to express my sincere gratitude to all of you that came across my way. Thank you!

My special thanks I would like to address to Prof. Dr.-Ing. Christoph Odenbreit, Professor at the University of Luxembourg, holder of the ArcelorMittal Chair of Steel and Façade Engineering and the supervisor of my thesis. Thank you for offering me the opportunity to perform the very interesting and very innovative research work. Thank you for giving a faith in me and for assuring extraordinary, professional and pleasant supervision. Thank you for your time, all your invaluable remarks, remaining restless spirit, interesting discussions – sometimes to very late hours, your constructive critics and for having a support in your person. It was a pleasure and an honour to work with you.

I would like also to address my profound gratitude to Renata Obiala, PhD, Head of the Construction and Infrastructure Application Department of ArcelorMittal Global R&D. I truly appreciate your contribution in the continuous guidance of my research work, all the constructive critics received from your side, your technical expertise, willing to help, solid support in my work and positive attitude. Thank you for introducing me into the research and for the kick-off. Your contribution and support to my work is uncountable. Thank you for our professional and friendly discussions at the University and later during my stay in the offices of ArcelorMittal. I was lucky that I have met a person like you.

In a sincere expression of thanks, I would like to mention Dr. Eng. Teodora Bogdan, Senior Research Engineer at the ArcelorMittal Global R&D and a member of my supervision committee. First, I would like to thank for your technical advice, interesting discussions and constructive critics. I truly acknowledge your contribution to my work. However, most of all, I would like to thank you for your friendship, positive attitude and very pleasant atmosphere. I really enjoyed working with you on a common projects and having friendly talks in a free time.

My grateful thanks I would like to address to Prof. Dr. ir. Hervé Degée, Professor at the Hasselt University and member of my supervision committee. Thank you for joining the project, for your technical advice and for our interesting meetings proceeded with exhaustive discussions. In the same place, I would like to thank Prof. Dr.-Ing. Danielle Waldmann-Diederich, Professor at the University of Luxembourg and Chairman of my defence committee. Thank you for your contribution to my defence and for our interesting and inspirational discussions. I was always looking forward to having a meeting with you and to knowing your opinion. Finally yet importantly, I would like to thank Prof. Dennis Lam, PhD, Professor at the University of Bradford, for being a valuable member of my defence committee and for the participation in my dissertation committee meetings. Your feedback was always well seen.

During my research work, I had an occasion to experience numerous discussions with the world-class experts in the field of steel-concrete composite structures. Among all, I would like to especially thank to Prof. Dr.-Ing. Markus Schäfer from the University of Luxembourg, Prof. Dr. ir. André Plumier from the University of Liège and Prof. Dr. Ing. Quang-Huy Nguyen from the University of Rennes. Your valuable comments and provided literature guide my research and allow exploring the background of the behaviour of composite columns, as well as composite theory. Finally yet importantly, I would like to thank Prof. Dr.-Ing. Wolfgang Kurz from the Technische Universität Kaiserslautern for his support during the tests performed in the laboratory of TU Kaiserslautern and his valuable remarks.

For the continuous support in administrative tasks, I would like to thank Simone Drees and Annabella Simon. Thank you for management of my requests, your patience, understanding and friendly discussions. Moreover, I cannot omit Berta Rato. Thank you Berta for your significant work, your valuable remarks and support during application for the PhD Grant from FNR.

A big part of my research work was related to experimental investigations and I would like to thank all the support team of the laboratory of the University of Luxembourg. Especially, a big thank I would like to address to Logan Freitas for his enormous work and energy that he invest to help me with the preparation of all specimens and tests. I really enjoyed your company, your support and positive attitude at work and in private life. I would like also to thank Marc Seil for his support with laboratory work planning, measurement equipment and countless friendly discussions. Moreover, sincere thanks are addressed to Vincente Reis Adonis, Claude Collé, Ed Weyer, Ralph Reiter, Cédric Bruyere, Ken Adam, Gilbert Klein and Grace Ligbado. I was always able to count on your support and friendly talk in the corridor. Big thanks I would like to address to Valter de Matos, student of the University of Luxembourg, for his support during fabrication of test specimens.

I would like to thank all my colleagues. Special thanks to Andras Kozma, Valentino Vignieri. Yves Staudt, Job Duarte da Costa, Sebastian Nellinger and Matthias Braun who accompanied me during the research work in the research team of ArcelorMittal Chair of Steel and Façade Engineering at the University of Luxembourg. I will be missing our common brainstorming, problem-driven discussions,

off-topic discussions, all kind of discussions that I had the pleasure to carry with you. Thanks for common trips, all funny moments and for your continuous support. Gentlemen, it was a privilege to work with you!

During my research work, I had an amazing opportunity to join the R&D team of ArcelorMittal in Esch-sur-Alzette, Luxembourg. At this moment, I would like to thank again Renata Obiala and Teodora Bogdan but also in addition, I would like to express my sincere gratitude to Nicoleta Popa, Olivier Vassart and Boris Donnay for making this possible and for given acknowledge to the research project that I was dealing with. Such a distinction brought even more motivation into my work. Inside the ArcelorMittal, I have met an extraordinary team of professionals, which is the essence of the definition of the word "teamwork". My experience obtained there is invaluable and I would like to thank for it to Mike, François, Philippe, Jerome, Rodrigo, Bastien, Marion, Justine, Perla, Ludmila Antoine, Riccardo, Françoise, Thomas, Thibaut, Dario, Omer, Dennis, Micael, Rafael and Jean-Marc. However, special thanks I want to address to Rui Matos and Miguel Candeias, who were my officemates. I really enjoyed your company and all the discussions held. Moreover, I have learnt some Portuguese words – Obrigado!

A profound gratitude I want to express to Dr inż. Wioleta Barcewicz, an Assistant Professor at the Warsaw University of Technology and my former supervisor at the time of my Master and Bachelor studies. Dear Wioleta, thanks to you, I have found myself as a research at the University of Luxembourg and I still remember our discussion in your office after my Master Thesis defence in Warsaw as if it was yesterday. Time is passing fast. Thank you for inspiring me to do the research and for your support during my application for the position of doctoral researcher. I owe you my eternal gratitude for this.

At the end, I want to express my most sincere gratitude towards my family, who supported me and have not doubt in me for all that time. Disregarding the distance, your spirit and good energy pushed me forward and forward. Many thanks that you, nevertheless, stayed close. Finally, I want to profound thank my wife Magdalena for staying with me arm-by-arm in this sometimes hard and sometimes happy time. Your presence and your support at all levels cannot be measured or evaluated. You were always my strongest foundation in every action I took. Without you, it would be not possible at all. Moreover, during our stay in Luxembourg/Germany, you have blessed me with our beautiful daughter Hania for what I even cannot express how grateful I am. At the time of completing my research work, Hania is only, or maybe already, one year old. Currently, is excessively early for her to understand any written text but after some years, I hope she will find this dissertation and she will be proud of her father.

I would like to dedicate this work to two most important women in my life – my wife and daughter.

Luxembourg, in June 2019, *Maciej Piotr Chrzanowski*



Abstract

The PhD Thesis is dealing with the shear transfer in heavy steel-concrete composite columns with multiple encased steel profiles. In the conducted research, a focus was placed on two aspects of shear transfer: (1) local shear transfer at the steel-concrete interface and (2) global shear transfer between the embedded steel profiles. With reference to the current practice, gaps in the knowledge and in the available solutions have been identified.

The development of a novel, easy-applicable and efficient type of shear connectors for an application in composite columns with one or multiple-encased steel profiles satisfies the improvement need to assure local shear transfer between steel and concrete materials. The novel type of flat shear connectors has a form of reinforcement bars welded to the flanges of steel profiles. Three main orientations, in accordance to the steel beam longitudinal axis, were investigated: 1) transversal, 2) longitudinal and 3) angled under 45° - V-shaped. The force transfer mechanism of the proposed shear connectors considers the usage of the external stirrups to anchorage the compression struts and bear the tensile forces. In parallel, the steel-concrete bond phenomenon was examined and analysed.

In the consideration of the global shear transfer and in respect to the mechanical engineering model and behaviour of large composite columns with more than one embedded steel profile, the common practice so far is to assume a homogenous system with one stiffness and analyse it based on the Bernoulli beam theory. However, the results of the recent tests caused some doubts whether this approach is correct. The derivation away from the Bernoulli beam behaviour leads to a changed stiffness of the column and hence changed critical buckling load. An innovative hybrid conception has been proposed, where a transition towards the Vierendeel truss model embedded into the Timoshenko beam model is considered in order to govern the identified significant effects of shear deformation. Within this objective, big-scale beam/column members with two embedded steel profiles were examined in order to investigate an internal forces distribution and its bending and shear stiffness.

A complex interaction between the materials and lack of knowledge regarding composite behaviour in columns with multiple encased steel profiles opens opportunities to develop novel systems and design methods. The described objectives are investigated experimentally and by the FE numerical simulations. As an outcome, an analytical model for the resistance of the developed novel shear connectors and innovative mechanical engineering model for the description of the structural behaviour, as well as effective stiffness, of a composite member with more than one embedded steel profile are given.

Keywords: Steel-concrete composite columns; Multiple encased steel profiles; Shear transfer; Composite action; Shear connection; Structural behaviour; Effective stiffness

Streszczenie

Rozprawa doktorska dotyczy transferu ścinania w ciężkich słupach zespolonych stalowo-betonowych z wieloma obetonowanymi profilami stalowymi. Przeprowadzone badania skupiają się na dwóch aspektach transferu ścinania: (1) lokalny transfer ścinania na powierzchni między stalą a betonem, oraz (2) globalny transfer ścinania pomiędzy obetonowanymi profilami stalowymi. W odniesieniu do obecnej praktyki, braki w wiedzy oraz braki w dostępnych rozwiązaniach zostały zidentyfikowane.

Opracowanie nowatorskich, łatwych w aplikacji i efektywnych typów łączników zespalających dla słupów zespolonych z jednym lub wieloma obetonowanymi profilami stalowymi spełnia potrzebę ulepszenia lokalnego transferu ścinania między stalą a betonem. Nowatorskie płaskie łączniki zespalające wykonane są z prętów zbrojeniowych przyspawanych do półek profili stalowych. Trzy główne orientacje, w odniesieniu do osi podłużnej profilu stalowego: 1) poprzeczna, 2) podłużna i 3) ukośna pod kątem 45° - V-kształtna, zostały zbadane. Mechanizm transferu sił zaproponowanych łączników zespalających uwzględnia wykorzystanie zewnętrznych strzemion w celu zakotwienia ściskanych krzyżulców betonowych, oraz przeniesienia sił rozciągających. Równolegle, przeanalizowano i zbadano naturalne zespolenie między stalą a betonem.

W ramach globalnego transferu ścinania i w odniesieniu do modelu mechanicznego, oraz zachowania dużych słupów zespolonych z więcej jak jednym obetonowanym profilem stalowym, dotychczas normalnie przyjęta praktyka uwzględnia założenie homogenicznego systemu z jedną sztywnością i analizę w oparciu o teorię belek Bernoulli'ego. Jednakże, wyniki ostatnich badań wykazują pewne wątpliwości czy te założenie zostało prawidłowo przyjęte. Odbiegnięcie od założonego zachowania belki Bernoulli'ego prowadzi do zmienionej sztywności słupa i a co zatem zmienionej wartości siły krytycznej wyboczenia. Zaproponowana została innowacyjna koncepcja hybrydowa mająca na celu przejście w stronę modelu kratownicowego typu Vierendeel wbudowanego w model belki Timoshenko, który uwzględnia zidentyfikowane znaczne efekty deformacji od ścinania. W zakresie tego zadania, zostały zbadane konstrukcyjne elementy typu belka-słup o dużej skali z dwoma obetonowanymi profilami stalowymi.

Skomplikowana interakcja między materiałami i brak wiedzy w odniesieniu do zachowania zespolenia w słupach z wieloma obetonowanymi profilami stalowymi otwiera możliwości do opracowania innowacyjnych systemów, oraz metod projektowania. Opisane zadania są przeanalizowane eksperymentalnie i numerycznie poprzez symulacje MES. W rezultacie, model analityczny opisujący nośność opracowanych nowatorskich łączników do zespolenia konstrukcji i innowacyjny model inżynierski opisujący zachowanie konstrukcji, jak i również sztywność efektywną, elementów konstrukcyjnych z więcej jak jednym obetonowanym profilem stalowym zostały wyprowadzone.

Słowa klucz: Słupy zespolone stalowo-betonowe; Wiele obetonowanych profili stalowych; Transfer ścinania; Akcja zespolenia; Połączenie zespalające; Zachowanie konstrukcji; Sztywność efektywna

List of publications made out from this thesis

Based on the work described in this thesis, the following list of publications have been made until the day of publication of the thesis:

1. Chrzanowski, M.; Odenbreit, C.; Bogdan, T.; MultiCoSteel – Structural Behaviour of Heavy Composite Columns with Multiple Encased Steel Profiles for High Rise Buildings. Poster, 100 years of Engineering Education in Luxembourg, 2016. http://hdl.handle.net/ 10993/32320, http://hdl.handle.net/10993/32319.
2. Chrzanowski, M.; Odenbreit, C.; Bogdan, T.; Development of an innovative type of shear connection dedicated to the composite columns application. Poster, Proc. of Eurosteel 2017, CE/papers, Ernst&Sohn, Vol. 1, No. 2-3, 2017. https://doi.org/10.1002/cepa.96.
3. Chrzanowski, M.; Odenbreit C.; Obiala, R.; Bogdan, T.; Shear stresses analysis at the steel-concrete interface with the usage of bond eliminating products. Proc. of XI Congresse de Construção Metálica e Mista (XICMM), Coimbra, Portugal, 1027-1036, 2017.
4. Chrzanowski, M.; Odenbreit, C.; Obiala, R.; Bogdan, T.; Braun, M.; Degée, H.: Development of an innovative type of shear connector dedicated to fully embedded steel-concrete composite columns – experimental and numerical investigations. Proc. of 12th Intl. Conf. on Advances in Steel-Concrete Composite Structures (ASCCS 2018), Valencia, Spain, 427–434, 2018.
5. Chrzanowski, M.; Odenbreit, C.; Obiala, R.; Bogdan, T.; Degée, H.; Transfer of shear stresses at steel-concrete interface – Experimental tests and literature review. Steel Construction, Design and Research, Ernst&Sohn, Vol. 12, No. 1, 44-54, 2019. DOI: 10.1002/ stco.201800024.
6. Odenbreit, C.; Chrzanowski, M.; Obiala, R.; Bogdan, T.; Degée, H.; Characterisation of a new flat mechanical shear connection mean for steel-concrete composite columns. Structures, Elsevier, 2019. https://doi.org/10.1016/j.istruc.2019.03.001.
7. Chrzanowski, M.; Odenbreit, C.; Degée, H.; Obiala, R.; Bogdan, T.; Effective bending stiffness of heavy steel-concrete composite columns with multiple encased steel profiles. Proc. of 9th International Conference on Steel and Aluminium Structures (ICSAS19), Bradford, UK, 2019.

In the result, some figures, tables and parts of text can overlap. The listed papers and articles have been published before the publication date of the final version of this thesis. The above-listed publications are not directly referred in the text of the thesis and are not included in the references.

Table of Contents

List of Figures xvi
List of Tables xxvii
Nomenclature xxviii
1. Introduction 1
2. Overview and Structure of the Thesis 3
3. State of the Art 4
3.1. Steel-concrete composite construction 4
3.1.1. Basis of composite behaviour 5
3.1.2. Partial interaction 11
3.1.3. Composite columns 13
3.2. Beam and Truss Theories 16
3.2.1. Beam theories 16
3.2.1.1. Euler-Bernoulli beam theory 16
3.2.1.2. Timoshenko beam theory 17
3.2.2. Truss theories 18
3.2.2.1. Principal theory of trusses 18
3.2.2.2. Vierendeel truss theory 19
3.3. Shear connection 22
3.3.1. Shear transfer phenomena 22
3.3.2. Plain steel – concrete bond 24
3.3.3. Reinforcement bar – concrete bond 27
3.3.4. Mechanical shear connection means 32
3.4. Provisions for the design of composite columns 58
3.4.1. General considerations 58
3.4.2. International standards 59
3.4.3. EN 1994-1-1 64
3.4.4. Analytical models for the flexural stiffness found in the literature 74
3.4.5. Strut and tie model 75
3.4.6. Pivot/Fibre method 77
3.5. Composite columns with multiple encased steel profiles 78
3.5.1. Current approach 79
3.5.2. RFCS project ‘SmartCoCo’ 83
3.5.3. CTBUH project ‘ISRC Composite Column’ 92
3.5.4. International literature review 97
4. Motivation and Objectives 114

5. Local Shear Transfer at the Steel-Concrete Interface – Development and Characterisation of a Novel Type of Flat Mechanical Shear Connectors 116
5.1. General considerations 118
5.2. Development of a concept 119
5.2.1. Analysis of variants for the feasible geometry 119
5.2.2. Defining critical aspects 119
5.2.3. Identification of a solution 121
5.2.4. Detailing the concept 124
5.3. Investigation on steel-concrete bond 126
5.3.1. Small-scale push-out tests 126
5.3.2. Numerical simulations 129
5.3.3. Summary and comparison to the literature data 130
5.4. Push-out test campaign 134
5.4.1. Specimen properties 134
5.4.2. Specimen instrumentation 139
5.4.3. Test conduction and boundary conditions 143
5.4.4. Test results 146
5.4.4.1. Measured material properties 146
5.4.4.2. Load-slip response 147
5.4.4.3. Recorded strains 149
5.4.4.4. Displacements of concrete block 154
5.4.5. Observed failure pattern 156
5.4.5.1. Reference specimens 0v2 157
5.4.5.2. Specimens Cv2 with longitudinal connector 157
5.4.5.3. Specimens Av2 with transversal connector 158
5.4.5.4. Specimens Bv2 with V-shaped connector 160
5.4.6. Discussion of the results 163
5.5. Numerical simulations 166
5.5.1. Geometry and mesh 167
5.5.2. Material laws 170
5.5.2.1. Structural steel 170
5.5.2.2. Reinforcement steel 171
5.5.2.3. Concrete 172
5.5.3. Steel-concrete bond model 176
5.5.3.1. In Abaqus/Standard simulations 177
5.5.3.2. In Abaqus/Explicit simulations 178
5.5.4. Assembly, interactions, constraints and boundary conditions 179
5.5.5. Results and comparison to the experimental data 180

5.5.5.1. Reference specimen 0v2 181
5.5.5.2. Specimen Cv2 with longitudinal connector 181
5.5.5.3. Specimen Av2 with transversal connector 182
5.5.5.4. Specimen Bv2 with V-shaped connector 185
5.6. Analytical model for the resistance of flat shear connectors 189
5.6.1. Fundamental assumptions 189
5.6.2. Evaluation of the steel-concrete bond influence – specimen 0v2 190
5.6.3. Resistance of the longitudinal connector – specimen Cv2 193
5.6.3.1. Verification of the equation for the shear connector bond strength ($P_{R,b}$) 196
5.6.4. Resistance of the transversal connector – specimen Av2 197
5.6.4.1. Verification of the resistance of the weld ($P_{R,w}$) 212
5.6.4.2. Verification of the resistance of the connector material ($P_{R,m}$) 212
5.6.4.3. Verification of the maximum compression condition for concrete ($P_{R,c}$) 213
5.6.4.4. Verification of the maximum shear condition for concrete ($P_{R,s1}$) 216
5.6.4.5. Minimum spacing condition 217
5.6.5. Resistance of the V-shaped connector – specimen Bv2 218
5.6.5.1. Verification of the resistance of the weld ($P_{R,w}$) 234
5.6.5.2. Verification of the resistance of connector material ($P_{R,m}$) 235
5.6.5.3. Concrete stress state condition – identification of the tensile stresses 236
5.6.5.4. Verification of the maximum tension condition for concrete 237
5.6.5.5. Verification of the maximum compression condition for concrete ($P_{R,c}$) 238
5.6.5.6. Verification of the maximum shear condition for concrete ($P_{R,s1}$) 240
5.6.5.7. Verification of the vertical shearing condition for concrete ($P_{R,s2}$) 242
5.6.6. Summary and limitations to the analytical model 244
5.7. Summary and conclusions 248
6. Global Shear Transfer and Effective Stiffness in Composite Members with Two Encased Steel Profiles 251
6.1. General considerations 252
6.2. Pre-design of test specimens 253
6.2.1. Provisions from EN 1994-1-1 254
6.2.2. Provisions from EN 1992-1-1 255
6.2.3. Elastic analysis of the cross-sectional resistance in bending 256
6.3. Beam/column three-point bending tests 261
6.3.1. Specimen properties 261
6.3.2. Applied shear connectors 266
6.3.3. Specimen instrumentation 268
6.3.4. Test conduction and boundary conditions 277

6.3.5. Test results 280
6.3.5.1. Measured material properties 280
6.3.5.2. Load-deformation responses 281
6.3.5.3. Strains in the specimens 286
6.3.5.4. Recorded slip of the steel profiles 295
6.3.6. Observed failure patterns 298
6.3.6.1. Specimen VT-1 with the small distance between steel profiles 300
6.3.6.2. Specimen VT-2 with the big distance between steel profiles 305
6.3.7. Discussion of the results 311
6.4. Numerical simulations 326
6.4.1. Geometry and mesh 326
6.4.2. Material laws 330
6.4.2.1. Structural steel 330
6.4.2.2. Reinforcement steel 331
6.4.2.3. Concrete 332
6.4.2.4. Cohesive elements – shear connection 336
6.4.3. Assembly, interactions, constraints and boundary conditions 340
6.4.4. Results and comparison to the experimental data 343
6.4.4.1. Specimen VT-1 with the small distance between steel profiles 344
6.4.4.2. Specimen VT-2 with the big distance between steel profiles 351
6.5. An analytical model for the member stiffness 361
6.5.1. Fundamental assumptions 362
6.5.2. Identification of the reference load for the model verification 363
6.5.3. Vierendeel truss as a Timoshenko beam analogy model 369
6.5.3.1. Model for the global beam deflection 369
6.5.3.2. Derivation of the bending stiffness 370
6.5.3.3. Derivation of the shear stiffness 372
6.5.3.4. Discretisation of the member into Vierendeel truss elements 374
6.5.3.5. Calibration of the model 376
6.5.4. Other considered beam models 383
6.5.4.1. Euler-Bernoulli beam model 383
6.5.4.2. Timoshenko beam model 384
6.5.4.3. Morsch truss as a Timoshenko beam analogy model 385
6.5.5. Comparison of the investigated models with experimental and numerical data 387
6.5.6. Derivation of an equation for new effective bending stiffness 393
6.5.7. Analysis of the Euler critical buckling load 394
6.6. Summary and conclusions 397

7. Thesis Summary and Overall Conclusions 400
8. Outlook 407
Acknowledgements 410
References 411
Annex A – Preliminary numerical simulations and parametric study on the development of new mechanical shear connectors A.1
Annex B – Details on steel-concrete bond investigation B.1
Annex C – Details on the production, measurement equipment and opening of the push-out test specimens for flat mechanical shear connectors C.1
Annex D – Solver setup, energy balance and concrete material law in FE simulations of push-out tests for flat mechanical shear connectors D.1
Annex E – Details on the production and measurement equipment of big scale beam/column test specimens E.1
Annex F – Solver setup, energy balance and concrete material law in FE simulations of big scale beam/column tests F.1
Annex G – Calculations made in the evaluation of analytical models for effective stiffnesses of a column member with multiple encased steel profiles G.1

List of Figures

Fig. 1.1. Comparison of steel-concrete composite columns in design standards and modern high-rise buildings.....1

Fig. 2.1. Structure of the Thesis. 3

Fig. 3.1. Composite action on the example of simple supported two material beam – a) non-composite case and b) composite case with full interaction. (Source: Nethercot [127]).....5
Fig. 3.2. Definition of the shear flow – a) development model, b) connection model and c) general connection force-slip diagram. (Source: Leskelä [110]). 6
Fig. 3.3. Classification of the shear connection behaviour. (Adapted from: Leskelä [110]).....6
Fig. 3.4. A composite cross-section of two material parts with full shear connection and subjected to pure bending. (Source: Leskelä [110]).....7
Fig. 3.5. Relative slip in a beam composed from two materials and subjected to bending. (Source: Leskelä [110]). 9
Fig. 3.6. Plane problem of a stress state in a unit rectangular block of elastic material. (Source: Timoshenko [184]).....10
Fig. 3.7. A composite beam with flexible shear connection – a) strains distribution (Source: Leskelä [110]) and b) internal forces equilibrium (Source: Johnson [89]).....11
Fig. 3.8. Typical cross-sections of composite columns – a) fully encased steel profiles, b) partially encased steel profiles, c) filled rectangular steel tubes and d) filled circular steel tubes. (Source: Roik/Bergmann [159]).....13
Fig. 3.9. Single-symmetric cross-sections of composite columns. (Source: Roik/Bergmann [158]).....14
Fig. 3.10. Comparison of elasto-plastic and plastic block stress distributions in composite column cross-section. (Source: Leskela [110]).....14
Fig. 3.11. Load introduction to steel-concrete composite columns. (Source: EN 1994-1-1 [58]). 15
Fig. 3.12. Types of structural systems of columns – a) solid and b) lattice. (Adapted from Petersen [144]).....16
Fig. 3.13. Shear deformation in the Timoshenko beam. (Source: Timoshenko [183]).....17
Fig. 3.14. Typical examples of parallel-chord truss systems. (Source: Thrower [182]). 18
Fig. 3.15. Global and local equilibrium states in a truss system. 18
Fig. 3.16. Distribution of forces into truss elements acting on an equivalent beam – analogy to the Mörsch truss.....19
Fig. 3.17. Vierendeel truss bridge designed by Arthur Vierendeel in 1898, Brussels. (Source: Odenbreit [131]). 19
Fig. 3.18. Example of a Vierendeel truss system with denoted internal forces. (Source: Sakai [166]). 19
Fig. 3.19. Global distribution of forces and identification of the theoretical hinges in Vierendeel truss elements. (Source: Wickersheimer [201]).....20
Fig. 3.20. Internal forces distribution in a Vierendeel truss. (Source: Petersen [145]). 20
Fig. 3.21. Shear deformation of Vierendeel trusses (extreme case).....21
Fig. 3.22. Force transfer mechanisms contributing to steel-concrete bond. (Adapted from Goralski [66]).....23
Fig. 3.23. Measurement of roughness on a steel surface – a) after milling (B2 class) and b) polished (B4 class). (Source: Ivkovic [83]).....23
Fig. 3.24. Shear connection means in composite structures. (Source: Goralski [66]).....24
Fig. 3.25. General load-slip behaviour of steel-concrete bond. 25
Fig. 3.26. Two approaching fractal surfaces – microscopic interlocking mechanism. (Source: Hanaor [68]). 26
Fig. 3.27. Distribution of the steel-concrete bond strength over the interface length – a) fully embedded HEB200 profile (Source: Wium [202]), b) fully embedded W10x(22/45/77) profile (Source: Roeder [157]), c) concrete filled stainless steel square tube 120x4 (Source: Tao [181]) and d) strains in steel plate of steel-concrete-steel specimen at three points over the contact length (G6 top – G8 bottom) (Source: Berthet [14]). 27
Fig. 3.28. Reinforcement bar-concrete bond force transfer mechanisms. (Source: ACI 408R-03 [3]).....28
Fig. 3.29. Experimental bond stress versus slip relations of Ø16 and Ø20 reinforcement bars obtained from pull-out tests. (Source: Bigaj [15]).....29
Fig. 3.30. Bond and splitting in reinforced concrete with deformed bars – a) typical stress peaks in the elastic phase, b) development of slip and bearing action of the bar and c) resultant stresses. (Source: fib bulletin 10 [60]). 29
Fig. 3.31. Bearing action in concrete corbels due to reinforcement bar-concrete bond. (Source: Choi [30]).....29
Fig. 3.32. Development of compressive and tensile principal stresses in concrete due to reinforcement-concrete bond. (Source: ACI 408R-03 [3]).....30
Fig. 3.33. Splitting failure of reinforcement-concrete bond. (Source: Lundgren [114] and Carins [27]). 30
Fig. 3.34. Pull-out failure of reinforcement-concrete bond. (Source: Bigaj [15] and fib bulletin 10 [60]).....30
Fig. 3.35. Local bond stress-slip behaviour of reinforcement-concrete bond. (Source: fib bulletin 10 [60]). 31
Fig. 3.36. Behaviour of an unzipping shear connection. (Source: Leskelä [110]). 32
Fig. 3.37. Geometry of a shear stud – a) scheme (Source: Johnson [89]), b) different sizes of headed shear studs and c) stud welding detail (Source: Houston [75]).....33
Fig. 3.38. Push-out test of shear studs – a) specimen and b) load-slip curves. (Adapted from Ollgaard [134]). 34
Fig. 3.39. Typical load-slip curves for shear studs with 19-25mm shank. (Source: Hanswille [71]). 34

Fig. 3.40. Load-slip responses of headed stud connectors embedded in concrete slab – a) according to Lungershausen [115] for 4 studs Ø 22 mm and b) tests made by Lam et al [163] for 2 studs Ø 19 mm. 35
Fig. 3.41. Load-bearing mechanism of a shear stud in solid concrete slab. (Source: Lungershausen [115]). 35
Fig. 3.42. Additional frictional forces in composite columns chambers. (Source: Hanswille [71]). 36
Fig. 3.43. Bearing plate shear connectors in the concrete filled hollow sections. (Source: Hanswille [71]). 37
Fig. 3.44. Tests of gusset plate shear connector in the concrete filled hollow steel section – a) specimen and b) load-displacement curves. (Source: Roik [165]). 37
Fig. 3.45. Tests of internal ring shear connector in the concrete filled hollow steel section – a) specimen and b) load-displacement curves. (Source: Tao [181]). 38
Fig. 3.46. T-shaped connectors – a) view (Source: Valente [190]) and b) column application (Source: Roik [161]). 38
Fig. 3.47. Load-slip curve for T-shaped shear connector. (Source: Roik [161]). 39
Fig. 3.48. Application of channel shear connectors in bridge and building structures. (Source: Shariati [173]). 39
Fig. 3.49. Test of channel connector – a) test layout, b) test results (N-plain concrete, RC-reinforced concrete, FRC-fibre reinforced concrete, ECC-engineered mix) and c) deformed connector. (Source: Maleki [117, 118]). 40
Fig. 3.50. Helical shear connector. (Source: IS:11384-1985 [78]). 40
Fig. 3.51. Block shear connector for composite beams. (Source: BS 5400-5:1979 [26]). 40
Fig. 3.52. Load-slip behaviour of block and burl shear connectors in column application. (Source: Roik [162]). 41
Fig. 3.53. Bar passing connector –specimen layout and load-slip curve. (Adapted from Roik [161]). 42
Fig. 3.54. Push-out specimen layout with the stiffener type connector – a) strong axis orientation and b) weak axis orientation. (Source: SmartCoCo [175]). 43
Fig. 3.55. Load-slip curves of the stiffener connector – a) strong axis orientation (B) and b) weak axis orientation (D). (Source: SmartCoCo [175]). 43
Fig. 3.56. Examples of perfobond type of shear connectors. (Source: Neto [128]). 44
Fig. 3.57. Behaviour of concrete dowel in a perfobond shear connection. (Source: Braun [23]). 44
Fig. 3.58. Push-out test of the perfobond connector – a) specimen and b) load-slip curves. (Source: Neto [128]). 45
Fig. 3.59. Push-out test of the perfobond connector with steel sheeting – a) specimen and b) load-slip curves. (Source: Jeong [84]). 45
Fig. 3.60. Test of a composite pylon with perfobond connectors – a) specimen and b) load-displacement curves. (Source: Wang [198]). 46
Fig. 3.61. Composite dowel shear connectors – a) different types (Source: Alves [7]) and b) crestbond detail (Source: Veríssimo [193]). 47
Fig. 3.62. Crestbond connector – a) push-out specimen and b) load-slip behaviour. (Source: Veríssimo [193]). 47
Fig. 3.63. Failure modes of the composite dowels shear connectors. (Source: Valente [189]). 47
Fig. 3.64. Tail shear connectors. (Source: Kovács [104]). 48
Fig. 3.65. Beam tests of tail shear connectors. (Source: Kovács [104]). 48
Fig. 3.66. Typical forms of steel sheeting in composite slabs. (Source: Seres [171]). 49
Fig. 3.67. Motivation for the utilisation of the grouted shear connection. (Source: Schaumann [167]). 50
Fig. 3.68. Tests of the submerged grouted shear connection – a) specimen and b) test results. (Source: Schaumann [167]). 50
Fig. 3.69. Dry tests of the grouted shear connection – a) specimen and b) test results. (Source: Pan [138]). 50
Fig. 3.70. Grouted connection between steel girder and concrete slab. (Source: Papastergiou [139]). 51
Fig. 3.71. Grouted connection for steel girder – a) specimen and b) test results. (Source: Papastergiou [139]). 51
Fig. 3.72. Small-scale pin shear connectors and their production process. (Source: Classen [34]). 52
Fig. 3.73. Push-out tests of pin shear connectors – a) specimen and b) test results. (Source: Wolters [203]). 52
Fig. 3.74. Slim floor system with the reinforcement bars used as the shear connectors. (Source: Frangi [63]). 53
Fig. 3.75. Beam test results of slim installation floor system with the reinforcement bars used as the shear connectors. (Source: Frangi [64]). 53
Fig. 3.76. Push-out tests of epoxy shear connection – a) tested specimen and b) test results. (Source: Meaud [121]). 54
Fig. 3.77. Beam tests with epoxy shear connection – a) specimen and b) test results. (Source: Bouazaoui [21]). 54
Fig. 3.78. Shallow cellular floor beam – a) detail and b) construction application. (Source: Huo [76]). 55
Fig. 3.79. Load-slip curves of composite dowels obtained from push-out tests. (Source: Braun [24]). 55
Fig. 3.80. Demountable shear connectors – a) non-reusable expansion anchors (Source: Kwon [107]) and b) reusable bolt cylinder system (Source: Kozma [105]). 56
Fig. 3.81. Non-reusable and demountable shear connectors – a) AJAX bolt, b) threaded shear stud and c) Lindapter bolts. (Source: Versani [191]). 56
Fig. 3.82. Behaviour of AJAX bolts – a) load-slip curves after cycling load (Source: Mirza [122]), b) shear-tension interaction diagram (Source: Versani [191]) and c) load-slip curve in comparison to headed studs (Source: Uy [188]). 57
Fig. 3.83. Demountable shear connector system from Hilti. (Source: Cândido-Martins [28]). 57
Fig. 3.84. Load-slip behaviour of the reusable and demountable shear connectors – a) cylinder system and b) coupler system. (Source: Kozma [105]). 57
Fig. 3.85. Load-moment (N-M) interaction curves of composite column with fully encased I-section and considering different analysis approaches. (Source: Bridge [25]). 58

Fig. 3.86. Comparison of the EN 1994-1-1 and JGJ 138 for the fully encased composite column section –M-N interaction curves. (Source: AVEC BNT [11]).....63
Fig. 3.87. Comparison of the EN 1994-1-1 and JGJ 138 for the fully encased composite column section – buckling curves. (Source: AVEC BNT [11]).....63
Fig. 3.88. Typical cross-sections of composite columns covered by EN 1994-1-1. (Source: EN 1994-1-1 [58]). 64
Fig. 3.89. Interaction curve for the combined compression and uniaxial bending. (Source: EN 1994-1-1 [58]).....66
Fig. 3.90. Simplified N-M interaction curve and corresponding stress distribution. (Source: EN 1994-1-1 [58]). 68
Fig. 3.91. Interaction diagram for combined compression and bi-axial bending. (Source: Hanswille [71]).....69
Fig. 3.92. Load introduction mechanism in concrete encased columns. (Source: Hanswille [71]). 71
Fig. 3.93. Force distribution in shear connection for axial load and bending case – a) elastic model and b) plastic model. (Source: Hanswille [71]).....71
Fig. 3.94. Load introduction mechanism in concrete encased columns. (Source: Hanswille [71]). 72
Fig. 3.95. Design shear strength of steel-concrete bond according to EN 1994-1-1. (Source: EN 1994-1-1 [58]).....73
Fig. 3.96. Compression members with confining reinforcement. (Source: fib MC2010 [62]). 73
Fig. 3.97. The load path method and discretisation of stress trajectories into truss elements of strut and tie method. (Source: Schlaich [168]). 75
Fig. 3.98. Superposition of the strut and tie models. (Source: Schlaich [168]).....76
Fig. 3.99. Geometry of compression struts fields – a) 'fan', b) 'bottle' and c) 'prism'. (Source: Schlaich [168]). 76
Fig. 3.100. Fibre method and possible strain distributions in the reinforced concrete. (Source: EN 1992-1-1 [53]).....77
Fig. 3.101. Simplified model of the concrete for the rectangular stress distribution. (Source: EN 1992-1-1 [53]). 77
Fig. 3.102. Comparison of the N-M interaction diagrams based on different methods – a) direct comparison and b) comparison with plastic curves reduced by the factor α_M. (Source: Anwaar [9]). 78
Fig. 3.103. High-rise buildings in the scope of the last century. (Source: Al-Kodmany [6]). 79
Fig. 3.104. Construction of the IFC Tower Two, Hong-Kong – a) an elevation of mega-columns and b) plinth detail of a mega-column. (Source: Wong [204]). 79
Fig. 3.105. Construction of the East Pacific Center, Shenzhen – a) building elevation and b) detail of a column. (Source: Tran [185]).....80
Fig. 3.106. Construction of the World Financial Center in Shanghai, China – a) building elevation and b) section of a column. (Source: Tran [185]).....80
Fig. 3.107. Construction of the Shanghai Tower, China – a) building elevation and b) detail of a column. (Source: Tran [185]).....81
Fig. 3.108. Construction of the Ping Ahn Finance Center in Shenzhen, China – a) render of a building, b) building elevation under construction and c) detail of building core and heavy columns. (Source: Odenbreit [132]). 81
Fig. 3.109. Cross-section of heavy columns with multiple encased steel profiles – a) IFC Tower in Hong-Kong and b) Zlota 44 in Warsaw, Poland. (Source: Arup Hong-Kong and Besix).....81
Fig. 3.110. Composite shear wall system – a) with steel plate, b) with double steel plate and c) construction detail. (Source: Tran [185]). 82
Fig. 3.111. Composite shear wall under axial load on eccentricity according to JGJ 138. (Source: JGJ 138 [85]). 83
Fig. 3.112. Push-out test campaign within the SmartCoCo research project. (Source: SmartCoCo [175]). 84
Fig. 3.113. Test layout and cross-section of the shear wall bending tests conducted at the University of Rennes. (Source: SmartCoCo [175]). 85
Fig. 3.114. Load-deflection curves of the shear wall bending tests conducted at the University of Rennes. (Source: SmartCoCo [175]). 85
Fig. 3.115. Test layout of the shear wall tests conducted at the University of Liège. (Source: SmartCoCo [175]). 86
Fig. 3.116. Load-displacement curves from the shear wall tests conducted at the University of Liège. (Source: SmartCoCo [175]).....86
Fig. 3.117. Histograms of factor "R" – a) simplified design and b) proposed model. (Source: SmartCoCo [175]). 87
Fig. 3.118. Typical sections of composite members reinforced by several steel profiles considered in the generic design approach from project SmartCoCo – a) column and b) wall. (Source: SmartCoCo [175]).....88
Fig. 3.119. Decomposition scheme of composite into reinforced concrete section. (Source: SmartCoCo [175]). 89
Fig. 3.120. Shear transfer system according to SmartCoCo. (Source: SmartCoCo [175]). 89
Fig. 3.121. Internal Mörsch truss system according to SmartCoCo. (Source: SmartCoCo [175]).....90
Fig. 3.122. Truss model for the local shear transfer according to SmartCoCo. (Source: SmartCoCo [175]). 91
Fig. 3.123. Composite column with four embedded steel profiles according to SmartCoCo model – a) distribution of shear forces in a composite column section and b) N-M interaction curve. (Source: SmartCoCo [175]).....91
Fig. 3.124. Considered section of a composite column with four encased steel profiles within the project ISRC. (Source: CTBUH [82]). 92
Fig. 3.125. Test layouts for the composite columns with four encased steel profiles of the project ISRC – a) static tests and b) dynamic tests. (Source: CTBUH [82]).....92
Fig. 3.126. Geometry of the specimen for the static tests of the project ISRC. (Source: CTBUH [82]). 93
Fig. 3.127. Static test of the project ISRC. (Source: CTBUH [82]). 93
Fig. 3.128. Load-vertical displacement curves for the concentric tests of the project ISRC. (Source: CTBUH [82]).....94

Fig. 3.129. Load-vertical displacement curves for the eccentric tests of the project ISRC. (Source: CTBUH [82]). 94
Fig. 3.130. Horizontal deformation of specimens in the static tests of the project ISRC at different load steps (0.2, 0.4, 0.6, 0.8, 1.0 of P_u and failure) – a) concentric, b) eccentric 10% and c) eccentric 15%. (Source: CTBUH [82]). 94
Fig. 3.131. Comparison of the N-M interaction curves to the test and simulation results obtained from the static tests of the project ISRC. (Source: CTBUH [82]). 95
Fig. 3.132. Comparison of the analytical N-M interaction curves based on the design codes to the test results from the project ISRC. (Source: CTBUH [82]). 96
Fig. 3.133. Transformation principle of the composite cross-section into equivalent simplified composite cross-section. (Source: CTBUH [82]). 96
Fig. 3.134. Geometry of the shear walls analysed by Dan et al. (Source: Dan [35]). 97
Fig. 3.135. Cracking pattern of the tested shear walls by Dan et al. at different load stages. (Source: Dan [35]). 98
Fig. 3.136. Lateral load-total drift curves for the tested shear walls by Dan et al. – a) experimental curves and b) numerical curves. (Source: Dan [36]). 99
Fig. 3.137. Relative experimental stiffness degradation of the shear walls tested by Dan et al. – a) determination of the elastic limit of a shear wall response and b) relative stiffness-drift curves(Source: Dan [36]). 99
Fig. 3.138. Schematic definition of the analysed shear wall-frame structure by Liao et al. (Source: Liao [111]). 100
Fig. 3.139. Numerical model of the shear wall developed by Liao et al. (Source: Liao [111]). 100
Fig. 3.140. Cracking pattern of the shear wall with composite boundary columns – a) test and b) simulation. (Source: Liao [111]). 100
Fig. 3.141. Lateral load-drift curves for the shear walls analysed by Liao et al. (Source: Liao [111]). 101
Fig. 3.142. Distribution of bending moment and shear forces between the boundary steel reinforced columns and reinforced concrete wall panel in the shear walls tested by Liao et al. (Source: Liao [111]). 101
Fig. 3.143. Geometry of the shear wall specimens analysed by Qian et al. (Source: Qian [151]). 102
Fig. 3.144. Geometry of the shear wall specimens analysed by Ji et al. (Source: Ji [87]). 102
Fig. 3.145. Geometry of the shear wall specimens analysed by Ji et al. (Source: Qian [86]). 103
Fig. 3.146. Deformations of tested specimens shown in Fig. 3.145. (Source: Ji [86]). 103
Fig. 3.147. Cracking pattern of specimens shown in Fig. 3.143. (Source: Qian [151]). 104
Fig. 3.148. Cracking pattern of specimens shown in Fig. 3.144. (Source: Ji [87]). 104
Fig. 3.149. Lateral load-displacement curves for specimens shown in Fig. 3.143. (Source: Qian [151]). 105
Fig. 3.150. Test results for specimens shown in Fig. 3.144 – a) lateral load-displacement curves and b) strain distribution over the wall section in specimen SRCW3. (Source: Ji [87]). 105
Fig. 3.151. Test results for specimens shown in Fig. 3.145 – a) lateral load-displacement curves and b) stiffness degradation at different levels of deformation. (Source: Ji [86]). 105
Fig. 3.152. Cross-section of the buckling-restraining brace system with isolated cores. (Source: Zhu [214]). 106
Fig. 3.153. Model for the analysis of buckling-restraining brace system with isolated cores. (Source: Zhu [214]). 106
Fig. 3.154. Geometry of the test specimens with three steel cores tested by Chanou. (Source: Chanou [29]). 107
Fig. 3.155. Shear connection detail in the specimens tested by Chanou. (Source: Chanou [29]). 108
Fig. 3.156. Test layout of tests performed by Chanou. (Source: Chanou [29]). 108
Fig. 3.157. Push-out test of the perfobond connector in concrete filled tubes. (Source: Chanou [29]). 109
Fig. 3.158. Push-out test of the shear rib connector in concrete filled tubes with one core. (Source: Chanou [29]). 109
Fig. 3.159. Push-out test of the shear rib connector in concrete filled tubes with three cores. (Source: Chanou [29]). 110
Fig. 3.160. Load-lateral displacement curves of the tested concrete filled tubes with three steel cores. (Source: Chanou [29]). 110
Fig. 3.161. Strain distribution at the end of the concrete filled steel tube specimen with three internal steel cores and without mechanical shear connectors. (Source: Chanou [29]). 111
Fig. 3.162. Change of the flexural stiffness of concrete filled steel tube column specimens with three internal steel cores. (Source: Chanou [29]). 111
Fig. 3.163. Geometrical variants used for the parametric studies performed by Chanou on concrete filled composite columns with multiple internal steel cores. (Source: Chanou [29]). 112
Fig. 3.164. Modification of the plastic bending moment resistance due to the corresponding axial load. (Source: Chanou [29]). 112
Fig. 3.165. Reduction factor k_B for the effective bending stiffness used for the second-order analysis according to Chanou. (Source: Chanou [29]). 113
Fig. 3.166. Distribution of the reduction factor k_B proposed by Chanou in the function of eccentricity and boundary bending moment ratio. (Source: Chanou [29]). 113

Fig. 4.1. Aspects of the shear transfer in heavy steel-concrete composite columns with multiple encased steel profiles considered for the improvement in the scope of the dissertation. 115

Fig. 5.1. Construction detail of heavy steel-concrete composite columns – a) applied stud shear connectors and b) reinforcement detail. (Source: R. Wong [206].) 117
Fig. 5.2. Taken development and characterisation process of a new flat mechanical shear connectors. 118

Fig. 5.3. Analysis of the geometrical parameters for the introduced embossments on the flanges of a steel profile – a) concept of introduced embossments and b) considered geometrical parameters. 119
Fig. 5.4. Ishikawa diagram for the development process of new flat mechanical shear connectors. 120
Fig. 5.5. Layout for the preliminary FE simulations with an example of transversally placed embossments – a) scheme and b) FE model. 121
Fig. 5.6. A high concentration of shear stresses at notches in negative embossment variants. 122
Fig. 5.7. Numerically obtained load-slip curves of flange test models with the highest judgement rate. 124
Fig. 5.8. Radar diagrams of three selected variants of embossments considered for the application – a) for model FTp1v1a, b) for model FTp2 and c) for model FTp3. 124
Fig. 5.9. Considered variants of materials for the fabrication of the flat shear connectors – a) weld stripe (source: thefabricator.com [137]), b) plain steel bar and c) reinforcement bar. 125
Fig. 5.10. Variants of the novel flat shear connectors selected for the characterisation process. 125
Fig. 5.11. Geometry of the small-scale push-out test specimens for the investigation on bond strength. 127
Fig. 5.12. Load-slip curves obtained from the small-scale push-out tests – a) PS series, b) G series, c) PTFE series and d) comparison diagram. 128
Fig. 5.13. Load-slip curves form the numerical simulations of small-scale cube push-out tests – a) specimen PS, b) specimen G, c) specimen PTFE and d) comparison of numerical responses. 130
Fig. 5.14. Analysed database of the steel-concrete bond strength – a) scatter diagram and b) Gaussian distribution. 132
Fig. 5.15. Influence of surface treatment on bond strength. 133
Fig. 5.16. Overview of the column push-out test series – a) reference tests 0v2, b) transversal variant conn. Av2, c) angled, V-shaped variant conn. Bv2 and d) longitudinal variant conn. Cv2. 135
Fig. 5.17. Geometry of the CoPOT specimens. 136
Fig. 5.18. Technical drawing of reinforcement arrangement in the CoPOT specimens. 137
Fig. 5.19. Details of steel parts in the CoPOT specimens – a) reinforcement cage and b) steel profiles. 137
Fig. 5.20. Geometry detail of applied flat shear connectors in the CoPOT specimens – a) variant Av2, b) variant Bv2 and c) variant Cv2. 138
Fig. 5.21. Welded flat shear connectors to the steel profiles of CoPOT specimens – a) overview on the applied connectors and b) weld detail. 139
Fig. 5.22. Arrangement of the displacement transducers (DT) in the CoPOT tests – a) scheme and b) view in the laboratory. 139
Fig. 5.23. Details of glued strain gauges to steel parts in CoPOT specimens – a) on steel profile and b) on reinforcement cage. 142
Fig. 5.24. Test setup at the University of Luxembourg for the CoPOT – a) scheme and b) a view in the laboratory. 143
Fig. 5.25. Test setup at TU Kaiserslautern for the CoPOT – a) scheme and b) a view in the laboratory. 144
Fig. 5.26. Test procedure used for the column push-out tests. 145
Fig. 5.27. Assumed simplified load-spread due to the implemented recess in column push-out tests, ...145
Fig. 5.28. Experimental load-slip curves for the column push-out tests – a) specimen 0v2, b) specimen Av2, c) specimen Bv2 and d) specimen Cv2 148
Fig. 5.29. Strains in steel profiles in the series without mechanical shear connectors of CoPOT – a) specimen 0v2-1 and b) specimen 0v2-2. 149
Fig. 5.30. Strains in steel profiles in the series with transversal shear connectors of CoPOT – a) specimen Av2-1, b) specimen Av2-2 and c) specimen Av2-3. 150
Fig. 5.31. Strains in stirrups in the series with transversal shear connectors of CoPOT – a) specimen Av2-1, b) specimen Av2-2 and c) specimen Av2-3. 150
Fig. 5.32. Strains in steel profiles in the series with V-shaped shear connectors of CoPOT – a) specimen Bv2-1, b) specimen Bv2-2 and c) specimen Bv2-3. 151
Fig. 5.33. Strains in stirrups in the series with V-shaped shear connectors of CoPOT – a) specimen Bv2-1, b) specimen Bv2-2 and c) specimen Bv2-3. 151
Fig. 5.34. Strains in U-bars in the series with V-shaped shear connectors of CoPOT – a) specimen Bv2-1, b) specimen Bv2-2 and c) specimen Bv2-3. 151
Fig. 5.35. Strains in steel profiles in the series with longitudinal shear connectors of CoPOT – a) specimen Cv2-1, b) specimen Cv2-2 and c) specimen Cv2-3. 152
Fig. 5.36. Strains in stirrups in the series with longitudinal shear connectors of CoPOT – a) specimen Cv2-1, b) specimen Cv2-2 and c) specimen Cv2-3. 152
Fig. 5.37. Distribution of strains in the column push-out test specimen Av2. 154
Fig. 5.38. Distribution of strains in the column push-out test specimen Bv2. 154
Fig. 5.39. Distribution of strains in the column push-out test specimen Cv2. 154
Fig. 5.40. Lateral displacement of the concrete block base in series with transversal shear connectors of CoPOT – a) specimen Av2-1, b) specimen Av2-2 and c) specimen Av2-3. 155
Fig. 5.41. Lateral displacement of the concrete block base in series with longitudinal shear connectors of CoPOT – a) specimen Cv2-1, b) specimen Cv2-2 and c) specimen Cv2-3. 155
Fig. 5.42. Opening of the column push-out test specimens – a) cutting scheme and b) cutting process detail. 156

Fig. 5.43. Slide of steel profile in the test series 0v2 of CoPOT without mechanical shear connectors. 157
Fig. 5.44. Failure of specimen Cv2 of CoPOT with the longitudinal shear connectors – a) bottom view, b) scheme and c) detail of vertical crack on concrete surface. 157
Fig. 5.45. Executed and opened specimen Av2 of CoPOT with the transversal shear connector – a) central part with steel profile, b) concrete encasement and c) separated concrete cone. 158
Fig. 5.46. Cracks at the surface of the specimen Av2 of CoPOT with the transversal shear connector. 159
Fig. 5.47. Failure planes of the specimen Av2 of CoPOT with the transversal shear connector. 160
Fig. 5.48. Executed and opened specimen Bv2 of CoPOT with the V-shaped shear connector – a) central part with steel profile, b) concrete encasement and c) cracks at the surface of the specimen. 161
Fig. 5.49. Load decomposition scheme in the specimen Bv2 of CoPOT with the V-shaped shear connector. 162
Fig. 5.50. Resulting failure planes in the specimen Bv2 of CoPOT with the V-shaped shear connector. 162
Fig. 5.51. Failure detail in the specimen Bv2 of CoPOT with the V-shaped shear connector – a) planes next to the connector and b) planes in the concrete (given view according to cut (c) in Fig. 5.42). 163
Fig. 5.52. Comparison of the load-slip responses from column push-out test. 164
Fig. 5.53. Comparison of the initial load-slip responses from column push-out test. 164
Fig. 5.54. Distribution of stresses over the embedment length in the reference specimens 0v2 of CoPOT. 165
Fig. 5.55. Sequence of the performed numerical simulations for the flat mechanical shear connectors. 166
Fig. 5.56. Numerical model of the reference specimen 0v2 of CoPOT. 168
Fig. 5.57. Numerical model of CoPOT specimen Av2 with the transversal shear connector – a) steel profile with shear connector and b) embedment detail. 169
Fig. 5.58. Numerical model of CoPOT specimen Bv2 with the V-shaped shear connector – a) steel profile with shear connector and b) embedment detail. 169
Fig. 5.59. Numerical model of CoPOT specimen Cv2 with the longitudinal shear connector – a) steel profile with shear connector and b) embedment detail. 170
Fig. 5.60. Material law for the structural steel used in numerical simulations of column push-out tests. 171
Fig. 5.61. Material law for the reinforcement steel used in numerical simulations of column push-out tests. 171
Fig. 5.62. Stress-strain behaviour of the numerical concrete material law for the specimen 0v2 of CoPOT. 174
Fig. 5.63. Stress-strain behaviour of the numerical concrete material law for the specimen Av2 of CoPOT. 174
Fig. 5.64. Stress-strain behaviour of the numerical concrete material law for the specimen Bv2 of CoPOT. 175
Fig. 5.65. Stress-strain behaviour of the numerical concrete material law for the specimen Cv2 of CoPOT. 175
Fig. 5.66. Traction separation laws for bond model in the standard simulations of column push-out tests – a) plain steel-concrete and b) connector-concrete. 177
Fig. 5.67. Traction separation laws for bond model in the explicit simulations of column push-out tests – a) plain steel-concrete and b) connector-concrete. 179
Fig. 5.68. Layout of the column push-out FE simulation of the series Av2. 180
Fig. 5.69. Numerical load-slip curve of the CoPOT specimen 0v2 and comparison to test results. 181
Fig. 5.70. Numerical load-slip curve of the CoPOT specimen Cv2 and comparison to test results. 181
Fig. 5.71. Sequence of concrete damage in the numerical simulation of CoPOT specimen Cv2 – a) the initial stage, b) stage at the peak load and c) stage at the descending branch. 182
Fig. 5.72. Numerical load-slip curve of the CoPOT specimen Av2 and comparison to test results. 182
Fig. 5.73. Sequence of concrete damage in the numerical simulation of CoPOT specimen Av2 – a) the initial stage, b) stage before the peak load, c) stage after the peak load and d) stage at the descending branch. 183
Fig. 5.74. Analysis of the developed failure planes in the numerical simulation of CoPOT specimen Av2. 184
Fig. 5.75. Minimum principal stresses in the concrete of CoPOT specimen Av2 – stress state close to but before the peak load. 185
Fig. 5.76. Numerical load-slip curve of the CoPOT specimen Bv2 and comparison to test results. 185
Fig. 5.77. Sequence of concrete damage in the numerical simulation of CoPOT specimen Bv2 – a) the initial stage, b) stage before the peak load, c) stage at the peak load and d) stage at the descending branch. 186
Fig. 5.78. Analysis of the developed failure planes in the numerical simulation of the specimen Bv2 187
Fig. 5.79. Minimum principal stresses in the concrete of CoPOT specimen Bv2 – stage when the first damage occured. 188
Fig. 5.80. Mechanical model of the specimen 0v2 of CoPOT and simplified reaction conditions. 190
Fig. 5.81. Assumed distribution of strains in the steel profiles of the CoPOT series 0v2. 191
Fig. 5.82. Internal bending mechanism due to the support eccentricity condition of CoPOT specimens. 192
Fig. 5.83. Strut-and-tie model of the specimen Cv2 of CoPOT. 194
Fig. 5.84. Reinforcement bar-concrete bond strength according to fib ModelCode 2010 [62]. 196
Fig. 5.85. Strut-and-tie model of the specimen Av2 of CoPOT. 198
Fig. 5.86. Stresses on the contact surface of the transversal variant of flat shear connector (consider with Fig. 5.85). 199
Fig. 5.87. Principal stress state in the transversal variant of flat shear connector, specimen Av2 of CoPOT. 201
Fig. 5.88. Failure condition for the Mohr-Coulomb material [130] – a) for cement paste, b) for concrete. 202
Fig. 5.89. Internal friction angle for different strengths of concrete [130]. 203
Fig. 5.90. Ratio between fcc and fc in the modified Mohr-Coulomb material according to Nielsen [130]. 203
Fig. 5.91. Maximum shear stress state in the transversal variant of flat shear connector, specimen Av2 of CoPOT. 204

Fig. 5.92. Failure criterion for the modified Mohr-Coulomb material according to Nielsen [130] – a) overall definition and b) sliding failure. 204
Fig. 5.93. Model for the verification of weld in the transversal variant of flat shear connector, specimen Av2 of CoPOT. 206
Fig. 5.94. Detail of flat shear connector, transversal variant, specimen Av2 – a) view from the left side, b) view from the right side. 206
Fig. 5.95. Mechanical model for the evaluation of the resistance of connector material in the transversal variant of flat shear connector. 210
Fig. 5.96. Local strut-and-tie model of the V-shaped variant of flat shear connector of specimen Bv2 of CoPOT. 219
Fig. 5.97. Redistribution of forces in the V-shaped flat shear connector of the specimen Bv2 of CoPOT –a) general case and b) redistributed case. 220
Fig. 5.98. Vector representation of the resultant normal force acting on the V-shaped connector. 221
Fig. 5.99. Detail of the forces acting on the contact area of V-shaped shear connector – a) resulting forces acting at the connector-concrete interface and b) definition of the contact surface length. 222
Fig. 5.100. Stresses acting on the contact surface of the V-shaped variant of flat shear connector (consider with Fig. 5.99a). 223
Fig. 5.101. Principal stress state in the V-shaped flat shear connector of the specimen Bv2 of CoPOT. 225
Fig. 5.102. Maximum shear stresses state in the V-shaped flat shear connector of the specimen Bv2 of CoPOT. 227
Fig. 5.103. Vertical shear stress state in the V-shaped flat shear connector of the specimen Bv2 of CoPOT and resulting vertical shearing area between the arms of connector. 229
Fig. 5.104. Stresses distribution in weld for the Von Mises yield criterion, according to EN 1993-1-8 [57]. 230
Fig. 5.105. Resistances of flat shear connectors – a) transversal variant connector and b) V-shaped variant connector. 245

Fig. 6.1. A case study for the improvement of shear transfer in the heavy composite column – a) common solution and b) innovative approach with separated embedded steel profiles. 251
Fig. 6.2. Generalised cross-sections and static system of the investigated beam/column specimens. 252
Fig. 6.3. General cross-section of the beam/column test specimens – a) smaller specimen and b) bigger specimen. 253
Fig. 6.4. Typical cross-section of fully encased composite column with notation according to EN 1994-1-1 [58]. 254
Fig. 6.5. Detailed geometry of the cross-section of beam/column test specimens – a) smaller specimen and b) bigger specimen. 257
Fig. 6.6. Elastic strain analysis of the cross-section of beam/column specimen for the cases when the rupture of steel elements occurs. 258
Fig. 6.7. Elastic analysis of strains and stresses in the cross-section of smaller specimen. 259
Fig. 6.8. Elastic analysis of strains and stresses in the cross-section of bigger specimen. 259
Fig. 6.9. Schematic overview of the beam/column test specimens. 262
Fig. 6.10. Arrangement of reinforcement in the cross-section of beam/column specimens – a) specimen VT-1 and b) specimen VT-2 263
Fig. 6.11. Technical drawing of the reinforcement arrangement in beam/column specimen VT-1. 264
Fig. 6.12. Technical drawing of the reinforcement arrangement in beam/column specimen VT-2. 265
Fig. 6.13. Applied shear connectors in beam/column test specimens – a) geometry and arrangement, b) fabrication detail and c) weld detail. 267
Fig. 6.14. Arrangement of the displacement transducers (DT) in beam/column tests – a) specimen VT-1 and b) specimen VT-2. 269
Fig. 6.15. Arrangement of the inclinometers (IM) in beam/column specimens – a) specimen VT-1 and b) specimen VT-2. 270
Fig. 6.16. Strain gauges (DMS) on the reinforcement bars of beam/column specimens – a) specimen VT-1 and b) specimen VT-2. 272
Fig. 6.17. Strain gauges (DMS) in the cross-section of beam/column specimens – a) on the reinforcement bars and b) on the steel profiles. 273
Fig. 6.18. Strain gauges (DMS) on the steel profiles of beam/column specimens – a) specimen VT-1 and b) specimen VT-2. 274
Fig. 6.19. Detail of displacement transducer measuring the deflection of beam/column specimen. 276
Fig. 6.20. Detail of inclinometer on the beam/column specimen. 276
Fig. 6.21. Detail of strain gauge glued to the reinforcement bar of beam/column specimen. 276
Fig. 6.22. Detail of strain gauges glued to the steel profile of beam/column specimen. 276
Fig. 6.23. Test setup for the beam/column test specimens on the example of specimen VT-2 – a) scheme and b) view in the laboratory. 277
Fig. 6.24. Test layout of beam/column test specimen with the deformed shape and boundary conditions. 278
Fig. 6.25. Scheme of the loading protocol used during the beam/column tests. 279
Fig. 6.26. Deflection shape of the beam/column specimen VT-1. 281
Fig. 6.27. Deflection shape of the beam/column specimen VT-2. 282
Fig. 6.28. Load-deflection curve for the beam/column specimen VT-1, sensor DT-5, mid-span. 282
Fig. 6.29. Load-deflection curve for the beam/column specimen VT-1, sensor DT-4 and DT-6, mid-zone. 283

Fig. 6.30. Load-deflection curve for the beam/column specimen VT-1, sensor DT-1 to DT-3 and DT-7 to DT-8, side-zones. 283
Fig. 6.31. Load-deflection curve for the beam/column specimen VT-2, sensor DT-5, mid-span. 283
Fig. 6.32. Load-deflection curve for the beam/column specimen VT-2, sensor DT-4 and DT-6, mid-zone. 284
Fig. 6.33. Load-deflection curve for the beam column specimen VT-2, sensor DT-1 to DT-3 and DT-7 to DT-8, side-zones. 284
Fig. 6.34. Lateral expansion in the beam/column specimen VT-1. 284
Fig. 6.35. Lateral expansion in the beam/column specimen VT-2. 284
Fig. 6.36. Load/Bending moment-rotation curves for the beam/column specimen VT-2. 285
Fig. 6.37. Distribution of the sectional rotations over the length of the beam/column specimen VT-2. 285
Fig. 6.38. Strains in the beam/column specimen VT-1, longitudinal direction at measurement section 1 (MS-1). 286
Fig. 6.39. Strains in the beam/column specimen VT-1, longitudinal direction at measurement section 2 (MS-2). 286
Fig. 6.40. Strains in the beam/column specimen VT-1, longitudinal direction at measurement section 3 (MS-3). 287
Fig. 6.41. Strains in the beam/column specimen VT-1, longitudinal direction at measurement section 4 (MS-4). 287
Fig. 6.42. Distribution of longitudinal strains in the measurement sections of beam/column specimen VT-1. 288
Fig. 6.43. Strains in the beam/column specimen VT-2, longitudinal direction at measurement section 1 (MS-1). 289
Fig. 6.44. Strains in the beam/column specimen VT-2, longitudinal direction at measurement section 2 (MS-2). 289
Fig. 6.45. Strains in the beam/column specimen VT-2, longitudinal direction at measurement section 3 (MS-3). 289
Fig. 6.46. Strains in the beam/column specimen VT-2, longitudinal direction at measurement section 4 (MS-4). 289
Fig. 6.47. Distribution of longitudinal strains in the measurement sections of beam/column specimen VT-2. 290
Fig. 6.48. Strains in the webs of steel profiles under 45° in the beam/column specimen VT-1 291
Fig. 6.49. Strains in the webs of steel profiles under 45° in the beam/column specimen VT-2 291
Fig. 6.50. Strains in the stirrups of beam/column specimen VT-1, measurement section 1 (MS-1). 292
Fig. 6.51. Strains in the stirrups of beam/column specimen VT-1, measurement section 2 (MS-2). 292
Fig. 6.52. Strains in the stirrups of beam/column specimen VT-1, measurement section 3 (MS-3). 292
Fig. 6.53. Strains in the stirrups of beam/column specimen VT-1, measurement section 4 (MS-4). 292
Fig. 6.54. Strains in the stirrups of beam/column specimen VT-2, measurement section 1 (MS-1). 292
Fig. 6.55. Strains in the stirrups of beam/column specimen VT-2, measurement section 2 (MS-2). 292
Fig. 6.56. Strains in the stirrups of beam/column specimen VT-2, measurement section 3 (MS-3). 293
Fig. 6.57. Strains in the stirrups of beam/column specimen VT-2, measurement section 4 (MS-4). 293
Fig. 6.58. Strains in the lateral arms of stirrups in the beam/column specimen VT-1. 294
Fig. 6.59. Distribution of strains in the lateral arms of stirrups in the beam/column specimen VT-1 – a) on the top and b) on the bottom. 294
Fig. 6.60. Strains in the lateral arms of stirrups in the beam/column specimen VT-2. 294
Fig. 6.61. Distribution of strains in the lateral arms of stirrups in the beam/column specimen VT-2 – a) on the top and b) on the bottom. 295
Fig. 6.62. Load-end slip curves in the beam/column specimen VT-1, upper beam. 296
Fig. 6.63. Load-end slip curves in the beam/column specimen VT-1, lower beam. 296
Fig. 6.64. Load-mid slip curves in the beam/column specimen VT-1, upper beam. 296
Fig. 6.65. Load-mid slip curves in the beam/column specimen VT-1, lower beam. 296
Fig. 6.66. Load-end slip curves in the beam/column specimen VT-2, upper beam. 297
Fig. 6.67. Load-end slip curves in the beam/column specimen VT-2, lower beam. 297
Fig. 6.68. Load-mid slip curves in the beam/column specimen VT-2, upper beam. 297
Fig. 6.69. Load-mid slip curves in the beam/column specimen VT-2, lower beam. 297
Fig. 6.70. Shear deformation scheme of the tested beam/column specimens – a) undeformed shape and b) deformed shape. 299
Fig. 6.71. Opening scheme of the beam/column specimens. 300
Fig. 6.72. Diagonal cracks in the beam/column specimen VT-1. 300
Fig. 6.73. Development of the concrete crush zone in compression of beam/column specimen VT-1. 301
Fig. 6.74. Concrete spalling in the compression zone of beam/column specimen VT-1. 301
Fig. 6.75. Vertical cracks in the tension zone before the failure of beam/column specimen VT-1. 301
Fig. 6.76. Vertical cracks in the tension zone after the failure of beam/column specimen VT-1. 301
Fig. 6.77. A view on the tested beam/column specimen VT-1, south wall, right side. 302
Fig. 6.78. A view on the tested beam/column specimen VT-1, south wall, left side. 302
Fig. 6.79. Detail of compression failure zone in the beam/column specimen VT-1, south wall. 302
Fig. 6.80. Detail of compression failure in the beam/column specimen VT-1, north wall. 302
Fig. 6.81. Detail of compression failure in the beam/column specimen VT-1, top view. 303
Fig. 6.82. Detail of compression failure in the beam/column specimen VT-1, deformed reinforcement. 303
Fig. 6.83. Opened beam/column specimen VT-1 – view on the revealed steel profiles. 303
Fig. 6.84. Opened beam/column specimen VT-1 – steel-concrete interface next to the upper steel profile. 304
Fig. 6.85. Opened beam/column specimen VT-1 – steel-concrete interface next to the lower steel profile. 304
Fig. 6.86. Opened beam/column specimen VT-1 – detail of the flat shear connector. 304

Fig. 6.87. Opened beam/column specimen VT-1 – concrete damage around the flat shear connector.....304
Fig. 6.88. Vertical cut through the top concrete encasement in the support zone of beam/column specimen VT-1.....305
Fig. 6.89. Diagonal cracks in the beam/column specimen VT-2.....306
Fig. 6.90. Development of the concrete crush zone in compression of beam/column specimen VT-2. 306
Fig. 6.91. Concrete spalling in the compression zone of beam/column specimen VT-2. 306
Fig. 6.92. Vertical tensile cracks in the tension zone at the failure of beam/column specimen VT-2. 307
Fig. 6.93. Vertical cracks in the tension zone after the failure of beam/column specimen VT-2. 307
Fig. 6.94. View on the tested beam/column specimen VT-2, south wall.....307
Fig. 6.95. Detail of the support zone of tested beam/column specimen VT-2.....307
Fig. 6.96. Detail of the central zone of tested beam/column specimen VT-2.....308
Fig. 6.97. Detail of the compression failure zone of tested beam/column specimen VT-2 – a) top view and b) buckled reinforcement.....308
Fig. 6.98. Opened beam/column specimen VT-2 – view on the revealed steel profiles. 308
Fig. 6.99. Steel profiles in opened beam/column specimen VT-2 – method with a straight bar.....309
Fig. 6.100. Steel profiles in opened beam/column specimen VT-2 – method with a line.....309
Fig. 6.101. Interface in the opened beam/column specimen VT-2 – a) upper steel profile and b) lower steel profile.....309
Fig. 6.102. Examination of the concrete damage around the shear connector in the central zone of beam/column specimen VT-2 – a) view on the revealed shear connector and b) view on the concrete next to the connector in the outward direction.....310
Fig. 6.103. Top concrete encasement in the support zone of beam/column specimen VT-2.....310
Fig. 6.104. Load-strain diagram for DMS-23 of beam/column specimen VT-1, MS-4 – a) initial record and b) modified record.....311
Fig. 6.105. Comparison of longitudinal strains between the experimental values and fibre method – a) specimen VT-1 and b) specimen VT-2. 312
Fig. 6.106. Analysis of the bending moment in the specimen for undeformed and deformed states. 314
Fig. 6.107. Variation of stiffnesses at the different phases of beam/column tests – a) specimen VT-1 and b) specimen VT-2.....316
Fig. 6.108. Analysis of the deflection shapes of beam/column specimen VT-1.....317
Fig. 6.109. Analysis of the deflection shapes of beam/column specimen VT-2.....317
Fig. 6.110. Shear deformation in the artificially modified numerical model of specimen VT-2. 318
Fig. 6.111. Shear forces in deformed beam/column specimen VT-1 in reference to the imposed load. 319
Fig. 6.112. Shear forces in deformed beam/column specimen VT-2 in reference to the imposed load. 319
Fig. 6.113. Relative shear-strains curves in the stirrup of beam/column specimen VT-1, MS-1.....321
Fig. 6.114. Relative shear-strains curves in the stirrup of beam/column specimen VT-1, MS-2.....321
Fig. 6.115. Relative shear-strains curves in the stirrup of beam/column specimen VT-1, MS-3.....321
Fig. 6.116. Relative shear-strains curves in the stirrup of beam/column specimen VT-1, MS-4.....321
Fig. 6.117. Relative shear-strains curves in the stirrup of beam/column specimen VT-2, MS-1.....321
Fig. 6.118. Relative shear-strains curves in the stirrup of beam/column specimen VT-2, MS-2.....321
Fig. 6.119. Relative shear-strains curves in the stirrup of beam/column specimen VT-2, MS-3.....322
Fig. 6.120. Relative shear-strains curves in the stirrup of beam/column specimen VT-2, MS-4.....322
Fig. 6.121. Shear forces taken by stirrups in ref. to the imposed load in the beam/column specimen VT-1. 322
Fig. 6.122. Shear forces taken by steel profiles in ref. to the imposed load in the beam/column specimen VT-1.....322
Fig. 6.123. Shear forces taken by stirrups in reference to the imposed load in the beam/column specimen VT-2.....322
Fig. 6.124. Shear forces taken by steel profiles in ref. to the imposed load in the beam/column specimen VT-2.....322
Fig. 6.125. Distribution of relative slip over the length of beam/column specimen VT-1.....324
Fig. 6.126. Distribution of relative slip over the length of beam/column specimen VT-2.....324
Fig. 6.127. Tensile forces-slip curves for the lower steel profile of beam/column specimen VT-1.....325
Fig. 6.128. Tensile forces-slip curves for the lower steel profile of beam/column specimen VT-2.....325
Fig. 6.129. Geometry of beam/column specimen VT-1 used in the numerical simulations. 327
Fig. 6.130. Geometry of beam/column specimen VT-2 used in the numerical simulations. 327
Fig. 6.131. Mesh in the steel and concrete parts used in the FE simulations of beam/column specimen VT-1.....329
Fig. 6.132. Material law for structural steel used in the numerical simulations of beam/column tests.....330
Fig. 6.133. Material laws for reinforcement steel used in the numerical simulations for beam/column tests.....331
Fig. 6.134. Stress-strain behaviour implemented for the concrete material law in the numerical simulation of beam/column specimen VT-1. 336
Fig. 6.135. Stress-strain behaviour implemented for the concrete material law in the numerical simulation of beam/column specimen VT-2. 336
Fig. 6.136. Traction-separation law for the cohesive elements in the specimen VT-1 – a) normal direction, b) shear direction 1 and c) shear direction 2.....339
Fig. 6.137. Traction-separation law for the cohesive elements in the specimen VT-2 – a) normal direction, b) shear direction 1 and c) shear direction 2.....339

Fig. 6.138. Perspective view on the assembly of the numerical model of beam/column specimen VT-2 – a) with highlighted steel profiles, b) with highlighted concrete and c) with highlighted reinforcement cage. 341
Fig. 6.139. Applied symmetry conditions in the numerical model of beam/column specimen VT-2. 342
Fig. 6.140. Boundary conditions used in the FE models of beam/column specimens. 343
Fig. 6.141. Numerical load-deflection curve of beam/column specimen VT-1 for the node at the mid-span. 345
Fig. 6.142. Damage sequence in the numerical simulation of beam/column specimen VT-1 – a) damage at the phase before the failure, b) damage at the peak point and c) damage at the last phase of simulation. 346
Fig. 6.143. Deformation of embedded steel profiles at the peak load from the numerical simulation of beam/column specimen VT-1 – a) logarithmic strains and b) von Mises stresses. 347
Fig. 6.144. Strains and stresses limited to yielding values in the embedded steel profiles at the maximum deflection from the FE simulation of beam/column specimen VT-1 – a) logarithmic strains and b) stresses in y-direction. 348
Fig. 6.145. Zone of compression strains in the stirrups at the maximum deflection state obtained from the simulation of beam/column specimen VT-1. 348
Fig. 6.146. Shear stresses developed in the layer of cohesive elements at the peak load in the simulation of beam/column specimen VT-1. 349
Fig. 6.147. Degradation of cohesive elements at the end of simulation for the beam/column specimen VT-1. 349
Fig. 6.148. Relative slip of embedded steel profiles obtained from the numerical simulation of beam/column specimen VT-1 – a) state at the peak load and b) state at the end of the simulation. 350
Fig. 6.149. Principal stresses in the support zone obtained from the FE simulation of beam/column specimen VT-1 – a) maximum principal stresses and b) minimum principal stresses. 351
Fig. 6.150. Numerical load-deflection curve of beam/column specimen VT-2 for the node at the mid-span. 352
Fig. 6.151. Damage sequence in the FE simulation of beam/column specimen VT-2 – a) damage at the phase before the failure, b) damage at the peak point and c) damage at the last phase of simulation. 353
Fig. 6.152. Deformation of embedded steel profiles at the peak load from the FE simulation of beam/column specimen VT-2 – a) logarithmic strains and b) von Mises stresses. 354
Fig. 6.153. Strains and stresses limited to yielding values in the embedded steel profiles at the maximum deflection from the FE simulation of beam/column specimen VT-2 – a) logarithmic strains and b) stresses in y-direction. 355
Fig. 6.154. Zone of the compression strains in the longitudinal reinforcement obtained from the simulation of beam/column specimen VT-2 – a) at the peak load state and b) at the maximum deflection state. 355
Fig. 6.155. Zone of the compression strains in the stirrups obtained from the FE simulation of beam/column specimen VT-2 – a) at the peak load state and b) at the maximum deflection state. 356
Fig. 6.156. Shear stresses developed in the layer of cohesive elements at the peak load in the FE simulation of beam/column specimen VT-2. 357
Fig. 6.157. Degradation of cohesive elements at the end of simulation from the beam/column specimen VT-2. 357
Fig. 6.158. Relative slip of embedded steel profiles obtained from the FE simulation of beam/column specimen VT-1 – a) state at the peak load and b) state at the end of simulation. 358
Fig. 6.159. Principal stresses in the support zone obtained from the FE simulation of beam/column specimen VT-2 – a) maximum principal stresses and b) minimum principal stresses. 359
Fig. 6.160. Vierendeel action in a modified simulation of beam/column specimen VT-2. 360
Fig. 6.161. Simplified interaction curve and corresponding stress distributions in the characteristic points of method given in EN 1994-1-1 [58]. 364
Fig. 6.162. Stresses distribution for the design plastic bending resistance of the cross-section – a) for the specimen VT-1 and b) for the specimen VT-2. 365
Fig. 6.163. Reference points for the analytical model obtained from the plastic bending design resistances of beam/column specimens. 367
Fig. 6.164. Reference points for the analytical model obtained from the secant stiffness method for beam/column specimens – a) for the specimen VT-1 and b) for the specimen VT-2. 368
Fig. 6.165. Deflection of a transversally loaded beam [183]. 370
Fig. 6.166. Cross-section geometry of the beam/column specimen in steel units – a) for the specimen VT-1 and b) for the specimen VT-2. 371
Fig. 6.167. Vierendeel truss model for the evaluation of equivalent beam shear stiffness in the VTBM model – a) global model and b) considered detail. 373
Fig. 6.168. Distributions of internal forces in the considered detail of the Vierendeel truss system of VTBM model – a) normal forces, b) shear forces and c) bending moments. 373
Fig. 6.169. Discretisation scheme of beam/column specimen VT-1 into the theoretical Vierendeel truss system. 375
Fig. 6.170. Discretisation scheme of beam/column specimen VT-2 into the theoretical Vierendeel truss system. 375
Fig. 6.171. Defined geometry of cross-sections in steel units for the beam/column specimens – a) for the specimen VT-1 and b) for the specimen VT-2. 378
Fig. 6.172. Defined geometry of the discretised geometry of the specimen VT-1 into the Vierendeel truss system. 379
Fig. 6.173. Defined geometry of the discretised geometry of the specimen VT-2 into the Vierendeel truss system. 379
Fig. 6.174. Geometry of chords in the VTBM model – a) for the specimen VT-1 and b) for the specimen VT-2. 380

Fig. 6.175. Morsch truss model for the evaluation of shear stiffness in the beam/column specimens – a) global model and b) considered detail. 386
Fig. 6.176. Load-deflection curves of the investigated analytical models for the beam/column specimen VT-1. 388
Fig. 6.177. Load-deflection curves of the investigated analytical models for the beam/column specimen VT-2. 388
Fig. 6.178. Load-deflection curves of VTBM model with different stiffness reduction factors for the beam/column specimen VT-1. 389
Fig. 6.179. Load-deflection curves of VTBM model with different stiffness reduction factors for the beam/column specimen VT-2. 389
Fig. 6.180. Deflection shape of the specimen VT-1 according to the VTBM model and comparison to test results. 390
Fig. 6.181. Deflection shape of the specimen VT-2 according to the VTBM model and comparison to test results. 390
Fig. 6.182. Weighted deflection shape of the specimen VT-1 according to the VTBM model in order to converge to test results. 391
Fig. 6.183. Comparison of the VTBM load-deflection curve with international models for the specimen VT-1. 392
Fig. 6.184. Comparison of the VTBM load-deflection curve with international models for the specimen VT-2. 392

Fig. 7.1. Summary card of the analysed aspects of local and global shear transfer in heavy steel-concrete composite columns with multiple encased steel profiles. 406

Fig. 8.1. Outlook for further investigations on the local shear transfer aspect in heavy steel-concrete composite columns with multiple encased steel profiles – novel flat mechanical shear connectors. 408
Fig. 8.2. Outlook for further investigations on the global shear transfer aspect in heavy steel-concrete composite columns with multiple encased steel profiles – innovative structural model VTBM for stiffness evaluation. 409

List of Tables

Table 3.1. Axial strength reduction factors for flexural response of a column. (Source: AVEC BNT [11]). 62

Table 5.1. Judging table with considered parameters for the development of the geometrical concept of flat shear connectors....123
Table 5.2. Overview of the small-scale push-out test specimens. 127
Table 5.3. Overview of the composite column push-out test specimens. 135
Table 5.4. List of the used displacement transducers in the column push-out tests. 140
Table 5.5. Arrangement and list of the strain gauges used in the column push-out tests for the specimen 0v2. 141
Table 5.6. Arrangement and list of the strain gauges used in the column push-out tests for the specimen Av2. 141
Table 5.7. Arrangement and list of the strain gauges used in the column push-out tests for the specimen Cv2. 141
Table 5.8. Arrangement and list of the strain gauges used in the column push-out tests for the specimen Bv2. 142
Table 5.9. Material properties of the structural steel in column push-out tests. 146
Table 5.10. Material properties of the reinforcement steel in column push-out tests. 146
Table 5.11. Material properties of the concrete in column push-out tests. 147
Table 5.12. Column push-out test results. 149
Table 5.13. Strains in stirrups from column push-out tests. 153
Table 5.14. Verification of the normal separation measured in column push-out tests. 156
Table 5.15. Properties used to define the material law of structural steel in numerical simulations of CoPOT. 171
Table 5.16. Properties used to define the material law of reinforcement steel in numerical simulations of CoPOT. 172
Table 5.17. Interaction properties of bond in Abaqus/Standard simulations of column push-out tests. 177
Table 5.18. Interaction properties of bond in Abaqus/Explicit simulations of column push-out tests. 178
Table 5.19. Overview on the calibration of the proposed analytical model for flat shear connectors. 246
Table 5.20. Comparison of the analytical model for flat shear connectors to the test results. 247

Table 6.1. Evaluation of the imposed load in test specimens (consider with Fig. 6.7 and Fig. 6.8). 260
Table 6.2. Overview of the beam/column test specimens. 262
Table 6.3. List of the used displacement transducers and inclinometers in beam/column tests. 271
Table 6.4. List of the used strain gauges in beam/column tests. 275
Table 6.5. Material properties of the structural steel from beam/column specimens. 280
Table 6.6. Material properties of the reinforcement steel from beam/column specimens. 280
Table 6.7. Material properties of the concrete. 281
Table 6.8. Test results for the considered mid-span deflections of beam/column specimens. 282
Table 6.9. Strains in the shear reinforcement of beam/column specimens. 293
Table 6.10. Relative slip of the embedded steel profiles in beam/column specimens. 298
Table 6.11. Summary and comparison of the internal forces in beam/column specimens. 314
Table 6.12. Shear force transferred by the stirrups and steel profiles in the beam/column specimens. 323
Table 6.13. Material properties used to define the structural steel material law in the FE simulations of beam/column tests. 330
Table 6.14. Material properties used to define the reinforcement steel material law in the FE simulations of beam/column tests. 331
Table 6.15. Properties used to define the response of cohesive elements in the FE simulations of beam/column specimens. 339
Table 6.16. Investigated analytical models for the effective stiffness of beam/column specimens and comparison to test results. 387

Nomenclature

Abbreviations

1D	One-dimensional
2D	Two-dimensional
3D	Three-dimensional
ACI	American Concrete Institute
AISC	American Institute of Steel Construction
ANSI	American National Standards Institute
Approx.	Approximately
ASCE	American Society of Civil Engineers
ASD	Allowable strength design
Avg.	Average
B	The nomination of steel material for reinforcing concrete or back
BOT	Bottom
C	Concrete, cement or compression strut
ca.	Circa
Cal	Calculation
Calib	Calibration
CDP	Concrete Damaged Plasticity
ch	Chord
cm	Centimetre
Con	Connector
Const.	Constant
CoPOT	Composite column push-out test
CTBUH	Council on Tall Buildings and Urban Habitat
Cyl.	Cylinder
Dev	Deviation
DMS	Strain gauge (abbreviation from the German language)
DOF	Degree of freedom
DT	Displacement transducer
Dur	Durability
e.g.	"*exempli gratia*" – example given
EC	Eurocode
Eff	Effective
EN	European Norm
Eq.	Equation
Err	Error

et al.	*"et alia / et alii / et aliae"* – and others
Exp	Experimental
F	Front
FE	Finite Element
FEA	Finite Element Analysis
FEM	Finite Element Method
Fig.	Figure
G	Grease
GPa	Gigapascal
H	Horizontal
HOR	Horizontal
HP	High Performance
Hz	Hertz
i.e.	"*id est*" – in other words / that is
IM	Inclinometer
ISO	International Organization for Standardization
JSCE	Japan Society of Civil Engineers
kN	Kilonewton
kNm	Kilonewton-metre
L	Left
LE	Logarithmic strain
LRFD	Load and resistance factor design
LSP	Lower embedded steel profile
Lubr.	Lubricated
µm	Micrometre
m	Metre
Max	Maximum
MC	Model Code
Min	Minimum or minute
mm	Millimetre
MN	Meganewton
MPa	Megapascal
MS	Measurement section
MTBM	Mörsch truss beam model
N	Newton
n/a	Not available
No.	Number
Nom	Nominal
OoP	Out of plane
po	Post

POT	Push-out test
PS	Pure steel
PTFE	Polytetrafluoroethylene / Teflon
R	Right
RC	Reinforced concrete
Real	Realistic
Rebar	Reinforcement bar
Ref.	Reference
Resid	Residual
RFCS	Research Fund for Coal and Steel
S	The nomination of structural steel material or stress
s	Second
SC	Shear connector
SDEG	Stiffness degradation
SG	Strain gauge
SLS	Serviceability Limit State
SP	Steel profile
SSCPOT	Small-scale cube push-out test
T	Tension tie
TUK	Technische Universität Kaiserslautern
ULS	Ultimate Limit State
UniLux	University of Luxembourg
UP	Upper
USP	Upper embedded steel profile
V	Vertical
VER	Vertical
VT	Vierendeel test
VTBM	Vierendeel truss beam model
W	Water

Symbols

The convention of used symbols in the nomenclature of this dissertation is following, in general, the nomenclature given in the European Standards (EN). If another source is cited, like for example American Building Code ACI 318 or research paper, the nomenclature of the cited source is used. A list of symbols used in the dissertation is given below with distinction on Greek and Latin letters. Combinations of multiple symbols given in the list are foreseen in used indexes of other values.

Greek letters

α	Angle or factor correlating the slenderness of a stud connector

α_c	Angle defining the orientation of a flat shear connector, when $\alpha_c = 90^0$ then it is a transversal orientation
α_{cc}	Coefficient taking account of long term effects on the compressive strength of concrete and unfavourable effects resulting from the way how the load was introduced
α_i	Composite stiffness parameter, when $\alpha_i = 0$ then $(EI)_{com} = (EI)_{a+c}$
α_M	Coefficient including the strength reduction of a composite section due to the simplified design method and interaction of axial load
α_{s1}	Angle between the direction of maximum shear stresses and flange of steel profile
α_{VTBM}	Stiffness reduction factor correlating the stiffness value of EN 1994-1-1 to the stiffness value from the VTBM model
α_w	Angle of the slope of the weld used in flat shear connectors
β	Angle, coefficient depending on the form of bending moment function for the given load case or effective buckling length factor
β_c	Amplification factor of natural steel-concrete bond strength in composite columns due to the thickness of the concrete cover
β_{dns}	Reduction factor due to the sustained axial load
β_l	Effective buckling length factor
β_w	Factor for the weld strength with reference to welded steel materials
Δ	Difference
δ	Displacement or error
$\delta_{l,u}$	Longitudinal relative displacement at the ultimate load or slip at the ultimate load
${\delta_m}^f$	Total plastic displacement in the traction-separation law
$\delta_{n,u}$	Normal separation at the ultimate load
δ_s	Relative slip or shear deformation of a truss
δ_{s0}	Relative slip in the case of no shear connection
δ_u	Relative slip at the ultimate load
γ	Angle, transformation angle, strains in the tangential direction – shear strains, coefficient depending on the distribution form of bending moment or partial safety factor
γ_p	Transformation angle for the direction of the principal stresses
$\gamma_{s,max}$	Transformation angle for the direction of the maximum shear stresses
γ_{s2}	Transformation angle for the direction of the vertical shear stresses
ε	Strains in the normal direction – tension or compression strains
ε_a	Strains in the structural steel
ε_c	Compression strains in the concrete
$\varepsilon_{c,lim}$	Ultimate compressive strains of concrete
ε_{c1}	Compression strains in the concrete at the ultimate stress state
$\varepsilon_{c2,c}$	Compressive strains in the confined concrete at the ultimate stress state according to the simplified parabola-rectangle model
ε_{ct}	Tensile strains in the concrete
$\varepsilon_{cu2,c}$	Ultimate compressive strains of confined concrete according to the simplified parabola-rectangle model
ε_p	Plastic strains
ε_s	Strains in the reinforcement steel

$\varepsilon_{s,m}$	Mean strains in the stirrups
ε_y	Yielding strain
ε_{ys}	Yielding strain of the reinforcement steel
ε_u	Ultimate strain
ϵ	Eccentricity of hyperbolic yield function approach in the concrete plasticity law
η	Degree of shear connection, factor for the evaluation of bond strength, coefficient taking into account an increase of stiffness due to the existence of embedded steel profiles
$\eta_{E,a}$	Elastic modular conversion ratio to steel units
$\eta_{E,a,eff}$	Effective value of elastic modular conversion ratio to steel units in the VTBM model
θ	Angle or dispersion angle of the concrete strut
θ_c	Resultant angle from vector summation of redistributed reactions at the arm of flat shear connector
θ_{MTBM}	Inclination angle of the diagonal strut in the Mörsch truss model
κ_1	Load distribution factor for the resistance of the V-shaped flat shear connector
κ_2	Load distribution factor for the resistance of the V-shaped flat shear connector
κ_{com}	Curvature of a composite section
κ_i	Curvature of a section of part "i"
$\bar{\lambda}$	Relative slenderness
λ_A	Area correction factor for the vertical shearing in the V-shaped flat shear connector
λ_d	Factor for the effective contact area of flat shear connectors
λ_f	Force orientation factor for the resistance of flat shear connectors
λ_s	Calibration factor for the shear resistance of flat shear connectors based on test results
λ_u	Activation factor for the effective perimeter
μ	Friction ratio or relative bending moment
μ_d	Factor correlating the respective bending moment resistance of a composite column to the level of acting axial load
μ_m	Ratio for the evaluation of the density of shear connection, where $\mu_m = \gamma/\beta$
μ_{visc}	Viscosity parameter
ν	Poisson's ratio or strength reduction factor in shear for cracked concrete
ν_{ch}	Poisson's ratio of chords in a truss system
v_l	Shear flow
${v_l}^1$	Unit shear flow, where $v_l = {v_l}^1 V$
ν_{po}	Poisson's ratio of posts in a truss system
ν_s	Reduction factor for cohesion due to the micro-cracking of concrete
π	Mathematical constant
ρ	Density or parameter related to the reduced design bending resistance accounting for vertical shear
ρ_s	Reinforcement ratio
σ	Stresses in the normal direction – tension or compression stresses
σ_2	Confining stresses
σ_c	Compression stresses in the concrete
σ_{ct}	Tensile stresses in the concrete

σ_p	Plastic stresses in the normal direction
σ_{p1}	Maximal principal stresses
σ_{p2}	Minimal principal stresses
σ_s	Corresponding normal stresses in the direction of maximum shear stresses
σ_{x1}	Normal stresses in the direction rotated by a transformation angle
τ	Stresses in the tangential direction – shear stresses
τ_b	Bond shear stress or stiffness reduction factor of slender columns used in AISC 360
τ_{max}	Maximum shear stresses
$\tau_{R,bond}$	Bond strength of the plain steel-concrete interface
$\tau_{R,con}$	Bond strength of a flat shear connector
τ_{Rd}	Design shear strength, for example of bond
$\tau_{surf,i}$	Shear stresses at an interface
τ_{x1y1}	Shear stresses in the direction rotated by a transformation angle
φ	Axial strength reduction factor for the flexural response of a column or internal friction angle
φ_t	Creep coefficient
ϕ	Nominal diameter or strength reduction factor
χ	Reduction factor of axial strength for the relevant buckling mode
ψ	Factor, factor considering partial shear connection, parameter of contra flexure for the Vierendeel truss or dilation angle for the concrete plasticity law
ψ_A	Equation simplification factor for the transversal variant of flat shear connectors
ψ_B	Equation simplification factor for the V-shaped variant of flat shear connectors
$\psi_{B,s2,1}$	Equation simplification factor for the V-shaped variant of flat shear connectors and the vertical shearing failure pattern
$\psi_{B,s2,2}$	Equation simplification factor for the V-shaped variant of flat shear connectors and the vertical shearing failure pattern
ψ_M	Contra-flexure parameter and equation simplification factor in the VTBM model
ψ_Q	Axial-relativity parameter and equation simplification factor in the VTBM model
$\psi_{w,el}$	Geometrical factor for the weld resistance of flat shear connectors according to the elastic analysis
$\psi_{w,pl}$	Geometrical factor for the weld resistance of flat shear connectors according to the plastic analysis
Ω	Safety factor in AISC 360
ω_c	Factor for the concrete confinement taking into account an arrangement of the reinforcement cage
ω_{cc}	Transformation factor, which relates the Coulomb material compression strength to the concrete compression strength without confining stresses

Latin letters

$(EA)_{a+c}$	Sum of axial stiffnesses of structural steel and concrete parts
$(EA)_{com}$	Axial stiffness of a composite section
$(EA)_i$	Axial stiffness of a section of part “i”
$(EI)_{a+c}$	Sum of flexural stiffnesses of structural steel and concrete parts
$(EI)_{com}$	Flexural stiffness of a composite section

$(EI)_{eff,EC4}$	Effective flexural stiffness according to the EN 1994-1-1
$(EI)_{eff,II,EC4}$	Effective flexural stiffness according to the EN 1994-1-1 and for the second-order analysis
$(EI)_{eff,VTBM}$	Effective flexural stiffness according to the VTBM model considering bending and shear
$(EI)_{full}$	Flexural stiffness according to the EN 1994-1-1 without stiffness reduction factors
$(EI)_i$	Flexural stiffness of a section of part "i"
$(EI)_{MTBM}$	Equivalent beam bending stiffness for the Mörsch truss model
$(EI)_{v,gl}$	Equivalent beam bending stiffness for the Vierendeel truss model
A	Cross-sectional area or elongation after fracture
A_c	Cross-sectional area of concrete
A_{ch}	Cross-sectional area of the chord in a truss system
$A_{con,eff}$	Effective area of the connector contact surface
$A_{con,arm,eff}$	Effective area of the contact surface of a flat shear connector arm
$A_{cont,eff}$	Effective area of a contact surface
A_{ds}	Cross-sectional area of the diagonal strut in a Mörsch truss system
A_{po}	Cross-sectional area of the post in a truss system
$A_{s1,eff}$	Effective area of concrete in the plane of maximum shear stresses
$A_{s2,eff}$	Effective area of concrete in the vertical plane
A_v	Shear area
$A_{v,ch}$	Shear area of the chord in a truss system
$A_{v,po}$	Shear area of the post in a truss system
A_{sw}	Cross-sectional area of stirrups
A_w	Cross-sectional area of weld
a	Distance, span between posts in a truss system or index for the structural steel
a_w	Thickness of weld
B	Width of a composite section
b	Distance, width, width of a composite section, thickness, span between chords in a truss system or index for bond
b_f	Width of the flange of a steel profile
$b_{f,int}$	Width of the internal side of the flanges of a steel profiles
C	Parameter
c	Distance, concrete cover, cohesion or index for concrete part, for compression or for confinement
c_{nom}	Nominal thickness of the concrete cover
c_z	Thickness of the concrete encasement in a composite section with reference to z-axis
c_y	Thickness of the concrete encasement in a composite section with reference to y-axis
D	Depth of a composite section, damage factor or resultant internal compression force
d	Diameter, distance, depth, index for design action or index for design property
d_a	Distance between embedded steel profiles
d_c	Damage factor for compression in the CDP material law
d_{ch}	Depth of a chord section in a truss model

d_{po}	Depth of a post section in a truss model
d_t	Damage factor for tension in the CDP material law
dF	Change in forces (N, M, V)
ds	Infinitesimal deformed line element
dx / dy / dz	Infinitesimal line element
E	Modulus of elasticity / Young's modulus
E_a	Modulus of elasticity of structural steel
$E_{a,eff}$	Effective value of modulus of elasticity of structural steel in the VTBM model
E_{cd}	Design value of modulus of elasticity of concrete
E_{ch}	Modulus of elasticity of chord in a truss system
E_{cm}	Mean value of modulus of elasticity of concrete
$E_{cm,eff}$	Effective mean value of modulus of elasticity of concrete in the VTBM model
E_{ds}	Modulus of elasticity of diagonal strut in a truss system
E_{po}	Modulus of elasticity of post in a truss system
E_{red}	Reduced value of modulus of elasticity
E_s	Modulus of elasticity of reinforcement steel
$E_{s,eff}$	Effective value of modulus of elasticity of reinforcement steel in the VTBM model
e	Eccentricity of the axial force, eccentricity of the reaction force in push-out tests
e_i	Distance between centroids of two composed parts
e_{jk}	Distance from the centroid of part "j" to place "k"
e_{jo}	Distance from the centroid of part "j" to the centroid of a composite section
e_0	Plastic eccentricity, where $e_0 = M/N$
e_w	Eccentricity of the reaction force acting on the welded connection of flat shear connectors
F	Force
F_{α_c}	Resultant force acting on the contact surface of the V-shaped flat shear connector
F_{arm}	Force taken by one arm of a flat shear connector
$F_{f,D}$	Friction force due to the compression lateral force
F_L	Load, longitudinal force
F_N	Internal force in the normal direction
F_n	Normal force
F_Q	Internal force in the transversal direction
F_R	Resultant force or reaction force
F_s	Shear connection force resistance or force in stirrups
$F_{s,na}$	Total force taken by stirrups
F_t	Tangential force or tensile force
$F_{t,a}$	Tensile force in a steel profile
F_u	Ultimate force or peak force
f_b	Bond strength
f_{bd}	Design bond strength

f_c	Strength of concrete for compression
f_{ck}	Characteristic value of the compression strength of concrete
$f_{ck,cube}$	Characteristic value of the compression strength of concrete for cubic specimens
$f_{ck,c}$	Characteristic value of the compression strength of confined concrete
f_{cd}	Design value of the compression strength of concrete
f_{cm}	Mean compression strength of concrete
$f_{cm,c,cube}$	Mean compression strength of confined concrete for cubic specimens
$f_{cm,cc,cube}$	Mean compression strength of concrete for a modified Mohr-Coulomb law
$f_{cm,cube}$	Mean compression strength of concrete for cubic specimens
f_{ctd}	Design value of the tensile strength of concrete
f_{ctm}	Mean value of the tensile strength of concrete
f_d	Design value of a material strength
f_k	Characteristic value of a material strength
f_s	Stress in the reinforcement
f_{sd}	Design value of the yielding strength of reinforcement steel
f_u	Ultimate strength of a material
f_y	Yielding strength of a material
f_{yd}	Design value of the yielding strength of a material
f_{ywd}	Design value of the yielding strength of stirrups
G	Shear modulus
G_{ch}	Shear modulus of the chord in a truss system
G_{po}	Shear modulus of the post in a truss system
g	Index for gross section
H	Height of a part, height of a specimen
H_{ch}	Internal force in the chord of a truss system in the horizontal direction
h	Height, height of a composite section
h_{ch}	Height of a chord section in a truss system
h_{po}	Height of a post section in a truss system
i	Radius of gyration
$i, j, \ldots, k$	Symbolic definition of an order number in series
I	Moment of inertia / Second moment of area
I_a	Moment of inertia of a structural steel section
I_c	Moment of inertia of a concrete section
I_{ch}	Moment of inertia of a chord section in a truss system
I_{po}	Moment of inertia of a post section in a truss system
I_s	Moment of inertia of a reinforcement steel section
$I_{v,gl}$	Moment of inertia of an equivalent beam section for the Vierendeel truss system
I_w	Moment of inertia of weld
K	Stiffness

K_0	Calibration factor for the evaluation of effective stiffness in the analysis of second-order
K_c	Correction factor for the evaluation of effective stiffness
$K_{c,II}$	Correction factor for the evaluation of effective stiffness in the analysis of second-order
K_{init}	Initial stiffness
K_R	Stiffness at reload
K_{sc}	Constant stiffness of shear connection over the entire connection length
$K_{s,MTBM}$	Equivalent beam shear stiffness for the Mörsch truss model
K_{sv}	Equivalent beam shear stiffness for the Vierendeel truss model
k	Factor, moment magnification factor or index for the characteristic action and property
k_B	Stiffness reduction factor proposed by Chanou
k_{hlc}	Calibration factor for the compression resistance of flat shear connectors based on the test results and on the extrapolation of the problem to the 3D and the resistance of globally confined concrete
k_s	Stiffness of shear connector or inclination parameter for the Coulomb material
k_{ss}	Initial stiffness of shear connection in the tangential direction for the traction-separation law
L	Length
L_0	Length between the supports
L_{arm}	Length of the flat shear connector arm
L_l	Length between the maximum curvature place and place of the restrained slip
L_E	Load introduction length
L_{emb}	Embedment length
l_0	Effective length of a column
l_b	Anchorage length or bonded length
l_w	Length of weld
M	Bending moment
$\bar{M}$	Bending moment from the reaction of virtual work
M_{Ed}	Design value of bending moment obtained from the factored combination of actions
M_e	Bending moment due to the reaction acting on an eccentricity
$M_{max,Rd}$	Maximum design resistance of a section for bending moment
$M_{pl,Rd}$	Plastic design resistance of a section for bending moment
$M_{pl,Rk}$	Plastic characteristic resistance of a section for bending moment
M_R	Resistance to bending moment
$M_{R,pd}$	Ultimate bending moment resistance obtained from the pre-design process
$M_{R,pl,resid}$	Residual plastic resistance to the bending moment
m	Index for the mean value
N	Normal or axial force
$\bar{N}$	Normal or axial force from the reaction of virtual work
N_{cr}	Euler's elastic critical buckling load
N_{Ed}	Design value of axial load obtained from the factored combination of actions
$N_{G,Ed}$	Permanent part of design axial load
$N_{pl,Rd}$	Plastic design resistance of a section for normal force

$N_{pl,Rk}$	Plastic characteristic resistance of a section for normal force
$N_{pm,Rd}$	Plastic design resistance of concrete to the compressive normal force
n	Number, relative axial force, number of buckling mode or index for normal direction
n_a	Number of arms of a flat shear connector
n_j	Modular conversion ratio for part "j", where normally $n_j = E_i/E_j$
n_{po}	Number of posts in a truss system
P	Point load
P_{cr}	Euler's critical buckling load
P_{Ed}	Design value of a point load
P_{end}	Residual load-bearing capacity for the tested beam/column specimens
$P_{K,sec,pl}$	Load level evaluated from the secant stiffness method of plastic design
$P_{R,Av2}$	Resistance of the transversal variant of flat shear connectors
$P_{R,Bv2}$	Resistance of the V-shaped variant of flat shear connectors
$P_{R,b}$	Resistance of bond in flat shear connectors
$P_{R,Cv2}$	Resistance of the longitudinal variant of flat shear connectors
$P_{R,c}$	Resistance of flat shear connector for the compression failure of concrete
$P_{R,cb,cs}$	Resistance of flat shear connector for the interaction of bending and shear in elastic analysis
$P_{R,cb,el}$	Resistance of flat shear connector for the bending according to elastic analysis
$P_{R,cs,el}$	Resistance of flat shear connector for the shearing according to elastic analysis
$P_{R,cs,\mathrm{pl}}$	Resistance of flat shear connector for the shearing according to plastic analysis
$P_{R,m}$	Resistance of flat shear connector for the material failure
$P_{R,s1}$	Resistance of flat shear connector for the maximum shear failure of concrete
$P_{R,s2}$	Resistance of flat shear connector for the vertical shear failure of concrete
$P_{R,t}$	Resistance of concrete to tensile stresses in the analytical model for flat shear connectors and criterion for cracked concrete state
$P_{R,w}$	Resistance of flat shear connector for the weld failure
P_{Rd}	Design resistance of a shear connector
P_u	Ultimate point load
$P_{u,pd}$	Ultimate load resistance obtained from the pre-design process
p	Pressure
$\bar{Q}$	Shear force from the reaction of virtual work
q	Distributed load
R	Resistance, radius or reaction force
R_d	Design resistance
R_{eH}	Yielding strength
R_m	Tensile strength
R_n	Nominal strength
R_u	Required strength or ultimate resistance
r	Radius, radius of curvature of a beam or index for reinforcement

r_δ	Flexibility parameter
S	Static moment of area, first moment of area, stress or shear force
S_d	Design response
S_n	Nominal strength of a section
S_{SP}	Shear stiffness of a sub-section with steel profiles in the truss model of SmartCoCo
S_{RC}	Shear stiffness of a reinforced concrete sub-section in the truss model of SmartCoCo
s	Length of shear connection, slip, span or index for steel
s or w	Index for reinforcement steel
s_c	Span between shear connectors
s_w	Spacing of stirrups
T	Transversal shear force
T_{ch}	Transversal shear force in the chord of a truss system
T_{po}	Transversal shear force in the post of a truss system
t	Thickness, time, traction, index for tension or index for tangential direction
t_f	Thickness of the flange of a steel profile
t_n	Traction stress in the normal direction
t_s	Traction stress in the first shear direction
t_{ss}	Tangential shear stress component of traction vector for the traction-separation law
t_t	Traction stress in the second shear direction
t_w	Thickness of the web of a steel profile
U	Required strength calculated for factored loads or displacement
UR	Rotation
u	Perimeter, parameter or index for ultimate state
V or Q	Shear force
V_a	Shear force taken by steel profiles
$V_{a,Ed}$	Design value of shear forces taken by the structural steel section
V_{Ed}	Design value of shear forces obtained from the factored combination of actions
$V_{L,Ed}$	Design value of longitudinal shear forces acting on a shear connection
$V_{pl,Rd}$	Plastic design resistance of a section for shear forces
$V_{pl,Rk}$	Plastic characteristic resistance of a section for shear forces
$V_{Rd,s}$	Design resistance of reinforced concrete to shear assured by the stirrups
V_s	Shear force taken by the stirrups
V_{tot}	Total shear force
w	Deflection, density of concrete, crack width or index for wall, for stirrups or for weld
w_1	Crack width at the ultimate tensile stresses
w_b	Bending part of deflection of a beam
$w_{Bernoulli}$	Deflection of a beam according to the Euler-Bernoulli beam theory
w_c	Crack width at the fracture
$w_{K,sec,pl}$	Deflection correlating to the load evaluated from the secant stiffness method for plastic design

w_{max}	Maximal mid-span deflection
w_{MTBM}	Deflection of the equivalent beam according to the Mörsch truss model
w_s	Shear part of deflection of a beam
$w_{Timoshenko}$	Deflection of a beam according to the Timoshenko beam theory
w_u	Mid-span deflection with corresponding ultimate load
w_{VTBM}	Deflection of the equivalent beam according to the VTBM model
x	In plane 1st direction in a 3D/2D system, abscissa in the Cartesian coordinate system or sectional length of compressed concrete
y	In plane 2nd direction in a 3D/2D system, ordinate in the Cartesian coordinate system
Z	Resultant internal tensile force
z	Out of plane 3rd direction in a 3D system, internal lever arm between resultant tension and compression forces or distance from the neutral axis to the considered fibre of section
z_{real}	Internal lever arm for the realistic distribution of stresses in cross-section
z_{sb}	Internal lever arm for the plastic distribution of stresses in cross-section

1. Introduction

Research conducted within the scope of the given dissertation has been launched at the University of Luxembourg in the research team of ArcelorMittal Chair of Steel and Façade Engineering held by Prof. Dr.-Ing. Christoph Odenbreit and it was a common research project with ArcelorMittal Global R&D with offices in Esch-sur-Alzette in Luxembourg called “MultiCoSteel”. Of interest was to investigate the behaviour of heavy steel-concrete composite columns with multiple encased hot-rolled steel profiles in order to improve the current practice and to bring an understanding of such complex and novel structural elements. The aforementioned composite columns are used in high-rise buildings and a trend to build vertically becomes much more significant in the last century [6]. With the increased height of buildings, the available solutions included in the current design codes, like EN 1994-1-1 [58], stopped to satisfy the needs of structural engineers, investors and architects. Many high-rise buildings were constructed worldwide, where the applied solutions for composite columns went beyond the available design provisions and they required complex Finite Element analyses in order to evaluate their behaviour. In Fig. 1.1, a comparison between the typical cross-sections of composite columns, where the simplified design procedure is available, and the novel solutions with multiple encased steel profiles is shown.

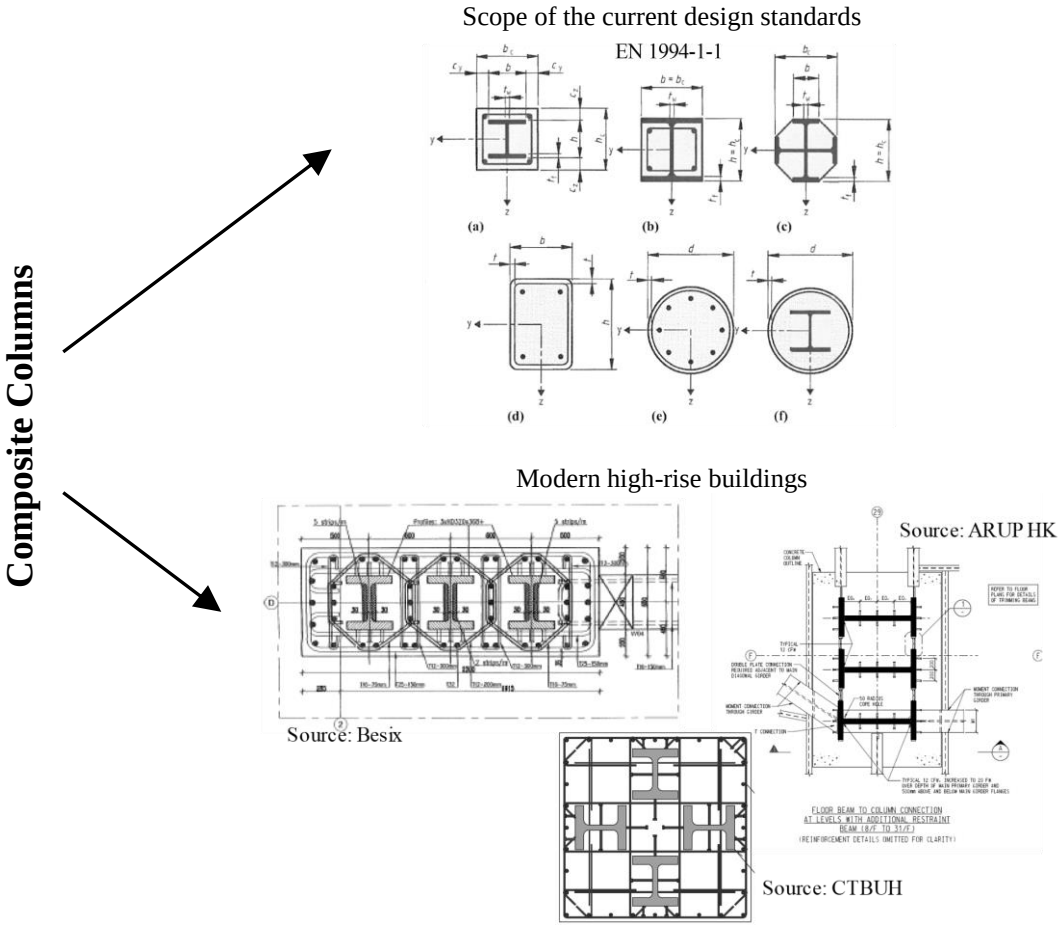


Fig. 1.1. Comparison of steel-concrete composite columns in design standards and modern high-rise buildings.

The shear connection at the steel-concrete interface in composite columns with embedded heavy steel profiles is commonly assured by the application of a big amount of shear studs, which brings an exhaustive application process, reduces the construction safety, lowers the economy of the solution and increase the complexity of the building erection process. A replacement of the current solution with a new and more efficient solution dedicated to the considered type of columns would be highly beneficial. Moreover, it has been identified that composite columns with multiple encased steel cores can diverge in their behaviour from a typically assumed Euler-Bernoulli beam model, which is commonly applied to analyse the behaviour of composite columns with one embedded steel profile. In the result, the divergence from the Euler-Bernoulli beam model can lead to the reduced value of the effective stiffness of a column in some cases. The possible overestimation of the stiffness would directly refer to the overestimation of the Euler's elastic buckling critical load and moment magnification factors in the second-order analysis. In the structural behaviour of the aforementioned columns, a sign of the shear deformation and transition towards the Vierendeel truss behaviour has been observed. An accurate assessment of the structural behaviour would significantly increase the safety of the construction, lower the construction costs and widen the application range of the complex composite columns with multiple steel cores. The identified aspects of improvement in the current practice can be commonly considered under the topic of the shear transfer. In the conducted research, a clear industrial impact can be observed.

The significance of the research and a need for the improvement of the current level of knowledge have been acknowledged by the Luxembourgish National Research Fund (FNR). The conducted research has been awarded with a PhD Grant within the scope of the AFR-PPP funding scheme, where the industrial project partner was ArcelorMittal Belval & Differdange S.A. In the result, close collaboration on the common research project in the topic of shear transfer in heavy steel-concrete composite columns has been formally established between three parties: FNR, University of Luxembourg and ArcelorMittal Global R&D. Within the project, the author spent a significant part of his working time in the industrial project partner facility. This experience allowed for industrial impact-driven research, which considers not only the theoretical value but also focuses on practical solutions, which are highly potential for a further application to the market.

To support the taken investigations, a collaboration with the Hasselt University, University of Liège, research unit INSA of the University of Rennes, Imperial College London, University of Bradford, GSI SLV Saarbrücken, Wallerich Lux S.A., Council of Tall Buildings and Urban Habitat (CTBUH), Arup Hong-Kong and China Academy of Building Research (CABR) Technology Co., Ltd was established. The established network of specialists in the field of research allowed for the in-depth analysis of the problem and other research projects in the field of composite columns with multiple encased steel profiles (SmartCoCo [175] and ISRC Composite Columns [82]). Finally, the coordinator of the RFCS research project SmartCoCo [175], Prof. Dr. ir. Hervé Degée, joined the project and became a member of the supervision committee.

2. Overview and Structure of the Thesis

This dissertation is dealing with the shear transfer in heavy steel-concrete composite columns with multiple encased steel profiles. In the investigated shear transfer, two aspects are considered, local shear transfer and global shear transfer. The local shear transfer is referring to the investigation of shear connection at the steel-concrete interface and development of a novel type of flat mechanical shear connectors dedicated to fully encased composite columns. The developed novel shear connectors are characterised and an analytical model for the evaluation of their resistance is given. The global shear transfer is referring to the load-flux in the steel-concrete composite specimens with two embedded steel profiles and distribution of the shear forces between the steel profiles and the reinforced concrete. In the result, the shear deformation of the aforementioned specimens is investigated and an innovative mechanical engineering model, involving the Vierendeel truss system and Timoshenko beam theory, is developed. Based on the proposed innovative mechanical engineering model, an equation for the new effective bending stiffness is derived, which incorporates the reduction of stiffness due to significant shear effects. The structure of the dissertation is presented in a process flow diagram in Fig. 2.1.

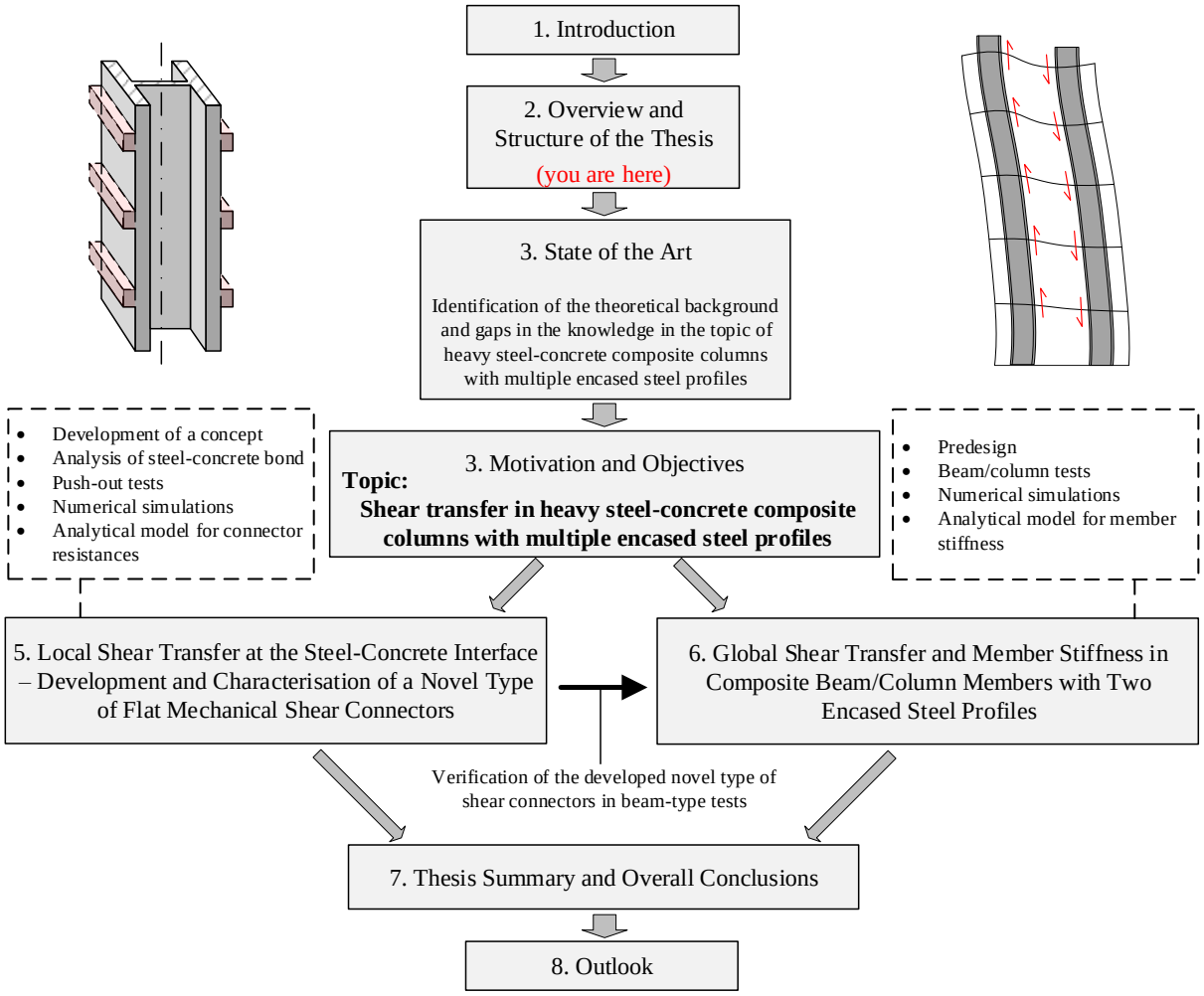


Fig. 2.1. Structure of the Thesis.

3. State of the Art

The topic of research introduced in Chapter 1 and summarized in Chapter 2 requires an extensive literature research in order to create a solid theoretical background for the further investigations and to identify gaps in the current state of the art. A good understanding of the structural behaviour of steel-concrete composite structures, especially composite columns, was essential in the taken investigation. An efficient combination of steel and concrete materials in composite structures requires shear connection to be assured at the steel-concrete interface. The aspect of shear connection, as a local shear transfer at the steel-concrete interface, had been analysed and the occurring force transfer phenomena – mechanical and non-mechanical, were investigated. In the scope of the investigation of shear connection, plain steel-concrete bond and reinforcement bar-concrete bond were considered. Furthermore, mechanical shear connection means, like for example shear studs, were identified and briefly analysed. An impact of the applied shear connection on the structural behaviour of composite members had been investigated in parallel with the global structural behaviour of composite columns in the light of different theoretical models. Based on the international design codes, provisions for the design of composite columns were reviewed and the focus was placed on the models for the effective flexural stiffness. Finally, recent investigations in the topic of composite columns with multiple encased steel profiles had been analysed, where the aspects of shear transfer and effective stiffness were considered.

The gathered information allowed identifying a need for the improvement of current solutions in terms of shear connection and lack of knowledge regarding the structural behaviour of columns with more than one embedded steel profile. In the result, the motivation and objectives for the conducted research are formulated afterward in Chapter 4.

3.1. Steel-concrete composite construction

Main structural materials used for the construction are steel and concrete. Both materials bring certain advantages and disadvantages for structural members. Constructions made from steel are light and have good performance with no distinction on tension or compression character of work. However, the structural steel material is relatively expensive, contain poor resistance to fire and environmental conditions without special treatments, as well as steel members are sensitive to the instabilities. On the other hand, reinforced concrete (RC) structures are cheaper, contain good fire and environmental protection properties and are efficient in compression. The biggest structural disadvantages of RC members are strong limitations in the tension zones, vulnerability to creep and shrinkage effects, brittle character of damage and requirement of a significant cross-sectional area in order to achieve a high load-bearing capacity. In addition, RC structures require more complicated erection process.

Efficient combination of steel and concrete materials in one composite member allow to benefit from both, where the concrete part is activated in compression and the steel part work in tension and compression. Due to the simultaneous and combined work of both materials in composite member as one material, the overall load-bearing performance and stiffness is increased [89, 110, 127]. In order to assure the described-above composite behaviour, the shear connection at the steel-concrete interface is required. The existence of steel profile in a composite cross-section greatly increases the ductility and energy dissipation properties of columns, which is highly desirable for seismic design [77]. Moreover, the concrete material provides an isolation layer for the steel material in fire and aggressive environmental conditions and the steel hollow sections provide a permanent formwork for the concrete.

3.1.1. Basis of composite behaviour

The considered idea of the steel-concrete composite behaviour, which is also defined as the composite theory [110], consists of axial and flexural theory of elastic behaviour of structural composite members made in steel and concrete. The pure axial behaviour of composite members allow summing the contributions of two materials, where certain limitations and corrections are introduced due to the correlation of strains between steel and concrete sections. This aspect mainly considers members subjected to compression, where the contribution of concrete in tension is normally neglected due to the poor tensile resistance properties. No restrictions are defined for the shear connection until a compressed member is not sensitive to buckling effects and the relative slip between the steel and concrete is prevented by boundary conditions. Typical composite flexural members consist of composite beams and composite slabs. However, also composite columns subjected to lateral forces, imperfections, effects of second-order and buckling exhibit flexural behaviour. The flexural behaviour of a composite member can benefit only when the shear connection is assured at the steel-concrete interface. However, the shear connection can be applied assuring full or partial interaction between the two materials, where assured full interaction prevent development of any relative slip at the steel-concrete interface. In Fig. 3.1, the idea of the composite behaviour with full interaction in a flexural composite member and comparison to the variant where no shear connection was provided are shown. The given example consists of a two-material simple supported beam according to Nethercot [127], where next to the given beam examples, strains distribution diagrams are given in composite cross-sections.

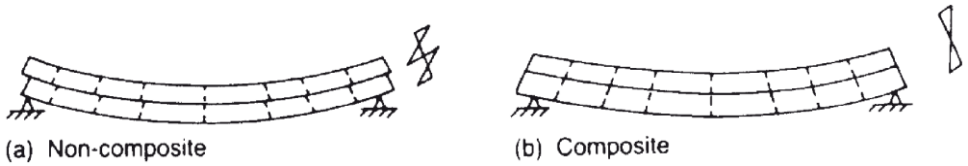
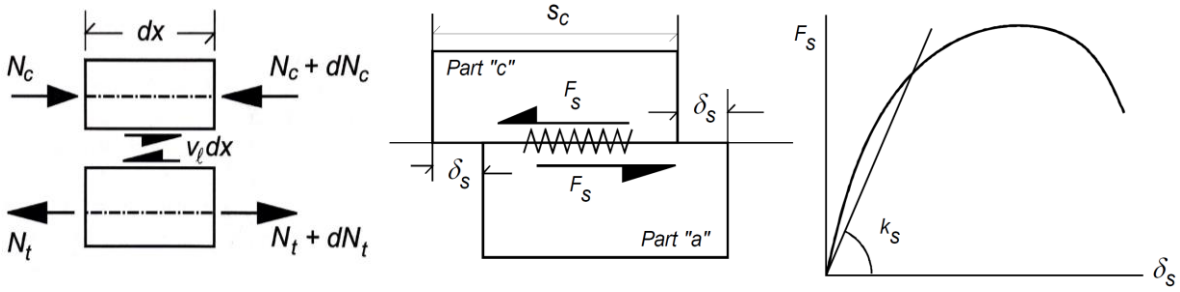


Fig. 3.1. Composite action on the example of simple supported two material beam – a) non-composite case and b) composite case with full interaction. (Source: Nethercot [127]).

In some cases, mainly for the simplified design purposes, the composite theory is considered with an assumed plastic distribution of stresses [58]. Application of the composite theory for the plastic design

requires sufficient ductility of the shear connection in order to allow for the redistribution of forces. In the result, in order to benefit from the composite behaviour and assure the simplified design process, the applied shear connection should provide a high initial stiffness and a wide range of ductility after exhibiting the maximum level of utilisation.

According to the identified-above character of the composite action, it can be observed that three the most important aspects in the flexural response that define the structural behaviour of a composite member are: (1) the shear connection, which defines the composite action, (2) the number and positions of neutral axes in a composite cross-section and (3) the resultant effective flexural stiffness of a composite member, which directly defines its structural performance.



a) b) c)

Fig. 3.2. Definition of the shear flow – a) development model, b) connection model and c) general connection force-slip diagram. (Source: Leskelä [110]).

$$v_l\,dx = dN, \qquad dN = |dN_c| = |dN_t|, \qquad v_l = \frac{dN}{dx} \tag{3.1}$$

The shear connection can be defined as the interface property, which resists the relative slip between two corresponding points on contact surfaces caused by the strains differences in these parts. The resultant force developed at the interface is commonly called the shear flow v_l and it refers to the area of contact interface. The shear flow refers to the longitudinal direction of composed parts and it is related to the change in the normal forces of each part as shown in Fig. 3.2 and described by Eq. 3.1. The applied shear connection resists the development of the relative slip δ_s and it can be characterised by the force-slip curve as shown in Fig. 3.2c. According to the defined behaviour, the shear connection can be classified as a ductile, rigid, brittle, softening, plastic and hardening as shown in Fig. 3.3.

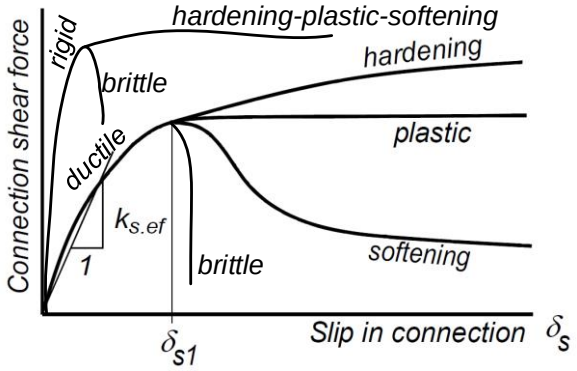


Fig. 3.3. Classification of the shear connection behaviour. (Adapted from: Leskelä [110]).

The full shear connection at the interface of an elastic flexural composite member results in the condition that the resultant curvature is the same in each part; therefore, the principle for the evaluation of effective bending stiffness of a composite section can be derived by using the fundamental relation for the beam curvature of flexural members [184] given in Eq. 3.2. From the forces equilibrium condition, the resultant relation for the evaluation of composite bending stiffness is given in Eq. 3.3.

$$\kappa_j = \frac{M}{(EI)_j} = \frac{M}{(EI)_{com}} \tag{3.2}$$

$$(EI)_{com} = \sum_{j=1}^{k} E_j I_j = \sum_{j=1}^{k} (EI)_j \tag{3.3}$$

The method shown above considers a general global bending model for the evaluation of the effective bending stiffness of a composite cross-section, where a conservative value of the composite bending stiffness equal to the sum of stiffnesses of the subsequent parts is obtained. In example according to Leskelä [110] shown in Fig. 3.4, the distance between centroids e_i of two parts "c" and "a" can be distinguished, where due to the global bending, the resultant normal forces N_a and N_c subjected to their centroids with opposite directions and bending moments M_a and M_c are inducted. Taking into account the full shear connection, the condition for the strain correlation at the interface "j" is given in Eq. 3.4. By considering the analysed example of a composite member as an elastic Euler-Bernoulli beam, the strains in each part are described in Eq. 3.5-3.6 as the resultants of internal forces. In the result, Eq. 3.4 can be transformed into Eq. 3.7, which defines the equilibrium of strains in each part.

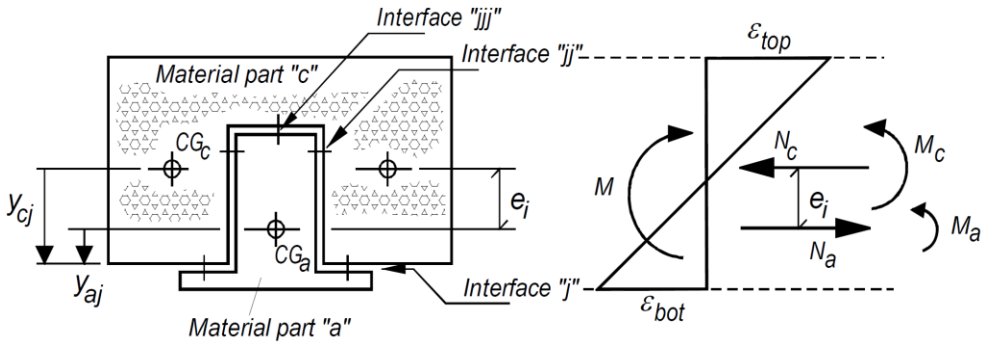


Fig. 3.4. A composite cross-section of two material parts with full shear connection and subjected to pure bending. (Source: Leskelä [110]).

$$\Delta\varepsilon_j = \varepsilon_{cj} - \varepsilon_{aj} = 0 \tag{3.4}$$

$$\varepsilon_{cj} = \frac{N_c}{(EA)_c} + \frac{M_c y_{cj}}{(EI)_c} \tag{3.5}$$

$$\varepsilon_{aj} = \frac{N_a}{(EA)_a} + \frac{M_a y_{aj}}{(EI)_a} \tag{3.6}$$

$$\frac{N_a}{(EA)_a} + \frac{M_a y_{aj}}{(EI)_a} = \frac{N_c}{(EA)_c} + \frac{M_c y_{cj}}{(EI)_c} \tag{3.7}$$

By applying the condition for the equilibrium of horizontal forces $N = N_a = -N_c$, Eq. 3.7 is transformed into Eq. 3.8. Due to the correlation of beam curvatures of each composed part, the relations given in Eq. 3.9 are respected. Finally, by applying Eq. 3.9 into Eq. 3.8, the resultant relation is obtained in Eq. 3.10, where $(EA)_{a+c} = (EA)_a + (EA)_c$ and $(EI)_{a+c} = (EI)_a + (EI)_c$.

$$N\left(\frac{1}{(EA)_c} + \frac{1}{(EA)_a}\right) = \frac{M_c y_{cj}}{(EI)_c} - \frac{M_a y_{aj}}{(EI)_a} \tag{3.8}$$

$$\frac{M_a}{(EI)_a} = \frac{M_c}{(EI)_c} = \frac{M}{(EI)_{com}} \quad \text{from which} \quad M_a = M\frac{(EI)_a}{(EI)_{com}} \text{ and } \quad M_c = M\frac{(EI)_c}{(EI)_{com}} \tag{3.9}$$

$$N\frac{(EA)_{a+c}}{(EA)_a(EA)_c} = \frac{M(y_{cj} - y_{aj})}{(EI)_{com}} = \frac{Me_i}{(EI)_{com}} \tag{3.10}$$

Considering the equilibrium of forces described in Fig. 3.4 in terms of bending moments, the equilibrium condition from Eq. 3.11 has to be respected. In order to derive the composite effective bending stiffness given in Eq. 3.12, the relations given in Eq. 3.9 and Eq. 3.10 are applied to Eq. 3.11. Eq. 3.12 can be simplified to Eq. 3.13 by defining the composite stiffness parameter α_i.

$$M = M_a + M_c + Ne_i \tag{3.11}$$

$$(EI)_{com} = {e_i}^2\frac{(EA)_a(EA)_c}{(EA)_{a+c}} + (EI)_{a+c} \tag{3.12}$$

$$(EI)_{com} = (1 + \alpha_i)(EI)_{a+c} \quad \text{, where} \quad \alpha_i = \frac{{e_i}^2}{(EI)_{a+c}}\frac{(EA)_a(EA)_c}{(EA)_{a+c}} \tag{3.13}$$

The identified composite stiffness factor α_i directly indicates an increase in composite stiffness due to the applied shear connection. When no shear connection is applied, the $\alpha_i = 0$ and the composite stiffness is equal to the sum of stiffnesses of composing parts $(EI)_{com} = (EI)_{a+c}$. In addition, when the distance between the centroids of two composing parts is equal to zero $e_i = 0$, for example in double symmetric cross-sections of composite columns, the composite stiffness factor also reaches zero value $\alpha_i = 0$ and the composite stiffness not contributes from the enforcement effects.

The relative slip at the steel-concrete interface of a composite member can be evaluated in reference to the characteristic behaviour of the shear connection and the effective composite stiffness discussed earlier. The relative slip at the interface "j" can be defined as the difference in strains between the two parts over the considered length of a member (dx). The resultant equation for the evaluation of slip is given in Eq. 3.14 below. It can be observed that change in the slip over the considered length is related to the distribution of bending moment over the considered member and distance between the centroids of two parts, which compose the composite cross-section, see Fig. 3.5.

$$d\delta_s = (\varepsilon_{cj} - \varepsilon_{aj})dx = \frac{Me_i}{(EI)_{a+c}}dx \tag{3.14}$$

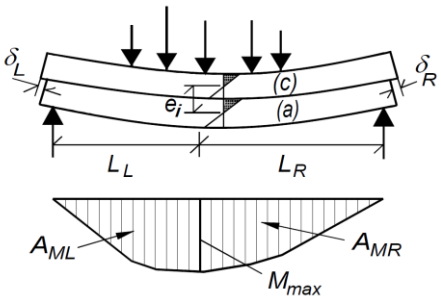


Fig. 3.5. Relative slip in a beam composed from two materials and subjected to bending. (Source: Leskelä [110]).

According to Eq. 3.14, it can be observed that if centroids of two parts are overlapping, the relative slip will be always zero ($e_i = 0 \rightarrow d\delta_s = \Delta\varepsilon_j dx = 0$). This remark is essential for the application in double-symmetric composite columns.

The shear flow for the case of full shear connection can be evaluated by considering conditions given in Eq. 3.10 and Eq. 3.12 and solving the equation given in Eq. 3.1. Eq. 3.15 describes the relation for the developed normal force in each part, which is changing over the length of a beam with relation to the acting bending moment. In the result, by placing Eq. 3.15 into Eq. 3.1, the resultant shear flow is defined by differentiating the developed normal force over the length of a beam as given in Eq. 3.16.

$$N(x) = \frac{M(x)e_i}{(EI)_{com}} \frac{(EA)_a (EA)_c}{(EA)_{a+c}} = \frac{M(x)}{e_i} \frac{\alpha_i}{1+\alpha_i} \tag{3.15}$$

$$v_l(x)dx = dN(x) \rightarrow v_l(x) = \frac{dN(x)}{dx} = \frac{1}{e_i} \frac{\alpha_i}{1+\alpha_i} \frac{dM(x)}{dx} = \frac{1}{e_i} \frac{\alpha_i}{1+\alpha_i} V(x) \quad \left[\frac{kN}{cm}\right] \tag{3.16}$$

From Eq. 3.16, it can be observed that the shear flow developed at the interface of two composing parts is related to the vertical shear forces acting in a composite member. The equation given in Eq. 3.16 can be simplified to Eq. 3.19 by applying relations given in Eq.3.17-3.18, where e_{ao} and e_{co} are distances from centroids of each part to the centroid of composite section.

$$e_{ao} = \frac{(EA)_c}{(EA)_{a+c}} e_i \qquad \text{and} \qquad e_{co} = \frac{(EA)_a}{(EA)_{a+c}} e_i \tag{3.17}$$

$$v_l{}^1 = \frac{1}{e_i} \frac{\alpha_i}{1+\alpha_i} = \frac{e_{ao}(EA)_a}{(EI)_{com}} = \frac{e_{co}(EA)_c}{(EI)_{com}} \quad \left[\frac{1}{cm}\right] \tag{3.18}$$

$$v_l = v_l{}^1 V \quad \left[\frac{kN}{cm}\right] \tag{3.19}$$

The shear flow evaluated in Eq. 3.16 or Eq. 3.19 is considered for the case of continuous shear connection and it refers to the unit length of interface. For local shear connections, the condition given in Eq. 3.16 has to be integrated over the length L_l between the place of maximum curvature and the place where the relative slip is blocked, e.g. from the mid-span to the end of a beam. In the result, the relation given in Eq. 3.20 is defined. Eq. 3.21 presents the evaluated form of Eq. 3.20. Factor ψ, where $0 \leq \psi \leq 1$, defines if the entire relative slip will be removed or only a certain part of it.

$$\int v_l(x)dx = \int \frac{dN(x)}{dx}dx \rightarrow V_l = \frac{e_i}{(EI)_{com}} \frac{(EA)_a(EA)_c}{(EA)_{a+c}} \int \frac{dM(x)}{dx}dx \tag{3.20}$$

$$V_l = \psi \frac{A_{M,l}}{L_l} \frac{e_i}{(EI)_{com}} \frac{(EA)_a(EA)_c}{(EA)_{a+c}} \tag{3.21}$$

From Eq. 3.16, Eq. 3.18-3.19 and Eq. 3.21, it can be observed that if the distance between the centroids of the composing parts in composite cross-section e_i is equal to zero, the resultant shear flow and shear connection forces are set to zero as well.

A similar observation that the shear flow is related to the vertical shear forces has been taken by Johnson [89]. By assuming the composite section as a homogenous isotropic elastic material, it can be observed that the elastic shear stresses evaluated according to the principal definition given in Eq. 3.22 have their associated complementary shear stresses at the right angle with equal values as shown in Fig. 3.6 and Eq. 3.23. The associated perpendicular stresses are considered as the shear flow occurring at the interface and its value can be evaluated according to Eq. 3.22. It can be observed that the method given by Johnson [89] gives a much more practical approach for the evaluation of shear flow but also brings a strongly simplified and conservative evaluation in comparison to method given by Leskelä [110].

$$\tau = \frac{V}{A_v} = \frac{VS}{It} \tag{3.22}$$

$$\left|(\tau_{xy})_1\right| = \left|(\tau_{xy})_2\right| = \left|(\tau_{xy})_3\right| = \left|(\tau_{xy})_4\right| \tag{3.23}$$

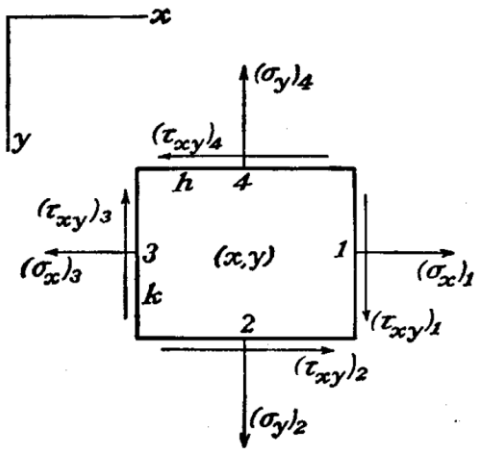


Fig. 3.6. Plane problem of a stress state in a unit rectangular block of elastic material. (Source: Timoshenko [184])

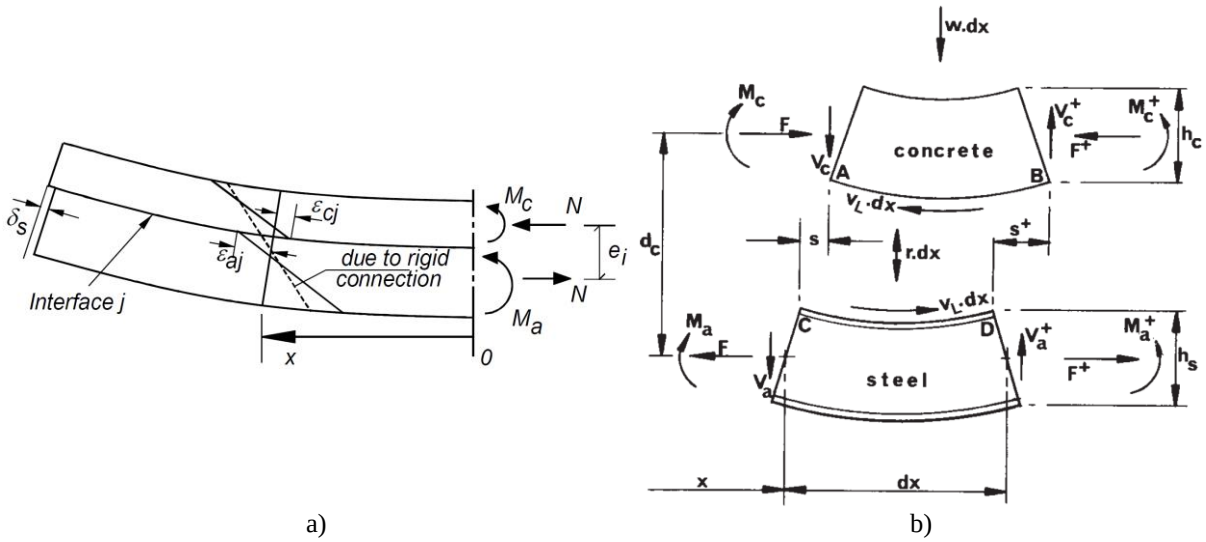
Based on the principal definition of the longitudinal shear (shear flow) given in Eq. 3.1, it can be concluded that maximum possible developed shear forces in the shear connection will be equal to the tensile/compression resistance of the weaker from composing parts. According to the aforementioned remark, a common practice for the evaluation of the required shear connection resistance is to set it equal to the tensile resistance of the steel part in a composite cross-section. Like this, the number of required mechanical shear connectors is easily evaluated in the conservative way.

3.1.2. Partial interaction

In the previous Section 3.1.1, the cases of full shear connection and no shear connection were considered in order to define the behaviour of a composite member according to the composite theory. The term of full shear connection is rather theoretical than practical since achieving a perfectly rigid shear connection is impossible – eventually, effects of slip can be small and have negligible impact on the composite behaviour. When in shear connection, a certain level of slip is allowed to develop, we are saying about partial shear connection. The partial shear connection allows for the development of a difference in strain at the interface of both composing parts in composite cross-section and release condition defined in Eq. 3.4 as given in Eq. 3.24 below. However, the partial shear connection still restrains development of the relative slip and the resultant value of straining $\Delta\varepsilon_j$ will be smaller than in the case of no shear connection $\Delta\varepsilon_{j,max}$. The resultant difference in strains at the interface is related to the stiffness of shear connection and it can be defined as the connection ductility. A change in the connection ductility, affects the resultant effective composite bending stiffness $(EI)_{com,eff}$, which can be defined in the same form as given in Eq. 3.13 but a new effective composite stiffness parameter $\alpha_{i,eff} \leq \alpha_i$ is employed, see Eq. 3.25. The new effective composite stiffness parameter reaches its maximum value of α_i when the straining at the interface $\Delta\varepsilon_j$ is set to zero.

$$\Delta\varepsilon_j(x) = \varepsilon_{cj}(x) - \varepsilon_{aj}(x) \neq 0 \tag{3.24}$$

$$(EI)_{com,eff}(x) = (EI)\left(\Delta\varepsilon_j(x)\right) = \left(1 + \alpha_{i,eff}(x)\right)(EI)_{a+c} \tag{3.25}$$



a) b)

Fig. 3.7. A composite beam with flexible shear connection – a) strains distribution (Source: Leskelä [110]) and b) internal forces equilibrium (Source: Johnson [89]).

By considering the difference in strains at the interface of two parts as shown in Fig. 3.7a and respecting the relation of the same curvature in a composite cross-section, the stress resultant can be related to the acting bending moment analogous to Eq. 3.15 and the new effective relation is given in Eq. 3.26 below.

$$N(x) = N\left(\Delta\varepsilon_j(x)\right) = \frac{M(x)}{e_i}\frac{\alpha_{i,eff}}{1+\alpha_{i,eff}} \tag{3.26}$$

According to Leskelä [110] the effective stiffness parameter $\alpha_{i,eff}$ can be defined by Eq. 3.27 and by following his example, it can be related to the flexibility parameter r_δ, which, in turn, is the ratio between the maximum present slip $\delta_{s,max}$ to the maximum slip for the case of no shear connection $\delta_{s0,max}$, see Eq. 3.28 and Eq. 3.29.

$$\alpha_{i,eff} = \alpha_i\left(1 - \frac{\Delta\varepsilon_{j,max}}{\kappa_{max}e_i}\right) \tag{3.27}$$

$$\alpha_{i,eff} = \frac{1-r_\delta}{1+\alpha_i r_\delta}\alpha_i \tag{3.28}$$

$$r_\delta = \frac{\delta_{s,max}}{\delta_{s0,max}} \tag{3.29}$$

In order to define the flexibility parameter given in Eq. 3.29, a shear connection stiffness has to be considered. By assuming a constant stiffness of the shear connection K_{sc} over the entire length of a beam, the relation given in Eq. 3.30 correlates the shear flow with the corresponding slip.

$$v_l(x) = K_{sc}\delta_s(x) \tag{3.30}$$

Finally, the normal forces in composing parts $N(x)$ have to be in equilibrium with the developed shear connection forces within the connection length "s", $\int v_l(s)ds$ (e.g. from the mid-span to the end of a beam). Thus, by assuming a maximum developed slip $\delta_{s,max}$, the maximum developed forces N_{max} given in Eq. 3.31 are related to the acting bending moment according to Eq. 3.26. In the result, relations given in Eq. 3.32 can be derived from which the flexibility parameter can be resolved in Eq. 3.33, where the value of $\mu_m = \gamma/\beta$ depends on the bending moment diagram, refer to [110].

$$N_{max} = \gamma K_{sc}\delta_{s,max}L \tag{3.31}$$

$$\frac{\alpha_{i,eff}}{1+\alpha_{i,eff}} = (1-r_\delta)\frac{\alpha_i}{1+\alpha_i} \quad \text{and} \quad \frac{M_{max}}{e_i} = \frac{\beta}{{e_i}^2}\frac{(EI)_{a+c}}{L}\delta_{s0,max} \tag{3.32}$$

$$r_\delta = \frac{1}{1+\mu_m\frac{K_{sc}L^2{e_i}^2}{(EI)_{a+c}}\cdot\frac{\alpha_i+1}{\alpha_i}} = \frac{\frac{\alpha_i}{\alpha_i+1}\frac{(EI)_{a+c}}{{e_i}^2}}{\frac{\alpha_i}{\alpha_i+1}\frac{(EI)_{a+c}}{{e_i}^2}+\mu_m K_{sc}L^2} \tag{3.33}$$

The term $\mu_m K_{sc}L^2$ in Eq. 3.33 represents the density of the shear connection. It can be observed that if the density rise, the end slip decreases. Moreover, the density is proportional to the span length due to the constitutive relation of connection stiffness $K_{sc}L^2 = k_s L^2/s_c$, therefore, with an increase of span length L the density rises but with increase of connection length s_c (span between shear connectors) the density decreases. The stiffness of one connector is represented by k_s.

3.1.3. Composite columns

The steel-concrete composite columns are flexural members subjected mainly to compression forces. Three main groups of composite columns due to the geometry of cross-section can be distinguished (classification according to Roik and Bergmann [159]): (i) with fully encased steel profiles, (ii) with partially encased steel profiles and (iii) with concrete filled hollow steel sections, see Fig. 3.8. Examples with combined cross-sections, e.g. concrete filled hollow sections with embedded inside steel profiles, can be identified as well. According to practical aspects, the composite theory defined-above in Section 3.1.1-3.1.2 and a simplification of the analysis, all the composite columns should have, but are not limited to, the double-symmetric and constant cross-sections over the length of a column. As discussed earlier in Section 3.1.1, the double-symmetry results in the prevented relative slip between the steel and concrete materials in bending for the uncracked concrete state. Moreover, a double-symmetry condition assures the same flexural performance in both ways of one bending direction. The bi-axial bending case can be analysed as the bi-directional interaction of both flexural performances [12, 160].

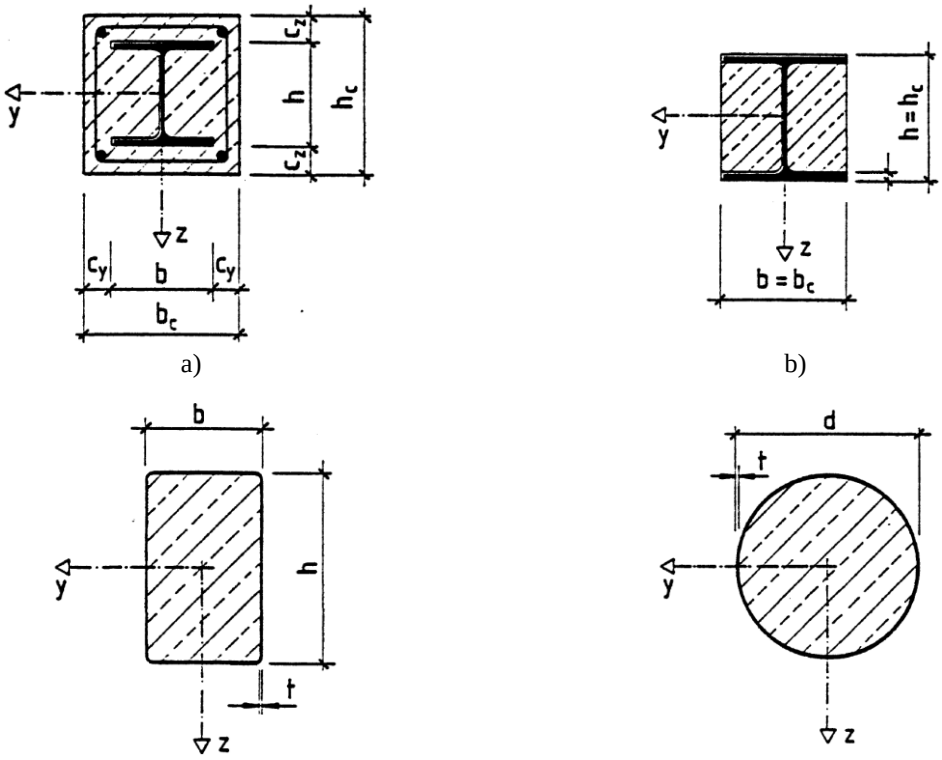


Fig. 3.8. Typical cross-sections of composite columns – a) fully encased steel profiles, b) partially encased steel profiles, c) filled rectangular steel tubes and d) filled circular steel tubes. (Source: Roik/Bergmann [159]).

The design of composite columns can be made according to the procedure based on the N-M interaction curves and with reference to the acting loads [12]. A simplified method is normally used in practice [110, 159], where plastic stress distribution over a composite cross-section is assumed. The usage of plastic stress distribution requires plastic deformations in steel and concrete. The elastic instabilities in steel parts should be prevented. In addition, the contribution of reinforcement bars can be included in the plastic design only when the buckling would not develop before their plastification. This

method has been adapted in the current European design code for composite structures EN 1994-1-1 [58] and it is described later more in detail in Section 3.4.3. The verification of single-symmetric composite cross-sections, examples shown in Fig. 3.9, can be made analogically to the double-symmetric cases as described by Roik and Bergmann [158] but an additional plastic eccentricity due to the change of the position of neutral axis in a composite cross-section has to be considered.

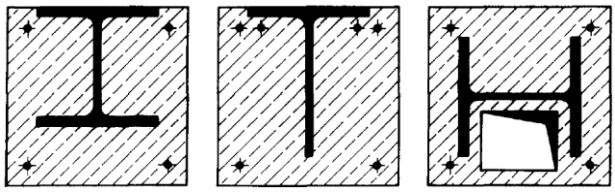


Fig. 3.9. Single-symmetric cross-sections of composite columns. (Source: Roik/Bergmann [158]).

Composite columns are vulnerable to instability and second-order effects. However, the failure mode due to the elastic buckling is possible only for slender columns, where $\bar{\lambda} > 2$ [159]. Normally, this is only a case for very slender columns. Nevertheless, geometrical imperfections of a column member and second-order effects can greatly enhance the first order bending moments, which can lead to the plastic failure of a column due to the combined bending and compression. These two aspects can be evaluated directly as described for example by Leskelä [110], Roik et al. [160] or Bergmann [12], where the buckling verification and elastic instability behaviour analysis are analogous to a typical steel column problem, which is described in detail by Petersen [144]. However, the second-order effects and member imperfections can be included in the analysis of a composite column in a simplified way by modifying the effective composite stiffness, including amplification factors for the first-order bending moments and by applying the European buckling curves together with buckling verification procedure [110, 159].

The idea of simplification to the plastic block stress distribution diagram is shown in Fig. 3.10. It can be observed that applied material laws defines a specific stress distribution in a composite cross-section. In addition, the internal lever arm between the realistic pair of resultant tension and compression forces due to bending z_{real} is bigger then in the case of plastic block distribution z_{sb}. However, according to Leskelä [110], the plastic block distribution is reliable due to the similar resulting plastic bending moment value as given in Eq. 3.34 because $F_{t,sb} = F_{c,sb} > F_{t,real} = F_{c,real}$.

$$M_{pl,Rd} = F_{t,real} \cdot z_{real} \approx F_{t,sb} \cdot z_{sb} \tag{3.34}$$

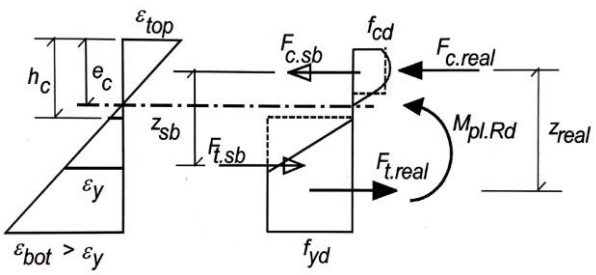


Fig. 3.10. Comparison of elasto-plastic and plastic block stress distributions in composite column cross-section. (Source: Leskela [110]).

The transversal shear in a composite column cross-section is split between the steel and concrete parts with relation to their bending stiffnesses according to the assumption about the same curvature in a composite cross-section, see Section 3.1.1. In the result, each part has to be able to resist the distributed shear separately. Impact of the acting significant transversal shear forces on the resistance of a composite cross-section is discussed later in Section 3.4.

In the composite theory described in Section 3.1.1-3.1.2, it has been identified that in flexural composite members with double-symmetric cross-sections, where the centroids of both parts are overlapping, the resultant longitudinal shear flow will not develop due to bending. This case reflects well a typical composite column. However, this assumption is only valid for the uncracked concrete state. When the concrete crack, the active concrete area will change and the centroid of concrete part will move away from its initial position. However, the developed centroid eccentricity e_i will be very small due to the existence of the reinforcement, therefore, the resultant local shear flow will be small as well. In practice, the induced shear flow due to concrete cracking is neglected [110]. On the other hand, the longitudinal shear flow is related to the developed transversal shear stresses based on the theory of elastic materials, as shown in Fig. 3.6, and can be evaluated according to Eq. 3.22.

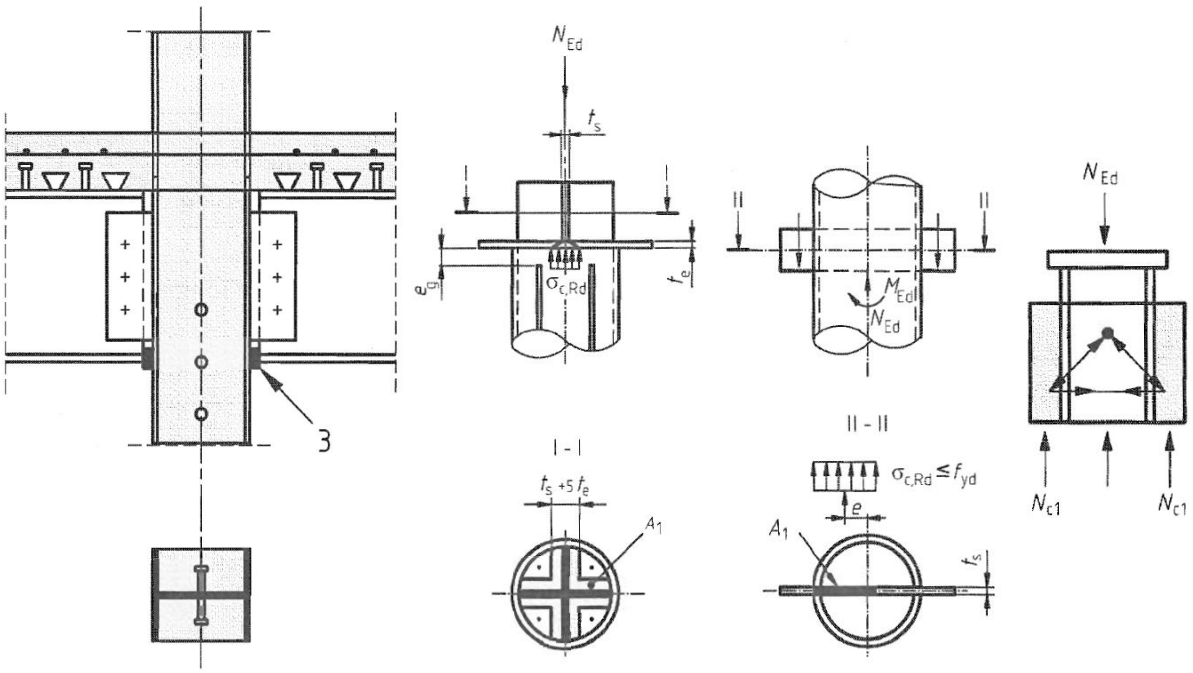
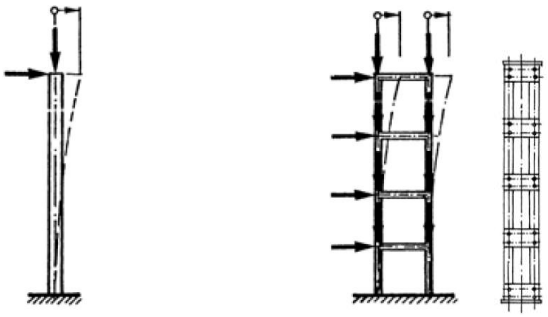


Fig. 3.11. Load introduction to steel-concrete composite columns. (Source: EN 1994-1-1 [58]).

Normally, loads from horizontal structural systems of a building (for example floor beams) are introduced to a composite column through the steel or concrete parts as shown in Fig. 3.11. The introduced vertical load has to be distributed to the entire composite cross-section by the shear connection in a load introduction zones. The developed shear forces between steel and concrete have to be resisted by the steel-concrete bond or by the applied mechanical shear connectors.

3.2. Beam and Truss Theories

A column can be defined as a three-dimensional load bearing compressed flexural member with a one direction significantly bigger than two other directions. With respect to the structural system, two main types of columns can be distinguished: (i) with solid section and (ii) of lattice system, like truss towers or build up members, see Fig. 3.12. In both cases, the global behaviour is normally described by the beam theories. However, the internal force transfer, stiffness and local behaviour can be described either by the beam theories or by the truss theories with respect of the used system.



a) b)

Fig. 3.12. Types of structural systems of columns – a) solid and b) lattice. (Adapted from Petersen [144]).

Regular steel-concrete composite columns are analysed as the common Euler-Bernoulli beams [110, 159]. In the case, when the effects of shear significantly contribute to the resultant curvature of a beam, or the composite action at the steel-concrete interface is harmed, the structural behaviour of a column member corresponds to the Timoshenko beam theory [183, 184].

Truss system analogies are commonly used is the reinforced concrete structures in order to describe the distribution of internal forces [168, 169]. The same truss analogy method applies to the composite structures in order to describe the distribution of forces in concrete from embedded steel bearing parts. Details about the mentioned strut-and-tie method are given in Section 3.4.5 and the principles of the truss system are given in Section 3.2.2. Another reference to the truss system analogy can be identified in the heavy steel-concrete composite columns with multiple encased steel profiles, where the Mörsch truss model can be used to describe the distribution of forces inside the composite member and between the embedded steel profiles [175]. However, in the conducted research, a divergence from the typically assumed truss system has been identified towards the Vierendeel truss system.

3.2.1. Beam theories

3.2.1.1. Euler-Bernoulli beam theory

The Euler-Bernoulli beam theory describes the flexural and axial behaviour of three-dimensional isotropic slender beams made of elastic material and subjected to small deformations due to pure bending. The effects of shear on the beam deformation are negligible. The resultant relation between the beam curvature and the bending moment can be described as given in Eq. 3.35. The differential

equations of the beam deformation curve are defined in Eq. 3.36. The detailed information about the Euler-Bernoulli beam theory and theory of elasticity can be found among others in [183, 184].

$$\kappa = \frac{1}{r} = \frac{M}{EI} \tag{3.35}$$

$$EI_z \frac{d^2y}{dx^2} = -M(x) \tag{3.36}$$

The application of the Euler-Bernoulli beam theory requires the following main assumptions:

- The theory of elasticity defines the material behaviour and the Hooke's law apply
- The Navier's assumption about plane sections that remain plane after the deformation apply
- Sections of a beam are always perpendicular to the neutral axis, also after the deformation
- Sections of beams are constant and do not deform under the applied load
- Through the entire length, beams consist of a constant cross-section

3.2.1.2. Timoshenko beam theory

The Timoshenko beam theory includes the shear deformation of a flexural member and it is a general case of the Euler-Bernoulli beam theory [183, 184]. The initially plain sections are no longer remain plain after the deformation due to the shear deformation of adjacent cross-sections along each other as shown in Fig. 3.13. At sections centroids, the shear strains and the slope of the deflection curve due to pure shear are equal. This fundamental relation for Timoshenko beam is described in Eq. 3.37, where y_1 reflects the shear part of the deflection, A_v is the effective shear area of a cross-section, G is the shear modulus defined according to the theory of elasticity and ν is the Poisson's ratio.

$$\frac{dy_1}{dx} = \frac{(\tau_{yx})_{y=0}}{G} = \frac{V(x)}{A_v G} \quad \text{, where} \quad G = \frac{2(1+\nu)}{E} \tag{3.37}$$

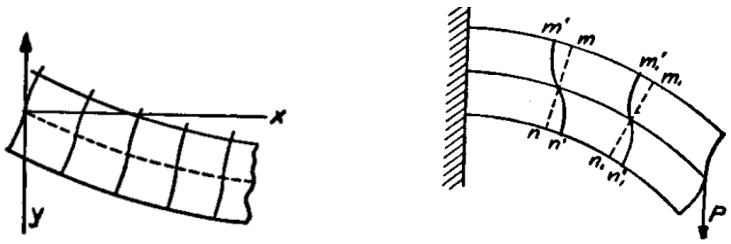


Fig. 3.13. Shear deformation in the Timoshenko beam. (Source: Timoshenko [183]).

According to the relation defined in Eq. 3.37, the relation for the beam curvature due to the pure shear is defined in Eq. 3.38. The resultant differential equation of a beam is defined in Eq. 3.39.

$$\kappa_1 = \frac{d^2y_1}{dx^2} = \frac{1}{A_v G}\frac{dV(x)}{dx} = -\frac{q(x)}{A_v G} \tag{3.38}$$

$$\frac{d^2y}{dx^2} = -\frac{M(x)}{EI_z} - \frac{q(x)}{A_v G} = -\frac{1}{EI_z}\left(M(x) + \frac{EI_z}{A_v G}q(x)\right) \tag{3.39}$$

3.2.2. Truss theories

3.2.2.1. Principal theory of trusses

The truss is a framed construction composed by a number of connected slender members with one dominating dimension (length). Each truss member is statically considered as a two-dimensional element with no flexural stiffness. In the result, only axial forces, tension or compression, are considered and their respective axial stiffnesses define the structural behaviour of the entire truss system [182]. In the analysis of a truss, each node is represented as a hinge. Internal forces in all truss elements are assumed to be parallel to the longitudinal axes of respective truss members and they are acting in the centroids of their cross-sections. Standard types of truss examples are shown in Fig. 3.14.

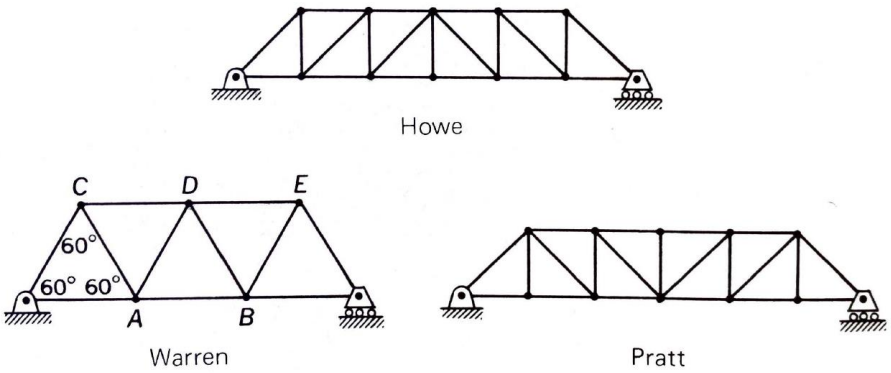


Fig. 3.14. Typical examples of parallel-chord truss systems. (Source: Thrower [182]).

The truss structures has to satisfy two equilibrium conditions, the first, global, where the imposed loads and reactions at supports (boundary conditions) have to be in the equilibrium and the second, local, where each node at a connection point between truss members has to be in the equilibrium, see Fig. 3.15. In order to define the global equilibrium of a truss, the entire system can be considered as a beam.

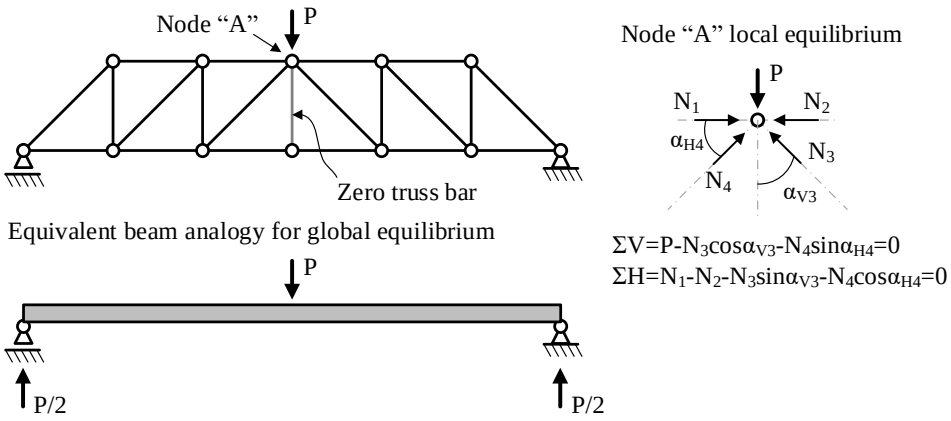


Fig. 3.15. Global and local equilibrium states in a truss system.

Considering the truss system analogy in a beam, which is subjected to bending and shear load, the distribution of loads into the axial forces in truss members are as shown in Fig. 3.16. The bending moment is distributed between two chords, where the shear load is fully taken by the diagonal strut.

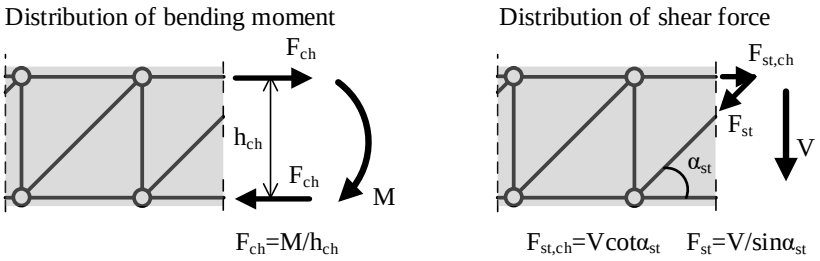


Fig. 3.16. Distribution of forces into truss elements acting on an equivalent beam – analogy to the Mörsch truss.

The deflection of a truss structure can be evaluated according to the principle of the virtual work. This is an energetic method based on the accumulated energy of strains. The relation between the strain energies and virtual work done by the external load can be formulated in Eq. 3.40.

$$\delta = \int \frac{\bar{N}(x)N(x)}{EA}dx + \int \frac{\bar{Q}(x)Q(x)}{GA_v}dx + \int \frac{\bar{M}(x)M(x)}{EI}dx \tag{3.40}$$

3.2.2.2. Vierendeel truss theory

The Vierendeel truss is a specific case of a truss system, which consist of rigid connections between the truss elements, no diagonal struts and only vertical posts as shown in Fig. 3.17-3.18. In regular Vierendeel trusses, the span between vertical posts is constant and the flexural stiffness of chords is much bigger than of posts. Sections and material properties of each group of members are constant. Due to the rigid connection at each node, in contrary to the regular truss systems, in parallel to axial forces, shear forces and bending moments are present in the Vierendeel truss elements as shown in Fig. 3.18.



Fig. 3.17. Vierendeel truss bridge designed by Arthur Vierendeel in 1898, Brussels. (Source: Odenbreit [131]).

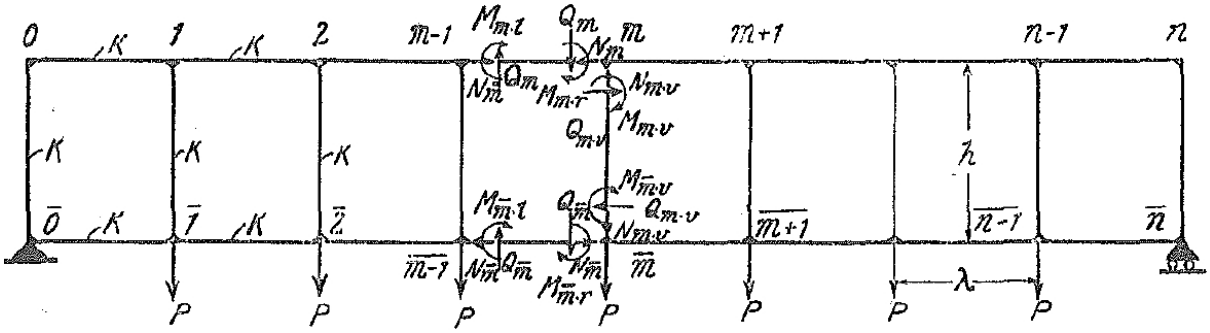


Fig. 3.18. Example of a Vierendeel truss system with denoted internal forces. (Source: Sakai [166]).

The Vierendeel truss can be considered as a simple supported beam in order to establish the global equilibrium of forces, where the correlating global forces distribution diagrams are obtained for bending

moments and transversal forces as shown in Fig. 3.19. In the Vierendeel truss elements, a characteristic local distribution of bending moments can be observed, where the antisymmetric character is present to assure equilibrium of forces at each node. The bending moment diagrams are striving to zero value at the mid-spans of each element and theoretical hinges can be assumed accordingly as shown in Fig. 3.19.

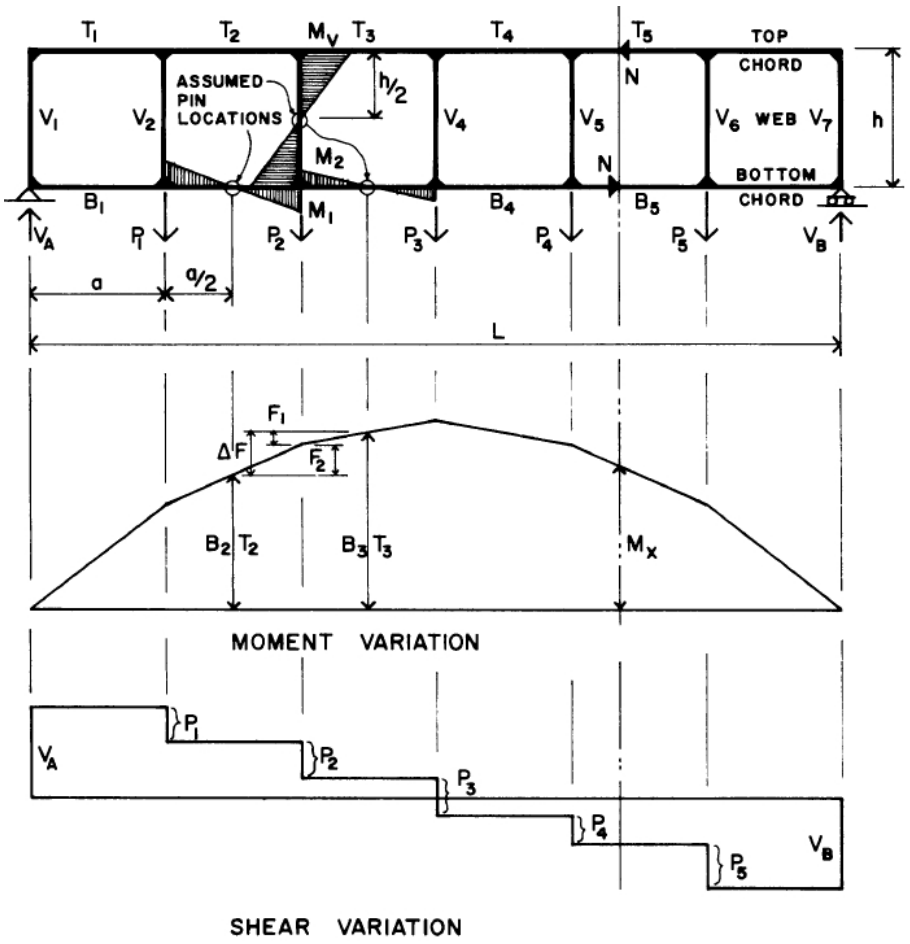


Fig. 3.19. Global distribution of forces and identification of the theoretical hinges in Vierendeel truss elements. (Source: Wickersheimer [201]).

According to the defined global equilibrium of forces and their local distributions, the internal forces in each truss element can be evaluated by applying Eq. 3.41-3.45, described also in Fig. 3.20.

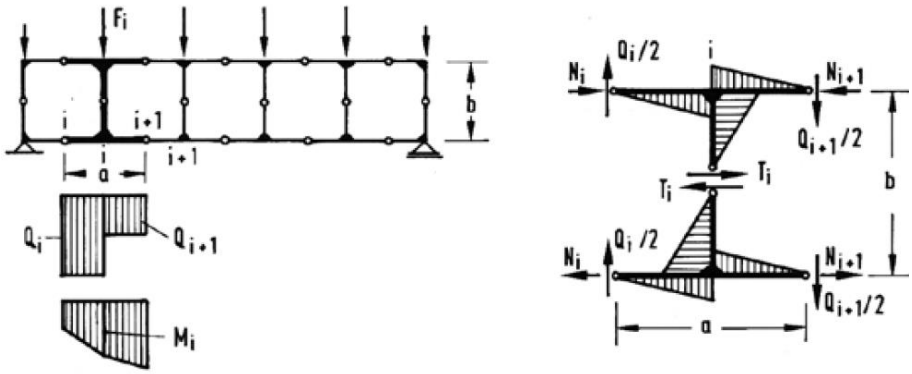


Fig. 3.20. Internal forces distribution in a Vierendeel truss. (Source: Petersen [145]).

$$N_i = \frac{M_{i-1} + M_i}{2b} \tag{3.41}$$

$$N_{i+1} = \frac{M_i + M_{i+1}}{2b} \tag{3.42}$$

$$T_i = \left(\frac{Q_i}{2} + \frac{Q_{i+1}}{2}\right)\frac{a}{b} \tag{3.43}$$

$$M_{i,H} = \frac{Q_i}{2}\frac{a}{2} = \frac{Q_i a}{4} \tag{3.44}$$

$$M_{i,V} = \frac{T_i}{2}\frac{b}{2} = \frac{T_i b}{4} \tag{3.45}$$

Shear forces Q_i are equally distributed on both chords of a Vierendeel truss by $Q_i/2$ and their value if derived from the global distribution of shear forces. Similar origin of the longitudinal forces in the chords N_i can be observed due to the global bending moment distribution and it is related to the depth of a truss system b. From the described load-bearing character of the Vierendeel truss elements, it can be observed that chords and posts are active in the transfer of normal forces, shear forces and bending moments. In the result, the structural behaviour of Vierendeel trusses will be defined by the axial, shear and flexural stiffnesses of chords and posts.

The deflection of a Vierendeel truss can be evaluated analogous to the typical truss system with the usage of the principle of virtual work, hence, Eq. 3.40 apply. In contradiction to typical truss systems, the Vierendeel trusses are vulnerable to the shear deformation effects [116, 145, 166], which result in the characteristic S-shape deformation of the vertical posts as shown in Fig. 3.21. The non-linear deformation of posts is related to the existence of internal transversal shear forces and bending moments. Moreover, a big difference between the sectional stiffnesses of chords and posts amplifies the effects of shear deformation in the Vierendeel truss systems. The chords of Vierendeel trusses undergo a characteristic for this type of truss deformation, where, when subjected to sagging bending, chords in the middle zone are following the sagging deflection with dependence on the bending and shear modes. However, close to the supports, the hogging bending deformation can be observed due to the shear effects as shown in Fig. 3.21. It can be observed that the deformation of the Vierendeel trusses is referring to the shear deformation described by the Timoshenko beam theory, see Fig. 3.13.

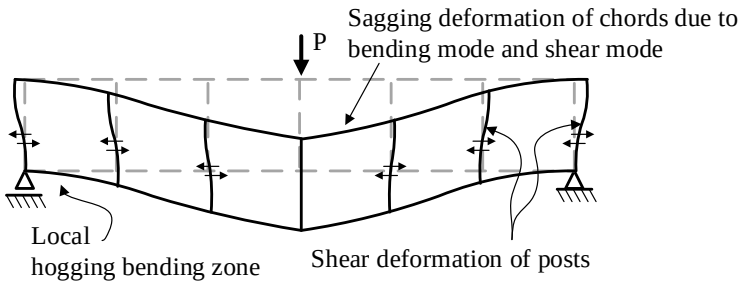


Fig. 3.21. Shear deformation of Vierendeel trusses (extreme case).

MacLeod in his work [116] proposed an approach for the global analysis of the Vierendeel trusses as beam analogy models. The analogous beam element consists of bending and shear stiffnesses and the equivalent beam moment of inertia is calculated according to the Steiner's rule considering only the contribution of chords. The eigenvalues of moment of inertia are neglected, which is a common approach for the parallel chord trusses [116]. The resultant deflection of an equivalent beam can be evaluated according to the Timoshenko beam theory, see Eq. 3.39.

The shear stiffness of an equivalent beam model is evaluated with respect to the principle differential relation between the truss slope, also called rotation, and acting transversal loads, see Eq. 3.37. The displacement of the truss is evaluated according to the principle of virtual work, where as a simplification, MacLoad considers only the bending part of the virtual work, refer Eq. 3.40. The resultant shear stiffness is described in Eq. 3.46, where the parameter of contraflexure ψ is described in Eq. 3.47. Subscripts "c" refer to chords and "p" to posts, value "a" is the span between the posts and value "b" is the span between the chords.

$$K_{sv} = \frac{24 E_c I_c}{a^2 [1 + 2\psi]} \tag{3.46}$$

$$\psi = \frac{I_c / a}{I_p / b} \tag{3.47}$$

In the method proposed by MacLeod [116], the Vierendeel truss elements have to be made from the same material, chords need to be parallel, truss is uniform along its length and the points of contraflexure (theoretical hinges) are in the mid-spans of truss elements. In order to assure the position of contraflexure at the mid-spans, cross-sections of both chords has to be the same. When parameter ψ reaches value higher than 1.0, the points of contraflexure move away from the mid-spans of truss elements.

3.3. Shear connection

3.3.1. Shear transfer phenomena

The shear flow at the steel-concrete interface can be resisted by (1) steel-concrete bond and (2) mechanical shear connection means [58, 110]. Steel-concrete bond is a natural property of the interface between the steel and concrete materials, which prevents the relative displacement and can transfer shear and normal forces within its resistance limit. Under the definition of steel-concrete bond, three internal mechanisms can be identified: (i) the chemical adhesion, (ii) the Coulomb friction and (iii) the surface roughness friction [66], see Fig. 3.22. The Coulomb friction phenomenon correlates the lateral pressure to the longitudinal frictional resistance at the contact interface between two specific materials [182]. The developed frictional forces are with respect to the corresponding static friction ratio μ, which is a contact surface property and it differs between materials in contact and contact surface treatments.

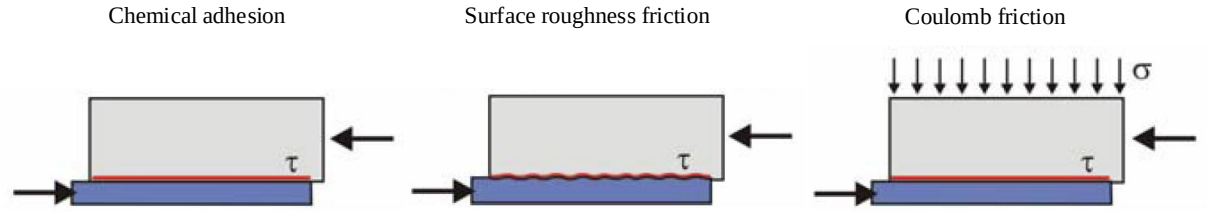


Fig. 3.22. Force transfer mechanisms contributing to steel-concrete bond. (Adapted from Goralski [66]).

The definition of the chemical adhesion term can be found as the ionic, covalent or hydrogen bonds, which are based on the connections that occurs when electrons of particles on two coincident surfaces are shared or swept. On the other hand, in the work of Kendall [94] on the adhesion of particles and Maugis [120] on solid bodies, it is described that the bonded connection can be achieved when two bodies (cells) are in a very close contact to each other due to the electron clouds. The attraction developed between two particles is described as the van der Waals forces or London forces. These investigations have their origins on the work done by Isaac Newton on the adhering marbles.

The surface roughness friction is related to the microscopic geometrical irregularities at both surfaces in contact. An example of the measured surface roughness for steel surface is shown in Fig. 3.23. The aforementioned microscopic imperfections are creating a mechanical bearing action when surfaces are relatively sliding among each other. The term of roughness friction describes the global behaviour of the phenomenon and, with contradiction to the typical Coulomb friction phenomenon, it does not require any lateral pressure to be developed. Surface roughness friction is always active when two surfaces are in contact and subjected to relative displacement. The strength of the surface roughness friction is related to the composed materials and their surface treatments. A relation to the Coulomb friction coefficient μ can be identified [83].

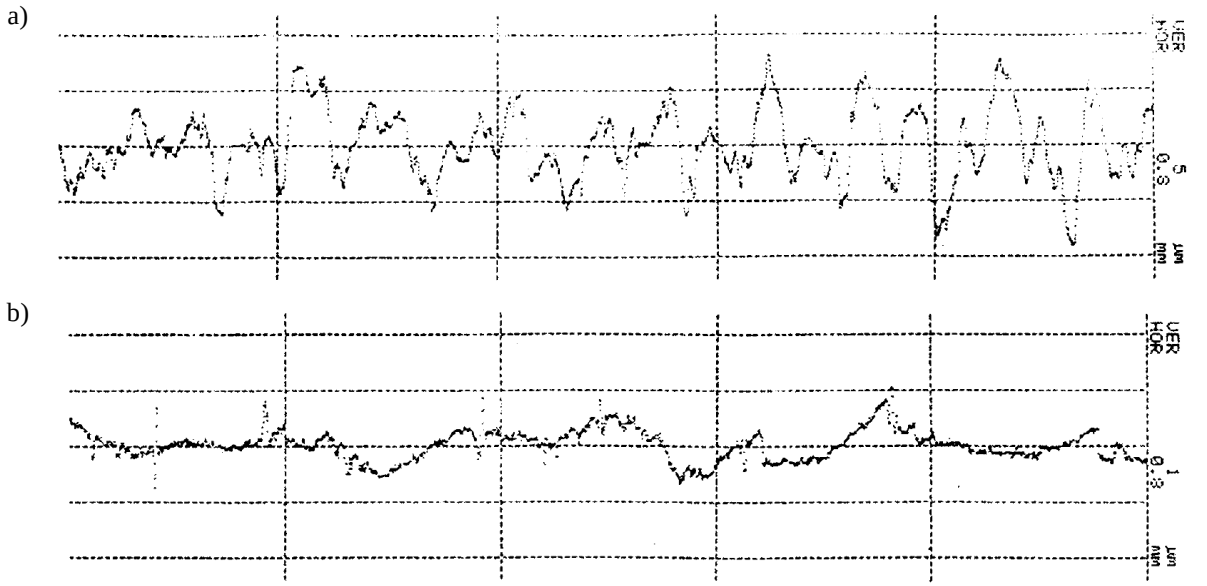


Fig. 3.23. Measurement of roughness on a steel surface – a) after milling (B2 class) and b) polished (B4 class). (Source: Ivkovic [83]).

When the developed shear flow at the steel-concrete interface exceeds the capacity of steel-concrete bond, additional mechanical shear connection means are required in order to prevent the relative slip between the steel and concrete. The mechanical shear connection means can be understand in the form of solid elements connected to the steel part and embedded in the concrete introducing a bearing reaction due to the relative slip. In Fig. 3.24, examples of the used mechanical shear connectors across the last century for steel-concrete composite beams (upper row) and columns (lower row) are shown. It can be observed that for composite columns, normally mechanical shear connectors are not required due to the double-symmetric cross-sections, as explained in Section 3.1. However, the applied shear connectors should assure the uniform distribution of forces in a column cross-section and prevent the possible relative slip due to the load introduction points. For such case, shear connectors used in composite beams are normally adapted for column application.

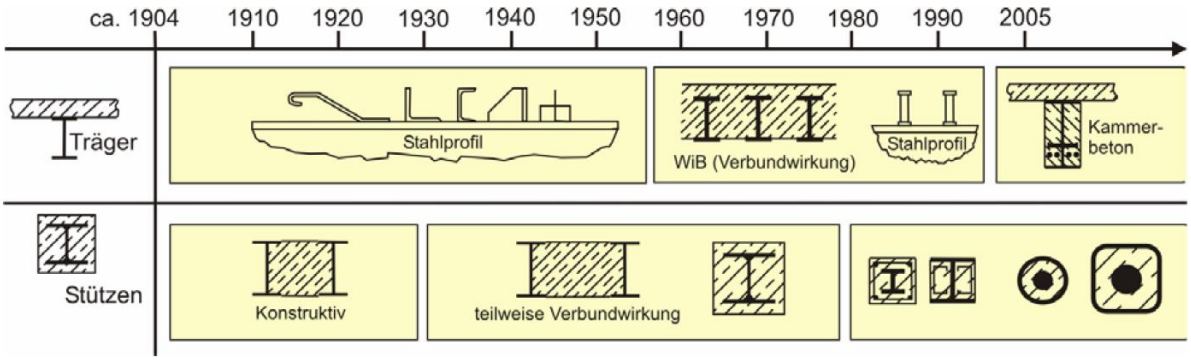


Fig. 3.24. Shear connection means in composite structures. (Source: Goralski [66]).

3.3.2. Plain steel – concrete bond

The plain steel-concrete bond rely on the natural connection between two materials and it refers to the nominally straight surfaces in such a way that the geometry of interface is not imposing any additional bearing action between the steel and concrete. It was mentioned above that, steel-concrete bond consists of the chemical adhesion, the Coulomb friction and the surface roughness friction, see Fig. 3.22. Each of these force-transferring phenomena bring a specific load-bearing character that contributes to the overall steel-concrete bond load-slip behaviour. A wide international literature can be identified on the investigation of steel-concrete bond, where the first investigations refer to plain steel bars used as the reinforcement for the concrete structures [60]. With the development of steel-concrete composite structures, the bond phenomenon started to be considered as the natural shear connection between the steel profiles and the concrete. In this Section, a general behaviour of bond is described, where an extensive database of bond strength values for composite columns is given in Section 5.3 together with the conducted individual research on its performance. The reference list consist of the work done by Roik [161-162], Wium [202], Roeder et al. [157], Xing et al. [209], Degée et al. [175], Tao et al. [177-181], Pecce et al. [142], Xu et al. [210], De Nardin et al. [41], Mollazadeh [124], Hotta et al. [74], Berthet et al. [14], Rana et al. [155], Wang et al. [197] and Qu et al. [152].

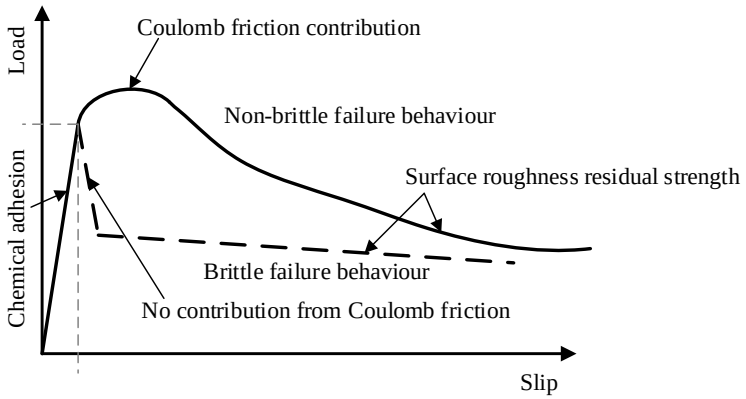


Fig. 3.25. General load-slip behaviour of steel-concrete bond.

In Fig. 3.25, a general load-slip behaviour of bond is given, where two failure modes can be distinguished – brittle and non-brittle. The steel-concrete bond, at the first stage of the load transfer, rely purely on the adhesive force transfer mechanism as it was identified for plain reinforcement bars [60] and for steel-concrete composite columns [162, 202]. This behaviour is very stiff and brittle [120]. The adhesive connection between steel and concrete irreversibly vanishes after the damage with small slip of approximately 0.5-1 mm [89, 162]. The ultimate strength of bond can be defined by the damage of the adhesive part [162] or can progress in a smoother manner with increased slip capacity due to the contribution of the Coulomb friction force-transfer mechanism [74, 202], as it is shown in Fig. 3.25. The contribution of the Coulomb friction mechanism rely on the activation of external lateral pressure and contact surfaces conditions [68]. This can be described in Eq. 3.48 by the principal linear relation of lateral pressure force F_n and the longitudinal reacting force F_t with dependence to the characteristic static friction ratio μ. The different conditions at the contact interface between steel and concrete will result in a different friction ratio between them and the level of the developed Coulomb friction forces will vary [182]. In the research done by Rabbat and Russell [154], the average friction ratio of dry concrete on a steel surface reached approximately 0.6. On the other hand, EN 1994-1-1 [58] recommends the usage of friction ratio of 0.5. For lubricated or polished surfaces the friction ratio will lower, where for surfaces with increased roughness, it will increase [68]. The amount of the lateral pressure on the contact interface can be related to the confining effects of external plates [74], shape of a steel profile [152], pressure of the concrete on the steel [202], reinforcement [157] or specimen geometry [162]. Moreover, the conducted research shows that boundary conditions have a significant influence on the level of the developed lateral pressure. A relation between the normal force imposing the pressure and the resultant tangential reaction can be defined as given in Eq. 3.49-3.50, with dependency on the angle between the reference normal direction to the surface and considered direction of acting load.

$$F_t = \mu \cdot F_n \tag{3.48}$$

$$\tan\theta = \frac{F_t}{F_n} \tag{3.49}$$

$$\mu = \tan\theta \tag{3.50}$$

In a typical push-out test, the Coulomb friction effects smoothly diminish after exhibiting a failure by the specimen [74], which can be observed also in Fig. 3.25 for the non-brittle behaviour. The dropping load is related to the redistribution of forces in the specimen due to interrupted composite action, reducing contact area due to the relative slip and eventual partially damaged contact between the steel and concrete due to the damage of a specimen. In both failure behaviours shown in Fig. 3.25, the load is not dropping to zero but a certain level of the residual strength sustains [162]. This load-bearing mechanism is related to the contribution of surface roughness and the microscopic interlocking mechanism between the two materials at the interface [83]. The mechanism of surface roughness friction can be well represented by the two approaching fractal surfaces as described in the work of Hanaor et al. [68] and shown in Fig. 3.26. When the upper and lower surfaces are relatively sliding in the plane of the diagram, the surface peaks are colliding to each other and the interlock mechanism develops. For the brittle failure behaviour shown in Fig. 3.25, the surface roughness friction activated directly after the adhesive failure [162]. Roik and Bergmann [159] defined the surface roughness friction load-bearing mechanism as the low bond strength value, which can be applied for the design purposes since the surface roughness friction always occurs between two sliding surfaces with no respect to the acting forces. This approach has been adapted in EN 1994-1-1 [58].

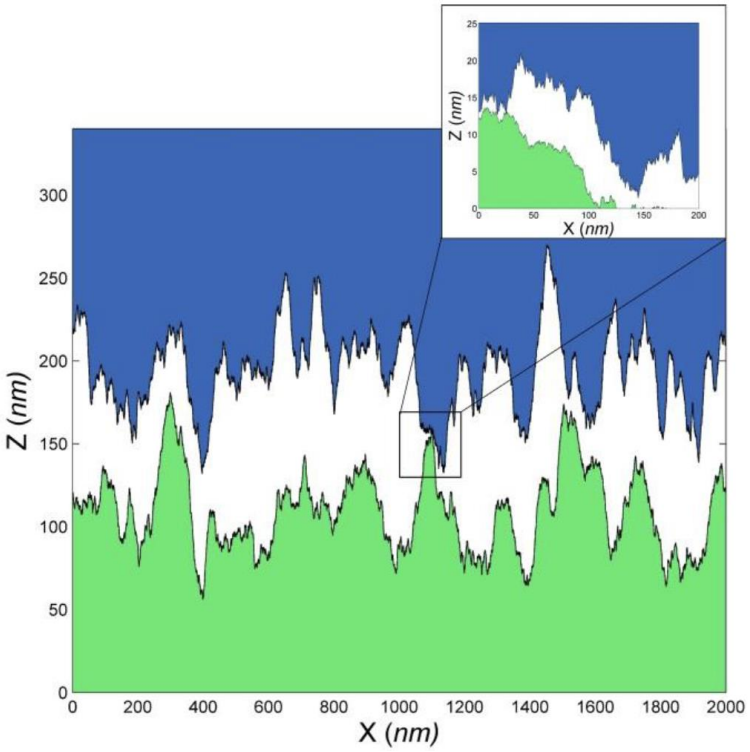


Fig. 3.26. Two approaching fractal surfaces – microscopic interlocking mechanism. (Source: Hanaor [68]).

Based on the work done by Wium [202], Roeder et al. [157], Tao et al. [181], De Nardin et al. [41], Berthet et al. [14], Wang et al. [197], Qu et al. [152] and Grzeszykowski et al. [67] on the evaluation of the steel-concrete bond, the uniform distribution of its strength over the contact perimeter and length of encased or concrete-filled steel profiles can be assumed. The exact distribution of bond over the

embedded length is non-linear, especially for the loads smaller than the ultimate load as it can be observed in Fig. 3.27. However, at loads close to the ultimate load, the strains/forces in steel reach nearly linear distribution, which proves the assumption about the uniform distribution of bond strength over the contact interface length. On the other hand, the evaluation of bond for lower loads, like for example in the serviceability limit state, the non-uniform distribution of bond should be taken into account.

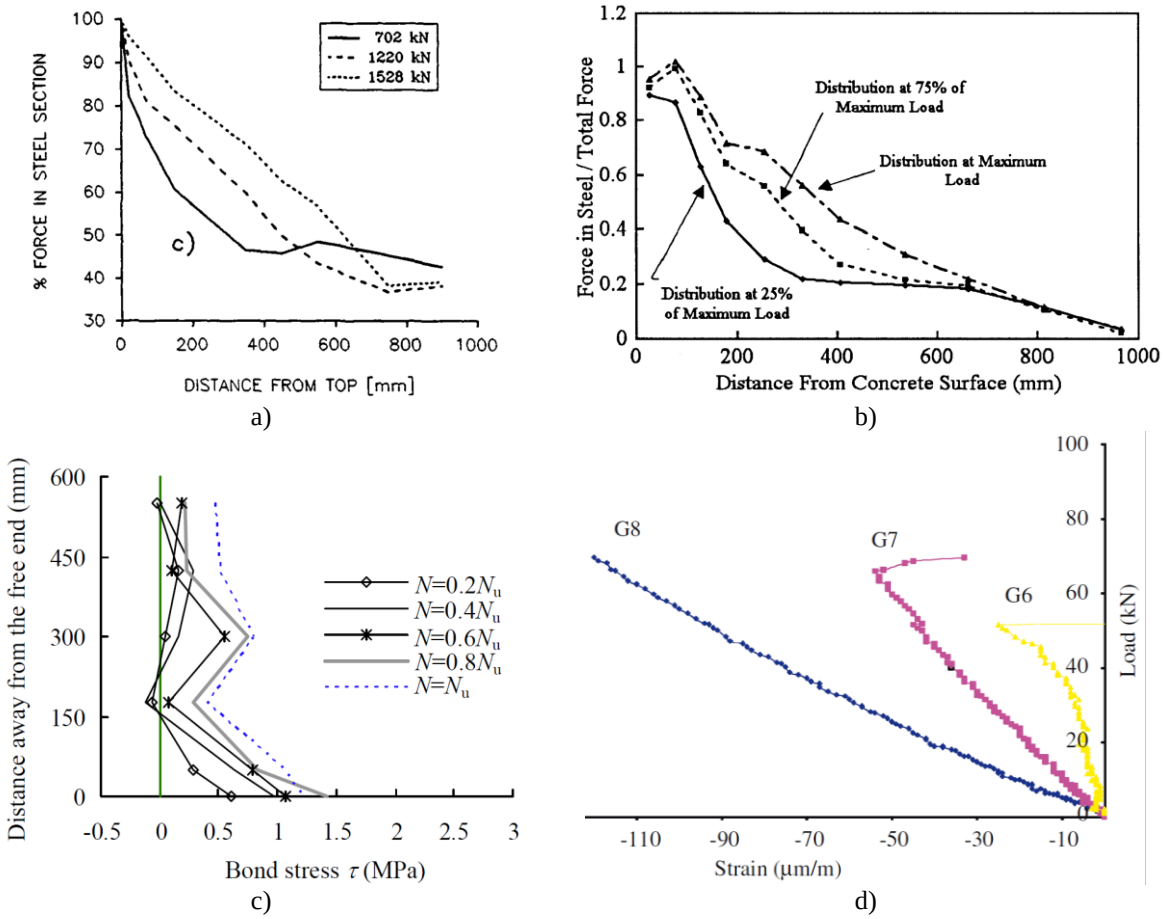


Fig. 3.27. Distribution of the steel-concrete bond strength over the interface length – a) fully embedded HEB200 profile (Source: Wium [202]), b) fully embedded W10x(22/45/77) profile (Source: Roeder [157]), c) concrete filled stainless steel square tube 120x4 (Source: Tao [181]) and d) strains in steel plate of steel-concrete-steel specimen at three points over the contact length (G6 top – G8 bottom) (Source: Berthet [14]).

3.3.3. Reinforcement bar – concrete bond

The reinforced concrete structures constitute a separate type of steel-concrete composite structures, where the steel reinforcing bars are embedded in the concrete. However, due to relatively small flexural and axial stiffnesses in comparison to the concrete part, the contribution of steel in the reinforced concrete sections is small and the global behaviour of members is dominated by the concrete behaviour. The presence of the reinforcement bars in the concrete allow transferring significantly higher tensile forces in comparison to the non-reinforced concrete structures. However, to transfer the tensile forces, the reinforcement bars requires an anchorage in the embedding concrete. The anchorage of the reinforcement bars is based on the same principle as the shear connection phenomenon in the steel-

concrete composite structures, where the shear flow between the steel bar and the concrete encasement develops due to the change in strains of steel and concrete parts over the anchorage length. The average bond stress over the anchorage length is defined in the technical report (bulletin 72) of International Federation for Structural Concrete fib [61] and in the work of Carins [27], where the value of bond stress f_b is related to the change of stresses in the reinforcement bar Δf_s, bar geometry and anchorage length l_b as given in Eq. 3.51.

$$f_b = \Delta f_s \cdot A_s / \pi \phi l_b \tag{3.51}$$

Where,

f_b is the average bond stress over the length l_b,

Δf_s is a change in bar stress over the length l_b,

A_s is the cross-sectional area of a bar,

ϕ is the nominal diameter of a bar,

l_b is the anchorage length over which Δf_s takes place.

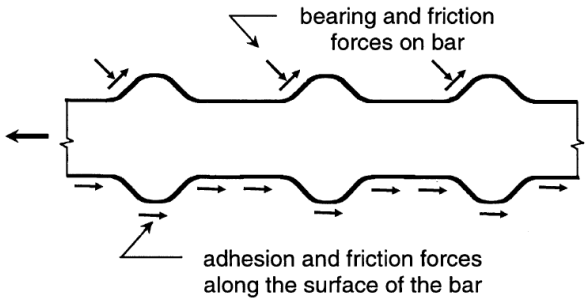


Fig. 3.28. Reinforcement bar-concrete bond force transfer mechanisms. (Source: ACI 408R-03 [3]).

Reinforcement bar-concrete bond consists of the natural plain steel-concrete bond phenomenon and an additional mechanical bearing action due to ribs on the surfaces of the bar as shown in Fig. 3.28. According to Bigaj [15], the activation of the load-bearing bond mechanism of the reinforcement bar can be divided into two main stages occurring one after another. First, where the plain steel-concrete bond govern the initial contact and the forces are transferred due to the adhesive connection and frictional interlocking of cementitious matrix and steel material. The second, where the bearing action of ribs against the concrete is activated with the development of a relative slip. Due to a significant discrepancy in the level of the bearing forces between these two stages and the fact that plain steel-concrete bond diminish shortly after loading, the overall performance of the reinforcement bar-concrete bond is defied mainly by the bearing action developed on the ribs of a bar [15, 114]. An example of the bond stress-slip curve obtained by Bigaj [15] is shown in Fig. 3.29, where the adhesive mechanism of reinforcement bar-concrete bond can be observed within the slip range of 0-0.15 mm and the bond stress value of approximately 5-7 MPa. The bearing reactions are transferred from the ribs of a bar to the concrete corbels localised between. A high concentration of forces in the front of a steel rib results in a cone-shaped crack initiated from the tip of a rib and progressing towards the surface of a steel bar, see

Fig. 3.30b. The investigation on the bearing angle and the resultant failure plane in concrete can be found in the work of Choi et al. [30], see Fig. 3.31. The resultant stresses, which are transferred to the surrounding concrete through the concrete corbels, can be defined in the shape of maximum compressive and tensile principal stresses as shown in Fig. 3.32. The resultant tensile stresses are forming a circumferential pattern around the reinforcement bar and the radial cracks develops as shown in Fig. 3.30c and Fig. 3.32.

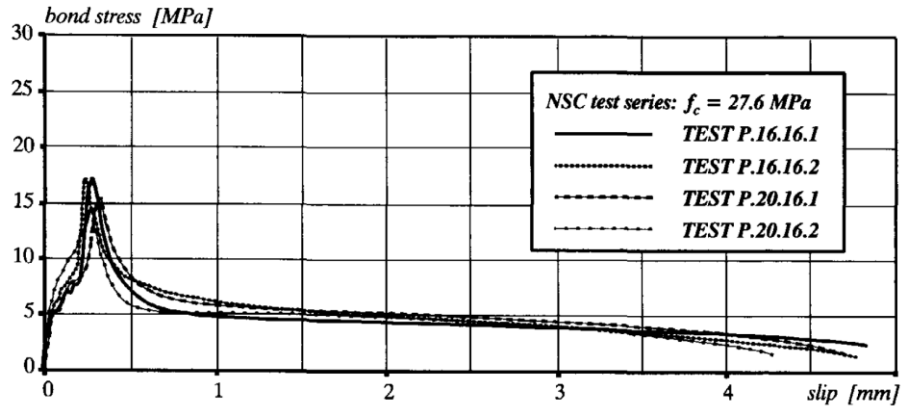


Fig. 3.29. Experimental bond stress versus slip relations of Ø16 and Ø20 reinforcement bars obtained from pull-out tests. (Source: Bigaj [15]).

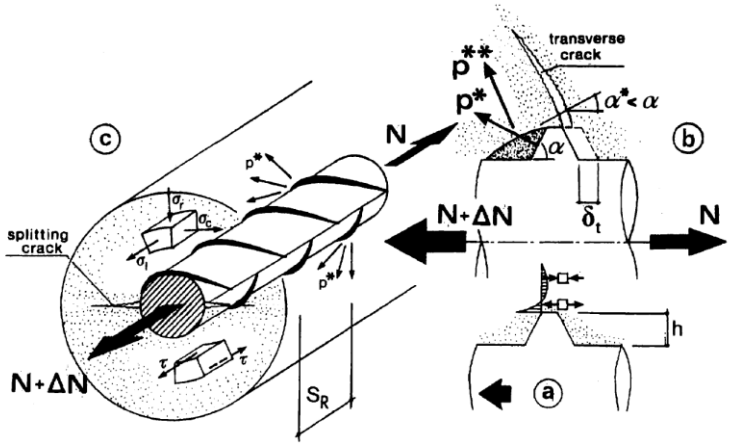


Fig. 3.30. Bond and splitting in reinforced concrete with deformed bars – a) typical stress peaks in the elastic phase, b) development of slip and bearing action of the bar and c) resultant stresses. (Source: fib bulletin 10 [60]).

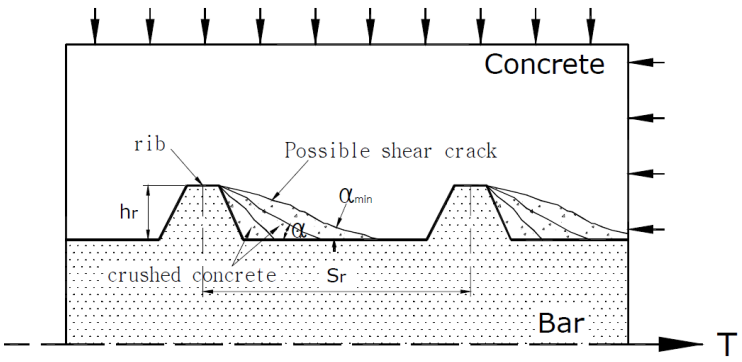


Fig. 3.31. Bearing action in concrete corbels due to reinforcement bar-concrete bond. (Source: Choi [30]).

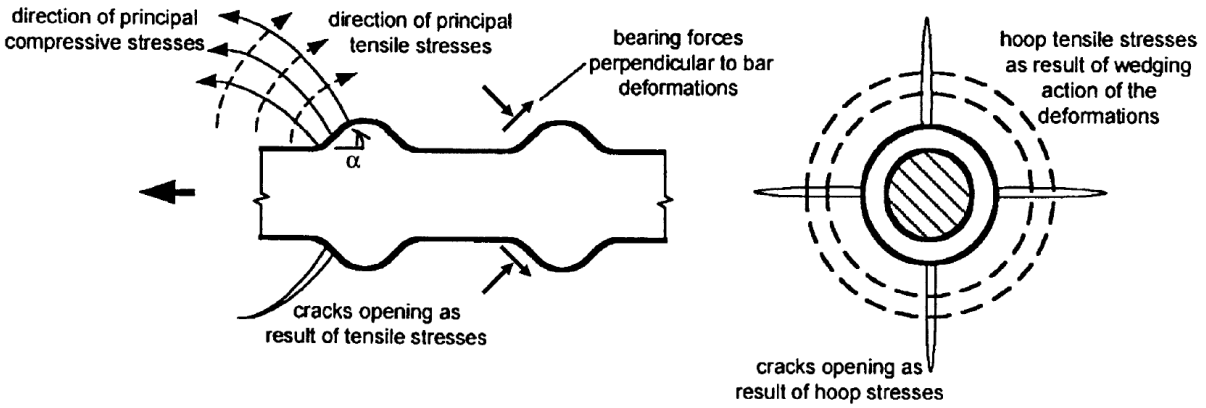


Fig. 3.32. Development of compressive and tensile principal stresses in concrete due to reinforcement-concrete bond. (Source: ACI 408R-03 [3]).

The resulting tensile stresses next to the embedded reinforcement bar, leads to two possible principal failure patterns: (i) the splitting failure and (ii) the pull-out failure [15, 60, 114]. The splitting failure occurs in the lower bond stresses than the pull-out failure and it is related to the transversal cracking of concrete and damage of bond between the reinforcement bar and concrete, see Fig. 3.33. When concrete is able to resist the splitting stresses around the reinforcement bar, for example due to the transversal reinforcement, the pull-out failure of the rebar is achieved and it is related to the longitudinally sheared concrete at the tips of ribs of the reinforcement bar as it is shown in Fig. 3.34.

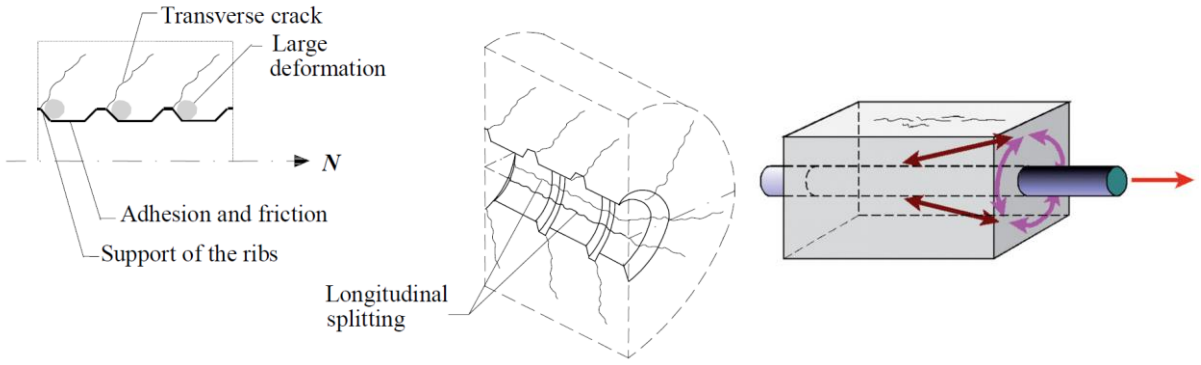


Fig. 3.33. Splitting failure of reinforcement-concrete bond. (Source: Lundgren [114] and Carins [27]).

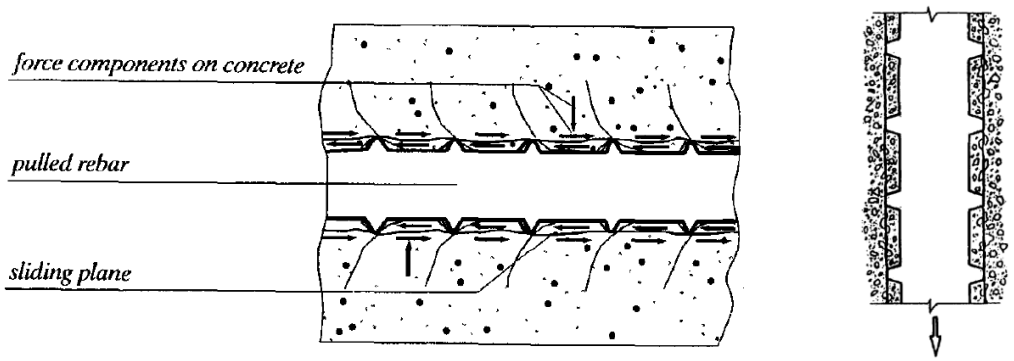


Fig. 3.34. Pull-out failure of reinforcement-concrete bond. (Source: Bigaj [15] and fib bulletin 10 [60]).

A general classification of the reinforcement bar-concrete bond behaviour can be found in fib bulletin 10 [60] and it is shown in Fig. 3.35, where the bond stress-bar slip curve with distinction on different failure modes and activated force transfer mechanisms is given. Stage I refers to the plain steel-concrete bond mechanism. Stage II corresponds to the activation of the bearing action by the ribs of a bar and development of radial microcracks. Stage III reflects the development of longitudinal splitting cracks over the anchorage length or, when the confinement of concrete allows for further development of the bearing action and the pull-out failure is reached. Stage IV describes the post-failure behaviour of reinforcement bar, where the friction effects are dominating in the force transfer.

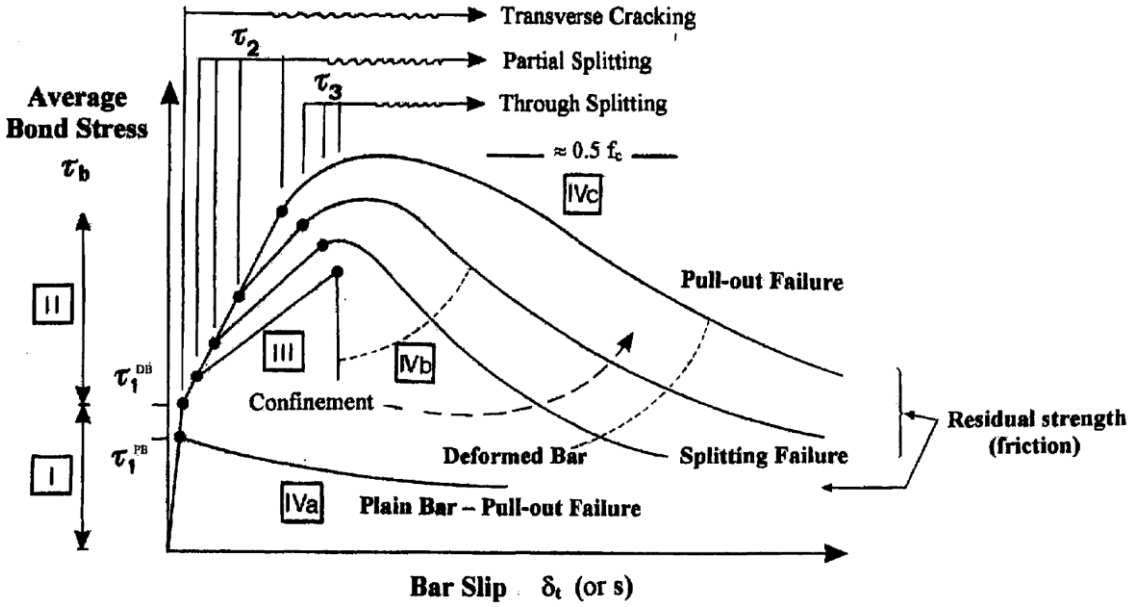


Fig. 3.35. Local bond stress-slip behaviour of reinforcement-concrete bond. (Source: fib bulletin 10 [60]).

From the analysed behaviour, it can be observed that the reinforcement-concrete bond behaviour is strictly related to the concrete material properties [27], geometry and arrangement of ribs over the reinforcement bar [40] and confinement of the concrete [20, 40, 211]. Moreover, the research data found in the literature allow identifying a vulnerability of the reinforcement-concrete bond strength to static or cyclic loading [45, 114], straining of the reinforcement bar [45, 125], corrosion level [119] or environmental and temperature effects [60]. According to the work of Prince et al. [150], the reusable concrete aggregate has no significant impact on the bond strength properties of the reinforcement bars.

Various descriptive equations for the evaluation of reinforcement bar-concrete bond can be found in the literature, like for example fib bulletin 10 [60], fib bulletin 72 [61], ACI 408R-03 [3], EN 1992-1-1 [53], Bigaj [15], Lundgren [114], Brantschen et al. [22] or Choi [30]. However, all the analytical models are relating the reinforcement bar-concrete bond strength to the material properties of concrete and the geometry of an embedded reinforcement bar. In Eq. 3.51, a general shape of the bond strength is given, where the change in bar stress is included. The change in stresses over the bar length can be also non-directly replaced by the respective concrete strength value, which will correlate the desired splitting or pull-out failure in the considered model [61].

3.3.4. Mechanical shear connection means

The definition of the mechanical shear connection mean for steel-concrete composite structures can be found as a structural device provided at the steel-concrete interface in order to assure the composite action between the steel and concrete materials by preventing the relative slip and to resist the developed shear flow [159]. In general, the shear connection should be always assured in composite structures [110]. A need for the usage of mechanical shear connectors arise especially in the steel-concrete composite beams and for the analysis of ultimate limit state. In the steel-concrete composite columns, the requirement for shear connection govern the load introduction points in order to transfer the imposed load to the entire composite cross-section of a column [110]. A distinction of the applied groups of shear connectors due to their working behaviour can be made into two groups: (i) plastic and (ii) unzipping. The plastic behaviour of a group of shear connectors allows for the uniform distribution of the shear flow between all applied connectors over the entire anchorage length. Moreover, it allows for the full utilisation of all connectors until the limit of the shear connection resistance (a specific limit of slip, where in EN 1994-1-1 [58], a minimum slip that has to be assured by the mechanical shear connectors is 6 mm). The unzipping behaviour governs a gradual and progressive damage in shear connection with increasing slip. In the result, after the damage of the first row of brittle connectors, only the residual strength of them contributes to the second row. The principle of the unzipping behaviour is shown in Fig. 3.36, where three states of developed slip are considered – initial elastic state and two with progressed development of a slip.

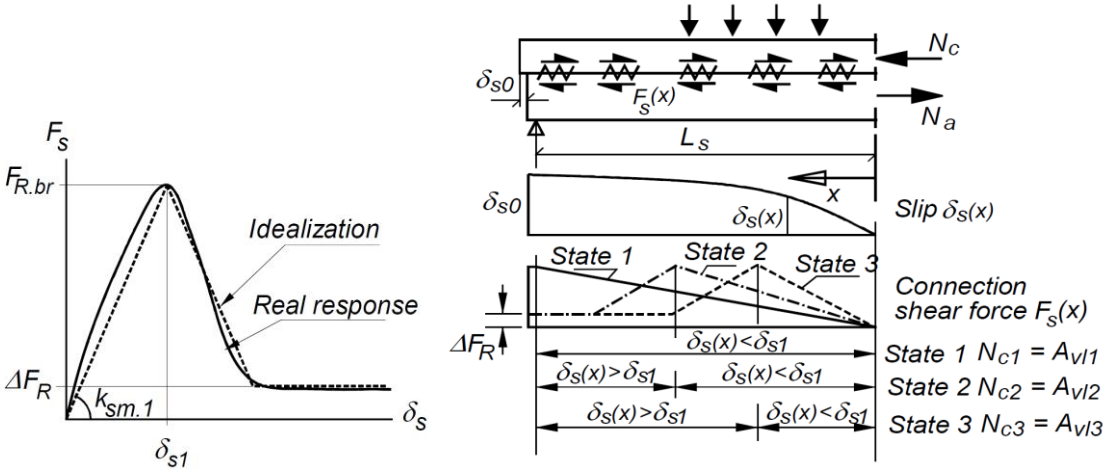


Fig. 3.36. Behaviour of an unzipping shear connection. (Source: Leskelä [110]).

Another requirement for the usage of mechanical shear connectors is the durability of the shear connection and normally a mechanical connection at the interface would be required due to the possible damage of natural steel-concrete bond by time [202], cycling loading [58, 161] or local cracking of the concrete [157].

For the evaluation of the performance of shear connectors, the following aspects shall be considered:

(1) the stiffness and the ductility of a shear connection,

(2) the resistance of a material of applied shear connectors,

(3) the resistance of a steel part to which connectors are fixed (normally not the case),

(4) the connection between the shear connector and the steel part,

(5) the resistance of the embedding concrete,

(6) the simultaneous or separate activation of plain steel-concrete bond.

The most common type of mechanical shear connectors provided at the steel-concrete interface are headed shear studs [115] and often in the literature can be found that term of shear connectors is directly related to this specific type of connectors. This type of shear connectors is also very often only covered in the design codes, like in EN 1994-1-1 [58] or JGJ138 [85]. However, the term of shear connectors is general and aside of headed shear studs, other types of shear connectors can be identified, like for example welded stiffeners [175], bar connectors [89], channel sections [89], T-section connectors [161], burls [162], perfobond solution [194] or bearing plates [69]. Besides the listed types of mechanical shear connectors other types can be identified. The recognised types of shear connectors are listed below with a short description in specific paragraphs.

Headed shear studs

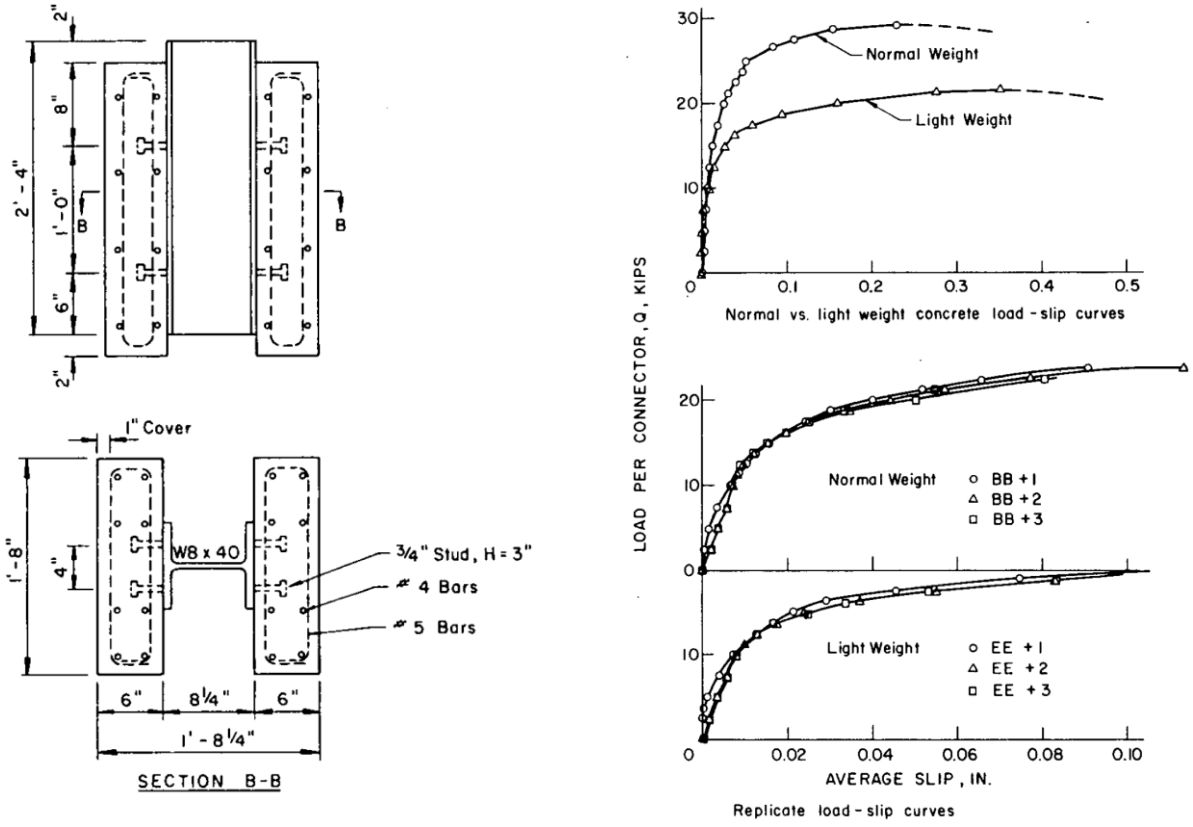
The geometry of headed shear stud connector consist of a cylindrical shank ended with a flat cylindrical head as shown in Fig. 3.37. The typical diameters of shanks varies between 13 mm and 25 mm, where welding of studs with diameter bigger than 20 mm becomes difficult and expensive [89]. Length of studs governs typically in 65-150 mm but longer studs are also in practice [89]. The thickness of a steel part t should not go beyond the ratio $d/t \leq 2.5$ [58, 89] to achieve full capacity of a stud.



a) b) c)

Fig. 3.37. Geometry of a shear stud – a) scheme (Source: Johnson [89]), b) different sizes of headed shear studs and c) stud welding detail (Source: Houston [75]).

The investigations on the behaviour of headed shear studs can be found in various international literature [73]. Ollgaard et al. [134] performed push-out tests on 16 mm and 19 mm diameter shear studs and two types of concrete, normal and lightweight, see Fig. 3.38. Hanswille et al. [71] give the load-slip behaviour of 19 mm, 22 mm and 25 mm shear studs, as shown in Fig. 3.39. Another examples of the load-slip behaviour of tested shear studs can be found among others in the work of Lungershausen [115] or Lam et al. [108], shown in Fig. 3.40.



a) b)

Fig. 3.38. Push-out test of shear studs – a) specimen and b) load-slip curves. (Adapted from Ollgaard [134]).

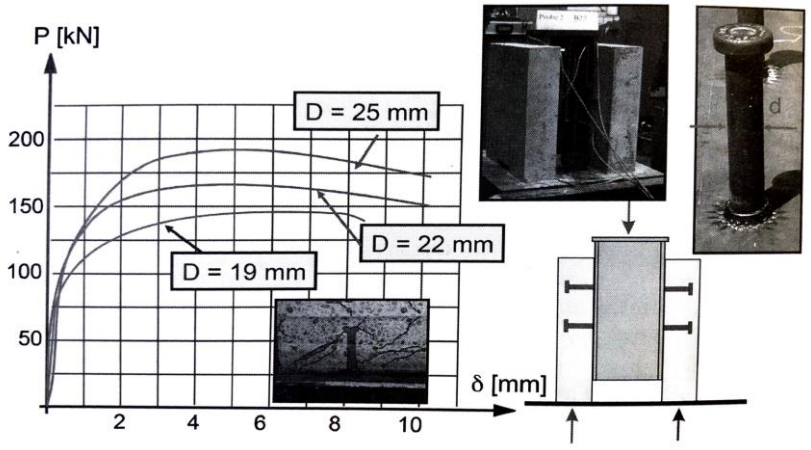
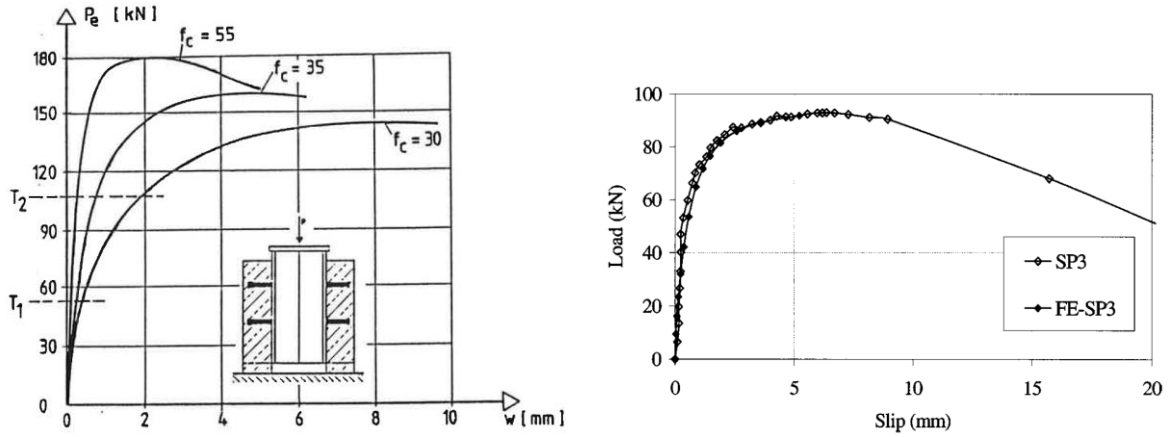


Fig. 3.39. Typical load-slip curves for shear studs with 19-25mm shank. (Source: Hanswille [71]).



a) b)

Fig. 3.40. Load-slip responses of headed stud connectors embedded in concrete slab – a) according to Lungershausen [115] for 4 studs Ø 22 mm and b) tests made by Lam et al [163] for 2 studs Ø 19 mm.

Lungershausen in his work [115] identified the load-bearing mechanism of shear studs and four stages of stud utilisation in solid concrete slabs were distinguished, named A-D, as shown in Fig. 3.41. In the stage A, at the base of the stud, the compression stresses form a compression strut, which impose the bearing action between shear stud and embedding concrete. When the local compression stresses are higher than concrete compression resistane, the stage B is activating, where the crushing of concrete develops next to the connector base and next top its tip on opposite sides. In the result, the shear stud is subjected to bending. An increase of slip results in singificant bending of the stud and the stage C can be observed. The tensile stresses develop in the shank of the stud and a compressive reaction under the head of the stud is activated. The copression stresses are spread over the concrete cone lying below the head of the stud and the Coulomb friction mechanism at the surface of a steel profile is activated. After reaching the maximum capacity, described as stage D, the shear connector fails under two major scenarios: (i) due to the failure of the concrete cone around the connector and separation of the concrete slab from the steel profile and (ii) due to the shearing of the shank of the stud. A mixed failure patterns can develop and they are strongly dependent on the used geometry and materials.

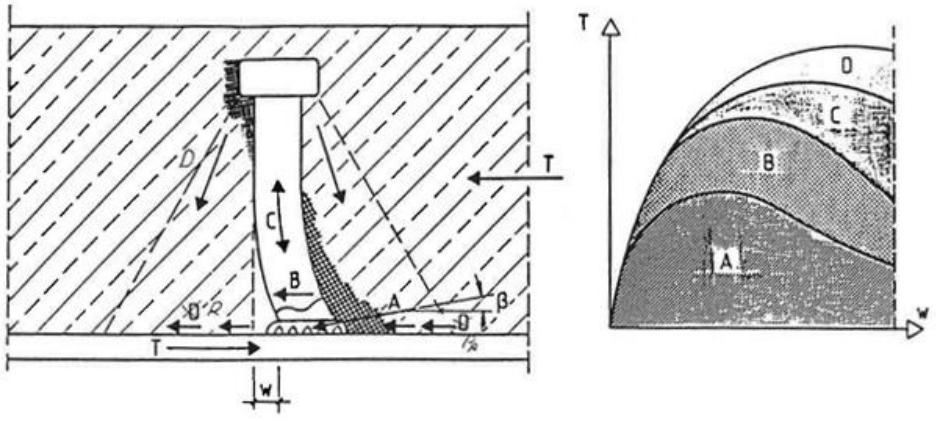


Fig. 3.41. Load-bearing mechanism of a shear stud in solid concrete slab. (Source: Lungershausen [115]).

More studies on the behaviour of headed shear studs can be found in the work of Hanswille et al. [70] about the resistance of studs subjected to cyclic loading, Nellinger [126] about the failure mechanisms of shear studs in deep steel decking, Chung et al. [31] about the additional shear and tension forces acting on the shear connection, Valente et al. [190] and Spremić [178] about the close spacing of studs or Jin et al. [88] about the influence of corrosion on the stud behaviour.

The application of shear studs in steel-concrete composite columns has been investigated in push-out tests among others by Roik et al. [161], Roik and Hanswille [163], Roik and Bergmann [159], Hanswille, Shafer and Bergmann [71] and Goralski [66]. When the shear studs are welded in the chambers of embedded H-shaped steel profiles, it was identified that the flanges of a steel profile create the confinement for concrete and due to the force transfer by the shear stud, an additional friction effect contributes to the shear connection, see Fig. 3.42.

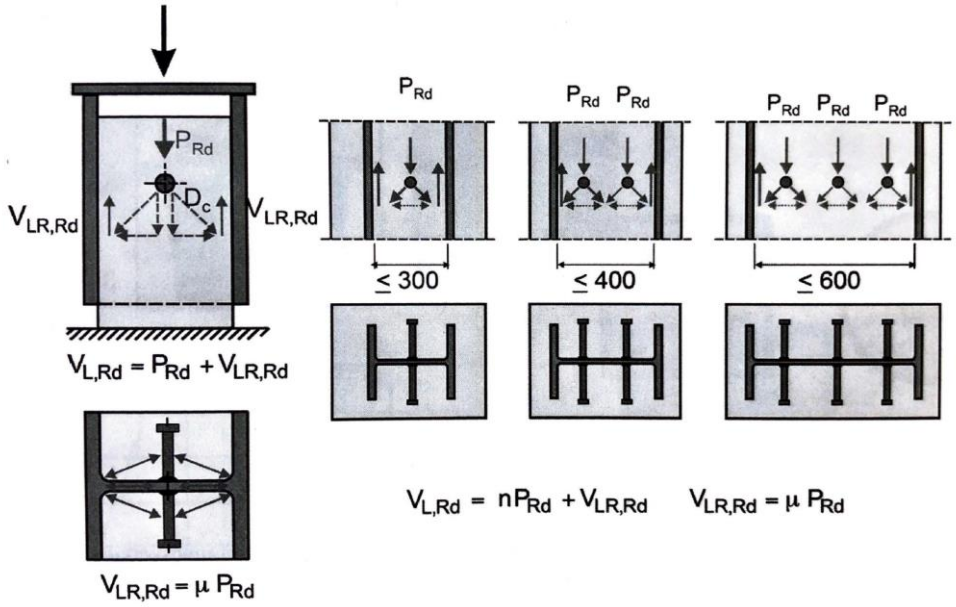


Fig. 3.42. Additional frictional forces in composite columns chambers. (Source: Hanswille [71]).

Application of shear studs has been investigated in concrete filled tubes for example by Tao et al. [177, 181] and De Nardin et al. [41], where the concrete is generally confined by the surrounding steel tube. Application of the mechanical shear connectors inside the steel tubes improved overall performance of the shear connection. Tao et al. [181] identified that due to the ageing, after three years, the natural bond at the interface between steel tube and concrete core was significantly reduced to a marginal value. Therefore, a need for the application of the mechanical shear connectors in concrete filled tubes has been identified in order to assure the long-term reliability of a structure.

Bearing plates in hollow sections

Three different types of mechanical shear connections can be distinguished in the group of bearing plates in hollow sections: (i) gusset plates, (ii) cap plates and (iii) internal rings/membranes. Gusset plates and cap plates shear connections were investigated by Hanswille, Roik and Schwalbenhofer [71,

163, 165] as a direct load introduction points in the concrete filled composite columns. The general overview of the analysed types of plate bearing connections are shown in Fig. 3.43. The load-displacement curves investigated by Roik et al. [165] for rectangular hollow profile 220x220x6.3 mm, 15 mm thick gusset plate connector and concrete grade B45 (currently C35/45) together with a test setup are shown in Fig. 3.44. It can be observed that steel plates of structural joins can efficiently work as a shear connector, however, a high concentration of compression stresses in the concrete under the bearing plates need to be considered [58, 71].

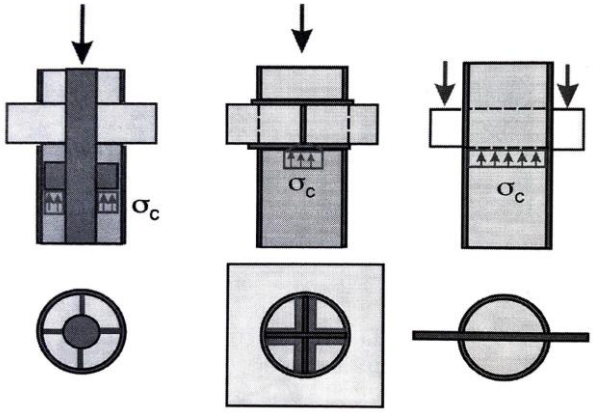
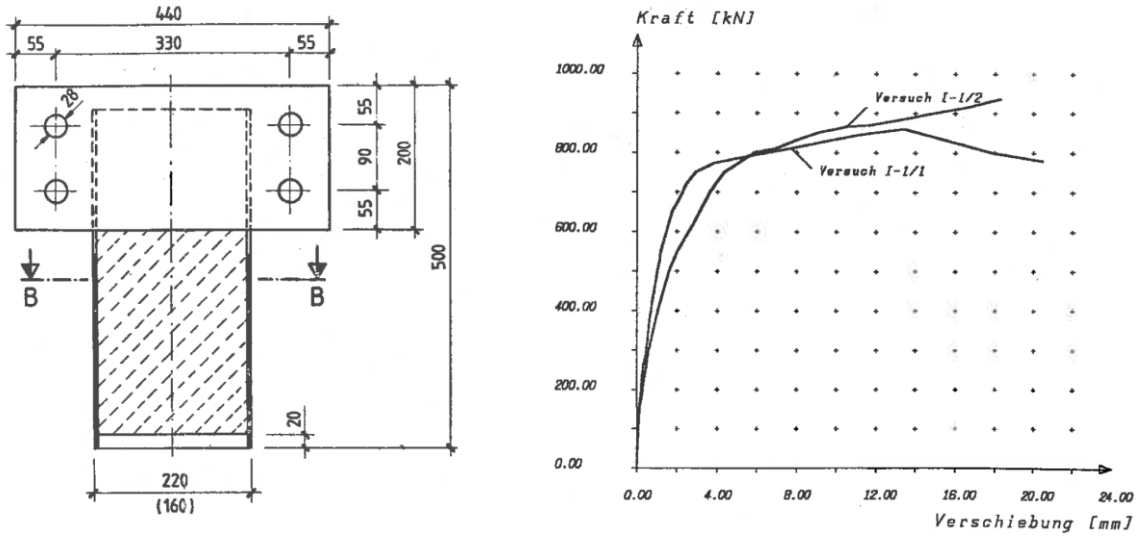


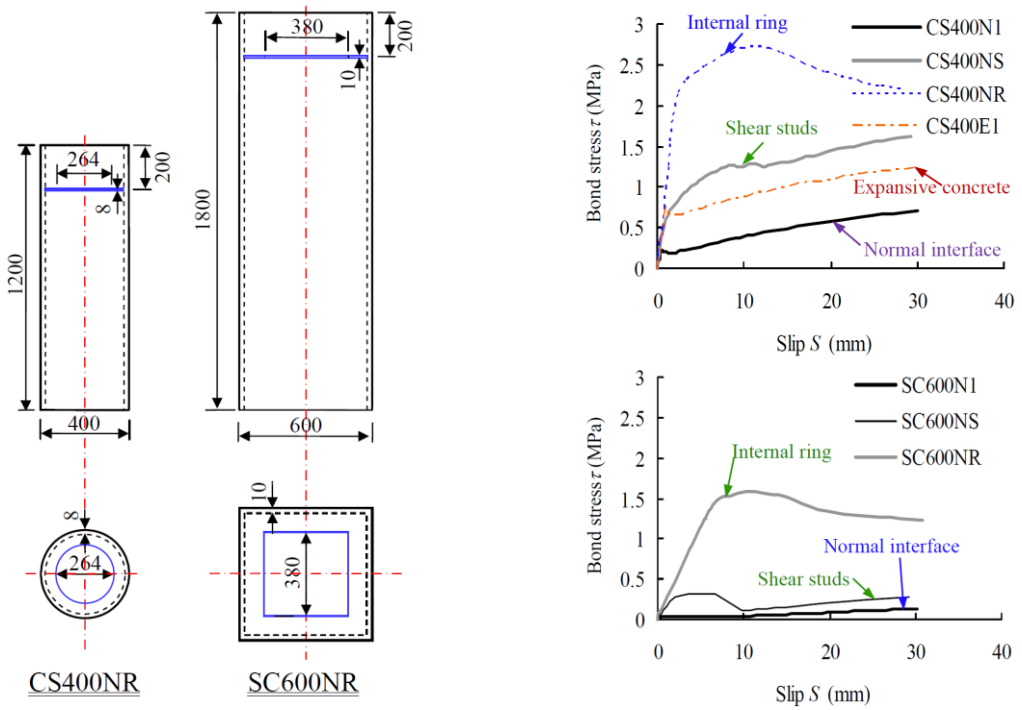
Fig. 3.43. Bearing plate shear connectors in the concrete filled hollow sections. (Source: Hanswille [71]).



a) b)

Fig. 3.44. Tests of gusset plate shear connector in the concrete filled hollow steel section – a) specimen and b) load-displacement curves. (Source: Roik [165]).

The investigation on internal rings in hollow sections can be found in the work of Tao et al. [181], where on the internal side of a steel tube, a steel ring in the form of flat steel plates was welded. An overview of the specimen layout and the experimental load-slip curves with comparison of different types of applied shear connection means is shown in Fig. 3.45. It can be observed that the introduced steel ring connector has significantly affected the load-slip behaviour and brought a good performance in comparison to the natural bond, expansive concrete mixture or commonly used shear studs. However, this type of connection requires further investigation, for example in specimens subjected to bending.

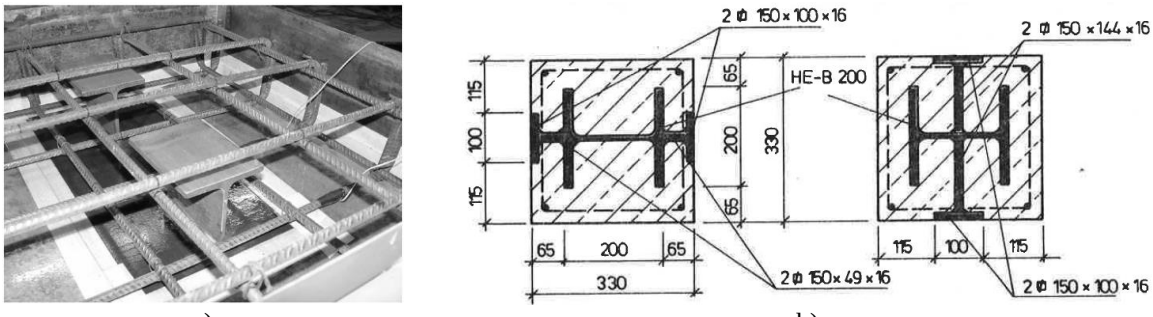


a) b)

Fig. 3.45. Tests of internal ring shear connector in the concrete filled hollow steel section – a) specimen and b) load-displacement curves. (Source: Tao [181]).

T-shaped connectors

The T-shaped shear connectors consist of T-shaped stub steel profile welded to the surfaces of steel profile, as shown in Fig. 3.46. The geometry of connector assure high load bearing capacity and high level of ductility. Due to the good performance, these type of connectors are considered as an efficient alternative for the high-strength concrete mixtures [190]. The investigations on the T-shaped shear connectors can be found in the work of Roik et al. [161] with the application to the fully embedded composite columns and in the work of Valente et al. [190], where typical push-out tests for testing of shear connectors were conducted.



a) b)

Fig. 3.46. T-shaped connectors – a) view (Source: Valente [190]) and b) column application (Source: Roik [161]).

The performance of the applied T-shaped shear connectors in composite columns is shown in Fig. 3.47, where their application to the flanges of a steel profile is considered. In the configuration, where the T-shaped connectors are welded inside the chambers of a steel profile, the load-bearing and ductility performance increases [161].

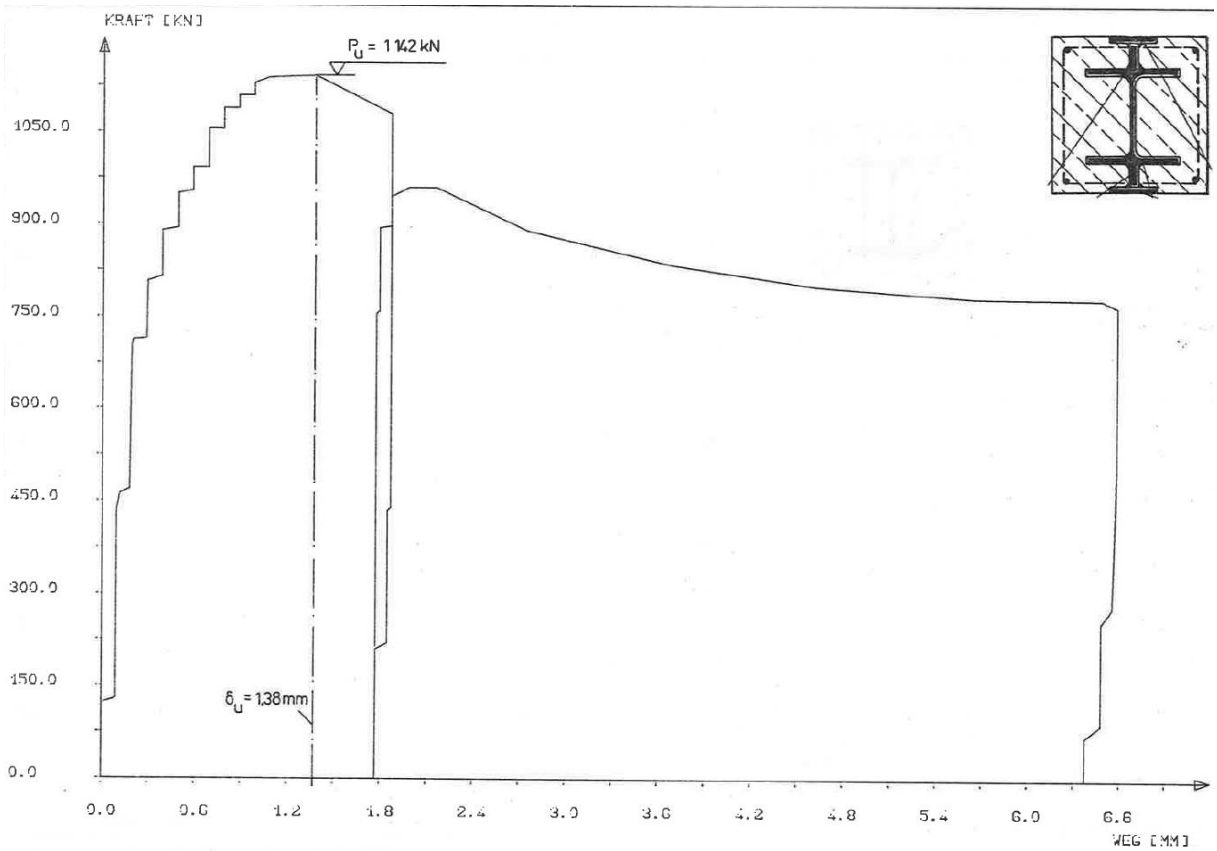


Fig. 3.47. Load-slip curve for T-shaped shear connector. (Source: Roik [161]).

Channel and Helical sections

The channel section shear connectors consist of the channel stub profiles welded with flanges to a steel profile. An application example in bridge and building structures is shown in Fig. 3.48. The behaviour of channel shear connectors can be found in the work of Shariati et al. [173] or Maleki et al. [117-118]. In Fig. 3.49, the test layout, the recorded load-slip performance and the deformed channel connector from tests made by Maleki [117-118] are shown.

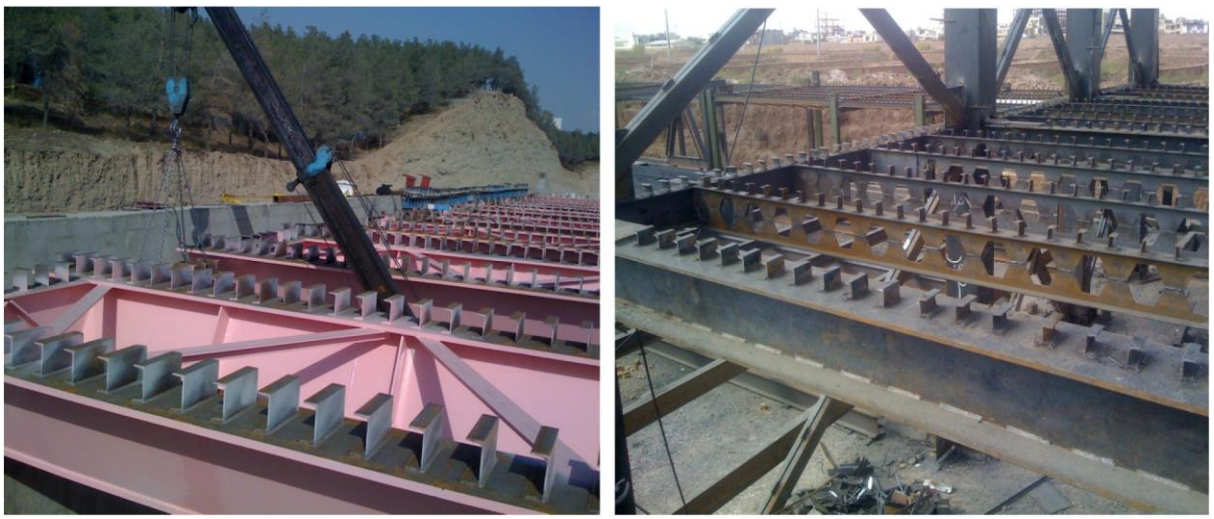
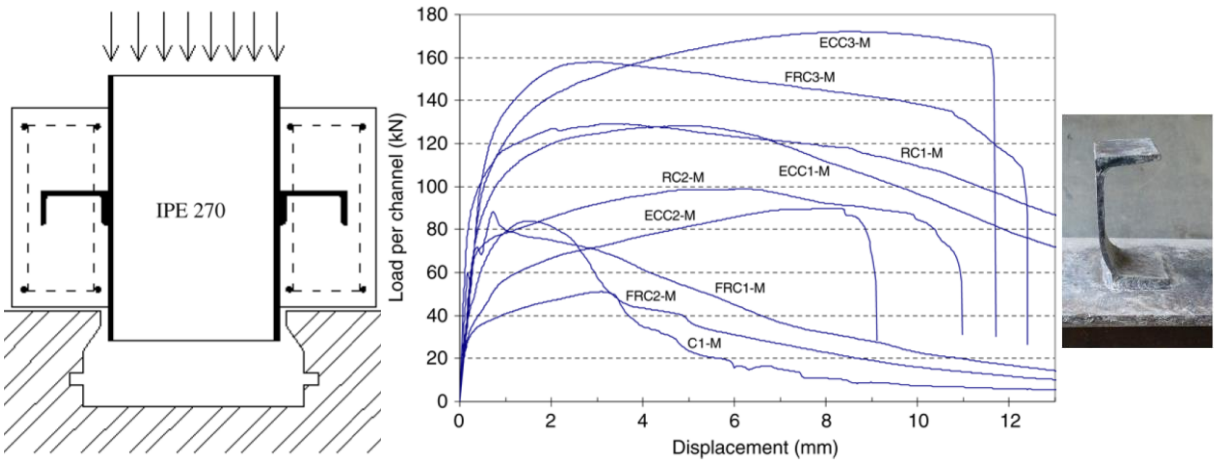


Fig. 3.48. Application of channel shear connectors in bridge and building structures. (Source: Shariati [173]).



a) b) c)

Fig. 3.49. Test of channel connector – a) test layout, b) test results (N-plain concrete, RC-reinforced concrete, FRC-fibre reinforced concrete, ECC-engineered mix) and c) deformed connector. (Source: Maleki [117, 118]).

The application of channel sections as the mechanical shear connection mean is foreseen in the Chinese design code JGJ138-2016 [85], American Specification AISC 360-16 [8], old British Standard BS 5400-5:1979 [26] and Indian Standard IS:11384-1985 [78]. The British and Indian Standards are giving the reference values of the design resistances. In addition, helical connectors shown in Fig. 3.50 can be found in Indian Standard [78], where the reference strength values are provided as well.

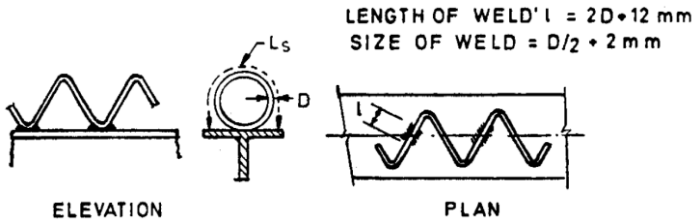


Fig. 3.50. Helical shear connector. (Source: IS:11384-1985 [78]).

Block connectors

The block connectors consist of the steel blocks welded to the surface of a steel profile with longer dimension. For the application in a beam, the block connectors are equipped with additional bar in the shape of a horseshoe welded to the block connector in order to prevent the uplift, see Fig. 3.51. Specifications can be found in British Standard BS 5400-5:1979 [26].

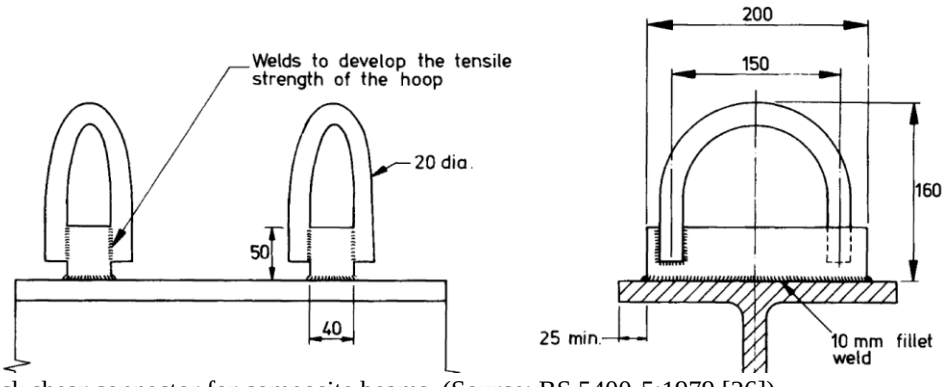


Fig. 3.51. Block shear connector for composite beams. (Source: BS 5400-5:1979 [26]).

The investigations on the behaviour of block connectors for column application can be found in the work of Roik et al. [161], see Fig. 3.52. Roik et al. [162] investigated also burl connectors visible in Fig. 3.52, originally named in German language as “Noppen”. Explaining further the figure: “stark bewehrt” – strong reinforcement, “schwach bewehrt” – weak reinforcement, “Schubleisten” – push strips (block connectors), “Kraft” – load, “Verschiebung” – movement, “Anordnung der Verbundmittel” – arrangement of the connectors. An investigation on the similar type of shear connectors called shear ribs can be found in the work of Chanou [29], see Section 3.5.4.

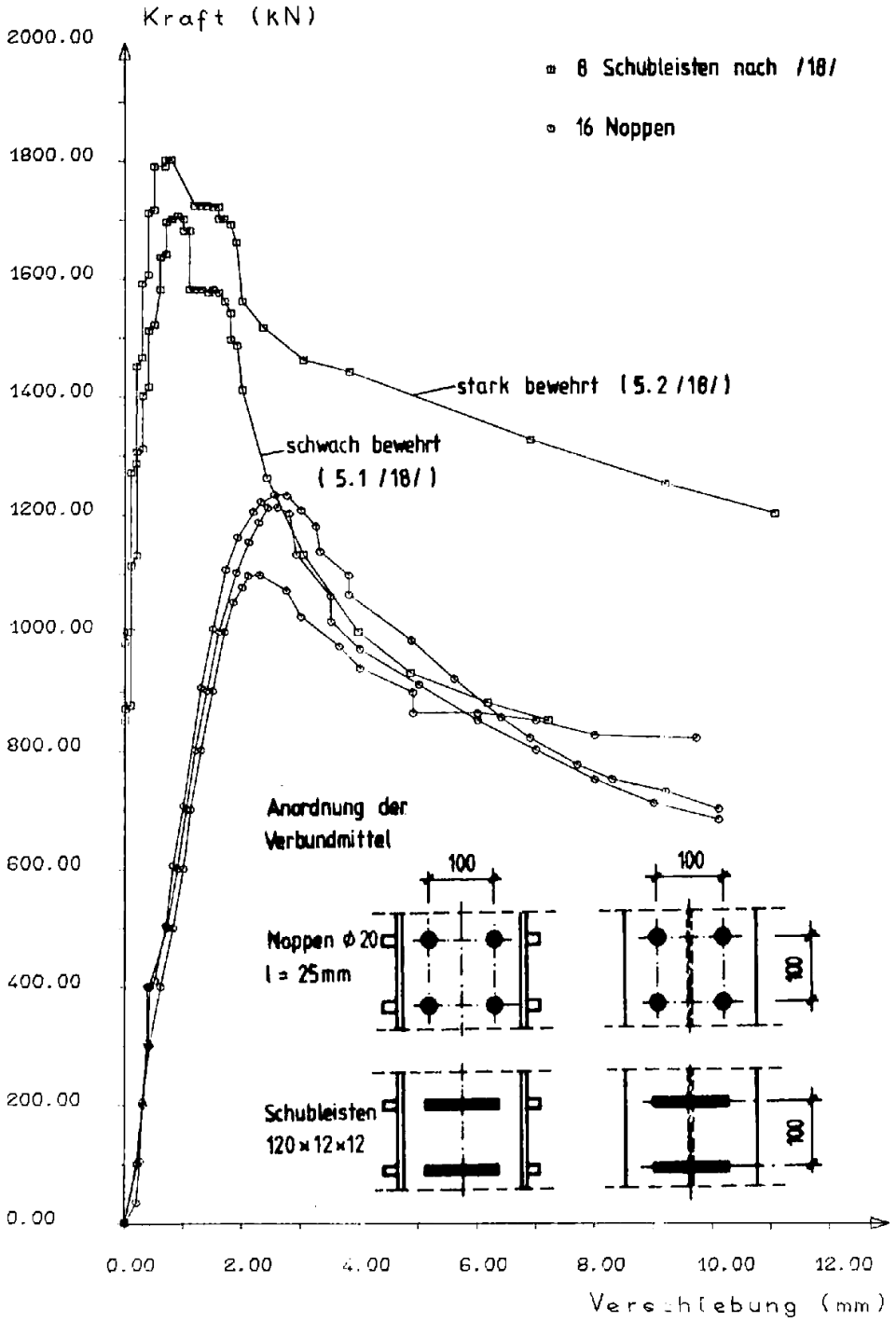


Fig. 3.52. Load-slip behaviour of block and burl shear connectors in column application. (Source: Roik [162]).

Bars passing through the flanges

Another type of shear connector analysed by Roik et al. [161] were bars passing through the flanges of a steel profile. The load-slip diagram with the recorded behaviour of connector is shown in Fig. 3.53. This type of connector showed significantly good performance in comparison to other types of connectors. However, fabrication of this type of connection requires drilling holes in a steel profile, which leads to the weakened cross-section and complex application process.

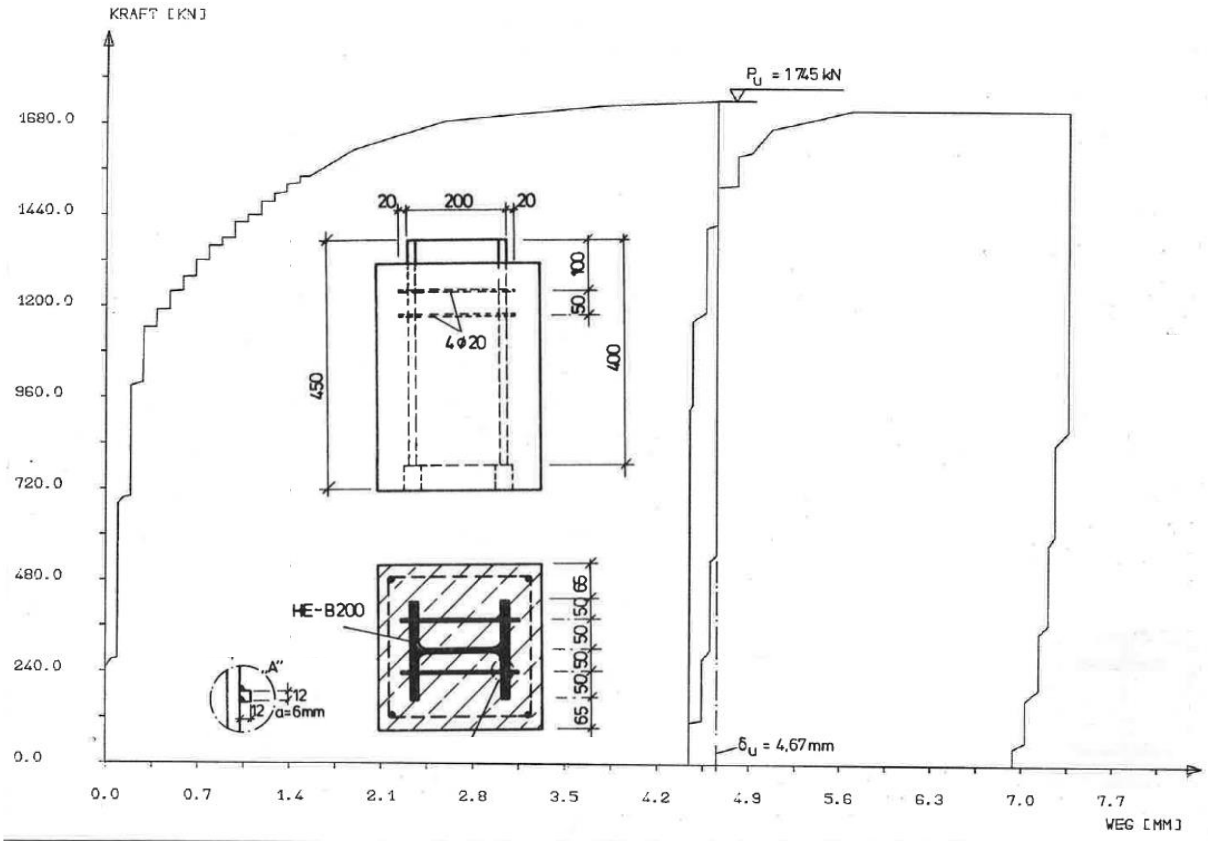
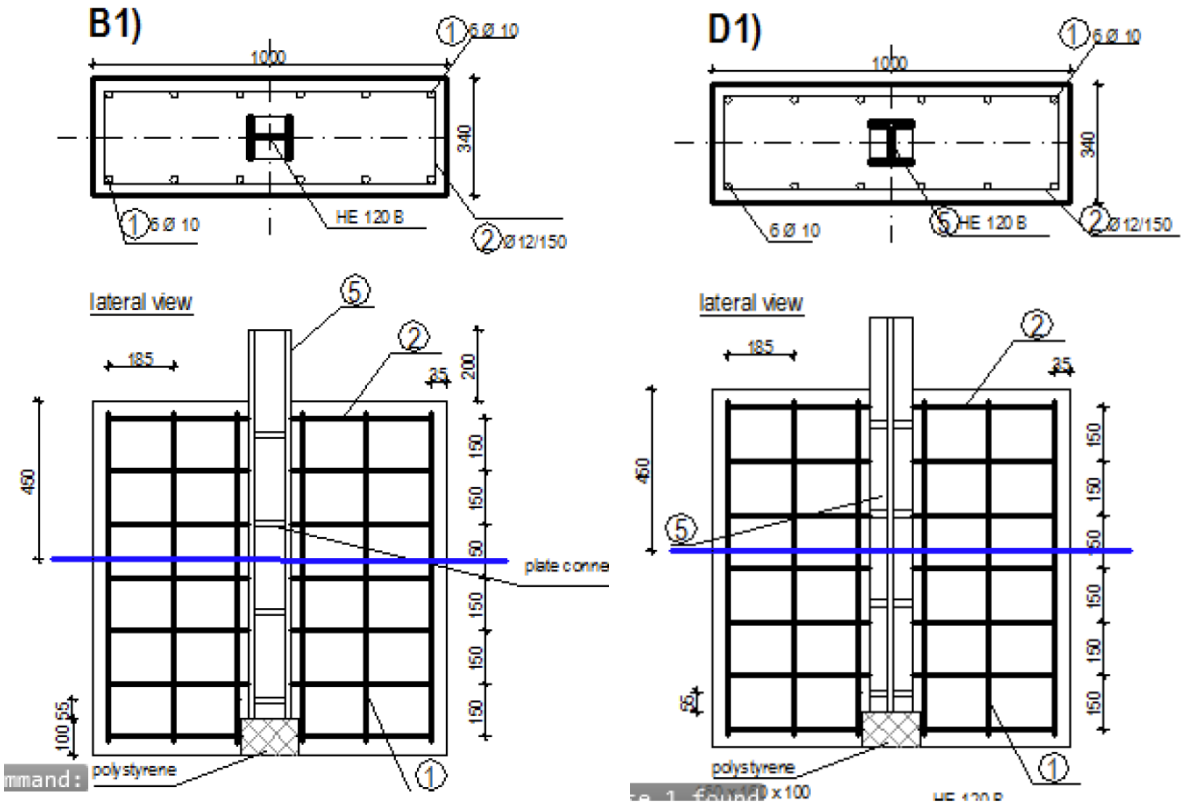


Fig. 3.53. Bar passing connector –specimen layout and load-slip curve. (Adapted from Roik [161]).

Welded stiffeners

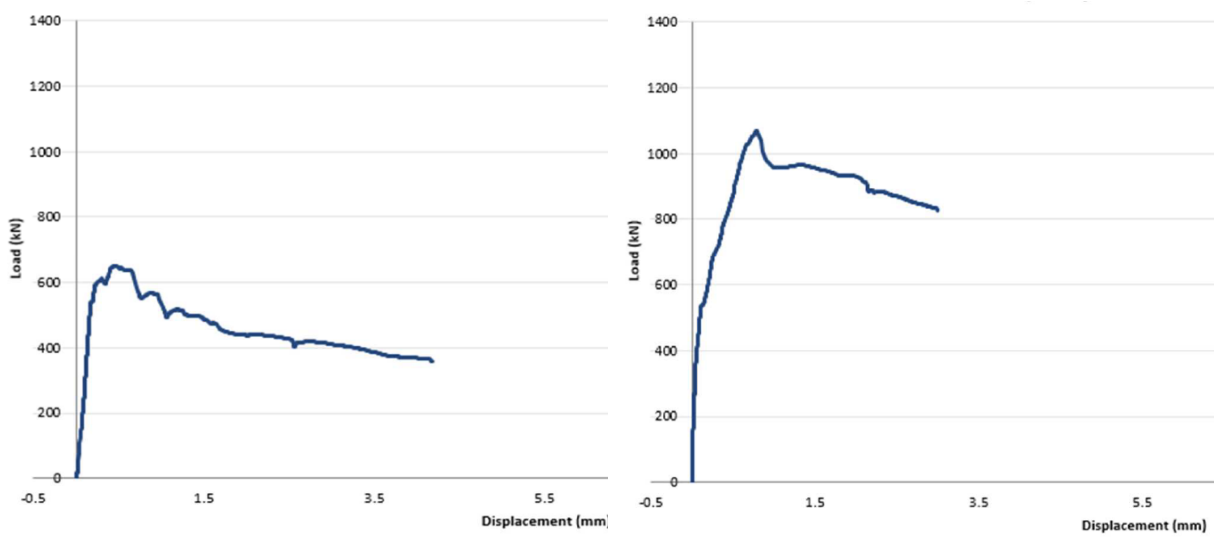
The stiffeners welded between the flanges of embedded steel profiles, which act as the mechanical shear connectors in steel-concrete composite columns were tested in the RFCS project SmartCoCo [175]. The shear connectors were tested in push-out tests with HEB 120 steel profiles centrally embedded in a wide concrete blocks as shown in Fig. 3.54. The results shown in Fig. 3.55 indicate that welded stiffener plates create a good alternative for the traditional shear studs in terms of load-bearing capacity, but the ductility of the connection is greatly reduced. The stiffener connectors were tested in two orientations of the steel profile – with the strong axis of the steel profile perpendicular and parallel to the longer side of the concrete block. It was identified that when the strong axis of the steel profile is parallel to the longer side of the concrete block, the additional reinforcement around the steel profile is not required, but for the second variant, the additional reinforcement greatly improves the performance of shear connection and prevent from the brittle damage of concrete. From the test campaign, it was

observed that steel-concrete bond and plate stiffener connector work simultaneously in the force transfer. A design proposal was derived for the stiffener type of shear connector, where the method is based on the strut and tie model and plasticity planes in the stiffener. The resistance of the connector is related to the concrete compression resistance and a condition for the thickness of the applied stiffener connector.



a) b)

Fig. 3.54. Push-out specimen layout with the stiffener type connector – a) strong axis orientation and b) weak axis orientation. (Source: SmartCoCo [175]).



a) b)

Fig. 3.55. Load-slip curves of the stiffener connector – a) strong axis orientation (B) and b) weak axis orientation (D). (Source: SmartCoCo [175]).

Perfobond connector

The perforbond shear connector consists of a perforated steel plate welded perpendicularly to a steel profile as shown in Fig. 3.56. Four main types of perfobond shear connections can be distinguished: (i) perfobond, (ii) T-Perfobond, (iii) I-Perfobond and (iv) 2T-Perfobond as also shown in Fig. 3.56. The perfobond connection base on the bearing action of the welded plate and the composite dowel action developed in the perforations, see Fig. 3.56 and Fig. 3.57. The perfobond connection can be reinforced by placing the reinforcement bars passing through the opening in the perfobond rib steel plate. A wide literature in the topic of the perfobond type of shear connectors can be found, like for example Neto et al. [128], Valente [189], Oguejiofor and Hosain [133], Klaiber and Wipf [100], Ahn et al. [5], Vianna et al. [195], Cândido-Martins et al. [28], Spremić et al. [178], Veldanda and Hosain [192], Su et al. [179], Kim et al. [99], Kvočák et al. [106], Wang et al. [198] and Jeong [84].

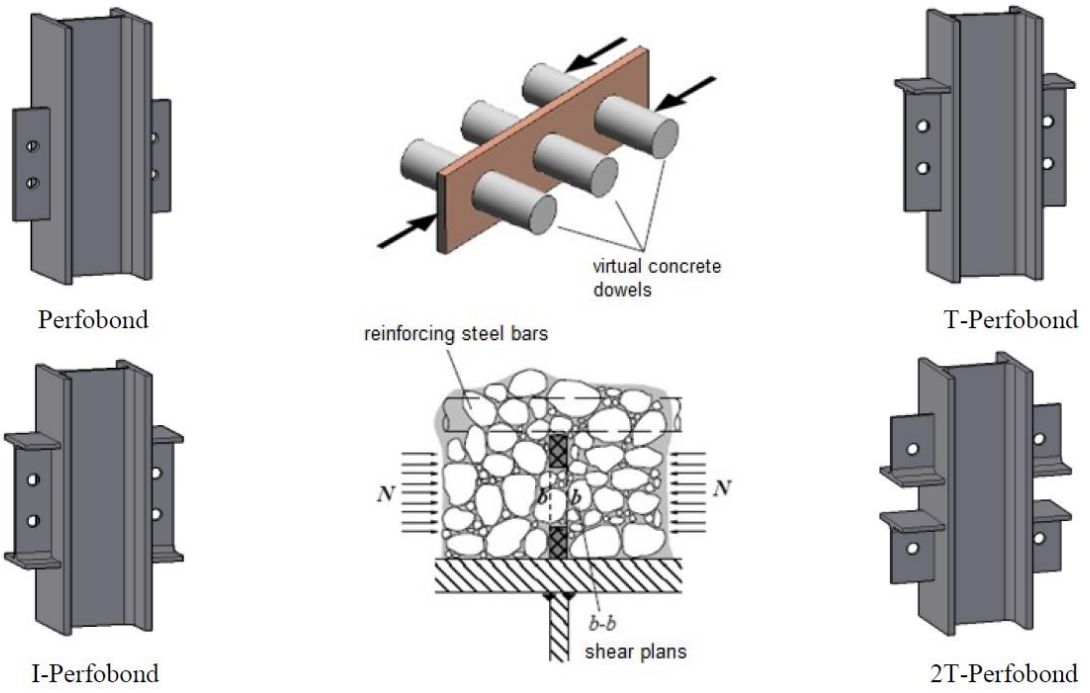


Fig. 3.56. Examples of perfobond type of shear connectors. (Source: Neto [128]).

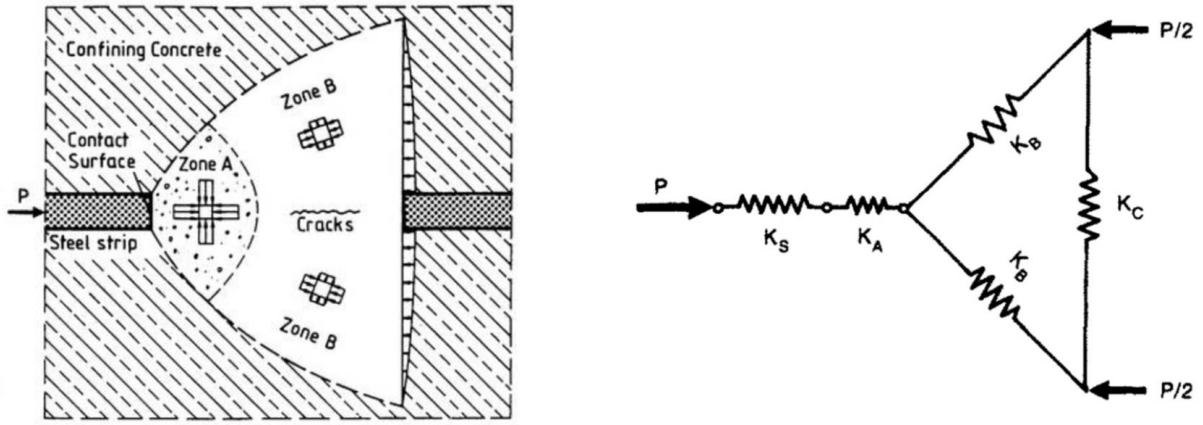
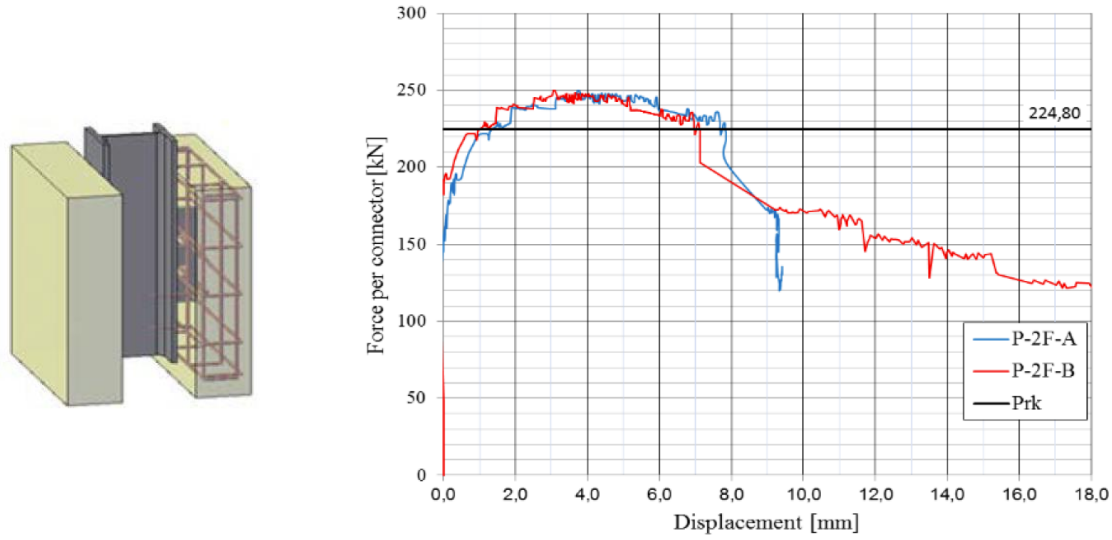


Fig. 3.57. Behaviour of concrete dowel in a perfobond shear connection. (Source: Braun [23]).

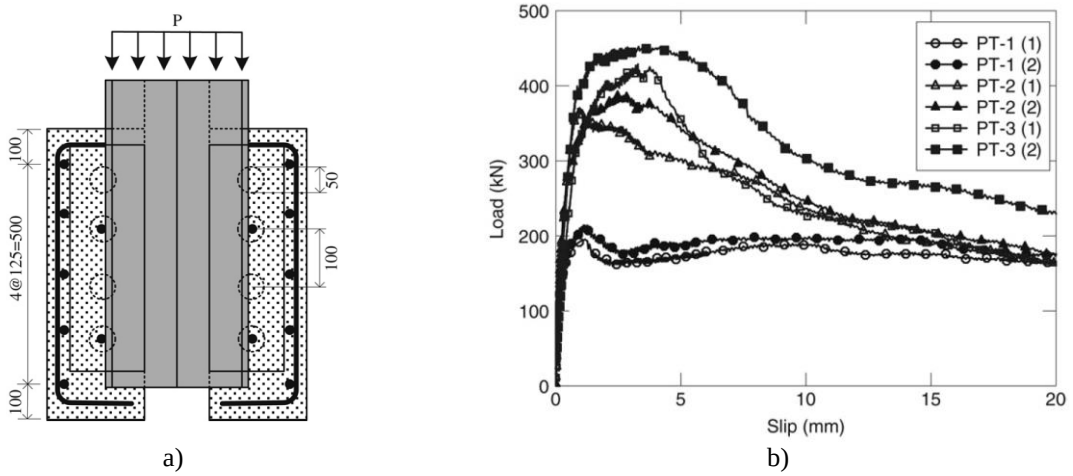
A typical load-displacement characteristic of the perfobond connection is shown in Fig. 3.58b, where one perfobond plate was placed on each side of the steel profile as shown in Fig. 3.58a. Neto et al. [128] analysed amount and spacing of the perfobond connectors, as well as presence of the reinforcing bars. It was observed that the increased number of connectors on the same height, placed parallel, resulted in an increased load bearing capacity but the ductility was greatly reduced. The existence of the reinforcement bars improved the performance of both, load-bearing capacity and ductility aspects. A conclusion can be draft that if the concrete grade rise, the ductility of the connection decrease.



a) b)

Fig. 3.58. Push-out test of the perfobond connector – a) specimen and b) load-slip curves. (Source: Neto [128]).

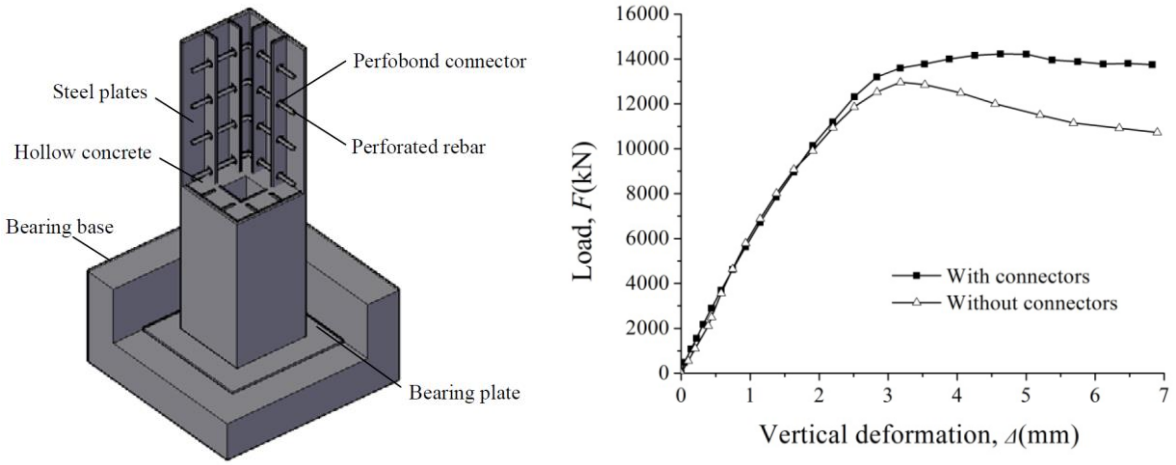
Application of the perfobond connectors in steel-concrete composite slabs has been analysed by Jeong et al. [84], where due to a small thickness of the steel sheeting, welding of shear studs would be not efficient. The performed push-out tests consisted of welded plates without perforation (series PT-1), plates with 50 mm holes in 100 mm spacing (series PT-2) and plates with the same perforation pattern as series PT-2 but with passing through 16x200 mm reinforcement (series PT-3). Specimen details and test results are shown in Fig. 3.59.



a) b)

Fig. 3.59. Push-out test of the perfobond connector with steel sheeting – a) specimen and b) load-slip curves. (Source: Jeong [84]).

Wang et al. [198] investigated the perfobond connectors impact on the bearing capacity of a composite pylon of a bridge. A model of the analysed case together with obtained results is shown in Fig. 3.60. The tested specimens consisted of concrete filled rectangular steel tube, where the concrete infill also consisted of a hollow in the centre. The shear connectors were placed in the longitudinal orientation with passing reinforcement bars. From the comparison of the specimen with and without perfobond connectors, it can be observed that presence of shear connectors greatly improved the ductile response of a pylon and prevented the normal separation between the steel tube and concrete infill.

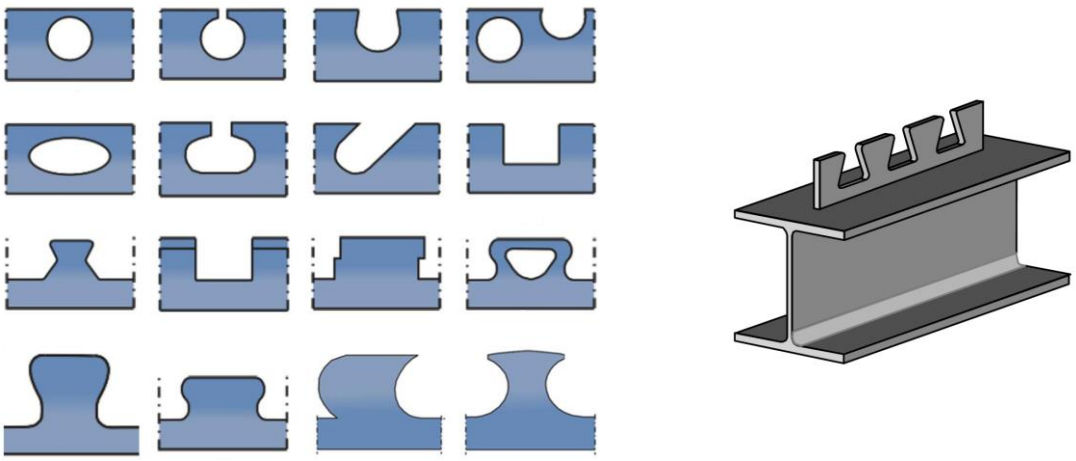


a) b)

Fig. 3.60. Test of a composite pylon with perfobond connectors – a) specimen and b) load-displacement curves. (Source: Wang [198]).

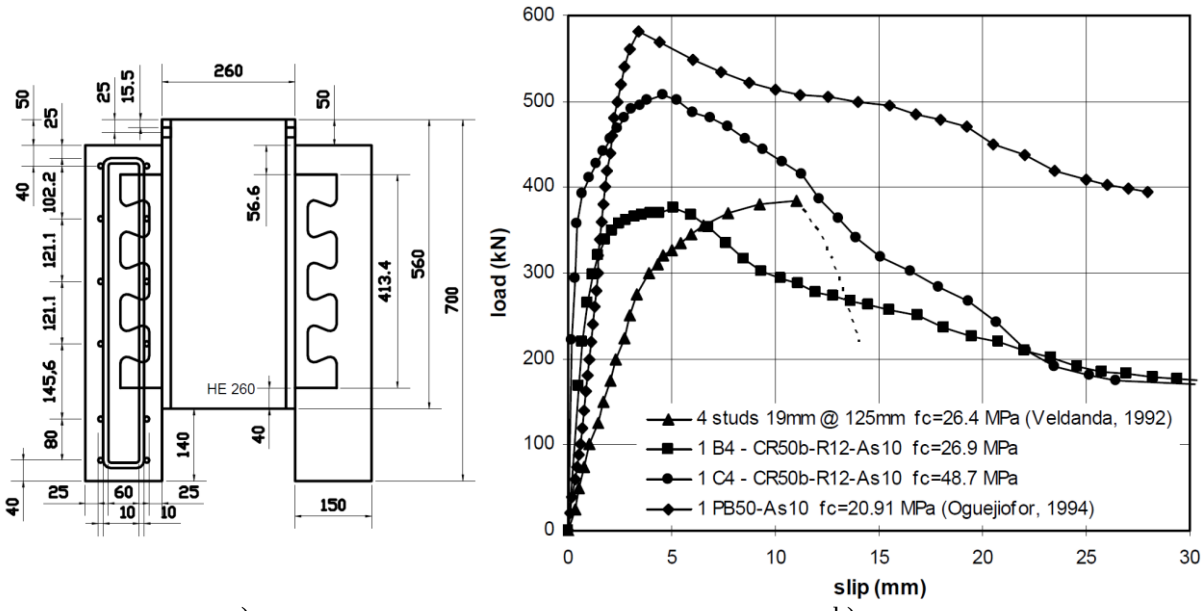
Crestbond, Puzzle and Clothoid connectors / Open perforated plates

The open perforated plate shear connectors derived from the perfobond shear connectors and they are commonly accounted to the composite dowels shear connectors [193]. Similar like in the perfobond connectors, they consist of welded perpendicular steel plates but the perforations have opened pattern, see Fig. 3.61. The opening and modified geometry of the perforations bring a bigger flexibility with the arrangement of the transversal reinforcement in the concrete slab during the construction process. Various types of composite dowel shear connectors can be distinguished as shown in Fig. 3.61, where the most common solutions are: (i) perfobond (1 row/1 column), (ii) crestbond (4 row/1 column), (iii) puzzle (4 row/2 column) and (iv) clothoid (4 row/4 column). The behaviour of the crestbond type of connector has been investigated by Veríssimo et al. [193] in standard push-out tests for shear connectors according to EN 1994-1-1 [58]. In Fig. 3.62, a test specimen layout and obtained load-slip curves for the crestbond connectors are given. On the diagram shown, a comparison to the shear studs and perfobond connectors is made. The possible failure patterns of the crestbond connectors are shown in Fig. 3.63, where the concrete shearing, concrete crushing, shearing of a connector and concrete prying failure modes are distinguished. A comprehensive analysis of the composite dowels in the open perforated connectors can be found in the work of Kopp et al. [103] and Classen et al. [32, 33].



a) b)

Fig. 3.61. Composite dowel shear connectors – a) different types (Source: Alves [7]) and b) crestbond detail (Source: Veríssimo [193]).



a) b)

Fig. 3.62. Crestbond connector – a) push-out specimen and b) load-slip behaviour. (Source: Veríssimo [193]).

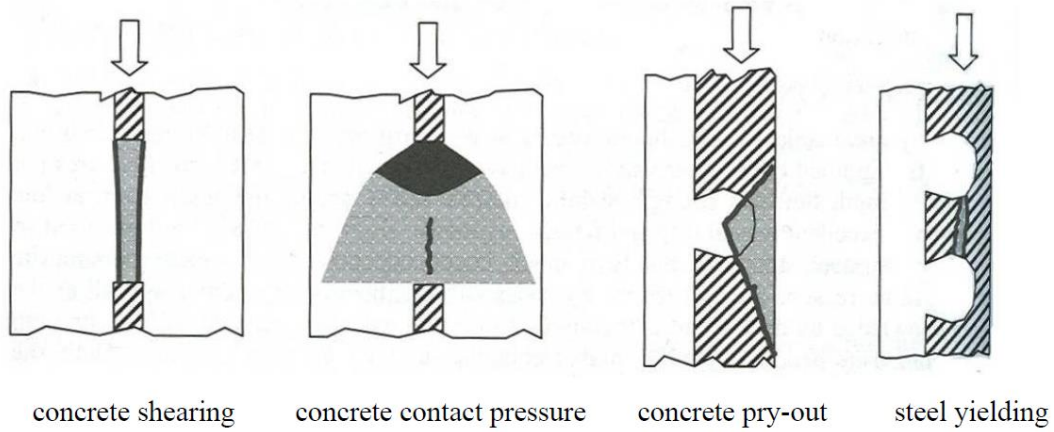


Fig. 3.63. Failure modes of the composite dowels shear connectors. (Source: Valente [189]).

Tail connectors

The tail connectors consist of trapezoidally-shaped rib plates with perforations as shown in Fig. 3.64, where the steel ribs are welded perpendicularly to a steel profile. This type of connectors comprises the plate bearing and composite dowel mechanisms in the longitudinal shear force transfer. The behaviour of the tail connectors in steel-concrete composite beams has been investigated by Kovács et al. [104]. The obtained load-relative slip performance is shown in Fig. 3.65.

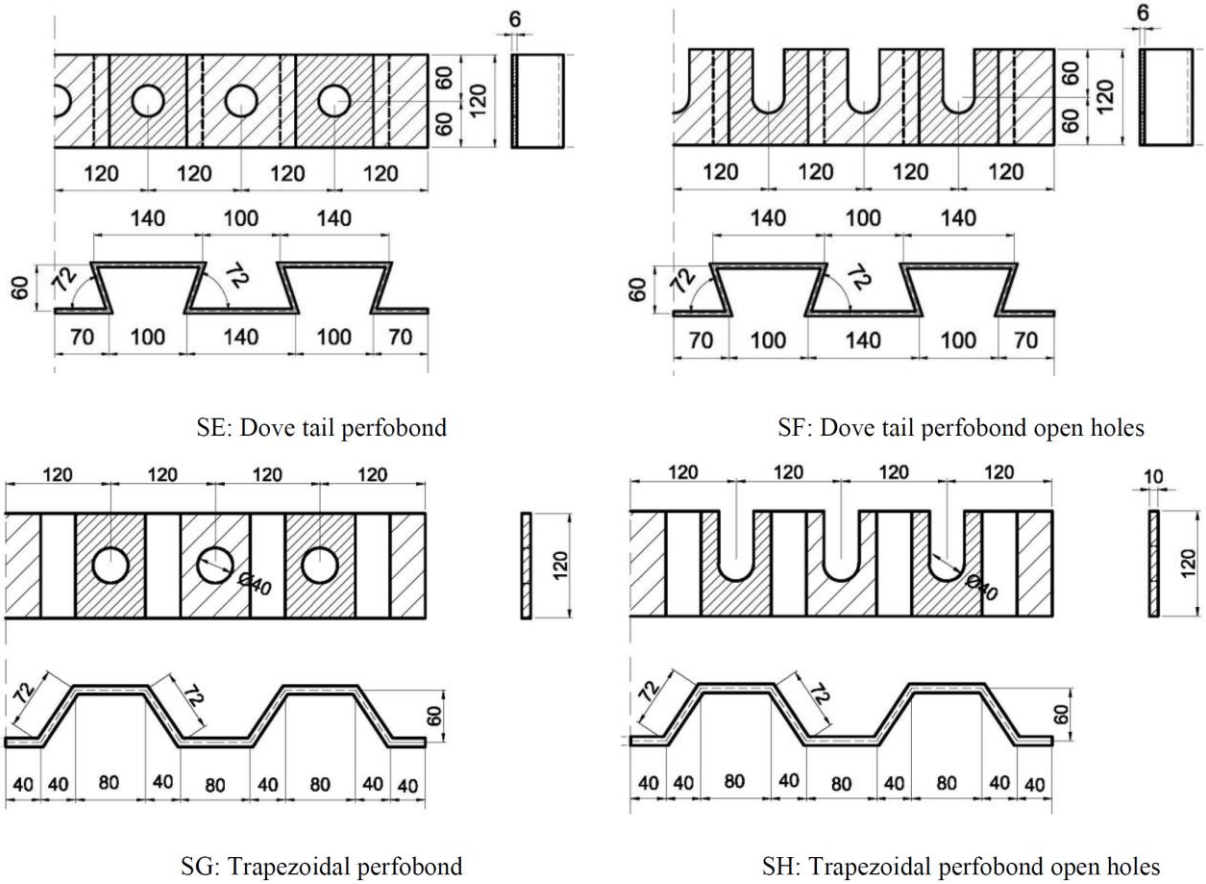


Fig. 3.64. Tail shear connectors. (Source: Kovács [104]).

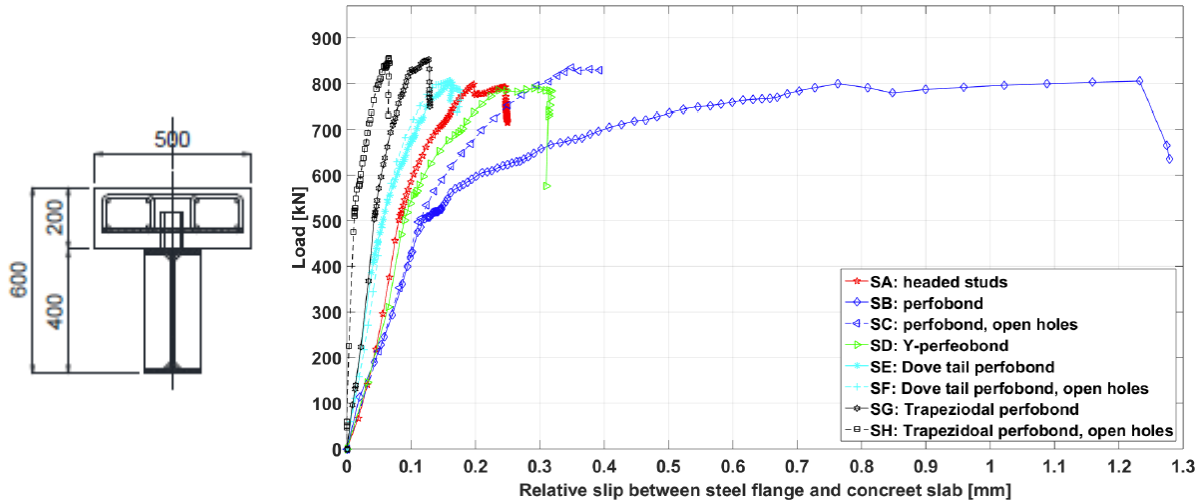


Fig. 3.65. Beam tests of tail shear connectors. (Source: Kovács [104]).

Steel sheeting

The steel sheeting is commonly used for steel-concrete composite slabs and consist of a special geometry, as well as perforations in order to reduce the amount of used concrete in a slab element and to assure the composite action between the steel and concrete parts. The application of steel sheeting in composite slabs is foreseen in the design codes, like for example EN 1994-1-1 [58]. Examples of the steel sheeting geometry with indicated different variants of shear connection are shown in Fig. 3.66. The specially shaped ribs in the steel sheeting creates the frictional interlock, which resists the relative slip. Moreover, in the steel sheeting, often various perforations are present in order to increase the shear connection strength at the interface by additional bearing effects between the perforation and the concrete. The end-anchorage of the steel sheeting should be assured by an additional mechanical shear connection mean, for example, shear studs.

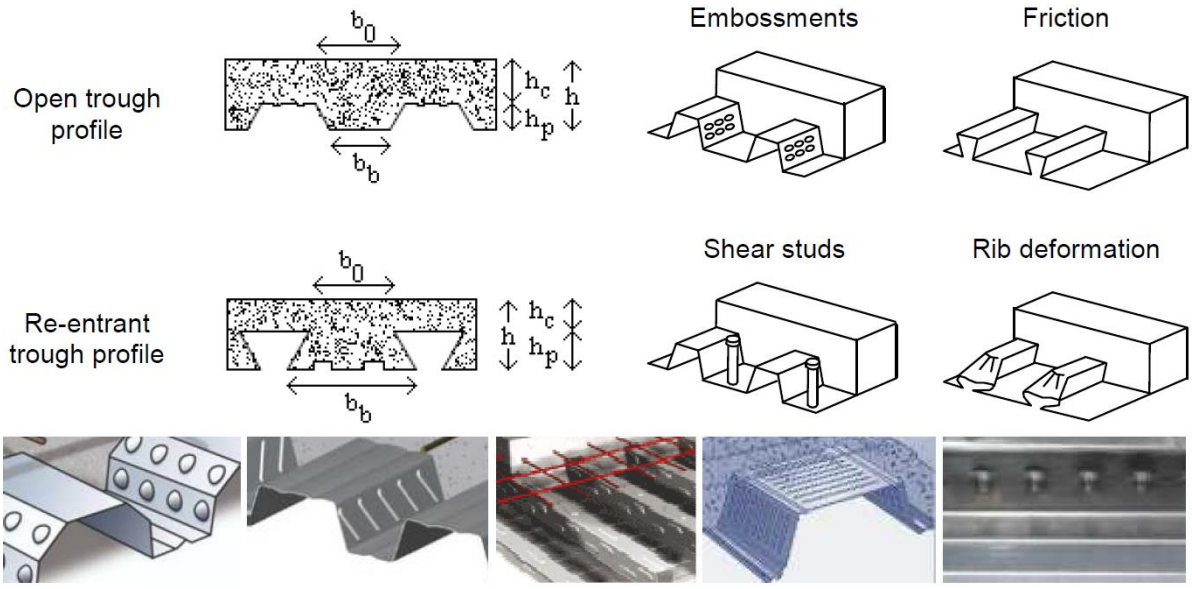


Fig. 3.66. Typical forms of steel sheeting in composite slabs. (Source: Seres [171]).

Grouted connections

The grouted shear connections consist of embossments on two consequent internal surfaces of a double tubular telescope connection with grout-filled space between the tubes as shown in Fig. 3.67. The investigation on this type of shear connection can be found in the work of Schaumann et al. [167] and Pan et al. [138], where the submerged and dry connections were tested respectively. In both cases, push-out tests were performed to analyse the performance of the grouted shear connection and in the next step, large-scale tests were performed in order to simulate a foundation column of an offshore wind turbine. In Fig. 3.68, the submerged specimen layout and experimental load-displacement curves are shown. For the dry tests, the specimen layout and test results are shown in Fig. 3.69, where the shear stresses were evaluated as the recorded force divided by the contact area between the inner tube and the grout.

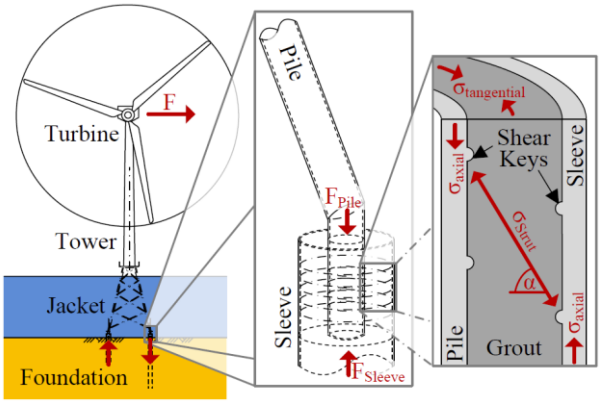
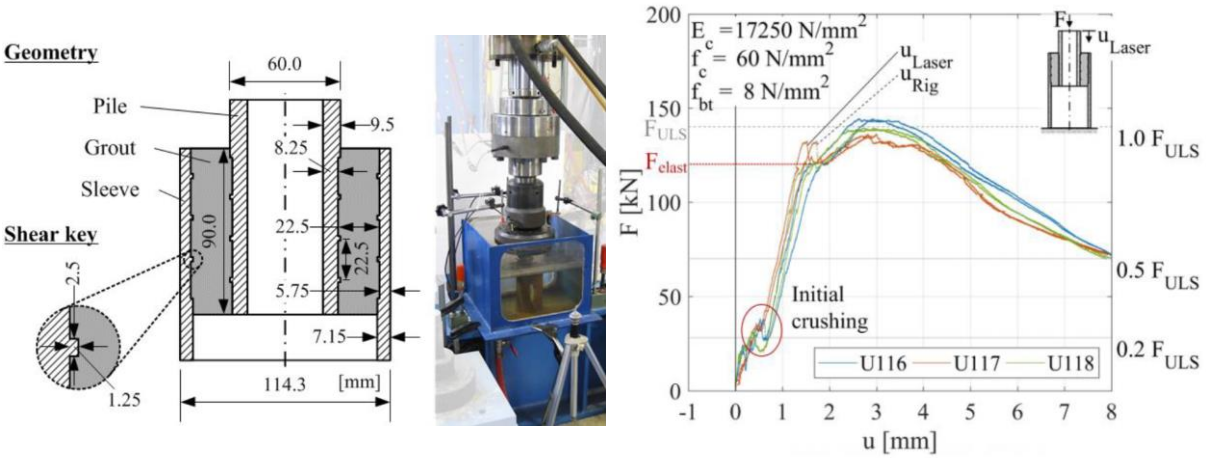
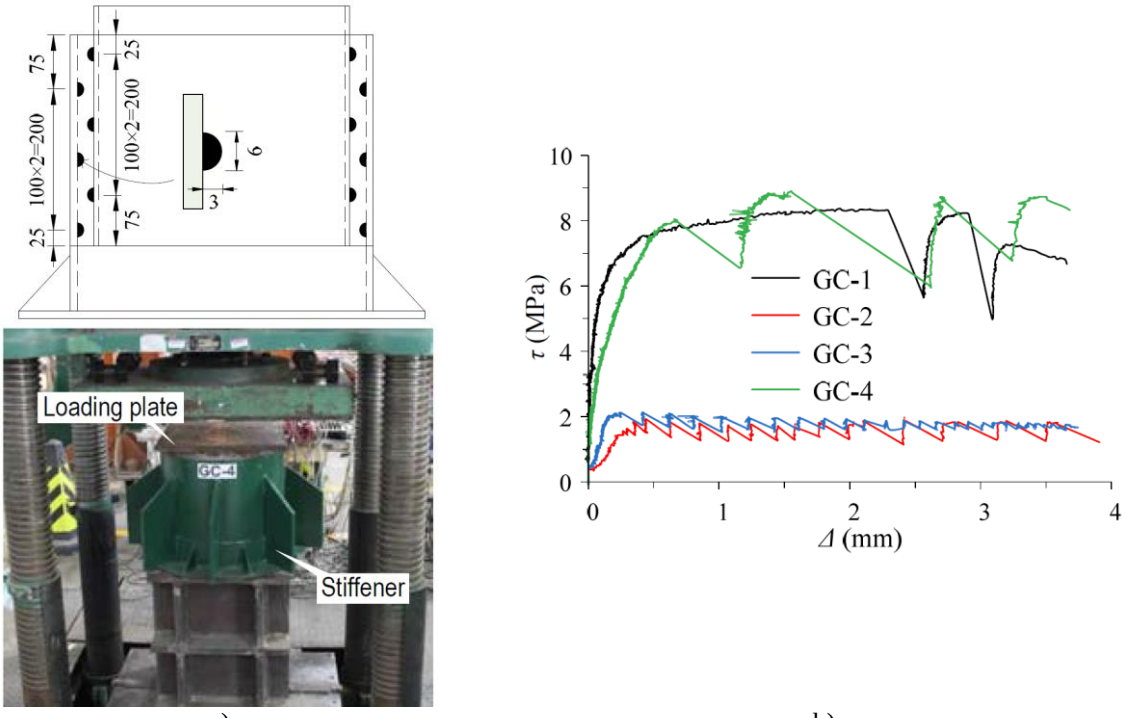


Fig. 3.67. Motivation for the utilisation of the grouted shear connection. (Source: Schaumann [167]).



a) b)

Fig. 3.68. Tests of the submerged grouted shear connection – a) specimen and b) test results. (Source: Schaumann [167]).



a) b)

Fig. 3.69. Dry tests of the grouted shear connection – a) specimen and b) test results. (Source: Pan [138]).

A separate type of grouted connection has been analysed by Papastergiou and Lebet [139, 140], where the cement grout was placed between the prefabricated concrete slab and perforated steel plate welded to a steel profile as shown in Fig. 3.70. The behaviour of the grouted connection for a bridge structure was analysed with respect to the cyclic loading, concrete grade and age. The obtained experimental load-slip response from the push-out tests is shown in Fig. 3.71, where pairs of specimens PR100_1 and PR100_2, and consequently each further pair, refer to one concrete grade and varies between the non-cycled and cycled specimens. The concrete grade varies between f_{cm}= 76.4-99.4 MPa. The concrete age varies between 32-185 days. Each first specimen from the pair was cycled only once, where each second specimen from the pair was cycled from 2E+06 to 5E+06 times.

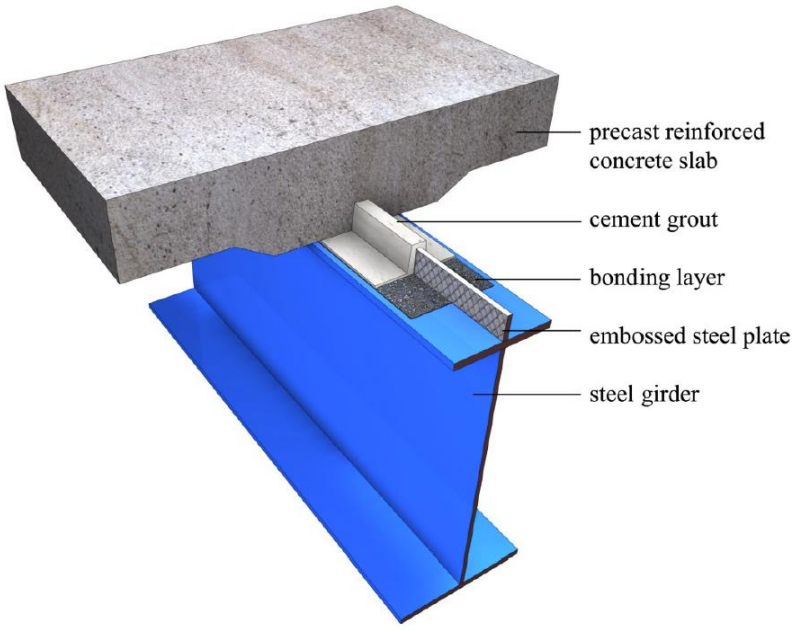
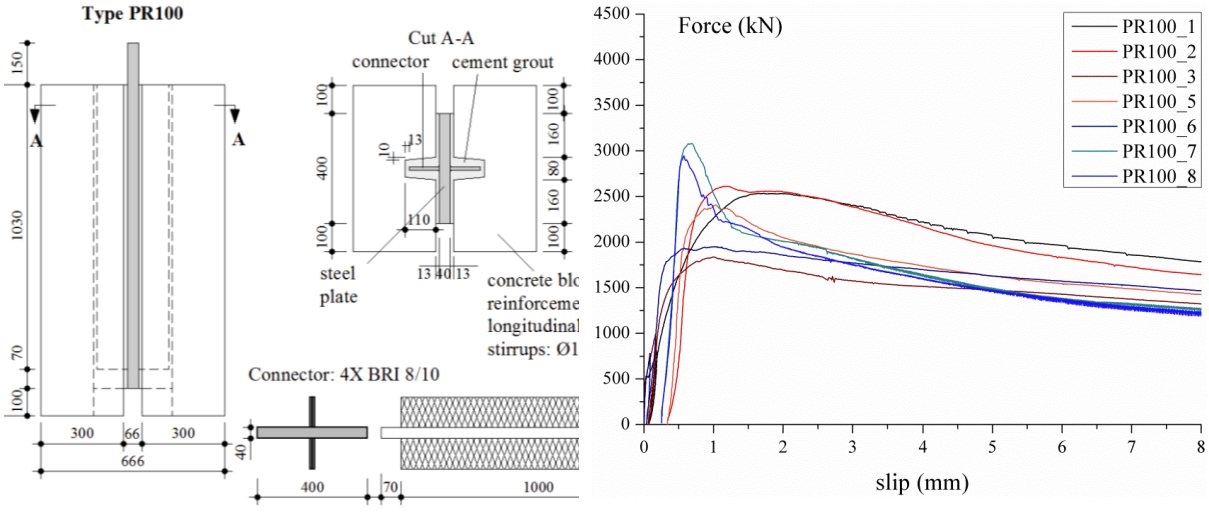


Fig. 3.70. Grouted connection between steel girder and concrete slab. (Source: Papastergiou [139]).



a) b)

Fig. 3.71. Grouted connection for steel girder – a) specimen and b) test results. (Source: Papastergiou [139]).

Small-scale pin connectors

The small-scale pin connectors consist of a pin shape created entirely in the welding process as shown in Fig. 3.72. This type of shear connectors has been developed at the University of Aachen, Germany with the application to the thin composite structures utilising high strength concrete grades. The investigation on the behaviour of the pin shear connectors can be found in the work of Classen et al. [34] and Wolters et al. [203]. The load-slip characteristic of the small-scale shear connectors was tested in push-out tests with the usage of high-strength concrete (HSC) and ultra-high-performance concrete (UHPC). The test setup and obtained results are shown in Fig. 3.73. An engineering model has been proposed by Classen et al. [34] for the evaluation of the resistance of pin shear connectors.

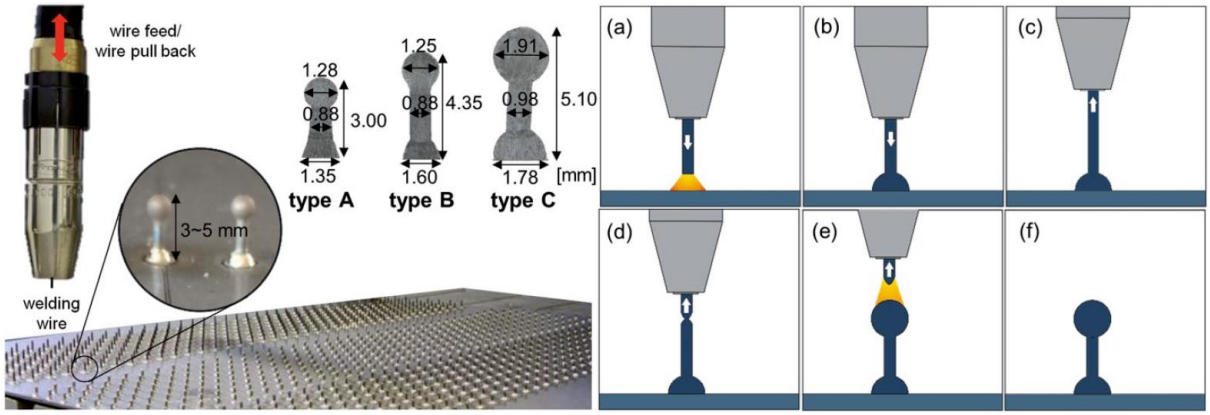
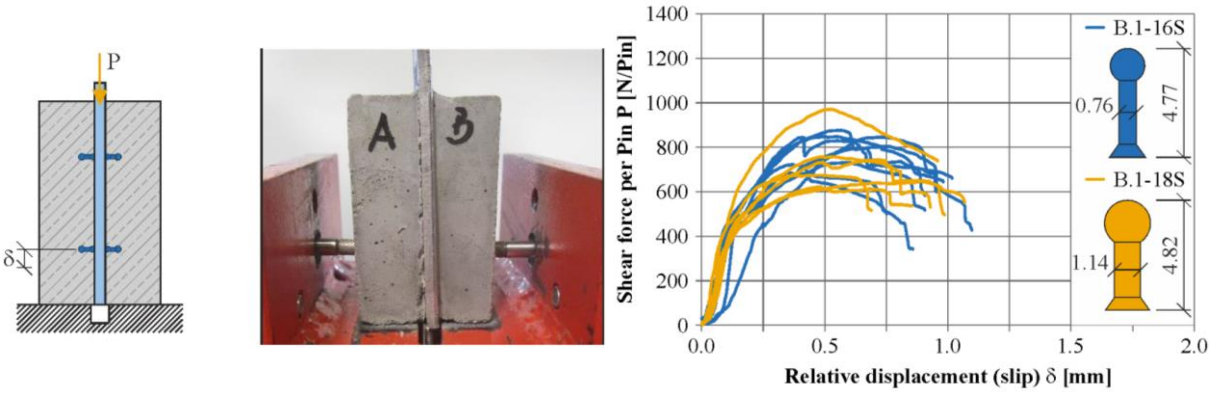


Fig. 3.72. Small-scale pin shear connectors and their production process. (Source: Classen [34]).



a) b)

Fig. 3.73. Push-out tests of pin shear connectors – a) specimen and b) test results. (Source: Wolters [203]).

Reinforcement bars

The application of regular reinforcement bars as the shear connector between the steel beam and concrete slab was investigated by Frangi, Fontana and Mensinger [63, 64]. The application of the reinforcement bars as shear connectors has been motivated by the development of the slim composite floor system, where the installation ducts were foreseen in the geometry of the floor structural system. The slim installation floor system is shown in Fig. 3.74. The performance of the slim floor system was tested in the four point bending tests and in two configurations as shown in Fig. 3.75. The resultant load-deflection curves are shown in Fig. 3.75, where "Beam I" refers to the configuration with concrete slab

on the top and “Beam II” refers to the configuration with concrete slab on the bottom. It can be observed that the applied reinforcement bars as shear connectors allowed for the development of the plastic bending capacity of the floor system.

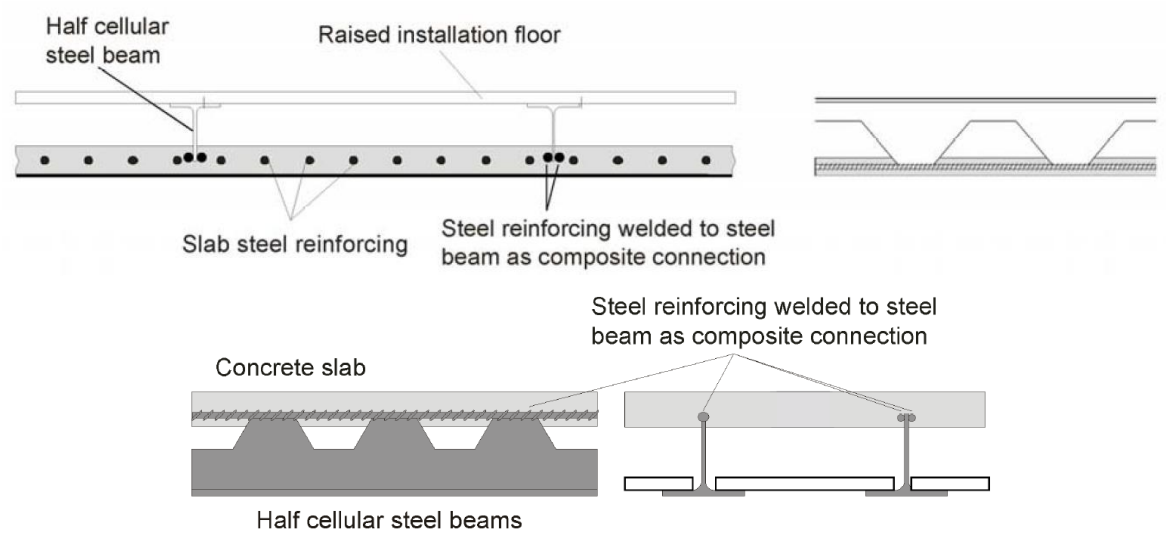


Fig. 3.74. Slim floor system with the reinforcement bars used as the shear connectors. (Source: Frangi [63]).

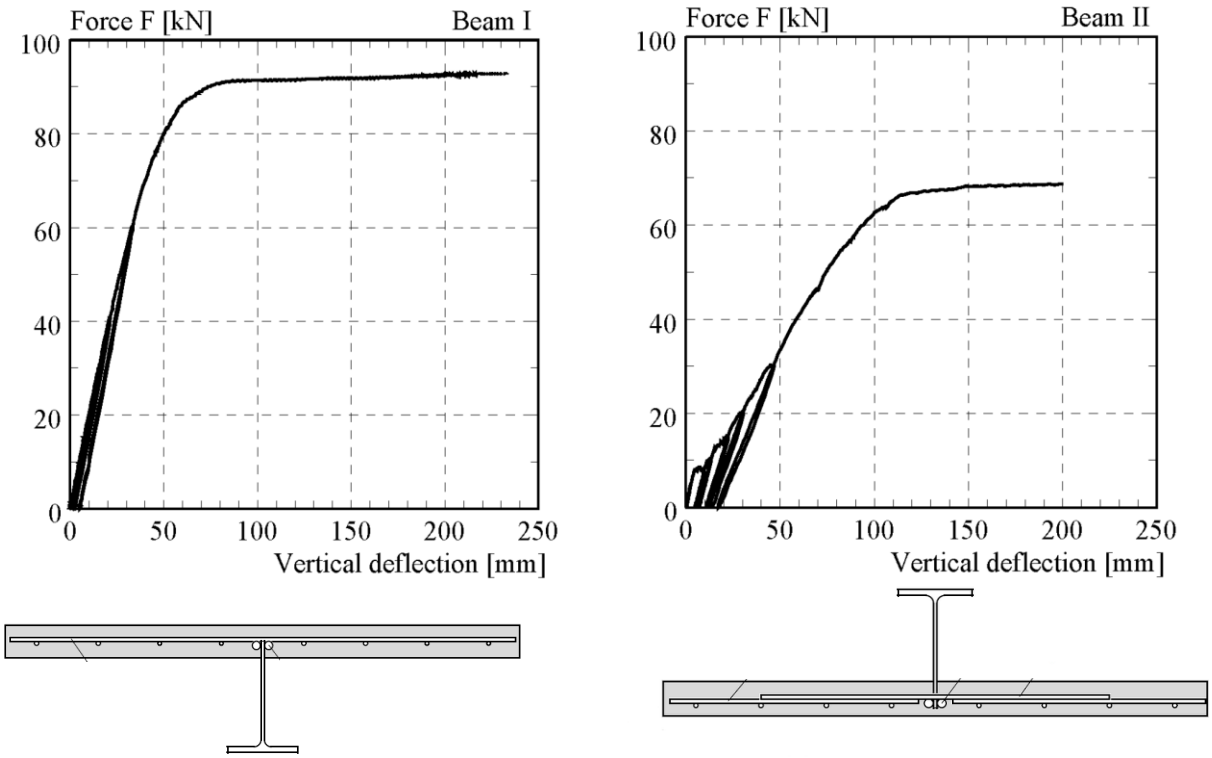
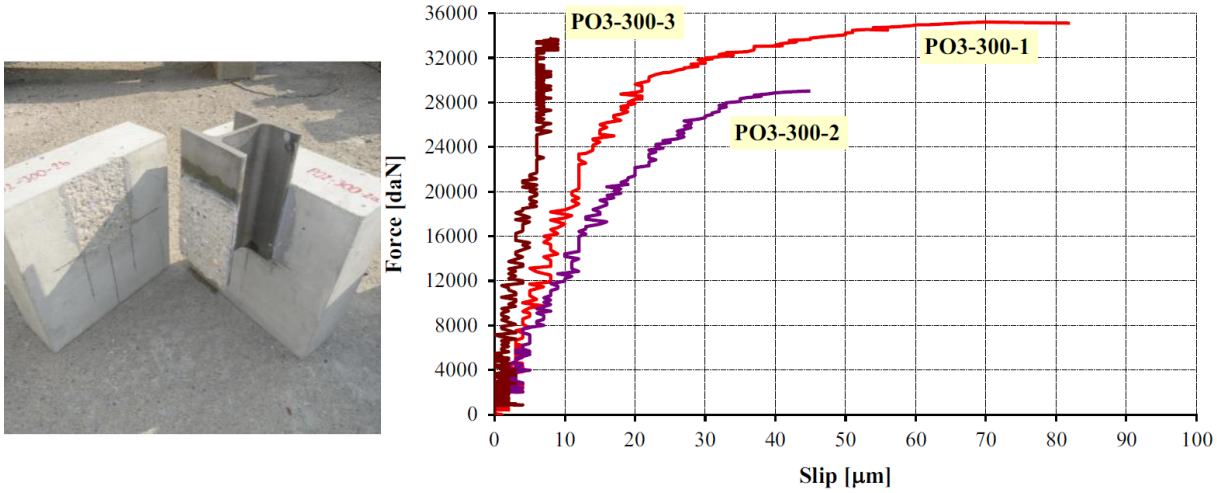


Fig. 3.75. Beam test results of slim installation floor system with the reinforcement bars used as the shear connectors. (Source: Frangi [64]).

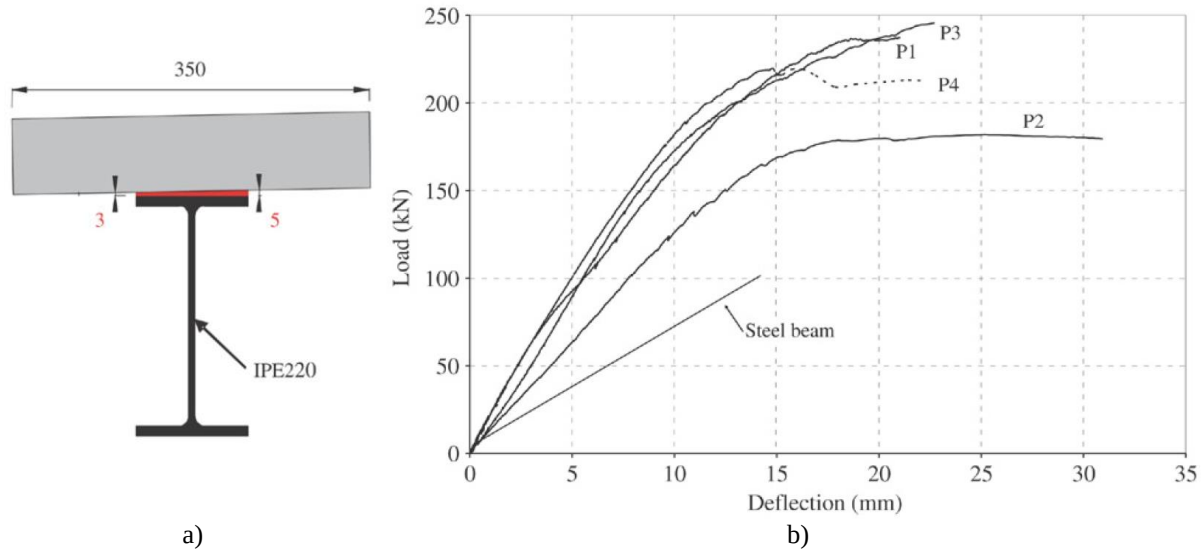
Epoxy bonded connection

An alternative connection type with reference to the typical shear connectors used in steel-concrete composite structures has been identified in the form of bonding products. Jurkiewiez et al. [93], Meaud et al. [121], Bouazaoui et al. [21], Kludka and Kurz [101] and Aboobucker et al. [1] analysed the epoxy as a type of shear connection mean. As a typical bonding product, the epoxy resin was tested since it shows a good hygrometry and temperature behaviour for the structural application [93]. Moreover, epoxy resin exhibit rigid connection. As an alternative bonding product, the polyurethane adhesive was tested, which allows for a bigger deformation at the steel-concrete interface but the strength of the connection is reduced [101]. Normally two types of failure could be observed: (i) failure of the concrete and (ii) adhesive failure due to the cohesion fracture. The behaviour of the epoxy shear connection has been tested in push-out tests, see Fig. 3.76, and in beam tests, see Fig. 3.77. The concrete strength in the push-out tests was 38.8-43.4 MPa, where for the beam tests, the concrete strength was 68 MPa.



a) b)

Fig. 3.76. Push-out tests of epoxy shear connection – a) tested specimen and b) test results. (Source: Meaud [121]).



a) b)

Fig. 3.77. Beam tests with epoxy shear connection – a) specimen and b) test results. (Source: Bouazaoui [21]).

Perforations in embedded steel profiles

The shear connection between the steel beam and the concrete slab in composite shallow slim floor systems is often achieved by introducing perforations in the steel profile and encasing it in the concrete, see Fig. 3.78. The encased perforations result in the development of the composite dowels, where the shear connection mechanism is analogous to the mechanism of composite dowels in the perfobond connectors or open perforated plate connectors. A transversal reinforcement passing through the perforations in the steel beam enhance the performance of the shear connection. An analysis of this type of connection can be found in the work of Leskelä [110] about box-shaped perforated shallow composite beams, Braun [23, 24] about the investigation on the load-bearing capacity behaviour of composite dowels or Huo [76] about the shear transfer in composite shallow cellular floor beams. The load-slip behaviour of composite dowels with reinforcement is shown in Fig. 3.79. Two possible composite dowel failure modes were identified in push-out tests for varied concrete strength, "Kinking" and "Shear".



a) b)

Fig. 3.78. Shallow cellular floor beam – a) detail and b) construction application. (Source: Huo [76]).

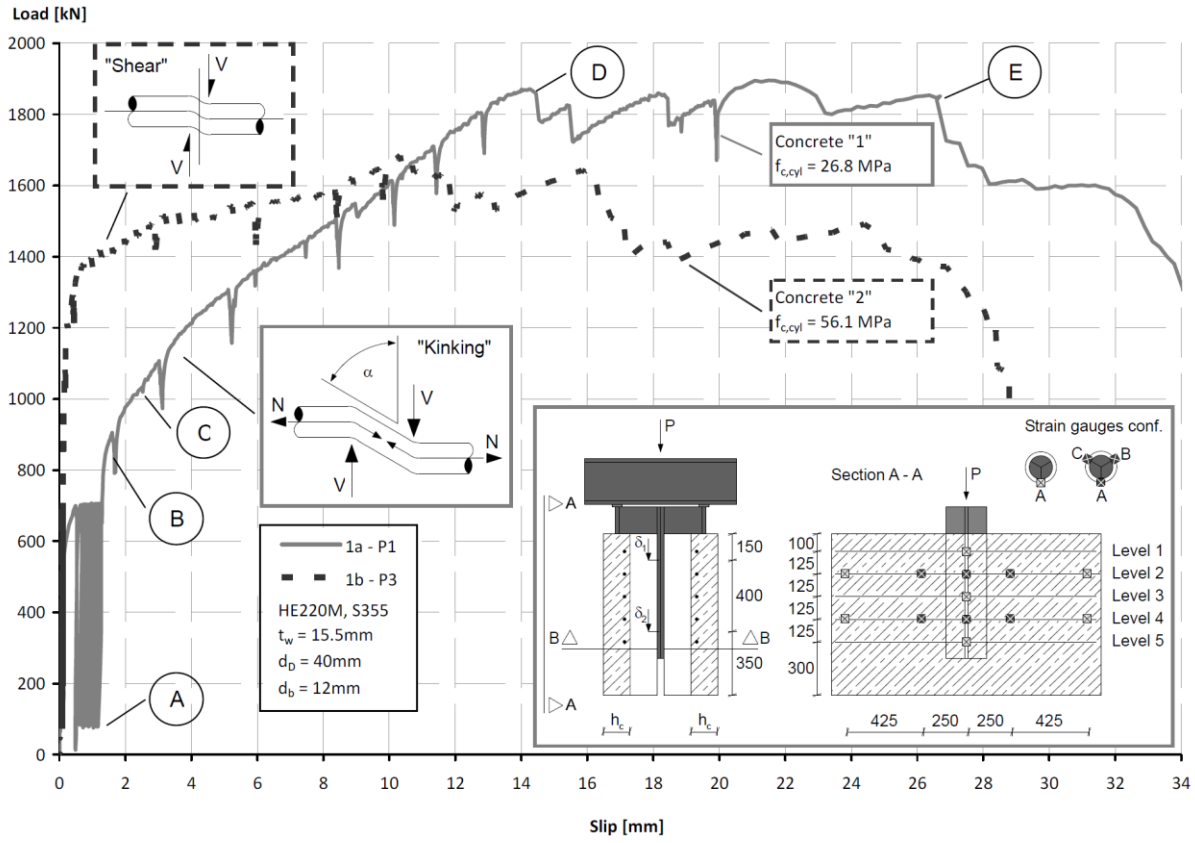
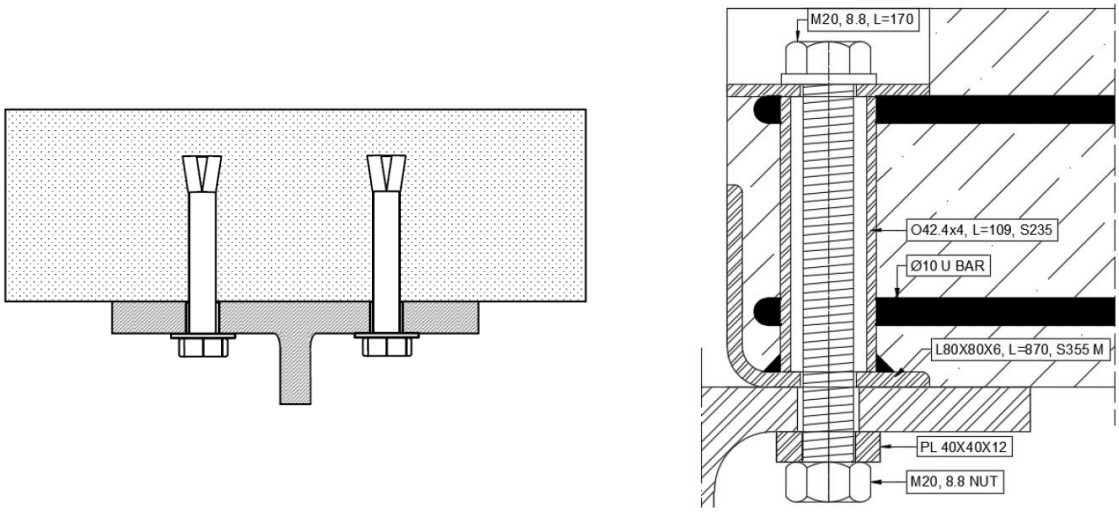


Fig. 3.79. Load-slip curves of composite dowels obtained from push-out tests. (Source: Braun [24]).

Demountable connectors

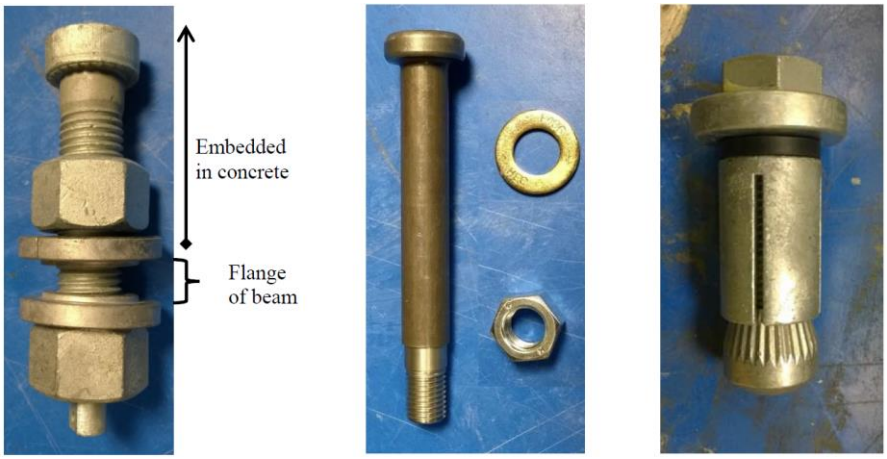
The demountable shear connectors mainly consist of different types of bolted connection systems. Two main groups of demountable shear connectors can be distinguished (i) non-reusable and b) fully reusable as shown in Fig. 3.80. The non-reusable shear connectors normally consist of anchor bolts or epoxy injected anchors used for the strengthening of existing composite structures [107]. The fully reusable shear connectors are based on the bolt-type connections with specially designed cylinder or coupler systems embedded in the concrete allowing for a circular economy of the composite structures. The reuse feature of composite elements positively affects the carbon footprint of the construction sector and allows for easy demountability and reusability of non-damaged composite elements [105].



a) b)

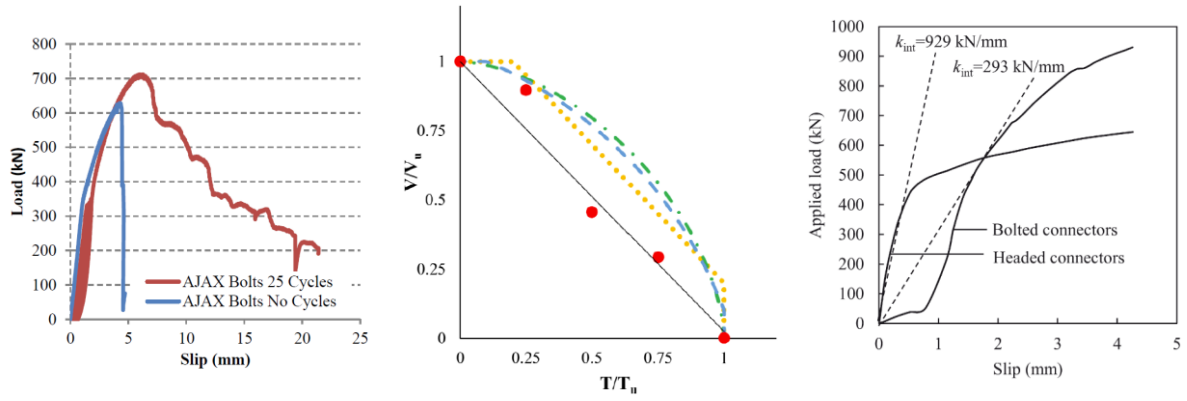
Fig. 3.80. Demountable shear connectors – a) non-reusable expansion anchors (Source: Kwon [107]) and b) reusable bolt cylinder system (Source: Kozma [105]).

The behaviour of anchor bolts, like for example AJAX bolts, Lindapter bolts, and threaded studs shown in Fig. 3.81, had been analysed by Mirza et al. [122], Uy et al. [188] and Versani et al. [191] in push-out tests and FE simulations. The load-slip behaviour of AJAX bolts is shown in Fig. 3.82.



a) b) c)

Fig. 3.81. Non-reusable and demountable shear connectors – a) AJAX bolt, b) threaded shear stud and c) Lindapter bolts. (Source: Versani [191]).



a) b) c)

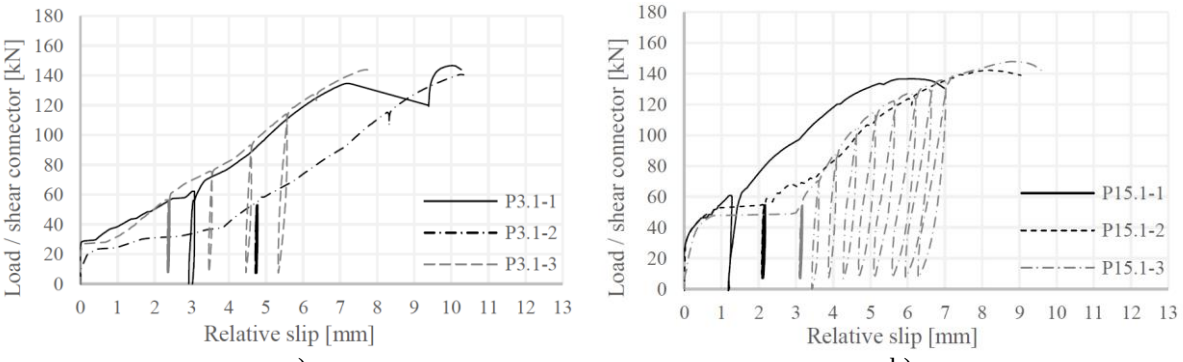
Fig. 3.82. Behaviour of AJAX bolts – a) load-slip curves after cycling load (Source: Mirza [122]), b) shear-tension interaction diagram (Source: Versani [191]) and c) load-slip curve in comparison to headed studs (Source: Uy [188]).

System solutions for the non-reusable shear connectors are also provided by the company Hilti AG with special connector system [28] shown in Fig. 3.83 and with epoxy anchored bolt systems HAS-E and HIT-TZ [107].



Fig. 3.83. Demountable shear connector system from Hilti. (Source: Cândido-Martins [28]).

The behaviour of fully reusable type of demountable shear connectors (Fig. 3.80b) is investigated in the RFCS project "REDUCE" with grant agreement RFCS-GA-710040 and the push-out investigation can be found in the work of Kozma et al. [105]. The obtained load-slip characteristics for the cylinder and coupler systems in the solid slabs are shown in Fig. 3.84.



a) b)

Fig. 3.84. Load-slip behaviour of the reusable and demountable shear connectors – a) cylinder system and b) coupler system. (Source: Kozma [105]).

3.4. Provisions for the design of composite columns

3.4.1. General considerations

The design of steel-concrete composite columns consists of the verification of the axial and biaxial bending resistances, where their interaction, acting shear forces, buckling instabilities, second order effects and imperfections have to be considered [71, 89, 110, 127, 158-160]. Three main approaches for the analysis based on the cross-sectional forces equilibrium and strains compatibility can be identified: (i) pure steel approach, (ii) reinforced concrete approach with additional steel reinforcement and (iii) composite approach [25]. In Fig. 3.85, the above-mentioned different approaches are compared on the example of N-M interaction diagram for fully encased I-steel section, where for the pure steel approach the enhancement for bending is neglected due to the lack of consideration of the reduced cracking of concrete with coexisting normal forces. On the presented diagram, Eq. 1 and Eq. 2 are rewritten below in Eq. 3.52 and Eq. 3.53 respectively, where they are based on the Australian design code AS 4100 [10] but a reference can be found also in EN 1993-1-1 [55] and ANSI/AISC 360 [8]. Where, M_{uo} is the pure bending moment capacity and N_{uo} is the pure axial compression capacity.

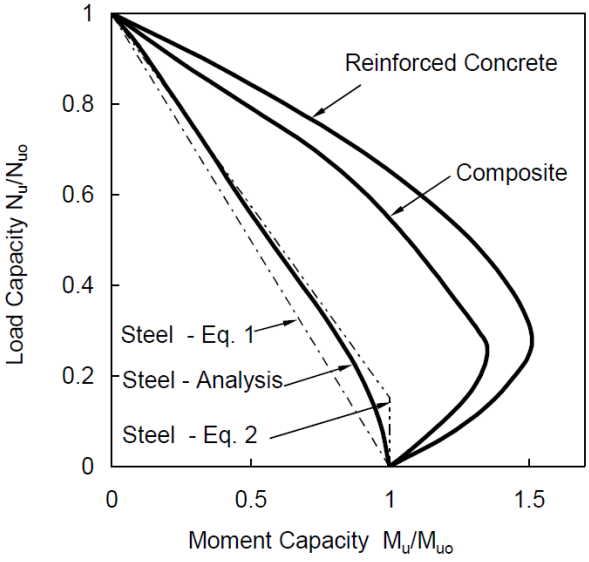


Fig. 3.85. Load-moment (N-M) interaction curves of composite column with fully encased I-section and considering different analysis approaches. (Source: Bridge [25]).

$$\frac{M_u}{M_{uo}} = 1 - \frac{N_u}{N_{uo}} \tag{3.52}$$

$$\frac{M_u}{M_{uo}} = 1.18\left(1 - \frac{N_u}{N_{uo}}\right) \leq 1.0 \tag{3.53}$$

The shear connection at the steel-concrete interface of composite columns should assure the force transfer from the load introduction point to the entire composite cross-section. Outside the load-introduction zones, the composite action should be assured considering concrete cracking and long-term effects. Normally, only double-symmetric cross-sections with one embedded steel profile are considered

in the design procedures and despite the composite theory, described in Section 3.1, the longitudinal shear is normally analysed in the conservative way according to the elastic analysis and following the principal relation $\tau_{zx} = \tau_{xz}$ with "x" and "z" corresponding to the longitudinal and transversal axes of the composite column. Cross-sectional geometries and detailing of the reinforcement, as well as concrete cover in the fully encased columns, should satisfy the requirements of application, efficiency and fire safety. Furthermore, the verification of the fatigue and serviceability limit design should be done in parallel but these aspects are not considered in the presented work.

The evaluation of the composite column cross-sectional resistances requires utilisation of the full shear connection at the steel-concrete interface, assurance of the shear reinforcement and assessment of the axial and flexural stiffnesses. Instabilities due to the compression forces, imperfections, eccentricities and acting bending and transversal loads impose a flexural reaction of a column. Therefore, evaluation of the flexural stiffness defines the general behaviour and allows for the assessment of the elastic critical buckling load, commonly called Euler's critical load. In the result, the obtained resultant resistances are strongly dependent on the considered stiffness of a column member.

3.4.2. International standards

The design provisions for composite columns in steel and concrete can be found in various international standards like for example the European design code EN 1994-1-1 [58], American building code ACI 318 [2], American Specification ANSI/AISC 360 [8], Japan standards for steel and composite structures and for concrete structures [91, 92] and Chinese design code JGJ 138 [85]. In addition, numerous literature can be identified in the topic of comparison of the design provisions between different standards, like for example the work of Bridge [25], Elnashai et al. [46], Weng et al. [200], Shanmugam et al. [172], Uy et al. [187], Furlong [65], Kim et al. [98], El-Tawil et al. [47], Eggemann [44] and Zhang et al. [11, 212-213]. Based on the revised literature, conclusions on the different overall design procedures for fully encased steel-concrete composite columns are listed below in the respective paragraphs, where focus was placed on the aspect of the effective flexural stiffness.

European design code EN 1994-1-1 [58]

In the European design code for composite structures, the Limit State design philosophy with safety factors for materials and loads is used. Three types of columns are considered: fully encased, partially encased and concrete filled tubular sections. A range of application is restricted by the geometrical and material conditions to fit with the background test database. Design process is based on the combined composite approach shown in Fig. 3.85. To establish the internal forces equilibrium, the plastic block stress distribution is used in the simplified design method. Long-term effects are considered to define the flexural stiffness. The buckling of composite columns is considered with the usage of steel buckling curves. Simplified design method is not applicable to the columns with more than one embedded steel profile and unsymmetric cross-sections. Details of the design procedure is described in Section 3.4.3.

American building code ACI 318 [2]

The building code of American Concrete Institute adapts the Limit State method of design with the respective load and capacity reduction factors as shown in Eq. 3.54, where S_n is the nominal strength of a section, ϕ is the strength reduction factor and U is the required strength calculated for factored loads. The design procedure is based on the reinforced concrete approach with consideration of the structural steel profile as an additional special reinforcement. Scope of the usage includes both, encased and filled, types of columns. The concrete compression strain limit is fixed on 3‰. Local buckling of a steel profile is considered as the failure of a column. The effective slenderness is calculated due to the moment magnification factors with respect to the reduced Euler's critical load. Effects of creep and cracked concrete are considered in the evaluation of stiffness, where two equations are considered as given in Eq. 3.55, where the second equation can be used for the case when the steel profile consists of a large percentage of the entire cross-section. I_{se} is referring to the reinforcement including structural steel and I_{sx} is referring only to the structural steel part. β_{dns} is the reduction factor due to the sustained axial load. The load-moment interaction curves are obtained based on the strain compatibility method and internal forces equilibrium. The shear transfer at the steel-concrete interface can be assured by the bonded connections and by direct bearings (mechanical shear connectors).

$$\phi S_n \geq U \tag{3.54}$$

$$(EI)_{eff} = \frac{\left(0.2E_cI_g + E_sI_{se}\right)}{1+\beta_{dns}} \quad \text{or} \quad (EI)_{eff} = \frac{\left(0.2E_cI_g\right)}{1+\beta_{dns}} + E_sI_{sx} \tag{3.55}$$

American specification ANSI/AISC 360 [8]

The design specification of American Institute of Steel Construction is based on the Limit State procedures including both, the load and resistance factor design (LRFD) and the allowable strength design (ASD). Eq. 3.56 represents two design concepts, where for the LRFD, R_u is the required strength with the LRFD load combinations, R_n is the nominal strength and ϕ is the resistance factor. For the ASD, R_a is the required strength with the ASD load combinations and Ω is the safety factor, which mostly govern the entire safety concept. The design methodology of the LRFD is similar to the procedure of ACI code but the composite section is considered as a steel profile strengthened by the surrounding concrete. The load-moment interaction curves are obtained in the bilinear polygons forms from the simplified analysis method, which are characteristic for the steel design approach. However, the design specification foresees also methods considering four-point interaction curves. Effective slenderness and geometrical properties include the presence of the concrete encasement. Effects of creep and shrinkage on the concrete are not considered. Shear transfer at the steel-concrete interface need to be assured by the direct (mechanical) shear connection means. The effective flexural stiffness is given in Eq. 3.57, where the factor reducing the contribution of concrete is defined in Eq. 3.58. The effective stiffness taken for the evaluation of resistances is taken in accordance to Eq. 3.59, where $\tau_b = 0.8$ for slender columns, otherwise $\tau_b = 1$.

$$R_u \leq \phi R_n \text{ (LRFD)} \quad \text{or} \quad R_a \leq R_n/\Omega \text{ (ASD)} \tag{3.56}$$

$$(EI)_{eff} = E_s I_s + E_s I_{sr} + C_1 E_c I_c \tag{3.57}$$

$$C_1 = 0.25 + 3\left(\frac{A_s + A_{sr}}{A_g}\right) \leq 0.7 \tag{3.58}$$

$$EI^* = 0.8\tau_b (EI)_{eff} \tag{3.59}$$

Japan standard for steel and composite structures JSCE [91, 92]

The design according to the Japan Society of Civil Engineers is based on Limit State design method, where partial safety factors consist of the material γ_m, structural member γ_b, structural analysis γ_a, action γ_f and structural γ_i factors as shown in Eq. 3.60-3.61. Where, S_d is the design response, R_d is the design resistance, F_k is the individual characteristic value of action and f_k is the characteristic value of material strength. The design procedures consists of the design of steel and composite structures, where the design of composite structures is based on the reinforced concrete structure approach. The full shear connection is assumed and the shear transfer at the steel-concrete interface shall be assured by the usage of the mechanical connectors. The design standard gives procedures for the verification of headed studs, perforated-plate dowels and block dowels with fixed diagonally semicircular rebars. The effective stiffness is evaluated according to the transformed cross-section and including the effects of creep, shrinkage, concrete cracking and second-order. The design standard allows considering the change of flexural stiffness in the function of bending moment as shown in Eq. 3.62-3.63, where Eq. 3.62 refers to the varied stiffness and Eq. 3.63 to the constant stiffness over the member length. The aforementioned equations are explained in the JSCE standard for concrete structures in the commentary to clause 7.4.5 [91].

$$\gamma_i \frac{S_d}{R_d} \leq 1.0 \tag{3.60}$$

$$\gamma_i \frac{\sum \gamma_a \cdot S(\gamma_f \cdot F_k)}{R(f_k/\gamma_m)/\gamma_b} \leq 1.0 \tag{3.61}$$

$$E_e I_e = \left(\frac{M_{crd}}{M_d}\right)^4 \frac{E_e I_g}{1 - \frac{\Delta M_{csg}}{M_d - P(d_p - c_g)}} + \left\{1 - \left(\frac{M_{crd}}{M_d}\right)^4\right\} \frac{E_e I_{cr}}{1 - \frac{\Delta M_{cscr}}{M_d - P(d_p - c_{cr})}} \tag{3.62}$$

$$E_e I_e = \left(\frac{M_{crd}}{M_{dmax}}\right)^3 \frac{E_e I_g}{1 - \frac{\Delta M_{csg}}{M_{dmax} - P(d_p - c_g)}} + \left\{1 - \left(\frac{M_{crd}}{M_{dmax}}\right)^3\right\} \frac{E_e I_{cr}}{1 - \frac{\Delta M_{cscr}}{M_{dmax} - P(d_p - c_{cr})}} \tag{3.63}$$

Based on the work of Uy et al. [187], the effective flexural stiffness of a composite column can be defined according to another Japanese standard, the AIJ standard from 1997, as given in Eq. 3.64.

$$K_e = E_s I_s + 0.2 E_c I_c \tag{3.64}$$

Chinese design code JGJ 138 [85]

The Chinese design code JGJ 138 [85] has been compared with the European design code EN 1994-1-1 [58] in the work of Zhang et al. [11, 212-213]. The JGJ 138 [85] is based on the Limit State design with partial safety factors for the design loads and design material strengths. In addition, safety factors for the design building life and the structure importance are defined. The fundamental limit state condition is given in Eq. 3.65, where S_d is the design action effect, R_d is the design resistance and γ_0 is the structure importance factor. The foreseen types of composite columns consist of fully encased steel profiles and concrete filled tubes. The relative slip is neglected and the design procedure does not requires the verification of the longitudinal shear for columns. The design is reduced to the verification of axial resistance in concentric and eccentric conditions, including large eccentricities and tensile work of a column. The bending verification of a column consist of compression case on an eccentricity and the acting bending moments are considered as an equivalent eccentricity of the axial force as given in Eq. 3.66. Effects of the shear forces are fully neglected. In the result, the load-moment interaction curves are not considered but they can be obtained by varying the axial resistance over the eccentricity and by considering two separate neutral axes – one for the concrete part and second for the steel part. The N-M interaction curves and buckling curves for fully encased columns are shown in Fig. 3.86 and Fig. 3.87 respectively. The flexural stiffness of column member is related to the radius of gyration and eventual reduction of stiffness is considered by the application of corresponding reduction factors based on the buckling curves from the Chinese design code for concrete structures GB50010-2010 as shown in Eq. 3.67 for the verification of axial resistance. The radius of gyration is defined in Eq. 3.68 and the respective reduction factors of resistances are given in Table 3.1.

$$\gamma_0 S_d \leq R_d \tag{3.65}$$

$$e_0 = M/N \tag{3.66}$$

$$N \leq 0.9\varphi\left(f_c A_c + f'_y A'_s + f'_a A'_a\right) \tag{3.67}$$

$$i = \sqrt{\frac{E_c I_c + E_a I_a}{E_c A_c + E_a A_a}} \tag{3.68}$$

Table 3.1.
Axial strength reduction factors for flexural response of a column. (Source: AVEC BNT [11]).

l_0/i	≤28	35	42	48	55	62	69	76	83	90	97	104
φ	1.0	0.98	0.95	0.92	0.87	0.81	0.75	0.70	0.65	0.60	0.56	0.52

Where, l_0 is the effective length of a column.

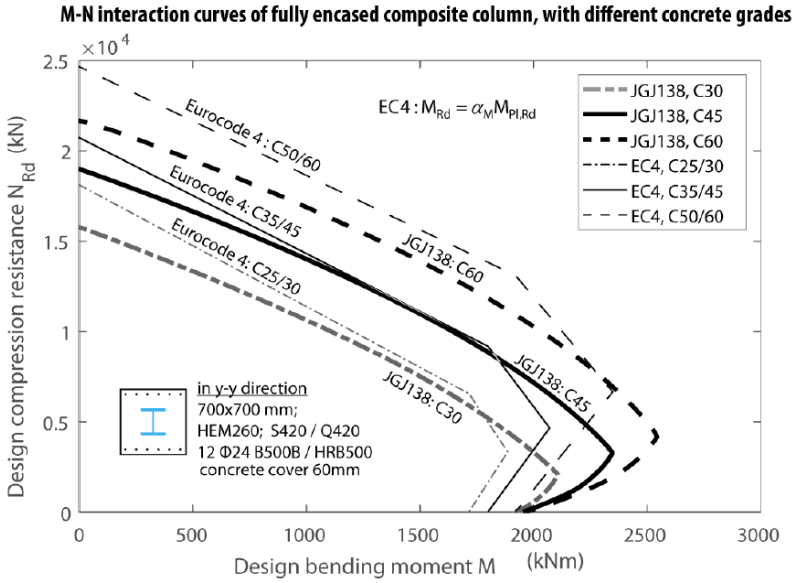


Fig. 3.86. Comparison of the EN 1994-1-1 and JGJ 138 for the fully encased composite column section –M-N interaction curves. (Source: AVEC BNT [11]).

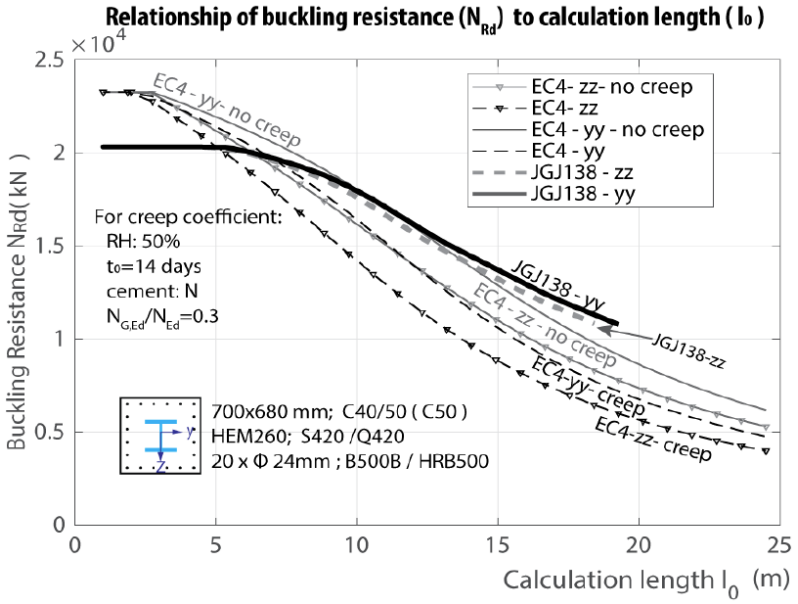


Fig. 3.87. Comparison of the EN 1994-1-1 and JGJ 138 for the fully encased composite column section – buckling curves. (Source: AVEC BNT [11]).

Australian and New Zealand design code AS/NZS 2327

According to the work of Uy et al. [187], in the common Australian and New Zealand design code AS/NZS 2327 (Draft 2015) the design of composite columns is based on the Limit State design method, where the safety capacity factors are applied to member resistances with respective values for different materials, considered actions or considered structural elements. The effective flexural stiffness can be defined in the form of Eq. 3.69 and Eq. 3.70 for former and new provisions respectively.

$$(EI)_e = \phi EI_s + \phi EI_r + \phi_c E_c I_c \quad \text{, where} \quad E_c = 5050\sqrt{f_c'} \text{ and } \phi = \phi_c = 1.0 \tag{3.69}$$

$$(EI)_e = E_s I_s + E_s I_{sr} + 0.6 E_c I_c \quad \text{, where} \quad E_c = w^{1.5}\left(0.024\sqrt{f_{cm}} + 0.12\right) \tag{3.70}$$

3.4.3. EN 1994-1-1

In Section 3.4.2, a concise description of the design methodology of steel-concrete composite columns in accordance to EN 1994-1-1 [58] was given. The background information and test data for the column design can be found among others in the work of Virdi and Dowling [196], Nethercot [127], Johnson [89-90], Leskelä [110], Roik et al. [158-165], Hanswille et al. [69, 71, 72], Bergmann [12] and Schwalbenhofer [170]. The given design provisions refer to the composite columns and composite compression members with fully and partially encased steel profiles and concrete filled tubes as shown in Fig. 3.88. In this section, the investigation is focused on the fully encased steel-concrete composite columns. In the design process, the local instabilities of a steel profile are neglected by assuring a minimum concrete cover according to the condition given in Eq. 3.71. Another two general limitations of the applicability of the design code refer to the used material grades and steel contribution ratio in the composite cross-section. Based on the background test database, the material grades are limited to S235-S460 for the structural steel, C20/25-C50/60 for the concrete and strength of the reinforcement steel between 400-600 MPa. The condition for steel contribution ratio is defined in Eq. 3.72 below.

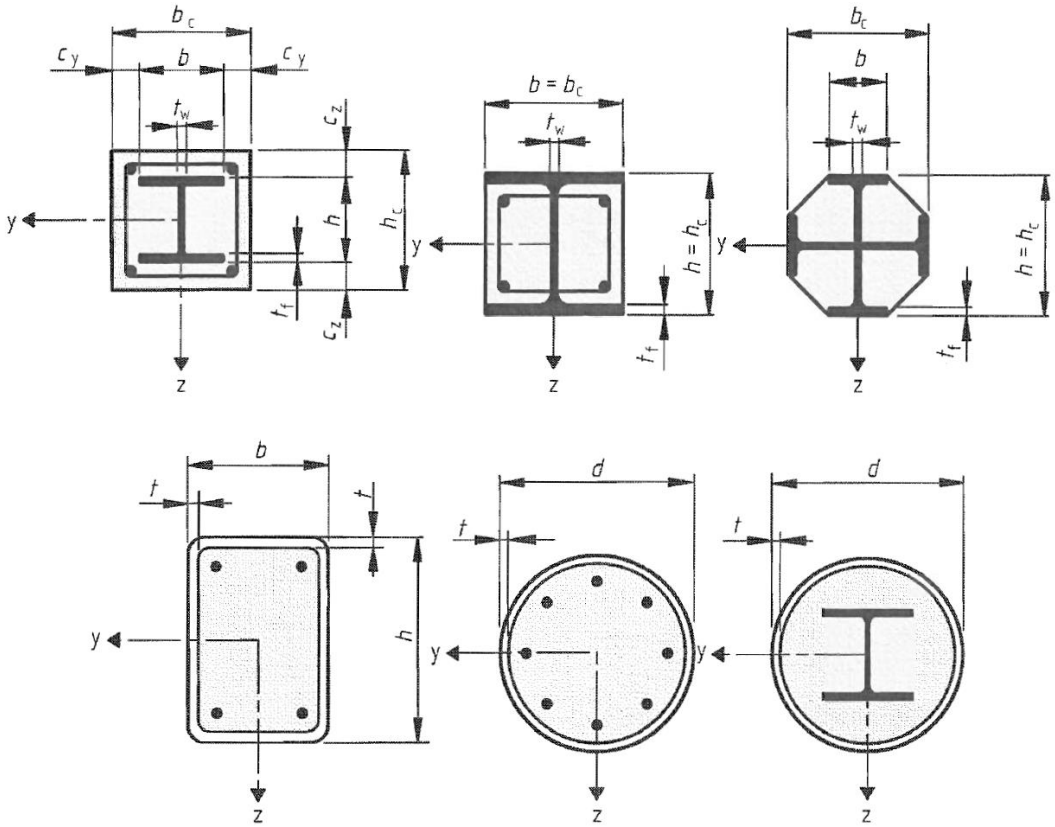


Fig. 3.88. Typical cross-sections of composite columns covered by EN 1994-1-1. (Source: EN 1994-1-1 [58]).

$$max\left\{40mm;\ \frac{b}{6}\right\} \leq c_z \tag{3.71}$$

$$0.2 \leq \delta = \frac{A_a f_{yd}}{N_{pl,Rd}} \leq 0.9 \tag{3.72}$$

The fully encased steel-concrete composite columns should be verified for (i) the cross-sectional resistances like compression, bending, shear, (ii) for the interaction of actions, (iii) for the instability effects, (iv) for the load introduction and (v) for the longitudinal shear verification in the zones outside the load introduction zones. In the verification, the second-order effects, long-term effects and column imperfections should be considered. To perform the verification process, two methods are considered: (1) general method, which includes non-symmetrical and non-uniform cross-sections over the column length and (2) simplified method, which requires double-symmetrical and uniform cross-sections over the column length. In both methods, the verification of the longitudinal shear in the load introduction zones is based on the elastic analysis, strut and tie method and the strength provisions are given only for the application of headed shear stud connectors. However, different types of connectors are allowable, when their performance is tested in accordance with EN 1994-1-1, Annex B [58]. A general information and rough design recommendations are given for the shear connection relayed on steel-concrete bond outside the load introduction zones.

The general method of design for composite columns is based on the non-linear Finite Element Analysis (FEA) according to the pre-defined set of provisions given in EN 1994-1-1 clause 6.7.2 [58]:

- The design process shall be based on the elasto-plastic analysis.
- The stability analysis should take into account effects of second-order theory, residual stresses, geometrical imperfections, local instabilities, cracking of concrete, creep and shrinkage of concrete and yielding of structural and reinforcement steels.
- The second-order effects shall be considered in any direction of possible column failure, if they affects the structural response significantly.
- It can be assumed that plain sections remain plain (the Euler-Bernoulli beam model apply).
- The full composite action can be assumed between steel and concrete.
- The tensile strength of concrete shall be neglected, where the tension stiffening effect on the flexural stiffness may be considered.
- The applied stress-strain relationships for concrete in compression should consider the non-linear behaviour, where for the steel parts, the bi-linear material laws without strain hardening effects should be implemented.
- The residual stresses and geometrical member imperfections can be included as an equivalent initial bow imperfection given in Table 6.5, EN 1994-1-1 [58].

The simplified design method of EN 1994-1-1 [58] is based on the Limit State method and the given provisions are established according to the composite approach, where the superposition method with the assured forces equilibrium and strain correlation between steel and concrete is adapted. The given guideline allows for the fast, easy and safe design process, which is based on the series of background tests. The verification of a composite column consists of structural integrity checks for (i) the axial

compression resistance including buckling stability reduction, (ii) the plastic bending resistance including two-plane bending and (iii) the interaction of compression and bending including one-axial bending and bi-axial bending cases. The verification of shear forces should be made for each part separately according to the given distribution ratio. Effects of shear forces on the bending resistance result in a reduced structural steel strength value over the shearing area. The interaction of axial forces and bending moments can be evaluated using the N-M interaction diagrams as shown in Fig. 3.89.

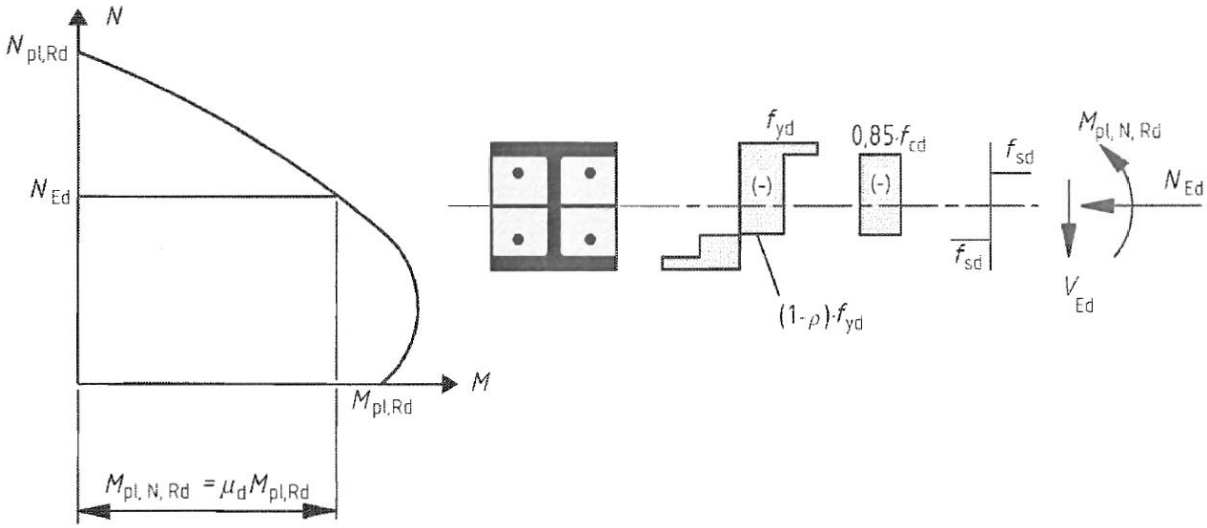


Fig. 3.89. Interaction curve for the combined compression and uniaxial bending. (Source: EN 1994-1-1 [58]).

The developed provisions of simplified design method were based on the test results and simulations performed by authors. In order to assure the applicability of the proposed method, the following limitations according to EN 1994-1-1 clause 6.7.3.1 [58] have to be respected:

- Only one embedded hot-rolled, cold-formed or welded steel profile can be utilised. The simplified method is not applicable to sections with two or more separately embedded structural steel profiles. This condition prevents a loss of flexural stiffness due to the slip between steel profiles and assures utilisation of the Euler-Bernoulli beam theory.
- The cross-section of a column need to be double-symmetric and uniform over the length.
- The cross-sectional resistances shall be calculated using the plastic block stress distribution.
- The relative slenderness of a column should be not greater than 2.
- The maximum concrete cover used in calculations should not exceed $c_{z,max} \leq 0.3h$ and $c_{y,max} \leq 0.4b$, where for notation see Fig. 3.88.
- The longitudinal rebars used in the calculation should not exceed 6% of the concrete area.
- The depth-to-width ratio of a composite section should fit within the limit between 0.2-5.0.
- The design stress-strain relation for concrete in compression can be used, where the simplification to the rectangular stress block according to EN 1992-1-1 clause 3.1.7(3) [53] can be applied.
- The tensile strength of concrete should be neglected.

According to the method of superposition, the plastic design resistance of a cross-section for normal force $N_{pl,Rd}$ can be evaluated according to Eq. 3.73, where factor 0.85 refers to the curing conditions, crack influence and behaviour of concrete in the concrete encased columns. For concrete filled columns, the factor of 1.0 is used instead of 0.85.

$$N_{pl,Rd} = A_a f_{yd} + 0.85 A_c f_{cd} + A_s f_{sd} \tag{3.73}$$

In Fig. 3.89, the effects of shear forces V_{Ed} are considered with the reduced structural steel strength over the height of the web of a steel profile. According to EN 1994-1-1 [58], the shear forces are affecting the N-M interaction curve if their part acting on the steel part $V_{a,Ed}$ exceeds 50% of the plastic design shear resistance $V_{pl,a,Rd}$. The distribution of shear forces between the structural steel and concrete parts can be done according to Eq. 3.74 and Eq. 3.75, where $M_{pl,a,Rd}$ is the plastic resistance moment of the steel section and $M_{pl,Rd}$ is the plastic resistance moment of the composite section. The steel material strength-reduction factor ρ can be evaluated according to Eq. 3.76. The shear forces acting on each part should be verified separately according to the provisions given in the respective design codes EN 1993-1-1 [55] for steel and EN 1992-1-1 [53] for concrete parts.

$$V_{a,Ed} = V_{Ed} \frac{M_{pl,a,Rd}}{M_{pl,Rd}} \tag{3.74}$$

$$V_{c,Ed} = V_{Ed} - V_{a,Ed} \tag{3.75}$$

$$\rho = \left(2V_{a,Ed}/V_{pl,a,Rd} - 1\right)^2 \tag{3.76}$$

The evaluation of the N-M interaction curve requires the verification of internal forces equilibrium in a composite cross-section with different ratios of axial and bending forces. For each different configuration of forces, the neutral axis of composite section is changing its position. Without application of computer-aided calculations, the evaluation of exact interaction curves would be not efficient. The EN 1994-1-1 [58] foresees application of the simplified interaction curves, which consist of four characteristic points and linear interpolation between the identified points. The schematic representation of a simplified interaction curve with corresponding stress state for the encased composite cross-section is shown in Fig. 3.90, where the factor of 0.85 refers to the concrete encased columns, similar like for the axial plastic resistance. The background information and detailed evaluation of the position of neutral axis, as well as the evaluation of respective resistances are described in the work of Johnson [90]. The load-moment interaction curves for the non-symmetrical cross-sections are described by Roik and Bergmann [158]. For the non-symmetric sections, an additional developing plastic eccentricity between the elastic and plastic centroids has to be considered in the acting moment of second-order. Moreover, in one direction of bending, two different moment resistances are obtained.

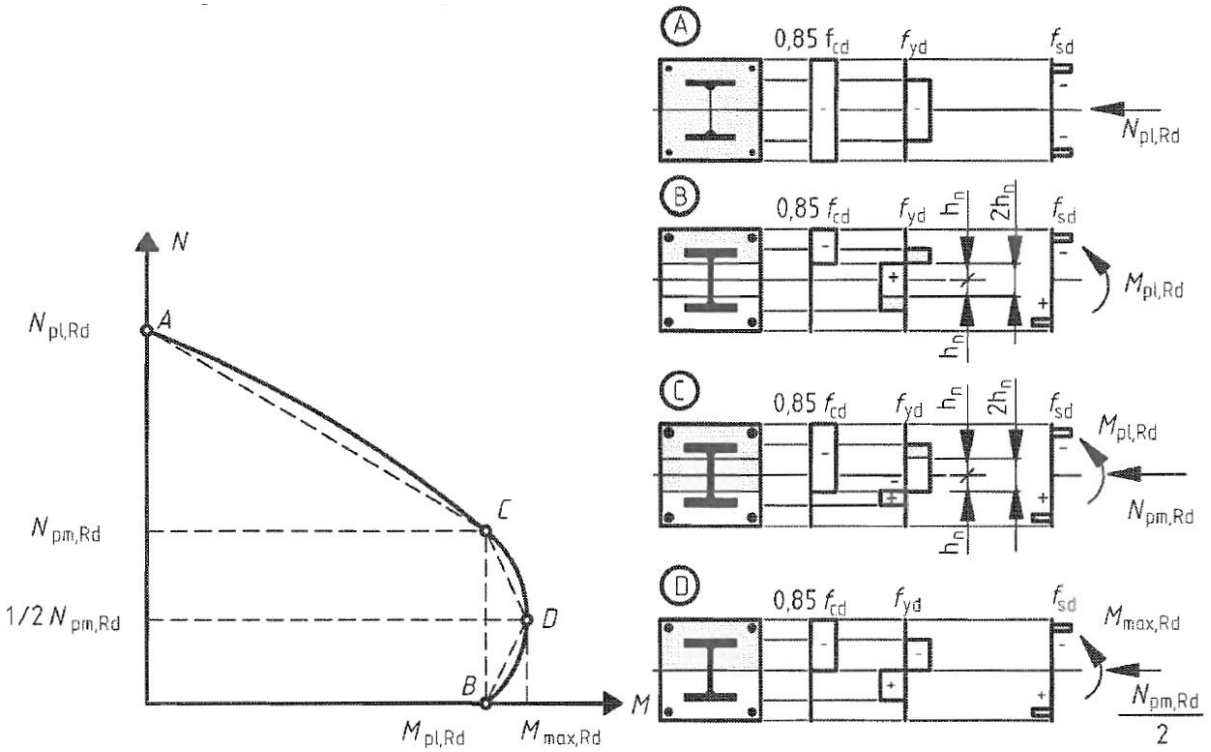


Fig. 3.90. Simplified N-M interaction curve and corresponding stress distribution. (Source: EN 1994-1-1 [58]).

The effective stiffness of a composite column according to EN 1994-1-1 [58] can be evaluated as the sum of stiffnesses of contributing parts, as it was described in Section 3.1. However, account should be taken for the long-term effects, creep, shrinkage, concrete micro- and macro-cracking and non-linear real behaviour of concrete by applying the effective value of concrete modulus of elasticity $E_{c,eff}$ and stiffness correction factor K_c given in Eq. 3.79 and 3.78 respectively. Factor φ_t is the creep coefficient and it can be obtained according to EN 1992-1-1 clause 5.4.2.2(2) [53].

$$(EI)_{eff} = E_a I_a + E_s I_s + K_c E_{cm} I_c \tag{3.77}$$

$$K_c = 0.6 \tag{3.78}$$

$$E_{c,eff} = E_{cm} \frac{1}{1 + (N_{G,Ed}/N_{Ed})\varphi_t} \tag{3.79}$$

In the work of Virdi and Dowling [196], the flexural stiffness is defined, which allows for the evaluation of the Euler's critical buckling load and respective relative slenderness ratio, see Eq. 3.80 and Eq. 3.81 respectively. Where, β_l is the effective buckling length factor, L is the column length between supports and $N_{pl,Rk}$ is the characteristic axial strength calaculated according to Eq. 3.73 with characteristic material properties.

$$N_{cr} = \frac{\pi^2 (EI)_{eff}}{(\beta_l L)^2} \tag{3.80}$$

$$\bar{\lambda} = \sqrt{\frac{N_{pl,Rk}}{N_{cr}}} \tag{3.81}$$

The second-order effects and member imperfections are taken into account by applying the reduced effective flexural stiffness as given in Eq. 3.82 and by applying the respective moment magnification factors defined in Eq. 3.83. Where, $K_0 = 0.9$ is the calibration factor due to test results and strains correlation, $K_{c,II} = 0.5$ is the correction factor including effects of the second-order and imperfections, β is the factor considering the distribution of bending moment (Table 6.4 from EN 1994-1-1 [58]) and $N_{cr,eff}$ is the effective Euler's critical buckling load evaluated including the effective stiffness from Eq. 3.82. Member imperfections are considered according to Table 6.5 of EN 1994-1-1 [58].

$$(EI)_{eff,II} = K_0\left(E_a I_a + E_s I_s + K_{c,II} E_{cm} I_c\right) \tag{3.82}$$

$$k = \frac{\beta}{1 - N_{Ed}/N_{cr,eff}} \geq 1.0 \tag{3.83}$$

The verification of the column cross-sectional resistances is done by satisfying the resistance conditions for the axial compression, for the combined compression and uniaxial bending and for the combined compression and biaxial bending, given in Eq. 3.84-3.86. Where, χ is the reduction factor for the relevant buckling mode, μ_d correlates the respective bending moment resistance to the level of acting simultaneously axial load and α_M is the coefficient including the reduction of strength. The superimposed bi-axial bending interaction curves are shown in Fig. 3.91.

$$\frac{N_{Ed}}{\chi N_{pl,Rd}} \leq 1.0 \tag{3.84}$$

$$\frac{M_{Ed}}{M_{pl,N,Rd}} = \frac{M_{Ed}}{\mu_d M_{pl,Rd}} \leq \alpha_M \tag{3.85}$$

$$\frac{M_{y,Ed}}{\mu_{dy} M_{pl,y,Rd}} \leq \alpha_M \qquad \frac{M_{z,Ed}}{\mu_{dz} M_{pl,z,Rd}} \leq \alpha_M \qquad \frac{M_{y,Ed}}{\mu_{dy} M_{pl,y,Rd}} + \frac{M_{z,Ed}}{\mu_{dz} M_{pl,z,Rd}} \leq 1.0 \tag{3.86}$$

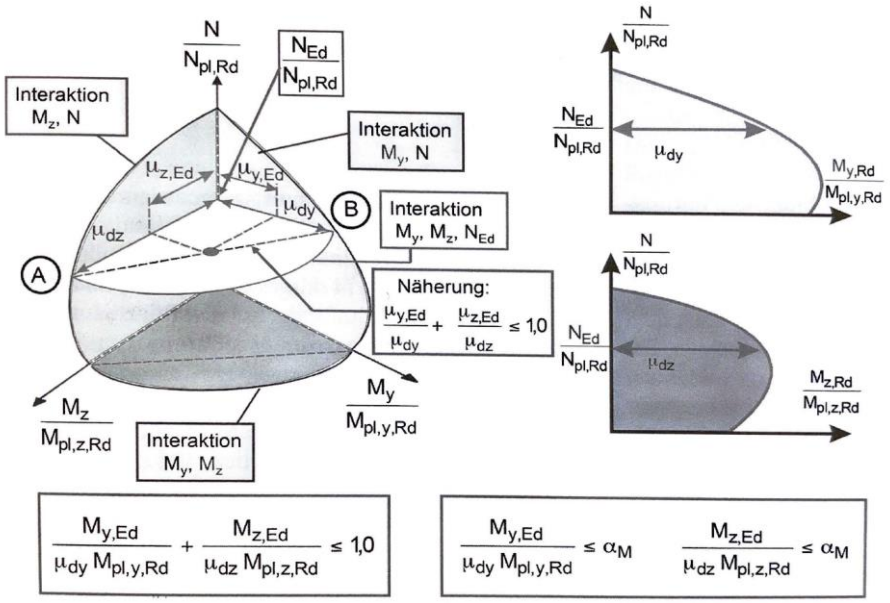


Fig. 3.91. Interaction diagram for combined compression and bi-axial bending. (Source: Hanswille [71]).

A common procedure for the verification of shear connection is given for the general and simplified design methods. The shear connection in fully encased steel-concrete composite columns has to be verified in the load introduction zones, where the load is imposed only to one part – steel or concrete. When the load is uniformly distributed over the steel and concrete parts, and in the zone outside the load introduction zones, the verification of shear connection is not required. Moreover, the shear connection is required in the areas of the change of a cross-section if the acting shear flow is exceeding the steel-concrete bond shear strength. The evaluation of shear forces should consider the change in sectional forces in steel or reinforced concrete parts over the load introduction length. An elastic analysis including creep and shrinkage effects should be taken out when the load is imposed only to the concrete part. Otherwise, the plastic and elastic analyses should be conducted in order to identify a more severe case. The load introduction length can be defined as the minimum value from 2d or L/3, where d is the minimum transverse dimension and L is the column length.

The resistances of headed stud shear connectors can be evaluated according to Eq. 3.87 and Eq. 3.88. Where, d is the diameter of of the shank of the stud (from 16 mm to 25 mm), α is factor correlating slenderness of the stud and γ_V is the partial safety factor. As the resultant resistance, the smaller from the two aforementioned resistances should be taken. When the shear studs are placed in the chambers of embedded steel profiles, the frictional mechanism can be added to the resistance of the shear connectors according to Fig. 3.42. The truss model with load-spread angle of 45° can be assumed for cases when the load is only introduced through the steel profile.

$$P_{Rd} = \frac{0.8 f_u \pi d^2/4}{\gamma_V} \tag{3.87}$$

$$P_{Rd} = \frac{0.29 \alpha d^2 \sqrt{f_{ck} E_{cm}}}{\gamma_V} \tag{3.88}$$

The verification of shear connection in composite columns can be found in the commentary work of Hanswille et al. [71] to EN 1994-1-1 [58]. The load transferred by the mechanical shear connectors in the load introduction zone is equal to the change in the forces between the steel profile and the surrounding concrete as given in Eq. 3.89 and shown in Fig. 3.92. Based on the aforementioned relation and plastic distribution ratios of internal forces given in Eq. 3.90, the equation for the resultant longitudinal shear forces acting on the shear connection $V_{L,Ed}$ can be defined in Eq. 3.91. The condition for the verification of shear connection capacity is given in Eq. 3.92, where n is the number of applied stud shear connectors and P_{Rd} is defined in Eq. 3.87-3.88.

$$\Delta N_{Ed} = V_{L,Ed} = N_{Ed} - N_{a,Ed} = N_{c+s,Ed} \tag{3.89}$$

$$N_{a,Ed} = N_{Ed} \frac{N_{pl,a}}{N_{pl,Rd}} \qquad N_{s,Ed} = N_{Ed} \frac{N_{pl,s}}{N_{pl,Rd}} \qquad N_{c,Ed} = N_{Ed} \frac{N_{pl,c}}{N_{pl,Rd}} \tag{3.90}$$

$$V_{L,Ed} = N_{c+s,Ed} = N_{Ed}\left(1 - \frac{N_{pl,a}}{N_{pl,Rd}}\right) \tag{3.91}$$

$$V_{L,Ed} \leq V_{L,Rd} = nP_{Rd} \tag{3.92}$$

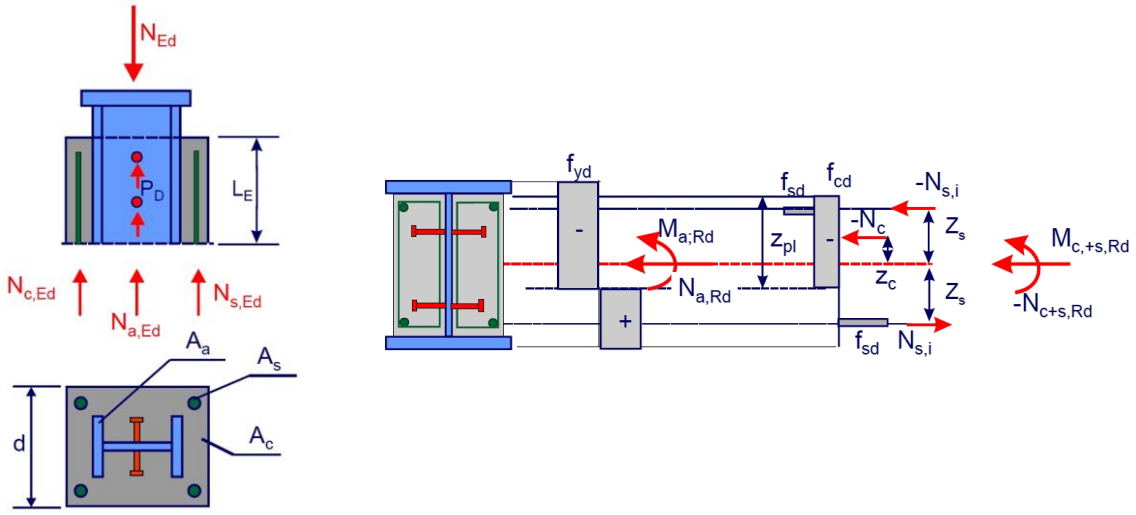
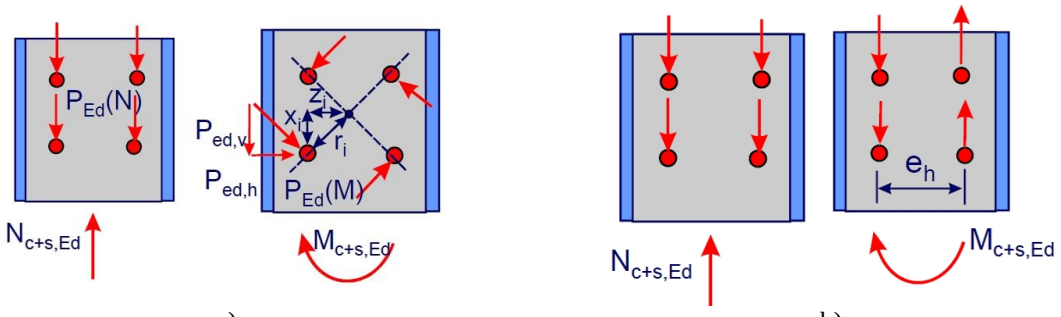


Fig. 3.92. Load introduction mechanism in concrete encased columns. (Source: Hanswille [71]).

When bending in the load introduction zone is considered, two models can be used for the verification of the shear studs (i) elastic model and (ii) plastic model, see Fig. 3.93. In the verification of axial force and bending moment, the resultant force acting on one critical shear stud is evaluated and compared to the resistance of a stud. The resulting actions acting on one stud are defined in Eq. 3.93 for the elastic model and in Eq. 3.94 for the plastic model.



a) b)

Fig. 3.93. Force distribution in shear connection for axial load and bending case – a) elastic model and b) plastic model. (Source: Hanswille [71]).

$$\max P_{Ed} = \sqrt{\left(\frac{N_{c+s,Ed}}{n} + \frac{M_{c+s,Ed}}{\Sigma r_i^2} x_i\right)^2 + \left(\frac{M_{c+s,Ed}}{\Sigma r_i^2} z_i\right)^2} \tag{3.93}$$

$$\max P_{Ed} = \frac{N_{c+s,Ed}}{n} + \frac{2M_{c+s,Ed}}{e_h n} \tag{3.94}$$

When the shear connectors are not placed in the chambers of a steel profile but attached to the flanges as shown in Fig. 3.94, the longitudinal shear has to be verified against the longitudinal shearing of concrete struts and longitudinal shearing of stirrups as given in Eq. 3.96-3.98. The new resultant

longitudinal shear acting on the shear connection can be evaluated based on Eq. 3.91 and by considering the ratio of non-directly connected concrete area to the entire area of a composite section as shown in Eq. 3.95. Where, A_{c1} is the non-directly connected concrete area, ν is the strength reduction factor for cracked concrete in shear and f_{ck} should be placed in MPa, θ is the concrete compression strut dilation angle and can be assumed as 45°, L_E is the load introduction length, A_s is the cross-sectional area of stirrup and s_w is the spacing of stirrups.

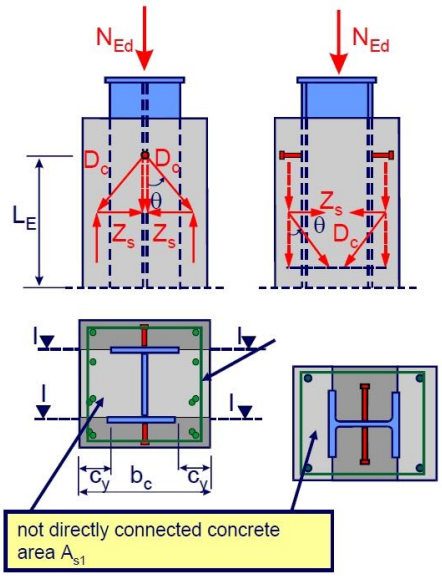


Fig. 3.94. Load introduction mechanism in concrete encased columns. (Source: Hanswille [71]).

$$V_{L,Ed} = N_{Ed}\left(1 - \frac{N_{pl,a}}{N_{pl,Rd}}\right)\frac{A_{c1}0.85f_{cd} + A_{s1}f_{sd}}{A_c 0.85f_{cd} + A_s f_{sd}} \tag{3.95}$$

$$V_{L,Rd,max} = 4\frac{c_y \nu 0.85 f_{cd}}{\cot\theta + \tan\theta} L_E \tag{3.96}$$

$$\nu = 0.6\left(1 - (f_{ck}/250)\right) \tag{3.97}$$

$$V_{L,Rd,s} = 4\frac{A_s}{s_w} f_{yd} \cot\theta \, L_E \tag{3.98}$$

The longitudinal shear in the zones outside the load introduction length can be verified according to the elastic analysis and by considering the critical shear plane I-I indicated in Fig. 3.94. The elastic shear stress can be analysed according to the equations given in Eq. 3.99. The provisions of EN 1994-1-1 [58] allow not to place any mechanical shear connection in the zones outside the load introduction zones if the resulting longitudinal shear stresses are not exceeding the natural bond strength at the steel-concrete interface. The bond strength values are given in Table 6.6 of EN 1994-1-1 [58] and they are varied for different types of columns, see Fig. 3.95. The values of bond strength in the aforementioned table are based on the experimental data base [161, 162]. An increase of the base value of the bond strength can be done with respect to the thickness of the concrete encasement around the steel profile as given in Eq. 3.100, where β_c is the amplification factor defined in Eq. 3.101, c_z is the thickness of the concrete encasement and $c_{z,min} = 40\ mm$ is the minimum concrete cover required.

$$\tau_{L,Ed} = \frac{\Delta N_{Ed}}{u_a L_E} \quad \text{or} \quad \tau_{L,Ed} = \frac{V_{Ed} S_{I-I}}{I b_{I-I}} \tag{3.99}$$

$$\tau_{Rd} = \beta_c \tau_{Rd,0} = \beta_c \cdot 0.3 \tag{3.100}$$

$$\beta_c = 1 + 0.02 c_z \left(1 - \frac{c_{z,min}}{c_z}\right) \leq 2.5 \tag{3.101}$$

Type of cross section	τ_{Rd} (N/mm^2)
Completely concrete encased steel sections	0,30
Concrete filled circular hollow sections	0,55
Concrete filled rectangular hollow sections	0,40
Flanges of partially encased sections	0,20
Webs of partially encased sections	0,00

Fig. 3.95. Design shear strength of steel-concrete bond according to EN 1994-1-1. (Source: EN 1994-1-1 [58]).

In order to describe the behaviour of concrete, the EN 1994-1-1 [58] is referring to the EN 1992-1-1 [53], where the provisions for the material properties and design of reinforced concrete structures are given. However, another European design code of International Federation for Structural Concrete (fib), fib ModelCode 2010 [62], gives an alternative model for the evaluation of concrete stress-strain behaviour, reinforcement-concrete bond and analysis of the concrete confinement. The proposed alternative model is widely used and in some cases, it brings a better correlation to the identified experimental behaviour. The model proposed for the concrete confinement is shown in Fig. 3.96 and described in Eq. 3.102-3.106. Where, $f_{ck,c}$ is the confined concrete compression strength and σ_2 is the confining stress imposed by the reinforcement cage. A more detailed explanation of the concrete behaviour can be found in the discussed fib ModelCode 2010 [62].

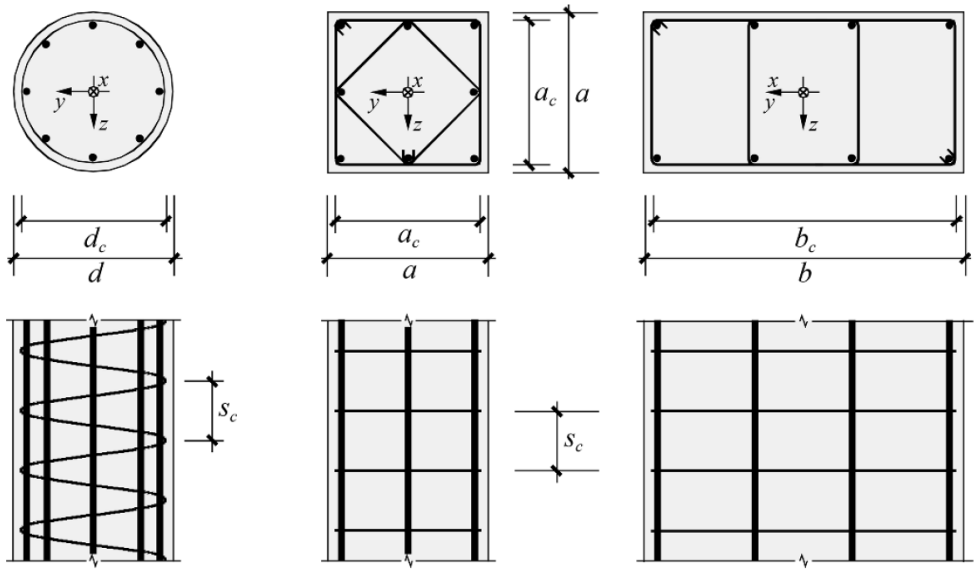


Fig. 3.96. Compression members with confining reinforcement. (Source: fib MC2010 [62]).

$$\frac{f_{ck,c}}{f_{ck}} = 1 + 3.5\left(\frac{\sigma_2}{f_{ck}}\right)^{\frac{3}{4}} \tag{3.102}$$

$$\varepsilon_{c2,c} = \varepsilon_{c2}\left[1 + 5\left(\frac{f_{ck,c}}{f_{ck}} - 1\right)\right] \tag{3.103}$$

$$\varepsilon_{cu2,c} = \varepsilon_{cu2} + 0.2\sigma_2/f_{ck} \tag{3.104}$$

$$\sigma_2 = \omega_c f_{cd}\left(1 - \frac{s_c}{a_c}\right)\left(1 - \frac{s_c}{b_c}\right)\left(1 - \frac{\Sigma {b_i}^2/6}{a_c b_c}\right) \tag{3.105}$$

$$\omega_c = min\left\{\omega_y = \frac{A_{sy} f_{yd}}{a_c s_c f_{cd}}, \omega_z = \frac{A_{sz} f_{yd}}{b_c s_c f_{cd}}\right\} \tag{3.106}$$

3.4.4. Analytical models for the flexural stiffness found in the literature

In the work of Kim et al. [98], the stiffnesses from different international design codes were compared with the experimental tests of concrete filled and concrete encased composite columns. In addition, another analytical model proposed by S. Ali Mirza and Timo K. Tikka [123] has been investigated and compared to other models. The proposed stiffness model of Mirza and Tikka is given in Eq. 3.107 and among a typical reduction for concrete cracking or creep effects, it correlates the effective flexural stiffness to the column slenderness and axial force eccentricity. Kim et al. [98] concluded that the model of Mirza and Tikka brought the best overall accuracy to the performed tests.

$$(EI)_{eff} = \left(0.313 + 0.00334\frac{L}{D} - 0.203\frac{e}{D}\right)E_c(I_g - I_{ss}) + 0.792E_{ss}I_{ss} + 0.788E_{sl}I_{sl} \tag{3.107}$$

Where,
L is the column effective length,
D is the depth of a column section in the direction of bending,
e is the axial force eccentricity,
E_c, E_{ss}, E_{sl} are the moduli of elasiticity of concrete, structural steel and longitudinal reinforcement respectively,
I_g, I_{ss}, I_{sl} are the moments of inertia of entire composite section, structural steel and longitudinal reinforcement in reference to centroid of entire section respectively.

In the work of Lippes [112], it was identified that for concrete filled circular tubes with an additional inner steel core, a modification to the model given in EN 1994-1-1 [58] for the effective flexural stiffness for second-order analysis should be introduced by applying additional reduction factor k_E, which varies from 0.7 to 1.0 with dependence on the column slenderness and plastic load eccentricity $e = M_{Ed}/N_{Ed}$. The proposed modified equation for the flexural stiffness by Lippes is given in Eq. 3.108. Reduction factor k_E has analogous origin like in the work of Chanou [29] described in Section 3.5.4.

$$(EI)_{eff,II} = k_E K_0\left(E_a I_a + E_s I_s + K_{c,II} E_{cm} I_c\right) \tag{3.108}$$

According to the CIDECT design guide [13], the flexural stiffness of concrete filled tube composite columns can be evaluated according to the model similar to the proposed in EN 1994-1-1 [58] but the

reduction factor for concrete part is changed. The CIDECT design guide covers only the concrete filled tube types of columns, therefore, a change in the flexural stiffness reduction factor to a smaller value is justified by the fact that the concrete inside the steel tube is not exposed to environmental conditions and the tube confinement reduces the stiffness reduction effects due to the concrete cracking. However, the design value of the concrete modulus of elasticity is introduced, where it is defined in Eq. 3.109. The resultant modified model for the flexural stiffness is shown in Eq. 3.110.

$$E_{cd} = E_{cm}/1.35 \tag{3.109}$$

$$(EI)_{eff,II} = E_a I_a + 0.8E_{cd} I_c + E_s I_s \tag{3.110}$$

3.4.5. Strut and tie model

The strut and tie method of design is based on the truss model developed by Ritter and Mörsch [156, 168, 169], which discretises the compressive and tensile stressed zones of a reinforced concrete structure in the discontinuities zones as shown in Fig. 3.97. This method of design has been developed by Schlaich and Schäfer [168, 169] and it is adopted in the current design codes [53, 62]. The discretisation into the truss elements is based on the elastic stress trajectories developed in the concrete structure with reference to the imposed load and boundary conditions. Multiple truss models can be developed for the same load case and boundary conditions if they are in the equilibrium. The superposition of two models, local and global, can be used in order to describe a complex stress distribution and they are equivalent with the complete detailed model as shown in Fig. 3.98.

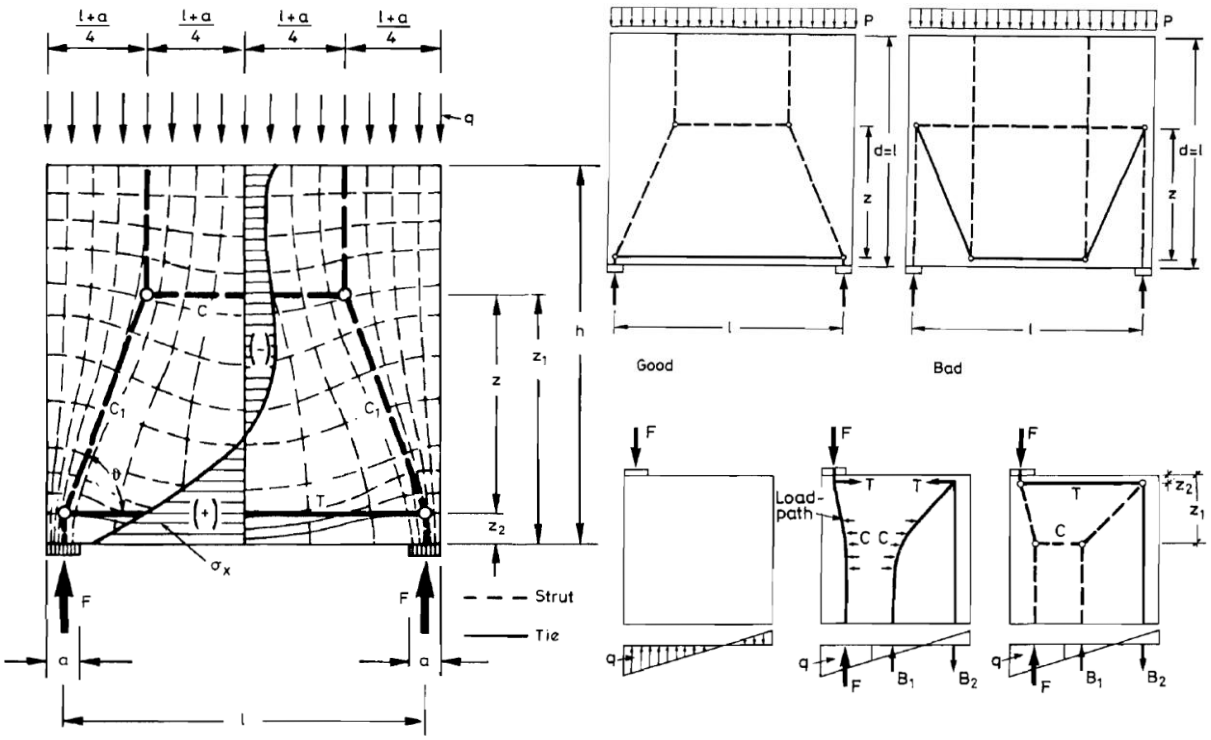


Fig. 3.97. The load path method and discretisation of stress trajectories into truss elements of strut and tie method. (Source: Schlaich [168]).

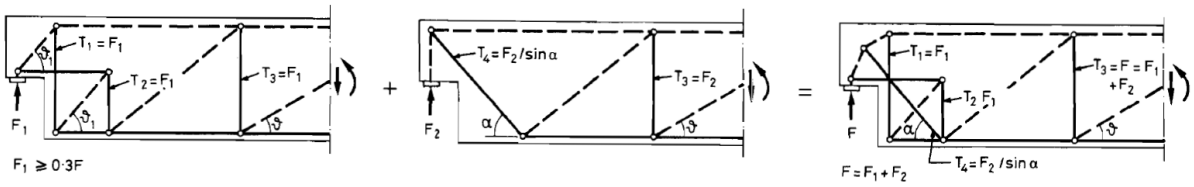


Fig. 3.98. Superposition of the strut and tie models. (Source: Schlaich [168]).

Analogically to the typical truss system, in strut and tie model, a compressive struts and tensile ties are distinguished. Each element is subjected to transfer only one type of axial forces. Effects of shear and bending on the concrete structure are discretised into system of compression and tensile forces. It is assumed that the stresses in struts and ties are constant over the entire sectional area and length. The compressive struts are representing the smeared compression stress fields, which consists of a certain geometry as shown in Fig. 3.99. The tensile ties are normally represented by the reinforcement bars distributed analogically to the identified tie truss elements. The resultant tensile stresses in the tie element are smeared over a certain area, therefore, the resultant stresses are taken by multiple reinforcement bars passing through the tensioned zone.

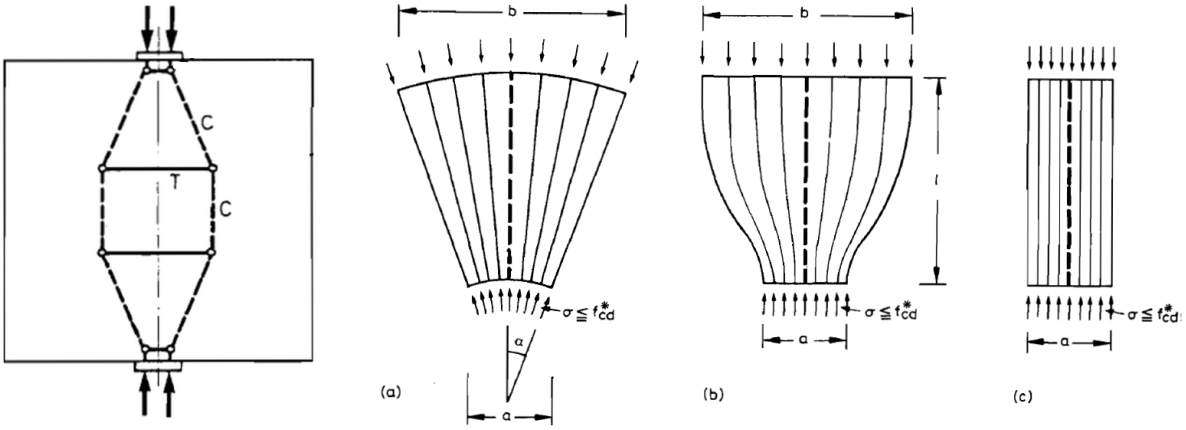


Fig. 3.99. Geometry of compression struts fields – a) 'fan', b) 'bottle' and c) 'prism'. (Source: Schlaich [168]).

The strut and tie elements are connecting in nodes, where the equilibrium of forces has to be respected. Due to the variation of interconnected truss elements, different configuration of nodes can be obtained. However, in the design codes [53, 62], normally four types of nodes are distinguished: (i) the compressed nodes CCC, (ii) nodes with two compressed and one tensioned arms CCT, (iii) nodes with two tensioned and one compressed arms CTT and (iv) the tensioned nodes TTT. Due to the requirement of equilibrium in each node, the concrete compression strength has to be higher than the occurring compression stresses and the applied reinforcement should be able to bear the developed tensile forces. The design of the compression struts consists of the verification of concrete compression strength with relation to the coexisting transversal stresses. If tensile stresses occur, the strength of compression strut is reduced by the factor of $0.6\nu'$ due to the cracked concrete state, where $\nu' = 1 - f_{ck}/250$. Details on the strut and tie method can be found in Schlaich et al. [169], where the design provisions are given in EN 1992-1-1 [53] and fib ModelCode 2010 [62].

3.4.6. Pivot/Fibre method

The fibre method is used for the evaluation of cross-sectional resistances with reference to the acting internal forces and it is based on the forces equilibrium and strain compatibility. The fibre method is commonly used in the design of reinforced concrete structures [53, 62] and steel-concrete composite structures [58] when bending occurs. Normally, it is assumed that strains varies linearly between the most compressed and the most tensioned fibres of the analysed cross-section (Euler-Bernoulli beam). In Fig. 3.100, three possible strain distributions are distinguished: (i) for the reinforcing steel (or structural steel) tension limit, (ii) for the concrete compression strain limit and (iii) for the concrete pure compression strain limit. The method allows introducing any strain limitation with respect to the analysed problem, like for example pure tension. The respected stress-strain material laws of steel and concrete elements are essential in the method. With reference to the conducted analysis – linear, non-linear, elastic, elasto-plastic or plastic, the respective material laws are applied [53, 55]. For the steel parts, the strain hardening effect is often neglected in the design process to move towards more conservative results. Similarly, the tensile strength of concrete is neglected completely. As a simplification, the plastic stress distribution in concrete with reduced acting length is assumed in order to simplify the calculations, see Fig. 3.101. The position of the neutral axis is related to the equilibrium of internal forces in a cross-section.

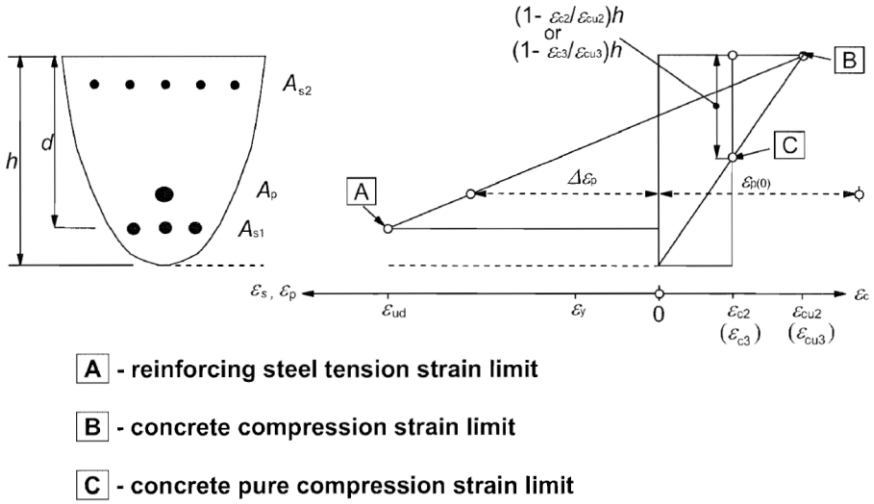


Fig. 3.100. Fibre method and possible strain distributions in the reinforced concrete. (Source: EN 1992-1-1 [53]).

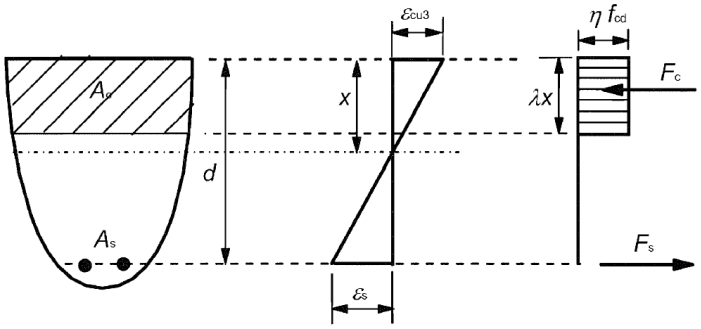


Fig. 3.101. Simplified model of the concrete for the rectangular stress distribution. (Source: EN 1992-1-1 [53]).

The analysis of the simplified design method of EN 1994-1-1 [58] and the exact non-linear method for the design of composite columns can be found in the work of Anwaar [9]. The comparison between the simplified method, exact plastic curve (named as Plastic_NL) and curve obtained based on the elasto-plastic analysis according to the fibre method (named as Strain Limited Design) is shown in Fig. 3.102.

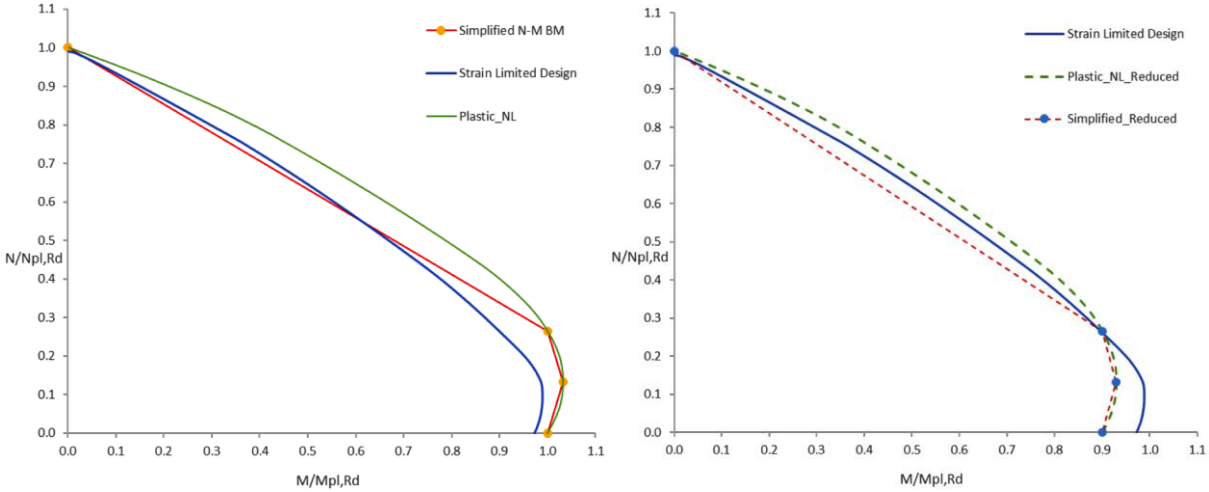


Fig. 3.102. Comparison of the N-M interaction diagrams based on different methods – a) direct comparison and b) comparison with plastic curves reduced by the factor α_M. (Source: Anwaar [9]).

3.5. Composite columns with multiple encased steel profiles

Steel-concrete composite columns are mainly used in tall buildings, where their significant compression and bending capacities with respect to small cross-sectional area are highly demanded. The continuous growth of economy and population, together with limited horizontal space, push the cities to grow vertically. In the result, the number and the height of high-rise buildings over the last decade has significantly raised [6], which can be observed on the diagram shown in Fig. 3.103. The tallest finished building in the world is the iconic Burj Khalifa (828m), however, other impressive high-rise buildings can be identified as well, like for example Shanghai Tower (632m), Makkah Clock Royal Tower (601m) or One World Trade Center (541m). The continuous growth of the skyscrapers is proceeding and a project under the construction, the Jeddah Tower in Saudi Arabia, if finished, it will reach the height of 1008m and become a new tallest building. A clear tendency is marked that people are building taller and taller, thus, the constructional solutions should govern the rising trend.

Together with the increased height of buildings, the constructional solutions covered by the current design procedures, like for example EN 1994-1-1 [58], stopped to satisfy the needs of investors, architects and structural engineers. In the modern high-rise buildings around the world, novel solutions of composite columns with multiple encased steel profiles can be identified [132, 143, 149, 185, 204-207], see Fig.3.104. These columns, together with the reinforced concrete and composite core, are the backbone of the high-rise buildings and they transfer the forces from the building to the ground.

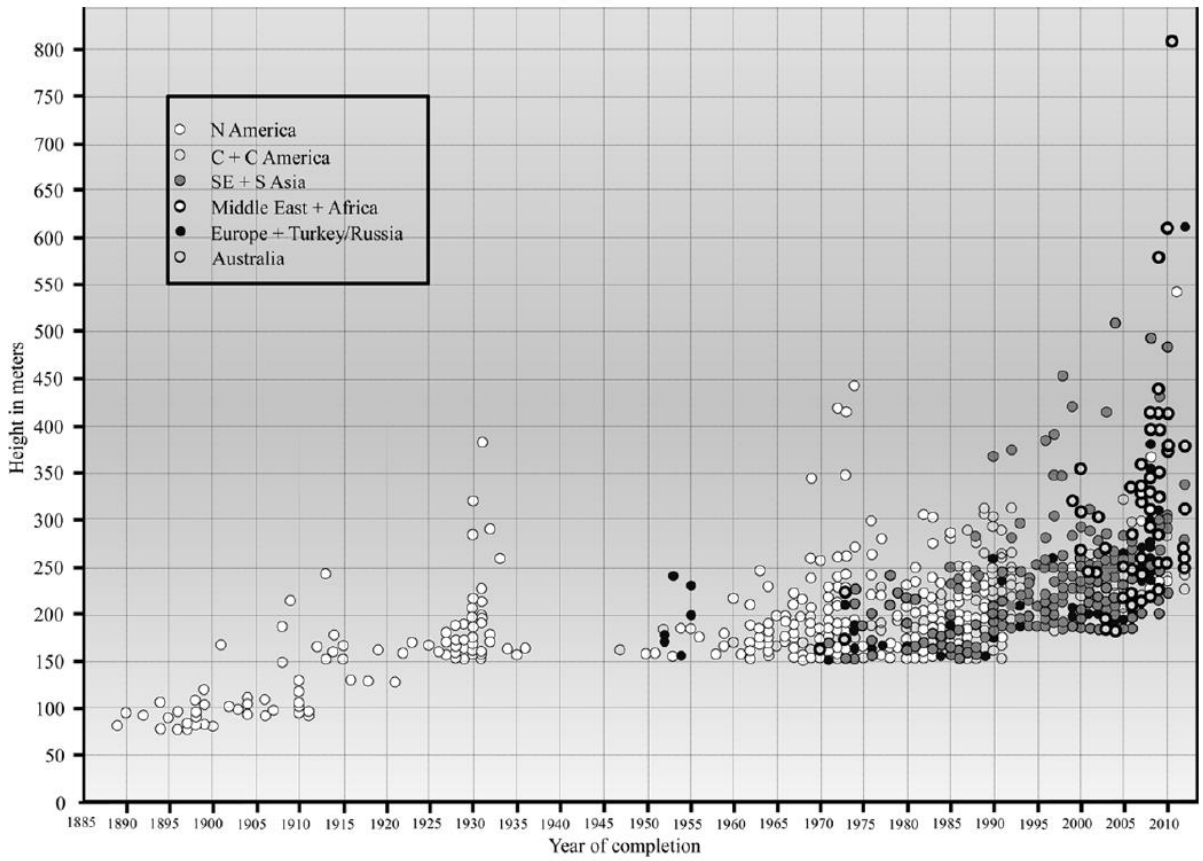


Fig. 3.103. High-rise buildings in the scope of the last century. (Source: Al-Kodmany [6]).



a) b)

Fig. 3.104. Construction of the IFC Tower Two, Hong-Kong – a) an elevation of mega-columns and b) plinth detail of a mega-column. (Source: Wong [204]).

3.5.1. Current approach

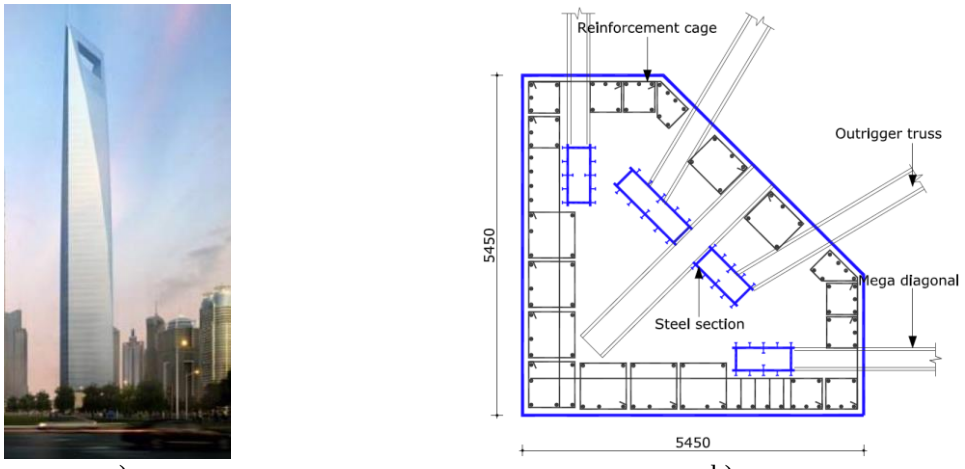
In the current design practice there is no available design guidance for the steel-concrete composite columns with more than one embedded steel profiles. Therefore, all the erected structures with this kind of columns adapted provisions given in the design codes and followed the available literature. Based on the consultations with design offices specialised in high-rise buildings, it was identified that the design

of heavy columns is based on the Finite Element simulations, rather than simplified analytical procedures – analogy to the general method of EN 1994-1-1 [58]. Moreover, often when designed columns are exceeding the scope of available design guidelines, individual test campaigns are taken out in order to investigate the behaviour of downscaled column specimens [82]. In the current practice, it is assumed that the Euler-Bernoulli beam theory describes the behaviour of columns with multiple encased steel profiles. However, in the conducted study, it was identified that main assumptions of this theory are harmed due to the significant shear deformations and according to high individual bending stiffness of steel cores. In the practice, the embedded steel profiles are interconnected but this strongly affects the efficiency of the used composite sections. In addition, on the example of a column with multiple encased steel profiles shown in Fig. 3.104, it can be observed that the cross-section is not uniform over the entire column length. Similar observations can be done for the East Pacific Center in Shenzhen, Shanghai Tower and World Finance Center in Shanghai, Ping Anh Finance Center in Shenzen, International Finance Center in Hong-Kong and Zlota 44 in Warsaw [132, 149, 185, 206], see Fig. 3.105-3.109, where multiple encased steel profiles were used.



a) b)

Fig. 3.105. Construction of the East Pacific Center, Shenzhen – a) building elevation and b) detail of a column. (Source: Tran [185]).



a) b)

Fig. 3.106. Construction of the World Financial Center in Shanghai, China – a) building elevation and b) section of a column. (Source: Tran [185]).



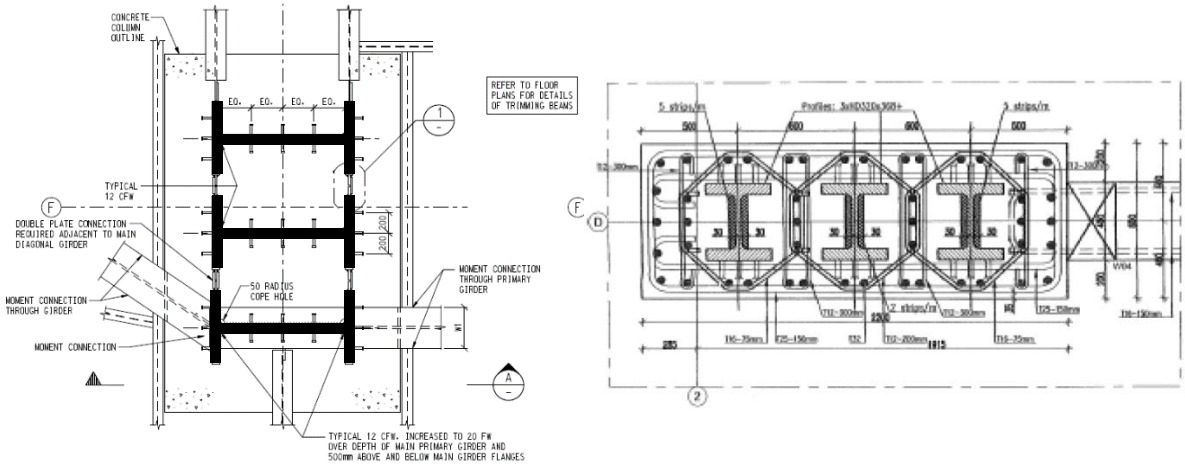
a) b)

Fig. 3.107. Construction of the Shanghai Tower, China – a) building elevation and b) detail of a column. (Source: Tran [185]).



a) b) c)

Fig. 3.108. Construction of the Ping Ahn Finance Center in Shenzhen, China – a) render of a building, b) building elevation under construction and c) detail of building core and heavy columns. (Source: Odenbreit [132]).



a) b)

Fig. 3.109. Cross-section of heavy columns with multiple encased steel profiles – a) IFC Tower in Hong-Kong and b) Zlota 44 in Warsaw, Poland. (Source: Arup Hong-Kong and Besix).

The shear connection in heavy steel-concrete composite columns is normally assured by headed stud connectors, see Fig. 3.105-3.109. Due to heavy forces transferred by the columns and their big scale, a big number of headed studs is required in order to transfer forces from steel to concrete, or in reverse. The protruding studs from steel profiles, see Fig. 3.109b, disturb in the arrangement of the reinforcement bars in a composite cross-section. In the result, works related to the application of the stud connectors, the complexity of structural detailing and the construction works on a building site are significant.

The shear walls are the wall composite structures with two embedded steel profiles at both ends of a wall element. In some cases, additional profiles are also placed between, in the wall panel. This type of structure is used to build the core of high-rise buildings and to resist heavy shear forces. Three main types of shear walls can be distinguished: (i) with not connected steel profiles, (ii) with internal steel plate and (iii) with double steel plate, see Fig. 3.110 and Fig. 3.111. Considering the type of shear wall without the internal steel plate between embedded steel profiles, an analogy to heavy composite columns with multiple encased steel profiles is clear. However, in shear walls, a big discrepancy between two sectional dimensions is present. In the result, the embedded steel profiles are in a big distance between each other. A design guidance for the shear walls can be found in the Chinese design code JGJ 138 in chapter 9 [85]. The flexural response is related to the equivalent plastic eccentricity of axial force and the flexural stiffness of structural steel is neglected. The equation for the verification of the axial load acting on the plastic eccentricity $e = M/N$ is given in Eq. 3.111-3.112, where for the nomenclature and details see JGJ 138 [85]. Further study on this topic is given in Section 3.5.4.

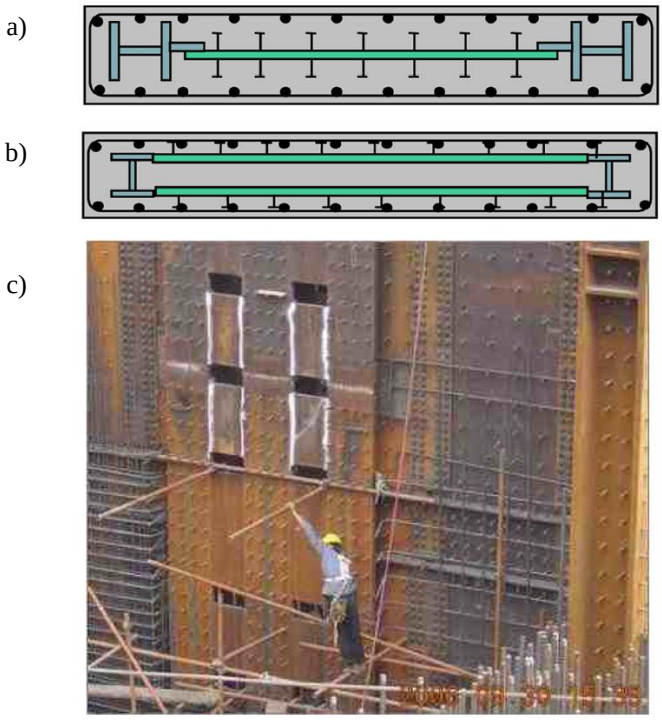


Fig. 3.110. Composite shear wall system – a) with steel plate, b) with double steel plate and c) construction detail. (Source: Tran [185]).

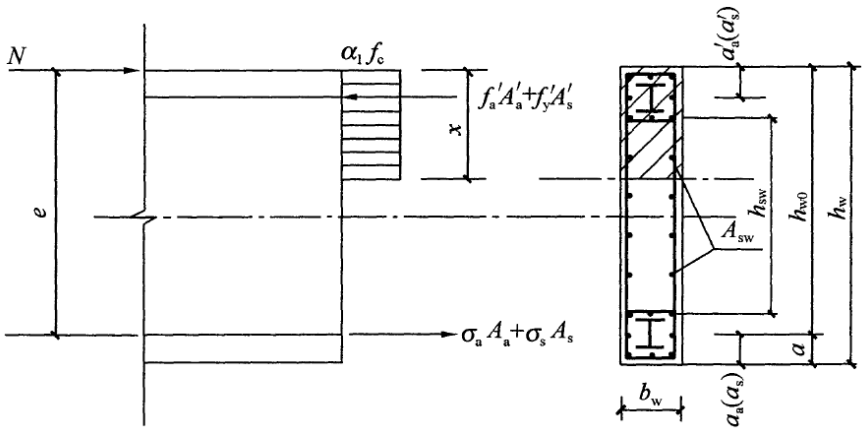


Fig. 3.111. Composite shear wall under axial load on eccentricity according to JGJ 138. (Source: JGJ 138 [85]).

$$Ne \le \alpha_1 f_c b_w x \left(h_{w0} - \frac{x}{2}\right) + f'_y A'_s (h_{w0} - a'_s) + f'_a A'_a (h_{w0} - a'_a) + M_{sw} \quad (3.111)$$

$$M_{sw} = \left[0.5 - \left(\frac{x - \beta_1 h_{w0}}{\beta_1 h_{sw}}\right)^2\right] f_{yw} A_{sw} h_{sw} \quad \text{or} \quad M_{sw} = 0.5 f_{yw} A_{sw} h_{sw} \quad (3.112)$$

Two major international research projects, which deal with the behaviour of columns with more than one embedded steel profile – RFCS project SmartCoCo [175] and CTBUH project ISRC Composite Column [82], can be identified. A brief description of each project is given in respective Sections 3.5.2 and 3.5.3. Among the identified projects, a number of research can be found in the literature, where a brief description of the main findings is given in Section 3.5.4. An analogous type of structures can be identified under the name of 'Sandwich Panels' but this type of structures is diverging from the system of composite columns much more than the composite shear walls, therefore it was omitted in the further analysis. In the work of Sohel et al. [176], the reference example concerning sandwich panels is given.

3.5.2. RFCS project 'SmartCoCo'

The research project of the Research Fund for Coal and Steel (RFCS) SmartCoCo, Smart Composite Components – Concrete Structures Reinforced by Steel Profiles [175] is dealing with the steel-concrete composite elements or connections that are not covered by the reinforced concrete, nor composite structures design procedures. The project fills the gaps in knowledge and delivers the generic design approach for the following type of structural elements (cited from the project report [175]):

- "Composite walls and columns reinforced by several fully encased steel sections;
- Columns of reinforced concrete buildings reinforced by one steel section over the height of one storey, without continuity above and under that storey;
- Composite elements transferring forces in zones of discontinuity of RC walls;
- Connections of steel or composite beams to reinforced concrete columns;
- Connections of reinforced concrete beams or flat slabs to steel or composite columns by means of steel shear keys."

The aspect of longitudinal shear has been tested in series of push-out tests conducted at the University of Liège, where plain steel-concrete bond, paint coating and variation of mechanical shear connectors in the form of headed studs and plate stiffeners were investigated. In Fig. 3.112, the push-out test specimen layout is shown.

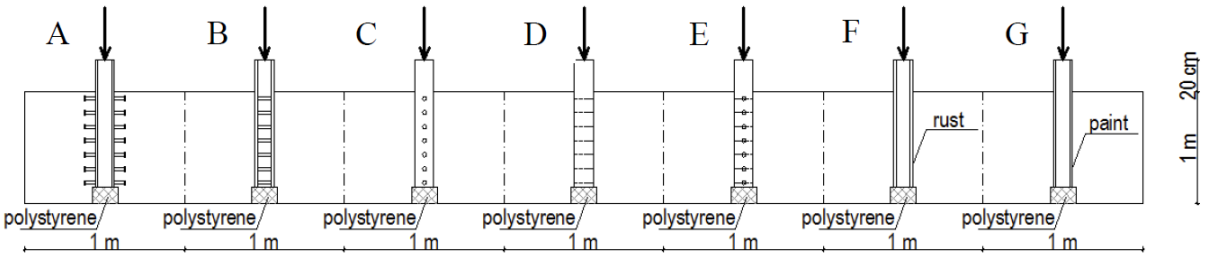


Fig. 3.112. Push-out test campaign within the SmartCoCo research project. (Source: SmartCoCo [175]).

Based on the conducted literature research within the project SmartCoCo, a generic design guide for the composite columns with multiple encased steel profiles is proposed. The derived method was confronted with the test results obtained from the conducted experimental campaign, revised and calibrated. Two series of tests on composite members with several encased steel profiles were conducted, one at the University of Rennes and the second at the University of Liège. Moreover, analytical and numerical studies were carried out at the University of Rennes in order to analyse the stability aspect of slender hybrid walls and columns with several encased steel profiles. In the result, a freeware software named “HBCOL” was developed and set available online. The developed software allows for the fast verification of predefined columns or shear walls with varied number and type of embedded steel profiles, as well as geometry of a cross-section. Based on the FE model, the numerical simulation adapts the strain compatibility and forces equilibrium methods. As an output, the N-M interaction curves can be obtained, which can include the second-order and long-term effects. In the evaluation process, the embedded steel profiles are discretised into the equivalent set of reinforcement bars and the procedure of EN 1992-1-1 [53] based on the plastic stress distribution is adapted. The same approach is used for the evaluation of the flexural stiffness of a column, where the nominal stiffness model of EN 1992-1-1 [53] is adapted.

The test campaign performed at the University of Rennes consisted of seven shear wall specimens, each with three embedded steel profiles HEB100 grade S460 oriented with the web perpendicular to the wall faces (bending according to the weak axis of steel profile). The steel profiles were embedded in 250x900 mm concrete block of 5000 mm length and C25/30 grade. The end slip of steel profiles was not restrained. The distance between supports was 3750 mm and the specimens were subjected to bending as shown in Fig. 3.113. The conducted tests correspond to three-point bending tests and no compression forces were applied. One test specimen (A-RC) was a pure reinforced concrete block and it stands as a reference test, two specimens (B-W and B-W-HC) were tested without mechanical shear connectors, two specimens (C-W and C-W-HC) were tested with 16 mm shear studs welded in the

chambers of steel profiles and two specimens (D-W and D-W-HC) were tested with welded plate stiffeners of 10 mm thickness. The spacing of the connectors was 200 mm, where in one test, the spacing was increased to 300 mm (D-W-HC). The arrangement of reinforcement was nominally identical and 8x Ø20 longitudinal bars grade B500B were used. The spacing of the stirrups was varied between two consequent nominally identical tests and the second test (-HC) consisted of doubled shear reinforcement in order to increase the concrete confinement. The load-deflection curves are given in Fig. 3.114.

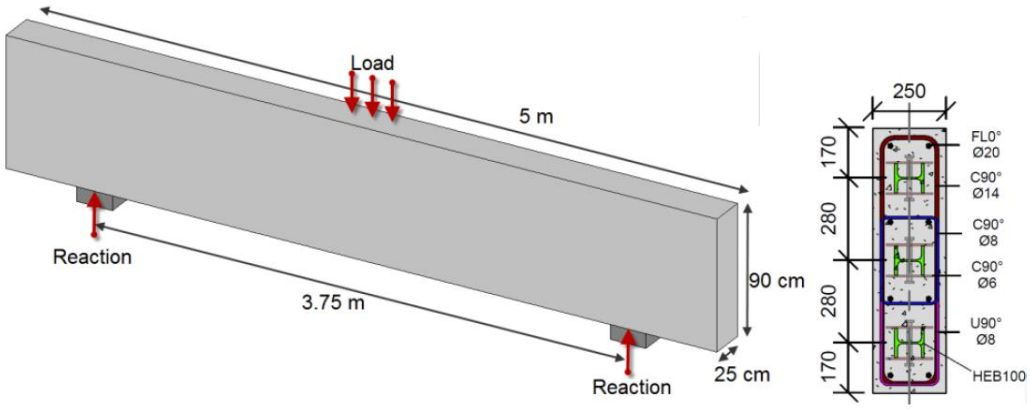


Fig. 3.113. Test layout and cross-section of the shear wall bending tests conducted at the University of Rennes. (Source: SmartCoCo [175]).

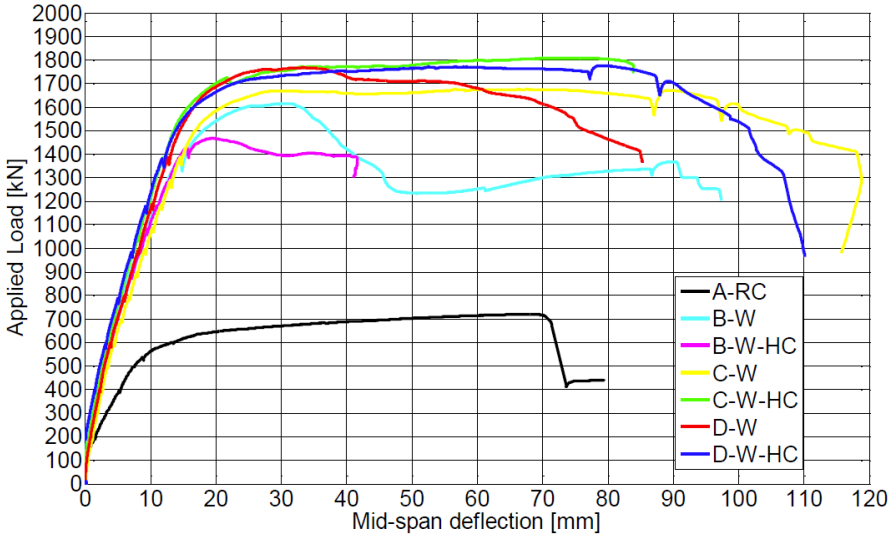


Fig. 3.114. Load-deflection curves of the shear wall bending tests conducted at the University of Rennes. (Source: SmartCoCo [175]).

The second series of tests on composite members with multiple encased steel profiles was conducted at the University of Liège. The test series consisted of six shear wall tests. The specimens had the system of a cantilever subjected to the lateral point load at the end. Analogically to the test series at the Univeristy of Rennes, 3x HEB100 steel profiles with grade S460 and C25/30 concrete blocks with dimensions of 240x800x2250 mm had been used. The reinforcement arrangement was also consistent, but the stirrups ratio was not varied between the subsequent nominally identical tests and the constant spacing of 100 mm had been applied. The tested specimens consisted in one reference test (ARC)

without embedded steel profiles, one specimen with embedded steel profiles and no mechanical shear connectors (BS), two specimens with applied shear studs (CS and CSN) and two specimens with welded plate stiffeners (DS and DSN). Each second test specimens were subjected to the additional normal compression force. The test layout and details of the specimen geometry are shown in Fig. 3.115. The obtained load-displacement curves are shown in Fig. 3.116.

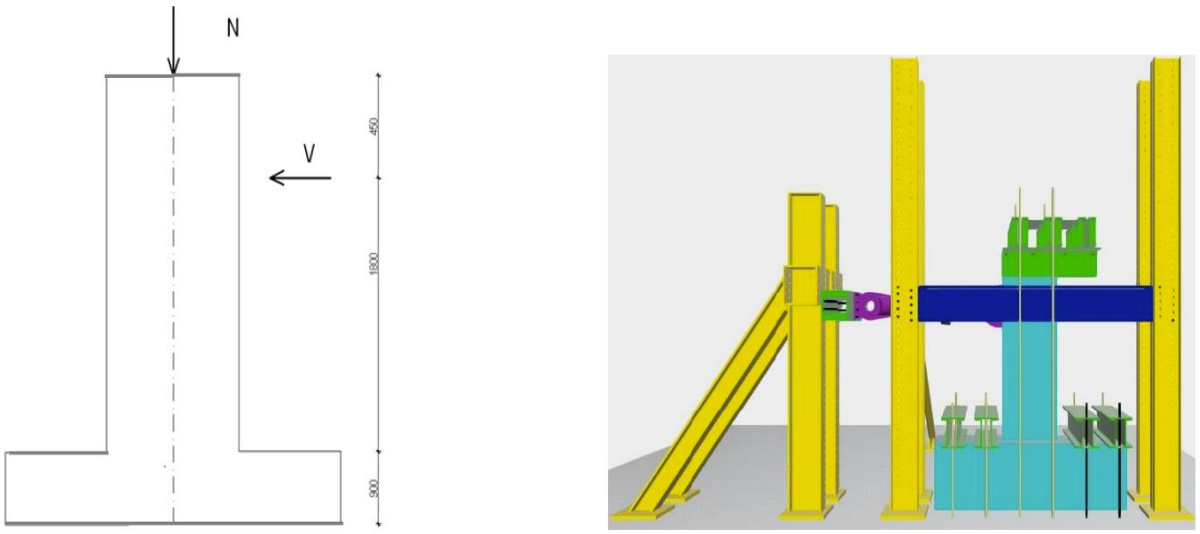


Fig. 3.115. Test layout of the shear wall tests conducted at the University of Liège. (Source: SmartCoCo [175]).

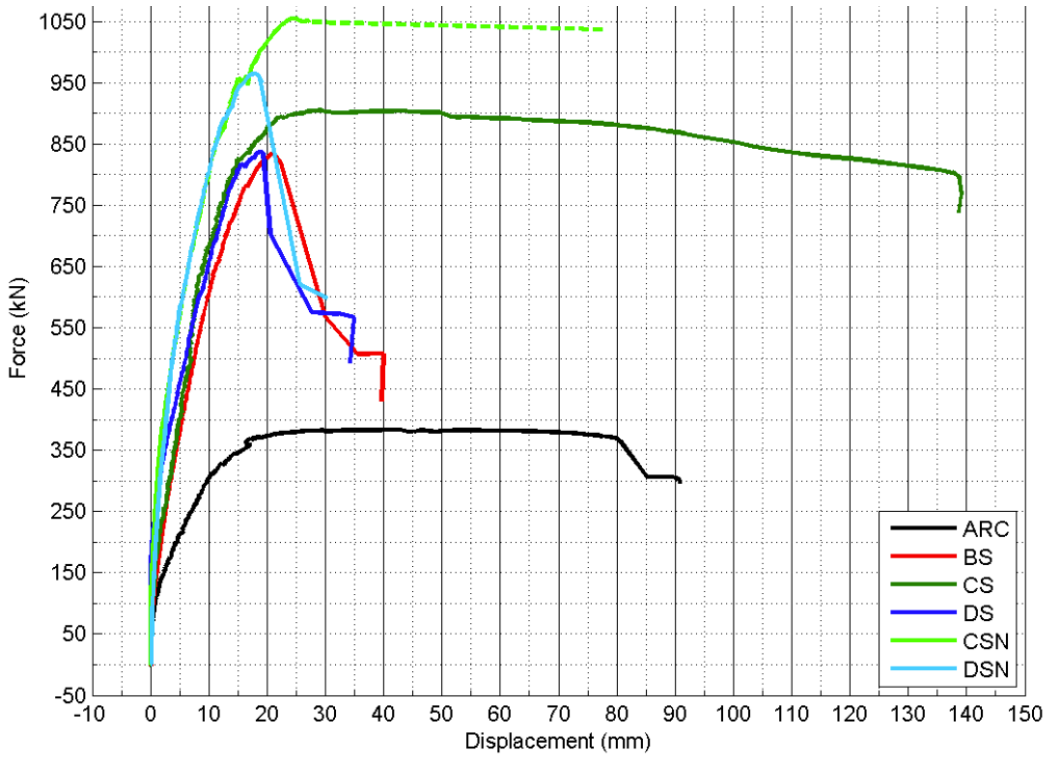


Fig. 3.116. Load-displacement curves from the shear wall tests conducted at the University of Liège. (Source: SmartCoCo [175]).

From both test series, it was identified that pure steel-concrete bond shear connection was enough to transfer the longitudinal shear flow developed at the steel concrete interface. Moreover, in each specimen, in comparison to the reference tests, a mixed flexural-shear failure pattern was observed,

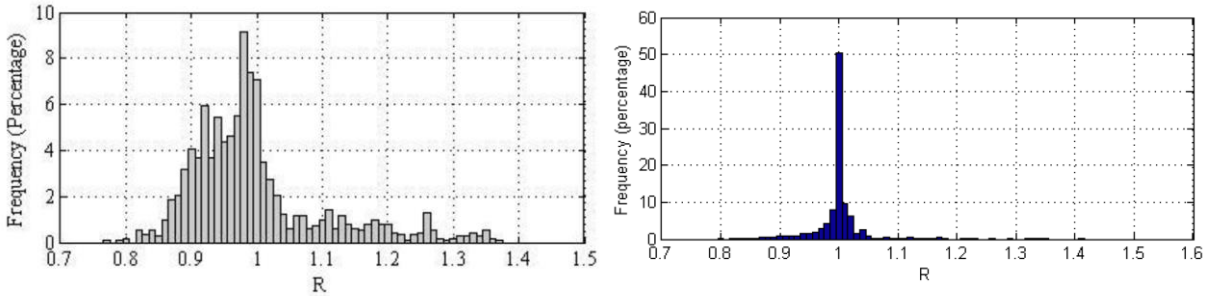
where at the damage initiation point, only pure bending failure was developed. In the later phase of the test, the shear damage dominated the entire response of the specimens. The contribution of embedded steel profiles in the load-bearing capacity had been identified and quantified.

The stability aspect and the effective flexural stiffness have been analysed at the University of Rennes based on the 1140 cases in a non-linear finite element parametric study. The parametric study consisted of five cross-sections with three and four embedded steel profiles. The impact of concrete material grade, two effective creep ratios, residual stresses and initial bow imperfections were analysed. The considered relative slenderness consisted of three variants 0.5, 1.0 and 2.0. In the taken analysis, effects of the second-order were considered. The moment magnification approach and the nominal stiffness method proposed by EN 1992-1-1 [53] had been adapted. The introduced modification envisaged in the consideration of a steel profile and introduction of a new stiffness reduction factor for the steel parts K_{sa}, which considers the effects of steel yielding, column slenderness and creep of concrete. The proposed new equation for the effective bending stiffness is given in Eq. 3.113 and the stiffness reduction factor for steel parts is defined in Eq. 3.114. Where, reduction coefficient for concrete K_c and the effective modulus of elasticity including effects of creep are based on EN 1992-1-1 [53]. The impact of the proposed model is shown in Fig. 3.117, where the ratio "R" defined in Eq. 3.116 is summarised and compared for the case of non-modified approach according to the simplified design procedures given in EN 1992-1-1 [53] and EN 1994-1-1 [58] to the proposed modified approach.

$$(EI)_{eff,II} = K_c E_{c,eff} I_c + K_{sa}(E_s I_s + E_a I_a) \tag{3.113}$$

$$K_{sa} = \frac{0.450\lambda^{0.147}}{1 + 1.433\varphi_{eff}\exp(-0.027\lambda)} \tag{3.114}$$

$$K_c = k_1 k_2 / (1 + \varphi_{eff}) \qquad k_1 = \sqrt{f_{ck}/20} \qquad k_2 = n\frac{\lambda}{170} \leq 0.20 \tag{3.115}$$



a) b)

Fig. 3.117. Histograms of factor "R" – a) simplified design and b) proposed model. (Source: SmartCoCo [175]).

$$R = \frac{R_{FE}}{R_{analytic}} \tag{3.116}$$

$$R_{FE/analytic} = \sqrt{\left(\frac{N_{FE/analytic}}{N_{pl,Rd}}\right)^2 + \left(\frac{M_{FE/analytic}}{M_{pl,Rd}}\right)^2} \tag{3.117}$$

The generic design approach was derived at the University of Liège by Prof. Plumier and it consists of design provision from EN 1992-1-1 [53], EN 1994-1-1 [58] and findings from the project SmartCoCo [175]. The developed model considers double symmetric members reinforced by several steel profiles. For columns, the larger dimension is not greater than 4 times the smaller dimension, where for walls, the length-to-thickness ratio is not smaller than 4, see Fig. 3.118. The design of composite columns with multiple encased steel profiles is based on the simplified N-M interaction curve following the method of EN 1994-1-1 [58]. For the global analysis of structures, the effective bending stiffness should be calculated according to Eq. 3.118, where for the stability checks, the model shown in Eq. 3.113 should apply. The long term effects should be considered by applying the effective value of the modulus of elasticity for concrete considering creep effects as given in EN 1994-1-1 [58].

$$(EI)_{eff} = K_e E_{cm} I_c + E_s I_s + E_a I_a \tag{3.118}$$

$$K_e = 0.5 \tag{3.119}$$

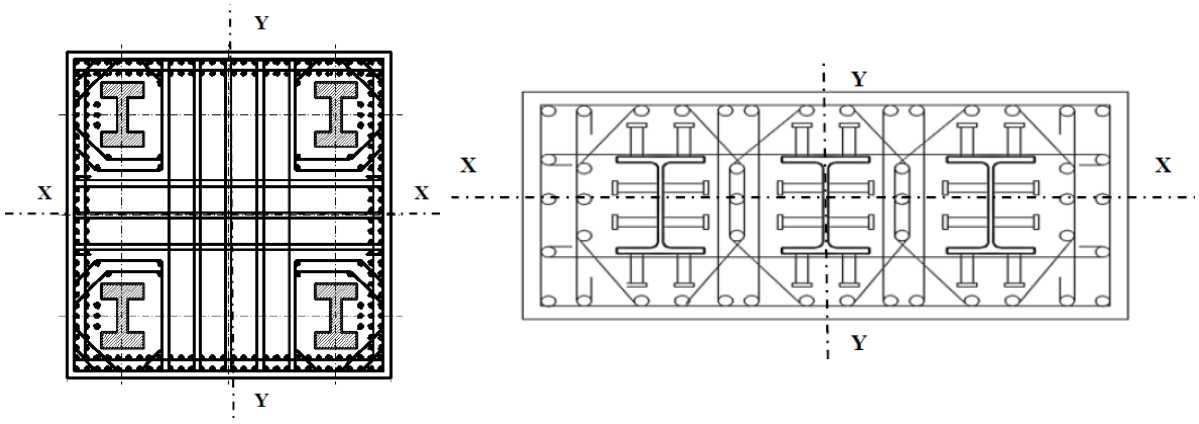


Fig. 3.118. Typical sections of composite members reinforced by several steel profiles considered in the generic design approach from project SmartCoCo – a) column and b) wall. (Source: SmartCoCo [175]).

An account for the influence of the axial force on the flexural stiffness is given and if the acting normal load is smaller than 20% of the plastic axial resistance, the stiffness can be calculated according to Eq. 3.120. Otherwise, Eq. 3.118 apply. The plastic axial resistance follows EN 1994-1-1 [58].

$$(EI)_{eff} = 0.5\left(1 + \frac{5N_{Ed}}{N_{pl,Rd}}\right)(K_c E_{cm} I_c + E_s I_s + E_a I_a) \tag{3.120}$$

The analysis of second-order effects should consider the flexural stiffness model shown in Eq. 3.113, where the plastic compression resistance should be evaluated according to the fibre method assuming strain correlation and internal forces equilibrium. For the statically indeterminate structures, the stiffness value should consider the effective modulus of elasticity for concrete following provisions of EN 1992-1-1 [53] as defined in Eq. 3.121-3.122. The second-order effects on slender columns should be considered by application of the moment magnification method analogically to the provisions given in EN 1994-1-1 [58] but the new effective flexural stiffness should be considered.

$$E_{cd,eff} = E_{cd}/(1+\varphi_{eff}) \tag{3.121}$$

$$E_{cd} = \frac{E_{cm}}{\gamma_{cE}} = \frac{E_{cm}}{1.2} \tag{3.122}$$

For the verification of composite members with multiple encased steel profiles, the steel sections can be replaced by the equivalent set of reinforcement bars, in such a way that minimum two equivalent bars represent each flange and web of a steel profile. The set of equivalent bars should exhibit the same plastic strength as the corresponding part of the steel profile. The decomposition scheme is shown in Fig. 3.119.

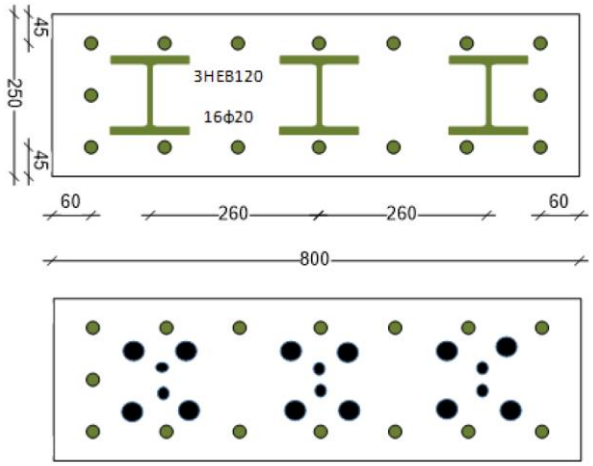


Fig. 3.119. Decomposition scheme of composite into reinforced concrete section. (Source: SmartCoCo [175]).

The shear transfer is assumed to distribute the shear forces between two systems proportionally to their relative shear stiffness. In the result, the subsection of the composite part with steel profiles and the subsection with pure reinforced concrete are considered. The model for the evaluation of internal forces base on the strut and tie method build on the Mörsch truss model. For the composite subsections, the entire shear is taken by the steel profiles and in the subsection consisting of the reinforced concrete part, the shear force is fully taken by the diagonal strut, see Fig. 3.120 and Fig. 3.121.

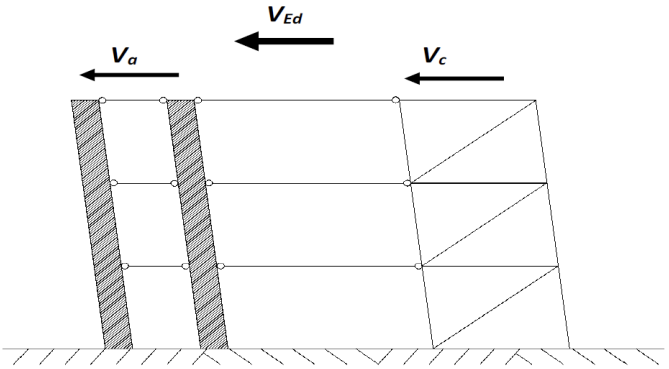


Fig. 3.120. Shear transfer system according to SmartCoCo. (Source: SmartCoCo [175]).

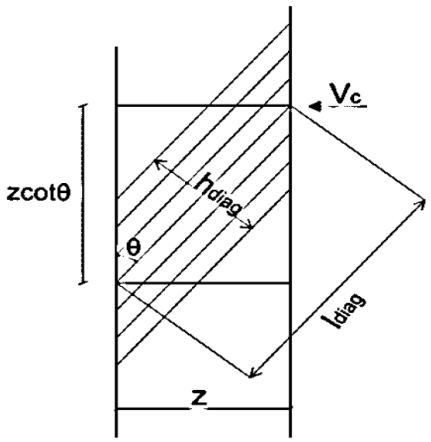


Fig. 3.121. Internal Mörsch truss system according to SmartCoCo. (Source: SmartCoCo [175]).

The respective shear stiffness of the composite and reinforced concrete subsections are defined in Eq. 3.123 and Eq. 3.124 respectively. Where, s is the spacing of stirrups, A_{sw} is the cross-sectional area of a stirrup, θ is the concrete strut dispersion angle (see Fig. 3.121), η is a coefficient, which takes into account the amplification of the concrete stiffness due to the existence of embedded steel profiles, b_w is the wall thickness, n is the number of embedded steel profiles and z is the distance between the external embedded steel profiles. Factor η is defined in Eq. 3.125, where further description of the introduced coefficient can be found in the SmartCoCo report [175].

$$S_{RC} = \frac{1}{\frac{s}{E_s A_{sw} \cot\theta} + \frac{1}{\eta E_c b_w \sin\theta \cos\theta}} \tag{3.123}$$

$$S_{SP} = \frac{nGA_v}{z \cot\theta} \tag{3.124}$$

$$\eta = \frac{E_c^e \cdot (z - \sum L_i) + E_c \cdot \sum L_i}{zE_c} \tag{3.125}$$

The distribution of shear forces between the subsections is based on the relative shear stiffness relation as shown in Eq. 3.126-3.128. The verification of shear forces in each subsection should be done according to the existing provisions [53, 55]. Additionally, the proposed model include verification of the von Mises stresses in each embedded steel profile and reduction of the axial strength due to the reduced area by the shear reduction factor ($A_{ir} = A_i - \rho A_{v,i}$). The aforementioned reduction factor and evaluation of the significance of the shear forces is based on the method given in EN 1994-1-1 [58], where originally, this factor is applied for the reduction of the material strength in bending.

$$V_{a,Ed} = V_{Ed} \frac{S_{SP}}{S_{SP} + S_{RC}} \tag{3.126}$$

$$V_{a,Ed,i} = \frac{V_{Ed} S_{SP}}{n(S_{SP} + S_{RC})} \tag{3.127}$$

$$V_{c,Ed} = V_{Ed} \frac{S_{RC}}{S_{SP} + S_{RC}} = V_{Ed} - V_{a,Ed} \tag{3.128}$$

According to the defined truss model, the longitudinal shear at the steel-concrete interface is related to the transferred shear forces by concrete subsection as shown in Fig. 3.122 and described in Eq. 3.129.

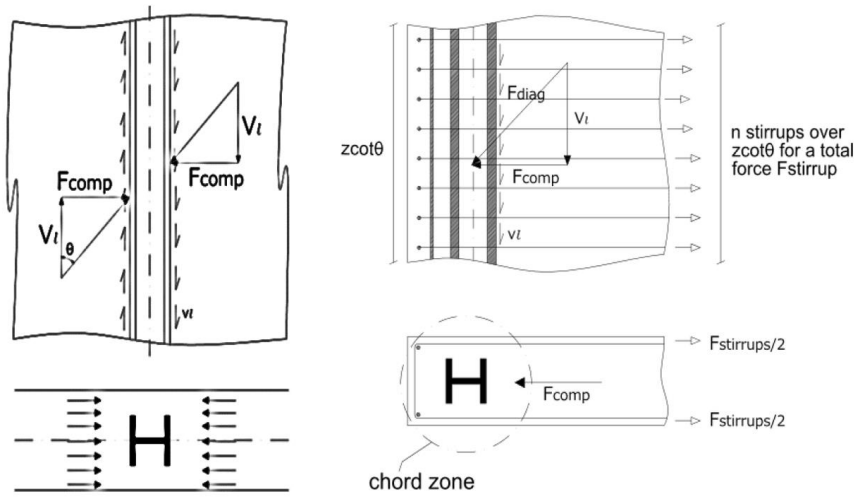


Fig. 3.122. Truss model for the local shear transfer according to SmartCoCo. (Source: SmartCoCo [175]).

$$V_{l,Ed} = V_{c,Ed} \cot\theta \qquad F_{comp,Ed} = F_{stirrup,Ed} = V_{c,Ed} \tag{3.129}$$

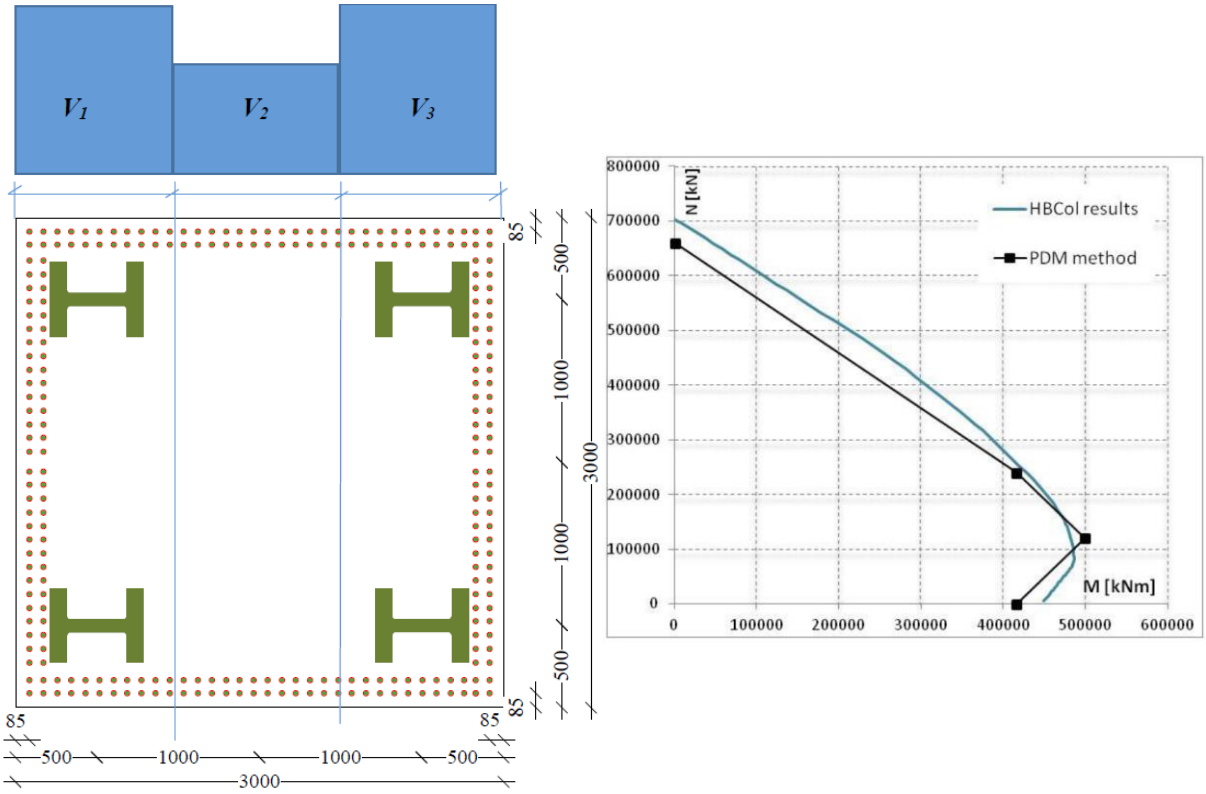


Fig. 3.123. Composite column with four embedded steel profiles according to SmartCoCo model – a) distribution of shear forces in a composite column section and b) N-M interaction curve. (Source: SmartCoCo [175]).

Shear forces distribution and comparison of the results from the HBCOL and proposed analytical model for a column with four embedded steel profiles are shown in Fig. 3.123. The simplified interaction curve incorporated an assumption that steel profiles and reinforcement bars can be simplified into a regular shape equivalent sections. This method was proposed by Plumier [175].

3.5.3. CTBUH project 'ISRC Composite Column'

The research project coordinated by the Council on Tall Buildings and Urban Habitat (CTBUH) called "Performance and Capacity of Isolated Steel Reinforced Concrete Columns and Design Approaches" (ISRC Composite Column) [82] had been conducted in collaboration with China Academy of Building Research (CABR) Technology, ArcelorMittal (AM) and Magnusson Klemencic Associates (MKA). The objectives of the project were to analyse the heavy composite column with four encased steel profiles subjected to axial load with the range of eccentricity equal to 0%, 10% and 15% and to validate the existing design provisions for the application. The conducted investigations consisted of experimental, numerical and analytical campaigns. The geometry of the analysed cross-section is shown in Fig. 3.124 and it was a case study for the real construction placed in China. The tested specimens consisted of six 1/4-scaled specimens tested in static loads character and four 1/6-scaled specimens subjected to dynamic cycling loads. In Fig. 3.124, the 1/4-scaled section is given, where the 1/6-scaled section is analogous but respectively smaller. Both test layouts are shown in Fig. 3.125.

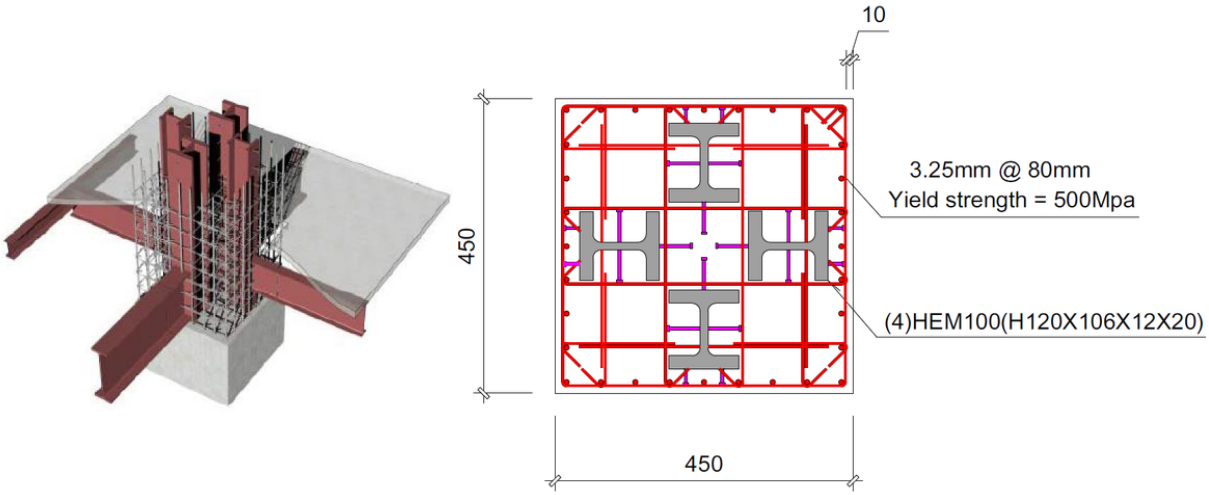
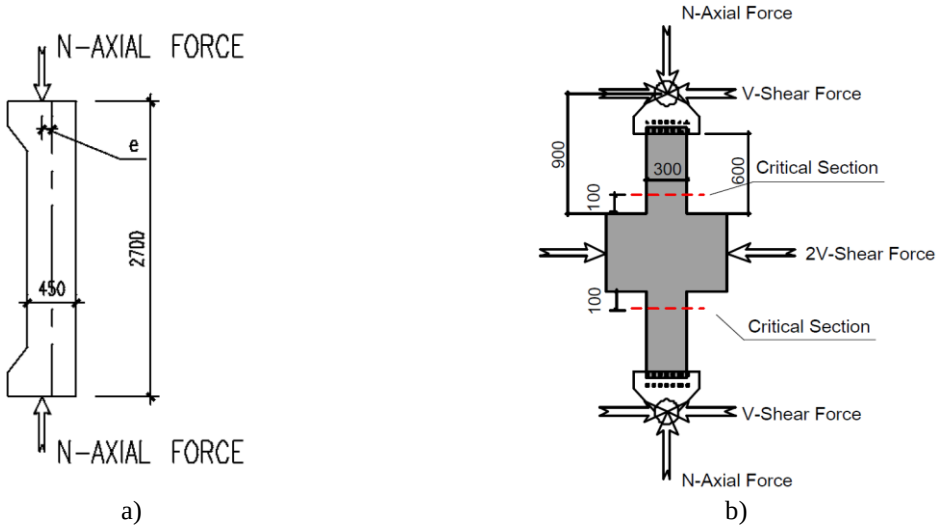


Fig. 3.124. Considered section of a composite column with four encased steel profiles within the project ISRC. (Source: CTBUH [82]).



a) b)

Fig. 3.125. Test layouts for the composite columns with four encased steel profiles of the project ISRC – a) static tests and b) dynamic tests. (Source: CTBUH [82]).

The static tests performed within the project are analysed. Details concerning the dynamic tests can be found in the report of the project [82]. The geometry of specimens used for the static tests is shown in Fig. 3.124 and Fig. 3.126, where four HEM100 steel profiles with grade S355 were embedded in a C50/60 concrete block. The reinforcement bars were comprising the Chinese standards and the grades of HRB 400 and HRB 500 were used for the longitudinal and transversal bars respectively. The shear connection between the steel profiles and the concrete was fully realized by the combination of 6x25 mm and 5x20 mm headed studs, where the smaller studs were placed on the external surfaces as shown in Fig. 3.124. The contribution of steel-concrete bond was neglected. The length of the specimen was 2700 mm but due to the test setup and pin support system, the unsupported length was 3590 mm. The test specimen placed in the testing frame is shown in Fig. 3.127.

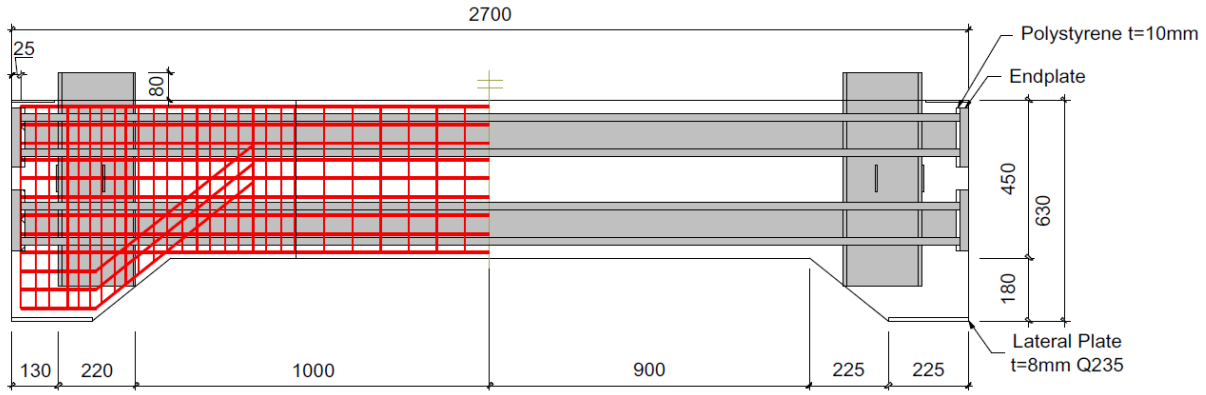


Fig. 3.126. Geometry of the specimen for the static tests of the project ISRC. (Source: CTBUH [82]).



Fig. 3.127. Static test of the project ISRC. (Source: CTBUH [82]).

The resultant load-vertical displacement curves from static tests are shown in Fig. 3.128 and Fig. 3.129, where three groups of specimens are distinguished – E00, E10 and E15 for the specimens with

corresponding 0%, 10% and 15% eccentricity e/h. The resultant trends of the horizontal deformation of columns are shown in Fig. 3.130. The comparison of the obtained results with the evaluated N-M interaction curves and numerical simulation curves are shown in Fig. 3.131. The interaction curves were obtained by applying the fibre method and simplified method derived in the SmartCoCo project [175]. Details concerning the FE simulations are available in the project report [82].

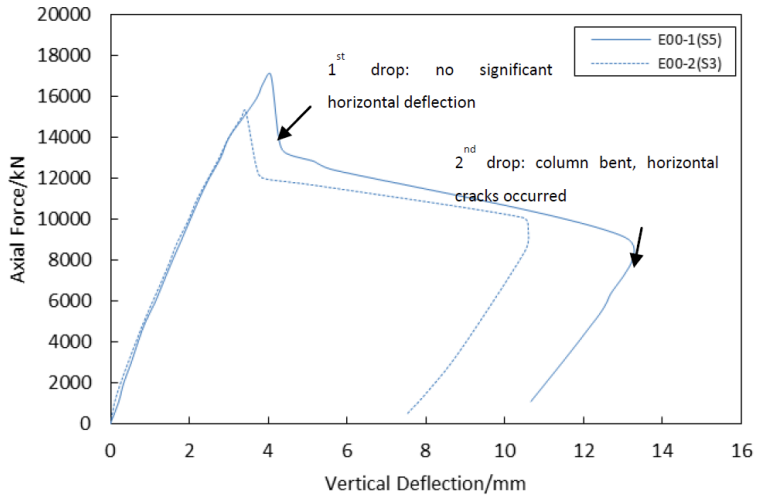


Fig. 3.128. Load-vertical displacement curves for the concentric tests of the project ISRC. (Source: CTBUH [82]).

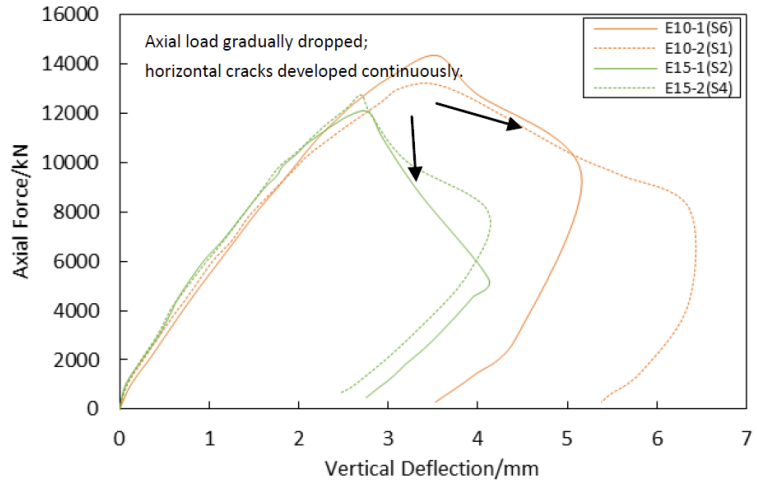


Fig. 3.129. Load-vertical displacement curves for the eccentric tests of the project ISRC. (Source: CTBUH [82]).

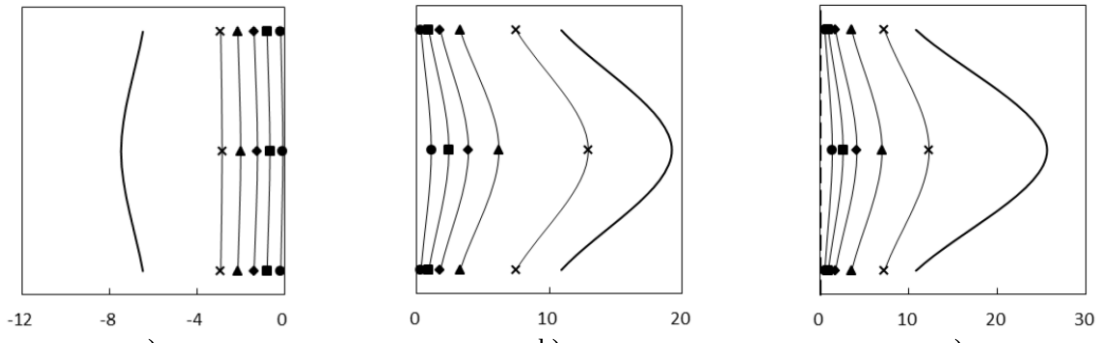


Fig. 3.130. Horizontal deformation of specimens in the static tests of the project ISRC at different load steps (0.2, 0.4, 0.6, 0.8, 1.0 of P_u and failure) – a) concentric, b) eccentric 10% and c) eccentric 15%. (Source: CTBUH [82]).

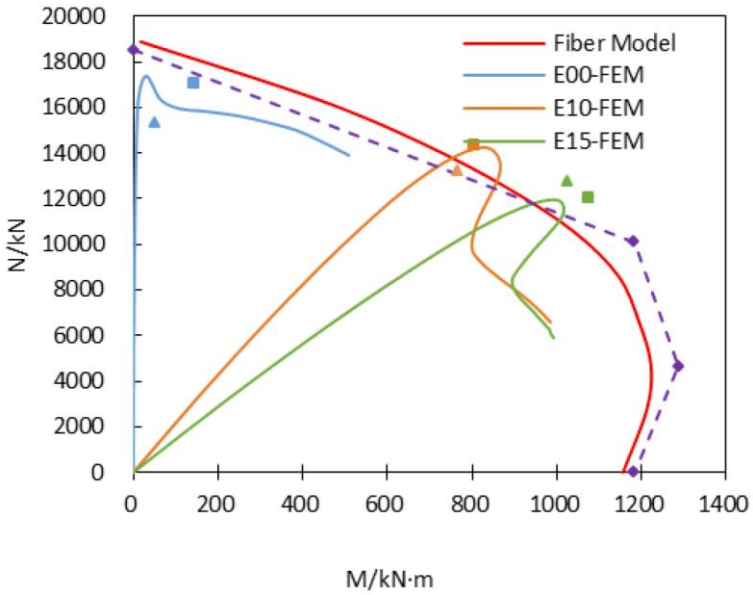


Fig. 3.131. Comparison of the N-M interaction curves to the test and simulation results obtained from the static tests of the project ISRC. (Source: CTBUH [82]).

From the records of strain gauges placed on the longitudinal reinforcement, steel profiles and concrete, authors identified the linear relation between the strains at different points of cross-section. Therefore, for the tested geometries, configuration and limitation of the applied eccentric load to 15%, the assumption about plane sections that remain plane had been verified. Moreover, the degradation of the stiffness of a column with the increased load was observed, where at the ultimate load, the reduction reached approximately 30-40% with dependence on the applied analytical model for stiffness evaluation (ACI 318 and EN 1994-1-1). Based on the taken observations, the corresponding reduction factors were proposed as 0.7 for the ACI 318 model [2] and 0.6 for the EN 1994-1-1 model [58].

In the analytical campaign, the provisions for the design from the American, Chinese and European design codes together with the method proposed in the project SmartCoCo [175] were checked if applicable to the considered cross-section of heavy composite column with four embedded steel profiles. The calculated resistances were compared to the obtained test results. It was found that the characteristic buckling resistance of the column correlates with the error of 10-20%, where the design values exhibited divergence to the test results of 40-80%. The most conservative results were obtained by applying ACI 318 building code [2], where three other standards/codes showed a similar correlation on the lower limit of the indicated convergence error. The interaction of bending and axial load has been compared on the basis of N-M interaction diagrams. The obtained results are shown in Fig. 3.132. The best accuracy was obtained by application of the Chinese Technical Specification of Steel-Reinforced Concrete Structures YB 9082, which is derived from the Japan design code AIJ-SRC. However, from Fig. 3.132, it can be observed that methods given by EN 1994-1-1 [58] or ACI 318 [2] exhibited similar convergence.

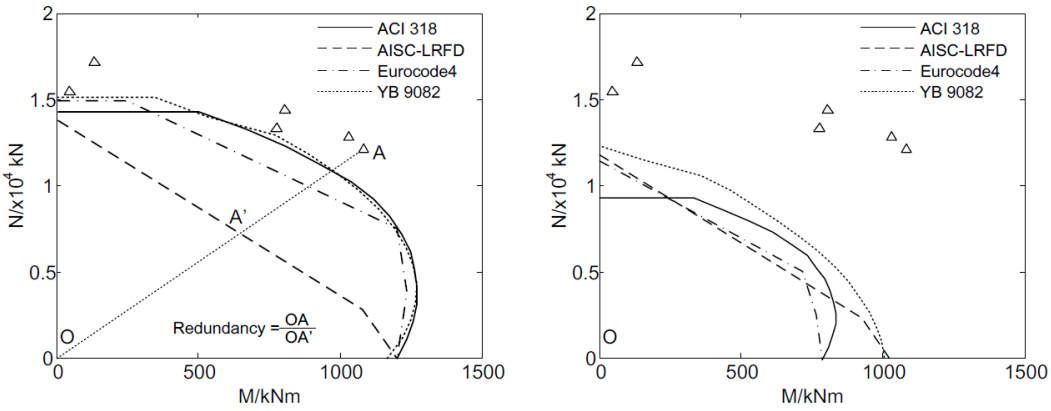


Fig. 3.132. Comparison of the analytical N-M interaction curves based on the design codes to the test results from the project ISRC. (Source: CTBUH [82]).

For the simplified design purposes, authors adapted method developed in the project SmartCoCo [175] and the composite cross-section has been transformed into the equivalent simplified composite cross-section as shown in Fig. 3.133. A similar adaptation has been made for the transfer of the shear forces between the respective subsections of the composite cross-section, but the original Mörsch truss model and distinction on the shear stiffness proposed by Plumier [175] were neglected and authors applied the flexural stiffnesses evaluated according to the design code provisions. However, this approach was also proposed by Plumier in one of his paper [146]. It was shown that the extended available design provisions from EN 1994-1-1 [58], JGJ 138 [85], ACI 318 [2] and AISC-LRFD [8] to the analysed composite column gave good convergence with the test results and safety margin.

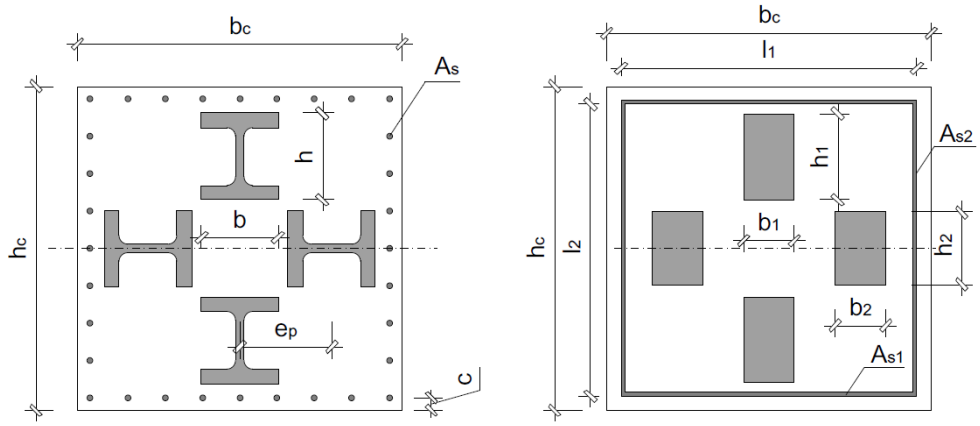


Fig. 3.133. Transformation principle of the composite cross-section into equivalent simplified composite cross-section. (Source: CTBUH [82]).

In the presented investigation on the composite column with four encased steel profiles, authors analysed the flexural stiffness of the column member fully utilising provisions from the considered design codes. However, the results shown in Fig. 3.130 (values in mm) for columns with eccentric load seem to harm the values that can be obtained by applying the pure Euler-Bernoulli beam model. This observation indicate that the proposed extension of the simplified design worked for the analysed case but the behaviour of the column and the shear transfer aspect still requires further analysis.

3.5.4. International literature review

In the international literature, number of publications can be identified that are dealing with the aspects of steel-concrete composite columns and shear walls with multiple encased steel profiles. However, the major part of the identified publications are related to the previously mentioned research projects SmartCoCo (RFCS) [175] and ISRC Composite Column (CTBUH) [82]. The separate research articles provide a background information of the analysed problems in the aforementioned research projects. Within the scope of the project SmartCoCo [175], the publications made by Plumier, Bogdan, Degée, Dragan, Nguyen, Tran, Keo, Somja and Hjiaj [17, 19, 42-43, 95-97, 129, 146-148, 185] can be identified. Similarly, series of publications made by Xiao, Deng, Chen, Zhao, Bogdan, Gerardy, Davies and Popa [16, 18, 208] have been produced based on the project ISRC of CTBUH [82]. The main conclusions are correlating to the observations and results described earlier in Sections 3.5.2 and 3.5.3. Beside the aforementioned, the following independent investigations were found:

Dan et al. [35-39]

The research project at the Polytechnic University of Timisoara in Romania called "Innovative Structural Systems Using Steel-Concrete Composite Materials and Fiber Reinforced Polymer Composites" supported by the CNCSIS-UEFISCSU (contracted in 2009) deals with the typical-geometry shear walls with two or three encased steel profiles. At the top of the specimens, the closing-frame top steel beam was used, see Fig. 3.134.

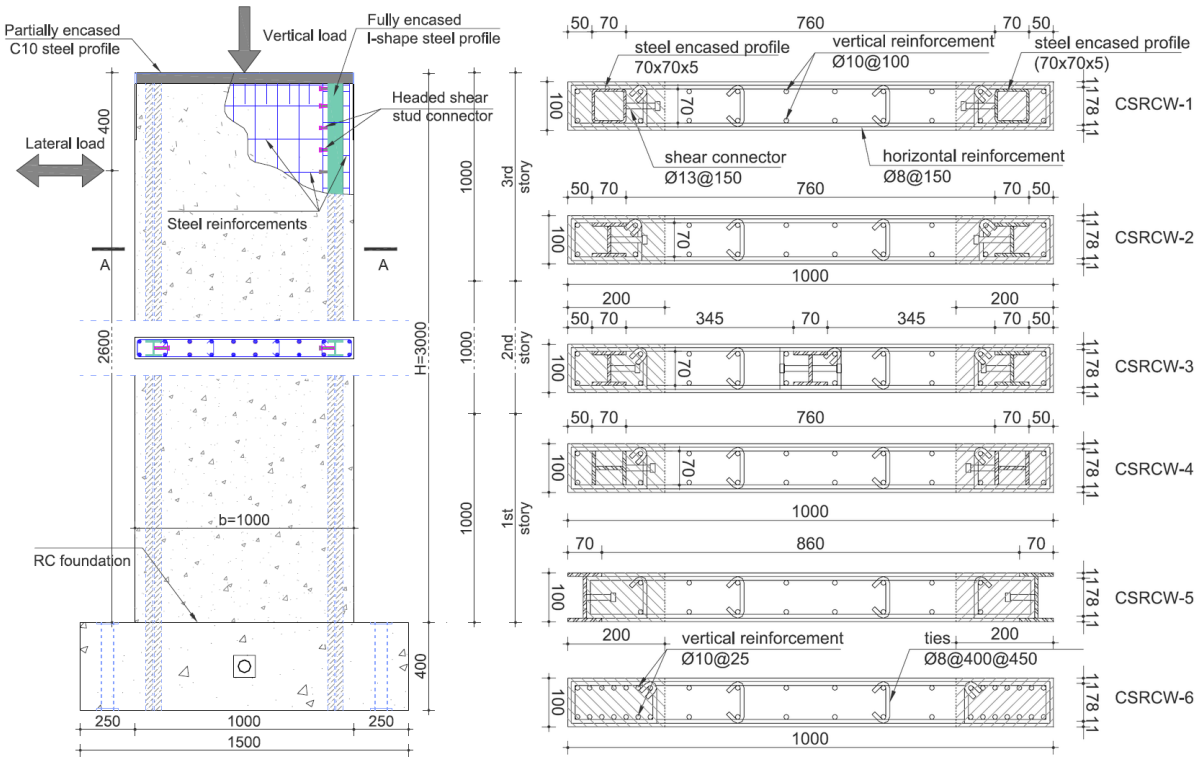


Fig. 3.134. Geometry of the shear walls analysed by Dan et al. (Source: Dan [35]).

The experimental campaign consisted of six specimens, where one pure reinforced concrete shear wall was tested as the reference. Headed studs assured the shear connection between steel profiles and

concrete. In the taken investigation, the number of embedded steel profiles, their shape and orientation were tested. The specimens were subjected to dynamic cycling loading. Numerical simulations in the software Atena 2D supported the conducted test campaign. The lateral load-drift characteristics were identified for each tested shear wall and the developed cracking failure patterns were analysed, see Fig. 3.135 and Fig. 3.136.

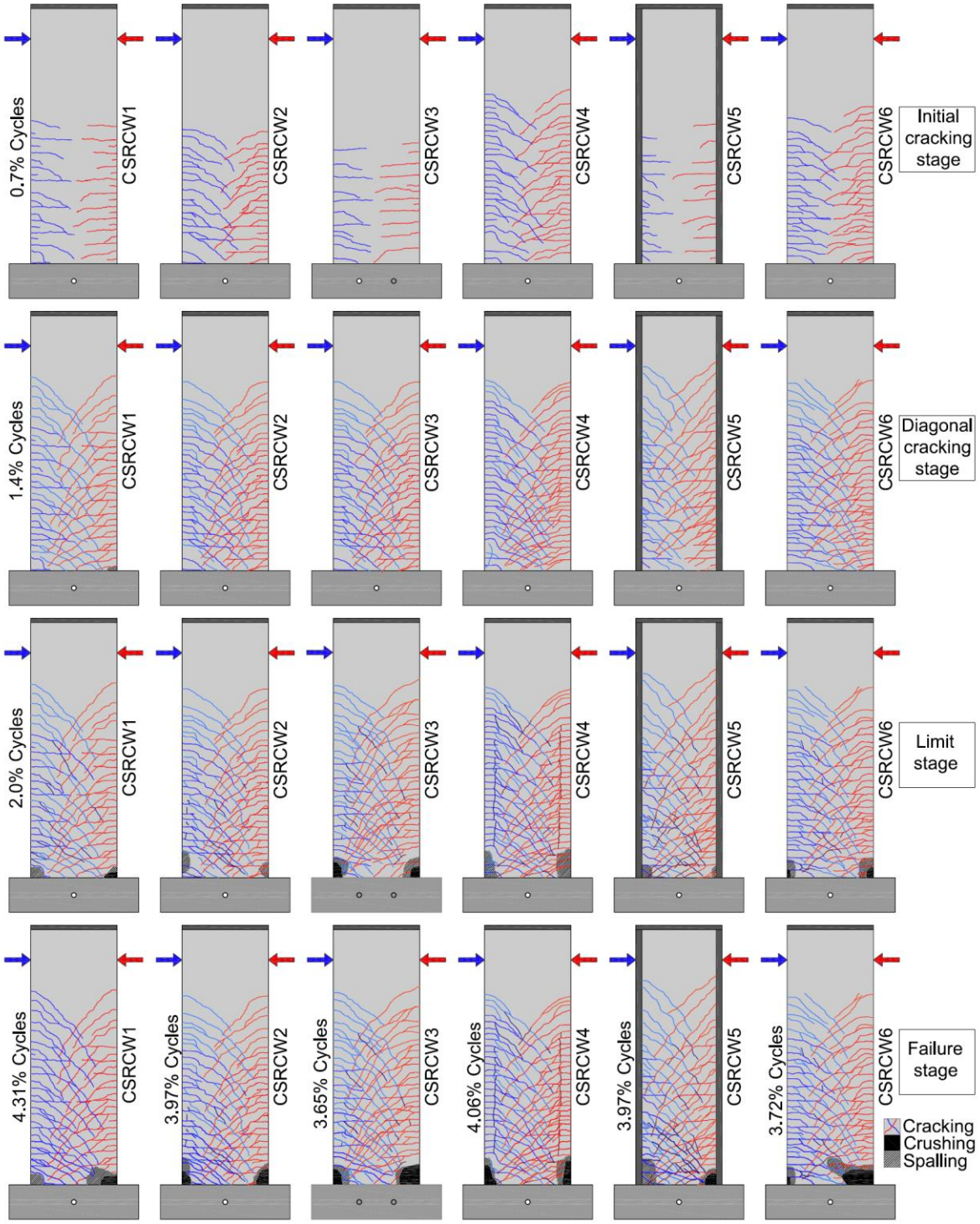
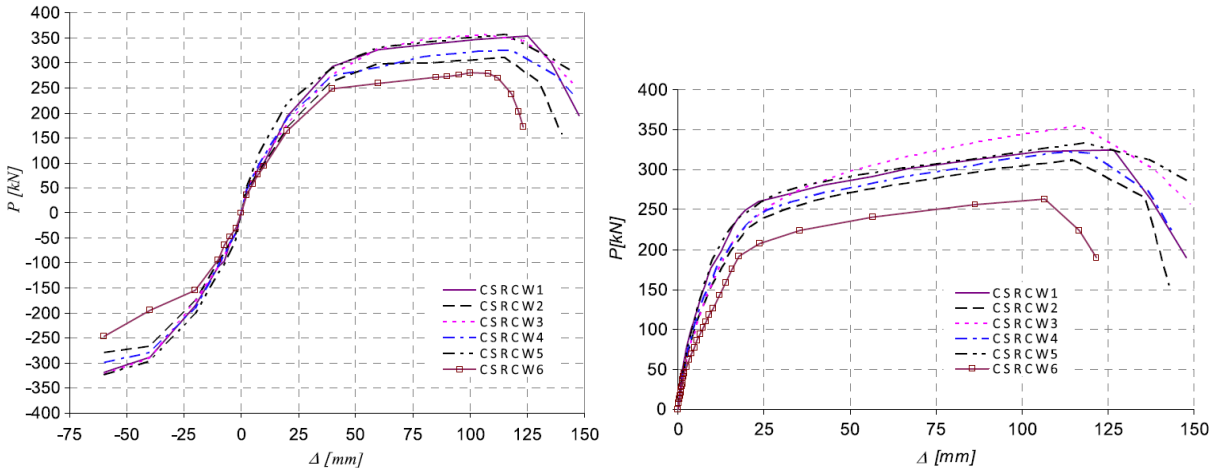


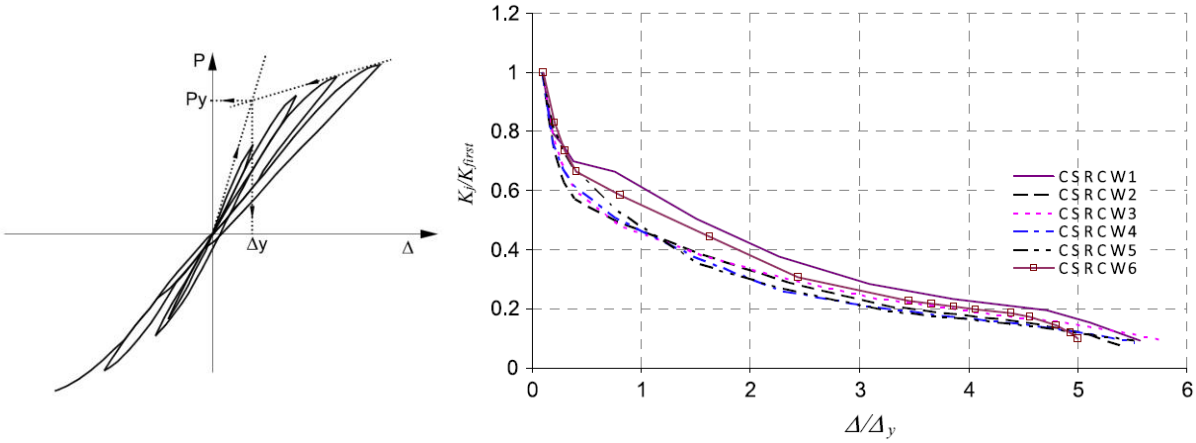
Fig. 3.135. Cracking pattern of the tested shear walls by Dan et al. at different load stages. (Source: Dan [35]).



a) b)

Fig. 3.136. Lateral load-total drift curves for the tested shear walls by Dan et al. – a) experimental curves and b) numerical curves. (Source: Dan [36]).

A positive impact of the applied steel profiles on the shear wall performance and energy dissipation was identified. The interaction of bending and shear forces defined the failure mode of the analysed shear walls and the importance of the second-order analysis had been highlighted. A correlation between the developed numerical model and test results was achieved as shown in Fig. 3.136. The degradation of the wall stiffness measured experimentally was analysed and the results are shown in Fig. 3.137.



a) b)

Fig. 3.137. Relative experimental stiffness degradation of the shear walls tested by Dan et al. – a) determination of the elastic limit of a shear wall response and b) relative stiffness-drift curves(Source: Dan [36]).

Liao et al. [111]

The work of Liao, Han and Tao [111] was done in order to develop and calibrate a numerical model to simulate the reinforced concrete shear walls with steel reinforced boundary columns. The analysed problem consisted of composite frame as shown in Fig. 3.138. The numerical model was developed in the software Abaqus and is shown in Fig. 3.139. Steel-concrete bond was modelled as the standard surface interaction, where the hard contact on pressure-overclosure relation had been applied and frictional relation between steel and concrete with friction ratio of $\mu = 0.6$ had been used. A slip of the longitudinal reinforcement was considered in the form of applied springs at the interface.

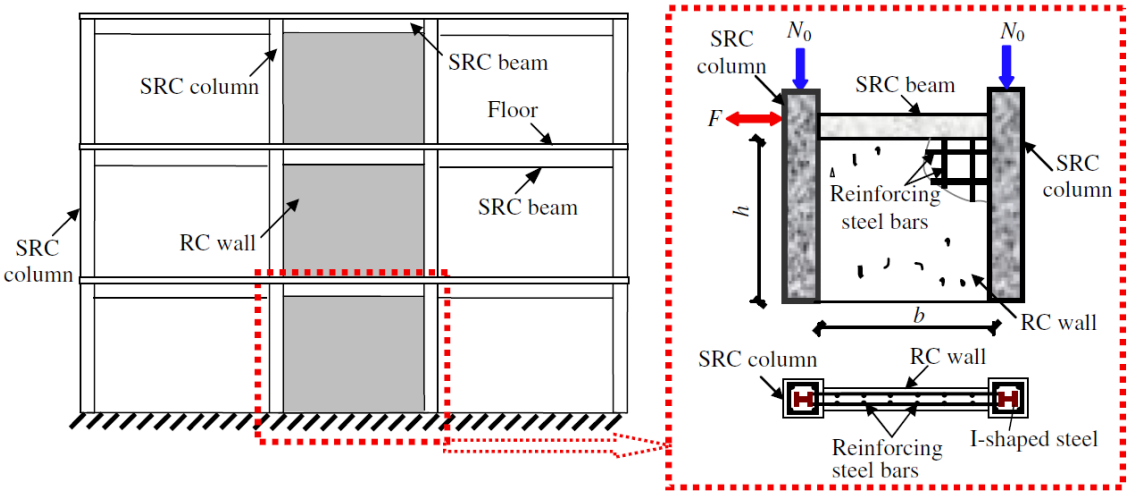


Fig. 3.138. Schematic definition of the analysed shear wall-frame structure by Liao et al. (Source: Liao [111]).

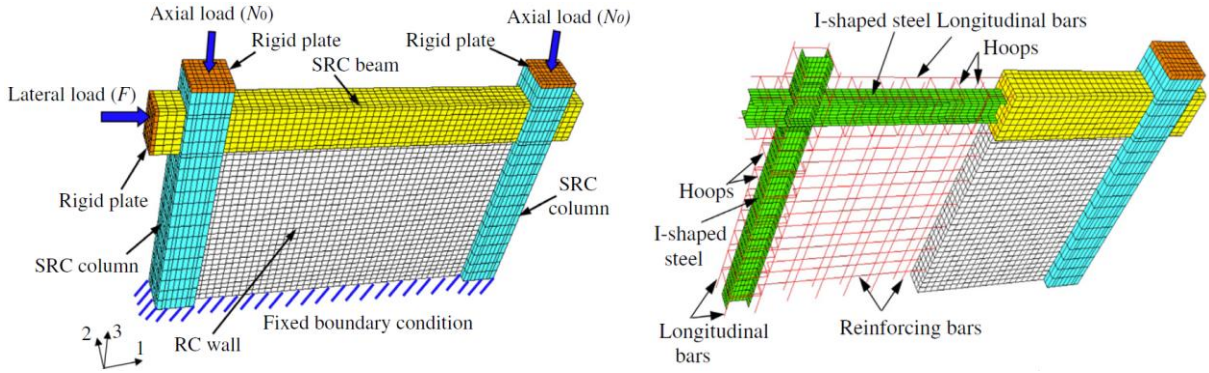
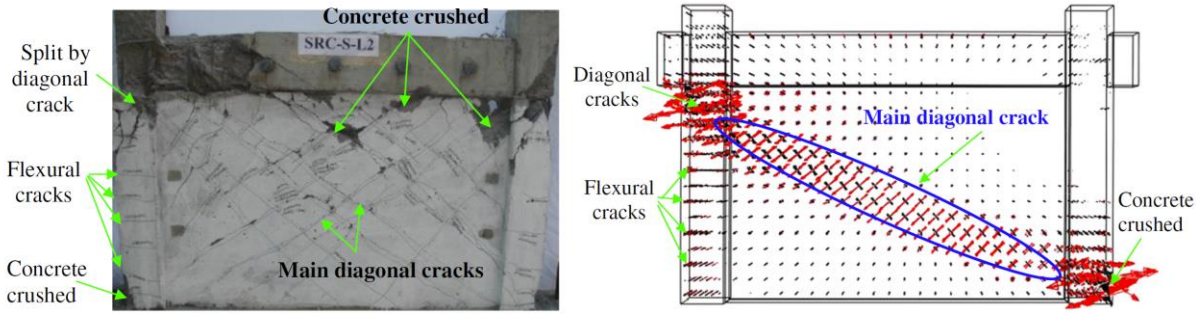


Fig. 3.139. Numerical model of the shear wall developed by Liao et al. (Source: Liao [111]).

The test campaign consisted of six specimens, where three main groups with varied geometry can be distinguished (-S-1, -L-1 and –L-2). Each group consisted of a pure reinforced concrete (RC) specimen and a steel reinforced concrete (SRC) specimen. The correlation between the developed numerical model of steel reinforced specimens and the corresponding experimental results is shown, see Fig. 3.140 and Fig. 3.141. Based on the calibrated numerical model, the structural behaviour of shear wall with steel reinforced boundary columns was analysed. The identified distribution of internal forces, shown in Fig. 3.142, indicated that the composite boundary columns took the major part of the bending action, where the shear forces were mainly bore by the reinforcement concrete wall part between them.



a) b)

Fig. 3.140. Cracking pattern of the shear wall with composite boundary columns – a) test and b) simulation. (Source: Liao [111]).

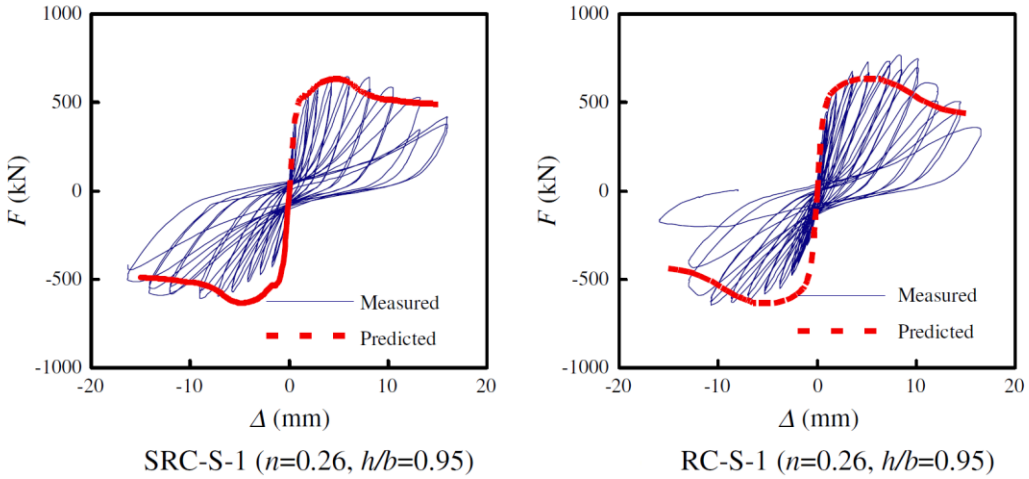


Fig. 3.141. Lateral load-drift curves for the shear walls analysed by Liao et al. (Source: Liao [111]).

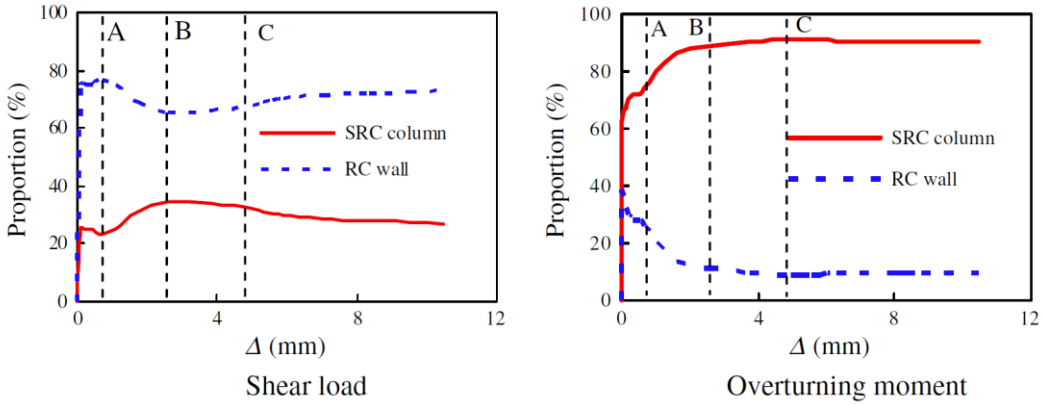


Fig. 3.142. Distribution of bending moment and shear forces between the boundary steel reinforced columns and reinforced concrete wall panel in the shear walls tested by Liao et al. (Source: Liao [111]).

Qian and Ji et al. [86-87, 151]

In the research work of Qian, Jiang, Ji, Sun and Lu [86-87, 151], the seismic behaviour of reinforced concrete shear walls with embedded steel profiles was investigated. Performed tests consisted of (i) the concrete filled and encased tubular steel profiles, (ii) the I-shaped and channel steel profiles and (iii) the double steel tubes at boundaries with sandwich wall panel between them. The analysed geometries are shown in Fig. 3.143-3.145 respectively. All test specimens were subjected to the dynamic cycling lateral loading imposed on the top of the wall panel. Simultaneously, the compressive axial force was imposed to all specimens. Tests shown in Fig. 3.144, were supported by the numerical simulations. The used concrete grade in all tests was C40 (European C25/30-C30/37), where the steel profiles were grade Q235 (European S235). The reinforcement bars consisted of deformed and plain steel bars. The deformed bars were HRB335 grade ($f_y = 335\ MPa$) and plain bars were HPB235 grade ($f_y = 235\ MPa$). In the test specimens shown in Fig. 3.145, tie bolts in the sandwich wall panels were used and the grade of bolts was 8.8. The failure patterns of tested specimens was govern by the significant bending and shear as shown in Fig. 3.146-3.148. Due to the bending action, the steel profiles yielded in the tensile zone and concrete crushed in the compressive zone. The identified load-drift curves are shown in Fig. 3.149-3.151. The embedded steel profiles enhance the performance of a wall element.

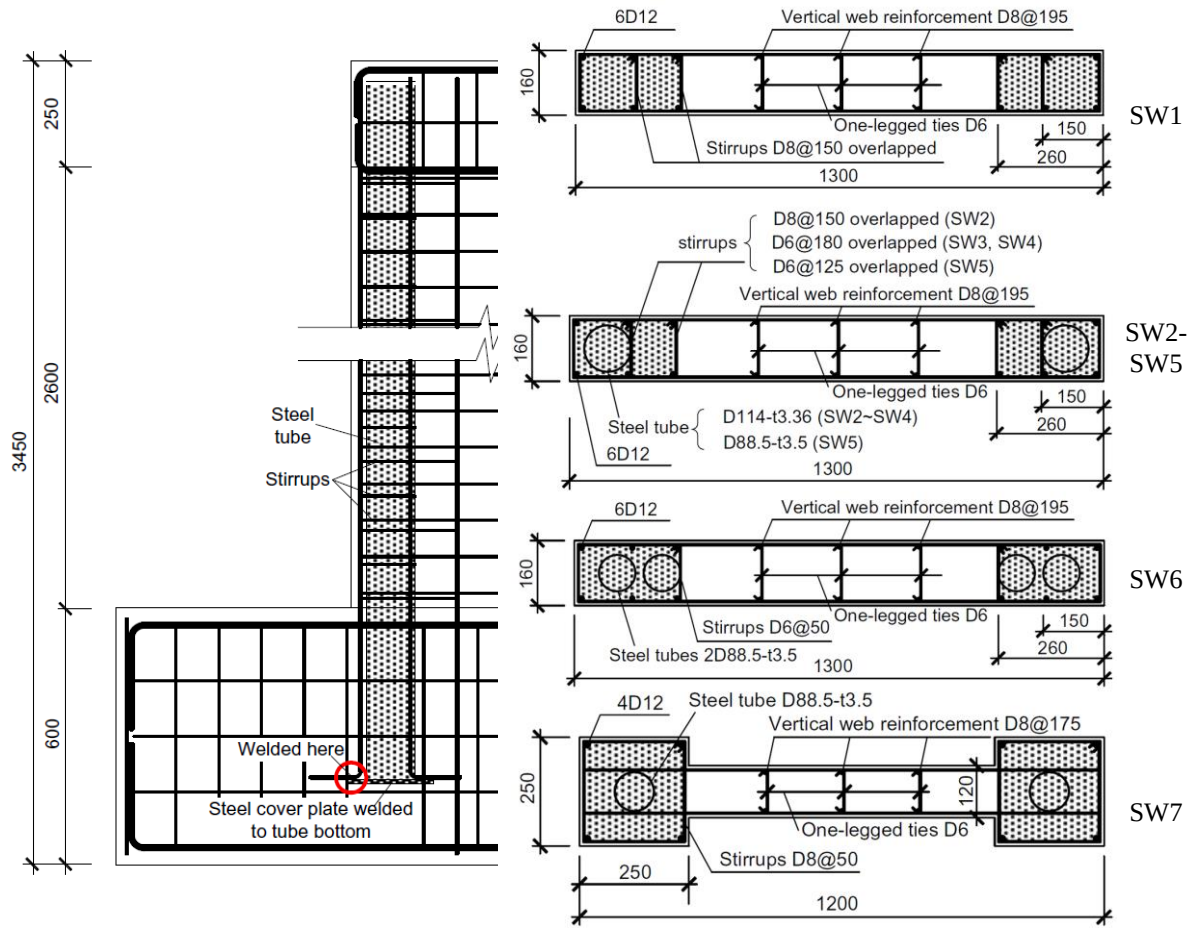


Fig. 3.143. Geometry of the shear wall specimens analysed by Qian et al. (Source: Qian [151]).

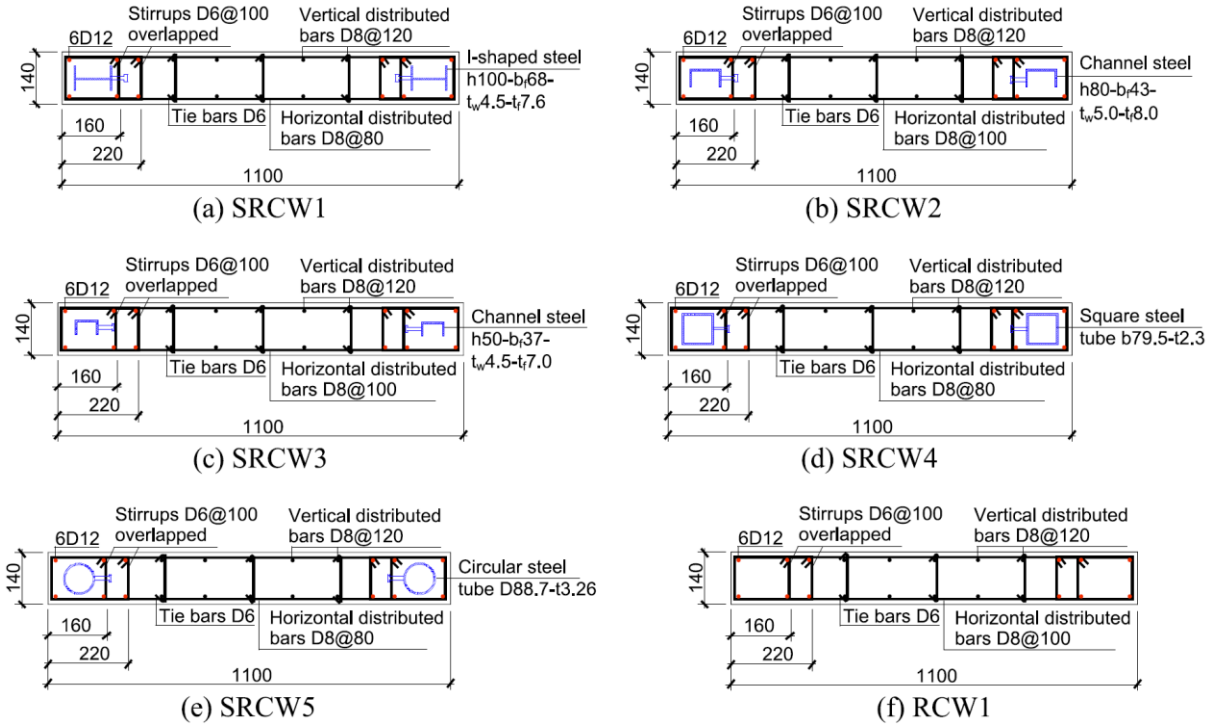


Fig. 3.144. Geometry of the shear wall specimens analysed by Ji et al. (Source: Ji [87]).

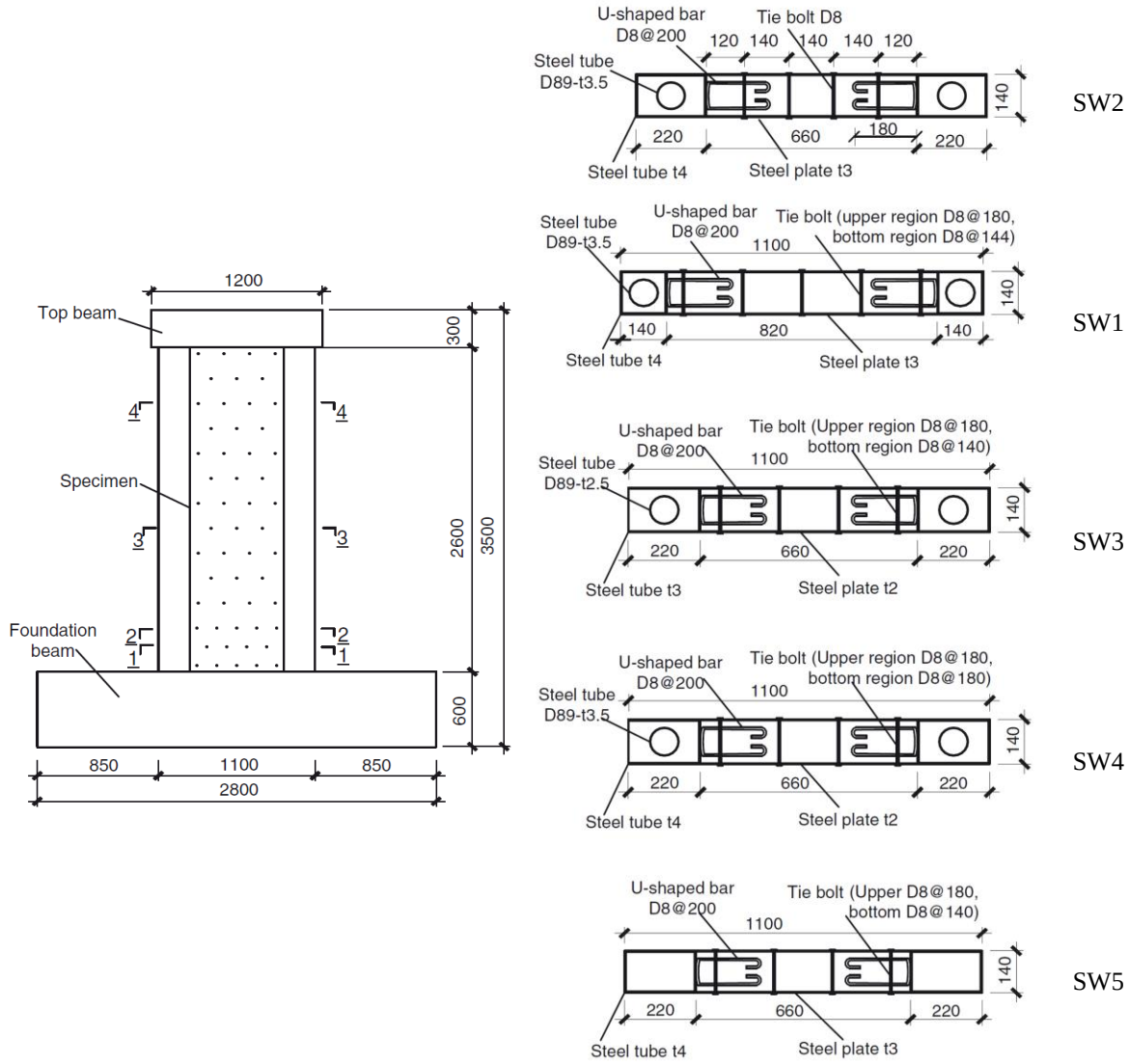


Fig. 3.145. Geometry of the shear wall specimens analysed by Ji et al. (Source: Qian [86]).

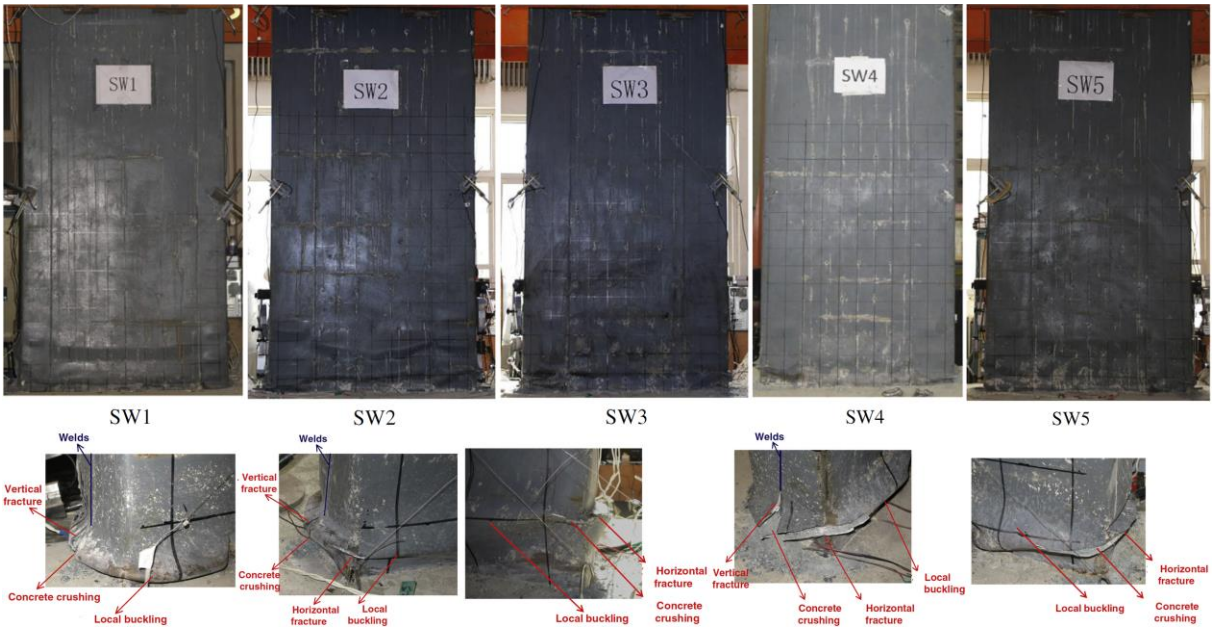


Fig. 3.146. Deformations of tested specimens shown in Fig. 3.145. (Source: Ji [86]).

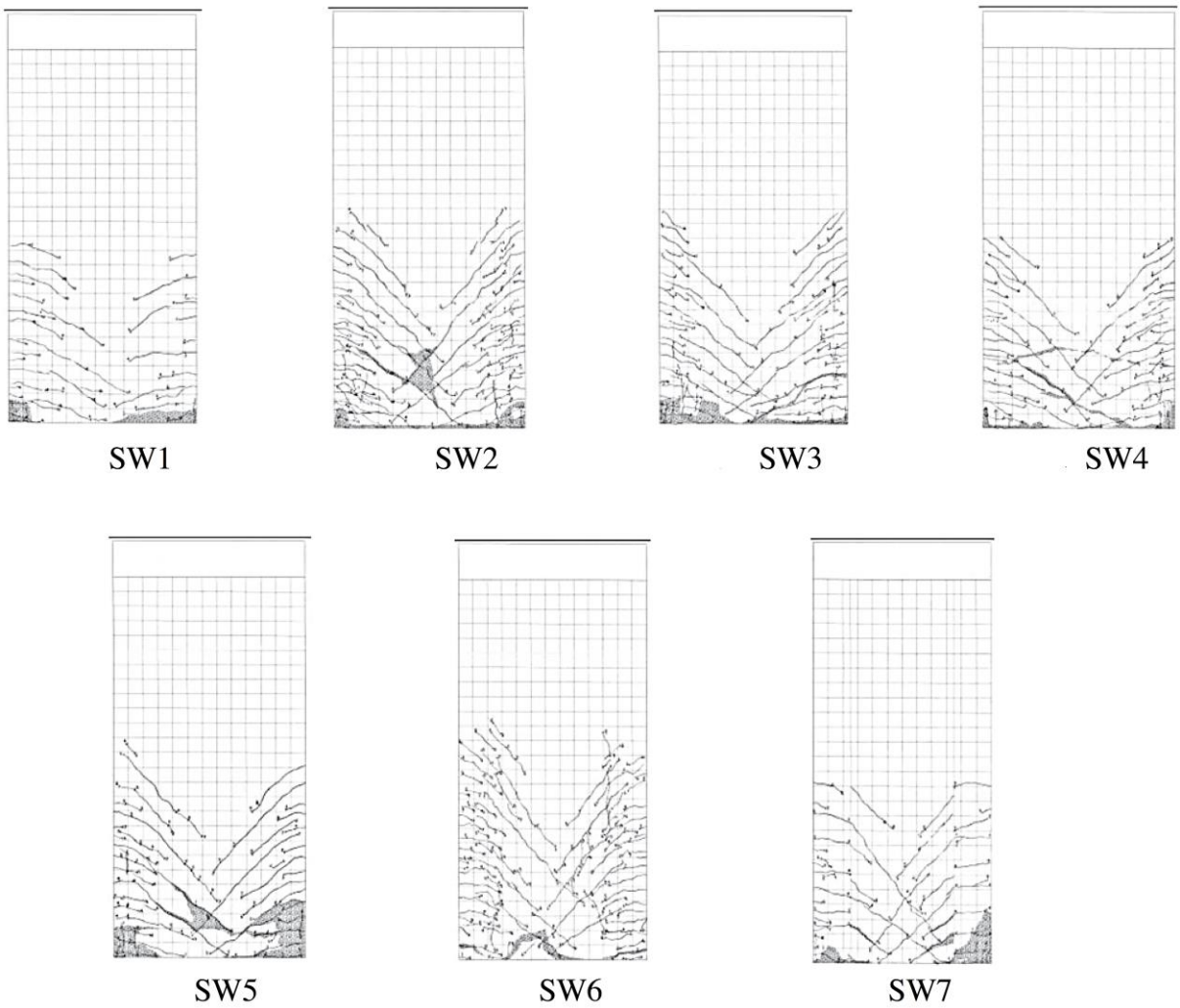


Fig. 3.147. Cracking pattern of specimens shown in Fig. 3.143. (Source: Qian [151]).

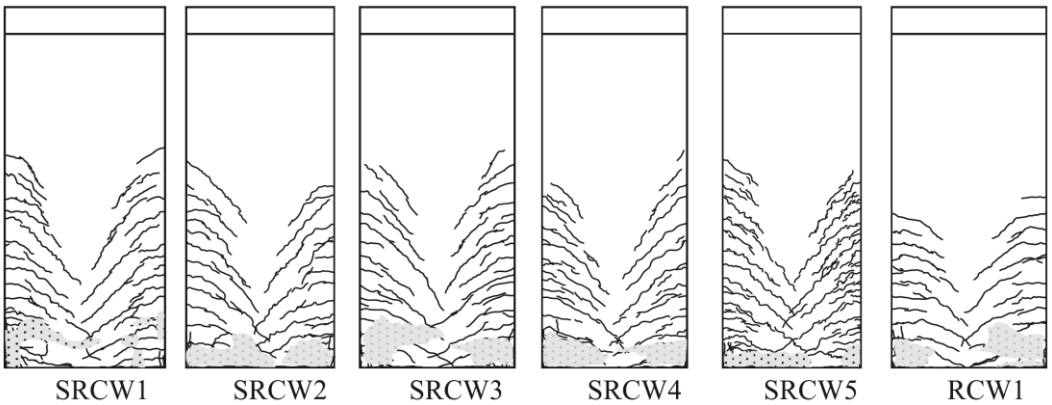


Fig. 3.148. Cracking pattern of specimens shown in Fig. 3.144. (Source: Ji [87]).

In Fig. 3.150b, the measured strain distribution over the depth of the tested shear wall specimen SRCW3 is given. For comparison, the strain distribution obtained from the numerical simulations is added. It can be observed that the non-linear character was obtained in the further phases of the test. Moreover, authors identified that the flexural stiffness of a shear wall is strongly dependent on the applied axial load and the model proposed by Adebar et al. (adopted by the Canadian Code) for the

reinforced concrete shear wall cores in high-rise buildings for seismic design, given in Eq. 3.130, estimates well the upper and lower boundaries of the flexural stiffness value. Where n is the axial force ratio and it can be defined by dividing the applied axial load by the plastic axial resistance.

$$EI_{eff} = \begin{cases} (0.6+n)EI_g \leq EI_g & \text{Upper-bound} \\ (0.2+2.5n)EI_g \leq 0.7EI_g & \text{Lower-bound} \end{cases} \tag{3.130}$$

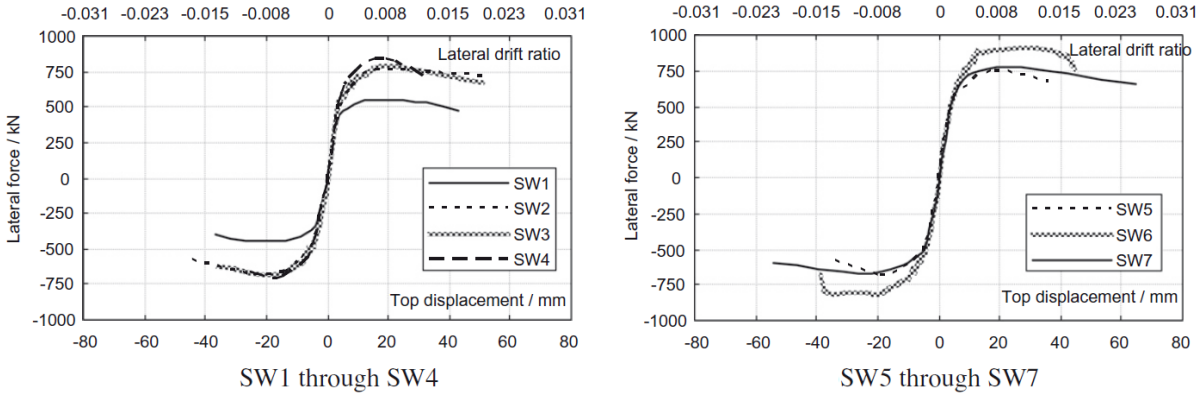


Fig. 3.149. Lateral load-displacement curves for specimens shown in Fig. 3.143. (Source: Qian [151]).

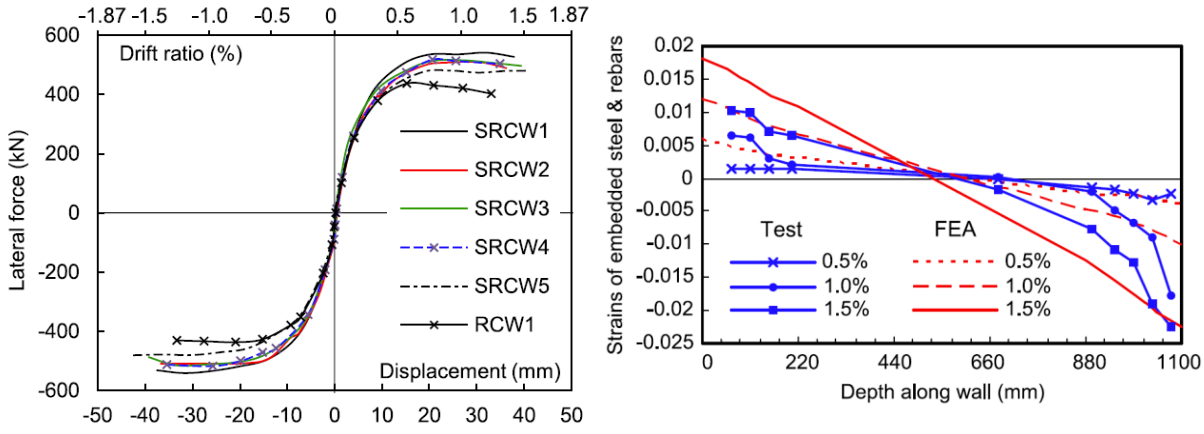


Fig. 3.150. Test results for specimens shown in Fig. 3.144 – a) lateral load-displacement curves and b) strain distribution over the wall section in specimen SRCW3. (Source: Ji [87]).

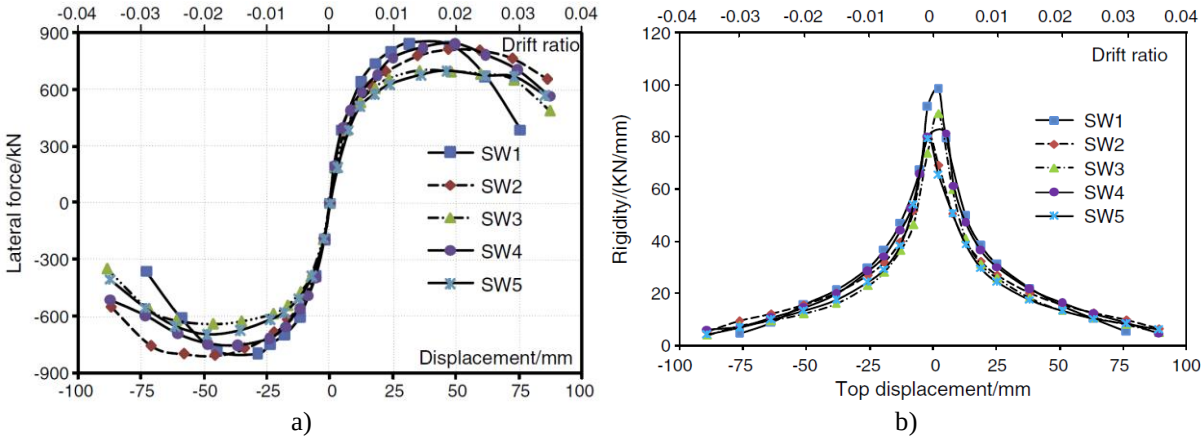


Fig. 3.151. Test results for specimens shown in Fig. 3.145 – a) lateral load-displacement curves and b) stiffness degradation at different levels of deformation. (Source: Ji [86]).

Zhu et al. [214]

An analogy to the composite columns with multiple encased steel profiles can be identified in the systems of buckling-restraining braces (BRB) with separated cores. In the work of Zhu and Guo [214], a bracing system with two concrete filled tubes, each with inner steel plate core, had been analysed numerically and analytically. The geometry of the analysed specimen is shown in Fig. 3.152. It was shown that in the developed system, the shear effects on the buckling deformation shape of the entire restraining brace system are significant and related to the big discrepancy between the individual stiffnesses of the core and interconnecting elements. The simplified analysed model is shown in Fig. 3.153 and the proposed equation for the critical buckling load is given in Eq. 3.131. Where, I_c refers to the entire core, $I_{e,c}$ to the concrete part and $I_{e,s}$ to the steel tube part. It was identified that the increased distance between the core elements increased the resultant buckling critical load.

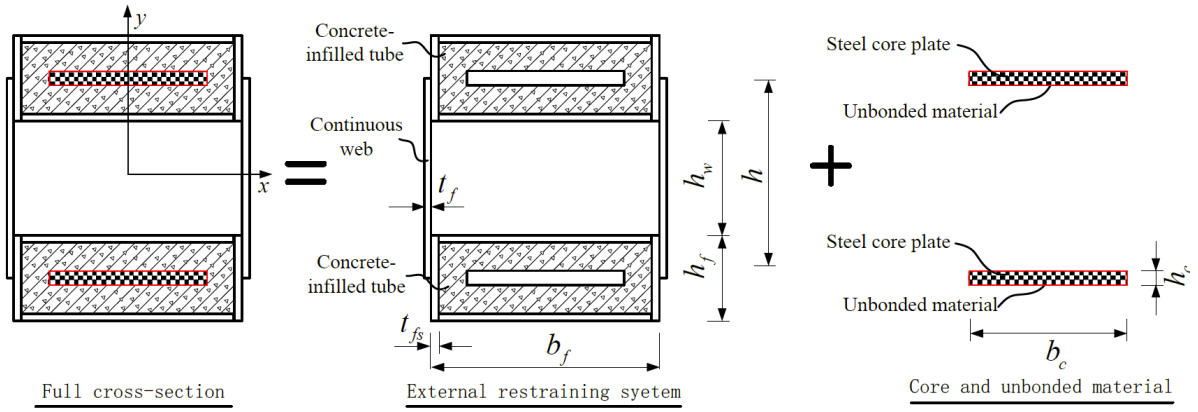


Fig. 3.152. Cross-section of the buckling-restraining brace system with isolated cores. (Source: Zhu [214]).

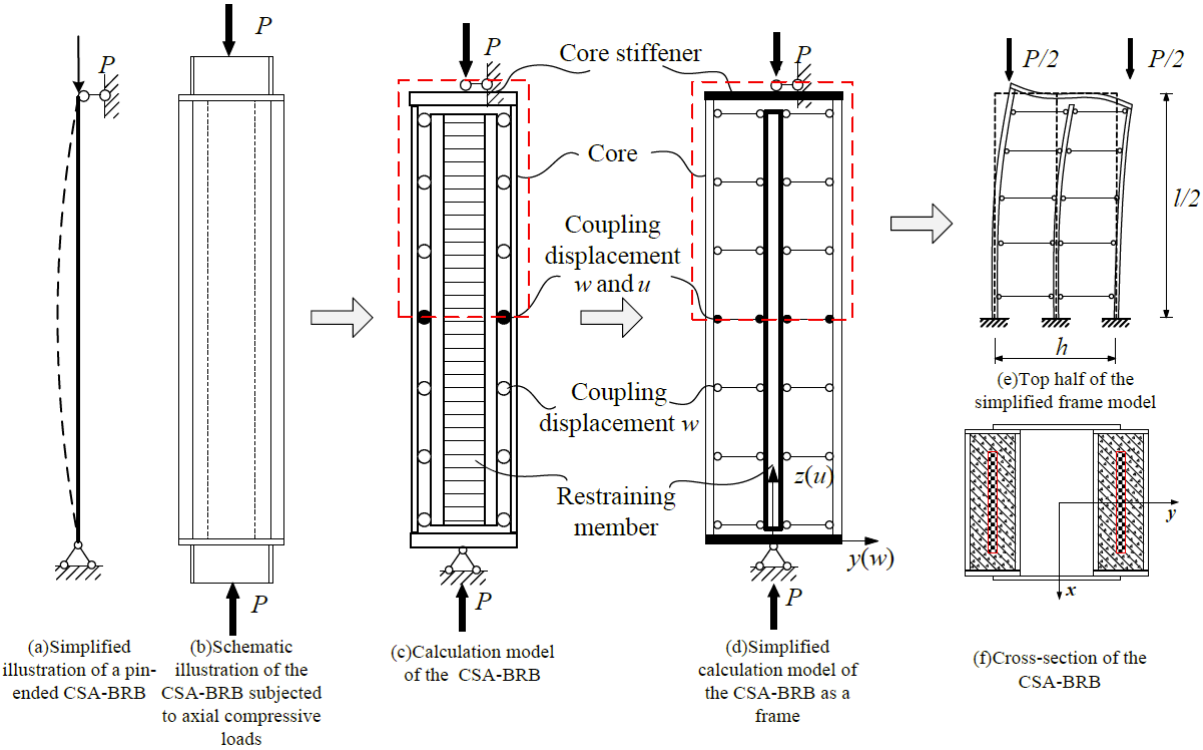


Fig. 3.153. Model for the analysis of buckling-restraining brace system with isolated cores. (Source: Zhu [214]).

$$P_{cr,x} = \frac{(4 + 3.192\beta)\left(2\pi^2 E_c I_{c,x} + \pi^2 E_e I_{e,x}\right)}{l^2(1 + 3.192\beta)} \tag{3.131}$$

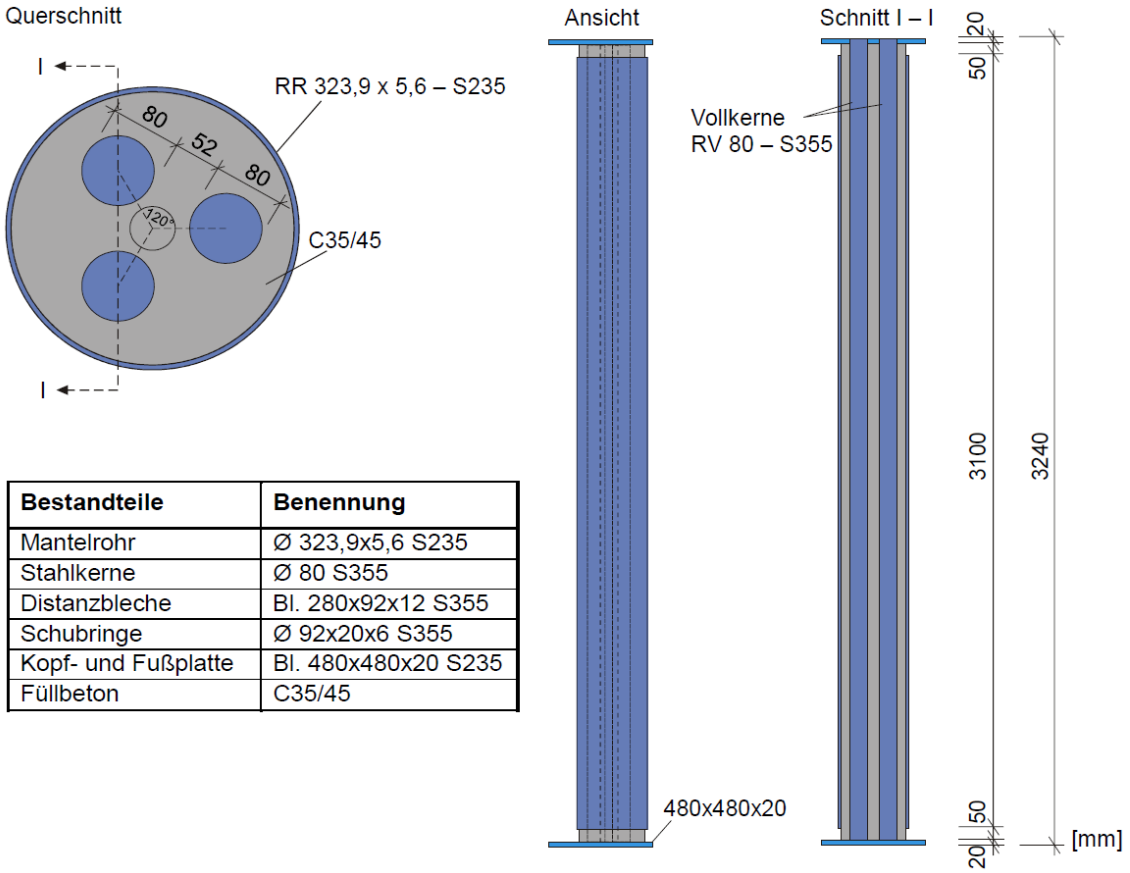
$$\beta = \frac{2(2E_c I_c + E_e I_e)}{E_s A_c h^2} \tag{3.132}$$

$$E_e I_e = E_s I_{e,s} + 0.8 E_c I_{e,c} \tag{3.133}$$

A correlation to the steel-concrete composite columns with multiple encased steel profiles is non-direct, where in composite columns, the interconnecting material is concrete between the encased steel profiles and in BRB systems are the steel plates. However, in both cases, each core element consists of much higher individual bending stiffness than the interconnecting part.

Chanou [29]

In his PhD Thesis, Chanou [29] analyses the structural behaviour of circular concrete filled steel tube composite columns with multiple solid circular steel cores. This type of composite columns is clearly beyond the scope of the simplified design method of EN 1994-1-1 [58] and can be classified as the heavy steel concrete composite columns with multiple encased steel profiles. Chanou in his work varies the number and the position of the steel cores in order to analyse the improvement of the structural behaviour and load-bearing capacity. The geometry of tested specimens is shown in Fig. 3.154-3.155.



Bestandteile	Benennung
Mantelrohr	Ø 323,9x5,6 S235
Stahlkerne	Ø 80 S355
Distanzbleche	Bl. 280x92x12 S355
Schubringe	Ø 92x20x6 S355
Kopf- und Fußplatte	Bl. 480x480x20 S235
Füllbeton	C35/45

Fig. 3.154. Geometry of the test specimens with three steel cores tested by Chanou. (Source: Chanou [29]).

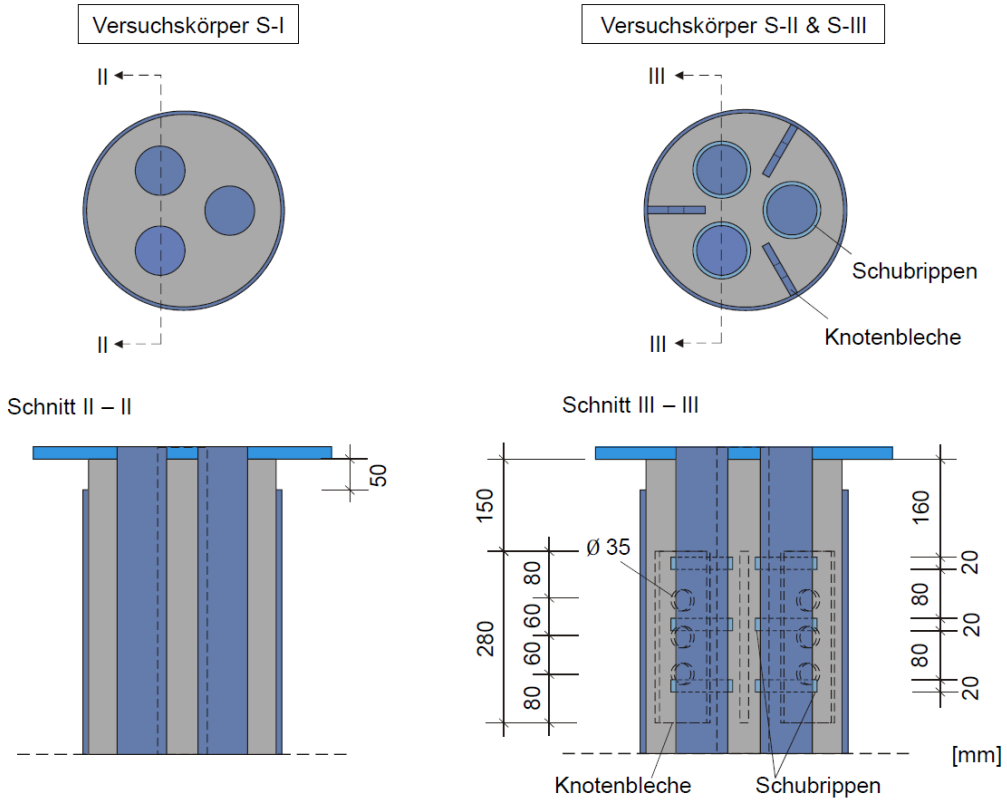


Fig. 3.155. Shear connection detail in the specimens tested by Chanou. (Source: Chanou [29]).

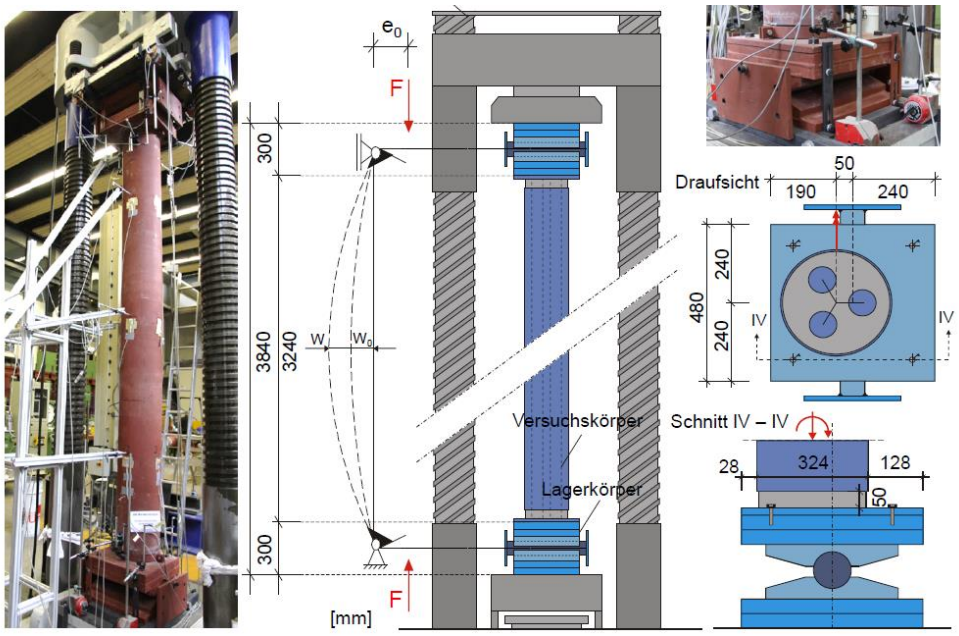


Fig. 3.156. Test layout of tests performed by Chanou. (Source: Chanou [29]).

The investigations are based on the conducted three big-scale column compression tests and developed numerical model. As an outcome, a proposal for the adaptation of the simplified design procedure of EN 1994-1-1 [58] was given, where modification for the effective flexural stiffness and plastic bending moment capacity is considered. The test layout is shown in Fig. 3.156. Two types of shear connectors are considered – perforbond plate and shear ribs, where the schematic geometry with test results are shown in Fig. 3.157-3.159. The shear ribs connectors were also tested with three internal

steel cores as shown in Fig. 3.159. From the conducted push-out tests with multiple steel cores, it can be observed that shear connection strength exhibited better performance due to increased amount of embedded cores (compare Fig. 3.158 and Fig. 3.159). In Fig. 3.158 and Fig. 3.159, the applied load is described in the function of relative ratio, which can be evaluated according to Eq. 3.134. Where, F is the applied load, f_{cm} is the mean concrete compression strength for cylindrical specimens, d_k is the diameter of the inner core, h_{SR} is the height of the shear rib connector and n_{SR} is the number of applied shear rib connectors.

$$\alpha_s = \frac{F}{f_{cm} \cdot \pi \cdot d_k \cdot h_{SR} \cdot n_{SR}} \tag{3.134}$$

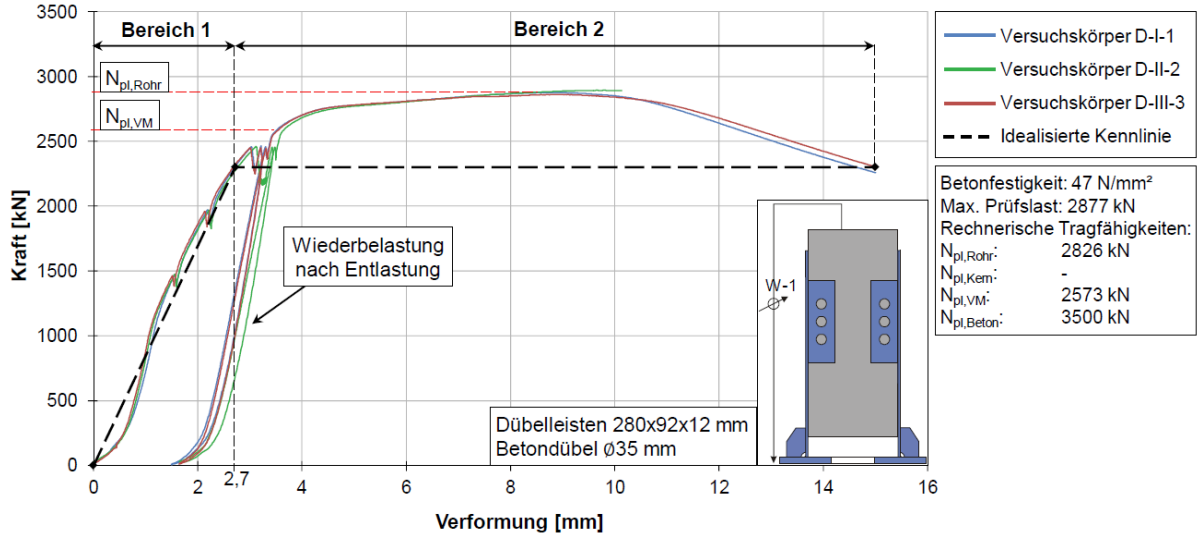


Fig. 3.157. Push-out test of the perfobond connector in concrete filled tubes. (Source: Chanou [29]).

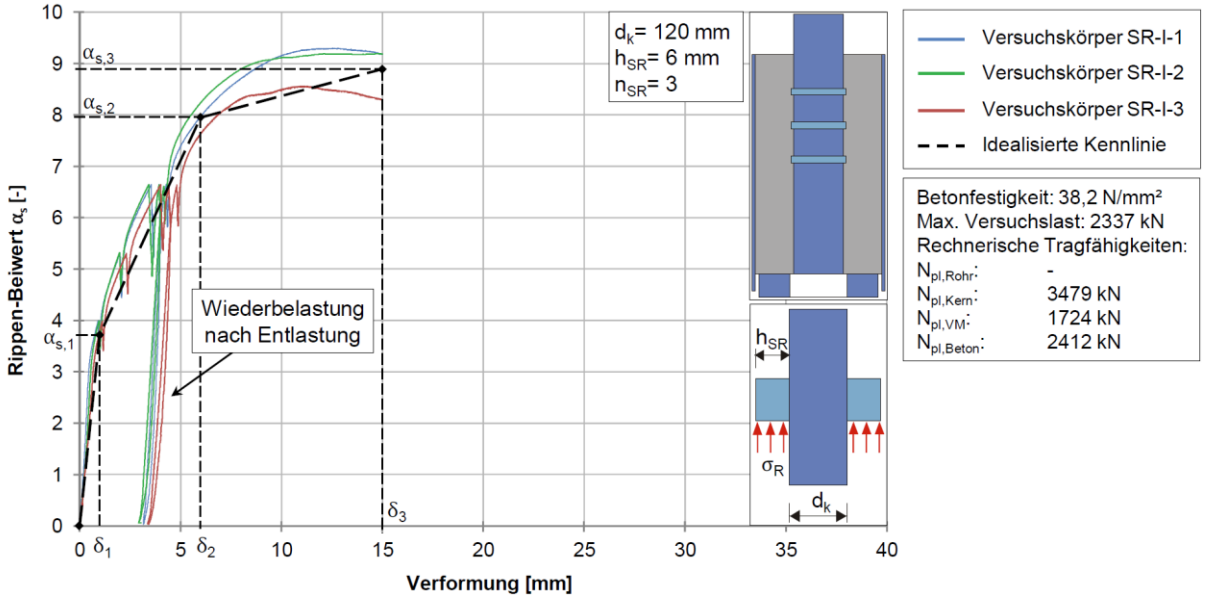


Fig. 3.158. Push-out test of the shear rib connector in concrete filled tubes with one core. (Source: Chanou [29]).

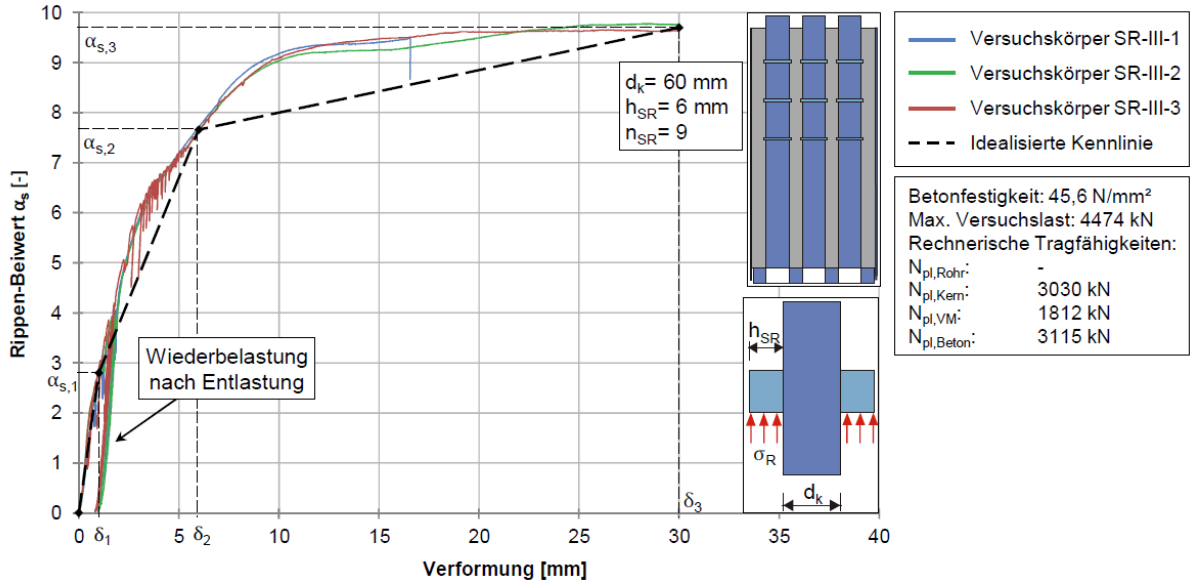


Fig. 3.159. Push-out test of the shear rib connector in concrete filled tubes with three cores. (Source: Chanou [29]).

The obtained test results from column compression tests are shown in Fig. 3.160, where the load-lateral displacement curves are given. It can be observed that the non-linear behaviour of columns can be observed very late, with loads corresponding to the ultimate load. After the tests, the external steel tubes were removed and the concrete cracking and crushing zones were identified. A typical bending failure of the Euler-Bernoulli beam has been observed with transversal cracks on the tensioned side and diagonal cracks with spalled concrete on the compression side. The analysis of the strains recorded in the external steel tube and internal steel cores reveals nearly linear distribution in the specimens with shear connectors. In the specimen without shear connectors, a divergence between strains in different steel parts can be observed, especially in the zones close to the load introduction, see Fig. 3.161.

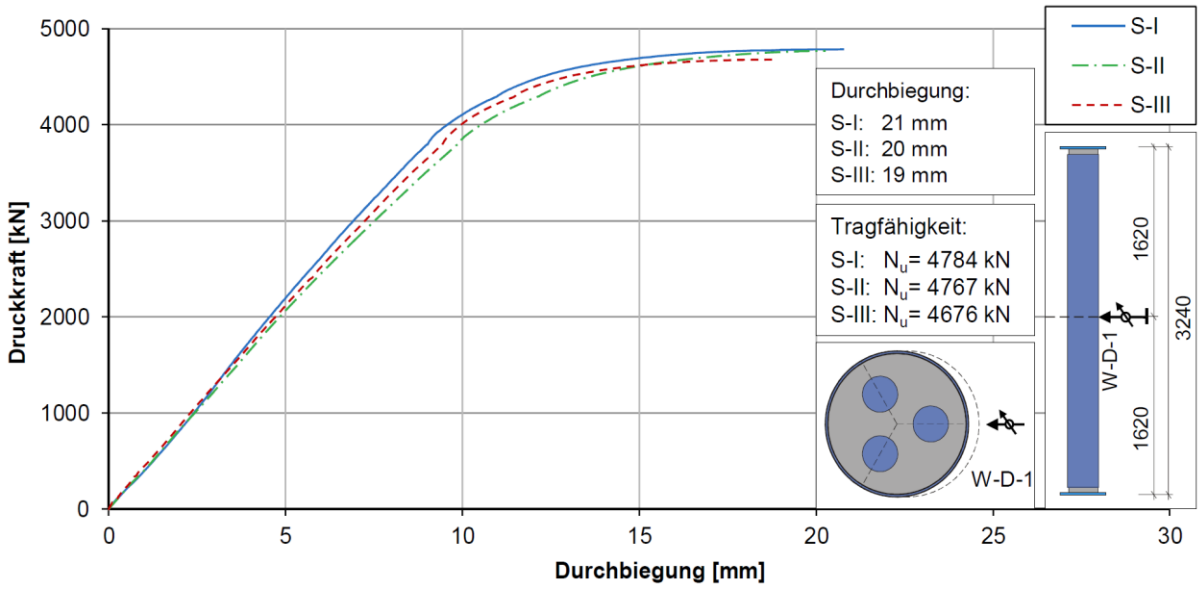


Fig. 3.160. Load-lateral displacement curves of the tested concrete filled tubes with three steel cores. (Source: Chanou [29]).

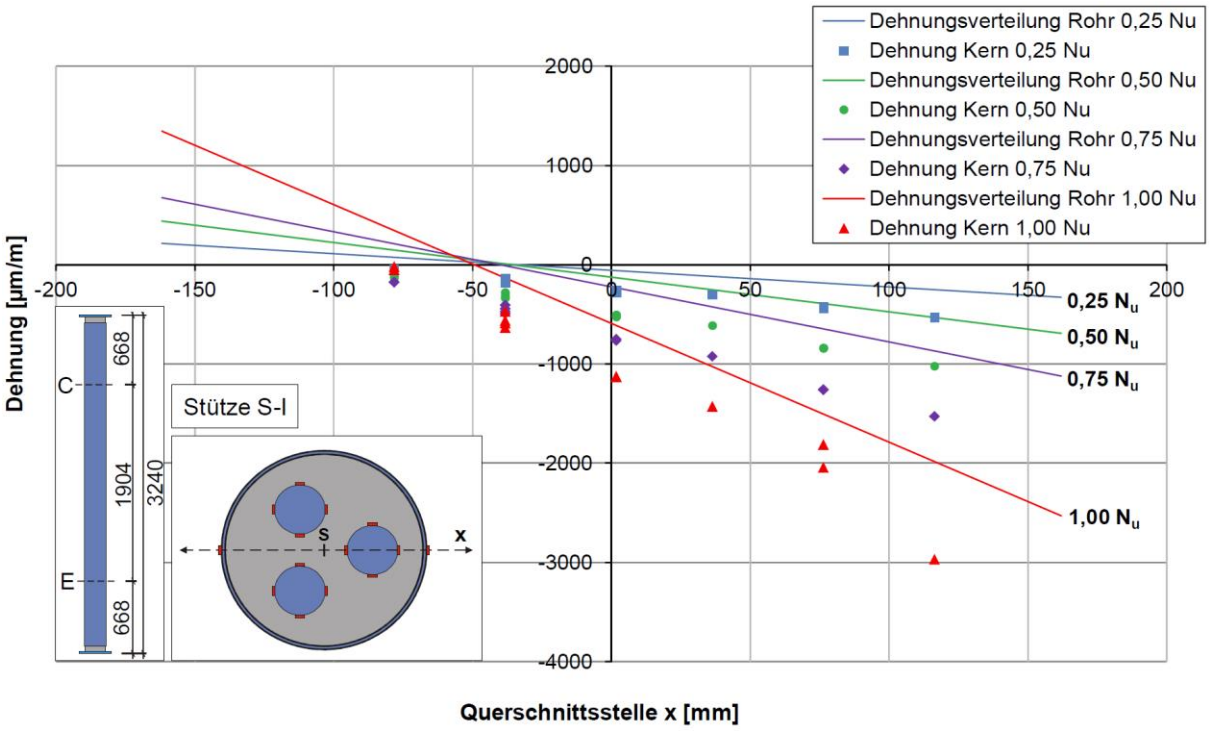


Fig. 3.161. Strain distribution at the end of the concrete filled steel tube specimen with three internal steel cores and without mechanical shear connectors. (Source: Chanou [29]).

Based on the recorded strains in cross-section localised in the middle of the specimen, the section curvature had been analysed and compiled with the resulting bending moment. Finally, a relation of the stiffness change over the increasing load level had been obtained according to the principle relation between the curvature and bending moment as shown in Fig. 3.162.

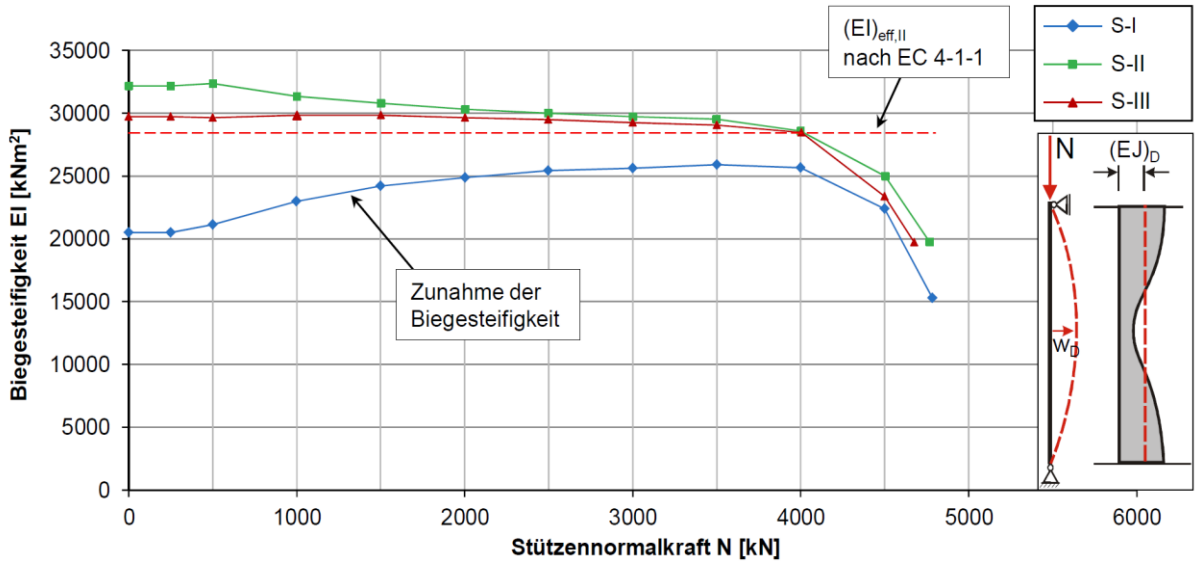


Fig. 3.162. Change of the flexural stiffness of concrete filled steel tube column specimens with three internal steel cores. (Source: Chanou [29]).

According to the obtained results from tests, the numerical models were developed and calibrated. This allowed for the extensive parametric studies considering different geometries of the cross-section of a column with varied number and arrangement of the steel cores. The considered geometrical variants

are shown in Fig. 3.163. For each variant, the N-M interaction curves obtained with plastic method and exact fibre method had been analysed. Moreover, the buckling behaviour of the considered cases were analysed and compared to the procedures given in EN 1994-1-1 [58]. In the result, equations for the plastic bending moment capacity reduction factors α_M had been derived with reference to the acting normal load. The derived equations are given in Eq. 3.135-3.136, where the visualised change in reference to the EN 1994-1-1 [58] is shown in Fig. 3.164.

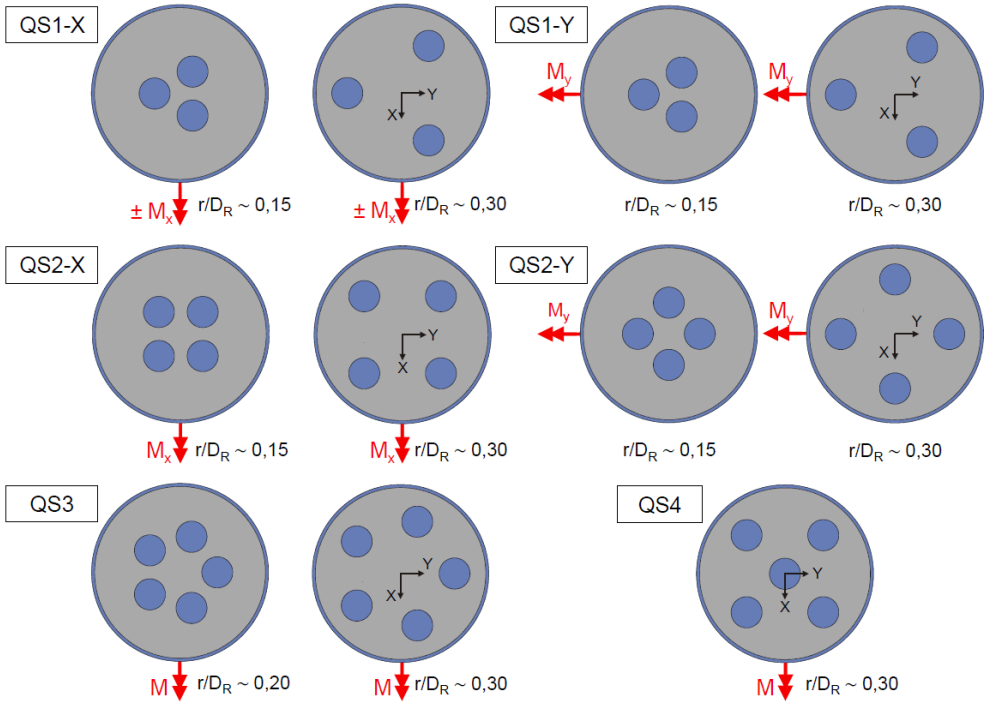


Fig. 3.163. Geometrical variants used for the parametric studies performed by Chanou on concrete filled composite columns with multiple internal steel cores. (Source: Chanou [29]).

$$\alpha_M(N_{Ed}) = 0.90 - 0.20\frac{N_{Ed}}{N_{pl,Rd}} \qquad \text{for} \qquad \frac{N_{Ed}}{N_{pl,Rd}} \leq 0.50 \tag{3.135}$$

$$\alpha_M(N_{Ed}) = 1.20 - 0.80\frac{N_{Ed}}{N_{pl,Rd}} \qquad \text{for} \qquad \frac{N_{Ed}}{N_{pl,Rd}} > 0.50 \tag{3.136}$$

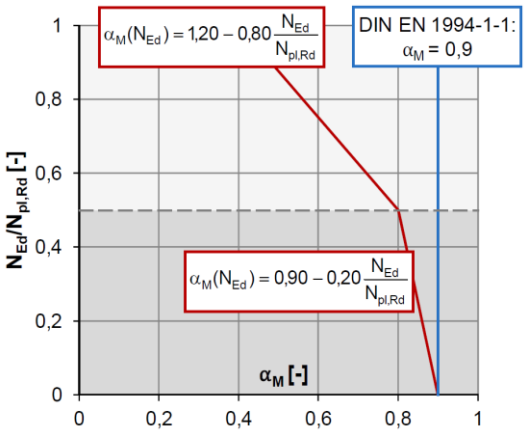


Fig. 3.164. Modification of the plastic bending moment resistance due to the corresponding axial load. (Source: Chanou [29]).

According to the performed buckling analysis with the usage of the European buckling curves given in EN 1993-1-1 [55], a modification to the equation for the effective bending stiffness used for the analysis of second-order given in EN 1994-1-1 [58] was proposed. It was observed that due to the interaction of bending moment and axial load acting on an eccentricity, a reduction of the stiffness should be implemented in the form of a reduction factor as given in Eq. 3.138. The value of reduction factor k_B had been calibrated based on the statistical evaluation and can be defined as given in Eq. 3.139. Alternatively, the reduction factor can be taken with reference to the predefined values of eccentricity and ratio of acting bending moments as shown in Fig. 3.165-3.166. If no bending moments at the column member ends are acting, then the reduction factor $k_B = 1.0$.

$$(EI)_{eff,II} = 0.9(E_a I_a + 0.5E_{cm} I_c) \tag{3.137}$$

$$(EI)_{II,mod} = k_B \cdot (EI)_{eff,II} \tag{3.138}$$

$$k_B\left(\psi, \frac{e_0}{D_R}\right) = 1 - \frac{1}{20} \cdot \frac{e_0}{D_R} \cdot (4 + 3\psi - \psi^2) \tag{3.139}$$

$$e_0 = M_{Ed}/N_{Ed} \tag{3.140}$$

Beiwert k_B		Bezogene Randexzentrizität e_0/D_R		
		0,0	0,5	1,0
$\psi = \frac{M_A}{M_B}$	-1,0	1,0*	1,0	1,0
	0,0		0,9	0,8
	1,0		0,8	0,7

Fig. 3.165. Reduction factor k_B for the effective bending stiffness used for the second-order analysis according to Chanou. (Source: Chanou [29]).

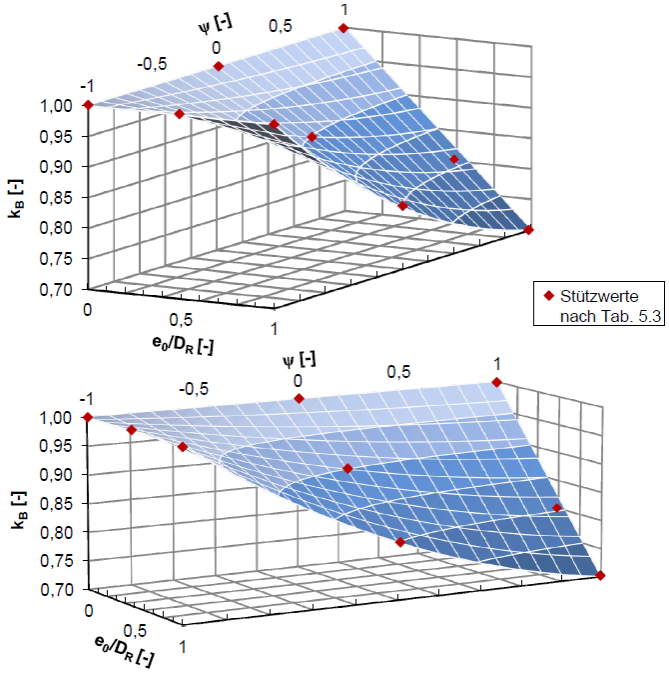


Fig. 3.166. Distribution of the reduction factor k_B proposed by Chanou in the function of eccentricity and boundary bending moment ratio. (Source: Chanou [29]).

4. Motivation and Objectives

In the previous chapters, the general description of the conducted research and the current level of knowledge in the topic of steel-concrete composite action, shear transfer, design of the composite columns and composite columns with multiple encased steel profiles are given. In the described state-of-the-art in Chapter 3, a gap in the knowledge can be identified in the domain of heavy steel-concrete composite columns with multiple encased steel profiles, where the steel profiles are not directly interconnected. These columns are out of the scope of available design codes and a limited literature is available, which deals with their structural behaviour. In the identified research projects dealing with composite columns and shear walls with more than one embedded steel profile, see Section 3.5, the approach, which considers fully Euler-Bernoulli beam model, is commonly applied. Due to a significant own flexural stiffness of embedded heavy steel profiles and significance of the shear forces on the member deformation, the fundamental assumptions of the Euler-Bernoulli beam model seems to be harmed and the resultant effective stiffness is normally overestimated. In the RFCS project SmartCoCo [175], a proposal was given to analyse the distribution of shear forces based on the Mörsch truss model, however, the member stiffness was considered in a common way by applying Euler-Bernoulli beam model with only modified stiffness reduction factors.

Besides the identified variety of mechanical shear connectors given in Section 3.3.4, a common practice is to use the shear studs in order to ensure the longitudinal shear transfer between the steel profiles and the concrete in contact. Shear studs brings a good performance in terms of ductility, load-bearing capacity and provide the same performance in any direction, where their application process is relatively fast. However, considering the scale of heavy composite columns with multiple encased steel profiles, either the shear studs have to be scaled accordingly, which would result in a much more difficult and expensive welding process, either a big number of smaller studs is required. In both scenarios, the protruding shear studs out from the steel profiles are consuming big amount of space in the composite cross-section and make the column erection process, as well as handling of heavy steel profiles on a building site, much more difficult. Besides, in some cases, shear studs are required to be welded during the construction process and after the assembly of a steel profile. Finally, the entire process of application of shear connectors become even more difficult and expensive.

In the conducted research, an analogy in the behaviour of composite columns with multiple encased steel profiles has been identified to the Vierendeel truss system. This observation allowed deriving a working hypothesis of the dissertation about the transition of mechanical engineering model from the typical Euler-Bernoulli beam model towards the innovative model consisting of the Vierendeel truss model embedded into the Timoshenko beam model. This innovative approach allows including shear deformation of a column related to the internal forces transfer between the stiff embedded steel profiles through the relatively weaker concrete and final application of a simple beam model for the global

description of the structural behaviour. The utilisation of a beam model allows for a possibility of application into the currently available design provisions. In addition, the conducted research is dealing with the development of an efficient and novel type of flat mechanical shear connectors dedicated to fully embedded composite columns, which is applicable to heavy steel profiles used normally in columns with multiple encased steel profiles. The developed new type of mechanical shear connectors should provide a solid alternative for the common practice and brings a potential for a fully automatized application process. Moreover, the utilisation of the shear connectors in a composite cross-section should be optimised in order to allow for easy arrangement of the reinforcement bars.

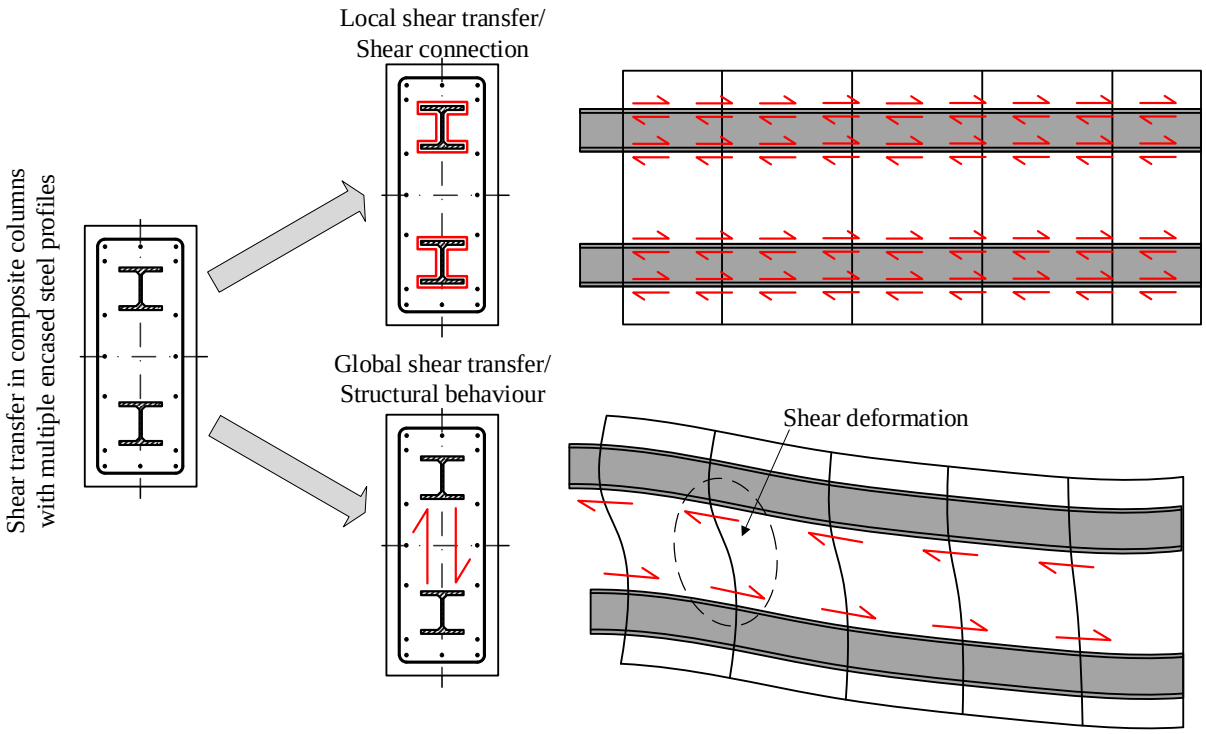


Fig. 4.1. Aspects of the shear transfer in heavy steel-concrete composite columns with multiple encased steel profiles considered for the improvement in the scope of the dissertation.

The described-above two aspects bring a novel approach to the current practice for heavy steel-concrete composite columns and are inherent with the general term of shear transfer, where the shear connection is dealing with local shear transfer at the steel-concrete interface and the structural behaviour is related to the global shear transfer within a column member. This dissertation deals with the shear transfer in heavy steel-concrete composite columns with multiple encased steel profiles and both identified fields of novelty are considered. In Fig. 4.1, the schematic visual representation of objectives for the conducted research is given. The taken investigations are based on experimental and numerical campaigns. As an outcome, analytical models for the resistances of the novel flat shear connectors and for the new effective bending stiffness of a composite columns with multiple encased steel profiles are given. The Luxembourgish National Research Fund (FNR) within the scope of AFR-PPP PhD Grant funds the conducted research and the working plan, as well as all objectives, were defined in the grant proposal with the Reference Number 11283614.

5. Local Shear Transfer at the Steel-Concrete Interface – Development and Characterisation of a Novel Type of Flat Mechanical Shear Connectors

The idea and impact of composite action on composite structures in steel and concrete is explained in Section 3.1. The assured shear connection at the steel-concrete interface allows for activation of both materials in the simultaneous force transfer, which leads to an increased performance. The most beneficial combination of shear connection properties consist of a high stiffness, high load-bearing capacity and a ductile failure behaviour. The ductility of the shear connection allows to include the simplified assumption about the plastic stress block distribution in the cross-section in the design process. EN 1994-1-1 [58] defines the ductility requirement limit as 6 mm. A brittle failure of the shear connection, like for example rupture of the connector, is the most unfavourable failure pattern.

Shear connection at the steel-concrete interface is realised by three phenomena: (i) adhesion, (ii) friction and (iii) mechanical connection. All three force-transfer mechanism are acting simultaneously and they contribute to the overall performance of the shear connection. By knowing the contribution of adhesion and friction parts, it is possible to evaluate the contribution of the pure mechanical connection part. The combination of adhesive and frictional mechanisms can be defined as steel-concrete bond. In the result, the shear connection at the steel-concrete interface is assured by two means: (1) bond and (2) mechanical connectors. In the common practice, for the push-out tests of shear connectors, the contribution of steel-concrete bond is often neglected from the consideration in the force transfer mechanism by greasing of the steel profiles. However, as described later in Section 5.3, the strength of bond is very sensitive to specimen conditions and its contribution in push-out tests of shear connectors for fully encased columns is still significant, even for greased profiles.

In Section 3.3.4, various types of mechanical shear connectors are described. The most common solution are headed shear studs, which are welded to the steel profile and embedded in the concrete. The behaviour of headed stud connectors in solid concrete slabs has been comprehensively investigated for example by Lungershausen [115] or Lam et al. 108]. A minor application of shear studs for anchor plates in the reinforcement concrete structures [54] and in chambers of encased steel profiles in composite columns [163] can be also recognised. According to the defined behaviour of the stud connectors, it can be osberved that shear studs require a certain value of relative slip to develop their full strength. Like this, the stiffness of the shear connection is seriously harmed and in the case of high strength concrete, a brittle failure of the stud – shearing of the shank, is the most probable.

Besides the typical application of shear studs for the mechanical shear connection, a minor usage of other types of shear connectors has been identified in Section 3.3.4. Among others, welded stiffeners between the flanges of steel profiles [175], welded channel sections [8], perfobond solution [195] and

bearing plate connectors in filled hollow sections [69] can been distinguished. However, the most of the available solutions on the market have been mainly developed for the composite beams and they are only adapted for the usage in the composite columns. In addition, all the identified shear connectors consumes a big part of cross-sectional area, they often require a big number of connectors and requires a manual application process, which is often related to the complex process.



a) b)

Fig. 5.1. Construction detail of heavy steel-concrete composite columns – a) applied stud shear connectors and b) reinforcement detail. (Source: R. Wong [206].)

Due to the fact that composite columns are mainly used in tall buildings, the replacement of the commonly used shear connectors with a new solution, which has a higher load bearing capacity with a simultaneously smaller size, provides the potential for fully automatic fabrication process and easier building erection process would be highly beneficial. This criterion is significant especially for high-rise buildings, where heavy composite columns with multiple encased steel profiles are implemented. In Fig. 5.1, construction details of discussed heavy steel-concrete composite columns are shown, where a scale of the problem in the current practice can be recognised. In Fig. 5.1a, it can be observed that due to the required shear connection, the entire surfaces of the visible steel profiles of a column are covered with stud connectors. Moreover, in Fig. 5.1b, it can be observed that a big amount of reinforcement is required for composite columns used in high-rise buildings, therefore, the space-consuming stud connectors protruding out from surfaces of steel profiles are not in favour. In addition, taking into account handling of the profiles at the building site, required working time to weld all the stud connectors, trained workers to do the work, a strong improvement need is revealed.

To satisfy the identified need for the improvement of shear connection in steel-concrete composite columns, especially in heavy columns with multiple encased steel profiles, a novel and efficient type of flat shear connectors has been proposed. The proposed solution consists of embossments introduced to the flanges of steel profiles under a specific arrangement. The development and characterisation processes of the proposed connectors are described in the further parts of this chapter.

5.1. General considerations

In the taken investigation, the development phase and the characterisation phase of a novel type of flat mechanical shear connectors are described as shown in Fig. 5.2. The main criteria in the development process were to introduce a new solution with a high load-bearing capacity, a high initial stiffness and a sufficient ductility. Moreover, the solution should be economic, feasible to typical composite columns and in the same time feasible to heavy jumbo steel profiles used in high-rise buildings. An easy-applicability to steel profiles and a potential for fully automatic fabrication process were set as additional assets. A concept of flat mechanical shear connectors in the form of introduced embossments on the flanges of embedded steel profiles has been proposed. The geometry, orientation and arrangement were investigated in a preliminary numerical sensivity study. In the last step in the developments process of a concept, the feasible materials and the fabrication methods were analysed.

After defining the concept, the proposed flat connectors in the form of welded reinforcement bars to the external surfaces of steel profiles under a specific arrangement were tested in the column type push-out tests with centrally embedded steel profiles in wide concrete blocks. The test campaign was supported by the numerical simulations in order to investigate the load-flux and failure sequence. In parallel, the plain steel-concrete bond and reinforcement bar-concrete bond were investigated in order to precisely analyse each contributing load-transferring phenomenon.

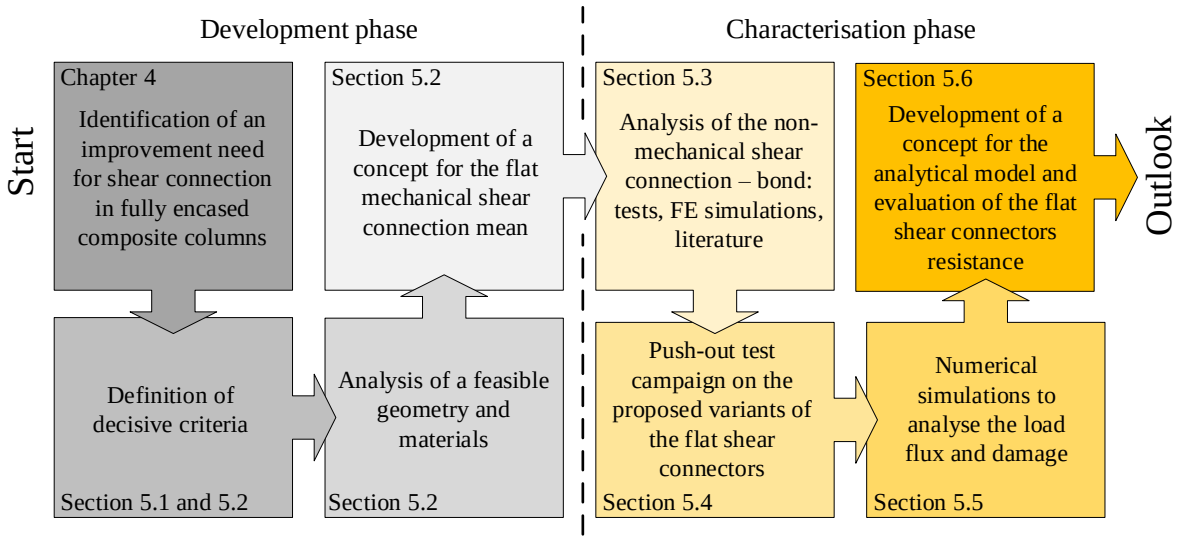


Fig. 5.2. Taken development and characterisation process of a new flat mechanical shear connectors.

In the final stage of the characterisation process, a conceptual analytical model has been derived in order to analytically describe the load transfer and resistance mechanisms of the proposed solution. The proposed analytical model is strictly limited to the tested specimens and based on test values.

5.2. Development of a concept

5.2.1. Analysis of variants for the feasible geometry

In the initial stage, different variants of possible connector geometries were considered and discussed. Among many ideas, where mesh geometries, different kind of plate geometries or custom shape geometries were analysed, an idea of imposing embossments to the steel profiles on the external surfaces of flanges in positive and negative material variants, see Fig. 5.3a, was revealed. A strong criterion in the development process was the possibility for the fully automatized fabrication process, thus, a more complex and protruding shapes were disqualified. The positive variant of connector referred to the added material to the flanges of steel profiles, for example by welding, where the negative variant referred to the subtraction of the material from the base steel profile, for example by cutting. The introduction of embossments to the flanges of steel profile was considered with varied geometry and arrangement parameters as shown in Fig. 5.3b.

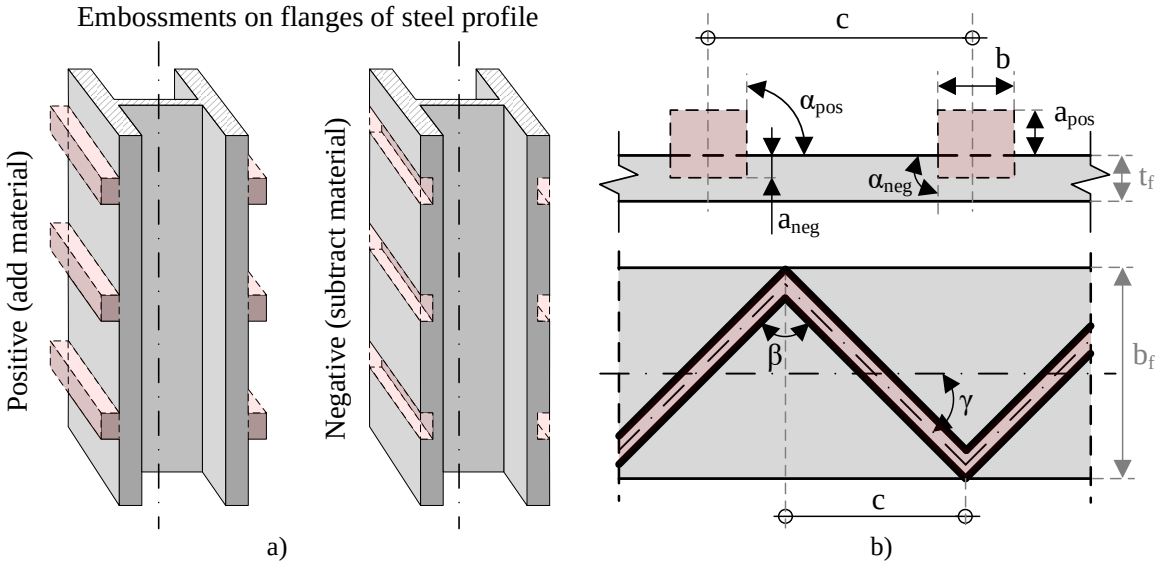


Fig. 5.3. Analysis of the geometrical parameters for the introduced embossments on the flanges of a steel profile – a) concept of introduced embossments and b) considered geometrical parameters.

5.2.2. Defining critical aspects

In addition to the aforementioned main aspects taken into account for the development process of a new type of flat shear connectors, an investigation was taken to identify all crucial aspects that could affect the final shape and performance of the proposed mechanical connectors. The taken investigation is presented in the form of the Ishikawa diagram as shown in Fig. 5.4. The given diagram is also commonly named as "5M+process" diagram, which defines the six main criterions affecting the performance of a product: (i) methods, (ii) machines, (iii) measurements, (iv) materials, (v) manpower and (vi) process. In each of the main criterion, various affecting aspects were considered.

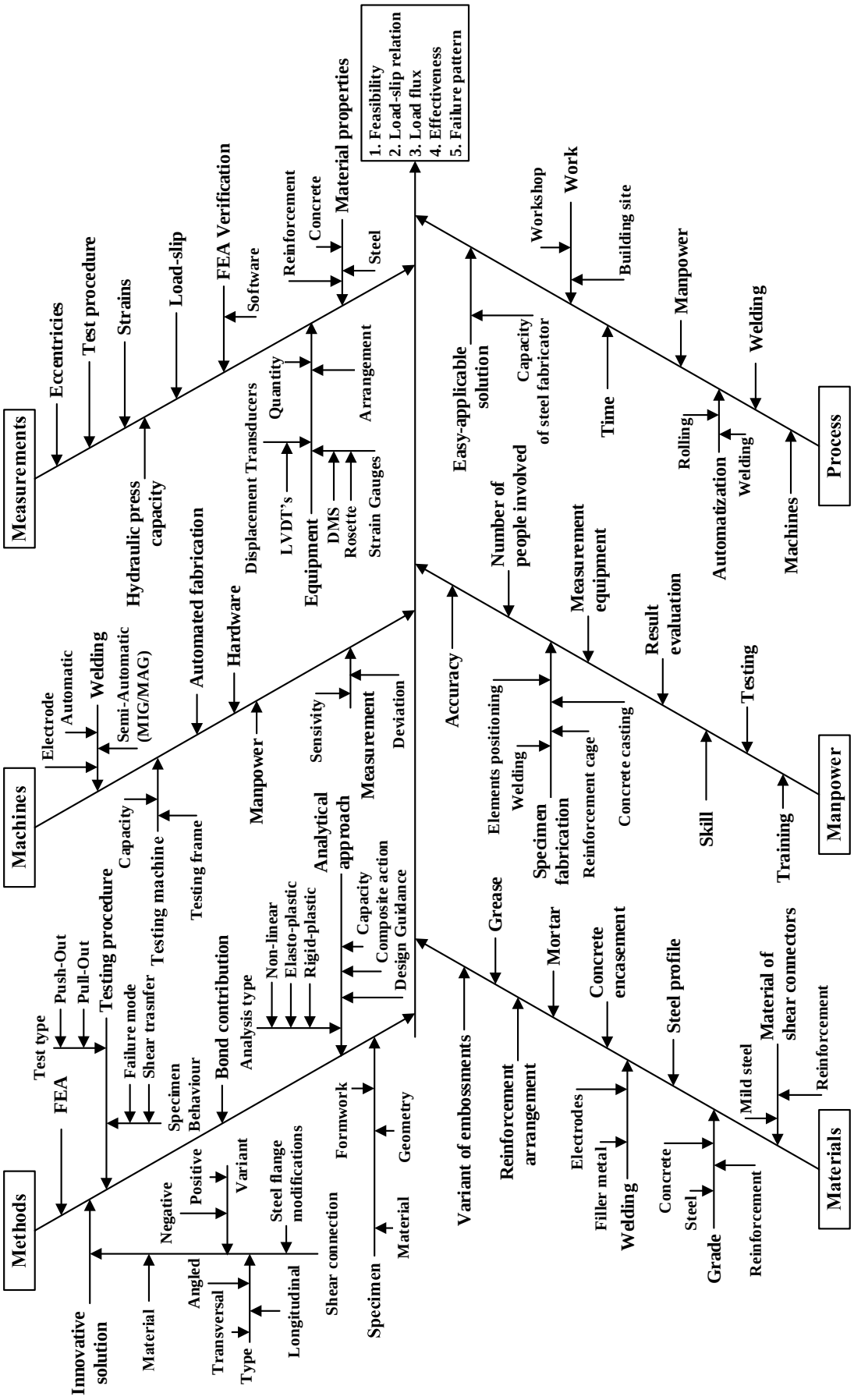


Fig. 5.4. Ishikawa diagram for the development process of new flat mechanical shear connectors.

5.2.3. Identification of a solution

The conducted preliminary study in order to identify the most performing geometry and arrangement of the introduced embossments on the flanges of steel profiles was done by using FE code Abaqus [174]. The created numerical models consisted in nominally identical and very simple geometry of a steel flange and respective concrete encasement as shown in Fig. 5.5, where an example with transversally placed embossments is given. In the performed simulations, only the arrangement and geometry of the embossments changed and the geometry of steel flange and concrete stayed the same. A geometry of the modelled steel flanges refers to the flange of HD400 steel profile, where it thickness is 40 mm. The length of the specimens was set to 1540mm, which allowed for a free arrangement of different geometrical variants of embossments. The concrete encasement had the corresponding dimensions to the steel flange part. The thickness of the encasement was set to 70 mm, which corresponds to the minimum required concrete cover by EN1994-1-1:2004 [58] for fully embedded HD400 steel profiles.

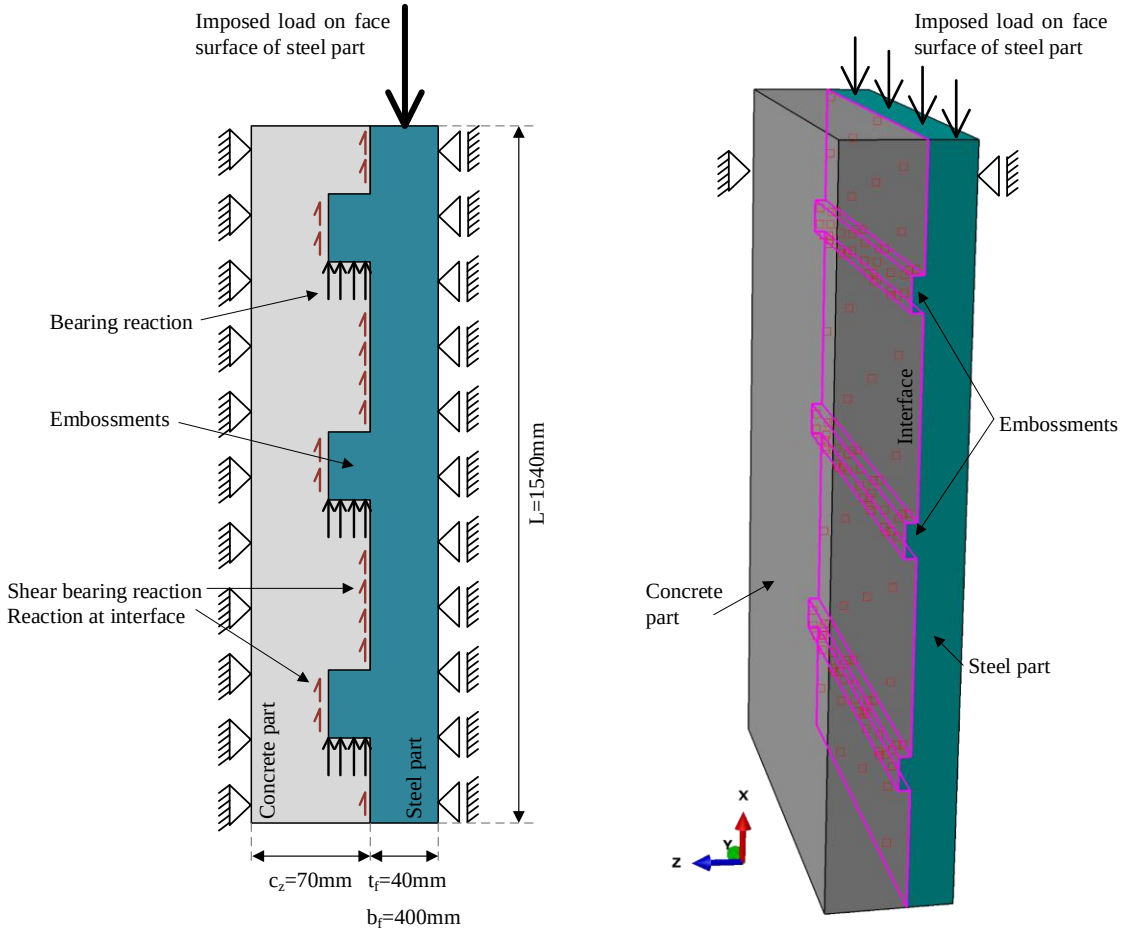


Fig. 5.5. Layout for the preliminary FE simulations with an example of transversally placed embossments – a) scheme and b) FE model.

Each of the modelled parts were discretised with 8-node brick finite elements C3D8R with the mesh size of approximately 10 mm, where in the zone of embossments the mesh was refined to 5 mm. The both applied material laws for steel and concrete parts consisted of a simplified linear elasto-plastic

material law, where the input values were based on the normative values for the steel grade S460 and for the concrete grade C50/60 respectively. These strongly simplified conditions were taken in order to fast and efficiently compare different geometrical arrangements of introduced embossments between each other, without reference to the external results.

The applied boundary conditions consisted in entirely fixed top surface of the concrete encasement and only released movement in the longitudinal direction for the bottom surface of the steel flange, see Fig. 5.5. The interaction between two materials was defined as the standard surface-to-surface contact formulation including pressure-overclosure relation defined as “hard contact” and tangential behaviour with defined small friction ratio of 0.05 to reduce its impact on the results. The relative movement of two parts was imposed as the uniformly distributed displacement of the face surface of steel part. For the analysis, the Abaqus/Standard solver was used.

The summary of the analysed models with varied parameters is given in Annex A. The varied parameter values are corresponding to the parameters defined in Fig. 5.5. The naming of the models considers the following pattern: FT – flange tests (series name), p/n – positive/negative variant of the embossments, following numbers 1/2/3 for positive and respectively 4/5/6 for negative variants refer to the major orientation of the embossments, where 1/4 – transversal orientation, 2/5 – longitudinal orientation and 3/6 – angled orientation. At the end of the names, respective sub-series symbols are given, where the geometrical parameters were varied between the subsequent sub-series.

In general, each negative variant of the introduced embossments showed a slightly smaller load-bearing capacity in comparison to the corresponding positive variants. Moreover, a high concentration of shear stresses in the concrete teeth, as shown in an example given in Fig. 5.6, was identified. These observations lead to the conclusion that the positive variants of embossments brings a better performance and less vulnerability for brittle shearing damage. In the result, a preselection was made that the negative variants of embossments are disqualified from the further analysis and the focus was placed in the positive variants of embossments.

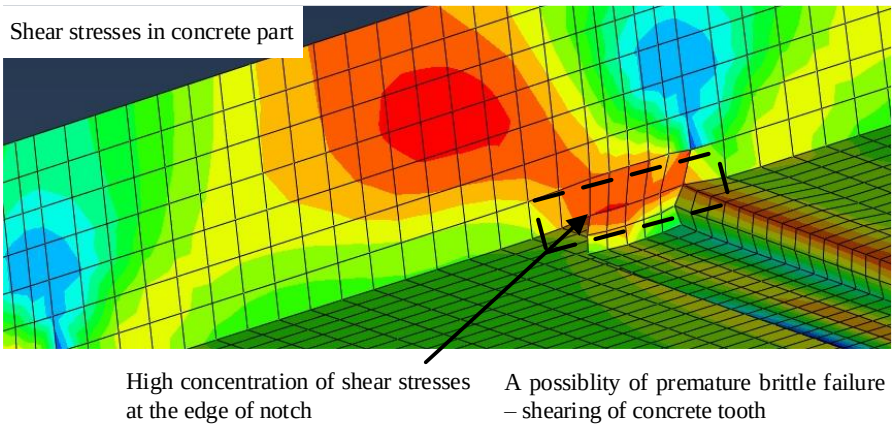


Fig. 5.6. A high concentration of shear stresses at notches in negative embossment variants.

Table 5.1.
Judging table with considered parameters for the development of the geometrical concept of flat shear connectors.

Specimen		Criteria, judgement scale: best (+++)(++)(+)(0)(-)(--)(---) worse								
Variant	Name	Load bearing capacity	Welding complexity	Material usage	Automated fabrication	Concrete cover	Space for rebars	Initial stiffness	Evaluation complexity	Judgement sum
Transversal – γ=90° positive embossment	**FTp1v1a**	**(+++)**	**(+)**	**(+++)**	**(++)**	**(+)**	**(++)**	**(++)**	**(++)**	**+16**
	FTp1v2	(++)	(++)	(++)	(+)	(+)	(++)	(+)	(+)	+12
	FTp1v3	(+++)	(+)	(0)	(++)	(0)	(++)	(++)	(++)	+12
	FTp1v3a	(+++)	(+)	(--)	(++)	(0)	(+)	(++)	(++)	+9
	FTp1v3b	(++)	(+)	(+++)	(+)	(-)	(+++)	(++)	(++)	+13
	FTp1v5	(++)	(+)	(+++)	(++)	(+)	(++)	(++)	(++)	+15
	FTp1v5a	(+++)	(0)	(---)	(+)	(-)	(+)	(+++)	(0)	+4
	FTp1v5b	(++)	(-)	(+++)	(-)	(-)	(++)	(++)	(0)	+6
Longitudinal – γ=0° positive embossment	**FTp2**	**(-)**	**(++)**	**(+)**	**(++)**	**(+)**	**(+)**	**(--)**	**(+++)**	**+7**
	FTp2v1a	(0)	(++)	(++)	(+++)	(0)	(+)	(-)	(-)	+6
	FTp2v2	(0)	(++)	(++)	(++)	(+)	(+)	(-)	(-)	+6
	FTp2v2a	(0)	(++)	(++)	(+)	(+)	(+)	(-)	(-)	+4
	FTp2v3	(0)	(++)	(0)	(+++)	(0)	(+)	(-)	(-)	+4
	FTp2v3a	(0)	(++)	(--)	(+++)	(0)	(0)	(-)	(-)	+1
	FTp2v4	(0)	(++)	(0)	(+++)	(0)	(+)	(-)	(-)	+4
	FTp2v4a	(0)	(++)	(-)	(+++)	(0)	(+)	(-)	(-)	+3
	FTp2v5	(0)	(+)	(0)	(+)	(0)	(+)	(-)	(-)	+1
	FTp2v5a	(0)	(+)	(0)	(+)	(-)	(+)	(-)	(-)	0
	FTp2v5b	(0)	(0)	(+)	(+)	(0)	(+)	(-)	(-)	+1
Angled – γ=45°/60° positive embossment	**FTp3**	**(+)**	**(+)**	**(++)**	**(++)**	**(0)**	**(+)**	**(+)**	**(0)**	**+8**
	FTp3v2	(+)	(+)	(++)	(+)	(+)	(+)	(0)	(-)	+6
	FTp3v3	(++)	(0)	(+)	(++)	(0)	(+)	(+)	(0)	+7
	FTp3v3a	(++)	(0)	(-)	(++)	(0)	(0)	(++)	(0)	+5
	FTp3v4	(+)	(0)	(+)	(++)	(0)	(+)	(+)	(0)	+6
	FTp3v5	(+)	(-)	(++)	(0)	(--)	(+)	(0)	(-)	0
	FTp3v5a	(++)	(-)	(+)	(+)	(-)	(+)	(++)	(0)	+5
	FTp3v5b	(++)	(--)	(0)	(-)	(---)	(0)	(+)	(-)	-4

The relative judgement of the considered positive variants of embossments was made in the form of a judging table and it is given in Table 5.1. The analysed models were grouped according to the major orientations – transversal γ=90°, longitudinal γ=0° and angled γ=45°/60°. From each group, the best performing and efficient model was selected in accordance to the defined judging criteria. In Fig. 5.7, a comparison of load-slip curves for the best performing solutions is given. To get a better overview, the shown load-slip curves were extended by other well performing solutions from the judging table. The load-slip characteristics of all models are given in Annex A.

The performance of the selected variants of embossments for the application is described in the form of radar diagrams in order to visualise strong and weak points of each as shown in Fig. 5.8. It can be observed that the transversal embossment model FTp1v1a indicated the highest load-bearing capacity from the selected models. The longitudinal embossment model FTp2 showed the poorest performance but due to the easy-applicability and reduced complexity of a solution it was analysed further.

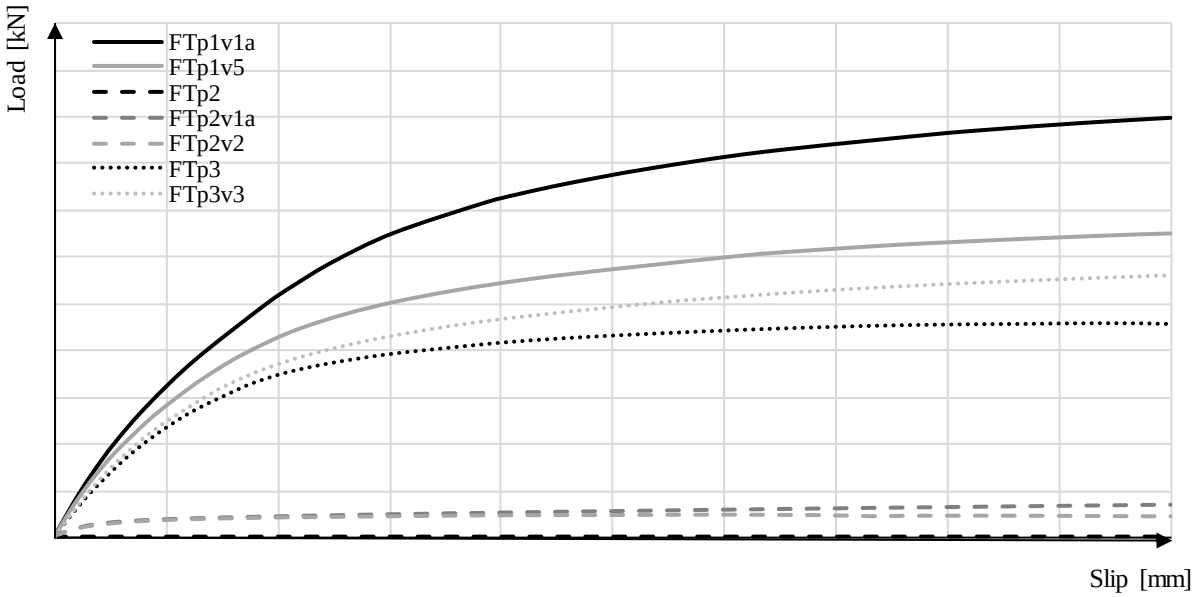


Fig. 5.7. Numerically obtained load-slip curves of flange test models with the highest judgement rate.

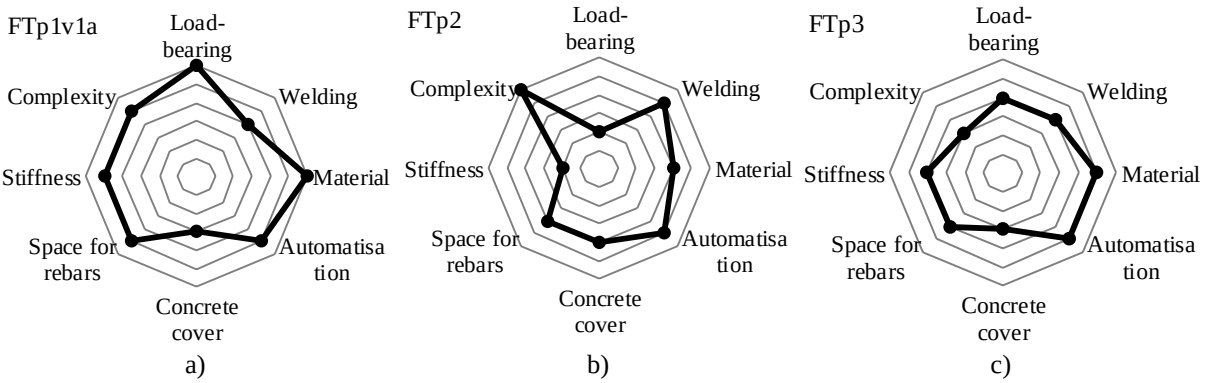


Fig. 5.8. Radar diagrams of three selected variants of embossments considered for the application – a) for model FTp1v1a, b) for model FTp2 and c) for model FTp3.

Based on the conducted investigation, the final layout of the concept for a novel flat mechanical shear connectors consisted of three geometrical variants: (1) transversal with 90° angle between the axes of the connector and steel profile, (2) angled, V-shaped, with 90° angle between the arms of the connector and 45° angle between the axes of arms and steel profile and (3) longitudinal, where axes of connector and steel profile are parallel. The aforementioned three variants were included in the further characterisation process described in the further parts of this chapter, refer to Fig. 5.2.

5.2.4. Detailing the concept

The preliminary geometry and arrangement of the novel type of flat mechanical shear connectors were specified in previous section. A feasible material for the fabrication of the connectors was selected in a second step. Three different material options were taken into consideration as shown in Fig. 5.9: (i) the weld stripe, (ii) the mild steel bar and (iii) the reinforcement bar. Investigation on each material variant and conducted welding tests in the laboratory revealed that production of connectors in the form of weld stripes would require to introduce an enormous amount of energy and heat to the steel profile.

In the result, the material composition of the structural steel would change. Thus, this variant of the material was not considered further. From the conducted welding tests, it was identified that there is no difference in welding of mild steel bars and reinforcement bars to the flat surfaces of flanges of steel profiles. Moreover, a consultation with the welding institute SLV Saarbrucken have not revealed any disadvantage of welding of the reinforcement bars to the steel profiles with reference to the mild steel bars. In the result, in terms of application, both materials – mild steel bars and reinforcement bars, were considered as feasible. Due to reinforcement bar-concrete bond, the reinforcement steel was selected as the feasible material for the characterisation process and test campaign.



a) b) c)

Fig. 5.9. Considered variants of materials for the fabrication of the flat shear connectors – a) weld stripe (source: thefabricator.com [137]), b) plain steel bar and c) reinforcement bar.

In reference to the geometry and arrangement of the new type of flat shear connectors identified in the preliminary parametric study, the final shape and geometry of the flat shear connectors was adapted for the need of laboratory testing. It was decided to test the developed shear connectors in a column-type push-out tests with fully embedded HEB120 steel profiles. Taking into account the selection of the reinforcement steel as the material for the fabrication of flat shear connectors, the exact geometrical ratios from the preliminary parametric study was not able to be respected. In the result, the preliminary study was adapted and reinforcement bars with diameter of Ø8 mm for the transversal and V-shaped variants and with diameter of Ø12 mm for the longitudinal variant were used. The detailed concept of the applied shear connectors to the embedded steel profiles is shown in Fig. 5.10.

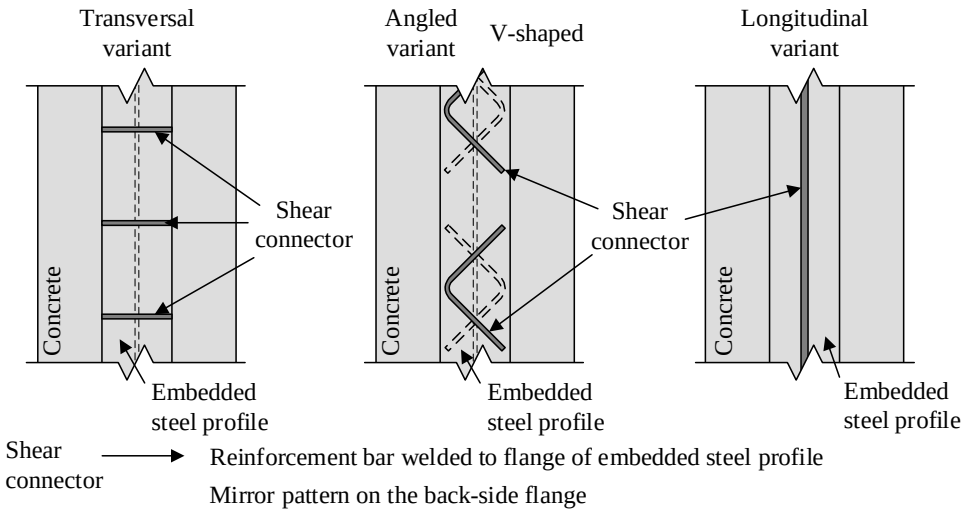


Fig. 5.10. Variants of the novel flat shear connectors selected for the characterisation process.

5.3. Investigation on steel-concrete bond

The characterisation process of the proposed novel type of flat shear connectors consists of experimental and numerical push-out investigations. Simultaneously to the mechanical connection, steel-concrete bond is active in the force transfer mechanism. Therefore, in order to analyse the part of forces transferred by the flat shear connectors, the experimental and numerical analysis of the steel-concrete bond contribution was required. A number of references in the literature can be found for the bond analysis and the literature data is summarised later in Section 5.3.3. A big scatter in the bond strength values can be identified and the relation to the specimen conditions was observed. Based on this, it can be concluded that the steel-concrete bond strength is not a universal value and it is sensitive to many aspects related to the geometry, interface conditions and concrete state of the tested specimens.

In the push-out tests of flat shear connectors, the aim was to analyse the pure mechanical part of the shear connection. In order to obtain the desired output, the contribution of steel-concrete bond was desired to be as small as possible. Clause B.2.3(2) of EN 1994-1-1:2004 [58] states that greasing of steel profiles should be applied in order to prevent the bond at the interface. No specific regulation is given for the greasing products. To understand the variation of bond strength values, the different mechanisms composing the bond phenomenon have to be considered as shown in Fig. 3.22. In order to analyse steel-concrete bond, an individual test campaign on small-scale specimens was considered and two bond-reducing products were applied, a high-performance demoulding oil and Teflon spray. The reasoning for the application of these products was in accordance to the identified force transferring mechanism of steel-concrete bond. An oil product can efficiently reduce the chemical adhesion, where the Teflon coating can prevent the development of frictional forces. In order to identify the best bond-reducing products from the two investigated, both of them were used in the experimental bond campaign described in Section 5.3.1. The individual bond test campaign allowed for the development and calibration of numerical simulations of steel-concrete bond with and without bond reducing products. Like this, the developed numerical model of bond can be later applied in the numerical simulations of novel flat shear connectors. A concise summary of the calibration is described in Section 5.3.2, where more details can be found in Annex B.

5.3.1. Small-scale push-out tests

In order to investigate the behaviour and ultimate strength of steel-concrete bond, small-scale cube push-out tests (SSCPOT) were performed. The test campaign consisted of 9 nominally identical specimens, which were composed from 10x30x150 mm steel bars vertically embedded in 150x150x150 mm concrete cubes. Below the steel bar, a recess was placed to allow for the relative slip so the imposed load was totally transferred through the steel-concrete interface. In the result, the embedded length of the steel bar was set to 100 mm and the height of the recess had 50 mm. The geometry of the SSCPOT

specimens is shown in Fig. 5.11. The applied material grades were S235 for the steel bar and C35/45 for the concrete cube. More details about the SSCPOT tests are given in Annex B.

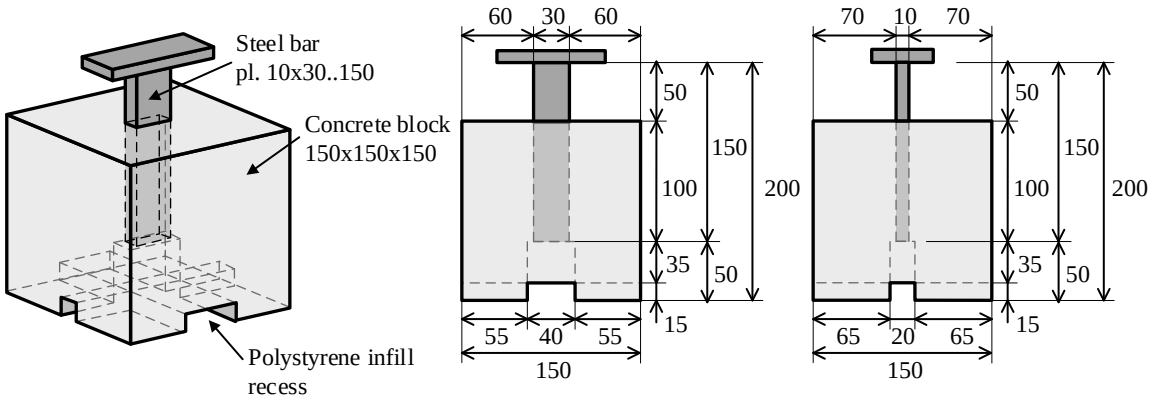


Fig. 5.11. Geometry of the small-scale push-out test specimens for the investigation on bond strength.

Three variants of steel surface treatment were examined: (i) the untreated steel surface, (ii) the steel surface coated with a demoulding oil and (iii) the steel surface coated with a Teflon spray. Each variant of the steel surface treatment consisted of three specimens. A summary of the test specimens is given in Table 5.2. The nominally identical specimens and test layout between each test series resulted in one reference series with the untreated steel surface and two series with investigated bond-reducing products. Like this, an impact of each applied bond-reducing product could be analysed and directly compared to the reference series.

Table 5.2.
Overview of the small-scale push-out test specimens.

Test name	Geo-metry	Sub-num-ber	Concrete part [mm]	Steel part [mm]	Embedded length/ contact area	Surface treatment	No. of tests	Results
PS	Fig. 5.11	-1 -2 -3	Cube: 150x150x150 with 20x40x50 recess at bottom	Steel bar: 10x30x150	100mm/ 80cm^2	Cleaning: No Coating: No	3	Fig. 5.12a mean bond strength 2.65 MPa
G	Fig. 5.11	-1 -2 -3	Cube: 150x150x150 with 20x40x50 recess at bottom	Steel bar: 10x30x150	100mm/ 80cm^2	Cleaning: No Coating: Demoulding oil	3	Fig. 5.12b mean bond strength 0.90 MPa
PTFE	Fig. 5.11	-1 -2 -3	Cube: 150x150x150 with 20x40x50 recess at bottom	Steel bar: 10x30x150	100mm/ 80cm^2	Cleaning: No Coating: PTFE Teflon spray	3	Fig. 5.12c mean bond strength 1.47 MPa

The WETCAST FormFluid HP made by the company Hebau GmbH [136] was used as the demoulding oil, where the applied Teflon spray was the PTFE-Spray from the company KimTec GmbH [135]. The recorded load-slip behaviours for each applied products in the respective test series are presented in Fig. 5.12. In Fig. 5.12d, a comparison diagram, which consists of all experimental curves,

was given in order to directly compare and quantify an impact of the bond reducing products on the bond behaviour in reference to the untreated steel surface specimens. It can be observed that both applied materials reduced the steel-concrete bond strength significantly, however, the reduction level obtained for the specimens coated with the demoulding oil was much higher than in the case of the Teflon spray.

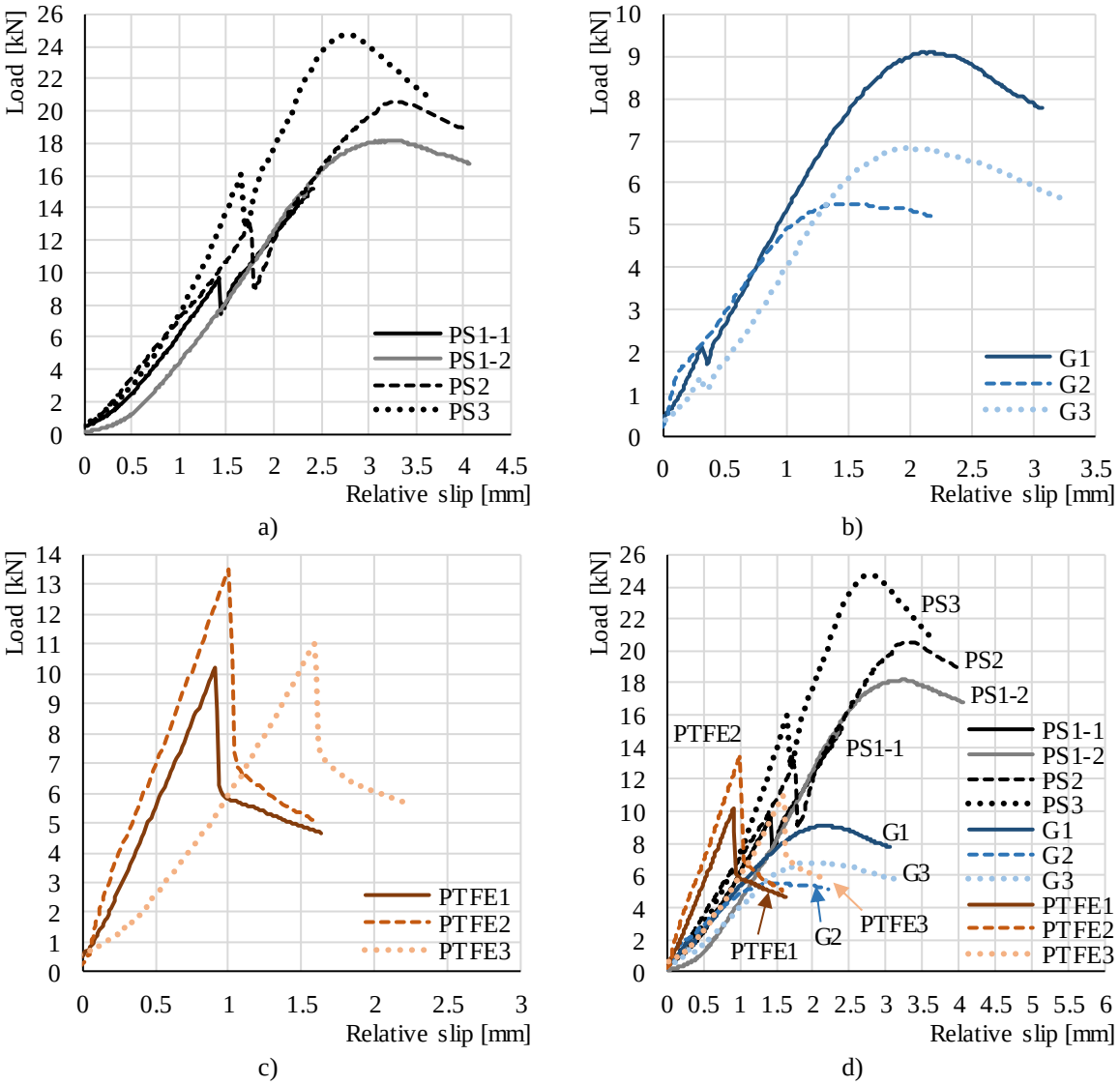


Fig. 5.12. Load-slip curves obtained from the small-scale push-out tests – a) PS series, b) G series, c) PTFE series and d) comparison diagram.

From the diagrams given in Fig. 5.12, it can be observed that at the beginning, the entire force was transferred by the chemical adhesion and later, with the development of a slip higher than 1-1.5 mm, the surface roughness friction and the Coulomb friction were activated. In a normal case condition, the combination of the Coulomb friction mechanisms together with the chemical adhesion contributed to the peak value of the steel-concrete bond strength. The surface roughness friction dominated the overall behaviour of bond at the late stage of the descending branch, where the load dropped gently with progressing slip. The descending and not constant branch of load was related to the partially vanishing pressure developed at the interface, where in the result, the Coulomb friction contribution was reducing.

Comparing the recorded load-slip curves with the series PS shown in Fig. 5.12a, a specific and characteristic behaviour of each bond-reducing product can be identified. From the response shown in Fig. 5.12b for the specimens with demoulding oil, it can be observed that the overall bond behaviour was very similar to the reference series but much weaker and the pure adhesive failure mechanism developed at the slip of only 0.5 mm. This observation clearly proves that the demoulding oil significantly reduced the chemical adhesive intermolecular connection. In the case of recorded response for specimens with Teflon coating shown in Fig. 5.12c, the chemical adhesion mechanism dominated the entire bond behaviour but the amplification of the bond strength due to the Column friction after the adhesive part failure was completely removed. The obtained results shows that the Teflon coating can be efficiently used to eliminate friction, but the smooth surface of the coated steel bar resulted in a much stronger chemical intermolecular connection and finally, the overall bond strength was much higher than for the case, where the demoulding oil was applied. Based on above, the demoulding oil solution was selected to be applied further in the column push-out tests of flat shear connectors.

5.3.2. Numerical simulations

The obtained results from the SSCPOT test campaign described in Section 5.3.1 were used in order to develop and validate a numerical model of steel-concrete bond, which can be later applied to the numerical simulations with flat shear connectors. The numerical simulations were performed with the usage of FE code Abaqus [174] and Abaqus/Standard solver was employed. The geometry and simulation layout were strictly reflecting the test campaign. The steel-concrete bond has been modelled as a standard surface-to-surface contact formulation where normal, tangential, cohesive and damage behaviours were defined. Details of the developed numerical models are given in Annex B. Three numerical models were created and calibrated so they correlate to the test results as shown in Fig. 5.13. The numerical load-slip responses were calibrated to converge with the mean values from the tests.

The obtained results from numerical simulations showed that steel-concrete bond can be numerically reproduced with a good accuracy and with desired stiffness, peak load and failure behaviour. The developed numerical model of bond shown in Fig. 5.13, is a simplified model which did not cover the non-linear damage evolution of bond. For the numerical simulations of flat shear connectors, described in Section 5.5, the model of bond was extended and governed all occurring phenomena.

The behaviour of bond obtained from the numerical simulations is very sensitive to the defined parameters. In the result, the extrapolation of the bond model to specimens with different geometries and conditions is limited and should be verified. The shown methodology how to model bond proves that it can be accurately included in the numerical simulations of push-out tests.

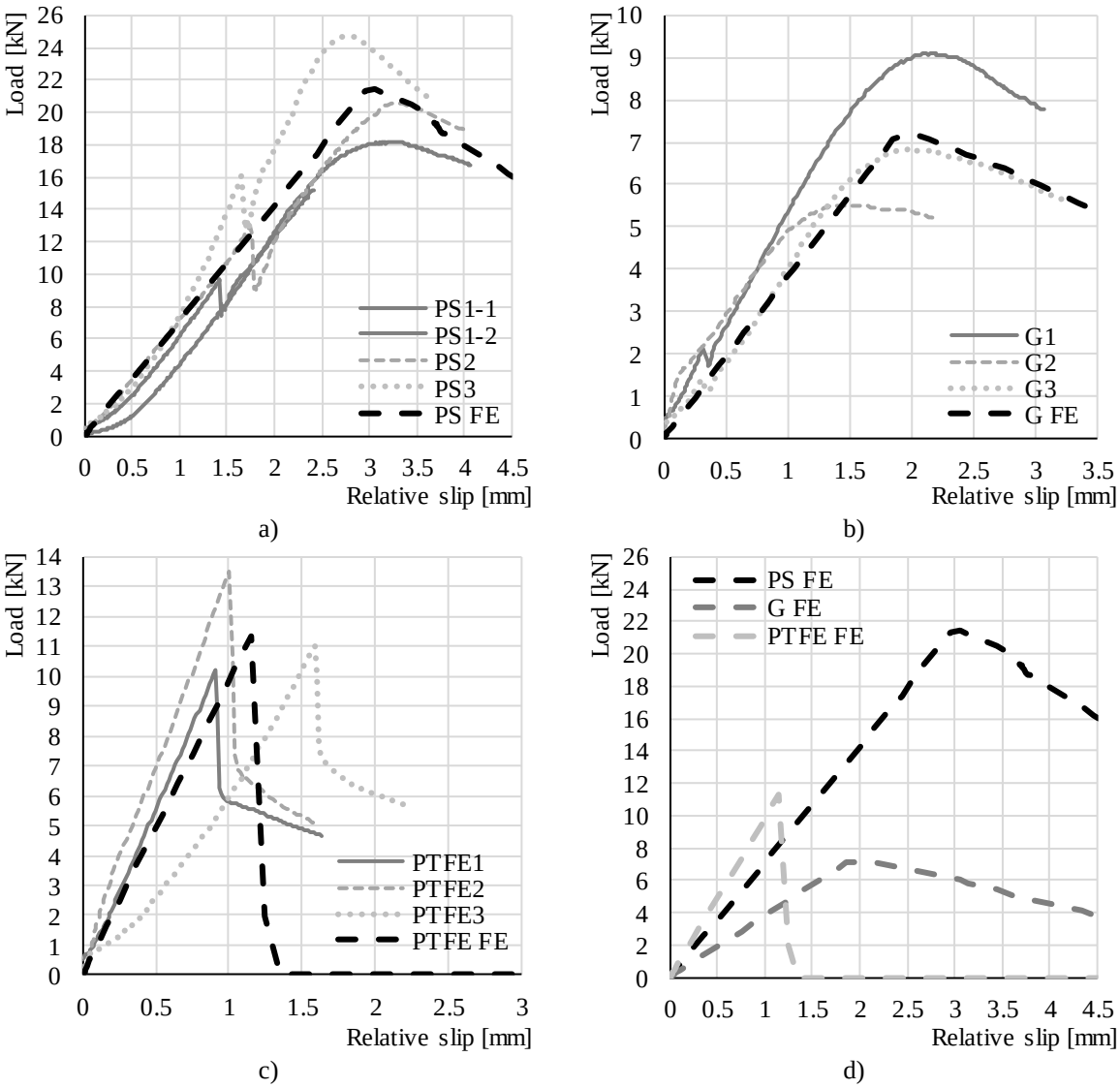


Fig. 5.13. Load-slip curves form the numerical simulations of small-scale cube push-out tests – a) specimen PS, b) specimen G, c) specimen PTFE and d) comparison of numerical responses.

5.3.3. Summary and comparison to the literature data

Besides the tested specimens from the SSCPOT test series described above, steel-concrete bond was tested in a column type of push-out tests - CoPOT series, used for the flat shear connector test campaign, see Section 5.4. One series of tests without any mechanical shear connectors were included in the test campaign as reference tests. In the test campaign, HEB120 steel profiles coated with the demoulding oil were used. The resultant bond strength values for CoPOT series were equal to 0.92 MPa and 0.81 MPa for two nominally identical specimens.

Additional data regarding the bond strength values between steel and concrete and the influence of different parameters on the bond strength can be found in the literature [14, 41, 74, 124, 142, 152, 155, 157, 162, 175, 181, 197, 202, 209, 210]. The data is summarized in Table B.3 in Annex B. Steel-concrete bond is sensitive to various parameters and the bond strength values cannot be directly extrapolated to specimens with different geometries and conditions. The influence of the most important parameters is

discussed below in respective paragraphs. In addition, the identified steel-concrete bond strength values are significant, even for greased surfaces, therefore, its contribution in the force transfer mechanism of shear connectors in push-out tests with fully embedded steel sections cannot be disregarded.

Influence of steel surface treatment

The steel surface treatment has the most critical influence on the steel-concrete bond strength. Specimens with rusted steel surfaces achieved the highest bond strength, see Table B.3, No. 46. Furthermore, specimens with failure scale from the rolling process exhibited higher resistance than specimens with cleaned steel surfaces (sandblasted or paint thinners), see Table B.3, No. 1 and No. 16-19. The poorest resistances were noticed in specimens with "greased" steel surfaces, see Table B.3, No. 2. Paint or Teflon were not as efficient as the greasing process, see Table B.3, No. 3 and No. 47.

Influence of concrete cover

Concrete cover was the parameter with the second-largest impact on the bond strength. A thin concrete cover (approx. 50 mm) and large steel-to-concrete area ratio resulted in bond with a weak shear resistance, see Table B.3, No. 16-32. At the same time, specimens with a thick concrete cover (> 100 mm) and small steel-to-concrete surface ratio reached high bond stress values, see Table B.3, No. 40-45. Concrete shrinkage can have a positive or negative influence on the steel-concrete bond strength depending on the geometry of the specimen (tension or compression orthogonal to the contact surface), see Table B.3, No. 5-12.

Influence of concrete confinement

Concrete confinement affects the frictional behaviour of the steel-concrete bond. The greater the confinement of the concrete, the higher is the shear resistance at the steel-concrete interface, see Table B.3, No. 33-39. A large impact on the resulting bond strength values was observed when a lateral pressure acted on the interface, e.g. transverse reinforcement anchoring tensile forces from compression struts, such as in push-out tests on shear connectors. The existence of transverse reinforcement without imposing a lateral pressure has a minor effect on the steel-concrete bond.

Influence of steel section geometry

The geometry of steel section has an impact on the concrete confinement level and confinement zones, e.g. zones between flanges of H-shaped steel sections or concrete- filled tube specimens. An impact on the bond strength is noticeable. It was observed that the steel-concrete bond strength (stress value) decreases as the scale of the steel profiles used increases, see Table B.3, No. 1-4 and 20-32.

Influence of time

In tests performed by Wium [202] it was observed that the steel-concrete bond was affected by the age of the specimen. The difference between two nominally identical specimens, tested six months apart, resulted in the bond values being reduced by approx. 15 %. This effect should be associated with creep and shrinkage effects, but is not investigated further in this article.

The data summarised in Table B.3 is presented in the form of a scatter diagram in Fig. 5.14a. From the visual representation of the summarised data, it can be observed that no clear tendency for the universal bond strength value can be concluded. The statistical evaluation of the considered database in the form of Gaussian curve shown in Fig. 5.14b indicates that the global mean value oscillates around the value of 1 MPa. However, this value cannot be considered as a general bond strength because in some cases, the bond strength can be much smaller or bigger. In dependency to the considered problem, design or experimental testing, the assumed values could be unfavourable.

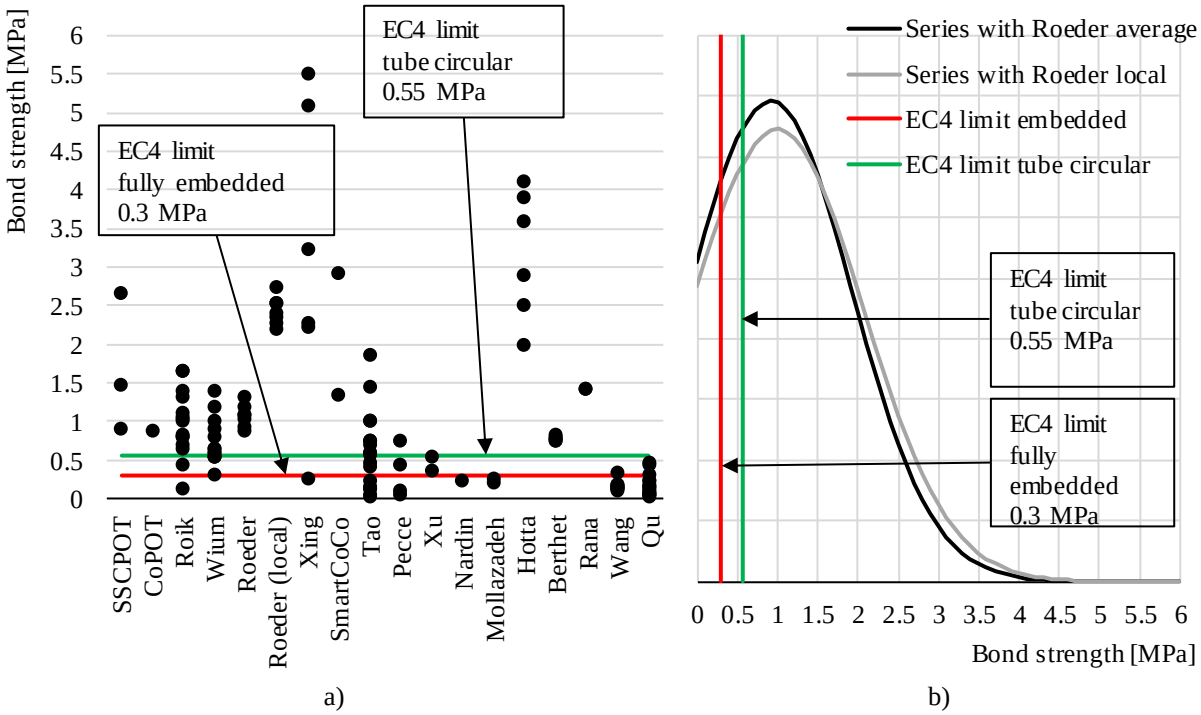


Fig. 5.14. Analysed database of the steel-concrete bond strength – a) scatter diagram and b) Gaussian distribution.

The steel surface treatment has been identified as the most affecting parameter on the steel-concrete bond strength. In order to give an overview on analysed surface treatment conditions a bar diagram is shown in Fig. 5.15. The hatched part with linear pattern refers to the minimum value identified from the analysed database, where the hatched part with dot-pattern gives a range up to the maximum identified value. It can be observed that the untreated steel surface brings the biggest variation of the bond strength value and its value can be very high. In the diagram shown, the maximum value of bond for untreated surface refers to plain bar profile and very thick concrete cover, refer to Xing et al. [209]. Greased or oiled steel surfaces gave the smallest identified bond strength.

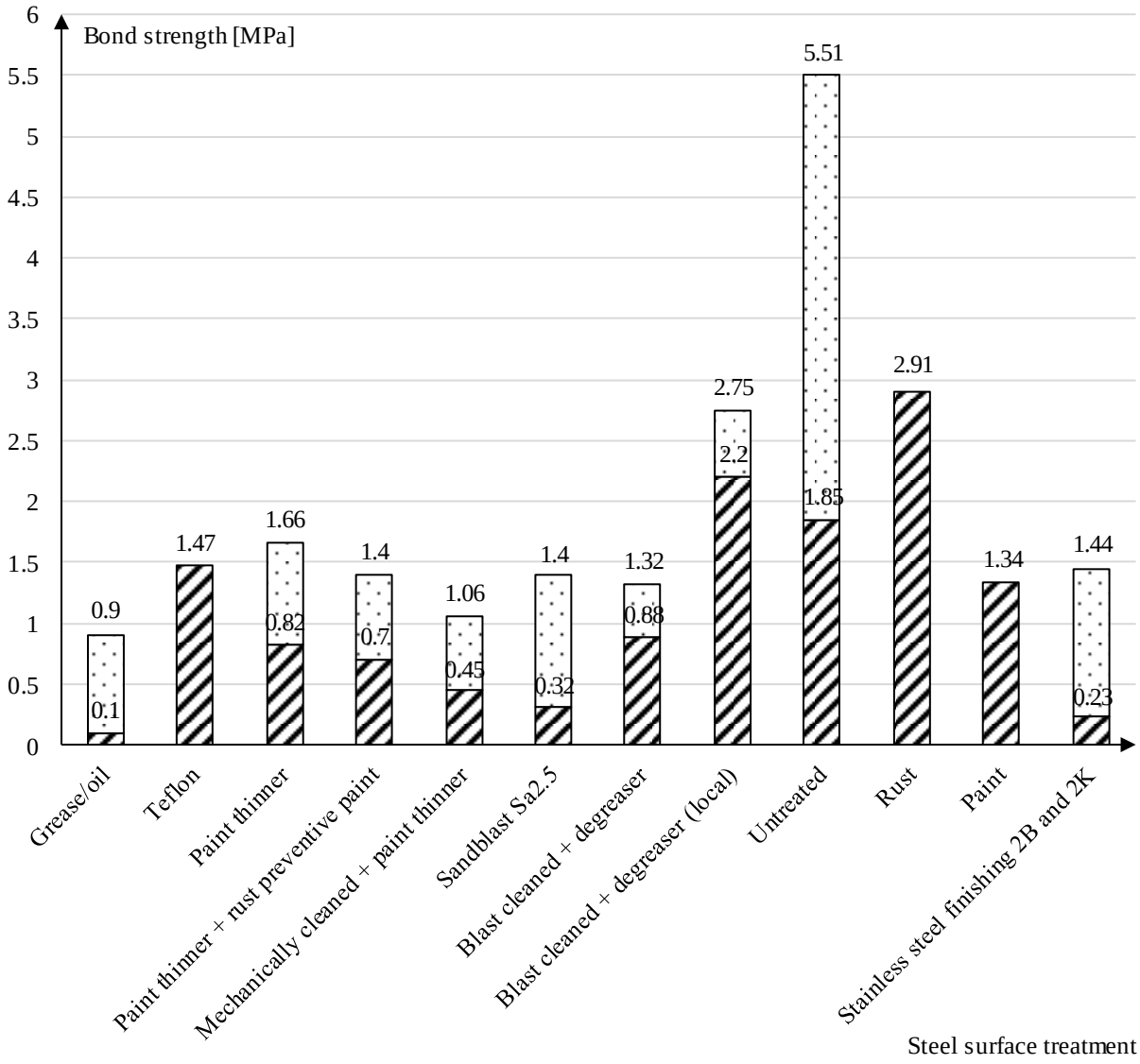


Fig. 5.15. Influence of surface treatment on bond strength.

According to the taken investigation on steel-concrete bond, it can be concluded that its contribution in the steel-concrete push-out tests is significant even for greased surfaces and it cannot be disregarded in the experimental testing of shear connectors for fully embedded steel profiles. The analysis of identified bond strength values indicated a big scatter, therefore, the bond strength cannot be directly extrapolated to different specimen conditions. However, according to the presented analysis a reference source is given. It has been shown that steel-concrete bond can be accurately modelled in the FE numerical simulations with the usage of the software Abaqus and its behaviour can be analysed. During the calibration process of numerical model of bond, a big sensivity of resultant strength to input parameters was identified, thus, the numerical simulations should be referred to test results.

5.4. Push-out test campaign

Concerning the load-slip behaviour of the shear connection in composite columns, not only the load capacity is of importance, but also the stiffness and the sufficient connection ductility. The investigated solutions of novel flat shear connectors are made of regular reinforcement bars, welded to the external surfaces of the flanges of steel profiles (creating embossments) under a specific arrangement as described in Section 5.2. An important necessity in the force transfer mechanism is the existence of a transversal reinforcement cage in the concrete and around the steel profile. The investigation and characterisation of the novel flat mechanical shear connectors is based on composite column type push-out tests (CoPOT) with fully embedded steel profiles and the mechanical bearing action between the connector and concrete together with steel-concrete bond and connector-concrete bond are considered. In the result, a portion of the force transferred by the non-mechanical shear connection can be distinguished and subtracted from the measured resistance of specimens to obtain the load bearing part of the mechanical connection. The investigation done in Section 5.3, shows that the shear resistance of steel-concrete bond in the column type push-out tests is significant and it cannot be neglected even if the steel profiles are greased.

Performed column push-out tests to characterise the developed novel flat shear connectors consisted of three variants – transversal, longitudinal and angled. Reference specimens without applied any mechanical shear connectors and nominally identical geometry were tested simultaneously. Failure patterns of each of the investigated connectors have been revealed. In order to investigate the load flux and precisely identify the failure sequence, numerical simulations in the Finite Element (FE) code Abaqus® [174] supported the test campaign.

5.4.1. Specimen properties

Experimental tests consisted of 11 column push-out tests (CoPOT). In the test campaign, 4 series were distinguished: (i) reference tests (0v2) without any mechanical shear connectors, (ii) transversal variant of the novel flat shear connector (Av2), (iii) angled, V-shaped, variant of the novel flat shear connector (Bv2) and (iv) longitudinal variant of the novel flat shear connector (Cv2), see Fig. 5.16. In each test series, three tests of nominally identical specimen had been performed, where in the reference test series 0v2, only two tests were conducted. The summary and an overview about the test specimens is shown in Table 5.3.

Besides the different connector shapes, all test specimens had nominally identical geometries and production conditions. The geometry of tested specimens referred to the push-out tests from the RFCS project SmartCoCo [175] and consisted of a centrally embedded HEB120 steel profile in a wide concrete block. The consistency between the specimens from two projects complemented results. The size of concrete block allowed for no geometrical restraint of the load flux in the internal force transfer

mechanism. All specimens for the test campaign were produced at the University of Luxembourg. During the fabrication process, the steel profiles surfaces were coated with the anti-adhesive release agent WETCAST FormFluid HP of the Company Hebau GmbH, in order to reduce the bond strength in the force transfer mechanism. The applied bond-reducing product was the same product as in the series G of the SSCPOT test series and detailed investigation about the influence of the applied release agent on steel-concrete bond is described in Section 5.3. No cleaning process of the steel profiles had been applied beforehand and the steel profiles were applied to the specimens in the state as delivered. Shear connectors were excluded from the anti-adhesive cover and cleaned afterward with a degreaser.

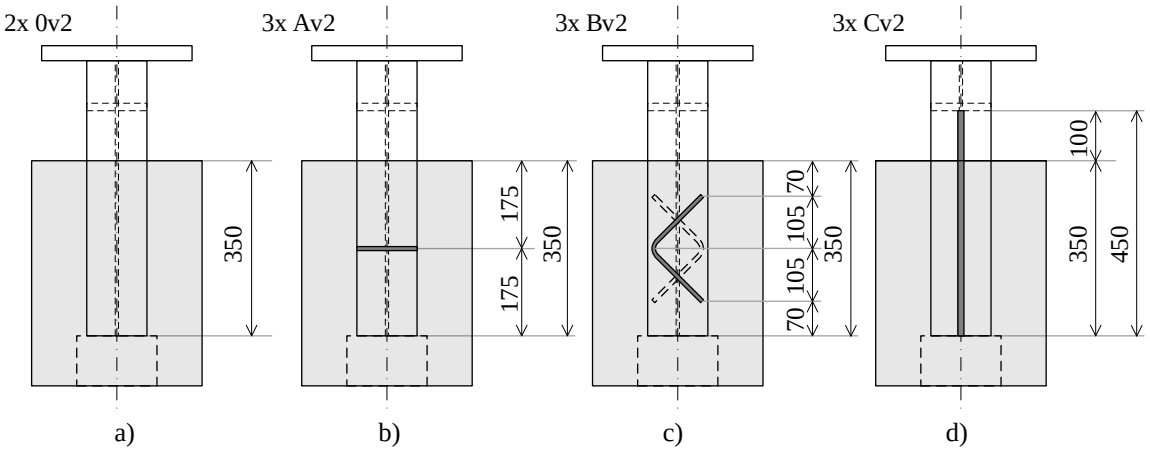


Fig. 5.16. Overview of the column push-out test series – a) reference tests 0v2, b) transversal variant conn. Av2, c) angled, V-shaped variant conn. Bv2 and d) longitudinal variant conn. Cv2.

Table 5.3.
Overview of the composite column push-out test specimens.

Series	Geo-metry	Sub-number	Material and geometry [mm]	Shear connection	Surface treatment	No. of tests	Re-sults
0v2	Fig. 5.17	-1 -2	Steel profile: HEB 120 L=550 S355 Concrete block: 340x1000x450 C25/30 with 160x340x100 recess at bottom, L_{emb}=350	Reference tests: without mechanical connectors	Cleaning: No Coating: Release agent – demoulding oil	2	Fig. 5.28a
Av2	Fig. 5.17, Fig. 5.20	-1 -2 -3	Steel profile: HEB 120 L=550 S355 Concrete block: 340x1000x450 C25/30 with 160x340x100 recess at bottom, L_{emb}=350	Mechanical flat shear connector, transversal variant	Cleaning: No Coating: Release agent – demoulding oil	3	Fig. 5.28b
Bv2	Fig. 5.17, Fig. 5.20	-1 -2 -3	Steel profile: HEB 120 L=550 S355 Concrete block: 340x1000x450 C25/30 with 160x340x100 recess at bottom, L_{emb}=350	Mechanical flat shear connector, angled, V-shaped variant	Cleaning: No Coating: Release agent – demoulding oil	3	Fig. 5.28c
Cv2	Fig. 5.17, Fig. 5.20	-1 -2 -3	Steel profile: HEB 120 L=550 S355 Concrete block: 340x1000x450 C25/30 with 160x340x100 recess at bottom, L_{emb}=350	Mechanical flat shear connector, longitudinal variant	Cleaning: No Coating: Release agent – demoulding oil	3	Fig. 5.28d

The applied steel profiles were 550 mm long and embedded in a 340x1000x450 mm (width x length x height) concrete block, see Fig. 5.17. Between the flanges of steel profiles and above the concrete encasement, two stiffeners were welded for each steel profile in order to prevent any local instability effects due to high compression loads. The distance of welded stiffeners from the concrete block allowed for a relative slip of 100 mm, see Fig. 5.17. At the bottom of each specimen, directly below the embedded steel profile, a recess with the dimension of 160x340x100 mm was placed centrally, see Fig. 5.17. In the result, the embedment length of steel profiles was 350 mm.

All the CoPOT test specimens were composed from nominally identical materials and the ordered grades were: (i) S355 JR+M for the structural steel, (ii) B500B R for the reinforcement steel and (iii) C25/30 for the concrete. Material properties were obtained experimentally for each applied material and supported by the delivery certificates. The measured values are given in Table 5.9-5.11.

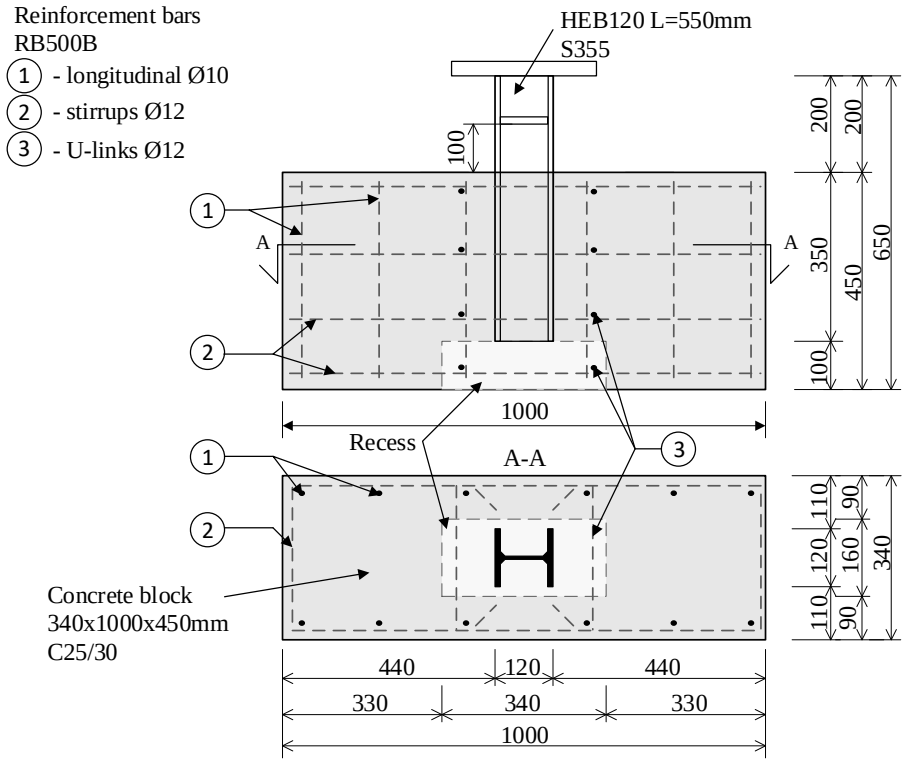


Fig. 5.17. Geometry of the CoPOT specimens.

The concrete block was reinforced with three types of ribbed bars: (1) longitudinal bars Ø10/180(185), L=380, (2) closed stirrups Ø12/116(117), L=2615 and (3) U-links Ø12/116(117), L=525 as shown in Fig. 5.17 and Fig. 5.18. The id numbers of bars are consistent between figures and text. The concrete cover of the reinforcement in the vertical direction was 50 mm for both, top and bottom sides, where the distance was measured from concrete surface to the centre of stirrups. In the horizontal direction, the concrete cover was 45 mm. The concrete cover of stirrups in horizontal direction was approximately 25 mm. The applied reinforcement cages contained bending diameter of reinforcement bars equal to 4xØ according to EN 1992-1-1:2004 [53]. In Fig. 5.19, a view on the fabricated reinforcement cage and used steel profiles is given.

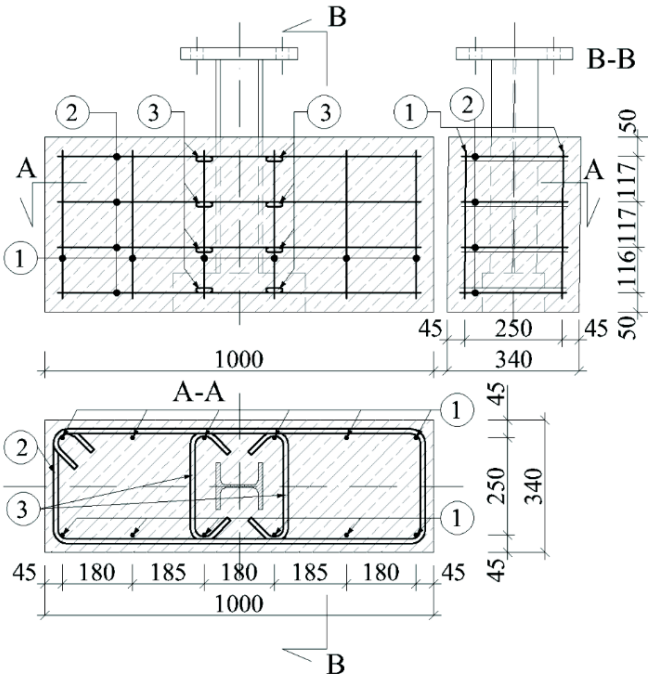


Fig. 5.18. Technical drawing of reinforcement arrangement in the CoPOT specimens.



a) b)

Fig. 5.19. Details of steel parts in the CoPOT specimens – a) reinforcement cage and b) steel profiles.

The applied flat shear connectors had been fabricated out of regular B500B R reinforcement bars with diameter Ø8 mm for the Av2 and Bv2 series and with diameter Ø12 mm for the Cv2 series. The bigger diameter of shear connectors was used for Cv2 series in order to obtain a comparable value of shear connection resistance to the two other test series. The connectors were welded to the external surfaces of the flanges of steel profiles as shown in Fig. 5.20 and Fig. 5.21. In order to limit the shear connection resistance to the capacity of the used test machine, only one connector was placed per flange of a steel profile. The detailed geometry and arrangement over the embedded length of the applied flat shear connectors is shown in Fig. 5.20. Nominal material properties of the connectors are the same as the properties for the reinforcement bars and they are given in Table 5.10.

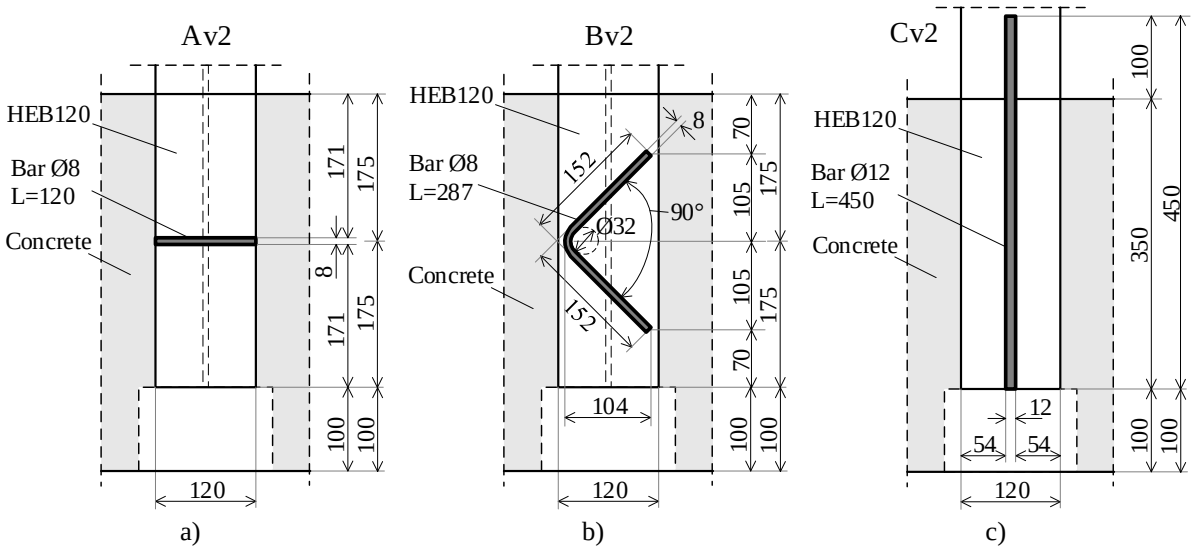
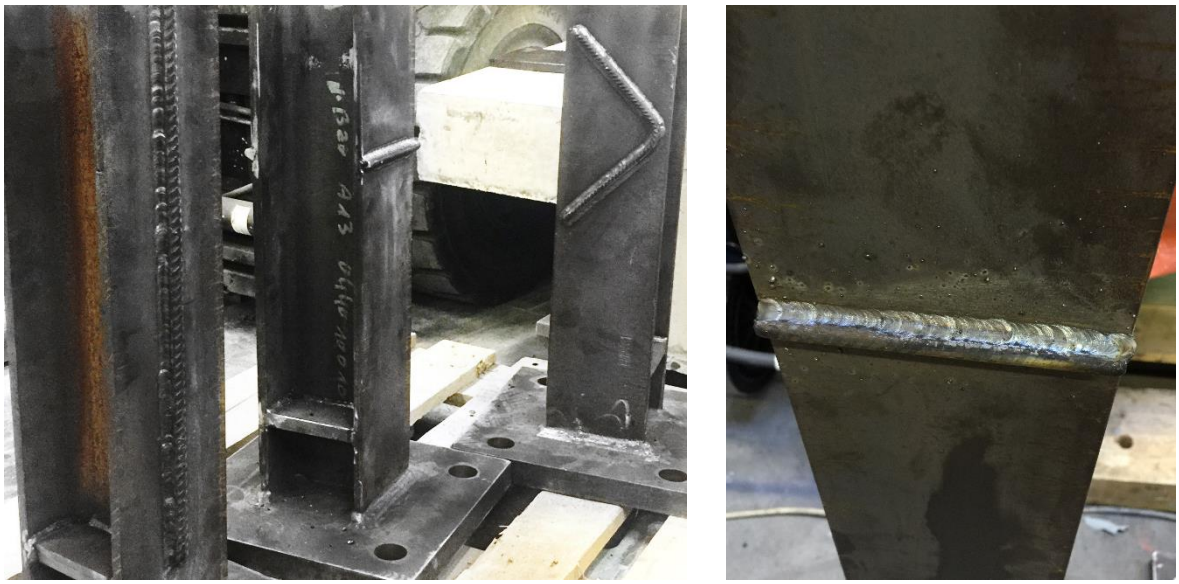


Fig. 5.20. Geometry detail of applied flat shear connectors in the CoPOT specimens – a) variant Av2, b) variant Bv2 and c) variant Cv2.

Flat shear connectors in all CoPOT test series were welded to the steel profiles with the usage of gas-coated electrode manual electric arc welding. The used welding technique allowed for the direct evaluation of quality of the produced welds. Like this, any possible imperfection that could affect the resistance of shear connection could be identified and eliminated. Covered electrode rods of company Oerlikon Citorex with size of Ø2.5 x 350 mm and Ø3.2 x 350 mm had been used to weld the connector diameters of Ø8 mm and Ø12 mm, respectively. The used electrode rods were classified as E 38 2 RB 1 2 according to ISO 2560 [79]. During the welding process, the steel profiles and connectors were prevented from an excessive overheating by applying appropriate welding procedure, however, due to the small scale of the applied shear connectors, a high heat flux concentration was recognised. Due to the extensive welding of relatively small reinforcement bars, the material properties of welded shear connectors can vary from the nominally defined properties.

On the top of embedded steel profiles, supporting plates were welded in order to connect the hydraulic press with the specimens, see Fig. 5.19, Fig. 5.21-5.22. The thickness of the supporting plates ensured the uniform distribution of the compression stresses over the entire cross-section of the steel profile at the top surface.

In the final stage of the specimen production process, the steel profiles, recess filament elements and reinforcement cages had been assembled and closed in the formwork. The reinforcement cages were fabricated with the usage of wires. The specimens had been cast with the concrete delivered by the company Bétons Feidt SA and the delivery certificate confirmed the ordered concrete material properties. The specimens were poured directly from the concrete truck, where the falling height was not higher than 500 mm. The specimen pouring process was split into three layers and between each layer, the concrete was vibrated. More information about the fabrication process of CoPOT specimens can be found in Annex C.

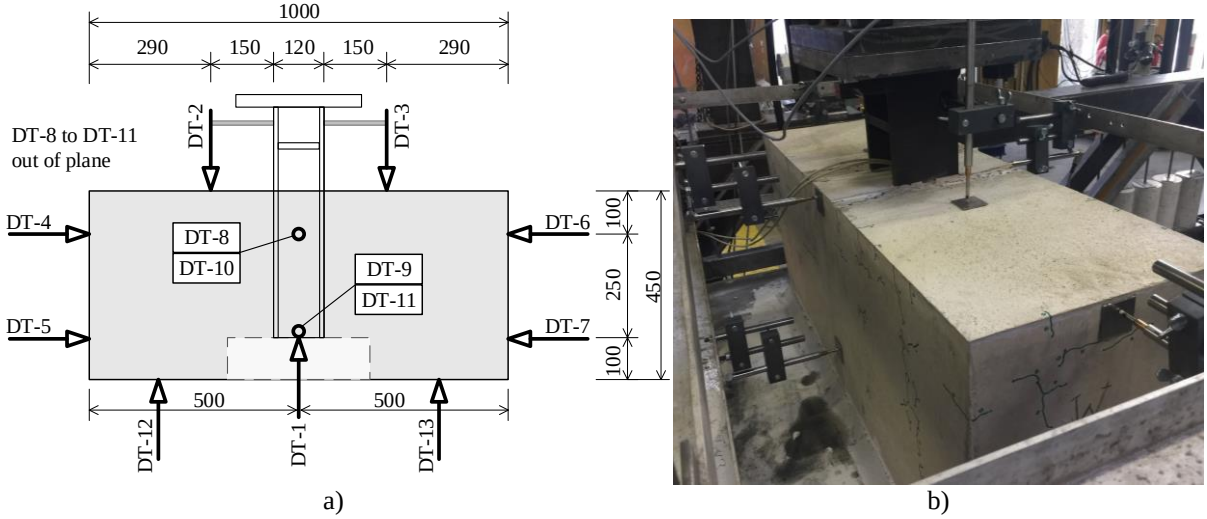


a) b)

Fig. 5.21. Welded flat shear connectors to the steel profiles of CoPOT specimens – a) overview on the applied connectors and b) weld detail.

5.4.2. Specimen instrumentation

From the performed CoPOT tests series, the load-slip behaviour was recorded. The imposed load and travel of the testing machine was recorded from an integrated load cell. The relative slip was recorded by a set of external linear variable displacement transducers. Besides the load-slip relation, the displacement of concrete block was measured on each wall of the specimen. Moreover, strains inside the specimens were measured by a set of strain gauges glued to the steel profiles and stirrups.



a) b)

Fig. 5.22. Arrangement of the displacement transducers (DT) in the CoPOT tests – a) scheme and b) view in the laboratory.

The position of the measurement equipment used to record the relative slip and deformation of the specimens is shown in Fig. 5.22. It consisted of a set of 13 linear variable displacement transducers (DT) distributed over each side of the specimen. A mean value of the signals from the sensors DT-2 and DT-3, see Fig. 5.22, was used to describe the relative slip between the steel profile and the concrete block.

The sensor DT-1 also measured the relative slip of the bottom part of the steel profile but it was used only for the verification. A two level record of the relative slip, top and bottom, allowed for a more accurate measurement. A list of all used displacement transducers is given in Table 5.4.

Table 5.4.
List of the used displacement transducers in the column push-out tests.

Sensor name	Range	Measuring value	Reference point
DT-1	100 mm	Displacement of the bottom face of the steel profile	Ground
DT-2	100 mm	Relative slip, L	Steel profile
DT-3	100 mm	Relative slip, R	Steel profile
DT-4	20 mm	Displacement of concrete block, L TOP	Testing frame
DT-5	20 mm	Displacement of concrete block, L BOT	Testing frame
DT-6	20 mm	Displacement of concrete block, R TOP	Testing frame
DT-7	20 mm	Displacement of concrete block, R BOT	Testing frame
DT-8	20 mm	Displacement of concrete block, F TOP	Testing frame
DT-9	20 mm	Displacement of concrete block, F BOT	Testing frame
DT-10	20 mm	Displacement of concrete block, B TOP	Testing frame
DT-11	20 mm	Displacement of concrete block, B BOT	Testing frame
DT-12	20 mm	Deflection of the support, L	Ground
DT-13	20 mm	Deflection of the support, R	Ground

Where,
L – left side, see Fig. 5.22,
R – right side, see Fig. 5.22,
F – front side, side in the front view in Fig. 5.22,
B – back side, side in the back side of the view in Fig. 5.22,
TOP – top part of the concrete block,
BOT – bottom part of the concrete block.

The displacement transducers DT-2 and DT-3 were fixed to the flanges of steel profile above the concrete and measured the distance to the top surface of the concrete block. Change of the measured distance indicated the developed relative slip at the steel-concrete interface. The sensors DT-4 to DT-11 were placed similarly, but the reference points were localized on the supporting frame fixed around the specimen. The sensors DT-1, DT-12 and DT-13 were fixed to the ground and pointed to the bottom face of the steel profile and concrete block.

In parallel to the measurements made by the displacement transducers, a set of strain gauges (SG) was used in each specimen. Applied strain gauges allowed for the measurement in one direction and were glued to the embedded part of steel profiles and to the reinforcement bars. The arrangements and lists of used strain gauges in each test series are given in Table 5.5-5.8. Strain gauges used for the measurements in steel profiles were glued to their webs, where strain gauges used for the reinforcement bars were glued to stirrups. Arrangement of strain gauges in series Bv2 consisted of three strain gauges glued to the steel profile, before the applied shear connector, between the arms of shear connector and after the applied shear connector. This arrangement allowed to investigate the level of forces transferred by each arm of the connector. Strain gauges applied to the reinforcement bars consisted of four sensors placed on stirrups and four sensors placed on U-bars in the transversal direction. Due to the geometry of the V-shaped flat shear connector, a minor torsion effect and tension forces in the direction of U-bars were expected. In Fig. 5.23, strain gauges are shown. More details can be found in Annex C.

Table 5.5.
Arrangement and list of the strain gauges used in the column push-out tests for the specimen 0v2.

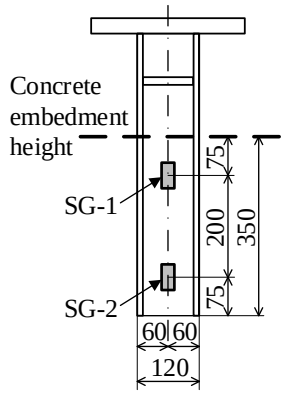
Arrangement on steel profile	Arrangement on reinforcement cage	No.	Sensor name	Position
	No Strain Gauges	1.	SG-1	Steel profile, web, upper
		2.	SG-2	Steel profile, web, lower

Table 5.6.
Arrangement and list of the strain gauges used in the column push-out tests for the specimen Av2.

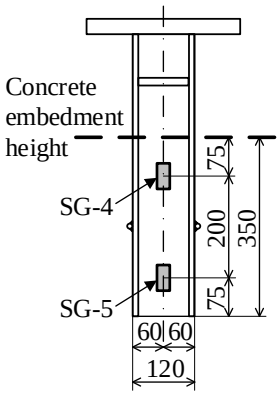
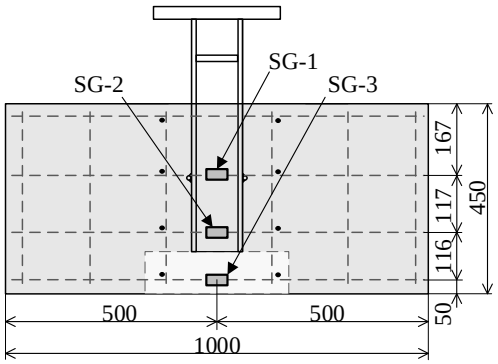
Arrangement on steel profile	Arrangement on reinforcement cage	No.	Sensor name	Position
		1.	SG-1	Stirrup, third from bottom
		2.	SG-2	Stirrup, second from bottom
		3.	SG-3	Stirrup, bottom
		4.	SG-4	Steel profile, web, upper
		5.	SG-5	Steel profile, web, lower

Table 5.7.
Arrangement and list of the strain gauges used in the column push-out tests for the specimen Cv2.

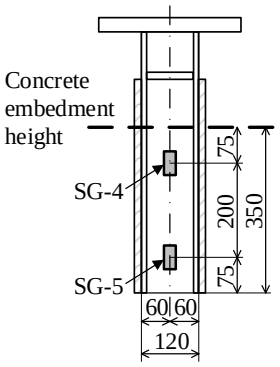
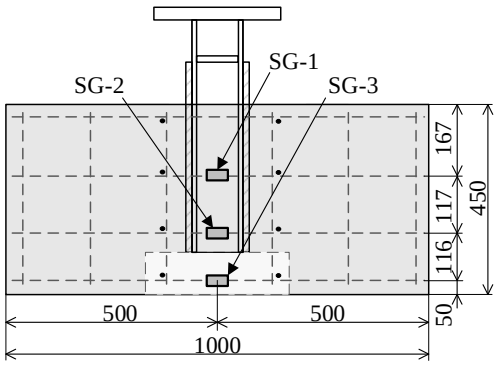
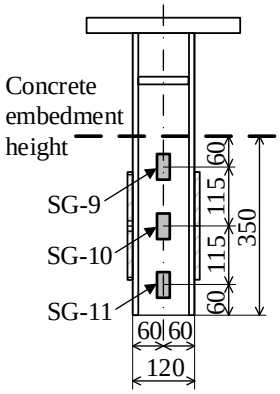
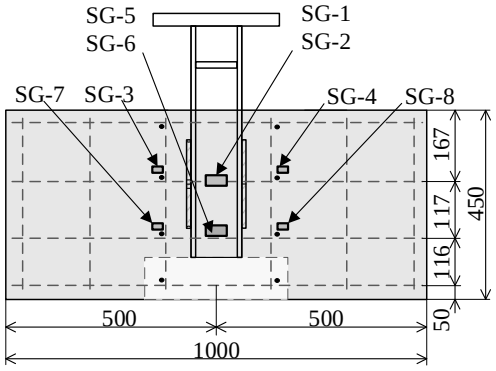
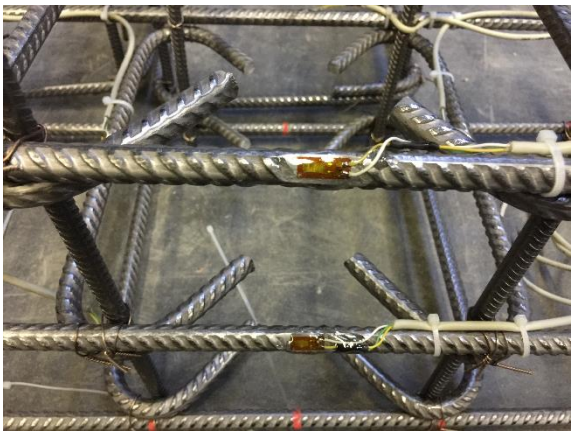
Arrangement on steel profile	Arrangement on reinforcement cage	No.	Sensor name	Position
		1.	SG-1	Stirrup, third from bottom
		2.	SG-2	Stirrup, second from bottom
		3.	SG-3	Stirrup, bottom
		4.	SG-4	Steel profile, web, upper
		5.	SG-5	Steel profile, web, lower

Table 5.8.
Arrangement and list of the strain gauges used in the column push-out tests for the specimen Bv2.

Arrangement on steel profile	Arrangement on reinforcement cage	No.	Sensor name	Position
		1.	SG-1	Stirrup, third from bottom, front side
		2.	SG-2	Stirrup, third from bottom, back side
		3.	SG-3	U-bar, left, third from bottom
		4.	SG-4	U-bar, right, third from bottom
		5.	SG-5	Stirrup, second from bottom, front side
		6.	SG-6	Stirrup, second from bottom, back side
		7.	SG-7	U-bar, left, second from bottom
		8.	SG-8	U-bar, right, second from bottom
		9.	SG-9	Steel profile, web, upper
		10.	SG-10	Steel profile, web, mid
		11.	SG-11	Steel profile, web, lower



a)

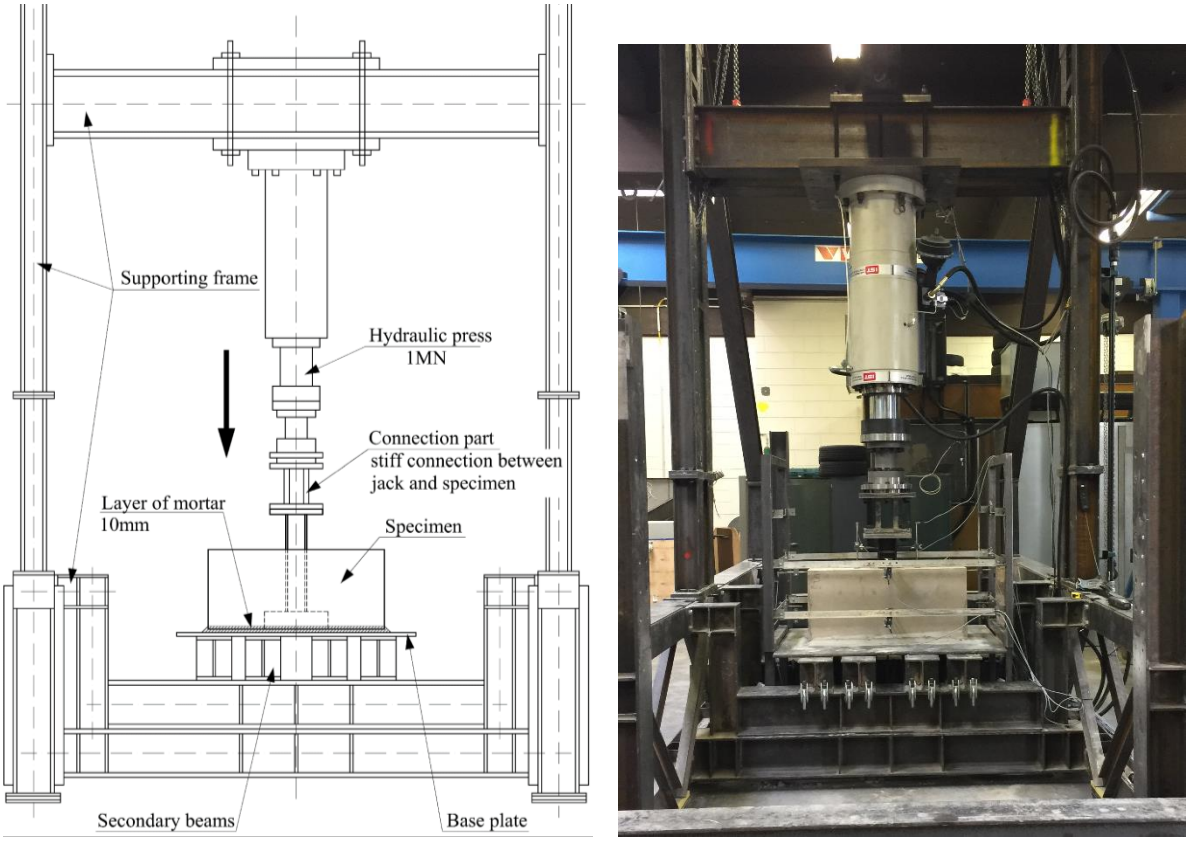


b)

Fig. 5.23. Details of glued strain gauges to steel parts in CoPOT specimens – a) on steel profile and b) on reinforcement cage.

5.4.3. Test conduction and boundary conditions

The test conduction was split between the laboratories of the University of Luxembourg (UniLux) and the Technische Universität Kaiserslautern (TUK). Only the specimens of the series Bv2 had been tested at TUK. The test layout in both laboratories was identical – the specimens were placed vertically on a rigid base and the force was introduced fully to the steel part, so that, the relative slip between the steel part and the concrete block was induced.

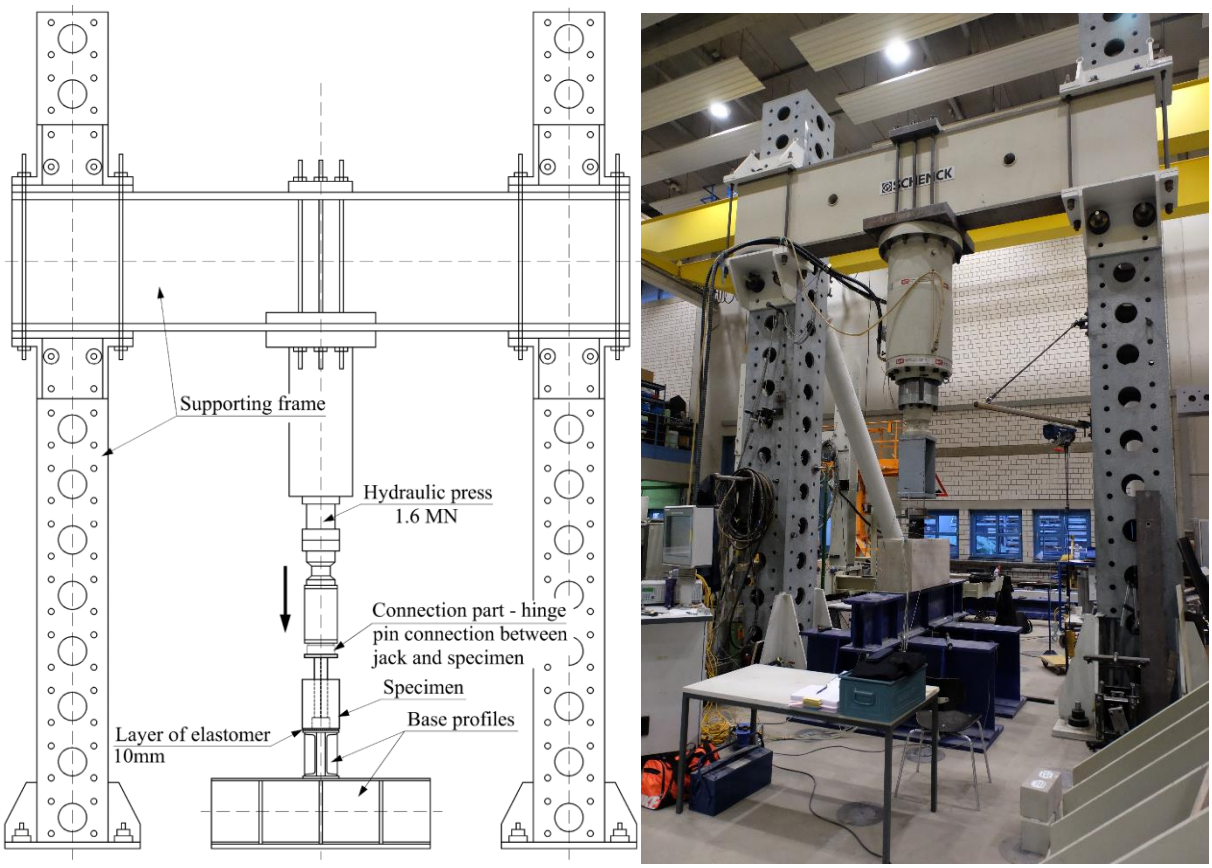


a) b)

Fig. 5.24. Test setup at the University of Luxembourg for the CoPOT – a) scheme and b) a view in the laboratory.

In the test campaign, two different test setups were used as shown in Fig. 5.24 and Fig. 5.25. The test specimens executed at the University of Luxembourg (0v2, Av2 and Cv2), were placed on a 10mm thick mortar bedding and connected on top to the hydraulic press with a connection device imposing a rigid connection, see Fig. 5.24. At the Technische Universität Kaiserslautern, the specimens of the series Bv2, were placed on a 10mm thick layer of elastomer and connected with the hydraulic press through a calotte, see Fig. 5.25. As observed after the test, the usage of different materials to support the specimens, affected the overall behaviour more than expected. The elastomer allowed for a bigger outward rigid-body movement of the bottom part of the concrete block, which imposed at the lower part a normal separation at the steel-concrete interface. Due to the resulting separation, the concrete area in direct compression under the connector was reduced and the load-bearing capacity of the Bv2 test specimens reduced accordingly. Moreover, the elastomer bedding resulted in a nearly uniform distribution of a reaction pressure field at the base of the specimens, thus, the resultant reaction centre

moved outward in comparison to the tests with mortar bedding, where a triangular reaction field was assumed. An increased distance to the reaction forces resulted in a higher load-dispersion angle and higher tension forces developed in the specimens. In comparison with the behaviour in a real column, the obtained performance of the Bv2 variant connector moved towards the safe side, if sufficient stirrup reinforcement would prevented this lateral separation.



a) b)

Fig. 5.25. Test setup at TU Kaiserslautern for the CoPOT – a) scheme and b) a view in the laboratory.

The test procedure defined in Eurocode 4: EN1994-1-1:2004 Annex B [58] was applied for all tests. The specimens were loaded in the displacement control mode with the shape of a ramp. A high rigidity of the applied shear connection required a small load increment speed and the displacement speed at the hydraulic press was set to 0.5 mm/min. In order to allow for the concrete relaxation and the investigation of the load drop characteristic, a pause of 4-5 min was used between each load increment (ca. 30-40 kN). The specimens were cycled 25 times between 5% and 40% of the expected ultimate load with the frequency of 0.015 Hz. After the cycles, quasi-static increments were applied up to the failure. After reaching the peak load, the specimens were continuously loaded with a constant displacement rate up to the relative slip of approximately 95 mm. In order to investigate the stiffness of the connection at different stages of damage, one to two reloads were made close to the peak load. The applied test procedure can be represented in the form of a diagram as shown in Fig. 5.26.

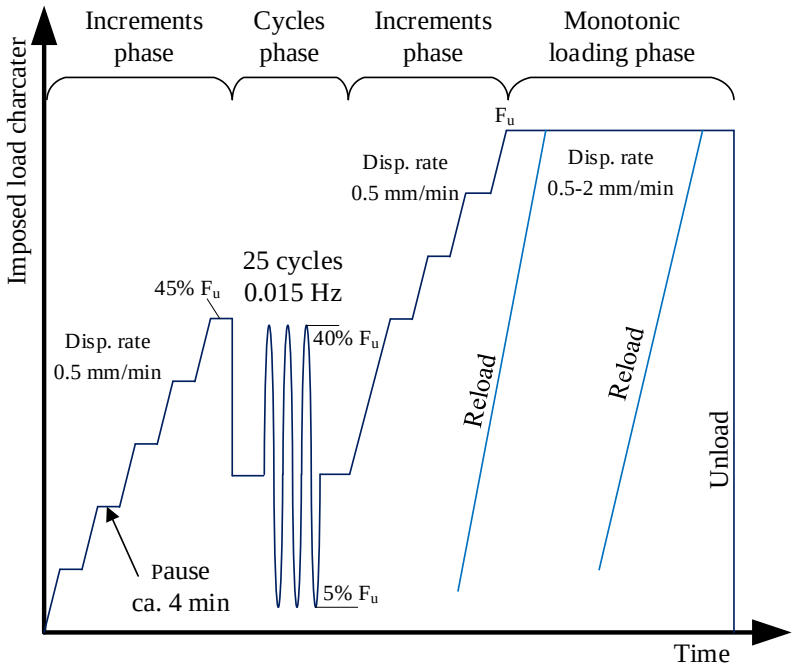


Fig. 5.26. Test procedure used for the column push-out tests.

The applied recess at the bottom of test specimens allowed the downward slide of the steel profiles with an assumed resultant load-spread in the concrete approximately under 30°-45°, see Fig. 5.27. The assumed load-spread angle reflects the situation in the mid-zone of the full column length member, where the forces distributed to the concrete from the steel profile are not constrained by a geometry at the base. The implemented recess in CoPOT test specimens resulted in a force eccentricity and development of tension and compression zones over the steel-concrete interface as shown in Fig. 5.27.

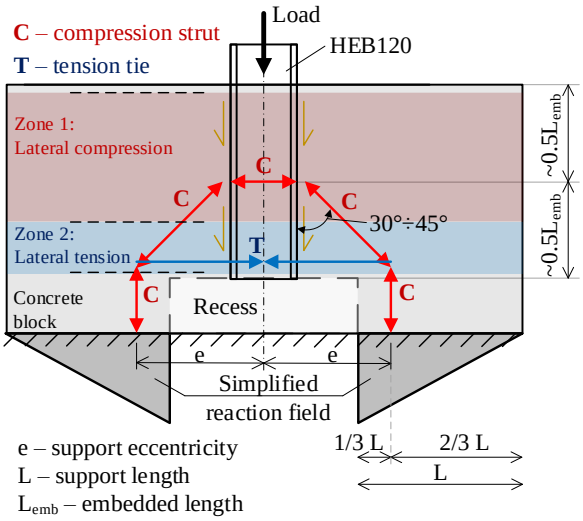


Fig. 5.27. Assumed simplified load-spread due to the implemented recess in column push-out tests,

5.4.4. Test results

From each CoPOT test, 20 signals were recorded, where for series Bv2 the amount raised to 26 signals and for series 0v2 reduced to 17 signals due to the varied amount of used strain gauges. All the signals were recorded by NI hardware and dedicated software NI SignalExpress. The data recording frequency was set to 1k Hz. The recorded data was compiled and post-processed in the DIAdem software. A high frequency at the recording required data reduction and curve smoothing, however, a higher accuracy and control over the recorded data was achieved.

In parallel to the CoPOT tests, material tests were conducted for each part used for fabrication of the specimens. The tests of structural steel consisted of four coupon tests with gauge length of 200 mm, width of 25 mm and thickness of 10 mm. The taken geometry resulted in a nominal cross-section area of 250 mm^2. The steel samples were cut out from the additionally delivered steel profile stubs for the material testing purposes and they originated from the same rolled material batch. The samples were taken from flanges of steel stub. Specimens used for the material tests of the reinforcement steel consisted of four straight bar tensile specimens per each tested diameter – Ø8, Ø10 and Ø12. The gauge length was set to 100 mm in each tested diameter.

5.4.4.1. Measured material properties

The material properties of the parts used to fabricate the specimens were obtained experimentally. Table 5.9 gives the properties of the structural steel. The properties of the reinforcement steel are given in Table 5.10. In Table 5.11, concrete material properties are shown. Two series of concrete properties are given due to the fact that each test with sub-number "3" (for example, Av2-3) was produced from the second batch of the delivered concrete. The concrete compression strength was measured at 28 days after the concreting date and in addition at the day of the test.

Table 5.9.
Material properties of the structural steel in column push-out tests.

Ordered grade: **S355 JR+M**	Value – min (EN 10025-1:2004 [48])	Value – expected (heat certificate)	Value – test (ISO 6892-1:2009 [80])	Unit
R_{eH}, yielding strength	355	409	455	[MPa]
R_m, tensile strength	470	501	527	[MPa]
A, elongation at fracture	22	32.34	26.5	[%]
E, modulus of elasticity	210 000	-	207 827	[MPa]

Table 5.10.
Material properties of the reinforcement steel in column push-out tests.

Ordered grade: **B500B**	Value – min (ISO 6935-2:2007 [81])	Value – test (ISO 6935-2:2007 [81])			Unit
		Ø8	**Ø10**	**Ø12**	
R_{eH}, yielding strength	500	583	584	528	[MPa]
R_m, tensile strength	540	671	684	639	[MPa]
A, elongation at fracture	$A_{gt} = 5$ / $A_5 = 14$	27.45	30.2	30.25	[%]
E, modulus of elasticity	200 000	208 478	207 270	201 109	[MPa]

Table 5.11.
Material properties of the concrete in column push-out tests.

Ordered grade: **C25/30**		Value – min	Value – test, 1st series (Specimens -1 and -2)	Value – test, 2nd series (Specimens -3)	Unit
28 days, cyl.	f_{cm}, mean compression strength for cylinders (age: 28 days)	33	40.92	-	[MPa]
28 days, cube	$f_{cm,cube}$, mean compression strength for cubes (age: 28 days)	40	44.93	40.59	[MPa]
0v2	$f_{cm,cube}$, mean compression strength for cubes (age: 28 days, the day of test 0v2)	-	44.93	40.59	[MPa]
Av2	$f_{cm,cube}$, mean compression strength for cubes (1st series age: 43 days, 2nd series age: 35 days, the day of test Av2)	-	55.55	45.92	[MPa]
Bv2	$f_{cm,cube}$, mean compression strength for cubes (1st series age: 57 days, 2nd series age: 50 days, the day of test Bv2)	-	58.41	51.92	[MPa]
Cv2	$f_{cm,cube}$, mean compression strength for cubes (age: 35 days, the day of test Cv2)	-	50.86	45.92	[MPa]
Cement		CEM IIB-S 42.5N			
W/C		0.59			
Exposition class		CAT2 – XC4, XF1, XA1			
Consistency class		F4			
Aggregate		B16			

Dimensions of cylinder specimens were 150x300mm
Dimensions of cube specimens were 150x150x150mm
Min values according to EN 206-1:2000 [59]
1st series for the specimens with sub-number 1 and 2, tests according to EN 12390-3:2001 [50]
2nd series for the specimens with sub-number 3, tests according to EN 12390-3:2001 [50]

5.4.4.2. Load-slip responses

From the executed tests, the load-slip relationships had been recorded and are shown in Fig. 5.28. It can be clearly seen that the applied flat shear connectors influenced the overall performance of the specimens. The data extracted from the obtained diagrams is summarised in Table 5.12. It can be observed that the longitudinal variant of the shear connector (Cv2) exhibited the smallest load-bearing capacity but the highest ductility after the failure and high stiffness. The residual strength after the failure sustained at the level of about 75% of the ultimate load until the end of the tests. The connector Av2 showed the highest resistance but it fails in the most brittle manner and the stiffness exhibited the smallest value. Finally, it can be observed that the V-shaped variant of the proposed shear connector (Bv2) brought a good compromise between the resistance, ductility and stiffness. Moreover, the economy aspect in Bv2 variant connector has a good ratio between the load-bearing capacity and used material, compare Fig. 5.20 or Fig. 5.21 with Fig. 5.28c. The impact of concrete material properties on the peak load in each flat connector variant is obvious, where assessment of the impact on the residual strength and the ductility would require additional tests with varied concrete grades.

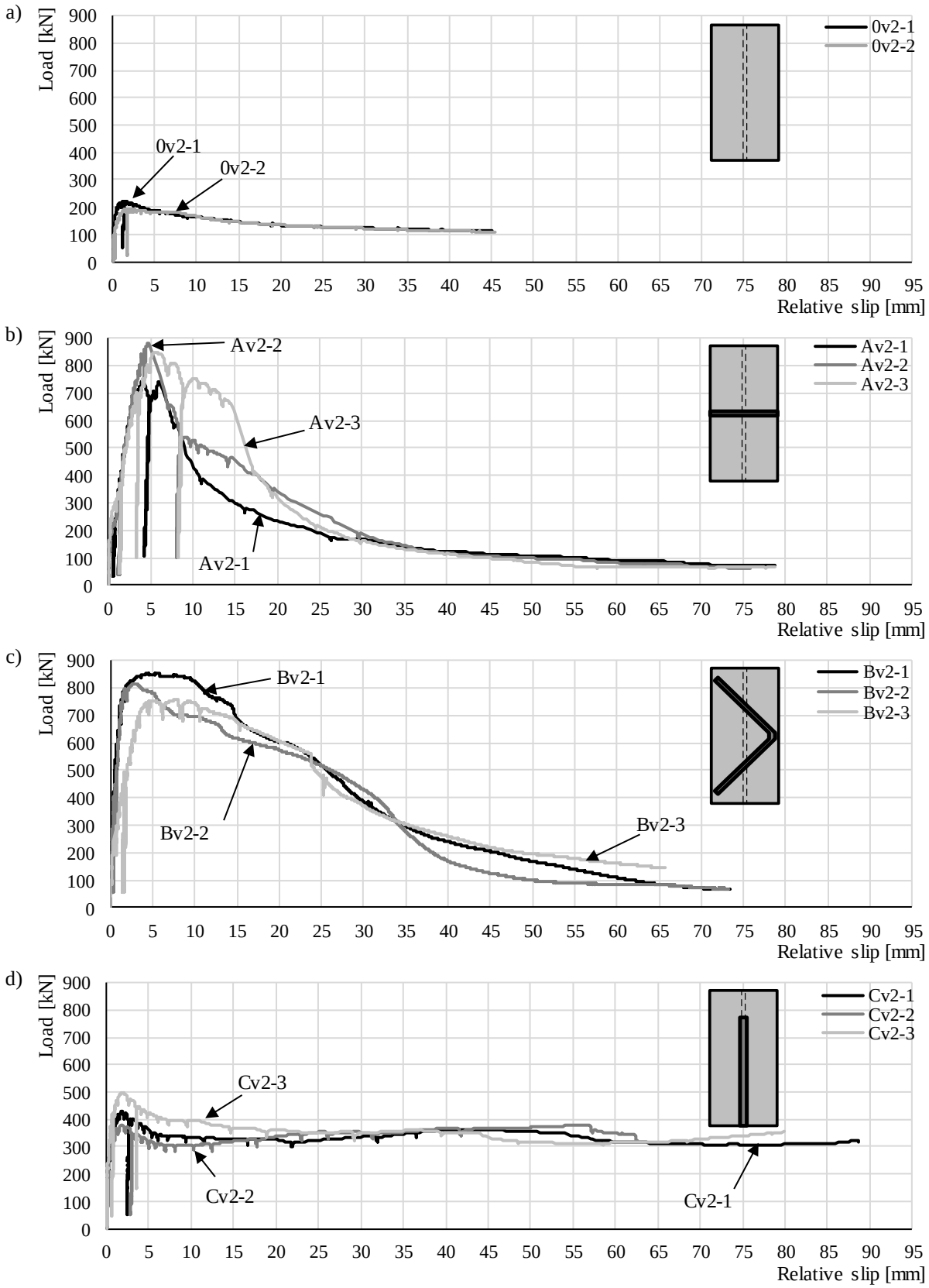


Fig. 5.28. Experimental load-slip curves for the column push-out tests – a) specimen 0v2, b) specimen Av2, c) specimen Bv2 and d) specimen Cv2

Table 5.12.
Column push-out test results.

Series	Test	F_u	F_6	δ_u	δ_1	δ_2	$\frac{\delta_2 - \delta_u}{\delta_u - \delta_1}$	$K_{0.5}$
		[kN]	[kN]	[mm]	[mm]	[mm]	[-]	[kN/mm]
0v2	1	221	182	1.49	0.52	3.43	1.99	389
	2	194	182	1.64	0.93	6.95	7.48	287
	Mean	**208**	**182**	**1.56**	**0.72**	**5.19**	**4.74**	**338**
Av2	1	746	740	4.06	2.97	6.89	2.60	390
	2	881	777	4.69	3.67	5.83	1.12	428
	3	847	844	5.64	4.35	8.44	2.17	545
	Mean	**825**	**787**	**4.80**	**3.66**	**7.05**	**1.96**	**454**
Bv2	1	854	843	4.51	1.39	11.78	2.33	968
	2	816	740	2.84	1.33	6.19	2.22	886
	3	757	741	8.00	3.21	14.66	1.39	520
	Mean	**809**	**775**	**5.12**	**1.98**	**10.88**	**1.98**	**791**
Cv2	1	429	344	1.87	1.08	3.55	2.13	545
	2	380	312	1.95	1.06	3.95	2.25	576
	3	496	410	1.90	1.08	3.93	2.48	740
	Mean	**435**	**355**	**1.91**	**1.07**	**3.81**	**2.29**	**620**

F_u is the peak load,
F_6 is the load level at 6 mm of relative slip,
δ_u is the relative slip at peak load,
δ_1 is the relative slip at 90% of peak load, before failure,
δ_2 is the relative slip at 90% of peak load, after failure,
$K_{0.5}$ is the shear connection stiffness at $\delta = 0.5$ mm.

5.4.4.3. Recorded strains

In the specimens 0v2, only strains in the steel profiles were measured and the recorded values are given in Fig. 5.29. Due to the applied arrangement of SG, the distribution of strains in the embedded steel profiles can be investigated. It can be clearly observed that steel-concrete bond transferred the imposed load from steel to concrete until the failure. The analysis of the recorded values of strains proves that steel profiles in both tests stayed in the elastic range and strains did not exceed 0.25‰.

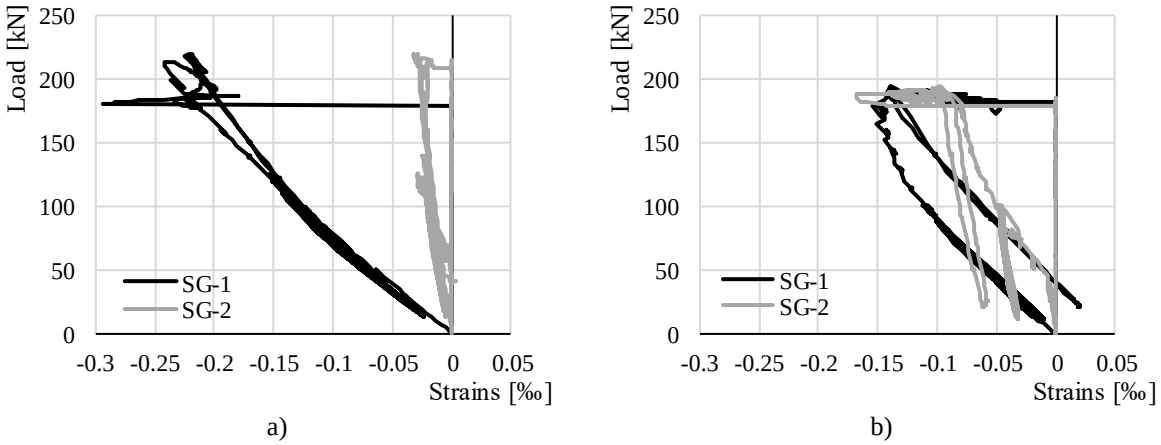


Fig. 5.29. Strains in steel profiles in the series without mechanical shear connectors of CoPOT – a) specimen 0v2-1 and b) specimen 0v2-2.

In the specimens Av2, strains were measured in the steel profiles and reinforcement bars. The obtained results are given in Fig. 5.30 and Fig. 5.31 respectively. The arrangement of strain gauges over the embedded steel profiles consisted of two sensors, one placed above the applied shear connector (DT-4) and the second below it (DT-5). It can be observed that nearly entire imposed load was transferred to the concrete between two measurement points. In each case, the steel profiles stayed in the elastic range of strains and they did not exceed 1.35‰. Strains recorded in stirrups allow for the evaluation of shear reinforcement activation and the load-spread dispersion angle. The measurement of strains was done on three subsequent layers of stirrups from the bottom – approximately at the level of shear connector (SG-1), 117 mm below (SG-2) and 233 mm below the shear connector (SG-3, sensor at the lowest stirrup). From the recorded values, it can be observed that only stirrup with sensor SG-3 yielded at the load level close to the 85% of Pu, where the yielding strain was $\varepsilon_{ys} = 2.625‰$.

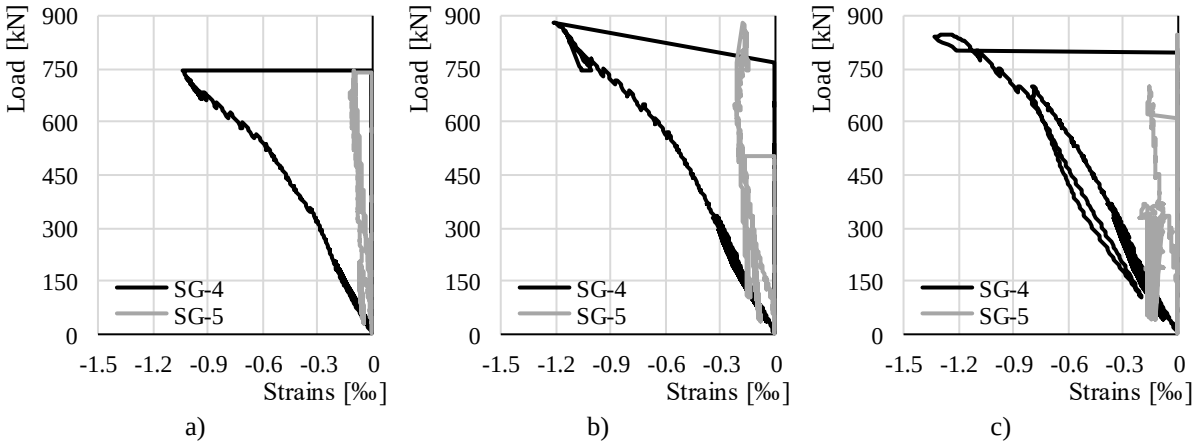


Fig. 5.30. Strains in steel profiles in the series with transversal shear connectors of CoPOT – a) specimen Av2-1, b) specimen Av2-2 and c) specimen Av2-3.

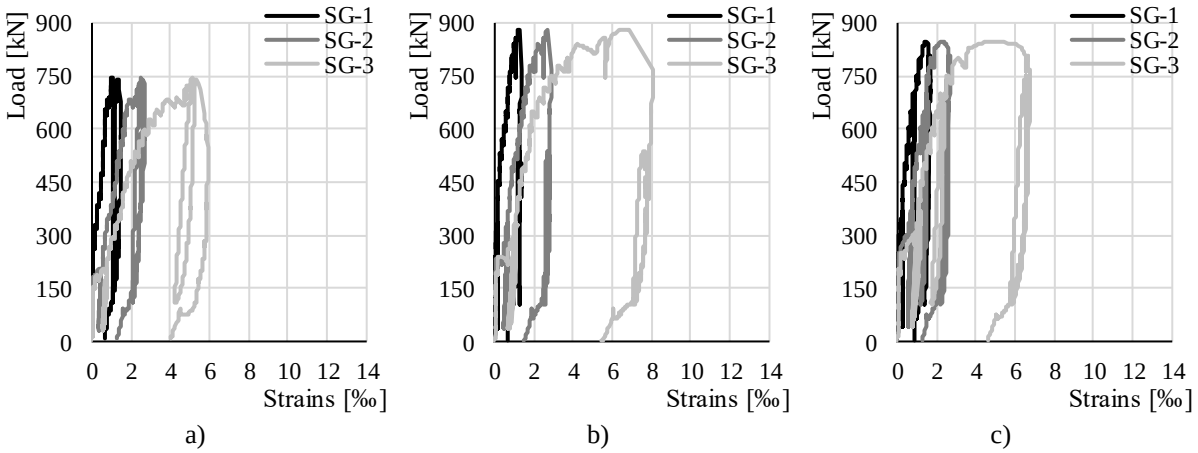


Fig. 5.31. Strains in stirrups in the series with transversal shear connectors of CoPOT – a) specimen Av2-1, b) specimen Av2-2 and c) specimen Av2-3.

In the specimens Bv2, strains were measured in the steel profiles and reinforcement bars. In the steel profiles, the measurement was done in three places – above the applied shear connector (SG-9), between the arms of the connector (SG-10) and below it (SG-11). The recorded strains, as shown in Fig. 5.32, shows that each arm of the applied shear connector transfer nearly equal part of load from steel to

concrete. Strains measured in stirrups are shown in Fig. 5.33. The applied sensors SG-1-2 and SG-5-6 are placed on both sides of the same stirrup but in different layer, see Table 5.8. The recorded strains allowed for the verification of forces distribution due to the bearing action of shear connector and a rough assessment of the resultant load-spread dispersion angle. Besides of strain in stirrups, in Bv2 series, strains in U-bars were measured and given in Fig. 5.34.

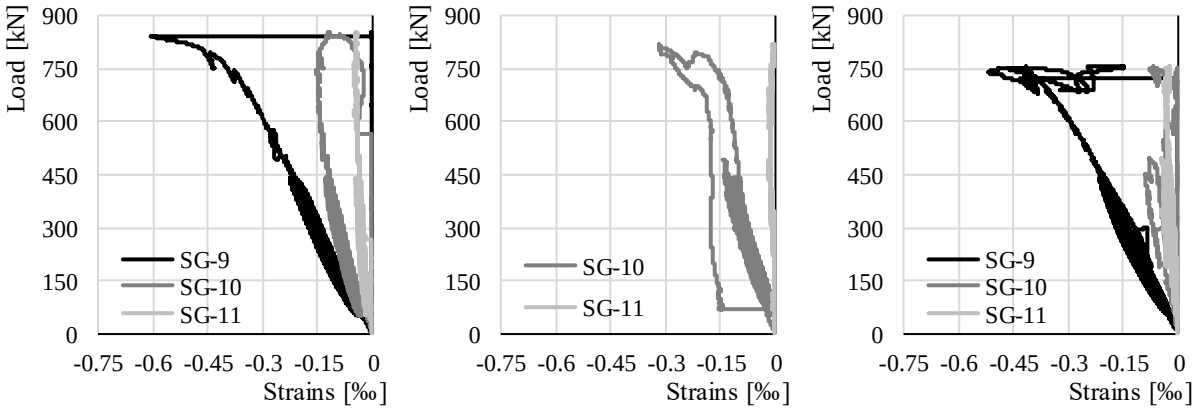


Fig. 5.32. Strains in steel profiles in the series with V-shaped shear connectors of CoPOT – a) specimen Bv2-1, b) specimen Bv2-2 and c) specimen Bv2-3.

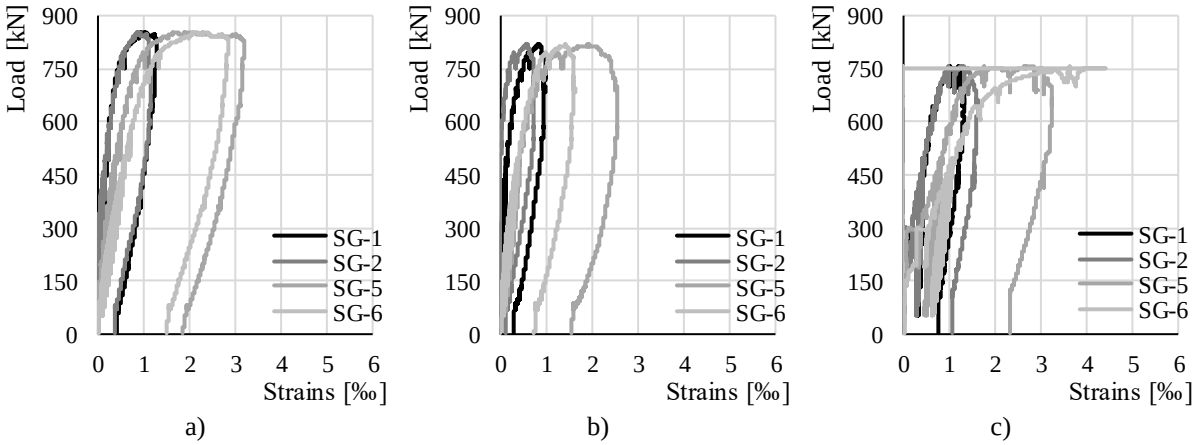


Fig. 5.33. Strains in stirrups in the series with V-shaped shear connectors of CoPOT – a) specimen Bv2-1, b) specimen Bv2-2 and c) specimen Bv2-3.

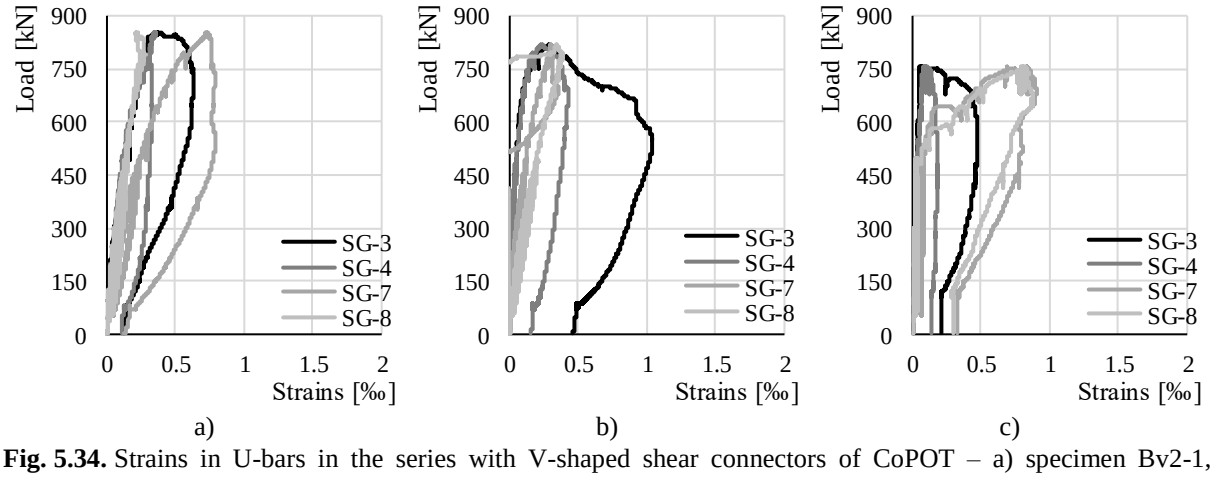


Fig. 5.34. Strains in U-bars in the series with V-shaped shear connectors of CoPOT – a) specimen Bv2-1, b) specimen Bv2-2 and c) specimen Bv2-3.

In the specimens Cv2, strains were recorded in the steel profiles and reinforcement bars. The recorded data is shown in Fig. 5.35 for the steel profiles and in Fig. 5.36 for the reinforcement bars. It can be observed that forces from steel were transferred to concrete over the embedment length and the maximum-recorded strains were approximately 0.45‰, which proves the elastic state of strains. Similarly, the strains recorded in stirrups indicated the elastic strain state over the entire test and an equally rising distribution of forces between subsequent layers of stirrups was revealed. A low utilisation of stirrups in the load transfer shows that the dominating load-transfer mechanism was developed at the connector-concrete interface, an analogy to the rebar pull-out failure.

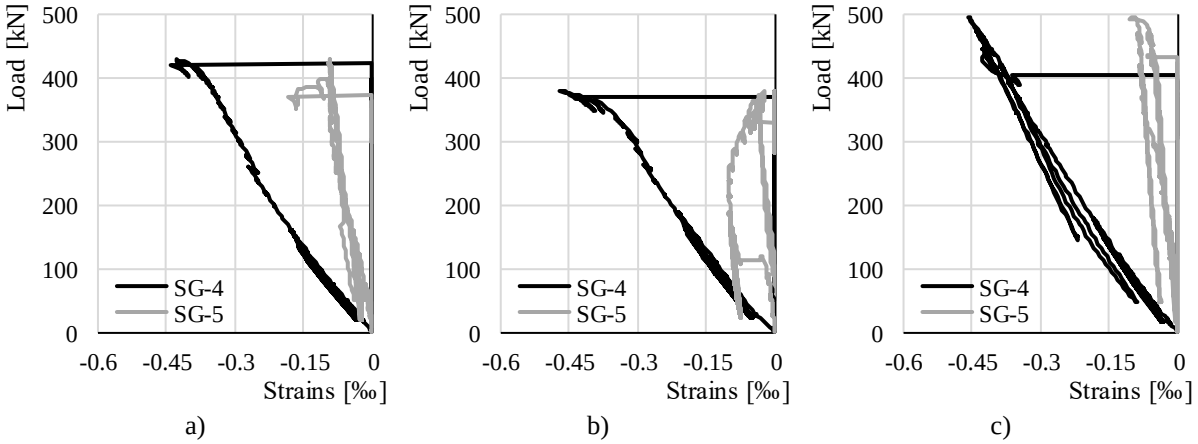


Fig. 5.35. Strains in steel profiles in the series with longitudinal shear connectors of CoPOT – a) specimen Cv2-1, b) specimen Cv2-2 and c) specimen Cv2-3.

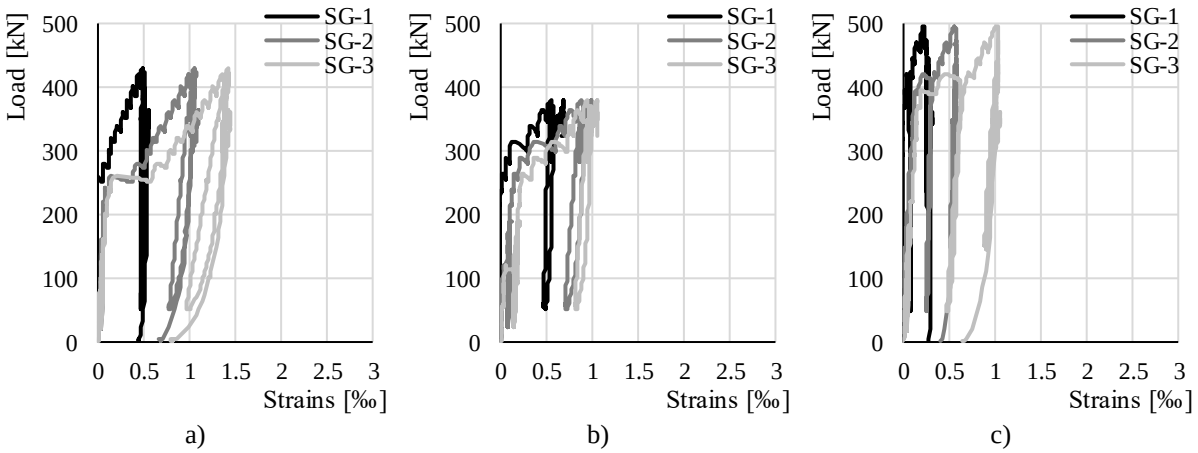


Fig. 5.36. Strains in stirrups in the series with longitudinal shear connectors of CoPOT – a) specimen Cv2-1, b) specimen Cv2-2 and c) specimen Cv2-3.

Based on the results shown in Fig. 5.31, Fig. 5.33 and Fig. 5.36, a summary with strains in stirrups at different load levels corresponding to 30%, 60%, 90% and 100% of the peak loads is given in Table 5.13. For the comparison, strains recorded in the U-bars in series Bv2 are included. The evaluated average values of strains are presented in a graphical way in Fig. 5.37-5.39 for each test series of CoPOT with shear connectors. From the given analysis, the load dispersion angle can be evaluated. Taking for the example series Av2 with transversally placed flat shear connectors and assuming that in the stirrup localised on the top layer, where no sensor was placed, strains are compressive or equal to zero, the

resultant tension force from all stirrups reached 290 kN. In the result, by analysing the angle between the vectors of imposed and tension forces, the dispersion angle reached 35°, see Fig. 5.37.

Table 5.13.
Strains in stirrups from column push-out tests.

Specimen	Load [kN]	SG-1 [‰]	SG-2 [‰]	SG-3 [‰]	SG-5 [‰]	SG-6 [‰]	SG-7 [‰]	SG-8 [‰]
Av2-1	746	1.0225	2.4937	5.1335	-	-	-	-
	672	0.7544	1.8510	3.6638	-	-	-	-
	448	0.4932	1.2173	1.7897	-	-	-	-
	224	0.0857	0.5238	0.7850	-	-	-	-
Av2-2	881	1.2150	2.6921	6.5877	-	-	-	-
	793	0.8762	1.9835	3.6431	-	-	-	-
	529	0.3585	1.1311	1.7156	-	-	-	-
	264	0.0590	0.4572	0.7271	-	-	-	-
Av2-3	847	1.4713	2.2772	5.0071	-	-	-	-
	762	1.0479	1.6106	2.7965	-	-	-	-
	508	0.4633	0.9941	1.4537	-	-	-	-
	254	0.0083	0.1022	0.2051	-	-	-	-
Av2 Average	825	1.2363	2.4876	5.5761	-	-	-	-
	742	0.8928	1.8150	3.3678	-	-	-	-
	495	0.4383	1.1142	1.6530	-	-	-	-
	248	0.0510	0.3611	0.5724	-	-	-	-
Bv2-1	854	0.9530	0.8663	0.3489	0.3468	1.7213	2.1699	0.7324
	769	0.4822	0.4953	0.2671	0.2893	0.8993	1.2060	0.5190
	512	0.1945	0.1835	0.1467	0.1283	0.4118	0.6255	0.2537
	256	0.0404	0.0072	0.0420	0.0458	0.1281	0.2236	0.0707
Bv2-2	816	0.8337	0.5628	0.2906	0.2343	1.9261	1.4194	0.2953
	734	0.4212	0.1585	0.1221	0.1220	0.8628	0.7493	0.2437
	490	0.1327	-0.0042	0.0503	0.0533	0.4166	0.3880	0.1183
	245	0.0232	-0.0293	0.0180	0.0069	0.1308	0.0992	0.0321
Bv2-3	757	1.2392	1.3314	0.0742	0.1061	2.8228	0.0000	0.8350
	681	0.7527	0.7590	0.0482	0.0689	1.2310	1.9256	0.4434
	454	0.3962	0.3926	0.0270	0.0268	0.7359	0.9728	0.0699
	227	0.0217	0.0317	0.0152	0.0124	0.0846	0.2659	0.0217
Bv2 Average	809	1.0086	0.9202	0.2379	0.2291	2.1567	1.1964	0.6209
	728	0.5520	0.4709	0.1458	0.1601	0.9977	1.2937	0.4020
	485	0.2411	0.1906	0.0747	0.0695	0.5214	0.6621	0.1473
	243	0.0285	0.0032	0.0251	0.0217	0.1145	0.1962	0.0415
Cv2-1	429	0.4848	1.0524	1.4197	-	-	-	-
	386	0.3644	0.8866	1.2282	-	-	-	-
	257	-0.0100	0.1265	0.1588	-	-	-	-
	129	-0.0110	0.0392	0.0468	-	-	-	-
Cv2-2	380	0.5566	0.8909	0.9506	-	-	-	-
	342	0.4100	0.7097	0.8004	-	-	-	-
	228	0.0002	0.1180	0.2059	-	-	-	-
	114	-0.0064	0.0279	0.0507	-	-	-	-
Cv2-3	496	0.2223	0.5591	1.0189	-	-	-	-
	446	0.1041	0.4010	0.8077	-	-	-	-
	298	-0.0149	0.0786	0.1230	-	-	-	-
	149	-0.0113	0.0290	0.0508	-	-	-	-
Cv2 Average	435	0.4212	0.8341	1.1297	-	-	-	-
	392	0.2929	0.6658	0.9454	-	-	-	-
	261	-0.0082	0.1077	0.1626	-	-	-	-
	130	-0.0096	0.0320	0.0494	-	-	-	-

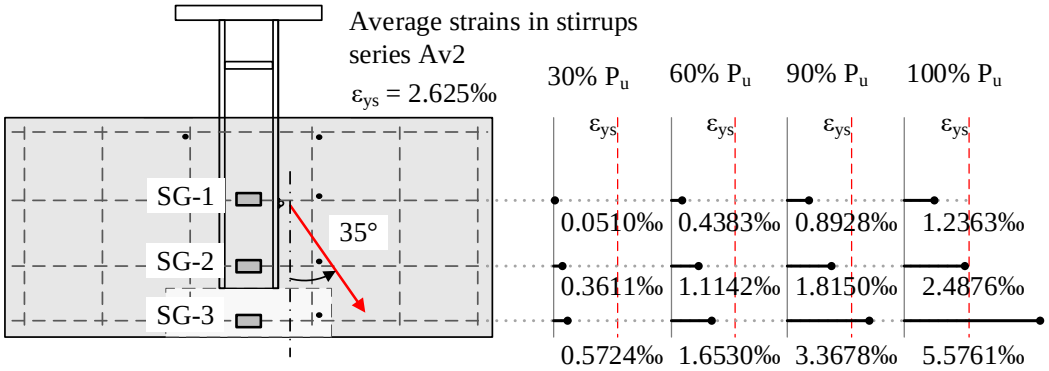


Fig. 5.37. Distribution of strains in the column push-out test specimen Av2.

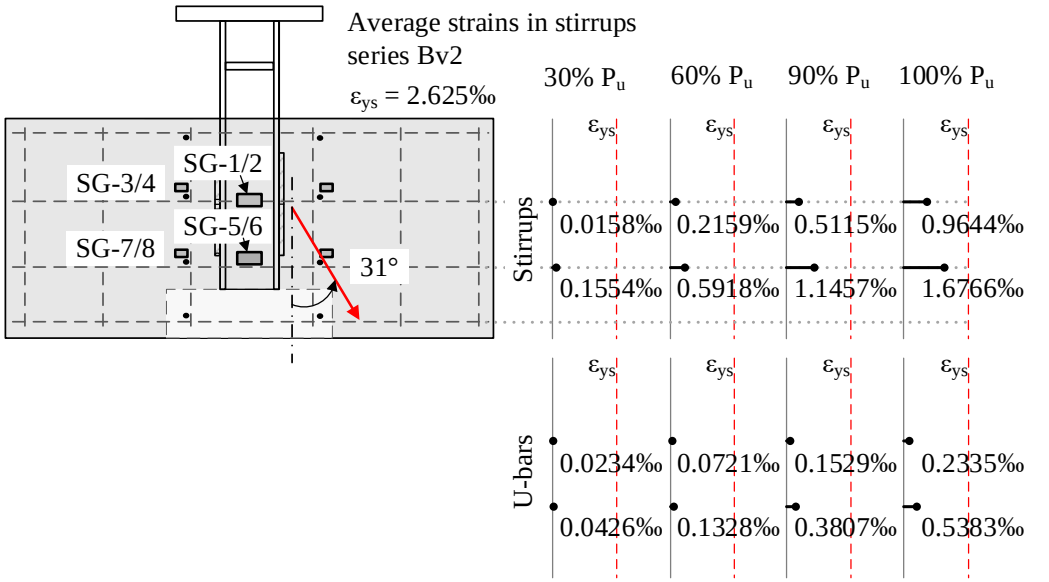


Fig. 5.38. Distribution of strains in the column push-out test specimen Bv2.

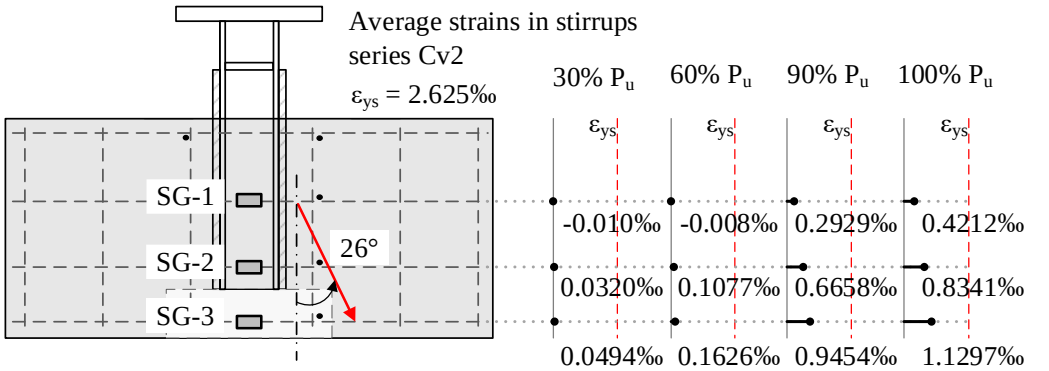


Fig. 5.39. Distribution of strains in the column push-out test specimen Cv2.

5.4.4.4. Displacements of concrete block

The displacements of walls in CoPOT tests were measured by the set of displacement transducers fixed to the supporting frame placed around tested specimens, see Fig. 5.22 and Table 5.4. The measured values were used to control the normal separation at the steel-concrete interface. During the tests of series 0v2 no displacements were measured. For series Bv2, no data is available due to reduced measurement equipment used for tests performed at the Technische Universität Kaiserslautern. Data

recorded during the tests of series Av2 and Cv2 are shown below in Fig. 5.40 and Fig. 5.41 respectively. Due to a small movement of the entire specimen as a rigid body, the measurements from two counter sides of the specimens (DT-5 and DT-7 according to Fig. 5.22) were summarised. Like this, the movement of the specimens was compensated. For the evaluation of normal separation, the summed values need to be divided by two in order to include a mean separation on one side of the steel profile.

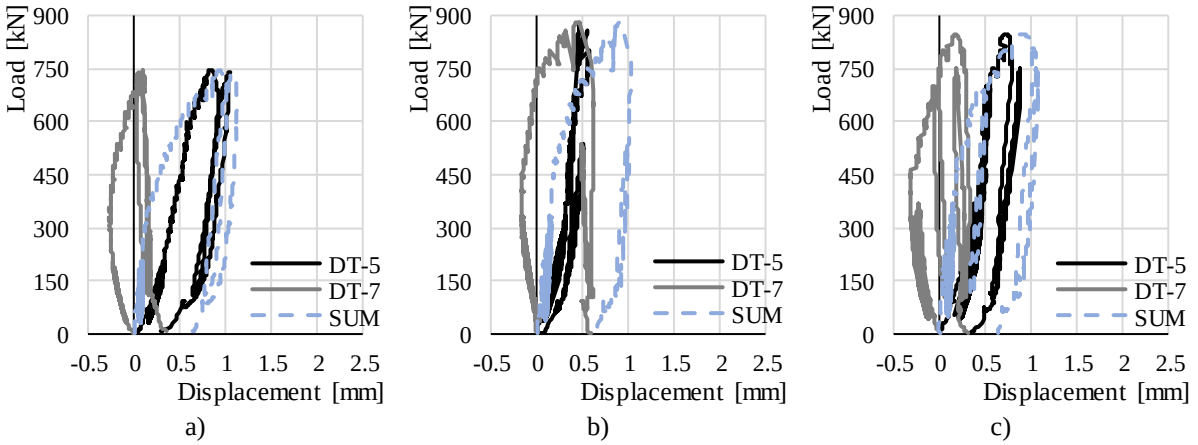


Fig. 5.40. Lateral displacement of the concrete block base in series with transversal shear connectors of CoPOT – a) specimen Av2-1, b) specimen Av2-2 and c) specimen Av2-3.

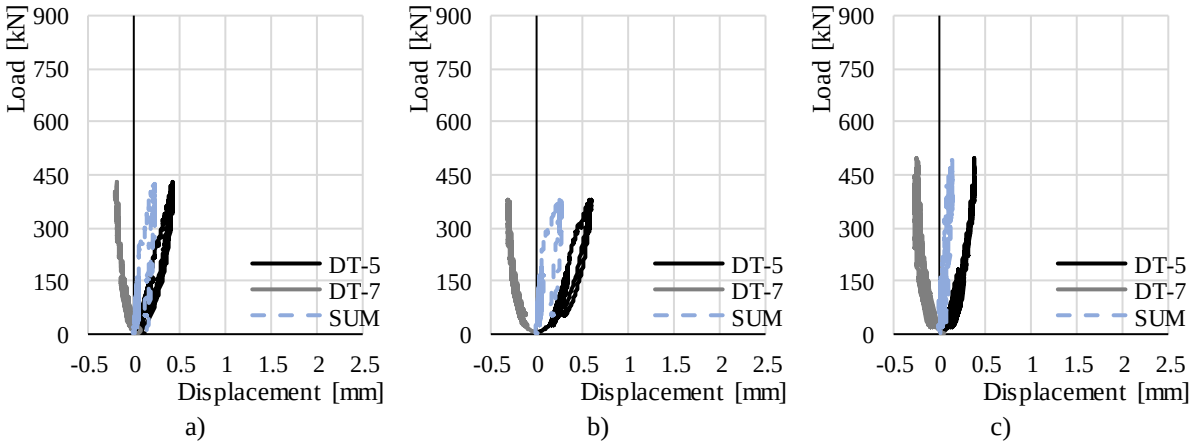


Fig. 5.41. Lateral displacement of the concrete block base in series with longitudinal shear connectors of CoPOT – a) specimen Cv2-1, b) specimen Cv2-2 and c) specimen Cv2-3.

The evaluation of the normal separation was made according to the procedure given in clause B.2.5(3) EN1994-1-1:2004 [58]. The aforementioned clause refers to the shear connectors composed of two separate elements, one to resist relative slip and the other to resist the normal separation. For the case of investigated flat shear connectors, the elements that prevented normal separation were stirrups around the embedded steel profiles. The defined condition for normal separation can be rewritten in Eq. 5.1, where the normal separation measured at 80% of the peak load should be smaller than half of the respective relative slip. A maximum mean displacement of the concrete block, thus normal separation, measured in the series Cv2 was smaller than 0.1 mm and smaller than 0.26 mm for the series Av2. The mean value of relative slip at load level corresponding to 80% Pu was 0.68 mm for the series Cv2 and 2.88 mm for the series Av2. By modifying the given condition in Eq. 5.1 to a more restrictive case,

where the maximum normal separation will be compared to the relative slip at 80% of the peak load, as described in Eq. 5.2, it can be observed that the introduced system with flat shear connectors satisfies the demand with a big reserve of capacity. The results are summarised in Table 5.14.

$$\delta_{n,u80\%} \leq 0.5 \cdot \delta_{l,u80\%} \tag{5.1}$$

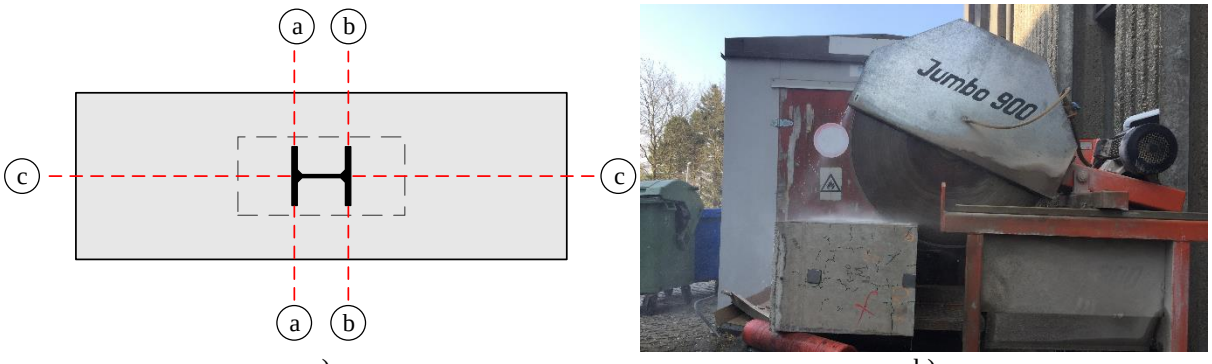
$$\delta_{n,u} \leq 0.5 \cdot \delta_{l,u80\%} \tag{5.2}$$

Table 5.14.
Verification of the normal separation measured in column push-out tests.

Specimen	$\delta_{l,u80\%}$ [mm]	$0.5 \cdot \delta_{l,u80\%}$ [mm]	$\delta_{n,u}$ [mm]	Verification (Eq. 5.2)
Av2-1	2.48	1.24	0.25	OK
Av2-2	2.99	1.49	0.23	OK
Av2-3	3.17	1.49	0.20	OK
Av2 mean	2.88	1.41	0.23	OK
Cv2-1	0.79	0.40	0.07	OK
Cv2-2	0.60	0.30	0.06	OK
Cv2-3	0.65	0.32	0.04	OK
Cv2 mean	0.68	0.34	0.06	OK

5.4.5. Observed failure pattern

The visual examination of the test specimen 0v2 showed no and for Cv2 only minor concrete damage, and the failure of the shear connection occurred locally at the steel-concrete interface by sliding. The specimens Av2 and Bv2 showed a significant crack pattern and therefore were opened with the concrete saw. The cutting pattern allowed the separation of the concrete encasement from the steel profile. The specimens have been cut in the planes of the flanges of steel profile (lines (a) and (b) in Fig. 5.42) and in the second step, in the plane of the web of steel profile (line (c) in Fig. 5.42).



a) b)

Fig. 5.42. Opening of the column push-out test specimens – a) cutting scheme and b) cutting process detail.

5.4.5.1. Reference specimen 0v2

In the reference tests (0v2), the forces from the steel profile to the concrete encasement had been fully transferred by steel-concrete bond. During the tests, no visible cracks developed at the concrete surfaces. A view from the bottom of the specimen, through the recess, showed that the steel profile slid downward without any surrounding concrete damage, see Fig. 5.43. The failure of the specimen occurred at the steel-concrete interface due to debonding. After reaching the ultimate load, the adhesive force transfer mechanism of bond vanished and the inelastic relative slip progress. A corresponding level of the residual strength was observed due to the remained Coulomb friction and the surface roughness friction between two relatively sliding materials. A detailed analysis of the bond behaviour of the respective materials has been conducted beforehand and described in Section 5.3.

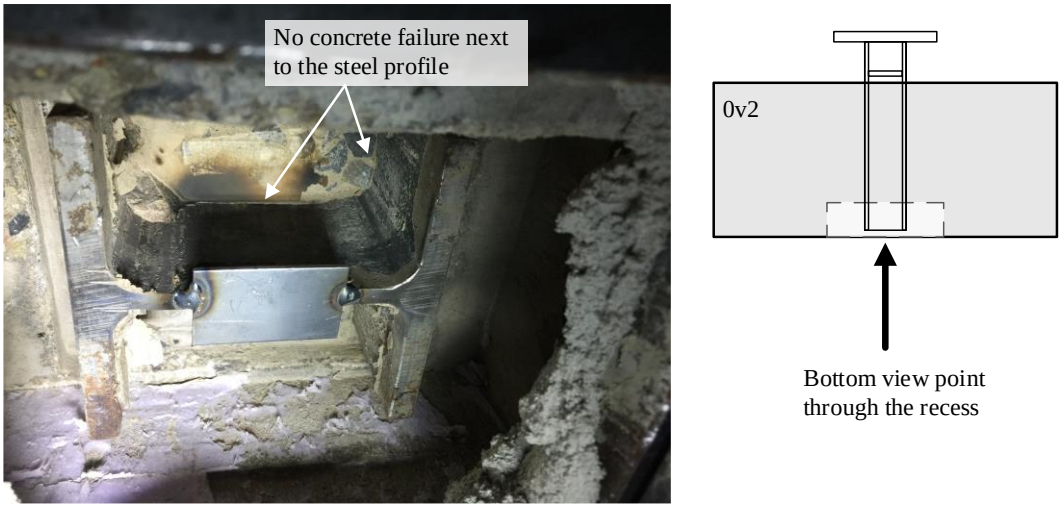


Fig. 5.43. Slide of steel profile in the test series 0v2 of CoPOT without mechanical shear connectors.

5.4.5.2. Specimen Cv2 with longitudinal connector

The failure pattern observed in the specimens Cv2 had a similar behaviour to the reference tests 0v2. The tested specimens and observed failure pattern are shown in Fig. 5.44 below.

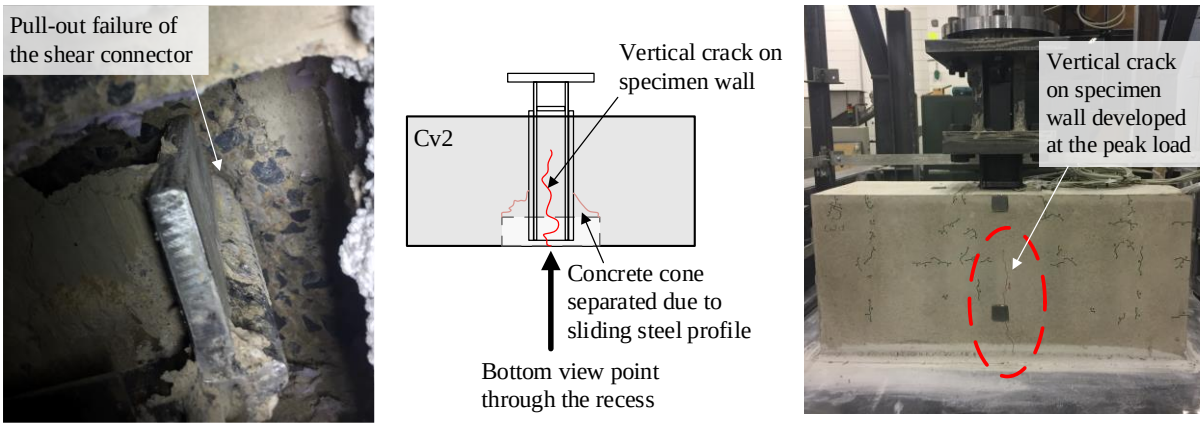


Fig. 5.44. Failure of specimen Cv2 of CoPOT with the longitudinal shear connectors – a) bottom view, b) scheme and c) detail of vertical crack on concrete surface.

The existence of the longitudinally welded rebars at the steel surface resulted in the additional rebar-type pull-out failure mechanism. At the concrete surface, a single vertical crack in the middle developed when the peak load was reached, see Fig. 5.44. This effect has been investigated for example by Bigaj [15] and Lundgren [114] for the embedded regular reinforcement bar. The steel profile slid downward and the failure of the specimen developed only at the interface. A minor concrete cone at the bottom of the connector followed the downward slide of the steel profile as shown in Fig. 5.44.

5.4.5.3. Specimen Av2 with transversal connector

The opened specimen Av2 with the transversal variant of the shear connector is shown in Fig. 5.45. The opening has been done according to the cutting lines (a) and (b) described in Fig. 5.42. It can be clearly observed that the failure of the specimens was subjected to cracks in the concrete under the applied shear connectors.

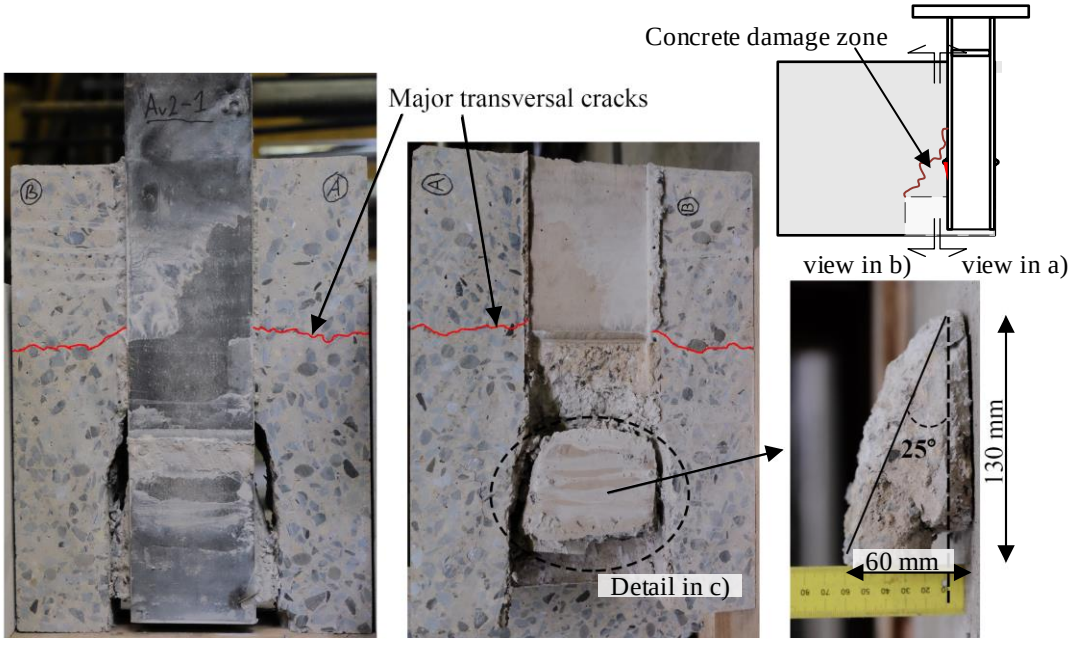


Fig. 5.45. Executed and opened specimen Av2 of CoPOT with the transversal shear connector – a) central part with steel profile, b) concrete encasement and c) separated concrete cone.

The major transversal cracks in the specimens, indicated in Fig. 5.45a and Fig. 5.45b, developed at the peak load and they represent the 38° oriented diagonal cracks developed at the concrete surface shown in Fig. 5.46. The concrete cone at the bottom of the steel profile separated due to the failure plane developed under 25° angle, see Fig. 5.45c, which corresponds to the development of the compression strut failure as explained in Fig. 5.47a and Fig. 5.47c. The failed zone around the shear connector is shown in Fig. 5.47b. A small portion of the concrete directly under the connector remained intact, which was related to the existence of a highly confined concrete area. The width and thickness of the confined area are directly related to the geometry of the shear connector. The applied transversal flat connectors had the length of 120 mm and diameter of 8 mm. The height of the confined area was 30 mm, which resulted in the shear plane under 15° towards the embedded steel profile.

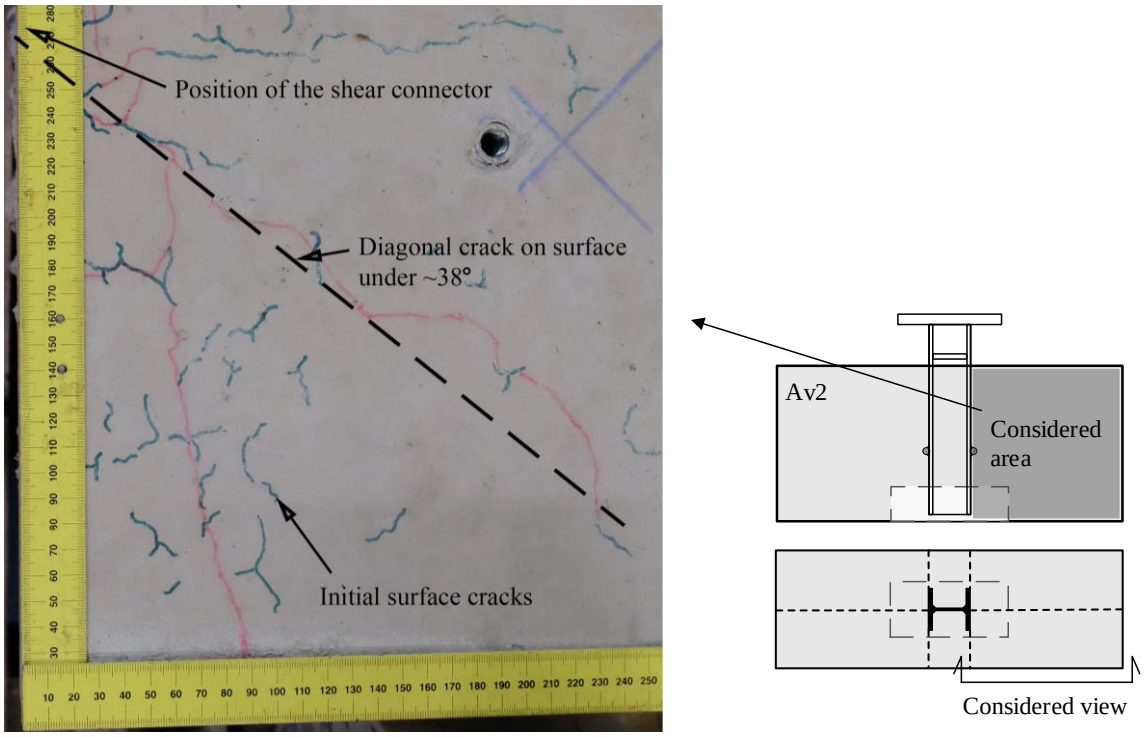


Fig. 5.46. Cracks at the surface of the specimen Av2 of CoPOT with the transversal shear connector.

Due to the geometry of the specimen, mainly the geometry of the recess at the bottom, the concrete failure occurred at angles of 0°, 25° and 50°, as shown in Fig. 5.47. The first zone, with the parallel plane (0°), is corresponding to the highly locally confined concrete area directly under the connector and has a corresponding length of 30 mm. The second zone, with the failure plane orientation of 25°, is corresponding to the broken out concrete cone as shown in Fig. 5.45c. The third failure zone, with 50° ended directly at the edge of the recess. The mid-cut of the concrete encasement (cutting line (c) in Fig. 5.42) revealed the mean failure plane developed behind the failure zones 2 and 3, described in Fig. 5.47a and Fig. 5.47c. The geometry of the implemented recess and the height of the failure zone 1, described in Fig. 5.47a and Fig. 5.47b, resulted in the inclination of the mean failure plane under 32°, which correlates to the diagonal crack in Fig. 5.46 and load dispersion angle from Fig. 5.37.

The failure of the specimen happened only in the concrete. The steel parts of the connection, which consisted of the rebar Ø8 mm and the respective weld, remained in a proper state. It can be concluded, that the resulting failure planes in the concrete block were strongly related to the specimen geometry and support conditions. In the same time, a minimum reinforcement ratio and size of the concrete encasement, refer to [53, 58, 62, 168, 169], is necessary for the development of the strut and tie model shown in Fig. 5.47a. The shear connection failure is described by the formulated shear plane under 15° in the zone directly under the connector, as shown in Fig. 5.47b. Simultaneously, the mean failure plane under 32°, shown in Fig. 5.47c, indicated the direction of the maximum compression stresses in the concrete encasement, compare to Fig. 5.47a. More details of the failure pattern identified from the opened specimens Av2 are given in Annex C.

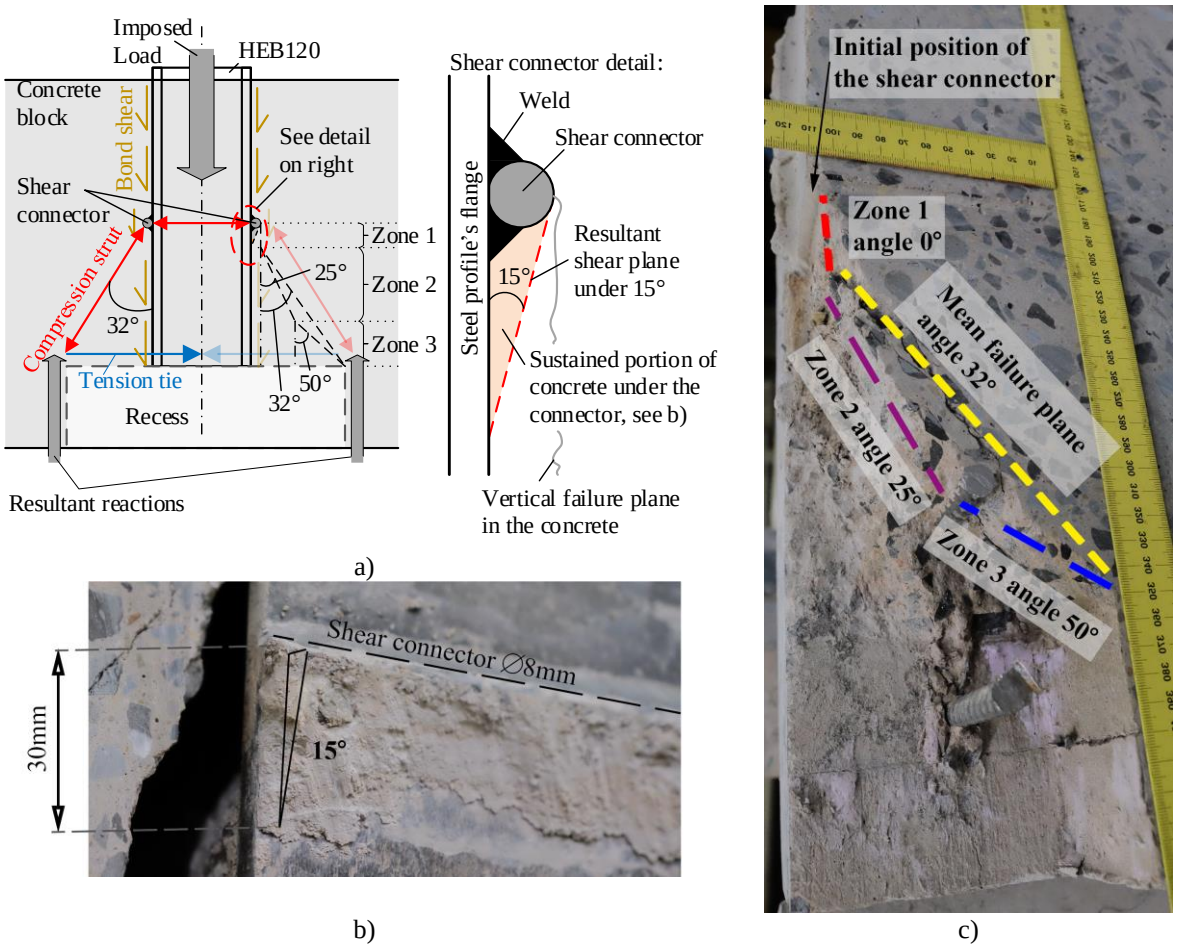


Fig. 5.47. Failure planes of the specimen Av2 of CoPOT with the transversal shear connector.

5.4.5.4. Specimen Bv2 with V-shaped connector

The opened specimen Bv2 according to the cut plane (a) and (b) (see Fig. 5.42) is shown in Fig. 5.48. Two main zones can be distinguished, the first zone, where the concrete failure developed between the arms of the connector in a parallel plane to the steel flange and the second zone, where the inclination of the failure plane reached 16°, see Fig. 5.48 and Fig. 5.50-5.51.

In the opening sections of the specimen Bv2, major transversal and vertical cracks can be identified, see Fig. 5.48a and Fig. 5.48b. The transversal cracks progressed to the concrete external surface where they showed an inclination of ~20° towards the vertical direction, see Fig. 5.48c. The aforementioned inclination angle of the surface crack correlates to the failure plane in zone 2 indicated in Fig. 5.48 and Fig. 5.50-5.51. The identified vertical cracks at the cut sections shown in Fig. 5.48 are related to the fact, that the shear connectors, due to their inclination, imposed two-directional reactions into the concrete block, see Fig. 5.49, where in the redistributed case between the two arms of the applied connector, a horizontally oriented tension tie developed.

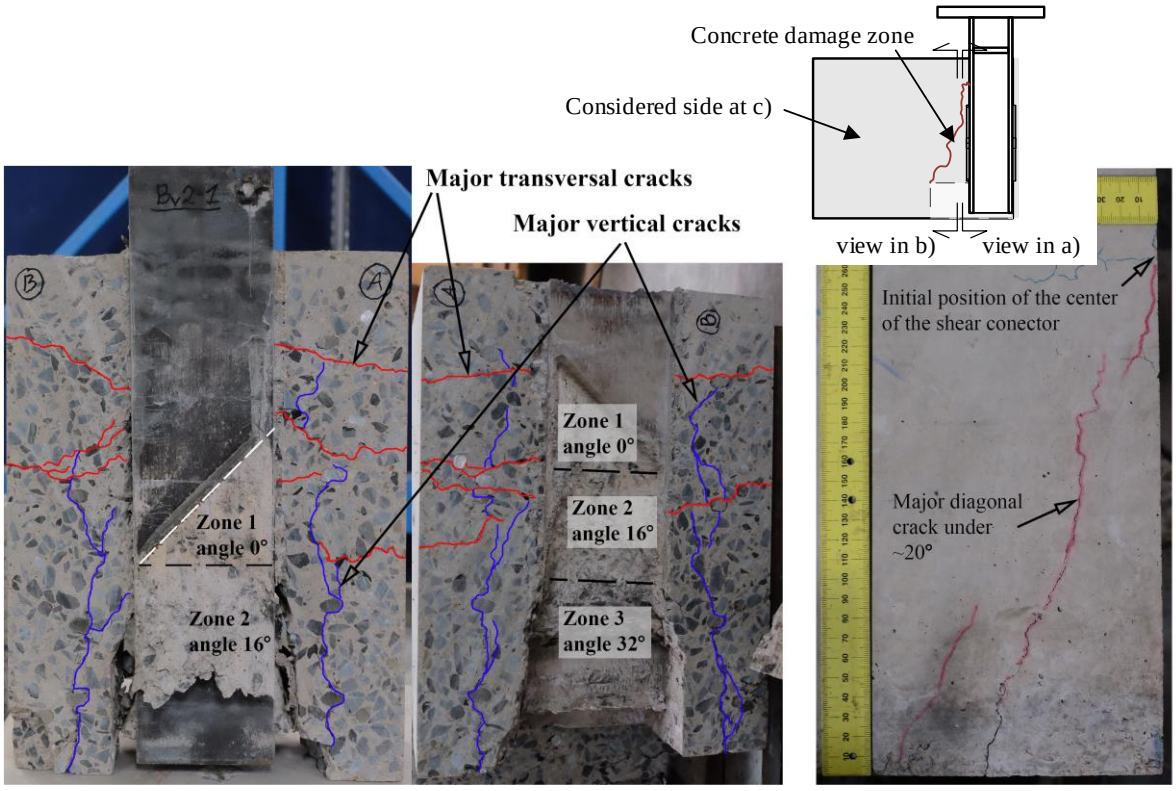


Fig. 5.48. Executed and opened specimen Bv2 of CoPOT with the V-shaped shear connector – a) central part with steel profile, b) concrete encasement and c) cracks at the surface of the specimen.

The inclination angle in the zone 2 is related to the global redistribution of the bearing forces between the arms of connector, which is described in Fig. 5.49. The existence of the zone 1 developed analogically to the zone 1 of specimen Av2, with the difference that the arms of the shear connector created a nearly perfect shear plane due to the small distance between them. The shear plane developed over the whole width of the connector due to the progressing development of the damage, starting from the connector's corner.

The failure detail of the specimen Bv2 is shown in Fig. 5.50 and Fig. 5.51. The correlation of two failure planes under 0° and 16°, to the failure planes from Fig. 5.48, can be identified. In addition, directly below the shear connector, an additional failure plane oriented under 32° had been observed. The development of the third failure plane was accompanied by the concrete cone separation due to the compression strut failure. The brake out of the concrete cone was related to the close localisation to the bottom of the specimen and to the existence of the recess. The mid-cut of the concrete encasement according to the cutting line (c) in Fig. 5.42, revealed that behind the 16° failure plane, diagonally oriented cracks developed, see Fig. 5.51b. Similar cracks are characteristic for the typical rebar pull-out failure [15, 114].

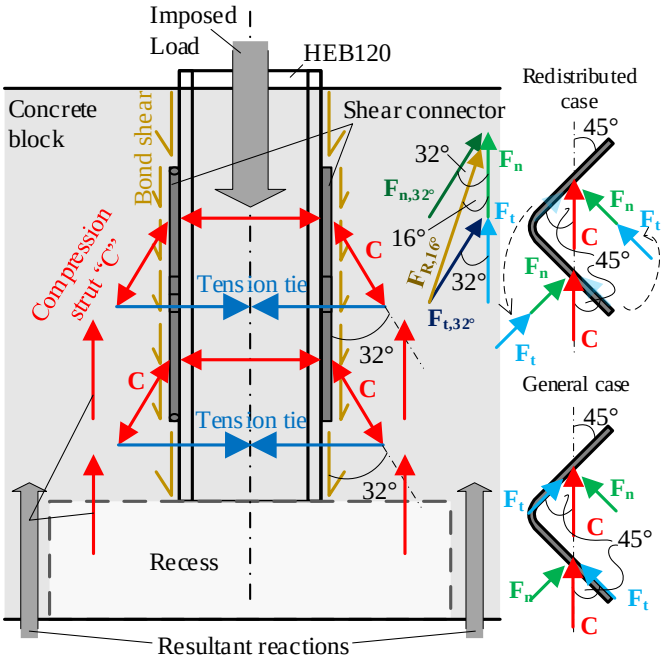


Fig. 5.49. Load decomposition scheme in the specimen Bv2 of CoPOT with the V-shaped shear connector.

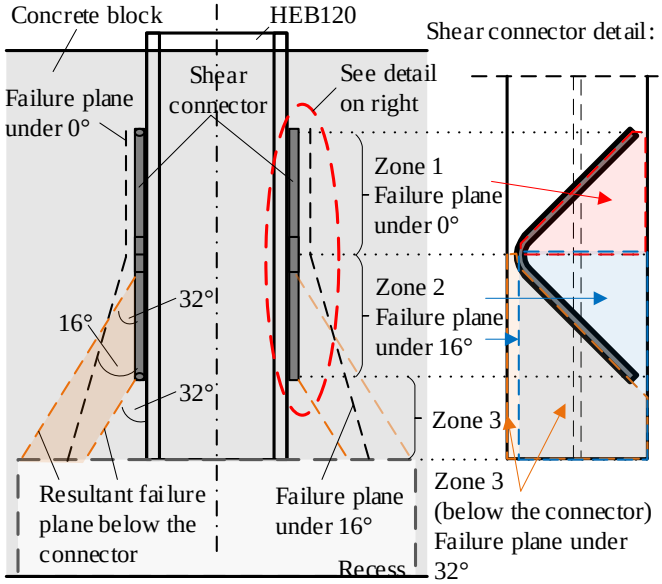


Fig. 5.50. Resulting failure planes in the specimen Bv2 of CoPOT with the V-shaped shear connector.

The shear connection resistance is related not to the resulting concrete cone break out but it is related to the local resistance of the confined concrete subjected to combined shearing and compression between the arms of the connector and the compression strut failure in the concrete encasement. Similar like for the connector Av2, an appropriate amount of stirrups and size of the concrete encasement is required in order to assure the development of the truss system described in Fig. 5.49. More details of the failure pattern identified for series Bv2 are given in Annex C.

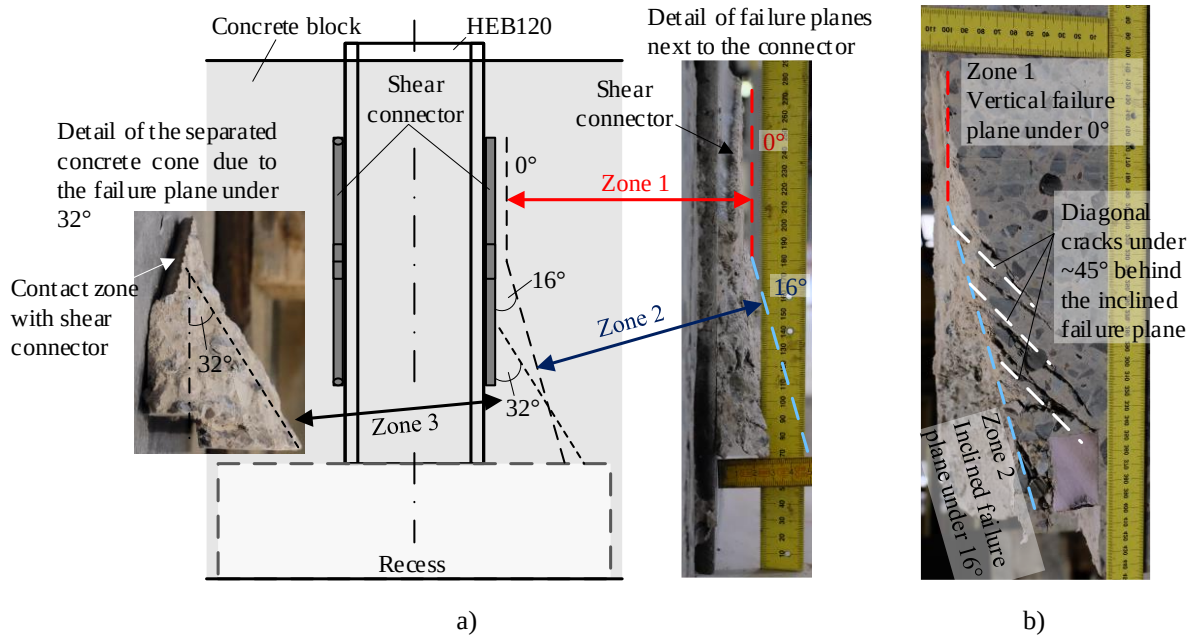


Fig. 5.51. Failure detail in the specimen Bv2 of CoPOT with the V-shaped shear connector – a) planes next to the connector and b) planes in the concrete (given view according to cut (c) in Fig. 5.42).

5.4.6. Discussion of the results

The selected representative load-slip curves for each CoPOT test series, including the reference test, are shown in Fig. 5.52. On the diagram, the load levels corresponding to the 90% of the respective peak loads are marked. The intersection points between the load-slip curves and the respective 90% peak load lines are corresponding to slip values δ_1 and δ_2 given in Table 5.12. The width of the 90% line between the intersection points, before and after the failure, indicates the plasticity zone of the shear connection. It can be clearly observed that the V-shaped flat shear connectors (Bv2) reached a high level of the plasticity plateau in terms of a slip capacity (10.39 mm) and in comparison to series Av2 (2.16 mm), the plastic capacity is nearly 5 times bigger. However, for both test series, the ductility requirement defined in EN 1994-1-1:2004 [58] as a slip capacity of 6 mm (indicated in Fig. 5.52 as the red vertical dashed line) is satisfied. In Fig. 5.52, it can be observed that each load-slip curve, besides series Cv2, after exhibiting a failure converged to a common value in the range of 65-100 kN, which corresponds to the pure surface roughness friction force transfer mechanism at the plain steel-concrete interface. In the series Cv2, the surface roughness friction mechanism refers to the sliding connector on the concrete surface, thus, the load-bearing resistance is heavily amplified to the level of approximately 300 kN. A similar effect is not recognised in the series Bv2 due to a significant concrete cone brake out and separation between the connector and concrete.

In Fig. 5.53, a close view on the first initial 10 mm of the load-slip curves shown in Fig. 5.52 is given. From the zoomed diagram, it can be observed that specimens from series Cv2 and Bv2, which benefit from the connector-concrete bond phenomenon, reached a much higher stiffness than the specimen from series Av2. In the other hand, in the initial response of the specimen Av2, the pure plain steel-concrete

bond part can be clearly distinguished, where after the adhesive part failure, the mechanical bearing action contributed. In the result, the increased load-bearing capacity was obtained but the stiffness of the connection was reduced due to the movement of the force transfer from one mechanism to the other.

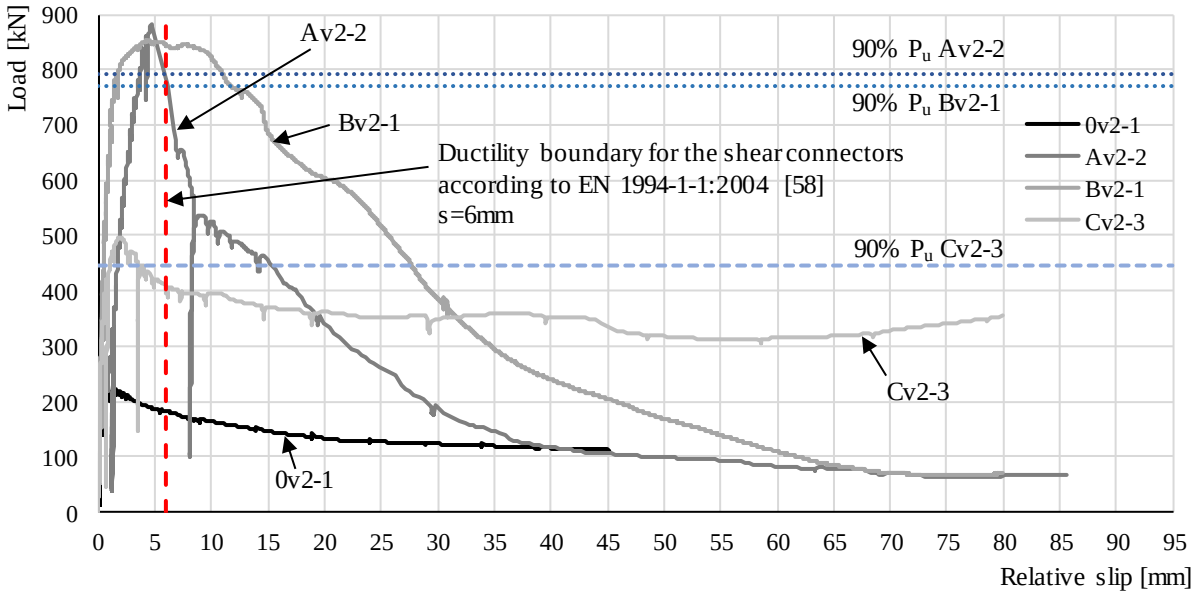


Fig. 5.52. Comparison of the load-slip responses from column push-out test.

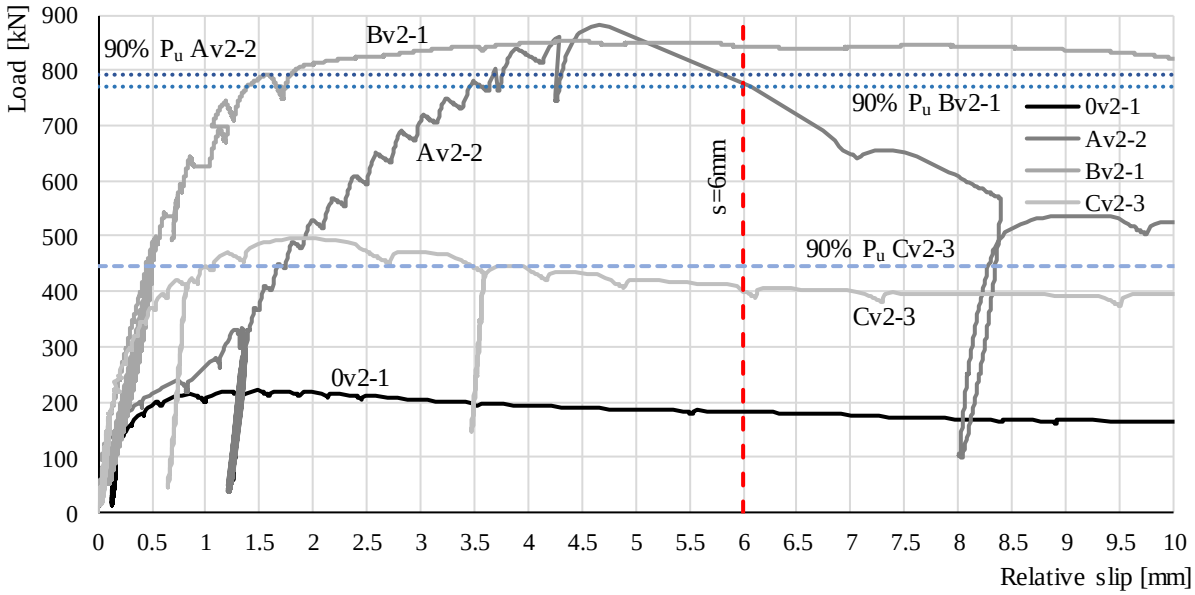


Fig. 5.53. Comparison of the initial load-slip responses from column push-out test.

Based on the analysis above, it can be observed that the V-shaped variant of flat shear connector brings the best compromise and benefit the most from the simultaneously activated load-transferring phenomena – chemical adhesion, friction and mechanical bearing action. In terms of overall performance of the shear connection, the transversal variant of proposed flat shear connectors, besides its brittle failure character and reduced stiffness, showed excellent load-bearing properties in comparison to the economical aspect and satisfied the ductility requirement of 6 mm of slip. In the result, both solutions can be defined as a feasible for application. However, by neglecting the economy aspect, which

is impossible to be assessed accurately at this stage of research, the V-shaped variant brings the best performance from the developed and characterised flat shear connectors.

The proper evaluation of the pure mechanical shear connection load-bearing capacity requires excluding the part of the forces transferred by the steel-concrete bond. According to the measured strains in the reference tests 0v2 without any mechanical shear connectors, a rough estimation of the distribution character of the bond strength over the embedded area can be done. Based on the records from strain gauges given in Fig. 5.29, a visual representation of the resulting stresses over the steel profile at the load level equal to the 90% of the peak load is given in Fig. 5.54 below. According to the evaluated stresses from the measured strains, a linear distribution of stresses over the embedment length can be assumed for the further consideration. A linear distribution of the stresses over the embedment length results in the uniformly distributed bond strength over the entire contact area at the steel-concrete interface. In the result, an assumption was taken that a mean bond strength value can be evaluated by dividing the transferred force by the respective contact area. Roeder et al. [157] made a similar conclusion in his research. The assumed concept had been verified in the numerical simulations described later in Section 5.5. The assumed simplified concept about uniformly distributed bond strength had been applied in the analytical model for the flat shear connectors resistance, which is described in Section 5.6.

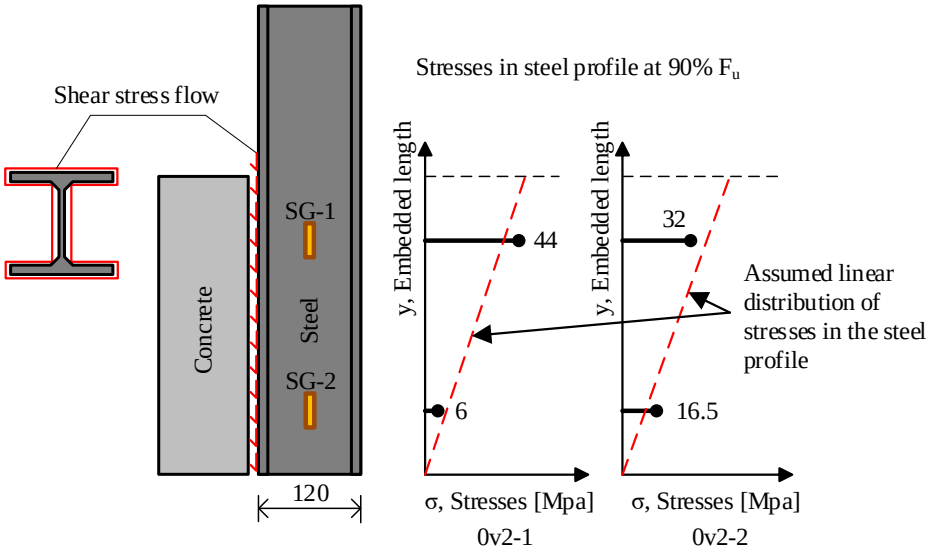


Fig. 5.54. Distribution of stresses over the embedment length in the reference specimens 0v2 of CoPOT.

5.5. Numerical simulations

Conducted numerical finite element simulations were performed in the FE code Abaqus® [174] of Dassault Systèmes Simulia Corp. with the aim of investigating precisely the load flux and damage sequence in the CoPOT tests. Created models reflected the experimental specimens and test layout. In order to extend the investigation on flat shear connectors by numerical results, a precise calibration of simulations according to the obtained beforehand test results was essential. Under the calibration, the following aspects were considered: (i) load-slip behaviour, (ii) failure pattern, (iii) cracking of concrete (damage) and (iv) quasi-static character of simulations when the Abaqus/Explicit solver was used. The sequence of analysed simulations as shown in Fig. 5.55 (0v2→Cv2→Av2→Bv2) allowed for a good understanding of the occurring phenomena and behaviour of specimens.

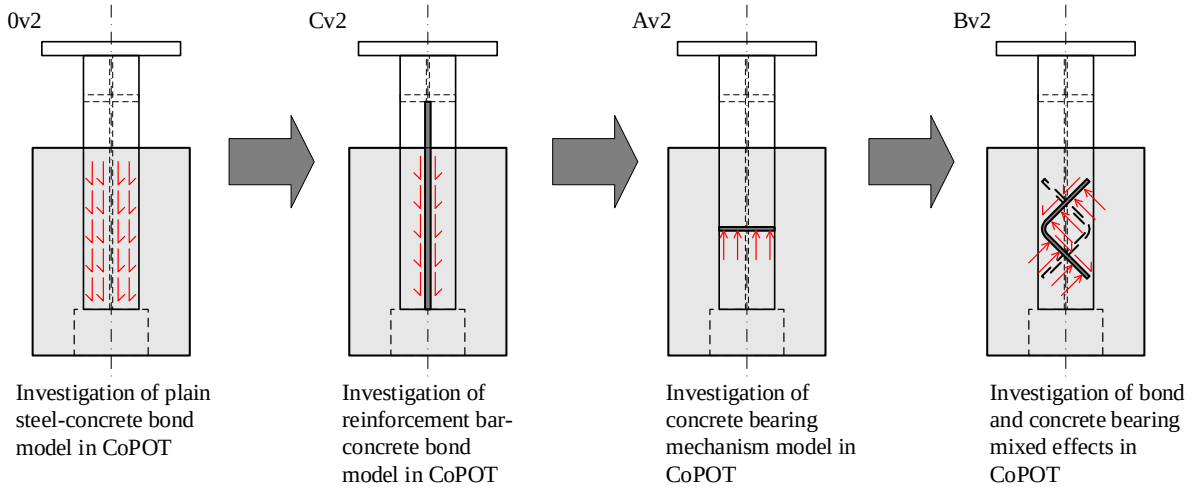


Fig. 5.55. Sequence of the performed numerical simulations for the flat mechanical shear connectors.

The developed numerical model of steel-concrete bond described in Section 5.3 and Annex B had been adapted for the simulations of CoPOT tests. The linear model based on traction-separation law was extended to a complex model incorporating the non-linear behaviour after the debonding, which includes a gradual release of bond strength with the progressing slip and remained load-bearing capacity due to the surface roughness phenomenon observed in the experimental campaign. Moreover, simultaneously to plain steel-concrete bond, the connector-concrete bond had been defined and implemented in the analogous way.

The Abaqus/Explicit solver was employed to simulate the test procedure and care had been taken to keep the simulations in the quasi-static state. An exemption was made for the specimen Cv2, where the Abaqus/Standard solver was implemented. The exemption was enforced due to the identified problem of non-realistic finite element distortion due to the defined high-strength cohesion relation at the connector-concrete interface. In another words, a high occurring tangential cohesive shear resistance at the connector-concrete interface, which reflected the reinforcement bar-concrete bond, imposed in the dynamic explicit simulations unrealistic high finite element distortions of the concrete encasement due

to the dynamic effects. A dynamic character of the explicit simulations of specimen Cv2 lead to the hourglassing of finite elements due to multiple small dynamic impacts at the interface. In the result, a strong connection between two relatively sliding parts imposed a non-realistic loss of stability in weaker finite elements lying at the contact surface in the concrete part. In contradiction to the other specimens, the behaviour of the specimen Cv2 was heavily related to the above-mentioned effect due to the major force transferring mechanism related to the connector-concrete bond. The chosen Abaqus/Standard solver tracked more accurately the cohesion damage at the interface due to the assured forces equilibrium and prevented the unrealistic progress of stability loss in the concrete part.

Application of two different solvers for the CoPOT simulations resulted in the modelling of bond phenomenon in two ways: (i) with the usage of cohesive elements in Abaqus/Explicit simulations and (ii) with the usage of contact properties in Abaqus/Standard simulations. The reasoning, explanation and differences between two methods are described later in Section 5.5.3.

5.5.1. Geometry and mesh

The modelled geometry reflected the geometry of tested specimens described in Section 5.4 and shown in Fig. 5.17 and Fig. 5.20. The embedded steel profiles, the concrete blocks and the applied shear connectors were modelled as solid bodies with the respective dimensions. The rounding between the web and flanges of the steel profile was simplified by the fazing length equal to 0.67 times radius of the original rounding. By removing the non-linear parts of the steel profile cross-section, the efficiency of the numerical simulations was greatly increased. The solid bodies of applied flat shear connectors were merged together with the steel profile part but different section assignments remained. This allowed varying material properties in the same part. The space for embedded steel profile in the concrete block part had been cut in the assembly module directly from the geometry of steel part. In the result, matching surfaces at the interface were obtained. The reinforcement bars were modelled as one-dimensional beam elements merged into one part and creating the entire reinforcement cage part. Finally, all the created parts were assembled according to the defined geometry of the specimens in CoPOT test campaign as shown in Fig. 5.56. Due to the geometry of the CoPOT specimens Bv2 and arrangement of the applied V-shaped flat shear connectors, no symmetry or anti-symmetry boundary conditions could be applied in the numerical simulations. In the result, all the specimens were fully modelled.

Created parts of the steel profile with shear connectors and the concrete block were discretised with solid 8-node brick finite elements C3D8R. The second-order accuracy for deformation of finite elements was enabled in the concrete part. The applied linear finite elements with reduced integration are the recommended elements from the Abaqus library [174] for the usage in solid structures subjected to significant deformations and contact-based problems. However, a good accuracy of results requires a sufficiently refined mesh. In order to increase the accuracy with more coarse meshes, the quadratic finite elements with reduced integration C3D20R are suggested by Abaqus manual [174]. Taking into account

the simulation efficiency and optimisation of the simulation computing power and time, the linear quadrilateral elements with refined mesh brought better results. The reinforcement bars were discretised with 1D quadratic beam elements B32. The beam elements were selected for the reinforcement bars of the CoPOT specimens, instead of typical truss elements, in order to include effects of significant shear forces developed in the specimens due to the occurred load transfer.

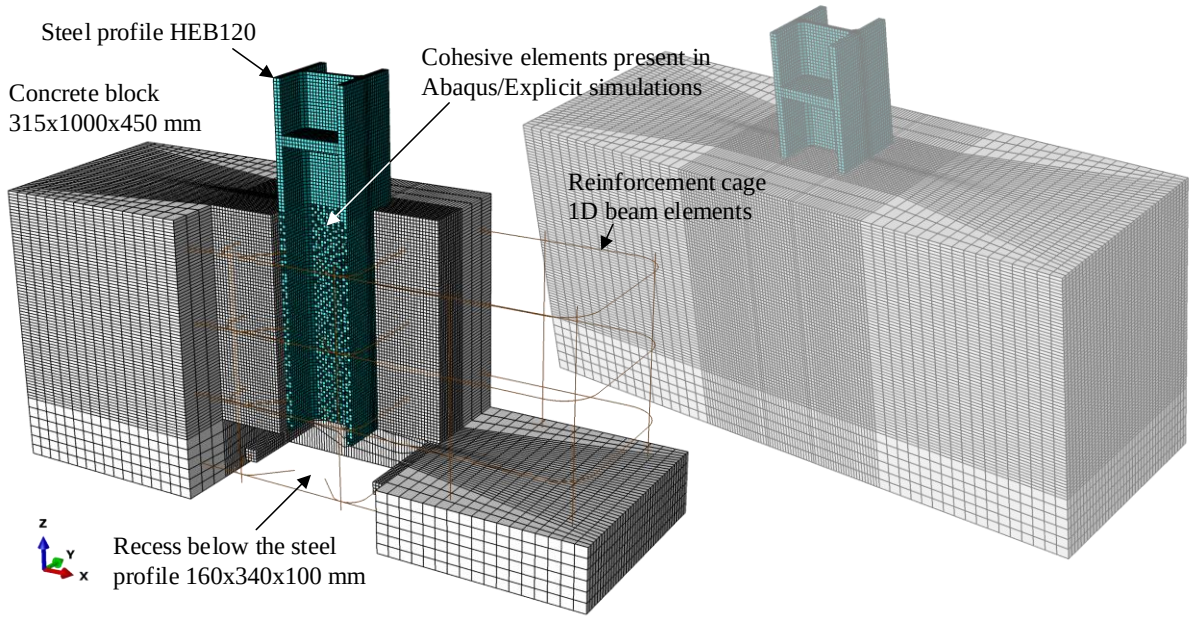


Fig. 5.56. Numerical model of the reference specimen 0v2 of CoPOT.

The size of the applied mesh for the steel part with included flat shear connectors was approximately 5 mm, where for the specimen Cv2, the size was increased to 10 mm in order to increase the simulation efficiency with no loss of accuracy. The concrete part was globally discretised with a mesh of 20 mm, where in the zone next to the embedded steel profile, including the embedment height, the size of mesh was adjusted to the mesh size of the steel part. The reinforcement bars were globally discretised with the mesh of 20 mm, where rounding in stirrups were refined to 5 mm. The details of meshes and assembly for each numerical model with applied flat shear connectors are shown in Fig. 5.57-5.59. It can be observed that both meshes, on the steel part and on the concrete part, had coinciding nodes. The cohesive properties of steel-concrete bond are implemented to the nodes of finite elements, therefore, the coherent meshes created good conditions for the accurate analysis. The size of mesh in the contact zone was related to the cohesive contact length, which required sufficiently small elements [186].

In Abaqus/Explicit simulations, cohesive elements were applied between the contact surfaces of plain steel and concrete, as well as between connector and concrete surfaces. Cohesive elements allow modeling the interaction between two surfaces in the form of a zero-thickness material. The mesh of applied cohesive elements consisted of the COH3D8 finite elements, which were created as a zero offset from the mesh of the steel part. The definition of the cohesive finite elements is analogous to above-described C3D8R elements but a full integration is used. More details are given in Section 5.5.3.

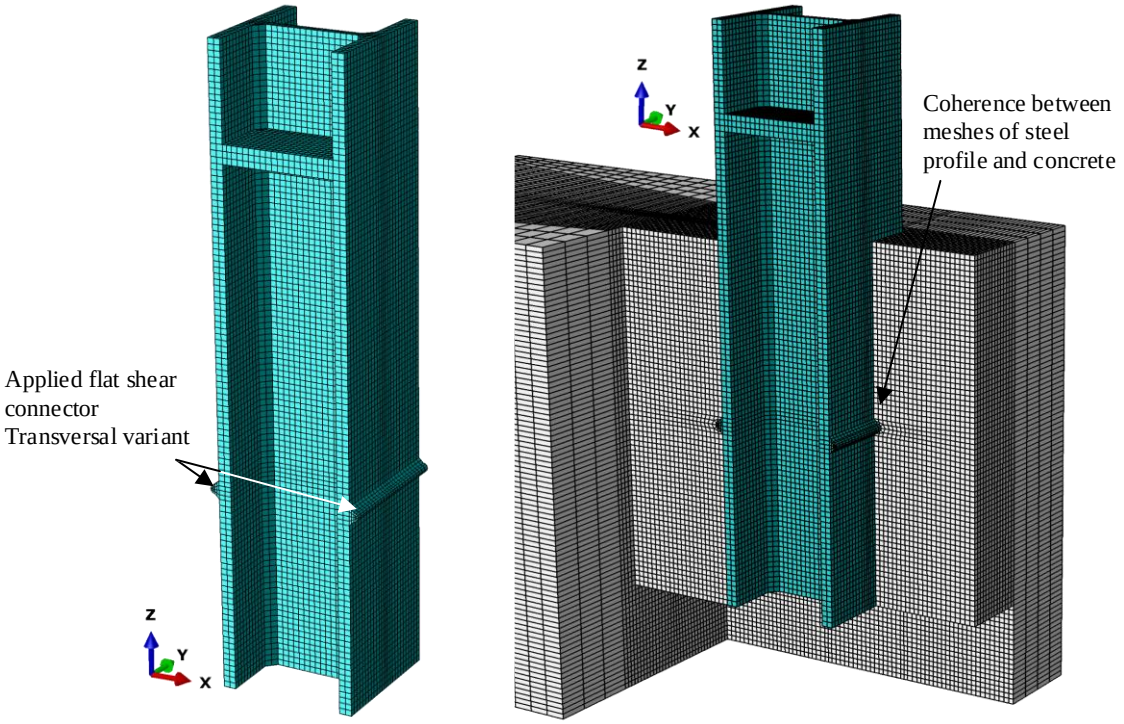


Fig. 5.57. Numerical model of CoPOT specimen Av2 with the transversal shear connector – a) steel profile with shear connector and b) embedment detail.

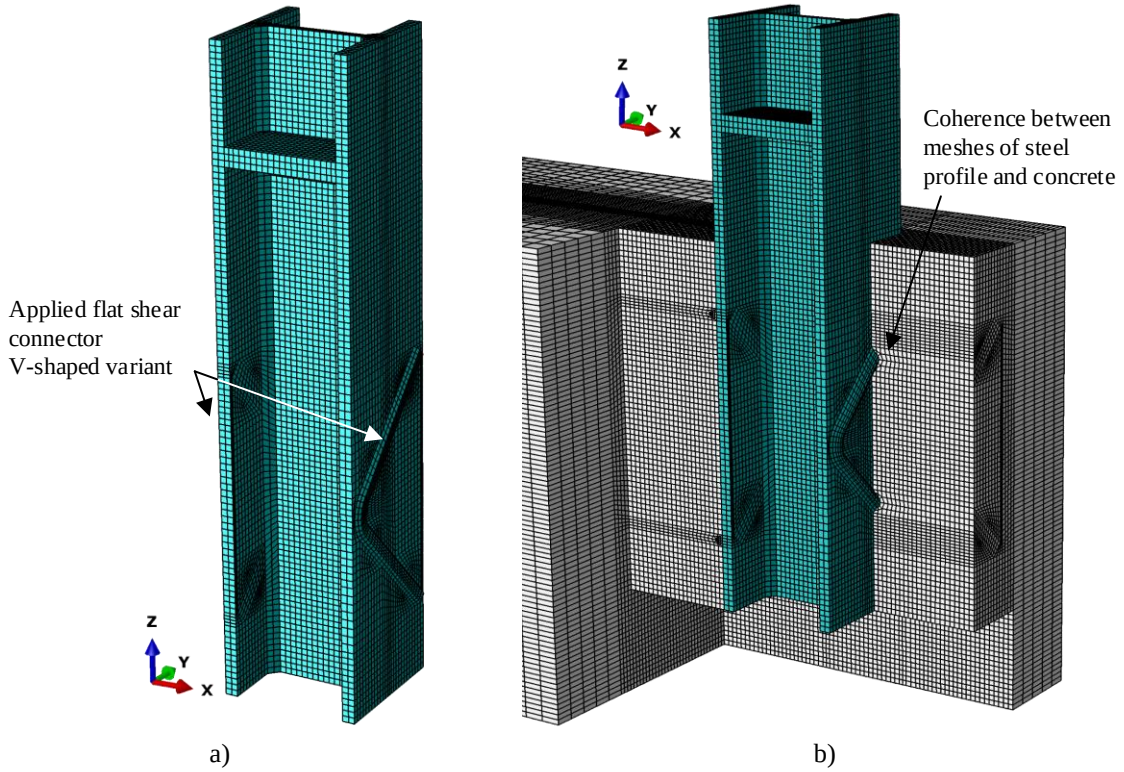


Fig. 5.58. Numerical model of CoPOT specimen Bv2 with the V-shaped shear connector – a) steel profile with shear connector and b) embedment detail.

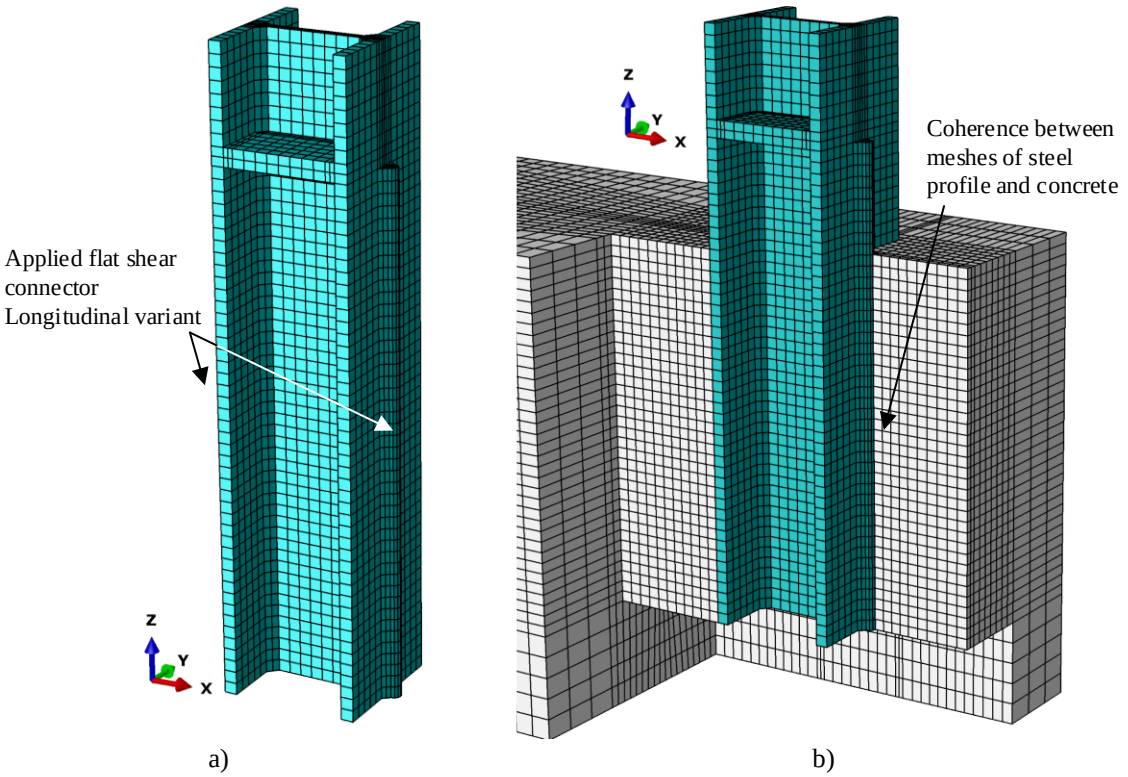


Fig. 5.59. Numerical model of CoPOT specimen Cv2 with the longitudinal shear connector – a) steel profile with shear connector and b) embedment detail.

5.5.2. Material laws

The applied material laws were based on the European design codes EN 1993-1-1:2005 [55] for the structural steel, EN 1992-1-1:2004 [53] for the reinforcement steel and fib ModelCode 2010 [62] for the concrete. Experimental material tests, which were performed in parallel, defined the respective input parameters. The measured material properties are given in Table 5.9-5.11.

5.5.2.1. Structural steel

The applied material law for the structural steel consisted of elasto-plastic linear material law, where the effects of strain hardening and damage were considered. The effect of steel damage included only the reduction in the material strength due to an excessive elongation and change of the section shape due to the defined Poisson's ratio. The stiffness remained unchanged after exhibiting the damage and necking effects were not considered. The input data was based on the performed coupon tests according to ISO 6892-1:2009 [80] and the obtained results are presented in Table 5.9. The applied stress-strain relation was identical for all specimens and it is shown in Fig. 5.60. A summary of the implemented parameters in Abaqus is given in Table 5.15. The values of mass density and Poisson's ratio were based on EN 1991-1-1:2002 [52] and EN 1993-1-1:2005 [55] respectively. In order to reflect the realistic behaviour of steel material, the applied stress-strain curve consisted of horizontal part at the ultimate strength level, which was calibrated based on the experimental material tests.

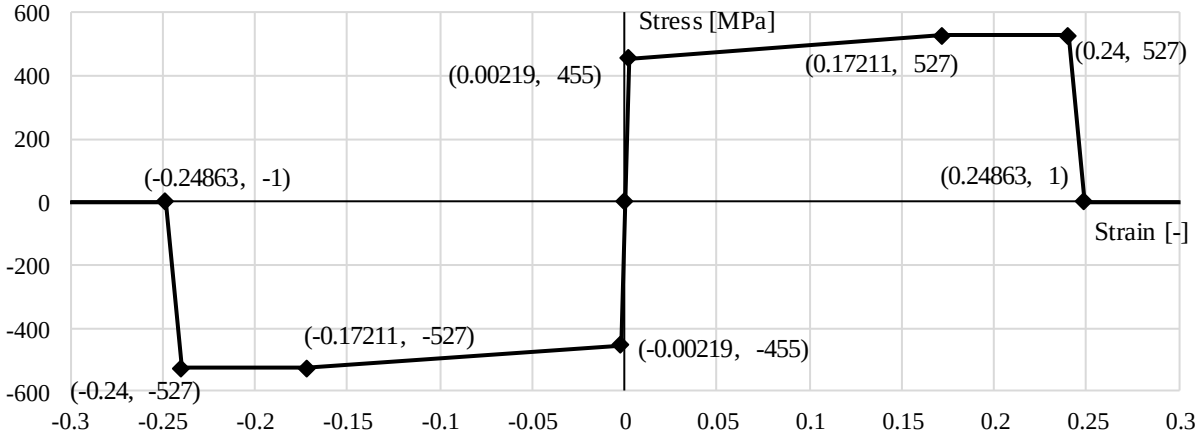


Fig. 5.60. Material law for the structural steel used in numerical simulations of column push-out tests.

Table 5.15.
Properties used to define the material law of structural steel in numerical simulations of CoPOT.

Structural Steel Grade S355					
Behaviour	Density	Elastic - Isotropic		Plastic - Isotropic	
Input number	Mass Density ρ	Young's Modulus E	Poisson's Ratio ν	Yield Stress σ_p	Plastic Strain ε_p
	[tonne/mm^3]	[MPa]	[-]	[MPa]	[-]
1	7.85E-009	207827	0.3	455	0
2	-	-	-	527	0.172105
3	-	-	-	527	0.24
4	-	-	-	1	0.248627

5.5.2.2. Reinforcement steel

The material law of reinforcement bars was analogous to the material law of steel part but with individual input data from the experimental material tests of reinforcement steel. The measured properties of three different diameters of the applied bars are given in Table 5.10. The applied stress-strain relationships in numerical simulations are shown in Fig. 5.61, where the summary with input data is given in Table 5.16. Flat shear connectors had modelled no damage in order to compensate the observation from the tests of not damaged shear connectors.

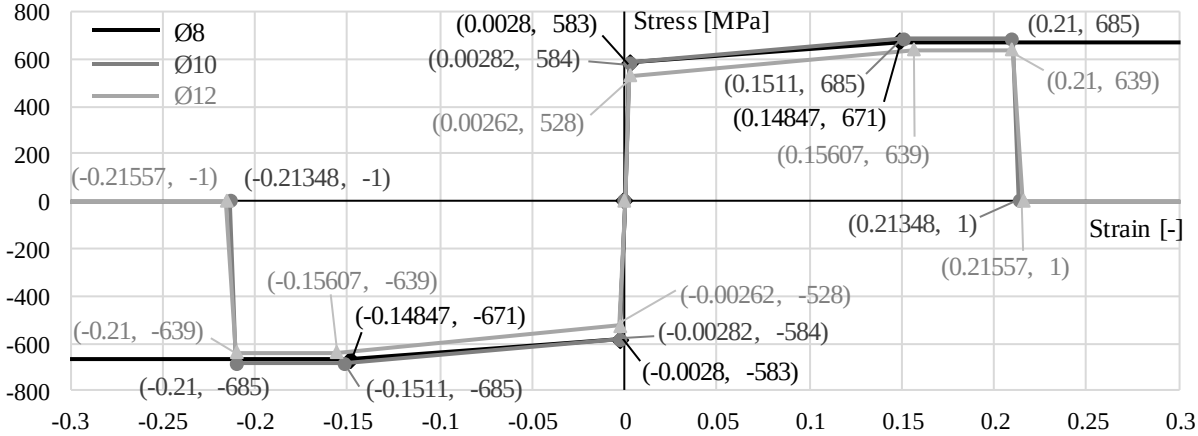


Fig. 5.61. Material law for the reinforcement steel used in numerical simulations of column push-out tests.

Table 5.16.
Properties used to define the material law of reinforcement steel in numerical simulations of CoPOT.

Reinforcement Steel Grade B500B					
Behaviour	Density	Elastic - Isotropic		Plastic - Isotropic	
Input number	Mass Density ρ	Young's Modulus E	Poisson's Ratio ν	Yield Stress σ_p	Plastic Strain ε_p
	[tonne/mm^3]	[MPa]	[-]	[MPa]	[-]
Diameter Ø8					
1	7.85E-009	208478	0.3	583	0
2	-	-	-	671	0.148472
Diameter Ø10					
1	7.85E-009	207269	0.3	584	0
2	-	-	-	685	0.151103
3	-	-	-	685	0.21
4	-	-	-	1	0.213483
Diameter Ø12					
1	7.85E-009	201109	0.3	528	0
2	-	-	-	639	0.156072
3	-	-	-	639	0.21
4	-	-	-	1	0.215571

5.5.2.3. Concrete

For the concrete part, the Concrete Damaged Plasticity (CDP) model of the Abaqus material library [174] was taken with the plasticity parameters Dilation Angle=25°, Eccentricity=0.1, fb0/fc0=1.16, Kc=0.667 and Viscosity Parameter=0.0001, according to the work of Kmiecik et al. [102] and Szczecina et al. [180]. The input parameters base on the concrete compression material tests performed during test campaign, see Table 5.11, and fib ModelCode 2010 [62].

The applied CDP material law for concrete is a plasticity-based non-linear elasto-plastic continuum damage model for quasi-brittle materials, where the Drucker-Prager plastic flow hyperbolic function and yield function proposed by Lubliner et al. [113] with modifications proposed by Lee and Fenves [109] are implemented and described in Eq. 5.3 and Eq. 5.4 respectively. The CDP is the recommended material law for the reinforced concrete due to its plasticity-based nature, where the modelled material is losing its stiffness with progressing damage, thus, by reaching the yielding criterion. This behaviour supports well the existence of reinforcement bars in the concrete. The CDP material law can reflect well the combined elastic/inelastic behaviour of concrete with inclusion of damage by defining the specific uniaxial compression and tension behaviour and transposing it to the multiaxial stress state with respect to the above-mentioned plastic flow and yielding functions. The damage after reaching the yielding criterion is defined as the relative ratio of the occurring stresses to the material resistance. The cyclic loading behaviour and stiffness degradation were controlled by the stiffness recovery factors used to define the stiffness degradation level after unload from one state, compression or tension, to the other.

$$\dot{\boldsymbol{\varepsilon}}^{\boldsymbol{pl}} = \dot{\lambda}\frac{\partial G(\bar{\boldsymbol{\sigma}})}{\partial \bar{\boldsymbol{\sigma}}} \quad \text{and} \quad G = \sqrt{(\epsilon\sigma_{t0}\tan\psi)^2 + \bar{q}^2} - \bar{p}\tan\psi \tag{5.3}$$

$$F(\bar{\boldsymbol{\sigma}}, \bar{\boldsymbol{\varepsilon}}^{\boldsymbol{pl}}) = \frac{1}{1-\alpha}\left(\bar{q} - 3\alpha\bar{p} + \beta(\bar{\boldsymbol{\varepsilon}}^{\boldsymbol{pl}})\langle\hat{\bar{\sigma}}_{max}\rangle - \gamma\langle-\hat{\bar{\sigma}}_{max}\rangle\right) - \bar{\sigma}_c(\bar{\varepsilon}_c^{pl}) \leq 0 \tag{5.4}$$

Where, the explanation of the above-described functions is given in Abaqus manual [174].

The uniaxial behaviour of concrete was evaluated according to fib ModelCode 2010 [62] and based on the experimentally obtained values of concrete compression strength. The applied respective stress-strain relations are described in Eq. 5.5 and in Eq. 5.6-5.9 for compression and tension respectively. The concrete confinement effect has been included by substituting the respective values by the confined values calculated according to fib Model Code clause 7.2.3.1.6 [62]. The elasticity properties of the concrete were defined by the values of Young's modulus and Poisson's Ratio. The applied elastic behaviour of concrete consisted of isotropic linear elastic law based on the Hooke's law for three dimensional problems.

$$\frac{\sigma_c}{f_{cm}} = -\left(\frac{\frac{E_{cm}}{E_{c1}} \cdot \frac{\varepsilon_c}{\varepsilon_{c1}} - \left(\frac{\varepsilon_c}{\varepsilon_{c1}}\right)^2}{1 + \left(\frac{E_{cm}}{E_{c1}} - 2\right) \cdot \frac{\varepsilon_c}{\varepsilon_{c1}}}\right) \tag{5.5}$$

$$\sigma_{ct} = E_{cm} \cdot \varepsilon_{ct} \quad \text{, for } \sigma_{ct} \leq 0.9 \cdot f_{ctm} \tag{5.6}$$

$$\sigma_{ct} = f_{ctm} \cdot \left(1 - 0.1 \cdot \frac{0.00015 - \varepsilon_{ct}}{0.00015 - 0.9 \cdot f_{ctm}/E_{cm}}\right) \quad \text{, for } 0.9 \cdot f_{ctm} < \sigma_{ct} \leq f_{ctm} \tag{5.7}$$

$$\sigma_{ct} = f_{ctm} \cdot \left(1.0 - 0.8 \cdot \frac{w}{w_1}\right) \quad \text{, for } w \leq w_1 \tag{5.8}$$

$$\sigma_{ct} = f_{ctm} \cdot \left(0.25 - 0.05 \cdot \frac{w}{w_1}\right) \quad \text{, for } w_1 < w \leq w_c \tag{5.9}$$

$$w_1 = G_F/f_{ctm} \quad \text{, when } \sigma_{ct} = 0.2 \cdot f_{ctm} \tag{5.10}$$

$$w_c = 5 \cdot G_F/f_{ctm} \quad \text{, when } \sigma_{ct} = 0 \tag{5.11}$$

It has been identified that the value of dilation angle is strongly related to the type of used concrete, its strength, level of confinement and load character. Moreover, the definition of the accurate stress-strain relation in the plastic response of the concrete, as well as an accurate reflection of the concrete damage required sensivity studies. The considered parameters in the conducted sensivity study consisted of: (i) influence of the confinement effect on the concrete behaviour (according to fib ModelCode 2010 [62] and EN 1992-1-1:2004 [53]), (ii) value of the confining stresses, (iii) consideration of cubic or cylinder values for concrete compression strengths and their all derivatives in the concrete behaviour model according to fib ModelCode 2010 [62], (iv) dilation angle, (v) viscosity parameter and (vi) maximuam allowable concrete damage level. In the result, it has been identified that the confining stresses reached 3.6 MPa in the CoPOT specimens and this value refers well to the prediction from fib ModelCode 2010 [62] with removed reduction safety coefficients. The identified dilation angle of 25° was found to be feasible for the simulations of CoPOT tests. The value of the applied dilation angle was related to a more concentrated and shear-dominated character of the load flux in the concrete.

From the conducted parametric study, the concrete compression strength for cubic specimens has been identified as feasible for the definition of the concrete behaviour in CoPOT simulations. The properties were calculated based on the experimentally obtained compression strengths of concrete given in Table 5.11. For the evaluation, a mean value from the 1st and 2nd series was taken. Due to measured different concrete compression strengths for each test series, four respective concrete material laws were defined. For simulations of test series 0v2 and Cv2, the confinement effects were neglected in order to reduce the complexity of simulation and to verify if the failure in the specimens can develop only at the steel-concrete interface. The applied stress-strain behaviours for each simulation series are shown in Fig. 5.62-5.65. The applied input parameters in the definition of the CDP concrete material law are summarised in Annex D.

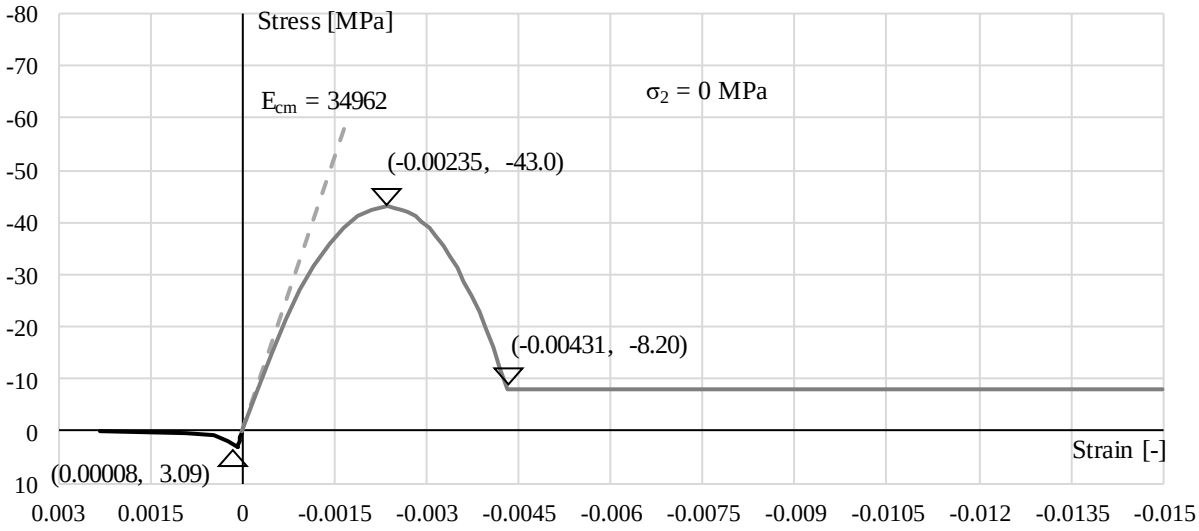


Fig. 5.62. Stress-strain behaviour of the numerical concrete material law for the specimen 0v2 of CoPOT.

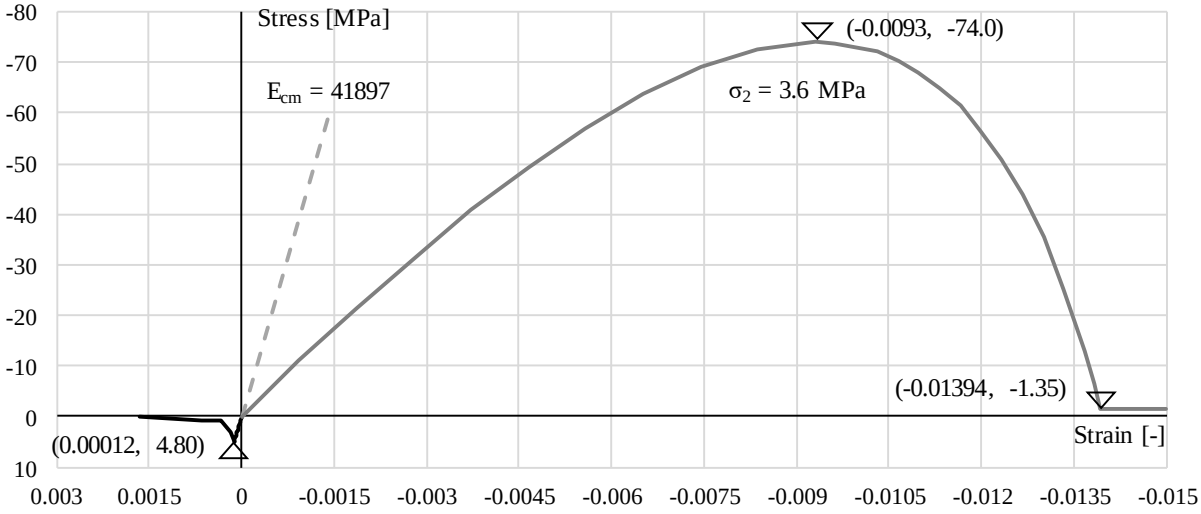


Fig. 5.63. Stress-strain behaviour of the numerical concrete material law for the specimen Av2 of CoPOT.

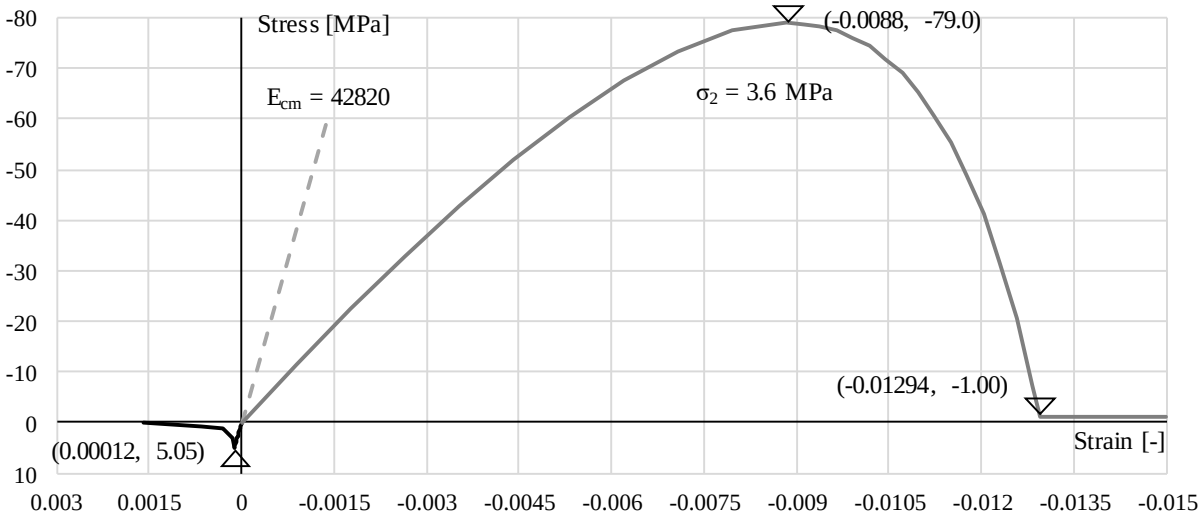


Fig. 5.64. Stress-strain behaviour of the numerical concrete material law for the specimen Bv2 of CoPOT.

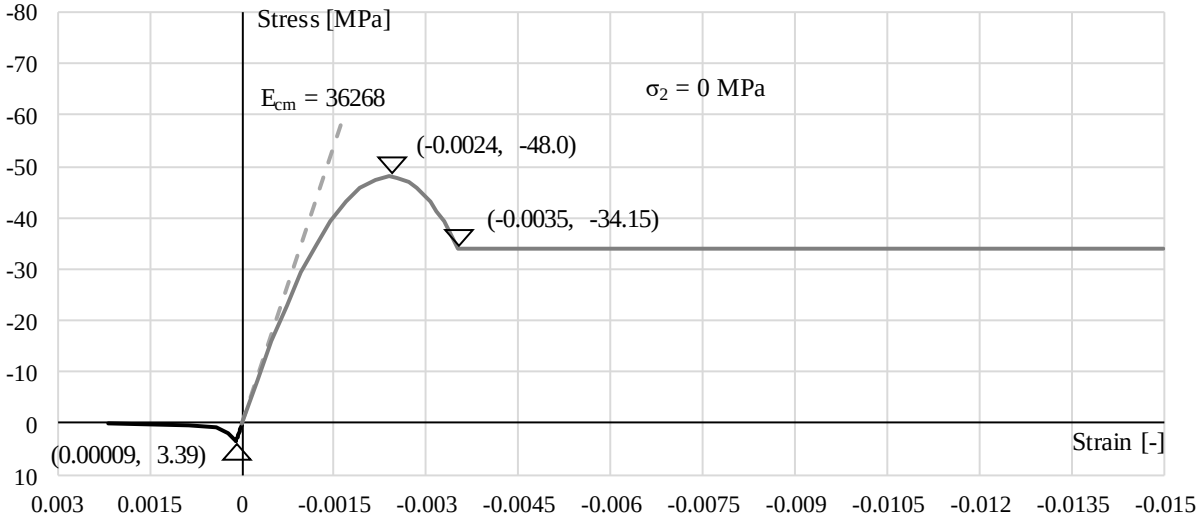


Fig. 5.65. Stress-strain behaviour of the numerical concrete material law for the specimen Cv2 of CoPOT.

For series Cv2, a different value of the dilation angle was used in the simulation. The simulation of the test Cv2 was performed with the usage of Abaqus/Standard solver, thus, the concrete material law required adjustment, like for example viscosity parameter. However, the change in the dilation angle was mainly related to the fact that in the series Cv2, the load transfer mechanism of flat shear connectors did not contain mechanical bearing action and nearly all forces were transferred by connector-concrete bond. Due to the different load-transfer mechanism, the response of the concrete changed. A higher value of the applied dilation angle spread the load over a bigger part of the concrete behind the contact interface. In the result, the splitting stresses and the pull-out failure of the specimen at the interface was obtained.

5.5.3. Steel-concrete bond model

An essential aspect of the FE simulations of push-out tests with flat shear connectors was the accurate modelling of steel-concrete bond, which has a significant contribution to the force transferring mechanism, see Fig. 5.28. First investigations in Abaqus showed that the numerical simulation of bond cannot be realized by the common method of implementing only the Coulomb frictional behaviour at the interface. In the numerical software, the Coulomb friction requires a lateral force to be activated. The results of the reference tests 0v2 showed that the bond mechanism is active at large displacements even without a lateral pressure and even after reaching the ultimate load, see Fig. 5.28a. Therefore, the method to implement the steel-concrete bond in numerical simulations described in Section 5.3 was adapted and extended to the non-linear definition of the damage evolution.

The numerical modelling of steel-concrete bond in the FE code Abaqus® [174] can be realized in two different ways: (a) with the usage of cohesive elements and (b) with cohesive interaction properties. It has been found, that the Abaqus/Explicit solver works better with the cohesive elements approach, where Abaqus/Standard solver works well with the cohesive interaction properties approach. In the explicit simulations, the cohesive finite elements COH3D8 with zero thickness were used at the interface. The interaction between the steel and the concrete in static simulations of specimen Cv2 was defined as the standard surface-to-surface contact.

The post-failure behaviour of bond was defined using a tabular definition in order to reproduce the behaviour shown in Fig. 5.28a. Normally, in Abaqus, the tabular damage definition is described in terms of a stiffness reduction. An equation, which correlates the demanded shear damage factor in terms of forces D_d with the requested by Abaqus shear damage factor in terms of stiffnesses D_r has been derived based on the damage definition used by Abaqus for cohesive behaviour and implemented elastic traction-separation law [174]. The resultant relation is described in Eq. 5.12 below.

$$D_r = 1 - \frac{(1 - D_d) \cdot t_{ss}}{k_{ss} \cdot \left(\delta_i + {}^{t_{ss}}/_{k_{ss}}\right)} \tag{5.12}$$

Where, D_r is the requested damage factor in terms of stiffness, D_d is the demanded damage factor in terms of forces, t_{ss} is the shear strength value, k_{ss} is the initial stiffness of the shear connection, δ_i is the plastic (inelastic) part of the displacement of the considered location.

Besides steel-concrete bond, connector-concrete bond was modelled in the analogic way. The properties of the connector-concrete bond were based on the reinforcement bar-concrete bond performance available in the literature [15, 60, 61, 114] and based on the performed Cv2 tests. It has been identified that the simplified linear definition of connector-concrete bond brought a good accuracy when working simultaneously with the non-linear bond model of plain steel and concrete. Implementation of two non-linear cohesive behaviours in one model greatly reduce the efficiency of a simulation.

5.5.3.1. In Abaqus/Standard simulations

The interaction between steel and concrete in the static simulations of specimen Cv2 was defined as the standard surface-to-surface contact with the finite sliding formulation and node-to-surface discretisation method [174]. In the interaction properties, the pressure-overclosure, tangential, cohesive and damage behaviours were defined. An appropriate assignment of the master/slave surface definition was essential in the performed simulations and the concrete surface had the master properties. In the result, each sliding slave node into the zone of master nodes can be activated according to the specified cohesive behaviour. Counter definition of the master/slave properties would result in the activation of the nodes only initially in contact. The connector-concrete interaction was defined analogous. The applied interaction properties for plain steel-concrete bond and connector-concrete bond are given in Table 5.17. The used values of interaction properties were calibrated according to the CoPOT test results. The respective traction separation laws for plain steel-concrete bond and connector-concrete bond are shown in Fig. 5.66, where the applied non-linear and linear bond models are shown.

Table 5.17.
Interaction properties of bond in Abaqus/Standard simulations of column push-out tests.

Property	Symbol	Unit	Plain steel-concrete bond with oiled surf	Connector-concrete bond
Friction coefficient	μ	[-]	0.14	1.4
Stiffness – normal direction	k_{nn}	[MPa/mm]	0	200
Stiffness – shear 1&2 direction	$k_{ss/tt}$	[MPa/mm]	1.2	60
Max nominal stress – normal direction	t_{nn}	[MPa]	1	1
Max nominal stress – shear 1&2 direction	$t_{ss/tt}$	[MPa]	0.79	9.5
Damage evolution type			Displacement	Displacement
Damage softening character			Tabular (97 points)	Linear
Total plastic displacement	$\delta_m{}^f$	[mm]	Tabular definition	5
Viscosity parameter	μ_{visc}	[-]	0.001	0.001

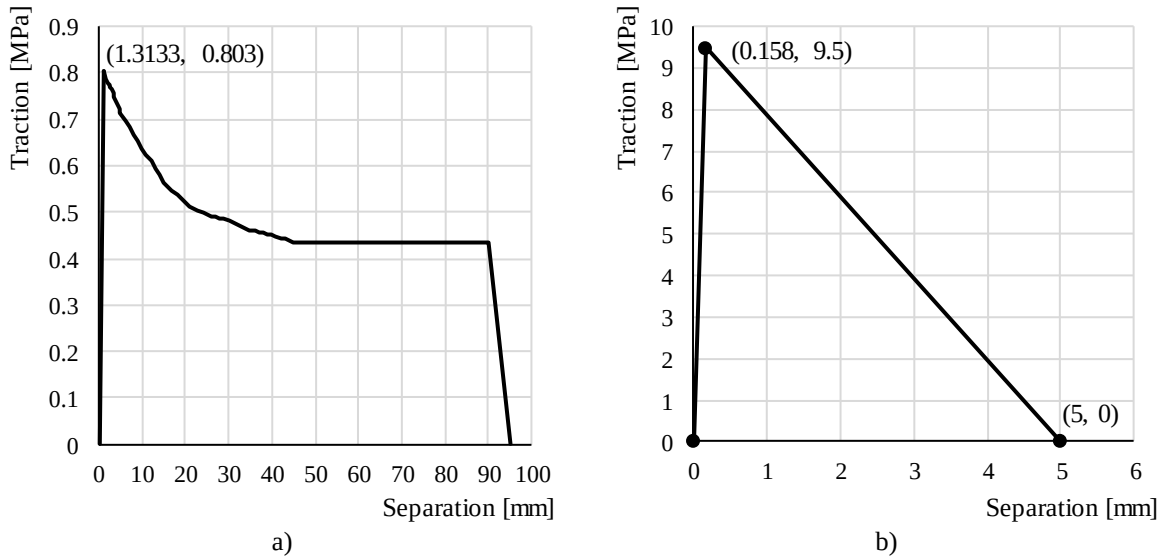


Fig. 5.66. Traction separation laws for bond model in the standard simulations of column push-out tests – a) plain steel-concrete and b) connector-concrete.

In order to assure an accurate implementation of the cohesive and damage behaviours, a sufficiently small mesh [186] and load increments were required. It was essential to enforce Abaqus solver to proceed with small maximum increments. Solver setup is given in Annex D.

5.5.3.2. In Abaqus/Explicit simulations

Both, the plain steel-concrete bond and connector-concrete bond were modelled in explicit simulations as a layer of cohesive elements with zero thickness at the interface. The material law of the applied cohesive elements was defined by the linear elastic traction-separation law, which describes the stress-displacement behaviour [174]. The uncoupled elastic stiffness matrix, where the off-diagonal terms are set to zero, defined the elastic relation between the traction (stress) vector and separation (displacement) vector. The quadratic nominal stress criterion was used to define the damage initiation point [174]. In parallel, the pressure-overclosure behaviour and tangential behaviour at the interface were defined as contact properties of the general contact feature. The applied properties of bond models are summarised in Table 5.18. The applied traction-separation material laws for the cohesive elements are shown in Fig. 5.67, where the non-linear material law for plain steel-concrete bond and simplified linear material law for connector-concrete bond models are given. Similar like in the case of standard simulations, the combination of two non-linear traction-separation laws drastically reduces the efficiency of simulations. Implemented simplified traction-separation law for connector-concrete bond brought a good accuracy.

Table 5.18.
Interaction properties of bond in Abaqus/Explicit simulations of column push-out tests.

Property	Symbol	Unit	Plain steel-concrete bond with oiled surf	Connector-concrete bond
Friction coefficient	μ	[-]	0.1	1.4
Stiffness – normal direction	k_{nn}	[MPa/mm]	0.1	0.1
Stiffness – shear 1&2 direction	$k_{ss/tt}$	[MPa/mm]	0.625	60
Max nominal stress – normal direction	t_{nn}	[MPa]	0.01	0.01
Max nominal stress – shear 1&2 direction	$t_{ss/tt}$	[MPa]	0.803	15 for Bv2 25 for Av2
Damage evolution type			Displacement	Displacement
Damage softening character			Tabular (97 points)	Linear
Total plastic displacement	$\delta_m{}^f$	[mm]	Tabular definition	5
Viscosity parameter	μ_{visc}	[-]	0.001	0.001

In Table 5.18, the maximum nominal strength for shear directions in bond model at the connector-concrete interface varies between the series Av2 and Bv2. The experimental connector-concrete bond strength value of 15 MPa had been identified from the tests Cv2 and literature [15, 60, 61] and this values worked well for the simulations of series Bv2. For the simulations of series Av2, an adjustment was made in order to obtain the desired response of the specimen and to correlate to test results. Impact of the imposed modification is not significant and the value could stay unchanged. However, the imposed modification moved the obtained failure pattern and the resultant load-slip curve closer to the

test results. A good reflection of the tests was crucial in order to analyse the developed load-flux and failure sequence in the concrete part.

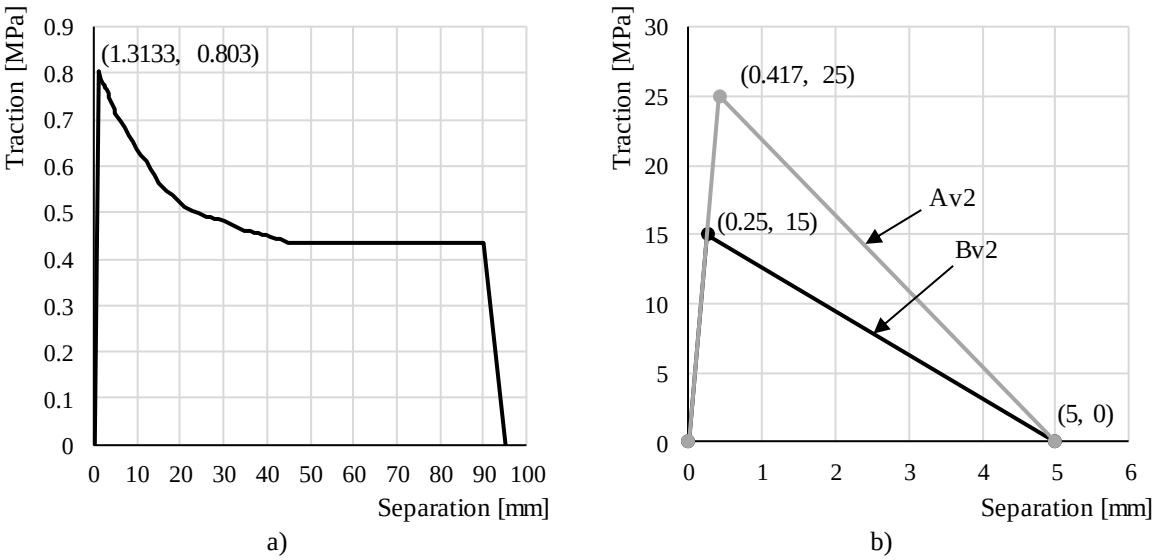


Fig. 5.67. Traction separation laws for bond model in the explicit simulations of column push-out tests – a) plain steel-concrete and b) connector-concrete.

5.5.4. Assembly, interactions, constraints and boundary conditions

The assembly of the performed simulations with applied boundary conditions and indicated interaction surfaces are shown in Fig. 5.68 on the example of series Av2. The reinforcement cage was embedded in the concrete block by applying the respective constraint with tied relation. The interaction between steel and concrete had been defined as the general contact feature in Abaqus [174], where the interaction properties defined the normal and tangential behaviour at the respective interfaces between the concrete and plain steel or connector parts. According to the Abaqus manual [174], in explicit simulations, particular attention has to be given to the possible development of non-physical forces at the interface, therefore, the verification of the energy balance with a sufficiently small difference in internal energy and external work, as well as sufficiently small fraction of the kinetic energy in respect to the internal energy were crucial.

At the base of the specimen, only the vertical degree of freedom (DOF) was blocked. At the same time, the top surface of the steel profile was coupled with the kinematic constraints on all DOF to the reference point localised 200 mm above it. The reference point at the top had released only the vertical movement DOF. In order to load the specimen, the reference point was pushed down up to a maximum displacement of 95 mm. In the Abaqus/Explicit simulations, the imposed displacement speed was 0.25 mm/s and the smooth step character had been used. In Abaqus/Standard simulations, sufficiently small increments were used due to the cohesive behaviour.

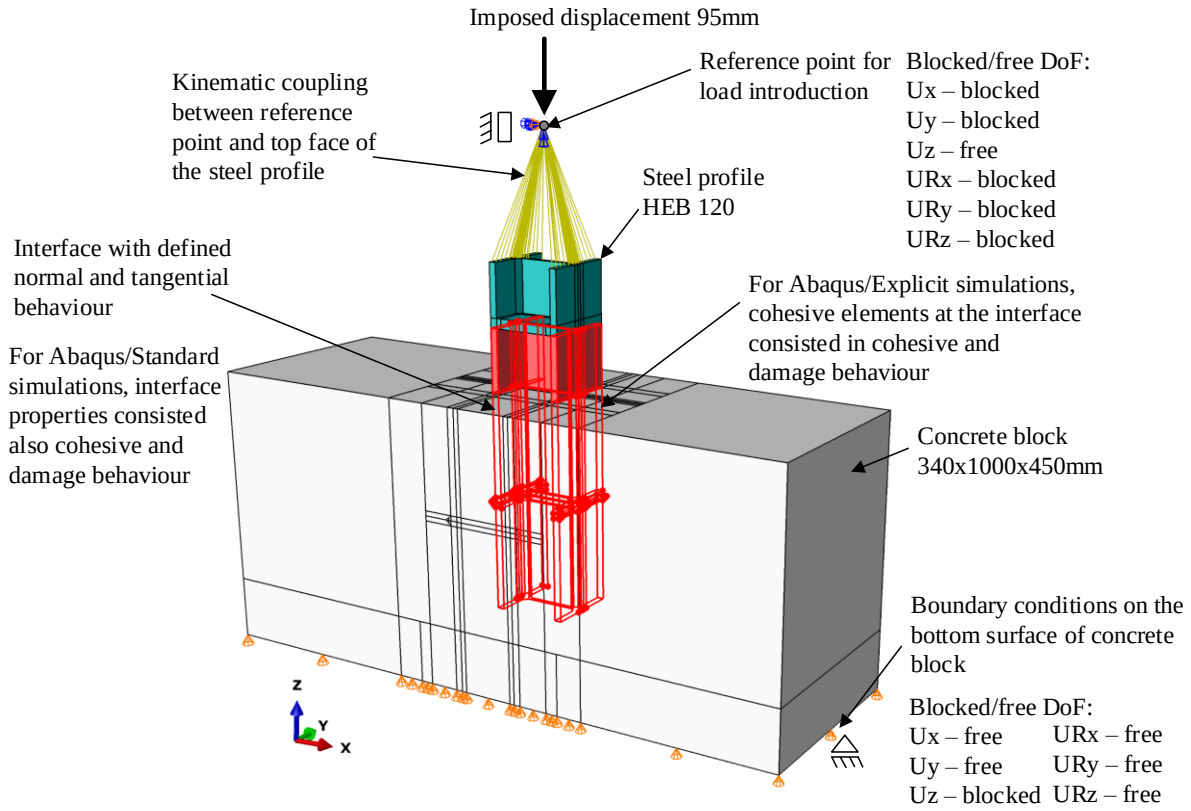


Fig. 5.68. Layout of the column push-out FE simulation of the series Av2.

In addition, self-contact properties were added to the concrete surface at the interface between steel and concrete parts. The self-contact formulation prevented that the concrete material protruded inside itself after an extensive deformation under the displaced connector.

The created cohesive elements in Abaqus/Explicit simulations were tied to the respective surfaces of the steel or concrete parts. In the formulation of tie constraint, the surfaces of cohesive elements consisted of slave surface definition so they followed the deformation and displacement of the master surfaces defined on the steel and concrete surfaces.

5.5.5. Results and comparison to the experimental data

The calibration process of the performed numerical simulations consisted of 267 simulations. It has been identified that the accuracy of the conducted simulations for series Av2 and Bv2 is valid only until the relative slip of 10-15 mm. Further part of simulations comprise a significant deformation of concrete under the sliding shear connectors and lack of discontinuities in the concrete material law introduces a non-realistic response of the specimens. However, in the scope of the obtained calibrated response, the most important parts of the load-slip behaviour are included – the ascending part, peak zone part and wide part of the descending branch. A good convergence between the experimental and numerical curves was obtained. In the presented diagrams of numerically obtained load-slip curves, the test results from Fig. 5.28 are included in the background for a comparison. The numerical simulations were calibrated in order to converge with the mean value from the test results.

5.5.5.1. Reference specimen 0v2

The obtained numerical load-slip response of the specimen without mechanical shear connectors – series 0v2, is shown in Fig. 5.69. It can be observed that the implemented numerical model of bond reflects the experimental behaviour with a high accuracy including the remained load-bearing capacity due to the surface roughness friction mechanism. In the zoomed part of the initial ascending branch, it can be observed that the adhesive stiffness of steel-concrete bond was higher than defined in the numerical simulations. However, to overcompensate the frictional behaviour at the peak zone from the tests, the stiffness of bond in numerical simulations was intentionally reduced in order to correlate to the peak point. No concrete damage was observed after the simulation, thus, the failure of the specimen was fully related to the debonding.

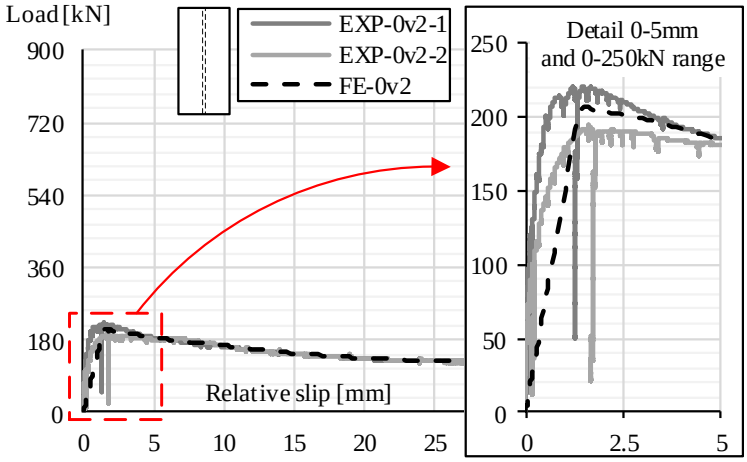


Fig. 5.69. Numerical load-slip curve of the CoPOT specimen 0v2 and comparison to test results.

5.5.5.2. Specimen Cv2 with longitudinal connector

In Fig. 5.70, the numerically obtained load-slip curve for series Cv2 is given.

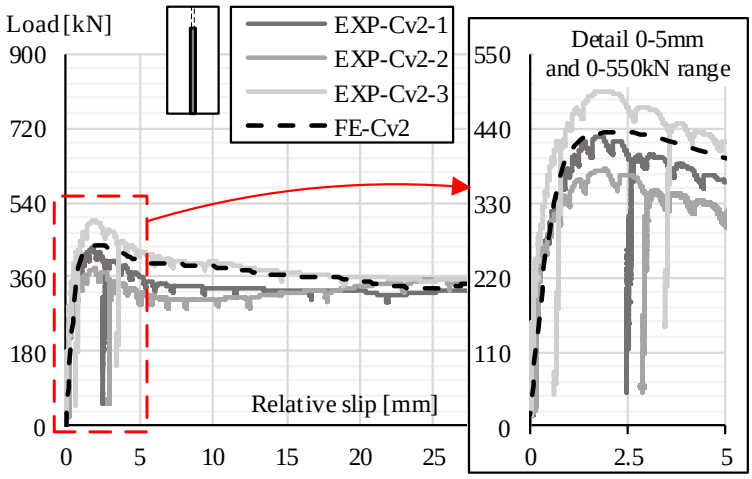
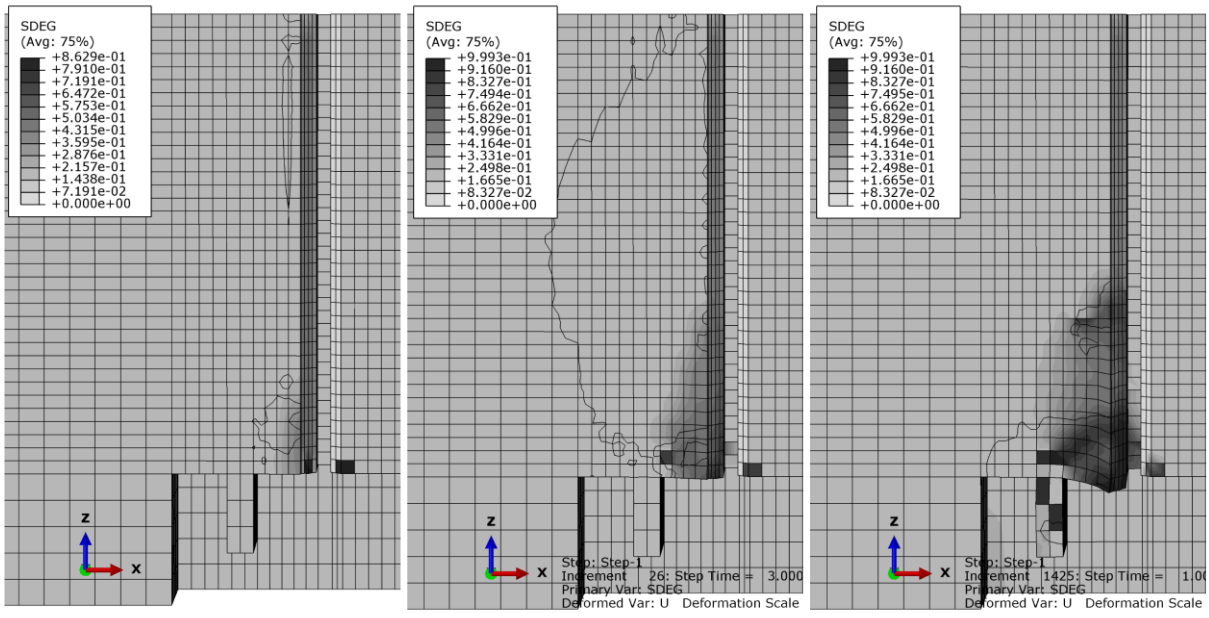


Fig. 5.70. Numerical load-slip curve of the CoPOT specimen Cv2 and comparison to test results.

From Fig. 5.70, it can be observed that good correlation to the experimental curves was obtained and the initial stiffness was well reproduced due to the implemented connector-concrete bond model in parallel to the plain steel-concrete bond.

In Fig. 5.71, the damage sequence is shown. It can be observed that at the initial stage shown in Fig. 5.71a, the damage developed only at the connector-concrete interface. With progressing slip, the damaged concrete formulated a concrete cone localised at the edge of connector and recess. A good correlation to test campaign observations can be identified, see Fig. 5.44.



a) b) c)

Fig. 5.71. Sequence of concrete damage in the numerical simulation of CoPOT specimen Cv2 – a) the initial stage, b) stage at the peak load and c) stage at the descending branch.

5.5.5.3. Specimen Av2 with transversal connector

In Fig. 5.72, the numerically obtained load-slip curve for series Av2 is shown. A good correlation to test results can be observed. The oscillation of the numerical curve is related to the progressing damage of concrete under the connector and due to released energy. Dynamic reaction of shear connector under a big portion of concrete occured despite performed quasi-static simulations, see Annex D.

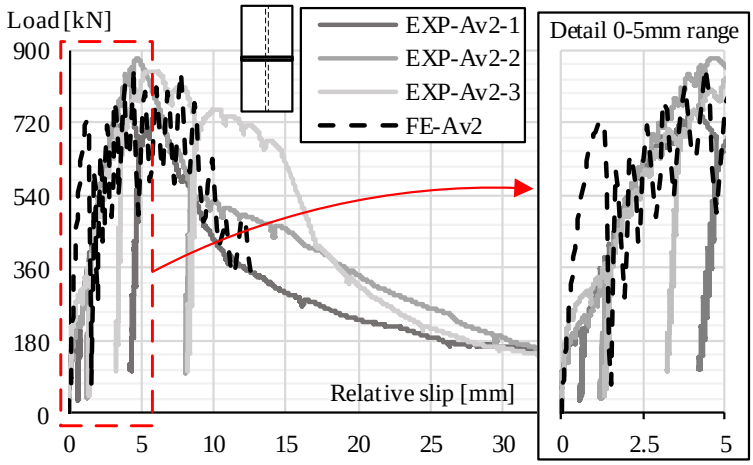


Fig. 5.72. Numerical load-slip curve of the CoPOT specimen Av2 and comparison to test results.

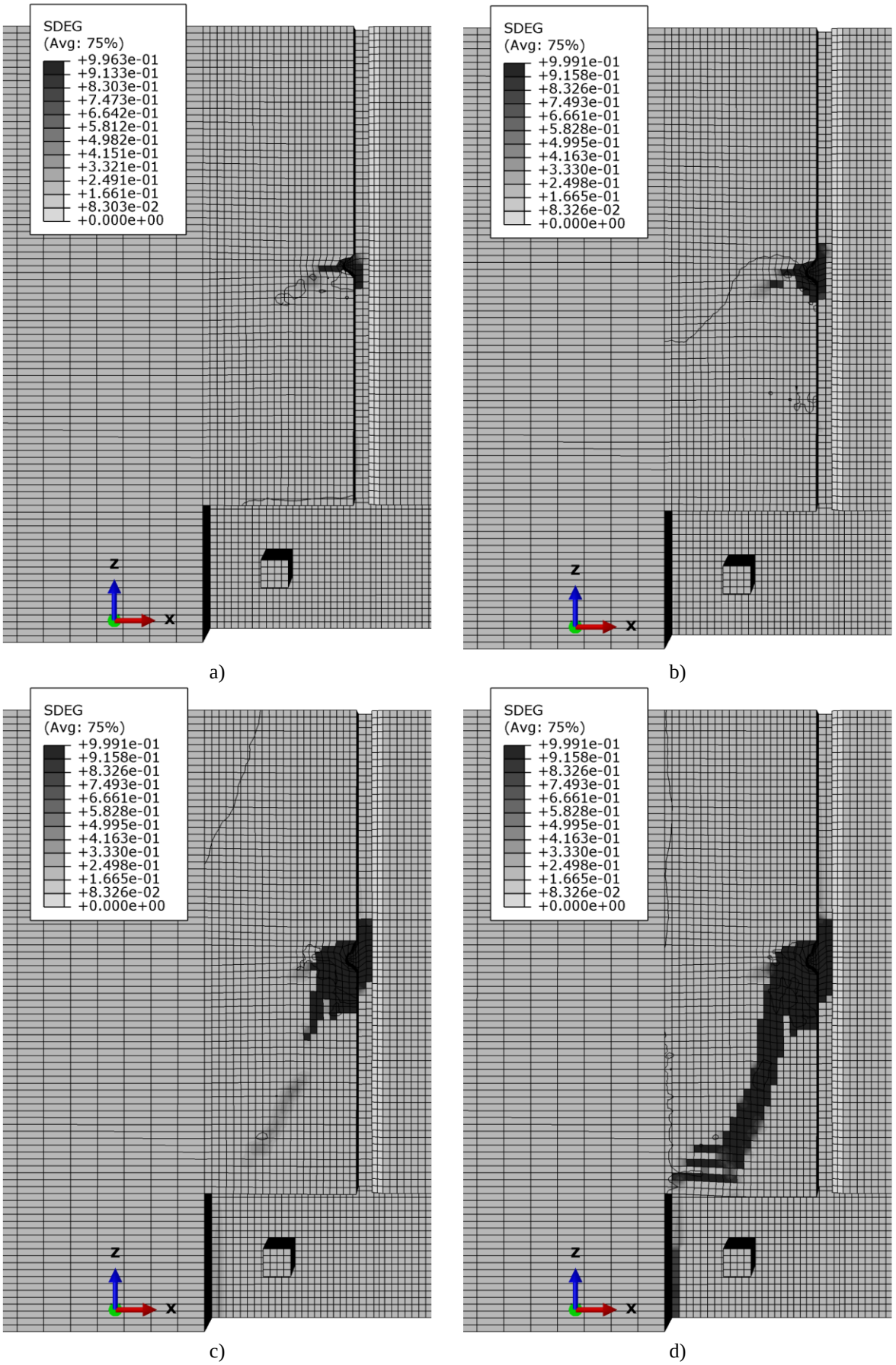


Fig. 5.73. Sequence of concrete damage in the numerical simulation of CoPOT specimen Av2 – a) the initial stage, b) stage before the peak load, c) stage after the peak load and d) stage at the descending branch.

From Fig. 5.72, it can be observed that the amplitude peaks of the numerical response fits between the obtained test curves. In the zoomed part of the initial ascending branch, the first minor peak is revealed, which does not correlate to the test curves. This effect is related to the simultaneous work of cohesive and mechanical bearing mechanisms due to perfectly matching geometries of steel and concrete parts. In the test campaign such perfect match is impossible, thus, the first peak had not been obtained. It can be observed that, after the drop of the first peak, the branch of load-slip curve continues to ascend with good correlation to test results.

In Fig. 5.73, the damage sequence is shown. It can be observed that before the concrete compression strut failure, a small portion of damaged concrete under the connector was formulated, see Fig. 5.73b. This portion of the damaged concrete correlate to the portion of concrete under the connector identified after opening of the specimens Av2 shown in Fig. 5.47. The developed damage in the concrete due to the concrete compression strut visible in Fig. 5.73c-d is shown more in detail in Fig. 5.74, where drawn lines reflecting the identified failure planes from Fig. 5.47. A clear tendency between the two obtained failure patterns – experimental and numerical, can be identified.

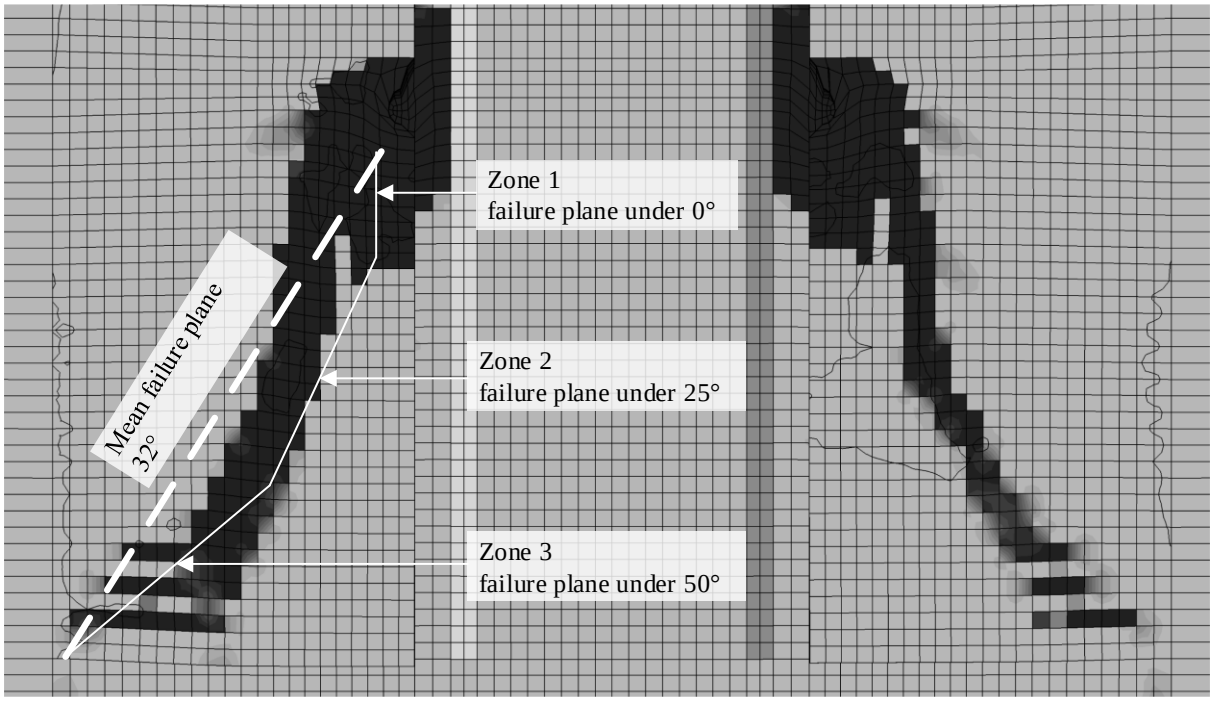


Fig. 5.74. Analysis of the developed failure planes in the numerical simulation of CoPOT specimen Av2.

In Fig. 5.75, minimum principal stresses in the concrete encasement are shown. The presented principal stresses are corresponding to the state close to the peak load, before the failure. Based on the given figure, an estimation of the orientation of the developed concrete compression strut was made and the angle of 32°-38° was identified to the vertical direction. In addition, from Fig. 5.75, the average value of the acting compression stresses under the shear connector were identified on the level of 230 MPa. These high values of stresses could be obtained in the concrete due to the existence of a highly locally confined concrete localised directly under the connector.

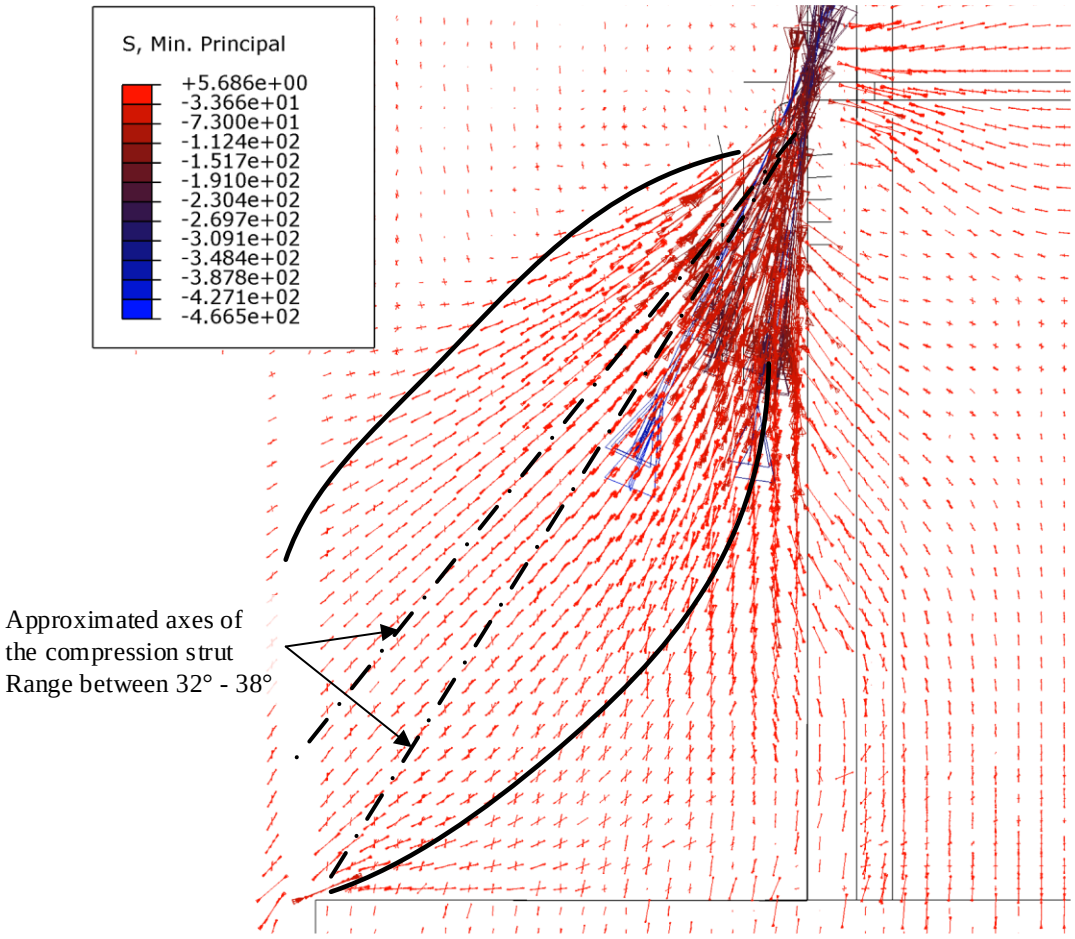


Fig. 5.75. Minimum principal stresses in the concrete of CoPOT specimen Av2 – stress state close to but before the peak load.

5.5.5.4. Specimen Bv2 with V-shaped connector

In Fig. 5.76, the numerical load-slip response of the series Bv2 is shown. A good correlation to the test results is visible. Similarly like in the case of series Av2, the first minor peak of load can be identified. It can be observed that the identified peak followed the curves of two test series, where after the drop, it converged to the response of the third tested specimen. Due to significant contribution of the connector-concrete bond, the identified effect correlated to the realistic behaviour of tested specimens.

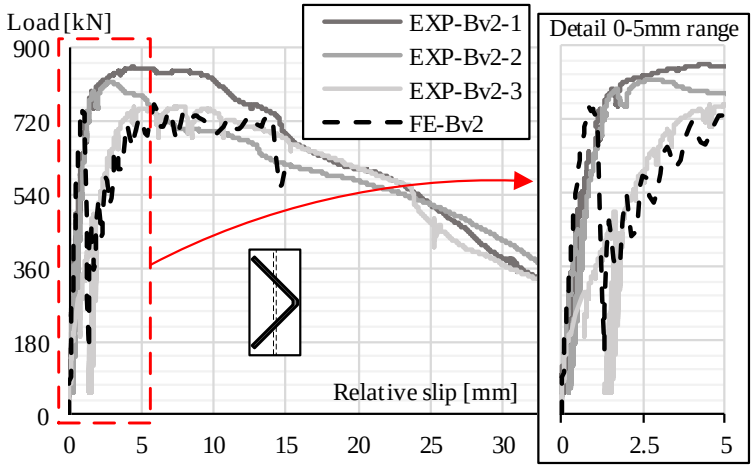


Fig. 5.76. Numerical load-slip curve of the CoPOT specimen Bv2 and comparison to test results.

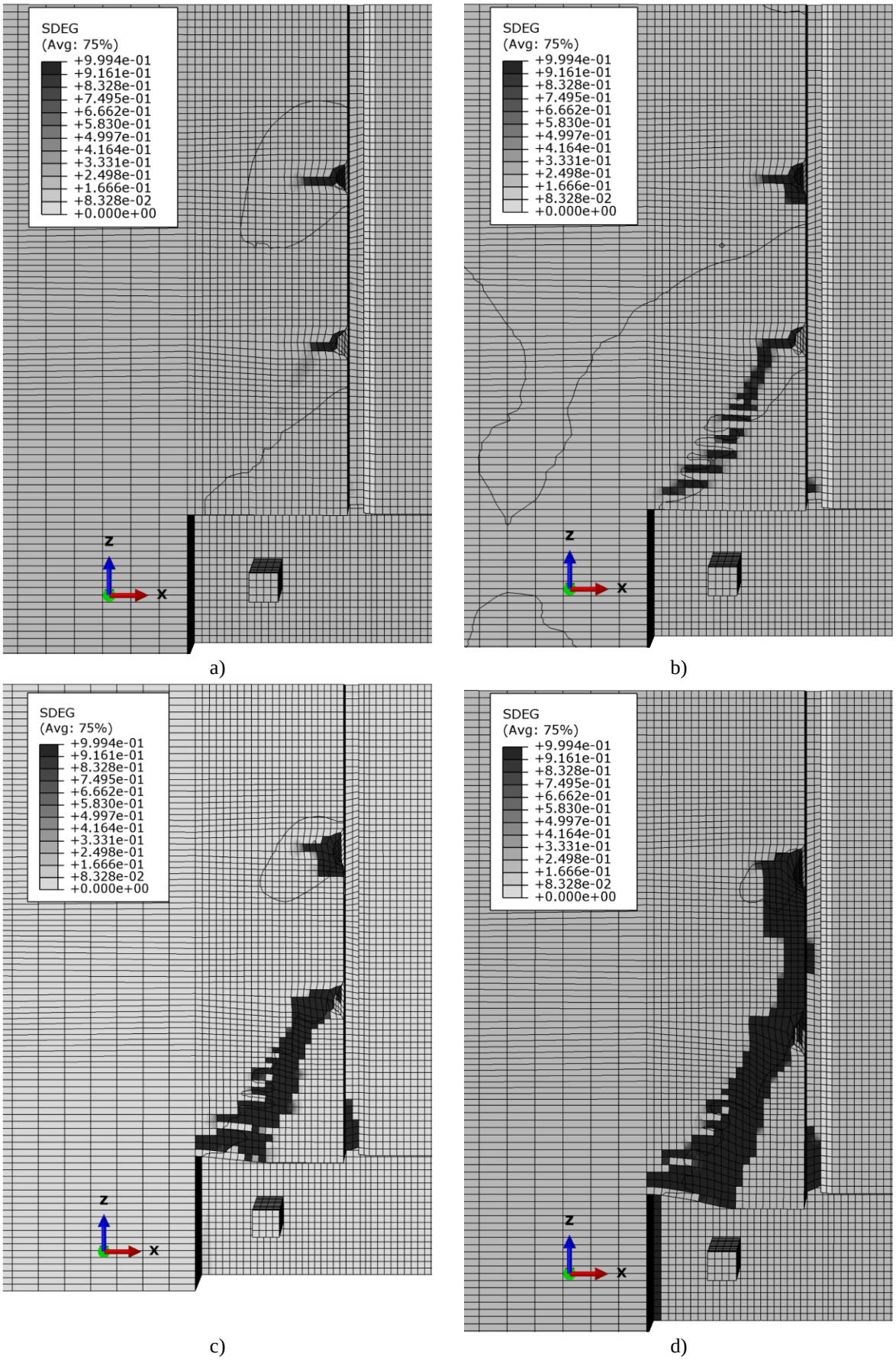


Fig. 5.77. Sequence of concrete damage in the numerical simulation of CoPOT specimen Bv2 – a) the initial stage, b) stage before the peak load, c) stage at the peak load and d) stage at the descending branch.

From Fig. 5.76, it can be observed that the oscillation in the numerically obtained load-slip curve are much smaller than in the case of the series Av2. Both simulations had nearly identical simulation parameters. The dynamic effects visible in the load-slip curve in the form of oscillations are damped in the case of series Bv2 due to (i) bigger implemented shear connector (two arms), (ii) distributed pressure of the connector on the concrete between two arms and (iii) due to significant contribution of the connector-concrete bond in the force transfer mechanism.

In Fig. 5.77, the damage sequence of the series Bv2 is shown. In the identified concrete damage, a coherence to the mechanism identified in series Av2 can be identified, see Fig. 5.73. The development of the compression strut failure under the lower arm of connector, instead of a small crushing portion of concrete under it, was related to a small distance between the lower embedded arm of the connector and top surface of the recess. Due to the same geometrical aspect, in the failure of the concrete compression strut under the lower arm of connector, characteristic scattered tensile horizontal cracks can be identified due to pushing out the concrete cone, see Fig. 5.77b-d and compare to Fig. 5.51b. With the development of the relative slip, the concrete compression strut failure at the bottom formulated characteristic failure planes. Between the arms of the connector, the horizontally oriented failure plane developed in the concrete, see Fig. 5.77d.

In Fig. 5.78, the fully developed damage in the concrete is shown. The characteristic developed failure planes from tests shown in Fig. 5.51 are indicated in Fig. 5.78 in the form of lines. A good coherence between the two obtained failure patterns, numerical and experimental, can be observed.

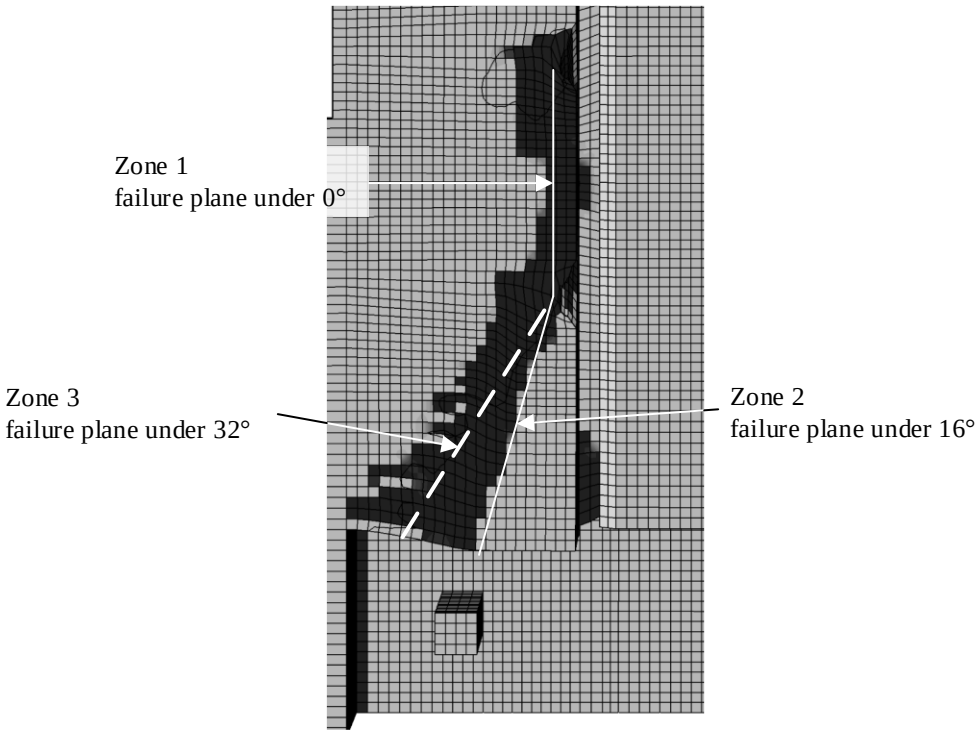


Fig. 5.78. Analysis of the developed failure planes in the numerical simulation of the specimen Bv2

Based on the obtained good calibration of the numerical model according to test observations, the load-flux in the concrete part has been analysed. In Fig. 5.79, the distribution of minimum principal stresses is shown. The shown principal stresses in the concrete are corresponding to the state before reaching the peak load, particularly, at the stage before development of damage in the concrete under the connector arms, see Fig. 5.77b. It can be observed that under each arm, compression struts were formulated. The approximated range of the struts orientations varies between 22° and 32° for the lower arms and between 32° and 40° for the upper arms. The observations from the numerical simulations supported the test observations from the opening of the test specimens Bv2, where the concrete compression strut orientation angle can be identified under 32° as shown in Fig. 5.51a in the broke out concrete cone under the applied shear connector (Zone 3).

The analysis of the minimum principal stresses under the arms of the V-shaped flat shear connectors revealed that the average maximum compression stresses reached approximately 125 MPa. It can be observed that the developed compression stresses greatly overcame the concrete compression strength defined in the material properties. This effect was possible due to a global and local confinement of the concrete under the connectors.

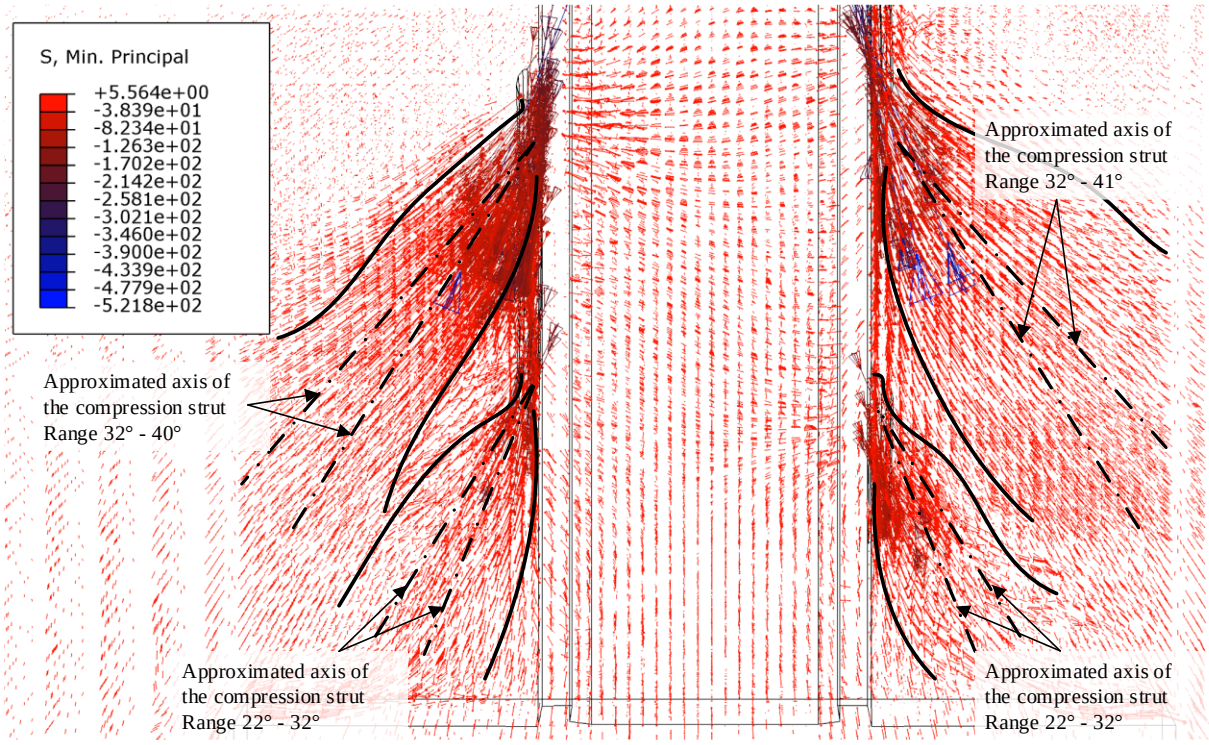


Fig. 5.79. Minimum principal stresses in the concrete of CoPOT specimen Bv2 – stage when the first damage occured.

5.6. Analytical model for the resistance of flat shear connectors

The developed analytical model is analytically summarising the resistance of flat mechanical shear connectors, which were proposed and characterised in this dissertation. The given analytical model is based on the obtained results from the performed 11 column push-out laboratory tests and 270 numerical simulations. The comprehensive analysis of results and exhaustive investigation of the failure patterns in CoPOT specimens allowed identifying the characteristic load flux in each specimen and settling the fundamental theoretical assumptions, which finally lead to the analytical description of the load bearing capacities of proposed flat shear connectors.

In this section, an interest was to evaluate the resistance of flat shear connectors, where the global verification of specimens can be performed according to the existing provisions of design codes, like for example EN 1994-1-1 [58], EN 1992-1-1 [53], EN 1993-1-1 [55] or fib Model Code 2010 [62]. However, based on the steps taken to establish the resistance of flat shear connectors, like for example the identification of inclination angle for the compression strut in concrete, certain design recommendations are given.

Due to the limited experimental database, the developed analytical model cannot be extrapolated to other cases and be considered as the general design guidance of the proposed type of flat shear connectors. Nevertheless, it applies for the tested configurations and it provides a clear explanation of the occurring failure mechanisms.

5.6.1. Fundamental assumptions

The analytical model has been developed to describe the load bearing capacity of the proposed novel type of flat shear connectors. A mechanical model of each connector variant and a set of equations were derived to explain the load transferring mechanisms and possible failure modes. In the performed investigations, the reference tests without shear connectors were included in order to asses forces transferred by plain steel-concrete bond. An appropriate estimation of these forces, including the Coulomb friction part, allowed evaluating forces transferred purely by the mechanical connection.

The delivered analytical model for each variant is based on main principal assumptions:

- The analytical model is referring only to the column push-out tests described in Section 5.4,
- The analysis is based on the theory of elasticity (the elastic material assumption),
- The stirrups are stiff enough to anchor the tensile forces without a deformation (the infinite stiffness of stirrups assumption or the rigid body assumption),
- Each used material is assumed to be homogenous (the homogenous material assumption),
- No safety concept has been implemented (the test values assumption),
- Long-term effects have been disregarded.

5.6.2. Evaluation of the steel-concrete bond influence – specimen 0v2

The concluded force transferring mechanism of reference tests without mechanical shear connectors is shown in Fig. 5.80. Due to the connection at the interface and existing support eccentricity “e”, the inclined compression strut in concrete developed. To obtain the forces equilibrium, the tensile force at the bottom part of the specimen (Zone 2 in Fig. 5.80) and the compression force at the top part of the specimen (Zone 1 in Fig. 5.80) have been identified. Due to the acting lateral forces at the steel-concrete interface, the Coulomb friction force activated and it contributed to the overall shear connection strength. Due to the same mechanism, the tensile lateral force at the bottom of the specimen enforced an earlier failure of bond in comparison to the upper parts of interface. The described behaviour can justify the non-brittle failure of the specimen 0v2. The position of concentrated vertical reaction forces is related to the assumed simplified distribution of the pressure on the base and the size of applied recess. These conditions are defining the size of the reaction support eccentricity. The failure of the specimen occurred at the interface due to the steel-concrete bond failure.

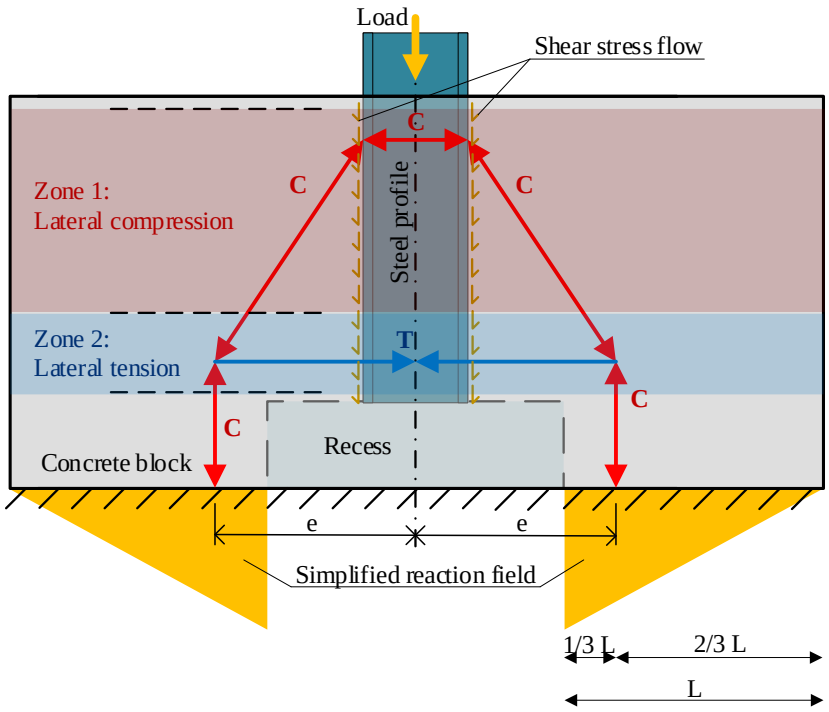


Fig. 5.80. Mechanical model of the specimen 0v2 of CoPOT and simplified reaction conditions.

According to the data collected from the strain gauges glued to the webs of steel profiles during the experimental campaign, as shown in Fig. 5.29 and Fig. 5.54, the simplification about the uniform distribution of bond strength over the contact area was assumed. The approximated linear relation of compression strains over the embedded length justify the taken simplification, see Fig. 5.81.

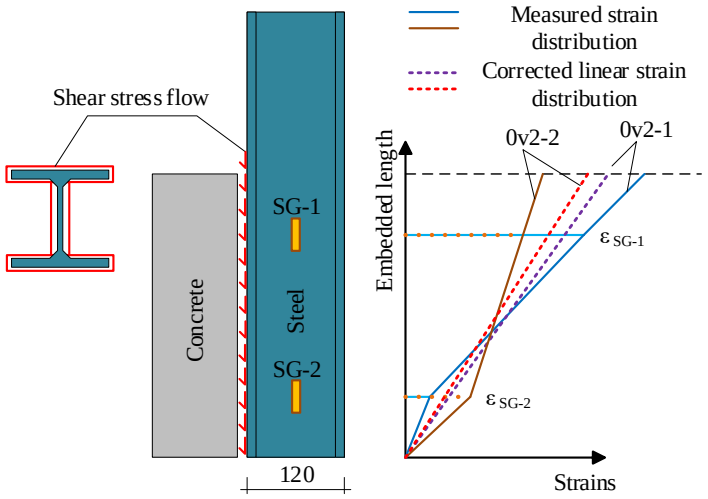


Fig. 5.81. Assumed distribution of strains in the steel profiles of the CoPOT series 0v2.

In general, steel-concrete bond is defined as the tangential shear strength due to the chemical adhesion and friction phenomena at the steel-concrete interface. A relation between the force acting on a contact area and the resulting shear stresses can be defined in Eq. 5.13 by applying the simplification of equal shear stress distribution. The effective steel-concrete contact area is defined in Eq. 5.14.

$$\tau_{surf,i} = \frac{F_i}{A_{cont,eff}} \left[{}^{kN}/_{cm^2} \right] \tag{5.13}$$

$$A_{cont,eff} = L_{emb,s} \cdot u_{s,eff} \, [cm^2] \tag{5.14}$$

Where,

$L_{emb,s}$ is the embedded length of the steel profile and

$u_{s,eff}$ is the effective embedded perimeter of the steel profile.

The assessment of frictional forces developed at the steel-concrete interface during the tests allowed subtracting their contribution from the overall recorded strength and obtaining the pure adhesive resistance. The consideration of this aspect is essential, since the Coulomb friction forces are strongly dependent on the specimen geometry and boundary conditions. According to Fig. 5.27 and Fig. 5.80, the support eccentricity reached the value of 280mm. According to the developed eccentricity of reaction forces and based on the theory of elasticity, a generalised value of lateral compression force acting on the steel-concrete interface can be calculated according to Eq. 5.15-5.17. For the simplification, it was assumed that the neutral axis of the lateral bending mechanism in the concrete was localised in the mid-height of the complete concrete block, see Fig. 5.82.

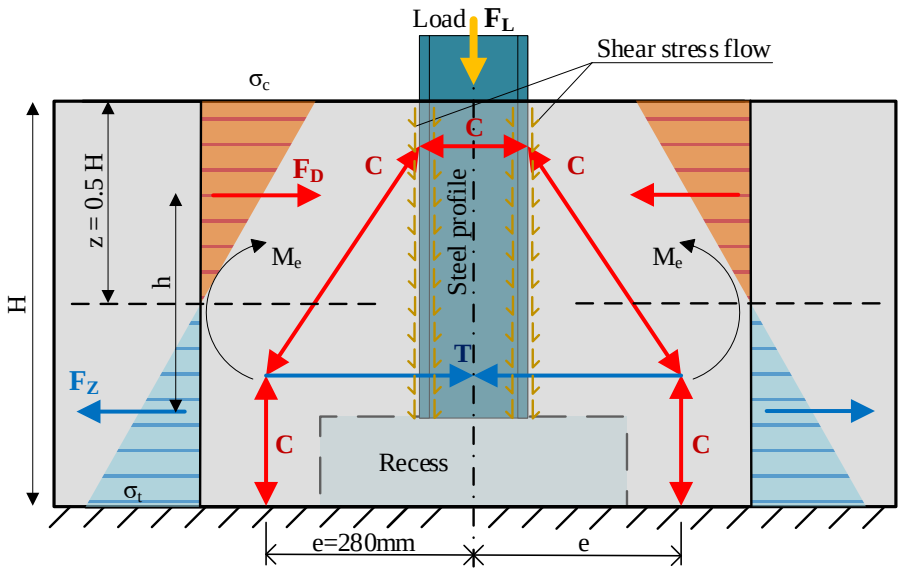


Fig. 5.82. Internal bending mechanism due to the support eccentricity condition of CoPOT specimens.

$$M_e = 0.5 \cdot F_L \cdot (e - 0.5 \cdot h_{HEB})\ [kNcm] \tag{5.15}$$

Where,

F_L is the imposed load.

$$\sigma_c = \frac{M_e \cdot z}{I_c}\ \left[\frac{kN}{cm^2}\right] \tag{5.16}$$

Where,

$z = 0.5 \cdot H$ and it is the distance to the most compressed fibre and

I_c is the moment of inertia of the complete vertical concrete cross-section.

$$F_{f,D} = \mu \cdot \left(0.5 \cdot \sigma_c \cdot 0.5H \cdot b_f\right)\ [kN] \tag{5.17}$$

Where,

μ is the friction ratio for the oil coated steel-concrete interface and

b_f is the width of the steel profile's flanges.

Due to the horizontal compression force developed at the upper part of the specimen - between the flanges of the steel profile, the Coulomb friction forces were also activated from the internal side of the of the flanges. Following this remark, Eq. 5.17 is then modified to Eq. 5.18.

$$F_{f,D} = \mu \cdot \left(0.5 \cdot \sigma_c \cdot 0.5H \cdot b_f\right) + \mu \cdot \left(0.5 \cdot \sigma_c \cdot 0.5H \cdot b_{f,int}\right)\ [kN] \tag{5.18}$$

Where,

$b_{f,int}$ is the width of the internal side of the flanges of steel profile (excluding web and radius).

Considering the geometry of specimen, the friction ratio of 0.1 and the obtained mean peak load from tests in Eq. 5.15-5.18, the generalised frictional force which is contributing to the shear strength of the steel-concrete bond reaches value of 9.4 kN. In the next step, subtracting the obtained frictional force from the obtained experimental mean peak load gives the force, which has been transferred purely by the adhesive part of bond – 198.1 kN. Finally, this force can be used in Eq. 5.13 and the adhesive strength of the bond can be obtained as shown in Eq. 5.19.

$$\tau_{surf,i} = \frac{F_i}{A_{c,eff}} = \frac{198.1}{2401} = 0.0825 \left[{}^{kN}/_{cm^2}\right] = 0.825\ [MPa] \tag{5.19}$$

5.6.3. Resistance of the longitudinal connector – specimen Cv2

The analytical model to estimate the load-bearing capacity for the longitudinal variant of flat shear connector covers the interfacial load transferring mechanism – connector-concrete bond. In the considered case, the imposed load has been transferred from the steel profile to the concrete via plain steel-concrete bond and connector-concrete bond (rebar-concrete bond) simultaneously. The assessment of the resistance of connector required exclusion of the Coulomb friction effects and the forces which were transferred via steel-concrete bond, see Eq. 5.20.

$$F_{connector} = \left(F_{test} - F_{bond\ steel\ prof} - F_{friction}\right)/2 \tag{5.20}$$

Where, 2 is the number of the applied connectors.

Following the procedure described in Section 5.6.2 for the specimen 0v2 without any mechanical shear connectors, it is possible to calculate the frictional forces developed on the plain steel surface and on the surfaces of connectors. A difference in the friction ratios has to be respected – $\mu = 0.1$ for plain steel and $\mu = 1.4$ for connectors, where the given values are referring to the conducted numerical simulations. In the result, using Eq. 5.15-5.18, implementing the geometry of specimen Cv2 and the experimental data obtained from the tests, the force transferred by one connector was calculated and it reached 103.2 kN. The obtained force transferred by one connector resulted in its resistance of 15.6 MPa, according to Eq. 5.13. The obtained results found a good correlation to the results obtained by Bigaj [15] (rebar ultimate pull-out bond strength of 15 MPa).

The strut-and-tie model for the specimen Cv2 visualising the forces distribution is shown in Fig. 5.83. An analogy in the developed force distribution model to the model of embedded reinforcement bar can be observed. Taking into account an assumption that stirrups are stiff enough to bare the resulting transversal tension forces without a deformation and the visual examination of specimens after the tests, the possible failure mode of the specimen can be obtained on the connectors-concrete interface in the tangential direction due to shear. This type of failure reflects the pull-out failure of the embedded rebar. The splitting failure mechanism is prevented due to the imposed confinement in the form of stirrups.

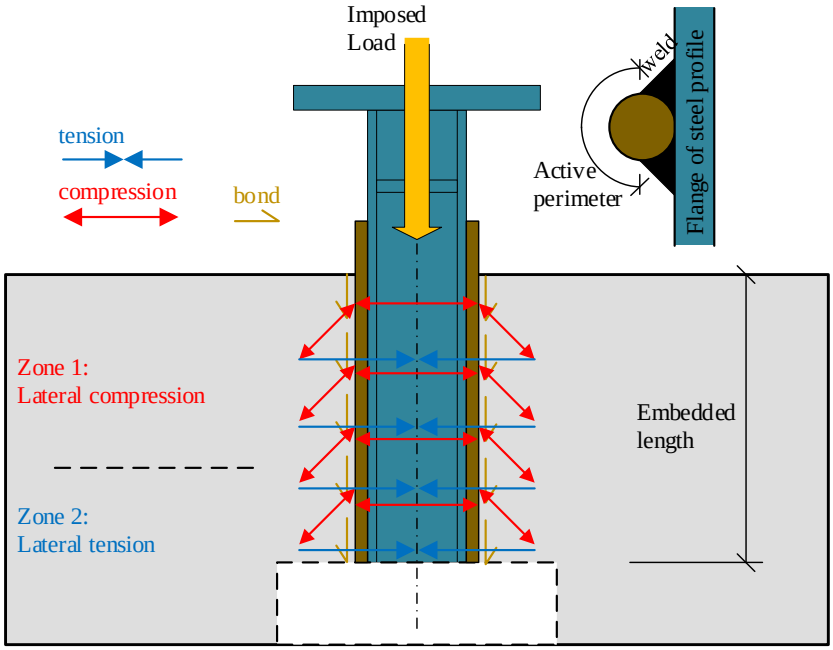


Fig. 5.83. Strut-and-tie model of the specimen Cv2 of CoPOT.

In Fig. 5.83, it could be observed that the contact area of shear connectors is not totally activated due to the implemented weld. Based on the theoretical model of the fillet welds, it was assumed that the applied welds reached the mid-height of the connector diameter and their slope was under 45°. Therefore, the effective area activation factor for the connector-concrete bond has been taken as $\lambda_u = 0.5$. In addition, it was assumed that the weld contact area was included in the plain steel-concrete bond.

The taken assumptions and observations finally lead to the overall shape of the equation that describes the load-bearing capacity of the longitudinal variant of flat shear connectors, see Eq. 5.21. In the described equation, an assumption about uniformly distributed shear stresses over the total embedded area, according to Fig. 5.81, has been implemented.

$$P_{R,b,Cv2} = \lambda_u \cdot u_{con} \cdot L_{emb} \cdot \tau_{R,con}\ [kN] \tag{5.21}$$

Where,
λ_u is the effective perimeter activation factor,
u_{con} is the perimeter of the flat shear connector,
L_{emb} is the embedded length and
$\tau_{R,con}$ is the bond shear strength of the flat shear connector.

Knowing the geometry of connector, the unknown would be only a proper estimation of the bond shear strength of shear connector. Based on the collected experimental data, an investigation to find the most feasible analytical equation to calculate the connector-concrete shear bond strength was taken. In

EN 1992-1-1 [53] and fib ModelCode 2010 [62], equations to calculate the reinforcement bar-concrete anchorage strength are provided, see Eq. 5.22 and Eq. 5.23, respectively. In each case, the given equations are referring the bond strength of rebar to the compression strength of concrete, where EC2 [53] refers the bond strength to the tension strength of concrete, but on the other hand, the tension strength of concrete is calculated based on its compression strength.

$$f_{bd} = 2.25 \cdot \eta_1 \cdot \eta_2 \cdot f_{ctd}\ [MPa] \tag{5.22}$$

Where,

η_1 is the factor including bond conditions (taken as 1.0 for good bond conditions)

η_2 is the factor relating bond to the used diameter of rebar (taken as 1.0 for ϕ<32mm)

f_{ctd} is the concrete tension strength (here three characteristic values were investigated $f_{ctk,0.95}$, $f_{ctk,0.05}$ and f_{ctm} calculated based on EC2 [53])

$$\tau_{bmax} = 2.5\sqrt{f_{cm}}\ [MPa] \tag{5.23}$$

Where,

The taken equations is for good bond conditions and pull-out failure (see Fig. 5.84)

f_{cm} is the mean concrete compression strength.

To find the best fitting equation that will give the closest value to the one calculated according to Eq. 5.13 with the force obtained from the test, the both models from EC2 [53] and fib MC2010 [62] were investigated and different values of the concrete compression strength has been implemented. For the same grade of concrete, the values for cylindrical and cubic compression strengths, as well as, for the confined and unconfined concrete were checked. The concrete confinement laws from both, EC2 [53] and fib MC2010 [62], were considered. The confinement stress was calculated according to the fib MC2010 [62] provisions. From the conducted sensivity study, it was identified that the equation of fib MC2010 [62] for the unconfined cylindrical concrete compression strength reflects the most accurately the evaluated connector-concrete bond shear strength. Values obtained from Eq. 5.21 by applying the bond strength according to EC2 [53] gave always a conservative solution. Based on the remark above, Eq. 5.21 can be updated by the definition of the bond strength of connector according to the provisions given in fib MC2010 [62] as given in Eq. 5.23. In the result, Eq. 5.24 describes the final shape of the equation for the resistance of the longitudinal variant of flat shear connector.

$$P_{R,b,Cv2} = 2.5 \cdot \pi \cdot \lambda_u \cdot d \cdot L_{emb} \cdot \sqrt{f_{cm}}\ [kN] \tag{5.24}$$

	1	2	3	4	5	6
	Pull-out (PO)		Splitting (SP)			
	$\varepsilon_s < \varepsilon_{s,y}$		$\varepsilon_s < \varepsilon_{s,y}$			
	Good bond cond.	All other bond cond.	Good bond cond.		All other bond cond.	
			Unconfined	Stirrups	Unconfined	Stirrups
τ_{bmax}	$2.5\sqrt{f_{cm}}$	$1.25\sqrt{f_{cm}}$	$2.5\sqrt{f_{cm}}$	$2.5\sqrt{f_{cm}}$	$1.25\sqrt{f_{cm}}$	$1.25\sqrt{f_{cm}}$
$\tau_{bu,split}$	—	—	$7.0\cdot\left(\frac{f_{cm}}{25}\right)^{0.25}$	$8.0\cdot\left(\frac{f_{cm}}{25}\right)^{0.25}$	$5.0\cdot\left(\frac{f_{cm}}{25}\right)^{0.25}$	$5.5\cdot\left(\frac{f_{cm}}{25}\right)^{0.25}$
s_1	1.0 mm	1.8 mm	$s(\tau_{bu,split})$	$s(\tau_{bu,split})$	$s(\tau_{bu,split})$	$s(\tau_{bu,split})$
s_2	2.0 mm	3.6 mm	s_1	s_1	s_1	s_1
s_3	c_{clear} [1)]	c_{clear} [1)]	$1.2s_1$	$0.5c_{clear}$ [1)]	$1.2s_1$	$0.5c_{clear}$ [1)]
a	0.4	0.4	0.4	0.4	0.4	0.4
τ_{bf}	$0.40\tau_{max}$	$0.40\tau_{max}$	0	$0.4\tau_{bu,split}$	0	$0.4\tau_{bu,split}$

1) c_{clear} is the clear distance between ribs

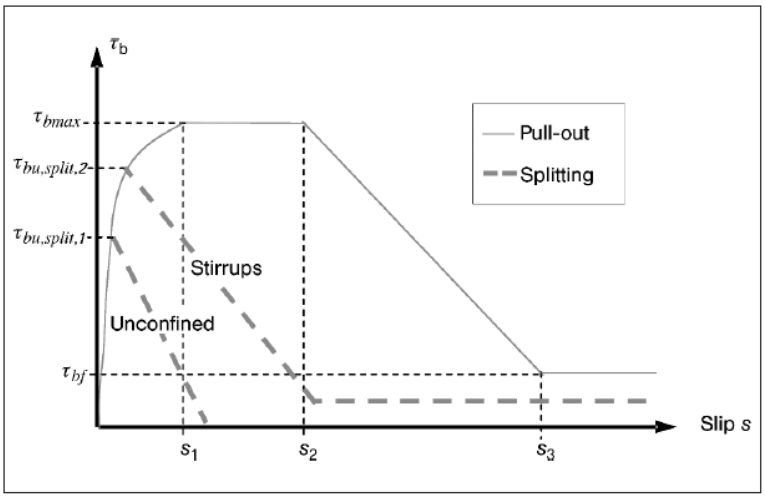


Fig. 5.84. Reinforcement bar-concrete bond strength according to fib ModelCode 2010 [62].

5.6.3.1. Verification of the equation for the shear connector bond strength ($P_{R,b}$)

Considering the geometry of the investigated connectors and the concrete material properties from the tests Cv2 in Eq. 5.24, the calculated resistance is given in Eq. 5.25.

$$P_{R,b,Cv2} = 2.5 \cdot \pi \cdot 0.5 \cdot 12 \cdot 350 \cdot \sqrt{39.2} = 103.3\ [kN] \tag{5.25}$$

Where, $f_{cm} = 39.2\ [MPa]$ is the mean compression strength of concrete for cylindrical specimens, at the day of test.

The obtained value from Eq. 5.25 gives the accuracy ratio of $103.3/103.2 = 1.00$, in reference to the experimental data, where the pure resistance of flat shear connector was distinguished. The given values are referring to one connector of diameter ϕ12 and embedded length of 350mm.

As supplementary calculations, the verification of weld can be done according to the directional method given in EN 1993-1-8 [57]. Due to the used orientation of the connector over the steel profile, only the parallel shear stresses has to be considered in the weld. Based on that conclusion, the weld resistance can be calculated according to Eq. 5.26.

$$P_{R,w,Cv2} = \sum a_w \cdot l_w \cdot \frac{f_u}{\sqrt{3} \cdot \beta_w} \; [kN] \tag{5.26}$$

Where,

$\sum a_w \cdot l_w$ is the weld geometry,

f_u is the ultimate strength of steel material and

β_w is the weld factor according to EN 1993-1-8 [57].

Reorganising Eq. 5.26, a minimal length of the weld can be calculated according to Eq. 5.27.

$$l_{w,min,Cv2} = \frac{\sqrt{3} \cdot P_{R,b,Cv2} \cdot \beta_w}{\sum a_w \cdot f_u} \; [cm] \tag{5.27}$$

In the considered case of the test Cv2 and according to Eq. 5.27, the minimum required length of the weld on both sides of the connector was 36 mm. This show, that application of the intermittent filled welds could lead to a more economical solution without harming the resistance of connector.

5.6.4. Resistance of the transversal connector – specimen Av2

The transversal variant of flat shear connector in its force transfer mechanism is incorporating three main mechanisms: (i) plain steel-concrete bond, (ii) connector-concrete bond and (iii) the mechanical bearing action. The methods described earlier to evaluate the plain steel-concrete bond and connector-concrete bond for specimens 0v2 and Cv2 apply. By calculating the mentioned above quantities, it was possible to distinguish the part of force, which was transferred purely by the mechanical connection. In summary, the mean ultimate load imposed to the specimens during the tests was 824.8 kN, the force taken by the plain steel-concrete bond was 197.2 kN and the force taken by the connector-concrete bond was 23.6 kN, in both cases including the Coulomb friction. In the result, the force that has been transferred only by the mechanical connection was 562.8 kN (281.4 kN per each connector). The scheme of the force distribution model (strut-and-tie model) of specimen Av2 is shown in Fig. 5.85.

In the model shown in Fig. 5.85, the concrete compression strut is inclined under 32°. The inclination angle has been correlated to the observations from CoPOT specimens opening, see Fig. 5.47. Form the shear connection detail, also visible in Fig. 5.85, an angle β can be identified, which is the angle between the tangential direction of the connector contact area and direction of the compression strut. It can be found that $\beta = \alpha_w + \theta$, where $\alpha_w = 45^o$ and it is the slope of the weld. In the result, $\beta = 77^o$ and accordingly $\beta_1 = 13^o$.

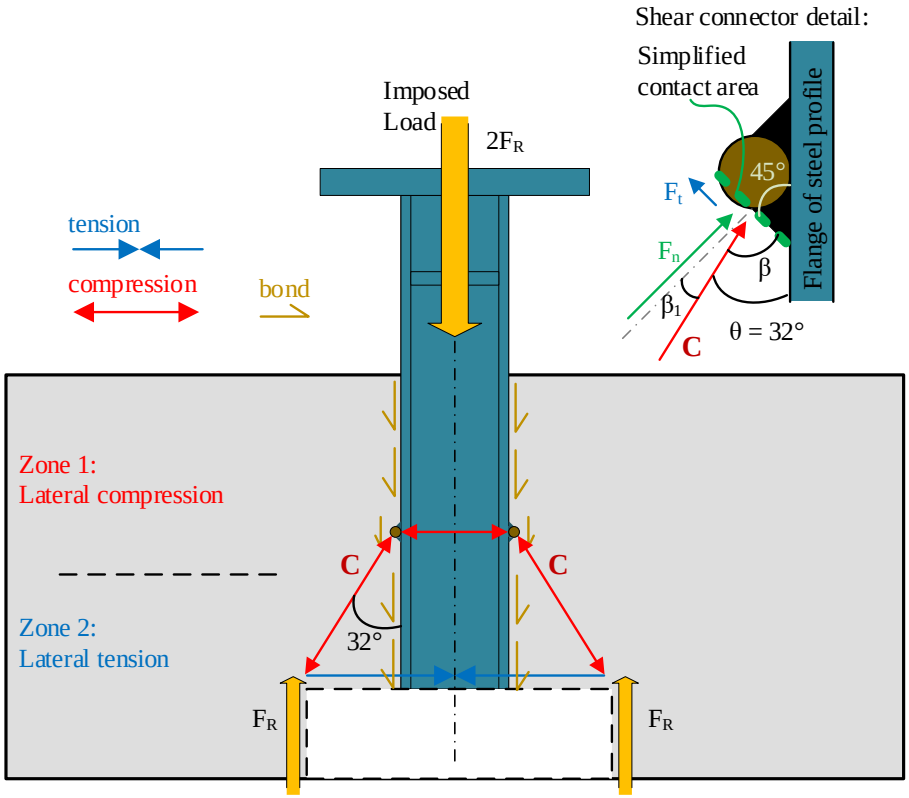


Fig. 5.85. Strut-and-tie model of the specimen Av2 of CoPOT.

The values of resulting forces acting on the connector contact area in normal and tangential directions, F_n and F_t from Fig. 5.85 respectively, can be calculated as follows:

$$C = \frac{F_R}{\cos\theta}\ [kN] \tag{5.28}$$

$$F_n = C \cdot \sin\beta\ [kN] \tag{5.29}$$

$$F_t = C \cdot \cos\beta\ [kN] \tag{5.30}$$

The contact area of flat shear connector can be calculated with a simplified and straightened shape, as shown in Fig. 5.85. The considered geometrical simplification is neglecting the rounded shape of the connector and the straight surface of the weld towards the connector peak point is extended. In the result, the considered area is slightly smaller than the realistic value, which leads to a solution that is more conservative. Eq. 5.31 describes the considered connector contact area.

$$A_{con,eff} = \lambda_d \cdot d \cdot L_{con}\ [cm^2] \tag{5.31}$$

Where,

λ_d is the effective area factor which correlates the contact area width to the diameter of the flat shear connector, and it is taken as $\lambda_d = \sqrt{2}$,

d is the flat shear connector diameter and

L_{con} is the flat shear connector length.

Knowing forces acting on the bearing contact area between the connector and concrete (Eq. 5.29-5.30), it is possible to calculate stresses acting on the contact interface as given in Eq. 5.32-5.33. Considering the situation in the plain strain state, the local coordinate system has been taken that the "x" axis is directed in the normal direction to the contact surface as shown in Fig. 5.86. The stresses has been represented as vectors.

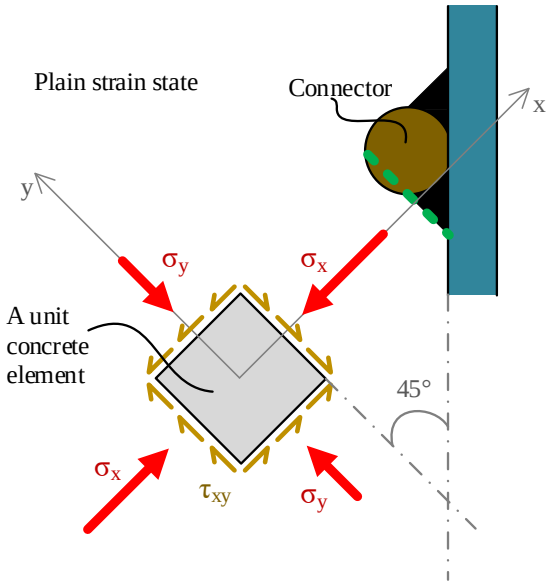


Fig. 5.86. Stresses on the contact surface of the transversal variant of flat shear connector (consider with Fig. 5.85).

$$\sigma_x = \frac{F_n}{A_{con,eff}} = \frac{C \cdot \sin\beta}{\lambda_d \cdot d \cdot L_{con}} = \frac{F_R \cdot \sin\beta}{\lambda_d \cdot d \cdot L_{con} \cdot \cos\theta} \left[{}^{kN}/_{cm^2}\right] \tag{5.32}$$

$$\tau_{xy} = \frac{F_t}{A_{con,eff}} = \frac{C \cdot \cos\beta}{\lambda_d \cdot d \cdot L_{con}} = \frac{F_R \cdot \cos\beta}{\lambda_d \cdot d \cdot L_{con} \cdot \cos\theta} \left[{}^{kN}/_{cm^2}\right] \tag{5.33}$$

To know the complete stress state acting on a unit concrete element shown in Fig. 5.86, the stresses acting in "y" direction are remaining. Those stresses are imposing a confinement stresses to the concrete element and they are directly related to the acting stresses σ_x. According to the observations taken from the experimental campaign, particularly to the failure pattern discovered in the specimens Av2 and highly confined concrete area identified under the connector (see Fig. 5.47), an assumption of full confinement has been implemented. The taken assumption brings a simplification to the concrete stress state and according to it, the strains in the transversal directions (ε_y) are equal to 0. This relation has been confirmed in numerical simulations. Based on the theory of elasticity, Hooke's law and equilibrium conditions, the transversally confining stresses can be calculated as given in Eq. 5.34-5.37.

$$\varepsilon_y = \frac{\sigma_y - \sigma_x \cdot \nu}{E} = 0 \tag{5.34}$$

$$\sigma_y - \sigma_x \cdot \nu = 0 \tag{5.35}$$

$$\sigma_y = \sigma_x \cdot \nu \tag{5.36}$$

$$\sigma_y = \frac{F_n}{A_{con,eff}} \cdot \nu = \frac{C \cdot \sin\beta}{\lambda_d \cdot d \cdot L_{con}} \cdot \nu = \frac{F_R \cdot \sin\beta \cdot \nu}{\lambda_d \cdot d \cdot L_{con} \cdot \cos\theta} \left[{}^{kN}/_{cm^2} \right] \tag{5.37}$$

Where, ν is the Poisson ratio and the value of 0.2 is taken for the concrete.

According to the model shown in Fig. 5.85 and evaluated stresses at the connector-concrete bearing interface, the shear connection resistance is related to:

1) the strength of embedding concrete,
2) the strength of weld and
3) the strength of connector material.

The identified failure mechanisms are described and characterised below in the respective paragraphs.

The strength of embedding concrete has to be verified in (i) the maximum compression condition and (ii) the maximum shear condition. To analyse these conditions, the principal stresses direction for the maximum compression stresses has to be considered, as well as, the direction where the shear stresses reached the maximum value - 45° rotated direction from the principal direction [184]. Using Cauchy stress tensor definition, the stress transformation equations are given in Eq. 5.38-5.39, where γ is the transformation angle. Differencing the transformation equations over the transformation angle result in two characteristic angles for the maximum normal stresses and one angle for the maximum tangential stresses as given in Eq. 5.40-5.41. Implementing the respective angles back to the transformation equations from Eq. 5.38 and Eq. 5.39, the equations describing the principal stress state and maximum shear stress state are obtained and given in Eq. 5.42-5.45.

$$\sigma_{x1} = \frac{\sigma_x + \sigma_y}{2} + \frac{\sigma_x - \sigma_y}{2} \cdot \cos 2\gamma + \tau_{xy} \cdot \sin 2\gamma \tag{5.38}$$

$$\tau_{x1y1} = -\frac{\sigma_x - \sigma_y}{2} \cdot \sin 2\gamma + \tau_{xy} \cdot \cos 2\gamma \tag{5.39}$$

$$\tan 2\gamma_p = \frac{2\tau_{xy}}{\sigma_x - \sigma_y} \tag{5.40}$$

$$\tan 2\gamma_{s,max} = -\left(\frac{\sigma_x - \sigma_y}{2\tau_{xy}}\right) \tag{5.41}$$

$$\sigma_{p1,p2} = \frac{\sigma_x + \sigma_y}{2} \pm \sqrt{\left(\frac{\sigma_x - \sigma_y}{2}\right)^2 + {\tau_{xy}}^2} \tag{5.42}$$

$$\tau_p = 0 \tag{5.43}$$

$$\tau_{max} = \sqrt{\left(\frac{\sigma_x - \sigma_y}{2}\right)^2 + {\tau_{xy}}^2} \tag{5.44}$$

$$\sigma_s = \frac{\sigma_x + \sigma_y}{2} \tag{5.45}$$

Where,

σ_{x1} is the normal stress in the considered direction,

τ_{x1y1} is the tangential stress in the considered direction,

$\sigma_{p1,p2}$ is the principal stress in direction 1 or direction 2, with considered "+" or "-", respectively,

τ_p is the shear stress in the principal direction (always zero),

τ_{max} is the maximum tangential shear stress,

σ_s is the corresponding normal stress to the maximum shear stress direction,

γ is the rotation angle from the initial state defining the considered direction,

γ_p is the angle defining the principal direction and

$\gamma_{s,max}$ is the angle defining the maximum shear stress direction.

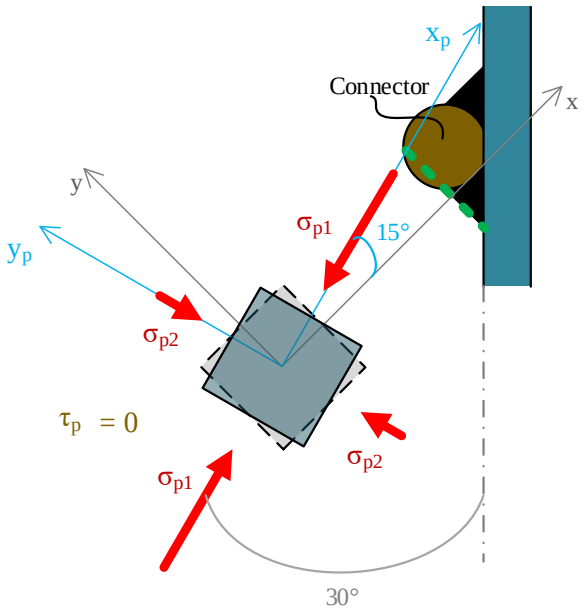
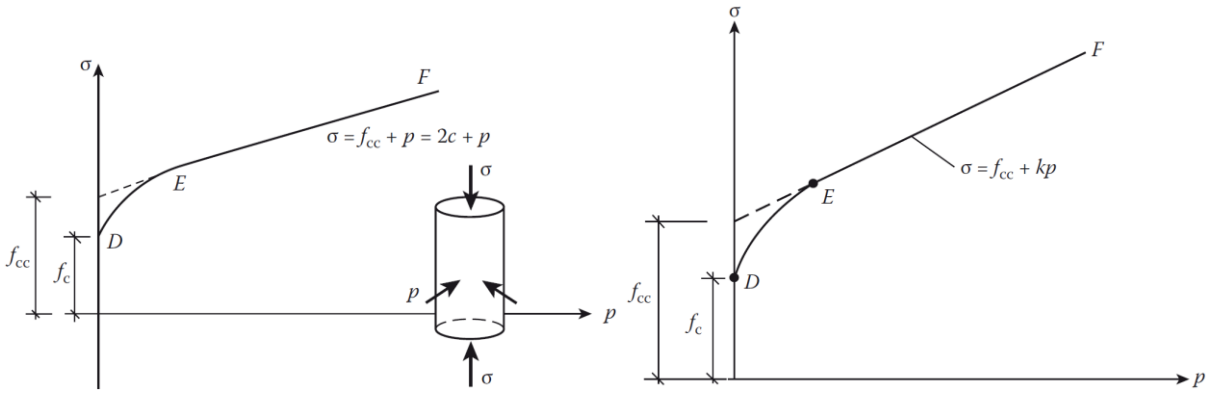


Fig. 5.87. Principal stress state in the transversal variant of flat shear connector, specimen Av2 of CoPOT.

According to Eq. 5.40, the orientation of the maximum compression principal stress under a $\gamma_p = 15^o$ has been identified. Direction of the considered principal stresses creates with the vertical direction an angle of 30°, which refers well to the concrete compression strut orientation identified during the experimental campaign as shown in Fig. 5.47. The stress state in the principal direction of concrete unit element is shown in Fig. 5.87.

Considering the principal stress state under the contact surface with the flat shear connector, the concrete is subjected to the maximum possible compression stresses. Therefore, the resistance of flat shear connector is related to the compression strength of concrete. The concrete compression strength is amplified by the existence of the lateral confining stresses in the direction of second principal stresses, which are defined by Eq. 5.42. Different models to evaluate the compression strength of confined

concrete have been investigated, in particular model given by EN 1992-1-1 [53] and fib MC2010 [62]. It was identified that EC2 [53] brings a more conservative value than the model of fib MC2010 [62]. However, the calculated compression strength of confined concrete was still not reflecting the obtained strength acquired from the tests Av2. Investigation of the background of the fib model of confined concrete allowed to identify a model proposed by Nielsen [130], which is similar to the model proposed by fib MC2010 [62] but it excludes the safety concept. The modified Mohr-Coulomb material law for concrete described by Nielsen [130], see Fig. 5.88, gave the best accuracy. Finally, the resistance of flat shear connector due to the concrete compression failure condition is defined in Eq. 5.46. Substituting the minority sign by equality sing and implementing Eq. 5.32-5.33 and Eq. 5.37 into Eq. 5.48, the resulting equation for the resistance is obtained and it is defined in Eq. 5.52.



a) b)

Fig. 5.88. Failure condition for the Mohr-Coulomb material [130] – a) for cement paste, b) for concrete.

$$\sigma_1 = \frac{\sigma_x + \sigma_y}{2} + \sqrt{\left(\frac{\sigma_x - \sigma_y}{2}\right)^2 + {\tau_{xy}}^2} < f_{cm,c,cube} \tag{5.46}$$

$$\frac{\sigma_x + \sigma_y}{2} + \sqrt{\left(\frac{\sigma_x - \sigma_y}{2}\right)^2 + {\tau_{xy}}^2} = \left(f_{cm,cc,cube} + k_s \cdot \sigma_2\right) \tag{5.47}$$

$$\frac{\sigma_x + \sigma_y}{2} + \sqrt{\left(\frac{\sigma_x - \sigma_y}{2}\right)^2 + {\tau_{xy}}^2} = \omega_{cc} \cdot f_{cm,cube} + k_s \cdot \left(\frac{\sigma_x + \sigma_y}{2} - \sqrt{\left(\frac{\sigma_x - \sigma_y}{2}\right)^2 + {\tau_{xy}}^2}\right) \tag{5.48}$$

$$\frac{F_R \cdot (0.5 \cdot \sin\beta \cdot (1+\nu) + \psi_A)}{\lambda_d \cdot d \cdot L_{con} \cdot \cos\theta} - k_s \cdot \frac{F_R \cdot (0.5 \cdot \sin\beta \cdot (1+\nu) - \psi_A)}{\lambda_d \cdot d \cdot L_{con} \cdot \cos\theta} = \omega_{cc} \cdot f_{cm,cube} \tag{5.49}$$

$$\psi_A = \sqrt{0.25 \cdot (1-\nu)^2 \cdot \sin^2\beta + \cos^2\beta} \tag{5.50}$$

$$\frac{F_R}{\lambda_d \cdot d \cdot L_{con} \cdot \cos\theta} \cdot \left((k_s + 1) \cdot \psi_A - 0.5 \cdot (k_s - 1) \cdot \sin\beta \cdot (1+\nu)\right) = \omega_{cc} \cdot f_{cm,cube} \tag{5.51}$$

$$P_{R,c} = \frac{\lambda_d \cdot \cos\theta \cdot L_{con} \cdot d \cdot \omega_{cc} \cdot f_{cm,cube}}{(k_s + 1) \cdot \psi_A - 0.5 \cdot (k_s - 1) \cdot \sin\beta \cdot (1+\nu)} \; [kN] \tag{5.52}$$

Where,

$f_{cm,c,cube}$ is the mean compression strength of confined concrete for cube specimens,

$f_{cm,cc,cube}$ is the compressive strength for a Coulomb material based on Fig. 5.88,

k_s is the inclination parameter for the Coulomb material and $k_s = \left(\mu + \sqrt{1+\mu^2}\right)^2$,

μ is the tangent of internal friction angle of concrete and $\mu = \tan\varphi$,

φ is the internal friction angle of concrete taken according to Fig. 5.89,

σ_2 is the confining pressure (in Fig. 5.88, it is denoted as "p"), in our case $\sigma_2 = \sigma_{p2}$,

ω_{cc} is the transformation factor which relates the Coulomb's material compression strength to the concrete compression strength without confining stresses (see Fig. 5.88), taken according to Fig. 5.90,

ψ_A is the coefficient, which simplifies the equation form and

$P_{R,c}$ is the shear connector's resistance for the concrete compression failure mode (substituted from F_R).

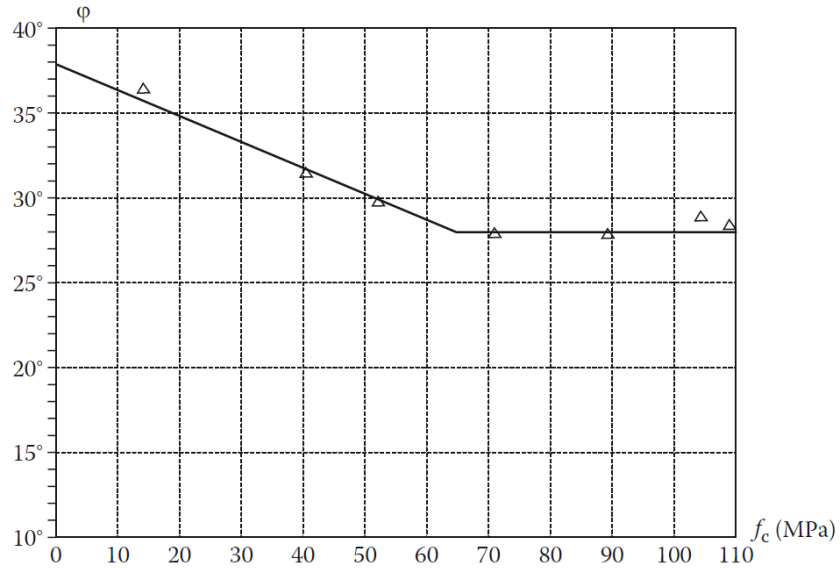


Fig. 5.89. Internal friction angle for different strengths of concrete [130].

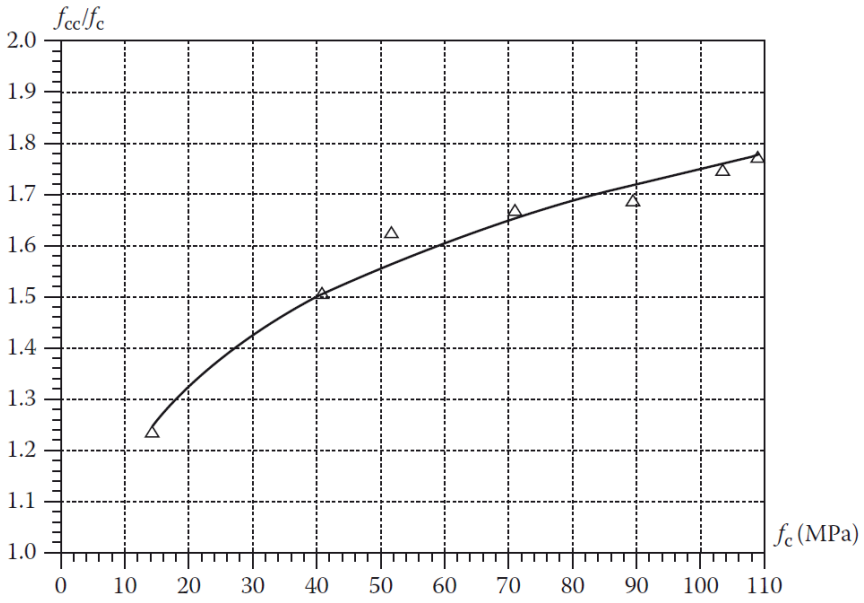


Fig. 5.90. Ratio between f_{cc} and f_c in the modified Mohr-Coulomb material according to Nielsen [130].

According to Eq. 5.41, the orientation of maximum shear stresses under a $\gamma_{s,max} = -30^o$ has been identified. Direction of the considered shear stress creates with the vertical direction an angle of $\alpha_{s1} = 15^o$, which refers well to the identified during the experimental campaign shear plane localised directly under the connector (see Fig. 5.47 and Eq. 5.50). The stress state in the maximum shear direction of concrete unit element is shown in Fig. 5.91.

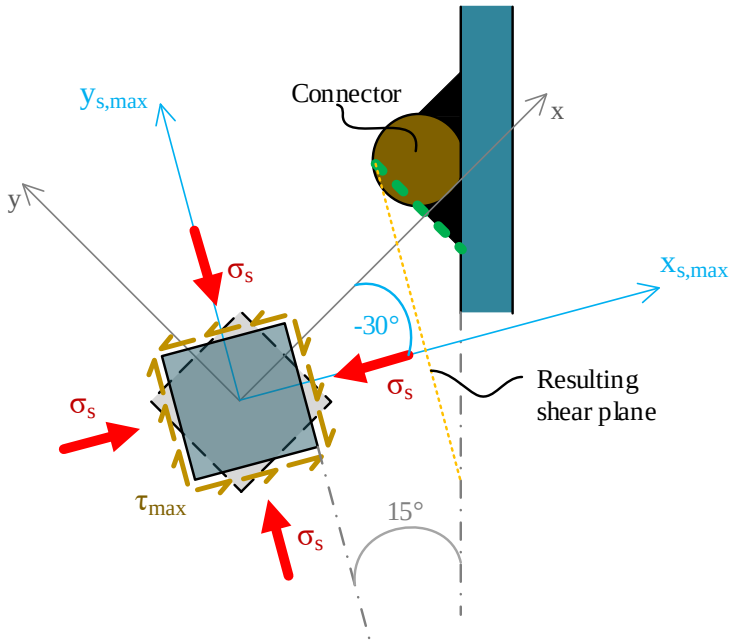


Fig. 5.91. Maximum shear stress state in the transversal variant of flat shear connector, specimen Av2 of CoPOT.

In the maximum shear stress state, the concrete is subjected to the significant shear stresses over the area in the resulting shear plane defined in Fig. 5.91. In the same time, the accompanying normal stresses σ_s are creating the confinement stresses. The effective shearing area can be defined in reference to the diameter of shear connector and resulting inclination angle of shear plane, as given in Eq. 5.54. Finally, the resistance of flat shear connector is related to the shearing strength of concrete over the effective area. To evaluate the shear strength of concrete, the modified Mohr-Coulomb material law proposed my Nielsen [130] has been implemented, see Fig. 5.92.

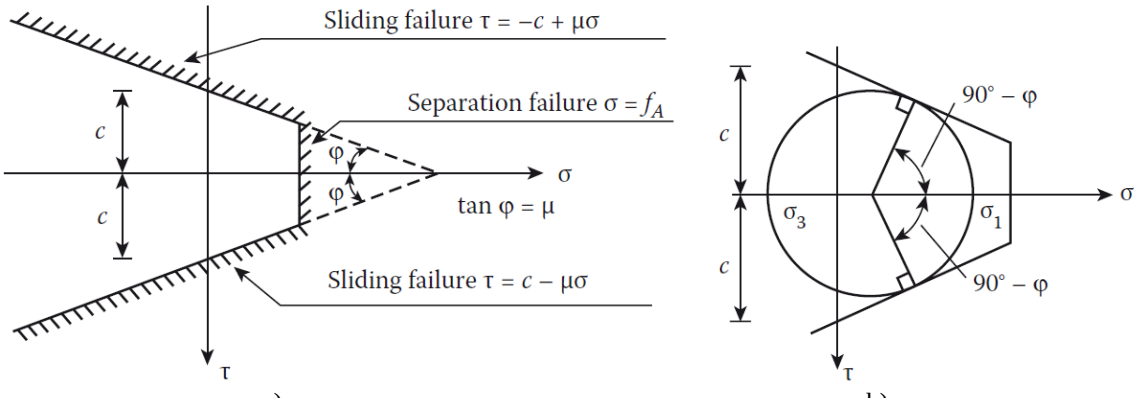


Fig. 5.92. Failure criterion for the modified Mohr-Coulomb material according to Nielsen [130] – a) overall definition and b) sliding failure.

The sliding failure, represented in Fig. 5.92, is reflecting the considered shear failure of concrete due to the occurring maximum shear stresses in the specimen. To define the shear strength of concrete, material constants, like cohesion and friction angle, have to be defined. Moreover, the external confining pressure is essential to define the amplified shear strength of concrete. The overall condition for the resistance of flat shear connector is defined in Eq. 5.55. Implementing Eq. 5.32-5.33, Eq. 5.37 and Eq. 5.54 into Eq. 5.55, the resulting resistance is defined in Eq. 5.59.

$$\alpha_{s1} = \alpha_w + \gamma_{s,max}\ [^o] \tag{5.53}$$

$$A_{s,eff} = \frac{d}{\sin(\alpha_s)} \cdot L_{con}\ [cm^2] \tag{5.54}$$

$$\tau_{max} = \sqrt{\left(\frac{\sigma_x - \sigma_y}{2}\right)^2 + {\tau_{xy}}^2} < \sigma_s \cdot \tan\varphi + c \tag{5.55}$$

$$\sqrt{\left(\frac{\sigma_x - \sigma_y}{2}\right)^2 + {\tau_{xy}}^2} = \frac{\sigma_x + \sigma_y}{2} \cdot \tan\varphi + \nu_s \cdot \frac{1}{2 \cdot \sqrt{k_s}} \cdot f_{cm,cube} \tag{5.56}$$

$$\frac{F_R \cdot \psi_A \cdot \sin(\alpha_{s1})}{d \cdot L_{con} \cdot \cos\theta} = \frac{F_R \cdot \sin\beta \cdot (1+\nu) \cdot \sin(\alpha_{s1})}{2 \cdot d \cdot L_{con} \cdot \cos\theta} \cdot \mu + \nu_s \cdot \frac{1}{2 \cdot \sqrt{k_s}} \cdot f_{cm,cube} \tag{5.57}$$

$$\frac{F_R \cdot \sin(\alpha_{s1})}{d \cdot L_{con} \cdot \cos\theta} \cdot (\psi_A - 0.5 \cdot \sin\beta \cdot (1+\nu) \cdot \mu) = \frac{\nu_s}{2\sqrt{k_s}} \cdot f_{cm,cube} \tag{5.58}$$

$$P_{R,s1} = \frac{\nu_s \cdot \cos\theta \cdot d \cdot L_{con} \cdot f_{cm,cube}}{2\sqrt{k_s} \cdot (\psi_A - 0.5 \cdot \sin\beta \cdot (1+\nu) \cdot \mu) \cdot \sin(\alpha_{s1})}\ [kN] \tag{5.59}$$

Where,

α_{s1} is the angle between the resulting shear and vertical directions,

$A_{s,eff}$ is the effective shearing area,

c is the cohesion of concrete material and $c = \nu_s \cdot \frac{1}{2\sqrt{k_s}} \cdot f_{cm,cube}$ [130],

ν_s is the concrete cohesion reduction factor due to micro cracking and it is taken as 0.5 [130],

for ψ_A see Eq. 5.50 and

$P_{R,s1}$ is the resistance of flat shear connector for the maximum shear condition (substituted from F_R).

The strength of weld can define the global resistance of the transversal variant of flat shear connector. Therefore, the verification according to the theory of elasticity and von Mises yield criterion has been made, which correlates to the method given in EN 1993-1-8 [57]. To achieve a more conservative and simplified solution, the vertical reaction force F_R has been assumed as the force acting on the welded connection, see Fig. 5.85. In Fig. 5.93, the mechanical model for the weld verification has been given, where the shear connector has been considered as the cantilever fixed to the flange of

steel profile and the resultant force is imposed to its centre. The vertical force imposed to the connection is acting on the weld with an eccentricity e_w. The eccentricity has been conservatively assumed up to the surface of flange. To verify the resistance of weld and check the yielding criterion, the failure planes in (i) the critical plane of weld, (ii) the rotated to the vertical direction critical plane of weld, (iii) the vertical plane in the centroid of weld and (iv) the vertical plane at the base of weld have been investigated. The geometry of the weld has been assumed as the filled weld with full penetration, which can be confirmed by the visual examination of the opened specimen and shown in Fig. 5.94. In the result, the height of weld until the middle of the shear connector diameter and the inclination slope of weld of 45° have been assumed.

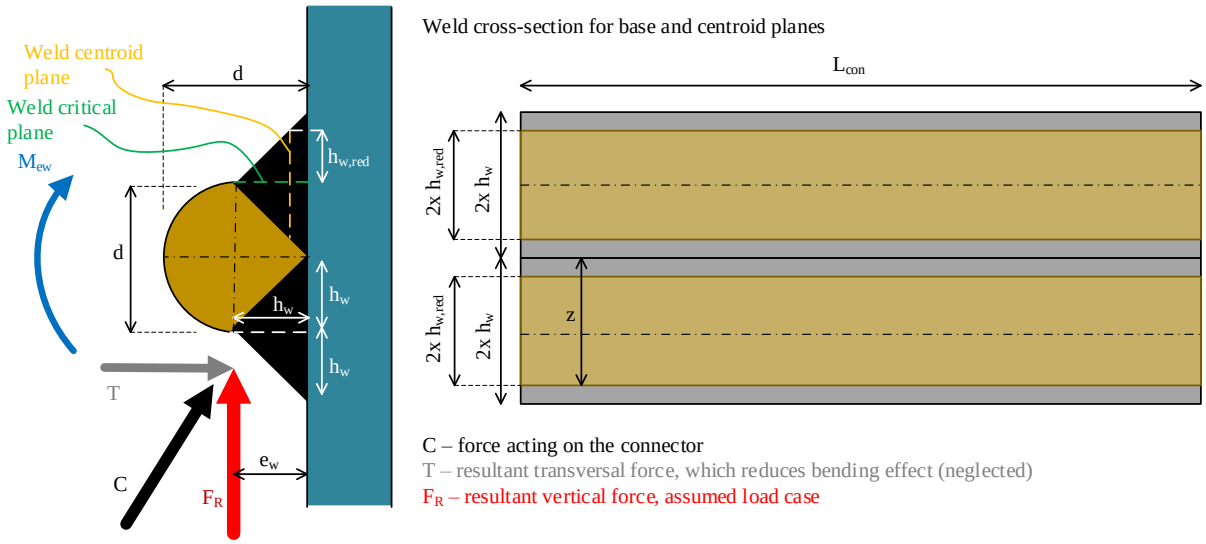


Fig. 5.93. Model for the verification of weld in the transversal variant of flat shear connector, specimen Av2 of CoPOT.



a) b)

Fig. 5.94. Detail of flat shear connector, transversal variant, specimen Av2 – a) view from the left side, b) view from the right side.

The consideration of different failure planes in the weld for the verification process impose different cross-sectional properties of the weld and different stress components to the von Mises yield criterion, see Eq. 5.62. However, only the input values are changing and the verification procedure, as well as, the principal resistance condition are the same. The sensivity study of different possible failure planes and observations from the experimental campaign show that the weld failure would develop most probably

in centroid plane shown in Fig. 5.93, which is oriented in the vertical direction and it is in the alignment to the imposed load. This failure pattern is the most probable and decisive failure mechanism because the shear plane will be formed in the direction of the major acting force – vertical reaction F_R. Verification of the weld in the critical plane, like suggests EN 1993-1-8 [57], in the case when the vertical reaction force is acting in shear, leads to the case when the failure of weld is achieved earlier than given by the experimental results. However, this case is in contradiction to the real orientation of the considered critical plane. Considering horizontal orientation of the critical plane, like in Fig. 5.93, the bending moment is acting on shear stresses and reaction force on normal stresses. This failure variant leads to the weld resistance very close to the obtained load-bearing capacity of specimen – but the specimen failure during tests did not happened due to weld failure. Therefore, the described variants including critical plane of weld were considered as a not realistic case and the verification has been made according to the previously mentioned centroid plane of the weld. The resistance condition and the resulting equation for the resistance of shear connector weld is given in Eq. 5.60-5.66. In Eq. 5.66, the resistance of weld due to the elastic model has been derived by inserting Eq. 5.64 and Eq. 5.65 into the resistance condition given in Eq. 5.62. In order to analyse the elastic stresses in the centroid plane, the geometrical factor $\psi_{w,el}$ given in Eq. 5.67 has to be considered. The plastic stress distribution model has been analysed as well and implemented into the von Mises yielding criterion. However, the resulting resistance was always higher than the elastic variant which leads to the less critical solution. In order to include the plastic stress distribution for the verification of weld, the plastic geometrical factor $\psi_{w,pl}$ given in Eq. 5.68 has to be implemented into Eq. 5.66.

$$e_w = h_w = 0.5d\ [cm] \tag{5.60}$$

$$M_{ew} = F_R \cdot e_w\ [kNcm] \tag{5.61}$$

$$\sqrt{{\sigma_\perp}^2 + 3 \cdot ({\tau_\perp}^2 + {\tau_\parallel}^2)} \leq \frac{f_u}{\beta_w \cdot \gamma_{M2}} \tag{5.62}$$

$$\tau_\parallel = 0 \tag{5.63}$$

$$\sigma_M = \frac{M_{ew} \cdot z}{I_w}\ \left[{kN}/{cm^2}\right] \rightarrow\ \sigma_M = \{\sigma_\perp\ or\ \tau_\perp\} \tag{5.64}$$

$$\sigma_F = \frac{F_R}{A_w}\ \left[{kN}/{cm^2}\right] \rightarrow\ \sigma_F = \{\sigma_\perp\ or\ \tau_\perp\} \tag{5.65}$$

$$P_{R,w} = \frac{f_u}{\beta_w \cdot \psi_w}\ [kN] \tag{5.66}$$

$$\psi_{w,el} = \sqrt{\frac{{e_w}^2 \cdot z^2}{{I_w}^2} + 3 \cdot \frac{1}{{A_w}^2}}\ \left[\frac{1}{cm^2}\right] \tag{5.67}$$

$$\psi_{w,pl} = \sqrt{\frac{{e_w}^2}{d^2 \cdot {A_{w,t}}^2} + 3 \cdot \frac{1}{{A_w}^2}} \left[\frac{1}{cm^2}\right] \tag{5.68}$$

Where,

e_w is the weld eccentricity measured from the position of force to the flange of steel profile,

h_w is the height of the used weld and $h_w = 0.5d$,

M_{ew} is the resulting bending moment in the welded connection due to the eccentricity e_w,

z is the distance from the weld centre of gravity to the most external fibre in tension,

I_w is the moment of inertia of the welded connection,

A_w is the cross-sectional area of the welded connection,

$A_{w,t}$ is the area of the weld subjected to tension,

$\sigma_\perp$, $\tau_\parallel$, $\tau_\perp$ are the stresses acting on the welded connection according to EN 1993-1-8 [57],

f_u is the ultimate strength of the welded material,

β_w is the weld parameter related to the steel grade

$P_{R,w}$ is the resistance of flat shear connector for the weld failure condition.

The strength of connector material is evaluated analogically to the verification of weld – the connectors is considered as a cantilever fixed to the flange of steel profile, see Fig. 5.93. In order to analyse the resistance of connector material, instead of the weld, the internal forces at the point where the weld ends and the cross-sectional properties of connector material at the aforementioned point are considered. The analysed case is shown in Fig. 5.95.

The elastic resistances for shear, bending and their interaction, define the resistance of connector material. In addition, the plastic resistance for shear is verified. The base fundamental equations and the derived equations for the resistance of connector material are described in Eq. 5.69-5.79. In Eq. 5.72-5.74, the bending resistance has been evaluated. In Eq. 5.75, the plastic shear resistance has been defined. In Eq. 5.76-5.79, the equations including interaction of both bending and shear are given.

Normally, the plastic shear resistance of the connector material given in Eq. 5.75 yields the smallest resistance from the considered values included in Eq. 5.80.

$$\tau_E = \frac{V_E \cdot S_{con}}{I_{con} \cdot t} \leq \frac{f_y}{\sqrt{3}} \tag{5.69}$$

$$V_E = F_R \cdot \left(1 - \frac{h_w}{d}\right) [kN] \tag{5.70}$$

$$P_{R,cs,el} = \frac{f_y \cdot L_{con} \cdot d}{1.5 \cdot \sqrt{3} \cdot \left(1 - \frac{h_w}{d}\right)} [kN] \tag{5.71}$$

$$\sigma_E = \frac{M_E \cdot z}{I_{con}} \leq f_y \tag{5.72}$$

$$M_E = \frac{F_R \cdot (d - h_w)^2}{2d} \; [kNcm] \tag{5.73}$$

$$P_{R,cb,el} = \frac{f_y \cdot L_{con} \cdot d^3}{3 \cdot (d - h_w)^2} \; [kN] \tag{5.74}$$

$$V_{pl,R} = \frac{A_{con} \cdot f_y}{\sqrt{3}} = \frac{d \cdot L_{con} \cdot f_y}{\sqrt{3}} = P_{R,cs,pl} \; [kN] \tag{5.75}$$

$$\sigma_E = \frac{M_E \cdot z}{I_c} \leq (1 - \rho) f_y \tag{5.76}$$

$$\rho = \left(\frac{2 \cdot V_E}{V_{pl,R}} - 1 \right)^2 \tag{5.77}$$

$$If, \quad \frac{V_E}{V_{pl,R}} < 0.5 \quad then\ bending\ and\ shear\ interaction\ can\ be\ neglected \tag{5.78}$$

$$P_{R,cb,cs} = \frac{(1 - \rho) \cdot f_y \cdot L_c \cdot d^3}{3 \cdot (d - h_w)^2} \; [kN] \tag{5.79}$$

$$P_{R,m} = min\{P_{R,cs,el};\ P_{R,cb,el};\ P_{R,cb,cs};\ P_{R,cs,pl}\} \tag{5.80}$$

Where,

τ_E is the resultant elastic shear stresses acting in the considered plane,

V_E is the resultant shear force acting in the considered plane,

S_{con} is the moment of area for the plane in the mid-height of shear connector cross-section,

I_{con} is the moment of inertia for the considered cross-section of shear connector,

t is the thickness of the cross-section in the transversal direction to the acting stresses ($t = L_{con}$),

f_y is the yielding strength of the connector material,

h_w is the height of the implemented weld (see Fig. 5.93),

$P_{R,cs,el}$ is the resistance of shear connector for the material elastic shearing condition,

$P_{R,cb,el}$ is the resistance of shear connector for the material elastic bending condition,

$P_{R,cb,cs}$ is the resistance of shear connector for the material bending and shear interaction condition and

$P_{R,m}$ is the resultant resistance of shear connector material.

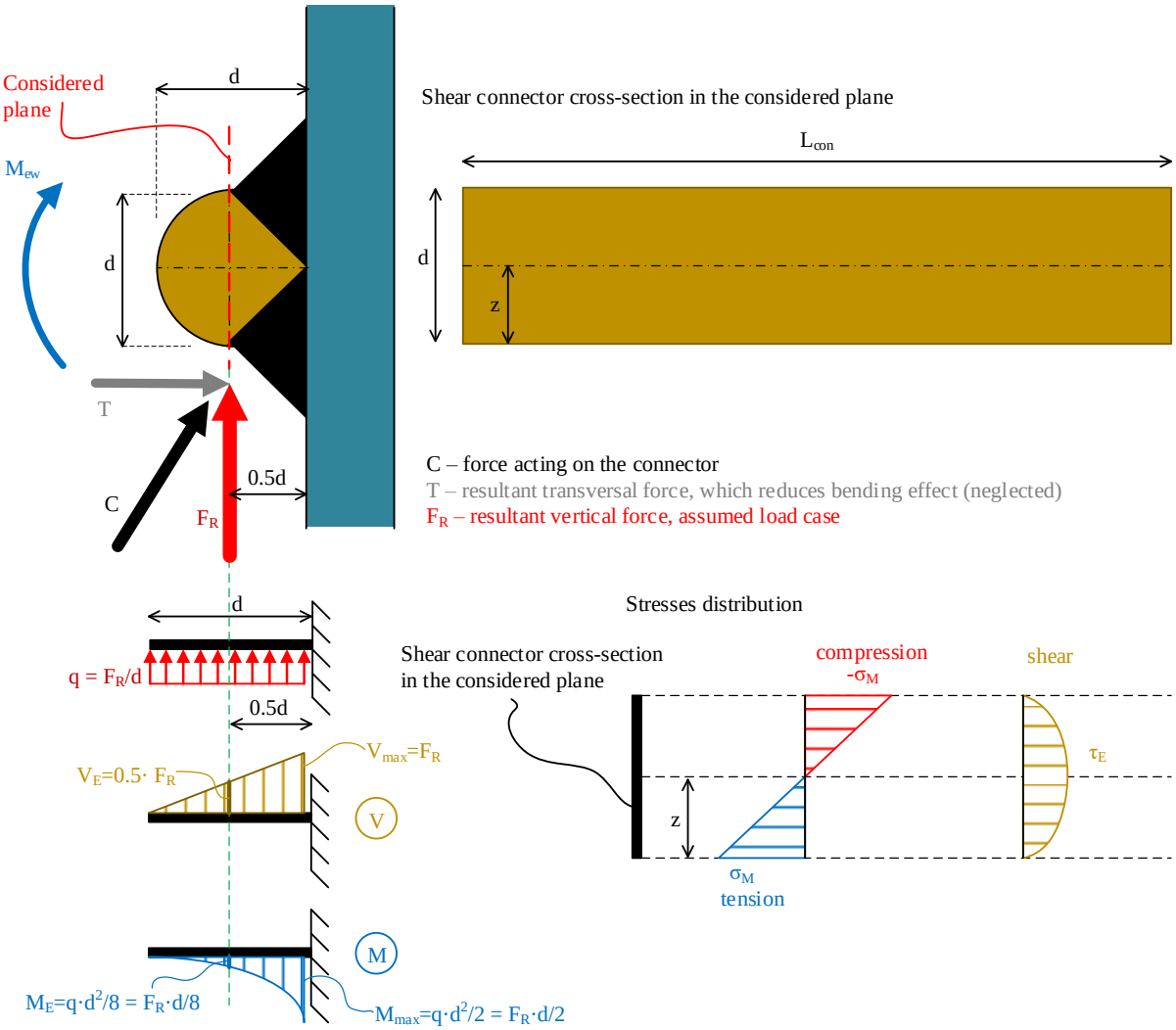


Fig. 5.95. Mechanical model for the evaluation of the resistance of connector material in the transversal variant of flat shear connector.

The resistance of embedding concrete to the maximum compression stresses and maximum shear stresses are supported in both cases by the connector-concrete bond resistance. The connector-concrete bond strength has been evaluated according to the procedure given for the specimen Cv2 described in Section 5.6.3 and given in Eq. 5.24. Due to different orientation of the connector with reference to the imposed load, transversal and not longitudinal, the effective area activation factor λ_u required an adjustment and it was assumed that the active area in connector-concrete bond reduces to 0.25 of the total perimeter. The reduction of the area activation factor is related to the fact that, in transversal orientation, the upper part of the connector perimeter is not transferring forces in shear but the load transfer is more related to the normal separation. The contributing part of the connector-concrete bond resistance has been denoted as $P_{R,b}$ and given in Eq. 5.81.

$$P_{R,b} = 2.5 \cdot \pi \cdot \lambda_u \cdot d \cdot L_{con} \cdot \sqrt{f_{cm}} \tag{5.81}$$

Where, $\lambda_u = 0.25$ and f_{cm} is considered for cylindrical values.

Finally, the resistance of transversal variant of flat shear connectors has to be taken as the minimum of the investigated possible failure modes. The summary and the judging criterion is given in Eq. 5.82.

$$P_{R,Av2} = min\begin{cases} P_{R,w} = \dfrac{f_u}{\beta_w \cdot \psi_w} \\ P_{R,m} = min\{P_{R,cs,el};\ P_{R,cb,el};\ P_{R,cb,cs};\ P_{R,cs,pl}\} = \dfrac{d \cdot L_{con} \cdot f_y}{\sqrt{3}} \\ P_{R,c} + P_{R,b} = \dfrac{\lambda_d \cdot \cos\theta \cdot L_{con} \cdot d \cdot \omega_{cc} \cdot f_{cm,cube}}{(k_s + 1) \cdot \psi_A - 0.5 \cdot (k_s - 1) \cdot \sin\beta \cdot (1 + \nu)} + P_{R,b} \\ P_{R,s1} + P_{R,b} = \dfrac{\nu_s \cdot \cos\theta \cdot d \cdot L_{con} \cdot f_{cm,cube}}{2\sqrt{k_s} \cdot (\psi_A - 0.5 \cdot \sin\beta \cdot (1 + \nu) \cdot \mu) \cdot \sin(\alpha_{s1})} + P_{R,b} \end{cases} \quad (5.82)$$

The above-described analytical model has been derived based on the observations from the experimental campaign and numerical simulations. It has been based on the fundamental equations of the theory of elasticity and plasticity with implemented modified Mohr-Coulomb material law for concrete described by Nielsen [130]. The procedure to estimate the resistance of shear connector has been supported by the design provisions given in EN 1994-1-1 [58], EN 1992-1-1 [53], EN 1993-1-1 [55], EN 1993-1-8 [57] and fib ModelCode 2010 [62]. The obtained results according to Eq. 5.82 are in good correlation to the obtained behaviour from the test specimens. However, to get a convergence with the experimental values of the specimen load-bearing capacity, calibration factors have to be implemented to the resistances for compression ($P_{R,c}$) and shear ($P_{R,s1}$) of concrete, where the verification is described in Sections 5.6.4.1-5.6.4.5. To distinguish the character of the implemented calibration factor, they have the following nomenclature and meaning:

- $\boldsymbol{k_{hlc}}$ is the calibration factor used for the compression strength of concrete and, among others, it is mainly related to the existence of the global confinement of the concrete due to the applied reinforcement cage around the embedded steel profile and extrapolation of the proposed plain model to the 3D problem. Its value was calibrated based on the experimental results and it is amplifying the confined concrete strength to reach the experimental values.
- $\boldsymbol{\lambda_s}$ is the calibration factor used for the concrete shear strength and it is related to the existence of the global confinement of the concrete due to the reinforcement cage, extrapolation of the plain model to the 3D problem and it is related to the local behaviour of concrete, like for example micro and macro carking effects around the shear connector. Its value has been calibrated based on the experimental results.

The aforementioned calibration factors are implemented to the derived analytical models for the resistances of flat connectors from specimens Av2 and Bv2 (transversal and V-shaped variants, respectively). The calibration factors are indicated in red colour in order to increase their visibility.

5.6.4.1. Verification of the resistance of the weld ($P_{R,w}$)

In the resistance model of weld given in Eq. 5.60-5.68, no calibration factors are implemented. The both stresses distribution, elastic and plastic, have been investigated and the corresponding resistances are calculated in Eq. 5.92 and Eq. 5.93, respectively.

$$d = 0.8\ [cm] \tag{5.83}$$

$$e_w = \frac{d}{2} = 0.4\ [cm] \tag{5.84}$$

$$z = \frac{d}{2} + {}^{2}/_{3}\, h_w = \frac{d}{2} + {}^{2}/_{3} \cdot \frac{d}{2} = 0.4 + 0.267 = 0.667\ [cm] \tag{5.85}$$

$$I_w = \frac{2 \cdot l_w \cdot (2h_w)^3}{12} + A_{w,t} \cdot \left(\frac{d}{2}\right)^2 = \frac{2 \cdot 12 \cdot (0.8)^3}{12} + (2 \cdot 0.267 \cdot 12) \cdot \left(\frac{0.8}{2}\right)^2 = 2.35\ [cm^4] \tag{5.86}$$

$$A_w = 2 \cdot \left(2 \cdot {}^{2}/_{3} \cdot h_w \cdot l_w\right) = 2 \cdot \left(2 \cdot {}^{2}/_{3} \cdot 0.4 \cdot 12\right) = 12.8\ [cm^2] \tag{5.87}$$

$$\psi_{w,el} = \sqrt{\frac{{e_w}^2 \cdot z^2}{{I_w}^2} + 3 \cdot \frac{1}{{A_w}^2}} = \sqrt{\frac{0.4^2 \cdot 0.667^2}{2.35^2} + 3 \cdot \frac{1}{12.8^2}} = 0.18\left[\frac{1}{cm^2}\right] \tag{5.88}$$

$$\psi_{w,pl} = \sqrt{\frac{{e_w}^2}{d^2 \cdot {A_{w,t}}^2} + 3 \cdot \frac{1}{{A_w}^2}} = \sqrt{\frac{0.4^2}{0.8^2 \cdot 6.4^2} + 3 \cdot \frac{1}{12.8^2}} = 0.16\left[\frac{1}{cm^2}\right] \tag{5.89}$$

$$f_u = 527\ [MPa] = 52.7\left[\frac{kN}{cm^2}\right] \quad \text{Value from Table 5.9} \tag{5.90}$$

$$\beta_w = 0.9 \quad \text{Value from EN 1993-1-8 [57] for S355} \tag{5.91}$$

$$P_{R,w,el} = \frac{f_u}{\beta_w \cdot \psi_w} = \frac{52.7}{0.9 \cdot 0.18} = 331.66\ [kN] \quad > 293.2\ [kN] \tag{5.92}$$

$$P_{R,w,pl} = \frac{f_u}{\beta_w \cdot \psi_w} = \frac{52.7}{0.9 \cdot 0.16} = 374.76\ [kN] \quad > 293.2\ [kN] \tag{5.93}$$

Comparing the calculated resistances from Eq. 5.92 and Eq. 5.93 to the experimentally obtained forces F_R = 293.2 kN (value is including the portion of force from connector-concrete bond), it can be observed that the weld resistance was higher than the acting forces. The obtained utilisation ratio $P_{R,w}/F_R$ reached 1.13 for the elastic stress distribution and 1.28 for the plastic stress distribution. In both cases, the weld failure would not develop, which corresponds well to the test observations.

5.6.4.2. Verification of the resistance of the connector material ($P_{R,m}$)

In the resistance model of connector material, no calibration factors are implemented. The calculations are based on the analytical model given in Eq. 5.69-5.80. Eq. 5.83 defines the shear connector diameter. To analyse acting shear forces V_E, the model shown in Fig. 5.95 and Eq. 5.70 was

used. From the condition given in Eq. 5.100, it has been obtained that the shear and bending interaction can be omitted due to a big plastic shear resistance capacity. However, a verification of the aforementioned condition can be done according to Eq. 5.76-5.79.

$$L_{con} = 12\ [cm] \tag{5.94}$$

$$h_w = 0.4\ [cm] \tag{5.95}$$

$$f_y = 583\ [MPa] = 58.3\ \left[\frac{kN}{cm^2}\right] \tag{5.96}$$

$$P_{R,cs,el} = \frac{f_y \cdot L_{con} \cdot d}{1.5 \cdot \sqrt{3} \cdot \left(1 - \frac{h_w}{d}\right)} = \frac{58.3 \cdot 12 \cdot 0.8}{1.5 \cdot \sqrt{3} \cdot \left(1 - \frac{0.4}{0.8}\right)} = 430.84\ [kN] \tag{5.97}$$

$$P_{R,cb,el} = \frac{f_y \cdot L_{con} \cdot d^3}{3 \cdot (d - h_w)^2} = \frac{58.3 \cdot 12 \cdot 0.8^3}{3 \cdot (0.8 - 0.4)^2} = 746.24\ [kN] \tag{5.98}$$

$$P_{R,cs,pl} = \frac{d \cdot L_{con} \cdot f_y}{\sqrt{3}} = \frac{0.8 \cdot 12 \cdot 58.3}{\sqrt{3}} = 323.13\ [kN] \tag{5.99}$$

$$\frac{V_E}{V_{pl,R}} = \frac{146.32}{323.13} = 0.45 < 0.5 \quad bending\ and\ shear\ interaction\ can\ be\ neglected \tag{5.100}$$

$$P_{R,m} = min\{430.84;\ 746.24;\ 323.13\} = 323.13\ [kN] \qquad > 293.2\ [kN] \tag{5.101}$$

Where, V_E according to the Eq. 5.70 and the acting force is taken from the test results.

Comparison of the calculated resistance from Eq. 5.101 to the value of transferred force by one connector of 293.2 kN from tests, shows that the resistance of shear connector material was bigger than the acting forces. The utilisation ratio of 1.1 has been obtained and the failure of connector material is prevented, which was also the case in the experimental campaign.

5.6.4.3. Verification of the maximum compression condition for concrete ($P_{R,c}$)

The verification of the maximum compression condition for concrete requires utilisation of the calibration factor k_{hlc}. The calibration factor has been placed in the front of the confined concrete strength amplifying its value. The verification procedure given in Eq. 5.46-5.52 has been updated and rewritten in Eq. 5.102-5.108 below. The calculation example is following the updated model. In the calculation procedure the shear connector geometry dimensions from Eq. 5.83 and Eq. 5.94 were used.

$$\sigma_1 = \frac{\sigma_x + \sigma_y}{2} + \sqrt{\left(\frac{\sigma_x - \sigma_y}{2}\right)^2 + {\tau_{xy}}^2} < k_{hlc} \cdot f_{cm,c,cube} \tag{5.102}$$

$$\frac{\sigma_x+\sigma_y}{2}+\sqrt{\left(\frac{\sigma_x-\sigma_y}{2}\right)^2+{\tau_{xy}}^2}=k_{hlc}\cdot\left(f_{cm,cc,cube}+k_s\cdot\sigma_2\right) \tag{5.103}$$

$$\frac{\sigma_x+\sigma_y}{2}+\sqrt{\left(\frac{\sigma_x-\sigma_y}{2}\right)^2+{\tau_{xy}}^2}=k_{hlc}\cdot\omega_{cc}\cdot f_{cm,cube}+k_{hlc}\cdot k_s\cdot\left(\frac{\sigma_x+\sigma_y}{2}-\sqrt{\left(\frac{\sigma_x-\sigma_y}{2}\right)^2+{\tau_{xy}}^2}\right) \tag{5.104}$$

$$\frac{F_R\cdot(0.5\cdot\sin\beta\cdot(1+\nu)+\psi_A)}{\lambda_d\cdot d\cdot L_{con}\cdot\cos\theta}-k_{hlc}\cdot k_s\cdot\frac{F_R\cdot(0.5\cdot\sin\beta\cdot(1+\nu)-\psi_A)}{\lambda_d\cdot d\cdot L_{con}\cdot\cos\theta}=k_{hlc}\cdot\omega_{cc}\cdot f_{cm,cube} \tag{5.105}$$

$$\psi_A=\sqrt{0.25\cdot(1-\nu)^2\cdot\sin^2\beta+\cos^2\beta} \tag{5.106}$$

$$\frac{F_R}{\lambda_d\cdot d\cdot L_{con}\cdot\cos\theta}\cdot\left((k_{hlc}\cdot k_s+1)\cdot\psi_A-0.5\cdot(k_{hlc}\cdot k_s-1)\cdot\sin\beta\cdot(1+\nu)\right)=k_{hlc}\cdot\omega_{cc}\cdot f_{cm,cube} \tag{5.107}$$

$$P_{R,c}=\frac{\lambda_d\cdot\cos\theta\cdot L_{con}\cdot d\cdot k_{hlc}\cdot\omega_{cc}\cdot f_{cm,cube}}{(k_{hlc}\cdot k_s+1)\cdot\psi_A-0.5\cdot(k_{hlc}\cdot k_s-1)\cdot\sin\beta\cdot(1+\nu)}\ [kN] \tag{5.108}$$

Assuming $k_{hlc}=1$, the shear connector resistance is given in Eq. 5.120.

$$\lambda_d=\sqrt{2} \tag{5.109}$$

$$\theta=32^o \tag{5.110}$$

$\omega_{cc}=1.44$ according to Fig. 5.90 and cylindrical concrete strength from test Av2 – 32 MPa (5.111)

$f_{cm,cube}=50.7\ [MPa]=5.07\ \left[\frac{kN}{cm^2}\right]$ is the value in the day of test Av2, see Table 5.11 (5.112)

$\varphi=33^o$ according to Fig. 5.89 and cylindrical concrete strength from test Av2 – 32 MPa (5.113)

$$\mu=\tan\varphi=\tan 33^o=0.65 \tag{5.114}$$

$$k_s=\left(\mu+\sqrt{1+\mu^2}\right)^2=\left(0.65+\sqrt{1+0.65^2}\right)^2=3.392 \tag{5.115}$$

$$\alpha_w=45^o \tag{5.116}$$

$$\beta=\alpha_w+\theta=45^o+32^o=77^o \tag{5.117}$$

$\nu=0.2$ according to EN 1992-1-1 [53] (5.118)

$$\psi_A=\sqrt{0.25\cdot(1-\nu)^2\cdot\sin^2\beta+\cos^2\beta}=\sqrt{0.25\cdot(1-0.2)^2\cdot\sin^2 77^o+\cos^2 77^o}=0.45 \tag{5.119}$$

$$P_{R,c} = \frac{\lambda_d \cdot \cos\theta \cdot L_{con} \cdot d \cdot k_{hlc} \cdot \omega_{cc} \cdot f_{cm,cube}}{(k_{hlc} \cdot k_s + 1) \cdot \psi_A - 0.5 \cdot (k_{hlc} \cdot k_s - 1) \cdot \sin\beta \cdot (1 + \nu)}$$
$$= \frac{\sqrt{2} \cdot \cos 32^o \cdot 12 \cdot 0.8 \cdot 1 \cdot 1.44 \cdot 5.07}{(1 \cdot 3.392 + 1) \cdot 0.45 - 0.5 \cdot (1 \cdot 3.392 - 1) \cdot \sin 77^o \cdot (1 + 0.2)} \quad (5.120)$$
$$= 145.53[kN] \quad < 281.4\ [kN]$$

The result obtained from Eq. 5.120 shows smaller resistance that it was actually obtained from the performed tests Av2 – 281.4 kN, where the value contains only a pure mechanical force transferred per one connector. Comparing the obtained values, the utilisation ratio reached 0.52. A good convergence to the experimental test data is obtained when the $k_{hlc} = 1.37$. The value of the calibration factor is proposed based on the global confined concrete compression strength ratio to the unconfined compression strength of concrete. The described relation is given in Eq. 5.125. The concrete confinement has been calculated based on the provisions given in fib ModelCode 2010 [62] with the adjusted confining stress taken equal to $\sigma_2 = 2.8$ MPa. The adjusted confining stress value corresponds to the value that can be obtained using procedure given in fib ModelCode [62], see Eq. 5.123. The calculation of the calibrated resistance is shown in Eq. 5.126.

$$f_{ck,cube} = f_{cm,cube} - 10 = 50.7 - 10 = 40.7\ [MPa] = 4.07\ \left[\frac{kN}{cm^2}\right] \quad (5.121)$$

$$\omega_c = min\left\{\frac{A_{sy} \cdot f_{yk}}{a_c \cdot s_c \cdot f_{ck,cube}}; \frac{A_{sz} \cdot f_{yk}}{b_c \cdot s_c \cdot f_{ck,cube}}\right\} = 0.057 \quad (5.122)$$

$$\sigma_2 = \omega_c \cdot f_{ck,cube} = 0.057 \cdot 40.7 \cong 2.3\ [MPa] \qquad \text{adjusted to } \sigma_2 = 2.8\ [MPa] \quad (5.123)$$

$$f_{cm,c,cube,fib} = f_{ck,cube} + 3.5 \cdot f_{ck,cube} \cdot \left(\frac{\sigma_2}{f_{ck,cube}}\right)^{\frac{3}{4}} + 10$$
$$= 40.7 + 3.5 \cdot 40.7 \cdot \left(\frac{2.8}{40.7}\right)^{\frac{3}{4}} + 10 = 69.9\ [MPa] \quad (5.124)$$

$$k_{hlc} = \frac{f_{cm,c,cube,fib}}{f_{cm,cube}} = \frac{69.9}{50.7} = 1.37 \quad (5.125)$$

$$P_{R,c} = \frac{\sqrt{2} \cdot \cos 32^o \cdot 12 \cdot 0.8 \cdot 1.37 \cdot 1.44 \cdot 5.07}{(1.37 \cdot 3.392 + 1) \cdot 0.45 - 0.5 \cdot (1.37 \cdot 3.392 - 1) \cdot \sin 77^o \cdot (1 + 0.2)}$$
$$= 281.72[kN] \quad \cong 281.4\ [kN] \quad (5.126)$$

Where,

ω_c is the confinement ratio due to the reinforcement cage geometry and used materials [62],

A_{sy} is the area of transversal reinforcement in “y” direction,

A_{sz} is the area of transversal reinforcement in “z” direction,

f_{yk} is the yielding strength of the reinforcement,

a_c is the spacing of longitudinal reinforcement in "y" direction,

b_c is the spacing of longitudinal reinforcement in the "z" direction,

s_c is the spacing of transversal reinforcement,

$f_{ck,cube}$ is the characteristic compression strength of concrete for cubes (a modification in Eq. 5.122 to cubic values has been made. A similar modification has been implemented in Eq. 5.124)

The utilisation ratio of the calibrated resistance of shear connector gives the value very close to 1. Based on the observations from the opening of specimens, see Fig. 5.47, it was impossible to clearly identify if the concrete compression failure around the shear connector occurs together with the shearing failure or not. However, according to the numerical simulations – see Fig. 5.73, it was identified that the concrete failed in compression under the connector and it formulates the shear plane. Based on the observations above, it was assumed that the both failure mechanisms, compression and shear of concrete can occur simultaneously. Therefore, the resistances for compression and shear were calibrated to oscillate around the utilisation ratio of 1.

5.6.4.4. Verification of the maximum shear condition for concrete ($P_{R,s1}$)

The verification of the maximum shear condition for concrete requires utilisation of the calibration factor λ_s. The calibration factor has been placed in the front of the concrete shear strength modifying its value. The verification procedure given in Eq. 5.55-5.59 has been updated and rewritten in Eq. 5.127-5.131 below. The calculation example is following the updated model. In the calculation procedure the geometry of shear connector from Eq. 5.83 and Eq. 5.94 were used. The angle of compression strut inclination θ was taken as given in Eq. 5.110. Mean compression strength of concrete for cubes is defined in Eq. 5.112. Angle defining the distribution of forces at the connector contact surface β has been taken according to Eq. 5.117. Factors k_s, ψ_A, and μ have been defined in Eq. 5.115, Eq. 5.119 and Eq. 5.114, respectively. The resulting shear area inclination angle α_{s1} is defined in Fig. 5.91 and its value used in calculation is 15°. ν_s is the cohesion of concrete reduction factor due to micro cracking and it is taken as 0.5 [130].

$$\tau_{max} = \sqrt{\left(\frac{\sigma_x - \sigma_y}{2}\right)^2 + {\tau_{xy}}^2} < \lambda_s \cdot (\sigma_s \cdot \tan\varphi + c) \tag{5.127}$$

$$\sqrt{\left(\frac{\sigma_x - \sigma_y}{2}\right)^2 + {\tau_{xy}}^2} = \lambda_s \cdot \frac{\sigma_x + \sigma_y}{2} \cdot \tan\varphi + \lambda_s \cdot \nu_s \cdot \frac{1}{2 \cdot \sqrt{k_s}} \cdot f_{cm,cube} \tag{5.128}$$

$$\frac{F_R \cdot \psi_A \cdot \sin(\alpha_{s1})}{d \cdot L_{con} \cdot \cos\theta} = \lambda_s \cdot \frac{F_R \cdot \sin\beta \cdot (1+\nu) \cdot \sin(\alpha_{s1})}{2 \cdot d \cdot L_{con} \cdot \cos\theta} \cdot \mu + \lambda_s \cdot \nu_s \cdot \frac{1}{2 \cdot \sqrt{k_s}} \cdot f_{cm,cube} \tag{5.129}$$

$$\frac{F_R \cdot \sin(\alpha_{s1})}{d \cdot L_{con} \cdot \cos\theta} \cdot (\psi_A - 0.5 \cdot \lambda_s \cdot \sin\beta \cdot (1+\nu) \cdot \mu) = \frac{\lambda_s \cdot \nu_s}{2\sqrt{k_s}} \cdot f_{cm,cube} \tag{5.130}$$

$$P_{R,s1} = \frac{\lambda_s \cdot \nu_s \cdot \cos\theta \cdot d \cdot L_{con} \cdot f_{cm,cube}}{2\sqrt{k_s} \cdot (\psi_A - 0.5 \cdot \lambda_s \cdot \sin\beta \cdot (1+\nu) \cdot \mu) \cdot \sin(\alpha_{s1})} \; [kN] \tag{5.131}$$

Assuming $\lambda_s = 1$, the shear connector resistance is given by Eq. 5.132.

$$\begin{aligned} P_{R,s1} &= \frac{\lambda_s \cdot \nu_s \cdot \cos\theta \cdot d \cdot L_{con} \cdot f_{cm,cube}}{2\sqrt{k_s} \cdot (\psi_A - 0.5 \cdot \lambda_s \cdot \sin\beta \cdot (1+\nu) \cdot \mu) \cdot \sin(\alpha_{s1})} \\ &= \frac{1 \cdot 0.5 \cdot \cos 32^o \cdot 0.8 \cdot 12 \cdot 50.7}{2\sqrt{3.392} \cdot (0.45 - 0.5 \cdot 1 \cdot \sin 77^o \cdot (1+0.2) \cdot 0.65) \cdot \sin(15^o)} \\ &= 307.93[kN] \qquad > 281.4\ [kN] \end{aligned} \tag{5.132}$$

The result obtained from Eq. 5.132 shows bigger resistance that it was actually obtained during the experimental campaign – 281.4 kN, where the value contains only a pure mechanical force transferred per one connector. Comparing the obtained values, the utilisation ratio reached 1.1. From the opening of test specimen, it can be clearly observed that the specimen failed in the maximum shear stress plane, see Fig. 5.47. A good convergence to the experimental test data is obtained when the $\lambda_s = 0.98$. The calculation of the calibrated resistance is shown in Eq. 5.133. The value of the calibration factor was proposed based on the test results.

$$\begin{aligned} P_{R,s1} &= \frac{\lambda_s \cdot \nu_s \cdot \cos\theta \cdot d \cdot L_{con} \cdot f_{cm,cube}}{2\sqrt{k_s} \cdot (\psi_A - 0.5 \cdot \lambda_s \cdot \sin\beta \cdot (1+\nu) \cdot \mu) \cdot \sin(\alpha_{s1})} \\ &= \frac{0.98 \cdot 0.5 \cdot \cos 32^o \cdot 0.8 \cdot 12 \cdot 50.7}{2\sqrt{3.392} \cdot (0.45 - 0.5 \cdot 0.98 \cdot \sin 77^o \cdot (1+0.2) \cdot 0.65) \cdot \sin(15^o)} \\ &= 272.37[kN] \qquad \leq 281.4\ [kN] \end{aligned} \tag{5.133}$$

The utilisation ratio of the calibrated resistance to the experimental value reached 0.97.

5.6.4.5. Minimum spacing condition

Knowing the resistance of flat shear connector, the global force equilibrium has to be assured by placing the transversal reinforcement to anchor the resultant lateral tension forces, see Fig. 5.85. According to the aforementioned condition, a limitation on the minimum shear connector spacing can be derived based on the geometry and spacing of the applied stirrups – the spacing between the consequent shear connectors has to be big enough to allow for placing enough amount of stirrups. The minimum spacing of the transversal variant of flat shear connectors is also related to the developed shear failure in the concrete at the plane, where the maximum shear stresses develop. The spacing between the consequent shear connectors has to be big enough to allow for the development of shear plane

towards the steel profile, like indicated in Fig. 5.91. According to the above, conditions for the minimum spacing can be derived as given in Eq. 5.134-5.136. Eq. 5.136 is based on the stress transformation equation to obtain the transformation angle for the maximum shear stresses given in Eq. 5.41.

$$s_{con,min} = max\{s_{con,w};\ s_{con,s1}\} \tag{5.134}$$

$$s_{con,w} = \frac{P_{R,con} \cdot \tan\theta \cdot s_w}{f_{yw} \cdot A_{sw}}\ [mm] \tag{5.135}$$

$$s_{con,s1} = \Delta_d \cdot d + \frac{d}{\tan\left(\alpha_w - tan^{-1}\left(\frac{1-\nu}{2 \cdot \cot\beta}\right) \cdot \frac{180}{\pi} \cdot 0.5\right)} \tag{5.136}$$

Where,

$s_{con,w}$ is the spacing of the connectors due to the stirrups condition,

$s_{con,s1}$ is the spacing of the connectors due to the maximum shear plane condition,

$P_{R,con}$ is the resistance of flat shear connector,

s_w is the spacing of the stirrups (according to EN 1992-1-1 [53]),

f_{yw} is the yielding strength of stirrups,

A_{sw} is the cross-sectional area of stirrup and

Δ_d is the dilation factor for connector diameter (a factor which includes deviations of the connector geometry and used weld), a proposal that $\Delta_d = 2$ is given.

Implementing the geometry and material of the specimen Av2, $P_{R,con} = 272.37\ [kN]$, the minimum spacing of the stirrups defined in EN 1992-1-1 [53] as $s_w = s_{w,min} = 33\ [mm]$ and $\Delta_d = 2$, the minimum spacing of the shear connectors (from axis to axis) reached approximately 100 mm.

5.6.5. Resistance of the V-shaped connector – specimen Bv2

The analytical model for the angled, V-shaped variant of flat shear connector has been built in the analogical way like for the transversal variant of connector used in the specimen Av2. In the forces distribution model, the same force transferring mechanisms were considered. The inclination angle of concrete compression strut under the arms of the connector has been calibrated based on the test results of specimen Bv2 (sheared concrete cone below the shear connector, see Fig. 5.49-5.51) and the numerical simulations. It was identified that the inclination of compression strut reached the value of 32° analogous to the specimen Av2. The verification of the resistance of V-shaped flat shear connector, among others, consists of the same failure modes as in the case of specimen Av2 – the verification of the maximum compression strength of concrete, the maximum shear strength of concrete, the strength of weld and the strength of connector material due to shear and bending actions. According to the specific geometry of connector, an additional failure mode of concrete in the vertical shear has to be considered. The mean ultimate load imposed to the specimens during the tests was 809.2 kN, where the force taken by plain steel-concrete bond was 195.9 kN and the force taken by the connector-concrete

bond was 56.4 kN, in both cases including the Coulomb friction. In the result, the force that has been transferred only by the mechanical connection was 511.7 kN (255.9 kN per each connector). A scheme of the force distribution model around the shear connector (local strut-and-tie model) of the specimen Bv2 is shown in Fig. 5.96 and Fig. 5.97. The proposed model allows for the verification of the resistance of shear connector and for the global verification of the specimen, the given strut-and-tie model has to be extended to a more detailed model, which would exactly correlate with the reaction forces.

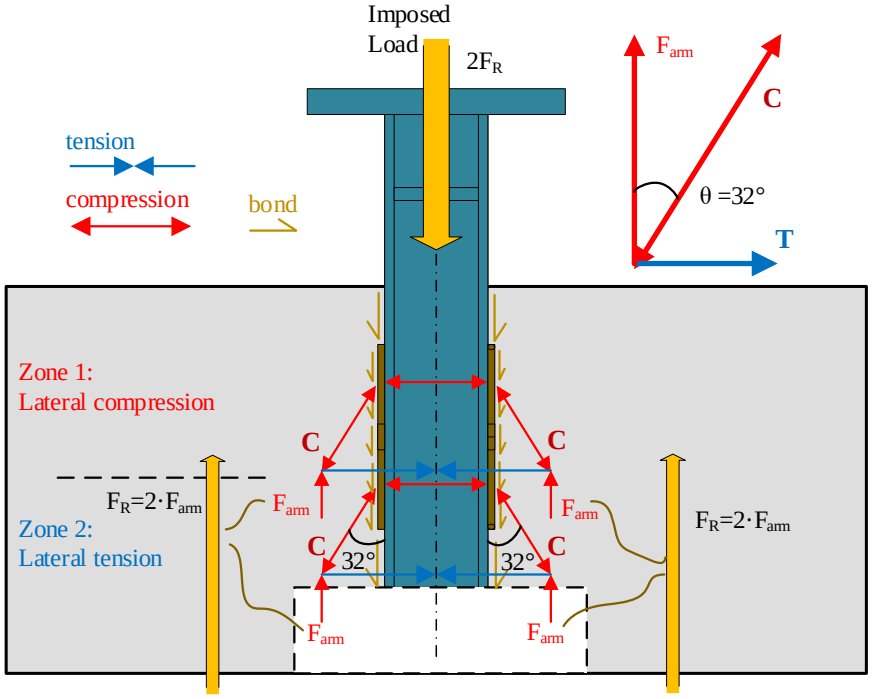


Fig. 5.96. Local strut-and-tie model of the V-shaped variant of flat shear connector of specimen Bv2 of CoPOT.

In Fig. 5.96, an analogical force distribution for the specimen Bv2 to the specimen Av2 is shown. The geometry of shear connector consists of two arms inclined under 45° to the longitudinal axis of the embedded steel profiles and between them, an angle of 90° is kept. The geometry of the connector is creating a characteristic "V" shape as shown in Fig. 5.97. Each arm of the connector is able to transfer forces simultaneously, therefore, it was assumed that the reaction force F_R is split equally on two arms of connector, $F_{arm} = 0.5 \cdot F_R$. This assumption is justified by the test results shown in Fig. 5.32 and it was confirmed in numerical simulations.

In Fig. 5.97, a transversal view on the face of shear connector, in reference to the Fig. 5.96, was given. Due to the geometry of shear connector, mainly the orientation angle α_c, the vertical reaction F_{arm} is distributed into a set of two forces acting in normal and tangential direction on each arm of the connector - F_{n,α_c} and F_{t,α_c}, respectively. The force F_{t,α_c} is acting in the tangential direction of the arm of connector and it is imposing sliding forces of the concrete over the arm of connector in the local longitudinal direction. Considering the global equilibrium of forces for both arms of connector embedded in concrete, the sliding force from one arm will increase the normal force acting on the second arm and vice versa, see Fig. 5.97b. Finally, the resultant force acting on the connector arm can be defined

as force F_{α_c} acting in the normal direction, where $F_{\alpha_c} = F_{n,\alpha_c} + F_{t,\alpha_c}$ is considering the sum of vectors and not scalars. Between the resultant forces in each arm, transversal tension reaction forces are induced to establish the redistributed equilibrium state, see Fig. 5.97b.

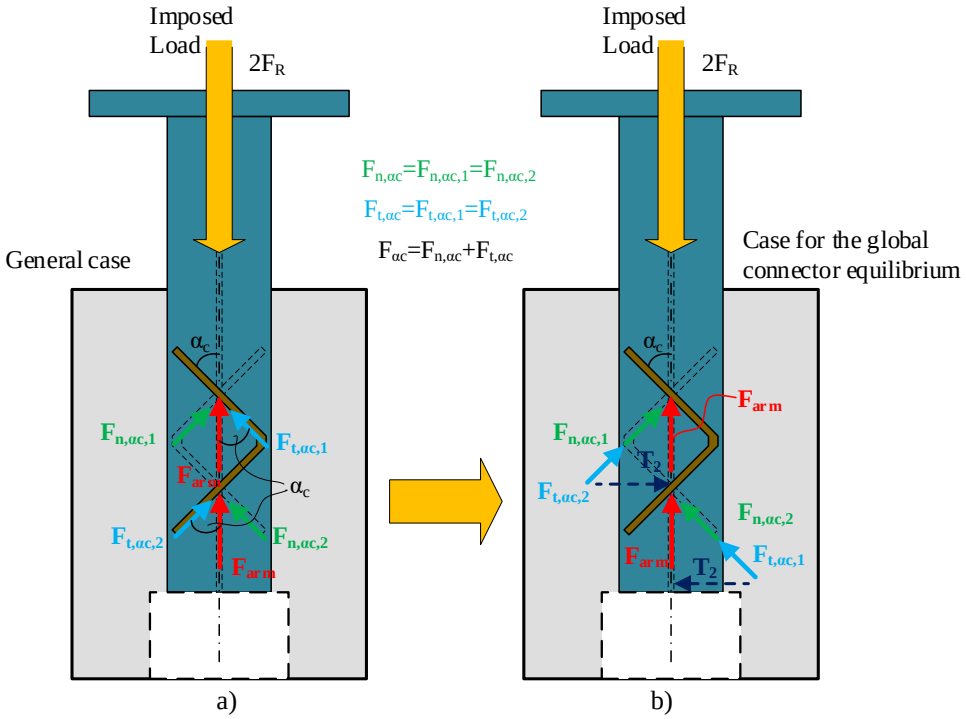


Fig. 5.97. Redistribution of forces in the V-shaped flat shear connector of the specimen Bv2 of CoPOT –a) general case and b) redistributed case.

The forces shown in Fig. 5.96 and Fig. 5.97 can be calculated in reference to the overall reaction force F_R according to Eq. 5.137-5.142.

$$F_{arm} = \frac{F_R}{n_a} \; [kN] \tag{5.137}$$

$$C = \frac{F_{arm}}{\cos\theta} = \frac{F_R}{n_a \cdot \cos\theta} \; [kN] \tag{5.138}$$

$$T = C \cdot \sin\theta = \frac{F_R}{n_a \cdot \cos\theta} \cdot \sin\theta = \frac{F_R}{n_a} \cdot \tan\theta \; [kN] \tag{5.139}$$

$$T_2 = F_{arm} \; [kN] \tag{5.140}$$

$$F_{n,\alpha_c} = F_{arm} \cdot \sin\alpha_c = \frac{F_R}{n_a} \cdot \sin\alpha_c \; [kN] \tag{5.141}$$

$$F_{t,\alpha_c} = F_{arm} \cdot \cos\alpha_c = \frac{F_R}{n_a} \cdot \cos\alpha_c \; [kN] \tag{5.142}$$

Where, n_a is the number of connector arms – in our case $n_a = 2$,

Considering the sum of forces F_{n,α_c} and F_{t,α_c} to obtain the resultant normal force F_{α_c}, the superposition of vectors with the respect to angle θ according to Fig. 5.98 has to be considered. It can

be observed that the resultant force F_{α_c} is acting under the resultant angle θ_c which is smaller than the angle θ. To find the resulting force F_{α_c}, the horizontal projection $F_{\alpha_c,H}$ and vertical projection $F_{\alpha_c,V}$ of it has to be found first. When these forces are known, the resulting load dispersion angle θ_c can be calculated according to Eq. 5.145. The procedure to calculate F_{α_c} is defined in Eq. 5.143-5.149 and the result is obtained by implementing Eq. 5.141 and Eq. 5.142.

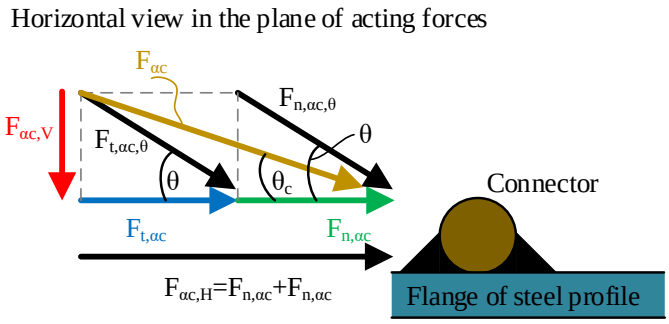


Fig. 5.98. Vector representation of the resultant normal force acting on the V-shaped connector.

$$F_{\alpha_c,H} = F_{n,\alpha_c} + F_{t,\alpha_c}\ [kN] \tag{5.143}$$

$$F_{\alpha_c,V} = F_{n,\alpha_c} \cdot \tan\theta\ \ [kN] \tag{5.144}$$

$$\theta_c = \tan^{-1}\left(\frac{F_{\alpha_c,V}}{F_{\alpha_c,H}}\right) \cdot \frac{180^o}{\pi} = \tan^{-1}\left(\frac{\sin\alpha_c \cdot \tan\theta}{\sin\alpha_c + \cos\alpha_c}\right) \cdot \frac{180^o}{\pi}\ [^o] \tag{5.145}$$

$$F_{\alpha_c} = \sqrt{{F_{\alpha_c,V}}^2 + {F_{\alpha_c,H}}^2}\ [kN] \tag{5.146}$$

$$F_{\alpha_c} = \sqrt{\left(F_{n,\alpha_c} \cdot \tan\theta\right)^2 + \left(F_{n,\alpha_c} + F_{t,\alpha_c}\right)^2}\ [kN] \tag{5.147}$$

$$F_{\alpha_c} = \sqrt{\left(\frac{F_R}{n_a} \cdot \sin\alpha_c \cdot \tan\theta\right)^2 + \left(\frac{F_R}{n_a} \cdot \sin\alpha_c + \frac{F_R}{n_a} \cdot \cos\alpha_c\right)^2}\ [kN] \tag{5.148}$$

$$F_{\alpha_c} = \frac{F_R}{n_a} \cdot \sqrt{\sin^2\alpha_c \cdot \tan^2\theta + (\sin\alpha_c + \cos\alpha_c)^2}\ [kN] \tag{5.149}$$

The resulting normal force F_{α_c} is acting on the contact area under the angle θ_c, see Fig. 5.99a. The contact area of connector is defined analogically to the transversal variant of connector as shown in Fig. 5.85 and Eq. 5.31, where the contact area has a simplified straight geometry related to the connector diameter and slope of weld. In the case of V-shaped connector, the length of arm will substitute the entire length of connector due to the geometry and distribution of forces between the arms of connector. The length of the arm is defined as shown in Fig. 5.99b. Between the direction of the resulting acting force and the tangential direction of the contact surface, an angle β can be identified, where it can be defined as $\beta = \alpha_w + \theta_c$. Analogically, angle $\beta_1 = 90 - \alpha_w - \theta_c$. For our considered case and according to Eq. 5.145, the angle $\theta_c = 16^o$, therefore $\beta = 45^o + 16^o = 61^o$ and $\beta_1 = 29^o$.

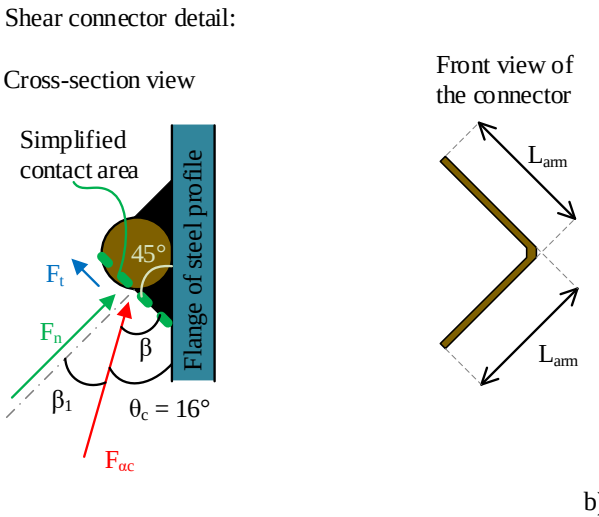


Fig. 5.99. Detail of the forces acting on the contact area of V-shaped shear connector – a) resulting forces acting at the connector-concrete interface and b) definition of the contact surface length.

According to the load distribution shown in Fig. 5.99a, the resultant normal and tangential forces acting on the simplified contact area can be calculated according to Eq. 5.150-5.154.

$$\beta = \alpha_w + \theta_c \tag{5.150}$$

$$F_n = F_{\alpha_c} \cdot \sin\beta \tag{5.151}$$

$$F_t = F_{\alpha_c} \cdot \cos\beta \tag{5.152}$$

$$F_n = \frac{F_R}{n_a} \cdot \sqrt{\sin^2\alpha_c \cdot \tan^2\theta + (\sin\alpha_c + \cos\alpha_c)^2} \cdot \sin\beta \tag{5.153}$$

$$F_t = \frac{F_R}{n_a} \cdot \sqrt{\sin^2\alpha_c \cdot \tan^2\theta + (\sin\alpha_c + \cos\alpha_c)^2} \cdot \cos\beta \tag{5.154}$$

The stresses that are acting on the contact surface can be calculated by dividing the resultant forces F_n and F_t given in Eq. 5.153 and Eq. 5.154 by the simplified contact area which is defined in Eq. 5.155. Considering the situation in the plain strain state, the local coordinate system has been taken that the "x" axis is directed in the normal direction to the contact surface as shown in Fig. 5.100, where stresses has been represented as vectors. In the result, the acting stresses on the contact surface of V-shaped flat shear connector are defined in Eq. 5.156 and Eq. 5.157.

$$A_{con,arm,eff} = \lambda_d \cdot d \cdot L_{arm}\ [cm^2] \tag{5.155}$$

$$\sigma_x = \frac{F_n}{A_{con,arm,eff}} = \frac{F_R \cdot \sin\beta \cdot \sqrt{\sin^2\alpha_c \cdot \tan^2\theta + (\sin\alpha_c + \cos\alpha_c)^2}}{n_a \cdot \lambda_d \cdot d \cdot L_{arm}} \left[{}^{kN}/_{cm^2}\right] \tag{5.156}$$

$$\tau_{xy} = \frac{F_t}{A_{con,arm,eff}} = \frac{F_R \cdot \cos\beta \cdot \sqrt{\sin^2\alpha_c \cdot \tan^2\theta + (\sin\alpha_c + \cos\alpha_c)^2}}{n_a \cdot \lambda_d \cdot d \cdot L_{arm}} \left[{}^{kN}/_{cm^2}\right] \tag{5.157}$$

Defining load distribution factors as:

$$\kappa_1 = \sin\beta \cdot \sqrt{\sin^2\alpha_c \cdot \tan^2\theta + (\sin\alpha_c + \cos\alpha_c)^2} \tag{5.158}$$

$$\kappa_2 = \cos\beta \cdot \sqrt{\sin^2\alpha_c \cdot \tan^2\theta + (\sin\alpha_c + \cos\alpha_c)^2} \tag{5.159}$$

The acting stresses σ_x and τ_{xy} can be simplified to Eq. 5.160 and Eq. 5.161:

$$\sigma_x = \frac{F_R \cdot \kappa_1}{n_a \cdot \lambda_d \cdot d \cdot L_{arm}} \left[kN/cm^2\right] \tag{5.160}$$

$$\tau_{xy} = \frac{F_R \cdot \kappa_2}{n_a \cdot \lambda_d \cdot d \cdot L_{arm}} \left[kN/cm^2\right] \tag{5.161}$$

Where,

λ_d is the effective area factor which correlates the contact area width to the connector diameter, and it is taken as $\lambda_d = \sqrt{2}$ and

L_{arm} is the length of the arm of connector (see Fig. 5.99b).

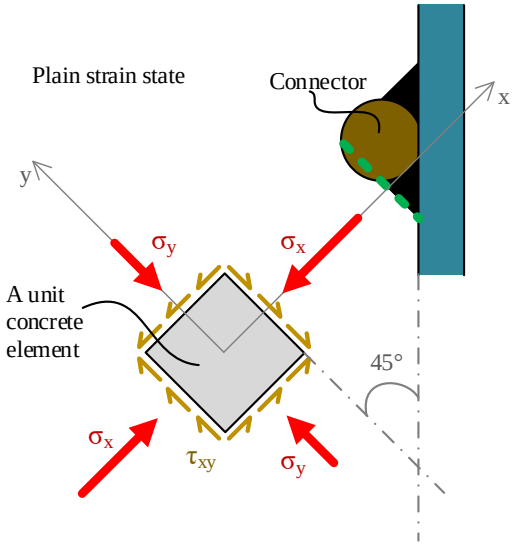


Fig. 5.100. Stresses acting on the contact surface of the V-shaped variant of flat shear connector (consider with Fig. 5.99a).

In order to calculate the stresses σ_y, which are imposing a confinement to the concrete in the considered stress state as shown in Fig. 5.100, an assumption of full confinement has to be implemented similarly like for the case of specimen Av2. The taken assumption brings a simplification to the concrete stress state, where the strains in the transversal directions (ε_y) are set equal to 0. Based on the theory of elasticity, Hooke's law and equilibrium conditions, the transversally confining stresses can be calculated according to the Poisson's ratio, see Eq. 5.162-5.165.

$$\varepsilon_y = \frac{\sigma_y - \sigma_x \cdot \nu}{E} = 0 \tag{5.162}$$

$$\sigma_y - \sigma_x \cdot \nu = 0 \tag{5.163}$$

$$\sigma_y = \sigma_x \cdot \nu \tag{5.164}$$

$$\sigma_y = \frac{F_R \cdot \kappa_1}{n_a \cdot \lambda_d \cdot d \cdot L_{arm}} \cdot \nu = \frac{F_R \cdot \kappa_1 \cdot \nu}{n_a \cdot \lambda_d \cdot d \cdot L_{arm}} \left[kN/cm^2\right] \tag{5.165}$$

Where, ν is the Poisson ratio and the value of 0.2 is taken for the concrete.

According to the model shown in Fig. 5.96-5.97 and evaluated stresses at the connector-concrete bearing interface, the shear connection resistance is related to:

1) the strength of embedding concrete,
2) the strength of weld and
3) the strength of connector material.

The identified failure mechanisms are described and characterised below in the respective paragraphs.

The strength of embedding concrete consists of three main failure modes that has to be verified: (i) the maximum compression condition, (ii) the maximum shear condition and (iii) the vertical shear condition. In reference to the specimen Av2, the two first failure modes are analogical. The third failure mode for the V-shaped connector has to be additionally analysed due to the geometry of the applied connector and possible shearing of concrete in the vertical direction between the arms of connector. The indicated possible failure modes have been also identified in the failure sequence obtained from the numerical simulations, see Fig. 5.77. To analyse the principal stresses and the maximum shear stresses Eq. 5.38-5.45 apply, where the main equations are repeated below in Eq. 5.166-5.168.

$$\sigma_{p1,p2} = \frac{\sigma_x + \sigma_y}{2} \pm \sqrt{\left(\frac{\sigma_x - \sigma_y}{2}\right)^2 + {\tau_{xy}}^2} \tag{5.166}$$

$$\tau_{max} = \sqrt{\left(\frac{\sigma_x - \sigma_y}{2}\right)^2 + {\tau_{xy}}^2} \tag{5.167}$$

$$\sigma_s = \frac{\sigma_x + \sigma_y}{2} \tag{5.168}$$

It has been identified that for the case of V-shaped connector, the tensile stresses in maximum principal stresses direction can be obtained. Therefore, Eq. 5.169-5.171 gives the condition for the concrete stress state. When the condition is fulfilled, the concrete is subjected to the lateral tension in the principal direction and the concrete confinement is $\sigma_2 = 0$ for the corresponding verification of the maximum compression of concrete. Moreover, when the concrete is subjected to tensile stresses, the concrete tensile strength can be verified in order to check the concrete state – cracked or uncracked. Cracked concrete state can affect the specimen behaviour and application of the proposed analytical model. The verification of the influence of concrete state on the shear connection strength is out of the scope of the conducted investigation.

$$\frac{\sigma_x + \sigma_y}{2} - \sqrt{\left(\frac{\sigma_x - \sigma_y}{2}\right)^2 + {\tau_{xy}}^2} < 0 \tag{5.169}$$

$$\frac{F_R \cdot \kappa_1 \cdot (1+\nu)}{2 \cdot n_a \cdot \lambda_d \cdot d \cdot L_{arm}} < \sqrt{\left(\frac{F_R \cdot \kappa_1 \cdot (1-\nu)}{2 \cdot n_a \cdot \lambda_d \cdot d \cdot L_{arm}}\right)^2 + \frac{F_R \cdot \kappa_2}{n_a \cdot \lambda_d \cdot d \cdot L_{arm}}^2} \tag{5.170}$$

$$\frac{\kappa_1 \cdot (1+\nu)}{2 \cdot \psi_B} < 1 \tag{5.171}$$

$$\psi_B = \sqrt{0.25 \cdot {\kappa_1}^2 \cdot (1-\nu)^2 + {\kappa_2}^2} \tag{5.172}$$

Where, ψ_B is the coefficient, which simplifies the equation form.

According to Eq. 5.40 and implementing Eq. 5.160-5.165, the maximum compression principal stresses direction has been identified under $\gamma_p = 27^o$ from the initial direction "x", see Fig. 5.101. The rotation of the unit concrete element by the indicated angle, results in the principal compression stresses orientation under 18° to the vertical direction. The identified angle is in good correlation to the angle θ_c defined in Eq. 5.145 (16°) and also to the observations made from the experimental campaign – inclined shear plane under 16°, see Fig. 5.51.

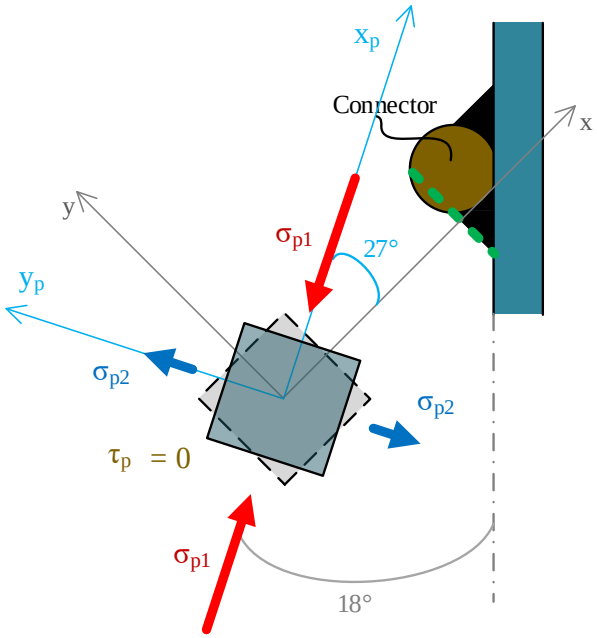


Fig. 5.101. Principal stress state in the V-shaped flat shear connector of the specimen Bv2 of CoPOT.

The resistance condition to verify the maximum compression stresses is governing the same condition like in the case of specimen Av2, where the confined concrete strength of modified Mohr-Coulomb material according to the model proposed by Nielsen [130], see Fig. 5.88, has been implemented. The resistance condition given in Eq. 5.46 is repeated in Eq. 5.173. The final shape of the equation defining the resistance of shear connector is obtained by implementing Eq. 5.160, Eq. 5.161 and Eq. 5.165 into Eq. 5.173 and replacing the minority sign by the equality sign. The resulted resistance for the concrete compression failure is defined in Eq. 5.179.

$$\sigma_1 = \frac{\sigma_x + \sigma_y}{2} + \sqrt{\left(\frac{\sigma_x - \sigma_y}{2}\right)^2 + {\tau_{xy}}^2} < f_{cm,c,cube} \tag{5.173}$$

$$\frac{\sigma_x + \sigma_y}{2} + \sqrt{\left(\frac{\sigma_x - \sigma_y}{2}\right)^2 + {\tau_{xy}}^2} = \left(f_{cm,cc,cube} + k_s \cdot \sigma_2\right) \tag{5.174}$$

$$\frac{\sigma_x + \sigma_y}{2} + \sqrt{\left(\frac{\sigma_x - \sigma_y}{2}\right)^2 + {\tau_{xy}}^2} = \omega_{cc} \cdot f_{cm,cube} + k_s \cdot \left(\frac{\sigma_x + \sigma_y}{2} - \sqrt{\left(\frac{\sigma_x - \sigma_y}{2}\right)^2 + {\tau_{xy}}^2}\right) \tag{5.175}$$

$$\frac{F_R \cdot \kappa_1 \cdot (1+\nu)}{2 \cdot n_a \cdot \lambda_d \cdot d \cdot L_{arm}} + \sqrt{\left(\frac{F_R \cdot \kappa_1 \cdot (1-\nu)}{2 \cdot n_a \cdot \lambda_d \cdot d \cdot L_{arm}}\right)^2 + \frac{F_R \cdot \kappa_2}{n_a \cdot \lambda_d \cdot d \cdot L_{arm}}^2} = \omega_{cc} \cdot f_{cm,cube} + \\ + k_s \cdot \left(\frac{F_R \cdot \kappa_1 \cdot (1+\nu)}{2 \cdot n_a \cdot \lambda_d \cdot d \cdot L_{arm}} - \sqrt{\left(\frac{F_R \cdot \kappa_1 \cdot (1-\nu)}{2 \cdot n_a \cdot \lambda_d \cdot d \cdot L_{arm}}\right)^2 + \frac{F_R \cdot \kappa_2}{n_a \cdot \lambda_d \cdot d \cdot L_{arm}}^2}\right) \tag{5.176}$$

$$\frac{F_R \cdot (0.5 \cdot \kappa_1 \cdot (1+\nu) + \psi_B)}{n_a \cdot \lambda_d \cdot d \cdot L_{arm}} - k_s \cdot \frac{F_R \cdot (0.5 \cdot \kappa_1 \cdot (1+\nu) - \psi_B)}{n_a \cdot \lambda_d \cdot d \cdot L_{arm}} = \omega_{cc} \cdot f_{cm,cube} \tag{5.177}$$

$$\frac{F_R}{n_a \cdot \lambda_d \cdot d \cdot L_{arm}} \cdot ((k_s + 1) \cdot \psi_B - 0.5 \cdot (k_s - 1) \cdot \kappa_1 \cdot (1+\nu)) = \omega_{cc} \cdot f_{cm,cube} \tag{5.178}$$

$$P_{R,c} = \frac{n_a \cdot \lambda_d \cdot d \cdot L_{arm} \cdot \omega_{cc} \cdot f_{cm,cube}}{(k_s + 1) \cdot \psi_B - 0.5 \cdot (k_s - 1) \cdot \kappa_1 \cdot (1+\nu)} \; [kN] \tag{5.179}$$

Where, ω_{cc} according to Fig. 5.90 and $k_s = \left(\mu + \sqrt{1+\mu^2}\right)^2$ based on Fig. 5.89, where $\mu = \tan\varphi$.

When the condition defined in Eq. 5.171 is fulfilled, the concrete confinement is not active and in Eq. 5.179, the factors $\omega_{cc} = 1$ and $k_s = 0$ are taken directly.

The condition for the cracked or uncracked concrete, due to the possible tensile stresses in the maximum principal direction, is defined in Eq. 5.180-5.181. The aforementioned condition has to be verified when the condition given by Eq. 5.171 is fulfilled. Otherwise, no tensile stresses will develop. From Eq. 5.181, a limitation in the shear connector resistance can be derived in order to keep the concrete in the uncracked state. The connector strength limitation then can be defined in Eq. 5.182.

$$\sqrt{\left(\frac{\sigma_x - \sigma_y}{2}\right)^2 + {\tau_{xy}}^2} - \frac{\sigma_x + \sigma_y}{2} < f_{ctm} \tag{5.180}$$

$$\frac{F_R \cdot (\psi_B - 0.5 \cdot \kappa_1 \cdot (1+\nu))}{n_a \cdot \lambda_d \cdot d \cdot L_{arm} \cdot f_{ctm}} < 1 \qquad \text{then, the concrete will be in the uncracked state} \tag{5.181}$$

$$P_{R,t} = \frac{n_a \cdot \lambda_d \cdot d \cdot L_{arm} \cdot f_{ctm}}{\psi_B - 0.5 \cdot \kappa_1 \cdot (1+\nu)} \; [kN] \tag{5.182}$$

Where, f_{ctm} is the concrete tensile strength and can be calculated according to [53] or [62].

According to Eq. 5.41, the orientation of maximum shear stresses under a $\gamma_{s,max} = -18^o$ has been identified. The direction of considered shear stress creates with the vertical direction an angle of $\alpha_{s1} = 27^o$, which was calculated according to Eq. 5.183. The concrete stress state in the maximum shear direction is shown in Fig. 5.102.

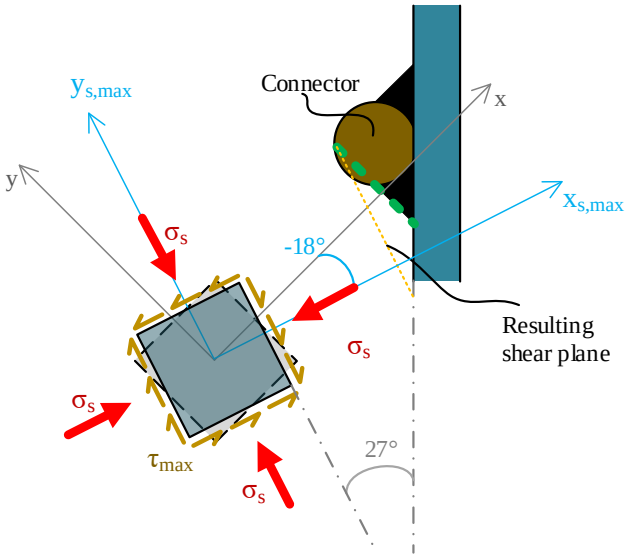


Fig. 5.102. Maximum shear stresses state in the V-shaped flat shear connector of the specimen Bv2 of CoPOT.

In the maximum shear stress state presented in Fig. 5.102, the concrete is subjected to the maximum possible shear stresses over the area in the resulting shear plane. The accompanying normal stresses σ_s are imposing confining stresses to the concrete. The effective shearing area can be defined in reference to the diameter of connector, its length and resulting shear plane inclination angle α_{s1}. Due to the connector orientation angle α_c, the resulting shear plane has to be projected to the vertical direction, where the failure occurred due to the direction of the imposed displacement of steel profile. Therefore, to the equation for the resultant effective shearing area $A_{s,eff}$, a projection factor $\lambda_p = 1/\sin\alpha_c$ is implemented, see Eq. 5.184.

$$\alpha_{s1} = \alpha_w + \gamma_{s,max}\ [^o] \tag{5.183}$$

$$A_{s,eff} = \lambda_p \cdot \frac{d}{\sin(\alpha_{s1})} \cdot L_{arm}\ [cm^2] \tag{5.184}$$

The resistance of shear connector is related to the concrete shearing strength. To evaluate the concrete shear strength, the modified Mohr-Coulomb material law proposed my Nielsen [130] has been implemented. The overall condition for the shear resistance is defined in Eq. 5.185. Implementing Eq. 5.160-5.161, Eq. 5.165 and Eq. 5.184 into Eq. 5.186, the resulting resistance of shear connector is defined in Eq. 5.190.

$$\tau_{max} = \sqrt{\left(\frac{\sigma_x - \sigma_y}{2}\right)^2 + {\tau_{xy}}^2} < \sigma_s \cdot \tan\varphi + c \tag{5.185}$$

$$\sqrt{\left(\frac{\sigma_x - \sigma_y}{2}\right)^2 + {\tau_{xy}}^2} = \frac{\sigma_x + \sigma_y}{2} \cdot \tan\varphi + \nu_s \cdot \frac{1}{2 \cdot \sqrt{k_s}} \cdot f_{cm,cube} \tag{5.186}$$

$$\sqrt{\left(\frac{F_R \cdot \kappa_1 \cdot (1-\nu) \cdot \sin(\alpha_{s1})}{2 \cdot n_a \cdot \lambda_p \cdot d \cdot L_{arm}}\right)^2 + \frac{F_R \cdot \kappa_2 \cdot \sin(\alpha_{s1})^2}{n_a \cdot \lambda_p \cdot d \cdot L_{arm}}} = \frac{F_R \cdot \kappa_1 \cdot (1+\nu) \cdot \sin(\alpha_{s1})}{2 \cdot n_a \cdot \lambda_p \cdot d \cdot L_{arm}} \cdot \tan\varphi + \nu_s \cdot \frac{1}{2 \cdot \sqrt{k_s}} \cdot f_{cm,cube} \tag{5.187}$$

$$\frac{F_R \cdot \psi_B \cdot \sin(\alpha_{s1})}{n_a \cdot \lambda_p \cdot d \cdot L_{arm}} = \frac{F_R \cdot \kappa_1 \cdot (1+\nu) \cdot \sin(\alpha_{s1})}{2 \cdot n_a \cdot \lambda_p \cdot d \cdot L_{arm}} \cdot \mu + \nu_s \cdot \frac{1}{2 \cdot \sqrt{k_s}} \cdot f_{cm,cube} \tag{5.188}$$

$$\frac{F_R \cdot \sin(\alpha_{s1})}{n_a \cdot \lambda_p \cdot d \cdot L_{arm}} \cdot (\psi_B - 0.5 \cdot \kappa_1 \cdot (1+\nu) \cdot \mu) = \frac{\nu_s \cdot f_{cm,cube}}{2 \cdot \sqrt{k_s}} \tag{5.189}$$

$$P_{R,s1} = \frac{n_a \cdot \lambda_p \cdot \nu_s \cdot d \cdot L_{arm} \cdot f_{cm,cube}}{2 \cdot \sqrt{k_s} \cdot (\psi_B - 0.5 \cdot \kappa_1 \cdot (1+\nu) \cdot \mu) \cdot \sin(\alpha_{s1})} \; [kN] \tag{5.190}$$

The last possible failure mode of concrete for the angled variant of connector is the vertical shearing between the arms of connector, see Fig. 5.103. The shear strength is based on the same principle as the calculation of the resistance according to the maximum possible shear stresses defined in Eq. 5.185. Therefore, the modified Mohr-Coulomb material strength proposed by Nielsen [130] is considered. A new internal rotation angle to the vertical direction $\alpha_{s2} = \gamma_{s2} = -\alpha_w$ has to be respected. In the result, a new effective shearing area has to be defined and the acting stresses has to be evaluated according to the vertical orientation of the internal unit concrete element.

The new effective shearing area can be simplified as the half area of a diamond shape with the base length equal to the L_{arm} and the sharp angle between the two consequent base lengths of $2\alpha_c$. Due to the taken simplification, the area correction factor $\lambda_A = 1.05$ has to be implemented. The value of the λ_A has been obtained by direct comparison of the simplified area of the diamond to the exact area between the arms of the connector, thus, in different geometry connector, λ_A can change. The shearing area between the arms of connector is defined in Eq. 5.192.

$$\alpha_{s2} = \gamma_{s2} = -\alpha_w \; [^o] \tag{5.191}$$

$$A_{s2,eff} = 0.5 \cdot \lambda_A \cdot {L_{arm}}^2 \cdot \sin 2\alpha_c \; [cm^2] \tag{5.192}$$

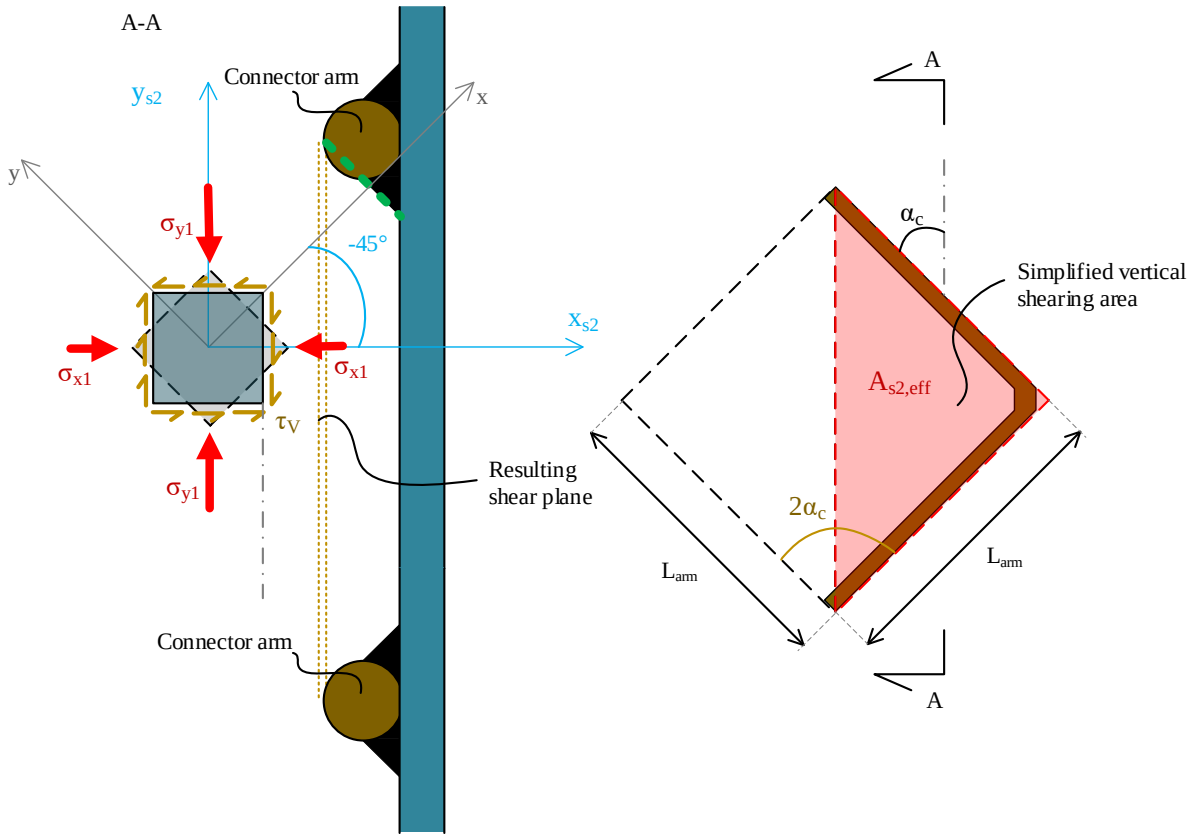


Fig. 5.103. Vertical shear stress state in the V-shaped flat shear connector of the specimen Bv2 of CoPOT and resulting vertical shearing area between the arms of connector.

In order to calculate the resulting shear stresses at the vertical shearing area, the stress transformation equations defined in Eq. 5.38-5.39, repeated here in Eq. 5.193-5.194, were used with the defined transformation angle of $\gamma = \gamma_{s2} = \alpha_{s2} = -\alpha_w = -45^o$. The adapted shear resistance condition is rewritten in Eq. 5.195. By implementing Eq. 5.160-5.161 and Eq. 5.165 into the Eq. 5.196, where the quality sign have replaced the minority sing from Eq. 5.195, the resistance to the vertical shearing of concrete is defined in Eq. 5.202.

$$\sigma_{x1} = \frac{\sigma_x + \sigma_y}{2} + \frac{\sigma_x - \sigma_y}{2} \cdot \cos 2\gamma + \tau_{xy} \cdot \sin 2\gamma = \sigma_x \cdot \cos^2\gamma + \sigma_y \cdot \sin^2\gamma + 2 \cdot \tau_{xy} \cdot \sin\gamma \cdot \cos\gamma \tag{5.193}$$

$$\tau_{x1y1} = -\frac{\sigma_x - \sigma_y}{2} \cdot \sin 2\gamma + \tau_{xy} \cdot \cos 2\gamma = \tau_{xy} \cdot (\cos^2\gamma - \sin^2\gamma) + (\sigma_y - \sigma_x) \cdot \sin\gamma \cdot \cos\gamma \tag{5.194}$$

$$\tau_{x1y1} < \sigma_{x1} \cdot \tan\varphi + c \tag{5.195}$$

$$\tau_{xy} \cdot (\cos^2\gamma - \sin^2\gamma) + (\sigma_y - \sigma_x) \cdot \sin\gamma \cdot \cos\gamma = (\sigma_x \cdot \cos^2\gamma + \sigma_y \cdot \sin^2\gamma + 2 \cdot \tau_{xy} \cdot \sin\gamma \cdot \cos\gamma) \cdot \mu + \nu_s \cdot \frac{1}{2 \cdot \sqrt{k_s}} \cdot f_{cm,cube} \tag{5.196}$$

$$\frac{F_R \cdot \kappa_2}{0.5 \cdot n_a \cdot \lambda_A \cdot {L_{arm}}^2 \cdot \sin 2\alpha_c} \cdot (\cos^2\gamma_{s2} - \sin^2\gamma_{s2})$$

$$+\left(\frac{F_R \cdot \kappa_1 \cdot \nu}{0.5 \cdot n_a \cdot \lambda_A \cdot {L_{arm}}^2 \cdot \sin 2\alpha_c} - \frac{F_R \cdot \kappa_1}{0.5 \cdot n_a \cdot \lambda_A \cdot {L_{arm}}^2 \cdot \sin 2\alpha_c}\right) \cdot \sin\gamma_{s2} \cdot \cos\gamma_{s2}$$

$$= \left(\frac{F_R \cdot \kappa_1}{0.5 \cdot n_a \cdot \lambda_A \cdot {L_{arm}}^2 \cdot \sin 2\alpha_c} \cdot \cos^2\gamma_{s2} + \frac{F_R \cdot \kappa_1 \cdot \nu}{0.5 \cdot n_a \cdot \lambda_A \cdot {L_{arm}}^2 \cdot \sin 2\alpha_c} \cdot \sin^2\gamma_{s2}\right.$$

$$\left. + 2 \cdot \frac{F_R \cdot \kappa_2}{0.5 \cdot n_a \cdot \lambda_A \cdot {L_{arm}}^2 \cdot \sin 2\alpha_c} \cdot \sin\gamma_{s2} \cdot \cos\gamma_{s2}\right) \cdot \mu + \nu_s \cdot \frac{1}{2 \cdot \sqrt{k_s}} \cdot f_{cm,cube} \quad (5.197)$$

$$\frac{F_R \cdot \psi_{B,s2,1}}{0.5 \cdot n_a \cdot \lambda_A \cdot {L_{arm}}^2 \cdot \sin 2\alpha_c} = \frac{F_R \cdot \psi_{B,s2,2} \cdot \mu}{0.5 \cdot n_a \cdot \lambda_A \cdot {L_{arm}}^2 \cdot \sin 2\alpha_c} + \frac{\nu_s \cdot f_{cm,cube}}{2 \cdot \sqrt{k_s}} \quad (5.198)$$

$$\psi_{B,s2,1} = \kappa_2 \cdot (\cos^2\gamma_{s2} - \sin^2\gamma_{s2}) + \kappa_1 \cdot (\nu - 1) \cdot \sin\gamma_{s2} \cdot \cos\gamma_{s2} \quad (5.199)$$

$$\psi_{B,s2,2} = \kappa_1 \cdot (\cos^2\gamma_{s2} + \nu \cdot \sin^2\gamma_{s2}) + 2 \cdot \kappa_2 \cdot \sin\gamma_{s2} \cdot \cos\gamma_{s2} \quad (5.200)$$

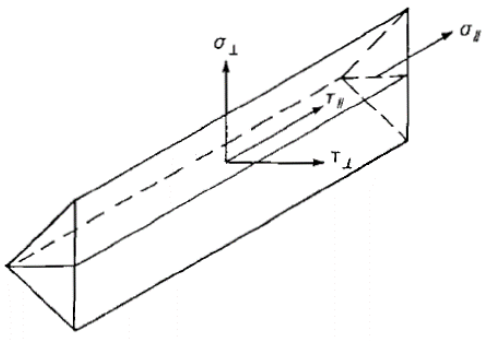
$$\frac{F_R}{0.5 \cdot n_a \cdot \lambda_A \cdot {L_{arm}}^2 \cdot \sin 2\alpha_c} \cdot (\psi_{B,s2,1} - \psi_{B,s2,2} \cdot \mu) = \frac{\nu_s \cdot f_{cm,cube}}{2 \cdot \sqrt{k_s}} \quad (5.201)$$

$$P_{R,s2} = \frac{n_a \cdot \lambda_A \cdot \nu_s \cdot \sin 2\alpha_c \cdot {L_{arm}}^2 \cdot f_{cm,cube}}{4 \cdot \sqrt{k_s} \cdot (\psi_{B,s2,1} - \psi_{B,s2,2} \cdot \mu)} \; [kN] \quad (5.202)$$

Where,

$\psi_{B,s2,1}$ and $\psi_{B,s2,2}$ are the coefficients, which simplify the equation form for the vertical shearing and $P_{R,s2}$ is the resistance of shear connector for the vertical shear condition (substituted from F_R).

The strength of weld of the specimen Bv2 has been analysed in accordance to the procedure described for the specimen Av2. Due to the geometry of the angled connector, different resulting forces are acting on the welded connection. To verify the most critical case, two force distribution models has been investigated. One, where the forces are acting like in general case described in Fig. 5.97a and the second, where the forces are acting according to the redistributed scheme shown in Fig. 5.97b. The main difference of two aforementioned models is in the definition of the resultant stress tensor for the von Mises yield criterion, see Fig. 5.104.



$$[\sigma_\perp^2 + 3\,(\tau_\perp^2 + \tau_\parallel^2)]^{0,5} \le f_u / (\beta_w\,\gamma_{M2}) \quad \text{and} \quad \sigma_\perp \le 0.9\,f_u / \gamma_{M2}$$

Fig. 5.104. Stresses distribution in weld for the Von Mises yield criterion, according to EN 1993-1-8 [57].

It has been found that the model with forces acting according to the redistributed equilibrium state yields a more critical solution, thus, a more conservative approach is obtained. Therefore, this model has been assumed for the verification of the weld strength of the shear connector. In the result, the verification procedure of the V-shaped connector is identical as for the transversal connector given in Fig. 5.93 and Eq. 5.60-5.68. The resistance condition defined in Eq. 5.62 is rewritten in Eq. 5.203. In the equation for the resistance of connector defined in Eq. 5.204, the force orientation factor λ_f has been introduced, which is referring to the number of connector arms and their inclination to the longitudinal axis of the steel profile α_c.

$$\sqrt{{\sigma_\perp}^2 + 3 \cdot ({\tau_\perp}^2 + {\tau_\parallel}^2)} \leq \frac{f_u}{\beta_w \cdot \gamma_{M2}} \tag{5.203}$$

$$P_{R,w} = \frac{\lambda_f \cdot f_u}{\beta_w \cdot \psi_w} \; [kN] \tag{5.204}$$

$$\lambda_f = n_a \cdot \sin \alpha_c \tag{5.205}$$

$$\psi_{w,el} = \sqrt{\frac{{e_w}^2 \cdot z^2}{{I_w}^2} + 3 \cdot \frac{1}{{A_w}^2}} \; \left[\frac{1}{cm^2}\right] \tag{5.206}$$

$$\psi_{w,pl} = \sqrt{\frac{{e_w}^2}{d^2 \cdot {A_{w,t}}^2} + 3 \cdot \frac{1}{{A_w}^2}} \; \left[\frac{1}{cm^2}\right] \tag{5.207}$$

Similarly, like in the case of transversal variant of connector, two stress distribution models have been investigated – elastic stress distribution and plastic stress distribution. Each model can be included in the equation for the resistance of connector by implementing of appropriate ψ_w coefficient given in Eq. 5.206-5.207.

The strength of connector material for the specimen Bv2 is verified with the identical procedure that has been defined for the specimen Av2. Here the model for the definition of the resulting forces acting on the connector is analogical to the model used for the weld resistance verification, see Fig. 5.95. Thus, the same force orientation factor λ_f will be implemented to the procedure defined in Eq. 5.69-5.80 and rewritten here in Eq. 5.208-5.217.

$$\tau_E = \frac{V_E \cdot S_{arm}}{I_{arm} \cdot t} \leq \frac{f_y}{\sqrt{3}} \tag{5.208}$$

$$P_{R,cs,el} = \frac{\lambda_f \cdot f_y \cdot L_{arm} \cdot d}{1.5 \cdot \sqrt{3} \cdot \left(1 - \frac{h_w}{d}\right)} \; [kN] \tag{5.209}$$

$$\sigma_E = \frac{M_E \cdot z}{I_{arm}} \leq f_y \tag{5.210}$$

$$P_{R,cb,el} = \frac{\lambda_f \cdot f_y \cdot L_{arm} \cdot d^3}{3 \cdot (d - h_w)^2} \; [kN] \tag{5.211}$$

$$V_{pl,R} = \frac{\lambda_f \cdot A_{arm} \cdot f_y}{\sqrt{3}} = \frac{\lambda_f \cdot d \cdot L_{arm} \cdot f_y}{\sqrt{3}} = P_{R,cs,pl} \; [kN] \tag{5.212}$$

$$\sigma_E = \frac{M_E \cdot z}{I_c} \leq (1 - \rho) f_y \tag{5.213}$$

$$\rho = \left(\frac{2 \cdot V_E}{V_{pl,R}} - 1 \right)^2 \tag{5.214}$$

$$If, \quad \frac{V_E}{V_{pl,R}} < 0.5 \quad then\ bending\ and\ shear\ interaction\ can\ be\ neglected \tag{5.215}$$

$$P_{R,cb,cs} = \frac{\lambda_f \cdot (1 - \rho) \cdot f_y \cdot L_c \cdot d^3}{3 \cdot (d - h_w)^2} \; [kN] \tag{5.216}$$

$$P_{R,m} = min\{P_{R,cs,el};\ P_{R,cb,el};\ P_{R,cb,cs};\ P_{R,cs,pl}\} \tag{5.217}$$

Analogically to the specimen Av2, the plastic shear resistance of the connector material for the Bv2 specimen given in Eq. 5.212 yields the smallest resistance from values included in Eq. 5.217.

The resistance of embedding concrete to the maximum compression stresses, maximum shear stresses and vertical shear stresses are supported in each case by the connector-concrete bond strength. The connector bond strength was derived in accordance to the procedure given for the specimens Cv2, see Eq. 5.24. Due to the different orientation of the connector in accordance to the imposed displacement, the effective area activation factor λ_u has to be adjusted. For a simplification, it has been assumed that the activation factor for the angled type of connector will consists of the same value as for the case of transversal variant connector and $\lambda_u = 0.25$. The contributing part of the connector-concrete bond resistance has been denoted as $P_{R,b}$ and Eq. 5.81 has been rewritten below in Eq. 5.218.

$$P_{R,b} = 2.5 \cdot \pi \cdot \lambda_u \cdot d \cdot L_{con} \cdot \sqrt{f_{cm}} \tag{5.218}$$

Where,

$\lambda_u = 0.25$,

f_{cm} is considered for cylindrical values and

L_{con} is taken as a total axial length of the connector (both arms).

Finally, the resistance of V-shape flat shear connector has to be taken as the minimum of the investigated possible failure modes. The summary of the investigated failure modes and the judging criterion are given in Eq. 5.219. In addition, the concrete stress state condition for the identification of possible tensile stresses in the principal direction under the connector, the concrete state condition and the resistance limitation due to the uncracked concrete state, are given in Eq. 5.220-5.222 respectively.

$$P_{R,Bv2} = min\begin{cases} P_{R,w} = \dfrac{\lambda_f \cdot f_u}{\beta_w \cdot \psi_w} \\ P_{R,m} = min\{P_{R,cs,el};\ P_{R,cb,el};\ P_{R,cb,cs};\ P_{R,cs,pl}\} = \dfrac{\lambda_f \cdot d \cdot L_{arm} \cdot f_y}{\sqrt{3}} \\ P_{R,c} + P_{R,b} = \dfrac{n_a \cdot \lambda_d \cdot d \cdot L_{arm} \cdot \omega_{cc} \cdot f_{cm,cube}}{(k_s + 1) \cdot \psi_B - 0.5 \cdot (k_s - 1) \cdot \kappa_1 \cdot (1 + \nu)} + P_{R,b} \\ P_{R,s1} + P_{R,b} = \dfrac{n_a \cdot \lambda_p \cdot \nu_s \cdot d \cdot L_{arm} \cdot f_{cm,cube}}{2 \cdot \sqrt{k_s} \cdot (\psi_B - 0.5 \cdot \kappa_1 \cdot (1 + \nu) \cdot \mu) \cdot \sin(\alpha_{s1})} + P_{R,b} \\ P_{R,s2} + P_{R,b} = \dfrac{n_a \cdot \lambda_A \cdot \nu_s \cdot \sin 2\alpha_c \cdot {L_{arm}}^2 \cdot f_{cm,cube}}{4 \cdot \sqrt{k_s} \cdot (\psi_{B,s2,1} - \psi_{B,s2,2} \cdot \mu)} + P_{R,b} \end{cases} \quad (5.219)$$

$$\frac{\kappa_1 \cdot (1 + \nu)}{2 \cdot \psi_B} < 1 \quad \text{then, tensile stresses in the principal direction will occur} \quad (5.220)$$

$$\frac{F_R \cdot (\psi_B - 0.5 \cdot \kappa_1 \cdot (1 + \nu))}{n_a \cdot \lambda_d \cdot d \cdot L_{arm} \cdot f_{ctm}} < 1 \quad \text{then, the concrete will be in the uncracked state} \quad (5.221)$$

$$P_{R,t} = \frac{n_a \cdot \lambda_d \cdot d \cdot L_{arm} \cdot f_{ctm}}{\psi_B - 0.5 \cdot \kappa_1 \cdot (1 + \nu)}\ [kN] \quad \text{Limitation to keep the uncracked state of concrete} \quad (5.222)$$

The above-described analytical model has been derived based on the observations from the experimental campaign and numerical simulations. It has been based on the fundamental equations of the theory of elasticity and plasticity with the implemented modified Mohr-Coulomb material law for concrete described by Nielsen [130]. The procedure to estimate the resistance of shear connector is supported by the design provisions given in EN 1994-1-1 [58], EN 1992-1-1 [53], EN 1993-1-1 [55], EN 1993-1-8 [57] and fib ModelCode 2010 [62]. The obtained results according to Eq. 5.219 are in good correlation to the obtained behaviour from the test specimens. However, to get a convergence with the experimental values of the resistance of connector, calibration factors have to be implemented to the concrete compression strength ($P_{R,c}$) and concrete shear strength ($P_{R,s1}$ and $P_{R,s2}$). The verification is described in Sections 5.6.5.1-5.6.5.7. To distinguish the character of the implemented calibration factor, they have the following nomenclature and meaning:

- $\boldsymbol{k_{hlc}}$ is the calibration factor used for the compression strength of concrete and, among others, it is mainly related to the existence of the global confinement of the concrete due to the applied reinforcement cage around the embedded steel profile and extrapolation of the proposed plain model to the 3D problem. Its value was calibrated based on the experimental results and it is amplifying the confined concrete strength to reach the experimental values.
- $\boldsymbol{\lambda_s}$ is the calibration factor used for the concrete shear strength and it is related to the existence of the global confinement of the concrete due to the reinforcement cage,

extrapolation of the plain model to the 3D problem and it is related to the local behaviour of concrete, like for example micro and macro carking effects around the shear connector. Its value has been calibrated based on the experimental results.

The calibration factors are indicated in red colour in order to increase their visibility.

In the sensivity study of the calibration factors, a relation has been found that the both calibration factors for the specimen Bv2 are possibly dependent on the shear connector orientation angle α_c. The aforementioned relation is proposed in Eq. 5.223-5.224. However, their value is fully based on the test results and the relations from Eq. 5.223-5.224 are given only for an overview.

$$k_{hlc,Bv2} = \frac{k_{hlc}}{\sin \alpha_c} \tag{5.223}$$

$$\lambda_{s,Bv2} = \frac{\lambda_s}{\sin \alpha_c} \tag{5.224}$$

5.6.5.1. Verification of the resistance of the weld ($P_{R,w}$)

In the resistance of the weld, no calibration factors are considered. The both stresses distributions, elastic and plastic, have been investigated and the corresponding resistances of shear connector are calculated in Eq. 5.236 and Eq. 5.237, respectively. The aforementioned equations consist of the force direction factor λ_f, which is defined in Eq. 5.235. The length of weld used for the verification has been reduced to the straight part of the arm of connector. In the result, according to the geometry of connector, the value of $l_w = 132$ mm is considered.

$$d = 0.8\ [cm] \tag{5.225}$$

$$e_w = \frac{d}{2} = 0.4\ [cm] \tag{5.226}$$

$$z = \frac{d}{2} + {}^{2}/_{3}\, h_w = \frac{d}{2} + {}^{2}/_{3} \cdot \frac{d}{2} = 0.4 + 0.267 = 0.667\ [cm] \tag{5.227}$$

$$l_w = 132\ [mm] \tag{5.228}$$

$$I_w = \frac{2 \cdot l_w \cdot (2h_w)^3}{12} + A_{w,t} \cdot \left(\frac{d}{2}\right)^2 = \frac{2 \cdot 13.2 \cdot (0.8)^3}{12} + (2 \cdot 0.267 \cdot 13.2) \cdot \left(\frac{0.8}{2}\right)^2 = 2.59\ [cm^4] \tag{5.229}$$

$$A_w = 2 \cdot \left(2 \cdot {}^{2}/_{3} \cdot h_w \cdot l_w\right) = 2 \cdot \left(2 \cdot {}^{2}/_{3} \cdot 0.4 \cdot 13.2\right) = 14.08\ [cm^2] \tag{5.230}$$

$$\psi_{w,el} = \sqrt{\frac{{e_w}^2 \cdot z^2}{{I_w}^2} + 3 \cdot \frac{1}{{A_w}^2}} = \sqrt{\frac{0.4^2 \cdot 0.667^2}{2.59^2} + 3 \cdot \frac{1}{14.08^2}} = 0.16 \left[\frac{1}{cm^2}\right] \tag{5.231}$$

$$\psi_{w,pl} = \sqrt{\frac{{e_w}^2}{d^2 \cdot {A_{w,t}}^2} + 3 \cdot \frac{1}{{A_w}^2}} = \sqrt{\frac{0.4^2}{0.8^2 \cdot 7.04^2} + 3 \cdot \frac{1}{14.08^2}} = 0.14 \left[\frac{1}{cm^2}\right] \tag{5.232}$$

$$f_u = 527\ [MPa] = 52.7\left[\frac{kN}{cm^2}\right] \quad \text{value from Table 5.9} \tag{5.233}$$

$$\beta_w = 0.9 \quad \text{value from EN 1993-1-8 [57] for S355} \tag{5.234}$$

$$\lambda_f = n_a \cdot \sin\alpha_c = 2 \cdot \sin 45^o = 1.414 \tag{5.235}$$

$$P_{R,w,el} = \frac{\lambda_f \cdot f_u}{\beta_w \cdot \psi_w} = \frac{1.414 \cdot 52.7}{0.9 \cdot 0.16} = 515.94\ [kN] \quad > 284.1\ [kN] \tag{5.236}$$

$$P_{R,w,pl} = \frac{\lambda_f \cdot f_u}{\beta_w \cdot \psi_w} = \frac{1.414 \cdot 52.7}{0.9 \cdot 0.14} = 582.98\ [kN] \quad > 284.1\ [kN] \tag{5.237}$$

Comparing the calculated resistances from Eq. 5.236 and Eq. 5.237 with the experimentally obtained forces F_R = 284.1 kN for one connector, where the value includes the portion of force from connector-concrete bond, it can be observed that the weld resistance is higher than the acting forces. The utilisation ratio $P_{R,w}/F_R$ reached 1.82 for the elastic stress distribution and 2.05 for the plastic stress distribution.

5.6.5.2. Verification of the resistance of connector material ($P_{R,m}$)

In the resistance of the connector material, no calibration factors are implemented. The calculations are based on the analytical model given in Eq. 5.208-5.217. Eq. 5.225 defines the shear connector diameter. To analyse V_E, the model shown in Fig. 5.95 and Eq. 5.70 was used. In the performed calculation, from the condition given in Eq. 5.245, it was obtained that the shear and bending interaction can be omitted. However, the verification of aforementioned condition can be done according to Eq. 5.213-5.216. Similarly, like for the verification of weld, the reduced length of shear connector to only straight parts of its arms are considered in order to simplify the calculation and obtain a more conservative solution. The reduced length of shear connector arm is defined in Eq. 5.238. In Eq. 5.242-5.244, the force direction factor in relation to the orientation of shear connector against the longitudinal direction of the embedded steel profile has been implemented in order to consider the correct force distribution.

$$L_{con,red} = 13.2\ [cm] \tag{5.238}$$

$$h_w = 0.4\ [cm] \tag{5.239}$$

$$f_y = 583\ [MPa] = 58.3\ \left[\frac{kN}{cm^2}\right] \tag{5.240}$$

$$\lambda_f = n_a \cdot \sin\alpha_c = 2 \cdot \sin 45^o = 1.414 \tag{5.241}$$

$$P_{R,cs,el} = \frac{\lambda_f \cdot f_y \cdot L_{con,red} \cdot d}{1.5 \cdot \sqrt{3} \cdot \left(1 - \frac{h_w}{d}\right)} = \frac{1.414 \cdot 58.3 \cdot 13.2 \cdot 0.8}{1.5 \cdot \sqrt{3} \cdot \left(1 - \frac{0.4}{0.8}\right)} = 670.23\ [kN] \tag{5.242}$$

$$P_{R,cb,el} = \frac{\lambda_f \cdot f_y \cdot L_{con,red} \cdot d^3}{3 \cdot (d - h_w)^2} = \frac{1.414 \cdot 58.3 \cdot 13.2 \cdot 0.8^3}{3 \cdot (0.8 - 0.4)^2} = 1160.88\ [kN] \quad (5.243)$$

$$P_{R,cs,pl} = \frac{\lambda_f \cdot d \cdot L_{con,red} \cdot f_y}{\sqrt{3}} = \frac{1.414 \cdot 0.8 \cdot 13.2 \cdot 58.3}{\sqrt{3}} = 502.67\ [kN] \quad (5.244)$$

$$\frac{V_E}{V_{pl,R}} = \frac{100.02}{355.44} = 0.28 < 0.5 \qquad bending\ and\ shear\ interaction\ can\ be\ neglected \quad (5.245)$$

$$P_{R,m} = min\{670.23;\ 1160.88;\ 502.67\} = 502.67\ [kN] \qquad > 284.1\ [kN] \quad (5.246)$$

Where, V_E has been analysed according to Eq. 5.70 and the acting force has been taken from the tests.

Comparison of the calculated resistance from Eq. 5.246 to the force transferred by one connector – 284.1 kN, shows that the shear connectors material resistance is higher than the forces to which connectors have been subjected to. The utilisation ratio of 1.77 is obtained.

5.6.5.3. Concrete stress state condition – identification of the tensile stresses

The condition for the concrete stress state has been defined in Eq. 5.171 and it verifies if in the maximum principal direction, tensile stresses can develop. The condition refers to the load distribution angles and to the relation between the two normal stresses acting on the concrete in the plain strain state (in the proposed model to the Poisson's ratio ν). Before the condition can be checked, the load distribution factors, which simplifies the equation form given in Eq. 5.158-5.159 and Eq. 5.172 have to be calculated. The force distribution angles are defined in Eq. 5.247-5.249 based on Fig. 5.96-5.97 and Fig. 5.99. The verification procedure is given in Eq. 5.247-5.254.

$$\theta = 32^o \quad (5.247)$$

$$\alpha_c = 45^o \quad (5.248)$$

$$\beta = \alpha_w + \theta_c = 45^o + 16^o = 61^o \quad (5.249)$$

$$\nu = 0.2 \qquad \text{according to EN 1992-1-1 [53]} \quad (5.250)$$

$$\kappa_1 = \sin\beta \cdot \sqrt{\sin^2\alpha_c \cdot \tan^2\theta + (\sin\alpha_c + \cos\alpha_c)^2} = \sin 61^o \cdot \sqrt{\sin^2 45^o \cdot \tan^2 32^o + (\sin 45^o + \cos 45^o)^2} = 1.30 \quad (5.251)$$

$$\kappa_2 = \cos\beta \cdot \sqrt{\sin^2\alpha_c \cdot \tan^2\theta + (\sin\alpha_c + \cos\alpha_c)^2} = \cos 61^o \cdot \sqrt{\sin^2 45^o \cdot \tan^2 32^o + (\sin 45^o + \cos 45^o)^2} = 0.72 \quad (5.252)$$

$$\psi_B = \sqrt{0.25 \cdot {\kappa_1}^2 \cdot (1 - \nu)^2 + {\kappa_2}^2} = \sqrt{0.25 \cdot 1.30^2 \cdot (1 - 0.2)^2 + 0.72^2} = 0.89 \quad (5.253)$$

$$\frac{\kappa_1 \cdot (1 + \nu)}{2 \cdot \psi_B} = \frac{1.30 \cdot (1 + 0.2)}{2 \cdot 0.89} = 0.88 < 1 \quad (5.254)$$

According to the calculation from Eq. 5.254, it has been proven that tensile stresses will develop in the maximum principal stress direction. Therefore, the verification of concrete crack state can be done to check if the concrete is in cracked or uncracked state. Moreover, the confinement stresses for the verification of concrete strength for the maximum compression case will be equal to zero.

5.6.5.4. Verification of the maximum tension condition for concrete

The condition checked in Eq. 5.254 shows that the tensile stresses develop in the maximum principal stress direction. In the result, the concrete can be in the cracked or uncracked state. The condition to verify the concrete crack state is given in Eq. 5.181, where the shear connector resistance limit is defined in Eq. 5.182, which limits the connector resistance to keep the concrete in the uncracked state. For the verification of the two aforementioned conditions, the calibration factor $k_{hlc,Bv2} = 2.2$ have been adapted to increase the strength of concrete accordingly. The concrete tensile strength f_{ctm} has been calculated according to the provisions given in EN 1992-1-1 [53]. The equation relating the concrete tensile strength to its compression strength is given in Eq. 5.255. The evaluation of concrete crack state is given in Eq. 5.260-5.262, where Eq. 5.247-5.253 and Eq. 5.257-5.259 are implemented. In Eq. 5.260, the experimental value of $F_R = 255.9$ kN has been used and the resulting value is given in Eq. 5.261.

$$f_{ctm} = 0.3 \cdot \left(f_{ck,cube}\right)^{\frac{2}{3}} \quad \text{for} < \text{C50/60}$$
$$f_{ctm} = 2.12 \cdot \ln\left(1 + 0.1 \cdot f_{ck,cube}\right) \quad \text{for} > \text{C50/60} \qquad \text{for } f_{ck,cube} \text{ see Eq. 5.278} \tag{5.255}$$

$$f_{ctm} = 0.3 \cdot \left(f_{ck,cube}\right)^{\frac{2}{3}} = 0.3 \cdot (45.2)^{\frac{2}{3}} = 3.8\ [MPa] = 0.38\ \left[\frac{kN}{cm^2}\right] \tag{5.256}$$

$$n_a = 2 \tag{5.257}$$

$$d = 0.8\ [cm] \tag{5.258}$$

$$L_{arm} = 15.2\ [cm] \tag{5.259}$$

$$\frac{F_R \cdot (\psi_B - 0.5 \cdot \kappa_1 \cdot (1 + \nu))}{n_a \cdot \lambda_d \cdot d \cdot L_{arm} \cdot k_{hlc,Bv2} \cdot f_{ctm}} < 1 \qquad \text{then, the concrete will be in the uncracked state} \tag{5.260}$$

$$\frac{255.9 \cdot (0.89 - 0.5 \cdot 1.30 \cdot (1 + 0.2))}{2 \cdot \sqrt{2} \cdot 0.8 \cdot 15.2 \cdot 2.2 \cdot 0.38} = 0.98 < 1 \qquad \text{concrete in the uncracked state} \tag{5.261}$$

$$P_{R,t} = \frac{n_a \cdot \lambda_d \cdot d \cdot L_{arm} \cdot k_{hlc,Bv2} \cdot f_{ctm}}{\psi_B - 0.5 \cdot \kappa_1 \cdot (1 + \nu)} = \frac{2 \cdot \sqrt{2} \cdot 0.8 \cdot 15.2 \cdot 2.2 \cdot 0.38}{0.89 - 0.5 \cdot 1.30 \cdot (1 + 0.2)} = 265.86[kN] > 255.9\ [kN] \tag{5.262}$$

From Eq. 5.262, it can be observed that the tensile strength of concrete has higher value than the experimentally obtained failure load and the utilisation ratio is 1.04. Therefore, it can be concluded that during the test Bv2, the concrete under the connector was in the uncracked state until the failure.

Removing the calibration factor from Eq. 5.261 and Eq. 5.262 would result in the cracked concrete state and the utilisation ratio of the Eq. 5.262 would reach 0.47.

5.6.5.5. Verification of the maximum compression condition for concrete ($P_{R,c}$)

The verification of maximum compression condition for concrete requires utilisation of the calibration factor $k_{hlc,Bv2}$. The calibration factor has been placed in the front of the confined concrete strength amplifying its value. The verification procedure given in Eq. 5.173-5.179 has been updated and rewritten in Eq. 5.263-5.269 below.

$$\sigma_1 = \frac{\sigma_x + \sigma_y}{2} + \sqrt{\left(\frac{\sigma_x - \sigma_y}{2}\right)^2 + {\tau_{xy}}^2} < k_{hlc,Bv2} \cdot f_{cm,c,cube} \tag{5.263}$$

$$\frac{\sigma_x + \sigma_y}{2} + \sqrt{\left(\frac{\sigma_x - \sigma_y}{2}\right)^2 + {\tau_{xy}}^2} = k_{hlc,Bv2} \cdot \left(f_{cm,cc,cube} + k_s \cdot \sigma_2\right) \tag{5.264}$$

$$\frac{\sigma_x + \sigma_y}{2} + \sqrt{\left(\frac{\sigma_x - \sigma_y}{2}\right)^2 + {\tau_{xy}}^2} = k_{hlc,Bv2} \cdot \omega_{cc} \cdot f_{cm,cube} + k_{hlc,Bv2} \cdot k_s \cdot \left(\frac{\sigma_x + \sigma_y}{2} - \sqrt{\left(\frac{\sigma_x - \sigma_y}{2}\right)^2 + {\tau_{xy}}^2}\right) \tag{5.265}$$

$$\frac{F_R \cdot \kappa_1 \cdot (1+\nu)}{2 \cdot n_a \cdot \lambda_d \cdot d \cdot L_{arm}} + \sqrt{\left(\frac{F_R \cdot \kappa_1 \cdot (1-\nu)}{2 \cdot n_a \cdot \lambda_d \cdot d \cdot L_{arm}}\right)^2 + \left(\frac{F_R \cdot \kappa_2}{n_a \cdot \lambda_d \cdot d \cdot L_{arm}}\right)^2} = k_{hlc,Bv2} \cdot \omega_{cc} \cdot f_{cm,cube} + k_{hlc,Bv2} \cdot k_s \cdot \left(\frac{F_R \cdot \kappa_1 \cdot (1+\nu)}{2 \cdot n_a \cdot \lambda_d \cdot d \cdot L_{arm}} - \sqrt{\left(\frac{F_R \cdot \kappa_1 \cdot (1-\nu)}{2 \cdot n_a \cdot \lambda_d \cdot d \cdot L_{arm}}\right)^2 + \left(\frac{F_R \cdot \kappa_2}{n_a \cdot \lambda_d \cdot d \cdot L_{arm}}\right)^2}\right) \tag{5.266}$$

$$\frac{F_R \cdot (0.5 \cdot \kappa_1 \cdot (1+\nu) + \psi_B)}{n_a \cdot \lambda_d \cdot d \cdot L_{arm}} - k_{hlc,Bv2} \cdot k_s \cdot \frac{F_R \cdot (0.5 \cdot \kappa_1 \cdot (1+\nu) - \psi_B)}{n_a \cdot \lambda_d \cdot d \cdot L_{arm}} = k_{hlc,Bv2} \cdot \omega_{cc} \cdot f_{cm,cube} \tag{5.267}$$

$$\frac{F_R}{n_a \cdot \lambda_d \cdot d \cdot L_{arm}} \cdot \left(\left(k_{hlc,Bv2} \cdot k_s + 1\right) \cdot \psi_B - 0.5 \cdot \left(k_{hlc,Bv2} \cdot k_s - 1\right) \cdot \kappa_1 \cdot (1+\nu)\right) = k_{hlc,Bv2} \cdot \omega_{cc} \cdot f_{cm,cube} \tag{5.268}$$

$$P_{R,c} = \frac{n_a \cdot \lambda_d \cdot d \cdot L_{arm} \cdot k_{hlc,Bv2} \cdot \omega_{cc} \cdot f_{cm,cube}}{\left(k_{hlc,Bv2} \cdot k_s + 1\right) \cdot \psi_B - 0.5 \cdot \left(k_{hlc,Bv2} \cdot k_s - 1\right) \cdot \kappa_1 \cdot (1+\nu)} \; [kN] \tag{5.269}$$

The value of ω_{cc} can be obtained according to Fig. 5.90 by selecting the corresponding factor in accrodance to the compression strength of concrete. In the analysed case, the value $\omega_{cc} = 1.465$ for the $f_c = f_{ck,Bv2} = 35.3$ MPa. The inclination parameter for Coulomb material $k_s = \left(\mu + \sqrt{1+\mu^2}\right)^2$ can be calculated by implementing the relation $\mu = \tan\varphi$, where the friction angle φ can be obtained from

Fig. 5.89, by using f_c value defined above. Finally, $\varphi = 32.5^o$ and $\mu = 0.637$, which give the value of $k_s = 3.322$ are obtained.

According to the verification made in Eq. 5.254, no concrete confinement in the principal stresses direction will occur. In the result, factors $\omega_{cc} = 1$ and $k_s = 0$ are taken.

Assuming $k_{hlc,Bv2} = 1$ and implementing Eq. 5.247-5.253 into Eq. 5.269, the shear connector resistance is given in Eq. 5.277.

$$n_a = 2 \tag{5.270}$$

$$d = 0.8\ [cm] \tag{5.271}$$

$$L_{arm} = 15.2\ [cm] \tag{5.272}$$

$$\lambda_d = \sqrt{2} \tag{5.273}$$

$$\omega_{cc} = 1 \tag{5.274}$$

$$k_s = 0 \tag{5.275}$$

$$f_{cm,cube} = 55.2\ [MPa] = 5.52\ \left[\frac{kN}{cm^2}\right] \quad \text{is the value in the day of test Bv2, see Table 5.11} \tag{5.276}$$

$$P_{R,c} = \frac{n_a \cdot \lambda_d \cdot d \cdot L_{arm} \cdot k_{hlc,Bv2} \cdot \omega_{cc} \cdot f_{cm,cube}}{\left(k_{hlc,Bv2} \cdot k_s + 1\right) \cdot \psi_B - 0.5 \cdot \left(k_{hlc,Bv2} \cdot k_s - 1\right) \cdot \kappa_1 \cdot (1 + \nu)}$$

$$= \frac{2 \cdot \sqrt{2} \cdot 0.8 \cdot 15.2 \cdot 1 \cdot 1 \cdot 5.52}{(1 \cdot 0 + 1) \cdot 0.89 - 0.5 \cdot (1 \cdot 0 - 1) \cdot 1.30 \cdot (1 + 0.2)} = 114.07[kN] \tag{5.277}$$

$$< 255.9\ [kN]$$

The result obtained from Eq. 5.277 shows smaller resistance that it was obtained from the experimental campaign – 255.9 kN, where the value consists of only a pure mechanical force transferred per one connector. Comparing the obtained values, the utilisation ratio reached 0.45. A good convergence to the experimental test data is obtained when the $k_{hlc,Bv2} = 2.2$. The value of calibration factor was proposed based on Eq. 5.223. The ratio of the compression strength of globally confined concrete to the unconfined compression strength was applied as shown in Eq. 5.282. The resultant calibration factor is described in Eq. 5.283. The concrete confinement has been calculated based on the provisions given in fib ModelCode 2010 [62] with the adjusted confining stress taken equal to $\sigma_2 = 4.7$ MPa. The value of adjusted confining stress corresponds to the value that can be obtained using the procedure given in fib ModelCode [62], when the safety concept is removed, see Eq. 5.279-5.280. The calculation of the calibrated resistance is shown in Eq. 5.284.

$$f_{ck,cube} = f_{cm,cube} - 10 = 55.2 - 10 = 45.2\ [MPa] = 4.52\ \left[\frac{kN}{cm^2}\right] \tag{5.278}$$

$$\omega_c = max\left\{\frac{A_{sy}\cdot f_{yk}}{a_c\cdot s_c\cdot f_{ck,cube}};\ \frac{A_{sz}\cdot f_{yk}}{b_c\cdot s_c\cdot f_{ck,cube}}\right\} = 0.086$$

Here a modification to the method has been introduced. The min value has been changed with the max value – a less conservative approach. (5.279)

$$\sigma_2 = \omega_c\cdot f_{ck,cube} = 0.086\cdot 45.2 \cong 4.0\ [MPa] \qquad \text{adjusted to } \sigma_2 = 4.7\ [MPa] \tag{5.280}$$

$$f_{cm,c,cube,fib} = f_{ck,cube} + 3.5\cdot f_{ck,cube}\cdot\left(\frac{\sigma_2}{f_{ck,cube}}\right)^{\frac{3}{4}} + 10$$
$$= 45.2 + 3.5\cdot 45.2\cdot\left(\frac{4.7}{45.2}\right)^{\frac{3}{4}} + 10 = 84.2\ [MPa] \tag{5.281}$$

$$k_{hlc} = \frac{f_{cm,c,cube,fib}}{f_{cm,cube}} = \frac{84.2}{55.2} = 1.53 \tag{5.282}$$

$$k_{hlc,Bv2} = \frac{k_{hlc}}{\sin\alpha_c} = \frac{1.53}{\sin 45^o} = 2.2 \tag{5.283}$$

$$P_{R,c} = \frac{n_a\cdot\lambda_d\cdot d\cdot L_{arm}\cdot k_{hlc,Bv2}\cdot\omega_{cc}\cdot f_{cm,cube}}{\left(k_{hlc,Bv2}\cdot k_s + 1\right)\cdot\psi_B - 0.5\cdot\left(k_{hlc,Bv2}\cdot k_s - 1\right)\cdot\kappa_1\cdot(1+\nu)}$$
$$= \frac{2\cdot\sqrt{2}\cdot 0.8\cdot 15.2\cdot 2.2\cdot 1\cdot 5.52}{(2.2\cdot 0+1)\cdot 0.89 - 0.5\cdot(2.2\cdot 0-1)\cdot 1.30\cdot(1+0.2)}$$
$$= 250.95[kN] \qquad \cong 255.9\ [kN] \tag{5.284}$$

The utilisation ratio of the calibrated resistance of shear connector defined in Eq. 5.284, gives the value very close to 1. From the observations made during the opening of CoPOT specimens, see Fig. 5.48 and Fig. 5.51, it was impossible to clearly identify if the concrete compression failure around the shear connector occurred simultaneously with the shearing failures. According to the numerical simulations shown in Fig. 5.77, it can be observed that the concrete failed in compression under the connector and it formulates the shear plane. Based on the observations above, it was assumed that the both failure mechanisms, compression and shear of concrete, occurred simultaneously.

5.6.5.6. Verification of the maximum shear condition for concrete ($P_{R,s1}$)

The verification of maximum shear condition for concrete requires utilisation of the calibration factor $\lambda_{s,Bv2}$. The calibration factor has been placed in the front of the concrete shear strength modifying its value. The verification procedure given in Eq. 5.185-5.190 has been updated and rewritten in Eq. 5.285-5.290 below. The calculation example is following the updated model. In the calculation procedure, the shear connector geometry dimensions from Eq. 5.270-5.272 were used. The angles of force distribution and the simplification factors from Eq. 5.247-5.253 have been implemented. Mean compression strength of concrete for cubes is defined in Eq. 5.276. The resulting inclination angle of shear plane α_{s1} is defined

in Fig. 5.102 and the value of 27° was used in calculation. ν_s is the concrete cohesion reduction factor due to the micro cracking and it is taken as 0.5 [130]. The inclination parameter for Coulomb material $k_s = \left(\mu + \sqrt{1+\mu^2}\right)^2$ has been used where $\mu = \tan\varphi$ and the friction angle φ can be obtained from Fig. 5.89 by using f_c value as the characteristic compression strength of concrete for cylindrical specimens, $f_c = f_{ck,Bv2} = 35.3$ MPa. In summary, $\varphi = 32.5^o$, $\mu = 0.637$ and $k_s = 3.322$.

$$\tau_{max} = \sqrt{\left(\frac{\sigma_x - \sigma_y}{2}\right)^2 + {\tau_{xy}}^2} < \lambda_{s,Bv2} \cdot (\sigma_s \cdot \tan\varphi + c) \tag{5.285}$$

$$\sqrt{\left(\frac{\sigma_x - \sigma_y}{2}\right)^2 + {\tau_{xy}}^2} = \lambda_{s,Bv2} \cdot \frac{\sigma_x + \sigma_y}{2} \cdot \tan\varphi + \lambda_{s,Bv2} \cdot \nu_s \cdot \frac{1}{2 \cdot \sqrt{k_s}} \cdot f_{cm,cube} \tag{5.286}$$

$$\begin{aligned}\sqrt{\left(\frac{F_R \cdot \kappa_1 \cdot (1-\nu) \cdot \sin(\alpha_{s1})}{2 \cdot n_a \cdot \lambda_p \cdot d \cdot L_{arm}}\right)^2 + \frac{F_R \cdot \kappa_2 \cdot \sin(\alpha_{s1})^2}{n_a \cdot \lambda_p \cdot d \cdot L_{arm}}} \\ = \lambda_{s,Bv2} \cdot \frac{F_R \cdot \kappa_1 \cdot (1+\nu) \cdot \sin(\alpha_{s1})}{2 \cdot n_a \cdot \lambda_p \cdot d \cdot L_{arm}} \cdot \tan\varphi + \lambda_{s,Bv2} \cdot \nu_s \cdot \frac{1}{2 \cdot \sqrt{k_s}} \cdot f_{cm,cube}\end{aligned} \tag{5.287}$$

$$\frac{F_R \cdot \psi_B \cdot \sin(\alpha_{s1})}{n_a \cdot \lambda_p \cdot d \cdot L_{arm}} = \lambda_{s,Bv2} \cdot \frac{F_R \cdot \kappa_1 \cdot (1+\nu) \cdot \sin(\alpha_{s1})}{2 \cdot n_a \cdot \lambda_p \cdot d \cdot L_{arm}} \cdot \mu + \lambda_{s,Bv2} \cdot \nu_s \cdot \frac{1}{2 \cdot \sqrt{k_s}} \cdot f_{cm,cube} \tag{5.288}$$

$$\frac{F_R \cdot \sin(\alpha_{s1})}{n_a \cdot \lambda_p \cdot d \cdot L_{arm}} \cdot \left(\psi_B - 0.5 \cdot \lambda_{s,Bv2} \cdot \kappa_1 \cdot (1+\nu) \cdot \mu\right) = \frac{\lambda_{s,Bv2} \cdot \nu_s \cdot f_{cm,cube}}{2 \cdot \sqrt{k_s}} \tag{5.289}$$

$$P_{R,s1} = \frac{n_a \cdot \lambda_{s,Bv2} \cdot \lambda_p \cdot \nu_s \cdot d \cdot L_{arm} \cdot f_{cm,cube}}{2 \cdot \sqrt{k_s} \cdot \left(\psi_B - 0.5 \cdot \lambda_{s,Bv2} \cdot \kappa_1 \cdot (1+\nu) \cdot \mu\right) \cdot \sin(\alpha_{s1})} \; [kN] \tag{5.290}$$

Assuming $\lambda_{s,Bv2} = 1$, the shear connector resistance is given by Eq. 5.291.

$$\begin{aligned}P_{R,s1} &= \frac{n_a \cdot \lambda_{s,Bv2} \cdot \lambda_p \cdot \nu_s \cdot d \cdot L_{arm} \cdot f_{cm,cube}}{2 \cdot \sqrt{k_s} \cdot \left(\psi_B - 0.5 \cdot \lambda_{s,Bv2} \cdot \kappa_1 \cdot (1+\nu) \cdot \mu\right) \cdot \sin(\alpha_{s1})} \\ &= \frac{2 \cdot 1 \cdot \sqrt{2} \cdot 0.5 \cdot 0.8 \cdot 15.2 \cdot 5.52}{2 \cdot \sqrt{3.322} \cdot (0.89 - 0.5 \cdot 1 \cdot 1.30 \cdot (1+0.2) \cdot 0.637) \cdot \sin(27^o)} \\ &= 146.80[kN] \qquad < 255.9\ [kN]\end{aligned} \tag{5.291}$$

The result obtained from Eq. 5.291 shows a smaller resistance that it was actually obtained during the experimental campaign – 255.9 kN, where the value contains only a pure mechanical force transferred per one connector. The comparison of obtained values gives the utilisation ratio of 0.57. From the opening of CoPOT specimens, it can be clearly observed that the specimen did not failed in the maximum shear stress plane, see Fig. 5.51. A good convergence to the experimental test data is

obtained when the $\lambda_{s,Bv2} = 1.3$. Where the calibration factor is based on Eq. 5.224 and it is defined in Eq. 5.292. The calculation of calibrated resistance is given in Eq. 5.293. The value of calibration factor $\lambda_s = 0.92$ was proposed based on the test results.

$$\lambda_{s,Bv2} = \frac{\lambda_s}{\sin \alpha_c} = \frac{0.92}{\sin 45^o} = 1.3 \tag{5.292}$$

$$\begin{aligned} P_{R,s1} &= \frac{n_a \cdot \lambda_{s,Bv2} \cdot \lambda_p \cdot \nu_s \cdot d \cdot L_{arm} \cdot f_{cm,cube}}{2 \cdot \sqrt{k_s} \cdot \left(\psi_B - 0.5 \cdot \lambda_{s,Bv2} \cdot \kappa_1 \cdot (1+\nu) \cdot \mu\right) \cdot \sin(\alpha_{s1})} \\ &= \frac{2 \cdot 1.3 \cdot \sqrt{2} \cdot 0.5 \cdot 0.8 \cdot 15.2 \cdot 5.52}{2 \cdot \sqrt{3.322} \cdot (0.89 - 0.5 \cdot 1.3 \cdot 1.30 \cdot (1+0.2) \cdot 0.637) \cdot \sin(27^o)} \\ &= 308.08[kN] \quad > 255.9\ [kN] \end{aligned} \tag{5.293}$$

The obtained shear resistance from Eq. 5.293 is higher than the experimental value. The utilisation ratio reached 1.20. However, taking into account no visible failure in the plane of maximum shear stresses in Fig. 5.51, the proposed calibration factor was taken as feasible due to the close convergence with the calibration factor from the model for the transversal variant of flat shear connector, see Eq. 5.133. Moreover, in the vertical shearing case, the identical calibration factor is implemented, which gives the coherence between different failure modes.

5.6.5.7. Verification of the vertical shearing condition for concrete ($P_{R,s2}$)

The verification of vertical shear condition for concrete requires utilisation of the calibration factor $\lambda_{s,Bv2}$. The calibration factor has been placed in the front of the concrete shear strength modifying its value. The verification procedure given in Eq. 5.195-5.202 has been updated and rewritten in Eq. 5.294-5.301 below. The calculation example is following the updated model. In the calculation procedure the shear connector geometry dimensions from Eq. 5.270-5.272 were used. The angles of force distribution and the simplification factors from Eq. 5.247-5.253 have been implemented. Mean compression strength of concrete for cubes is defined in Eq. 5.276. The resulting inclination angle of shear plane $\alpha_{s2} = \gamma_{s2}$ is defined in Fig. 5.103 and its value used in calculation is -45°. The effective shearing area is defined in Eq. 5.192. Analogous to the case of maximum shear, $\mu = 0.637$, $\nu_s = 0.5$ and $k_s = 3.322$.

$$\tau_{x1y1} < \lambda_{s,Bv2} \cdot (\sigma_{x1} \cdot \tan\varphi + c) \tag{5.294}$$

$$\begin{aligned} \tau_{xy} \cdot (\cos^2\gamma - \sin^2\gamma) + (\sigma_y - \sigma_x) \cdot \sin\gamma \cdot \cos\gamma \\ = \lambda_{s,Bv2} \cdot (\sigma_x \cdot \cos^2\gamma + \sigma_y \cdot \sin^2\gamma + 2 \cdot \tau_{xy} \cdot \sin\gamma \cdot \cos\gamma) \cdot \mu + \\ + \lambda_{s,Bv2} \cdot \nu_s \cdot \frac{1}{2 \cdot \sqrt{k_s}} \cdot f_{cm,cube} \end{aligned} \tag{5.295}$$

$$\frac{F_R \cdot \kappa_2}{0.5 \cdot n_a \cdot \lambda_A \cdot {L_{arm}}^2 \cdot \sin 2\alpha_c} \cdot (\cos^2\gamma_{s2} - \sin^2\gamma_{s2}) + \left(\frac{F_R \cdot \kappa_1 \cdot \nu}{0.5 \cdot n_a \cdot \lambda_A \cdot {L_{arm}}^2 \cdot \sin 2\alpha_c} - \frac{F_R \cdot \kappa_1}{0.5 \cdot n_a \cdot \lambda_A \cdot {L_{arm}}^2 \cdot \sin 2\alpha_c}\right) \cdot \sin\gamma_{s2} \cdot \cos\gamma_{s2} = \lambda_{s,Bv2} \cdot \left(\frac{F_R \cdot \kappa_1}{0.5 \cdot n_a \cdot \lambda_A \cdot {L_{arm}}^2 \cdot \sin 2\alpha_c} \cdot \cos^2\gamma_{s2} + \frac{F_R \cdot \kappa_1 \cdot \nu}{0.5 \cdot n_a \cdot \lambda_A \cdot {L_{arm}}^2 \cdot \sin 2\alpha_c} \cdot \sin^2\gamma_{s2} + 2 \cdot \frac{F_R \cdot \kappa_2}{0.5 \cdot n_a \cdot \lambda_A \cdot {L_{arm}}^2 \cdot \sin 2\alpha_c} \cdot \sin\gamma_{s2} \cdot \cos\gamma_{s2}\right) \cdot \mu + \lambda_{s,Bv2} \cdot \nu_s \cdot \frac{1}{2 \cdot \sqrt{k_s}} \cdot f_{cm,cube} \quad (5.296)$$

$$\frac{F_R \cdot \psi_{B,s2,1}}{0.5 \cdot n_a \cdot \lambda_A \cdot {L_{arm}}^2 \cdot \sin 2\alpha_c} = \frac{\lambda_{s,Bv2} \cdot F_R \cdot \psi_{B,s2,2} \cdot \mu}{0.5 \cdot n_a \cdot \lambda_A \cdot {L_{arm}}^2 \cdot \sin 2\alpha_c} + \frac{\lambda_{s,Bv2} \cdot \nu_s \cdot f_{cm,cube}}{2 \cdot \sqrt{k_s}} \quad (5.297)$$

$$\psi_{B,s2,1} = \kappa_2 \cdot (\cos^2\gamma_{s2} - \sin^2\gamma_{s2}) + \kappa_1 \cdot (\nu - 1) \cdot \sin\gamma_{s2} \cdot \cos\gamma_{s2} \quad (5.298)$$

$$\psi_{B,s2,2} = \kappa_1 \cdot (\cos^2\gamma_{s2} + \nu \cdot \sin^2\gamma_{s2}) + 2 \cdot \kappa_2 \cdot \sin\gamma_{s2} \cdot \cos\gamma_{s2} \quad (5.299)$$

$$\frac{F_R}{0.5 \cdot n_a \cdot \lambda_A \cdot {L_{arm}}^2 \cdot \sin 2\alpha_c} \cdot (\psi_{B,s2,1} - \lambda_{s,Bv2} \cdot \psi_{B,s2,2} \cdot \mu) = \frac{\lambda_{s,Bv2} \cdot \nu_s \cdot f_{cm,cube}}{2 \cdot \sqrt{k_s}} \quad (5.300)$$

$$P_{R,s2} = \frac{n_a \cdot \lambda_{s,Bv2} \cdot \lambda_A \cdot \nu_s \cdot \sin 2\alpha_c \cdot {L_{arm}}^2 \cdot f_{cm,cube}}{4 \cdot \sqrt{k_s} \cdot (\psi_{B,s2,1} - \lambda_{s,Bv2} \cdot \psi_{B,s2,2} \cdot \mu)} \; [kN] \quad (5.301)$$

Assuming $\lambda_{s,Bv2} = 1$, the shear connector resistance is given by Eq. 5.304.

$$\psi_{B,s2,1} = \kappa_2 \cdot (\cos^2\gamma_{s2} - \sin^2\gamma_{s2}) + \kappa_1 \cdot (\nu - 1) \cdot \sin\gamma_{s2} \cdot \cos\gamma_{s2} = 0.72 \cdot \left(\cos^2(-45^o) - \sin^2(-45^o)\right) + 1.30 \cdot (0.2 - 1) \cdot \sin(-45^o) \cdot \cos(-45^o) = 0.06 \quad (5.302)$$

$$\psi_{B,s2,2} = \kappa_1 \cdot (\cos^2\gamma_{s2} + \nu \cdot \sin^2\gamma_{s2}) + 2 \cdot \kappa_2 \cdot \sin\gamma_{s2} \cdot \cos\gamma_{s2} = 1.30 \cdot \left(\cos^2(-45^o) + 0.2 \cdot \sin^2(-45^o)\right) + 2 \cdot 0.72 \cdot \sin(-45^o) \cdot \cos(-45^o) = 0.52 \quad (5.303)$$

$$P_{R,s2} = \frac{n_a \cdot \lambda_{s,Bv2} \cdot \lambda_A \cdot \nu_s \cdot \sin 2\alpha_c \cdot {L_{arm}}^2 \cdot f_{cm,cube}}{4 \cdot \sqrt{k_s} \cdot (\psi_{B,s2,1} - \lambda_{s,Bv2} \cdot \psi_{B,s2,2} \cdot \mu)} = \frac{2 \cdot 1 \cdot 1.05 \cdot 0.5 \cdot \sin 2 \cdot 45^o \cdot 15.2^2 \cdot 5.52}{4 \cdot \sqrt{3.322} \cdot (0.06 - 1 \cdot 0.52 \cdot 0.637)} = 190.95[kN] < 255.9\,[kN] \quad (5.304)$$

The result obtained from Eq. 5.304 shows smaller resistance that it was actually obtained from the Bv2 tests – 255.9 kN, where the value is containing only a pure mechanical force transferred per one connector. Comparing the obtained values, the utilisation ratio reached 0.75. From the opening of CoPOT specimens, it can be clearly observed that the specimen failed in the vertical shear stress plane, see Fig. 5.51. A good convergence to the experimental test data is obtained when the same calibration factor like for the maximum shear resistance is used, $\lambda_{s,Bv2} = 1.3$.

$$\lambda_{s,Bv2} = \frac{\lambda_s}{\sin \alpha_c} = \frac{0.92}{\sin 45^o} = 1.3 \tag{5.305}$$

$$P_{R,s2} = \frac{n_a \cdot \lambda_{s,Bv2} \cdot \lambda_A \cdot \nu_s \cdot \sin 2\alpha_c \cdot {L_{arm}}^2 \cdot f_{cm,cube}}{4 \cdot \sqrt{k_s} \cdot (\psi_{B,s2,1} - \lambda_{s,Bv2} \cdot \psi_{B,s2,2} \cdot \mu)}$$
$$= \frac{2 \cdot 1.3 \cdot 1.05 \cdot 0.5 \cdot \sin 2 \cdot 45^o \cdot 15.2^2 \cdot 5.52}{4 \cdot \sqrt{3.322} \cdot (0.06 - 1.3 \cdot 0.52 \cdot 0.637)} = 254.22[kN] \tag{5.306}$$
$$\leq 255.9\ [kN]$$

The obtained vertical shear resistance from Eq. 5.306 is close the experimental value and the utilisation ratio is close to 1. The existence of the described failure mode is proven by the identification of the vertical failure plane in Fig. 5.51 and Fig. 5.77. The identical calibration factor like for the maximum shear failure gives a good accuracy in the assessment of the failure sequence.

5.6.6. Summary and limitations to the analytical model

The analytical models to estimate the resistance of proposed novel type of flat mechanical shear connectors dedicated to fully embedded steel-concrete composite columns have been proposed. Within the performed investigation, three variants of flat shear connectors were considered: (i) the longitudinal variant of connector (Cv2), (ii) the transversal variant of connector (Av2) and (iii) the angled, V-shaped, variant of connector (Bv2). The model for the pure bond type connection, including Coulomb friction effect, has been developed based on tests without mechanical connectors (0v2).

The analytical models for the resistances of proposed flat shear connectors are rewritten below in Eq. 5.307 for the specimen Cv2, in Eq. 5.308 for the specimen Av2 and in Eq. 5.309 for the specimen Bv2. The occurring failure modes are shown in Fig. 5.105. An overview on the calibration of the proposed analytical model is shown in Table 5.19-5.20.

$$P_{R,b,Cv2} = 2.5 \cdot \pi \cdot \lambda_u \cdot d \cdot L_{emb} \cdot \sqrt{f_{cm}}\ [kN] \tag{5.307}$$

$$P_{R,Av2} = min \begin{cases} P_{R,w} = \dfrac{f_u}{\beta_w \cdot \psi_w} \\ P_{R,m} = min\{P_{R,cs,el};\ P_{R,cb,el};\ P_{R,cb,cs};\ P_{R,cs,pl}\} = \dfrac{d \cdot L_{con} \cdot f_y}{\sqrt{3}} \\ P_{R,c} + P_{R,b} = \dfrac{\lambda_d \cdot \cos\theta \cdot L_{con} \cdot d \cdot k_{hlc} \cdot \omega_{cc} \cdot f_{cm,cube}}{(k_{hlc} \cdot k_s + 1) \cdot \psi_A - 0.5 \cdot (k_{hlc} \cdot k_s - 1) \cdot \sin\beta \cdot (1 + \nu)} + P_{R,b} \\ P_{R,s1} + P_{R,b} = \dfrac{\lambda_s \cdot \nu_s \cdot \cos\theta \cdot d \cdot L_{con} \cdot f_{cm,cube}}{2\sqrt{k_s} \cdot (\psi_A - 0.5 \cdot \lambda_s \cdot \sin\beta \cdot (1 + \nu) \cdot \mu) \cdot \sin(\alpha_{s1})} + P_{R,b} \end{cases} \tag{5.308}$$

$$P_{R,Bv2} = min \begin{cases} P_{R,w} = \dfrac{\lambda_f \cdot f_u}{\beta_w \cdot \psi_w} \\ P_{R,m} = min\{P_{R,cs,el};\ P_{R,cb,el};\ P_{R,cb,cs};\ P_{R,cs,pl}\} = \dfrac{\lambda_f \cdot d \cdot L_{arm} \cdot f_y}{\sqrt{3}} \\ P_{R,c} + P_{R,b} = \dfrac{n_a \cdot \lambda_d \cdot d \cdot L_{arm} \cdot k_{hlc,Bv2} \cdot \omega_{cc} \cdot f_{cm,cube}}{(k_{hlc,Bv2} \cdot k_s + 1) \cdot \psi_B - 0.5 \cdot (k_{hlc,Bv2} \cdot k_s - 1) \cdot \kappa_1 \cdot (1+\nu)} + P_{R,b} \\ P_{R,s1} + P_{R,b} = \dfrac{n_a \cdot \lambda_{s,Bv2} \cdot \lambda_p \cdot \nu_s \cdot d \cdot L_{arm} \cdot f_{cm,cube}}{2 \cdot \sqrt{k_s} \cdot (\psi_B - 0.5 \cdot \lambda_{s,Bv2} \cdot \kappa_1 \cdot (1+\nu) \cdot \mu) \cdot \sin(\alpha_{s1})} + P_{R,b} \\ P_{R,s2} + P_{R,b} = \dfrac{n_a \cdot \lambda_{s,Bv2} \cdot \lambda_A \cdot \nu_s \cdot \sin 2\alpha_c \cdot {L_{arm}}^2 \cdot f_{cm,cube}}{4 \cdot \sqrt{k_s} \cdot (\psi_{B,s2,1} - \lambda_{s,Bv2} \cdot \psi_{B,s2,2} \cdot \mu)} + P_{R,b} \end{cases} \quad (5.309)$$

$$\frac{\kappa_1 \cdot (1+\nu)}{2 \cdot \psi_B} < 1 \qquad P_{R,t} = \frac{n_a \cdot \lambda_d \cdot d \cdot L_{arm} \cdot k_{hlc,Bv2} \cdot f_{ctm}}{\psi_B - 0.5 \cdot \kappa_1 \cdot (1+\nu)}$$

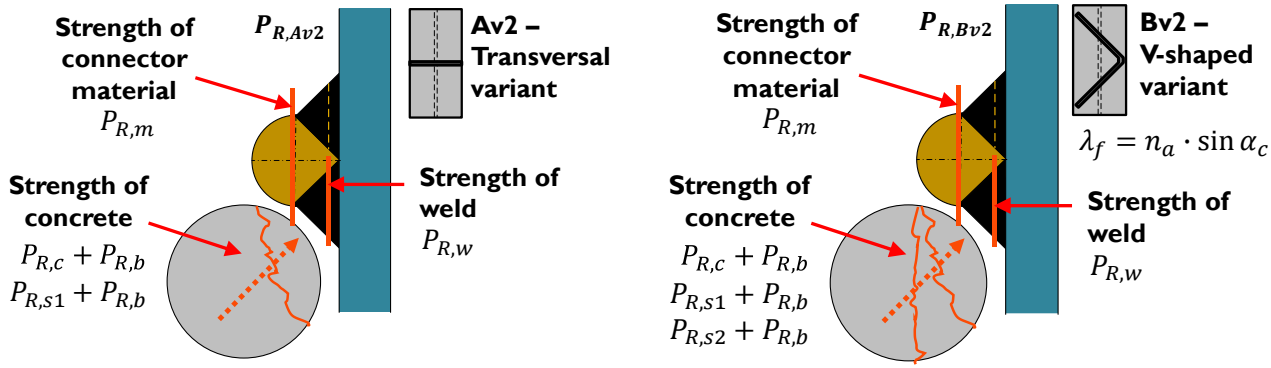
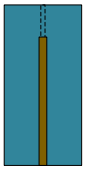
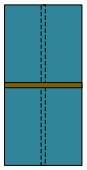
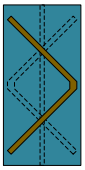


Fig. 5.105. Resistances of flat shear connectors – a) transversal variant connector and b) V-shaped variant connector.

It could be observed that the analytical models for all three variants of connectors are coherent. Moreover, the analytical model for the specimen Av2 can be considered as the specific case of the analytical model for specimen Bv2, when $\alpha_c = 90^o$.

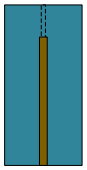
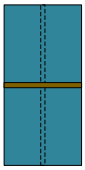
The developed analytical models are based on the six fundamental assumptions: (1) The analytical model is strictly referring only to the performed column push-out tests (CoPOT) described in this thesis in Section 5.4, (2) The elastic material assumption (3) The infinite stiffness of stirrups assumption or the rigid body assumption, (4) the homogenous material assumption, (5) The test values assumption and (6) Long-term effects have been disregarded. According to the first assumption, the given analytical models were calibrated strictly on the basis of performed tests and numerical simulations. The extrapolation of the delivered model to the specimens with other geometry and conditions is not recommended without additional experimental and numerical verification. The proposed calibration factors were based on the test results and their value have to be verified by additional investigations.

Table 5.19.
Overview on the calibration of the proposed analytical model for flat shear connectors.

Flat shear connector	Longitudinal variant			Transversal variant					Angled, V-shaped, variant				
Miniature													
Specimen name	Cv2			Av2					Bv2				
Failure mode	P_R [kN]	Calib factor	$\frac{P_R}{P_{R,exp}}$	P_R [kN]	Calib factor	$P_{R,cal}$ [kN]	$\frac{P_R}{P_{R,exp}}$	$\frac{P_{R,cal}}{P_{R,exp}}$	P_R [kN]	Calib factor	$P_{R,cal}$ [kN]	$\frac{P_R}{P_{R,exp}}$	$\frac{P_{R,cal}}{P_{R,exp}}$
Bond	103.3	-	1.00	-	-	-	-	-	-	-	-	-	-
Max compres-sion	-	-	-	157.5	**1.37**	**293.7**	0.54	**1.00**	143.7	**2.2**	**280.6**	0.51	**0.99**
Max shear	-	-	-	319.9	**0.98**	**284.3**	1.09	**0.97**	176.4	**1.3**	**337.7**	0.62	**1.19**
Vertical shear	-	-	-	-	-	-	-	-	220.6	**1.3**	**283.9**	0.78	**1.00**
Weld	1004	-	9.73	331.7	-	331.7	1.13	1.13	515.9	-	515.9	1.82	1.82
Material	*1280.3	-	*12.41	323.1	-	323.1	1.10	1.10	502.7	-	502.7	1.77	1.77
$P_{R,exp}$, per connector	103.2			293.2					284.1				

Where,
P_R is the resistance of respective shear connector and it is calculated according to Eq. 5.307-5.309 (the value is including connector-concrete bond), where calibration factors are excluded,
$P_{R,cal}$ is the calibrated resistance of the respective shear connector and is calculated according to Eq. 5.307-5.309 (the value is including connector-concrete bond), where calibration factors are included,
$F_{R,exp}$ is the force transferred by the shear connector from the respective experimental series, per one connector (the value is including connector-concrete bond).
* the material resistance for the Cv2 specimen has been given only for the overview purpose because the connector-concrete bond resistance will be always smaller in the used configuration. Calculations according to Eq. 5.75.

Table 5.20.
Comparison of the analytical model for flat shear connectors to the test results.

Flat shear connector	Longitudinal variant			Transversal variant					Angled, V-shaped, variant				
Miniature													
Specimen name	Cv2			Av2					Bv2				
Plain steel-concrete bond contribution	194.1 [kN]			197.2 [kN]					195.9 [kN]				
Coulomb friction contribution	34.3 [kN]			41.2 [kN]					45.1 [kN]				
Failure mode	F_R [kN]	Calib factor	$\frac{F_R}{F_{R,exp}}$	F_R [kN]	Calib factor	$F_{R,cal}$ [kN]	$\frac{F_R}{F_{R,exp}}$	$\frac{F_{R,cal}}{F_{R,exp}}$	F_R [kN]	Calib factor	$F_{R,cal}$ [kN]	$\frac{F_R}{F_{R,exp}}$	$\frac{F_{R,cal}}{F_{R,exp}}$
Bond	434.8	-	1.00	-	-	-	-	-	-	-	-	-	-
Max compres-sion	-	-	-	553.4	**1.37**	**825.8**	0.67	**1.00**	528.5	**2.2**	**802.2**	0.65	**0.99**
Max shear	-	-	-	878.2	**0.98**	**807.1**	1.06	**0.98**	593.9	**1.3**	**916.5**	0.73	**1.13**
Vertical shear	-	-	-	-	-	-	-	-	682.2	**1.3**	**808.8**	0.84	**1.00**
Weld	2236.4	-	5.14	901.8	-	901.8	1.09	1.09	1272.9	-	1272.9	1.57	1.57
Material	*2789	-	*6.42	884.7	-	884.7	1.07	1.07	1246.4	-	1246.4	1.54	1.54
$F_{R,exp}$	434.7			824.8					809.2				

Where,
$F_R = 2P_R + F_b + F_f$ is the resultant resistance of the respective specimen calculated according to Eq. 5.307-5.309 and including contribution of plain steel-concrete bond (F_b) and Coulomb friction (F_f), where calibration factors are excluded,
$F_{R,cal} = 2P_{R,cal} + F_b + F_f$ is the calibrated resistance of the respective specimen calculated according to Eq. 5.307-5.309 and including contribution of plain steel-concrete bond (F_b) and Coulomb friction (F_f), where calibration factors are included,
$F_{R,exp}$ is the mean peak load transferred by the specimen from the respective experimental test series,
For F_b and F_f see Table 5.20.
* the material resistance for the Cv2 specimen has been given only for the overview purpose because the connector-concrete bond resistance will be always smaller in the used configuration. Calculations according to Eq. 5.75.

5.7. Summary and conclusions

In Chapter 5, the development and characterisation process of the novel flat shear connectors dedicated to fully embedded steel-concrete composite columns are described. In the scope of the performed investigation, the development process of concept, the analysis of non-mechanical shear connection means, the experimental campaign on push-out tests of flat shear connectors, numerical simulations and derivation of the analytical model for the resistance of connectors were done. The proposed novel solution of flat shear connectors was developed for fully encased composite columns application and has an aim to be applicable to the regular composite columns and heavy composite column used in high-rise buildings. The proposed new connectors have a high potential for fully automatized application process at the level of beam-finishing workshop or profile production process.

In Section 5.2, the development process of concept for the introduced new flat type of mechanical shear connectors is described. The given concept consisted of embossments imposed to the flanges of steel profiles. The feasible geometry of the proposed new connectors was derived based on the preliminary numerical study performed with the usage of FE code Abaqus [174]. The simulated different variants of flat shear connectors were judged based on the criteria defined in the Ishikawa diagram presented in Fig. 5.4. Based on the taken sensivity study, three variants of flat shear connectors were considered for further experimental and numerical analyses. The proposed solution consisted of reinforcement bars welded to the external surfaces of steel profile flanges under (i) transversal orientation, (ii) angled, V-shaped, orientation and (iii) longitudinal orientation as shown in Fig. 5.10.

The characterisation process of the proposed novel flat shear connectors was based on the push-out tests performed according to EN 1994-1-1:2004 Annex B [58]. It was identified that steel-concrete bond cannot be neglected by greasing of steel profiles in the column type push-out tests and its contribution in the force transfer was significant. In order to accurately analyse the forces transferred by the introduced flat connectors, steel-concrete bond was analysed in parallel. Based on tests made in the laboratory, FE numerical simulations and literature review, steel-concrete bond was analysed and described in Section 5.3. It has been identified that steel-concrete bond consisted of three main force transferring mechanisms: (i) chemical adhesion, (ii) Coulomb friction and (iii) surface roughness friction. It has been found that the steel-concrete bond strength is strongly sensitive to surface treatment conditions, size of the concrete encasement, concrete confinement, geometry of the applied steel profiles and time. Therefore, it was not possible to reveal a one general value for all applications. Based on the conducted tests and in reference to the literature, a wide database of bond strength values is provided in Table B.3 of Annex B. The statistical evaluation of gathered data is shown in Fig. 5.14, where the diagram comparing different surface treatment conditions is given in Fig. 5.15.

In Section 5.4, the experimental campaign on the introduced novel flat mechanical shear connectors is described. Four test series were conducted with one reference series without any mechanical shear connection mean and one series per considered variant of the applied flat shear connectors, see Fig. 5.16. The push-out test specimens consisted of 11 nominally identical specimens, where the HEB120 steel profile was embedded centrally in the wide concrete block. In each case, the steel surface was covered with the anti-adhesive oil agent in order to minimise the impact of steel-concrete bond on the load transfer. The obtained test results were shown in Fig. 5.28, where the impact of the applied flat shear connectors on the load-slip behaviour can be observed. Due to the geometry of specimen, especially due to the placed recess under the steel profile, the eccentricity in the load transfer was identified, which imposed the lateral compression zone at the steel-concrete interface as shown in Fig. 5.27. The developed lateral pressure amplified the contribution of the Coulomb friction mechanism in the steel-concrete bond strength. The summary of performances for the applied flat shear connectors was given in Table 5.12. It was observed that the longitudinal variant of flat shear connector brought the worst load-bearing capacity but assured the highest ductility together with high initial stiffness. The transversal variant of flat shear connectors reached the highest load-bearing capacity but its failure proceeded in the most brittle way, where the initial stiffness was harmed due to the load-bearing mechanisms – interchange from the bond contribution to the mechanical bearing action. Finally, the test series Bv2 with V-shaped flat shear connectors showed the best compromise between the obtained load-bearing capacity, initial stiffness and connection ductility. Moreover, the V-shaped connectors can be classified as efficient in terms of application and production. After the tests, specimens of series Av2 and Bv2 were opened, see Fig. 5.45-5.51. The characteristic failure pattern for each applied variant of shear connectors was identified and it is shown in Fig. 5.47 for the series Av2 and in Fig. 5.51 for series Bv2. From the identified failure patterns, the characteristic failure planes in concrete were observed. For both test series, it was found that the concrete compression struts were oriented under 32° to the vertical direction. In addition, in series Bv2, the additional shear plane under 16° was identified due to the redistributed model of bearing reactions on the arms of connector, see Fig. 5.49. It was observed that the geometry of the tested specimens had an influence on the identified failure planes.

In Section 5.5, the numerical simulations of column push-out tests are described. In the conducted investigation, the numerical model of steel-concrete bond was proposed. The obtained results from simulation of reference tests 0v2 shown in Fig. 5.69, proves the applicability of the proposed numerical model of plain steel-concrete bond. In Fig. 5.70, Fig 5.72 and Fig. 5.76, the numerically obtained load-slip curves of series Cv2, Av2 and Bv2 respectively were compared to the test results and a good correlation was met. The numerically obtained damage patterns of concrete for each test series, see Fig. 5.71 for Cv2, Fig. 5.74 for Av2 and Fig. 5.78 for Bv2, refer well to the test observations. Due to the obtained good calibration of numerical models, the failure sequences of test specimens were analysed together with the developed load flux, see Fig. 5.73 and Fig. 5.77. It was identified that the shear failure

of concrete under the connector occurred first but the peak resistance of the shear connection was related to the failure of compression strut. The vertical failure plane in series Bv2 developed at the end of test as a resultant of the damaged concrete under the connector and further slip of the steel profile, see Fig. 5.77. The orientation of concrete compression struts in series Av2 and Bv2 were confirmed in the numerical simulations by analysing the minimum principal stresses.

In Section 5.6, the concept of analytical model describing the resistances of flat shear connectors is given. The developed analytical model is strictly limited to the tested specimens and described in Section 5.4. The analysis of load transfer in the series Cv2 allowed deriving the equation relating the applied geometry of shear connectors and the compression strength of concrete to the value of connector-concrete bond resistance, see Eq. 5.24. In the derived equation, the provision from the fib ModelCode 2010 [62] for the pull-out failure of reinforcement bar was employed. The resistances of the transversal and V-shaped variants of flat shear connectors, test series Av2 and Bv2 respectively, consisted of the same failure modes: (i) the concrete failure due to the maximum compression condition, (ii) the concrete failure due to the maximum shear condition, (iii) the concrete cracking due to the maximum tension condition, (iv) the failure of weld and (v) the failure of connector material. In addition, in the series Bv2, the failure due to the vertical shearing was considered. For both series Av2 and Bv2, the calibration of evaluated resistances was required in order to converge with the obtained tests results. Equations describing the resistance of the transversal variant of flat shear connector are given in Eq. 5.308, where equations for the resistance of the V-shape variant of flat shear connector are given in Eq. 5.309. The calibration overview of the proposed model is shown in Table 5.19 and Table 5.20. The applied calibration factors are amplifying the strength of concrete and are based on the test results. However, in the condition for compression resistance of concrete, a relation to the ratio between the confined and unconfined strengths of concrete was identified. The correction factors for the shear resistances of concrete were taken purely empirically.

Comparison of the proposed analytical models for the resistance of series Av2 and Bv2 revealed that analytical model proposed for the series Av2 is a special case of the analytical model for series Bv2. By applying specific input values, like for example the number of connector arms or the orientation angle to the longitudinal axis of steel profile, to the analytical model for series Bv2, the resistance of series Av2 can be obtained.

Based on the taken investigation, the new type of flat shear connectors is proposed, verified and characterised. However, in order to develop a general design model for the proposed new mechanical connectors, additional experimental and numerical studies on specimens with different geometries, materials, flat shear connectors and boundary conditions are necessary. The proposed concept of the analytical model from Section 5.6 considers only the case for the tested specimens but brings a solid basis for further and broader considerations.

6. Global Shear Transfer and Effective Stiffness in Composite Members with Two Encased Steel Profiles

The second aspect for the improvement in shear transfer of steel-concrete composite columns with multiple encased steel profiles refers to the geometry of cross-section. There is a possibility to eliminate the commonly used interconnections between the embedded steel profiles and bring an innovative approach to analyse the section with separated steel profiles as shown in Fig. 6.1. Considering the case where the hot-rolled, or welded, steel profiles are completely separated in the cross-section, as it is shown in Fig. 6.1b, the shear transfer between the steel profiles is occurring through the concrete.

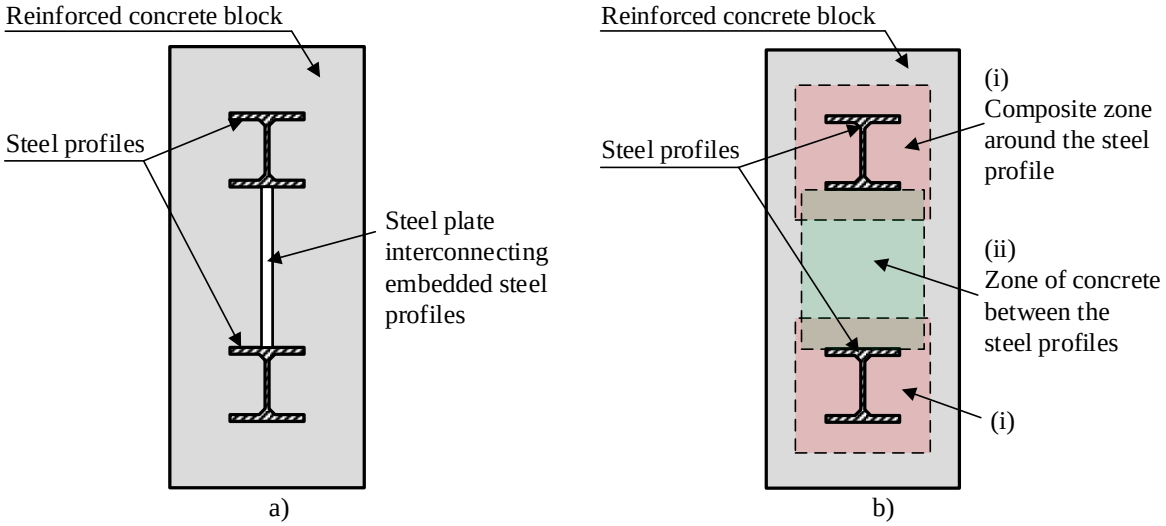


Fig. 6.1. A case study for the improvement of shear transfer in the heavy composite column – a) common solution and b) innovative approach with separated embedded steel profiles.

The concept to analyse the sectional load-bearing capacities of heavy composite columns with multiple encased steel profiles was investigated in the recent RFCS project 'SmartCoCo' [175]. The proposed method is extending the simplified method provided by the EN 1994-1-1 [58]. In the same manner, the effective bending stiffness of columns with more than one embedded steel profiles was based on the nominal stiffness method given in the EN 1992-1-1 [53]. A big discrepancy between the individual bending stiffnesses of two consequent zones: (i) the composite zone with embedded steel profile and (ii) the zone of concrete between the steel profiles, can be identified, see Fig. 6.1b. This leads to a conclusion that, the homogenous Euler-Bernoulli beam model commonly used to describe the global behaviour of a column could be harmed and a requirement for the new effective model describing the realistic behaviour of considered columns is revealed.

The work presented in this chapter, is dealing with the analytical concept to describe the structural behaviour of composite columns with two encased steel profiles and to derive an innovative model for the effective stiffness, which can be implemented into the common design procedure given in EN 1994-1-1 [58]. The investigation is based on the performed tests and numerical simulations.

6.1. General considerations

To investigate the stiffness aspect of the column with more than one embedded steel profile, as shown in Fig. 6.1b, two specimens were investigated experimentally and numerically. The aforementioned specimens consisted of two embedded steel profiles with different spacing between them. The investigated generalised cross-sections of specimens are shown in Fig. 6.2, where the two cases of analysed cross-sections are given: (1) with a small distance between the steel profiles and (2) with a big distance between the steel profiles. In each case, the double symmetric cross-section was considered. The difference in the distance between the embedded steel profiles affects the global stiffness of specimens, which allows investigating the working hypothesis and examine the applicability of the Euler-Bernoulli beam model describing the behaviour of considered column members. In the result, the transition towards the Vierendeel truss model could be investigated with two different internal discretisation models of the truss elements. In general, the geometry of both specimens was nominally identical, where the height of cross-section varied due to the respected distance between the steel profiles. The embedded steel profiles protruded from the concrete block in the longitudinal direction at the both ends of specimens so the end-slip was unconstrained. The length of specimens and the distance between the supports was 6700 mm and 6000 mm respectively. The static system of tests was reflecting the simple supported beam with concentrated load imposed in the middle, see Fig. 6.2. The considered static system involves the most critical case for the shear deformation of specimens.

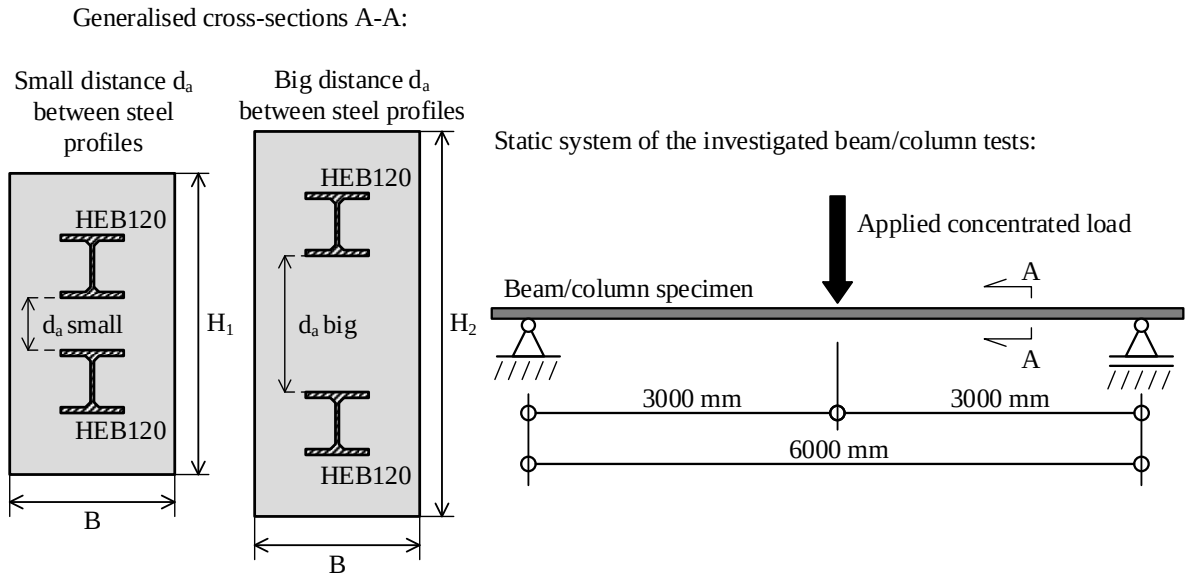


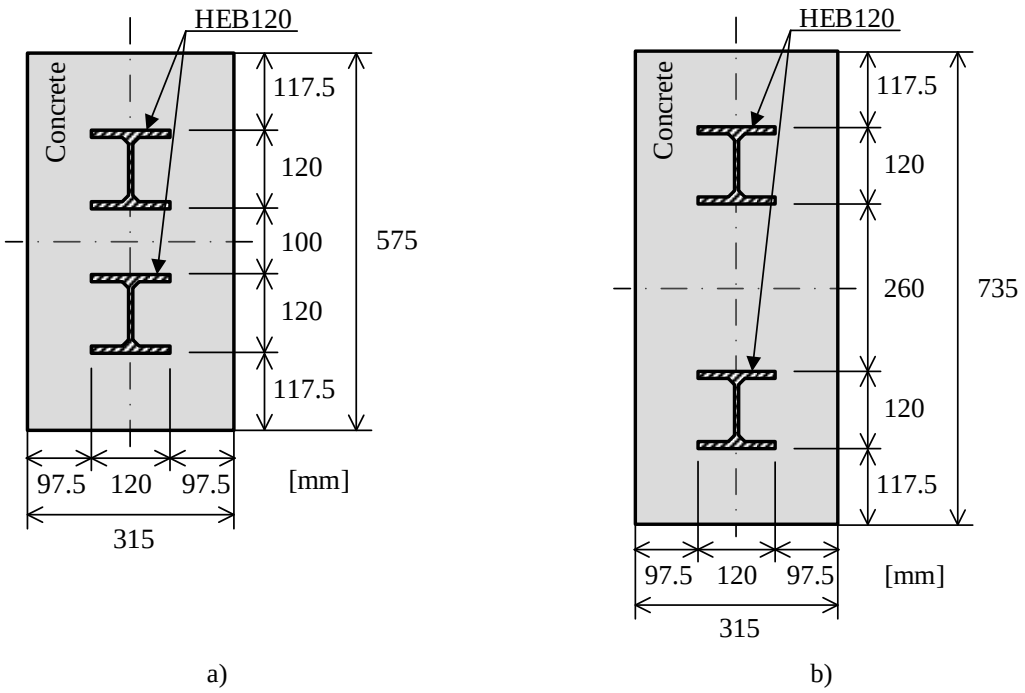
Fig. 6.2. Generalised cross-sections and static system of the investigated beam/column specimens.

To obtain a good geometrical correlation between the two performed test campaigns within the presented research, the applied steel profiles for beam/column tests were identical like in the experimental campaign of flat shear connectors – HEB120, see Section 5.4.

The specimens were detailed in the pre-design process according to the available recommendations from the existing European design standards and elastic analysis of cross-sections with assumed full interaction between the steel and concrete. The pre-design process was essential to predict the load-bearing capacity of specimens, their behaviour and to evaluate the possible failure patterns.

6.2. Pre-design of test specimens

The pre-design process of the test specimens have been divided into three phases: (1) predefining the geometry of the specimen to reach the test objective and technological limitations, (2) detailing the composite section and (3) the verification of stresses. Heavy composite columns with multiple encased steel profiles are intended to resist heavy compression and lateral forces in the building structural systems and those forces are very often exceeding any possible capacities of testing machines. Therefore, the scale and geometry of the test specimen has been carefully defined.



a) b)

Fig. 6.3. General cross-section of the beam/column test specimens – a) smaller specimen and b) bigger specimen.

In the first phase of pre-design process, main criteria for the specimen geometry were considered. The exact values of distances between the embedded steel profiles were established with respect to the internal equilibrium of forces due to bending for the imposed concentrated point load as shown in Fig. 6.2. In the result, the distance between the steel profiles of 100 mm has been engaged for the smaller section specimen and 260 mm for the bigger section specimen as shown in Fig. 6.3. The width of both specimens was 315 mm. The concrete cover of embedded steel profiles was 97.5 mm over the width and 117.5 mm over the height of composite cross-section. The size of concrete cover correlated to the specimens from the push-out test campaign of flat shear connectors and it was defined in accordance to

EN 1994-1-1 [58]. All the mentioned above geometrical parameters resulted in the cross-sectional dimensions of 315x575 mm for the smaller specimen and 315x735 mm for the bigger specimen as indicated in Fig. 6.3.

After defining of the general geometry of specimens, the cross-sections were detailed in the second phase of the pre-design process. To design an appropriate amount, geometry and distribution of the reinforcement cages, the provisions given in EN 1994-1-1 [58] and EN 1992-1-1 [53] were considered and described in the respective Sections 6.2.1 and 6.2.2.

Finally, in the third phase, the detailed cross-sections were verified with the elastic analysis to predict the possible failure modes of the specimens and to evaluate their load-bearing capacities. The performed analyses are described in Section 6.2.3.

6.2.1. Provisions from EN 1994-1-1

The provisions given in the EN 1994-1-1 [58] were used to define the size of concrete cover for the applied steel profiles and to define the minimum ratio of the longitudinal and transversal reinforcement. According to the clause 6.7.3.1 (2), the maximum concrete cover that can be included in the calculations of the simplified design method should be not more than 0.3h and 0.4b for the two respective directions z and y, see Fig. 6.4. In the same time, the minimum concrete cover of 40 mm is defined by the clause 6.7.4.3 (4) and clause 6.7.5.1 (1-2) to ensure the safe transmission of bond forces. Based on the above-mentioned provisions, the concrete cover distances are defined in Fig. 6.3 and in Eq. 6.1-6.2 for the smaller specimen and in Eq. 6.3- Eq. 6.4 for the bigger specimen.

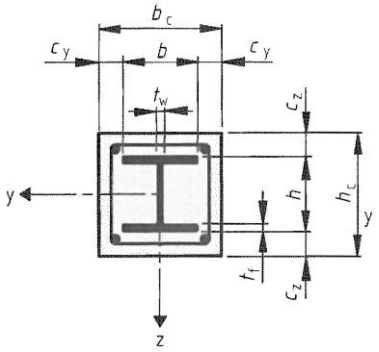


Fig. 6.4. Typical cross-section of fully encased composite column with notation according to EN 1994-1-1 [58].

$$\min c_z = 40\ mm \leq \quad c_{z,1} = 117.5\ mm \quad \leq \max c_z = 0.3 \cdot h = 0.3 \cdot 575 = 172.5\ mm \tag{6.1}$$

$$\min c_y = 40\ mm \leq \quad c_{y,1} = 97.5\ mm \quad \leq \max c_y = 0.4 \cdot b = 0.4 \cdot 315 = 126\ mm \tag{6.2}$$

$$\min c_z = 40\ mm \leq \quad c_{z,2} = 117.5\ mm \quad \leq \max c_z = 0.3 \cdot h = 0.3 \cdot 735 = 220.5\ mm \tag{6.3}$$

$$\min c_y = 40\ mm \leq \quad c_{y,2} = 97.5\ mm \quad \leq \max c_y = 0.4 \cdot b = 0.4 \cdot 315 = 126\ mm \tag{6.4}$$

In the clause 6.7.5.2 (4), the minimum longitudinal and transversal reinforcement are specified that should be implemented in the fully embedded composite cross-sections. For the longitudinal

reinforcement, the minimum bar diameter of 8 mm and the maximum spacing of 250 mm should be used. For the transversal reinforcement, the minimum bar diameter of 6mm and maximum spacing of 200 mm should be used. In the clause 6.7.5.2 (1) it is stated that, if the longitudinal reinforcement is accounted for the section resistance, a minimum degree of reinforcement of 0.3% should be used. For the further detailing of the reinforcement, clause 6.7.5.2 (2) is referring to the EN 1992-1-1 [53].

6.2.2. Provisions from EN 1992-1-1

In EN 1992-1-1 [53], the provisions for the design of reinforcement in clause 9.5.2 (1-4) for the longitudinal reinforcement and clause 9.5.3 (1-6) for the transversal reinforcement are given. For the longitudinal reinforcement, the minimum bar diameter of 8 mm should be used and the minimum total amount of the bars should be not less than $0.002A_c$, where, A_c is the concrete area. In the same time, the amount of longitudinal reinforcement should not exceed $0.04A_c$ for the zone outside the lap locations and $0.08A_c$ for the zone at laps. The spacing between the longitudinal bars should not exceed the distance of 150 mm from the restrained bars in the compression zone. For the transversal reinforcement, the minimum required bar diameter of 6mm is foreseen. The maximum spacing of stirrups can be taken as the minimum value of the following: (i) 20 times the minimum diameter of the longitudinal bars, (ii) the lesser dimension of the column or (iii) 400 mm. It is also specified that, in the load introduction zones, the above-mentioned maximum spacing has to be reduced by factor 0.6 over the length of the larger dimension of the cross-section. The verification of transversal reinforcement due to the acting shear forces in the specimen can be done according to the clause 6.2.3 (3). The aforementioned condition is given in Eq. 6.5 below, where A_{sw} is the applied shear reinforcement area, s is the spacing of the transversal reinforcement, z is the inner lever arm corresponding to the bending moment in the element under consideration, f_{ywd} is the yield strength of the shear reinforcement and θ is the angle between the concrete compression strut and the member axis perpendicular to the shear force – a value of 45° was taken.

$$V_{Rd,s} = \frac{A_{sw}}{s} \cdot z \cdot f_{ywd} \cdot \cot\theta \tag{6.5}$$

The clause 8.2 (2) of EN 1992-1-1 [53] specifies in overall the minimum spacing between the two reinforcement bars and the value should not be smaller than: (i) the bar diameter, (ii) the aggregate size plus 5 mm or (ii) 20 mm. The above-mentioned provision is referring to the appropriate concrete cover conditions. The provisions for the anchorage of reinforcement bars are defined in Section 8.4 and 8.5 of the EN 1992-1-1 [53] for the longitudinal and transversal bars, respectively.

Section 4 of EN 1992-1-1 [53] gives provisions for the concrete cover of reinforcement bars. This aspect had a direct influence on the geometry of reinforcement cages used in the beam/column specimens and contributed to the overall dimensions of cross-sections. Clause 4.4.1.1 (2), given in Eq.

6.6, defines the nominal concrete cover for the reinforcement bars. The definition of the minimum cover and contributing values are defined in Eq. 6.7-6.12. The deviation value for the concrete cover is defined by clause 4.4.1.3 (1) and it has a value of 10mm as given in Eq. 6.13.

$$c_{nom} = c_{min} + \Delta c_{dev} \tag{6.6}$$

$$c_{min} = max\{c_{min,b};\ c_{min,dur} + \Delta c_{dur,\gamma} - \Delta c_{dur,st} - \Delta c_{dur,add};\ 10mm\} \tag{6.7}$$

$$c_{min,b} = \phi_{bar} \text{ (diameter of bar)} \tag{6.8}$$

$$c_{min,dur} = 10mm, \text{ according to clause 4.4.1.2 (5) and exposition class XC3} \tag{6.9}$$

$$\Delta c_{dur,\gamma} = 0mm, \text{ clause 4.4.1.2 (6)} \tag{6.10}$$

$$\Delta c_{dur,st} = 0mm, \text{ clause 4.4.1.2 (7)} \tag{6.11}$$

$$\Delta c_{dur,add} = 0mm, \text{ clause 4.4.1.2 (8)} \tag{6.12}$$

$$\Delta c_{dev} = 10mm \tag{6.13}$$

$$c_{nom} = max\{\phi_{bar}; 10mm\} + 10\text{mm} \tag{6.14}$$

The resulting equation described in Eq. 6.14 outlines the nominal concrete cover of the reinforcement bars in the considered beam/column specimens with respect the applied bar diameter.

6.2.3. Elastic analysis of the cross-sectional resistance in bending

The verification of cross-sections in the elastic analysis is based on the fibre method described in Section 3.4.6 and shown in Fig. 3.100. The provisions described in Sections 6.2.1 and 6.2.2 completed the geometries of cross-sections shown in Fig. 6.3. The longitudinal reinforcement should not affect significantly the behaviour of specimens, therefore, a minimum amount according to the provisions of EN 1994-1-1 [58] and 1992-1-1 [53] was designed. The longitudinal reinforcement was defined with 8 mm diameter and double symmetric distribution in the cross-section. The reinforcement ratio of 0.389% for the smaller specimen and 0.304% for the bigger specimen was obtained as shown in Fig. 6.5.

The transversal reinforcement implemented in the beam/column specimens prevented them to fail in shear. According to the provisions described in Section 6.2.2 above, the applied bars had the diameter of 12 mm and they were distributed with the spacing of 120 mm for both specimens. In the load introduction zones, the spacing of stirrups reduced to 90mm. According to Eq. 6.5, the utilisation ratio of shear reinforcement reached 50-55%, where the maximum shear forces were specified in the performed elastic analysis as described in the further part of this section. The big safety margin mentioned above was considered as a reasonable due to a possible error of the predefined failure load in comparison to test results.

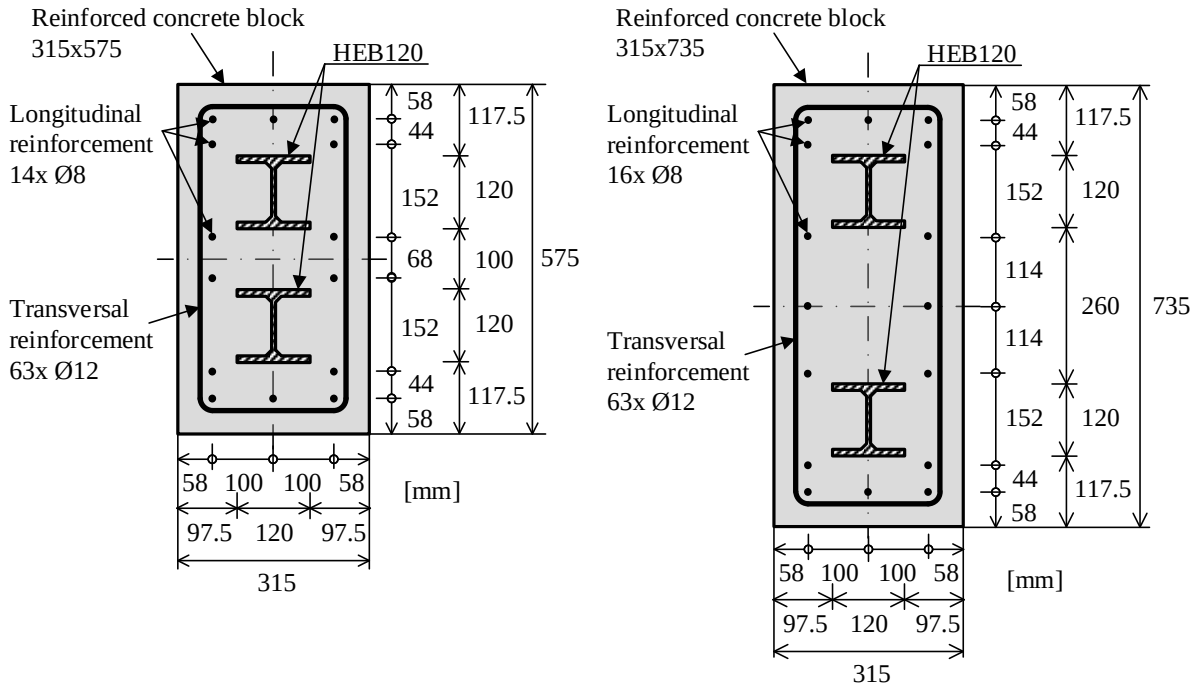


Fig. 6.5. Detailed geometry of the cross-section of beam/column test specimens – a) smaller specimen and b) bigger specimen.

The elastic analysis of strains and stresses in the considered cross-sections requires the usage of specific material laws for each contributing material. For the concrete material law, the simplified model with rectangular stress distribution described in clause 3.1.7 (3) of EN 1992-1-1 [53] was implemented with the assumed concrete grade of C35/45 (initially foreseen concrete grade for tests). Based on the assumed concrete grade, the effective factors λ and η for the rectangular stress distribution in concrete had values of 0.8 and 1, respectively. The concrete properties were taken according to EN 1992-1-1 Table 3.1 [53]. For the reinforcement steel material, the simplified bi-linear material law with strain hardening described in clause 3.2.7 (2) of EN 1992-1-1 [53] was used, where the modulus of elasticity of 200 GPa, according to clause 3.2.7 (4) and the properties according to Table C.1 of EN 1992-1-1 [53] were taken. The considered reinforcement grade was B500B R. The structural steel material law was taken according to Figure C.2 of EN 1993-1-5 [56] including the elasto-plastic behaviour with linear strain hardening. The properties of structural steel were based on Table 3.1 of EN 1993-1-1 [55], where the modulus of elasticity of 210 GPa, according to clause 3.2.6 (1) of EN 1993-1-1 [55], and the ultimate strain of $15 \cdot \varepsilon_y$, where ε_y is the yielding strain according to clause 3.2.2 (1) of EN 1993-1-1 [55] were considered. For all the material laws, the characteristic values of properties were used, where for the concrete, the characteristic values for cubic specimens were implemented.

For the verification of considered composite cross-sections with two embedded steel profiles, a pure bending state was considered according to the defined static system of beam/column tests shown in Fig. 6.2. In the result, the bending failure of specimens was considered. In the defined failure mechanism, three possible cases can be distinguished: (1) the failure due to concrete compression, (2) the failure due

to rupture of the reinforcement in tension and (3) the failure due to rupture of the steel profile in tension. It was identified, that the last two cases with tensile failure of steel bring an unrealistic strain distribution within cross-section as shown in Fig. 6.6 on the example of smaller specimen. Therefore, the concrete compression failure was considered as the possible failure mode of the analysed specimens and the detailed elastic analysis was performed with fixed ultimate strains for the concrete in the most compressed fibre. In the performed analyses, full interaction between the steel and concrete, as well as, reinforcement and concrete was assumed. In the result, the linear strain distribution over the total cross-section was obtained.

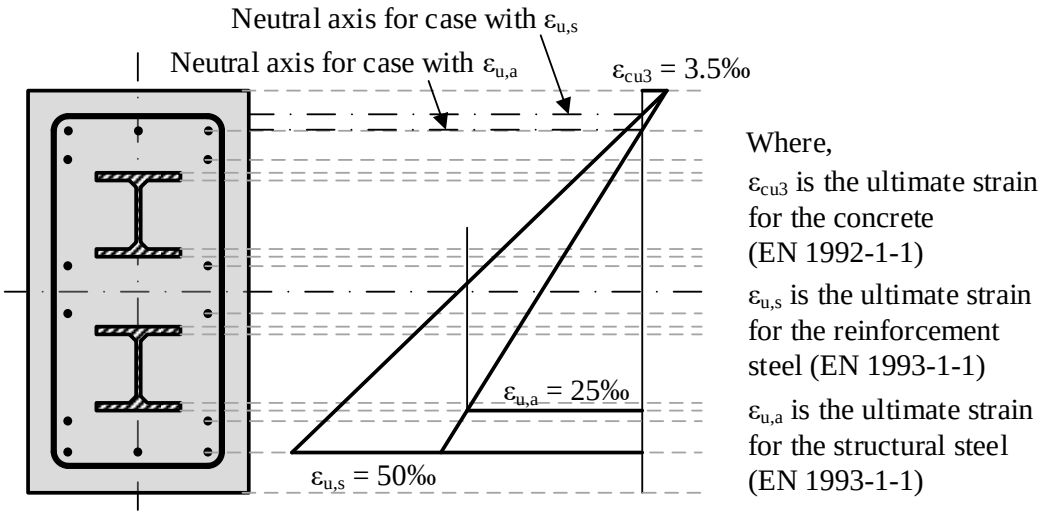


Fig. 6.6. Elastic strain analysis of the cross-section of beam/column specimen for the cases when the rupture of steel elements occurs.

Analysing the case for the failure of cross-section in bending due to the compression stresses in concrete, the neutral axis located in the web of upper steel profile, 154 mm from the top edge of the cross-section in the smaller specimen and 159 mm from the top edge in the bigger specimen. The exact position of the neutral axis was evaluated in the iterative process until the internal equilibrium of forces was reached. The resulted strain distribution and the following stresses distributions for each material are shown in Fig. 6.7 and Fig. 6.8 for the smaller and bigger specimens, respectively. The resulting stresses were obtained by implementing the assumed above material laws, where for the concrete, the tension resistance had been neglected. From the distribution of stresses, the internal resulting total compression force (D) and total tension force (Z) was calculated by including the respective area on which the previously evaluated stresses are acting. The internal lever arm “e” on which the forces D and Z are acting was found due to the position of the centre of gravity for all compression forces and all tension forces. Using the fundamental equation for the maximum bending moment of simple supported beam with the point load placed in the mid-span, the resulting imposed load P was calculated from the sectional moment-force relation. The calculations summary is presented in Table 6.1, where all the contributing compression forces and all the contributing tensile forces were listed.

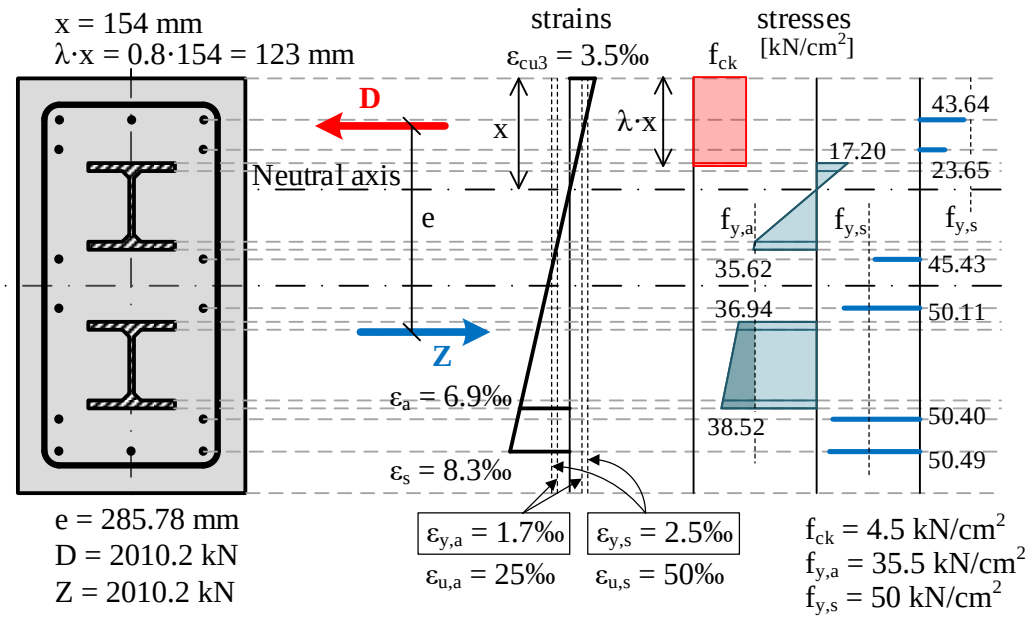


Fig. 6.7. Elastic analysis of strains and stresses in the cross-section of smaller specimen.

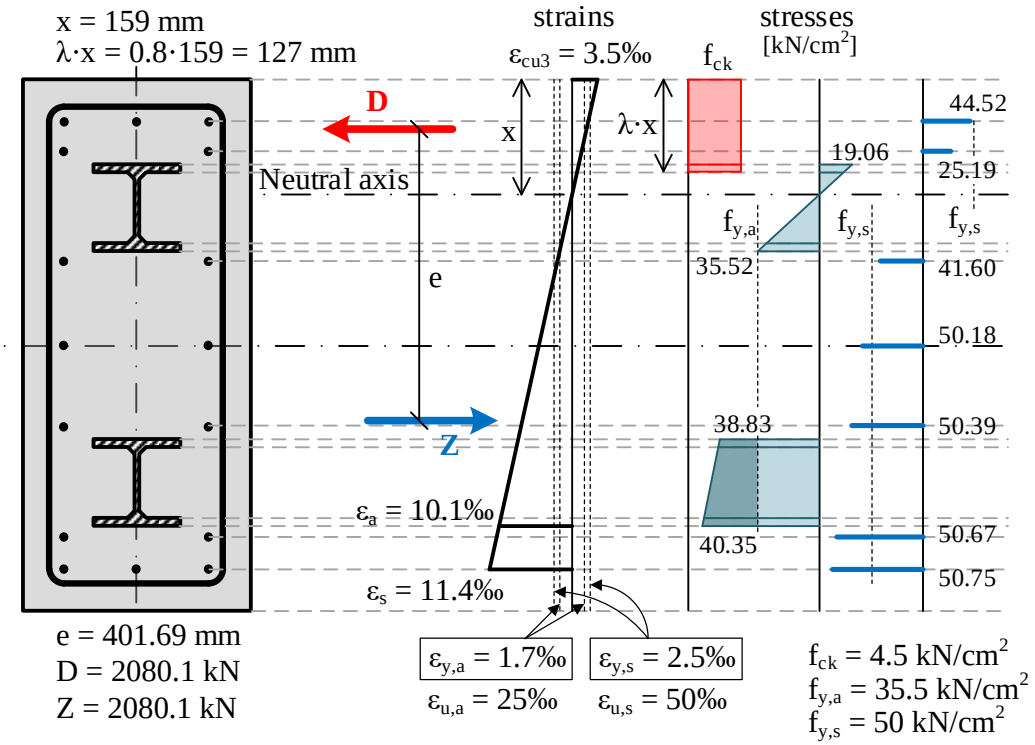


Fig. 6.8. Elastic analysis of strains and stresses in the cross-section of bigger specimen.

Table 6.1.
Evaluation of the imposed load in test specimens (consider with Fig. 6.7 and Fig. 6.8).

	ID	Compression				ID	Tension			
		Resulting Force	Arm to n.e.	$D = \sum F_i$	e1		Resulting Force	Arm to n.e.	$Z = \sum F_i$	e2
		[kN]	[cm]	[kN]	[cm]		[kN]	[cm]	[kN]	[cm]
Smaller specimen	Fc,1	1672.65	9.50	2010.2	8.66	Fa,3	82.55	4.86	2010.2	19.92
	Fc,2	45.90	3.34			Fa,4	78.32	7.39		
	Fa,1	192.34	3.02			Fa,5	390.18	7.94		
	Fa,2	9.72	1.67			Fa,6	488.52	18.95		
	Fs,1	65.81	9.60			Fa,7	240.32	24.42		
	Fs,2	23.77	5.20			Fa,8	507.46	29.85		
						Fs,3	45.67	10.00		
						Fs,4	50.38	16.80		
						Fs,5	50.67	32.00		
						Fs,6	76.13	36.40		
	e	$e = e_1 + e_2 = 8.66 + 19.92 = 28.58\ [cm]$								
	P	$M_{Ed} = \frac{P \cdot L}{4} \rightarrow P = \frac{4 \cdot M_{Ed}}{L} = \frac{4 \cdot Z \cdot e}{L} = \frac{4 \cdot 2010.2 \cdot 28.58}{600} = 383\ [kN]$								
Bigger specimen	Fc,1	1672.65	10.03	2080.1	9.00	Fa,3	68.67	4.51	2080.1	31.17
	Fc,2	83.01	3.66			Fa,4	388.77	7.24		
	Fa,1	218.15	3.55			Fa,5	54.90	7.80		
	Fa,2	13.79	2.02			Fa,6	513.42	34.42		
	Fs,1	67.13	10.13			Fa,7	252.18	39.84		
	Fs,2	25.32	5.73			Fa,8	531.74	45.32		
						Fs,3	41.82	9.47		
						Fs,4	50.44	20.87		
						Fs,5	50.65	32.27		
						Fs,6	50.94	47.47		
						Fs,7	76.53	51.87		
	e	$e = e_1 + e_2 = 9.00 + 31.17 = 40.17\ [cm]$								
	P	$M_{Ed} = \frac{P \cdot L}{4} \rightarrow P = \frac{4 \cdot M_{Ed}}{L} = \frac{4 \cdot Z \cdot e}{L} = \frac{4 \cdot 2080.1 \cdot 40.17}{600} = 557\ [kN]$								

Where,
n.e. – Neutral axis,
Fc,i; Fa,i; Fs,i – Resulting forces in the considered area (c – concrete, a – structural steel, s – reinforcement steel), where the number "i" refers to the considered portion with numbering starting from the top, for example Fs,1 refers to the force in the reinforcement bars at the first row from the top,
P – Imposed concentrated load in the mid-span of specimen length (see Fig. 6.2),
e – Internal lever arm of bending mechanism, between the resultant compression and tension forces,
e1; e2 – Internal arms of the resulting compression and tension forces, respectively,
L – Length of the specimen between the supports.

According to the performed analysis, the failure of beam/column specimens due to the compression in the top fibres of specimens was evaluated. From the performed analysis, it was found that the failure load in both cases is less than 1MN, which was the nominal capacity of the testing machine. A certain margin of the machine loading capacity was preserved due to the normally higher values of material properties obtained from the tests. Based on the above-described analysis, the beam/column test specimens were designed and fabricated accordingly.

6.3. Beam/column three-point bending tests

Three-point bending tests were performed to experimentally investigate the structural behaviour of column members with two separately embedded steel profiles, examine the internal forces distribution and analyse the effective stiffness. In order to identify the transfer of shear forces in the considered specimens, the axial compression force was not considered and the specimens were subjected only to bending and shear. In the result, due to the type of tests and type of specimens, the beam/column tests definition was introduced. In addition, in both beam/column specimens, the developed novel flat shear connectors of V-shaped variant were implemented and their behaviour in the beam-type tests was analysed. In the taken test campaign, the two aspects of innovation were considered: (1) replacing the traditional shear connectors by the more efficient variant and (2) analysis of the specimens without interconnected embedded multiple steel profiles.

In the experimental campaign, two beam/column tests specimens with the total length of 6700 mm were fabricated and tested. The geometry, used materials, surface treatment conditions and applied shear connection were nominally the same in both specimens. Two steel profiles HEB 120 L=6700 mm were embedded in the concrete block. The orientation of the embedded steel profiles in the composite cross-sections incorporate bending of them according to the strong axis.

The specimens were varied between each other only with a clear distance between the embedded steel profiles and the specimens were identified with the name VT-1 for the smaller specimen and VT-2 for the bigger specimen. Due to the varied distance between the embedded steel profiles, the height of specimens and the reinforcement arrangement were adjusted accordingly. The overview on the performed tests is shown in Table 6.2.

6.3.1. Specimen properties

The tested specimens, in both cases, had the double symmetric rectangular composite cross-section with dimensions of 315x575 mm for specimen VT-1 and 315x735 mm for specimen VT-2, as it is shown in Fig. 6.5. In each specimen, the embedded steel profiles were HEB120 L=6700 mm of S355JR+M grade. The steel profiles were embedded in the C30/37 concrete block. The concrete grade used in tests was lower in comparison to the concrete grade defined in the pre-design process due to the fact that the experimentally obtained material properties are usually higher than the nominal values given in the design standards. The total length of specimens was 6700 mm, where the used concrete blocks had length of 6500 mm. On each side of the specimens, the steel profiles were protruding from the concrete block by 100 mm. The non-restrained ends of steel profiles allowed for the development of relative slip between the steel profiles and concrete. In the result, the stiffness of shear connection and its influence on the global behaviour could be investigated. The schematic overview of beam/column specimens is shown in Fig. 6.9.

Table 6.2.
Overview of the beam/column test specimens

Name	Distance between steel profiles	Mechanical shear connection	Concrete part	Steel part	Steel surface treatment	No of tests	Load-defl. curve
VT-1	100 mm	Flat shear connector, V-shaped (Fig. 5.20b) 12 connectors per steel profile, symmetric distribution over the length, antisymmetric between the flanges	C30/37 315x575 L=6500mm	S355JR+M 2x HEB120 L=6700mm	Cleaning: No Coating: Anti-adhesive release agent	1	Fig. 6.28
VT-2	260 mm	Flat shear connector, V-shaped (Fig. 5.20b) 12 connectors per steel profile, symmetric distribution over the length, antisymmetric between the flanges	C30/37 315x735 L=6500mm	S355JR+M 2x HEB120 L=6700mm	Cleaning: No Coating: Anti-adhesive release agent	1	Fig. 6.31

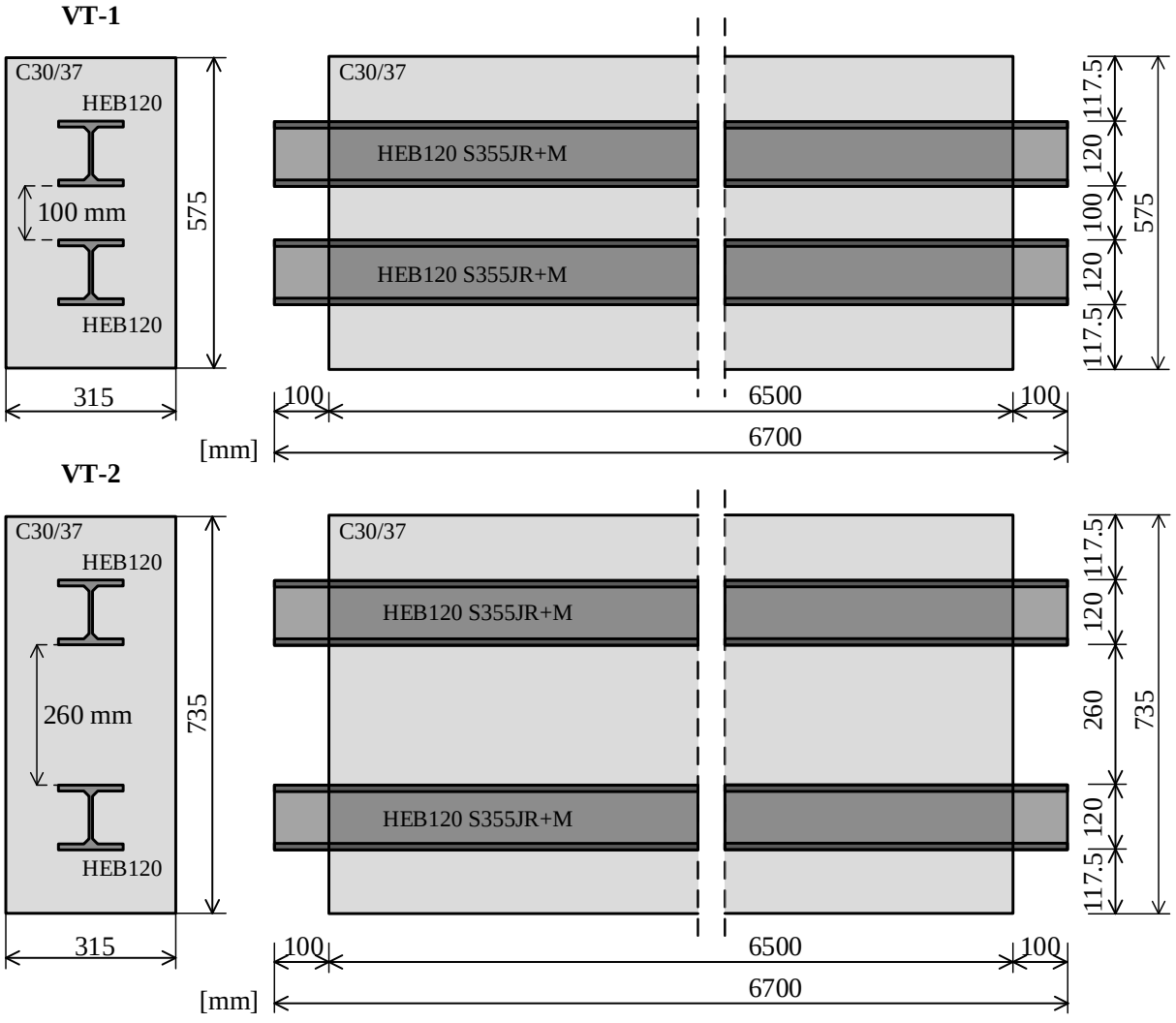


Fig. 6.9. Schematic overview of the beam/column test specimens.

The reinforcement cage around the embedded steel profiles was used to prevent the shear failure of specimens and to assure the shear transfer. The stirrups around steel profiles anchored the forces transferred by the shear connectors. The detailing of the longitudinal and transversal reinforcement was made in the pre-design process and the schematic view on the arrangement of reinforcement in the cross-section is shown in Fig. 6.5. In both specimens, the reinforcement cages were similar. The change of clear distance between the embedded steel profiles affects the reinforcement arrangement. In the specimen VT-2, in comparison to the specimen VT-1, two longitudinal bars were added in the middle of cross-section and the spacing of transversal reinforcement was adapted due to the increased length of load transition zones next to the supports and at mid-span. The technical drawings of reinforcement arrangements in the cross-sections are shown in Fig. 6.10. The longitudinal arrangement of shear reinforcement is shown in Fig. 6.11 for the specimen VT-1 and in Fig. 6.12 for the specimen VT-2.

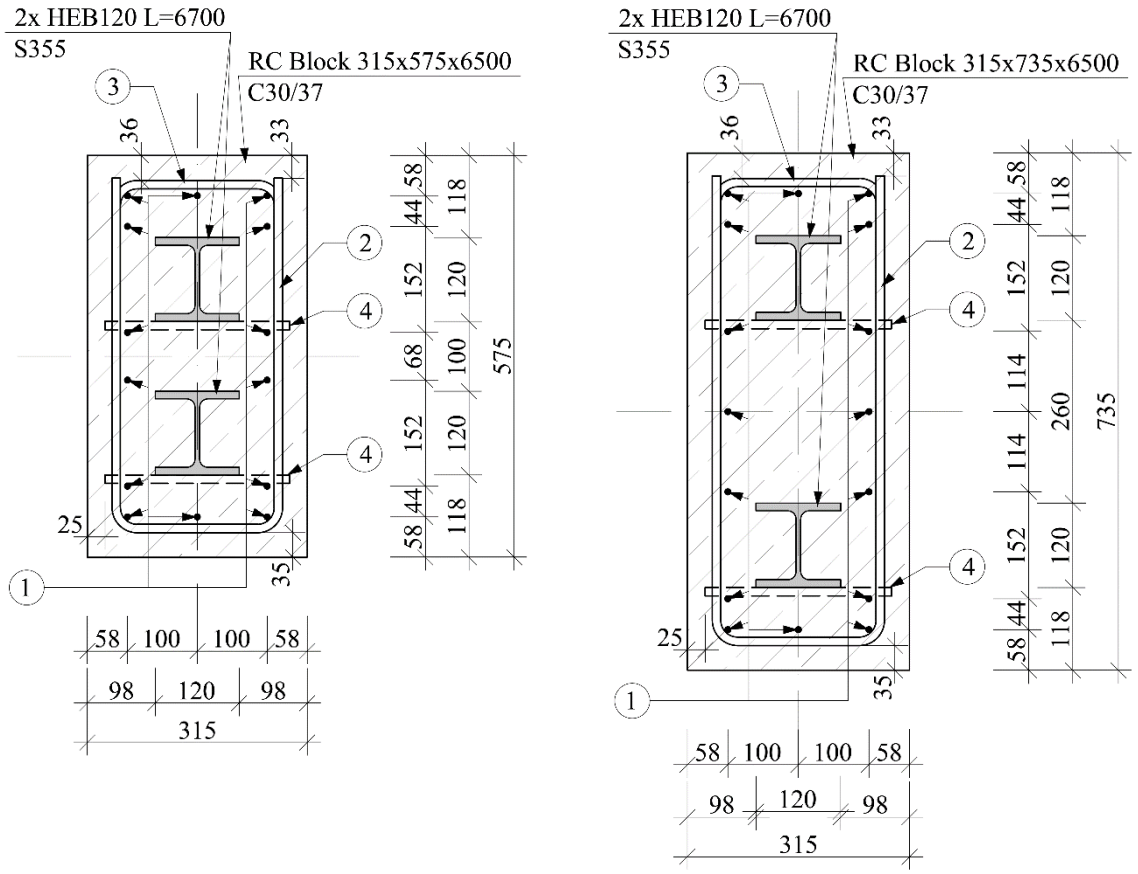


Fig. 6.10. Arrangement of reinforcement in the cross-section of beam/column specimens – a) specimen VT-1 and b) specimen VT-2

The stirrups were composed from Pos. (2) and Pos. (3), as it is shown in Fig. 6.10. Both of the aforementioned bars had the U-shape and, after assembly, they created a closed section. This type of stirrups were used in order to assure a less-complex fabrication process of beam/column specimens. Small straight reinforcement bars, denoted as Pos. (4) on Fig. 6.10, had no structural meaning and they were used only for the purpose to position steel profiles. The anchorage lengths of the reinforcement bars were designed according to EN1992-1-1 [53].

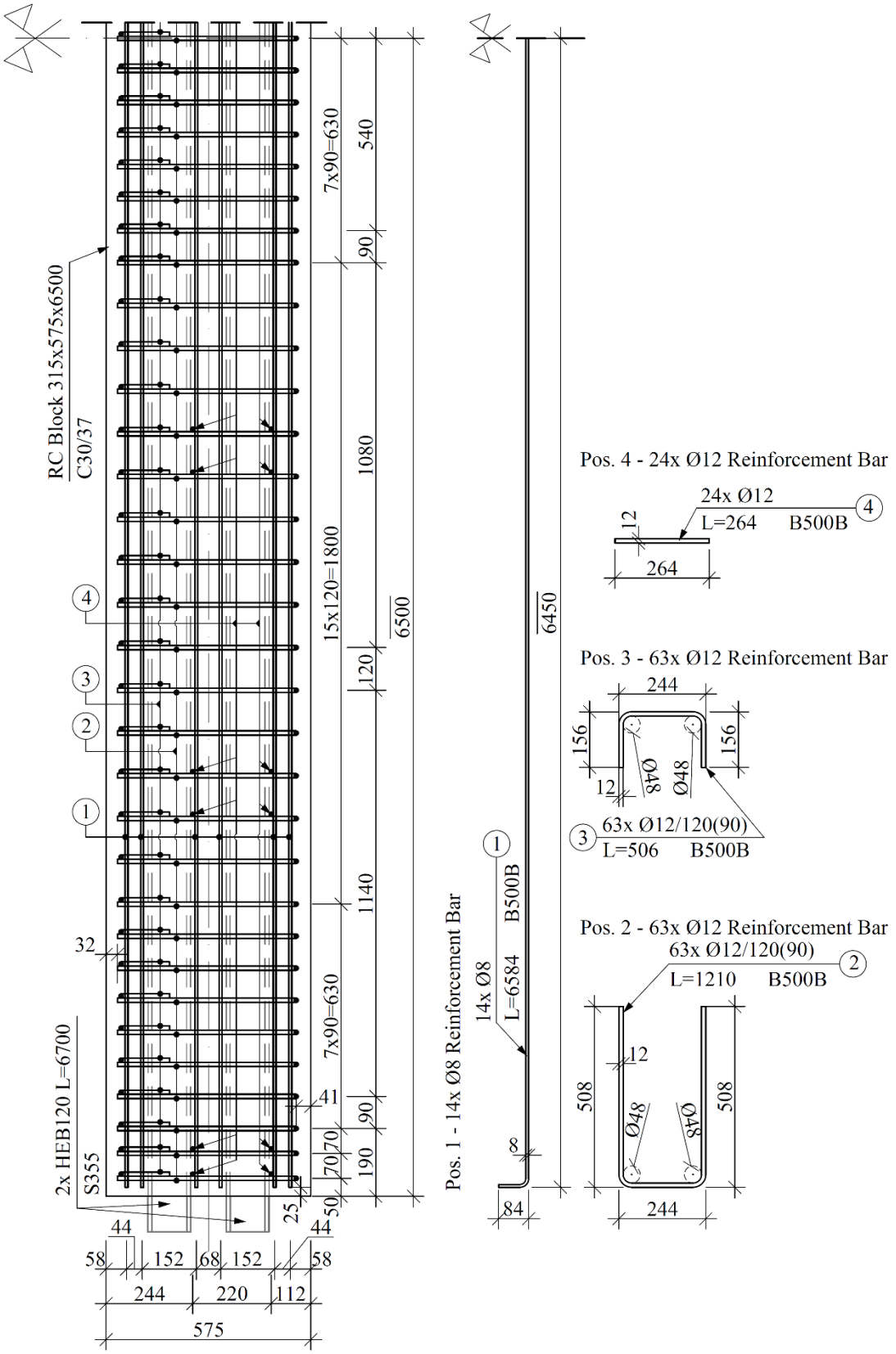


Fig. 6.11. Technical drawing of the reinforcement arrangement in beam/column specimen VT-1.

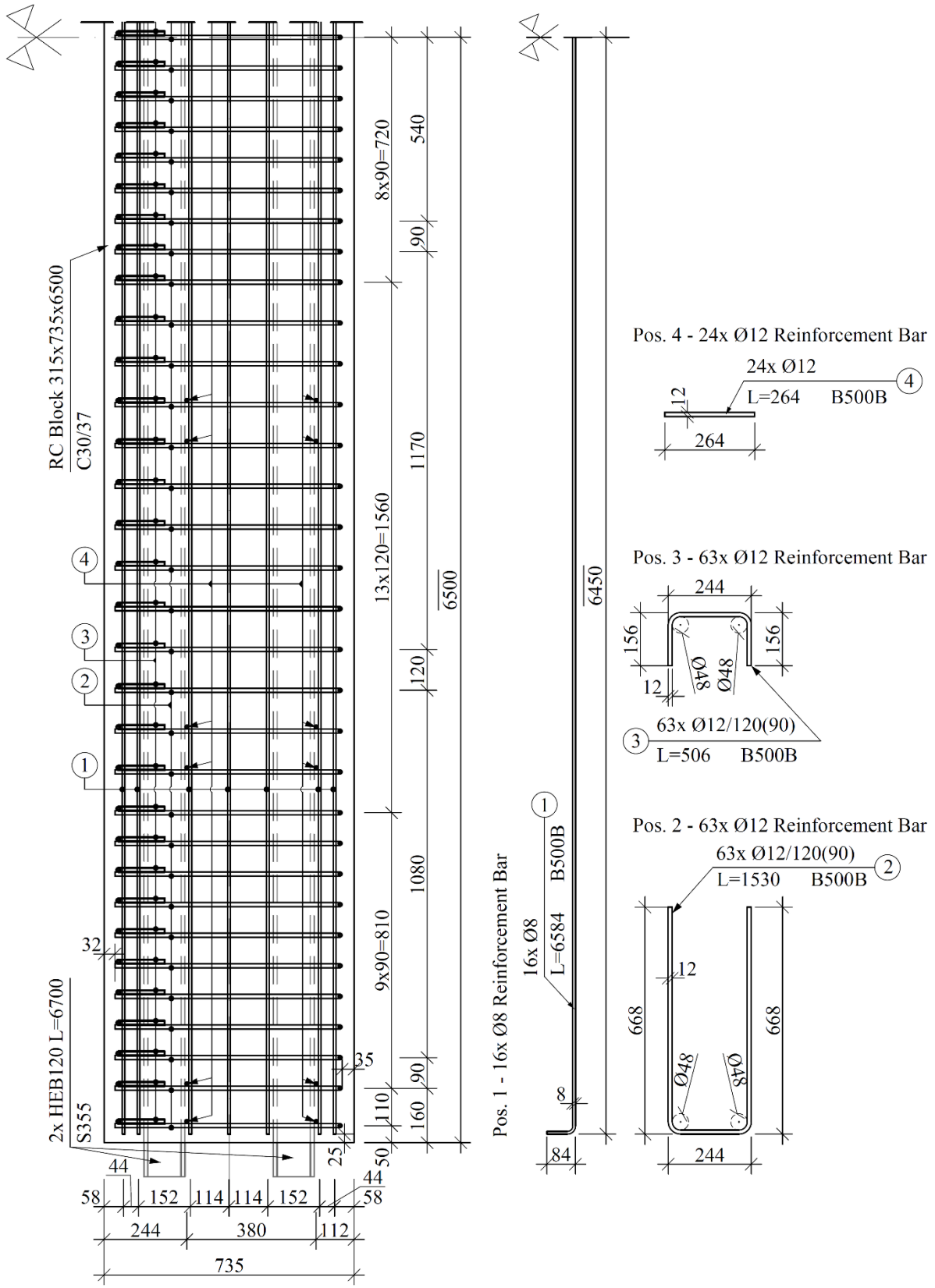


Fig. 6.12. Technical drawing of the reinforcement arrangement in beam/column specimen VT-2.

Both specimens were produced in the laboratory of the University of Luxembourg. The fabrication process of specimens was divided into five main work packages: (i) fabrication of the reinforcement cages, (ii) welding of the shear connectors, (iii) fabrication of the formwork, (iv) final assembly of the

specimens, and (v) concreting, where the sequence of work followed the given order. The fabricated specimens were reflecting the technical drawings well and no significant deviations have been identified. Details on the fabrication process of beam/column specimens are given in Annex E.

The used HEB120 steel profiles had not been subjected to any cleaning process beforehand and they were utilised to the specimens in the state 'as delivered'. During the assembly process, surfaces of the steel profiles were coated with the bond-reducing product in order to maintain nominally identical shear connection conditions as in the push-out test campaign of flat shear connectors described in Section 5.4. The technical name of the applied bond-reducing product is WETCAST – FormFluid HP of the company HEBAU GmbH and it is a high-performance anti-adhesive release agent with oil consistency. The impact of the used product on steel-concrete bond was investigated in Section 5.3-5.4. The steel profiles were coated approximately 24 hours before the concreting.

Both specimens were concreted from the same concrete delivery and at the same day. After the concreting process, the specimens were water-cured according to EN 13670 [51] and they stayed inside the laboratory hall during the hardening process. The plastic foil covered the specimens for the first 4 days in order to limit the excessive drying of the external surfaces of concrete and to assure a high humidity level for the cement hydration process. The specimen VT-2 was executed after 35 days of concrete hardening, where the specimen VT-1 was tested at the concrete age of 51 days.

6.3.2. Applied shear connectors

The novel type of flat mechanical shear connectors developed and characterised in Chapter 5 were applied to the beam/column specimens. According to the investigated performance of various flat connectors in push-out test campaign, the V-shaped variant indicated the best compromise between the load-bearing capacity, ductility and economy and it was selected for the application to the beam/column specimens. The connectors were made from the regular reinforcement bars grade B500B and diameter Ø8 mm. All the connectors were welded to the flanges of steel profiles on external surfaces using fillet welds with full penetration on both sides of the connector as shown in Fig. 6.13c. The semi-automatic gas metal arc welding technique – MAG was used. The geometry and arrangement of applied shear connectors is shown in Fig. 6.13a-b. Twelve connectors per one steel profiles had been applied in each specimen. The connectors were placed symmetrically over the length of steel profiles and antisymmetrically between the two flanges of the same steel profile. For both test specimens, VT-1 and VT-2, the arrangement and the used geometry of the shear connectors were identical, see Fig. 6.13b.

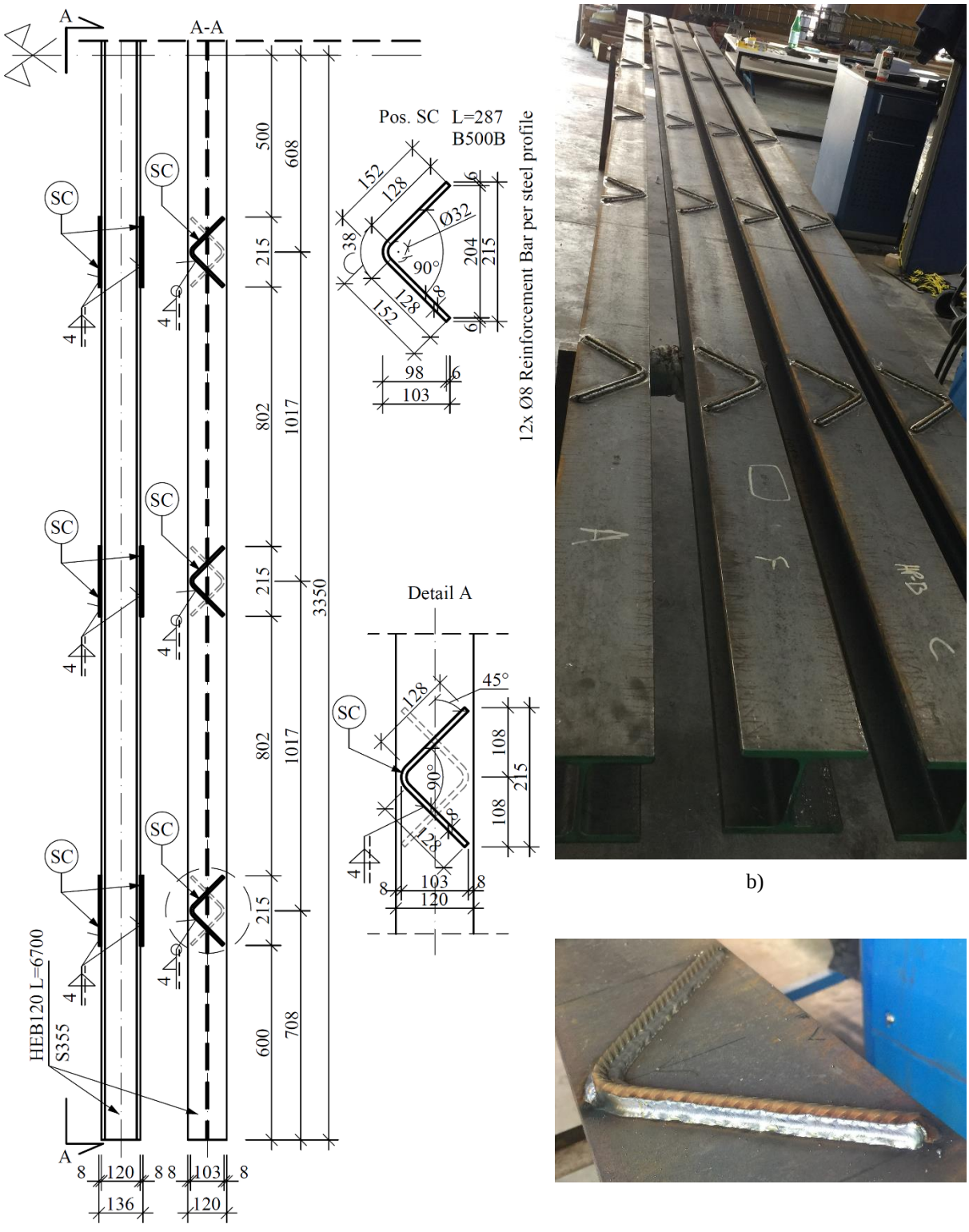


Fig. 6.13. Applied shear connectors in beam/column test specimens – a) geometry and arrangement, b) fabrication detail and c) weld detail.

The application of developed flat shear connectors from the push-out test campaign allowed for the verification of the performance of applied connectors in the beam-type tests, where the normal separation at the steel-concrete interface could develop due to the acting bending moment and deformation of the specimens. To prevent the normal separation, the activation of surrounding

reinforcement in the concrete, which is an integral part of the force transferring system for the considered flat shear connectors, was required.

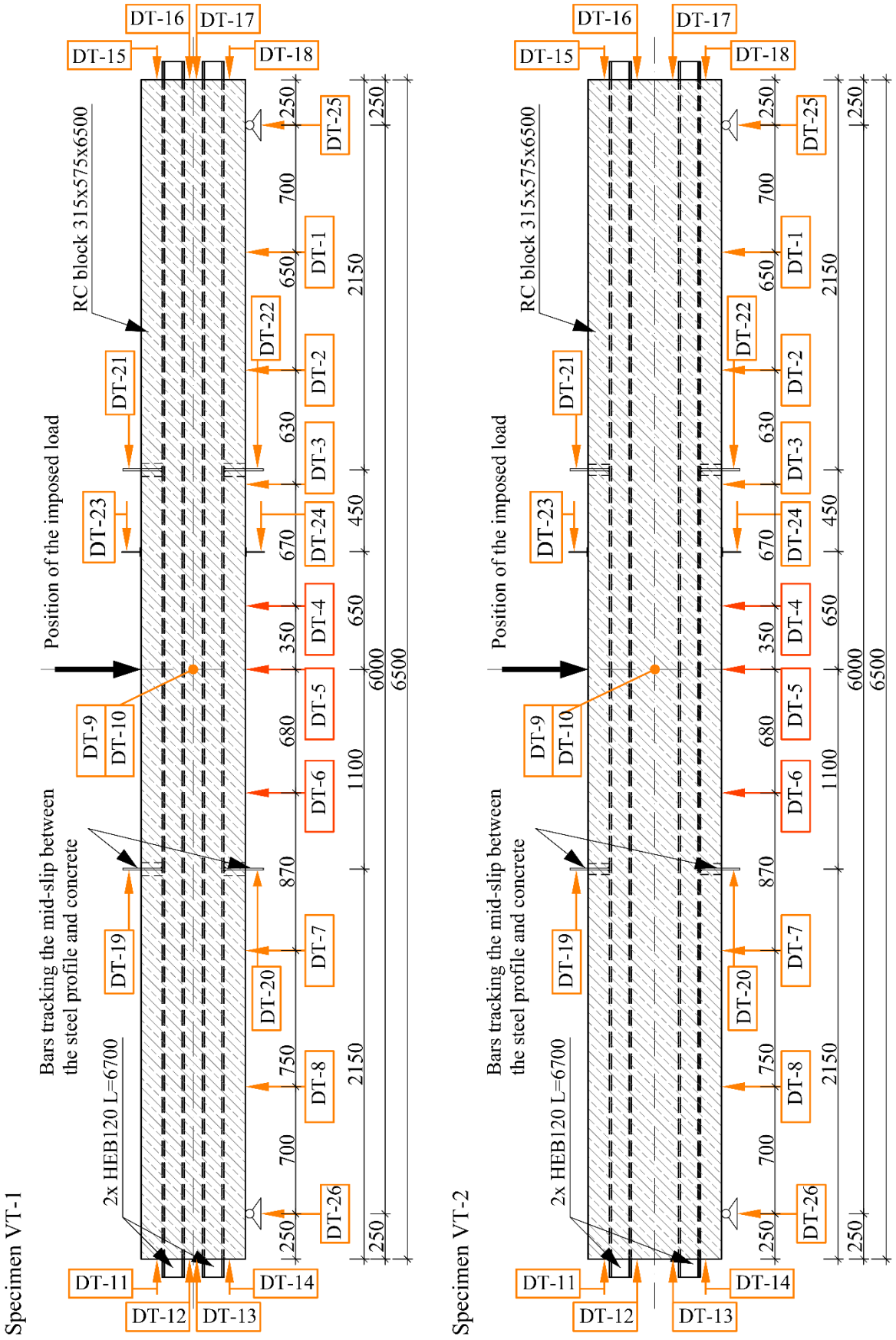
Surfaces of the applied shear connectors were not covered with the bond reducing agent. During the application process of release agent to the steel profiles, the surfaces of flat shear connectors were secured with a tape and after its removal, the connectors were cleaned with a degreaser.

Due to the extensive heat transfer during the welding process and small geometry of the flat shear connectors, the material properties of applied shear connectors can vary from the raw material, from which they have been fabricated – the reinforcement bar steel grade B500B.

6.3.3. Specimen instrumentation

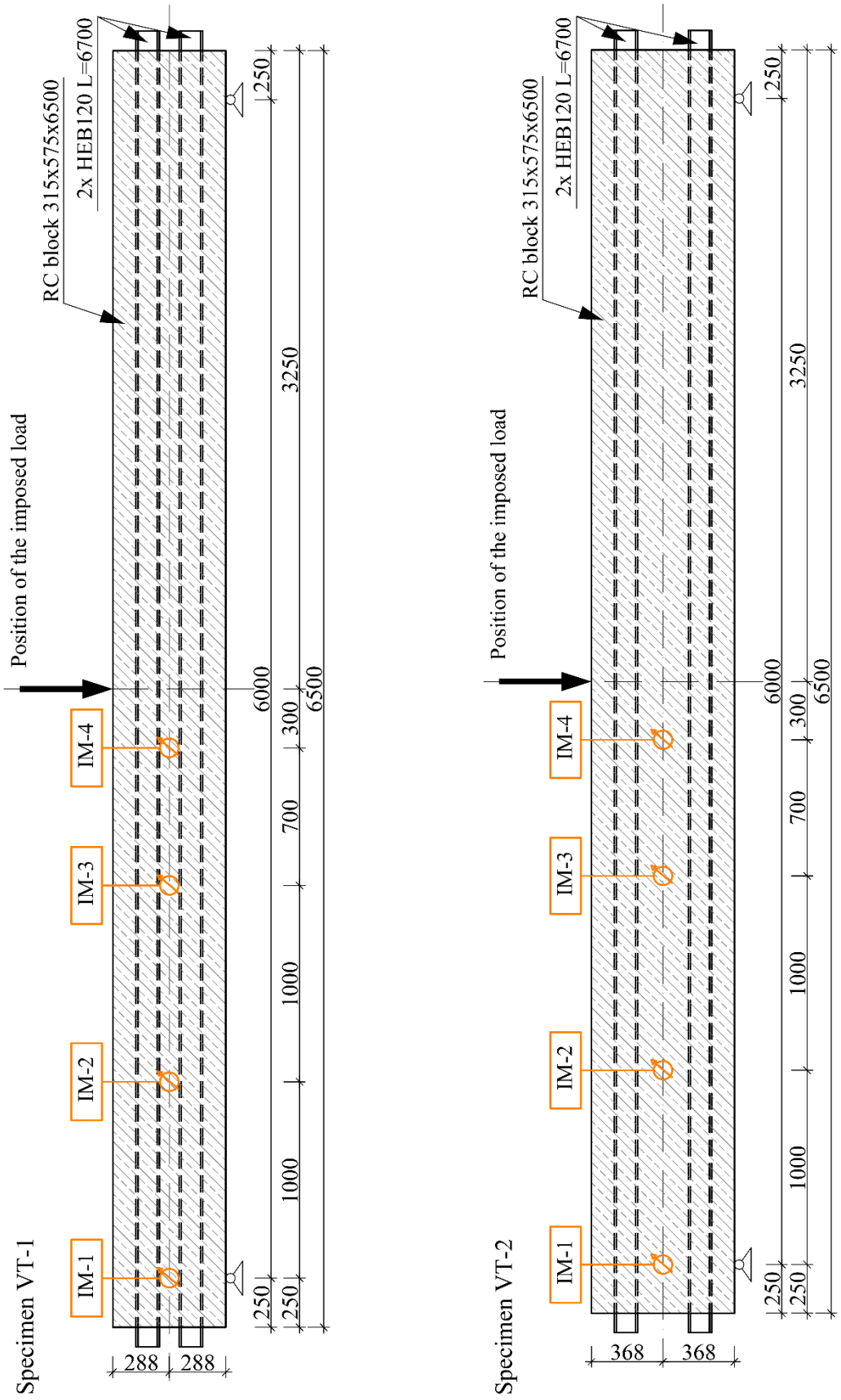
The arrangement of measurement equipment in both beam/column specimens was nominally identical. Per one specimen, sets of 26 Displacement Transducers (DT), 48 Strain Gauges (DMS) and 4 Inclinometers (IM) were used. The DT were pointed to the external surfaces of specimens. The DMS were glued to the flanges and webs of steel profiles and to the bars of reinforcement cages. The IM were fixed to the one sidewall of specimen. The arrangements of aforementioned sensors are shown in Fig. 6.14-6.20. It could be observed, that the DMS glued to the steel profiles and reinforcement bars created characteristic measurement sections. The IM were placed accordingly to the position of the measurement sections. On the walls of specimens, a grid was drawn to visually trace the deformation of specimens with a set of two cameras. The grid was reflecting the position of steel profiles and characteristic points like axes, mid-height, mid-span or supports of specimens. The grid span over the length of specimen had 150 mm, besides the first lines from the support and mid-span, where 100 mm and 50 mm spans were used.

In the set of DT, two types of sensors were used: (i) the mechanical linear variable displacement transducers with the range up to 100 mm and (ii) 3 laser displacement transducers with the range up to 500 mm to measure the deflection of the specimen in the mid-zone, points DT-4÷6 in Fig. 6.14. The reference point for DT measuring the deflection of specimens was the ground. Therefore, two DT measured the deflection of supports, points DT-25 and DT-26 in Fig. 6.14, to eliminate an offset imposed by the deformation of testing frame. The summary list of used DT and IM with the measuring values, ranges and reference points is given in Table 6.3. One type of DMS was used for all the measurement points – linear variable strain gauges. The orientation of DMS followed in each case the longitudinal axis of the element to which they were glued, where the DMS glued to the webs of steel profiles were oriented under 45° to the longitudinal axis of steel profiles. The summary list of the glued DMS with corresponding position is given in Table 6.4.



a) b)

Fig. 6.14. Arrangement of the displacement transducers (DT) in beam/column tests – a) specimen VT-1 and b) specimen VT-2.



a) b)

Fig. 6.15. Arrangement of the inclinometers (IM) in beam/column specimens – a) specimen VT-1 and b) specimen VT-2.

Table 6.3.
List of the used displacement transducers and inclinometers in beam/column tests.

Sensor Name	Range	Measuring value	Reference point
Displacement Transducers (DT)			
DT-1	100 mm	Deflection, R	Ground
DT-2	100 mm	Deflection, R	Ground
DT-3	100 mm	Deflection, R	Ground
DT-4 (laser)	500 mm	Deflection, middle zone	Ground
DT-5 (laser)	500 mm	Deflection, mid-span	Ground
DT-6 (laser)	500 mm	Deflection, middle zone	Ground
DT-7	100 mm	Deflection, L	Ground
DT-8	100 mm	Deflection, L	Ground
DT-9	100 mm	Wall lateral deformation, F	Testing frame
DT-10	100 mm	Wall lateral deformation, B	Testing frame
DT-11	50 mm	End slip of the steel profile, L USP TOP	Web of the steel profile, USP
DT-12	50 mm	End slip of the steel profile, L USP BOT	Web of the steel profile, USP
DT-13	50 mm	End slip of the steel profile, L LSP TOP	Web of the steel profile, LSP
DT-14	50 mm	End slip of the steel profile, L LSP BOT	Web of the steel profile, LSP
DT-15	50 mm	End slip of the steel profile, R USP TOP	Web of the steel profile, USP
DT-16	50 mm	End slip of the steel profile, R USP BOT	Web of the steel profile, USP
DT-17	50 mm	End slip of the steel profile, R LSP TOP	Web of the steel profile, LSP
DT-18	50 mm	End slip of the steel profile, R LSP BOT	Web of the steel profile, LSP
DT-19	20 mm	Mid slip of the steel profile, L USP TOP	Top surface of the concrete, L
DT-20	20 mm	Mid slip of the steel profile, L LSP BOT	Bottom surface of the concrete, L
DT-21	20 mm	Mid slip of the steel profile, R USP TOP	Top surface of the concrete, R
DT-22	20 mm	Mid slip of the steel profile, R LSP BOT	Bottom surface of the concrete, R
DT-23	50 mm	Compression strain of the concrete	Top surface of the concrete
DT-24	50 mm	Tensile strain of the concrete	Bottom surface of the concrete
DT-25	100 mm	Deflection of the support, R	Ground
DT-26	100 mm	Deflection of the support, L	Ground
Inclinometers (IM)			
IM-1	360°	Rotation of the *measurement section 1	Wall/gravity
IM-2	360°	Rotation of the *measurement section 2	Wall/gravity
IM-3	360°	Rotation of the *measurement section 3	Wall/gravity
IM-4	360°	Rotation of the *measurement section 4	Wall/gravity

Where,
L – Left side (bottom in Fig. 6.14),
R – Right side (top in Fig. 6.14),
F – Front side (side visible in Fig. 6.14),
B – Back side (back side of the view in Fig. 6.14),
USP – Upper embedded steel profile,
LSP – Lower embedded steel profile,
TOP – Top side of the embedded steel profile (upper flange),
BOT – Bottom side of the embedded steel profile (lower flange),
*Reference numbers of the measurement sections are defined from the side towards the middle of the specimen.
*Measurement sections are defined according to the arrangement of the DMS in Fig. 6.16 and Fig. 6.18.

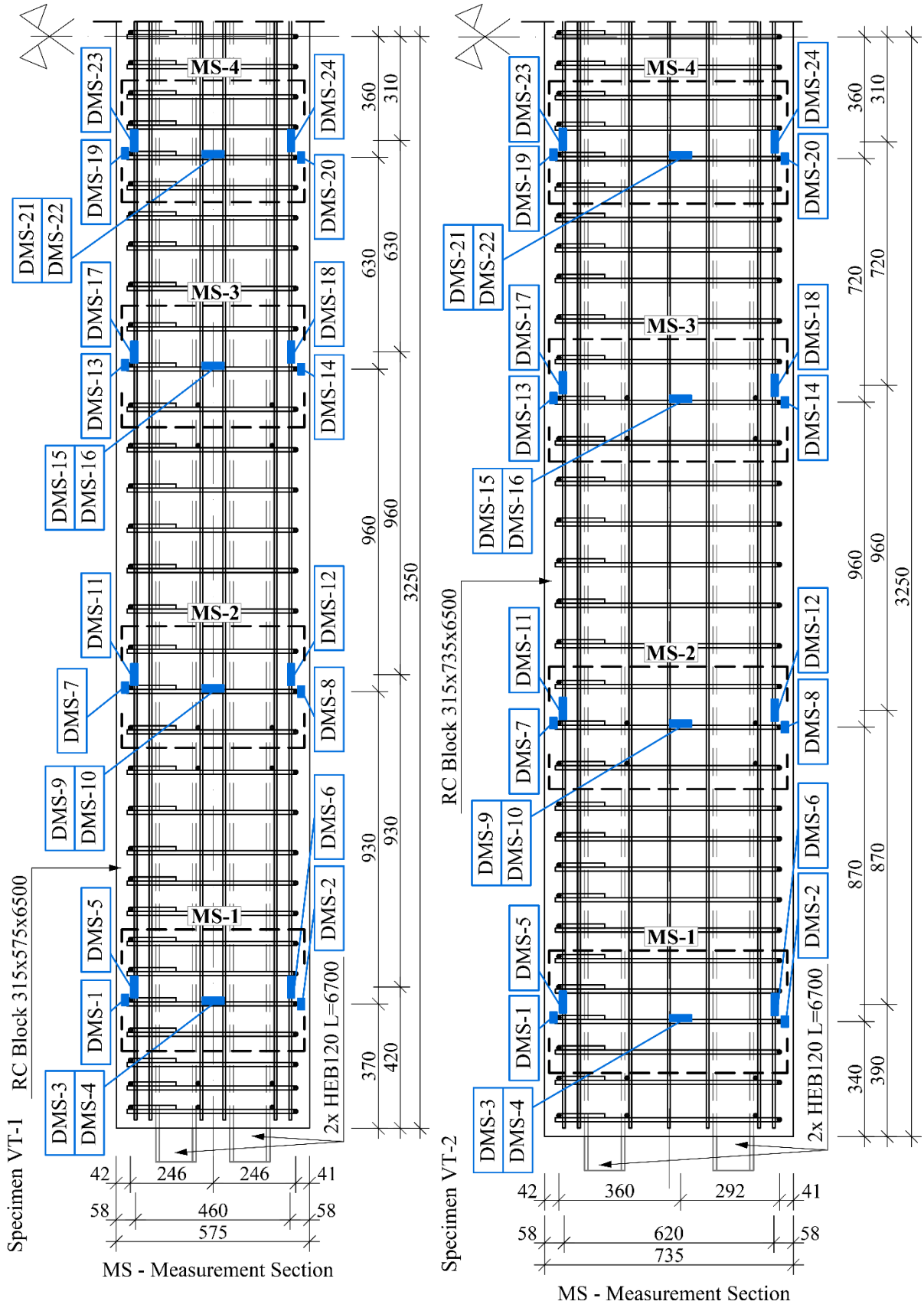
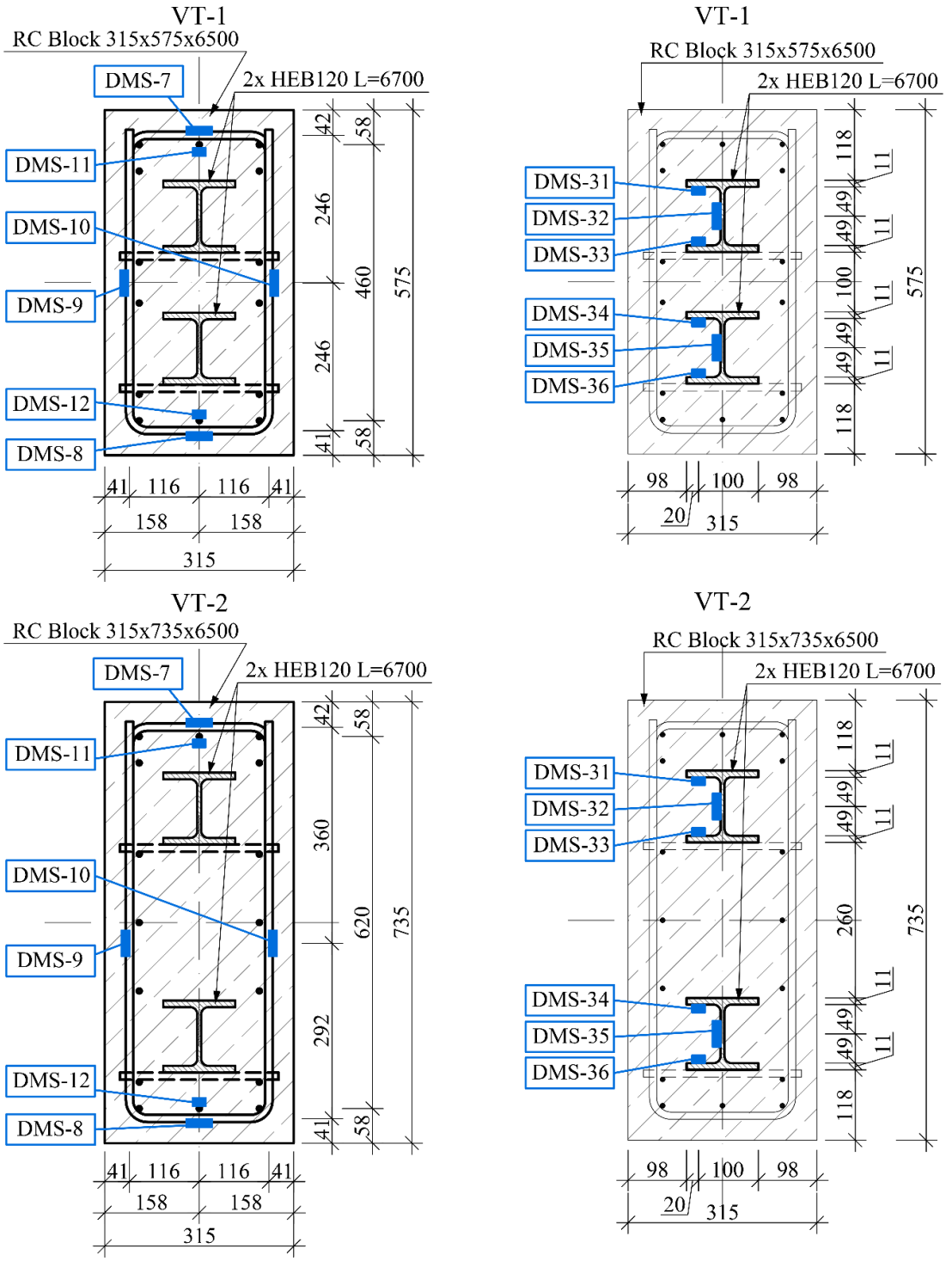


Fig. 6.16. Strain gauges (DMS) on the reinforcement bars of beam/column specimens – a) specimen VT-1 and b) specimen VT-2.



Indicated numbers of DMS are referring to the sencond measurement section (compare with Fig. 6.16)

a)

Indicated numbers of DMS are referring to the sencond measurement section (compare with Fig. 6.18)

b)

Fig. 6.17. Strain gauges (DMS) in the cross-section of beam/column specimens – a) on the reinforcement bars and b) on the steel profiles.

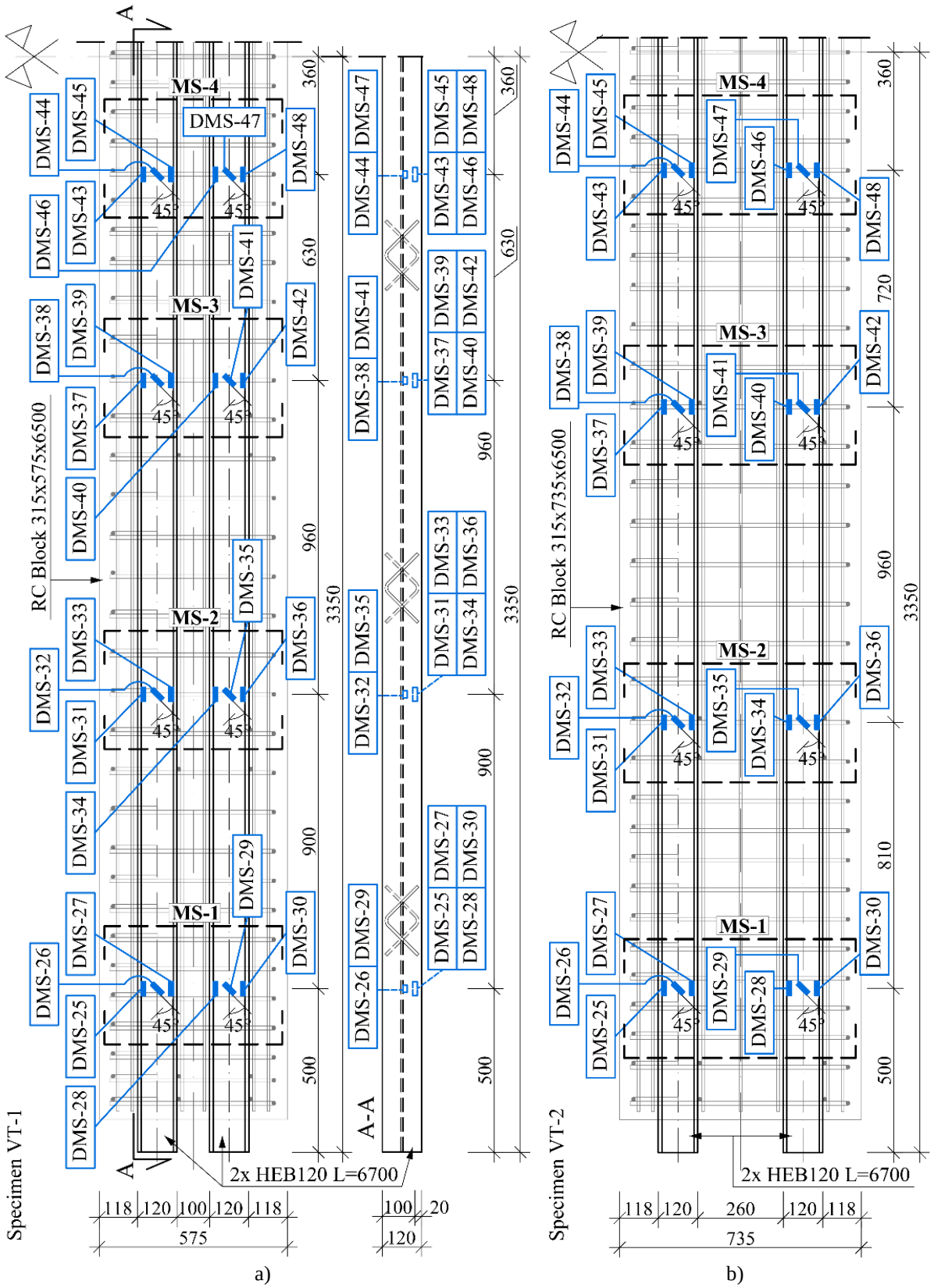


Fig. 6.18. Strain gauges (DMS) on the steel profiles of beam/column specimens – a) specimen VT-1 and b) specimen VT-2.

Table 6.4.
List of the used strain gauges in beam/column tests.

Strain Gauge (DMS)	Measuring value	Position	Measurement section (MS)	*Orientation
DMS-1	Strain, reinforcement bar	HOR stirrup TOP	1	Transversal, OoP
DMS-2	Strain, reinforcement bar	HOR stirrup BOT		Transversal, OoP
DMS-3	Strain, reinforcement bar	VER stirrup L		90°
DMS-4	Strain, reinforcement bar	VER stirrup R		90°
DMS-5	Strain, reinforcement bar	Longitudinal bar TOP		0°
DMS-6	Strain, reinforcement bar	Longitudinal bar BOT		0°
DMS-7	Strain, reinforcement bar	HOR stirrup TOP	2	Transversal, OoP
DMS-8	Strain, reinforcement bar	HOR stirrup BOT		Transversal, OoP
DMS-9	Strain, reinforcement bar	VER stirrup L		90°
DMS-10	Strain, reinforcement bar	VER stirrup R		90°
DMS-11	Strain, reinforcement bar	Longitudinal bar TOP		0°
DMS-12	Strain, reinforcement bar	Longitudinal bar BOT		0°
DMS-13	Strain, reinforcement bar	HOR stirrup TOP	3	Transversal, OoP
DMS-14	Strain, reinforcement bar	HOR stirrup BOT		Transversal, OoP
DMS-15	Strain, reinforcement bar	VER stirrup L		90°
DMS-16	Strain, reinforcement bar	VER stirrup R		90°
DMS-17	Strain, reinforcement bar	Longitudinal bar TOP		0°
DMS-18	Strain, reinforcement bar	Longitudinal bar BOT		0°
DMS-19	Strain, reinforcement bar	HOR stirrup TOP	4	Transversal, OoP
DMS-20	Strain, reinforcement bar	HOR stirrup BOT		Transversal, OoP
DMS-21	Strain, reinforcement bar	VER stirrup L		90°
DMS-22	Strain, reinforcement bar	VER stirrup R		90°
DMS-23	Strain, reinforcement bar	Longitudinal bar TOP		0°
DMS-24	Strain, reinforcement bar	Longitudinal bar BOT		0°
DMS-25	Strain, steel profile	USP, top flange	1	0°
DMS-26	Strain, steel profile	USP, web		45°
DMS-27	Strain, steel profile	USP, bottom flange		0°
DMS-28	Strain, steel profile	LSP, top flange		0°
DMS-29	Strain, steel profile	LSP, web		45°
DMS-30	Strain, steel profile	LSP, bottom flange		0°
DMS-31	Strain, steel profile	USP, top flange	2	0°
DMS-32	Strain, steel profile	USP, web		45°
DMS-33	Strain, steel profile	USP, bottom flange		0°
DMS-34	Strain, steel profile	LSP, top flange		0°
DMS-35	Strain, steel profile	LSP, web		45°
DMS-36	Strain, steel profile	LSP, bottom flange		0°
DMS-37	Strain, steel profile	USP, top flange	3	0°
DMS-38	Strain, steel profile	USP, web		45°
DMS-39	Strain, steel profile	USP, bottom flange		0°
DMS-40	Strain, steel profile	LSP, top flange		0°
DMS-41	Strain, steel profile	LSP, web		45°
DMS-42	Strain, steel profile	LSP, bottom flange		0°
DMS-43	Strain, steel profile	USP, top flange	4	0°
DMS-44	Strain, steel profile	USP, web		45°
DMS-45	Strain, steel profile	USP, bottom flange		0°
DMS-46	Strain, steel profile	LSP, top flange		0°
DMS-47	Strain, steel profile	LSP, web		45°
DMS-48	Strain, steel profile	LSP, bottom flange		0°

* The given orientation is referring to the longitudinal axis of the specimen, as shown in Fig. 6.16 and 6.18.
Where,
HOR – Horizontal arm,
VER – Vertical arm,
TOP – Top part of the considered element,
BOT – Bottom part of the considered element,

L – Left side of the considered element, according to Fig. 6.17,
R – Right side of the considered element, according to Fig. 6.17,
OoP – Out of plane,
USP – Upper embedded steel profile,
LSP – Lower embedded steel profile

The fixation details of each type of the used sensors is shown in Fig. 6.19-6.22. The displacement transducers were fixed to the supporting structures (steel bars Ø12) with the usage of plastic clamps. The applied plastic clamps had anti-conductor properties. The inclinometers were fixed directly to the specimens, where between the wall of the specimen and the sensor, an isolation layer made out of rubber was present. The strain gauges were glued to the reinforcement bars and to the steel profiles after grinding, polishing and de-greasing of the steel surface. In order to prevent a mechanical damage of the strain gauges and to prevent from the electrical conduction, a layer of silicone and a second layer of adhering clay (putty) were placed. Cables used to connect the sensors and hardware were distributed inside the specimen in such order that the impact on the concrete cover was minimal and that they were passing through the compressed part of the specimen. More details about the measurement equipment and application process are given in Annex E.

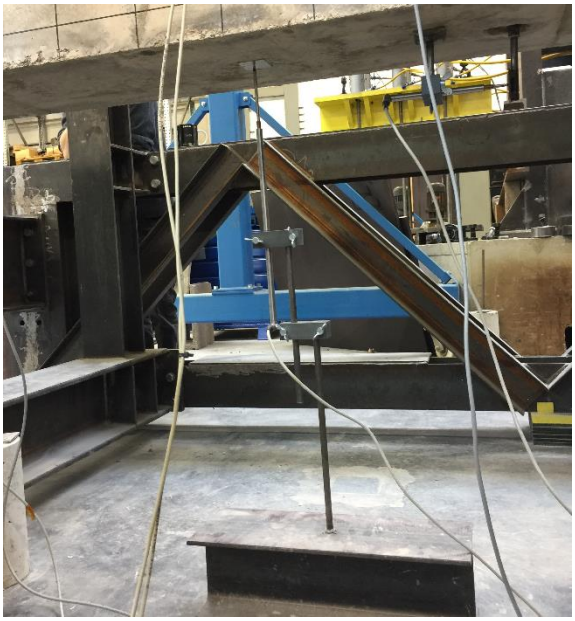


Fig. 6.19. Detail of displacement transducer measuring the deflection of beam/column specimen.

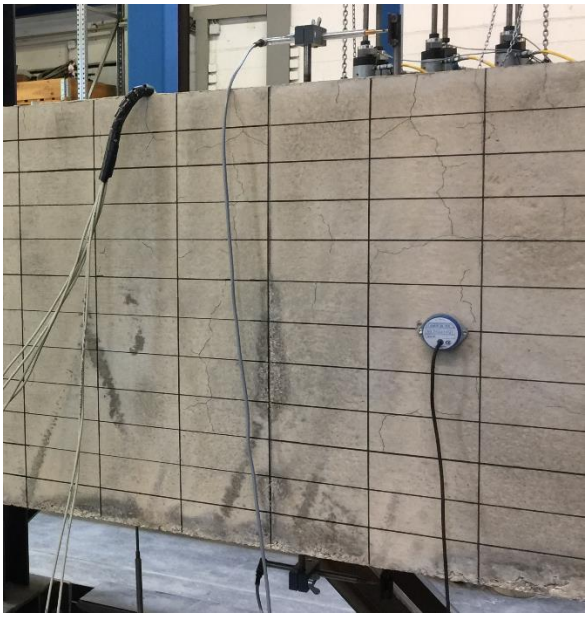


Fig. 6.20. Detail of inclinometer on the beam/column specimen.



Fig. 6.21. Detail of strain gauge glued to the reinforcement bar of beam/column specimen.

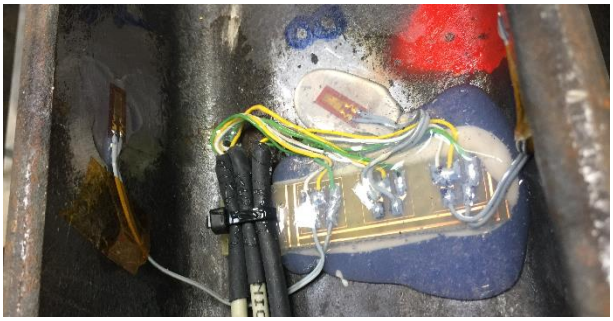
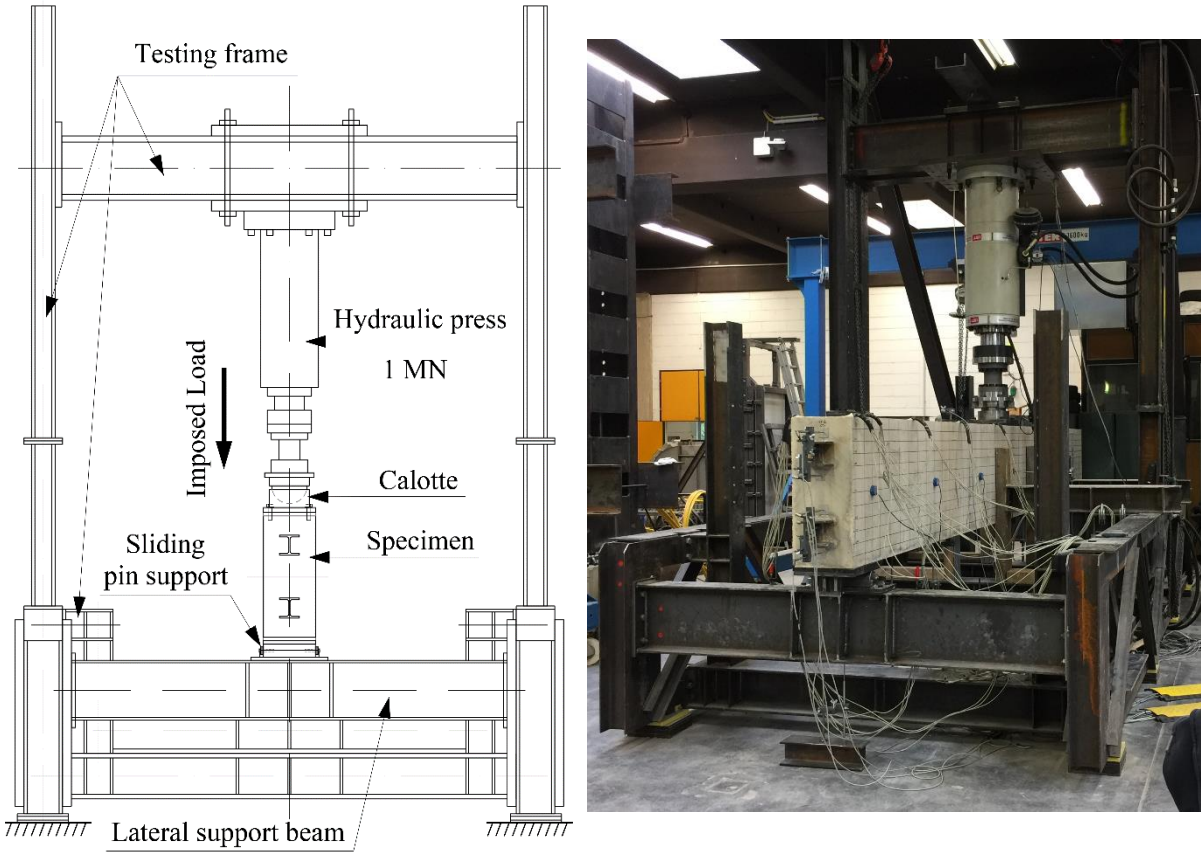


Fig. 6.22. Detail of strain gauges glued to the steel profile of beam/column specimen.

6.3.4. Test conduction and boundary conditions

The performed three-point bending tests had the static system reflecting the simple supported beam with the point load imposed in the mid-span, as it is shown in Fig. 6.2. The span between the supports was 6000 mm and the specimens were placed on a pin sliding supports, 250 mm from the edges of the concrete block. To perform the tests, a hydraulic press with the nominal capacity of 1 MN was used. The jack and the testing frame were fully integrated. The specimens were supported on the lateral bottom beams of the testing frame. The point load was imposed to the specimen in the mid-span through the calotte and through the load transition plate. The aforementioned plate was 40 mm thick and it was fixed to the specimen with 4 anchor bolts. Between the specimen and the force transition plates, which were also used at the supports, a 20 mm layer of rubber was placed in order to assure a uniformly distributed pressure over the contact surface. The test setup is presented in Fig. 6.23. The test layout with the view on the deformed shape and boundary conditions is shown in Fig. 6.24.



a) b)

Fig. 6.23. Test setup for the beam/column test specimens on the example of specimen VT-2 – a) scheme and b) view in the laboratory.

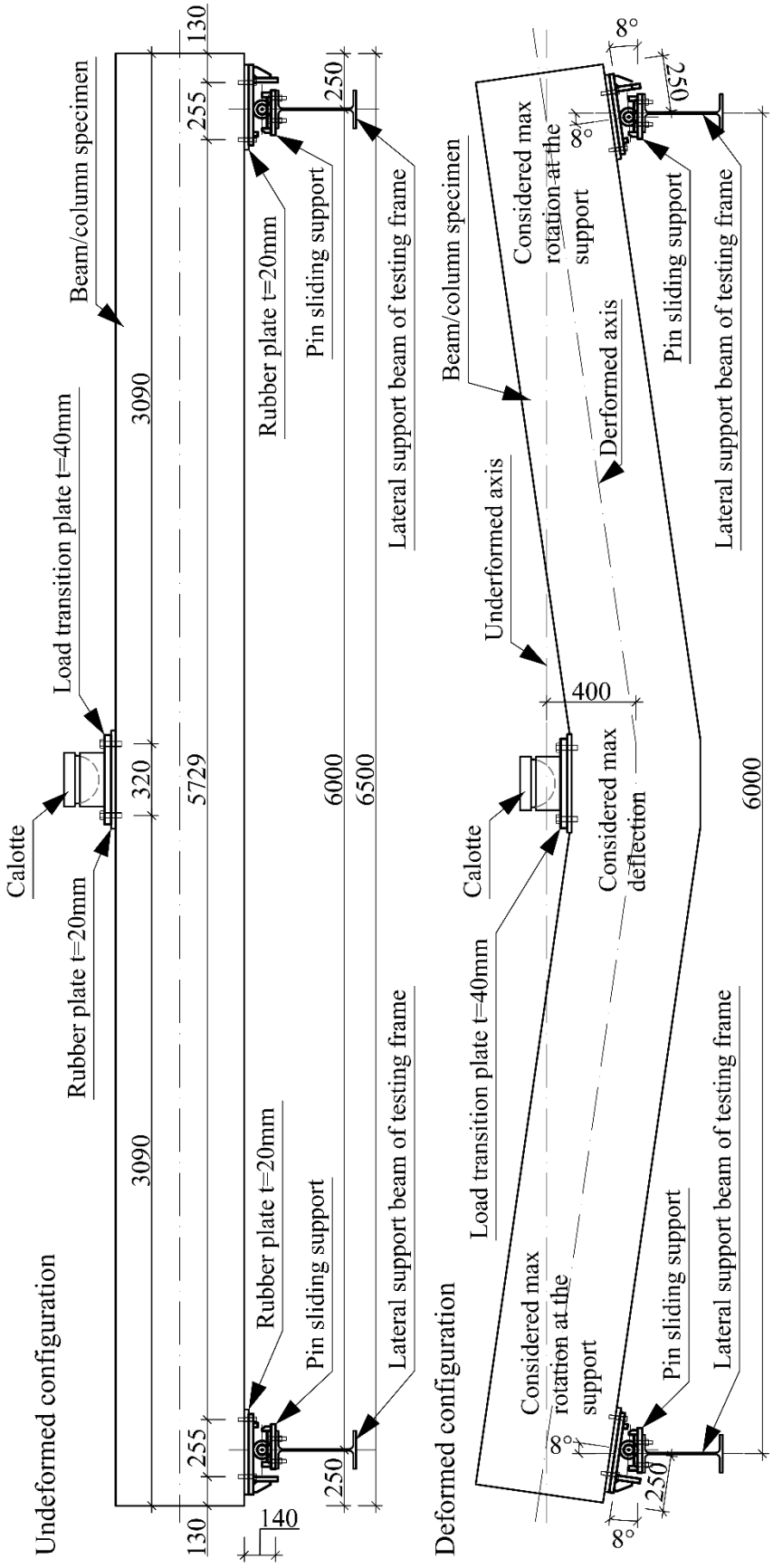


Fig. 6.24. Test layout of beam/column test specimen with the deformed shape and boundary conditions.

The test procedure defined in EN1994-1-1 Annex B [58] was adapted for the performed beam/column tests. The applied test procedure included (i) load increments in the first phase of test until the ultimate load, (ii) the dynamic cycles phase after reaching 45% of the expected ultimate load and (iii) the monotonic loading phase after reaching the ultimate load and until the end of the test, see Fig. 6.25. The load increments and monotonic loading phases were done in the displacement control mode. The load increments had the shape of ramp, where a small speed of imposed load was respected in order to avoid dynamic effects. At the beginning of test, the loading rate was set to 0,5 mm/min of the displacement of jack to avoid the rigid body movement of the specimens. After reaching a certain level of load (approx. 50 kN), the load rate was increased to 1-2 mm/min, with dependency on the stiffness of specimens. Between each load increment, a pause of minimum 4 minutes was respected allowing for the concrete relaxation, investigating of the load-drop during the pause and increasing an accuracy of the recorded values. In the result, the tests were performed in the quasi-static manner. The dynamic cycles phase was controlled in the force control mode. After reaching 45% of the expected ultimate load, the specimens were cycled 25 times with an amplitude from 5% to 40% of the expected ultimate load. The cycling frequency was 0,015Hz, which resulted in the cycling time approx. 25-30 min. After the cycling part of test, the increments continued up to the failure of specimens with the jack displacement rate of 2 mm/min. In the post-failure phase of test, the specimens were monotonically loaded with a constant jack displacement rate of 7 mm/min until the deflection of specimens reached 180-215 mm. The obtained maximum values of deflection exceeded the deflection value of L/40, where "L" refers to the length of specimen. During the tests, at least three reloads were performed in order to investigate the stiffness degradation of specimens at the different load levels and at the different states of the specimen, before the failure and after it.

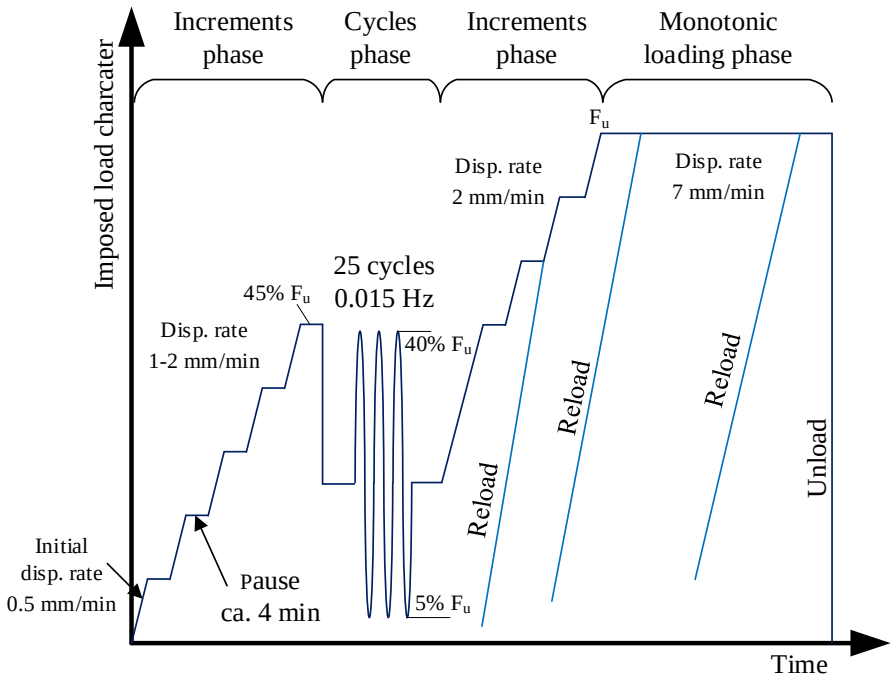


Fig. 6.25. Scheme of the loading protocol used during the beam/column tests.

6.3.5. Test results

From each beam/column test, 80 signals from the equipped sensors, listed in Table 6.3 and Table 6.4, were recorded and analysed. All the signals were recorded with the usage of National Instruments hardware and dedicated brand software – SignalExpress. The recording frequency was 1k Hz. The post processing of the recorded data, including the data reduction, was done with the usage of NI DIAdem software. In parallel to the beam/column tests, the material tests of the structural steel, reinforcement steel and concrete were performed.

6.3.5.1. Measured material properties

Material properties of the used parts were obtained experimentally from the respective material tests. The tensile coupon tests of structural steel were performed according to ISO 6892-1 [80], where the tensile tests of reinforcement steel were conducted according to ISO 6935-2 [81]. The compression strength of concrete was tested according to EN 12390-3 [50].

The industrial project partner ArcelorMittal delivered the structural steel material. The rolling heat certificate, obtained after the delivery, proves the ordered steel grade and specifies the minimal mechanical properties of steel material. The summary of measured steel properties is given in Table 6.5. The value of the modulus of elasticity was evaluated as a tangent of the elastic branch from the resultant stress-strain curve obtained from the tensile tests.

Table 6.5.
Material properties of the structural steel from beam/column specimens.

Ordered grade: S355 JR+M	Value – min (EN 10025-1 [48])	Value – expected (heat certificate)	Value – test (ISO 6892-1 [80])	Unit
R_{eH}, yielding strength	355	427	462	[MPa]
R_m, tensile strength	470	531	560	[MPa]
A, elongation at fracture	22	28.57	30.52	[%]
E, modulus of elasticity	210 000	-	207 708	[MPa]

The reinforcement steel was delivered by the company Ferrac Sàrl and at the delivery, the geometry and grade of the ordered bars were confirmed by a certificate. The geometry of ordered bars consisted of two diameters, Ø8 and Ø12. The summary of the reinforcement steel properties for each bar diameter is given in Table 6.6, where the modulus of elasticity was evaluated according to the elastic part of obtained stress-strain curve.

Table 6.6.
Material properties of the reinforcement steel from beam/column specimens.

Ordered grade: B500B	Value – min (ISO 6935-2 [81])	Value – test (ISO 6935-2 [81])		Unit
		Ø8	Ø12	
R_{eH}, yielding strength	500	572	530	[MPa]
R_m, tensile strength	540	674	633	[MPa]
A, elongation at fracture	$A_{gt} = 5$ / $A_5 = 14$	17.83	18.25	[%]
E, modulus of elasticity	200 000	206 165	202 531	[MPa]

The concrete mixture was delivered by the concrete manufacturer Betons Feidt. The ordered concrete grade, C30/37, and accompanying properties (e.g. w/c ratio or consistency class) were confirmed upon the delivery by the delivery receipt. Both beam/column specimens were concreted from the same batch of concrete. The compression strength of concrete was tested at the concrete age of 28 days using the cylindrical and cubic specimens. In addition, at the day after the beam/column tests, the compression tests of concrete were performed only on cubic specimens in order to obtain properties of the concrete at the testing date. The summary of concrete material properties is shown in Table 6.7.

Table 6.7.
Material properties of the concrete.

Ordered grade: C30/37	Value – min (EN 206-1 [59])	Value – test (EN 12390-3 [50])	Unit
f_{cm}, mean compression strength for cylinders (age: 28 days)	38	35.57	[MPa]
$f_{cm,cube}$, mean compression strength for cubes (age: 28 days)	47	38.98	[MPa]
$f_{cm,cube}$, mean compression strength for cubes (age: 35 days, the day of test VT-2)	-	47.75	[MPa]
$f_{cm,cube}$, mean compression strength for cubes (age: 51 days, the day of test VT-1)	-	44.25	[MPa]
Cement	Mix of CEMIIB-S 42.5N and CEMII/BM32.5R		
W/C	0.50		
Exposition class	CAT3 – SC4, XD2, XF2, XA2		
Consistency class	F4		
Aggregate	B08		

6.3.5.2. Load-deformation responses

The deflections of specimens were recorded by the displacement transducers positioned on the ground, see Table 6.3 and Fig. 6.14 – DT-1 to DT-8. Simultaneously, sensors DT-25 and DT-26 recorded the deflection of testing frame during the tests. The true deflections of specimens were evaluated by the subtraction of the measured deformations of testing frame from the deformations of specimens measured in reference to the ground. The deformation shapes at different load levels are presented in Fig. 6.26 for the specimen VT-1 and Fig. 6.27 for the specimen VT-2.

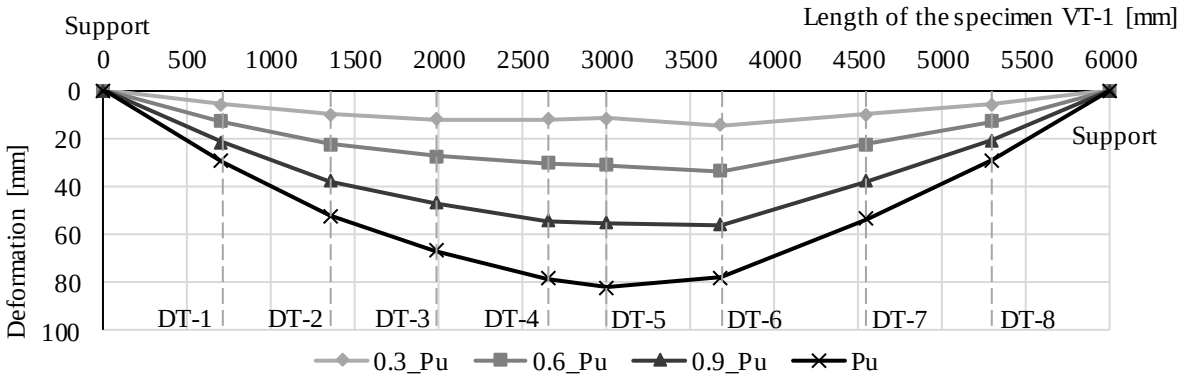


Fig. 6.26. Deflection shape of the beam/column specimen VT-1.

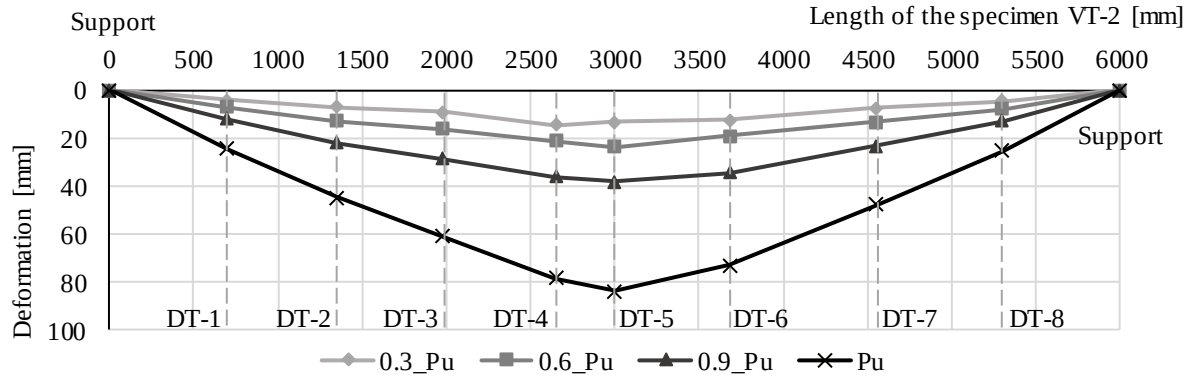


Fig. 6.27. Deflection shape of the beam/column specimen VT-2.

The obtained load-deflection curves for each considered displacement transducer are presented in Fig. 6.28-6.30 for the specimen VT-1 and in Fig. 6.31-6.33 for the specimen VT-2. In Table 6.8, the extracted values for the deflection at the mid-span, shown in Fig. 6.28 and Fig. 6.31, are summarised. The peak point values (P_u and w_u) and the corresponding reloads on the specimens are explained in Fig. 6.28 and Fig. 6.31 for the specimens VT-1 and VT-2, respectively.

Table 6.8.
Test results for the considered mid-span deflections of beam/column specimens.

Specimen	P_u [kN]	P_{end} [kN]	w_u [mm]	w_{max} [mm]	K_{init} [kN/mm]	K_{R1} [kN/mm]	K_{R2} [kN/mm]	K_{R3} [kN/mm]	K_{R4} [kN/mm]
VT-1	417	304	82.2	213.3	9.84	12.12	10.86	9.55	8.42
VT-2	598	525	84.0	184.6	15.95	29.07	24.60	23.47	-

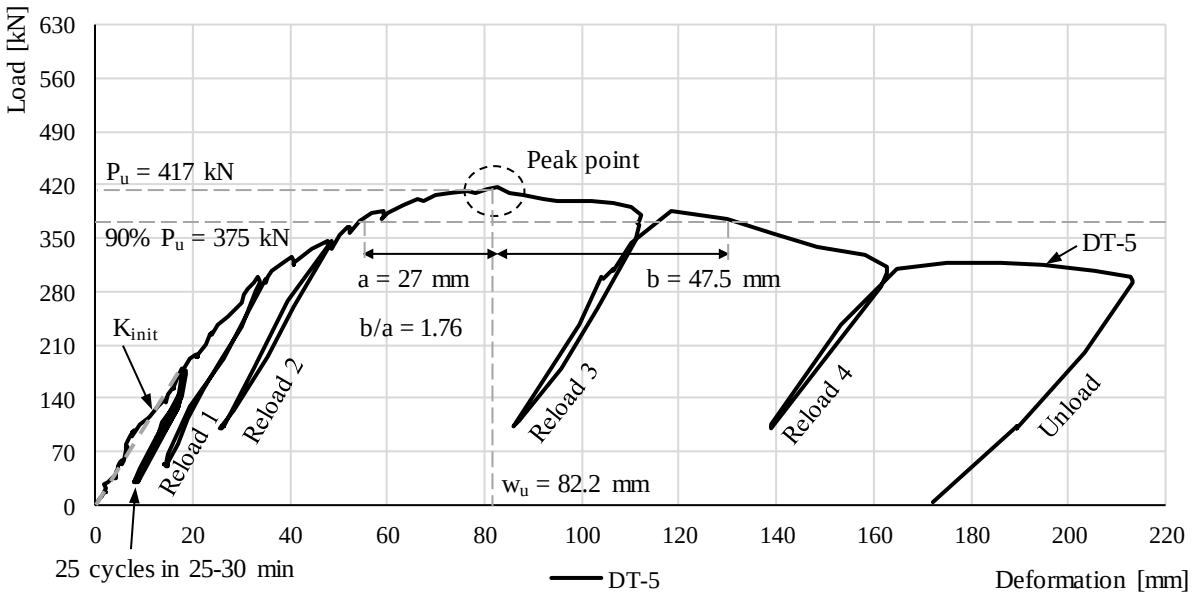


Fig. 6.28. Load-deflection curve for the beam/column specimen VT-1, sensor DT-5, mid-span.

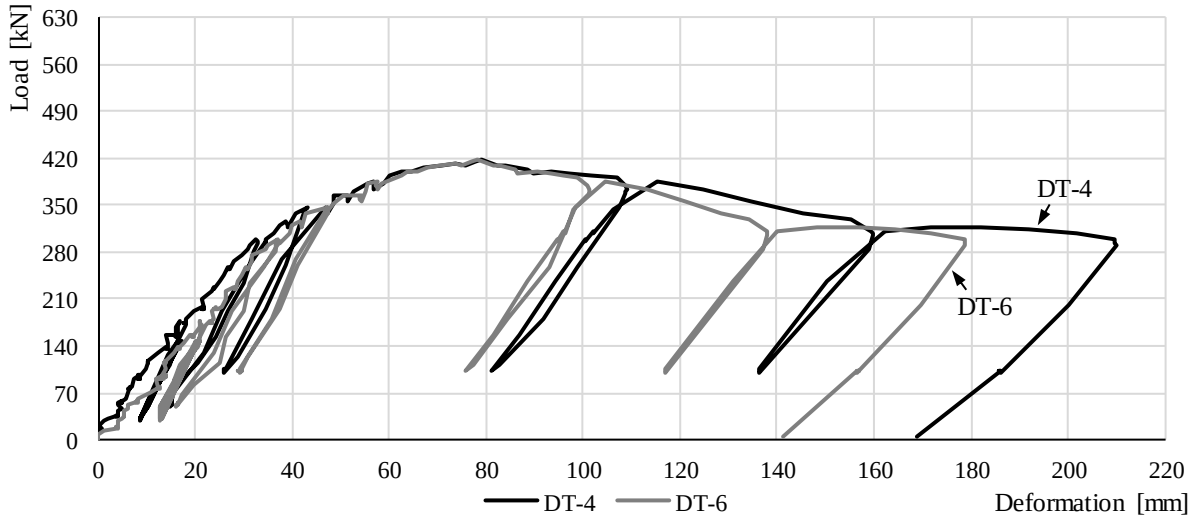


Fig. 6.29. Load-deflection curve for the beam/column specimen VT-1, sensor DT-4 and DT-6, mid-zone.

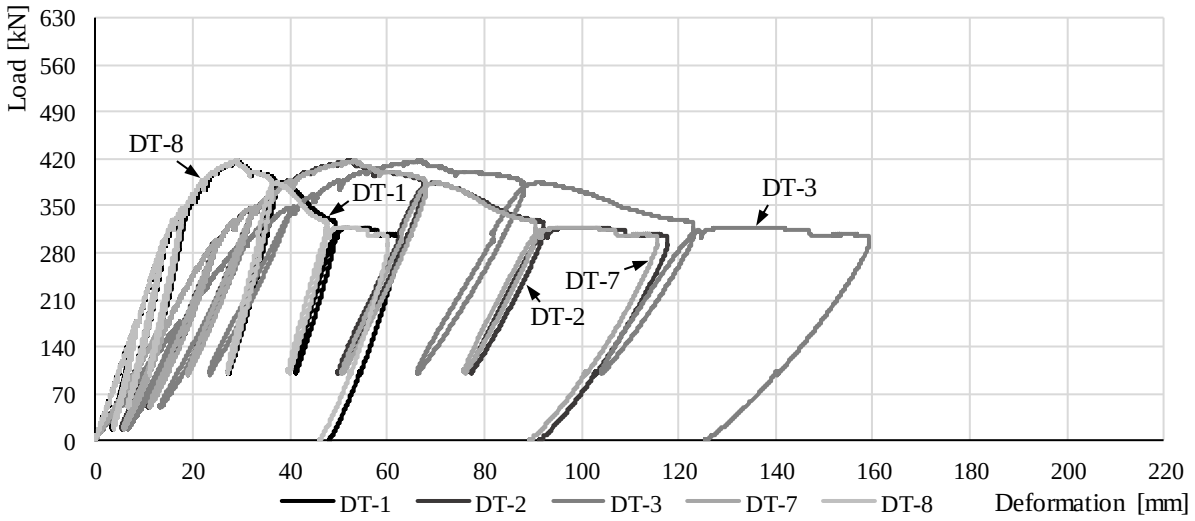


Fig. 6.30. Load-deflection curve for the beam/column specimen VT-1, sensor DT-1 to DT-3 and DT-7 to DT-8, side-zones.

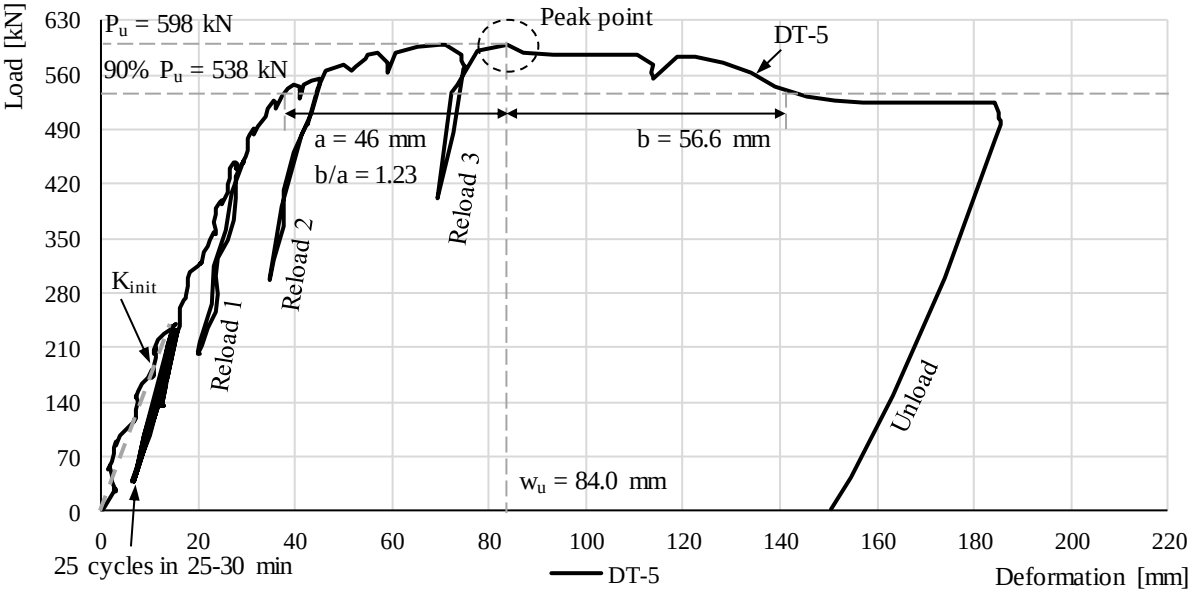


Fig. 6.31. Load-deflection curve for the beam/column specimen VT-2, sensor DT-5, mid-span.

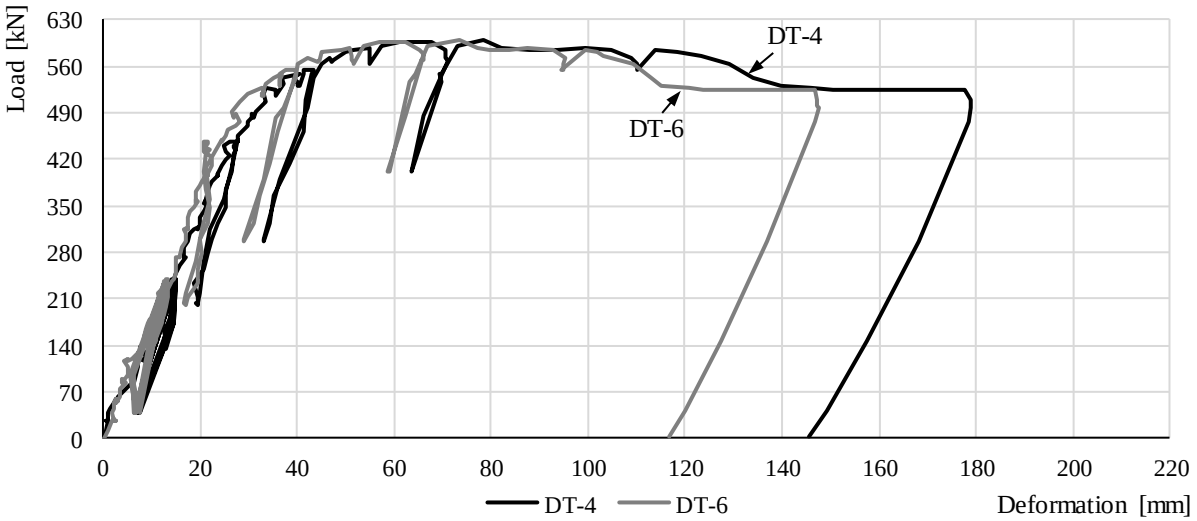


Fig. 6.32. Load-deflection curve for the beam/column specimen VT-2, sensor DT-4 and DT-6, mid-zone.

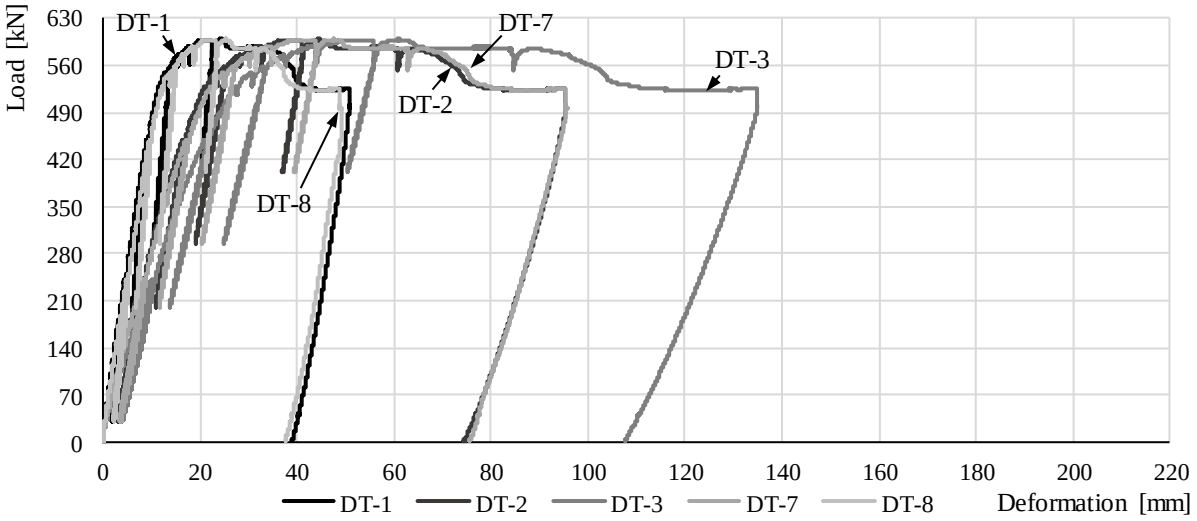


Fig. 6.33. Load-deflection curve for the beam column specimen VT-2, sensor DT-1 to DT-3 and DT-7 to DT-8, side-zones.

Sensors DT-9 and DT-10, see Table 6.3, measured the lateral expansion of specimens at the mid-span and the mid-height. Until the failure of specimens, the movement and lateral expansion by approximately 0.5 mm were observed in both specimens, see Fig. 6.34 for the specimen VT-1 and Fig. 6.35 for the specimen VT-2. The observed effect is not significant. Further recorded values are related to the spalling of concrete after reaching the failure of specimens.

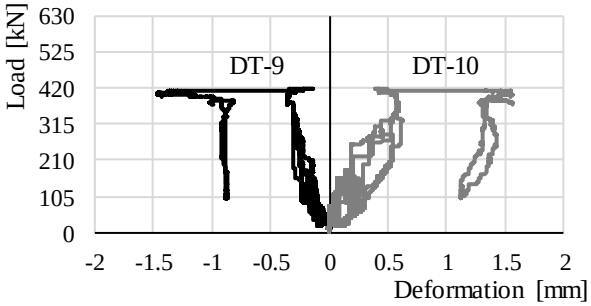


Fig. 6.34. Lateral expansion in the beam/column specimen VT-1.

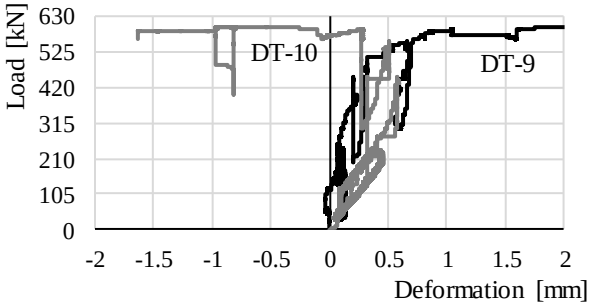


Fig. 6.35. Lateral expansion in the beam/column specimen VT-2.

The data recorded by the applied inclinometers is presented in Fig. 6.36. Only records from the test VT-2 are available. According to the diagram presented below, it can be observed, that the rotation measured by the IM-1 and IM-2 was very similar and the values were bigger than the rotation measured by the IM-3 and IM-4. The distribution of the sectional rotations over the length of specimen is presented in Fig. 6.37. It can be observed that change in the global curvature character is visible starting from the beginning of test. In the zone of the drastic change of curvature at higher loads, a plastic hinge developed in the mid-zone of specimen and the rotation significantly diverged.

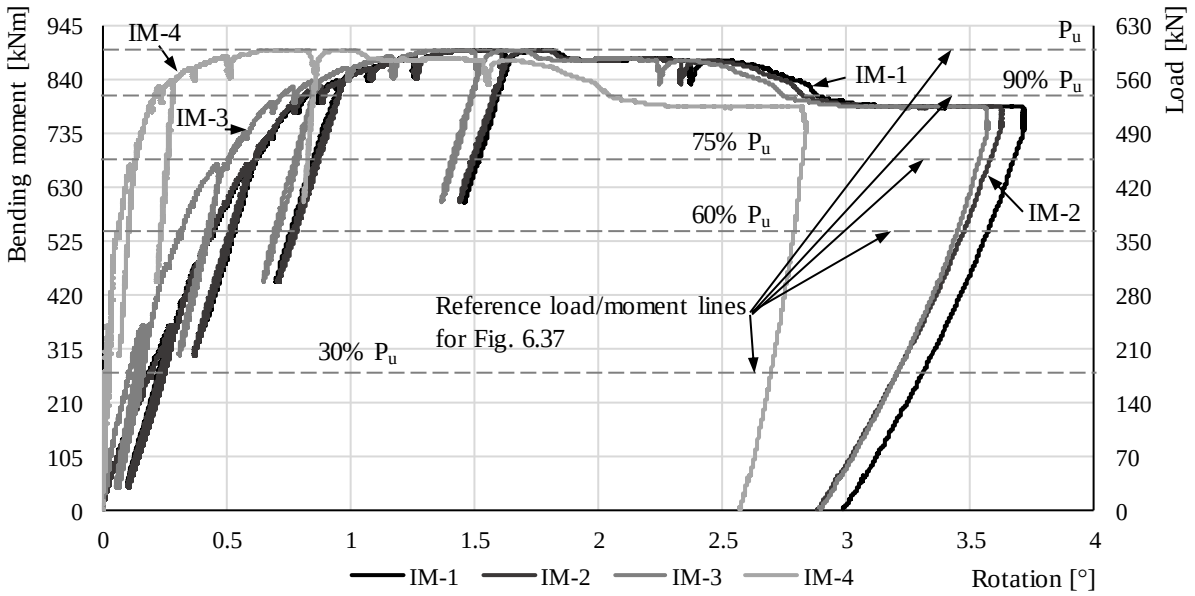


Fig. 6.36. Load/Bending moment-rotation curves for the beam/column specimen VT-2

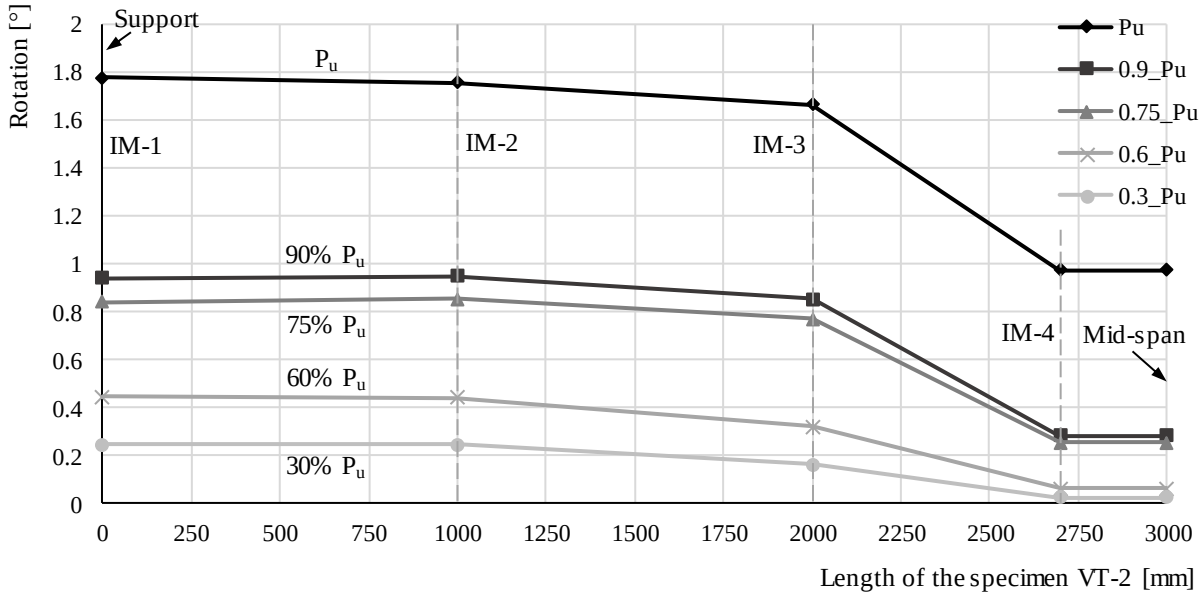


Fig. 6.37. Distribution of the sectional rotations over the length of the beam/column specimen VT-2.

6.3.5.3. Strains in the specimens

Strains in the specimens were recorded by the set of 48 DMS shown in Fig. 6.16-6.18 and listed in Table 6.4. The recorded strains in the reinforcement bars indicated the distribution of forces in the specimens and gave the information about the level of transferred forces by the structural elements. The DMS glued to the flanges of steel profiles supported the information about the distribution of strains in the measurement sections defined in Fig. 6.18. The DMS glued to the webs of steel profiles were intended to measure the shear forces developed in the steel profiles due to the composite force transferring mechanism. The information obtained from the above-mentioned sensors gives a wide spectrum on the global behaviour of tested beam/column specimens.

The distribution of strains in the considered measurement sections in the longitudinal direction (DMS on the longitudinal reinforcement bars and flanges of steel profiles) brought a relevant information about the sectional tension-compression zones, the resulting stresses and forces, the position of the neutral axis in the cross-sections and their curvatures. The recorded strains in the longitudinal reinforcement bars and flanges of steel profiles at the consequent measurement sections are shown in Fig. 6.38-6.41 for the specimen VT-1 and in Fig. 6.43-6.46 for the specimen VT-2. The corresponding schematic overviews of strains distributions in the specimens at different load levels are given in Fig. 6.42 for the specimen VT-1 and in Fig. 6.47 for the specimen VT-2. The DMS-25 and DMS-43 had been damaged during the test VT-1 and the recorded data is missing. In the test VT-2, the reinforcement bar localised at the bottom of specimen experienced an extensive elongation and due to the cable detaching, the data from the DMS-24 in the later phases of test is missing.

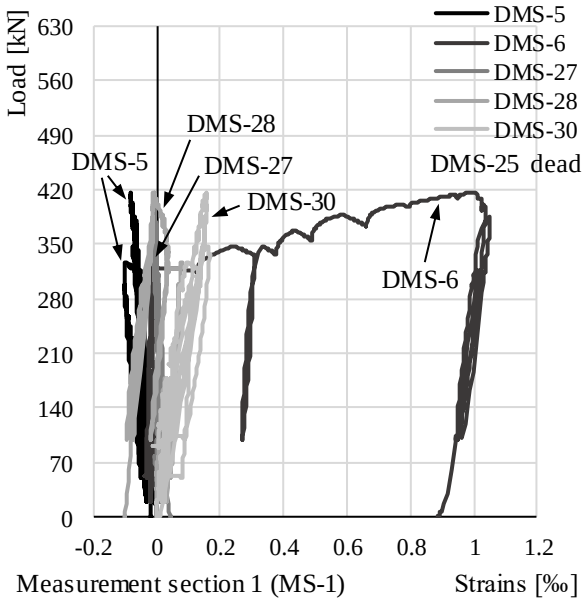


Fig. 6.38. Strains in the beam/column specimen VT-1, longitudinal direction at measurement section 1 (MS-1).

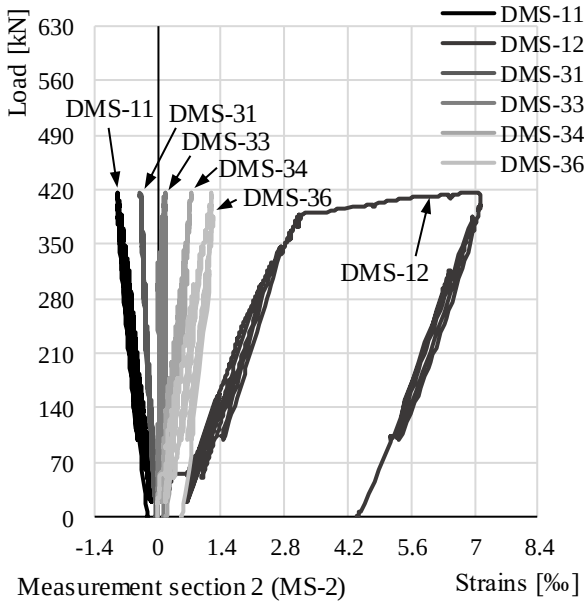


Fig. 6.39. Strains in the beam/column specimen VT-1, longitudinal direction at measurement section 2 (MS-2).

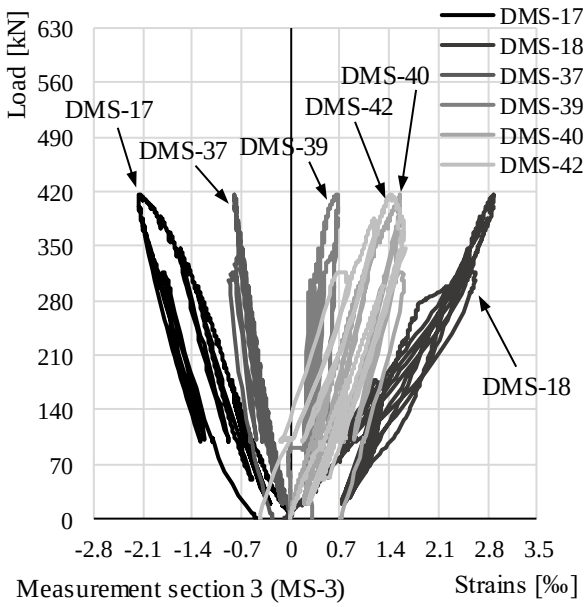


Fig. 6.40. Strains in the beam/column specimen VT-1, longitudinal direction at measurement section 3 (MS-3).

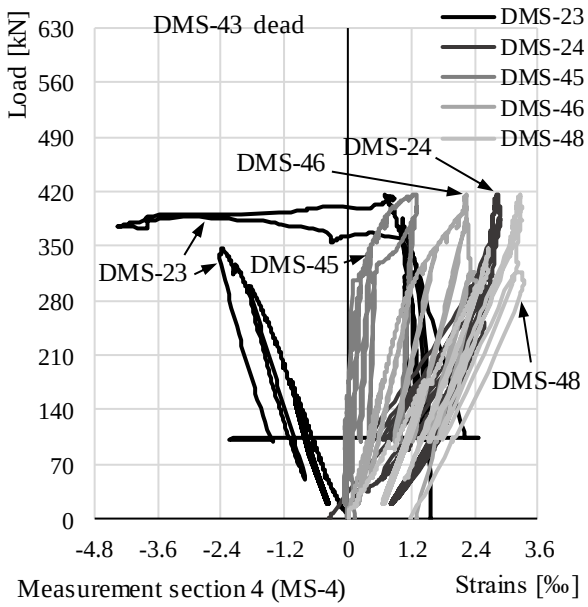


Fig. 6.41. Strains in the beam/column specimen VT-1, longitudinal direction at measurement section 4 (MS-4).

Considering the specimen VT-1, as shown in Fig. 6.42, it can be observed that in the upper part of specimen, the compression zone developed, where in the lower part of specimen, the tensile zone was present. This characteristic distribution of strains is related to the global bending mechanism to which the specimens were subjected during the tests. From the obtained distribution of strains, it can be observed, that both embedded steel profiles were subjected to bending. The neutral axis of the global bending mechanism was localised in the upper embedded steel profile, while the steel profile embedded at the bottom was subjected to the internal local bending mechanism due to the composite action and force transfer. In the first phase of test, it can be observed that the strains distributions over the height of measurement sections can be assumed to be linear due to the elastic range of strains in each material and due to the full shear connection. In the later phase of test, when the load reached level close to the peak load, the steel materials yielded in the most tensioned places and the concrete cracked extensively in the tensile zone. Moreover, the relative slip between the steel profiles and concrete was present. The aforementioned phenomena affected the linearity of strain distributions. In the result, a disturbed character of strains distributions, nonlinear, can be observed at the stages of 90% and 100% of the peak load. According to Table 6.5 and Table 6.6, the yielding strains for the structural steel was 2.22 ‰, where for the reinforcement steel the yielding strain reached 2.77 ‰. This observation with reference to Fig. 6.42, reveals that the steel profile embedded at the bottom yielded at the load close but bigger than 60% of the peak load (P_u), however, the ultimate strains have not been reached. A similar situation can be observed for the longitudinal reinforcement positioned at the bottom of specimen. The upper embedded steel profile not yielded, where the longitudinal reinforcement bars localised on the top were subjected to yielding due to the compression stresses at the peak load.

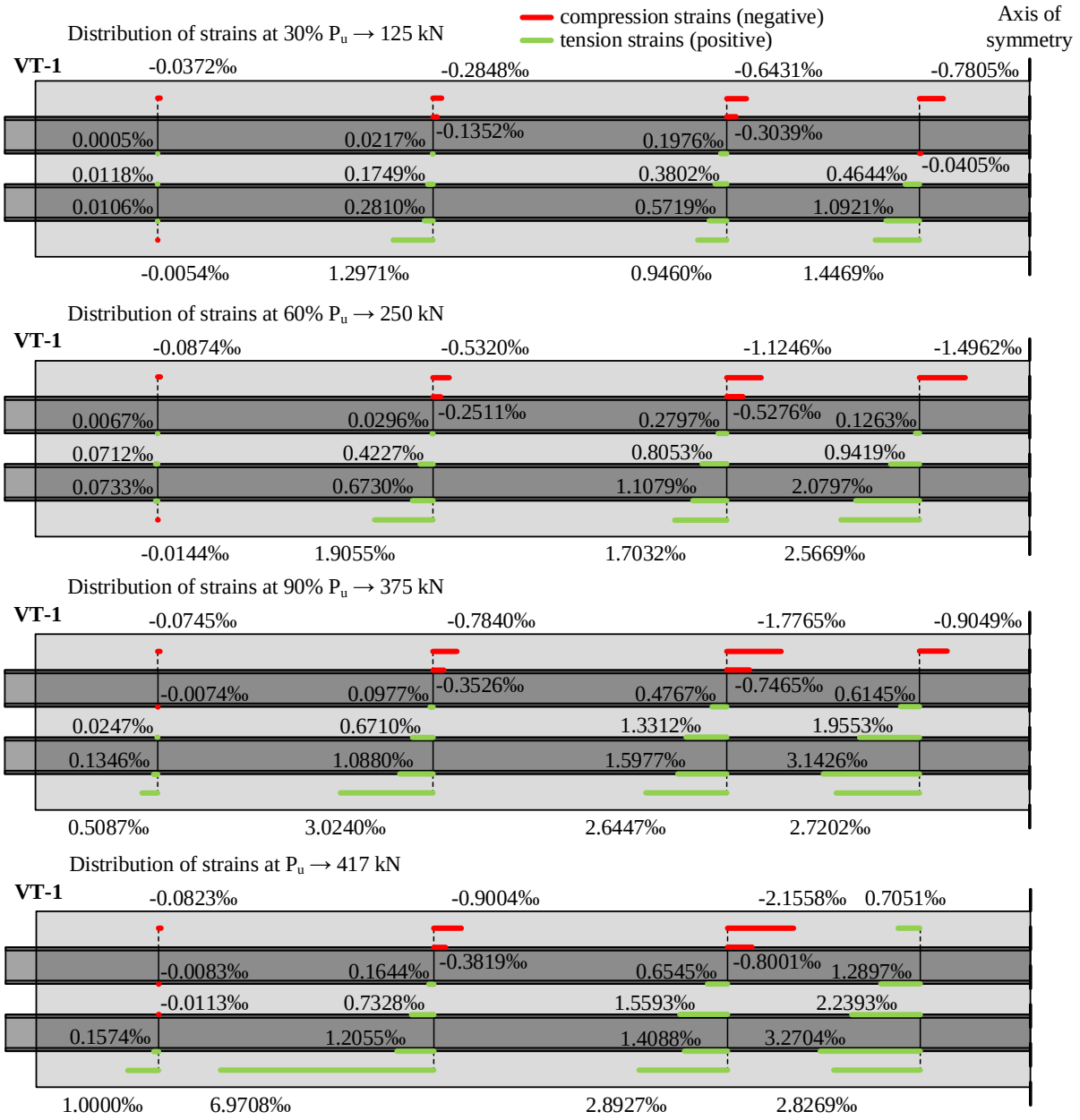


Fig. 6.42. Distribution of longitudinal strains in the measurement sections of beam/column specimen VT-1.

In the specimen VT-2, similar observations that are described for the specimen VT-1, were identified. In Fig. 6.47, a similar strains distribution character in the measurement sections can be seen, where the individual bending mechanism of the embedded steel profiles is visible. The two resulting zones, compression on the top and tension on the bottom, are distinguished. Similarly, like in the case of specimen VT-1, the neutral axis of cross-section was identified in the upper embedded steel profile. The material properties of steel elements were identical like in the case of specimen VT-1 and the measured values are given in Table 6.5 and Table 6.6 for the structural and reinforcement steels, respectively. The values of yielding strains were identical like in the case of specimen VT-1 and they reached 2.22 ‰ for the structural steel material and 2.77 ‰ for the reinforcement steel material. Yielding of the most tensioned fibres of steel profiles and reinforcement bars localised at the bottom of specimen developed with the load close but smaller than 90% of the peak load. A similar effect was identified in the

compression zone, where strains in the longitudinal reinforcement bars at the top reached nearly yielding strains with the load equal to 90% of the peak load. The comparison of Fig. 6.42 and 6.47 shows that yielding of the steel elements in the specimen VT-1 occurred earlier than in the specimen VT-2. In addition, it can be observed that the linearity of strains distributions over the height of measurement sections was disturbed in the specimen VT-2 at the earlier stages of test. The non-linearity in the specimen VT-2 occurred with the load level equal to 60% of the peak load.

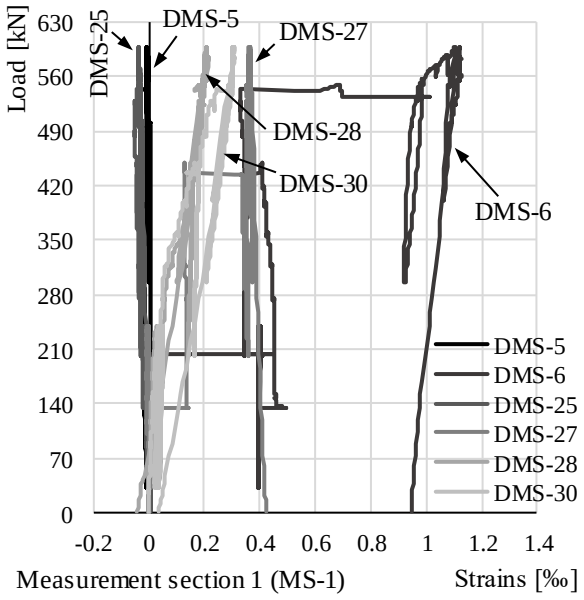


Fig. 6.43. Strains in the beam/column specimen VT-2, longitudinal direction at measurement section 1 (MS-1).

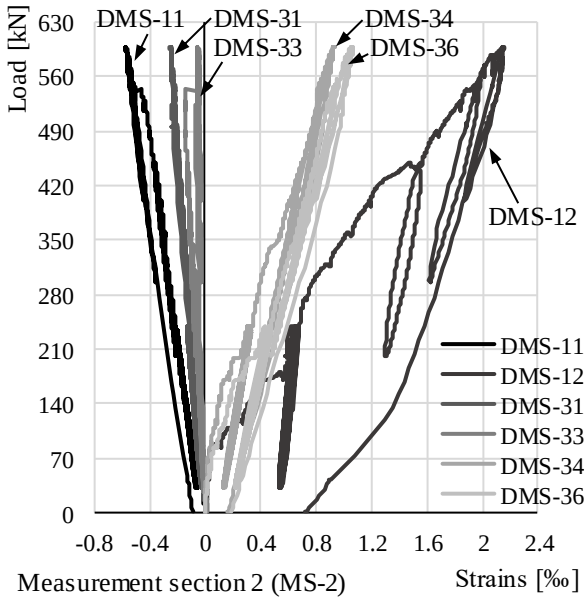


Fig. 6.44. Strains in the beam/column specimen VT-2, longitudinal direction at measurement section 2 (MS-2).

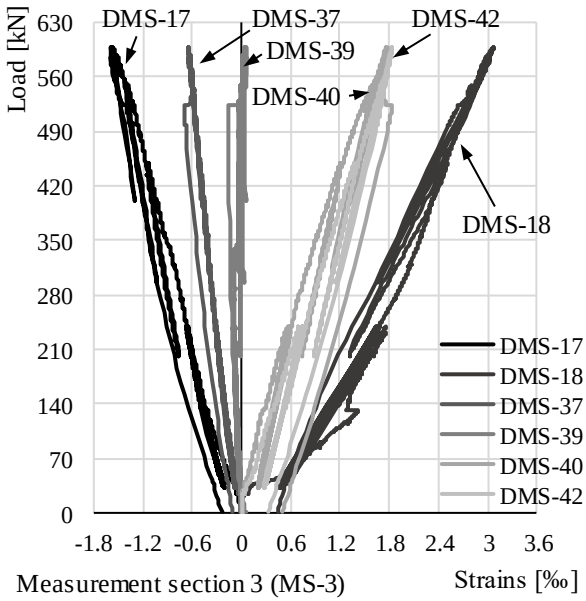


Fig. 6.45. Strains in the beam/column specimen VT-2, longitudinal direction at measurement section 3 (MS-3).

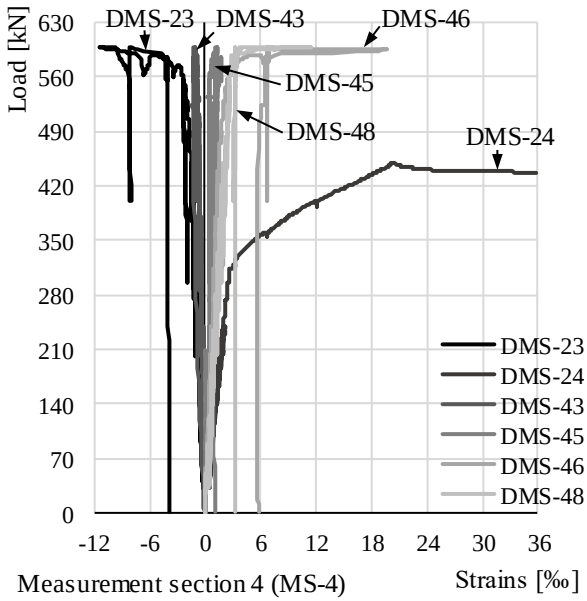


Fig. 6.46. Strains in the beam/column specimen VT-2, longitudinal direction at measurement section 4 (MS-4).

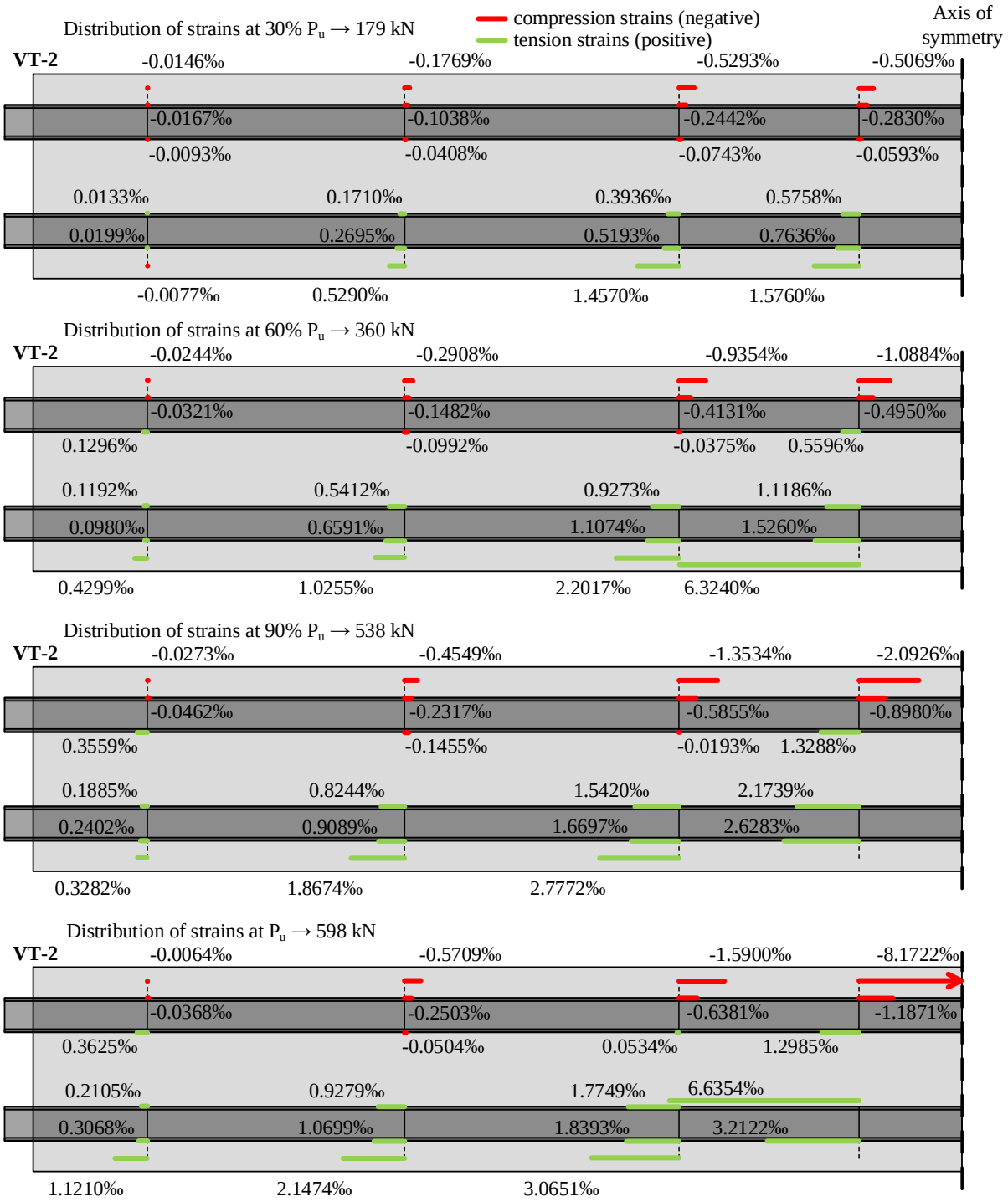


Fig. 6.47. Distribution of longitudinal strains in the measurement sections of beam/column specimen VT-2.

In Fig. 6.48 and Fig. 6.49, strains measured in the webs of the steel profiles under 45° are given for the specimen VT-1 and VT-2, respectively. Compression strains developed in the webs of steel profiles correspond to the developed shear stresses in steel profiles. The DMS that recorded tensile elongation had been mainly localised in the mid-spans of specimens and the tensile elongation of steel profile dominated the shear strains. The data presented in Fig. 6.48-6.49 proves the activation of steel profiles in the global shear forces transfer starting from the beginning of tests. The given information is respected qualitatively, since the recorded values are not free from an error due to existing accompanying

tension/compression stresses resulted from the global bending behaviour. An information about the three-dimensional stress state in the webs of steel profiles would be required for the quantitative analysis.

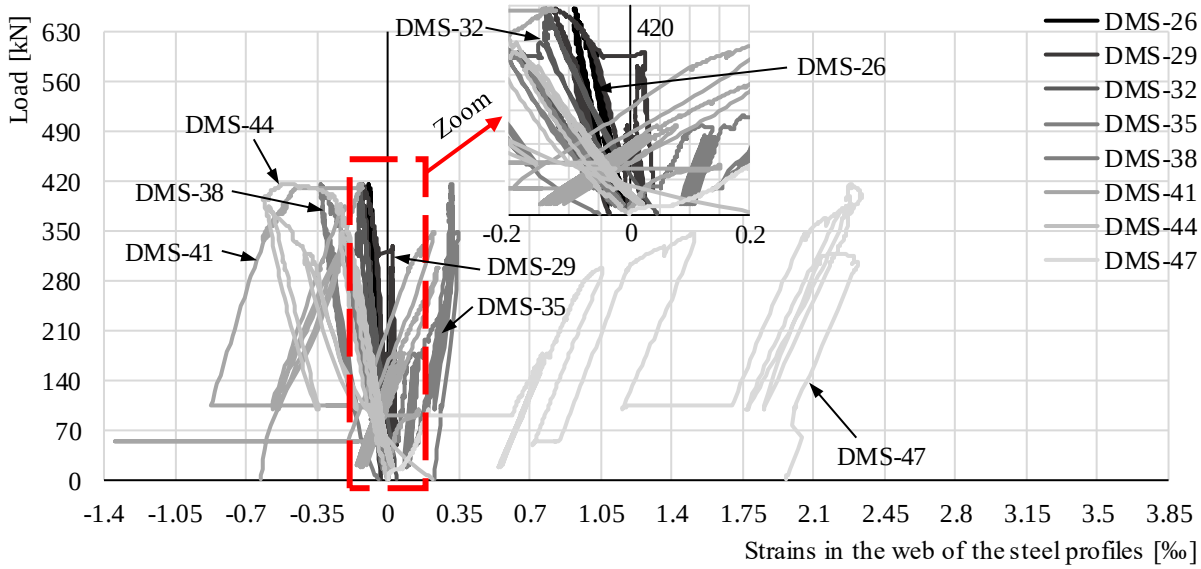


Fig. 6.48. Strains in the webs of steel profiles under 45° in the beam/column specimen VT-1.

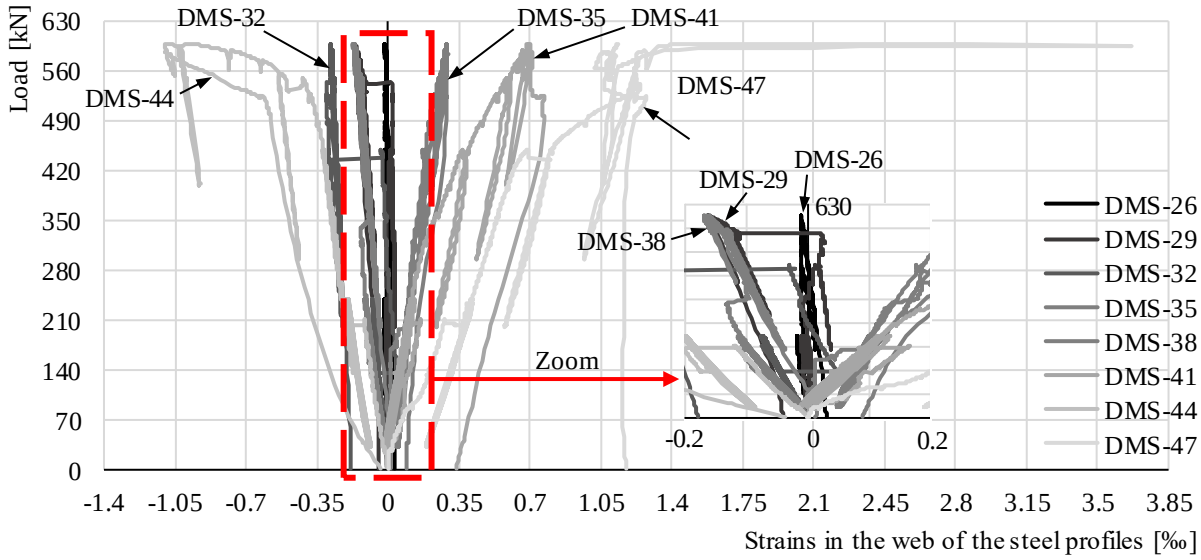


Fig. 6.49. Strains in the webs of steel profiles under 45° in the beam/column specimen VT-2.

In the measurement sections indicated in Fig. 6.16, the DMS glued to the side arms of stirrups, for example DMS-9 and DMS-10 in Fig. 6.16 and Fig. 6.17, recorded the strains of shear reinforcement subjected to the transfer of shear forces in the specimens. Based on the gathered data, the activation of shear reinforcement in the shear force transfer mechanism could be investigated. The recorded data is presented in Fig. 6.50-6.53 for the specimen VT-1, where the recorded data for the specimen VT-2 is given in Fig. 6.54-6.57. On the presented diagrams, it can be observed that the strains are varied between the subsequent measurement sections. The aforementioned variation can be related to the different stirrups spacing in the different parts of specimens, see Fig. 6.11 and Fig. 6.12, and due to the resulting flow of shear forces inside the specimens.

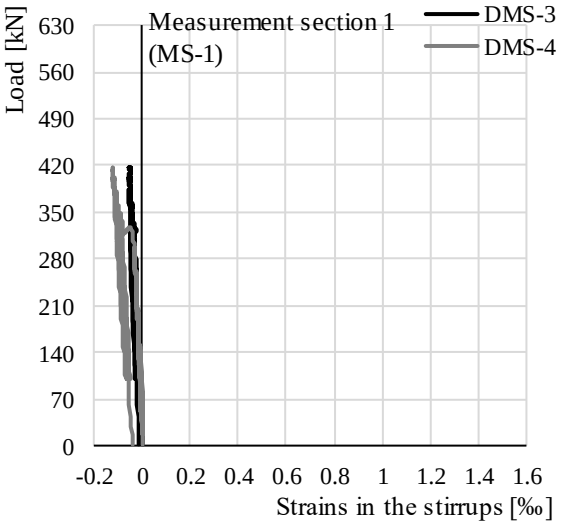


Fig. 6.50. Strains in the stirrups of beam/column specimen VT-1, measurement section 1 (MS-1).

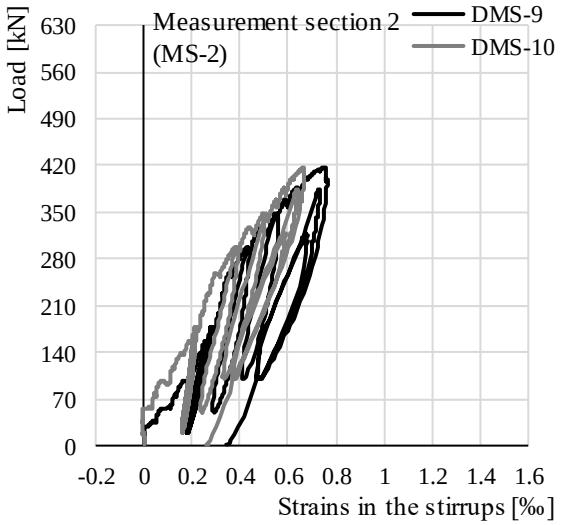


Fig. 6.51. Strains in the stirrups of beam/column specimen VT-1, measurement section 2 (MS-2).

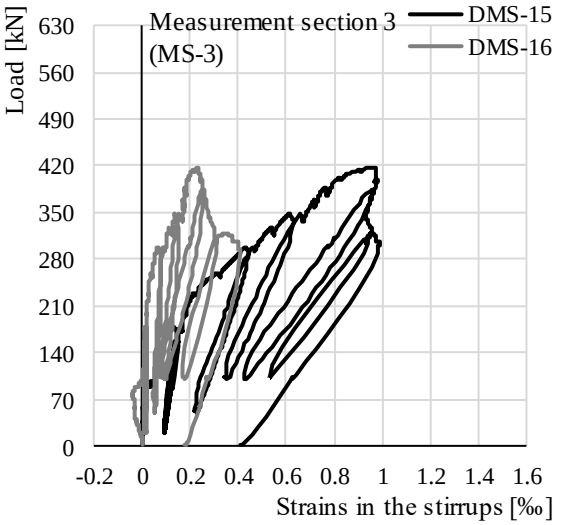


Fig. 6.52. Strains in the stirrups of beam/column specimen VT-1, measurement section 3 (MS-3).

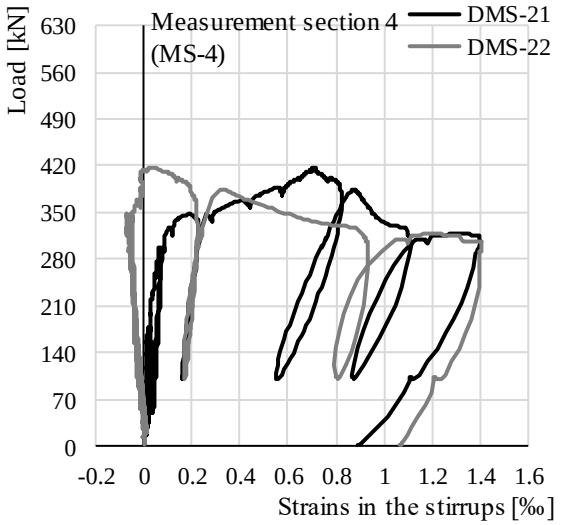


Fig. 6.53. Strains in the stirrups of beam/column specimen VT-1, measurement section 4 (MS-4).

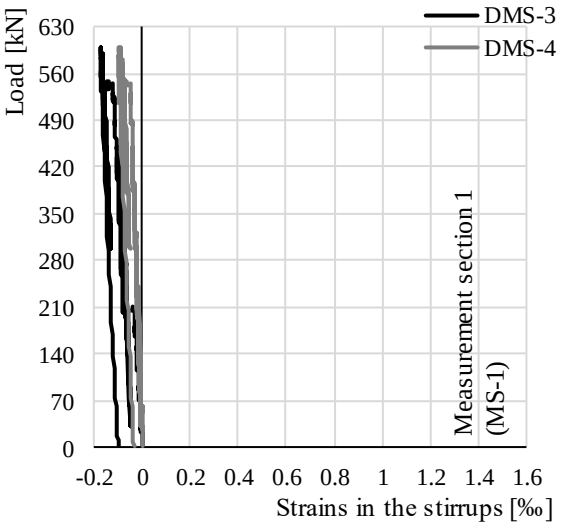


Fig. 6.54. Strains in the stirrups of beam/column specimen VT-2, measurement section 1 (MS-1).

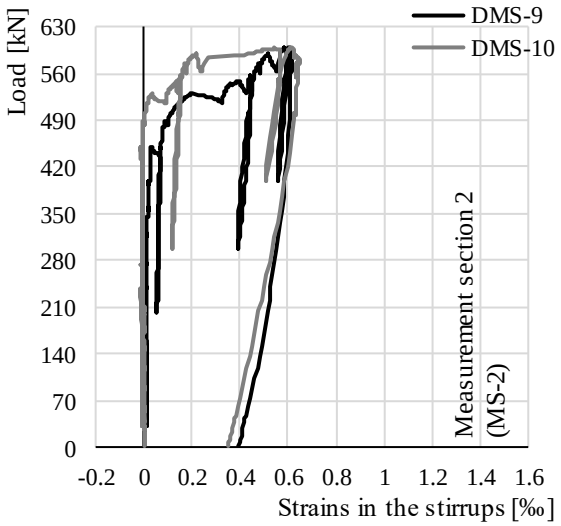


Fig. 6.55. Strains in the stirrups of beam/column specimen VT-2, measurement section 2 (MS-2).

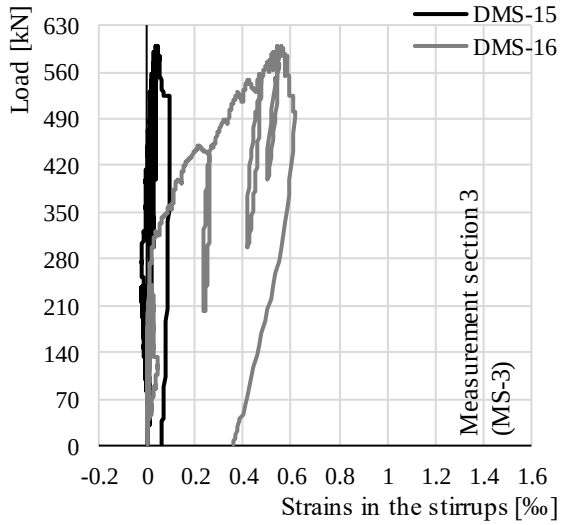


Fig. 6.56. Strains in the stirrups of beam/column specimen VT-2, measurement section 3 (MS-3).

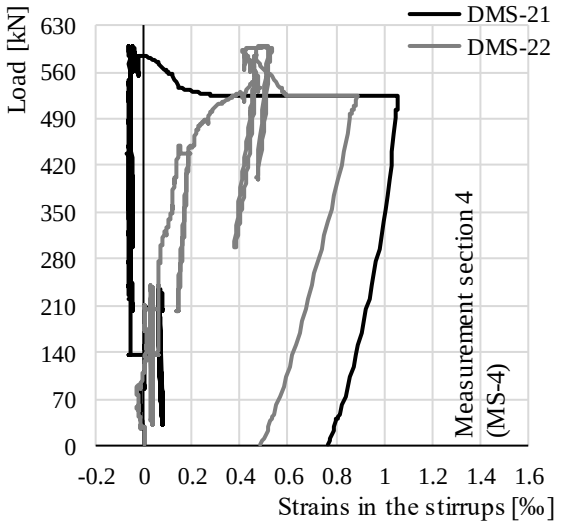


Fig. 6.57. Strains in the stirrups of beam/column specimen VT-2, measurement section 4 (MS-4).

Data from Fig. 6.50-6.57 is summarised in Table 6.9 below.

Table 6.9.
Strains in the shear reinforcement of beam/column specimens.

Specimen	Load	MS-1		MS-2		MS-3		MS-4	
		DMS-3	DMS-4	DMS-9	DMS-10	DMS-15	DMS-16	DMS-21	DMS-22
	[kN]	[‰]	[‰]	[‰]	[‰]	[‰]	[‰]	[‰]	[‰]
VT-1	417	-0.0537	-0.1252	0.7517	0.6656	0.9633	0.2303	0.7113	0.0375
	375	-0.0478	-0.1100	0.6133	0.5682	0.7374	0.1771	0.4743	-0.0186
	250	-0.0294	-0.0258	0.3429	0.2875	0.2794	0.0312	0.0438	-0.0505
	125	-0.0185	-0.0114	0.2171	0.1315	0.0559	0.0070	0.0067	-0.0279
VT-2	598	-0.1714	-0.0976	0.6047	0.6160	0.0404	0.5604	-0.0640	0.5114
	538	-0.1223	-0.0480	0.3454	0.1093	0.0159	0.4075	-0.0652	0.4379
	360	-0.0852	-0.0324	0.0149	-0.0090	-0.0077	0.0883	-0.0671	0.1173
	179	-0.0302	-0.0171	-0.0022	0.0031	-0.0195	0.0276	0.0041	0.0048

Strains recorded in the lateral arms of stirrups – the closing parts of stirrups at the bottom and on the top, for example DMS-7 and DMS-8 in Fig. 6.16 and Fig. 6.17, indicated the level of pressure that the steel profile imposed on the external concrete encasement. With this information, a simultaneous secondary lateral force dispersion mechanism can be investigated and the hogging or sagging bending character of the zones in specimens can be analysed. The recorded data from tests is shown in Fig. 6.58 for the specimen VT-1 and in Fig. 6.60 for the specimen VT-2. The overview on the resulting distribution of strains in the measurement sections is given in Fig. 6.59 and Fig. 6.61 for the specimen VT-1 and VT-2 respectively. The peak of strains that was measured by DMS-19 for both, specimen VT-1 and VT-2, resulted from the fact that the stirrups were localised in the zone of high compression stresses in concrete. Thus, the high value of recorded strains was a result of the local lateral expansion of concrete due to the extensive concrete cracking and spalling. Moreover, the longitudinal reinforcement bars buckled in the mid-zone due to the compression forces developed in the top part of specimens. This additionally impose tensile stresses in the top parts of stirrups, which held the longitudinal bars.

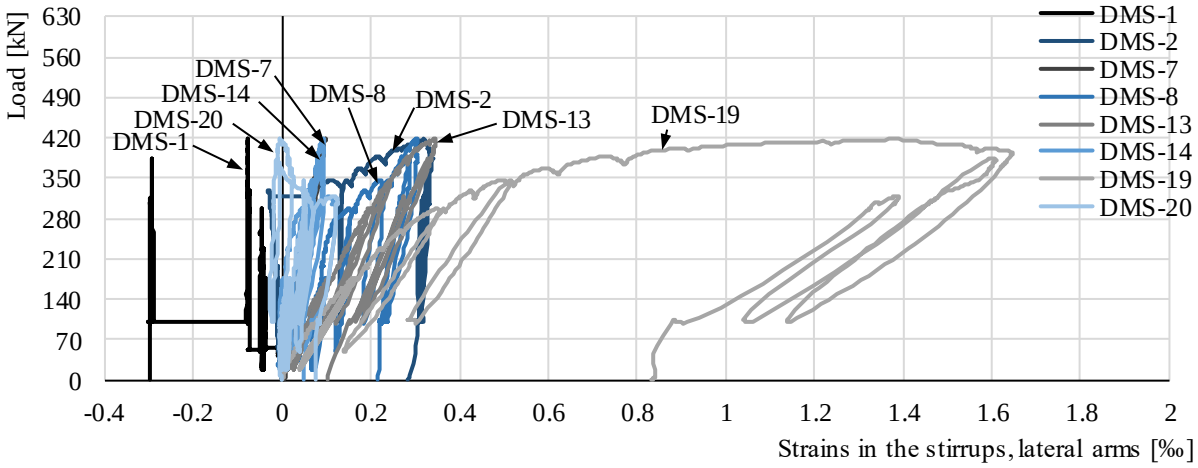


Fig. 6.58. Strains in the lateral arms of stirrups in the beam/column specimen VT-1.

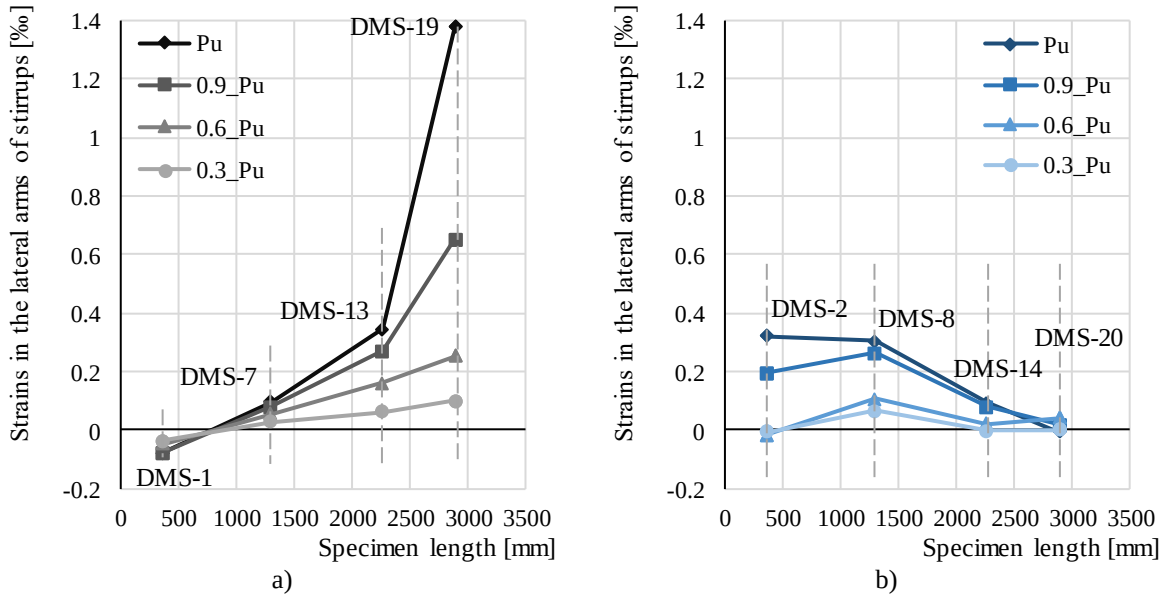


Fig. 6.59. Distribution of strains in the lateral arms of stirrups in the beam/column specimen VT-1 – a) on the top and b) on the bottom.

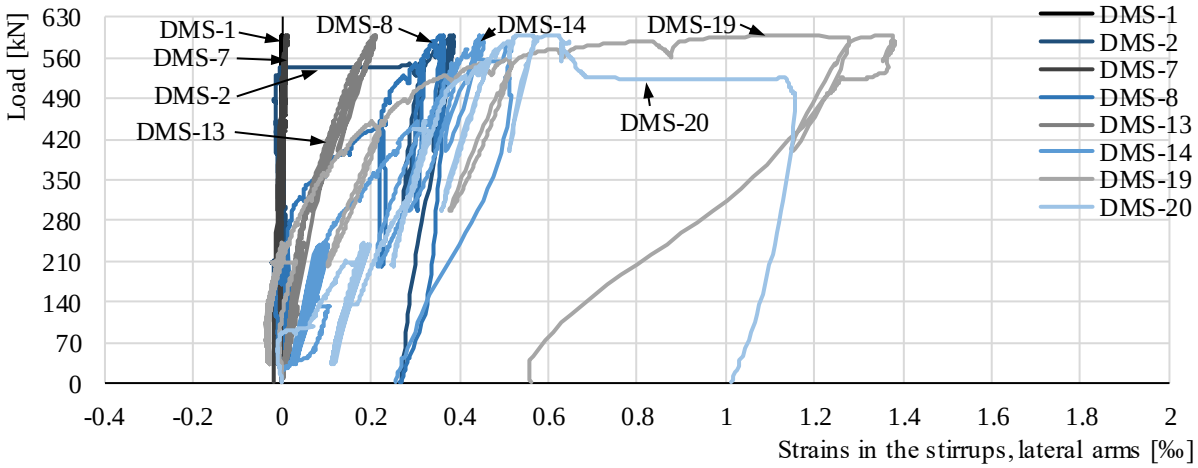


Fig. 6.60. Strains in the lateral arms of stirrups in the beam/column specimen VT-2.

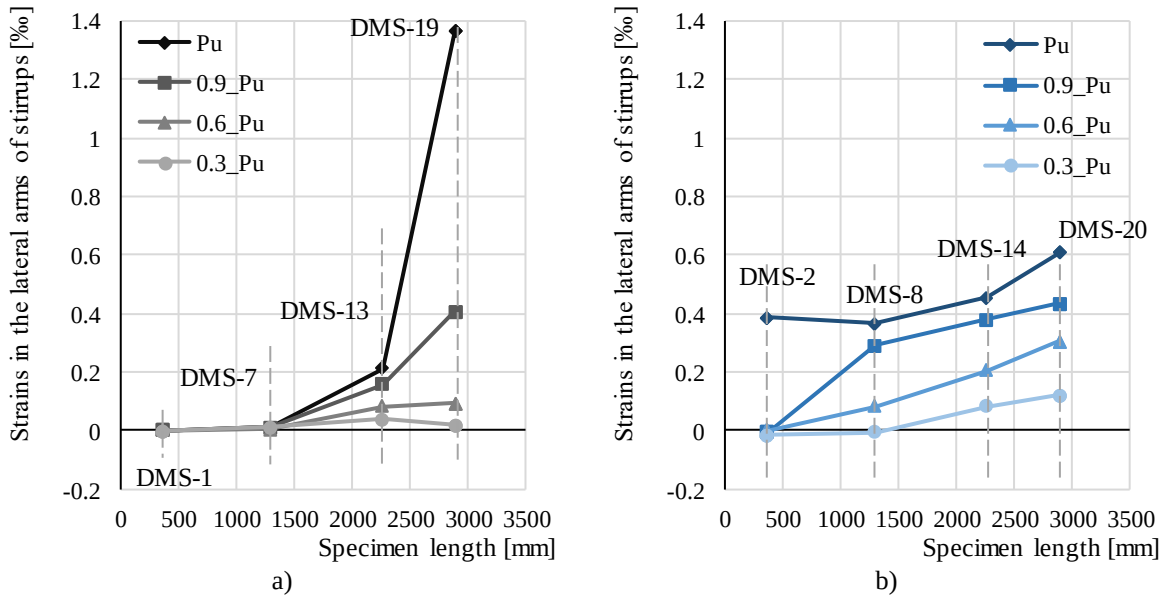


Fig. 6.61. Distribution of strains in the lateral arms of stirrups in the beam/column specimen VT-2 – a) on the top and b) on the bottom.

6.3.5.4. Recorded slip of the steel profiles

The relative slip of steel profiles against concrete was measured by the set of linear variable displacement transducers localised at the end of each embedded steel profile and at the point 1100 mm away from the mid-span. The considered displacement transducers have been numbered DT-11 to DT-22, where their arrangement is shown in Fig. 6.14 and listed in Table 6.3. Sensors DT-11 to DT-18 were fixed with plastic clamps to supporting bars welded to the webs of steel profiles and pointed towards concrete surface. Sensors DT-19 to DT-22 were fixed with plastic clamps to supporting bars anchored to the concrete surface and pointed towards reference points welded to the flanges of steel profiles. More details about sensors placement is given in Annex E. By measuring the slip of steel profiles at not only their ends but also at intermediate points, a rough assessment of the distribution and development of the relative slip over the embedded length was made. The analysis of relative slip verifies the development of composite action in tested beam/column specimens and proves the applicability of used flat shear connectors. Records from the tests are shown in Fig. 6.62-6.65 for the specimen VT-1 and in Fig. 6.66-6.69 for the specimen VT-2.

The comparison of relative slips on the upper and lower steel profiles embedded in the concrete shows that the upper steel profile slid away from the concrete, where the lower steel profile slid inside. The identified behaviour is typical for the steel-concrete composite structural elements in bending. It can be observed that the upper steel profile had undergo nearly no slip and in both specimens, the slip value was smaller than 0.1 mm. The lower embedded steel profile had experienced a not significant relative slip and the values of end-slip at peak load reached 1.43 mm for the specimen VT-1 and 1 mm for the specimen VT-2. The recorded slip values of embedded steel profiles are given in Table 6.10.

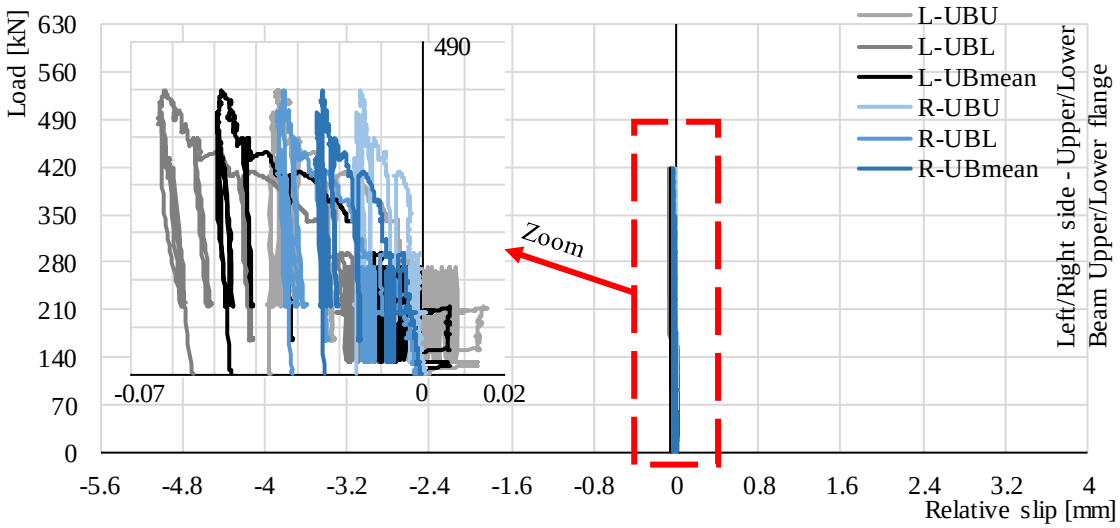


Fig. 6.62. Load-end slip curves in the beam/column specimen VT-1, upper beam.

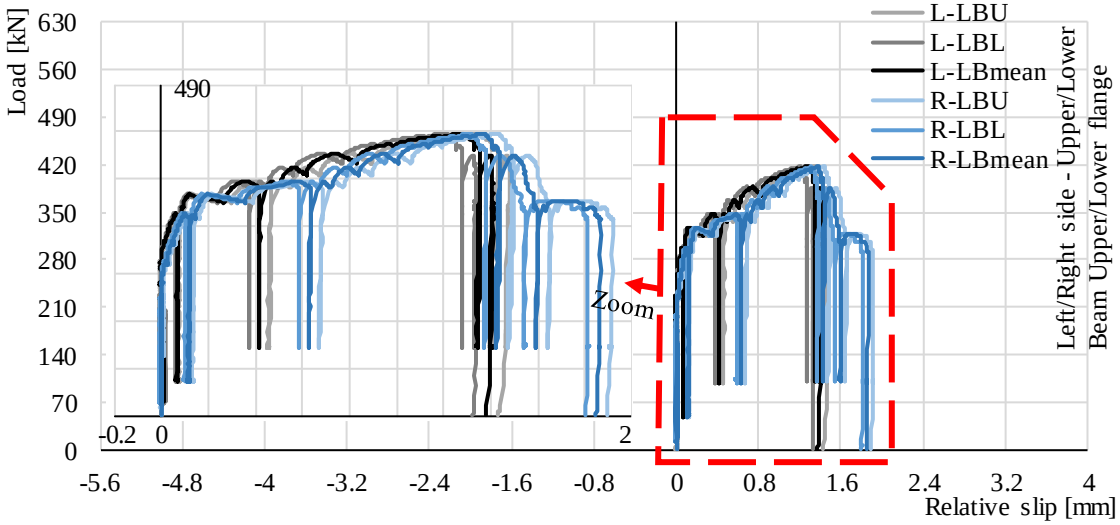


Fig. 6.63. Load-end slip curves in the beam/column specimen VT-1, lower beam.

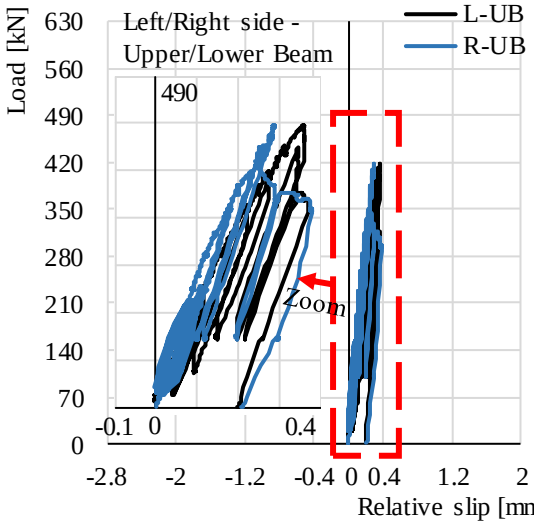


Fig. 6.64. Load-mid slip curves in the beam/column specimen VT-1, upper beam.

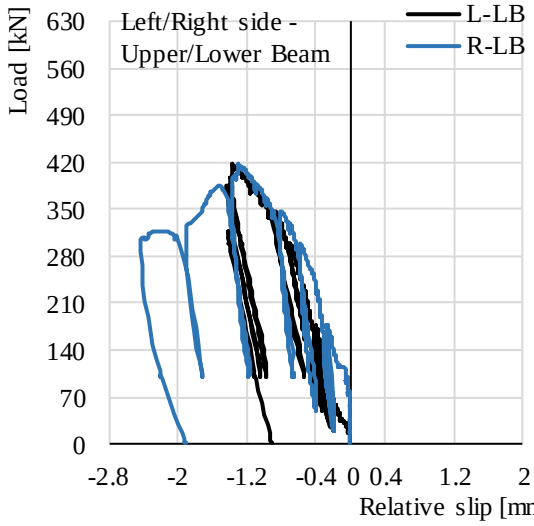


Fig. 6.65. Load-mid slip curves in the beam/column specimen VT-1, lower beam.

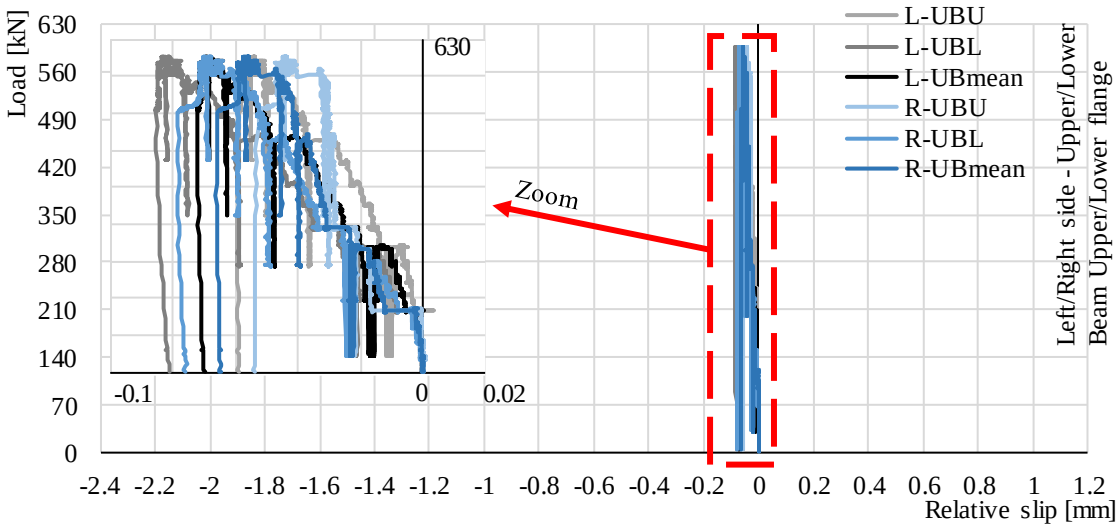


Fig. 6.66. Load-end slip curves in the beam/column specimen VT-2, upper beam.

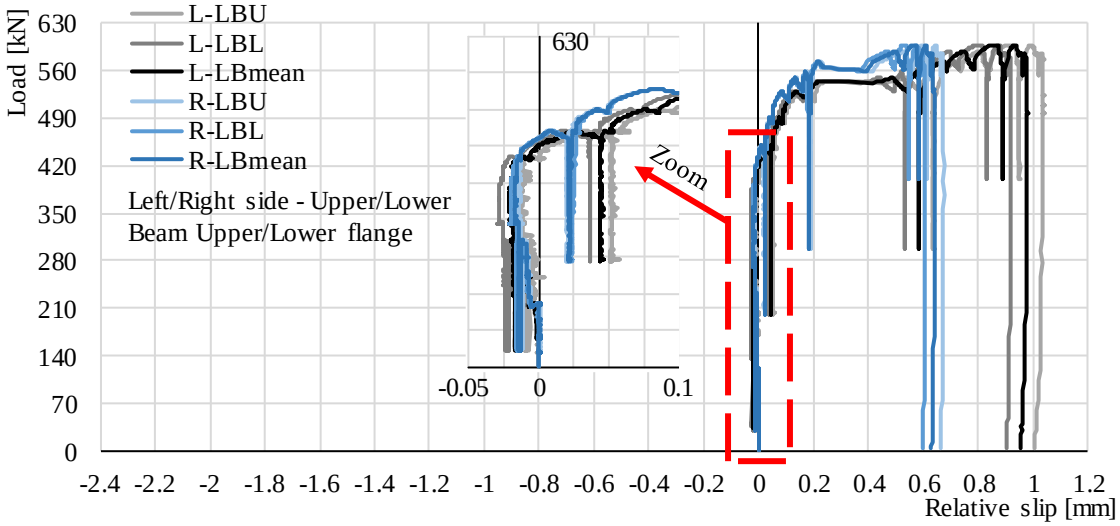


Fig. 6.67. Load-end slip curves in the beam/column specimen VT-2, lower beam.

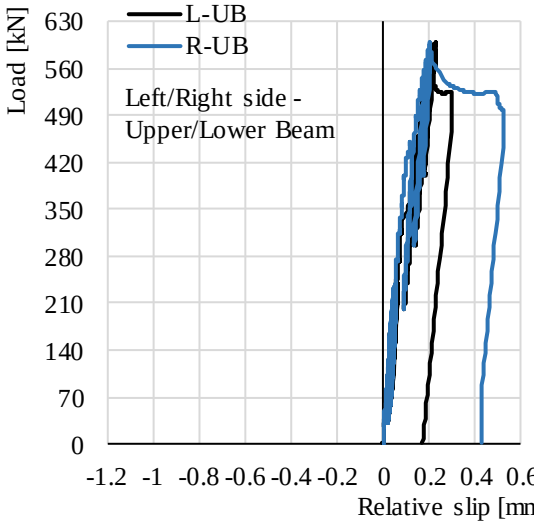


Fig. 6.68. Load-mid slip curves in the beam/column specimen VT-2, upper beam.

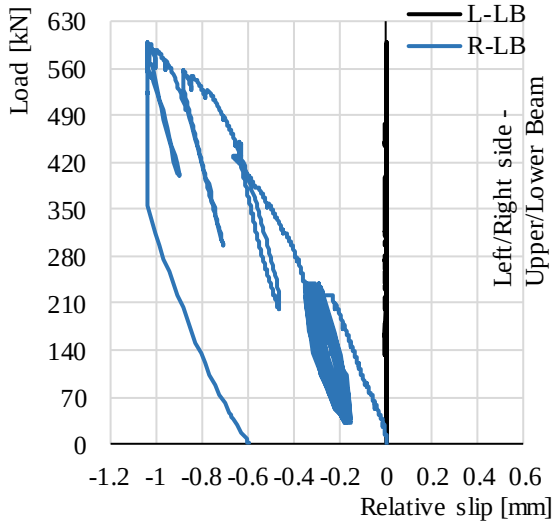


Fig. 6.69. Load-mid slip curves in the beam/column specimen VT-2, lower beam.

Table 6.10.
Relative slip of the embedded steel profiles in beam/column specimens.

Specimen	Load	End-slip								Mid-slip			
		Upper steel profile				Lower steel profile				Up profile		Low profile	
		L-UBU	R-UBU	L-UBL	R-UBL	L-LBU	R-LBU	L-LBL	R-LBL	L-UB	R-UB	L-LB	R-LB
	[kN]	[mm]											
VT-1	MAXs	-0.04	-0.02	-0.06	-0.03	1.48	1.92	1.34	1.82	0.37	0.38	-1.43	-2.43
	417	-0.03	-0.01	-0.06	-0.03	1.35	1.43	1.20	1.31	0.36	0.29	-1.37	-1.29
	375	-0.03	-0.01	-0.06	-0.03	0.70	0.92	0.59	0.81	0.30	0.26	-1.07	-1.03
	250	-0.01	0.00	-0.03	-0.02	0.01	0.05	0.00	0.03	0.18	0.14	-0.58	-0.42
	125	0.01	0.00	-0.01	-0.01	0.01	0.01	-0.01	0.00	0.08	0.08	-0.31	-0.16
VT-2	MAXs	-0.06	-0.05	-0.09	-0.08	1.04	0.68	0.92	0.61	0.30	0.52	0.00	-1.04
	598	-0.06	-0.04	-0.08	-0.07	1.00	0.65	0.88	0.58	0.23	0.20	0.00	-1.04
	538	-0.05	-0.03	-0.07	-0.06	0.22	0.12	0.18	0.11	0.18	0.17	0.00	-0.81
	360	-0.02	-0.03	-0.04	-0.04	-0.01	-0.01	-0.03	-0.02	0.11	0.08	0.00	-0.51
	179	0.00	-0.02	-0.01	-0.01	0.00	-0.01	-0.01	-0.01	0.04	0.04	0.00	-0.18

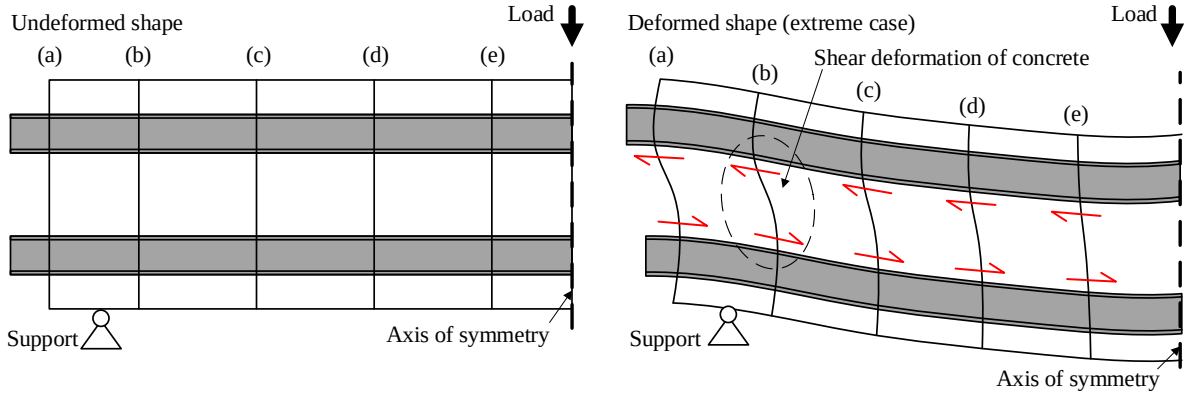
L/R-UBU – Left/Right side – Upper Beam Upper flange
L/R-UBL – Left/Right side – Upper Beam Lower flange
L/R-LBU – Left/Right side – Lower Beam Upper flange
L/R-LBL – Left/Right side – Lower Beam Lower flange
L/R-UB – Left/Right side – Upper Beam
L/R-LB – Left/Right side – Lower Beam
MAXs – maximum recorded slip value from the sensor

Values indicated in Table 6.10 are rounded to two decimal places. However, values below 0.1 mm shall not be respected due to the tolerance of measurement equipment. Based on the aforementioned remark, it can be assumed that the upper embedded steel profile had not experienced any slip and full shear connection was assured. At the load level close to the peak load, a small amount of slip developed in the mid-span of the upper embedded steel profile due to the global failure of the specimen, concrete cracking and damage at the steel-concrete interface.

6.3.6. Observed failure patterns

Tested beam/column specimens VT-1 and VT-2 were subjected to bending and shear due to the applied test layout given in Fig. 6.2. The predicted failure modes of specimens in the elastic analysis, as shown in Fig. 6.7 and Fig. 6.8, gave good correlation to the failure modes obtained from the tests. Both specimens failed due to the concrete compression in bending at the mid-span. The existence of two embedded steel profiles in each specimen affected the global failure mechanism. In the result, the pure bending failure was only observed in the mid-zone of specimens and the bending-shear failure developed in the zones close to the supports. The presence of stiff steel profiles in reference to the weaker surrounding concrete amplified the shear failure effect. Between the embedded steel profiles, the transfer of forces occurred due to the assured shear connection at the steel-concrete interface – this aspect is discussed more in detail later in Section 6.3.7. Thus, the concrete localised in the aforementioned transition zone was subjected not only to bending but also to significant shear forces. The observed shear failure symptoms in the zones close to the supports, major diagonal cracks and minor horizontal cracks at the concrete surfaces, it can be deducted that the shear deformation developed in the concrete between

the embedded steel profiles. This conclusion is supported by the observations about the level of the assured shear connection at the steel-concrete interface and the principle of composite action described in Section 3.1. The schematic representation of aforementioned shear deformation effect on the tested beam/column specimens is shown in Fig. 6.70 as the deformation of lines (a-e). The shear deformation cannot be directly observed from the visual examination of tested specimens due to too high stiffness of the concrete. This aspect is discussed later in Section 6.3.7. From Fig. 6.50-6.57, it can be observed that no yielding of stirrups occurred, thus, the diagonal cracking of concrete was not related to the elongation of the reinforcement bars. Moreover, the progressing bending damage, from the mid-span towards the supports, was restrained by the activated steel profiles and the shear failure started to be dominant in the zones closer to the supports due to the resulting shear deformation of specimens.



a) b)

Fig. 6.70. Shear deformation scheme of the tested beam/column specimens – a) undeformed shape and b) deformed shape.

The visual examination of tested specimens confirms the observations from Fig. 6.62-6.69 and Table 6.10 about the relative slip. The behaviour of both specimens respected the full composite action during the tests and no slip was visually observed. Moreover, no damage at the external surfaces of the specimens developed due to the failure of shear connection. The above-mentioned facts state, that the applied novel flat shear connectors described in Section 5.4 worked efficiently in the tested beam/column specimens and their applicability in the beam-type tests was proven.

The above-described failure pattern of tested specimens was analysed in detail for each tested specimen. To investigate the developed failure patterns, the specimens were opened with the usage of the concrete saw in order to reveal the embedded steel profiles. Moreover, to investigate crucial points for the investigation, like for example concrete around the applied shear connector, additional cuts in the specimen were done. The scheme of the opening of specimens is shown in Fig. 6.71.

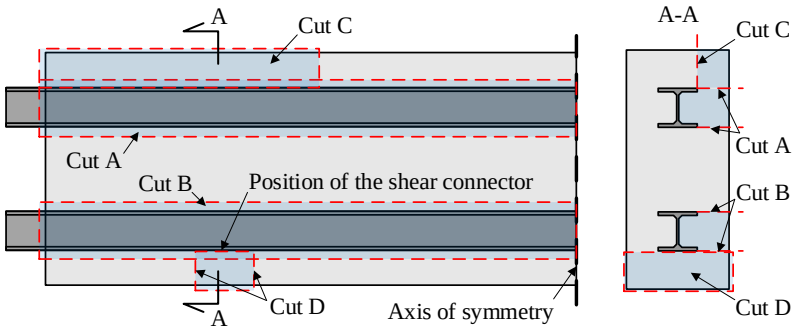


Fig. 6.71. Opening scheme of the beam/column specimens.

6.3.6.1. Specimen VT-1 with the small distance between steel profiles

The failure pattern of specimen VT-1 can be summarised in the following sequence: (1) the development of vertical tensile cracks at the bottom of specimen due to bending at the loads smaller than the peak load, (2) the development of diagonal cracks in the zones close to the supports at the load close to the peak load but below it, (3) the progressing vertical tensile cracks and development of the zone of crushed concrete in the compression zone due to bending at the mid-span at the peak load, (4) the extensive concrete crushing in the compression zone at the mid-span and propagating vertical and diagonal cracks with accompanying load drop, (5) the significant concrete spalling in the concrete compression zone and significant vertical cracks in the tension zone at the mid-span. An example of the developed diagonal cracks during the test are shown in Fig. 6.72. In the specimen VT-1, it has been observed that the diagonal cracks were less significant than in the specimen VT-2. A similar observation was done for the horizontal cracks. The developed concrete crushing zone in compression is shown in Fig. 6.73, where the fully formulated failure zone of concrete in compression with the concrete spalling is shown in Fig. 6.74. The development of vertical tensile cracks at the mid-span is shown in Fig. 6.75 and Fig. 6.76 for the state before reaching the peak load and after it, respectively.

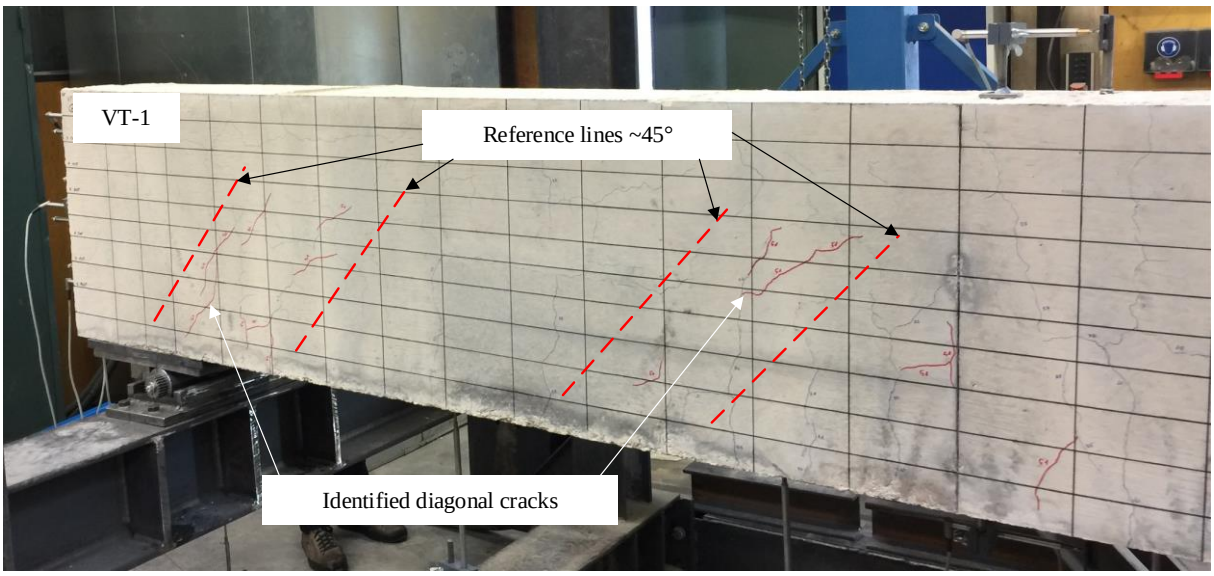


Fig. 6.72. Diagonal cracks in the beam/column specimen VT-1.

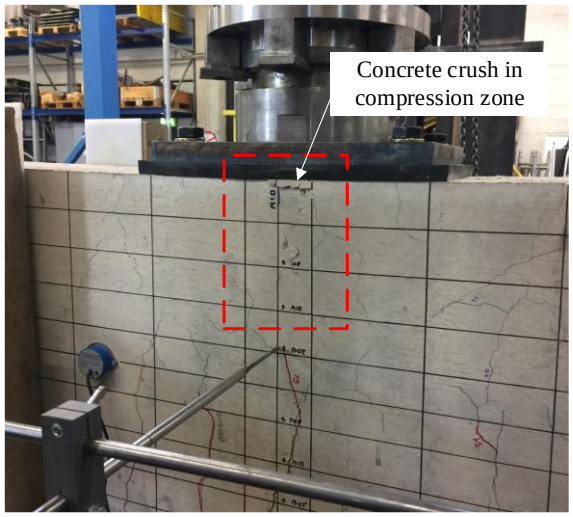


Fig. 6.73. Development of the concrete crush zone in compression of beam/column specimen VT-1.



Fig. 6.74. Concrete spalling in the compression zone of beam/column specimen VT-1.

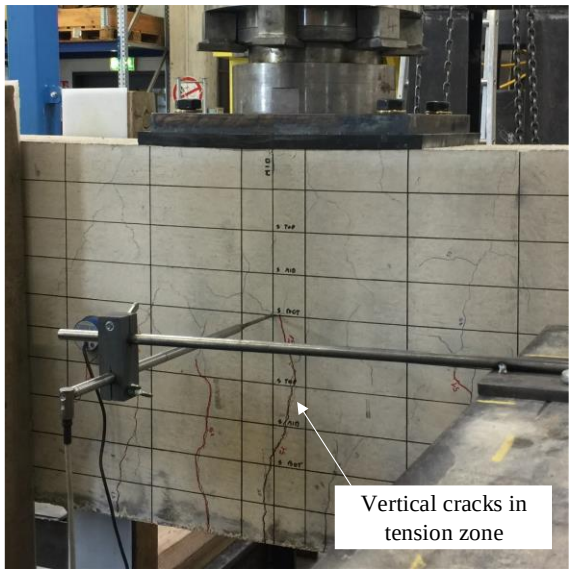


Fig. 6.75. Vertical cracks in the tension zone before the failure of beam/column specimen VT-1.

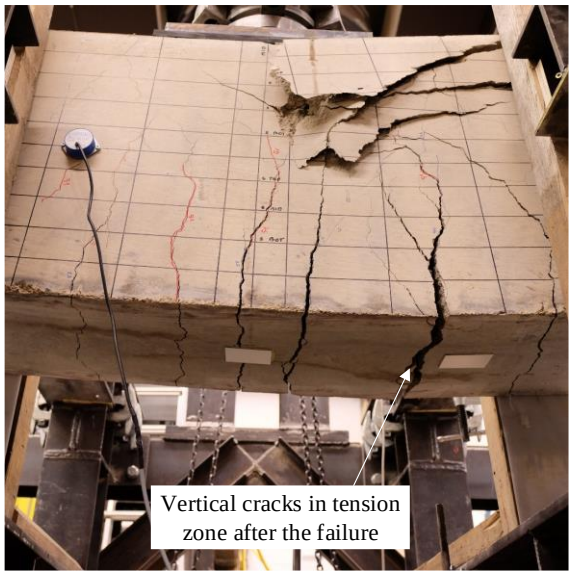


Fig. 6.76. Vertical cracks in the tension zone after the failure of beam/column specimen VT-1.

After the test, the specimen was removed from the testing frame and the separated parts of concrete were detached. Like this, the zone of concrete compression failure could be visually analysed. The overview on the tested specimen VT-1 is shown in Fig. 6.77 and Fig. 6.78 in the first plane. The central zone with pure bending failure pattern and the support zones with the bending-shear failure pattern can be distinguished. The diagonal and horizontal cracks in the support zones developed on each four sides of specimen. From the global deformation shape, it can be observed that the specimen plastified in the mid-span and the plastic hinge developed. The deformation of the side-parts of specimen is not directly visible after the test due to the rotational capacity of the aforementioned plastic hinge, which took over the total deformation.

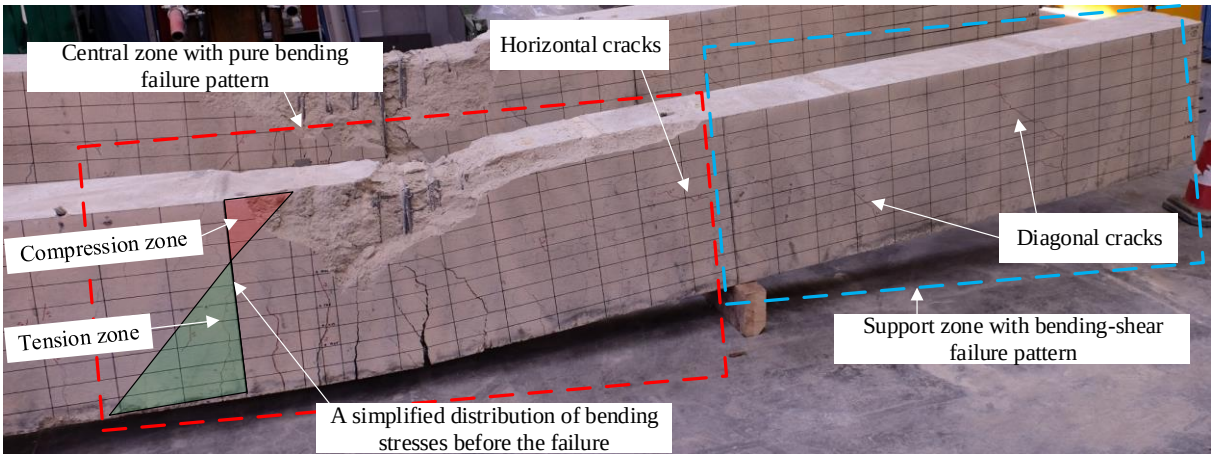


Fig. 6.77. A view on the tested beam/column specimen VT-1, south wall, right side.

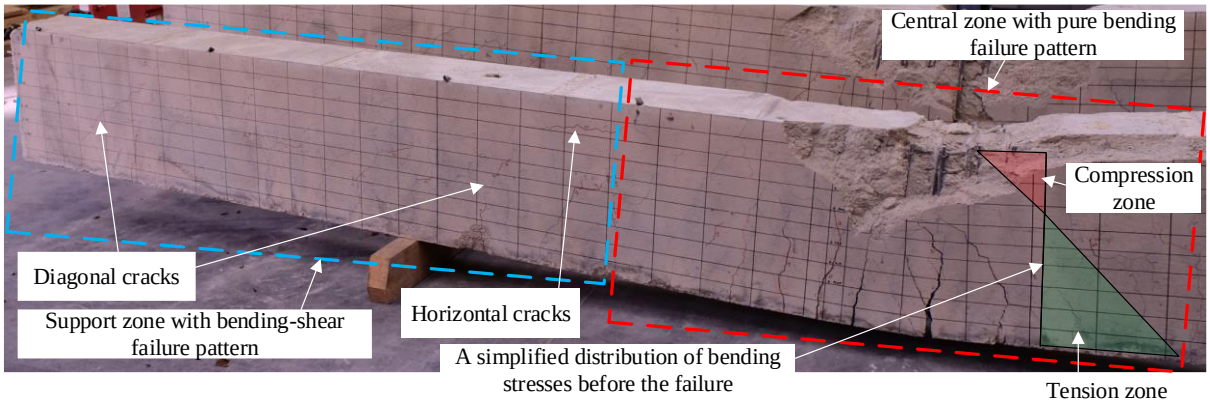


Fig. 6.78. A view on the tested beam/column specimen VT-1, south wall, left side.

Details of the compression zone are shown in Fig. 6.79-6.82. It can be observed that the concrete crushed over the total width of the specimen. The size of the compression zone reached approximately 240x700 mm in height and length. Due to the developed significant compression forces, the longitudinal reinforcement bars buckled despite existence of the anchoring transversal reinforcement bars. Deformed longitudinal reinforcement bars are visible in Fig. 6.81 and Fig. 6.82.

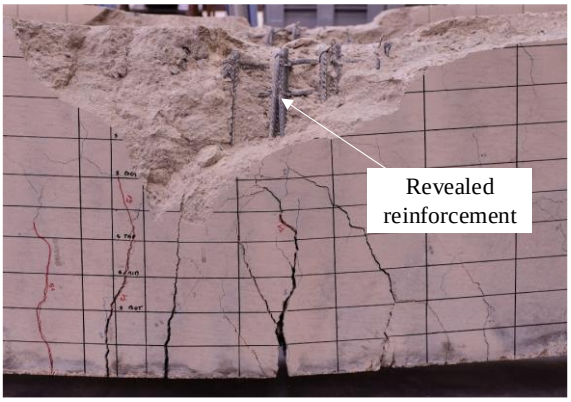


Fig. 6.79. Detail of compression failure zone in the beam/column specimen VT-1, south wall.

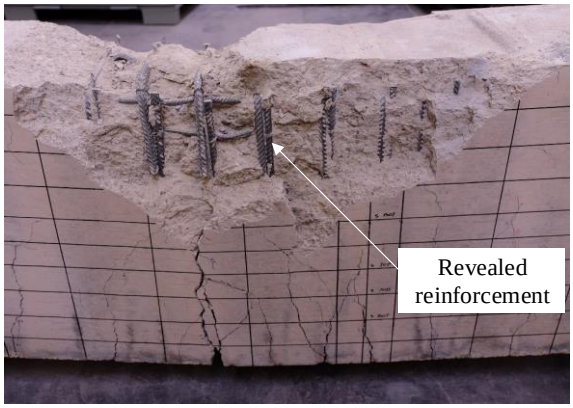


Fig. 6.80. Detail of compression failure in the beam/column specimen VT-1, north wall.



Fig. 6.81. Detail of compression failure in the beam/column specimen VT-1, top view.



Fig. 6.82. Detail of compression failure in the beam/column specimen VT-1, deformed reinforcement.

The specimen were opened according to the cutting planes defined in Fig. 6.71. The opening of specimen had four main objectives: (1) to reveal the deformation shape of steel profiles, (2) to investigate the conditions of steel-concrete interface, (3) to verify the damage of concrete around the shear connectors and (4) to investigate possible symptoms of the Vierendeel truss behaviour. The view on the revealed steel profiles shown in Fig. 6.83 indicates that the steel profiles followed the deformation of specimen and they deformed in the middle forming the plastic hinge, where the rest of steel profiles remains straight after the test. In Fig. 6.84 and Fig. 6.85, it is visible that the steel-concrete interface remained in the undamaged state. In order to investigate the resulting conditions around the applied flat shear connectors, the concrete was separated from the steel profile in the zone where the shear connector was applied according to cut D from Fig. 6.71. In Fig. 6.86 and Fig. 6.87, the revealed shear connector localised at the lower flange of lower steel profile is shown. The analysed shear connector was subjected to the maximal relative slip during the beam/column test and it was localised in the last row before the end of embedment length.

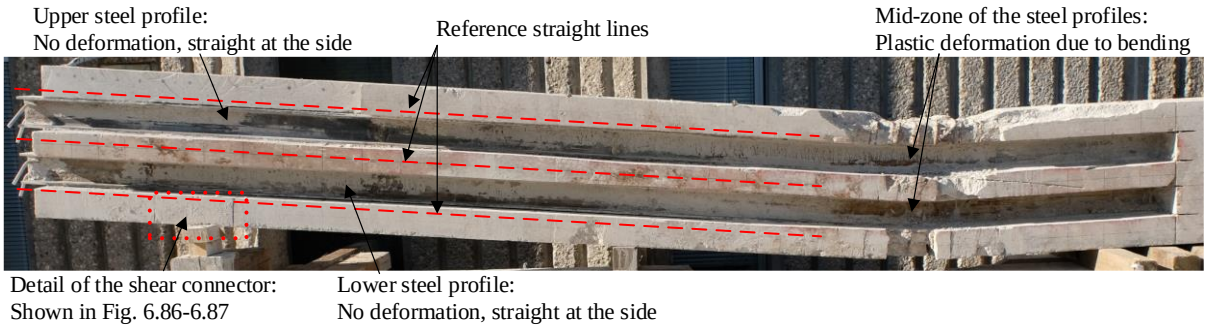


Fig. 6.83. Opened beam/column specimen VT-1 – view on the revealed steel profiles.



Fig. 6.84. Opened beam/column specimen VT-1 – steel-concrete interface next to the upper steel profile.



Fig. 6.85. Opened beam/column specimen VT-1 – steel-concrete interface next to the lower steel profile.

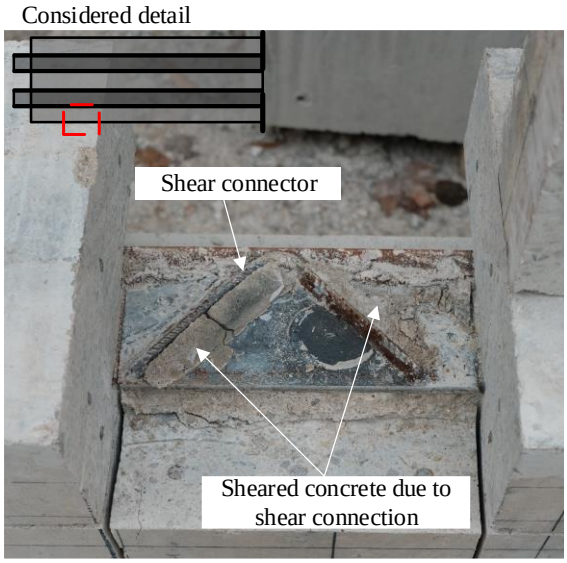


Fig. 6.86. Opened beam/column specimen VT-1 – detail of the flat shear connector.

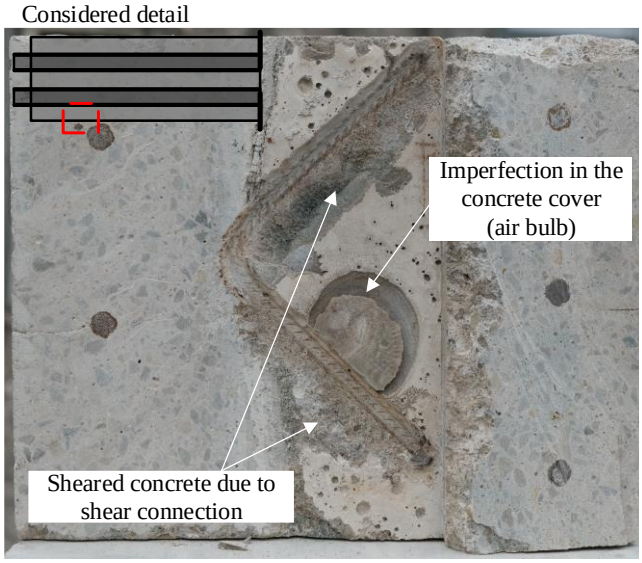


Fig. 6.87. Opened beam/column specimen VT-1 – concrete damage around the flat shear connector.

In Fig. 6.87, an imperfection in the concrete cover next to the shear connector was observed. However, the discovered air bulb was localised on the not directly bearing side of the shear connector arm. Thus, its existence had not affected the shear connector behaviour in reference to the observed level of damaged concrete around the shear connector. The sheared part of concrete localised directly next to the arms of the connector, see Fig. 6.86 and Fig. 6.87, is reflecting well the resistance model of flat shear connectors described in Section 5.6.5.6. Based on the identified above concrete damage around the shear connector, the level of developed relative slip in the specimen VT-1 and identified behaviour of the applied flat shear connectors, it can be concluded that the shear connector not reached its resistance. The developed inelastic slip was accompanied with the development of shear plane in the direction of

maximum shear flow. However, the developed failure is not affecting the further admissibility of the shear connectors due to the confinement of concrete.

The view on the opened top concrete encasement above the upper steel profile in the support zone is shown in Fig. 6.88. The cut was made according to the line C from Fig. 6.71. In Fig. 6.88, the vertical cracks can be observed in the revealed part of the concrete encasement. The identified cracks are not significant, besides the indicated zones. The observed cracks are in contradiction to the typical Euler-Bernoulli beam model, in which, the compression occurs in top fibres over the entire length of beam subjected to sagging bending. The presence of vertical cracks is proven also in numerical simulations, which is described later in Section 6.4. It can be concluded that a certain tensile stresses developed in the considered top support zone of concrete encasement. Due to the taken observations, a strong analogy can be identified with the Vierendeel truss model, where the contra-curvature (hogging bending) is present in the zones above to the support for the simple supported Vierendeel trusses subjected globally to sagging bending.

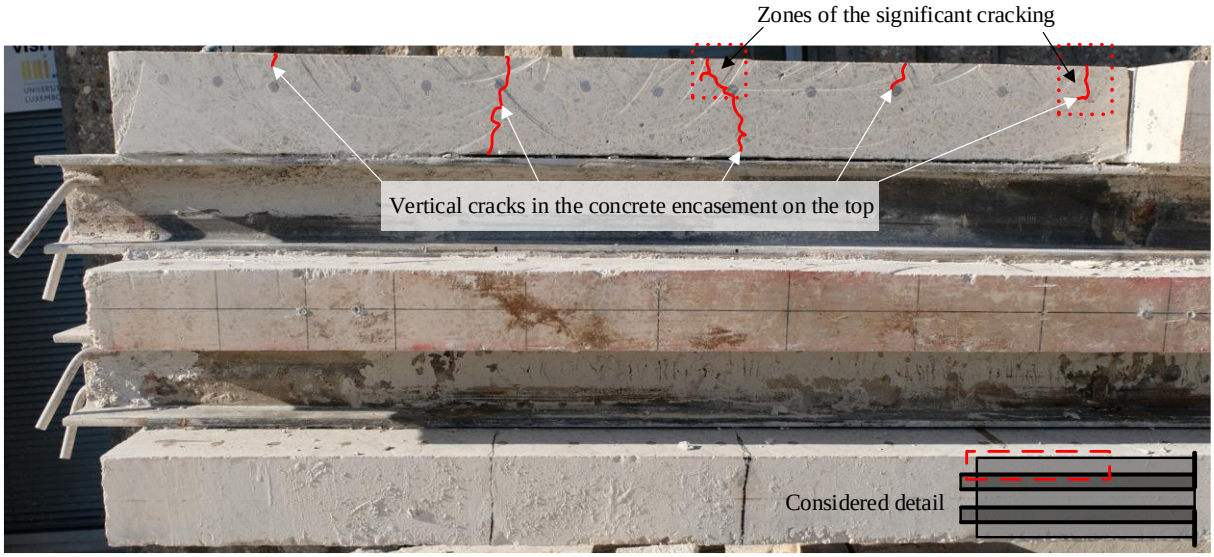


Fig. 6.88. Vertical cut through the top concrete encasement in the support zone of beam/column specimen VT-1.

6.3.6.2. Specimen VT-2 with the big distance between steel profiles

The failure pattern of specimen VT-2 was analogical to the failure pattern investigated in the specimen VT-1. The failure progressing sequence was identical, where the bending failure zone in the mid-span and the bending-shear failure zones close to the supports were present. The effects of shear forces and the shear deformation of specimen were more visible in the case of specimen VT-2 and they were accompanied by more significant diagonal and horizontal cracks in the support zone as shown in Fig. 6.89. The progressing damage of specimen in the mid zone due to bending was characterised by the development of vertical cracks in the tension zone and the concrete crushing in the compression zone. Both phenomena of tension and compression damage are shown in Fig. 6.90-6.93.

Similar like in the case of specimen VT-1, the specimen VT-2 was removed from the testing frame after the test and the separated parts of concrete were detached. This process allowed for the individual investigation of the zone of concrete compression failure. The overview on the tested specimen VT-2 is shown in Fig. 6.94, where the details of support and central zones are shown in Fig. 6.95 and Fig. 6.96. The central zone with pure bending failure pattern and the support zones with bending-shear failure pattern are indicated. From the global deformation shape, it can be observed that the specimen plastified in the middle analogically to the specimen VT-1. The deformation of specimen was related to the existence of plastic hinge developed during the test in the mid-span. In the result, outside the central zone, the specimen remained straight.

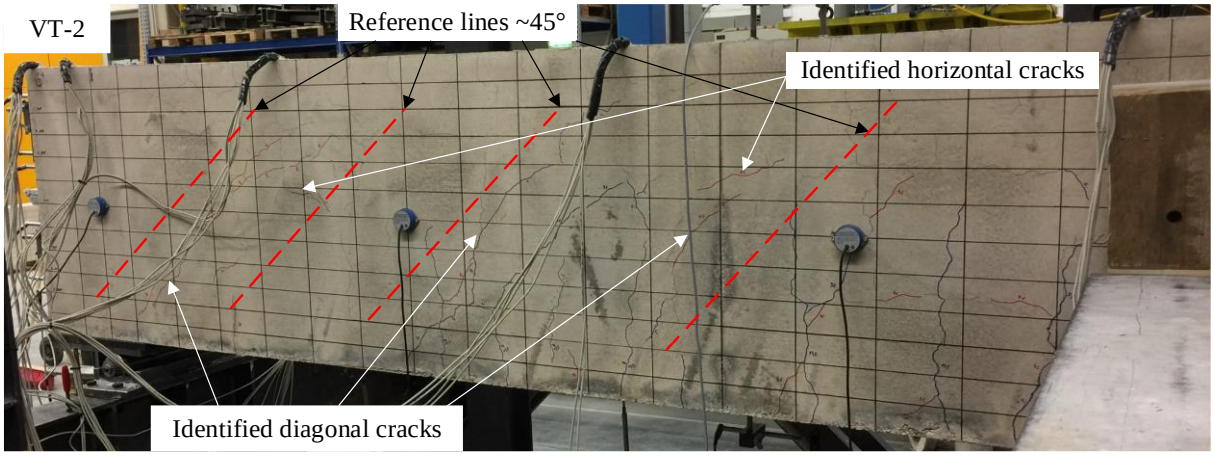


Fig. 6.89. Diagonal cracks in the beam/column specimen VT-2.

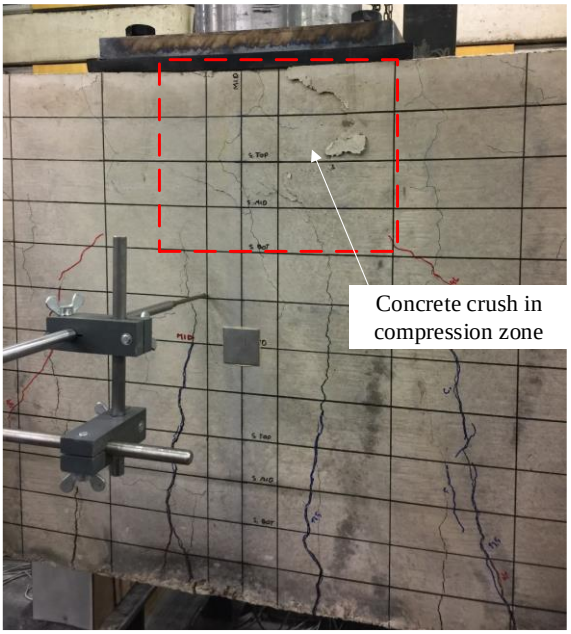


Fig. 6.90. Development of the concrete crush zone in compression of beam/column specimen VT-2.



Fig. 6.91. Concrete spalling in the compression zone of beam/column specimen VT-2.

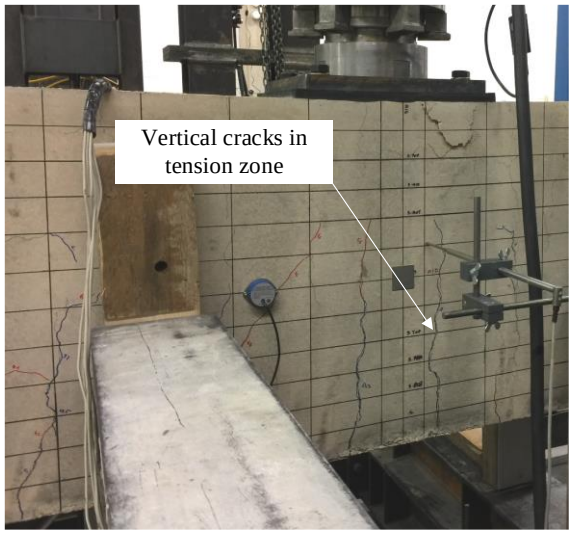


Fig. 6.92. Vertical tensile cracks in the tension zone at the failure of beam/column specimen VT-2.

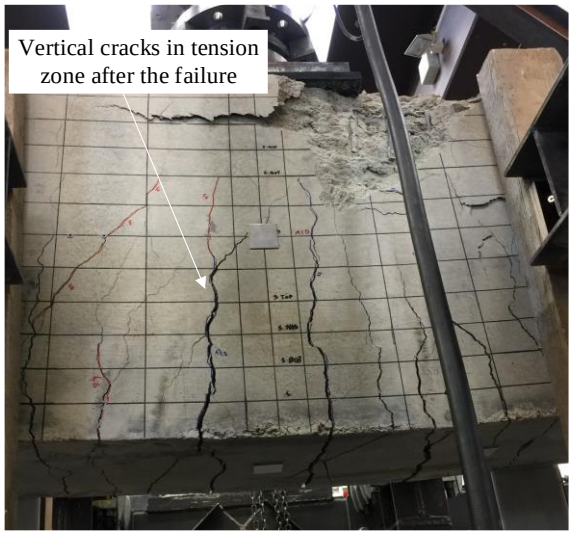


Fig. 6.93. Vertical cracks in the tension zone after the failure of beam/column specimen VT-2.

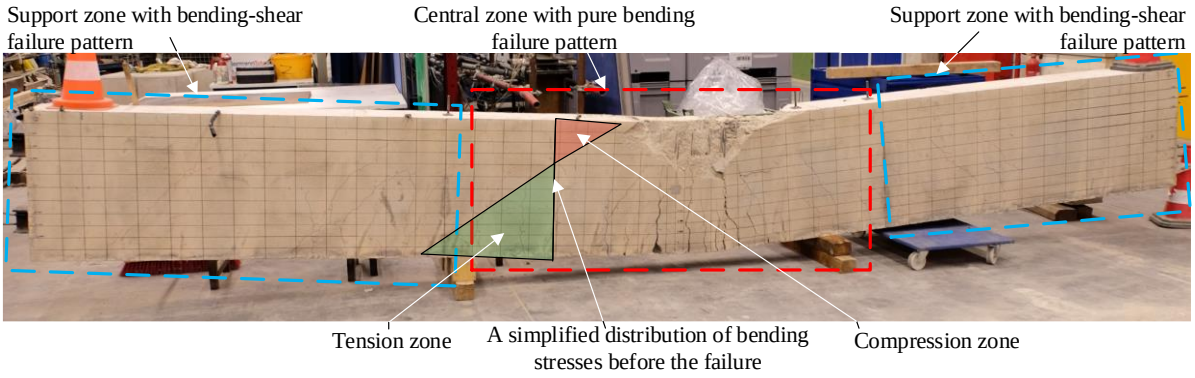


Fig. 6.94. View on the tested beam/column specimen VT-2, south wall.

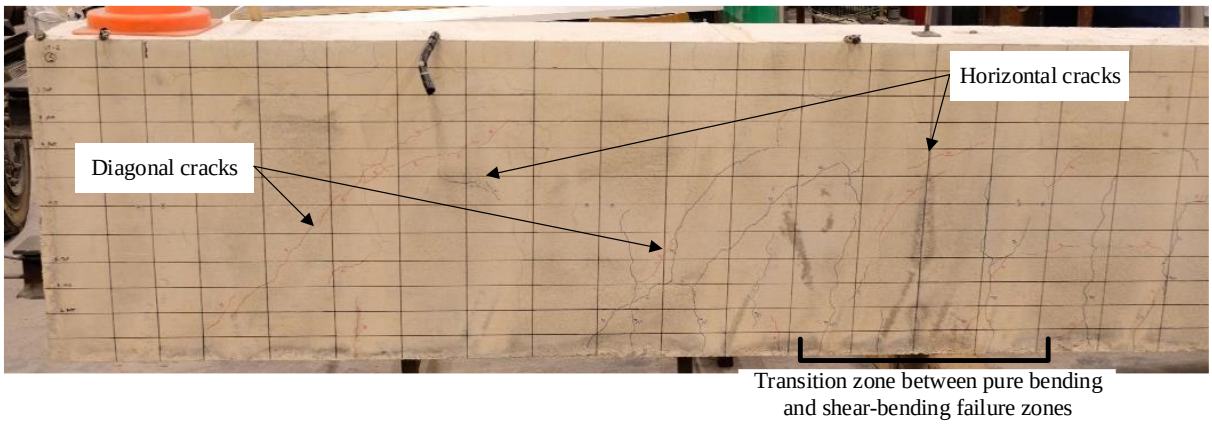


Fig. 6.95. Detail of the support zone of tested beam/column specimen VT-2.

From Fig. 6.96, it can be observed that the zone of concrete compression damage reached 300x1000 mm in size and it developed through the total width of the specimen. Similar like in the case of specimen VT-1, the significant compression forces resulted in the revealed reinforcement cage and buckled longitudinal reinforcement bars, as it is shown in Fig. 6.97.

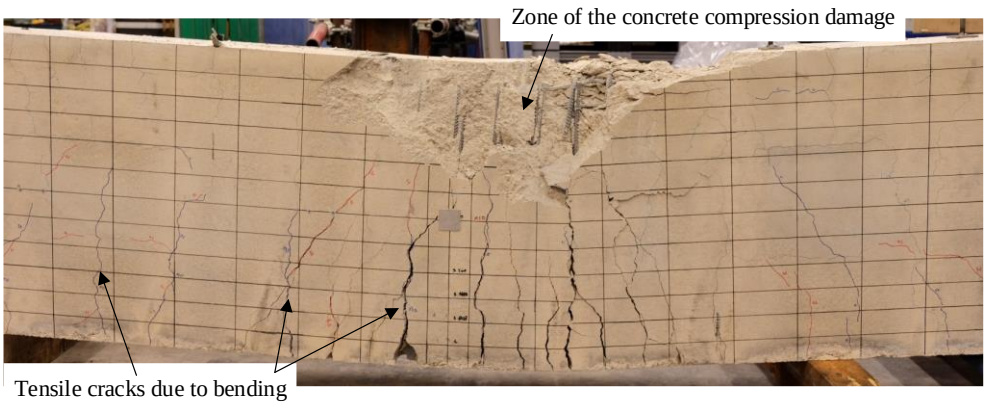


Fig. 6.96. Detail of the central zone of tested beam/column specimen VT-2.



a) b)

Fig. 6.97. Detail of the compression failure zone of tested beam/column specimen VT-2 – a) top view and b) buckled reinforcement.

The opened specimen VT-2 with revealed steel profiles is shown in Fig. 6.98. After the opening of specimen, the straightness of steel profiles in the support zones was checked with the usage of straight bar and line as shown in Fig. 6.99 and Fig. 6.100. Moreover, the state of steel-concrete interface was investigated and no damage was observed as shown in Fig. 6.101. Due to the high loads and big deformations, the examination of concrete around the shear connectors in the tensile zone at the mid-span was done. It was observed that no damage developed around the shear connectors and no normal separation developed at the interface. The revealed shear connector is shown in Fig. 6.102.

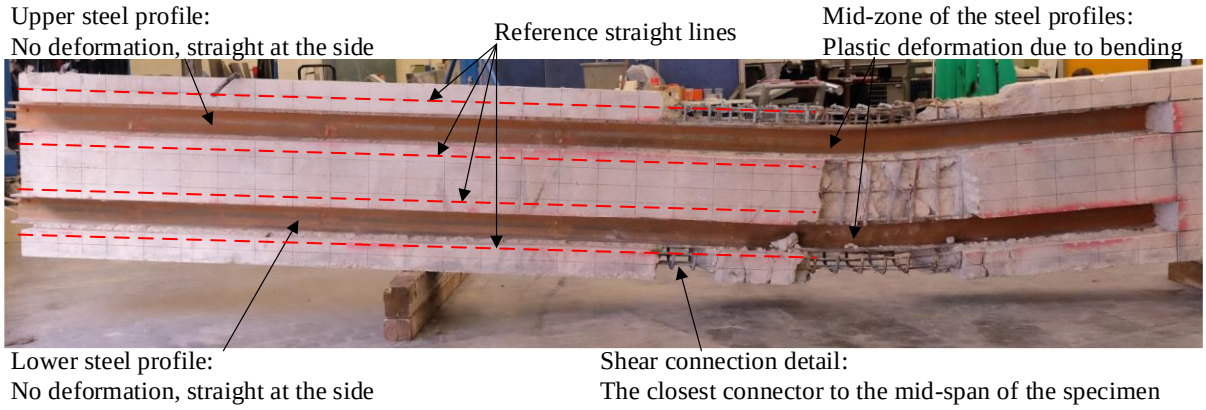


Fig. 6.98. Opened beam/column specimen VT-2 – view on the revealed steel profiles.

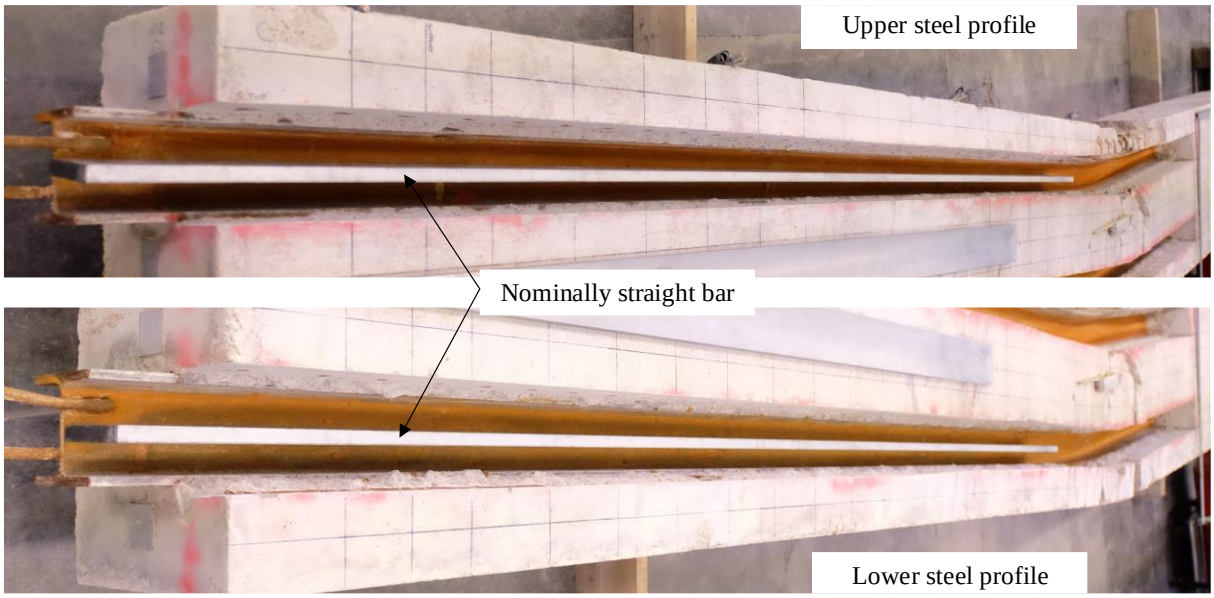


Fig. 6.99. Steel profiles in opened beam/column specimen VT-2 – method with a straight bar.

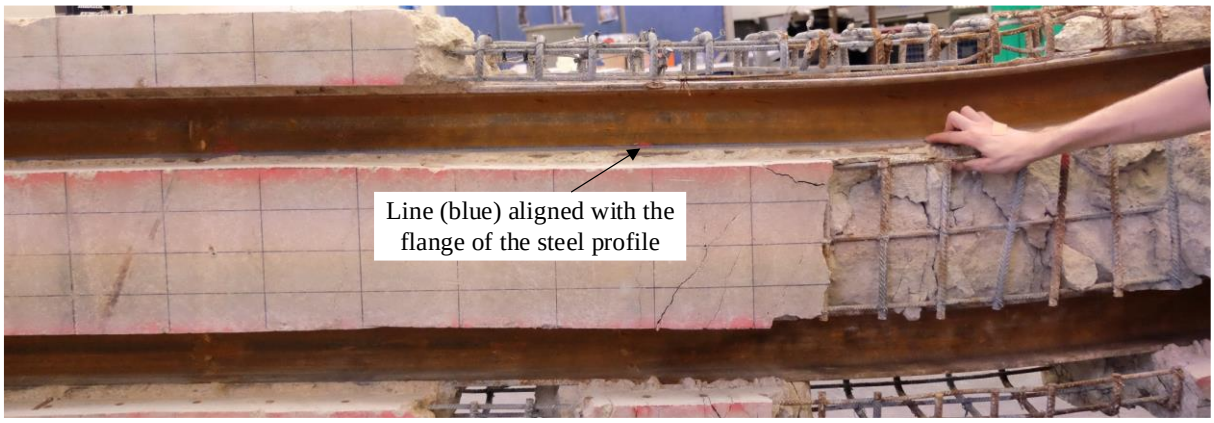
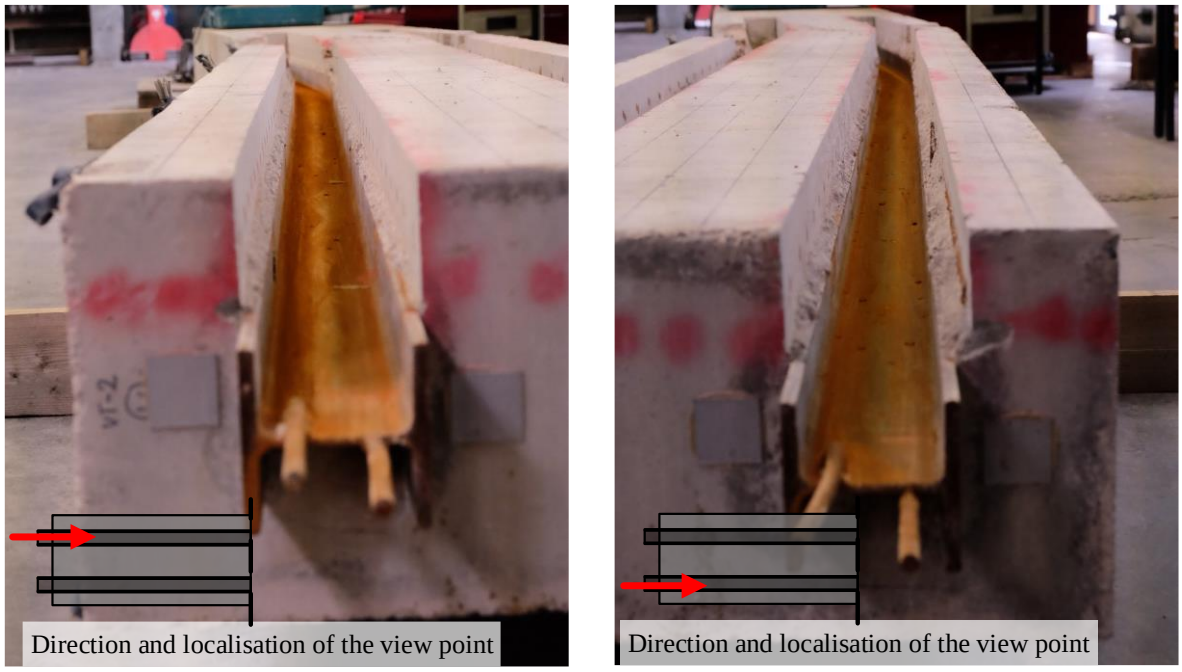
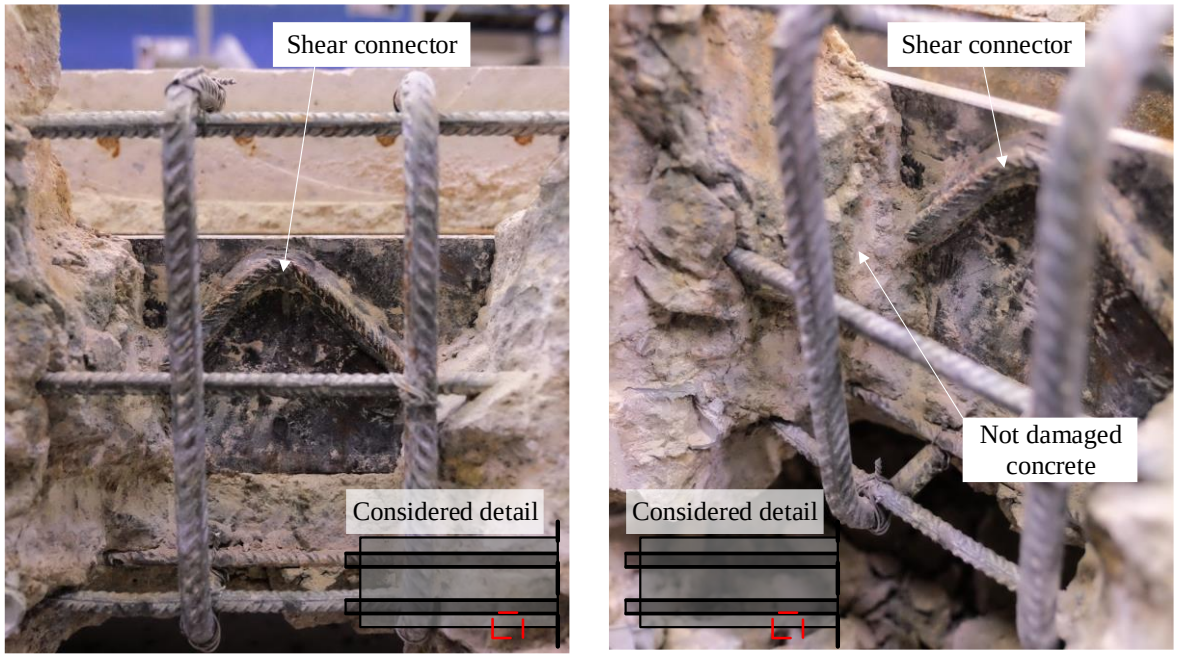


Fig. 6.100. Steel profiles in opened beam/column specimen VT-2 – method with a line.



a) b)

Fig. 6.101. Interface in the opened beam/column specimen VT-2 – a) upper steel profile and b) lower steel profile.



a) b)

Fig. 6.102. Examination of the concrete damage around the shear connector in the central zone of beam/column specimen VT-2 – a) view on the revealed shear connector and b) view on the concrete next to the connector in the outward direction.

Analogous to the specimen VT-1, the top concrete encasement, above the upper embedded steel profile in the support zone, was cut according to the line C from Fig. 6.71 and it is shown in Fig. 6.103. It can be observed that vertical cracks characteristic for the Vierendeel-like behaviour occurred and moved towards central part of the specimen VT-2 in comparison to the specimen VT-1. A clear analogy to the Vierendeel truss model can be observed, where tension in the top part of support zone occurs.

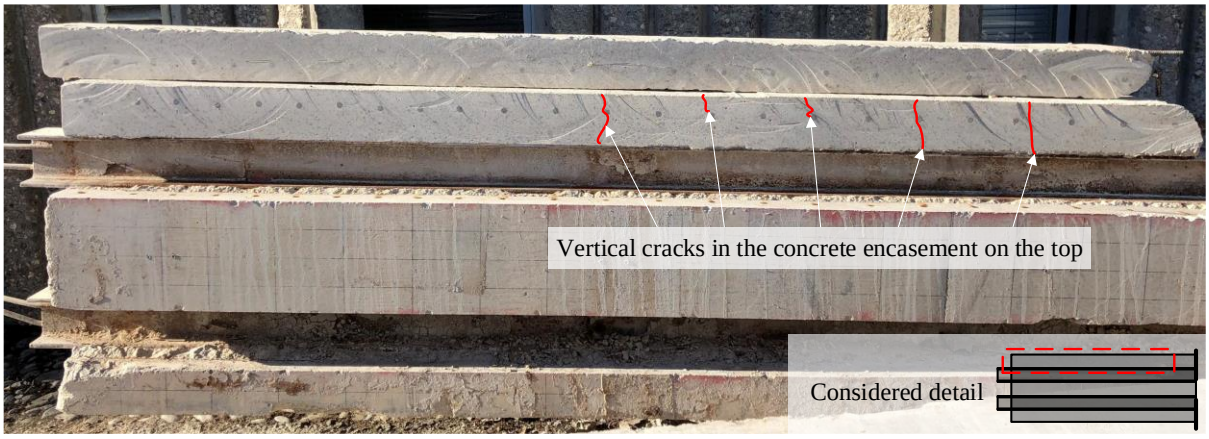


Fig. 6.103. Top concrete encasement in the support zone of beam/column specimen VT-2.

6.3.7. Discussion of the results

According to the test results from Section 6.3.5 and failure pattern revealed in Section 6.3.6, a specific behaviour of beam/column specimens was identified. In order to understand the observed phenomena, analyse the force flow and to investigate the resulting deformations, the previously presented test results are discussed and evaluated. The discussion is divided in the respective paragraphs.

Pre-design, longitudinal strains and bending resistance

In Fig. 6.7 and Fig. 6.8 of Section 6.2.3, the fibre method to evaluate the cross-sectional resistances of beam/column specimens according to the elastic strains distributions is shown. In the aforementioned strain distribution diagrams, the concrete compression strains at failure (3.5‰) were fixed and the equilibrium state was established. Based on the above and with respect to the used static system given in Fig. 6.2, the analysed cross-sections were subjected to the maximum bending moments at the mid-span. In the test campaign, no sensors were placed at the mid-span in order to avoid a big disturbance of measurements due to the damage zone. The measurement section MS-4 was localised in a distance of 360 mm from the centre. For the specimen VT-1, strains in the MS-4 in the longitudinal reinforcement bar on top were re-evaluated from the diagram given in Fig. 6.41 for DMS-23. In the aforementioned diagram, a non-realistic sudden offset of strains was observed. This effect related to an error of strain gauge during the test. The corrected diagram with an imposed offset of -0.00382 in strains is shown in Fig. 6.104. The comparison of the experimental and analytical values of longitudinal strains is shown in Fig. 6.105. In the measurement sections from the test results part, approximated strains were introduced and these strains are assumed based on the recorded values in order to maintain the linear strains distribution in the measurement sections. The approximated strains in the MS-4 showed similar values in comparison to the predicted values in the pre-design process.

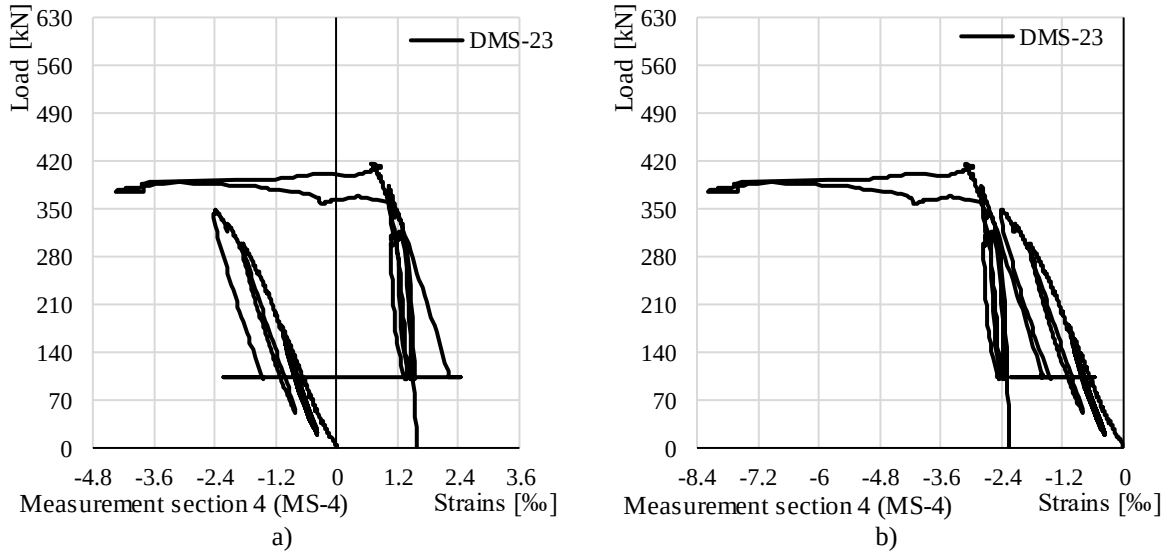


Fig. 6.104. Load-strain diagram for DMS-23 of beam/column specimen VT-1, MS-4 – a) initial record and b) modified record.

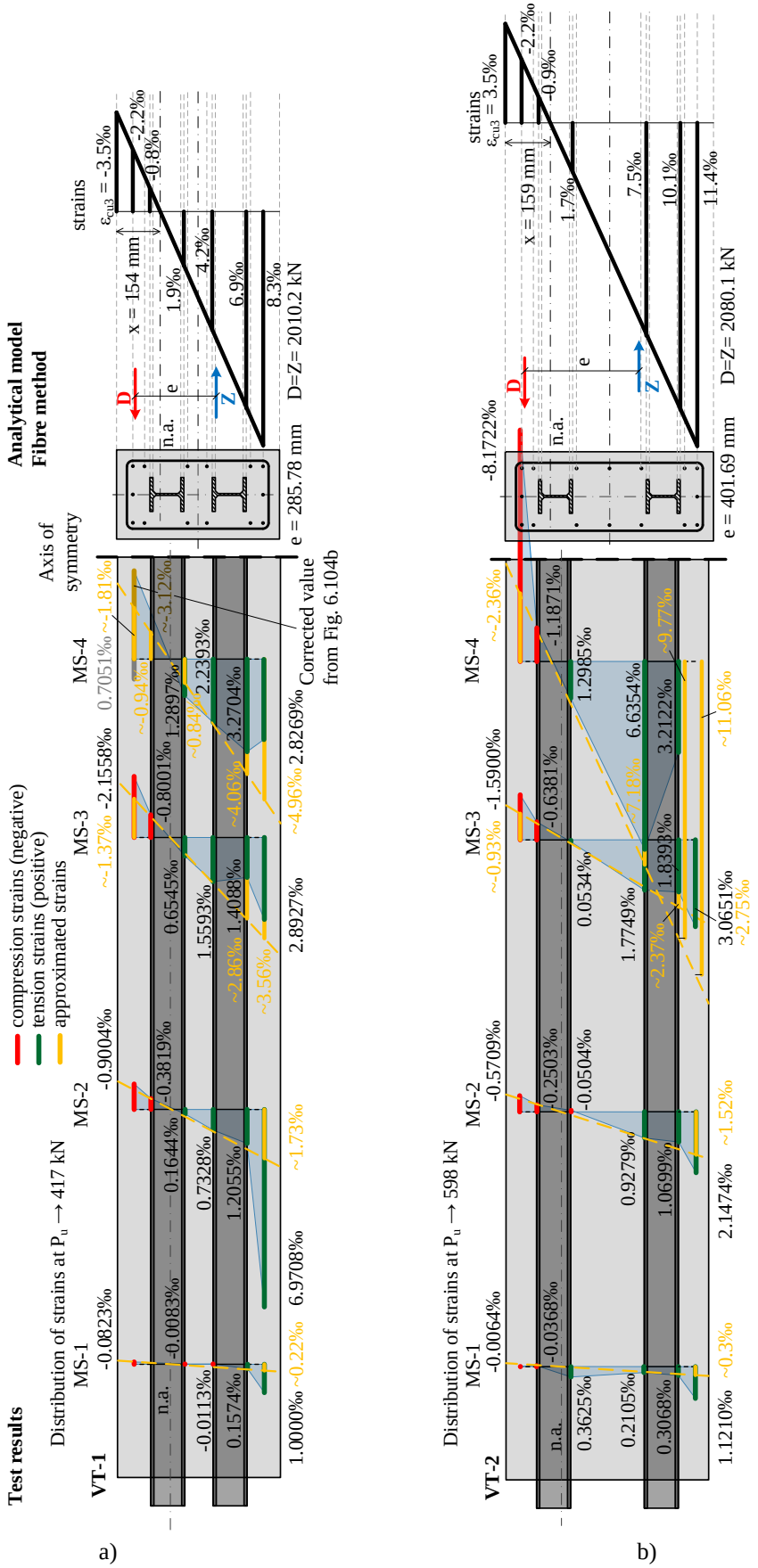


Fig. 6.105. Comparison of longitudinal strains between the experimental values and fibre method – a) specimen VT-1 and b) specimen VT-2.

The analysis shown in Fig. 6.105 indicates that the predicted linear elastic strain distribution in the cross-sections gives a good approximation of the realistic strain distribution obtained from the tests. However, it has to be respected, that the linearity of the experimental strain distribution is disturbed at the peak loads and the resulted values are related to the level of shear connection. Based on Fig. 6.38-6.47, it can be observed that the strains in steel profiles were recorded starting from the first load increments, thus, the steel profiles were activated in the bending force transfer mechanism directly at the beginning of the test.

In Table 6.1, the estimation of failure loads is given. The analytically obtained value is close to the peak load obtained from the tests and the relative error of 8% for the specimen VT-1 and 7% for the specimen VT-2 were identified. The error is calculated according to Eq. 6.15.

$$\delta_{err,P} = 1 - \frac{P_{analytic}}{P_{experimental}} \tag{6.15}$$

$$\delta_{err,P,VT-1} = 1 - \frac{383}{417} = 1 - 0.92 = 0.08 = 8\% \tag{6.16}$$

$$\delta_{err,P,VT-2} = 1 - \frac{557}{598} = 1 - 0.93 = 0.07 = 7\% \tag{6.17}$$

The differences between the predicted and experimental values of ultimate loads are not big. However, for the analytical evaluation, the normative values of material properties were used, where the used concrete grade was C35/45 and for the tests, the concrete grade C30/37 was used. The normative compression strength of concrete used for the calculations was 45 MPa and this value is referring to the characteristic value for cubic specimens. In the tests, the compression strength of concrete for cubic specimens at the day of test reached 44.25 MPa for the specimen VT-1 and 47.75 MPa for the specimen VT-2, see Table 6.7. It can be observed that the experimental values of the compression strength of concrete were close to the values used in the pre-design process for the higher grade. For the steel parts, the material grades not changed, where grade S355 was used for the structural steel and grade B500B was used for the reinforcement steel. The nominal values of the strengths of steel materials together with the measured properties are given in Table 6.5 and Table 6.6. In Fig. 6.105 and in the fibre method, the predicted pair of internal compression and tension forces (“D” and “Z”) acting on the internal lever arm (“e”) due to bending are defined. For the specimen VT-1, the predicted forces Z=D were equal to 2010.2 kN and they acted on 285.78 mm arm, which yielded the elastic bending moment of 574.5 kNm. For the specimen VT-2, the predicted forces Z=D were equal to 2080.1 kN and they acted on 401.69 mm arm, which in turns yields the elastic bending moment of 835.6 kNm. Based on the fibre method and the approximated strain distribution from test given in Fig. 6.105 in the measurement section MS-4, it was evaluated that the bending moments reached values of 620 kNm for the specimen VT-1 and 895 kNm for the specimen VT-2. The position of neutral axis from the analytical calculations with respect to the approximated strains in MS-4 is not referring exactly to the position identified graphically in Fig. 6.105.

From the fibre method, the position of neutral axis in specimen VT-1, is localised in 153 mm from the top fibres, where from Fig. 6.105, the position was found at 188 mm. According to Eq. 6.15 and with respect to bending moments, the pre-designed bending moment resistances give the error of 7.3% for the specimen VT-1 and 6.6% for the specimen VT-2. The evaluation is summarised in Table 6.11.

Table 6.11.
Summary and comparison of the internal forces in beam/column specimens.

Specimen	Pre-design			Test							$\frac{P_{u,pd}}{P_{u,test}}$	$\frac{M_{R,pd}}{M_{R,test}}$
	$P_{u,pd}$	$M_{R,pd}$	$Z = D$	P_u	M_R	P_{end}	$M_{R,pl,resid}$	$M_{R,pl,resid}$ reduced	$Z = D$	w		
	[kN]	[kNm]	[kN]	[kN]	[kNm]	[kN]	[kNm]	[kNm]	[kN]	[mm]		
VT-1	383	575	2010	417	620	304	456	454	1987	180	0.92	0.93
VT-2	557	836	2080	598	895	525	787	785	2260	180	0.93	0.93

Where,
P_u – is the ultimate load (peak load),
P_{end} – is the residual load-bearing capacity of tested specimens, see Table 6.8,
$P_{u,pd}/M_{R,pd}$ – is the ultimate load / bending moment resistance from the pre-design process,
$P_{u,test}/M_{R,test}$ – is the ultimate load / bending moment resistance from the tests,
$M_{R,pl,resid}$ – is the residual plastic bending resistance of tested specimens according to P_{end},
Z and D – are the resultant normal forces in the cross-section developed due to bending,
w – is the considered sagging deflection of tested specimens for the deformed state of static system,

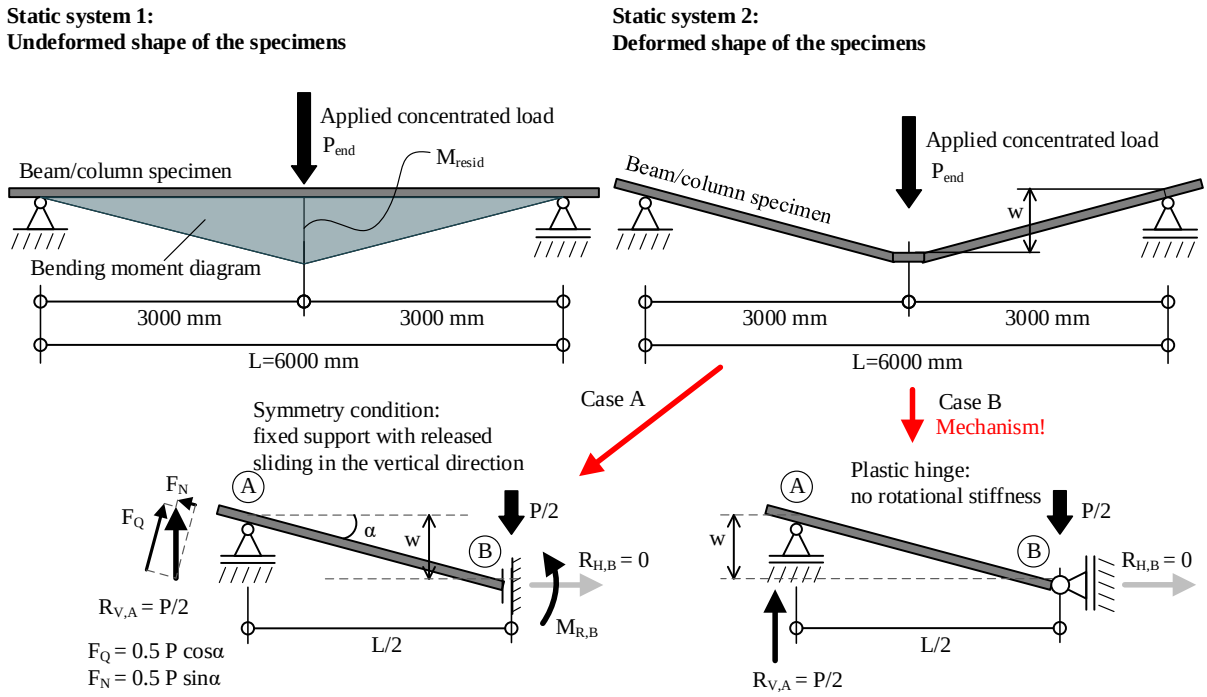


Fig. 6.106. Analysis of the bending moment in the specimen for undeformed and deformed states.

$$M_{resid} = \frac{P_{end} \cdot L}{4} \qquad \text{For } P_{end} \text{ see Table 6.8} \qquad (6.18)$$

$$M_{resid,def} = \frac{P_{end} \cdot L}{4} \qquad \leftarrow \text{For case A} \qquad (6.19)$$

$$M_{resid,def} = 0 \qquad \leftarrow \text{For case B} \qquad (6.20)$$

From Fig. 6.28 for the specimen VT-1 and Fig. 6.31 for the specimen VT-2, it can be observed that the load-deflection curves are stabilised in terms of load at the end of descending branches and they converged to the constant values of 304 kN for the specimen VT-1 and 525 kN for the specimen VT-2, see also Table 6.8. Form the observed behaviour, it can be concluded that the residual load-bearing capacity, after the specimen failure, can be defined as the residual plastic bending moment resistance of considered specimens. Therefore, the aforementioned resultant bending moments are calculated according to the present static system of specimen as shown in Fig. 6.106. In the result, the residual plastic bending resistance can be evaluated for two cases: (i) for the underformed shape of specimen and (ii) including the deformed shape. Considering the underformed shape and using Eq. 6.18, the bending moments reached 456 kNm for the specimen VT-1 and 787 kNm for the specimen VT-2. For the case with deformed shape, the considered static system is referring to the permanently deformed shape of the specimens after the development of the plastic hinge at the mid-span, see Fig. 6.83 and Fig. 6.98. Due to the applied roller and assuring sliding of the support, the horizontal reaction shown in Fig. 6.106 is set to zero. Resultant tensile normal forces (F_N) in the specimens did not impose a reduction in the bending moments due to the equilibrium of internal forces. Therefore, the residual plastic bending moment resistances in the case with deformed shape specimens are identical to the undeformed case, see Eq. 6.18-6.19. For the deformed shape, two boundary cases were considered, see Fig. 6.106: (A) where the symmetry condition is utilised at the mid span of the specimen and where the full rotational constraint is present, and (B) where the hinge is considered at the mid-span of the specimen. For the second case, where no rotational restraint is present, the residual plastic bending resistance is set to zero and the entire system would become a mechanism with a free movement of a rigid body. However, by considering the case, where the full rotational restraint is present, an overestimation of the bending capacity is done. In reality, the developed plastic hinge during the test formulated a spring with certain rotational stiffness. Therefore, in the considered static system like in the case A, the evaluated bending moment resistance will be higher. This approach was further adapted for the evaluation and the non-conservative character of the results was taken into consideration. In order to move towards a less non-conservative results, the equilibrium condition can be released and the bending moment reduction effect due to the normal force can be included in the residual plastic bending resistance ($M_{R,pl,resid}$ reduced). By considering the sagging deflection of 180 mm for both specimens and including the horizontal reaction from the normal force $F_H = 0.5P \sin\alpha \cos\alpha$, the reduced residual plastic bending resistances reached 454 kNm for the specimen VT-1 and 785 kNm for the specimen VT-2. The obtained results are included in Table 6.11.

Deformations in the specimens

In Fig. 6.28-6.33, the load-deformation curves for each specific displacement transducers measuring the deflection of specimens are shown. It can be observed that for both specimens, the recorded responses were analogous. Four main test phases can be clearly distinguished: (i) the initial phase, where

the ascending branch of the load-deflection relation can be assumed as linear, (ii) before failure non-linear phase, where the ascending branch of the curve started to flatten and finally reaching the peak point, (iii) after failure second non-linear phase, where the descending branch of the load-deflection curve started to drop after the peak load and (iv) the last phase where the load-deflection curve stabilised and converged to the constant value of load-bearing capacity. By analysing the load-deflection curves at the mid-span, see Fig. 6.28 and Fig. 6.31, a zone of plasticity at 90% of the peak load can be distinguished. In the aforementioned zone, the phase (ii) and phase (iii) described above are present. For the specimen VT-1 this zone reached 74.5 mm in deflection range and started at deflection of 55 mm. For the specimen VT-2, the plasticity zone reached 102.6mm and started at deflection of 38 mm. It can be observed, that the plasticity of the specimen VT-2 is higher than for the variant with smaller distance. Moreover, it can be observed that the stiffness, peak load and the residual load-bearing capacity are also higher for the specimen VT-2. In the same time, the peak load was achieved with a similar deflection for both specimens, see Table 6.8. Analysing the stiffness values given in Table 6.8, it can be observed that the relative change in stiffness of the specimen VT-1, in reference to the maximum value at Reload 1, reached 81% for K_{init}, 100% for K_{R1}, 90% for K_{R2}, 79% for K_{R3} and 70% for K_{R4}. Analogous for the specimen VT-2, the stiffness reached 55% for K_{init}, 100% for K_{R1}, 85% for K_{R2} and 81% for K_{R3}. The graphical representation of the above-mentioned variation of stiffness is shown in Fig. 6.107.

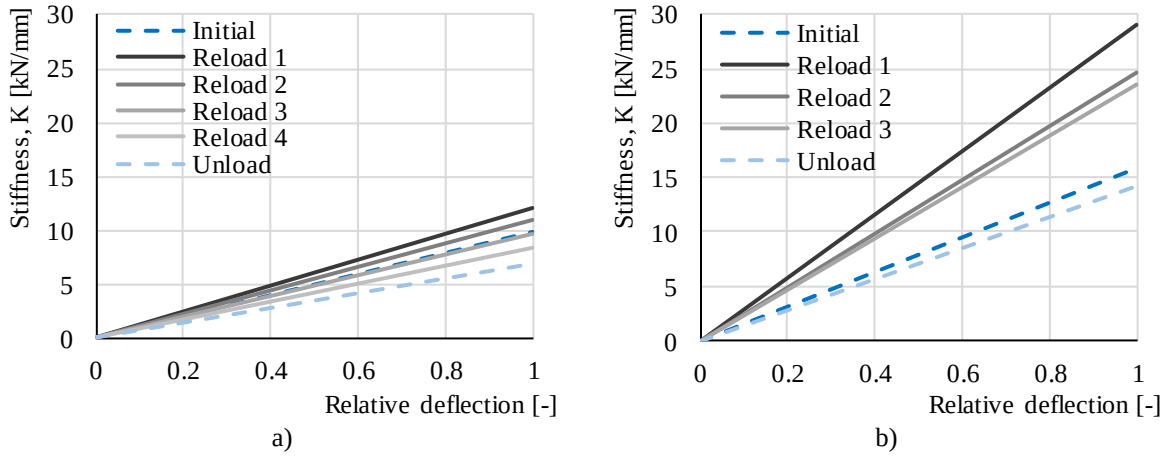


Fig. 6.107. Variation of stiffnesses at the different phases of beam/column tests – a) specimen VT-1 and b) specimen VT-2.

The analysis of deflections over the lengths of specimens, shown in Fig. 6.26 for the specimen VT-1 and in Fig. 6.27 for the specimen VT-2, reveals the global characters of the resultant deflections of specimens at different load levels. In the specimen VT-1, an equal progress of the deflection can be observed between the subsequent load steps. In the specimen VT-2, a significant progress of the deflection occurred between the subsequent load levels at 90% of the peak load and at 100% of the peak load. In Fig. 6.108, the deflection characters of specimen VT-1 were compared to the polynomial functions of 3rd order and linear functions at each considered load level. A closer correlation to the non-linear cubic functions can be observed with limited accuracy for each load case. The 3rd order polynomial

function of deflection curve shape is characteristic for the Euler-Bernoulli beams, where only bending deflection mode is considered. The linear functions are representing the pure shear deformation of the beam. Combination of both systems is characteristic for the Timoshenko beam theory, where shear effects on the beam curvature are summed with bending effects. In the same time, for the specimen VT-2, it can be observed that the deflection curves at each load level are dominated by the shear deflection mode characteristic for the Timoshenko beams as shown in Fig. 6.109. In the result, it can be observed the deflection curves of specimen VT-2 are correlated closer to the linear functions.

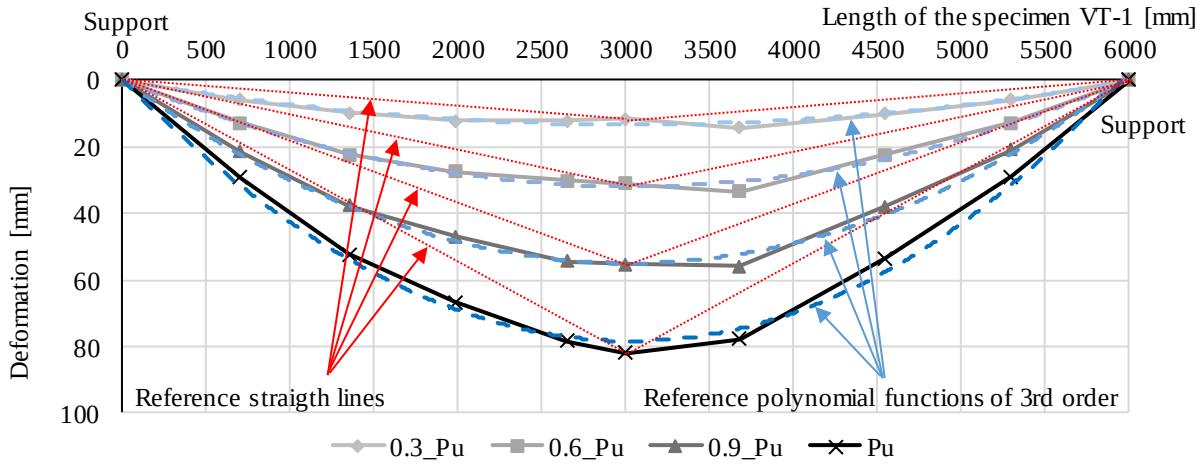


Fig. 6.108. Analysis of the deflection shapes of beam/column specimen VT-1.

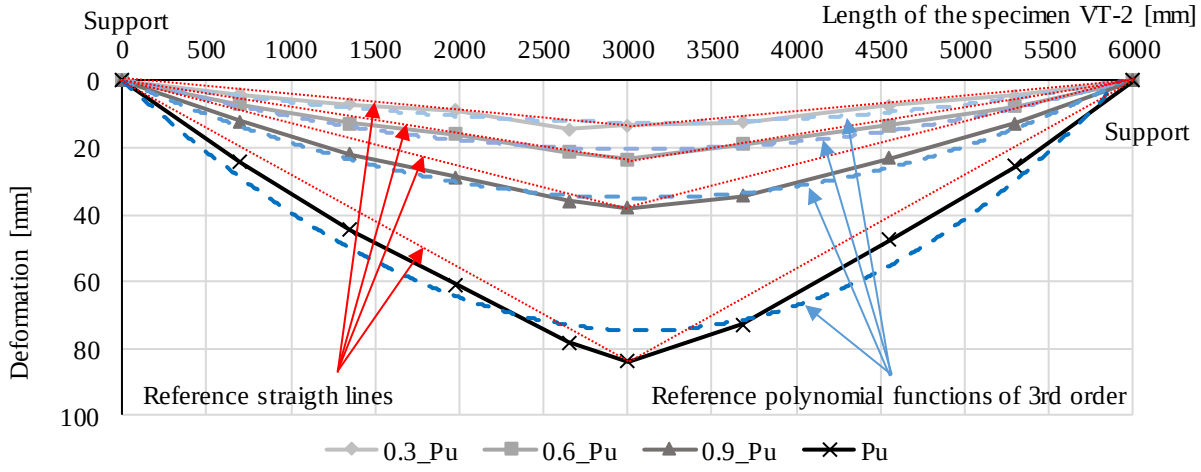


Fig. 6.109. Analysis of the deflection shapes of beam/column specimen VT-2.

For both cases presented in Fig. 6.108 and Fig. 6.109 above, the resultant deflection curves obtained from tests are between the indicated reference 3rd order polynomial and linear functions. However, a clear tendency can be observed that for the specimen VT-1, where the distance between the embedded steel profiles is small, a closer character to cubic function is visible. In the same time, for the specimen VT-2, where the distance between the embedded steel profiles is big, the deflection character was dominated by the shear deflection mode. Besides the different shapes of deflection curves for both specimens, the resultant values of deflections incorporate a significant influence of shear deflection mode. This aspect is analysed in detail later in Section 6.5.5.

The shear deflection mode visible in Fig. 6.109 for the specimen VT-2 clearly harms the main assumptions of Euler-Bernoulli beam theory about sections that after deformation stay perpendicular to the deformed axis of beam and the assumption about plane sections that remain plane after the deformation. However, by applying the approximated linear strains distribution shown in Fig. 6.105, thus by considering the plane sections assumption, the evaluation of the cross-section strength brought a good convergence to the test results. The described above behaviour correspond to the Timoshenko beam theory, which includes significant shearing effect on the beam deformation and it is a more overall definition of the Euler-Bernoulli beam theory. In the result, it can be concluded that the shear deflection mode was also present in the specimen VT-1, however, due to a bigger slenderness of the specimen and closer distance between the embedded steel profiles, it was not directly visible.

Taking into account the observed shear deflection mode from the beam deflection characteristic given in Fig. 6.109, the observed shear-bending failure pattern of specimen visible in Fig. 6.72 and Fig. 6.89 and the shear deformation scheme of specimens according to the steel-concrete composite theory, see Fig. 6.70, the direct relation between the aforementioned phenomena can be identified. The dominating shear deflection mode was accompanied by more extensive diagonal cracks in the support zone, like for the case of the specimen VT-2. Moreover, for the same specimen, a bigger disturbance in the linearity of strains distribution shown in Fig. 6.47 was observed. In the same time, a higher level of shear connection (less recorded slip, see Table 6.10) suggested the development of a higher level of shear deformation shown in Fig. 6.70. In Fig. 6.110, the shear deformation of the specimen was artificially obtained in numerical analysis by a significant reduction of the stiffness of concrete part and by implementing the full shear connection.

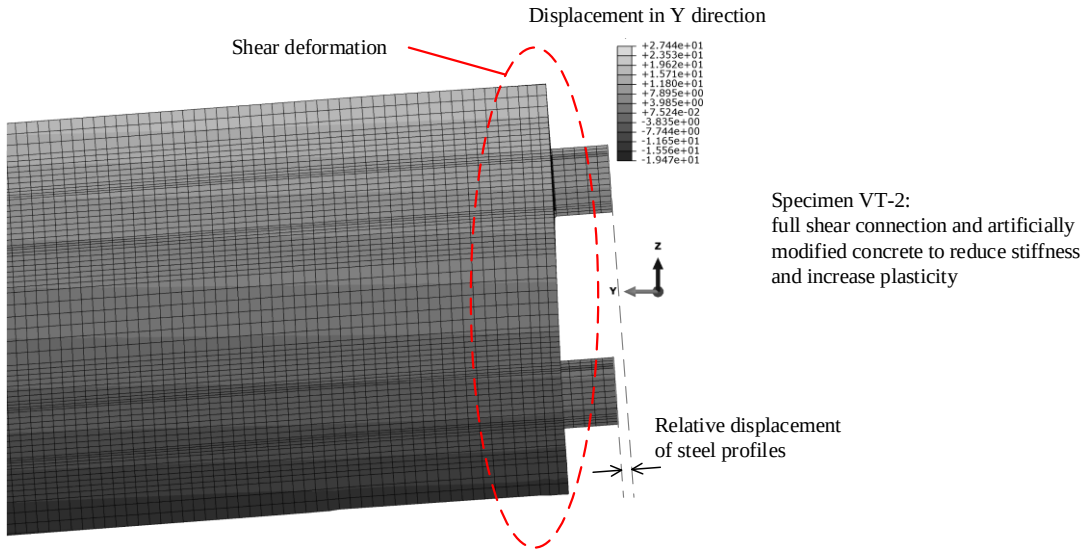


Fig. 6.110. Shear deformation in the artificially modified numerical model of specimen VT-2.

Activation of steel profiles in the force transfer mechanism

The analysis of strains recorded in the shear reinforcement shown in Fig. 6.50-6.57 and summarised in Table 6.9, allows for the verification of the level of shear forces transition between the embedded steel profiles and reinforced concrete. According to the defined static system, the shear forces distribution over the half-length of specimen is constant and it is equal to the half of imposed load. Considering the deformed shape of specimens, the marginal reduction of shear forces due to the progressing deformation is negligible, see Fig. 6.111 and Fig. 6.112.

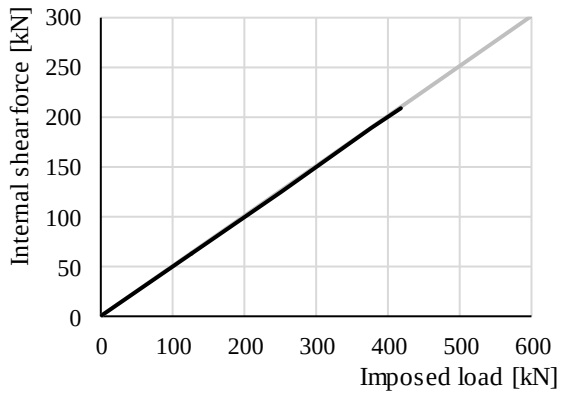


Fig. 6.111. Shear forces in deformed beam/column specimen VT-1 in reference to the imposed load.

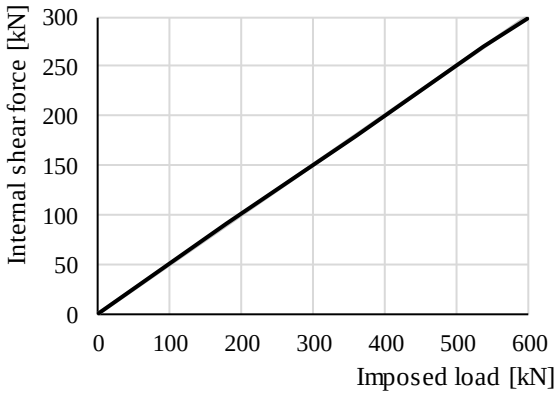


Fig. 6.112. Shear forces in deformed beam/column specimen VT-2 in reference to the imposed load.

The level of force taken by the stirrups is related to the recorded mean strains from both arms of the stirrup $\varepsilon_{s,m}$, the length of inner lever arm in the specimen z, the spacing of stirrups s and the concrete compression strut dispersion angle θ. According to Fig. 6.50-6.57, strains in the reinforcement stayed in the elastic range and the resultant force can be calculated using Eq. 6.21 and applying the Hooke's law. The considered force refer to one stirrup. Thus, to include the smeared shear transfer due to the size of concrete compression strut, the respective number of activated stirrups was calculated by using Eq. 6.23. Finally, the transferred force by the shear reinforcement is defined by Eq. 6.24. By knowing the shear forces transferred by the shear reinforcement, the shear forces bore by the steel profiles can be evaluated using Eq. 6.25 by subtracting the forces in reinforcement from the total imposed shear force. The section MS-1 was omitted in the evaluation. In addition, a case with global mean value of strains recorded in the stirrups was introduced for the global estimation of shear forces transferred by the shear reinforcement. The obtained results are summarised in Table 6.12, where the values are calculated for the respective measurement sections with assumed concrete compression strut angle $\theta = 45^0$. For the global case the angle θ was varied between 35° and 45°. Considering the globally averaged strains in the shear reinforcement and the variation in the dispersion angle of concrete compression struts, the spacing of stirrups was varied between 90 and 120 mm, see Fig. 6.11 and Fig. 6.12, in order to consider the maximum and minimum boundary values for the global shear force transfer case. To calculate the inner lever arm "z", the procedure from EN 1992-1-1 [53] was applied and the effective depth of the specimen "d" was assumed equal to the height between the top compressed fibre of concrete and the

centre of the tensioned bottom longitudinal reinforcement bar. For the specimen VT-1, the value of inner lever arm reached 465.3 mm and for the specimen VT-2 the inner lever arm reached 609.3 mm. The sum of the area of stirrups, mentioned in Eq. 6.21 and in Table 6.12, is referring to the areas of both arms in one stirrup. Modulus of elasticity of reinforcement steel is given in Table 6.6.

$$F_{s,i} = \varepsilon_{s,m,i} \cdot E_s \cdot \Sigma A_{s,i} \tag{6.21}$$

$$z = 0.9 \cdot d \tag{6.22}$$

$$n_{s,a} = \frac{z}{s} \cdot \cot\theta \tag{6.23}$$

$$V_s = F_{s,na} = F_{s,i} \cdot n_{s,a} \tag{6.24}$$

$$V_a = V_{tot} - V_s \tag{6.25}$$

The level of forces transferred by shear reinforcement in relation to the total imposed load are shown in Fig. 6.113-6.116 for specimen VT-1 and in Fig. 6.117-6.120 for specimen VT-2. It can be observed that in the specimen VT-1, the forces transferred by the stirrups reached 20-40% of the total imposed load at the peak load. In the same time, for the specimen VT-2, stirrups transferred 10-20% of the imposed load.

From Table 6.12, for the load equal to the 90% of the peak load and for the globally approximated strains in stirrups, it can be observed that the steel profiles took from 23% to 60% of the total acting shear force for the specimen VT-1 and from 64% to 81% for the specimen VT-2. The visual representation of the performed analysis is shown in Fig. 6.121 and Fig. 6.122 for the specimen VT-1 and in Fig. 6.123 and Fig. 6.124 for the specimen VT-2. It is visible that in the specimen with bigger distance between the embedded steel profiles, the activation of steel profiles in the transfer of shear forces is more significant. The proven existence of shear forces transfer justifies the presence of individual bending mechanism developed in each steel profile during the beam/column tests. Based on the above, an analogy to the Vierendeel truss system can be recognised, where the embedded steel profiles, in relation to the Vierendeel truss system, are representing shear- and bending-bearing chords.

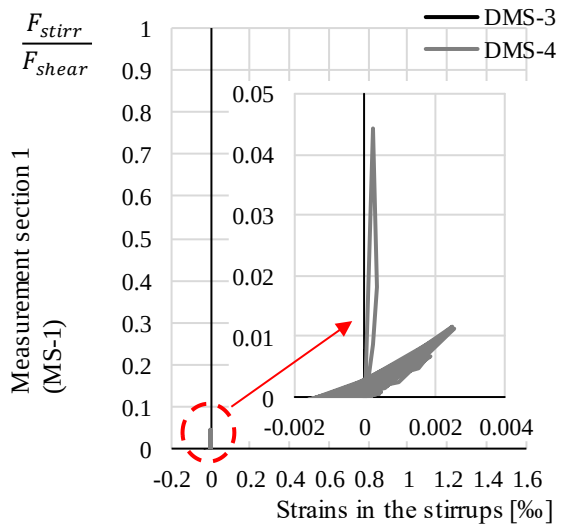


Fig. 6.113. Relative shear-strains curves in the stirrup of beam/column specimen VT-1, MS-1.

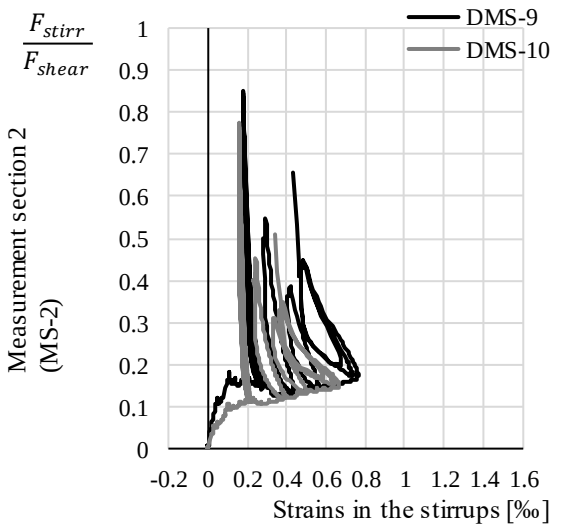


Fig. 6.114. Relative shear-strains curves in the stirrup of beam/column specimen VT-1, MS-2.

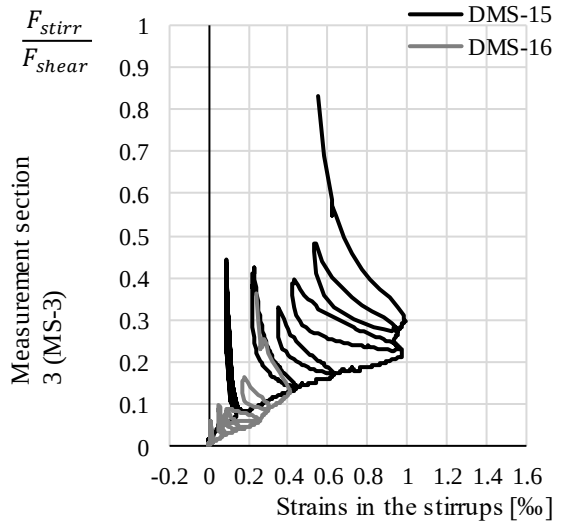


Fig. 6.115. Relative shear-strains curves in the stirrup of beam/column specimen VT-1, MS-3.

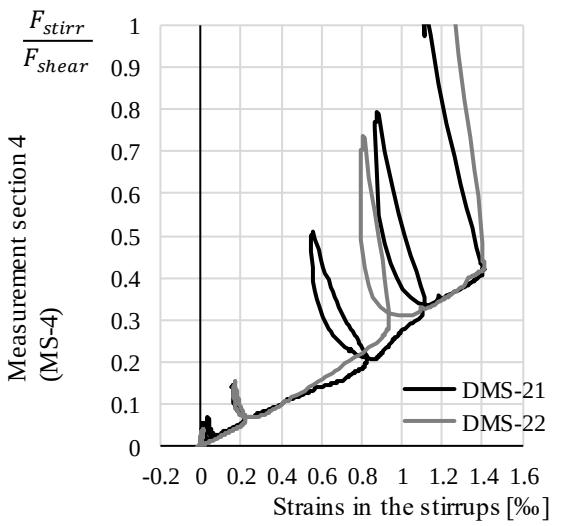


Fig. 6.116. Relative shear-strains curves in the stirrup of beam/column specimen VT-1, MS-4.

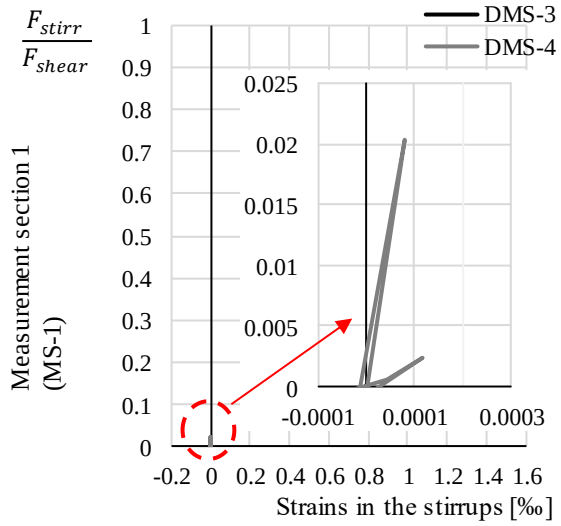


Fig. 6.117. Relative shear-strains curves in the stirrup of beam/column specimen VT-2, MS-1.

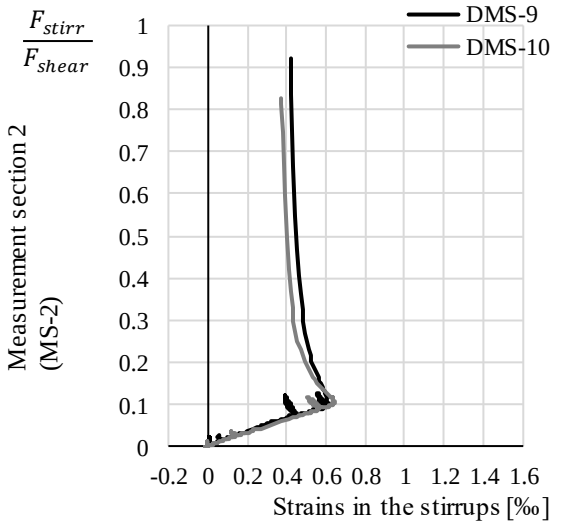


Fig. 6.118. Relative shear-strains curves in the stirrup of beam/column specimen VT-2, MS-2.

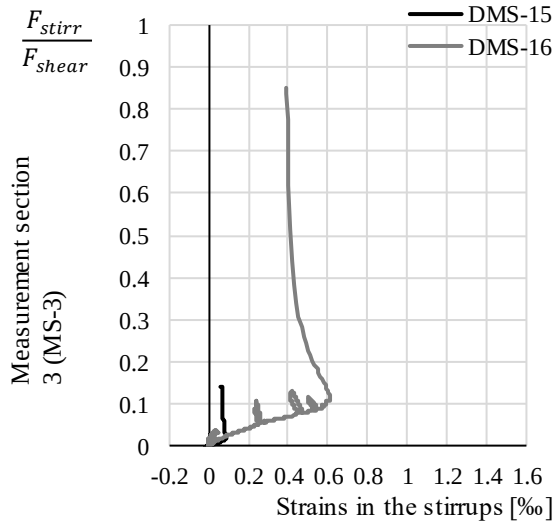


Fig. 6.119. Relative shear-strains curves in the stirrup of beam/column specimen VT-2, MS-3.

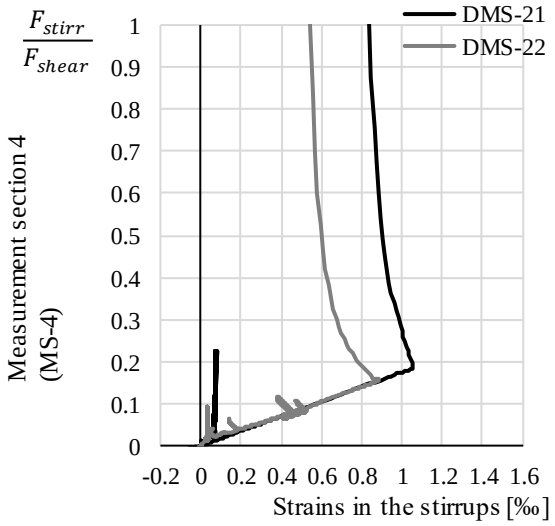


Fig. 6.120. Relative shear-strains curves in the stirrup of beam/column specimen VT-2, MS-4.

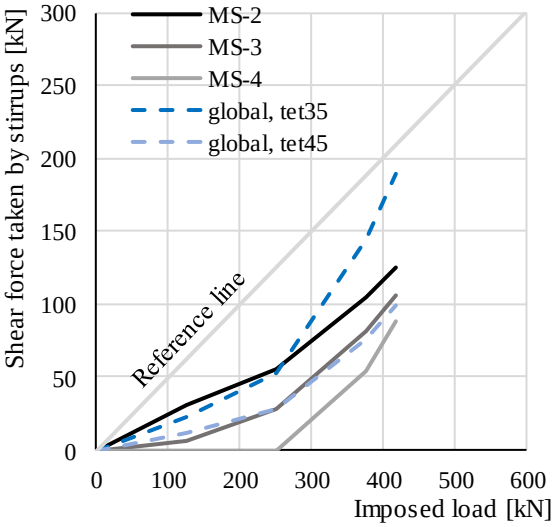


Fig. 6.121. Shear forces taken by stirrups in ref. to the imposed load in the beam/column specimen VT-1.

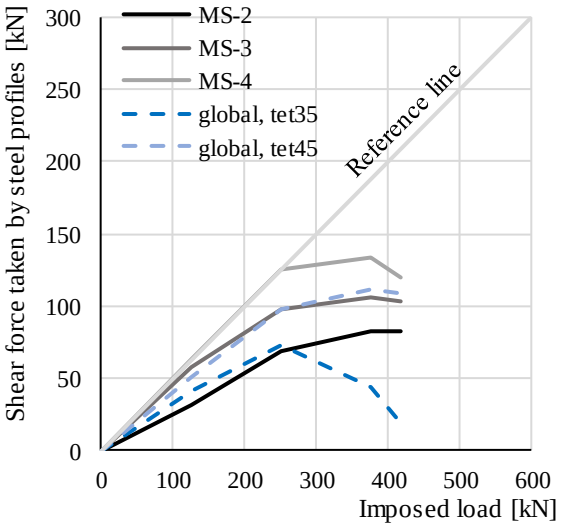


Fig. 6.122. Shear forces taken by steel profiles in ref. to the imposed load in the beam/column specimen VT-1.

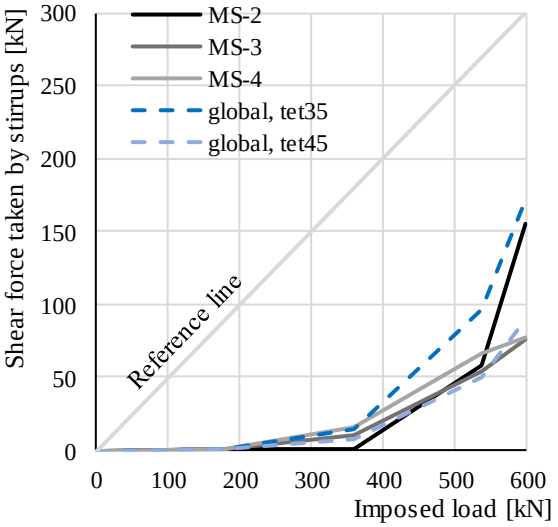


Fig. 6.123. Shear forces taken by stirrups in reference to the imposed load in the beam/column specimen VT-2.

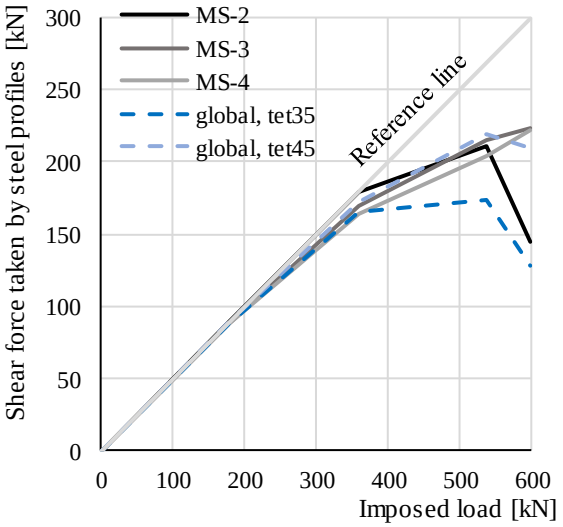


Fig. 6.124. Shear forces taken by steel profiles in ref. to the imposed load in the beam/column specimen VT-2.

Table 6.12.
Shear force transferred by the stirrups and steel profiles in the beam/column specimens.

Position	$\varepsilon_{s,m,i}$	$\Sigma A_{s,i}$	$F_{s,i}$	z	s	θ	$n_{s,a}$	V_{tot}	V_s	V_a	V_a/V_{tot}
	[‰]	[cm2]	[kN]	[mm]	[mm]	[°]	[-]	[kN]	[kN]	[kN]	[-]
VT-1											
At P_u											
MS-2	0.7087		32.46		120	45	3.9		125.88	82.65	0.40
MS-3	0.5968		27.34		120	45	3.9		106.01	102.52	0.49
MS-4	0.3744	2.26	17.15	465.3	90	45	5.2	208.53	88.67	119.86	0.57
global	0.5600		25.65		90	35	7.4		189.40	19.13	0.09
					120	45	3.9		99.56	109.07	0.52
At $0.9P_u$											
MS-2	0.5908		27.06		120	45	3.9		104.94	82.62	0.44
MS-3	0.4573		20.95		120	45	3.9		81.23	106.34	0.57
MS-4	0.2278	2.26	10.44	465.3	90	45	5.2	187.56	53.96	133.60	0.71
global	0.4253		19.48		90	35	7.4		143.86	43.71	0.23
					120	45	3.9		75.55	112.01	0.60
At $0.6P_u$											
MS-2	0.3152		14.44		120	45	3.9		55.99	69.19	0.55
MS-3	0.1553		7.11		120	45	3.9		27.59	97.60	0.78
MS-4	-0.003	2.26	-0.15	465.3	90	45	5.2	125.18	0.00	125.18	1.00
global	0.1557		7.13		90	35	7.4		52.67	72.51	0.58
					120	45	3.9		27.66	97.52	0.78
At $0.3P_u$											
MS-2	0.1743		7.99		120	45	3.9		30.97	31.49	0.50
MS-3	0.0315		1.44		120	45	3.9		5.59	56.86	0.91
MS-4	-0.011	2.26	-0.48	465.3	90	45	5.2	62.46	0.00	62.46	1.00
global	0.0651		2.98		90	35	7.4		22.01	40.44	0.65
					120	45	3.9		11.56	50.90	0.81
VT-2											
At P_u											
MS-2	0.6103		27.96		*110	45	5.5		154.87	144.31	0.48
MS-3	0.3004		13.76		*110	45	5.5		76.23	222.95	0.75
MS-4	0.2495	2.26	11.43	609.3	90	45	6.8	299.18	77.38	221.80	0.74
global	0.3867		17.72		90	35	9.7		171.30	127.88	0.43
					120	45	5.1		89.96	209.22	0.70
At $0.9P_u$											
MS-2	0.2273		10.41		*110	45	5.5		57.69	211.54	0.79
MS-3	0.2117		9.70		*110	45	5.5		53.72	215.50	0.80
MS-4	0.2121	2.26	9.72	609.3	90	45	6.8	269.23	65.79	203.43	0.76
global	0.2171		9.94		90	35	9.7		96.14	173.08	0.64
					120	45	5.1		50.49	218.74	0.81
At $0.6P_u$											
MS-2	0.0030		0.13		*110	45	5.5		0.75	179.02	1.00
MS-3	0.0403		1.85		*110	45	5.5		10.23	169.54	0.94
MS-4	0.0509	2.26	2.33	609.3	90	45	6.8	179.77	15.79	163.98	0.91
global	0.0314		1.44		90	35	9.7		13.91	165.86	0.92
					120	45	5.1		7.30	172.47	0.96
At $0.3P_u$											
MS-2	0.0004		0.02		*110	45	5.5		0.11	89.42	1.00
MS-3	0.0041		0.19		*110	45	5.5		1.03	88.50	0.99
MS-4	0.0045	2.26	0.20	609.3	90	45	6.8	89.53	1.38	88.15	0.98
global	0.0030		0.14		90	35	9.7		1.32	88.21	0.99
					120	45	5.1		0.69	88.84	0.99

Where,
* the measurement point was localised at the transition zone between two stirrups spacing zones, 120 and 90 mm, an average value was taken including the amount of bars included in each zone.

Analysis of the relative slip between steel and concrete

From the measured relative slips of the embedded steel profiles, see Fig. 6.62-6.69 and Table 6.10, it was observed that for the upper embedded steel profile, the full shear connection was achieved in both specimens and the recorded slip was negligible. For the lower embedded steel profiles, the maximum relative displacement against the concrete of 2 mm was recorded. However, at the peak load, the relative slip reached only 1.5 mm. Based CoPOT from Chapter 5, the shear connectors in beam/column tests reached only 30% of their utilisation at the peak load and respectively 40% at the end of beam/column test. This can be justified by opening detail of the shear connector given in Fig. 6.86 and Fig. 6.87, where the developed concrete failure is not significant with reference to the failure pattern investigated in the push-out test campaign and shown in Fig. 5.48 and Fig. 5.51. The numerical simulations of damage propagation shown in Fig. 5.77 confirms the early stage utilisation of shear connector.

From Fig. 6.63 and Fig. 6.67, it can be observed that the end-slip of lower embedded steel profiles developed fully at loads close to the peak load. Values recorded at the mid-lengths are affected by the concrete cracking due to the DT fixed to the concrete surface, see Annex E. The diagram visualising the development of relative slip over the length of specimens at different load levels is shown in Fig. 6.125 for the specimen VT-1 and in Fig. 6.126 for the specimen VT-2.

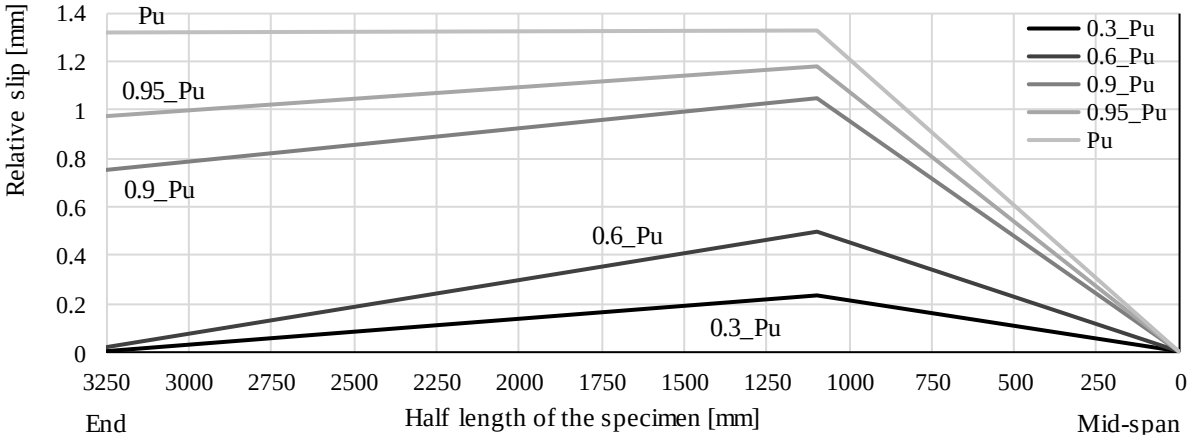


Fig. 6.125. Distribution of relative slip over the length of beam/column specimen VT-1.

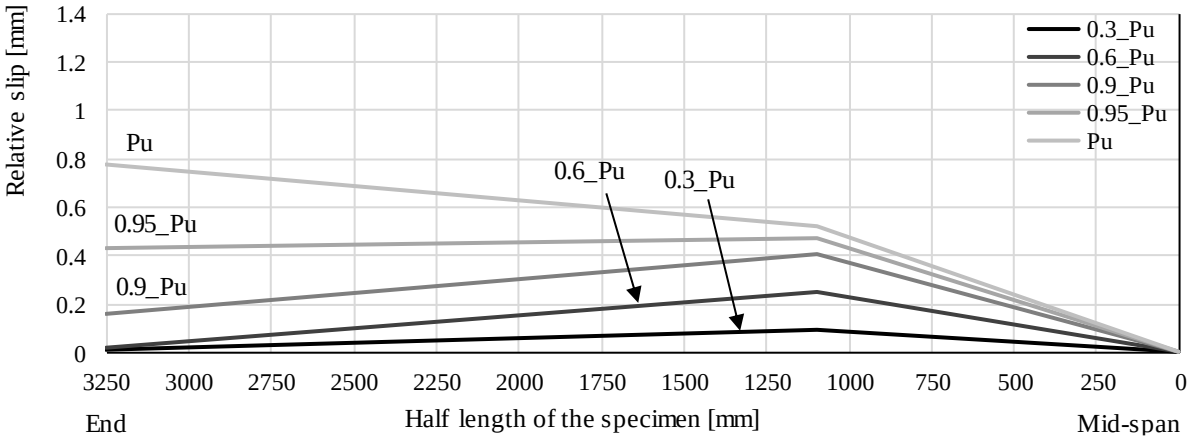


Fig. 6.126. Distribution of relative slip over the length of beam/column specimen VT-2.

In order to investigate the forces transferred by the shear connectors, the tensile forces developed in the embedded steel profiles were analysed in the function of the measured relative slip. The values of tensile forces developed in bottom steel profiles were evaluated based on the averaged strains from the measurement section MS-4, see Fig. 6.41 and Fig. 6.46 for the specimen VT-1 and VT-2 respectively. The evaluated data is presented below in Fig. 6.127 for the specimen VT-1 and in Fig. 6.128 for the specimen VT-2. The relative slip developed mainly after yielding of the embedded steel profiles.

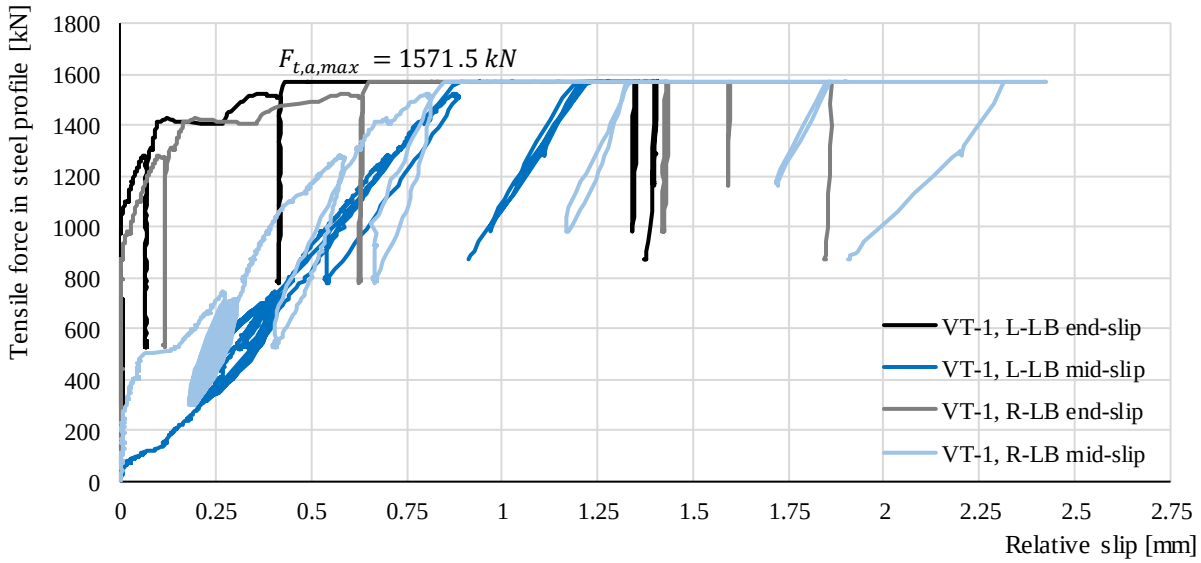


Fig. 6.127. Tensile forces-slip curves for the lower steel profile of beam/column specimen VT-1.

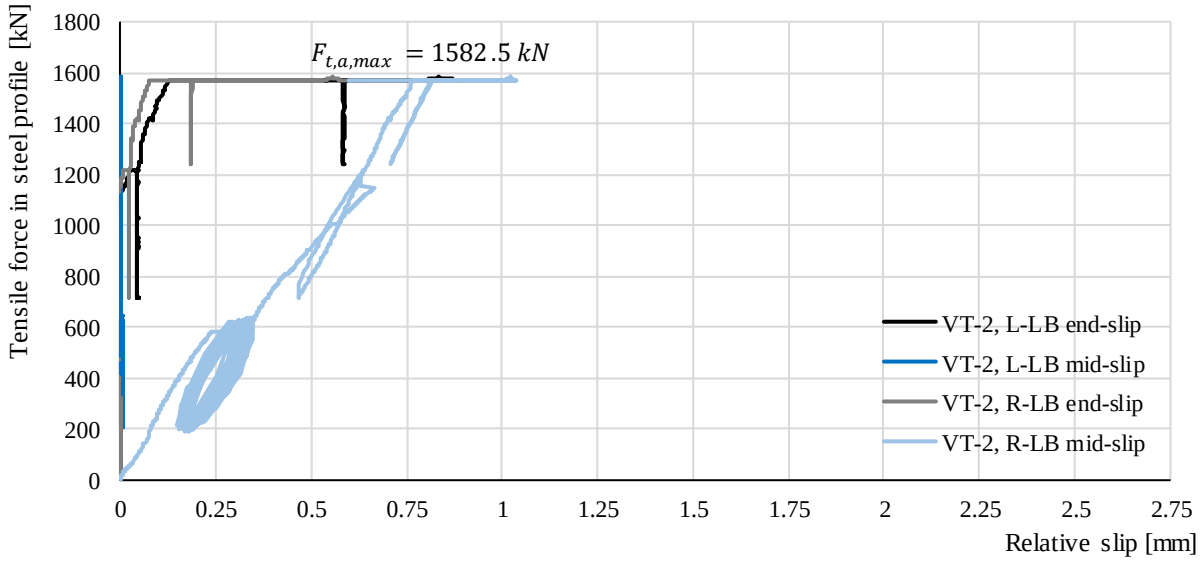


Fig. 6.128. Tensile forces-slip curves for the lower steel profile of beam/column specimen VT-2.

Based on the data presented above, it can be observed that the shear connectors assured nearly full shear connection at the steel-concrete interface, where the negligible small slip had no significant influence on the structural response of the specimens. The investigation of the relative slip in reference to the tensile forces developed in steel profiles revealed that the major part of the slip developed, when the steel profiles yielded. Based on this, it can be concluded that until the elasticity limit, the full shear connection was assured in both specimens.

6.4. Numerical simulations

Numerical simulations performed in FE code Abaqus® [174] supported the presented investigation on steel-concrete composite columns with multiple encased steel profiles. The performed simulations had the objective to simulate the experimental tests in order to investigate the load flux in the specimens and to support the observations made during the test campaign. No parametric studies, which would vary the geometrical or material grade conditions in the specimens, have been made. The obtained results and performed investigations during numerical simulations created a solid base and brought better understanding in the development process of analytical concept for the effective stiffness of tested composite columns with two separately embedded steel profiles.

The described below simulations had been made with the usage of dynamic solver Abaqus/Explicit, where the quasi-static simulations were defined by a proper setup of the solver, simulation speed, loading character, mass scaling and verification of the energy balance afterward. The applied parameters and verification of energies for the described below simulations are given in Annex F. The quasi-static simulations were crucial in order to avoid numerical problems with convergence, which can be encountered in the static simulations due to high deformation of specimens, complex interaction defined between the steel and concrete materials and local damage in the concrete. Moreover, quasi-static simulations correlate to the test procedure applied in the test campaign, where loads were applied over a certain time. In addition, the dynamic solver brings a better simulation efficiency for the composite structures in steel and concrete than the static solver does [153].

The calibration process of performed simulations required extensive sensivity study on the applied material laws, concrete confinement, interaction properties, modelling of steel-concrete bond and solver setup. The judgement of specimen behaviour in the simulated numerical models were made with reference to the obtained beforehand test results. As the main judging criteria, the load-deflection relation, the relative slip of embedded steel profiles and the failure pattern developed in both steel and concrete materials had been considered. The best compromise between the above-mentioned criteria defined the calibration level.

6.4.1. Geometry and mesh

Geometry of the numerical models reflected the geometry of experimental specimens including steel profiles, concrete block and reinforcement bars given in Fig. 6.9-6.12. The big scale of tested specimens would require a long computation time and high utilisation of computing nodes to perform FE simulations. In order to reduce the required hardware capacity and increase the calculation efficiency, double symmetry conditions were applied. In the result, one quarter of the whole specimen geometry had been modelled. The symmetry planes with geometries of the analysed numerical models are shown in Fig. 6.129 for the specimen VT-1 and in Fig. 6.130 for the specimen VT-2.

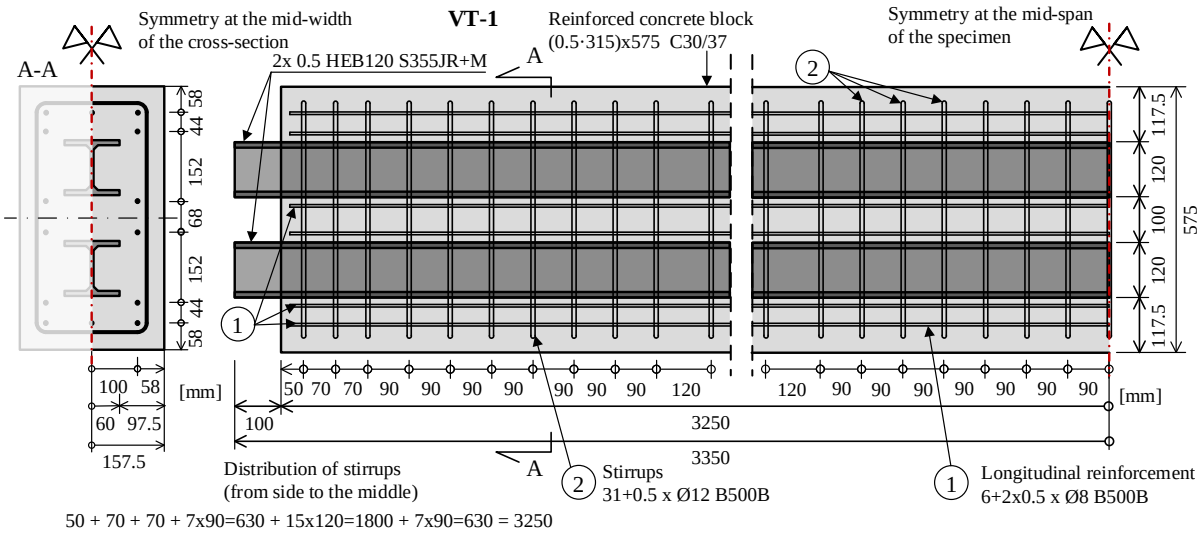


Fig. 6.129. Geometry of beam/column specimen VT-1 used in the numerical simulations.

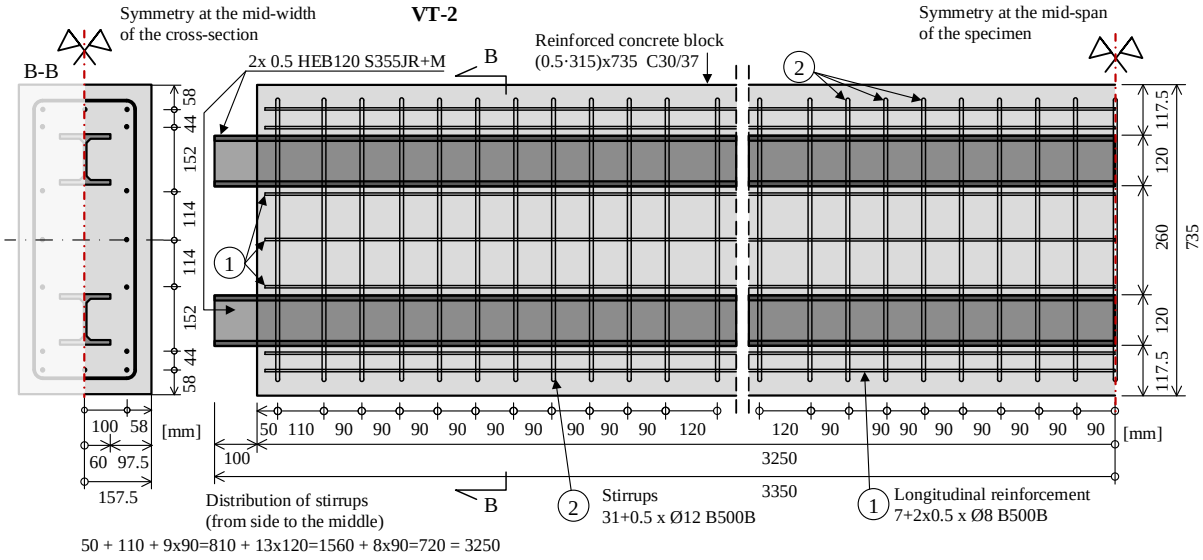


Fig. 6.130. Geometry of beam/column specimen VT-2 used in the numerical simulations.

Each of the implemented elements of the geometry of beam/column specimens shown in Fig. 6.129 and Fig. 6.130, were created as separate parts in Abaqus part creator module. The reinforcement bars were modelled as line 1D elements with cross-sectional area in the 3D space, where the steel profiles and concrete were defined as solid materials. The reinforcement cage was created with the usage of merge feature with retained boundaries of separate bars arranged in the assembly module, including bars with half-sectional area at the symmetry planes. In the result, one part with the whole reinforcement cage had been defined. The cross-sectional shape of steel profiles was simplified by replacing the rounding between the flanges and web with fazing distance equal to 0.67 radius of the original rounding. For HEB120 profile, the rounding radius is 12 mm, thus, the fazing distance was set to 8 mm, which resulted in similar areas of the simplified and original cross-sections. The final geometry of concrete was created in the assembly module of Abaqus by using the cut feature, where the volume of embedded parts of two steel profiles had been cut out from the original concrete block with rectangular cross-

section of 157.5x575x3250 mm for the specimen VT-1 and 157.5x735x3250 mm for the specimen VT-2. The cutting position of steel profiles in the concrete is defined in Fig. 6.129 and Fig. 6.130. In the result, matching parts of steel and concrete were obtained. Overlapping or gaps at contact surfaces are crucial to be prevented for the proper definition of interface behaviour in steel-concrete composites.

The applied flat mechanical shear connectors from the test campaign were not modelled as solid elements in the developed numerical models in order to reduce the complexity of simulations. Instead, the shear connectors were replaced by a specific interfacial resistance to shear smeared over the whole contact surface, which was applied together with steel-concrete bond in the form of cohesive elements. In the same time, the above-assumed simplification resulted in straight external surfaces of flanges in steel profiles and allowed for the regular discretisation of parts into the finite elements. The replacement and simplification of shear connectors into interface properties were based on the test observations about negligible slip that was developed in both embedded steel profiles during the beam/column tests, see Table 6.10 and Fig. 6.125-6.128, and high recorded shear connection stiffness that was measured in the push-out tests, see Table 5.12.

The steel profiles and concrete had been modelled as solid parts and for both, the Explicit C3D8R finite elements [174] with included sensivity for the second-order effects were used to discretise the defined geometry. The aforementioned finite elements (FE) are the linear eight-node brick elements with reduced integration, which are commonly used for the solid bodies in Abaqus simulations. They are characterised by high accuracy for the imposed deformations and allow for precise estimation of strains and stresses in the structure. Moreover, the Abaqus manual [174] and the literature, for example Qureshi [153], recommend them for the quasi-static simulations of composite structures in steel and concrete. The chosen FE were used in the steel profile part to create the structured mesh of hexahedral elements with a global seed of 10 mm. The mesh was refined over the thickness of flanges in steel profiles and fazing distances between the flanges and web to create an additional layer of FE (minimum 2 elements over the thickness of the considered zone). The same mesh was applied in the concrete part in the zones of embedded steel profiles, where the global mesh seed was set to 20 mm. The mesh seeding was adjusted in both, steel profile and concrete, parts to create coinciding nodes at the interface as it is shown in Fig. 6.131 for the specimen VT-1. For the specimen VT-2, an analogous mesh was used.

The reinforcement bars had been modelled as linear beam elements and the Explicit B32 quadratic finite elements [174] with three nodes were used. The reason for using beam elements with additional node in the middle, instead of commonly used truss elements with only two nodes, was to include the possible shearing effects of reinforcement bars. Moreover, the aforementioned FE were applied in the push-out test simulations and, for the consistency, they were applied also in the beam/column test simulations. The global mesh seeds for the reinforcement cage part was set to 20 mm, which correspond to global seed of concrete part. However, the modelled geometry of reinforcement cage included the

rounded corners, as it had place in the experimental campaign, and the seeding in the curved zones was refined to 5 mm in order to obtain a good approximation of curve by straight elements.

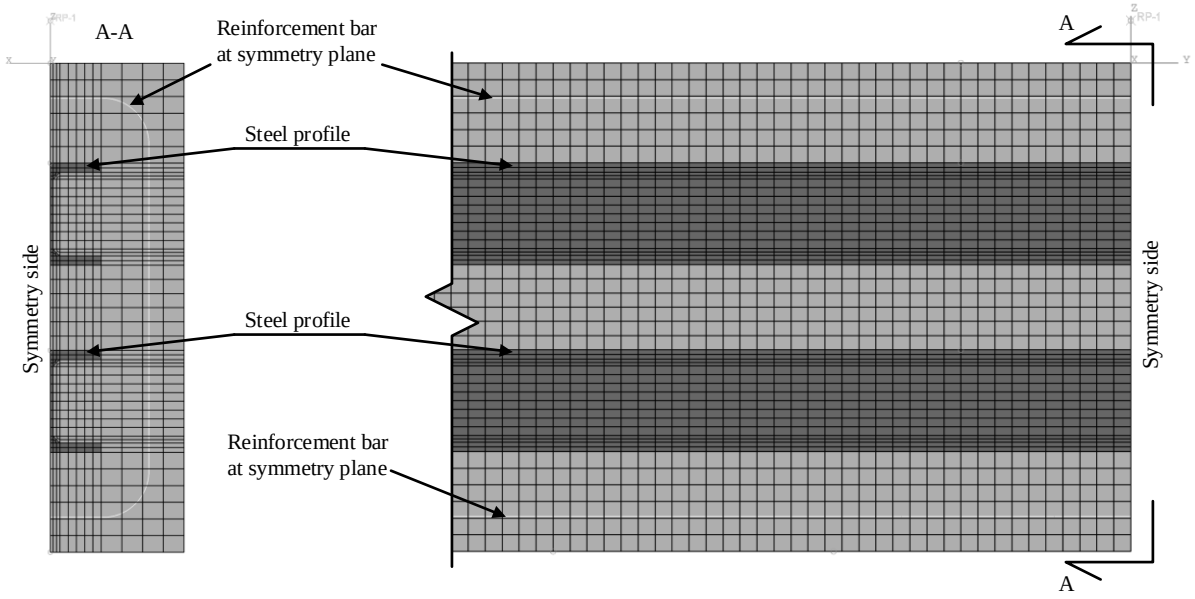


Fig. 6.131. Mesh in the steel and concrete parts used in the FE simulations of beam/column specimen VT-1.

To model the shear connection between the steel profiles and concrete, cohesive elements were applied. As it was stated earlier, by modelling of cohesive elements at the interface, two shear connection means were deployed and combined together – the steel-concrete bond and mechanical flat shear connectors from the test campaign. The applied cohesive elements at the interface between two materials not created any physical body in the model, since they were modelled as a layer of finite elements with zero thickness and specific traction-separation material law defining the connection behaviour between the connected parts. The application of cohesive elements to model steel-concrete bond phenomenon was described earlier in Section 5.5.3. The cohesive elements in beam/column test simulations were created by 0 mm offset of the FE from the mesh of steel profiles and by implementing the Explicit linear COH3D8 eight-node three dimensional finite elements [174]. The linear bulk viscosity of created elements was reduced to zero in order to assure the brittle behaviour of steel-concrete bond. The defined cohesive elements were set up to allow for degradation and finally element deletion after reaching its strength limit. During the simulations, the sensivity study revealed that a better behaviour of cohesive elements is obtained when the degradation limit is reduced to 90%. The created cohesive elements consisted in two surfaces, bottom and top, in order to tie them to the bounding materials. The respective surfaces of steel profiles and concrete lying on the interface were tied with the master formulation to the corresponding surfaces of cohesive elements. In the result, the surfaces of cohesive elements had slave characteristic and followed the deformation of master surfaces defined on steel and concrete parts.

6.4.2. Material laws

Specific material laws are required to define the desired material behaviour of each modelled parts in order to reflect accurately the test campaign. In each case, the main material properties were defined in the material tests performed within the test campaign and described in Section 6.3.5.1. The remaining properties were defined based on the current European Norms (EN) and International Standards (ISO). The material properties of cohesive elements were based on the test results obtained from the small-scale push-out tests campaign conducted for the bond investigation, see Section 5.3, and from the column push-out tests performed for the characterisation of novel flat mechanical shear connectors described in Section 5.4.

6.4.2.1. Structural steel

The applied material law for the structural steel consisted of elasto-plastic linear material law, where the strain hardening effect and damage were considered. The input data was based on the performed coupon tests according to ISO 6892-1 [80] and the obtained results are presented in Table 6.5. The applied stress-strain relation was identical for both specimens and it is shown in Fig. 6.132. The summary of implemented parameters in Abaqus is given in Table 6.13. The values of mass density and Poisson's ratio were based on EN 1991-1-1 [52] and EN 1993-1-1 [55] respectively. From the sensivity study, it was identified that Young's Modulus reduced to 90% brings better convergence to the observed behaviour of experimentally tested specimens.

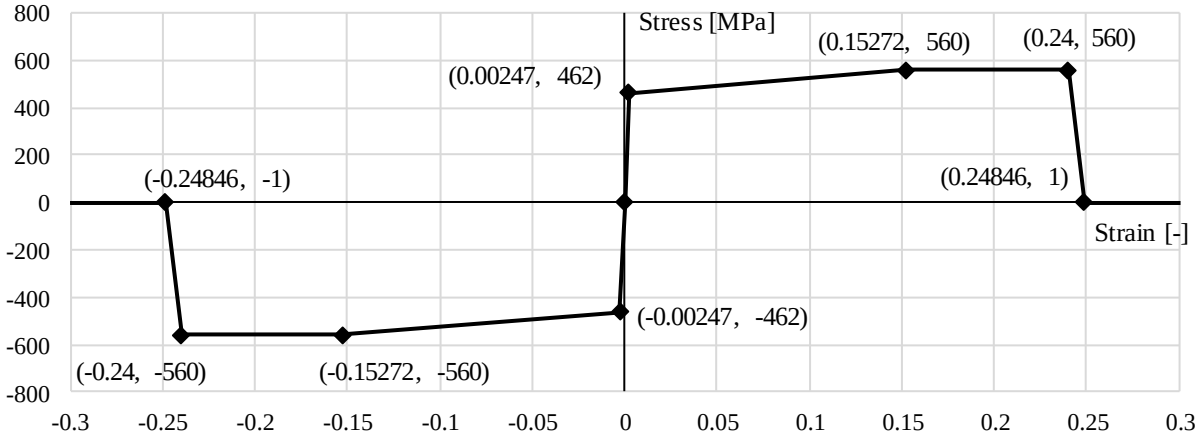


Fig. 6.132. Material law for structural steel used in the numerical simulations of beam/column tests.

Table 6.13.
Material properties used to define the structural steel material law in the FE simulations of beam/column tests.

Structural Steel Grade S355					
Behaviour	Density	Elastic - Isotropic		Plastic - Isotropic	
Input number	Mass Density ρ	Young's Modulus E_{red} = 0.9 E	Poisson's Ratio ν	Yield Stress σ_p	Plastic Strain ε_p
	[tonne/mm^3]	[MPa]	[-]	[MPa]	[-]
1	7.85E-009	0.9·207708 = 186937	0.3	462	0
2	-	-	-	560	0.15272
3	-	-	-	560	0.24
4	-	-	-	1	0.24846

6.4.2.2. Reinforcement steel

For the reinforcement bars, analogous material laws to the structural steel material law were applied. The linear elasto-plastic stress-strain relations were employed, where the strain hardening effect and damage were considered. The input data was based on the performed material tensile tests according to ISO 6935-2 [81] and the results are given in Table 6.6. For each diameter of applied reinforcement bars, Ø8 and Ø12, separate material laws were defined. In the result, the reinforcement cages in both specimens consisted of two material laws applied to the respective bars. The applied stress-strain relations for the implemented bars are shown in Fig. 6.133, where the input parameters are summarised in Table 6.14. The values of mass density and Poisson's ratio were based on EN 1992-1-1 [53] and EN 1993-1-1 [55] respectively. The sensivity study did not show any influence on the specimen behaviour by reducing the value of Young's Modulus for the reinforcement steel. However, the same reduction as in the case of structural steel was applied to the reinforcement steel material laws in order to maintain the same conditions for the steel parts.

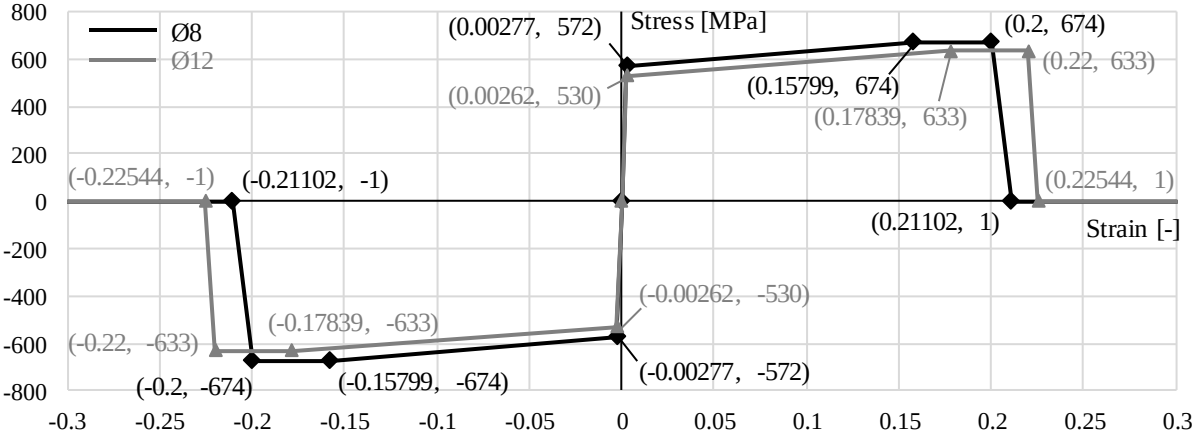


Fig. 6.133. Material laws for reinforcement steel used in the numerical simulations for beam/column tests.

Table 6.14.
Material properties used to define the reinforcement steel material law in the FE simulations of beam/column tests.

Reinforcement Steel Grade B500B					
Behaviour	Density	Elastic - Isotropic		Plastic - Isotropic	
Input number	Mass Density ρ	Young's Modulus E_{red} = 0.9 E	Poisson's Ratio ν	Yield Stress σ_p	Plastic Strain ε_p
	[tonne/mm^3]	[MPa]	[-]	[MPa]	[-]
Diameter Ø8					
1	7.85E-009	0.9·206165 = 185548	0.3	572	0
2	-	-	-	674	0.15799
3	-	-	-	674	0.2
4	-	-	-	1	0.21102
Diameter Ø12					
1	7.85E-009	0.9·202531 = 182278	0.3	530	0
2	-	-	-	633	0.17839
3	-	-	-	633	0.22
4	-	-	-	1	0.22544

6.4.2.3. Concrete

To simulate the concrete material in numerical simulations of both specimens, the Concrete Damage Plasticity (CDP) material law from the Abaqus materials library was applied [174]. The aforementioned material law is the plasticity-based non-linear elasto-plastic continuum damage model for quasi-brittle materials and its description is given in Section 5.5.2.3 of CoPOT series.

The input plasticity parameters for the applied concrete material law were based on the literature [102, 109, 113, 153, 174, 180], where the uniaxial compression and tension behaviours were calculated according to fib ModelCode 2010 [62]. The elastic behaviour of concrete material in Abaqus was defined separately by implementing elastic material behaviour from the Abaqus material library and by specifying the values of Young's modulus and Poisson's Ratio. The applied stress-strain relations are described in Eq. 6.38 for compression and in Eq. 6.39-6.42 for tension [62]. In the given relations, the concrete confinement effect was included by substituting the respective values by the confined values calculated according to fib Model Code 2010 clause 7.2.3.1.6 [62].

$$\frac{\sigma_c}{f_{cm}} = -\left(\frac{\frac{E_{cm}}{E_{c1}}\cdot\frac{\varepsilon_c}{\varepsilon_{c1}} - \left(\frac{\varepsilon_c}{\varepsilon_{c1}}\right)^2}{1+\left(\frac{E_{cm}}{E_{c1}}-2\right)\cdot\frac{\varepsilon_c}{\varepsilon_{c1}}}\right) \tag{6.38}$$

$$\sigma_{ct} = E_{cm}\cdot\varepsilon_{ct} \quad \text{, for } \sigma_{ct} \le 0.9\cdot f_{ctm} \tag{6.39}$$

$$\sigma_{ct} = f_{ctm}\cdot\left(1-0.1\cdot\frac{0.00015-\varepsilon_{ct}}{0.00015-0.9\cdot f_{ctm}/E_{cm}}\right) \quad \text{, for } 0.9\cdot f_{ctm} < \sigma_{ct} \le f_{ctm} \tag{6.40}$$

$$\sigma_{ct} = f_{ctm}\cdot\left(1.0-0.8\cdot\frac{w}{w_1}\right) \quad \text{, for } w \le w_1 \tag{6.41}$$

$$\sigma_{ct} = f_{ctm}\cdot\left(0.25-0.05\cdot\frac{w}{w_1}\right) \quad \text{, for } w_1 < w \le w_c \tag{6.42}$$

$$w_1 = G_F/f_{ctm} \quad \text{, when } \sigma_{ct} = 0.2\cdot f_{ctm} \tag{6.43}$$

$$w_c = 5\cdot G_F/f_{ctm} \quad \text{, when } \sigma_{ct} = 0 \tag{6.44}$$

A wide sensivity study of the parameters defining the material law was required in order to understand and accurately reflect the concrete behaviour observed in the beam/column tests. The considered parameters were: (i) the concrete confinement level and its influence on the concrete performance, (ii) the dilation angle ψ, which is the angle between the hydrostatic pressure and equivalent von Mises effective stress measured at high confining pressure, (iii) the viscosity parameter, which represents the relaxation time for the concrete after reaching the damage state, (iv) the modulus of elasticity E, which has direct influence on the elastic behaviour, stiffness and confinement of the material, (v) the concrete tensile resistance, (vi) the crack opening width w and w_1, (vii) the fracture energy G_F and (viii) the maximum allowable concrete damage level for tension d_t and compression d_c.

The effect of concrete confinement had a direct impact on the material behaviour. It was amplifying the strength and ductility capacity of the concrete. The confinement level was assessed according to the base material strength, geometry of the specimen and particularly to geometry of the implemented reinforcement cage. However, no single way of introducing the confinement effect to the stress-strain relation was identified. Three different variants with varied impact on each particular part of the stress-strain behaviour had been considered: (i) by direct modification of the stress-strain relation given in Eq.6.38-6.42 with confined values of E_{cm}, E_{c1}, f_{cm}, f_{ctm}, ε_{c1}, $\varepsilon_{c,lim}$, w_1 and w_c, (ii) by increasing the plasticity plateau at the maximum compression stresses by implementing a horizontal branch and varying the range of confined strains and (iii) by combination of both. In the performed sensivity study, it was identified that the direct modification of the stress-strain relation by confined values brings the best reflection to the realistic behaviour from the test campaign in both specimens. The existence of embedded steel profiles in both specimens affects the level of concrete confinement, especially in the zone between them. The confining stresses had been identified at the level of $\sigma_2 = 1.7$ MPa for the specimen VT-1 and $\sigma_2 = 0.8$ MPa for the specimen VT-2. The difference in the confining stresses were related to the bigger clear distance between the embedded steel profiles in the specimen VT-2, which resulted in a smaller confinement effect in comparison to the specimen VT-1. The given values of confinement were identified according to clause 7.2.3.1.6 of fib ModelCode 2010 [62] and calibrated in the sensivity study based approach with reference to test results.

The dilation angle control the load spread between the subsequent finite elements in the model with reference to the confining pressure and multiaxial stress behaviour. The investigated range of dilation angle was from 0 to 35 degrees. It was identified, that smaller dilation angles refer well to more concentrated load flux cases and the material damage is more concentrated. Where on the other hand, bigger values of dilation angle gives a wide load spread over the specimen and the damage is more smeared over a bigger volume of material. Based on the taken observations, it was concluded that smaller values of the dilation angle represents well more shear-based load transfer, where bigger dilation angle gives a more realistic behaviour of the material for bending cases. A value of dilation angle equal to 25° for both specimens had been recognised as the most feasible due to the resultant damage pattern obtained during the simulations and resultant distribution of stresses.

During the numerical sensivity study, a high initial stiffness in both specimens was observed with comparison to the experimental load-deformation responses. It was identified that the elastic response of massive concrete part affects the behaviour of the specimen in the low load phase of the simulations. In literature, like for example Pauw [141] or Wendner et al. [199], a big scatter in the test results of modulus of elasticity with roughly taken low boundary value of 17 GPa can be found. This leads to a remark that experimentally obtained values could be lower in some cases than the values predicted in the design standards. The difference can be justified by, among others, different material densities, different test and specimen treatment conditions applied and non-isotropic material. In the considered

experimental beam/column specimens, a significant impact on the stiffness reduction and contribution in the composite section could also have micro cracking and shrinkage developed between the concrete casting day and testing day. In addition, the values of the modulus of elasticity given in the current design standards are not including the non-linear behaviour of the concrete material, as they are linearly approximated at the point of $0.4f_{cm}$ from the stress-strain relation. Based on the above and considering additionally a more aggressive environment next to the beam/column test specimens in comparison to the concrete samples for the material testing, a simplification to reduce the modulus of elasticity of concrete was applied. In the result, the value of the modulus of elasticity in both specimens had been reduced by 50% in reference to the value calculated according to fib ModelCode 2010 provisions [62] including increased concrete compression strength due to the confinement effect. In the result, the Young's Modulus for concrete was assumed with the value of approximately 19 GPa in both specimens.

The tensile resistance of concrete was evaluated based on the provisions given in the fib ModelCode 2010 [62], where it is related to its compression strength. Based on the fact, that the concrete compression strength had been affected by the confinement effect, the tensile resistance was analogically increased with respect to the obtained compression strengths. However, in the design guidance there is no reference between the concrete confinement and the tensile resistance. In the numerical sensivity study, it was observed that for the specimen where higher confining stresses were present, the concrete tensile resistance should be reduced by 25% in reference to the value calculated including confinement effect. In the specimen VT-2, no reduction of the tensile resistance was applied. This observation gives a remark that high confining pressure can overestimate the tensile resistance of concrete in the specimen.

The viscosity parameter, crack opening and fracture energy are controlling the material tensile damage, thus the tensile stiffness reduction. Where, the crack opening width and fracture energy are defining directly the yielding point and damage evolution, the viscosity parameter defines the zone of the concrete affected by the yielding elements and smear the effect over them. The aforementioned parameters were adjusted in order to obtain a desired concrete cracking pattern in the shape of developed plastic strains and stiffness loss. It was observed that the considered parameters had no significant influence on the overall specimen behaviour, besides the size of the tensile zone of damaged concrete. The viscosity parameter was set according to the investigation made by Szczecina et al. [180] and the value was set to 0.0001 for both specimens. The fracture energy was analysed according to the provisions given in fib ModelCode 2010 [62] and it was strictly related to the concrete compression strength. The crack opening was analysed based on the same aforementioned design standard and in Eq. 6.43-6.44 the applied definition is shown. Small deviations from the normative values had been checked, however, the original values calculated including the concrete confinement effect brings a good correlation to the realistic cracking pattern observed during the test campaign.

In simulations of both specimen, the tensile damage of cocncrete was set to 99%, which reflects the full loss of concrete stiffness in the affected finite elements after reaching the total crack opening width. This value had been not varied during the sensivity study and it reflects well the behaviour observed in test campaign. In other words, finite elements of concrete material after reaching the full damage were withdrawn from the force transfer and could freely deform. In the result, the internal forces were redistributed onto surrounding finite elements, which reflects well the crack propagation process from the test campaign. In order to reflect the brittle character of tensile failure in concrete and to include the effect of aggregate interlocking on the stiffness maintenance during the crack development, the tensile damage parameters in the damage evolution had been modified, see Table F.3-F.4 of Annex F.

The level of maximum concrete damage due to compression stresses required a parametric study in order to identify the effective damage limit, which could correlate to the behaviour of concrete in the crushed state from the tests. By controlling the level of maximum concrete stiffness degradation, the level of redistribution of internal forces between the subsequent finite elements was changing. In the result, the load flux in the specimens was greatly affected by the damage parameter. It was identified, that for the specimen VT-1, the maximum concrete damage of 98% represents well the behaviour of concrete from the tests. Where in the same time, for the specimen VT-2, the maximum concrete damage was limited to 90%. It can be observed that the difference is not significant between the simulations of two specimens, however, in the bigger specimen, a bigger portion of crushed concrete retained his compression strength due to the confinement from the undamaged parts, therefore, an adjustment of the concrete damage was needed.

Due to the varied geometry between the two specimens and different properties of concrete, two different sets of the parameters defining the numerical material laws were obtained during the sensivity study. The evaluation of the uniaxial tension and compression behaviours of concrete was based on the mean concrete compression strength measured during experimental campaign in material compression tests for both specimens, see Table 6.7. The resultant uniaxial stress-strain behaviour for confined concrete, defined according to Eq. 6.38-6.42, is shown in Fig. 6.134 for the specimen VT-1 and in Fig. 6.135 for the specimen VT-2. From the given diagrams, it can be observed, that in the applied numerical material law, the ductility of concrete has been significantly affected by the confinement effect. The linear representations of the applied reduced values of Young's Modulus are included in Fig. 6.134 and Fig. 6.135. The concrete density was taken according to EN 1991-1-1 [52]. The input data is summarised in Annex F, Table F.3 for the specimen VT-1 and Table F.4 for the specimen VT-2.

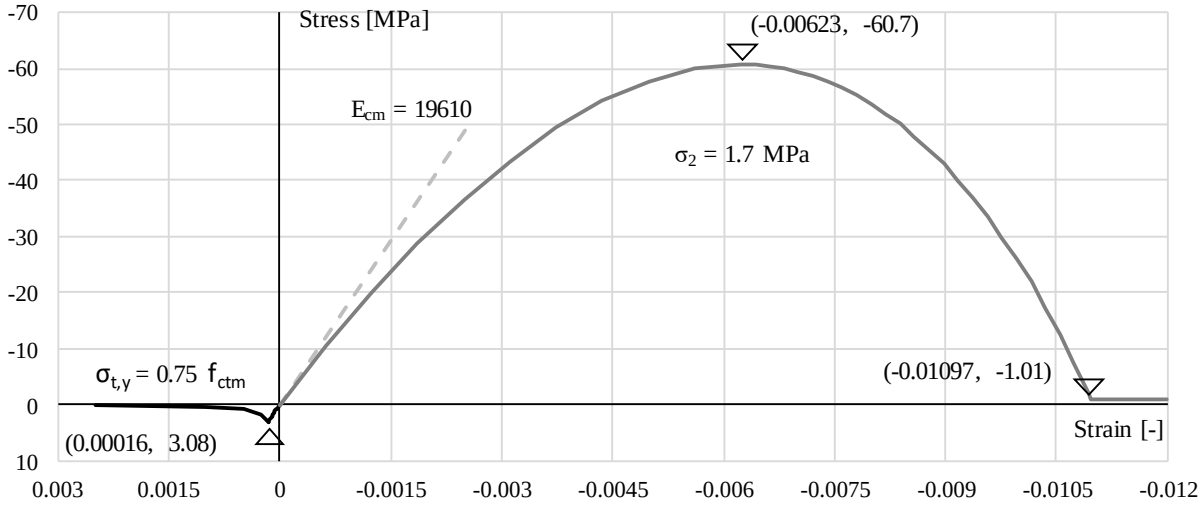


Fig. 6.134. Stress-strain behaviour implemented for the concrete material law in the numerical simulation of beam/column specimen VT-1.

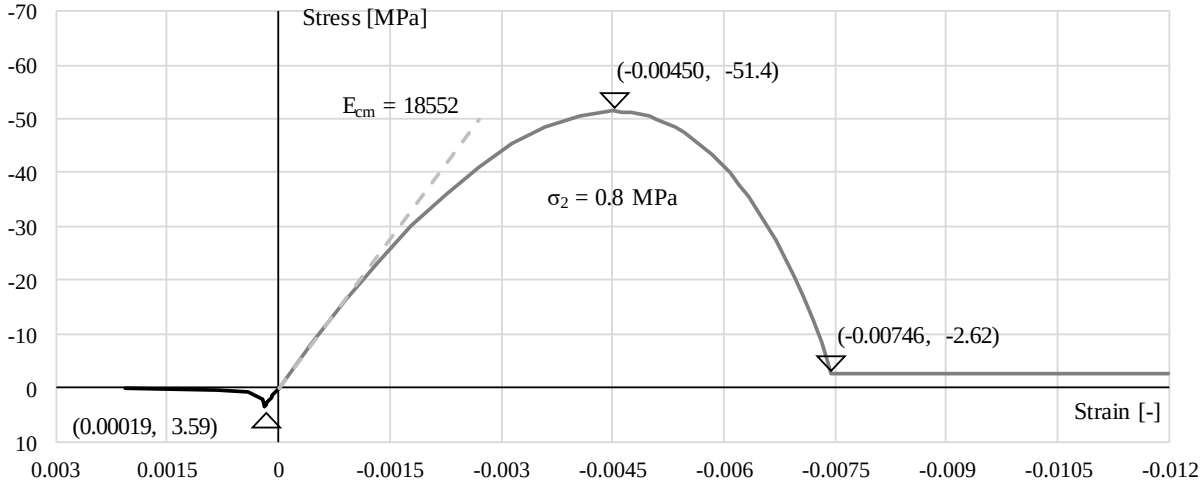


Fig. 6.135. Stress-strain behaviour implemented for the concrete material law in the numerical simulation of beam/column specimen VT-2.

6.4.2.4. Cohesive elements – shear connection

The material law defined for the cohesive elements applied at the steel-concrete interface was not reflecting any realistic material but the interaction properties between the steel and concrete surfaces. The applied material law was based on the traction-separation law with quadratic stress damage formulation, where the behaviour is linear in the first phase and the damage initiation consisted in quadratic interaction function involving the nominal stress ratios [174]. The aforementioned criterion is described in Eq. 6.45. The first linear phase of the behaviour was controlled by the elastic material properties, which had been defined using traction type of elastic response, where the moduli of elasticity for normal direction and two shear directions were specified. The linear elastic behaviour of cohesive elements sustained until reaching the peak point, which was defined by the aforementioned damage initiation criterion. In the applied traction-separation law, analogically to the formulation of elastic behaviour, three directions of nominal strengths were considered – normal and two shear directions, as

it can be seen in Eq. 6.45. The described damage criterion is only activated in tension and shear, where in compression no damage will occur.

$$\left\{\frac{\langle t_n \rangle}{t_n^0}\right\}^2 + \left\{\frac{t_s}{t_s^0}\right\}^2 + \left\{\frac{t_t}{t_t^0}\right\}^2 = 1 \tag{6.45}$$

After reaching the damage initiation point, thus, the effective resistance to combined shear and tension actions, the damage evolution softening behaviour can be defined as linear, exponential or user-defined. In other words, the material capacity for the stiffness and strength reduction can be described in three aforementioned variants. The resultant plastic displacements or fracture energy define the material damage capacity after initiation. Furthermore, the damage evolution character between the three considered actions can be set to be equal and independent from the considered direction or a specific relation can be defined by implementing mode-mix ratios. In the performed numerical simulations of the beam/column specimens, the linear damage evolution law based on the defined total plastic deformation with mode-independent mode-mix had been specified. After reaching the total degradation of the stiffness and in the same time, the total defined plastic deformation, the cohesive element deleted from the model.

The existence of cohesive elements with zero thickness are not affecting the contact interactions defined separately for the assembly of parts. Therefore, the defined cohesive material at the interface allows for the definition of tangential and normal contact properties defined in the interaction module of Abaqus. However, according to Abaqus manual [174], due to the combined contact properties and zero thickness cohesive elements at the interface, there is a risk of the development of non-physical forces in dynamic simulations. Therefore, the verification of energies with respect to the quasi-static character of the performed simulations was crucial, see Annex F.

The input data for the definition of the cohesive elements behaviour was based on the results obtained from the small-scale push-out tests, column push-out tests of flat shear connectors and from the numerical simulations, all described previously in Chapter 5. Due to the assumed earlier simplification of the beam/column numerical models, the implemented parameters were including two phenomena: (i) the performance of steel-concrete bond between plain steel and concrete parts and (ii) the performance of flat V-shaped mechanical shear connectors smeared equally over the contact surfaces. The applied shear connection is greatly affecting the global behaviour of specimens. A sensivity study was required in order to correlate the numerical response to the experimental behaviour of the specimens. An observation had been taken that in the specimen VT-1, a weaker shear connection strength than in the specimen VT-2 was required in order to simulate accurately the experimental behaviour. This observation refers well to the analysis of relative slip shown in Fig. 6.127 and Fig. 6.128, where in the specimen VT-2, a nearly two times smaller end slip was observed than in the specimen VT-1. The

evaluation of cohesive elements strength is described in Eq. 6.46. In the given evaluation, it is assumed that the total resistance of mechanical shear connectors is distributed uniformly over the whole interface. The analysis of shear connection stiffness revealed that in the specimen VT-2, a more ductile connection was required than in the specimen VT-1. This observation can be justified by the scatter of test results for the V-shaped flat shear connector push-out test series, see Fig. 5.28c and Table 5.12, and due to the applied CDP concrete material law, which is not respecting the discontinuities in the material due to cracking. The evaluation of shear connection stiffness is given in Eq. 6.52, where the stiffness values was related to the ductility performance of the V-shaped flat shear connector measured in the experimental campaign, see Table 5.12. Based on the experimental data (Eq. 6.57-6.59), the stiffness values are given in Eq. 6.53-6.55. The behaviour of cohesive elements in the normal direction was assumed to be negligible and the implemented values were taken empirically. The total plastic displacement in the definition of damage evolution was taken based on the experimental performance of the V-shaped flat shear connector given in Fig. 5.28c. The resultant value was calculated according to Eq. 6.60. The applied traction separation laws for all three directions is shown in Fig. 6.136 for the specimen VT-1 and in Fig. 6.137 for the specimen VT-2. The summary with implemented parameters is given in Table 6.15.

$$t_s^0 = t_t^0 = \tau_{R,bond} + \frac{P_{R,Bv2,i} \cdot n_{sc}}{U_{HEB120} \cdot L_{emb}} \cong 1.6\ [MPa] \tag{6.46}$$

Where,

$\tau_{R,bond} \approx 0.8\ [MPa]$, see Table B.3 or Table 5.20 (6.47)

$P_{R,Bv2,i} = 284.1\ [kN]$, see Table 5.19 (6.48)

$n_{sc} = 6$, see Fig. 6.13 (6.49)

$U_{HEB120} = 686\ [mm^2/mm]$, according to steel tables (6.50)

$L_{emb} = 3250\ [mm]$, see Fig. 6.129 and Fig. 6.130 (6.51)

$$k_s = k_t = \frac{\{t_s^0;\ t_t^0\}}{\delta_{u,Bv2}} \left[\frac{MPa}{mm}\right] \tag{6.52}$$

$$\{k_s;\ k_t\}_{min} = 0.2 \left[\frac{MPa}{mm}\right] \tag{6.53}$$

$$\{k_s;\ k_t\}_{max} = 0.55 \left[\frac{MPa}{mm}\right] \tag{6.54}$$

$$\{k_s;\ k_t\}_{m} = 0.31 \left[\frac{MPa}{mm}\right] \tag{6.55}$$

Where,

$\{t_s^0;\ t_t^0\} = 1.6\ [MPa]$, see Eq. 6.46 (6.56)

$\delta_{u,Bv2,min} = 2.84\ [mm]$, see Table 5.12 (6.57)

$\delta_{u,Bv2,max} = 8.00\ [mm]$, see Table 5.12 (6.58)

$\delta_{u,Bv2,m} = 5.12\ [mm]$, see Table 5.12 (6.59)

$\delta_m^f = 50\ mm - \delta_{u,Bv2,m} = 45\ [mm]$, see Fig. 5.28c (6.60)

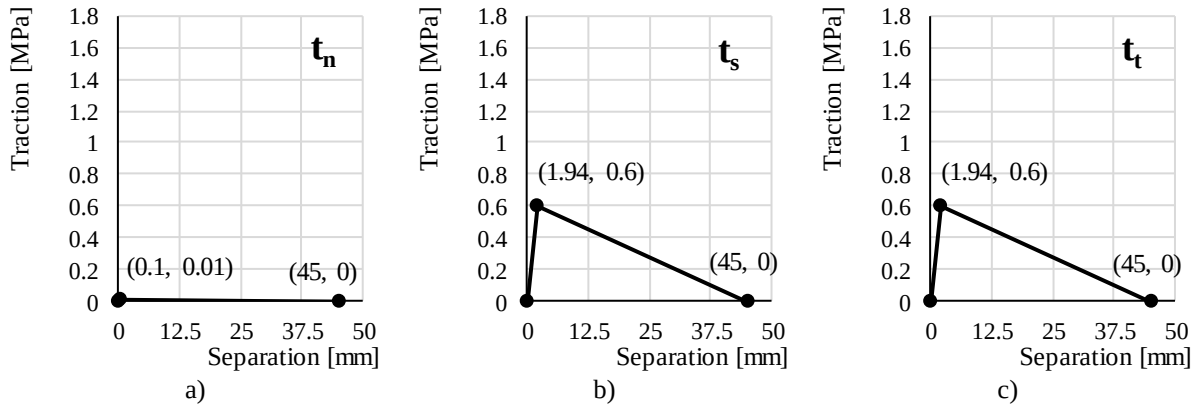


Fig. 6.136. Traction-separation law for the cohesive elements in the specimen VT-1 – a) normal direction, b) shear direction 1 and c) shear direction 2.

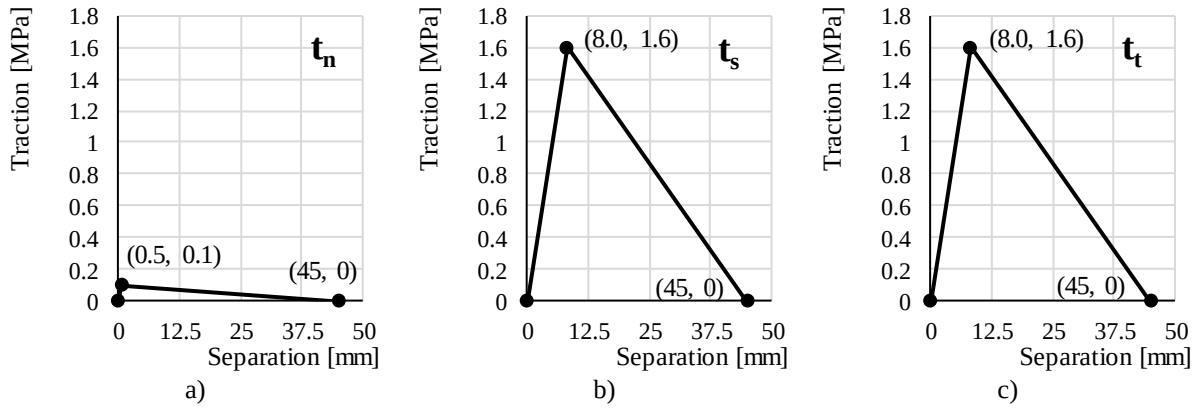


Fig. 6.137. Traction-separation law for the cohesive elements in the specimen VT-2 – a) normal direction, b) shear direction 1 and c) shear direction 2.

Table 6.15.
Properties used to define the response of cohesive elements in the FE simulations of beam/column specimens.

Behaviour	Density	Elastic			Damage initiation			Damage evolution
		Traction			Quads (quadratic stress criterion)			Displacement - linear
Direction:		normal	shear 1	shear 2	normal	shear 1	shear 2	Mode-independent
Specimen	ρ	k_n	k_s	k_t	t_n	t_s	t_t	$\delta_{m,f}$
	[tonne/ mm^3]	[MPa/ mm]	[MPa/ mm]	[MPa/ mm]	[MPa]	[MPa]	[MPa]	[mm]
VT-1	1E-010	0.1	0.31	0.31	0.01	0.6	0.6	45
VT-2	1E-010	0.2	0.2	0.2	0.1	1.6	1.6	45

The applied density of cohesive elements was assumed empirically and the taken value was following the suggestions given in Abaqus manual [174] about taking a value of ten times smaller than the lowest density of the connected parts in order not to impose any significant dynamic effects in the quasi-static simulations with the usage of Abaqus/Explicit solver. In the result, the taken value of density for the cohesive elements was assumed as 1E-010 tonne/mm^3.

6.4.3. Assembly, interactions, constraints and boundary conditions

The developed numerical models were assembled from four instances, which had been created from three parts: (i) steel profile, (ii) concrete block and (iii) reinforcement cage. The steel profile part was present in two instances, as specimen consisted in two embedded steel profiles. The cohesive elements were assigned to the steel profile part by default, as they were created by the offset from the mesh of steel profile. The assemblies are strictly reflecting the geometries of specimens from the experimental camping. The view of assembled cross-section is given in Fig. 6.131 and the perspective view with separately highlighted all the parts for the model of specimen VT-2 is shown in Fig. 6.138. The model of specimen VT-1 was assembled in an analogous way. In Fig. 6.129 and Fig. 6.130, the double symmetry planes are defined. The applied symmetry conditions consisted of restrained displacement in the normal direction and restrained rotations over the global principal axes in two tangential directions of the considered surfaces. The described symmetry conditions are shown in Fig. 6.139. From Fig. 6.138c, it can be noticed that two longitudinal bars and one stirrup are lying in the planes of symmetry, where the equivalent bars with half of the cross-sectional area were applied.

The layer of cohesive elements modelled at the interface between the structural steel and concrete required a constraint relation to interconnect all materials. As it was mentioned earlier, the corresponding surfaces were tied together with the master/slave formulation. Tie constraint between surfaces created a rigid connection between the respective nodes lying on each surface. The master surfaces are considered by Abaqus as the reference surfaces and the constraint properties are applied to the slave nodes, when approaching. This means, that one master node can react with multiple slave nodes but one slave node can react only with one master node. When the nodes on the mesh are adjusted to be coincident, as in the case of the performed beam/column simulations, there is no difference which surface is defined as master or slave. However, Abaqus manual [174] suggest applying the slave formulation to the surfaces of cohesive elements and master to the surfaces of sliding parts. Like this, the slave surfaces mimic the movement and imperfections of master surfaces and brings a more realistic numerical representation of the modelled problem.

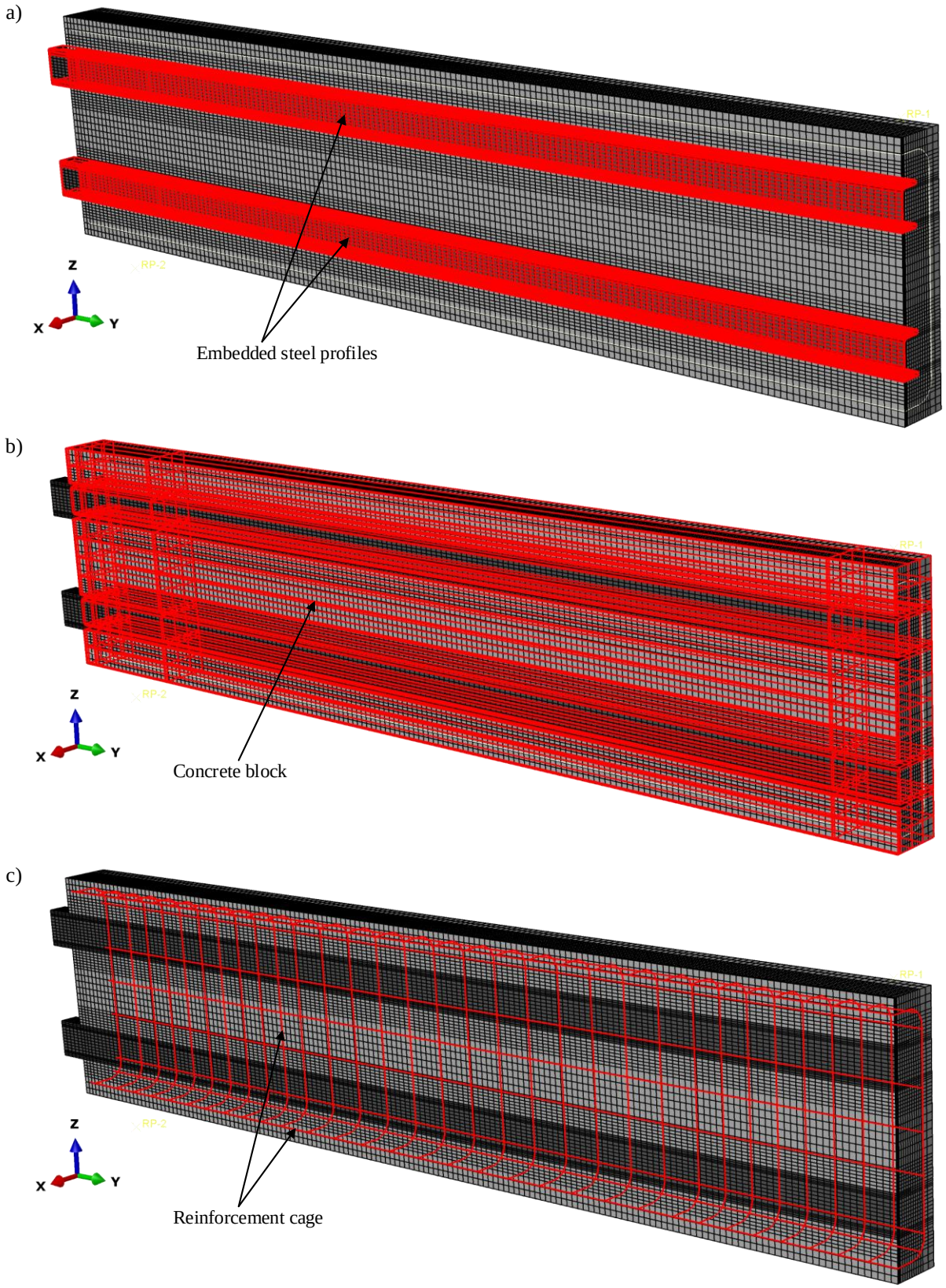


Fig. 6.138. Perspective view on the assembly of the numerical model of beam/column specimen VT-2 – a) with highlighted steel profiles, b) with highlighted concrete and c) with highlighted reinforcement cage.

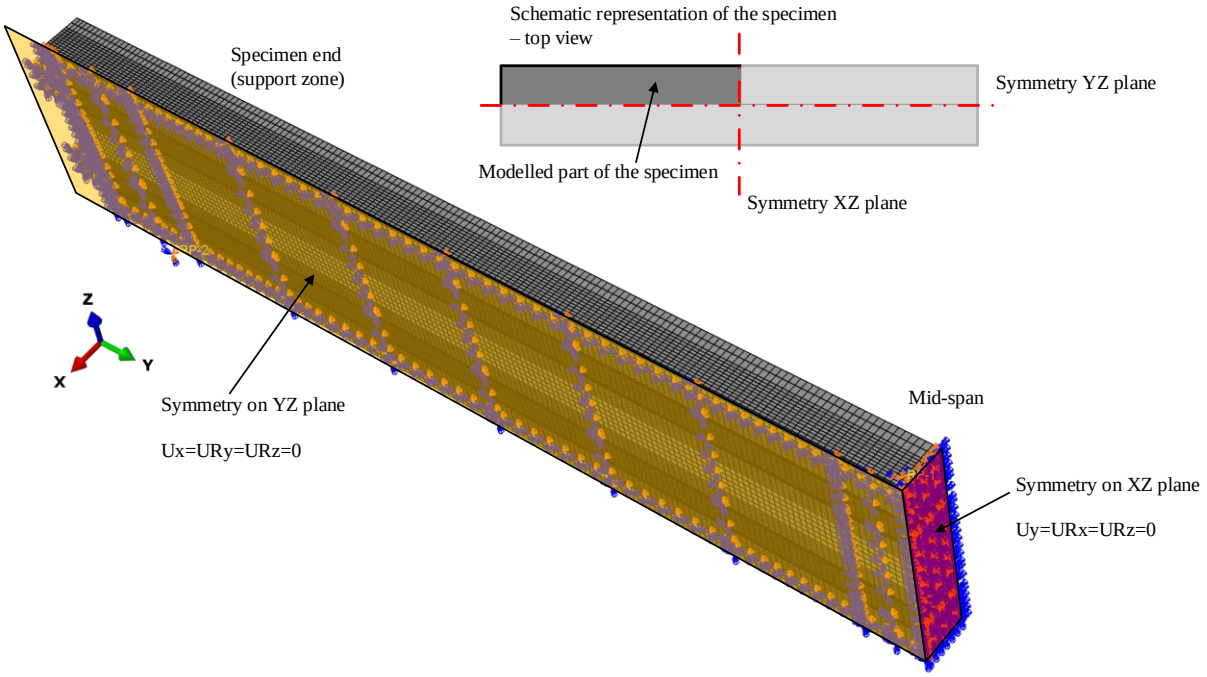


Fig. 6.139. Applied symmetry conditions in the numerical model of beam/column specimen VT-2.

Besides the cohesive elements, on the steel-concrete interface, the contact interaction properties were modelled. The defined interactions were reflecting normal direction behaviour of interaction, where the hard-contact formulation was applied, and tangential direction behaviour, where the Coulomb friction was defined. In the definition of the frictional behaviour, a penalty formulation with friction coefficient of 0.1 was applied for both specimens. The value of friction coefficient was taken and calibrated based on the previous numerical simulations of small-scale cube push-out tests and column push-out tests, see Section 5.3.2 and Section 5.5 respectively. The applied value reflects the reduced frictional behaviour at the interface due to the greased steel profiles with the anti-adhesive release agent. The defined general contact in the Explicit simulations in combination with the cohesive elements allowed for the precise definition of shear connection at the steel-concrete interface.

In order to define the interaction between modelled reinforcement cage and concrete block, the constraint ‘embedded’ had been used [174]. In the constraint definition, the embedded region was the whole part of reinforcement cage, where the host region was the entire concrete part. The default values of tolerances were used [174]. With the applied relation between the reinforcement bars and concrete, a full interaction was assumed.

In order to reflect the test setup and allow for easy and fast control of the reaction forces, as well as displacements, the reference points had been introduced in the places of load introduction points. The reference points were not lying on the surfaces of specimens but on certain offsets in order to reflect the test setup supporting structures, like the load transition plate and sliding pin support shown in Fig. 6.24. The applied offsets on the reference points created eccentricities, which in turn, are affecting the second order behaviour of the specimen. The reference points were lying in the symmetry planes and their

arrangement for both specimens VT-1 and VT-2 is given in Fig. 6.140. The size of the offset in reference point 'support' included the thickness of the roller used for the sliding support in beam/column tests. The modelled load transition points were coupled to the respective surfaces on the beam/column models, which were selected according to the test setup configuration and sizes of the load-transition plates under the hydraulic press and above the support. The kinematic coupling type had been applied for both cases, where all degrees of freedom were constrained between the control reference points and reacting surfaces.

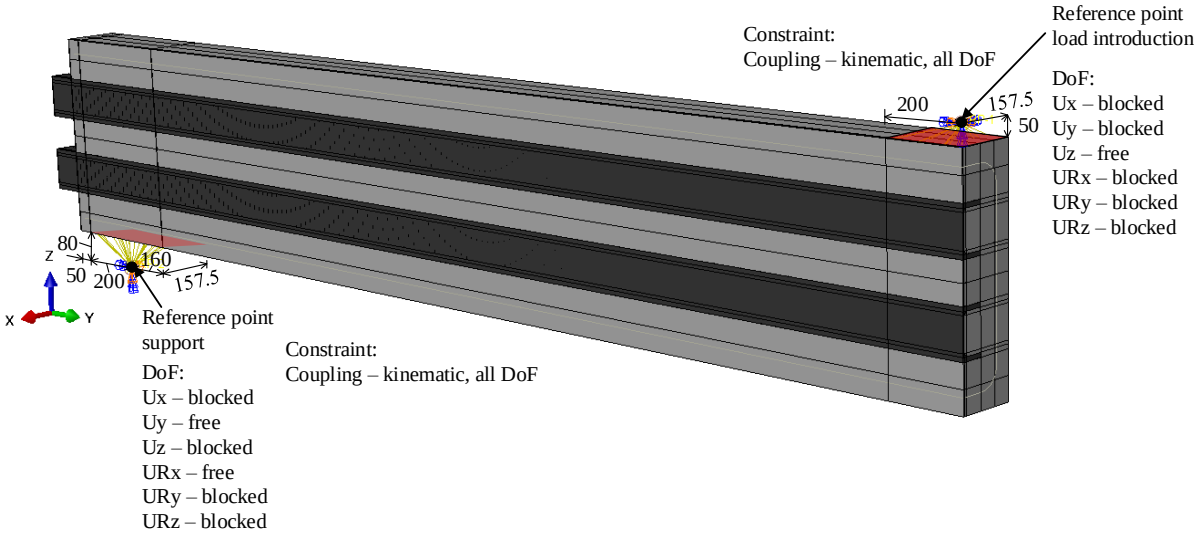


Fig. 6.140. Boundary conditions used in the FE models of beam/column specimens.

The load was imposed in both simulations as the displacement of reference point 'load introduction', which due to the coupling constraint, imposed the same displacement on the selected region in the top surface. The imposed displacement of 200 mm had the characteristic of smooth step, where three phases can be distinguished: (i) the soft non-linear ascending branch, (ii) the linear middle branch and (iii) the soft non-linear stabilising branch [174]. The imposed displacement over a time of 800 s resulted in the simulation speed of 0.25 mm/s, which respects the quasi-static character of the simulations, see Annex F. In theory, the simulation speed for the quasi-static simulations is referring to the mechanical wave propagation speed in the tested materials. Qureshi [153] has proved it that the speed of 0.25 mm/s is feasible for the quasi-static simulations of steel-concrete composite structures.

6.4.4. Results and comparison to the experimental data

As an outcome from the performed numerical simulations, the load-deflection curves, deformations, relative slips, concrete damage patterns and the distributions of strains and stresses in the assembled parts were considered. In order to compare the obtained results from the performed simulations in terms of load flux and specimen behaviour to the experimental results, five main calibration criteria were considered: (i) the energy balance respecting the quasi-static simulation, (ii) the load-deflection curve measured at the mid-span, (iii) the concrete damage pattern, (iv) the stresses and plastification of the

embedded steel profiles and (v) the verification of shear connection at the steel-concrete interface. A good compromise in correlation between the above-mentioned criteria brought a judgement about the calibration of numerical models and the reliability of obtained results. Observations taken from the numerical simulations supported the behaviour observed from the test campaign described in Section 6.3.5 and 6.3.6, where the developed failure of beam/column specimens and taken measurements from the tests were investigated. The obtained numerical results allowed to extend the investigations on values of strains, stresses or deformations. Moreover, based on the obtained numerical responses, the specific behaviour of specimens was distinguished, which proves the working hypothesis of analogy to the Vierendeel truss behaviour.

In the calibration process of simulated tests, 88 numerical simulations for the specimen VT-1 and 98 numerical simulations for the specimen VT-2 were performed. A high number of simulations allowed for the comprehensive investigation of varied input parameters. It was found that under a specific combination of the parameters, a significant difference in the global behaviour of specimens can be obtained, like for example more or less visible Vierendeel-like behaviour, later called as “Vierendeel action”.

6.4.4.1. Specimen VT-1 with the small distance between steel profiles

In Fig. 6.141, the numerically obtained load-deflection curve for the specimen VT-1 is shown. The described relation is showing the resultant reaction force in z-direction from the reference point ‘load introduction’ and the displacement of the node localised at the bottom surface of the specimen at the intersection axis of the symmetry planes. The obtained results of reaction force had been post-processed and the low-pass Butterworth filter [174] with cut-off frequency of 0.005 Hz was used. The application of the aforementioned filter simplified the load-deflection curve and eliminated the recorded noise-based amplitude peaks coming from the vibration response of model due to the dynamic nature of simulation. The dynamic peaks in the amplitude of reaction force were related to the applied mass scaling and the vulnerability of numerical model to vibration – big span between the supports. The applied mass scaling allowed for more efficient simulation time but the developed kinetic energy had be verified that is not reaching significant values in comparison to the internal energy, see Annex F. Finally, from Fig. 6.141, it can be observed that good correlation between the experimental and numerical load-deflection curves was obtained, where not only the peak but also ascending and descending branches are in good comparison to the test curve. Level of the residual load-bearing capacity relied on the capacity to redistribute forces from the damage zone localised at symmetry in mid-span towards the sides of specimen. From the sensivity study, it was identified that the peak load value and the level of residual strength were highly sensitive to the defined concrete material law and performance of the applied shear connection. Modification of both aspects not only change the load-deflection curve but also significantly affects the resulting deformation and damage pattern.

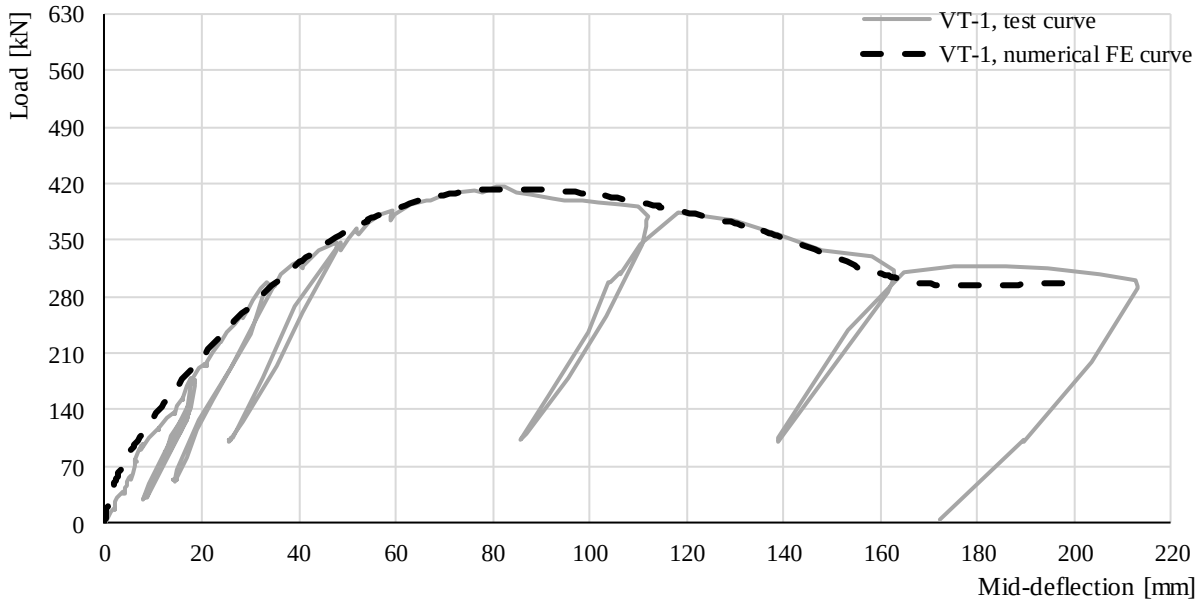


Fig. 6.141. Numerical load-deflection curve of beam/column specimen VT-1 for the node at the mid-span.

The damage sequence obtained from the numerical simulations reflected well the damage sequence observed in test specimens. Following the load-deflection curve shown in Fig. 6.141, in the ascending branch of the curve, the vertical cracks due to bending appeared. Formulation of the peak point was related to the development of compression damage zone in the top part of concrete and under the load introduction point. Finally, the descending branch and stabilisation zone were accompanied with the progressing damage in the zone next to the symmetry plane and progressing shear damage of concrete between the embedded steel profiles (in Abaqus can be observed as combination of tension and compression damage of CDP material). The described damage sequence is shown in Fig. 6.142, where the test specimen behaviour can be compared from Fig. 6.72-6.82. The characteristic zone of compression damage in the concrete part and the zone of crushed concrete observed from the tests are correlating. The resulting tensile vertical cracks and inclined diagonal shear cracks reflected well the test results. Moreover, in the final phase of simulation, the major horizontal tensile crack in the top part of concrete under the load introduction point is well reproduced from the test observations, compare Fig. 6.142c and Fig. 6.74 or Fig. 6.77.

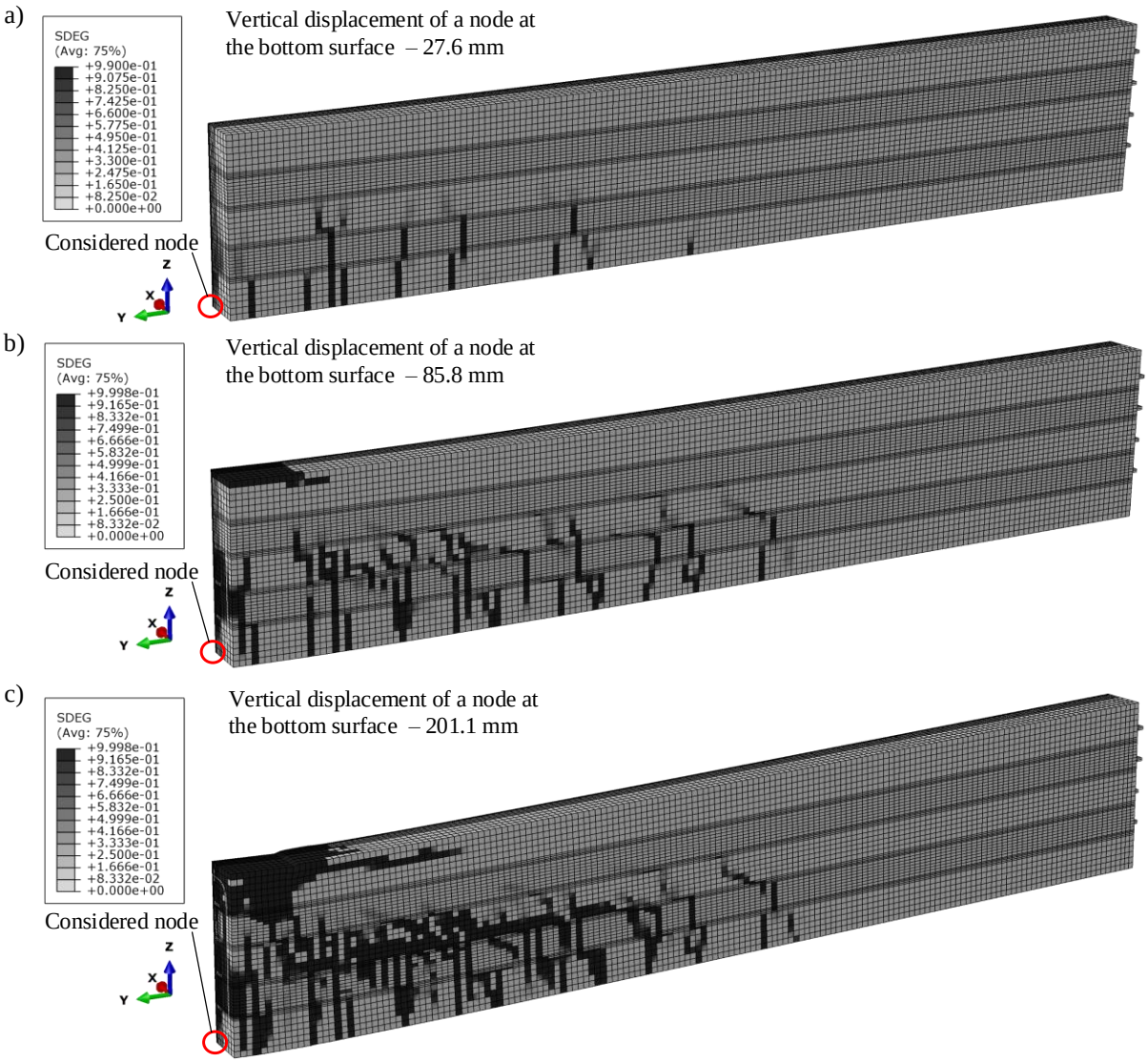


Fig. 6.142. Damage sequence in the numerical simulation of beam/column specimen VT-1 – a) damage at the phase before the failure, b) damage at the peak point and c) damage at the last phase of simulation.

In Fig. 6.143, the deformation of the embedded steel profiles obtained from the numerical simulation is given. It can be observed that the strains obtained numerically are in good comparison to the experimentally obtained values shown in Fig. 6.42 at the peak load. Moreover, the distribution of tensile and compression strains is shown and the local plastification of embedded steel profile at the bottom can be identified. The shown distribution of strains is confirming the position of neutral axis due to the global bending, which was localised in the web of upper embedded steel profile. In Fig. 6.143b, the resultant von Mises stresses are shown, where it can be observed that the top flange of the upper embedded steel profiles not yielded but the bottom flange with the part of the web of bottom embedded steel profile plastified in the zone next to the symmetry condition at the mid-span.

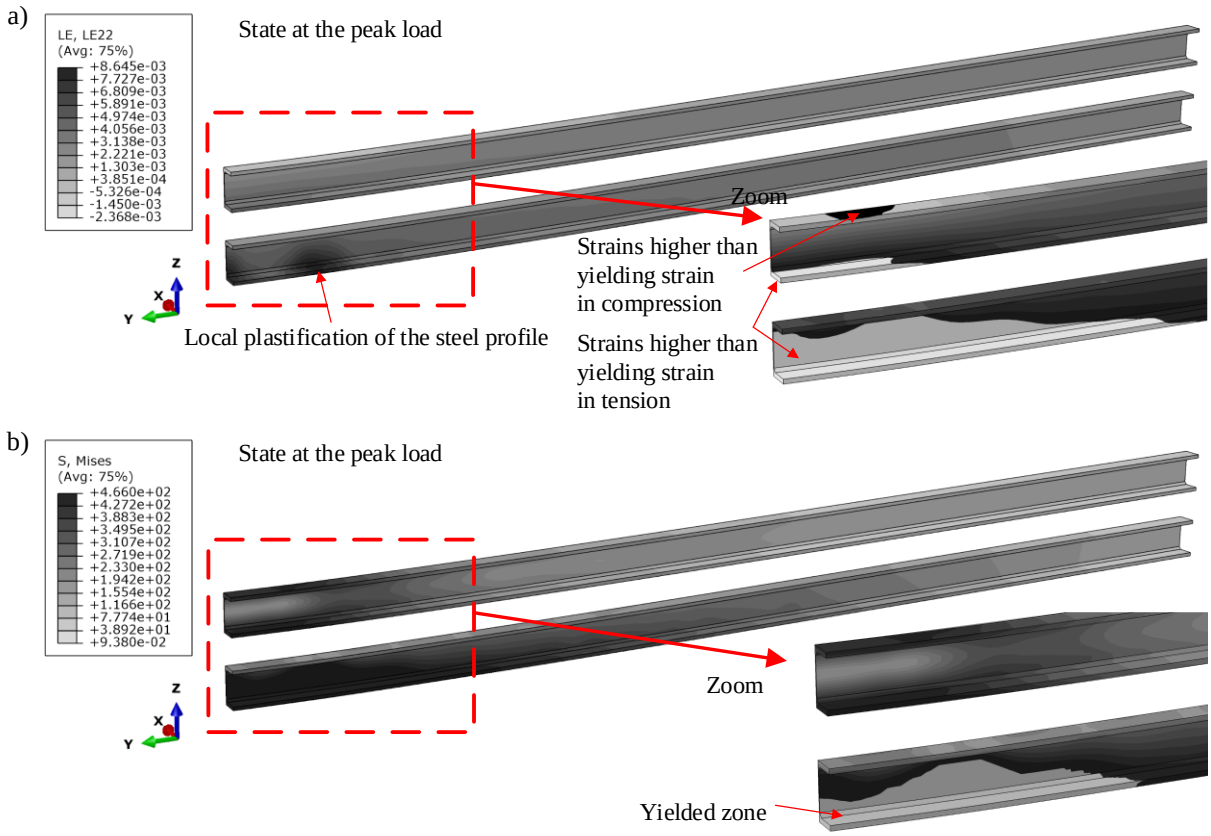


Fig. 6.143. Deformation of embedded steel profiles at the peak load from the numerical simulation of beam/column specimen VT-1 – a) logarithmic strains and b) von Mises stresses.

In Fig. 6.144, the logarithmic strains and stresses in the y-direction are shown for the state at the end of simulation, where the deflection reached maximal value. The zones of yielding stresses shown in Fig. 6.144b are not corresponding to the zones of the inelastic strains shown in Fig. 6.144a due to the redistribution of forces after the development of plastic hinge at the mid-span of specimen (in Abaqus in the zone close to the symmetry condition). The steel profiles outside the yielding zone remained straight, which was also observed from the tests and shown in Fig. 6.83.

The longitudinal reinforcement was subjected to higher deformation in the numerical simulation in comparison to test results. The distribution of logarithmic strains at the peak load indicated yielded bars with higher strains in comparison to the measured values during the test and shown in Fig. 6.42. The numerically obtained strains in the stirrups correlated to the experimental values given in Table 6.9, where in the numerical simulations a comparable character of the strains distribution was obtained with scattered values between 0.6-1‰. The compressive strains in the stirrups were observed above the support and further over a certain distance towards the mid-span at the bottom of specimen. At the state of maximum deflection, the aforementioned zone of compressive strains in stirrups extended over the bottom part of the specimen at a distance from the support equal approximately to two times the height of the specimen, see Fig. 6.145. The development of the compression strains in the shear reinforcement suggests that non-typical beam-like bending mechanism was present. The vertical compression in the bottom fibres of specimen subjected to sagging bending could be observed due to the developed

Vierendeel action, which imposed a point of contraflexure and certain restraint in the bottom fibres. The developed contra-curvature at the zone close to the support partially prevented sagging bending and imposed compression to the stirrups. This effect could be observed only due to the presence of the embedded stiff steel profiles and assured shear connection with the concrete.

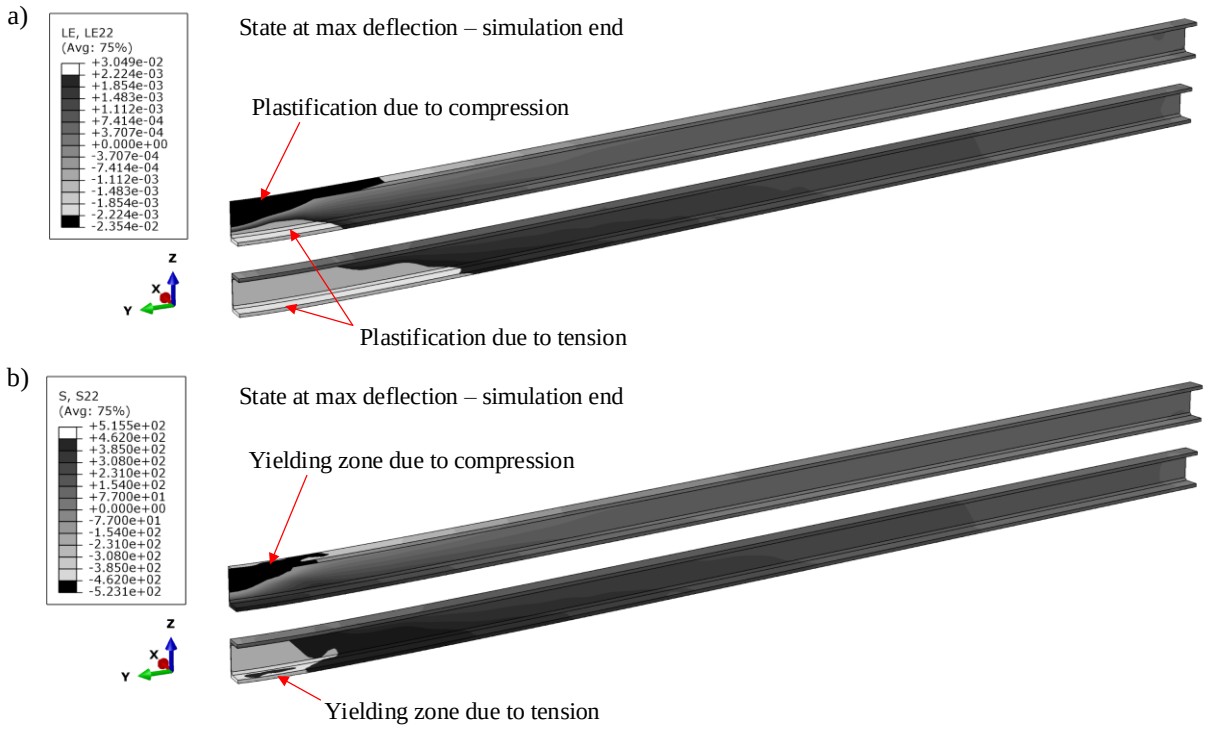


Fig. 6.144. Strains and stresses limited to yielding values in the embedded steel profiles at the maximum deflection from the FE simulation of beam/column specimen VT-1 – a) logarithmic strains and b) stresses in y-direction.

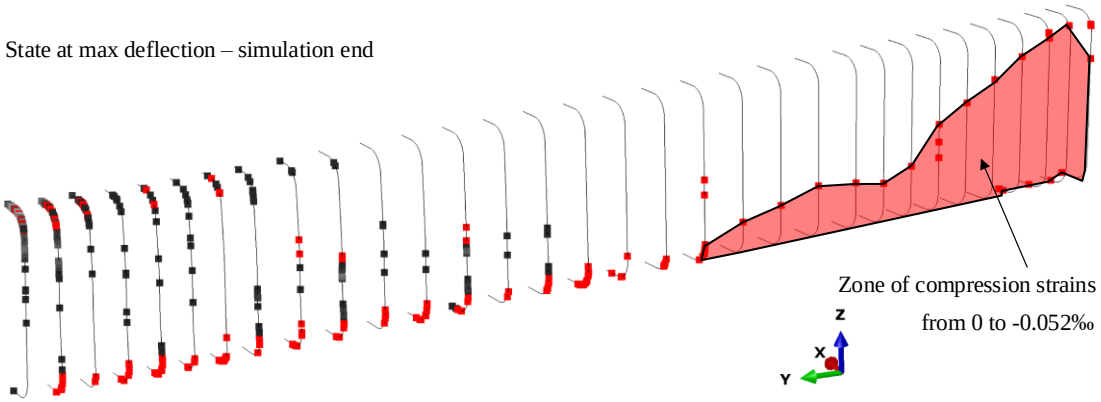


Fig. 6.145. Zone of compression strains in the stirrups at the maximum deflection state obtained from the simulation of beam/column specimen VT-1.

Due to the applied shear connection in the form of cohesive material, the utilisation of shear connection resistance can be described by the shear stresses developed in the layer of the cohesive elements as shown in Fig. 6.146. It can be observed that in the upper embedded steel profile, the shear connection had not been subjected to extensive stresses, where in the same time, in the bottom steel profile, the stresses of approximately 0.6 MPa at the peak load state were reached. The shear resistance of cohesive elements was achieved before reaching the peak load. However, the damage of shear

connection was restrained by the damage evolution law which required a relative slip to progress. The degradation of shear connection not developed at the peak load state and sustained nearly until the end of the simulation. The maximum degradation state of cohesive elements is shown in Fig. 6.147.



Fig. 6.146. Shear stresses developed in the layer of cohesive elements at the peak load in the simulation of beam/column specimen VT-1.

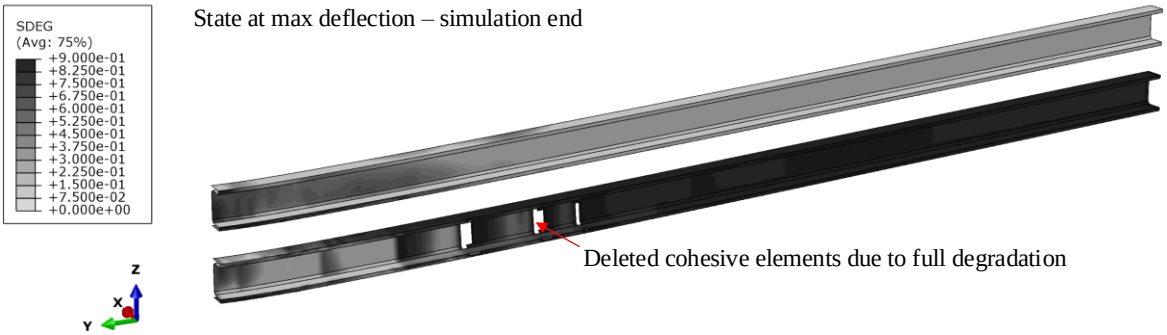


Fig. 6.147. Degradation of cohesive elements at the end of simulation for the beam/column specimen VT-1.

With the degradation of cohesive elements, the relative slip between the embedded steel profiles and the concrete developed. In Fig. 6.148, the contact interface slip obtained from the numerical simulation is shown. In the black area on the figure, the relative slip exceeded the values measured from the experimental tests – 1.43 mm for the peak load state and 2.43 mm for state at the end of the test, see Table 6.10. It can be observed that the indicated zones of higher slip are not equally distributed but they affected the final end-slip value, which reached approximately 4 mm at the peak load and 9.5 mm at the end of the simulation. However, it has to be respected that, due to the taken simplification in numerical simulations about the replacement of the mechanical shear connectors by the cohesive elements, the resultant slip obtained from simulation will be higher than in the corresponding test. The difference is related to the applied stiffness, strength and damage evolution in the material law of cohesive elements. The defined numerical properties of shear connection allowed for bigger deformation than the concrete damage developed around the shear connectors in beam/column tests, see Fig. 6.86 and Fig. 6.87.

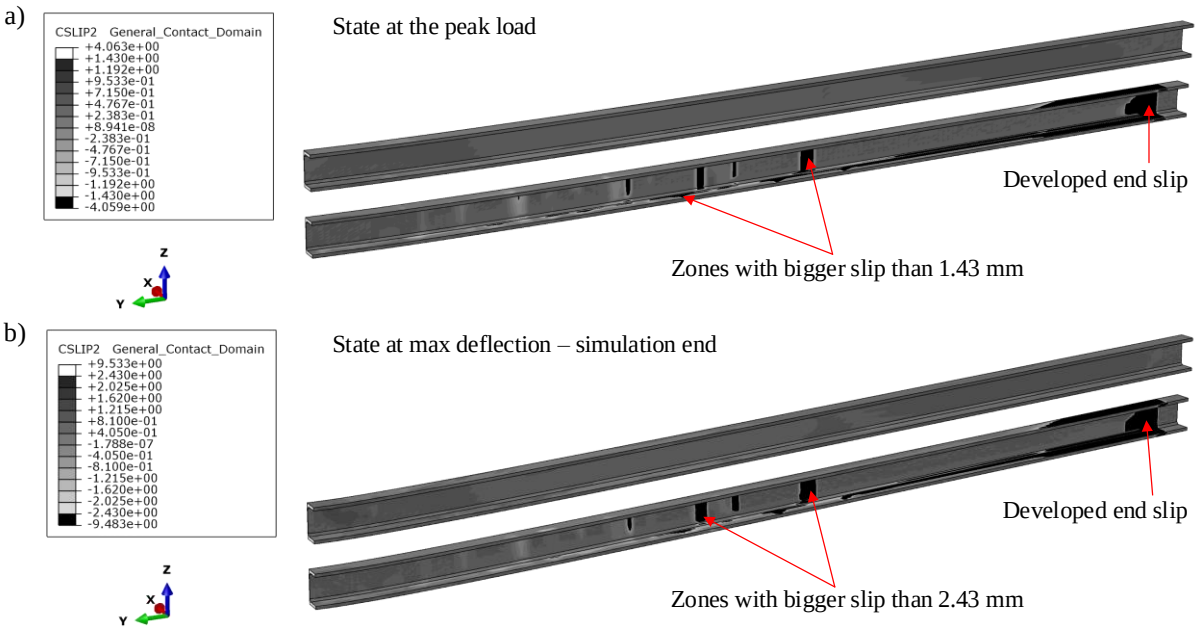


Fig. 6.148. Relative slip of embedded steel profiles obtained from the numerical simulation of beam/column specimen VT-1 – a) state at the peak load and b) state at the end of the simulation.

Comparing the result from Fig. 6.145 and Fig. 6.88, the vertical cracks above the support of specimen observed in the opened test specimen VT-1 are not directly visible in the numerical simulation. However, it has been observed that the maximum principal stresses in the considered zone above the support are positive and oriented approximately horizontal. Furthermore, the value of the minimum principal stresses in the same considered zone are positive and oriented clearly horizontally, which additionally proves the development of tensile stresses. The plot of identified principal stresses is given in Fig. 6.149. In the numerical model of specimen VT-1, the aforementioned effect is not significant but present, where in the numerical model of the specimen VT-2, a clear tensile stresses can be identified with the value close to the tensile resistance. The difference between the specimens is related to a more significant or less significant shear deformation of the specimen, see Section 6.3.6 and Section 6.3.7. Based on the identified tensile principal stresses above the support from the numerical simulation, it can be judged that the existence of identified vertical cracks from the test specimen opening indicated the characteristic Vierendeel truss-like behaviour of beam/column specimen. It is proven that the numerical simulations supported the observations from the tests and the Vierendeel action in the specimen was present.

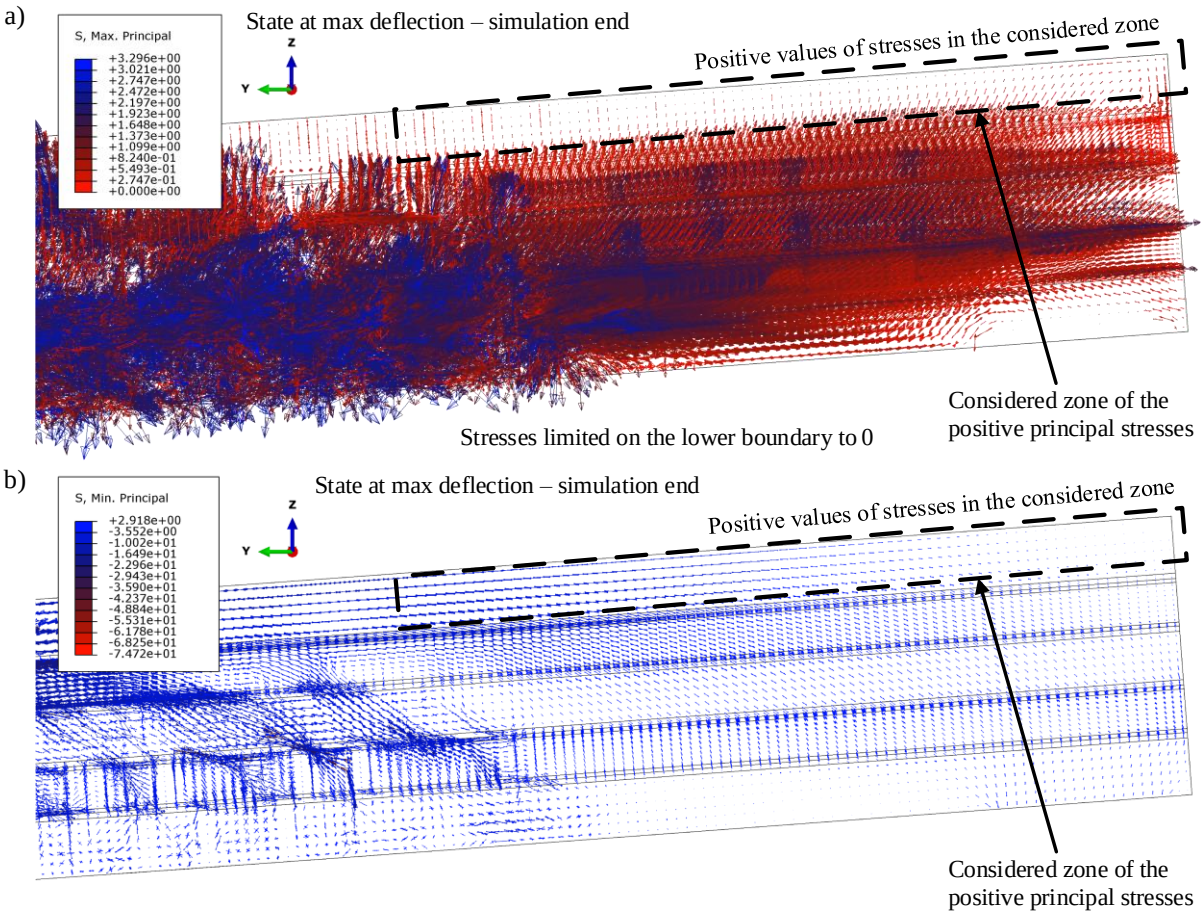


Fig. 6.149. Principal stresses in the support zone obtained from the FE simulation of beam/column specimen VT-1 – a) maximum principal stresses and b) minimum principal stresses.

6.4.4.2. Specimen VT-2 with the big distance between steel profiles

In Fig. 6.150, the numerically obtained load-deflection curve for the specimen VT-2 is shown. Identical like for the case of specimen VT-1, the described relation had been post processed and for the reaction force taken from the reference point 'load introduction' in z-direction, the Butterworth filter with cut-off frequency of 0.005 Hz was applied. The displacement described in the discussed diagram as the mid-deflection was taken from the node lying on the bottom surface of the specimen at the intersection of the symmetry planes. From Fig. 6.150, it can be observed that numerically obtained curve correlated well to the experimental response of specimen, including ascending and descending branches of the curve. The obtained numerical response was very sensitive to the defined level of the shear connection in the form of the shear strength of cohesive elements and applied concrete material law. A similar observations has been taken for the specimen VT-1.

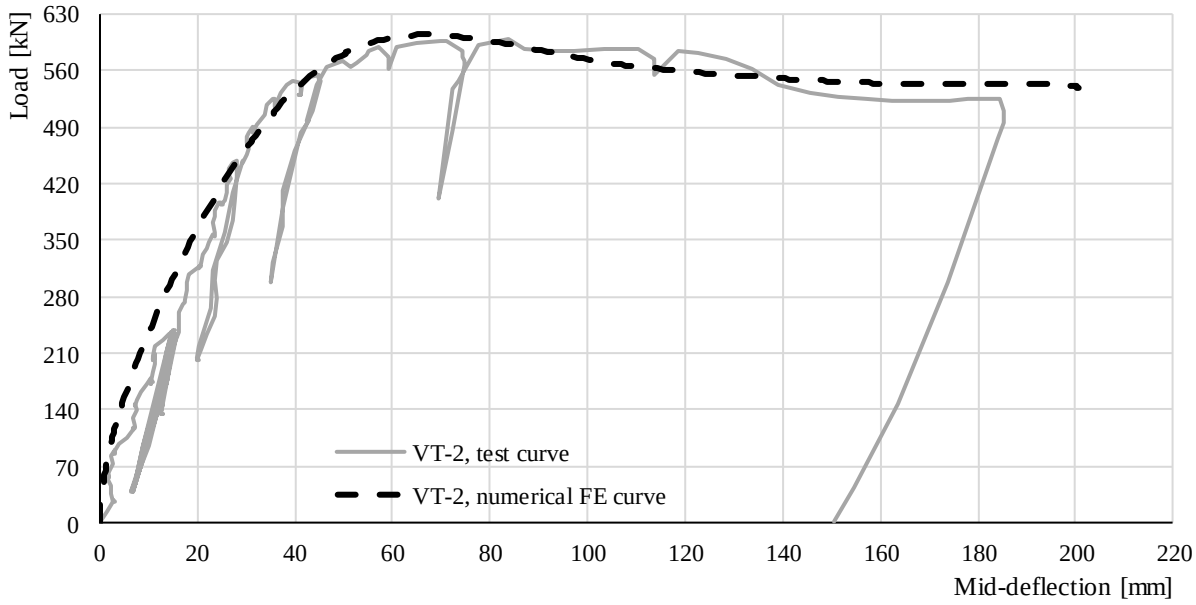


Fig. 6.150. Numerical load-deflection curve of beam/column specimen VT-2 for the node at the mid-span.

The obtained damage sequence in the concrete part from the numerical simulation given in Fig. 6.151 indicated good correlation to the observations from the test shown in Fig. 6.89-6.96. In the initial phase of test, the vertical tensile cracks due to bending formulated as shown in Fig. 6.151a. Together with approaching simulation state to the peak load level, the vertical cracks propagated and the horizontal cracks in the height of the steel profiles developed simultaneously with the concrete compression damage zone localised under the load introduction point, see Fig. 6.151b. In the last phase of the simulation, the concrete compression damage zone propagated together with the development of the more extensive zone of tensile and diagonal cracks on the wall of the specimen. The damage of the concrete part at the end of the simulation is shown in Fig. 6.151c. The resulting arrangement of the tensile vertical cracks and inclined diagonal shear cracks indicated good correlation to the test results. The characteristic horizontal cracks visible in the numerical simulation can be also observed in the experimentally obtained crack pattern of the beam/column specimen but with reduced impact. The difference between numerical and experimental observations are related to the fact that in the numerical model, the shear connection is uniformly distributed over the entire interface between the steel and concrete parts, where in the experimental specimen, the shear connection was assured in the discretised manner. In the result, a significant force transfer over the total embedment length was assured in numerical simulation, which imposed higher strains in concrete.

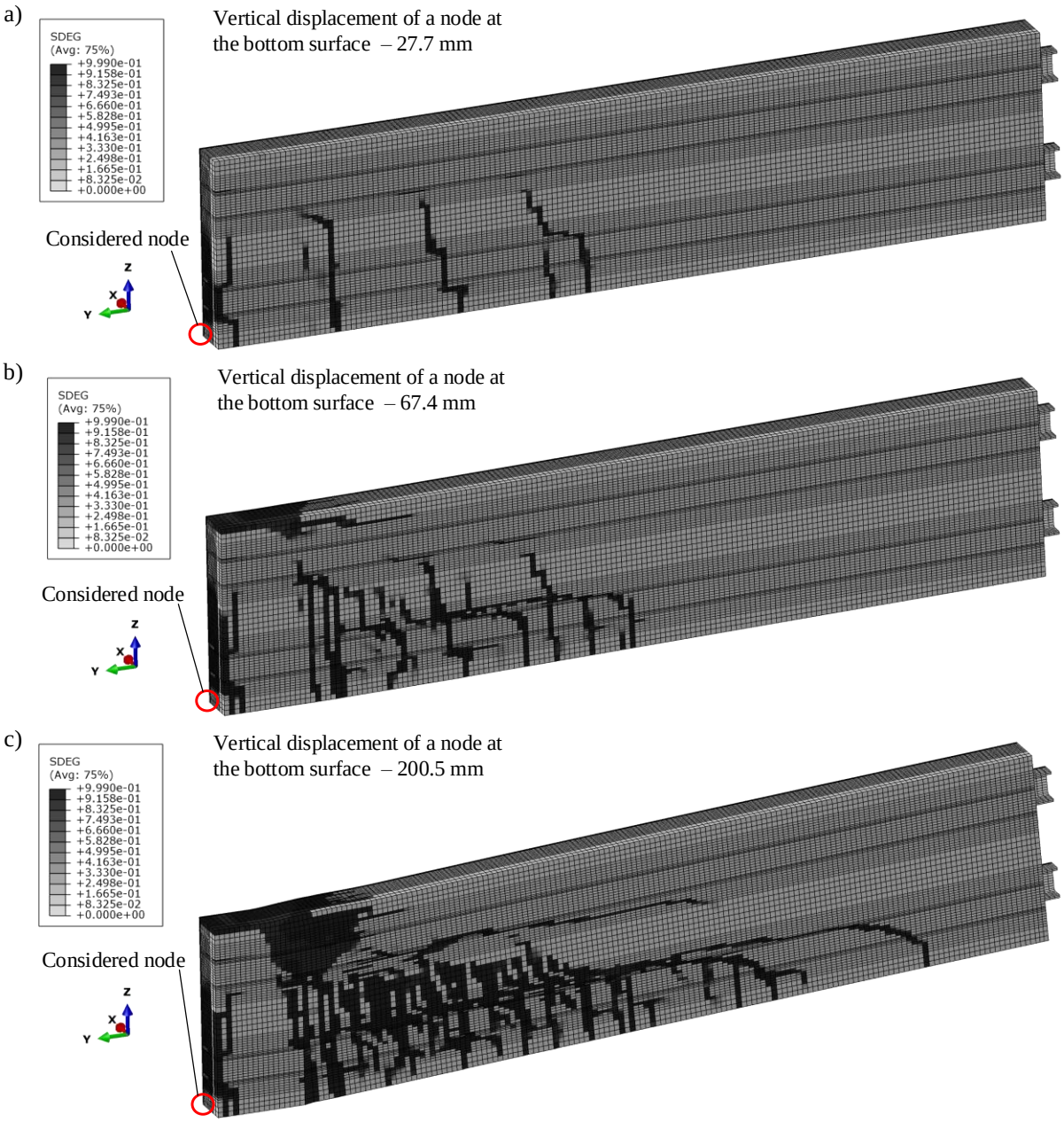


Fig. 6.151. Damage sequence in the FE simulation of beam/column specimen VT-2 – a) damage at the phase before the failure, b) damage at the peak point and c) damage at the last phase of simulation.

In Fig. 6.152, strains and von Mises stresses developed in the embedded steel profiles during the numerical simulation are shown. A good correlation to the experimentally measured strains shown in Fig. 6.47 at the peak load can be observed. Similarly like in the case of the specimen VT-1, a local pastification point in the bottom embedded steel profile can be observed. However, by limiting strains to the yielding strain in the plot, as shown in detail "zoom", two zones with higher strains can be identified – one in the compression in the top flange of upper embedded steel profile and second in tension in the bottom part of bottom embedded steel profile. The distribution of strains from simulation confirmed the evaluated position of neutral axis in the web of upper profile, which was also observed from the recorded strains in the beam/column test. From Fig. 6.152b, it can be observed that the upper

steel profiles had not yielded but the bottom flange with the part of the web of bottom embedded steel profile plastified in three zones next to the symmetry condition at the mid-span.

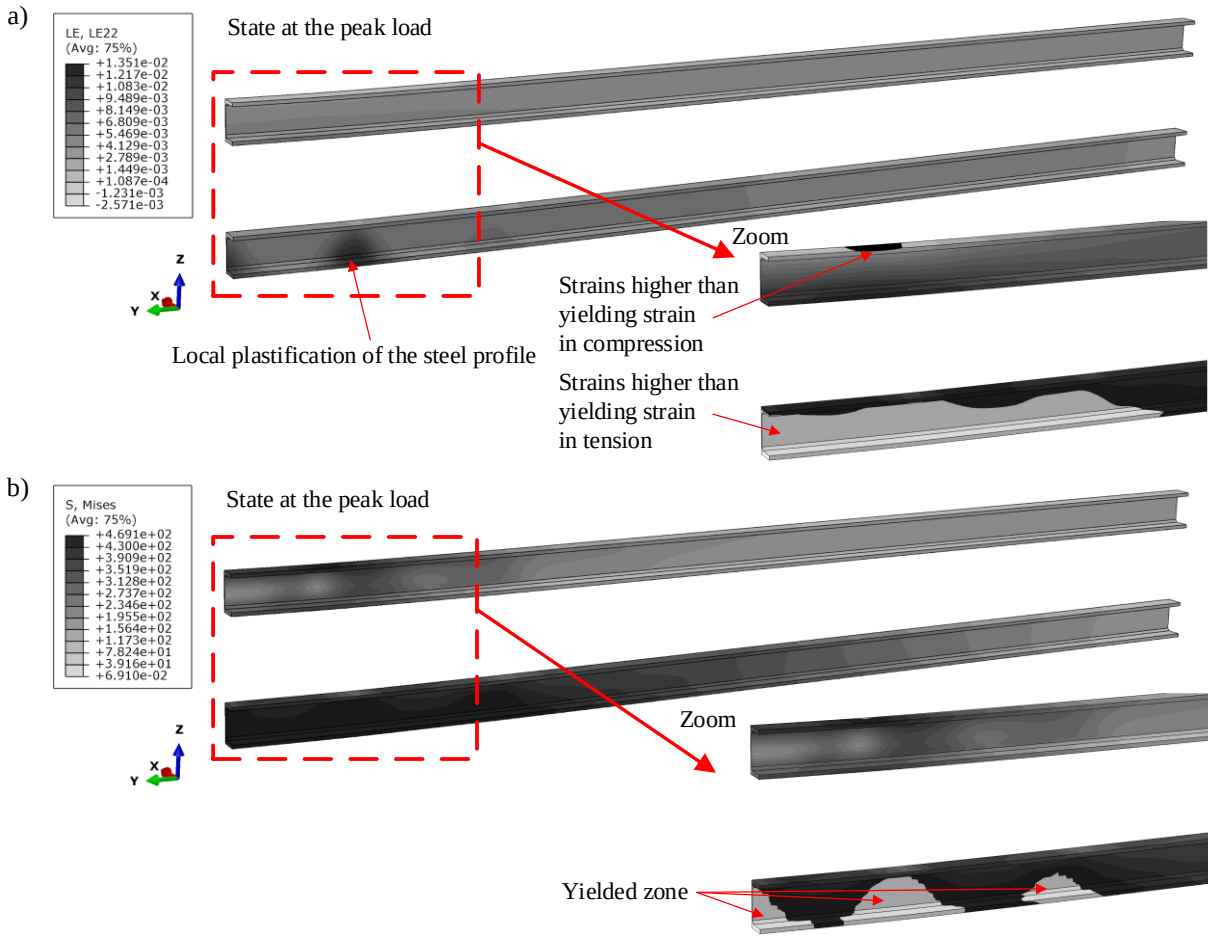


Fig. 6.152. Deformation of embedded steel profiles at the peak load from the FE simulation of beam/column specimen VT-2 – a) logarithmic strains and b) von Mises stresses.

Similar like in the case of specimen VT-1, the calibration and verification of numerical model for the specimen VT-2 in terms of strains was made until the peak load state, where the experimental measurement results are reliable. Afterward, the recorded data from tests is not free from an error in the measurement due to the significant deformation of specimen and the damage of measurement equipment, like for an example detaching of cables. In Fig. 6.153, the logarithmic strains and stresses in the y-direction are shown for the state at the end of simulation, where the maximum deflection was reached. From the presented deformation shapes of embedded steel profiles, it can be observed that the profiles outside the central zone remained straight, which was also observed from the test campaign and shown in Fig. 6.98-6.101. In the mentioned-above central zone, wide plastification zones can be noticed in both, compression and tension parts, as shown in Fig. 6.153a. In Fig. 6.153b, corresponding yielding zones can be identified. The localisation, shape and size of the developed zones of plastified material correspond to the deformation shape of specimen and the formulation of plastic hinge in its centre.

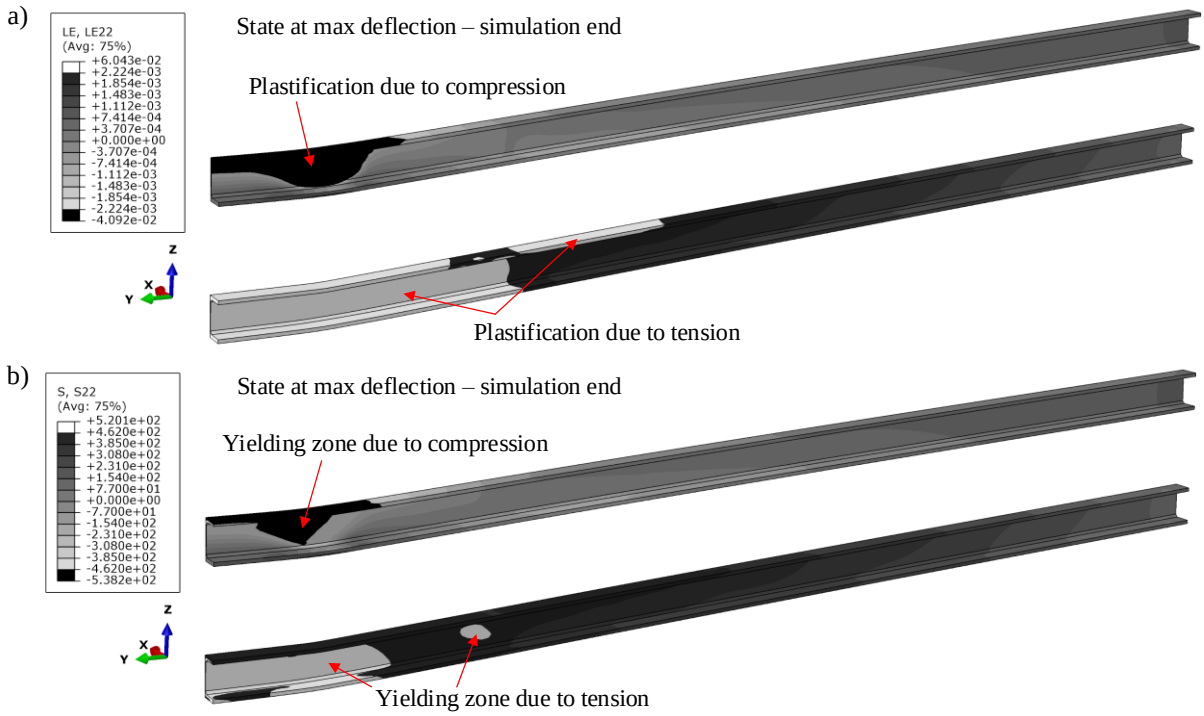


Fig. 6.153. Strains and stresses limited to yielding values in the embedded steel profiles at the maximum deflection from the FE simulation of beam/column specimen VT-2 – a) logarithmic strains and b) stresses in y-direction.

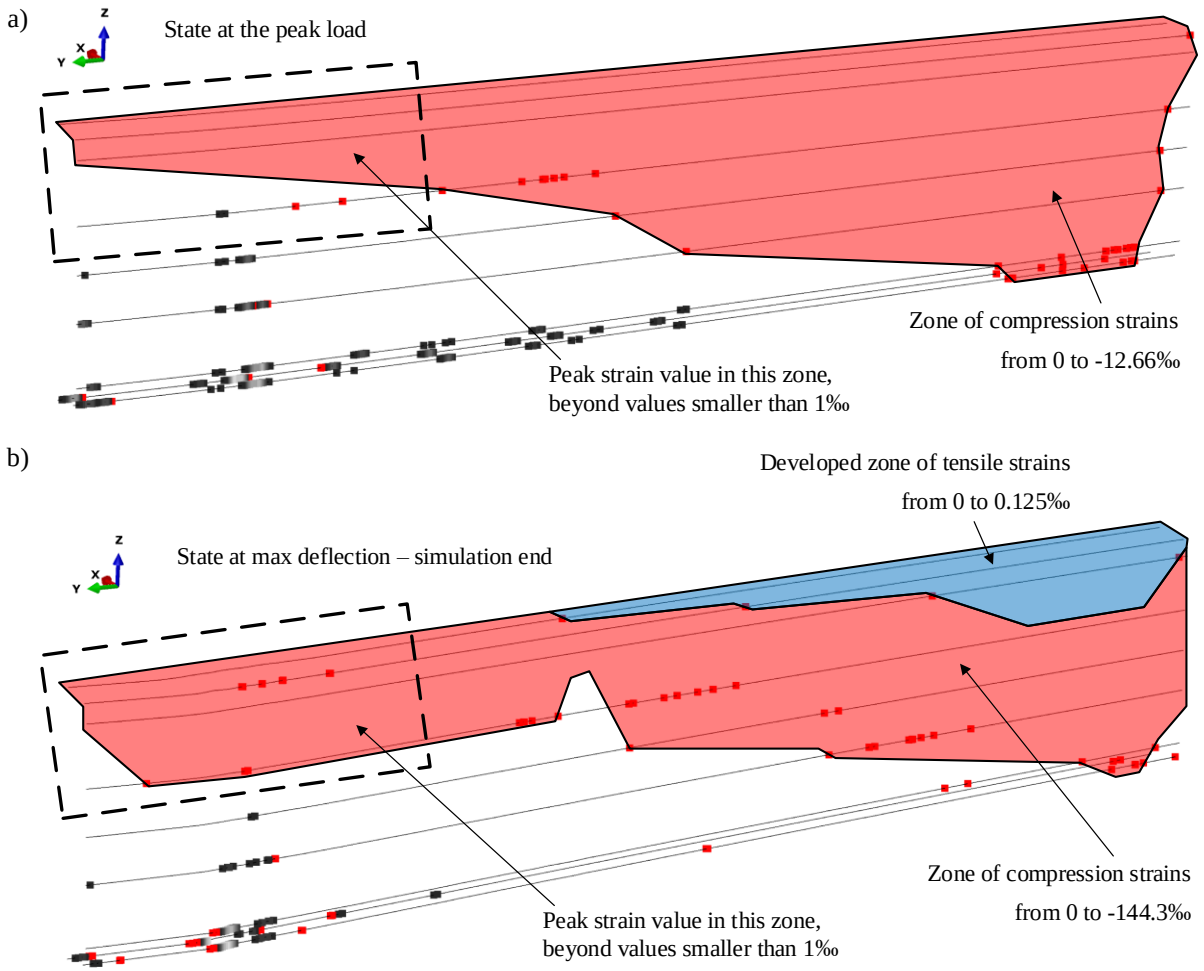


Fig. 6.154. Zone of the compression strains in the longitudinal reinforcement obtained from the simulation of beam/column specimen VT-2 – a) at the peak load state and b) at the maximum deflection state.

The resultant strains in the longitudinal reinforcement brought good correlation to the experimentally obtained values, however, in overall higher values from simulation were obtained. The difference is related to the applied concrete material law and the kinematic constraint between the concrete and reinforcement bars, as it was observed also for the specimen VT-1. In Fig. 6.154, the schematic representation of the developed compression stresses zone in the longitudinal reinforcement bars is given. It can be observed, by comparing Fig. 6.154a and Fig. 6.154b, that at the simulation end, a zone of tensile stresses formulated in the top part above the support, where at the peak load all the reinforcement bars were subjected to compression. The development of the aforementioned tensile zone in this characteristic place, suggest activation of the Vierendeel action together with higher deformation of the specimen, thus higher shear deformation.

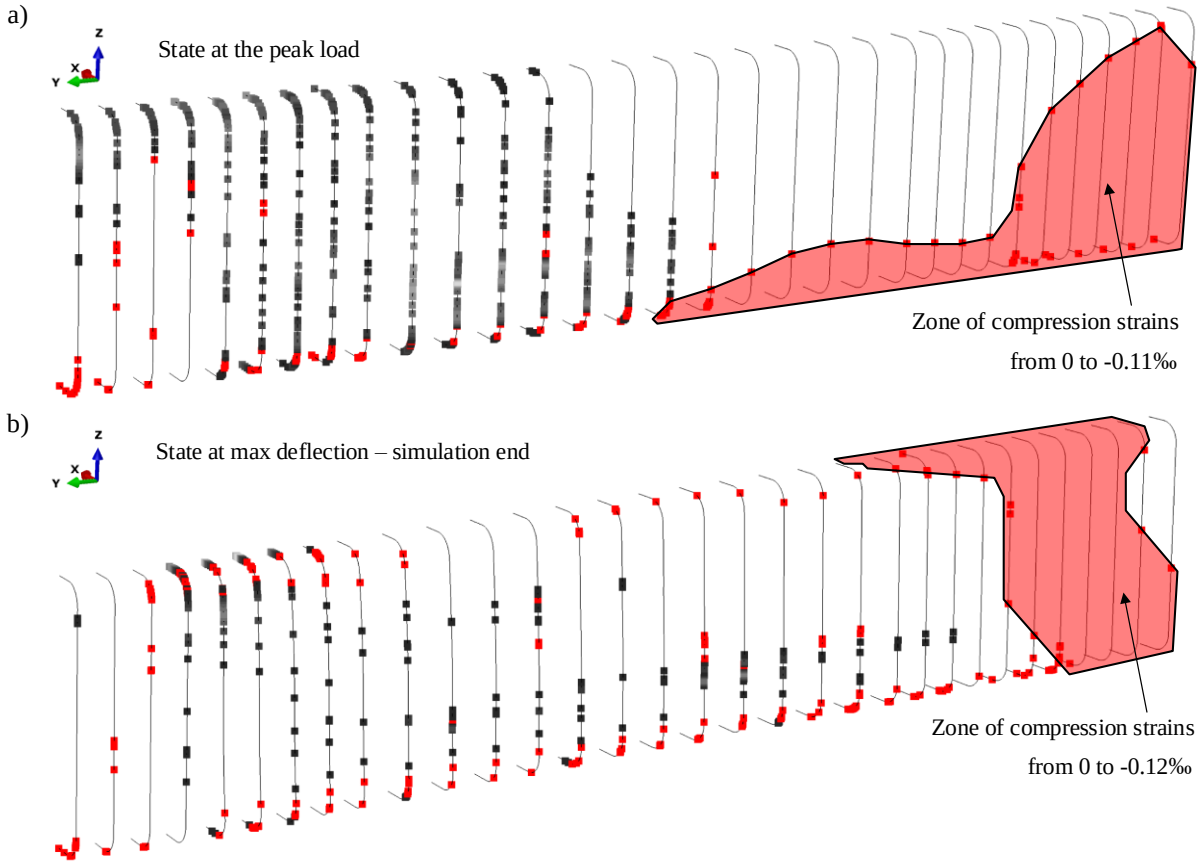


Fig. 6.155. Zone of the compression strains in the stirrups obtained from the FE simulation of beam/column specimen VT-2 – a) at the peak load state and b) at the maximum deflection state.

The numerically obtained strains in the stirrups brought good correlation to the experimental values. According to the measurements from tests given in Table 6.9, similar strains distribution was obtained from numerical simulations with scatter between 0‰ to 1.5‰. From Fig. 6.155a, a zone of compression strains above the support and at the bottom of the specimen can be identified with a length equal approximately to two times the height of specimen. Analogous observation was made for the specimen VT-1. After reaching the final stage of simulation, the compression zone reduced only to the zone next to the support and extended in height, see Fig. 6.158b. The existence of compression strains in the

stirrups at the bottom can be explained be the activation of the Vierendeel action in the specimen and imposed compression forces due to the contra-curvature developed in the zone next to the support. The described effect vanished with the increased deformation and development of the plastic hinge in the mid-span of the specimen due to the redistribution of internal forces.

From the analysis of shear stresses developed in the cohesive elements, the verification of shear connection can be made. In Fig. 6.156, the plot of shear stresses in the cohesive elements developed at the peak load is given. It can be observed that the shear connection in the upper embedded steel profile not exhibited extensive stresses, similarly like in the case of specimen VT-1. In the bottom steel profile, shear stresses of approximately 1.05 MPa were reached, which are much lesser than the specified strength of cohesive elements (1.6 MPa). This means, that the full shear connection was assured as it was observed in test campaign, see Table 6.10. From Fig. 6.157, the damage state of the cohesive elements at the end of simulation shows that some elements fully degraded even if the peak shear stresses had not been reached. This effect was observed due to the defined quadratic damage formulation, where the normal separation contribute to the resistance of cohesive elements. The normal direction of traction-separation law had been defined as 'weak', see Table 6.15, the normal separation that developed at the external surfaces of the flanges contributed greatly to the total damage of the layer of shear connection. In the same time, nearly no degradation of the cohesive elements developed over the upper embedded steel profile.

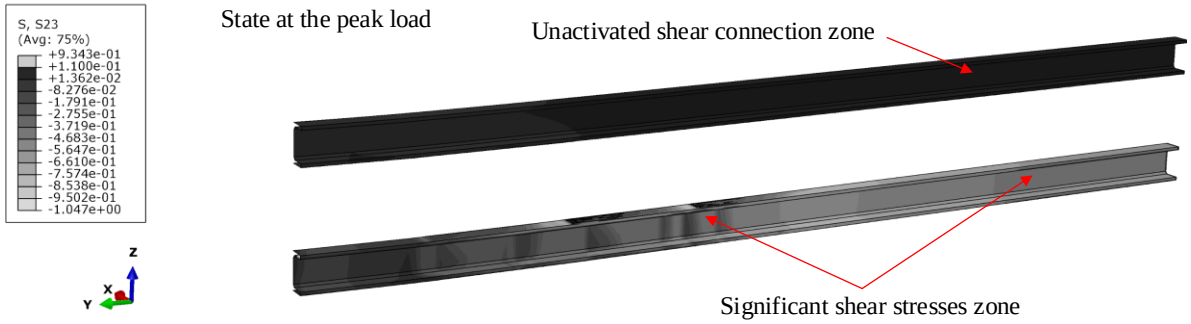


Fig. 6.156. Shear stresses developed in the layer of cohesive elements at the peak load in the FE simulation of beam/column specimen VT-2.

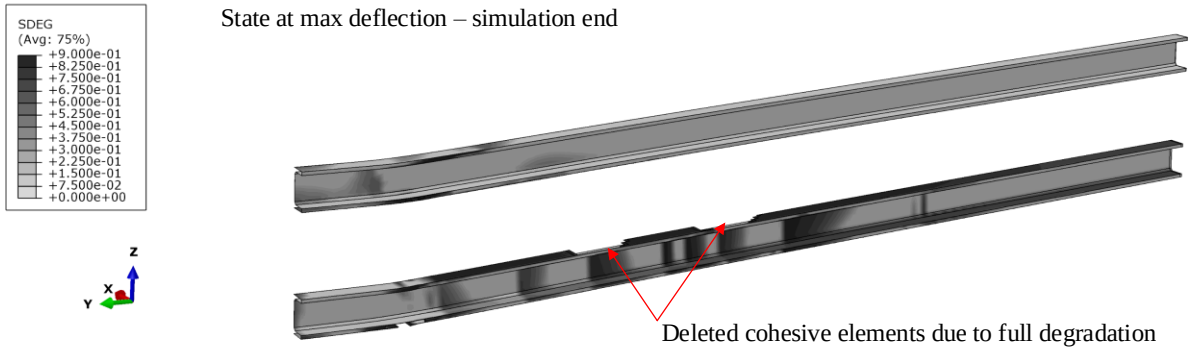


Fig. 6.157. Degradation of cohesive elements at the end of simulation from the beam/column specimen VT-2.

Analogically to the experimental tests, in numerical simulations the embedded steel profiles in the specimen VT-2 experienced smaller end-slip than the profiles from the specimen VT-1. In Fig. 6.158, the contact interface slip is shown for the state at the peak load and at the simulation end. The plotted slip was limited to the values recorded from the experimental campaign and given in Table 6.10. In the black or white area on the figure, the relative slip exceeded the experimental values of 1.04 mm for both states of the simulation. It can be observed that the indicated zones of higher slip are irregular. The value of the end-slip reached approximately 4.5 mm at the peak load and 7.9 mm at the end of the simulation. Due to the modelled mechanical shear connection as the cohesive elements distributed equally over the entire interface, the difference between the values obtained numerically and experimentally can be observed. The reasoning and justification of this effect was described earlier for the case of specimen VT-1 in Section 6.4.4.1. In simulation of the specimen VT-2, smaller stiffness of the traction material law for the cohesive elements had been applied in reference to the specimen VT-1, see Table 6.15. The change in the shear connection stiffness greatly affected the developed elastic and inelastic part of the relative slip. From Fig. 6.158b, it can be observed that, in the upper embedded steel profile, zones of significant slip were developed (white area) with nearly no degradation of the cohesive elements, compare to Fig. 6.157. This means that a small amount of inelastic slip and big amount of elastic slip contributed to the final value.

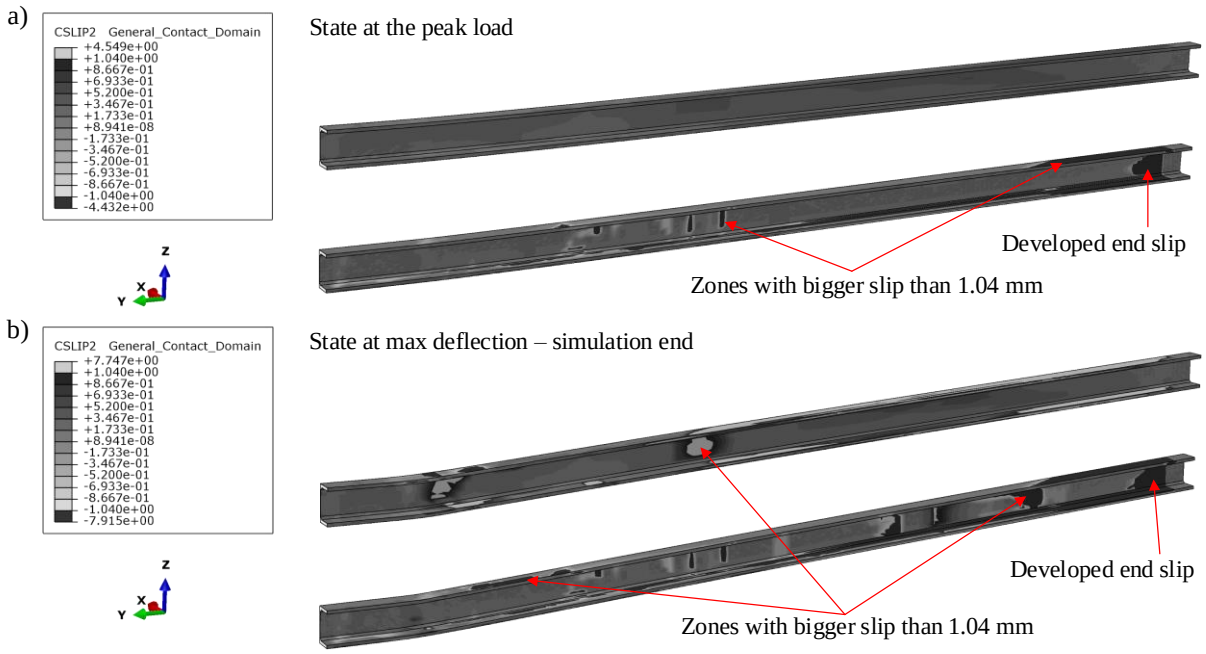


Fig. 6.158. Relative slip of embedded steel profiles obtained from the FE simulation of beam/column specimen VT-1 – a) state at the peak load and b) state at the end of simulation.

From Fig. 6.151, similar like in the case of specimen VT-1, the vertical cracks in the top part of concrete above the support are not directly visible. However, the distribution of maximum principal stresses given in Fig. 6.159a shows high concentration of the maximum positive stresses with horizontal orientation and the value of approximately 2.5-3.5 MPa. The identified values of maximum principal

stresses are close to the value of tensile strength of concrete. The value of concrete tensile strength applied in the concrete material law in numerical simulations was evaluated analytically according to the provisions given in fib Model Code 2010 [62] based on the compression strength of concrete obtained from the material tests, where the confinement effects were respected. Due to the scatter in the material tests of concrete properties, as shown for example in Table 6.7 or in the literature [199], and assumed uniform concrete confinement level in the entire concrete part, it can be concluded that the tensile strength present in the tests could differ from the evaluated value. In the result, the numerical simulations were less sensitive to the local concrete cracking effects. Therefore, the cracks observed from the tests, as shown in Fig. 6.88 and Fig. 6.103, were not directly visible in the conducted numerical simulations. In Fig. 6.159b, the minimum principal stresses in the support zone of specimen are shown. In the considered zone in the top part of concrete above the support, the minimum principal stresses reached small positive value, which additionally proves the tensile stresses acting in the aforementioned zone. Additionally, in Fig. 6.159b, the formulated diagonal compression struts between the embedded steel profiles can be clearly observed in the form of diagonally oriented maximum compression principal stresses.

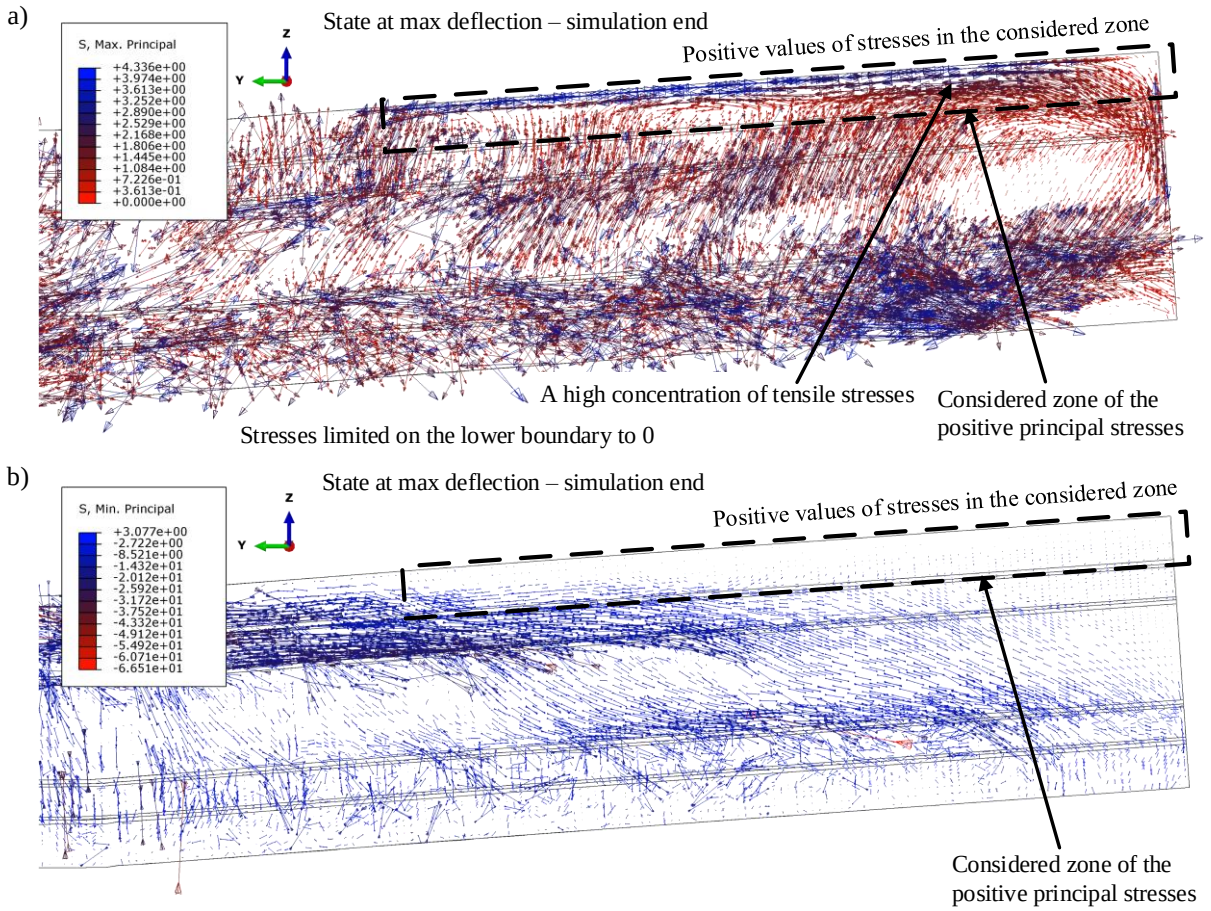


Fig. 6.159. Principal stresses in the support zone obtained from the FE simulation of beam/column specimen VT-2 – a) maximum principal stresses and b) minimum principal stresses.

In the sensivity study for the numerical model of specimen VT-2, it was identified that a clear Vierendeel-type behaviour can be obtained under a specific input parameters. In Fig. 6.160, a model with clear Vierendeel deflection character and vertical cracks in the top part of concrete in the zone above the support is shown. This specific behaviour of specimen was achieved by slight modification of the concrete material law and applied shear connection strength. In comparison to the calibrated model, the concrete confinement stresses were reduced to 0.5 MPa and the dilation angle was increased to 30°. This allowed for smaller concrete tension and compression strengths and reduced stiffness. The changed dilation angle imposed more smeared character of the force transfer inside the concrete part, which in turn, allowed for less concentrated damage and simultaneous activation of the wider zone of specimen in the force transfer. A higher level of the activation of specimen in the force transfer was also related to the applied strength of shear connection at the interface between steel and concrete parts. A higher value of the strength of cohesive elements not imposed a significant change in the shear connection resistance but it restrained the damage initiation point. In the result, the stiffer and stronger shear connection allowed for the development of more significant shear deformation (Vierendeel action) – an analogy to the rigid connection between posts and chords in the typical Vierendeel trusses can be identified.

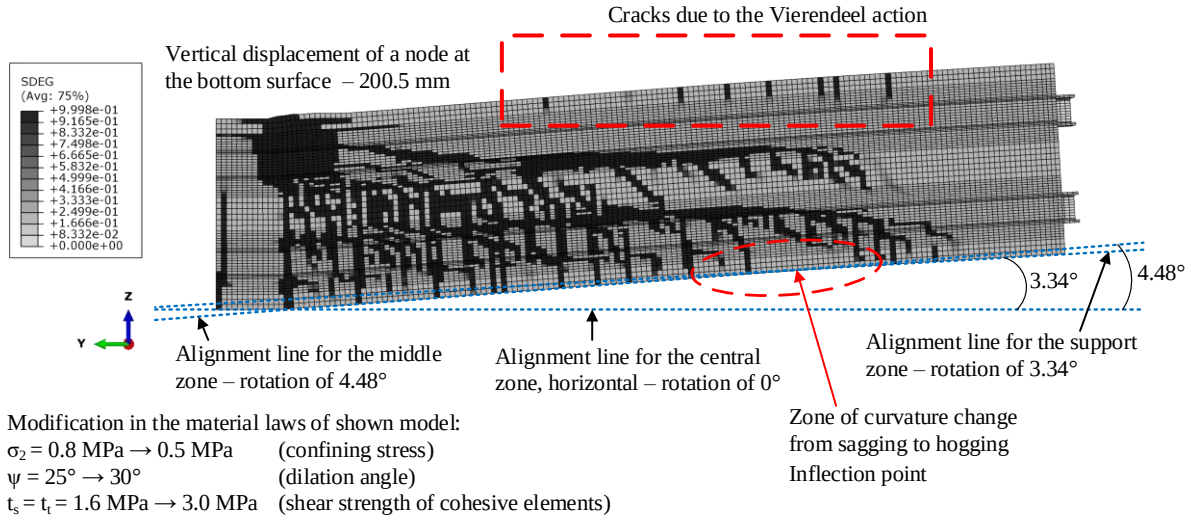


Fig. 6.160. Vierendeel action in a modified simulation of beam/column specimen VT-2.

Form Fig. 6.160, the zone of curvature change, from sagging to hogging, can be clearly identified. This effects is also characteristic for the typical Vierendeel trusses [166, 201] and it is related to the shear deformation, which is described in Fig. 6.70. In the considered specimen, the effect is not as obvious as in the Vierendeel truss system because the concrete localised between the embedded steel profiles reflects the smeared posts. Moreover, in the truss system, a big discrepancy between the stiffnesses of chords and posts is present, where in the considered composite specimen the difference is not so significant. Still, in the modified FE model, a change in the inclination of the bottom surface can be observed, where the relative difference between the surface directly above the support and the middle part was 1.14°.

6.5. An analytical model for the member stiffness

The obtained results from the experimental campaign and numerical simulations, described in Sections 6.3 and 6.4, comprehensively describe the behaviour of analysed beam/column specimens. From the taken observations, a strong analogy to the Vierendeel truss system behaviour was identified. In the same time, it was observed that the analysed specimens behaved like beam member in the global consideration. According to Fig. 6.83, Fig. 6.98, Fig. 6.108-6.109, Fig 6.142 and Fig. 6.151, the shear mode in the resultant deflection was detected in both specimens. Based on the above, a next analogy to the Timoshenko beam rather than the Euler-Bernoulli beam was identified, where the Euler-Bernoulli beam theory is limited to slender beams, homogenous sections and small deflections [183]. Moreover, the Timoshenko beam theory is a higher-order theory including effects of shear on the reduced stiffness, deformation and vibrations of the considered element [183] and the Euler-Bernoulli beam theory is considered as a specific case of the Timoshenko beam theory. In the result, the Timoshenko beam theory has been adapted for the considered composite members, where the effects of shear are significant.

From the performed investigation on the steel-concrete composite columns with two embedded steel profiles, it was identified that the cross-section resistance to bending can be estimated by the fibre method assuming the linear strains distribution. The differences between the ultimate loads obtained from the performed pre-design, see Table 6.1, and the experimental results, see Table 6.8, were 8% for the specimen VT-1 and 7% for the specimen VT-2. A similar approach to evaluate the cross-section strength was presented in the RFCS project 'SmartCoCo' [175] or CTBUH report 'ISRC Composite Column' [82] described in Section 3.5.2 and Section 3.5.3 respectively. Other similarities can be found in the PhD Theses of Tran [185] and Chanou [29], where the pivot method described in EN 1992-1-1 [53] or the simplified M-N interaction curve according to EN 1994-1-1 [58] were applied to assess the cross-section capacity. In all the above-mentioned works, a common assumptions about the full shear connection, the linear strain distribution and Euler-Bernoulli beam model were applied.

A correlation with the above-mentioned literature and the performed investigation in terms of the cross-section resistance can be observed. However, in reference to the stiffness of composite columns, all the previously mentioned research are based on the provisions given in EN 1994-1-1 [58] or EN 1992-1-1 [53], which were derived for the composite sections with only one embedded steel profiles, double symmetry and specific ratio of steel contribution in the cross-section. Disregarding the application boundaries, a significant deviation from the procedures given in the current design codes was identified according to the obtained results from the performed tests, simulations and literature given in Section 3.5. It has been found that the stiffness of steel-concrete composite members with more than one embedded steel profile is greatly overestimated by the application of available provisions from the design codes and the commonly applied Euler-Bernoulli beam theory is insufficient for specific cases, where the shear effect is significant. The overestimation of stiffness value leads to an unsafe

evaluation of deformation, the flexural response of composite member and the Euler's critical buckling load, which is essential parameter for compressed members. In reference to the performed beam/column tests and FE simulations described in Section 6.3 and Section 6.4 respectively, it was observed that the main assumptions of Euler-Bernoulli beam theory are harmed and a more suitable theory to describe the global behaviour of specimens is the Timoshenko beam theory. However, the application of raw beam theory and including only the shear effects was insufficient and a modification was required. In this place, the observations from the performed tests and simulations suggested to implement the Vierendeel truss model in order to evaluate the shear stiffness of considered composite members. The global equilibrium of forces and stiffness of Vierendeel truss system can be considered globally as a beam element [116]. Based on that, an innovative hybrid theory was proposed to apply the Timoshenko beam theory with embedded Vierendeel truss model (VTBM) in order to accurately describe the behaviour of analysed specimens and to derive a new effective bending stiffness that could be implemented into the existing design provisions of composite columns. An analogy to the opposite approach proposed by MacLeod [116] can be identified, where the Timoshenko beam model was used to describe the global beam behaviour of a pure steel Vierendeel truss. In the presented work, the derived innovative model is aimed to be coherent with the EN 1994-1-1 [58], thus, the provisions from the Eurocodes are applied in the development process.

6.5.1. Fundamental assumptions

In the determination of VTBM concept for a composite column with two embedded steel profiles, the following fundamental assumptions were taken into account:

- The proposed analytical model is calibrated and limited only to the geometry and conditions of the investigated experimentally beam/column specimens described in Section 6.3. The extrapolation and wider application of the proposed model require additional tests and numerical simulations.
- The proposed analytical model is valid for the test values, including material properties. No safety concept has been considered.
- The theory of elasticity describes the behaviour of specimens in the proposed analytical model with the consideration of the deflection function of elastic beams and principle of virtual work.
- The static system of a simple supported beam with point load in the middle is the only considered case in the proposed analytical concept, see Fig. 6.2, where overhangs beyond the supports are neglected. Extension of the proposed model to different boundary conditions and load cases require further investigation. In the result, the analysed specimens are globally considered as beams subjected to bending and shear without normal forces.
- According to Fig. 6.2, only in-plane deformation is considered.
- The Timoshenko beam theory is used to describe the global behaviour of specimens, including the evaluation model for the bending stiffness.

- The Vierendeel truss model is used to evaluate the equivalent beam shear stiffness.
- The full shear connection is assured at the interface between the embedded steel profiles and concrete – full composite action apply. Additionally, no slip is present at the reinforcement bar-concrete interface.
- For the evaluation of the geometrical properties, full sections are taken into account. In the same time, the reduction factors of the moduli of elasticity for the respective contributing materials are implemented to the stiffness evaluation process in order to include the effects of
    - concrete micro and macro cracking,
    - creep and shrinkage of concrete,
    - non-linear compressive behaviour of concrete,
    - compatibility of strains between the steel and concrete parts,
    - strain limitations on the steel parts due to non-fully activated concrete section in the composite force transfer and
    - test specimen conditions.

An analogous approach that is given in EN 1994-1-1 [58] has been adapted.

- Reinforcement bars are not contributing to the equivalent beam shear stiffness.

Besides the fundamental assumptions defined above, minor assumptions were made across the development process of presented analytical concept. They are defined and described next to the respective place of application.

6.5.2. Identification of the reference load for the model verification

The considered system in the analytical model is an elastic beam without normal force, therefore, the resultant load-deflection relation will be linear including the second order effects. The point of consideration is localized at the mid-span, where the deflection reaches the maximum value. The obtained experimental load-deflection curves shown in Fig. 6.28 for the specimen VT-1 and in Fig. 6.31 for the specimen VT-2 are the reference data. Moreover, the respective curves obtained numerically shown in Fig. 6.141 for the specimen VT-1 and in Fig. 6.150 for the specimen VT-2 are supporting the investigation. In both, experimental and numerical, cases, the load-deflection character is linear only in the initial phase of the test, where close to the peak load, the non-linear behaviour can be observed. In the result, the proposed analytical model can be calibrated to converge with the initial stiffness branch of the test curve or overlap with one of the characteristic points chosen close to the peak load. However, it is possible that both desired responses are achieved by introducing the respective stiffness reduction factors, where this aspect is discussed later in Section 6.5.5. In this section, the identification of a reference point close to the peak load is discussed, where the selected point should consider the pure bending case due to the load case considered experimentally. In the considered point, the specimen experiences the largest reasonable deflection and the elastic stiffness, for the linear load-deflection

relation, reaches the smallest corresponding value. Moreover, the reduced stiffness results with reduction in the Euler's critical buckling load.

The position of reference point next to the peak load from the test curve was identified in the presented analysis independently with two methods: (i) by the evaluation of imposed point load, which refers to the plastic bending resistance of cross-section evaluated using design values, point "B" from the N-M interaction curve given by EN 1994-1-1 [58] and (ii) the method of secant stiffness capacity, which is the graphical method. Both methods are described and analysed below in the respective paragraphs.

Plastic bending design resistance method

For the evaluation of load corresponding to the plastic bending resistance of cross-section, the simplified N-M interaction curve given in EN 1994-1-1 [58] approach was adapted. The plastic bending resistance is defined as point "B" from the normative procedure and it is shown in Fig. 6.161.

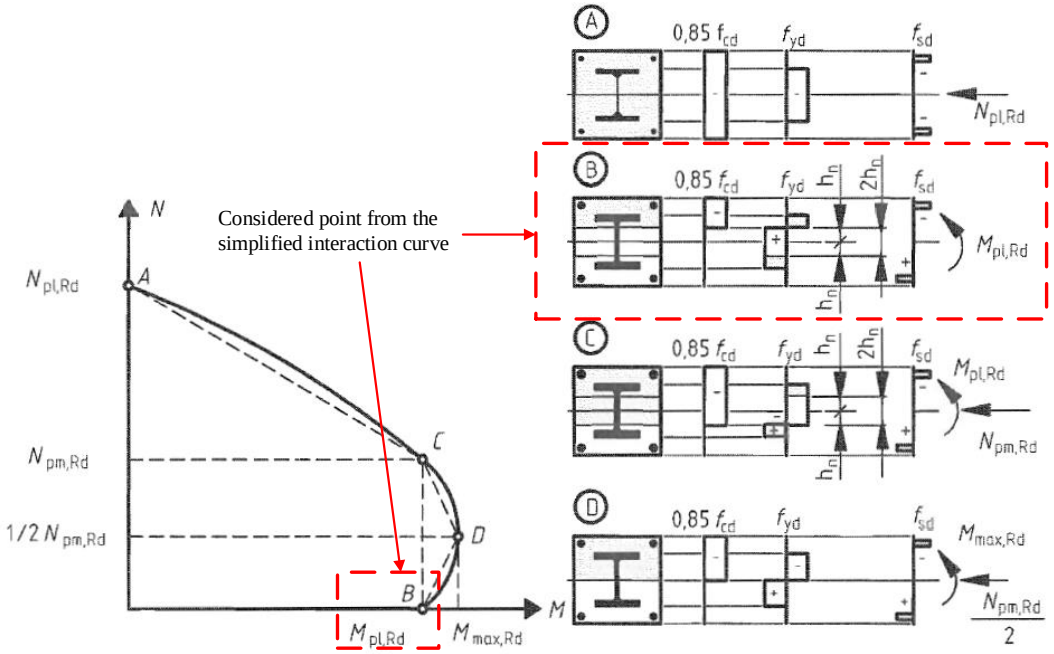


Fig. 6.161. Simplified interaction curve and corresponding stress distributions in the characteristic points of method given in EN 1994-1-1 [58].

The proposed evaluation method was adapted for the considered cross-sections with two embedded steel profiles shown in Fig. 6.5 and the neutral axis for the specimen VT-1 was localised in bottom flange of the upper embedded steel profile and for the specimen VT-2 in the fillet between the bottom flange and web of the upper embedded steel profile. The distribution of plastic block stresses due to the adapted method and identified neutral axes in the considered cross-sections are shown in Fig. 6.162. From the comparison of Fig. 6.7, Fig. 6.8, Fig. 6.105 and Fig. 6.162, it can be observed that the experimentally obtained position of neutral axes is localised between the positions identified in the pre-design according to the elastic analysis and in the simplified plastic design resistance.

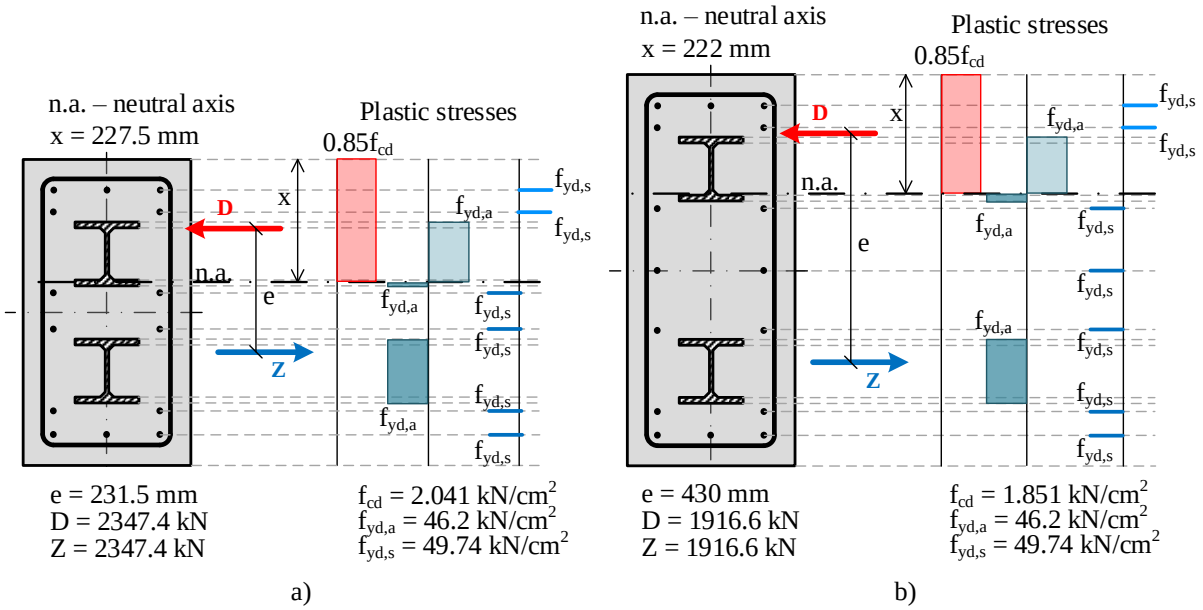


Fig. 6.162. Stresses distribution for the design plastic bending resistance of the cross-section – a) for the specimen VT-1 and b) for the specimen VT-2.

In reference to Fig. 6.162, the design values of material properties were calculated according to EN 1992-1-1 [53] for the concrete and reinforcement bars and according to EN 1993-1-1 [55] for the steel profiles. However, the experimentally measured material properties were adapted as the characteristic values for the evaluation of design values. For the concrete, a mean value for cube specimens was extracted from the material tests. Therefore, the simplified evaluation of characteristic values for the cylindrical specimens was performed beforehand. The evaluation of design material properties for the specimen VT-1 is shown below in Eq. 6.61-6.67 and in Eq. 6.68-6.74 for the specimen VT-2.

For the specimen VT-1 we have,

$$f_{cm,cube} = 47.75\ [MPa] \quad \text{experimentally obtained value for the specimen VT-1, see Table 6.7} \tag{6.61}$$

$$f_{ck,cube} = f_{cm,cube} - 10[MPa] = 37.75\ [MPa] \tag{6.62}$$

$$f_{ck} = f_{ck,cube} \cdot \frac{30}{37} = 37.75 \cdot 0.81 = 30.61\ [MPa] \quad \text{, where ratio 30/37 refers to the normative relation between the compression strengths of cylindrical and cubic specimens} \tag{6.63}$$

$$f_{cm} = f_{ck} + 8[MPa] = 38.61\ [MPa] \tag{6.64}$$

$$f_{cd} = \frac{\alpha_{cc} \cdot f_{ck}}{\gamma_c} = \frac{1 \cdot 30.61}{1.5} = 20.41\ [MPa] = 2.041\ [kN/cm^2] \tag{6.65}$$

$$f_{yd,a} = \frac{f_{yk,a}}{\gamma_{M0}} = \frac{462}{1.0} = 462\ [MPa] = 46.2\ [kN/cm^2] \tag{6.66}$$

$$f_{yd,s} = \frac{f_{yd,s}}{\gamma_s} = \frac{572}{1.15} = 497.4\ [MPa] = 49.74\ [kN/cm^2] \tag{6.67}$$

and for the specimen VT-2,

$$f_{cm,cube} = 44.25\ [MPa]$$ experimentally obtained value for the specimen VT-2, see Table 6.7 (6.68)

$$f_{ck,cube} = f_{cm,cube} - 10[MPa] = 34.25\ [MPa] \quad (6.69)$$

$$f_{ck} = f_{ck,cube} \cdot \frac{30}{37} = 34.25 \cdot 0.81 = 27.77\ [MPa]$$, where ratio 30/37 refers to the normative relation between the compression strengths of cylindrical and cubic specimens (6.70)

$$f_{cm} = f_{ck} + 8[MPa] = 35.77\ [MPa] \quad (6.71)$$

$$f_{cd} = \frac{\alpha_{cc} \cdot f_{ck}}{\gamma_c} = \frac{1 \cdot 27.77}{1.5} = 18.51\ [MPa] = 1.851\ [kN/cm^2] \quad (6.72)$$

$$f_{yd,a} = \frac{f_{yk,a}}{\gamma_{M0}} = \frac{462}{1.0} = 462\ [MPa] = 46.2\ [kN/cm^2] \quad (6.73)$$

$$f_{yd,s} = \frac{f_{yd,s}}{\gamma_s} = \frac{572}{1.15} = 497.4\ [MPa] = 49.74\ [kN/cm^2] \quad (6.74)$$

By identifying the position of neutral axis in the pure bending case, the resultant compression "D" and tension "Z" forces on internal lever arm "e" were estimated as shown in Fig. 6.162. The resultant compression and tension forces are equal due to the assured equilibrium in the cross-section. Based on the equilibrated internal forces in the cross-section, the resultant bending moment is evaluated according to Eq. 6.75, which will correspond to the plastic bending design resistance from the point "B" of simplified N-M interaction curve indicated in Fig. 6.161. Applying the considered static system of simple supported beam from Fig. 6.2, the imposed point force corresponding to the plastic bending resistances of cross-sections calculated in Eq. 6.76-6.77 can be evaluated according to Eq. 6.78.

$$M_{pl,Rd} = \{D = Z\} \cdot e \quad (6.75)$$

$$M_{pl,Rd,VT-1} = 2347.4 \cdot 0.2315 = 543.42\ [kNm] \quad (6.76)$$

$$M_{pl,Rd,VT-2} = 1916.6 \cdot 0.43 = 824.14\ [kNm] \quad (6.77)$$

$$M_{pl,Rd} = \frac{P_{M,pl,Rd} \cdot L}{4} \rightarrow P_{M,pl,Rd} = \frac{4 \cdot M_{pl,Rd}}{L} \quad (6.78)$$

$$P_{M,pl,Rd,VT-1} = \frac{4 \cdot 543.42}{6} = 362\ [kN] \quad (6.79)$$

$$P_{M,pl,Rd,VT-2} = \frac{4 \cdot 824.14}{6} = 549\ [kN] \quad (6.80)$$

Values of the plastic bending resistance calculated in Eq. 6.76 for the specimen VT-1 and in Eq. 6.77 for the specimen VT-2 are smaller than the values obtained from the pre-design process and evaluated from the test for the peak load, see Table 6.11. The relative difference for the specimen VT-1 reached 6% and 14% by considering the pre-design and test bending resistances respectively, where for the specimen VT-2 the difference of 1% and 9% was obtained respectively. In addition, in Table 6.11, the plastic bending residual resistances are given and they are smaller than the values obtained according to

the described-above simplified design code procedure, where the relative difference reached respectively 16% and 5% for the specimen VT-1 and specimen VT-2.

The identified loads in Eq. 6.79 and Eq. 6.80 are marked on the respective experimental load-deflection curves in Fig. 6.163 and the corresponding displacements are read. In the result, the reference points from the experimental curves corresponding to the pure design bending resistances for the proposed analytical model are defined.

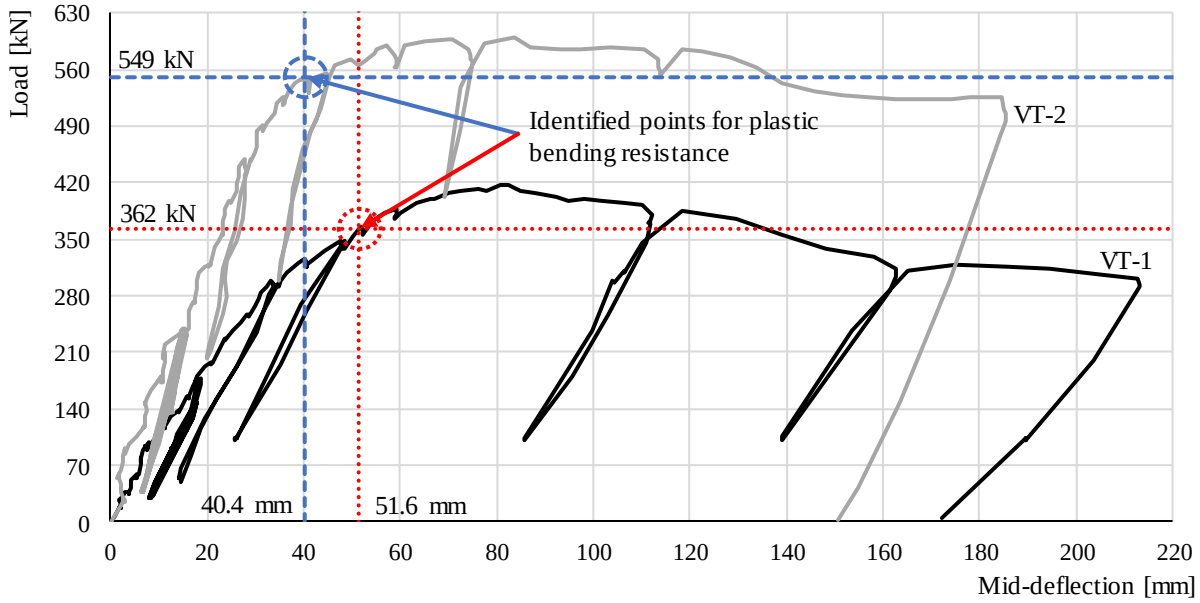


Fig. 6.163. Reference points for the analytical model obtained from the plastic bending design resistances of beam/column specimens.

Method of secant stiffness capacity

The method of secant stiffness capacity is a graphical method that allows identifying the point of interest from the experimentally obtained response for the plastic capacity estimation with respect to the certain remaining stiffness capacity. The method was originally developed for the moment resistant connections, therefore, in the considered adaptation for the composite beam/column specimens, no strict reference exist. It was assumed that the remaining stiffness capacity is equal to the 10% of initial stiffness. In Fig. 6.164, the described-above method was applied for the experimentally obtained load-deflection curves for both specimens. The applied procedure is listed below, where the listed points are corresponding to the points indicated in Fig. 6.164.

(1) Graphical identification of the initial stiffness K_{ini} from the given experimental load-deflection response as a tangent line to the experimental curve in the first phase of the test. A point after the cycles was taken as the limit of the initial phase of the test.

(2) Calculation of the reduced stiffness value equal to the 10% of initial stiffness value and marking the second reference line on the diagram.

(3) Translation of the reduced stiffness line obtained from ‘Step 2’ to the peak load zone of experimental curve and setting it in a tangential position.

(4) Finding an intersection point between the initial stiffness line and the translated reduced stiffness line. This point correspond to the reference load for the plastic bending design resistance – the horizontal dotted line.

(5) Finding the intersection point of the identified horizontal dotted line obtained from 'Step 4' and the experimental curve. The identified point on the experimental curve is referring to the load and displacement considered for the design plastic bending capacity.

(6) Identification of the secant stiffness line K_{sec}, which corresponds to the identified reference point on the experimental load-slip curve and evaluation of the corresponding deflection.

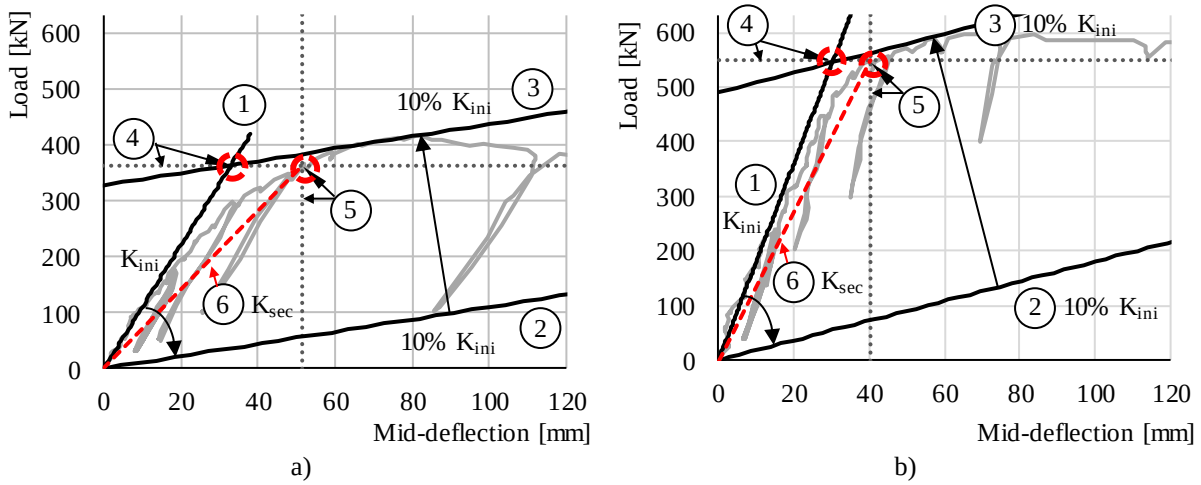


Fig. 6.164. Reference points for the analytical model obtained from the secant stiffness method for beam/column specimens – a) for the specimen VT-1 and b) for the specimen VT-2.

The obtained values from Fig. 6.164 are extracted and defined in Eq. 6.81-6.83 for the specimen VT-1 and in Eq. 6.84-6.86 for the specimen VT-2. The output values were graphically approximated and rounded to integer.

$$P_{K,sec,pl,VT-1} = 362\ [kN] \tag{6.81}$$

$$w_{K,sec,pl,VT-1} = 52\ [mm] \tag{6.82}$$

$$K_{sec,VT-1} = 7\ [kN/mm] \tag{6.83}$$

$$P_{K,sec,pl,VT-2} = 549\ [kN] \tag{6.84}$$

$$w_{K,sec,pl,VT-2} = 40\ [mm] \tag{6.85}$$

$$K_{sec,VT-2} = 14\ [kN/mm] \tag{6.86}$$

In order to verify and calibrate the proposed analytical model, the reference points from the experimental load-deflection curves were identified with two methods. By comparing the obtained results from both methods described in Eq. 6.79-6.80 and Eq. 6.81-6.86 it can be observed that nearly identical values were achieved. However, a further analysis would be required to confirm if the two presented methods are equivalent.

6.5.3. Vierendeel truss as a Timoshenko beam analogy model

From the experimental campaign described in Section 6.3 and numerical simulations described in Section 6.4, a strong analogy in the behaviour of analysed beam/column specimens to the simultaneous behaviours of Timoshenko beam and Vierendeel truss was identified. Therefore, the developed analytical concept for the evaluation of the effective stiffness of composite column specimens in steel and concrete with two embedded steel profiles consisted of both aforementioned theoretical models. The Timoshenko beam theory was applied to describe global behaviour of the specimens, where the shear effects on the stiffness reduction are considered. However, instead of assuming an isotropic and homogenous cross-section of the member, the discrete Vierendeel truss model was embedded in order to evaluate the reduced equivalent beam shear stiffness. The taken composition of the applied theories resulted in hybrid Vierendeel Truss Timoshenko Beam Model (VTBM). In the considered analytical model VTBM, the embedded steel profiles with surrounding concrete are considered as chords of the Vierendeel truss and the concrete localised between the embedded steel profiles reflects posts.

6.5.3.1. Model for the global beam deflection

In the VTBM model, the global deflection of considered specimens is described by the Timoshenko beam theory, where two deflection modes are distinguished: (i) bending and (ii) shear. This relation is described in Eq. 6.87. Each of the aforementioned deflection modes contribute to the resultant beam curvature due to the given load case and can be summed. By separate integration of each curvature caused by the bending and shear over the length of a beam, the resultant deflections for both modes are obtained. Assumptions about elastic beams and small deformations apply, which are crucial to define the relation between the applied actions and the resulting curvatures. Conditions given in Eq. 6.88 and in Eq. 6.90 describe relations between the load actions, curvatures and beam deflections with respect to the taken assumptions. The reference figure explaining the above-mentioned conditions is shown in Fig. 6.165. Differential equations applied for the description of respective beam curvatures are given in Eq. 6.89 for the bending mode and in Eq. 6.91 for the shear mode. Integration of these equations over the length of a beam resulted in equations for the beam deflections with respect to the considered static system. In Eq. 6.92 and Eq. 6.93, the derived functions of displacements are given.

Eq. 6.92 and Eq. 6.93 can be directly implemented into Eq. 6.87, which gives the resultant equation for the total deflection of a simple supported Timoshenko beam with point load in the mid-span. By including the respective stiffnesses notations given in Eq. 6.94 and Eq. 6.95, the final shape of the considered equation for the VTBM model is defined in Eq. 6.96. Value of the considered load has been identified in Section 6.5.2, where the respective stiffnesses are discussed in Section 6.5.3.2 for bending and in Section 6.5.3.3 for shear modes.

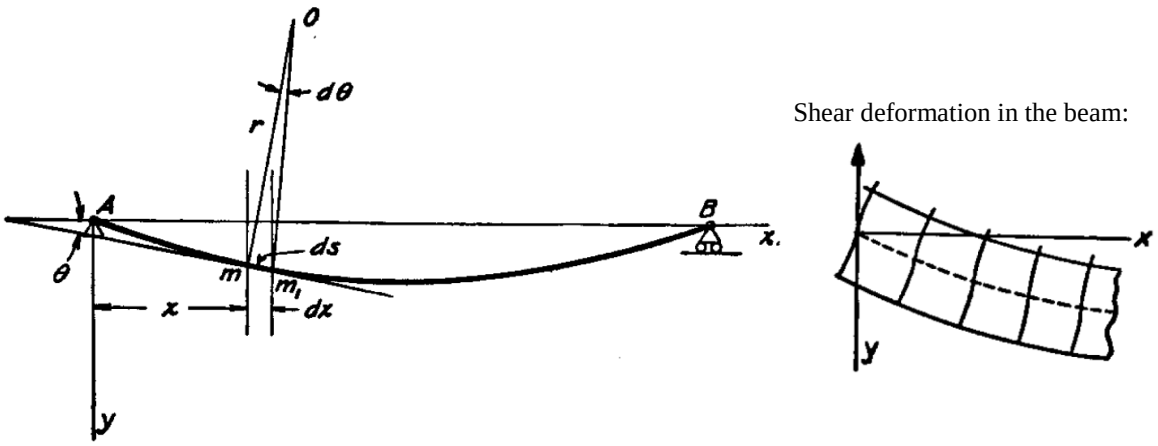


Fig. 6.165. Deflection of a transversally loaded beam [183].

$$w = w_b + w_s \tag{6.87}$$

$$\frac{1}{r} = \frac{M}{EI} \qquad ds = -r \cdot d\theta \qquad ds \approx dx \qquad \theta = \tan\theta = \frac{dy}{dx} \tag{6.88}$$

$$EI\frac{d^4 w_b}{dx^4} = q(x) \quad \text{, or} \quad EI\frac{d^2 w_b}{dx^2} = -M(x) \tag{6.89}$$

$$\frac{dw_s}{dx} = \frac{\tau_{yx}(x)}{G} = \frac{V(x)}{A_v \cdot G} \tag{6.90}$$

$$A_v G\frac{d^2 w_s}{dx^2} = \frac{dV(x)}{dx} = -q(x) \tag{6.91}$$

$$w_b = \frac{PL^3}{48EI} \quad \text{, for the simple supported beam with point load in the middle} \tag{6.92}$$

$$w_s = \frac{PL}{4A_v G} \quad \text{, for the simple supported beam with point load in the middle} \tag{6.93}$$

$$EI = (EI)_{v,gl} \quad \leftarrow \quad \text{equivalent beam global bending stiffness for the considered model} \tag{6.94}$$

$$A_v G = K_{sv} \quad \leftarrow \quad \text{equivalent beam shear stiffness for the considered Vierendeel model} \tag{6.95}$$

$$w = \frac{PL^3}{48 \cdot (EI)_{v,gl}} + \frac{PL}{4 \cdot K_{sv}} \tag{6.96}$$

6.5.3.2. Derivation of the bending stiffness

In the Vierendeel trusses, the bending stiffness is normally considered including only geometry of the chords, where posts are not contributing to the flexural response. Moreover, due to a big discrepancy between the vertical span of parallel chords and the height of chord in the typical Vierendeel trusses, the global moment of inertia is calculated by using a simplification that the eigenvalues of chords inertia can be neglected and the total value is based only on the Steiner rule. The described above simplified procedure brings sufficiently accurate results for the typical Vierendeel trusses made in steel. However, in the consideration of steel-concrete composite beam/column specimens from the experimental campaign, the moment of inertia eigenvalues of the theoretically discretised chords cannot be neglected.

The geometry of cross-sections in the analysed specimens are stocky in comparison to the typical lattice Vierendeel trusses, thus, the contribution of the chord moment of inertia eigenvalues are significant for the considered case.

According to the test observations about the development of bending failure shown in Fig. 6.73-6.78 for the specimen VT-1 and in Fig. 6.90-6.96 for the specimen VT-2, it can be noticed that the total height and width of specimens was activated in the bending force transfer. For example, in Fig. 6.73 it can be observed that the first concrete compression failure occurred in the top fibres of specimen section, where in Fig. 6.75, it can be observed that the tensile vertical cracks developed from the bottom fibres of the section. Based on the taken observations, it was assumed that the bending stiffness values should consider the entire geometry of the cross-section.

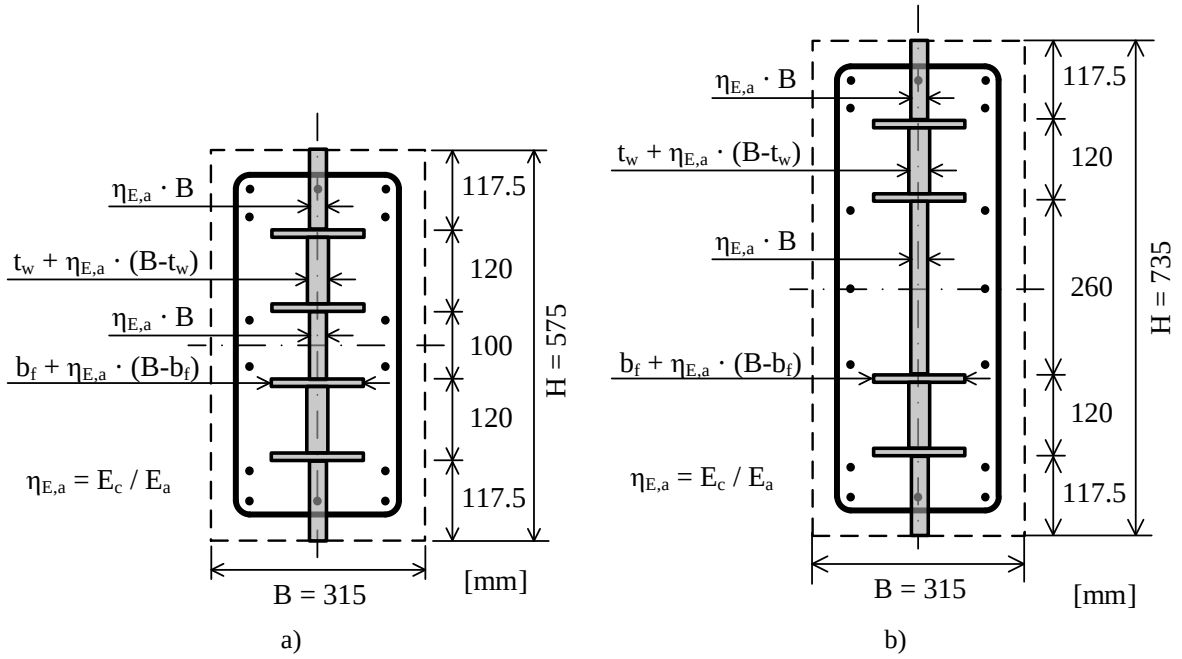


Fig. 6.166. Cross-section geometry of the beam/column specimen in steel units – a) for the specimen VT-1 and b) for the specimen VT-2.

In order to evaluate the effective bending stiffness of test specimens, the entire geometry was transformed into steel units by application of the relative elasticity ratio between the concrete and steel materials. Like this, the area of one material multiplied by the relative elasticity ratio yields the same stiffness, when the material properties of the second material are considered globally – transformation to the equivalent isotropic and homogenous cross-section [110]. In the considered case of beam/column specimens, the concrete area was transformed into the steel units by application of the relativity ratio given in Eq. 6.97, which gives the ratio of the concrete to steel Young's Moduli. It was assumed that the height of specimens stayed unchanged, thus, the widths of the subsequent parts of cross-sections were modified. The resultant geometries of cross-sections in steel units are shown in Fig. 6.166, where the fillet between the flanges and web of the steel profile was neglected. The reinforcement bars are omitted from the transformation process, however, their contribution to the global effective bending

stiffness is considered. According to the geometry given in Fig. 6.166, the resultant moments of inertia of transformed cross-sections were analysed and they notation is given in Eq. 6.98 for the specimen VT-1 and Eq. 6.99 for the specimen VT-2. The total moments of inertia of the applied sets of reinforcement bars given in Eq. 6.100 and Eq. 6.101 were evaluated based on the eigenvalues for circular cross-section and applied Steiner's rule. In the result, the equivalent beam bending stiffness of the developed VTBM model is defined in Eq. 6.102.

$$\eta_{E,a} = \frac{E_c}{E_a} \tag{6.97}$$

$I_{v,gl,VT-1}\ [cm^4]$, according to Fig. 6.166a, for value see Section 6.5.3.5 (6.98)

$I_{v,gl,VT-2}\ [cm^4]$, according to Fig. 6.166b, for value see Section 6.5.3.5 (6.99)

$$I_{s,total,VT-1} = \Sigma\left(\frac{\pi}{4}{r_{s,i}}^4 + A_{s,i} \cdot {z_{s,i}}^2\right) = 2314.54\ [cm^4] \tag{6.100}$$

$$I_{s,total,VT-2} = \Sigma\left(\frac{\pi}{4}{r_{s,i}}^4 + A_{s,i} \cdot {z_{s,i}}^2\right) = 4582.56\ [cm^4] \tag{6.101}$$

$$(EI)_{v,gl} = E_a \cdot I_{v,gl} + E_s \cdot I_{s,total} \tag{6.102}$$

6.5.3.3. Derivation of the shear stiffness

In the shear stiffness analysis of proposed model VTBM, the principle of virtual work was employed to analyse the shear part of deflection in the Vierendeel truss system. In the next step, the relation given in Eq. 6.90 was applied to correlate the obtained truss shear deflection with the beam shear stiffness. Application of the described method required a theoretical discretisation of the beam/column specimens into the Vierendeel truss elements – chords and posts. Respectively, chord elements are described with "ch" index and post elements are described with "po" index. The span between posts was defined as "a" value, where the span between chords was defined as "b" value. In order to investigate the pure shear deformation of the considered Vierendeel truss system, the symmetric portion of the entire truss, as shown in Fig. 6.167, was analysed. Due to the applied concentrated load P=2S, the acting shear force S/2 in the considered portion of the system imposed the resultant shear deformation, which in the result, was evaluated according to the principle of virtual work according to Eq. 6.103. Where for the bending moments and shear forces the internal forces distribution is clear, then for the normal forces distribution two scenarios are possible: (i) where the horizontal support at the point "A" from Fig. 6.167b will be considered or (ii) where the horizontal support at point "A" is disregarded. Finding the normal forces distribution with scenario (i), involves a much more complex situation than the scenario (ii). It was identified that from both scenarios Eq. 6.103 gives identical results, when the values "a" and "b" are constant. In the scenario (i) the normal forces are distributed over the total length "a" with the value equal to S/2 times the ratio of "a" over "b", where in the scenario (ii) the normal forces distribution is acting just on the half-length "a/2" but with increased value of S times the ratio of "a" over "b". Due to the reduced complexity of the problem, the scenario (ii) was considered. In Fig. 6.168, the distributions

of internal forces for the considered portion of Vierendeel truss are shown. The contributing partial deformations to the total shear deformation are given in Eq.6.104 for the normal forces, in Eq. 6.105 for the shear forces and in Eq. 6.106 for the bending moments. By placing the obtained partial shear deformations from Eq. 6.104-6.106 into Eq. 6.103 and implementing the elastic relation between the modulus of elasticity and shear modulus given in Eq. 6.107, the resultant deformation of Vierendeel truss according to the principle of virtual work is given in Eq. 6.108. Introducing the simplification factors defined in Eq. 6.109 and Eq. 6.110, Eq. 6.108 is simplified into the form described by Eq. 6.111. The evaluated shear deformation of the internal Vierendeel truss model from Eq. 6.111 is placed into the condition given in Eq. 6.90 and the resultant relation is defined in Eq. 6.112 by replacing the change of the shear deformation over the length, by the evaluated total shear deformation divided by the total length "a". In the result, in Eq. 6.113, the equivalent beam shear stiffness for the considered VTBM model is defined.

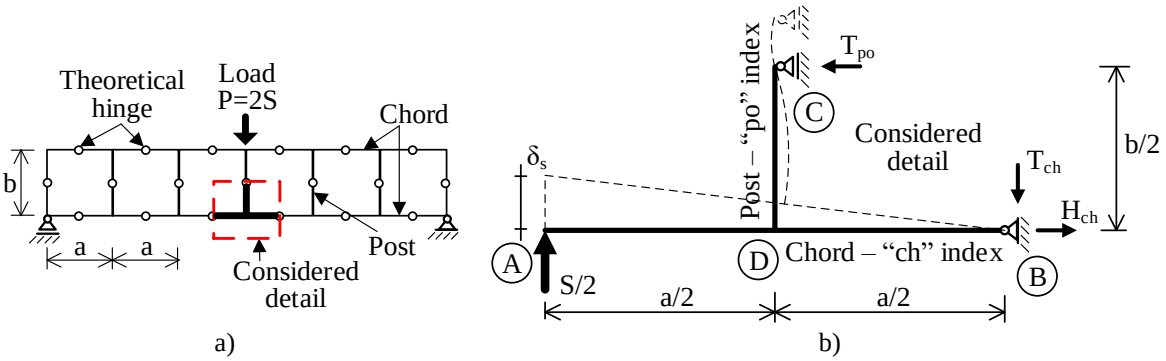


Fig. 6.167. Vierendeel truss model for the evaluation of equivalent beam shear stiffness in the VTBM model – a) global model and b) considered detail.

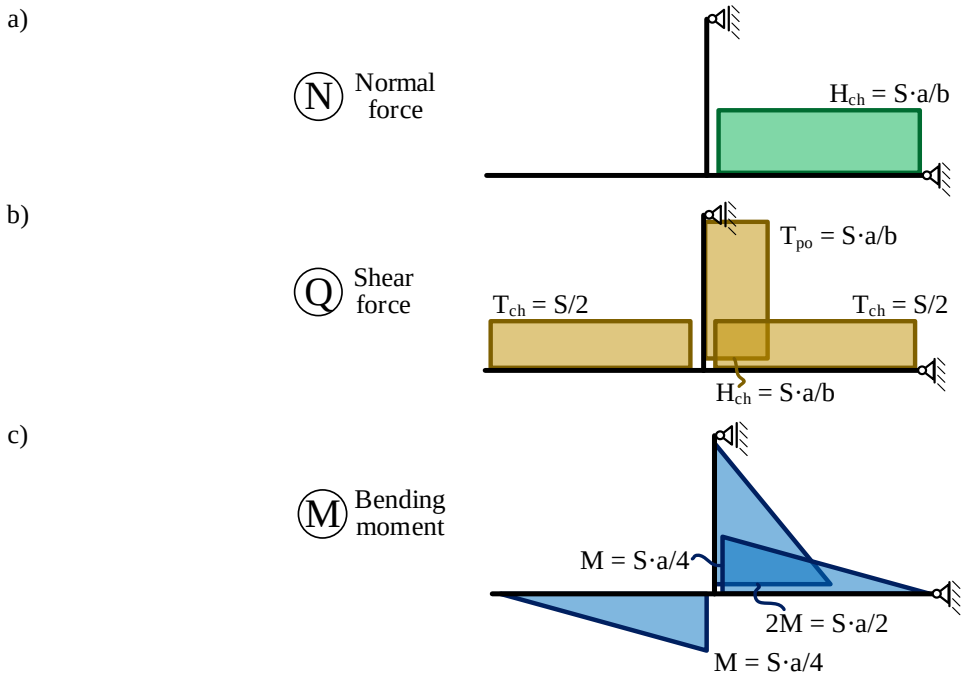


Fig. 6.168. Distributions of internal forces in the considered detail of the Vierendeel truss system of VTBM model – a) normal forces, b) shear forces and c) bending moments.

$$\delta = \int \frac{\bar{N}N}{EA}dx + \int \frac{\bar{Q}Q}{GA_v}dx + \int \frac{\bar{M}M}{EI}dx \tag{6.103}$$

$$\delta_{s,N} = \int \frac{\bar{N}N}{EA}dx = S \cdot a \cdot \left(\frac{a^2}{b^2 \cdot E_{ch} \cdot A_{ch}}\right) \tag{6.104}$$

$$\delta_{s,Q} = \int \frac{\bar{Q}Q}{GA_v}dx = S \cdot a \cdot \left(\frac{1}{2 \cdot G_{ch} \cdot A_{v,ch}} + \frac{a}{b \cdot G_{po} \cdot A_{v,po}}\right) \tag{6.105}$$

$$\delta_{s,M} = \int \frac{\bar{M}M}{EI}dx = S \cdot a \cdot \left(\frac{a^2}{24 \cdot E_{ch} \cdot I_{ch}} + \frac{a \cdot b}{12 \cdot E_{po} \cdot I_{po}}\right) \tag{6.106}$$

$$G = \frac{E}{2 \cdot (1 + \nu)} \tag{6.107}$$

$$\delta_s = Sa \cdot \left[\left(\frac{a^2}{b^2 E_{ch} A_{ch}}\right) + \left(\frac{(1+\nu_{ch})}{E_{ch}A_{v,ch}} + \frac{2a(1+\nu_{po})}{bE_{po}A_{v,po}}\right) + \left(\frac{a^2}{24E_{ch}I_{ch}} + \frac{ab}{12E_{po}I_{po}}\right)\right] \tag{6.108}$$

$$\psi_Q = \frac{E_{ch}A_{v,ch}/b(1+\nu_{ch})}{E_{po}A_{v,po}/a(1+\nu_{po})} \tag{6.109}$$

$$\psi_M = \frac{E_{ch}I_{ch}/a}{E_{po}I_{po}/b} \tag{6.110}$$

$$\delta_s = Sa \cdot \left[\frac{a^2}{b^2 E_{ch} A_{ch}} + \frac{(1+\nu_{ch})(1+2\psi_Q)}{E_{ch}A_{v,ch}} + \frac{a^2(1+2\psi_M)}{24E_{ch}I_{ch}}\right] \tag{6.111}$$

$$(A_v G)\frac{dw_s}{dx} = V(x) \rightarrow K_{sv} = \frac{S}{\delta_s/a} \tag{6.112}$$

$$K_{sv} = \frac{1}{\frac{a^2}{b^2 E_{ch} A_{ch}} + \frac{(1+\nu_{ch})(1+2\psi_Q)}{E_{ch}A_{v,ch}} + \frac{a^2(1+2\psi_M)}{24E_{ch}I_{ch}}} \tag{6.113}$$

The equation simplification factors ψ_Q and ψ_M defined in Eq. 6.109-6.110 define the shear relativity ratio and the contraflexure ratio in the considered Vierendeel truss systems. According to the identified values of aforementioned ratios, the characteristic for the Vierendeel truss behaviours can be analysed [116]. Where in the typical Vierendeel trusses made in steel, only the contraflexure ratio is considered.

6.5.3.4. Discretisation of the member into Vierendeel truss elements

To evaluate the equivalent beam bending stiffness given in Eq. 6.102, the full cross-section of specimen in the steel units is considered due to the identified bending failure pattern from the experimental campaign. However, evaluation of the equivalent beam shear stiffness given in Eq. 6.113 required discretisation of the composite cross-sections into Vierendeel truss elements with specified geometry. The discretisation scheme of the specimen VT-1 is shown in Fig. 6.169 and the discretisation scheme of the specimen VT-2 is shown in Fig. 6.170.

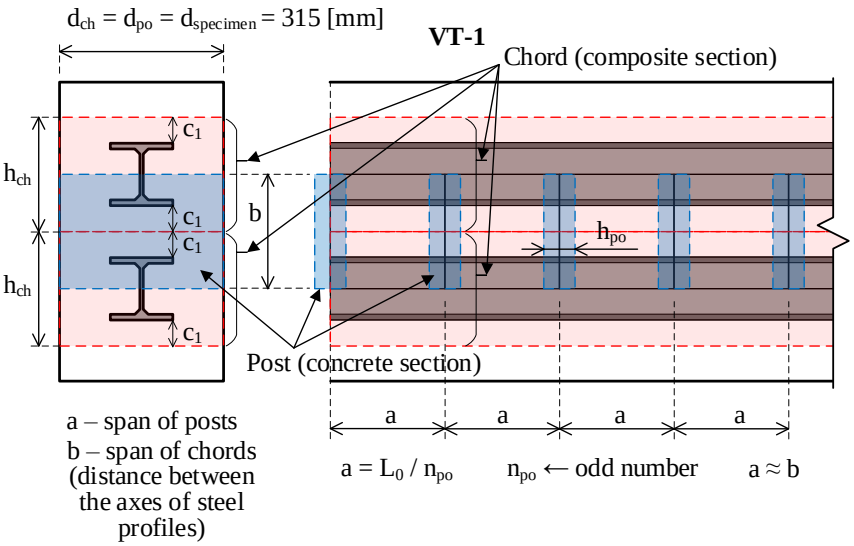


Fig. 6.169. Discretisation scheme of beam/column specimen VT-1 into the theoretical Vierendeel truss system.

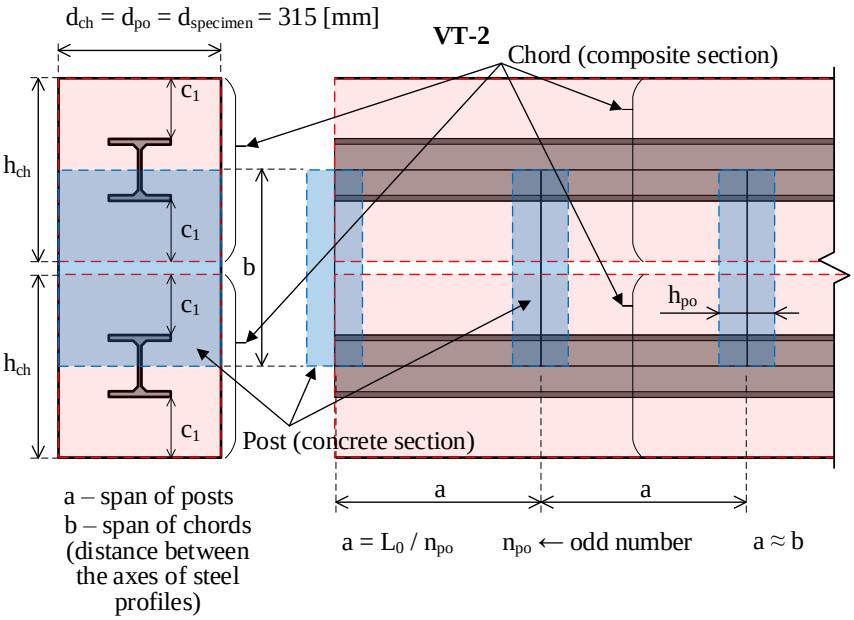


Fig. 6.170. Discretisation scheme of beam/column specimen VT-2 into the theoretical Vierendeel truss system.

It is assumed that chords are represented by the steel-concrete composite cross-sections transformed to the steel units and consist of one embedded steel profile with surrounding concrete. The aforementioned representation of chord geometry is intuitive to the fact that steel profiles consist of significant own bending stiffness in comparison to the concrete. Posts of the theoretical Vierendeel truss systems are represented by the pure concrete sections. In both cases, for chords and posts, double symmetric cross-sections are assumed. Due to the assumed geometrical representations of Vierendeel truss elements, the vertical span between chords “b” is taken to be equal to the span between the longitudinal axes of embedded steel profiles. In the result, the length of theoretical posts is taken to be equal to “b”. The horizontal span of posts “a” is taken as a result from the discretisation process with boundaries that $a \approx b$ and the number of posts should be an odd number in order to assure the symmetric distribution of posts, where one post is localised respectively at the beginning, end and mid-span of the

specimen length. The last boundary that allows for the discretisation of beam/column specimen geometry into the theoretical Vierendeel truss system is introduction an assumption that the total width of the cross-section is active in the force transfer mechanism. According to the taken set of assumptions and boundaries, the variables: (i) the height of chords h_{ch}, (ii) the height of posts h_{po} and (iii) the span of posts "a" were singular to define the remaining geometry of theoretical Vierendeel truss system.

From Fig. 6.169 and Fig. 6.170, it can be noticed that in the case of specimen VT-1, the area of chords neglects a certain area of concrete on the top and on the bottom edges of the entire beam/column cross-section, where in the case of specimen VT-2, the neglected area is localised in the middle. The observed situation is the resultant of taken assumption about the double symmetric cross-sections of chords. Moreover, according to the fact that chords are representing the major part of total cross-section, the area of posts is not significant. The rigid connection between the chords and posts in the theoretical Vierendeel truss model is reflected by the stiff shear connection from test specimens.

6.5.3.5. Calibration of the model

Calibration of the proposed VTBM model is referring to the point on the experimental load-deflection curve identified in Section 6.5.2. By appropriate definition of the geometry in the implemented analytical models for the equivalent beam bending and shear stiffnesses given in Eq. 6.102 and Eq. 6.113 respectively, the resultant function of specimen deflection given in Eq. 6.96 yields the linear load-deflection relation. However, based on the above, it can be concluded that the given VTBM model is calibrated only for the analysed test specimens described in Section 6.3 and wider application strongly requires additional experimental and numerical investigations.

The resultant stiffness of the analytically analysed specimens strictly depends on the applied moduli of elasticity of the contributing materials. For the steel materials, the base values were experimentally obtained and are given in Table 6.5 and Table 6.6 for the structural steel and reinforcement steel respectively. However, in the effective value of resultant stiffness, both moduli of elasticity of steel materials were reduced by 10% following the provisions given in clause 6.7.3.4 of EN 1994-1-1 [58]. The reduction on the stiffness of steel materials refers to the fundamental assumption taken in Section 6.5.1 about strain limitation of steel materials due to the reduced activation of concrete in the force transfer. The reduced values of the Young's Moduli for the structural and reinforcement steel material are given in Eq. 6.114 and Eq. 6.115 respectively.

$$E_{a,eff} = 0.9 \cdot E_a = 0.9 \cdot 207708 = 186937.2\ [MPa] \tag{6.114}$$

$$E_{s,eff} = 0.9 \cdot E_s = 0.9 \cdot 206165 = 185548.5\ [MPa] \tag{6.115}$$

The modulus of elasticity for the concrete material was evaluated based on the provision given in EN 1992-1-1 [53]. The transformed values of the mean compression strengths for cylindrical specimens given in Eq. 6.64 for the specimen VT-1 and in Eq. 6.71 for the specimen VT-2 were based on the

measured compression strengths for cubic specimens given in Table 6.7. In the result, the base values of concrete moduli of elasticity for both specimens are evaluated in Eq. 6.116 for the specimen VT-1 and in Eq. 6.117 for the specimen VT-2. Similar like in the case of steel materials, the effective values of reduced moduli of elasticity for concrete material were taken according to the fundamental assumptions about the nature of concrete macro and micro behaviour including second order effects, imperfections and specimen exposure conditions defined in Section 6.5.1. The applied reduction factor followed the provision given in clause 6.7.3.4 of EN 1994-1-1 [58] for the second-order analysis and the base value of concrete Young's Modulus was reduced by the factor of 0.9·0.5=0.45. The evaluated effective modulus of elasticity of concrete is defined in Eq. 6.118 for the specimen VT-1 and in Eq. 6.119 for the specimen VT-2.

$$E_{cm,VT-1} = 22 \cdot \left[\left(f_{cm,VT-1}\right)/10\right]^{0.3} = 22 \cdot [(38.61)/10]^{0.3} = 32.99\ [GPa] \tag{6.116}$$

$$E_{cm,VT-2} = 22 \cdot \left[\left(f_{cm,VT-2}\right)/10\right]^{0.3} = 22 \cdot [(35.77)/10]^{0.3} = 32.25\ [GPa] \tag{6.117}$$

$$E_{cm,eff,VT-1} = 0.45 \cdot E_{cm,VT-1} = 0.45 \cdot 32.99 = 14.85\ [GPa] \tag{6.118}$$

$$E_{cm,eff,VT-2} = 0.45 \cdot E_{cm,VT-2} = 0.45 \cdot 32.25 = 14.51\ [GPa] \tag{6.119}$$

According to the defined effective values of the moduli of elasticity for the materials, the effective conversion ratios are calculated in reference to Eq. 6.97 and they are given in Eq. 6.120 and Eq. 6.121 for the specimens VT-1 and VT-2 respectively. In the result, the geometry of considered cross-sections in steel units given in Fig. 6.166 can be defined and the resultant geometries are shown in Fig. 6.171. Based on Fig. 6.171, the effective global moments of inertia are defined in Eq. 6.122 for the specimen VT-1 and in Eq. 6.123 for the specimen VT-2. The obtained results from Eq. 6.114-115, Eq. 6.122-123 and from Eq. 6.100-101 are implemented into Eq. 6.102. In the result, the values of equivalent beam bending stiffnesses are defined in Eq. 6.124 for the specimen VT-1 and in Eq. 6.125 for the specimen VT-2. It can be observed that the evaluated values of equivalent beam bending stiffnesses for both specimens corresponds well to the values of effective bending stiffnesses that can be calculated according to clause 6.7.3.4 of EN 1994-1-1 [58] with the accuracy error less than 0.5%.

$$\eta_{E,a,eff,VT-1} = \frac{E_{cm,eff,VT-1}}{E_{a,eff}} = \frac{14850}{186937.2} = 0.079 \tag{6.120}$$

$$\eta_{E,a,eff,VT-2} = \frac{E_{cm,eff,VT-2}}{E_{a,eff}} = \frac{14510}{186937.2} = 0.078 \tag{6.121}$$

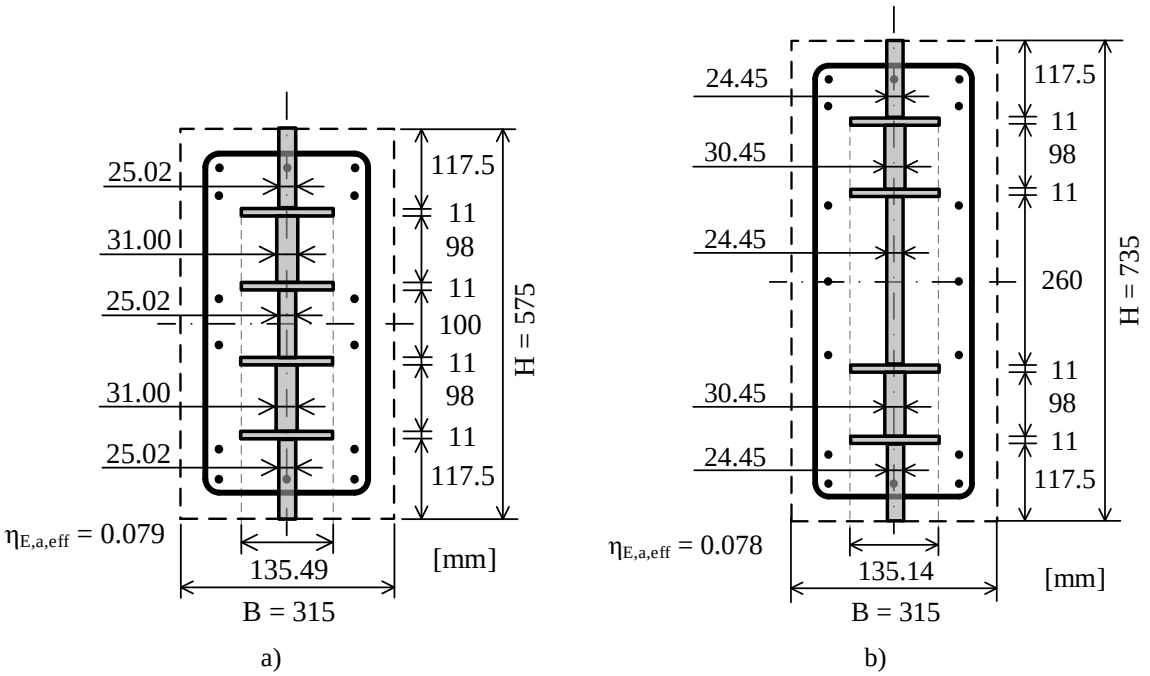


Fig. 6.171. Defined geometry of cross-sections in steel units for the beam/column specimens – a) for the specimen VT-1 and b) for the specimen VT-2.

$$I_{v,gl,VT-1} = 48477.72[cm^4] \tag{6.122}$$

$$I_{v,gl,VT-2} = 104276.13[cm^4] \tag{6.123}$$

$$(EI)_{v,gl,VT-1} = E_{a,eff} I_{v,gl,VT-1} + E_{s,eff} I_{s,total,VT-1} = 18693.72 \cdot 48477.72 + 18554.85 \cdot 2314.54 = 949174936\ [kNcm^2] \tag{6.124}$$

$$(EI)_{v,gl,VT-2} = E_{a,eff} I_{v,gl,VT-2} + E_{s,eff} I_{s,total,VT-2} = 18693.72 \cdot 104276.13 + 18554.85 \cdot 4582.56 = 2034337478\ [kNcm^2] \tag{6.125}$$

According to the defined effective values of the moduli of elasticity for the applied materials given in Eq. 6.114-6.115 and Eq. 6.118-6.119, the geometries of discretised Vierendeel truss elements shown in Fig. 6.169 for the specimen VT-1 and in Fig. 6.170 for the specimen VT-2 were evaluated. The spans between the chords "b" was equal to the distances between the axes of the embedded steel profiles and the values are defined in Eq. 6.126-6.127 for the respective specimens. According to the assumed geometrical constraint that a ≈ b, the values of spans between the posts "a" were evaluated with reference to the support length of specimens L_0 = 6000 mm. The obtained number of posts and the values of "a" are given in Eq. 6.128-6.129 for the respective specimens. The defined geometry is shown in Fig. 6.172 for the specimen VT-1 and in Fig. 6.173 for the specimen VT-2.

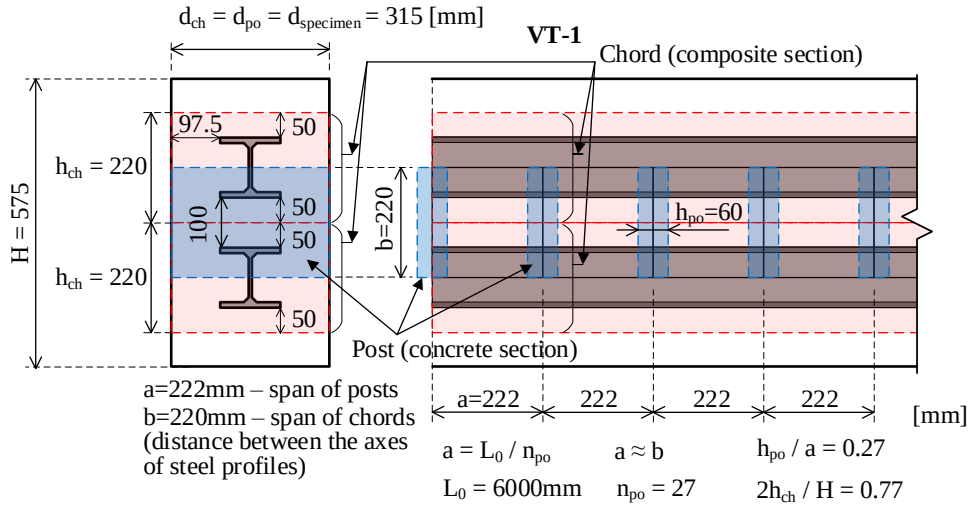


Fig. 6.172. Defined geometry of the discretised geometry of the specimen VT-1 into the Vierendeel truss system.

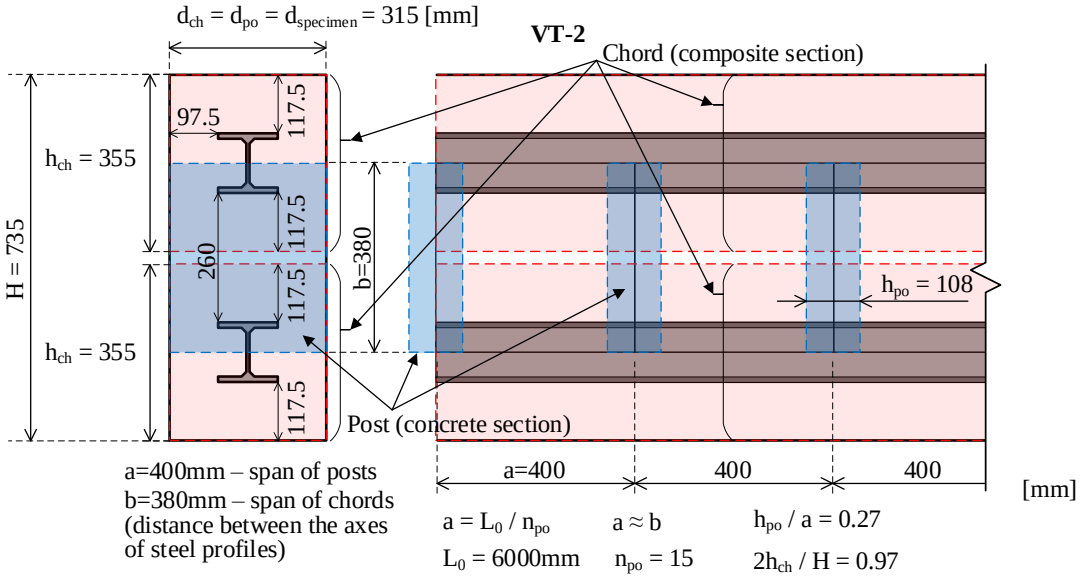


Fig. 6.173. Defined geometry of the discretised geometry of the specimen VT-2 into the Vierendeel truss system.

$$b_{VT-1} = 220\ [mm] \tag{6.126}$$

$$b_{VT-2} = 380\ [mm] \tag{6.127}$$

$$n_{po,VT-1} = 27 \quad \rightarrow \quad a_{VT-1} = \frac{L_0}{n_{po,VT-1}} = \frac{6000}{27} \cong 222\ [mm] \tag{6.128}$$

$$n_{po,VT-2} = 15 \quad \rightarrow \quad a_{VT-2} = \frac{L_0}{n_{po,VT-2}} = \frac{6000}{15} = 400\ [mm] \tag{6.129}$$

Considering the cross-sections of chords, it was assumed that they are double symmetric, therefore, the height of chords is limited to the concrete encasement or to the clear distance between the embedded steel profiles. For the specimen VT-1, see Fig. 6.172, the height of chord was limited by the clear distance between the steel profiles, where in the case of the specimen VT-2, see Fig. 6.173, the opposite situation took place, where the concrete encasement introduced the limit of height. In both cases, the cross-sections consisted in steel and concrete materials, therefore, the discretised chords were

transformed to the steel units sections by applying the effective conversion ratios given in Eq. 6.120 and Eq. 6.121 for the specimen VT-1 and VT-2 respectively. The resultant geometries of chords sections are shown in Fig. 6.174, where the geometrical and elastic material properties are defined in Eq. 6.130-6.134 for the specimen VT-1 and in Eq. 6.135-6.139 for the specimen VT-2.

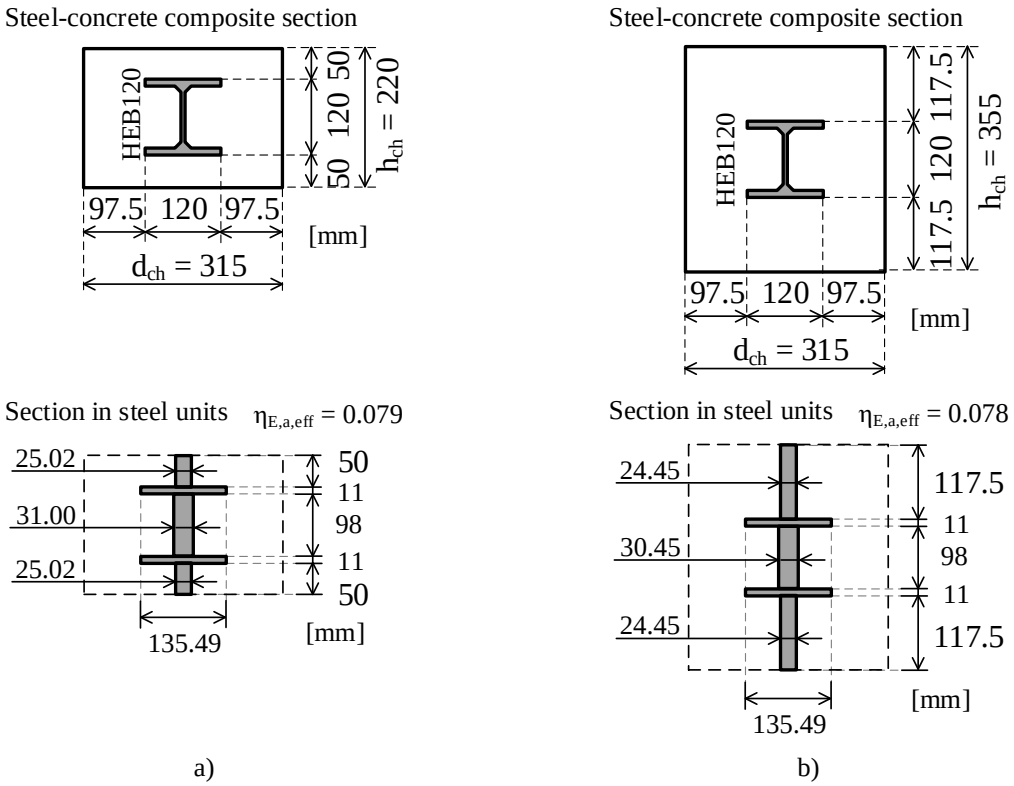


Fig. 6.174. Geometry of chords in the VTBM model – a) for the specimen VT-1 and b) for the specimen VT-2.

Chord properties for the specimen VT-1 are:

$$A_{ch,VT-1} = 85.21\ [cm^2] \tag{6.130}$$

$$I_{ch,VT-1} = 2991.19\ [cm^4] \tag{6.131}$$

$$A_{v,ch,VT-1} = 41.26\ [cm^2] \tag{6.132}$$

$$E_{ch,VT-1} = E_{a,eff} = 18693.72\ [kN/cm^2] \tag{6.133}$$

$$\nu_{ch,VT-1} = 0.3 \tag{6.134}$$

Chord properties for the specimen VT-2 are:

$$A_{ch,VT-2} = 117.03\ [cm^2] \tag{6.135}$$

$$I_{ch,VT-2} = 9888.89\ [cm^4] \tag{6.136}$$

$$A_{v,ch,VT-2} = 65.63\ [cm^2] \tag{6.137}$$

$$E_{ch,VT-2} = E_{a,eff} = 18693.72\ [kN/cm^2] \tag{6.138}$$

$$\nu_{ch,VT-2} = 0.3 \tag{6.139}$$

The remaining parts to evaluate the equivalent beam shear stiffness for the considered specimens are the cross-section geometries of posts in the assumed theoretical Vierendeel truss model. It was assumed that posts consisted only of pure concrete sections. From Fig. 6.172 and Fig. 6.173, it can be observed that the length of posts is equal to the vertical span between the embedded steel profiles "b" and for the specimen VT-1 it is equal to 220 mm, where for the specimen VT-2 it is equal to 380 mm. The width of posts is assumed equal to the total widths of specimens and in the same time, to the widths of chords. Therefore, the remaining parameter to be defined is the height of osts. This parameter was calibrated in the iterative process in order to converge the deflection value from the VTBM model, described by Eq. 6.96, with the reference point identified in Section 6.5.2. In the result, it was identified that for both specimens, the height of posts should be equal to 27% of the span between them, see Fig. 6.172 and Fig. 6.173. The defined discretisation models for posts give regular rectangular cross-sections of posts with dimensions of 60x315 mm for the specimen VT-1 and 108x315 mm for the specimen VT-2, where bending according to the weak axis is considered. The geometrical and material properties of the assumed cross-sections of posts are defined in Eq. 6.140-6.144 for the specimen VT-1 and in Eq. 6.145-6.149 for the specimen VT-2.

Post properties for the specimen VT-1 are:

$$A_{po,VT-1} = 189.00\ [cm^2] \tag{6.140}$$

$$I_{po,VT-1} = 567.00\ [cm^4] \tag{6.141}$$

$$A_{v,po,VT-1} = 126.00\ [cm^2] \tag{6.142}$$

$$E_{po,VT-1} = E_{cm,eff,VT-1} = 1484.70\ [kN/cm^2] \tag{6.143}$$

$$\nu_{po,VT-1} = 0.2 \tag{6.144}$$

Post properties for the specimen VT-2 are:

$$A_{po,VT-2} = 340.20\ [cm^2] \tag{6.145}$$

$$I_{po,VT-2} = 3306.74\ [cm^4] \tag{6.146}$$

$$A_{v,po,VT-2} = 226.80\ [cm^2] \tag{6.147}$$

$$E_{po,VT-2} = E_{cm,eff,VT-2} = 1451.08\ [kN/cm^2] \tag{6.148}$$

$$\nu_{po,VT-2} = 0.2 \tag{6.149}$$

The defined geometry of internal Vierendeel truss system in the considered beam/column specimens allowed for the evaluation of equivalent beam shear stiffness values by placing Eq. 6.126-6.149 into Eq. 6.113 for the respective specimens. The supporting simplification factors defined in Eq. 6.109 and Eq. 6.110 are evaluated in Eq. 6.150-6.151 for the specimen VT-1 and in Eq. 6.152-6.153 for the specimen VT-2. The resultant values of the equivalent beam shear stiffnesses are given in Eq. 6.154 and in Eq. 6.155 for the specimen VT-1 and VT-2 respectively.

$$\psi_{Q,VT-1} = \frac{E_{ch,VT-1}A_{v,ch,VT-1}/b_{VT-1}\left(1+\nu_{ch,VT-1}\right)}{E_{po,VT-1}A_{v,po,VT-1}/a_{VT-1}\left(1+\nu_{po,VT-1}\right)} = \frac{(18693.72\cdot 41.26)/\left(22\cdot(1+0.3)\right)}{(1484.70\cdot 126.00)/\left(22.2\cdot(1+0.2)\right)} = 3.844 \tag{6.150}$$

$$\psi_{M,VT-1} = \frac{E_{ch,VT-1}I_{ch,VT-1}/a_{VT-1}}{E_{po,VT-1}I_{po,VT-1}/b_{VT-1}} = \frac{(18693.72\cdot 2991.19)/22.2}{(1484.70\cdot 567.00)/22} = 65.759 \tag{6.151}$$

$$\psi_{Q,VT-2} = \frac{E_{ch,VT-2}A_{v,ch,VT-2}/b_{VT-2}\left(1+\nu_{ch,VT-2}\right)}{E_{po,VT-2}A_{v,po,VT-2}/a_{VT-2}\left(1+\nu_{po,VT-2}\right)} = \frac{(18693.72\cdot 65.63)/\left(38\cdot(1+0.3)\right)}{(1451.08\cdot 226.80)/\left(40\cdot(1+0.2)\right)} = 3.622 \tag{6.152}$$

$$\psi_{M,VT-2} = \frac{E_{ch,VT-2}I_{ch,VT-2}/a_{VT-2}}{E_{po,VT-2}I_{po,VT-2}/b_{VT-2}} = \frac{(18693.72\cdot 9888.89)/40}{(1451.08\cdot 3306.74)/38} = 36.599 \tag{6.153}$$

$$K_{sv,VT-1} = \frac{1}{\frac{{a_{VT-1}}^2}{{b_{VT-1}}^2 E_{ch,VT-1}A_{ch,VT-1}} + \frac{\left(1+\nu_{ch,VT-1}\right)\left(1+2\psi_{Q,VT-1}\right)}{E_{ch,VT-1}A_{v,ch,VT-1}} + \frac{{a_{VT-1}}^2\left(1+2\psi_{M,VT-1}\right)}{24E_{ch,VT-1}I_{ch,VT-1}}}$$
$$= \frac{1}{\frac{22.2^2}{22^2\cdot 18693.72\cdot 85.21} + \frac{(1+0.3)(1+2\cdot 3.844)}{18693.72\cdot 41.26} + \frac{22.2^2\cdot(1+2\cdot 65.759)}{24\cdot 18693.72\cdot 2991.19}}$$
$$= 15613.11\ [kN] \tag{6.154}$$

$$K_{sv,VT-2} = \frac{1}{\frac{{a_{VT-2}}^2}{{b_{VT-2}}^2 E_{ch,VT-2}A_{ch,VT-2}} + \frac{\left(1+\nu_{ch,VT-2}\right)\left(1+2\psi_{Q,VT-2}\right)}{E_{ch,VT-2}A_{v,ch,VT-2}} + \frac{{a_{VT-2}}^2\left(1+2\psi_{M,VT-2}\right)}{24E_{ch,VT-2}I_{ch,VT-2}}}$$
$$= \frac{1}{\frac{40^2}{38^2\cdot 18693.72\cdot 117.03} + \frac{(1+0.3)(1+2\cdot 3.622)}{18693.72\cdot 65.63} + \frac{40^2\cdot(1+2\cdot 36.599)}{24\cdot 18693.72\cdot 9888.89}}$$
$$= 27777.07\ [kN] \tag{6.155}$$

The obtained equivalent beam shear stiffness values from Eq. 6.154 and Eq. 6.155 are greatly reduced in comparison to the values of shear stiffnesses calculated for the homogenous and isotropic cross-sections. The relative ratio of the proposed equivalent beam shear stiffnesses to the Timoshenko shear stiffnesses reached 0.024 for the specimen VT-1 and 0.034 for the specimen VT-2. The deflection of specimens is calculated with the proposed hybrid VTBM model by placing the obtained equivalent beam bending and shear stiffnesses from Eq. 6.124-6.125 and Eq. 6.154-6.155 respectively into Eq. 6.96. The resultant VTBM curves and their comparison to the experimental and numerical results, as well as other considered models, like for example pure Timoshenko beam, are given in Section 6.5.5.

6.5.4. Other considered beam models

In order to analyse the impact level of proposed VTBM model for the evaluation of effective stiffness and resulting deflection, other analytical models were considered for the tested beam/column specimens. In the additionally considered models, the most common Euler-Bernoulli beam model and the Timoshenko beam model were included. Moreover, an analogical model to the proposed VTBM model but with introduced internal Mörsch truss system instead of the Vierendeel truss system, namely the Timoshenko beam with embedded Mörsch truss model (MTBM) was analysed. The MTBM model was inspired by the research shown in the RFCS project SmartCoCo [175], where the shear forces distribution in columns with multiple encased steel profiles was verified based on the Mörsch truss system but the evaluation of the effective bending stiffness adapted methods from EN 1992-1-1 [53]. Details on the performed calculations are given in Annex G.

6.5.4.1. Euler-Bernoulli beam model

In the considered case, the test specimens VT-1 and VT-2 are fully analysed according to the Euler-Bernoulli beam theory, where the homogenous and isotropic cross-sections in steel units of the tested beam/column specimens are considered. The analogous cross-sections are shown in Fig. 6.166, where here the conversion ratios reach the values of 0.159 for the specimen VT-1 and 0.155 for the specimen VT-2. Alternatively, the effective bending stiffness of considered specimens are analysed according to the provisions given in clause 6.7.3.3 (3) or clause 6.7.3.4 of EN 1994-1-1 [58], where the stiffness reduction factors are considered. The static system of analysed specimens given in Fig. 6.2 apply, where according to the considered beam theory, the maximum beam deflection can be evaluated according to Eq. 6.156. In the result, three variants of the Euler-Bernoulli beam deflections were evaluated: (i) with full cross-section without any reduction in stiffness, (ii) with effective bending stiffness according to EN 1994-1-1 [58] and (iii) with effective bending stiffness including the second-order effects according to EN 1994-1-1 [58]. The evaluated respective stiffnesses are defined in Eq. 6.157-6.159 for the specimen VT-1 and in Eq. 6.160-6.162 for the specimen VT-2.

$$w_{Bernoulli} = \frac{PL^3}{48EI} \tag{6.156}$$

, where the bending stiffness for the specimen VT-1 is

$$(EI)_{full,VT-1} = 1860517201\ [kNcm^2] \tag{6.157}$$

$$(EI)_{eff,EC4,VT-1} = 1218115077\ [kNcm^2] \tag{6.158}$$

$$(EI)_{eff,II,EC4,VT-1} = 951763092\ [kNcm^2] \tag{6.159}$$

and the bending stiffness for the specimen VT-2 is

$$(EI)_{full,VT-2} = 3901759347\ [kNcm^2] \tag{6.160}$$

$$(EI)_{eff,EC4,VT-2} = 2597155591\ [kNcm^2] \tag{6.161}$$

$$(EI)_{eff,II,EC4,VT-2} = 2043904187\ [kNcm^2] \tag{6.162}$$

It can be observed that values given by Eq. 6.159 and Eq. 6.162 are in good correlation to the values evaluated form the VTBM model for the equivalent beam bending stiffness given in Eq. 6.124 and Eq. 6.125 for the specimen VT-1 and VT-2 respectively. The comparison of deflection curves is given in Section 6.5.5.

6.5.4.2. Timoshenko beam model

An analogous case like for the pure Euler-Bernoulli beam model described in Section 6.5.4.1 is considered for the application of Timoshenko beam theory. The shear effect on the beam curvature modifies the elastic load-deflection relation given in Eq. 6.156 into Eq. 6.163. For the considered Timoshenko beam model, the same three variants as in the Euler-Bernoulli beam model are considered, where (i) the full cross-section in steel units, (ii) the effective bending stiffness according to EN 1994-1-1 [58] and (iii) the effective bending stiffness with the consideration of second-order effects according to EN 1994-1-1 [58] are considered. The bending stiffnesses calculated according to the Euler-Bernoulli beam theory given in Eq. 6.157-6.162 are directly included as the bending stiffnesses in Eq. 6.163. The shear stiffnesses are evaluated assuming cross-section in steel units by considering the respective conversion ratios. The evaluated conversion ratios with corresponding elastic isotropic shear stiffnesses are given in Eq. 6.164-6.166 for the specimen VT-1 and in Eq. 6.167-6.169 for the specimen VT-2.

$$w_{Timoshenko} = \frac{PL^3}{48EI} + \frac{PL}{4A_v G} \tag{6.163}$$

, where the bending stiffness from Eq. 6.157-6.162 apply and

the shear stiffness for the specimen VT-1 is

$$\eta_{E,a,full,VT-1} = 0.159 \quad \rightarrow \quad (A_v G)_{full,VT-1} = 1472558\ [kN] \tag{6.164}$$

$$\eta_{E,a,EC4,VT-1} = 0.095 \quad \rightarrow \quad (A_v G)_{eff,EC4,VT-1} = 861043\ [kN] \tag{6.165}$$

$$\eta_{E,a,EC4,II,VT-1} = 0.079 \quad \rightarrow \quad (A_v G)_{eff,EC4,VT-1} = 638461\ [kN] \tag{6.166}$$

and the shear stiffness for the specimen VT-2 is

$$\eta_{E,a,full,VT-2} = 0.155 \quad \rightarrow \quad (A_v G)_{full,VT-2} = 1869714\ [kN] \tag{6.167}$$

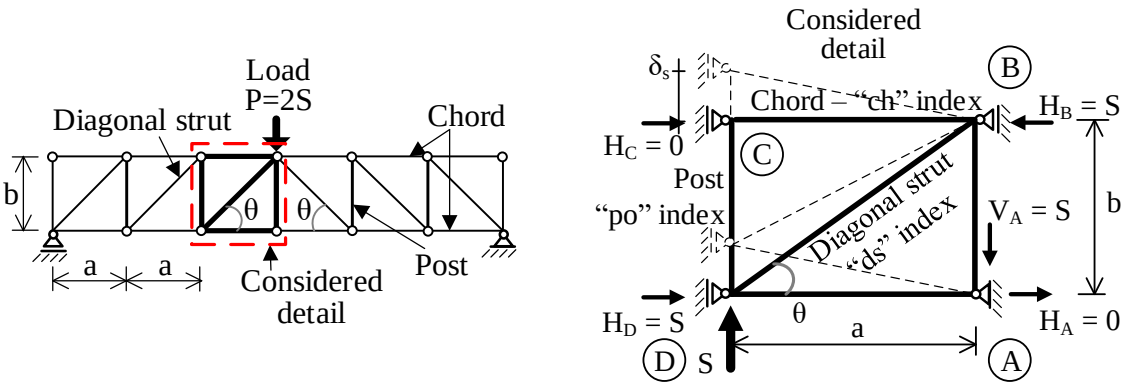
$$\eta_{E,a,EC4,VT-2} = 0.093 \quad \rightarrow \quad (A_v G)_{eff,EC4,VT-2} = 1105394\ [kN] \tag{6.168}$$

$$\eta_{E,a,EC4,II,VT-2} = 0.078 \quad \rightarrow \quad (A_v G)_{eff,EC4,VT-2} = 823745\ [kN] \tag{6.169}$$

The deflection curves and comparison of the results are given in Section 6.5.5.

6.5.4.3. Morsch truss as a Timoshenko beam analogy model

In the considered model of Timoshenko beam with embedded Mörsch truss system (MTBM), the procedure for the derivation of resultant deflection is analogical to the described-above VTBM model but instead of the Vierendeel truss, the Mörsch truss shown in Fig. 6.175 is considered. The effective values of the reduced moduli of elasticity of materials described in Eq. 6.114-6.119 apply. The bending stiffness of the considered systems are analysed analogically to the case of VTBM model, where the full cross-sections transformed into steel units are considered, see Fig. 6.171. The obtained values of bending stiffnesses are given in Eq. 6.170 for the specimen VT-1 and in Eq. 6.171 for the specimen VT-2. The principal of virtual work described in Eq. 6.103 apply in order to evaluate the shear deformation of the considered portion of truss shown in Fig. 6.175b. Due to the considered truss system, only normal forces are contributing to the shear deflection. By applying the shear effect condition on the Timoshenko beam curvature given in Eq. 6.90, the resultant equivalent beam shear stiffness for the MBTM model is given in Eq. 6.172. The discretisation of the specimens into the theoretical Mörsch truss system is assumed analogically to the VTBM model, where the diagonal struts were assumed with geometry corresponding to the geometry of the posts from the VTBM model and their cross-section consist of rectangular shape, pure concrete material and 60x315 mm dimensions for the specimen VT-1. In specimen VT-2, diagonal struts sections have 108x315 mm dimensions. The cross-section properties evaluated in Eq. 6.140-6.149 apply for the considered struts, see Eq. 6.173-6.176. Diagonal struts in the Mörsch truss system are responsible for the transfer of total shear forces, therefore, their geometry is taken as dominant in reference to vertical posts, where the distribution of areas in reference to the horizontal span “a” is taken as 38% for the diagonal struts and 10% for the vertical posts. Geometry of posts in the MTBM model is assumed as not significant due to a minor contribution in the force transfer and pure concrete rectangular cross-sections with dimensions of 22.2x315 mm for the specimen VT-1 and 40x315 mm for the specimen VT-2 are taken. The resulting section properties are defined in Eq. 6.177-6.180. The cross-sections of chords are taken identical like in the case of VTBM model and consist of steel-concrete composite sections. However, they do not contribute to the shear deformation. The vertical span between chords “b” and horizontal span between posts “a” are assumed identically like in the case of VTBM model. The taken values are described in Eq. 6.181-6.184 for the respective specimens. The taken vertical and horizontal distribution of chords and posts result in the defined inclination angle of diagonal struts and for the specimen VT-1 the angle $\theta = 44.71°$ (Eq. 6.185) is obtained, where for the specimen VT-2 the angle $\theta = 43.53°$ (Eq. 6.186) is reached. The geometry of discretised Mörsch truss system is applied into Eq. 6.172 with respect to each specimen and the resultant values of the equivalent beam shear stiffnesses are given in Eq. 6.187 and Eq. 6.188 for the specimen VT-1 and VT-2 respectively. The resultant deflections of specimens with the considered MTBM model are evaluated according to the Timoshenko beam theory by applying results from Eq. 6.170-6.171 and Eq. 6.187-6.188 into Eq. 6.189. Details on the performed calculations are given in Annex G.



a) b)

Fig. 6.175. Morsch truss model for the evaluation of shear stiffness in the beam/column specimens – a) global model and b) considered detail.

$$(EI)_{MTBM,VT-1} = 949174936\ [kNcm^2] \tag{6.170}$$

$$(EI)_{MTBM,VT-2} = 2034337478\ [kNcm^2] \tag{6.171}$$

$$K_{s,MTBM} = \frac{1}{\frac{1}{E_{ds}A_{ds}\sin^2\theta\cos\theta} + \frac{1}{E_{po}A_{po}\cot\theta}} \tag{6.172}$$

$$A_{ds,MTBM,VT-1} = 189.00\ [cm^2] \tag{6.173}$$

$$E_{ds,MTBM,VT-1} = 1484.70\ [kN/cm^2] \tag{6.174}$$

$$A_{ds,MTBM,VT-2} = 340.20\ [cm^2] \tag{6.175}$$

$$E_{ds,MTBM,VT-2} = 1451.08\ [kN/cm^2] \tag{6.176}$$

$$A_{po,MTBM,VT-1} = 70.00\ [cm^2] \tag{6.177}$$

$$E_{po,MTBM,VT-1} = 1484.70\ [kN/cm^2] \tag{6.178}$$

$$A_{po,MTBM,VT-2} = 126.00\ [cm^2] \tag{6.179}$$

$$E_{po,MTBM,VT-2} = 1451.08\ [kN/cm^2] \tag{6.180}$$

$$a_{MTBM,VT-1} = 222.22\ [mm] \tag{6.181}$$

$$b_{MTBM,VT-1} = 220\ [mm] \tag{6.182}$$

$$a_{MTBM,VT-2} = 400\ [mm] \tag{6.183}$$

$$b_{MTBM,VT-2} = 380\ [mm] \tag{6.184}$$

$$\theta_{MTBM,VT-1} = 44.71^0 \tag{6.185}$$

$$\theta_{MTBM,VT-1} = 43.53^0 \tag{6.186}$$

$$K_{s,MTBM,VT-1} = \frac{1}{\frac{1}{1484.70 \cdot 189 \cdot 0.352} + \frac{1}{1484.70 \cdot 70 \cdot 1.01}} = 50872.71\ [kN] \tag{6.187}$$

$$K_{s,MTBM,VT-2} = \frac{1}{\frac{1}{1451.08 \cdot 340.20 \cdot 0.344} + \frac{1}{1451.08 \cdot 126 \cdot 1.05}} = 90204.82\ [kN] \tag{6.188}$$

$$w_{MTBM} = \frac{PL^3}{48(EI)_{MTBM}} + \frac{PL}{4K_{s,MTBM}} \tag{6.189}$$

The deflection curves and the comparison of results is given in Section 6.5.5. The presented MTBM is considered with the corresponding geometry to the VTBM model in order to compare two approaches. The Mörsch truss system-based strut-and-tie models are widely applied with high accuracy to describe the distribution of forces inside the discontinuity zones of reinforce concrete structures [169]. For the composite columns with multiple encased steel sections the aforementioned model seems also feasible for the evaluation of internal forces distribution between the embedded elements, as it was shown in the RFCS project 'SmartCoCo' [175] and CTBUH project 'ISRC Composite Column' [82]. However, the observations taken from the experimental campaign and numerical simulations, described in Section 6.4 and 6.5, strongly indicated the Vierendeel-truss-like behaviour rather than the Mörsch-truss-like behaviour for the considered specimens. Moreover, the applied shear connection at the steel-concrete interface reflects more the rigid connections of the Vierendeel trusses instead of pin-connections used in Mörsch trusses. In addition, results shown in Section 6.5.5 indicate better convergence to the considered reference point of the VTBM model rather than the MTBM model.

6.5.5. Comparison of the investigated models with experimental and numerical data

In Table 6.16, the summary of investigated analytical models together with the evaluated values of bending and shear stiffnesses and the resulting deflections due to the considered reference load from Section 6.5.2 is given. In addition, the experimental and numerical results are given for the comparison.

Table 6.16.
Investigated analytical models for the effective stiffness of beam/column specimens and comparison to test results.

Specimen	VT-1							VT-2						
Considered model / test	L_0 [cm]	P [kN]	$(EI)_{eff}$ x10^6 [kNcm^2]	K_s x10^3 [kN]	w_s [cm]	w [cm]	w / w_{test}	L_0 [cm]	P [kN]	$(EI)_{eff}$ x10^6 [kNcm^2]	K_s x10^3 [kN]	w_s [cm]	w [cm]	w / w_{test}
Experimental	600	362	-	-	-	5.16	1.00	600	549	-	-	-	4.04	1.00
Numerical	600	362	-	-	-	4.97	0.96	600	549	-	-	-	4.22	1.04
VTBM	600	362	949.2	15.6	3.48	5.19	1.01	600	549	2034.3	27.8	2.96	4.18	1.03
MTBM	600	362	949.2	50.9	1.05	2.77	0.54	600	549	2034.3	90.2	0.76	1.97	0.53
Bernoulli, full	600	362	1860.5	-	-	0.88	0.17	600	549	3901.8	-	-	0.63	0.16
Bernoulli, EC4 eff	600	362	1218.1	-	-	1.34	0.26	600	549	2597.2	-	-	0.95	0.24
Bernoulli, EC4 eff,II	600	362	951.8	-	-	1.71	0.33	600	549	2043.9	-	-	1.21	0.30
Timoshenko, full	600	362	1860.5	1472.6	0.04	0.91	0.18	600	549	3901.8	1869.7	0.04	0.68	0.17
Timoshenko, EC4 eff	600	362	1218.1	861.0	0.06	1.40	0.27	600	549	2597.2	1105.4	0.08	1.03	0.25
Timoshenko, EC4 eff,II	600	362	951.8	638.5	0.08	1.80	0.35	600	549	2043.9	823.8	0.10	1.31	0.32

From Table 6.16, it can be noticed that the VTBM model reached convergence ratio to the test results close to 1.0, where the MTBM model reached convergence ratio of approximately 0.5. The Euler-Bernoulli beam and Timoshenko beam models gave convergence ratio in the range of 0.16-0.35.

The obtained resultant load-deflection curves from different considered analytical models are plotted in Fig. 6.176 for the specimen VT-1 and in Fig. 6.177 for the specimen VT-2. In the aforementioned figures, the experimental and numerical results were included for the reference.

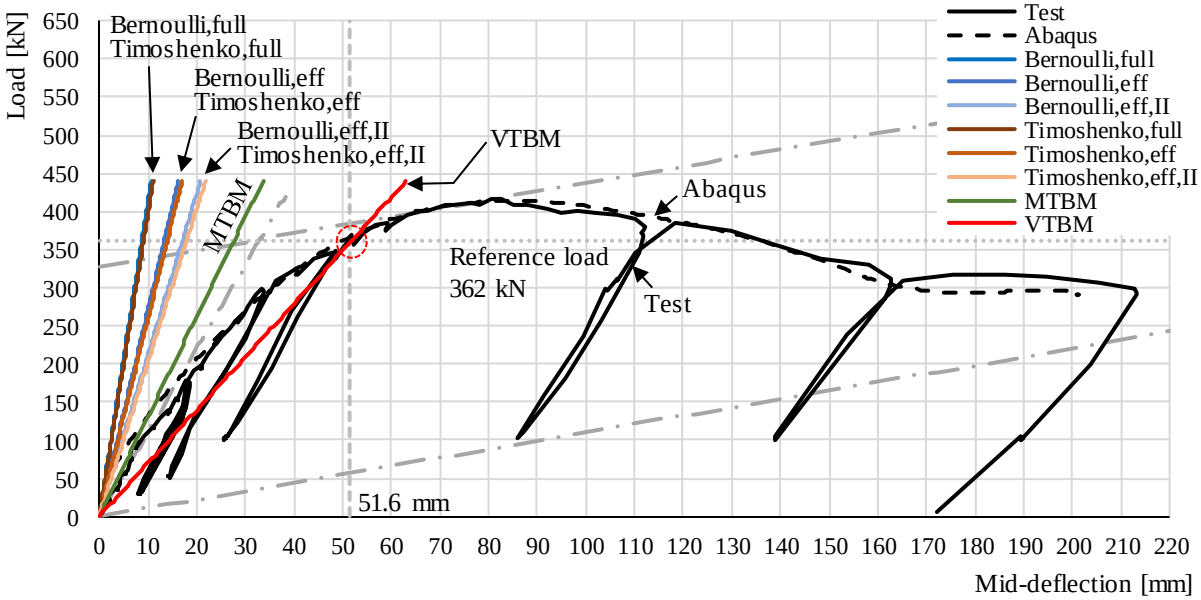


Fig. 6.176. Load-deflection curves of the investigated analytical models for the beam/column specimen VT-1.

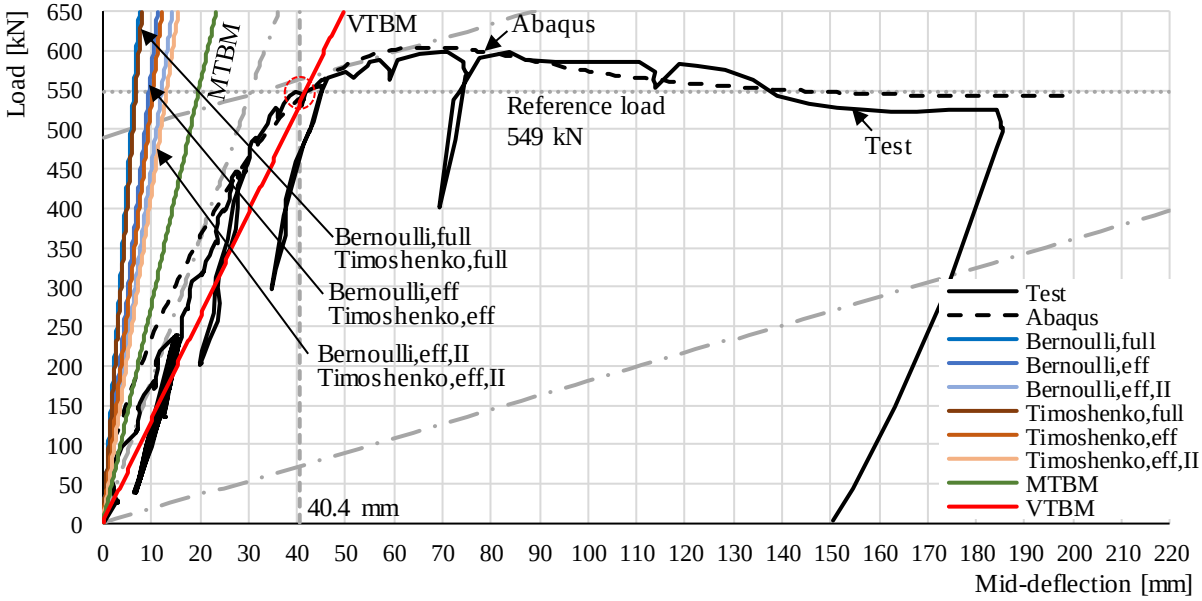


Fig. 6.177. Load-deflection curves of the investigated analytical models for the beam/column specimen VT-2.

From Fig. 6.176 and Fig. 6.177 it can be clearly observed that the VTBM model brings good correlation to the identified reference load point on the experimental curve. In the applied model, the reductions of the concrete Young's Modulus by factor 0.45 and the steel Young's Moduli by factor of 0.9 were done. These reduction factors are related to the nature of concrete behaviour and micro/macro

cracking effects from the test. An analogous approach is included in EN 1994-1-1 [58]. In the result, the reference point localised close to the peak load is accurately reached. However, by changing only the stiffness reduction factors and keeping the discretisation system unchanged, the initial stiffness behaviour is possible to be represented. Following the provisions given in clause 6.7.3.3 (3) of EN 1994-1-1 [58], the Young's Modulus of concrete is reduced by 0.6 and no reduction is applied to the steel parts. In the result, the load-deflection curve obtained for the VTBM model reflecting the initial phase of test is shown in Fig. 6.178 for the specimen VT-1 and in Fig. 6.179 for the specimen VT-2. In the above-mentioned diagrams, the original VTBM curves and VTBM curves with no applied reduction factors are included for the comparison.

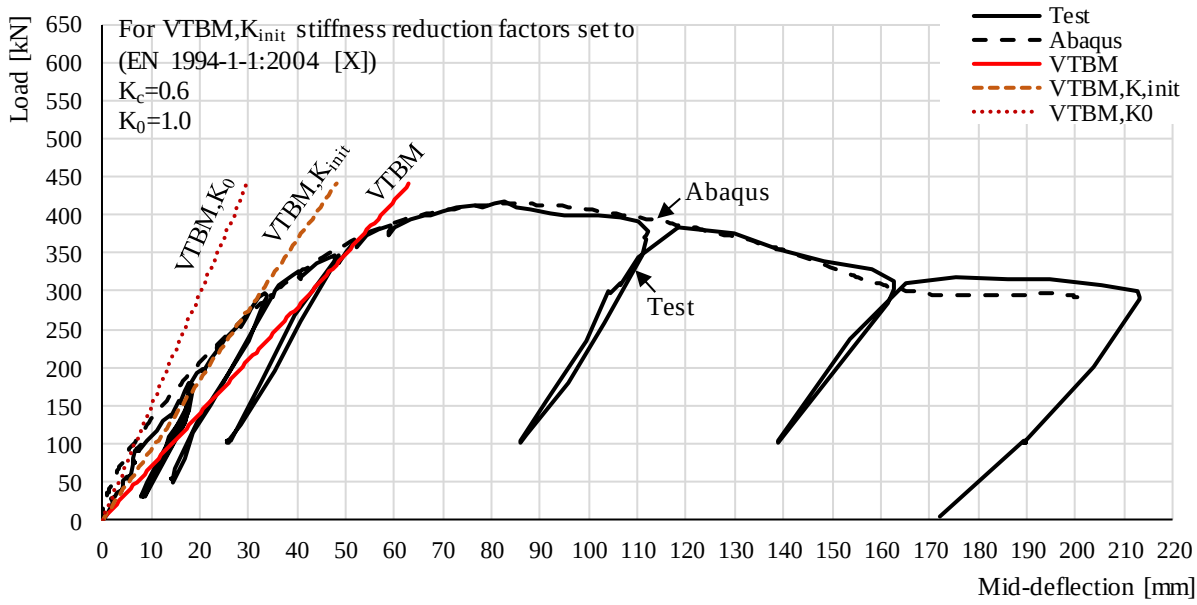


Fig. 6.178. Load-deflection curves of VTBM model with different stiffness reduction factors for the beam/column specimen VT-1.

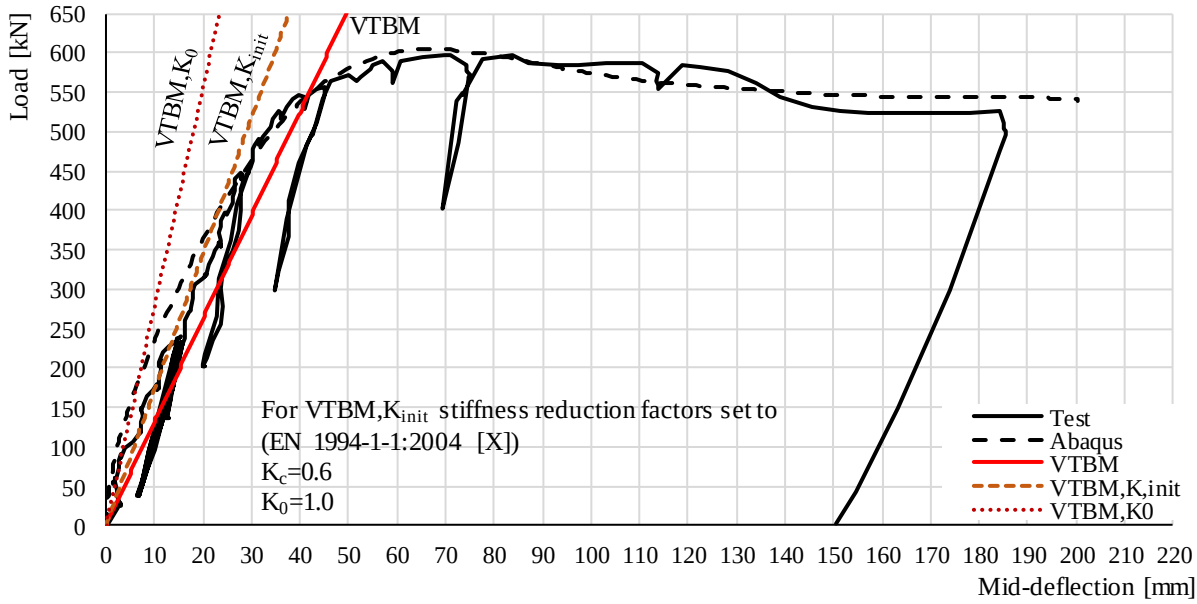


Fig. 6.179. Load-deflection curves of VTBM model with different stiffness reduction factors for the beam/column specimen VT-2.

Based on the results obtained from Table 6.16 and Fig. 6.176-6.179, it can be concluded that the proposed VTBM model can accurately consider the effective stiffness of considered beam/column specimens at the different stages of response – initial, elastic or plastic. The applied stiffness reduction factors followed the provisions given in EN 1994-1-1 [58].

According to the investigation above, it was shown that the proposed VTBM model brings good correlation to the experimental results. However, in the aforementioned investigation only the mid-span deflection was considered. It would be of interest to confront the entire deflection shape of specimens between the VTBM model and test results shown in Fig. 6.26-6.27. The comparison of deflection shapes is given in Fig. 6.180 for the specimen VT-1 and in Fig. 6.181 for the specimen VT-2. In both figures, the deflection shapes according to the new effective bending stiffness based on the VTBM model (EI_VTBM) are included. The derivation of the new effective bending stiffness is described in Section 6.5.6 below. The difference in the deflection shapes between the VTBM model and the EI_VTBM model is that the VTBM model consists of two deflection modes for bending and shear, where the EI_VTBM model consists only one deflection mode for bending. The resultant deflection shapes were evaluated according to the Timoshenko beam theory and the Euler-Bernoulli beam theory for the VTBM and EI_VTBM models respectively.

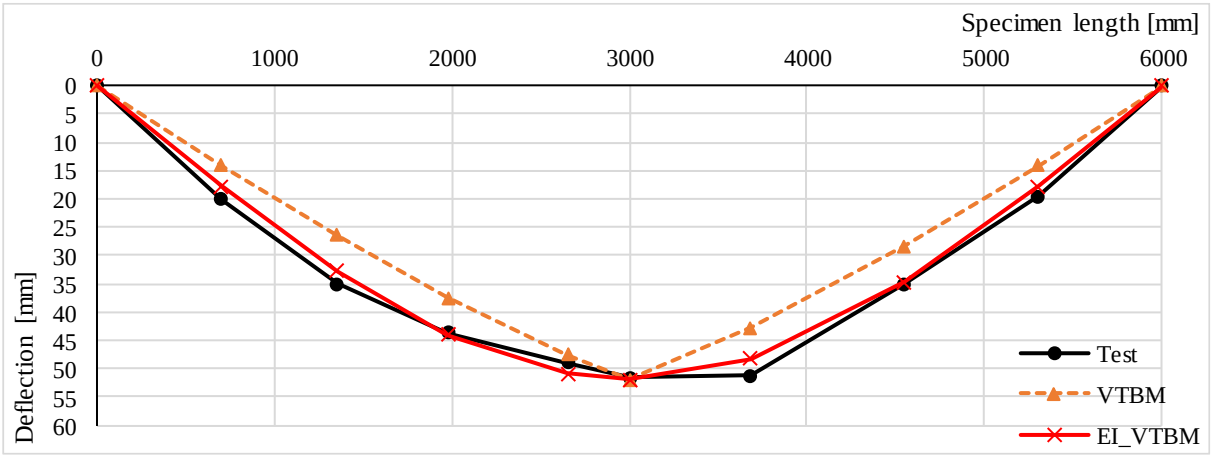


Fig. 6.180. Deflection shape of the specimen VT-1 according to the VTBM model and comparison to test results.

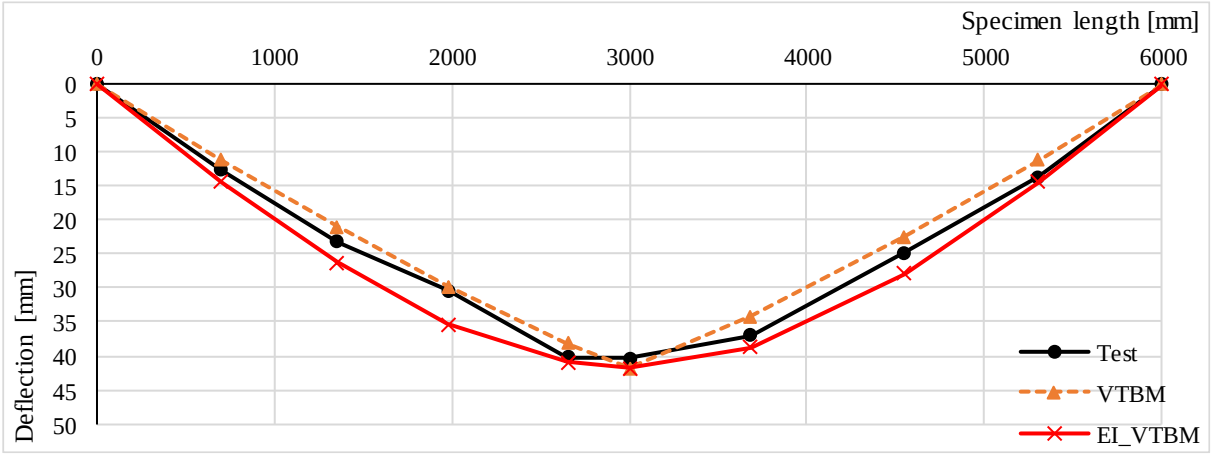


Fig. 6.181. Deflection shape of the specimen VT-2 according to the VTBM model and comparison to test results.

From Fig. 6.180 for the specimen VT-1, it can be observed that the EI_VTBM model fits better than the VTBM model to the deflection shape of the specimen obtained from the test. In the same time, from Fig. 6.181 for the specimen VT-2, it can be observed that the VTBM model fits well to the experimental deflection shape, the EI_VTBM model brings worse accuracy. The difference between the two figures shows that the specimen with the bigger distance between the embedded steel profiles was subjected to a more significant shear deformation effects than the specimen with the smaller distance. However, even if the specimen VT-1 showed bigger similarity to the Euler-Bernoulli beam deflection shape, the value of deflection obtained from the test is incorporating a significant part of shear deflection, which comes from the shear deformation effect and the identified analogy to the Vierendeel truss system. Based on the above described analysis, it can be concluded that the proposed VTBM model accurately described the behaviour of both specimens with respect that different variants of deflection shapes can be considered for different spacing between the embedded steel profiles. In the result, as an outlook, a weighting factors in relation to the distance between the embedded steel profiles could be introduced, which would modify the deflection modes in the VTBM model in order to obtain a respective more-bending or more-shear character of the global deflection shape. A purely empirical proposal of weighted deflection shape is shown in Fig. 6.182 for the specimen VT-1, where the bending mode deflection was amplified by factor 3.03, which in turn correlates to the ratio between the pure bending part of the deflection to the total deflection given in Table 6.16 for the VTBM model. Simultaneously, the shear deflection part was reduced to the marginal value by implementing the weighting factor of 0.02.

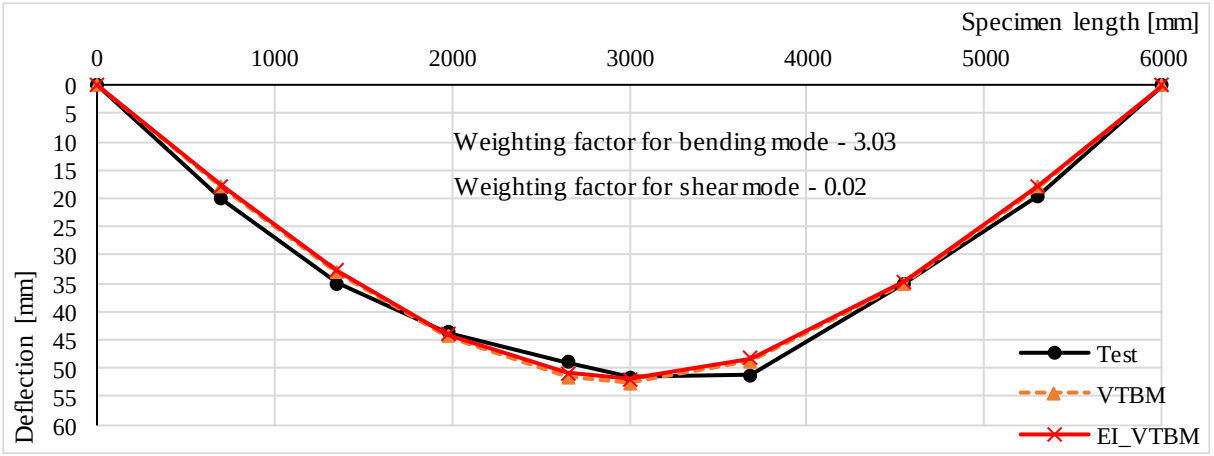


Fig. 6.182. Weighted deflection shape of the specimen VT-1 according to the VTBM model in order to converge to test results.

The proposed VTBM model and the corresponding resultant load-deflection curves were compared with the international analytical models available in the literature: (i) EN 1994-1-1 [58], (ii) ACI318 [2], (iii) AISC360 [8], (iv) Mirza/Tikka [123], (v) Lippes/Chanou [29, 112], (vi) SmartCoCo [175] and (vii) Adebar [87]. All the indicated models are briefly investigated in Chapter 3. In the calculations of respective effective flexural stiffnesses, the long-term effects and existence of the axial load were neglected. The calculation details are given in Annex G. The comparisons of resultant stiffnesses, evaluated for the geometry and conditions of the tested specimens described in Section 6.3, are given in

Fig. 6.183 and Fig. 6.184 for the specimen VT-1 and VT-2, respectively. It can be observed that for the analysed case, the analytical model for effective flexural stiffness proposed by the project SmartCoCo and the building code ACI318 gave the smallest value of stiffness. However, the convergence ratio to the proposed model VTBM is still low and it reached only 0.66 and 0.58 for the specimen VT-1 and VT-2, respectively.

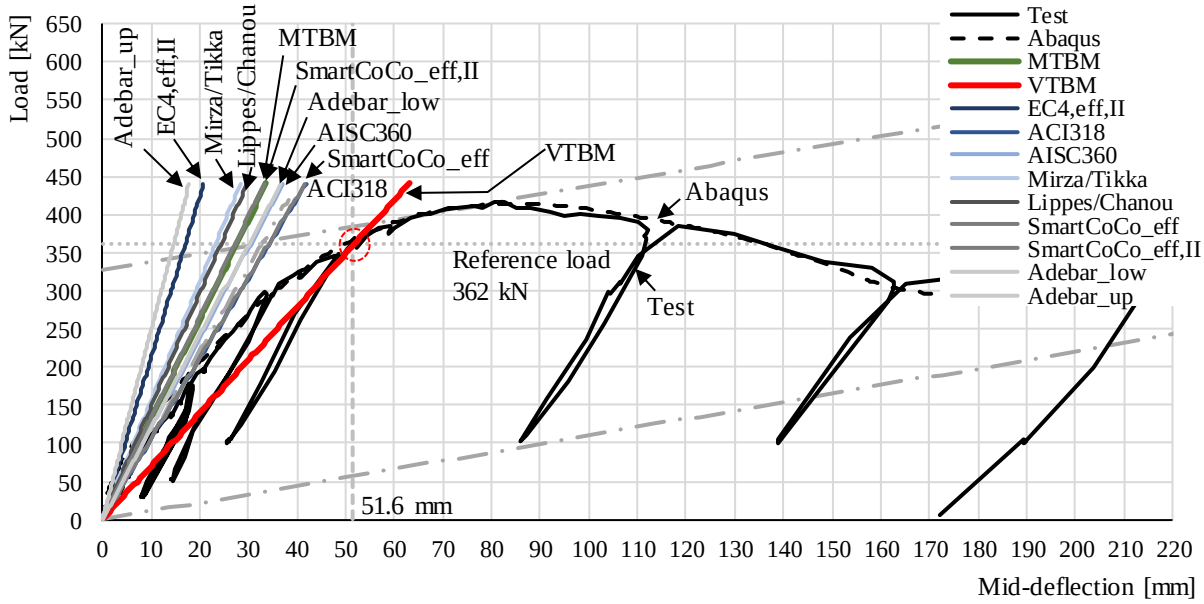


Fig. 6.183. Comparison of the VTBM load-deflection curve with international models for the specimen VT-1.

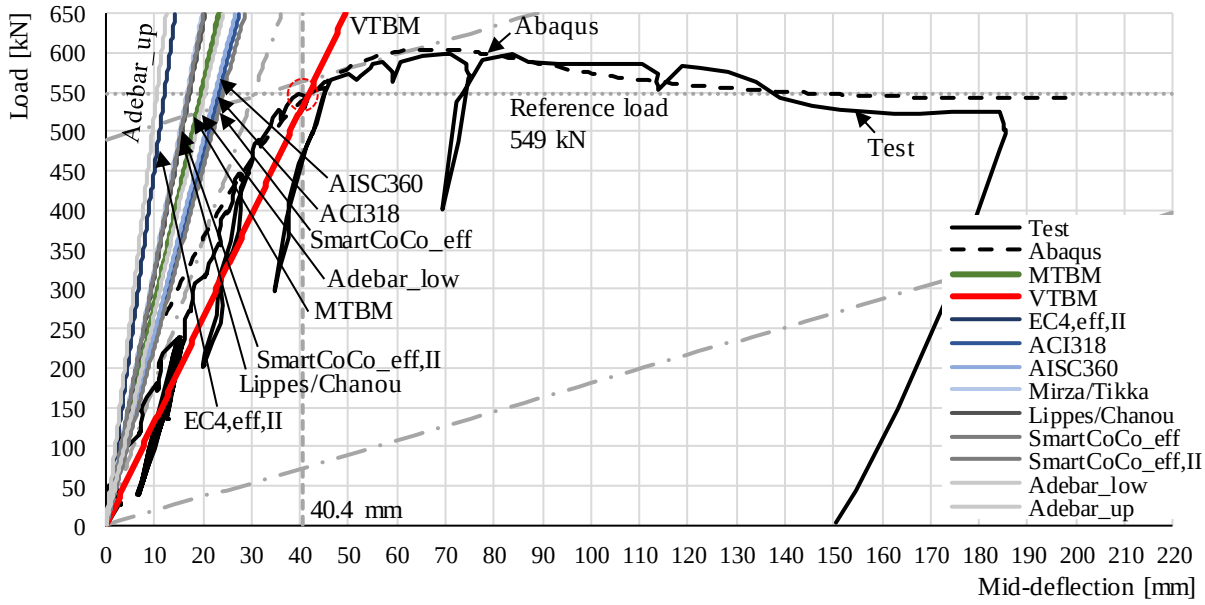


Fig. 6.184. Comparison of the VTBM load-deflection curve with international models for the specimen VT-2.

6.5.6. Derivation of an equation for new effective bending stiffness

According to the performed analysis in Section 6.5.4 and 6.5.5, it can be observed that the effective bending stiffness evaluated purely according to EN 1994-1-1 [58] brings a serious overestimation of the global beam stiffness in the considered steel-concrete composite specimens with two embedded steel profiles. The level of impact can be observed from the results named 'Bernoulli/Timoshenko,eff,II' in Fig. 6.176-6.177 and Table 6.16, which reflects the model considered in the EC4. In order to improve the existing provisions, a modification to the current procedure given in clause 6.7.3.3 and clause 6.7.3.4 of EN 1994-1-1 [58] is proposed based on the developed VTBM model. A new global effective bending stiffness can be evaluated by replacing the considered Timoshenko beam deflection in the VTBM model by the Euler-Bernoulli beam deflection as defined in Eq. 6.190. In the result, after transforming the equation, a new equation for the effective bending stiffness is proposed in Eq. 6.192. Based on the observations taken from the comparison of equivalent beam bending stiffness from the VTBM model and model given in EN 1994-1-1 [58], compare Eq. 6.124 and Eq. 6.125 to Eq. 6.159 and Eq. 6.162 respectively, it can be assumed that both methods are equivalent, as defined in Eq. 6.193. Therefore, in Eq. 6.192, a modification can be introduced by replacing the equivalent beam bending stiffness from the VTBM model by the effective bending stiffness evaluated according to the EN 1994-1-1 [58]. In the result, Eq. 6.192 transform to Eq. 6.194.

$$w_{VTBM} = \frac{PL^3}{48(EI)_{v,gl}} + \frac{PL}{4K_{sv}} = \frac{PL^3}{48(EI)_{eff,VTBM}} \tag{6.190}$$

$$\frac{PL^3}{48}\left(\frac{1}{(EI)_{v,gl}} + \frac{12}{L^2K_{sv}}\right) = \frac{PL^3}{48}\left(\frac{1}{(EI)_{eff,VTBM}}\right) \tag{6.191}$$

$$(EI)_{eff,VTBM} = \frac{L^2(EI)_{v,gl}K_{sv}}{L^2K_{sv} + 12(EI)_{v,gl}} \tag{6.192}$$

$$(EI)_{v,gl} = (EI)_{EC4,eff} \tag{6.193}$$

$$(EI)_{eff,VTBM} = \frac{L^2(EI)_{EC4,eff}K_{sv}}{L^2K_{sv} + 12(EI)_{EC4,eff}} \tag{6.194}$$

It can be observed that a relation between the current effective bending stiffness according to EN 1994-1-1 [58] and the new proposed effective bending stiffness based on the VTBM model can be defined in Eq. 6.195 by introducing the effective reduction factor α_{VTBM}, which correlates values of the effective bending stiffnesses between the two models. In the result, by transforming Eq. 6.196, the effective reduction factor can be defined in Eq. 6.198.

$$\alpha_{VTBM} \cdot (EI)_{EC4,eff} = (EI)_{eff,VTBM} \tag{6.195}$$

$$\alpha_{VTBM} \cdot (EI)_{EC4,eff} = \frac{L^2(EI)_{EC4,eff}K_{sv}}{L^2K_{sv} + 12(EI)_{EC4,eff}} \tag{6.196}$$

$$\alpha_{VTBM} = \frac{L^2 (EI)_{EC4,eff} K_{sv}}{(EI)_{EC4,eff}\left(L^2 K_{sv} + 12(EI)_{EC4,eff}\right)} \tag{6.197}$$

$$\alpha_{VTBM} = \frac{L^2 K_{sv}}{L^2 K_{sv} + 12(EI)_{EC4,eff}} = \frac{1}{1 + \frac{12(EI)_{EC4,eff}}{L^2 K_{sv}}} \tag{6.198}$$

$$\alpha_{VTBM,VT-1} = 0.33 \tag{6.199}$$

$$\alpha_{VTBM,VT-2} = 0.29 \tag{6.200}$$

$$(EI)_{eff,VTBM,VT-1} = 313626676\ [kNcm^2] \tag{6.201}$$

$$(EI)_{eff,VTBM,VT-2} = 591159436\ [kNcm^2] \tag{6.202}$$

The defined effective reduction factor in Eq. 6.198 visualises the reduction impact of the considered VTBM model in comparison to the current design procedure given in EN 1994-1-1 [58]. For the specimen VT-1, the aforementioned reduction factor reached 0.33 by implementing Eq. 6.159 and Eq. 6.154 into Eq. 6.198. For the specimen VT-2, the effective reduction factor α_{VTBM} reached 0.29 by analogous implementing Eq. 162 and Eq. 6.155 into Eq. 6.198. The obtained reduction values were defined in Eq. 6.199 and Eq. 6.200 respectively. Values of the new effective bending stiffnesses based on the VTBM model are evaluated simultaneously according to Eq. 6.194 and Eq. 6.195 and are given in Eq. 6.201 for the specimen VT-1 and in Eq. 6.202 for the specimen VT-2.

6.5.7. Analysis of the Euler critical buckling load

The characteristic property of each flexural column is the Euler's critical buckling load defined below in Eq. 6.203. The aforementioned critical load often defines the decisive load-bearing capacity of a column, especially for slender columns, when subjected to compression.

$$P_{cr} = \frac{\pi^2 (EI)}{(\beta L)^2} \tag{6.203}$$

Where,

(EI) is the bending stiffness of a column,

β is the buckling length factor and

L is the base length of a column.

Based on the investigation shown in Section 6.5.6 and the identified effective reduction factors given in Eq. 6.195-6.200 for the effective bending stiffness in reference to the procedures defined in EN 1994-1-1 [58], it can be clearly observed that the proposed modification linearly affects the critical buckling load. Therefore, the condition given in Eq. 6.204 can be defined based on Eq. 6.195 and transformed into Eq. 6.205. In the result, according to the proposed VTBM model, the bending stiffness present in the Euler's critical buckling load can be replaced by the new effective value defined in Eq. 6.194. Alternatively, the new form of the considered buckling load can be derived from the condition given in

Eq. 6.204-6.205. The resulting shape of the Euler's critical buckling load according to the VTBM model is defined in Eq. 6.206. Considering the geometry of tested specimens, the new effective critical buckling loads according to the VTBM model are given in Eq. 6.209 for the specimen VT-1 and in Eq. 6.210 for the specimen VT-2. For the comparison, the critical buckling load according to the stiffness model given in EN 1994-1-1 [58] is evaluated in Eq. 6.207-6.208 by implementing the bending stiffnesses valuse from Eq. 6.159 and Eq. 6.162 for both specimens respectively.

$$\alpha_{VTBM} \cdot (P_{cr})_{EC4,eff} = (P_{cr})_{eff,VTBM} \tag{6.204}$$

$$\alpha_{VTBM} = \frac{(P_{cr})_{eff,VTBM}}{(P_{cr})_{EC4,eff}} \tag{6.205}$$

$$(P_{cr})_{eff,VTBM} = \frac{\pi^2 \alpha_{VTBM}(EI)_{EC4,eff}}{(\beta L)^2} = \frac{\pi^2 (EI)_{eff,VTBM}}{(\beta L)^2} = \frac{\pi^2 L^2 (EI)_{EC4,eff} K_{sv}}{(\beta L)^2 \left(L^2 K_{sv} + 12(EI)_{EC4,eff}\right)} = \frac{\pi^2 (EI)_{EC4,eff} K_{sv}}{\beta^2 \left(L^2 K_{sv} + 12(EI)_{EC4,eff}\right)} \tag{6.206}$$

$$(P_{cr})_{EC4,eff,VT-1} = 26093.12\ [kN] \tag{6.207}$$

$$(P_{cr})_{EC4,eff,VT-2} = 56034.79\ [kN] \tag{6.208}$$

$$(P_{cr})_{eff,VTBM,VT-1} = 8598.25\ [kN] \quad \rightarrow \quad \alpha_{VTBM} = \frac{(P_{cr})_{eff,VTBM,VT-1}}{(P_{cr})_{EC4,eff,VT-1}} = 0.33 \tag{6.209}$$

$$(P_{cr})_{eff,VTBM,VT-2} = 16206.97\ [kN] \quad \rightarrow \quad \alpha_{VTBM} = \frac{(P_{cr})_{eff,VTBM,VT-2}}{(P_{cr})_{EC4,eff,VT-2}} = 0.29 \tag{6.210}$$

By assuming a certain buckling length factor, for example β=1.0, the relative slenderness of the tested beam/column specimens can be evaluated according to the proposed VTBM model and compared to the values evaluated according to clause 6.7.3.3 (2) of EN 1994-1-1 [58]. Eq. 6.211 gives the definition of the relative slenderness according to aforementioned clause from the design code. According to Eq. 6.212, the characteristic value of plastic resistance to compression can be estimated [58]. The critical buckling load is given in Eq. 6.203. By applying the geometries of tested beam/column specimens from Fig. 6.5, material properties from Table 6.5-6.6 for the steel parts and the characteristic strength of concrete evaluated in Eq. 6.63 for the specimen VT-1 and in Eq. 6.70 for the specimen VT-2, Eq. 6.212 gives the respective values of plastic resistance to compression in Eq. 6.213-6.214 for both specimens. The elastic critical buckling loads are evaluated in Eq. 6.207-6.210. In the result, the relative slenderness for the specimen VT-1 is given in Eq. 6.215-6.216 and for the specimen VT-2 in Eq. 6.217-6.218 for the respective considered model, EC4 or VTBM.

$$\bar{\lambda} = \sqrt{\frac{N_{pl,Rk}}{N_{cr}}} \tag{6.211}$$

$$N_{pl,Rk} = A_a f_{yk} + 0.85 A_c f_{ck} + A_s f_{sy} \tag{6.212}$$

$$N_{pl,Rk,VT-1} = 2 \cdot 34 \cdot 46.2 + 0.85 \cdot 1743 \cdot 3.06 + 14 \cdot 0.503 \cdot 57.2 = 8079\ [kN] \quad (6.213)$$

$$N_{pl,Rk,VT-2} = 2 \cdot 34 \cdot 46.2 + 0.85 \cdot 2247 \cdot 2.78 + 16 \cdot 0.503 \cdot 57.2 = 8906\ [kN] \quad (6.214)$$

$$\bar{\lambda}_{EC4,VT-1} = \sqrt{\frac{8079}{26093.12}} = 0.556 \quad (6.215)$$

$$\bar{\lambda}_{VTBM,VT-1} = \sqrt{\frac{8079}{8598.25}} = 0.969 \quad (6.216)$$

$$\bar{\lambda}_{EC4,VT-2} = \sqrt{\frac{8906}{56034.79}} = 0.399 \quad (6.217)$$

$$\bar{\lambda}_{VTBM,VT-2} = \sqrt{\frac{8906}{16206.97}} = 0.741 \quad (6.218)$$

$$\bar{\lambda}_{VTBM,VT-1} \Big/ \bar{\lambda}_{EC4,VT-1} = 1.74 \quad (6.219)$$

$$\bar{\lambda}_{VTBM,VT-2} \Big/ \bar{\lambda}_{EC4,VT-2} = 1.86 \quad (6.220)$$

From Eq. 6.219-6.220, it can be observed that the change in the slenderness is significant between the considered models. However, the values for relative slenderness obtained from Eq. 6.215-6.218 are small and they do not reached the unity. In clause 6.7.3.1 (1) of EN 1994-1-1 [58], the limit of relative slenderness is set to $\lambda \leq 2.0$ in order to apply the simplified design method. By assuming the buckling curve for the composite cross-sections of the tested specimens as "b", according to Table 6.5 from EN 1994-1-1 [58], the reduction factor for the relevant buckling mode χ can be evaluated according to clause 6.3.1.2 of EN 1993-1-1 [55]. In Eq. 6.221-6.222 and in Eq. 6.223-6.224, the evaluated reduction factors for buckling are given for the specimen VT-1 and VT-2 respectively.

$$\chi_{EC4,VT-1} = 0.858 \quad (6.221)$$

$$\chi_{VTBM,VT-1} = 0.617 \quad (6.222)$$

$$\chi_{EC4,VT-2} = 0.927 \quad (6.223)$$

$$\chi_{VTBM,VT-2} = 0.760 \quad (6.224)$$

$$\chi_{VTBM,VT-1} \Big/ \chi_{EC4,VT-1} = 0.72 \quad (6.225)$$

$$\chi_{VTBM,VT-2} \Big/ \chi_{EC4,VT-2} = 0.82 \quad (6.226)$$

The simplified procedure given in EN 1994-1-1 [58] for the verification of axial resistance adapted to the considered beam/column test specimens, shows that due to the applied VTBM model, the reduction of resistance in compression reached 18-28% as described in Eq. 6.225-6.226. Analogically, the moment magnification factors "k" for the second-order effects will be amplified, however, further analysis requires normal forces in the specimens.

6.6. Summary and conclusions

In Chapter 6, the behaviour of the composite columns in steel and concrete with two embedded steel profiles is investigated. The considered specimens consisted of two HEB120 S355 steel profiles embedded in the concrete block grade C30/37 and dimensions of 315x575x6500 mm for the specimen VT-1 and 315x735x6500 mm for the specimen VT-2. Both specimen had nominally identical geometry, where the clear distance between the embedded steel profiles was varied from 100 mm to 260 mm for the specimen VT-1 and specimen VT-2 respectively. In both analysed specimens, the reinforcement cage was present and arranged according to Fig. 6.10-6.12. The applied shear connection consisted in the novel flat mechanical shear connectors with V-shape variant developed and described in Section 5. The test layout and the considered static system for the evaluation of results consisted of the simple supported beam with the point load imposed at the mid-span. No axial compression force was imposed.

In Section 6.2, the pre-design process is described, where the fibre method with the elastic linear strains distribution was considered. It was identified that the performed calculations and the resultant predicted load-bearing capacities correlate to the experimental results. The relative error of ultimate load reached 8% for the specimen VT-1 and 7% for the specimen VT-2. The comparison was made in Table 6.11. However, the performed pre-design was based on the normative values of the materials properties, where in the tests, the same steel grades and smaller grade of concrete were applied. In the result, the considered material properties in the fibre method for the steel parts were smaller than the properties measured from the tests and simultaneously, the concrete compression strengths from tests reached similar values to the normative values of higher grade. From Fig. 6.105, it can be observed that the theoretically evaluated distribution of strains varies from the experimental values, however, the variation is not significant and the obtained strains from the fibre method can predict the resultant behaviour with good accuracy.

In Section 6.3, the experimental campaign on the beam/column tests specimens with two encased steel profiles is described. The deflection of specimens, rotations of measurement sections, relative slip at the steel-concrete interface, strains in steel were measured and analysed in order to investigate the behaviour and shear transfer in the beam/column specimens. After the tests, the specimens were opened in order to investigate the developed failure pattern, inelastic deformation of steel profiles and level of concrete damage next to the shear connectors. It was identified that the load-bearing capacity of the specimen VT-2 reached 598 kN and it was higher than the load-bearing capacity of the specimen VT-1, which was 417 kN. The peak loads were achieved in both specimens with corresponding deflection level of approximately 80 mm. From the obtained load-deflection curves at the mid-span given in Fig. 6.28 for the specimen VT-1 and in Fig. 6.31 for the specimen VT-2, the stabilised horizontal branches were identified, which refer to the residual plastic load-bearing capacity of specimens and plastic bending capacity of developed plastic hinge in the centre of both specimens. The analysis of measured stiffnesses

given in Fig. 6.107 showed that after the cycling part of the test, the stiffness of both specimens increased and it was reducing with the progressing deformation of specimens. Finally, the unload stiffness had a similar value to the initial stiffness recorded in the first phase of the tests. Moreover, it could be observed that in both specimens the shear deformation mode of deflection was significantly contributing to the overall deflection shape, especially in the specimen VT-2 as it shown in Fig. 6.108-6.109. It was identified that the shear deformation of specimens exist but due to the stiffness of the concrete, it is not possible to be directly observed from the visual examination of tests. From the recorded strains in the longitudinal direction, the recorded distribution of strains in both specimens showed a linear trend due to bending with neutral axis localised in the web of the upper embedded steel profile. However, at the load level close to the peak load, the disturbances in the linearity were observed. The load flux inside the specimens was identified based on the recoded strains in the stirrups and it was observed that the shear force taken by the steel profiles was significant as shown in Table 6.12 and Fig. 6.121-6.124. The recorded end-slip in both specimens was small and its maximum value reached 1.4 mm for the specimen VT-1 and 1 mm for the specimen VT-2 at the peak load. It was observed that the applied shear connection successfully transferred the entire developed tensile force from the embedded steel profiles to the concrete and the most part of relative slip developed after yielding of steel profiles, see Fig. 6.127-6.128. The identified shear deformation of specimens resulted in the characteristic shear diagonal cracking zones on the walls of specimens close to the supports, minor horizontal cracks in concrete on the level of embedded steel profiles and characteristic for the Vierendeel action vertical cracks above the support, see Fig. 6.72, 6.77-6.78, 6.88-89, 6.94-6.95. The global failure mode of both specimens was identified as the failure due to the compression in bending, where clearly formulated damage zones in compression and tension were observed. After opening of the specimens, it was observed that the steel profiles beyond the zone of the developed plastic hinge remained straight and the contact interface was undamaged. Moreover, investigation of the concrete next to the shear connector indicated the shear damage of concrete due to the described model in Section 5.6.5. The observed damage justifies the small amount of the developed end-slip. The experimentally observed and evaluated shear deformation and transfer of shear forces inside the specimens, together with the identified characteristic vertical cracks in the zone close to the support, allowed for the identification of a strong analogy to the Vierendeel truss system. However, the global system in both specimens behaved as a Timoshenko beam-like element.

In Section 6.4, the numerical simulations of previously tested beam/column specimens are described. The described simulations were conducted by using Abaqus FE code [174] and dynamic explicit solver with quasi-static simulation character. The obtained results from the numerical simulations supported the test observations and the characteristic yielding zones of materials were identified at different load levels. Moreover, by a precise simulation of materials, the obtained damage pattern in FE models extend the information about the failure pattern obtained from the tests. Due to a good calibration of models with the test results allowed for the reliable extended analysis of specimens behaviours and stress flows.

Therefore, a high concentration of the positive maximum principal stresses was identified in the zones above the support in both specimens as shown in Fig. 6.149 and especially in Fig. 6.159. Taken observations from the numerical simulations allowed to investigate the development of damage in concrete and the plastification of steel profiles in a step-by-step manner. Moreover, the identification of the Vierendeel action in the specimens was possible. The clear failure pattern and deformation shape due to the Viereneel action were observed in the adjusted model as shown in Fig. 6.160.

Based on the observations taken from Section 6.3 and Section 6.4, it was concluded that the investigated specimens behaved like the Timoshenko beam and Vierendeel truss in the same time. However, it was specified that the global behaviour of specimens and the deflection shape were govern by the Timoshenko beam theory, where the distribution of forces inside the specimens and the structural response reflected the Vierendeel truss. Accordingly, it was concluded that the investigated specimens with two embedded steel profiles behaved like the Timoshenko beam with embedded Vierendeel truss system describing the shear stiffness and load flux. The taken conclusion allowed for the derivation of the innovative hybrid analytical model VTBM (Vierendeel Truss Beam Model), where the global behaviour is described by the Timoshenko beam theory including shear effects but the shear stiffness of the beam is evaluated based on the distribution of forces inside the Vierendeel truss. The taken investigation is described in Section 6.5. Good correlation of the proposed analytical model to the performed tests was shown. For the comparison, other analytical models were also considered, see Table 6.16 and Fig. 6.176-6.177 and Fig. 6.183-6.184. The derived VTBM model is coherent with the method given in EN 1994-1-1 [58] and a new effective bending stiffness based on the provisions from the aforementioned design code was proposed. The reduction in the effective bending stiffness due to applied VTBM model reached 67% for the specimen VT-1 and 71% for the specimen VT-2 in comparison to the original values. In further investigation, it was shown that the modified effective bending stiffness affects the Euler's critical buckling load and all derivatives, like buckling resistance and moment amplification factors for the second-order analysis.

The given results, observations and conclusions are fully based on the considered beam/column specimens. Based on the obtained small end-slip values from the tests, the full shear connection was considered in the derived VTBM model and the influence of partial shear connection was omitted. A wider application of the given VTBM model requires calibration in additional experimental and numerical campaigns. Moreover, in the analysed specimens, no axial force was present and the considered static system reflected a beam.

Based on the obtained results from the beam/column tests, the application of the developed novel flat mechanical shear connectors described in Section 5.4 has been proven in the beam-type tests.

7. Thesis Summary and Overall Conclusions

In the first part of dissertation, the current level of knowledge regarding the structural behaviour, design and current practice for heavy steel-concrete composite columns with multiple encased steel profiles was defined. In addition, information about the steel-concrete composite theory, shear connection, general beam and truss theories, as well as design provisions of composite columns in the light of international standards, fulfilled the theoretical background of the conducted investigation. A good understanding of the current state-of-the-art allowed for a precise identification of gaps in the knowledge and potential aspects in the current practice that require improvement. In the result, novel solutions for the mechanical shear connectors dedicated to fully encased composite columns and innovative analytical model for the analysis of structural behaviour of heavy columns with multiple encased steel profiles were developed and characterised. The aforementioned aspects bring a big level of novelty into the topics of shear transfer and structural perception of composite column members with more than one embedded steel profile, where the shear connection aspect is dealing with the local shear transfer phenomenon and the structural behaviour is directly related to the global shear transfer phenomenon.

In Chapter 5, the investigation on the local shear transfer is described, where the development and characterisation process of a novel type of flat mechanical shear connectors are included. An important aspect during the characterisation process was analysis of plain steel-concrete bond, which contributes significantly to the load-bearing capacity and stiffness of shear connection at the steel-concrete interface in fully encased column push-out tests, even for the greased steel profiles. A wide literature review, conducted independent tests and numerical simulations allowed concluding a comprehensive database of bond strength, where main affecting criteria were discussed. The developed concept of flat mechanical shear connectors consisted of three variants of reinforcement bars welded parallel to the flanges of steel profile under transversal, longitudinal and V-shaped orientations. An integral part of the shear connection with the usage of proposed novel type of flat shear connectors is the reinforcement cage, which surrounds the embedded steel profile. The developed connectors were examined experimentally and numerically in order to investigate the internal load-flux, failure pattern and to derive a concept of analytical model for the prediction of their resistances. The application of novel shear connectors in a specimen subjected to major bending was verified by applying the V-shaped connector in the big-scale beam/column specimens, described in Chapter 6.

The investigations taken on the global shear transfer and the structural behaviour of composite columns with multiple encased steel profiles are described in Chapter 6. Series of laboratory tests on the big-scale specimens and series of numerical simulations were conducted in order to analyse the load distribution between each structural element of cross-section, to analyse the shear deformation and to derive an analytical model for the effective stiffness comprising both, bending and shear effects.

Beforehand, the pre-design of test specimens was made. The pre-design method was based on the fibre method, where the linear continuous strain distribution was assumed. The predicted load-bearing capacities correlated to the test results. The performed tests consisted of two specimens with two embedded steel profiles each. Both test specimens had nominally identical geometry and only the span between the embedded steel profiles varied. In the specimen with smaller distance between the embedded steel profiles, the deflection shape followed the Euler-Bernoulli beam deflection shape but the obtained values were much bigger than the theoretical model predicts. In the specimen with bigger distance between the embedded steel profiles, the deflection shape correlated to the Timoshenko beam deflection shape, where the effects of shear are considered in the shear deflection mode. From both tested specimens, the symptoms of shear deformation, the activation level of steel profiles in the transfer of shear forces and finally the need for the improvement of the procedures for the evaluation of effective stiffness were identified. The proposed innovative analytical model for the description of the structural behaviour of column with two encased steel profiles consisted of the Vierendeel truss model embedded into the Timoshenko beam model for the description of equivalent beam shear stiffness. The proposed model is limited only to the examined test specimen geometries and test conditions. The applied Vierendeel truss model reflects well the identified experimentally and numerically shear deformation developed in both specimens. Furthermore, the developed hybrid analytical model was compared and related to the model included in the EN 1994-1-1 [58] for the evaluation of effective stiffness of a composite column. In the result, a new reduction factor for the model included in the EN 1994-1-1 [58] has been proposed and a new equivalent effective bending stiffness applicable to the structural model of Euler-Bernoulli beam has been derived, where the reduction effects of shear deformations are embedded. Like this, the coherence between the current design code for composite structures and the proposed innovative analytical model has been obtained.

Based on the conducted research on the local and global shear transfer in heavy steel-concrete composite columns with multiple encased steel profiles, a list of general conclusions is given below. The detailed summary and conclusions for each considered aspect separately can be found in Section 5.7 and Section 6.6 for local and global shear transfers respectively.

1) A gap in the current level of knowledge in the topic of shear transfer in heavy steel-concrete composite columns with multiple encased steel profiles has been identified and addressed.
2) In the conducted research, both aspects of shear transfer (i) local and (ii) global were analysed analytically, laboratory tested and simulated numerically. As the outcome, a novel type of flat mechanical shear connectors and innovative analytical model for the structural behaviour and member stiffness have been delivered in the response for the local and global shear transfers respectively.
3) Steel-concrete bond was analysed in parallel to the characterisation process of a novel type of flat mechanical shear connectors. The taken investigations were based on the available

international literature and conducted independent tests on small-scale cube push-out tests and fully encased column push-out tests. The significance of plain steel-concrete bond contribution in the shear connection resistance has been identified, especially in the case of fully encased push-out test specimens. Therefore, its performance has to be considered, when shear connectors are investigated in this kind of tests. It has been shown that the performance of plain steel-concrete bond consists of three force-transferring phenomena: (1) the chemical adhesion, (2) the Coulomb friction and (3) the surface roughness friction, where they are active in the different phases of bond behaviour and they are overlapping close to the peak load. It has been found that the strength of bonded connection is mainly dependent on (i) the steel surface treatment, (ii) the size of concrete encasement, (iii) the concrete confinement, (iv) geometry of embedded steel profiles, (v) boundary conditions (development of lateral forces at the interface) and (vi) time. The summary of considered data is given in Table B.3 and statistically evaluated in Fig. 5.14. Impact of different steel surface treatment conditions on the bond strength is shown in Fig. 5.15.

4) In order to minimise the impact of plain steel-concrete bond on the shear connection resistance, two different bond-reducing products were examined and compared to the reference specimens without surface treatment. The considered products were high-performance demoulding oil and Teflon spray, where their identified ultimate bond strengths were 0.9 MPa and 1.47 MPa respectively with comparison to the reference strength value of 2.65 MPa obtained from the reference tests. It has been identified that the Teflon spray removed well the Coulomb friction forces but, on the other hand, the chemical adhesion strength was greatly amplified. In the result, the better performing bond-reducing product was the demoulding oil, which had a corresponding load-slip behaviour to the specimens with untreated steel surface but the resultant respective loads were much smaller.
5) The conducted experimental investigation on steel-concrete bond allowed for the development and calibration of a numerical model of bond, which considers all the force-transferring phenomena and reflect well the experimental behaviour.
6) The developed novel type of flat mechanical shear connectors in the form of welded reinforcement bars to the flanges of steel profiles were tested in fully encased column push-out tests. The obtained mean ultimate load levels from tests were (i) 825 kN for the transversal variant, (ii) 809 kN for the V-shaped variant and (iii) 435 kN for the longitudinal variant. The given values consist of two shear connectors, one on each side of a steel profile, and plain steel-concrete bond, which contribution was tested in reference tests and the ultimate load of 208 kN was recorded.
7) From the obtained load-slip curves, the performance of longitudinal variant showed the poorest load-bearing capacity but the highest ductility. The transversal variant of connector indicated the highest load-bearing capacity but the failure progressed in the most brittle

manner. The V-shaped variant of connector brings the best compromise between the load-bearing capacity and connection ductility and it was selected as the best performing variant. In addition, the V-shaped connector reached the highest stiffness of shear connection, where the stiffness of the longitudinal variant was slightly smaller. The stiffness of transversal variant of connector showed the smallest value. The resultant load-slip curves are shown in Fig. 5.28 and summarised in Table 5.12.

8) For each type of proposed shear connector variants, a specific failure pattern has been identified and described in Section 5.4.5. The failure of longitudinal variant shear connector is related to the rebar pull-out failure analogy, where the failure of transversal and V-shaped variants are related to the development of inclined internal failure planes in the concrete encasement. The failure of concrete is identified as the failure due to the maximum compression stresses or due to the maximal shear stresses. Additional failure pattern for the V-shaped variant of connector in the vertical direction between the arms of connector is identified. The orientation of concrete compression strut under the connector is identified under 32° in both, transversal and V-shaped, variants.
9) The developed novel shear connectors has been verified in beam tests performed for the analysis of structural behaviour in columns with multiple encased steel profilesThe observations from column push-out tests were reproduced with high accuracy in the numerical simulations performed in the FE code Abaqus [174] and are described in Section 5.5. The numerical models allow for the investigation of failure sequence developed in the concrete and identification of the load-flux. The orientation of the concrete compression strut has been confirmed under 32° from the test observations.
10) Based on the experimental and numerical observations, an analytical model for the resistance of the developed novel shear connectors has been derived, which considers three failure mechanisms: (i) the failure of weld, (ii) the failure of connector material and (iii) the failure of concrete encasement. The model for the longitudinal variant of connector considers only one failure mechanism, which defines the connector-concrete bond strength. The detailed description of developed resistance models are given in Section 5.6. The developed model is consistent between each variant of flat shear connector and the equations given for the resistance of V-shaped connector are the general shape of the model, where by applying specific input values, the equations for the resistances of transversal and longitudinal variants can be obtained. To correlate with experimental results, calibration factors were introduced, which amplify the strength of concrete material in compression and shear. The summary of the developed models is given in Fig. 5.105 and Table 5.19-5.20.
11) The global shear transfer and the structural behaviour of steel-concrete composite columns with multiple encased steel profiles have been analysed based on the beam/column specimens with two embedded steel profiles. The test campaign consisted of two specimens,

each with nominally identical geometry and only varied distance between the embedded steel profiles – 100 mm and 260 mm. The conducted test were three-point bending tests without imposed axial forces. The specimen with bigger distance between steel profiles reached higher load-bearing capacity (598 kN) in comparison to the specimen with smaller distance (417 kN). Both specimens exhibited failure at the corresponding level of mid-deflection at approximately 80 mm. A high level of ductility after the failure was observed in both specimens. The corresponding load-deformation curves are shown in Fig. 6.28 and Fig. 6.31.

12) The longitudinal strains in the measurement sections indicated the linear distribution. However, at loads close to the peak load, the linearity was disturbed. The aforementioned disturbance was more significant in the specimen with bigger distance between the embedded steel profiles. The strains distribution diagrams are shown in Fig. 6.42, Fig. 6.47 and Fig. 6.105. The obtained resultant internal forces correlate to the predesign based on the fibre method and linear strain distribution.
13) The deflection shape of two specimens varies between each other as shown in Fig. 6.108-6.109. In the specimen with smaller distance, the resultant deflection shape correlated more to the Euler-Bernoulli beam deflection shape, where in the specimen with bigger distance between steel profiles, the deflection shape reflected more the Timoshenko beam deflection shape. A bigger distance between the embedded steel profiles resulted in a more significant contribution of shear deformation to the deflection shape.
14) The activation of embedded steel profiles in the transfer of shear forces in the beam/column specimens with two embedded steel profiles has been analysed based on strains recorded in stirrups. It was observed that in both specimens, steel profiles took nearly over the entire shear force in the first phase of tests and in the last phase, they still contributed significantly. The steel profiles took 23-60% and 64-81% of the total shear forces at the load close to the peak load for the specimen with smaller and bigger distance between steel profiles, respectively. The activation of steel profiles is shown in Fig. 6.121-6.124.
15) The shear deformation of beam/column specimens with two embedded steel profiles and analogous behaviour to Vierendeel truss system have been identified based on the recorded strains and observed cracking pattern, especially in vertical cracks in the top part of the specimen in the support zones. The characteristic vertical cracks are shown in Fig. 6.88 and Fig. 6.103. These cracks correlate to the tension zones in the Vierendeel truss system.
16) The developed numerical models simulated the performed tests and allowed for the investigation of load-flux and the distribution of principal stresses in both specimens. The tensile principal stresses were localised in the top concrete part in the support zones, which correlates well to the vertical cracks revealed after the opening of test specimens.
17) An artificially modified numerical model for the beam/column specimen with bigger distance between two embedded steel profiles allowed for the clear revealing of the

Vierendeel-type behaviour in the specimen. The modified parameters changed the model not significantly and they are given in Fig. 6.160 together with the deformed shape.

18) Based on the taken observations from the beam/column tests and simulations with two embedded steel profiles, clear analogies to the Vierendeel truss and Timoshenko beam behaviours were concluded. The taken observations are a base for the derivation of an analytical model for the description of effective stiffness for the beam/column specimens.
19) The developed analytical model for the effective stiffness of composite member with two encased steel profiles is based on the Timoshenko beam deflection function, where the typical shear stiffness $A_v G$ is replaced by the equivalent beam shear stiffness K_{sv} evaluated based on the embedded Vierendeel truss model. In the result, an innovative hybrid Vierendeel truss beam model (VTBM) has been obtained.
20) The proposed VTBM model requires the discretisation of steel-concrete composite member into the Vierendeel truss members, where the chords are reflected by the composite area including embedded steel profiles and posts are reflected by the pure concrete sections. Double-symmetrical sections of chords and posts are assumed and the spacing between chords is equal to the distance between axes of embedded steel profiles. The span of posts is set approximately equal to the span of chords and the odd number of posts is required.
21) The innovative model for the effective stiffness of composite member with two encased steel profiles is related to the model given in EN 1994-1-1 [58] and in the result, a new equation for the effective flexural stiffness is proposed, which is directly applicable to the existing design provisions. The application range is limited to the tested specimens.
22) The VTBM model has been compared to the results obtained from tests, simulations and international models for the effective stiffness of composite columns. The comparison diagrams are shown in Fig. 6.176-6.177 and Fig. 6.183-6.184. The VTBM model correlates to the test results. It has been shown that available models from the literature overestimates the stiffness value. The closest correlation to the test results gives the models of ACI318 [2] and SmartoCoCo project [175], where the convergence ratio is 0.66 and 0.58 for the smaller and bigger specimen, respectively. The convergence ratio to the model given in EN 1994-1-1 [58] reaches values of 0.33 and 0.29, respectively.
23) The Euler's critical buckling load, the axial buckling resistance and the moment magnification factors are affected by the modified value of stiffness, see Section 6.5.7.
24) The derived analytical models for each shear transfer aspect have been proposed and calibrated according to the conducted tests. In the result, the applicability of the derived analytical models is limited to the specimens of geometries and test layouts considered in the conducted experiments. The validity of given models to the specimens with different geometries requires further investigations.

The summary card of the analysed local and global shear transfers is presented in Fig. 7.1 below.

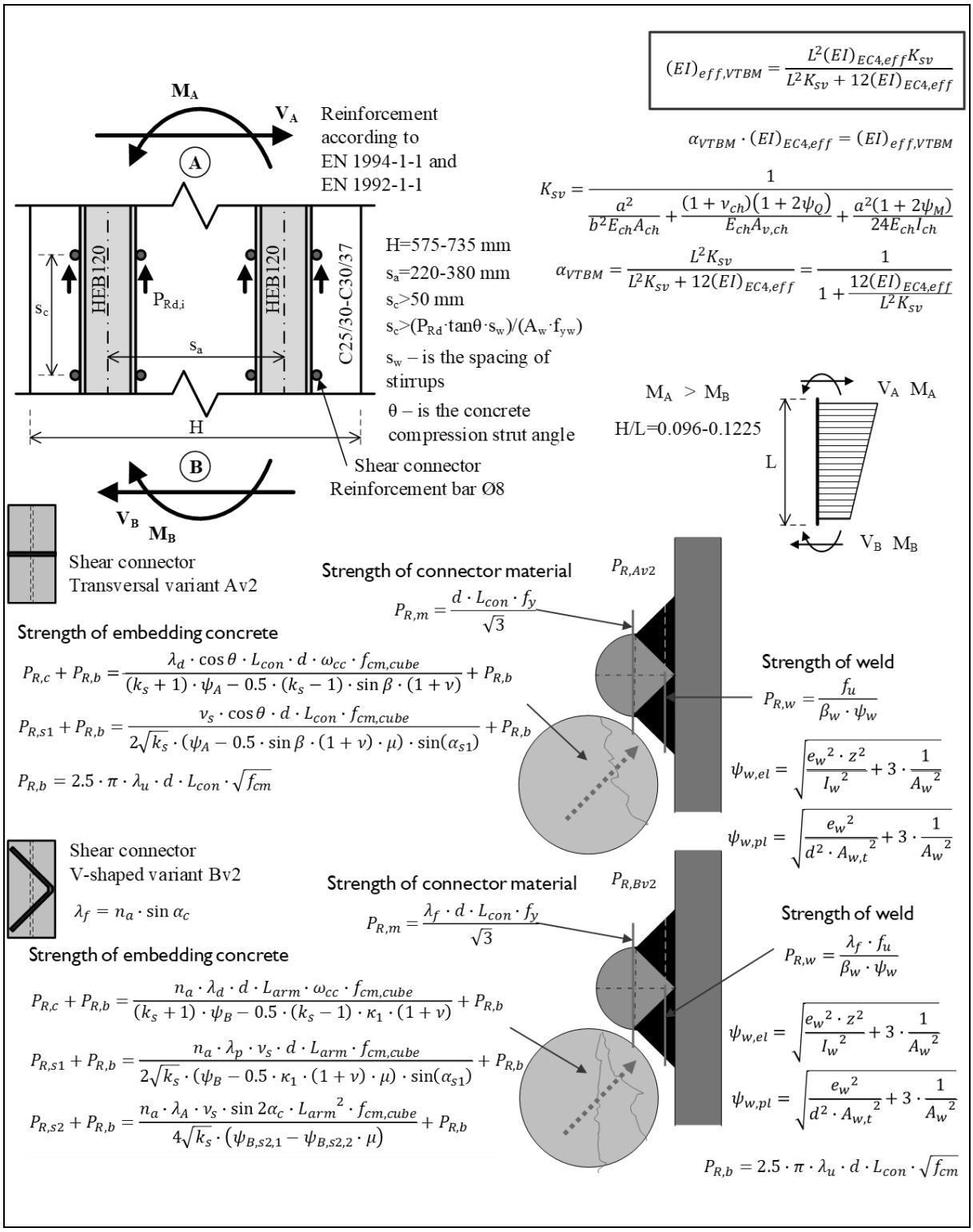


Fig. 7.1. Summary card of the analysed aspects of local and global shear transfer in heavy steel-concrete composite columns with multiple encased steel profiles.

8. Outlook

In the conducted research, the shear transfer aspect in heavy steel-concrete composite columns with multiple encased steel profiles has been analysed, where the novel type of flat mechanical shear connectors and innovative structural model for the evaluation of effective bending stiffness have been developed. The derived analytical models are concepts, which are fully based on the identified theoretical background, conducted tests and numerical simulations. In the result, the application of given innovations is limited only to the specimens with geometries and conditions from the performed tests. The extrapolation of identified behaviours to the different specimens requires further investigations, calibration and finally development of general models, which will have a wider scope of application. Therefore, a need for extensive parametric experimental and numerical studies is clear.

Based on the work done in the background of proposed analytical models described in Section 5.6 and Section 6.5, an outlook for further research in the domain of shear transfer in heavy steel-concrete composite columns with multiple encased steel profiles is drafted and described below in respective paragraphs for local and global aspects. The schematic representation of an outlook for the further required tests is shown in Fig. 8.1 for the novel flat shear connectors and in Fig. 8.2 for the effective flexural stiffness of steel-concrete composite columns with multiple encased steel profiles.

Local shear transfer – novel type of flat mechanical shear connectors

(1) Further investigations require experimental, numerical and analytical campaigns for the parametric studies and verification of identified failure modes.

(2) The calibration factors present in the proposed analytical model were based on the test results, where a correlation to the ratio of confined-to-unconfined concrete strength has been recognised. The proposed analytical model considers the plane strain state of problem, where the three-dimensional behaviour of concrete is omitted. The concrete confinement in the third direction requires consideration. A proof of aforementioned relations is needed.

(3) Based on the increased test database, the statistical evaluation of applied calibration factors and obtained resistances, as well as the application of safety concept are needed.

(4) The strut-and-tie model given for the V-shaped variant of flat shear connector considers only the local part, where the distribution of forces between each arm of connector was assumed as equal according to test observations. The proposed truss model should be complemented to the global equilibrium case, where reactions are related with imposed load.

(5) It has been shown that the tensile stresses occur in the direction of maximal principal stresses. The developed tensile stresses are verified against the tensile strength of concrete. A further investigation is needed in order to identify if the possible tensile maximal stresses are defining the connector resistance limit or only the concrete crack state. Moreover, the verification of connector performance after the crack opening is needed.

(6) It has been shown that boundary conditions and geometry of applied recess under the steel profile affects the overall performance of shear connection and internal strut-and-tie model. An investigation on the varied boundary conditions and resultant internal truss models is of great importance.

(7) An influence of long-term effects, like creep and shrinkage of concrete, on the performance of the flat shear connectors have to be analysed. In addition, the fatigue strength of flat shear connectors is needed to be assessed and verified.

(8) The performed push-out tests and numerical simulations consisted of strictly defined specimen and connector geometries, as well as material properties. A sensivity study on the following parameters in further investigations is crucial:

- number, diameter and spacing of the applied flat shear connectors,
- material of applied flat shear connectors, including smooth steel bars,
- material grades, including tests with high-strength concrete,
- size of the embedded steel profiles, including heavy jumbo HD profiles,
- thickness of the concrete encasement,
- ratio and maximum spacing of shear reinforcement,
- applied welds.

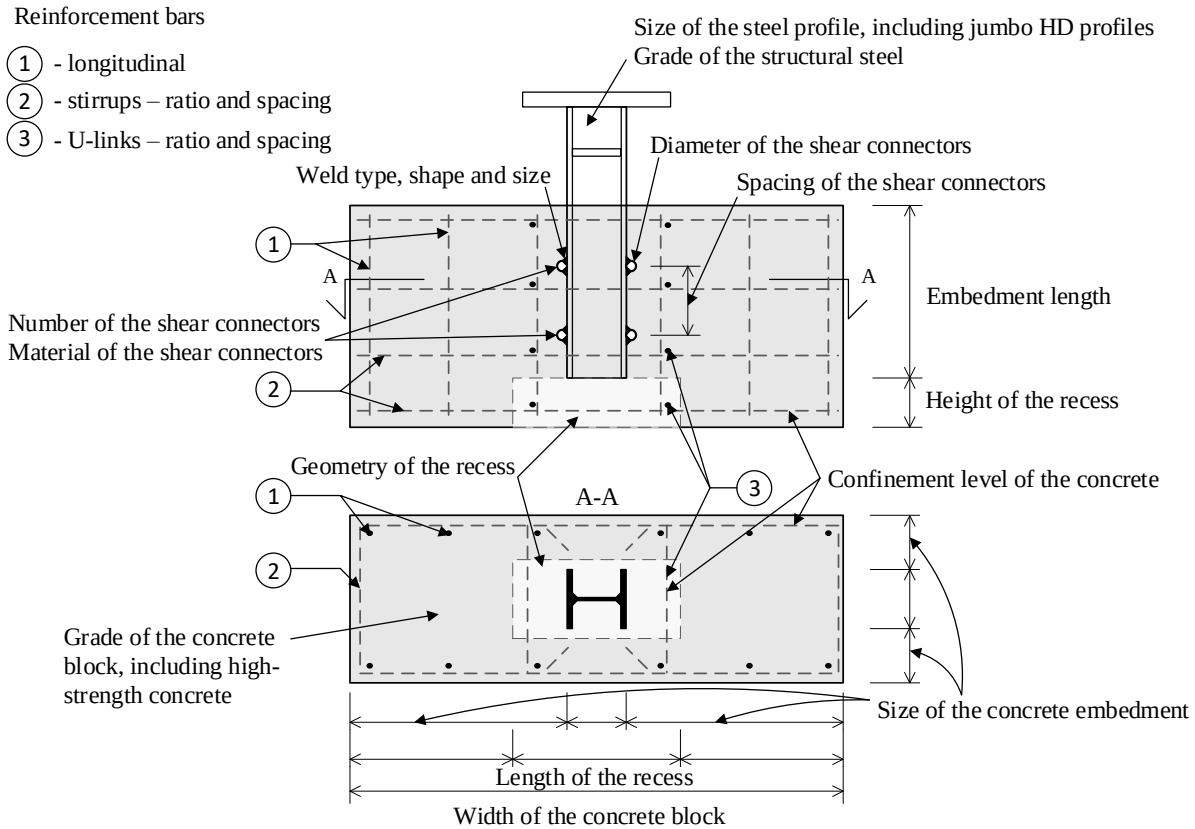


Fig. 8.1. Outlook for further investigations on the local shear transfer aspect in heavy steel-concrete composite columns with multiple encased steel profiles – novel flat mechanical shear connectors.

Global shear transfer – innovative Vierendeel truss beam model (VTBM) for effective stiffness

(1) Further investigations require experimental, numerical and analytical campaigns for the parametric studies and development of database for the structural response of composite columns with multiple encased steel profiles.

(2) Examination of more specimens with two encased steel profiles and varied geometries would allow developing a general model for the discretisation of Vierendeel truss system in a composite member. Moreover, bigger amount of tests and numerical simulations would allow for the verification of proposed model VTBM in wider range of geometries.

(3) Nominally identical tests to the performed beam/column tests but with bending according to the weak axis would be of interest in order to create the background data for the behaviour of columns with, for example, four embedded steel profiles in a rectangle pattern.

(4) The variation of number and arrangement of embedded steel profiles would allow for the extension of the proposed model VTBM to more complex geometries.

(5) The proposed VTBM model is assuming full shear connection at the steel-concrete interface. The extrapolation to the partial shear connection case is required.

(6) In the proposed VTBM model, the stiffness reduction factors followed recommendations given in EN 1994-1-1 [58] for the second-order analysis and they were applied to the moduli of elasticity of concrete and steel parts. The verification of applied factors is required.

(7) The conducted beam/column tests were the three-point bending tests and the imposed axial load was not present. A strong need is to perform tests with specimens subjected simultaneously to axial compression/tension forces, transversal shear and bending.

(8) The conducted beam/column tests were supported as a beam-like structure with hinge-sliding supports. Tests with column-like support system are required.

(9) Impact of the long-term effects, like creep and shrinkage of concrete, should be verified.

(10) Investigation on the weighting factors for the deflection in VTBM model is of interest.

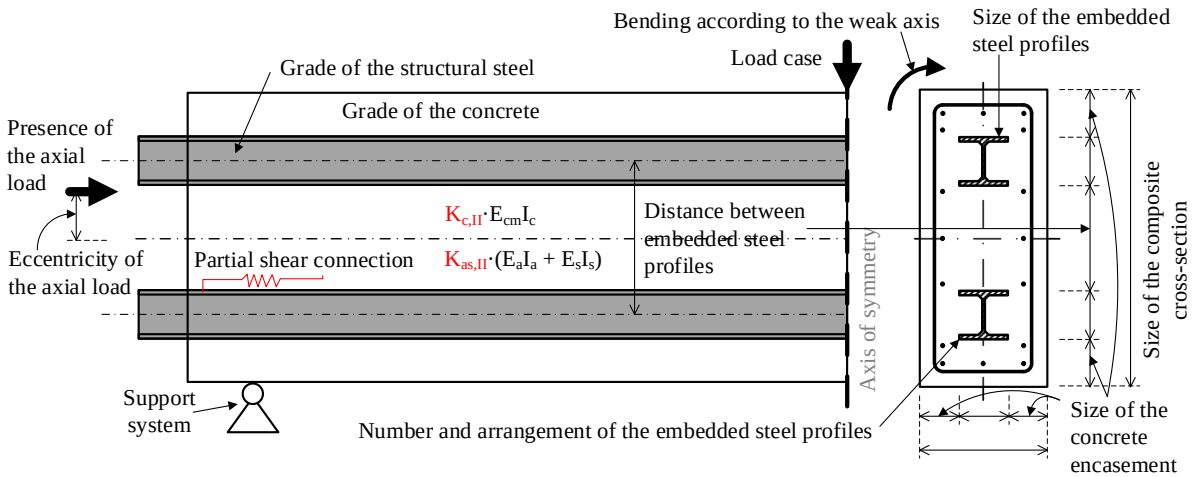


Fig. 8.2. Outlook for further investigations on the global shear transfer aspect in heavy steel-concrete composite columns with multiple encased steel profiles – innovative structural model VTBM for stiffness evaluation.

Acknowledgements

This thesis was written as the final deliverable of the MultiCoSteel research project, which was conducted at the University of Luxembourg and running in close collaboration with the industrial project partner ArcelorMittal Global R&D – Construction & Infrastructure Applications Department in Luxembourg. The aforementioned research project was funded and supported by the Luxembourgish National Research Fund within the scheme of the FNR AFR-PPP PhD grant (Call 2016-1), project reference 11283614.

The steel profiles used in the experimental campaign described in this thesis were granted and delivered by the project partner ArcelorMittal Belval & Differdnage S.A.

The high performance demoulding oil WETCAST FormFluid HP applied in the experimental campaign was granted and delivered by the official producer, company HEBAU GmbH.

Numerical simulations presented in the thesis were carried out using the HPC facilities of the University of Luxembourg, see http://hpc.uni.lu.

References

[1] Aboobucker, M.A.M.; Wang, T.Y.; Liew, J.Y.R.: An experimental investigation on shear bond strength between steel and fresh cast concrete using epoxy, Technical Paper, The IES Journal Part A: Civil & Structural Engineering, Taylor & Francis, Vol. 2, No. 2, 107-115, 2009.

[2] ACI 318-14, Building Code Requirements for Structural Concrete, with commentary ACI 318R-14, An ACI Standard and Report, ACI Committee 318, American Concrete Institute ACI, 2014.

[3] ACI 408R-03, Bond and Development of Straight Reinforcing Bars in Tension, ACI Committee 408 Report, American Concrete Institute ACI, 2003.

[4] Adebar, P.; Ibrahim, A.M.M.; Bryson, M.: Test of High-Rise Core Wall: Effective Stiffness for Seismic Analysis, ACI Structural Journal, American Concrete Institute ACI, Vol. 104, No. 5, Title No. 104-S52, September-October 2007.

[5] Ahn, J.-H.; Lee, C.-G.; Won, J.-H.; Kim, S.-H.: Shear resistance of the perfobond-rib shear connector depending on concrete strength and rib arrangement, Journal of Constructional Steel Research, Elsevier, 66, 1295-1307, 2010.

[6] Al-Kodmany, K.: The Logic of Vertical Density: Tall Buildings in the 21st Century City, International Journal of High-Rise Buildings, CTBUH Korea, Vol. 1, No. 2, 131-148, 2012.

[7] Alves, A.R.; Valente, I.B.; Vieira, W.B.; Veríssimo, G.S.: Prospective study on the behaviour of composite beams with an indented shear connector, Journal of Constructional Steel Research, Elsevier, 148, 508-524, 2018.

[8] ANSI/AISC 360-16, Specification for Structural Steel Buildings, An American National Standard, American Institute of Steel Construction AISC, USA, 2016.

[9] Anwaar, M.O.: Non-Linear Analysis of Composite Columns, Design methods according to (EN 1994-1-1) and Chinese code of design for composite column (JGJ-138:2016), Master's Thesis, University of Luxembourg, Luxembourg, November 2017.

[10] AS 4100-1998, Steel structures, Australian Standard, SAI Global Ltd., Standards Australia Ltd., 1998. ISBN 0-7337-1981-3.

[11] AVEC BNT, Analyse und Vergleich Europäischer und Chinesischer Bautechnischer Normen der Tragweksplanung, Unter besonderer Beachtung der Stahlbeton- und Stahlverbundbaunormen, Erasums + strategic partnership, European Union, University of Luxembourg, 2018. http://www.avec-bnt.de/.

[12] Bergmann, R.: Traglastberechnung von Verbundstützen, Technical Report, Mitteilung Nr. 81-2, Institut für Konstruktiven Ingenieurbau Ruhr-Universität Bochum, 1981.

[13] Bergmann, R.; Matsui, C.; Meinsma, C.; Dutta, D.: CIDECT 5, Design guide for concrete filled hollow section columns under static and seismic loading, Verlag TÜV Rheinland, 1995. ISBN 3-8249-0298-2.

[14] Berthet, J.F.; Yurtdas, I.; Delmas, Y.; Li, A.: Evaluation of the adhesion resistance between steel and concrete by push out test, International Journal of Adhesion & Adhesives, Elsevier, 31, 75-83, 2011.

[15] Bigaj, A.J.: Structural Dependence of Rotation Capacity of Plastic Hinges in RC Beams and Slabs, PhD Thesis, Delft University of Technology, The Netherlands, 1999. ISBN 90-407-1926-8.

[16] Bogdan, T.; Chrzanowski, M.: Mega columns with several reinforced steel profiles – experimental and numerical investigations, Proc. of 12th International Conference on Advances in Steel-Concrete Composite Structures (ASCCS2018), Universitat Politècnica de València, Valencia, Spain, June 27-29, 2018. Doi: http://dx.doi.org/10.4995/ASCCS2018.2018.6944.

[17] Bogdan, T.; Degée, H.; Plumier, A.; Campian, C.: A simple computational tool for the verification of concrete walls reinforced by embedded steel profiles, Proc. of 15th World Conference and Earthquake Engineering (15 WCEE), Lisbon, Portugal, September 2012.

[18] Bogdan, T.; Gerardy, J.-C.; Davies, D.W.; Popa, N.: Performance and capacity of composite "mega columns" with encased hot rolled steel sections, Proc. of Eurosteel 2017, September 13-15, Copenhagen, Denmark, CE/papers, Ernst&Sohn, Vol. 1, No. 2-3, 2017. https://doi.org/10.1002/cepa.96.

[19] Bogdan, T.; Plumier, A.; Degée, H.: A proposal for the design of concrete sections reinforced by multiple encased rolled steel sections, Proc. of Eurosteel 2014, September 10-12, Naples, Italy, ECCS European Convention for Constructional Steelwork, 2014. ISBN 9789291471218, 9291471216.

[20] Bompa, D.V.; Elghazouli, A.Y.: Bond-slip response of deformed bars in rubberised concrete, Construction and Building Materials, Elsevier, 154, 884-898, 2017.

[21] Bouazaoui, L.; Perrenot, G.; Delmas, Y.; Li, A.: Experimental study of bonded steel concrete composite structures, Journal of Constructional Steel Research, Elsevier, 63, 1268-1278, 2007. doi:10.1016/j.jcsr.2006.11.002.

[22] Brantschen, F.; Faria, D.M.V.; Fernández Ruiz, M.; Muttoni, A.: Bond behaviour of straight, hooked, U-shaped and headed bars in cracked concrete, Structural Concrete, Ersnt&Sohn, Vol. 17, No. 5, 2016. DOI: 10.1002/suco.201500199.

[23] Braun, M.: Investigation of the Load-Bearing Behaviour of CoSFB-Dowels, PhD Thesis, University of Luxembourg, Luxembourg, June, 2018.

[24] Braun, M.; Obiala, R.; Odenbreit, C.; Hechler, O.: CoSFB – Design and application of a new generation of slim-floor construction, Proc. of Eurosteel 2014, September 10-12, Naples, Italy, ECCS European Convention for Constructional Steelwork, 2014. ISBN 9789291471218, 9291471216.

[25] Bridge, R.Q.: Design of composite columns – Steel, concrete or composite approach?, Composite Construction in Steel and Concrete IV, American Society of Civil Engineers ASCE, 276-290, 2011. https://doi.org/10.1061/9780784406168.

[26] BS 5400-5:1979, Steel, concrete and composite bridges – Part 5: Code of practice for design of composite bridges, British Standard, BSI, Committee reference CSB/30, Draft for comment 75/10554, 1979.

[27] Cairns, J.: Bond and anchorage of embedded steel reinforcement in fib Model Code 2010, Technical Paper, Structural Concrete, Ernst&Sohn, No. 1, 2015. DOI: 10.1002/suco.201400043.

[28] Cândido-Martins, J.P.S.; Costa-Neves, L.F.; Vellasco, P.C.G. da S.: Experimental evaluation of the structural response of Perfobond shear connectors, Engineering Structures, Elsevier, 32, 1976-1985, 2010.

[29] Chanou, M.: Zum Tragverhalten von Hohlprofil-Verbundstützen mit Mehrkernquerschnitten, Heft 23, PhD Thesis, Institut für Konstruktiven Ingenieurbau, Bergische Universität Wuppertal, Germany, 2018. ISBN 978-3-940795-22-9.

[30] Choi, O.C.; Yang, S.Y.: Bearing angle model for bond of reinforcing bars to concrete, ACI Structural Journal, American Concrete Institute ACI, Vol. 114, No. 1, 245-253, 2017.

[31] Chung, K.F.; Shen, M.H.; Yam, C.H.: Structural behaviour of shear connections with solid and composite slabs under co-existing shear and tension forces, Proc. of 11th International Conference on Advances in Steel and Concrete Composite Structures (ASCCS2015), Tsinghua University, Beijing, China, December 3-5, 378-388, 2015.

[32] Classen, M.; Christou, G.; Hegger, J.: Composite dowels in cracked concrete, Experimental investigation, Proc. of Eurosteel 2017, September 13-15, Copenhagen, Denmark, CE/papers, Ernst&Sohn, Vol. 1, No. 2-3, 2017. https://doi.org/10.1002/cepa.96.

[33] Classen, M.; Herbrand, M.: Shear behaviour of composite dowels in transversely cracked concrete, Structural Concrete, Ernst&Sohn, No. 2, 2015. DOI: 10.1002/suco.201400100.

[34] Classen, M.; Herbrand, M.; Kueres, D.; Hegger, J.: Derivation of design rules for innovative shear connectors in steel-concrete composites through the systematic use of non-linear finite element analysis (FEA), Structural Concrete, Ernst&Sohn, No. 4, 2016. DOI: 10.1002/suco.201500217.

[35] Dan, D.; Fabian, A.; Stoian, V.: Nonlinear behavior of composite shear walls with vertical steel encased profiles, Engineering Structures, Elsevier, 33, 2794-2804, 2011. doi:10.1016/j.engstruct.2011.06.004.

[36] Dan, D.; Fabian, A.; Stoian, V.: Theoretical and experimental study on composite steel-concrete shear walls with vertical steel encased profiles, Journal of Constructional Steel Research, Elsevier, 67, 800-813, 2011. doi:10.1016/j.jcsr.2010.12.013.

[37] Dan, D.; Fabian, A.; Stoian, V.; Nagy-György, T.: Experimental Research on Composite Steel-Concrete Shear Walls with Steel Encased Profiles, Proc. of Eurosteel 2014, September 10-12, Naples, Italy, ECCS European Convention for Constructional Steelwork, 2014. ISBN 9789291471218, 9291471216.

[38] Dan, D.; Stoian, V.; Fabian, A.: Numerical analysis of composite steel concrete structural shear walls with steel encased profiles, BULETINUL INSTITUTULUI POLITEHNIC DIN IAŞI, Publicat de Universitatea Tehnică „Gheorghe Asachi" din Iaşi, Tomul LV (LIX), Fasc. 3, 2009.

[39] Dan, D.; Stoian, V.; Florut, S.-C.; Fabian, A.; Boita, E.: Experimental investigations on performance enhabcement of composite steel concrete shear walls by using steel fibre reinforced concrete, Proc. of Eurosteel 2017, September 13-15, Copenhagen, Denmark, CE/papers, Ernst&Sohn, Vol. 1, No. 2-3, 2017. https://doi.org/10.1002/cepa.96.

[40] Darwin, D.; Graham, E.K.: Effect of deformation height and spacing on bond strength of reinforcing bars, Second Printing, Technical Report, University of Kansas Center for Research, Inc., 1993.

[41] De Nardin, S.; El Debs, A.L.H.C.: Shear transfer mechanisms in composite columns: an experimental study, Steel and Composite Structures, Techno-Press, Vol. 7, No. 5, 377-390, 2007.

[42] Dragan, D.; Plumier, A.; Degée, H.: Experimental Study Regarding Shear Behavior of Concrete Walls Reinforced by Multiple Steel Profiles, High Tech Concrete: Where Technology and Engineering Meet, Springer, Cham, 2018. DOI 10.1007/978-3-319-59471-2_125.

[43] Dragan, D.; Plumier, A.; Degée, H.: Shear behavior of concrete walls reinforced by multiple steel profiles, Calibration of numerical model, Proc. of Eurosteel 2017, September 13-15, Copenhagen, Denmark, CE/papers, Ernst&Sohn, Vol. 1, No. 2-3, 2017. https://doi.org/10.1002/cepa.96.

[44] Eggemann, H.: Simplified Design of Composite Columns, Based on a Comparative Study of the Development of Building Regulations in Germany and the United States, Proc. of Second International Congress on Construction History, Cambridge, Construction History Society, Vol. 1, 1023-1041, 2006.

[45] Eligehausen, R.; Popov, E.P.; Bertero, V.V.: Local bond stress-slip relationships of deformed bars under generalized excitations, Report No. UCB/EERC-83/23, Earthquake Engineering Research Center, University of California, 1983.

[46] Elnashai, A.S.; El-Ghazouli, A.Y.; Dowling, P.J.: International Assessment of Design Guidance for Composite Columns, Journal of Constructional Steel Research, Elsevier, 15, 191-213, 1990.

[47] El-Tawil, S.; Sanz-Picón, C.F.; Deierlein, G.G.: Evaluation of ACI 318 and AISC (LRFD) Strength Provisions for Composite Beam-Columns, Journal of Constructional Steel Research, Elsevier, 34, 103-123, 1995.

[48] EN 10025-1, Hot-rolled products of structural steels – Part 1: General technical delivery conditions, European Standard, European Committee for Standardization, Brussels, 11.2004.

[49] EN 10088-4, Stainless steels – Part 4: Technical delivery conditions for sheet/plate and strip of corrosion resisting steel for construction purposes, European Standard, European Committee for Standardization, Brussels, 04.2009.

[50] EN 12390-3, Testing hardened concrete – Part 3: Compressive strength of test specimens, European Standard, European Committee for Standardization, Brussels, 12.2001.

[51] EN 13670, Execution of concrete structures, German version, European Standard, European Committee for Standardization, Brussels, 12.2009.

[52] EN 1991-1-1, Eurocode 1: Actions on structures – Part 1-1: General actions – Densities, self-weight, imposed loads for buildings, European Standard, European Committee for Standardization, Brussels, 04.2002.

[53] EN 1992-1-1, Eurocode 2: Design of concrete structures – Part 1-1: General rules and rules for buildings, European Standard, European Committee for Standardization, Brussels, 12.2004.

[54] EN 1992-4, Eurocode 2: Design of concrete structures – Part 4: Design of fastenings for use in concrete, European Standard, European Committee for Standardization, Brussels, 09.2016.

[55] EN 1993-1-1, Eurocode 3: Design of steel structures – Part 1-1: General rules and rules for buildings, European Standard, European Committee for Standardization, Brussels, 05.2005.

[56] EN 1993-1-5, Eurocode 3: Design of steel structures – Part 1-5: Plated structural elements, European Standard, European Committee for Standardization, Brussels, 10.2006.

[57] EN 1993-1-8, Eurocode 3: Design of steel structures – Part 1-8: Design of joints, European Standard, European Committee for Standardization, Brussels, 05.2005.

[58] EN 1994-1-1, Eurocode 4: Design of composite steel and concrete structures – Part 1-1: General rules and rules for buildings, European Standard, European Committee for Standardization, Brussels, 12.2004.

[59] EN 206-1, Concrete – Part 1: Specification, performance, production and conformity, European Standard, European Committee for Standardization, Brussels, 12.2000.

[60] fib bulletin 10, Bond of reinforcement in concrete, State-of-art report, Task Group 4.5 Bond Models, International Federation for Structural Concrete (fib), 2000. ISBN 2-88394-050-9.

[61] fib bulletin 72, Bond and anchorage of embedded reinforcement: Background to the fib Model Code for Concrete Structures 2010, Technical Report, Task Group 4.5 Bond models, International Federation for Structural Concrete (fib), 2014. ISBN 978-2-88394-112-0.

[62] fib Model Code for Concrete Structures 2010, Special Activity Group 5, International Federation for Structural Concrete (fib), Ernst&Sohn, 2000. ISBN 978-3-433-03061-5.

[63] Frangi, A.; Fontana, M.; Mensinger, M.: Design of composite slab system with integrated installation floor, Proc. of High Rise Towers and Tall Buildings Conference, Munich, 2010. DOI: 10.13140/2.1.3786.3686.

[64] Frangi, A.; Fontana, M.; Mensinger, M.: Innovative composite slab system with integrated installation floor, Structural Engineering International, International Association for Bridge and Structural Engineering IABSE, 19:4, 404-409, 2009. DOI: 10.2749/101686609789846948.

[65] Furlong, R.W.: Design Rules for Steel-Concrete Composite Columns: 1971 to 2011, Concrete International, American Concrete Institute ACI, Vol. 34, No. 4, 61-66, April 2012.

[66] Goralski, C.: Zusammenwirken von Beton und Stahlprofil bei kammerbetonierten Verbundträgern, PhD Dissertation, Rheinisch-Westfälischen Technischen Hochschule Aachen, 2006.

[67] Grzeszykowski, B.; Szmigiera, E.D.: Analysis of the load transfer between materials in composite concrete encased steel columns loaded axially, Proc. of Eurosteel 2017, September 13-15, Copenhagen, Denmark, CE/papers, Ernst&Sohn, Vol. 1, No. 2-3, 2017. https://doi.org/10.1002/cepa.96.

[68] Hanaor, D.A.; Gan, Y.; Einav, I.: Static friction at fractal interfaces, Tribology International, Elsvier, 93, 229-238, 2016.

[69] Hanswille, G.; Porsch, M.: Lasteinleitung bei ausbetonierten Hohlprofil-Verbundstützen, Stahlbau, Ernst&Sohn, Vol. 73, No. 9, 2004.

[70] Hanswille, G.; Porsch, M.; Ustundag, C.: Resistance of headed studs subjected to fatigue loading, Part I: Experimental study, Journal of Constructional Steel Research, Elsevier, 63, 475-484, 2007.

[71] Hanswille, G.; Schäfer, M.; Bergmann, M.: Verbundtragwerke aus Stahl und Beton, Bemessung und Konstruktion, Kommentar zu DIN EN 1994-1-1, Ausgabe Dezember 2010, Stahlbau Kalender 2018: Verbundbau – Fertigung, Ernst&Sohn, 2018. ISBN 978-3-433-03166-7.

[72] Hanswille, G; Bergmann, M.; Bergmann, R.: Design of composite columns with cross-sections not covered by Eurocode 4, Steel Construction, Design and Research, Ernst&Sohn, Vol. 10, No. 1, 10-16, 2017. https://doi.org/10.1002/stco.201710004.

[73] Hirama, C.; Ishikawa, T.; Hisagi, A.: Shear strength of headed stud push-out tests, Comprehensive literature review focusing on slab type, failure mode, and large-diameter headed stud, Proc. of Eurosteel 2017, September 13-15, Copenhagen, Denmark, CE/papers, Ernst&Sohn, Vol. 1, No. 2-3, 2017. https://doi.org/10.1002/cepa.96.

[74] Hotta, H.; Kihara, H.; Takiguchi, K.: A Fundamental study on shear bond strength of steel encased reinforced concrete members, Proc. of FRAMCOS-3, Fracture Mechanics of Concrete Structures, AEDIFICATIO Publishers, 1321-1330, 1998.

[75] Houston, W.; Houston, I.: How to properly specify weld studs for use with the drawn arc stud welding process in structural applications, Modern Steel Construction, Solid Bond, steelwise, June 2015.

[76] Huo, B.Y.: Experimental and analytical study of the shear transfer in composite shallow cellular beams, PhD Thesis, City University London, UK, November 2012. http://openaccess.city.ac.uk/1965/.

[77] INNO-HYCO, Innovative hybrid and composite steel-concrete structural solutions for building in seismic area, Technical Report, European Commission, Research Programme of the Research Fund for Coal and Steel, RFSR-CT-2010-00025, 2013.

[78] IS: 11384-1985, Code of practice for composite construction in structural steel and concrete, Indian Standard, Prefabricated and Composite Construction Sectional Committee BDC 32, Indian Standards Institution, New Delhi, India, 1986.

[79] ISO 2560, Welding consumables – Covered electrodes for manual metal arc welding of non-alloy and fine grain steels – Classification, International Standard, Third Edition, International Organization for Standardization, Geneva, Switzerland, 10.2009.

[80] ISO 6892-1, Metallic materials – Tensile testing – Part 1: Method of test at room temperature, International Standard, International Organization for Standardization, Geneva, Switzerland, 08.2009.

[81] ISO 6935-2, Steel for reinforcement of concrete – Part 2: Ribbed bars, International Standard, International Organization for Standardization, Geneva, Switzerland, 01.2007.

[82] ISRC Composite Column, Performance and capacity of isolated steel reinforced concrete columns and design approaches, Technical Report, Council on Tall Buildings and Urban Habitat, CTBUH, ArcelorMittal, China Academy of Building Research Technology Co., Ltd., CABR, Magnusson Klemencic Associates, MKA, 2014.

[83] Ivković, B.; Djurdjanović, M.; Stamenković, D.: The influence of the Contact Surface Roughness on the Static Friction Coefficient, Tribology in industry, Faculty of Engineering, University of Kragujevac, Serbia, Vol. 22, No. 3&4, 41-44, 2000.

[84] Jeong, Y.-J.; Kim, H.-Y.; Koo, H.-B.: Longitudinal shear resistance of steel-concrete composite slabs with perfobond shear connectors, Journal of Constructional Steel Research, Elsevier, 65, 81-88, 2009.

[85] JGJ 138, 组合结构设计规范[S]. Code for design of composite structures, Ministry of Housing and Urban-Rural Development of the People Republic of China, 2016.

[86] Ji, X.; Jiang, F.; Qian, J.: Seismic behavior of steel tube-double steel plate-concrete composite walls: Experimental tests, Journal of Constructional Steel Research, Elsevier, 86, 17-30, 2013. http://dx.doi.org/10.1016/j.jcsr.2013.03.011.

[87] Ji, X.; Sun, Y.; Qian, J.; Lu, X.: Seismic behavior and modeling of steel reinforced concrete (SRC) walls, Earthquake Engineering & Structural Dynamics, Wiley, 44, 955-972, 2015. DOI: 10.1002/eqe.2494.

[88] Jin, W.L.; Chen, J.; Jiang, A.Y.: Fatigue behaviour of corroded stud shear connectors, Proc. of 11th International Conference on Advances in Steel and Concrete Composite Structures (ASCCS2015), Tsinghua University, Beijing, China, December 3-5, 372-377, 2015.

[89] Johnson, R.P.: Composite Structures of Steel and Concrete. Beams, Slabs, Columns and Frames for Buildings, Third Edition, Blackwell Publishing, 2004. ISBN 1-4051-0035-4.

[90] Johnson, R.P.: Designers' Guide to Eurocode 4: Design of Composite Steel and Concrete Structures, EN 1994-1-1, Second Edition, ICE Publishing, Thomas Telford Ltd., 2012. ISBN 978-0-7277-4173-8.

[91] JSCE Standard Specifications for Concrete Structures – 2007, "Design", JSCE Guidelines for Concrete, No. 15, Japan Society of Civil Engineers, December 2010. ISBN: 978-0-87031-930-3.

[92] JSCE Standard Specifications for Steel and Composite Structures, First Edition, Japan Society of Civil Engineers, December 2009.

[93] Jurkiewiez, B.; Tout, F.; Ferrier, E.: Bonding connection in steel-concrete composite structures, Proc. of Eurosteel 2014, September 10-12, Naples, Italy, ECCS European Convention for Constructional Steelwork, 2014. ISBN 9789291471218, 9291471216.

[94] Kendall, K.; Kendall, M.; Rehfeldt, F.: Adhesion of Cells, Viruses and Nanoparticles, Springer, XV, 2011. ISBN 978-90-481-2584-5.

[95] Keo, P.; Nguyen, Q.-H.; Somja, H.; Hjiaj, M.: Derivation of the exact stiffness matrix of shear-deformable multi-layered beam element in partial interaction, Finite Elements in Analysis and Design, Elsevier, 112, 40-49, 2016. http://dx.doi.org/10.1016/j.finel.2015.12.004.

[96] Keo, P.; Nguyen, Q.-H.; Somja, H.; Hjiaj, M.: Geometrically nonlinear analysis of hybrid beam-column with several encased steel profiles in partial interaction, Engineering Structures, Elsevier, 100, 66-78, 2015. http://dx.doi.org/10.1016/j.engstruct.2015.05.030.

[97] Keo, P.; Somja, H.; Nguyen, Q.-H.; Hjiaj, M.: Simplified design method for slender hybrid columns, Journal of Constructional Steel Research, Elsevier, 110, 101-120, 2015. http://dx.doi.org/10.1016/j.jcsr.2015.03.006.

[98] Kim, C.S.; Park, H.G.; Chung, K.-S.; Choi, I.-R.: Eccentric Axial Load Capacity of High-Strength Steel-Concrete Composite Columns of Various Sectional Shapes, Journal of Structural Engineering, American Society of Civil Engineers ASCE, Vol. 140, No. 4, 2014. DOI: 10.1061/(ASCE)ST.1943-541X.0000879.

[99] Kim, S.-H.; Choi, J.-H.: Experimental study on shear connection in unfilled composite steel grid bridge deck, Journal of Constructional Steel Research, Elsevier, 66, 1339-1344, 2010.

[100] Klaiber, F.W.; Wipf, T.J.: An Alternate Shear Connector for Composite Action, Proc. of Mid-Continent Transportation Symposium, Ames, Iowa, USA, 115-120, 2000.

[101] Kludka, M.; Kurz, W.: Adhesives as a permanent shear connection for composite beams, International Conference on Composite Construction in Steel and Concrete, Composite Construction in Steel and Concrete VII, ASCE, 2013. https://doi.org/10.1061/9780784479735.046.

[102] Kmiecik, P; Kamiński, M.: Modelling of reinforced concrete structures and composite structures with concrete strength degradation taken into consideration, Archives of Civil and Mechanical Engineering, Elsevier, Vol. XI, No. 3, 623-636, 2011.

[103] Kopp, M.; Wolters, K.; Claßen, M.; Hegger, J.; Gündel, M.; Gallwoszus, J.; Heinemeyer, S.; Feldmann, M.: Composite dowels as shear connectors for composite beams – Background to the design concept for static loading, Journal of Constructional Steel Research, 147, 488-503, 2018.

[104] Kovács, N.; Kövesdi, B.; Kachichian, M.; Frank, M.F.: Full scale test on steel-concrete composite beams, Proc. of Eurosteel 2017, September 13-15, Copenhagen, Denmark, CE/papers, Ernst&Sohn, Vol. 1, No. 2-3, 2017. https://doi.org/10.1002/cepa.96.

[105] Kozma, A.; Odenbreit, C.; Braun, M.V.; Veljkovic, M.; Nijgh, M.P.: Push-out tests on demountable shear connectors of steel-concrete composite structures, Proc. of 12th International Conference on Advances in Steel-Concrete Composite Structures (ASCCS2018), Universitat Politècnica de València, Valencia, Spain, June 27-29, 2018. Doi: http://dx.doi.org/10.4995/ASCCS2018.2018.6944.

[106] Kvočák, V.; Dubecký, D.; Kožlejová, V.: Experimental verification of composite action using push-out tests, Proc. of Eurosteel 2017, September 13-15, Copenhagen, Denmark, CE/papers, Ernst&Sohn, Vol. 1, No. 2-3, 2017. https://doi.org/10.1002/cepa.96.

[107] Kwon, G.; Hungerford, B.; Kayir, H.; Schaap, B.; Ju, Y.K.; Klingner, R.; Engelhardt, M.: Strengthening Existing Non-Composite Steel Bridge Girders Using Post-Installed Shear Connectors, Technical Report, FHWA/TX-07/0-4124-1, The University of Texas at Austin, USA, 2007.

[108] Lam, D.; El-Lobody, E.: Behaviour of Headed Stud Shear Connectors in Composite Beam, Journal of Structural Engineering, ASCE, January 2005. DOI: 10.1061/(ASCE)0733-9445(2005)131:1(96).

[109] Lee, J.; Fenves, G.L.: Plastic-Damage Model for Cyclic Loading of Concrete Structures, Journal of Engineering Mechanics, American Society of Civil Engineers ASCE, Vol. 124, No. 8, 892-900, 1998.

[110] Leskelä, M.V.: Behaviour and design of steel-concrete composite structures, PG 0917, First Edition, Peikko Group Corporation, 2017.

[111] Liao, F.-Y.; Han, L.-H.; Tao, Z.: Performance of reinforced concrete shear walls with steel reinforced concrete boundary columns, Engineering Structures, Elsevier, 44, 186-209, 2012. http://dx.doi.org/10.1016/j.engstruct.2012.05.037.

[112] Lippes, M.: Zur Bemessung von Hohlprofil – Verbundstützen aus hochfesten Stählen und Betonen, PhD Thesis, Bergische Universität Wuppertal, Germany, November 2008. ISBN 978-3-940795-12-0.

[113] Lubliner, J.; Oliver, J.; Oller, S.; Oñate, E.: A plastic-damage model for concrete, International Journal of Solids and Structures, Pergamon Press plc, Vol. 25, No. 3, 299-326, 1989.

[114] Lundgren, K.: Three-Dimensional Modelling of Bond in Reinforced Concrete, Theoretical Model, Experiments and Applications, PhD Thesis, Chalmers University of Technology, Sweden, 1999. ISBN 91-7197-853-4

[115] Lungershausen, H.: Zur Schubtragfähigkeit von Kopfbolzendübeln, Tech. Rep., Mitteilung Nr. 88-7, Institut für Konstruktiven Ingenieurbau Ruhr-Universität Bochum, 1988.

[116] MacLeod, I.A.: Modern Structural Analysis, Modelling process and guidance, Thomas Telford, 2005. ISBN 0-7277-3279-X.

[117] Maleki, S.; Bagheri, S.: Behaviour of channel shear connectors, Part I: Experimental study, Journal of Constructional Steel Research, Elsevier, 64, 1333-1340, 2008. doi:10.1016/j.jcsr.2008.01.010.

[118] Maleki, S.; Bagheri, S.: Behaviour of channel shear connectors, Part II: Analytical study, Journal of Constructional Steel Research, Elsevier, 64, 1341-1348, 2008. doi:10.1016/j.jcsr.2008.01.006.

[119] Mancini, G.; Tondolo, F.: Effect of bond degradation due to corrosion – a literature survey, Structural Concrete, Ernst&Sohn, Vol. 15, No. 3, 2014. DOI: 10.1002/suco.201300009.

[120] Maugis, D.: Adhesion of Solids: Mechanical Aspects, CRC Press LLC, 2001.

[121] Meaud, C.; Jurkiewiez, B.; Ferrier, E.: Steel-concrete bonding connection: An experimental study and non-linear finite element analysis, International Journal of Adhesion & Adhesives, Elsevier, 54, 131-142, 2014. http://dx.doi.org/10.1016/j.ijadhadh.2014.05.010.

[122] Mirza, O.; Mashiri, F.R.; Canuto, C.; Lam, D.: Post fire behaviour of innovative shear connection for composite steel-concrete structures, Proc. of 11th International Conference on Advances in Steel and Concrete Composite Structures (ASCCS2015), Tsinghua University, Beijing, China, December 3-5, 462-469, 2015.

[123] Mirza, S.A.; Tikka, T.K.: Flexural Stiffness of Composite Columns Subjected to Major Axis Bending, Title no. 96-S03, ACI Structural Journal, American Concrete Institute ACI, 19-28, Jan.-Feb. 1999.

[124] Mollazadeh, M.H.: Load Introduction into Concrete-Filled Steel Tubular Columns, PhD Thesis, School of Mechanical, Aerospace and Civil Engineering, The University of Manchester, 2015.

[125] Muttoni, A.; Fernández Ruiz, M.: Influence of geometric, strain and size effects on bond in structural concrete, Bond in Concrete 2012, Brescia, Italy, 15-21, 2012.

[126] Nellinger, S.: On the behaviour of shear stud connections in composite beams with deep decking, PhD Thesis, University of Luxembourg, Luxembourg, November 2015.

[127] Nethercot, D.A.: Composite Construction, Spon Press, 2004. ISBN 0-203-45733-1.

[128] Neto, C.; Costa-Neves, L.F.; Vellasco, P.C.G. da S.; Jordão, S.; Ihaddoudene, A.N.T.: Experimental research of multiple perfobond connectors for composite girders, Proc. of Eurosteel 2017, September 13-15, Copenhagen, Denmark, CE/papers, Ernst&Sohn, Vol. 1, No. 2-3, 2017. https://doi.org/10.1002/cepa.96.

[129] Nguyen, Q.-H.; Hjiaj, M.; Tran, V.-T.: Development of design method for composite columns with several encased steel profiles under combined shear and bending, Proc. of Eurosteel 2014, September 10-12, Naples, Italy, ECCS European Convention for Constructional Steelwork, 2014. ISBN 9789291471218, 9291471216.

[130] Nielsen, M.P.; Hoang, L.C.: Limit Analysis and Concrete Plasticity, Third Edition, CRC Press, Taylor & Francis Group, 2011. ISBN 978-1-4398-0396-7.

[131] Odenbreit, C.: Basics in steel construction, Stahlbau II course script, Technical Report, University of Luxembourg, 2016.

[132] Odenbreit, C.: High Rise Buildings in Steel – from Past to Present, Proc. of the Journée Construction Acier 2015, Luxembourg, Luxembourg, 2015.

[133] Oguejiofor, E.C.; Hosain, M.U.: Numerical analysis of push-out specimens with perfobond rib connectors, Computers & Structures, Elsevier Science Ltd., Vol. 62, No. 4, 617-624, 1997.

[134] Ollgaard, J.G.; Slutter, R.G.; Fisher, J.W.: Shear strength of stud connectors in lightweight and normal weight concrete, Fritz Laboratory Reports, AISC Engineering Journal, AISC, April 1971, 71-10, 1971.

[135] Online source: http://www.kim-tec.de/produkte/pflege-und-wartungsprodukte/kim-tec-ptfe-spray-detail.

[136] Online source: https://hebau.de/produkte/optimierung-der-betonherstellung/trennmittel/wetcast-formfluid-hp.

[137] Online source: https://www.thefabricator.com/article/aluminumwelding/how-to-recognize-minimize-weld-smut.

[138] Pan, W.; Fan, J.; Li, W.: Experimental study on ultimate capacity of grouted connections in tripod support structure of offshore wind turbines, Proc. of 11th International Conference on Advances in Steel and Concrete Composite Structures (ASCCS2015), Tsinghua University, Beijing, China, December 3-5, 440-445, 2015.

[139] Papastergiou, D.: Connections by Adhesion, Interlocking and Friction for Steel-Concrete Composite Bridges under Static and Cyclic Loading, These No 5301 (2012), PhD Thesis, École Polytechnique Fédérale de Lausanne, Switzerland, 2012.

[140] Papastergiou, D.; Lebet, J.-P.: New steel-concrete connection for prefabricated composite bridges, Stahlbau, Ernst&Sohn, Vol. 80, No. 12, 2011. DOI: 10.1002/stab.201101493.

[141] Pauw, P.E.: Static Modulus of Elasticity of Concrete as Affected by Density, ACI Journal, American Concrete Institute ACI, Vol. 32, No. 6, Title No. 57-32, 679-687, 1960.

[142] Pecce, M.; Ceroni, F.: Bond tests of partially encased composite columns, Advanced Steel Construction an International Journal, The Hong Kong Institute of Steel Construction, Vol. 6, No. 4, 1001-1018, 2010.

[143] Peng, L.: Form Follows Function – The Composite Construction and Mixed Structures in Modern Tall Buildings, International Journal of High-Rise Buildings, CTBUH Korea, Vol. 3, No. 3, 191-198, 2014.

[144] Petersen, Ch.: Stahlbau, Grundlagen der Berechnung und baulichen Ausbildung von Stahlbauten, Fourth Edition, Springer Vieweg, 2013. ISBN 978-3-8348-8610-1.

[145] Petersen, Ch.: Stahlbau, Grundlagen der Berechnung und baulichen Ausbildung von Stahlbauten, Third Edition, Vieweg, 1993. ISBN 3-528-28837-X.

[146] Plumier, A.: A design method for walls with several encased steel profiles, Proc. of 11th International Conference on Advances in Steel and Concrete Composite Structures (ASCCS2015), Tsinghua University, Beijing, China, December 3-5, 603-611, 2015.

[147] Plumier, A.: Assessment of design expressions for walls with several encased steel profiles, Proc. of 11th International Conference on Advances in Steel and Concrete Composite Structures (ASCCS2015), Tsinghua University, Beijing, China, December 3-5, 612-619, 2015.

[148] Plumier, A.; Dragan, D.; Nguyen Q.-H.; Degée, H.: An Analytical Design Method for Steel-Concrete Hybrid Walls, Structures, Elsevier, In Press, 2016. http://dx.doi.org/10.1016/j.istruc.2016.12.007.

[149] Poon, D.C.K.; Hsiao, L.; Zhu, Y.; Pacitto, S.; Zuo, S.; Gottlebe, T.; Wang, S.: Structural Analysis and Design Challenges of the Ping An Tower under Consideration of the Upcoming China Code, Structures Congress, American Society of Civil Engineers ASCE, 528-540, April 14-16, 2011. https://doi.org/10.1061/9780784411711.

[150] Prince, M.J.R.; Singh, B.: Bond behaviour of normal- and high-strength recycled aggregate concrete, Structural Concrete, Ernst&Sohn, No. 1, 2015. DOI: 10.1002/suco.201300101.

[151] Qian, J.; Jian, Z.; Ji, X.: Behavior of steel tube-reinforced concrete composite walls subjected to high axial force and cyclic loading, Engineering Structures, Elsevier, 36, 173-184, 2012. doi:10.1016/j.engstruct.2011.10.026.

[152] Qu, X.; Chen, Z.; Nethercot, D.A.; Gardner, L.; Theofanous, M.: Push-out tests and bond strength of rectangular CFST columns, Steel and Composite Structures, Techno-Press, 19(1), 21-41, 2015.

[153] Qureshi, J.: Finite element modelling of steel-concrete composite structures, PhD Thesis, The University of Leeds, UK, November 2010.

[154] Rabbat, B.G.; Russell, H.G.: Friction Coefficient of Steel and Concrete or Grout, Journal of Structural Engineering, ASCE, Vol. 111, No. 3, 505-515, 1985.

[155] Rana, M.M.; Lee, C.K.; Al-Deen, S.: A study on the bond stress-slip behaviour between engineered cementitious composites and structural steel sections, Proc. of Eurosteel 2017, September 13-15, Copenhagen, Denmark, CE/papers, Ernst&Sohn, Vol. 1, No. 2-3, 2017. https://doi.org/10.1002/cepa.96.

[156] Ritter, W.: Die Bauweise Hennebique, Schweizerische Bauzeitung, Vol. 33/34, No. 5, 1899. http://doi.org/10.5169/seals-21306.

[157] Roeder, C.W.; Chmielowski, R.; Brown, C.B.: Shear Connector Requirements for Embedded Steel Sections, Journal of Structural Engineering, ASCE, 125(2), 142-151, 1999.

[158] Roik, K.; Bergmann, R.: Design Method for Composite Columns with Unsymmetrical Cross-Sections, Journal of Constructional Steel Research, Elsevier, 15, 153-168, 1990.

[159] Roik, K.; Bergmann, R.: Harmonisation of the European Construction Codes, Eurocode 3,4 and 8/part3, Report on Eurocode 4, Composite Columns, Report EC4/6/89, Minister für Raumordung, Bauwesen und Städtebau, RS II 1-674102-8630, 1989.

[160] Roik, K.; Bergmann, R.; Bode, H.; Wagenknecht, G.: Tragfähigkeit von einbetonierten Stahlstützen, Tech. Rep., Mitteilung Nr. 76-4, Institut für Konstruktiven Ingenieurbau Ruhr-Universität Bochum, 1976.

[161] Roik, K.; Bode, H.; Breit, M.: Momentfreie Anschlüsse an einbetonierte Stahlprofilstützen, Projekt 53, Studiengesellschaft für Anwendungstechnik von Eisen und Stahl e.V., 1980.

[162] Roik, K.; Breit, M.; Schwalbenhofer, K.: Untersuchung der Verbundwirkung zwischen Stahlprofil und Beton bei Stützenkonstruktionen, Projekt 51, Studiengesellschaft für Anwendungstechnik von Eisen und Stahl e.V., 1984.

[163] Roik, K.; Hanswille, G.: Beitrag zur Bestimmung der Tragfähigkeit von Kopfbolzendübeln, Stahlbau, Ernst&Sohn, Vol. 52, No. 10, 1983.

[164] Roik, K.; Schwalbenhofer, K.: Experimentelle und theoretische Untersuchungen zum plastischen Verhalten von Verbundstützen bei großen Deformationen, Stahlbau, Ernst&Sohn, 58, 321-329, 1989.

[165] Roik, K.; Schwalbenhofer, K: Experimentelle Untersuchungen zum plastischen Verhalten von Verbundstützen, Projekt 125, Studiengesellschaft für Anwendungstechnik von Eisen und Stahl e.V., 1988.

[166] Sakai, T.: Practical calculation formulae of parallel chord vierendeel trusses with constant stiffness for full loads derived from “Differenzengleichung” method, Bulletin, Memoirs of the Faculty of Engineering, Hokkaido Imperial University, 1939. http://hdl.handle.net/2115/37728.

[167] Schaumann, P.; Henneberg, J.; Raba, A.: Axially loaded grouted connections in offshore conditions using ordinary portland cement, Proc. of 12th International Conference on Advances in Steel-Concrete Composite Structures (ASCCS2018), Universitat Politècnica de València, Valencia, Spain, June 27-29, 2018. Doi: http://dx.doi.org/10.4995/ASCCS2018.2018.6944.

[168] Schlaich, J.; Schäfer, K.: Design and detailing of structural concrete using strut-and-tie models, The Structural Engineer, The Institution of Structural Engineers, Vol. 69, No. 6, 1991.

[169] Schlaich, J.; Schäfer, K.; Jennewein, M.: Toward a Consistent Design of Structural Concrete, Special Report, PCI Journal, Precast Concrete Institute, May-June, 74-150, 1987.

[170] Schwalbenhofer, K.: Zum Tragverhalten von Verbundstutzen und Verbundrahmenkonstruktionen bei großen Deformationen, Tech. Rep., Mitteilung Nr. 88-12, Institut für Konstruktiven Ingenieurbau Ruhr-Universität Bochum, 1988.

[171] Seres, N.: Behaviour and resistance of concrete encased embossments in composite slabs, PhD Thesis, Budapest University of Technology and Economics, Hungary, 2012.

[172] Shanmugam, N.E.; Lakshmi, B.: State of the art report on steel-concrete composite columns, Journal of Constructional Steel Research, Elsevier, 57, 1041-1080, 2001.

[173] Shariati, M.; Sulong, N.H.R.; Arabnejad K.H., M.M.; Mahoutian, M.: Shear resistance of channel shear connectors in plain, reinforced and lightweight concrete, Scientific Research and Essays, Academic Journals, Vol. 6, No. 4, 977-983, 2011. DOI: 10.5897/SRE10.1120.

[174] SIMULIA User Assistance 2017, Abaqus, Dassault Systèmes Simulia Corp., Providence, RI, USA.

[175] SmartCoCo, Smart Composite Components - Concrete Structures Reinforced by Steel Profiles, Technical Report, European Commission, Research Programme of the Research Funds for Coal and Steel, TGS8, RFSR-CT-2012-00031, 2016.

[176] Sohel, K.M.A.; Liew J.Y.R.; Yan, J.B.; Zhang, M.H.; Chia, K.S.: Behaviour of steel-concrete-steel sandwich structures with lightweight cement composite and novel shear connectors, Composite Structures, Elsevier, Vol. 94, No. 12, 3500-3509, 2012. https://doi.org/10.1016/j.compstruct.2012.05.023.

[177] Song, T.-Y.; Tao, Z.; Uy, B.; Han, L.-H.: Bond strength in full-scale concrete-filled steel tubular columns, Proc. of the 2015 World Congress on Advances in Structural Engineering and Mechanics (ASEM15), Incheon, Korea, August 25-29, 2015.

[178] Spremić, M.; Gluhović, N.; Marković, Z.; Dobrić, J.; Filipović, A.: Comparison of headed studs with perfobond shear connectors – experimental and numerical analysis, Proc. of Eurosteel 2017, September 13-15, Copenhagen, Denmark, CE/papers, Ernst&Sohn, Vol. 1, No. 2-3, 2017. https://doi.org/10.1002/cepa.96.

[179] Su, Q.-T.; Wang, W.; Luan, H.-W.; Yang, G.-T.: Experimental research on bearing mechanism of perfobond rib shear connectors, Journal of Constructional Steel Research, Elsevier, 95, 22-31, 2014.

[180] Szczecina, M.; Winnicki, A.: Calibration of the CDP model parameters in Abaqus, Proc. of 2015 World Congress and Advances in Structural Engineering and Mechanics (ASEM15), Incheon, Korea, 2015.

[181] Tao, Z.; Song, T.-Y.; Uy, B.; Han, L.-H.: Bond behaviour in concrete-filled steel tubes, Journal of Constructional Steel Research, Elsevier, 120, 81-93, 2016.

[182] Thrower, J.R.: Technical statistics and strength of materials, Second Edition, Breton Publishers, PWS Publishers, 1986. ISBN 0-534-06384-5.

[183] Timoshenko, S.: Strength of Materials, Part I, Elementary Theory and Problems, Second Edition, Tenth Printing, D. Van Nostrand Company, Inc., 1948.

[184] Timoshenko, S.; Goodier, J.N.: Theory of Elasticity, Second Edition, McGraw-Hill Book C., Inc., 1951.

[185] Tran, V.T.: Experimental and numerical analysis of the steel-concrete composite walls with several fully encased steel profiles, PhD Thesis, Institut National des Sciences Appliquées (INSA) de Rennes , France, November 2015.

[186] Turon, A.; Dávila, C.G.; Camanho, P.P.; Costa, J.: An engineering solution for mesh size effects in the simulation of delamination using cohesive zone models, Engineering Fracture Mechanics, Elsevier, 74, 1665-1682, 2007. doi:10.1016/j.engfracmech.2006.08.025.

[187] Uy, B.; Kang, W.-H.; Hicks, S.: From design to reliable structures, HERA innovation in metals, The University of Sydney, 15 September 2017. https://hera.org.nz.

[188] Uy, B.; Patel, V.; Li, D.; Aslani, F.: Behaviour and Design of Connections for Demountable Steel and Composite Structures, Structures, Elsevier, In Press, 2016. http://dx.doi.org/10.1016/j.istruc.2016.06.005.

[189] Valente, I.: Experimental Studies on Shear Connection Systems in Steel and Lightweight Concrete Composite Bridges, PhD Thesis, University of Minho, Portugal, April 2007.

[190] Valente, I.; Cruz, P.J.S.: Experimental studies on shear connection between steel and lightweight concrete, Proc. of International Conference on Bridge Maintenance, Safety and Management, 2, Kyoto, Taylor and Francis, 2004. ISBN 04-1536-336-X. http://hdl.handle.net/1822/3125.

[191] Varsani, H.; Tan, E.L.; Singh, B.: Behaviour of innovative demountable shear connectors subjected to combined shear and axial tension, Proc. of Eurosteel 2017, September 13-15, Copenhagen, Denmark, CE/papers, Ernst&Sohn, Vol. 1, No. 2-3, 2017. https://doi.org/10.1002/cepa.96.

[192] Veldanda, M.R.; Hosain, M.U.: Behaviour of perfobond rib shear connectors: push-out tests, Canadian Journal of Civil Engineering, Canadian Science Publishing, 19, 1-10, 1992.

[193] Veríssimo, G.S.; Paes, J.L.R.; Valente, I.; Cruz, P.J.S.; Fakury, R.H.: Design and experimental analysis of a new shear connector for steel and concrete composite structures, Proc. of Third International Conference on Bridge Maintenance, Safety and Management, IABMAS'06, 16-19 July, Porto, Portugal, Taylor and Francis, 2006. ISBN 9780429158094. https://doi.org/10.1201/b18175.

[194] Vianna, J. da C.; Costa-Neves, L.F.; Vellasco, P.C.G. da S.; de Andrade, S.A.L.: Experimental assessment of Perfobond and T-Perfobond shear connector' structural response, Journal of Constructional Steel Research, Elsevier, 65, 408-421, 2009.

[195] Vianna, J. da. C.; de Andrade, S.A.L.; Vellasco, P.C.G. da S.; Costa-Neves, L.F.: Experimental study on Perfobond shear connectors in composite construction, Journal of Constructional Steel Research, Elsevier, 81, 62-75, 2013. http://dx.doi.org/10.1016/j.jcsr.2012.11.002.

[196] Virdi, K.S.; Dowling, P.J.: A unified design method for composite columns, IABSE Publications, International Association for Bridge and Structural Engineering IABSE, 36, 1976.

[197] Wang, L.; Chen, H.; Zhong, J.; Chen, H.; Xuan, W.; Mi, S.; Yang, H.: Study on the Bond-Slip Performance of CFSSTs Based on Push-Out Tests, Research Article, Advances in Materials Science and Engineering, Hindawi Publishing Corp., Vol. 2018, ID 2959827, 2018. https://doi.org/10.1155/2018/2959827.

[198] Wang, X.Z.; Zheng, S.J.; Liu, Y.Q.; Tang, L.; Gao, Y.: Mechanism of composite pylon with perfobond connectors under axial loads, Proc. of 11th International Conference on Advances in Steel and Concrete Composite Structures (ASCCS2015), Tsinghua University, Beijing, China, December 3-5, 412-416, 2015.

[199] Wendner, R.; Vorel, J.; Smith, J.; Hoover, C.G.; Bažant, Z.P.; Cusatis, G.: Characterization of concrete failure behaviour: a comprehensive experimental database for the calibration and validation of concrete models, Materials and Structures, Springer Netherlands, Vol. 48, 3603-3626, 2015. DOI 10.1617/s11527-014-0426-0.

[200] Weng, C.C.; Yen, S.I.: Comparisons of concrete-encased composite column strength provisions of ACI code and AISC specification, Engineering Structures, Elsevier, 24, 59-72, 2002.

[201] Wickersheimer, D.J.: The Vierendeel, Journal of the Society of Architectural Historians, JSTOR, Vol. 35, No. 1, 54-60, 1976. http://www.jstor.org/stable/988971.

[202] Wium, J.A.: Composite Columns: Force Transfer from Steel Section to Concrete Encasement, PhD Thesis, These No 1008 (1992), École Polytechnique Fédérale de Lausanne, Switzerland, 1992.

[203] Wolters, K.; Kopp, M.; Feldmann, M.; Claßen, M.; Schäfer, J.: Static shear capacity of small-scaled pin shear connectors, Proc. of Eurosteel 2017, September 13-15, Copenhagen, Denmark, CE/papers, Ernst&Sohn, Vol. 1, No. 2-3, 2017. https://doi.org/10.1002/cepa.96.

[204] Wong, R.W.M.: Construction of Two IFC, Presentation, City University of Hong Kong, Online, https://docplayer.net/48929926-Two-ifc-construction-of.html.

[205] Wong, R.W.M.: International Finance Centre, Phase II, Photo Essay, Construction & Contract News, China Trend Building Press Ltd., No. 1, 2003.

[206] Wong, R.W.M.: The construction of Super High-rise Composite Structures in Hong Kong, Presentation, 2nd International Structural Engineering and Construction Conference, Rome, Italy, 2003. http://personal.cityu.edu.hk/~bswmwong/photo_lib/pdf/composite.pdf.

[207] Wong, R.W.M.; Ho, M.F.: Structural and Construction Feature of the Hong Kong International Financial Center Phase II, Building for the Future: The 16th CIB World Building Congress, 2004. http://www.irbnet.de/daten/iconda/CIB10120.pdf.

[208] Xiao, C.; Deng, F.; Chen, T.; Zhao, Z.: Experimental study on concrete-encased composite columns with separate steel sections, Steel and Composite Structures, Techno-Press, Vol. 23, No. 4, 2017. DOI: https://doi.org/10.12989/scs.2017.23.4.000.

[209] Xing, G.; Zhou, C.; Wu, T.; Liu, B.: Experimental Study on Bond Behavior between Plain Reinforcing Bars and Concrete, Research Article, Advances in Materials Science and Engineering, Hindawi Publishing Corp., Vol. 2015, ID 604280, 2015. http://dx.doi.org/10.1155/2015/604280.

[210] Xu, K.-C.; Chen, M.-C.; Yuan, F.: Confined Expansion and Bond Property of Micro-Expansive Concrete-Filled Steel Tube Columns, The Open Civil Engineering Journal, Bentham Open, 5, 173-178, 2011.

[211] Zanuy, C.; Curbach, M.; Lindorf, A.: Finite element study on bond strength between concrete and reinforcement under uneven confinement condition, Structural Concrete, Ernst&Sohn, Vol. 14, No. 3, 2013. DOI: 10.1002/suco.201200019.

[212] Zhang, Q.; Schäfer, M.: Comparison of design for composite beam in steel and concrete according to Eurocode 4 and Chinese design codes, XI Conference on Steel and Composite Construction, CE/papers, Ernst&Sohn, Vol. 1, No. 4, 426-437, 2017. https://doi.org/10.1002/cepa.542.

[213] Zhang, Q.-J.; Schäfer, M.: Comparison of EN1994-1-1 and Chinese JGJ138-2016 for Design of Composite Structures of Steel and Concrete, Proc. of Ninth International Conference on advances in Steel Structures (ICASS'2018), 5-7 December, Hong Kong, China, The Hong Kong Institute of Steel Construction, 2018. DOI: 10.18057/ICASS2018.xxx.

[214] Zhu, B.; Guo, Y.-L.: Elastic buckling load and load resistance of core-separated assembled BRB confined by two concrete-infilled tubes, Proc. of Eurosteel 2017, September 13-15, Copenhagen, Denmark, CE/papers, Ernst&Sohn, Vol. 1, No. 2-3, 2017. https://doi.org/10.1002/cepa.96.

Annexes

Annex A – Preliminary numerical simulations and parametric study on the development of new mechanical shear connectors

Summary of the analysed models in the preliminary numerical study is given in Table A.1.

Table A.1.
Parametric study with considered parameters for the identification of the geometry of flat shear connectors.

Specimen		Considered parameters										
No	Name	positive/ negative	L	γ	β	α	a	b	c	dashed	dash angle	dash gap
			[mm]	[°]	[°]	[°]	[mm]	[mm]	[mm]	yes/no	[°]	[mm]
1	FT0	-	640	-	-	-	-	-	-	-	-	-
2	FTp1v1	positive	640	90	-	90	10	30	200	no	-	-
3	FTp2v1	positive	640	0	-	90	10	30	200	no	-	-
4	FTp3v1	positive	1540	45	90	90	10	30	400	no	-	-
5	FTn4v1	negative	640	90	-	90	10	30	200	no	-	-
6	FTn5v1	negative	640	0	-	90	10	30	200	no	-	-
7	FTn6v1	negative	1540	45	90	90	10	30	400	no	-	-
8	FTp1v1a	positive	1540	90	-	90	10	30	200	no	-	-
9	FTp2v1a	positive	1540	0	-	90	10	30	200	yes	90	200
10	FTn4v1a	negative	1540	90	-	90	10	30	200	no	-	-
11	FTn5v1a	negative	1540	0	-	90	10	30	200	yes	90	200
12	FTp1v2	positive	1540	90	-	135	10	20	200	no	-	-
13	FTp2v2	positive	1540	0	-	135	10	20	200	yes	90	200
14	FTp3v2	positive	1540	45	90	135	10	20	400	no	-	-
15	FTn4v2	negative	1540	90	-	135	10	20	200	no	-	-
16	FTn5v2	negative	1540	0	-	135	10	20	200	yes	90	200
17	FTn6v2	negative	1540	45	90	135	10	20	400	no	-	-
18	FTp2v2a	positive	1540	0	-	135	10	20	200	yes	135	200
19	FTn5v2a	negative	1540	0	-	135	10	20	200	yes	135	200
20	FTp1v3	positive	1540	90	-	90	15	30	200	no	-	-
21	FTp2v3	positive	1540	0	-	90	15	30	200	yes	90	200
22	FTp3v3	positive	1540	45	90	90	15	30	400	no	-	-
23	FTn4v3	negative	1540	90	-	90	15	30	200	no	-	-
24	FTn5v3	negative	1540	0	-	90	15	30	200	yes	90	200
25	FTn6v3	negative	1540	45	90	90	15	30	400	no	-	-
26	FTp1v3a	positive	1540	90	-	90	20	30	200	no	-	-
27	FTp2v3a	positive	1540	0	-	90	20	30	200	yes	90	200
28	FTp3v3a	positive	1540	45	90	90	20	30	400	no	-	-
29	FTn4v3a	negative	1540	90	-	90	20	30	200	no	-	-
30	FTn5v3a	negative	1540	0	-	90	20	30	200	yes	90	200
31	FTn6v3a	negative	1540	45	90	90	20	30	400	no	-	-
32	FTp1v3b	positive	1540	90	-	90	7	30	200	no	-	-
33	FTp1v4	positive	1540	90	-	90	10	40	200	no	-	-
34	FTp2v4	positive	1540	0	-	90	10	40	200	yes	90	200
35	FTp3v4	positive	1540	45	90	90	10	40	400	no	-	-
36	FTn4v4	negative	1540	90	-	90	10	40	200	no	-	-
37	FTn5v4	negative	1540	0	-	90	10	40	200	yes	90	200
38	FTn6v4	negative	1540	45	90	90	10	40	400	no	-	-
39	FTp1v4a	positive	1540	90	-	90	10	50	200	no	-	-
40	FTp2v4a	positive	1540	0	-	90	10	50	200	yes	90	200
41	FTp3v4a	positive	1540	45	90	90	10	50	400	no	-	-
42	FTn4v4a	negative	1540	90	-	90	10	50	200	no	-	-
43	FTn5v4a	negative	1540	0	-	90	10	50	200	yes	90	200

44	FTn6v4a	negative	1540	45	90	90	10	50	400	no	-	-
45	FTp1v5	positive	1540	90	-	90	10	30	300	no	-	-
46	FTp2v5	positive	1540	0	-	90	10	30	120	yes	90	200
47	FTp3v5	positive	1540	30/60	90	90	10	30	693/231	no	-	-
48	FTn4v5	negative	1540	90	-	90	10	30	300	no	-	-
49	FTn5v5	negative	1540	0	-	90	10	30	120	yes	90	200
50	FTn6v5	negative	1540	30/60	90	90	10	30	693/231	no	-	-
51	FTp1v5a	positive	1540	90	-	90	10	30	100	no	-	-
52	FTp2v5a	positive	1540	0	-	90	10	30	120	yes	90	100
53	FTp3v5a	positive	1540	60	60	90	10	30	231	no	-	-
54	FTn4v5a	negative	1540	90	-	90	10	30	100	no	-	-
55	FTn5v5a	negative	1540	0	-	90	10	30	120	yes	90	100
56	FTn6v5a	negative	1540	60	60	90	10	30	231	no	-	-
57	FTp1v5b	positive	1540	90	-	90	10	30	200	yes	90	100
58	FTp2v5b	positive	1540	0	-	90	10	30	120	yes	90	150
59	FTp3v5b	positive	1540	45/90	45	90	10	30	400	no	-	-
60	FTn4v5b	negative	1540	90	-	90	10	30	200	yes	90	100
61	FTn5v5b	negative	1540	0	-	90	10	30	120	yes	90	150
62	FTn6v5b	negative	1540	45/90	45	90	10	30	400	no	-	-

Geometries of numerical models listed in Tab. A.1. are shown below in Fig. A.1-A.62.

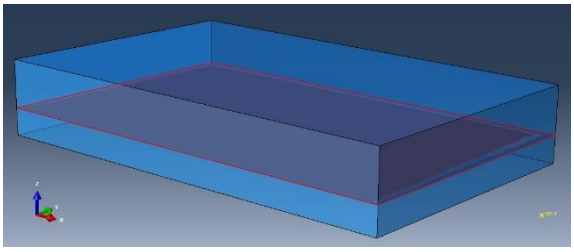


Fig. A.1. Specimen FT0

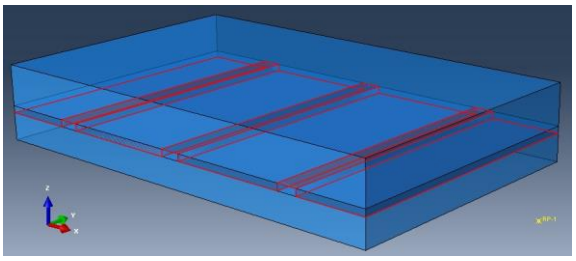


Fig. A.2. Specimen FTp1v1

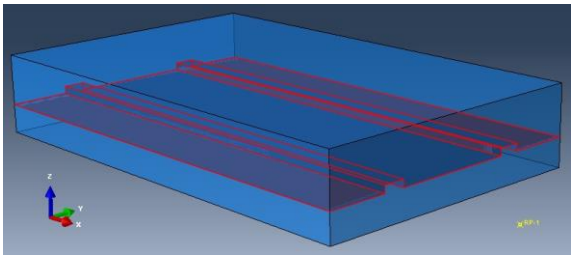


Fig. A.3. Specimen FTp2v1

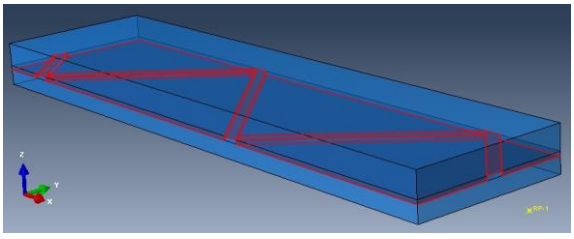


Fig. A.4. Specimen FTp3v1

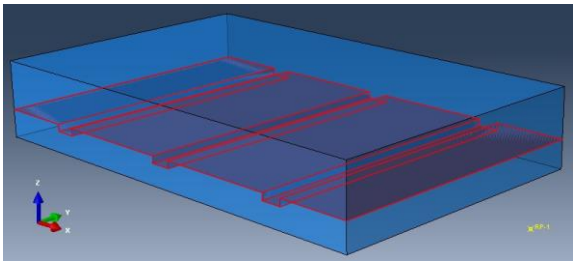


Fig. A.5. Specimen FTn4v1

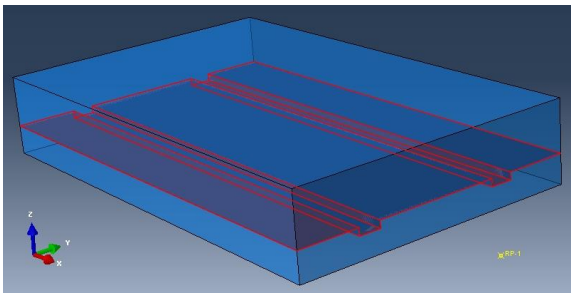


Fig. A.6. Specimen FTn5v1

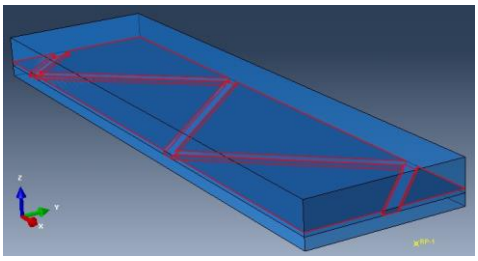


Fig. A.7. Specimen FTn6v1

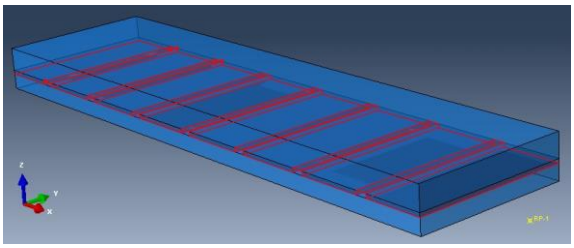


Fig. A.8. Specimen FTp1v1a

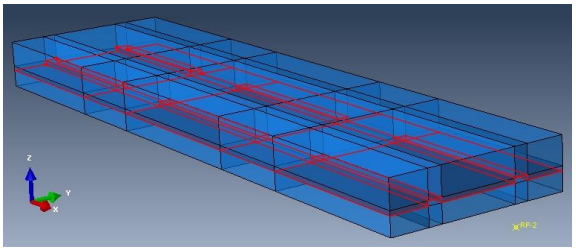


Fig. A.9. Specimen FTp2v1a

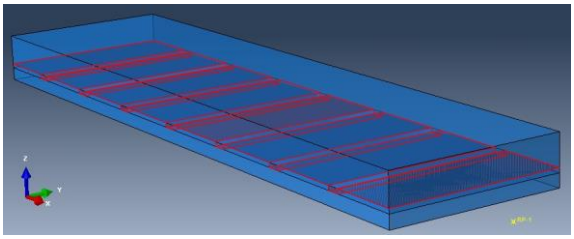


Fig. A.10. Specimen FTn4v1a

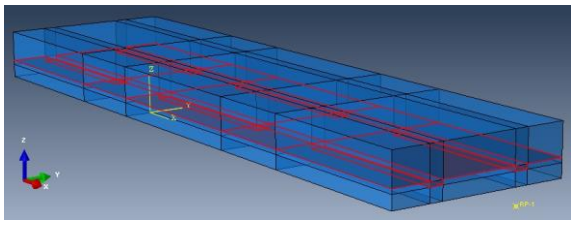


Fig. A.11. Specimen FTn5v1a

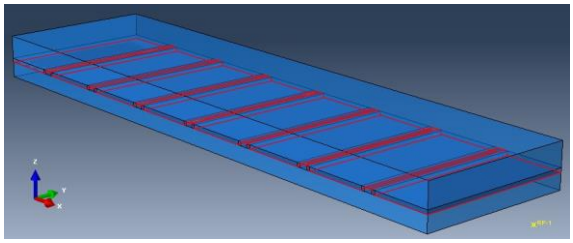


Fig. A.12. Specimen FTp1v2

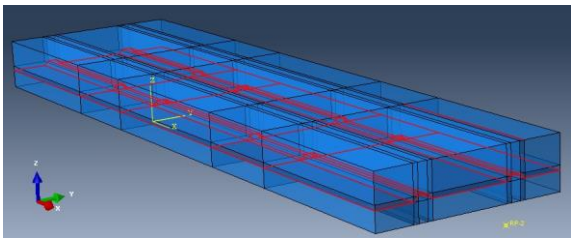


Fig. A.13. Specimen FTp2v2

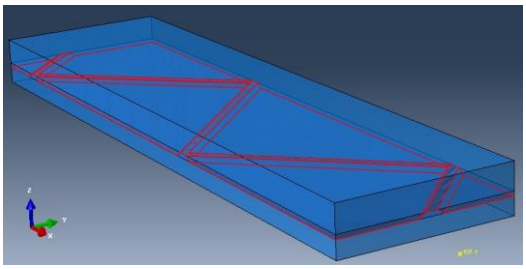


Fig. A.14. Specimen FTp3v2

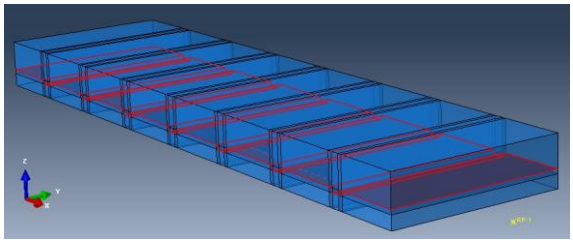


Fig. A.15. Specimen FTn4v2

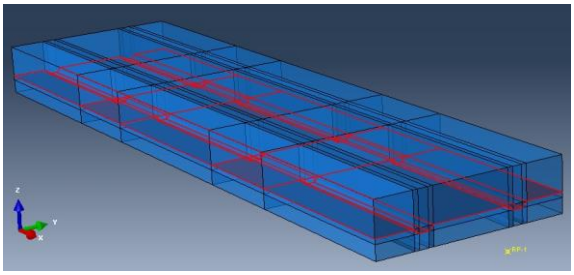


Fig. A.16. Specimen FTn5v2

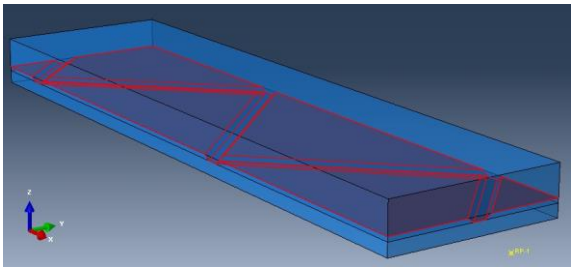


Fig. A.17. Specimen FTn6v2

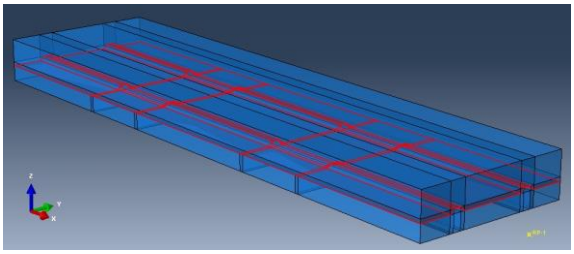


Fig. A.18. Specimen FTp2v2a

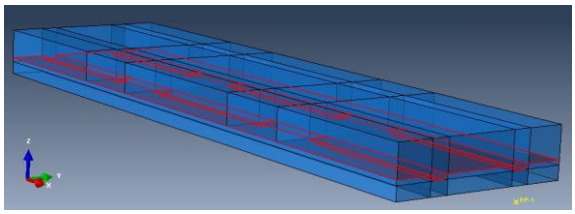


Fig. A.19. Specimen FTn5v2a

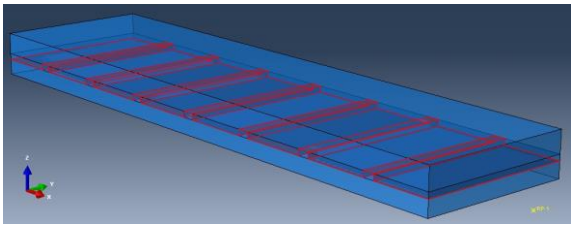


Fig. A.20. Specimen FTp1v3

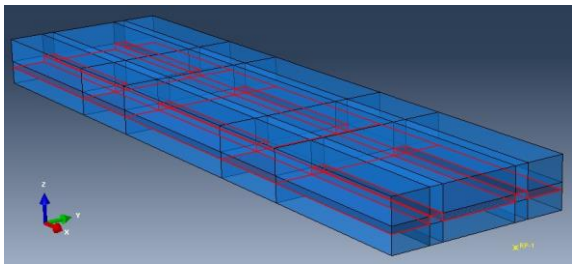


Fig. A.21. Specimen FTp2v3

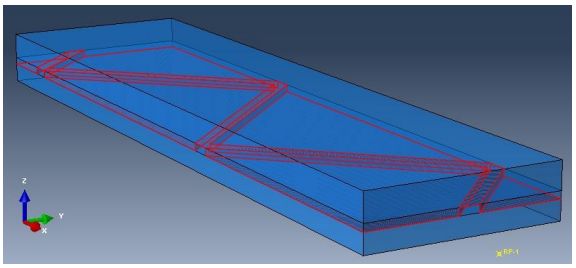


Fig. A.22. Specimen FTp3v3

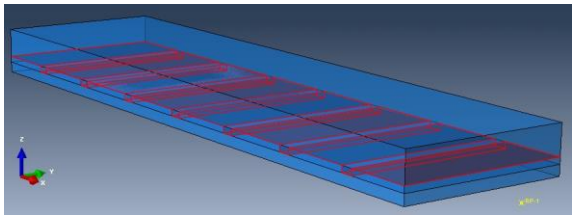


Fig. A.23. Specimen FTn4v3

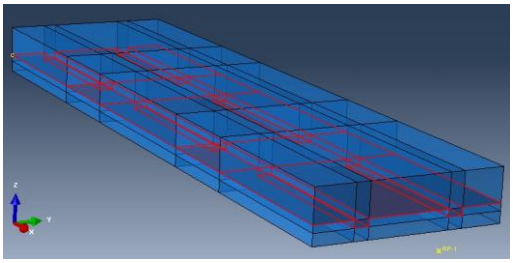


Fig. A.24. Specimen FTn5v3

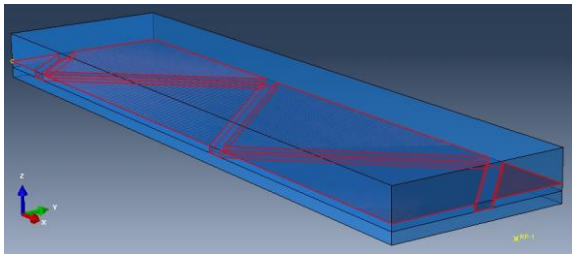


Fig. A.25. Specimen FTn6v3

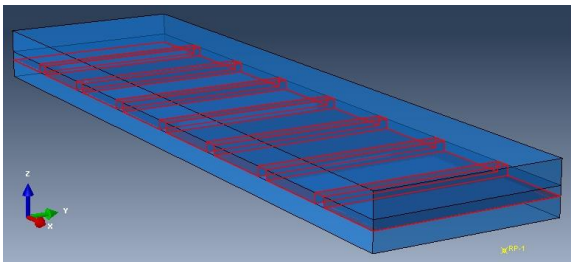


Fig. A.26. Specimen FTp1v3a

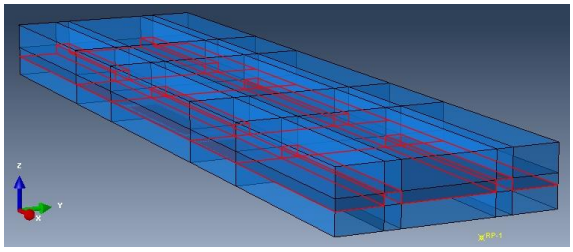


Fig. A.27. Specimen FTp2v3a

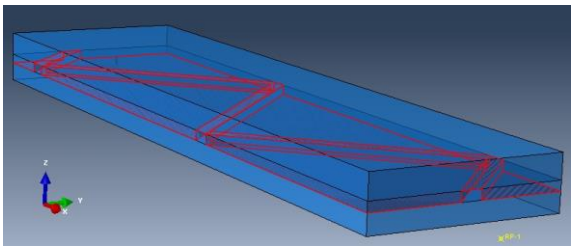


Fig. A.28. Specimen FTp3v3a

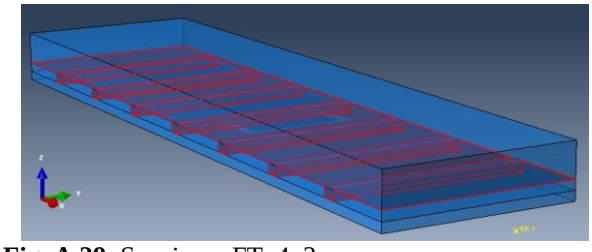


Fig. A.29. Specimen FTn4v3a

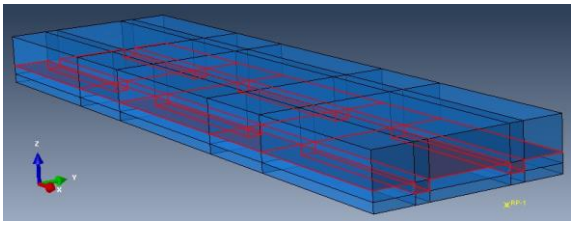


Fig. A.30. Specimen FTn5v3a

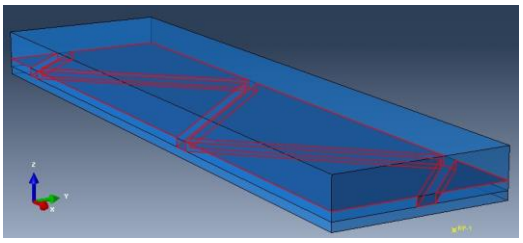


Fig. A.31. Specimen FTn6v3a

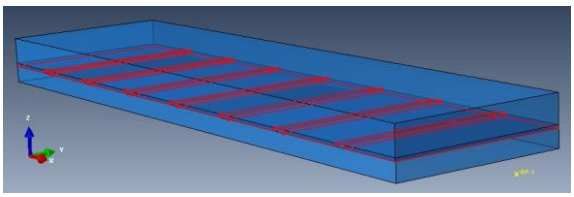


Fig. A.32. Specimen FTp1v3b

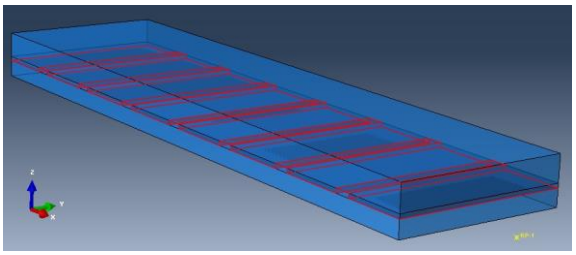


Fig. A.33. Specimen FTp1v4

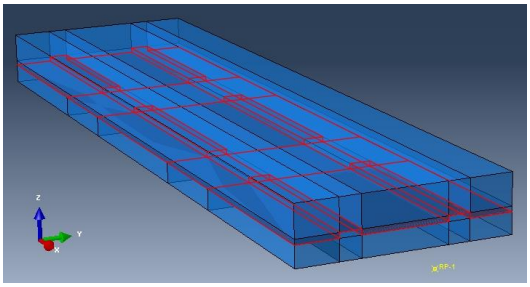


Fig. A.34. Specimen FTp2v4

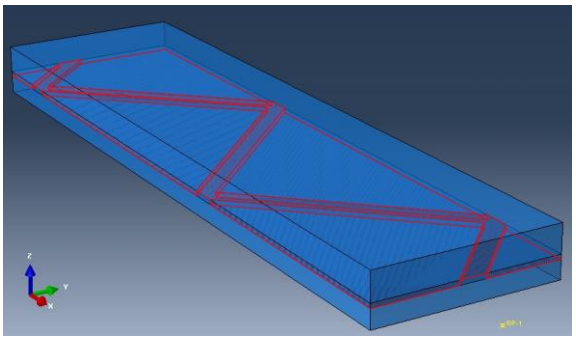


Fig. A.35. Specimen FTp3v4

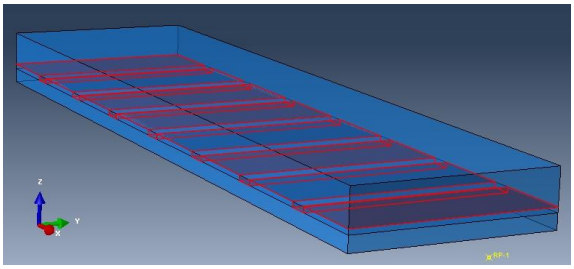


Fig. A.36. Specimen FTn4v4

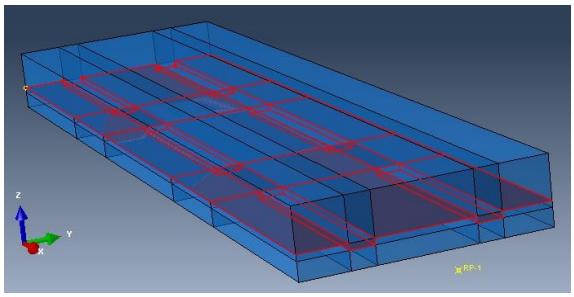


Fig. A.37. Specimen FTn5v4

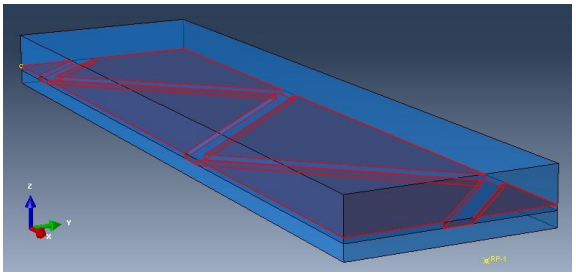


Fig. A.38. Specimen FTn6v4

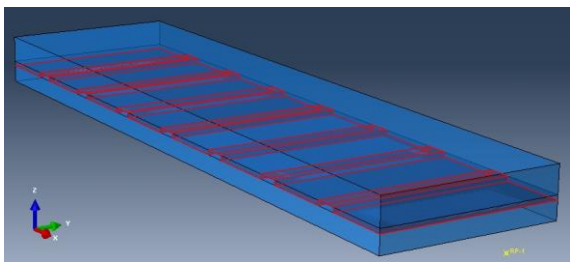


Fig. A.39. Specimen FTp1v4a

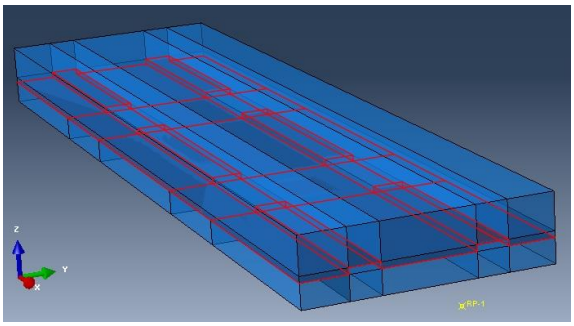


Fig. A.40. Specimen FTp2v4a

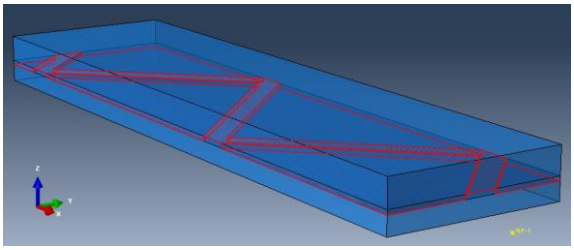


Fig. A.41. Specimen FTp3v4a

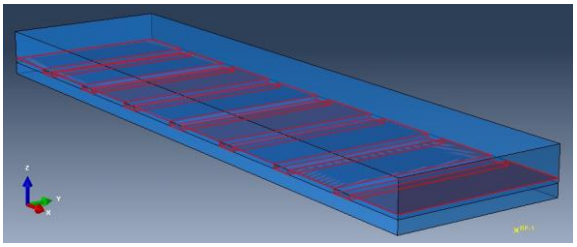


Fig. A.42. Specimen FTn4v4a

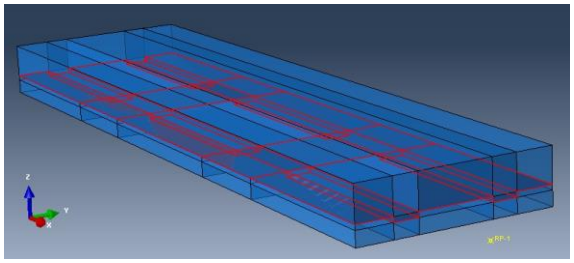


Fig. A.43. Specimen FTn5v4a

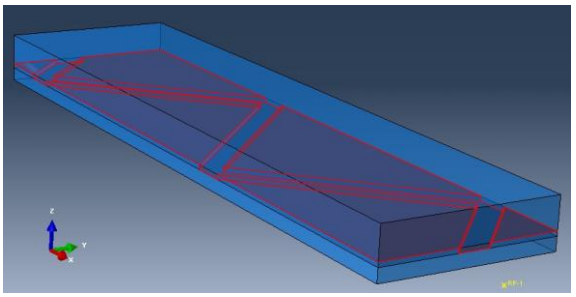


Fig. A.44. Specimen FTn6v4a

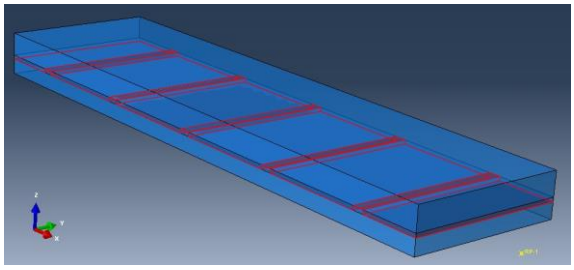


Fig. A.45. Specimen FTp1v5

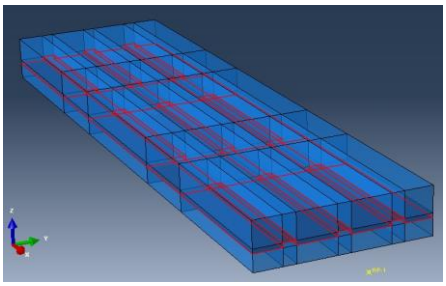


Fig. A.46. Specimen FTp2v5

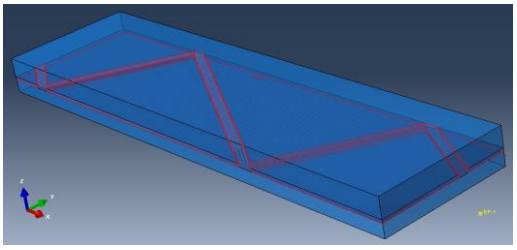


Fig. A.47. Specimen FTp3v5

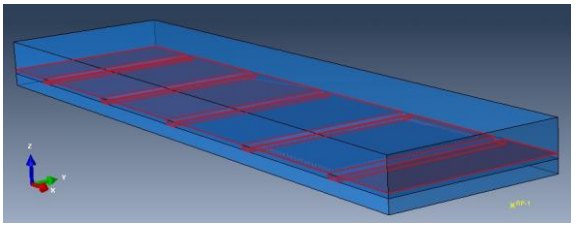


Fig. A.48. Specimen FTn4v5

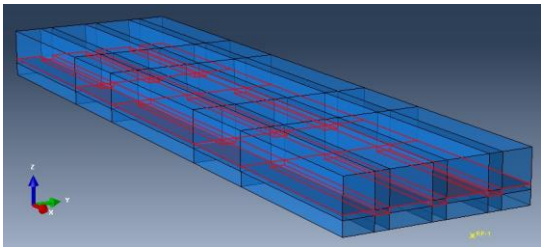


Fig. A.49. Specimen FTn5v5

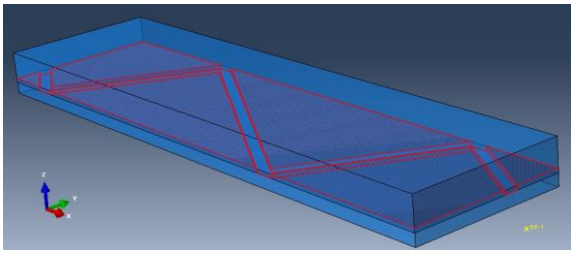


Fig. A.50. Specimen FTn6v5

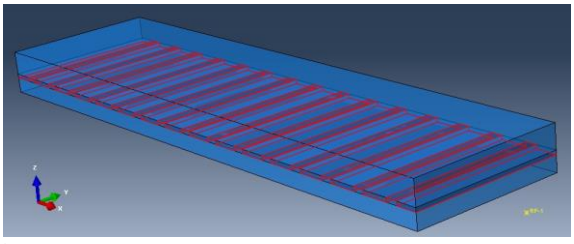


Fig. A.51. Specimen FTp1v5a

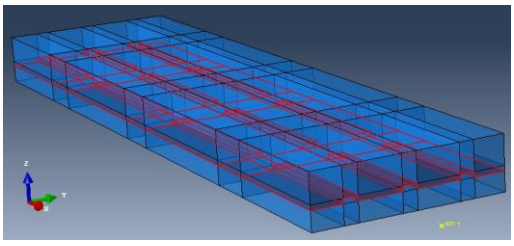


Fig. A.52. Specimen FTp2v5a

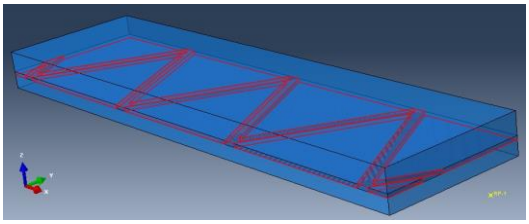


Fig. A.53. Specimen FTp3v5a

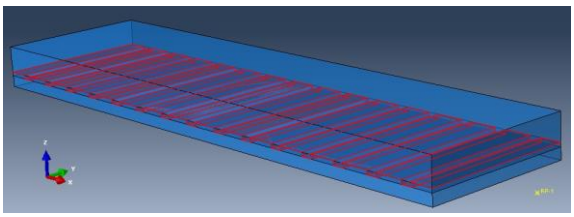


Fig. A.54. Specimen FTn4v5a

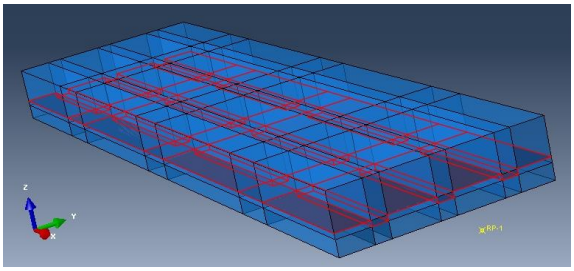


Fig. A.55. Specimen FTn5v5a

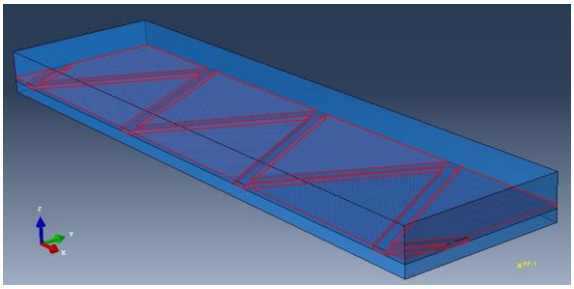


Fig. A.56. Specimen FTn6v5a

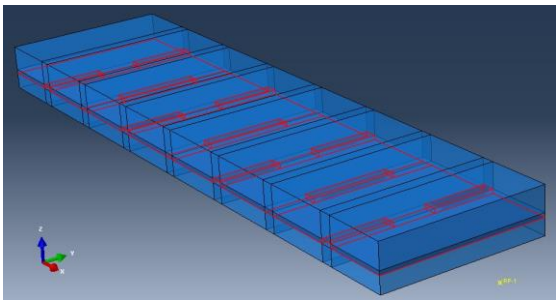


Fig. A.57. Specimen FTp1v5b

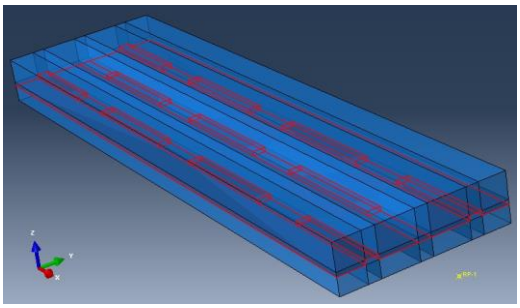


Fig. A.58. Specimen FTp2v5b

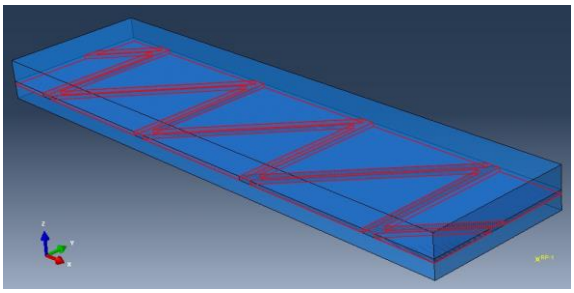


Fig. A.59. Specimen FTp3v5b

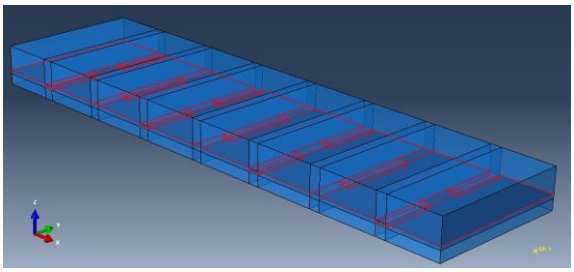


Fig. A.60. Specimen FTn4v5b

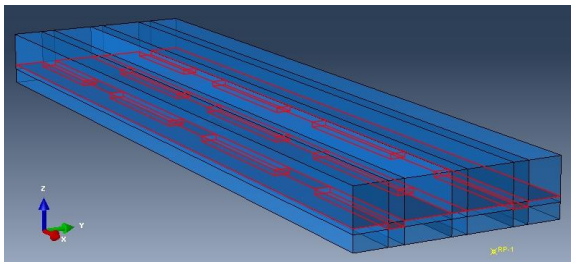


Fig. A.61. Specimen FTn5v5b

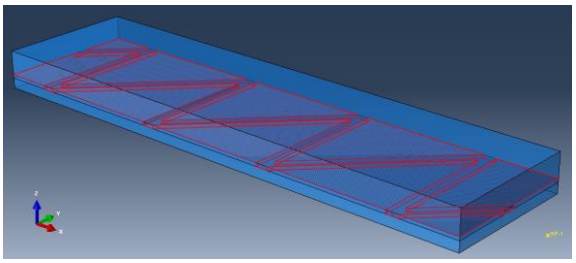


Fig. A.62. Specimen FTn6v5b

Obtained load-bearing capacities of all simulations are summarised in Fig. A.63.

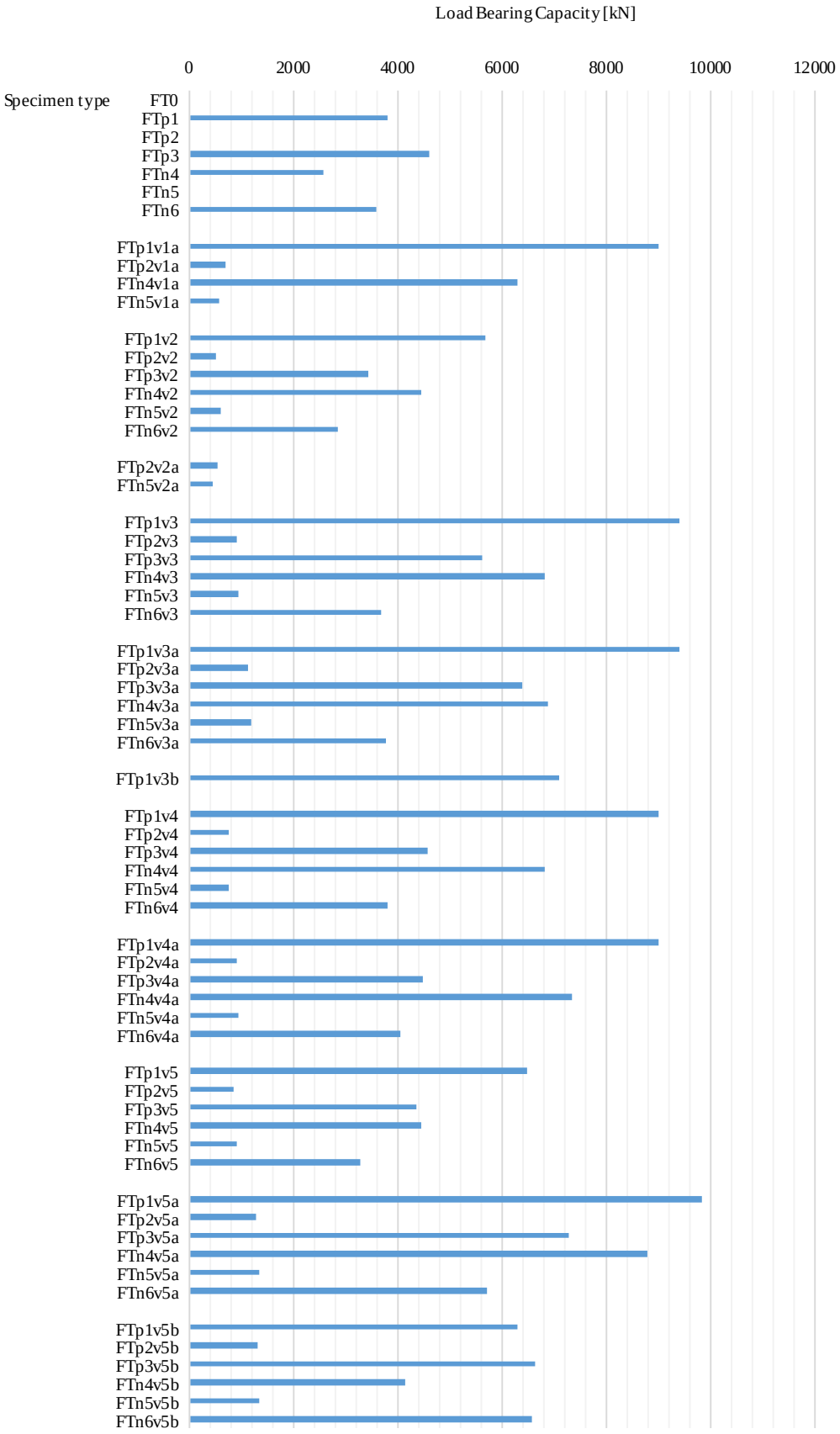


Fig. A.63. Comparison of obtained load-bearing capacities from preliminary numerical simulations of conceptual flat shear connectors.

The conducted simulations had only an aim to compare the performance of the introduced geometries on the flanges of steel profiles and not to investigate the real behaviour. Therefore, in order to perform fast and efficient simulations, simplified material laws for steel and concrete material were applied. In both cases, bi-linear elasto-plastic stress-strain relationships with no distinction on compression or tension behaviours were utilised. The taken grades were S460 for steel and C50/60 for concrete. The taken material laws are shown in Fig. A.64.

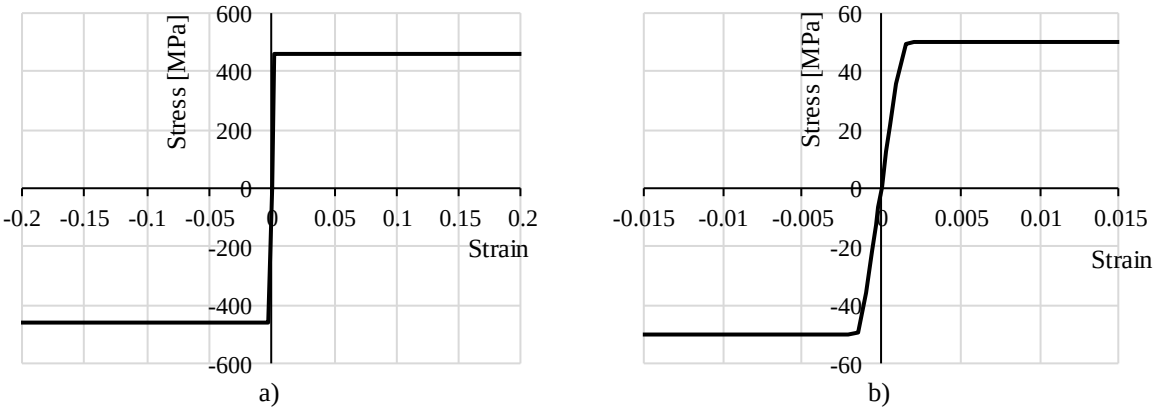


Fig. A.64. Simplified material laws applied for preliminary numerical simulations of conceptual flat shear connectors – a) structural steel and b) concrete.

Load-slip curves of positive variants of for each group of introduced embossments, transversal (FTp1), longitudinal (FTp2) and angled (FTp3), are shown and compared in Fig. A.65.

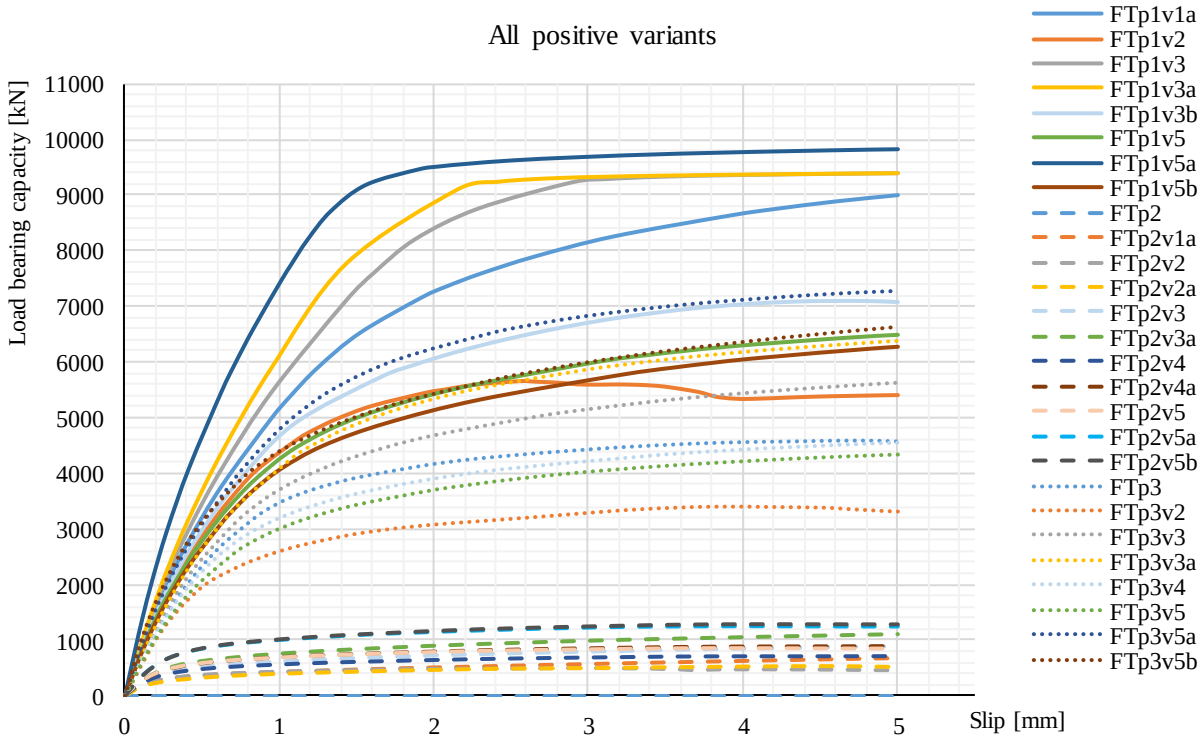


Fig. A.65. Comparison all load-slip curves of positive variants obtained from preliminary numerical simulations of conceptual flat shear connectors.

Annex B – Details on steel-concrete bond investigation

B.1. Small-scale push-out tests

B.1.1. Specimens properties, production and instrumentation

Test specimens for the investigation on plain steel-concrete bond consisted of 10x30x150 mm rectangular steel bar, 150x150x150 mm concrete block and no reinforcement bars have been applied. Detailed geometry of test specimens is shown in Fig. B.1. The specimens were nominally identical and the embedded length was 100 mm. At the bottom of specimens, a recess was placed in order to assure free downward slide of embedded steel bars. Grades of used materials were S235 for steel bars and C35/45 for concrete blocks. All steel bars were cut out from one longer 10x30 mm steel bar. Concrete was grated and delivered by the company BETONS matériaux S.a. Properties of the concrete were confirmed by the certificate of receipt. No individual material tests were performed. All Specimens were tested on the same day at concrete age of 21 days.

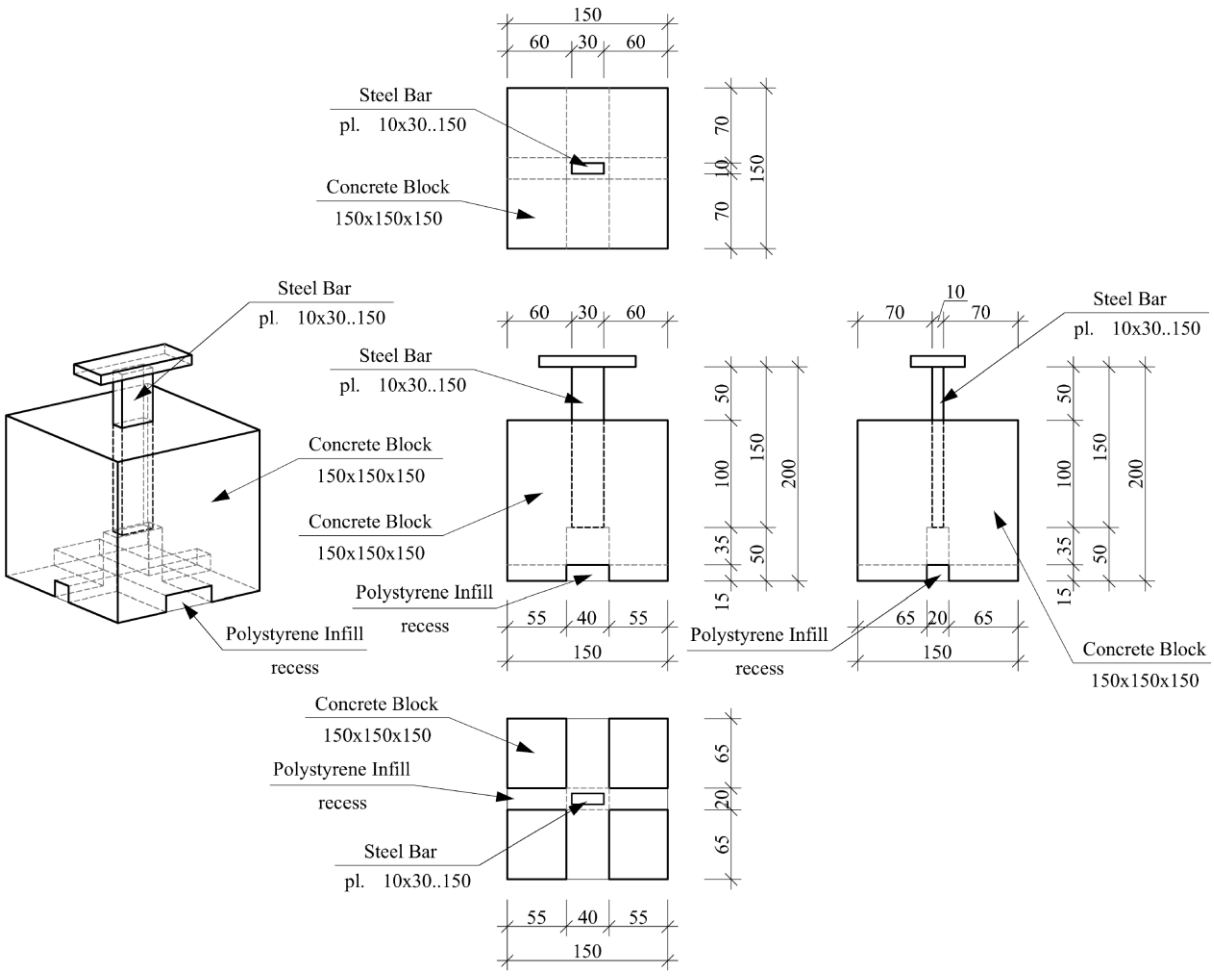
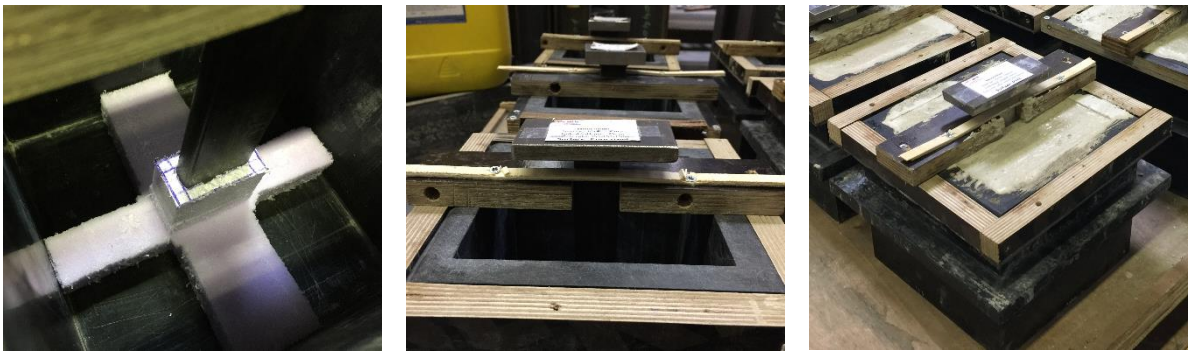


Fig. B.1. Geometry of small-scale cube push-out specimens.

For the fabrication of specimens, plastic moulds for the normative concrete cube specimens were used. A key aspect during fabrication process was to assure verticality of the embedded steel bar, therefore, a two-point fixation was used. At the bottom, a specially designed polystyrene infill was placed, which created a necessary space for the recess after removal and it prevent any movement of the steel bar as shown in Fig. B.2a. On the top, a timber collar around the plastic mould was applied, to which, a crossbeam out of timber was fixed in order to restraint any lateral movement of the steel bar as shown in Fig. B.2b. Thanks to the applied fixation of steel bar, its position during the concreting process stayed unchanged as shown in Fig. B.2c.



a) b) c)

Fig. B.2. Fabrication details of small-scale cube push-out test specimens – a) bottom fixation point detail, b) upper fixation point detail and c) concreted specimens.

Three variants of steel bar surface treatment were considered: (1) untreated, (2) coated with demoulding oil and (3) coated with PTFE spray. The steel bars were not subjected to any cleaning process beforehand. The demoulding oil was the WETCAST FormFluid HP product of company Hebau GmbH and it was profusely applied with a paintbrush approximately 3 hours before concreting. The PTFE spray was the PTFE-Spray product of company Kim-Tec GmbH and it was applied a day before the concreting by using a spryer. After application and drying out, the PTFE-Spray created a solid Teflon cover at the surfaces of steel bars. The thickness of the Teflon cover was approximately 25-40 μm (1-2 layers of spray application). A view on the coated steel parts is given in Fig. B.3.

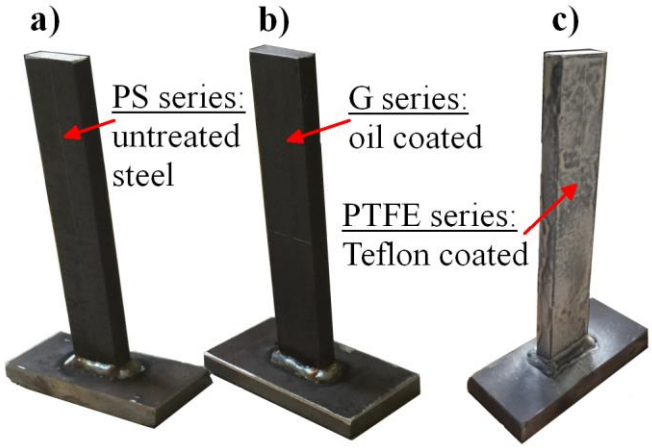


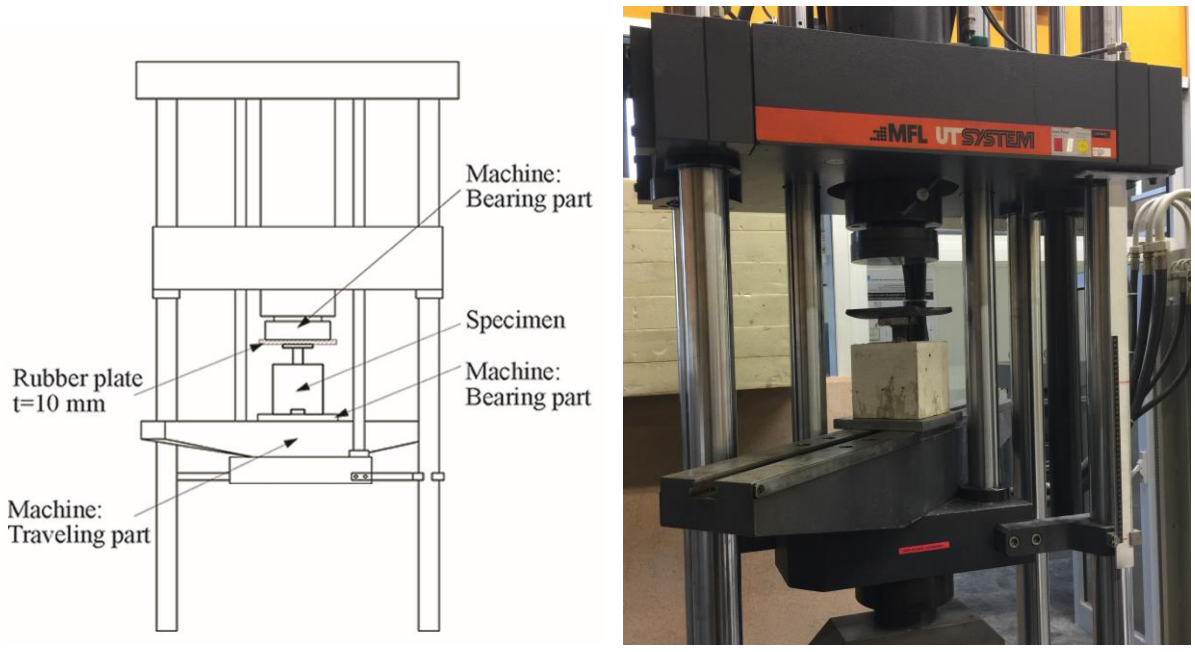
Fig. B.3. Detail of steel bars surface treatment in small-scale cube push-out tests – a) untreated, b) coated with demoulding oil and c) coated with PTFE spray.

An overview of the test specimens prepared for the testing is shown in Fig. B.4.



Fig. B.4. Small-scale cube push-out specimens.

The experimental tests were performed in the laboratory of the University of Luxembourg. The test layout was identical in each case and it is shown in Fig. B.5. The Zwick Roell Machine of 400 kN nominal capacity has been used (Type 065146.100, Series No. 807289/02). The hydraulic testing machine allowed positioning of the specimen between two bearing plates, where the load was imposed by the movement of the bottom traveling part and the specimens have been pushed against the top bearing part. Between the top bearing plate and the specimen, an elastomer plate has been placed to assure uniformly distributed pressure on the steel bar. The load was applied continuously in the shape of a ramp in the displacement control mode. The displacement speed at the beginning of the test was 0.2 mm/min (machine travel). After reaching the load of 20kN, the speed was increased to 0.5 mm/min. The displacement of the bottom traveling part of the machine and indications from the force sensor integrated in the machine were recorded. Due to high rigidity of the testing machine and small scale of the specimen, no external measurement equipment was placed. The tests have been stopped when the force dropped by approximately 10% after reaching the peak point.



a) b)

Fig. B.5. Test setup of small-scale push-out tests – a) scheme and b) testing machine.

B.1.2. Test results

The recorded displacement and force from the testing machine were set as the relative slip between the steel and concrete parts and corresponding load, respectively. However, the raw recorded data contained an error coming from the loss of stiffness due to machine displacement and deformation of the rubber plate. In order to subtract this error, a compliance test with only the rubber plate placed between the bearing plates was performed. In the result, an error correction function was able to be derived as a regression of the recorded load-displacement curve from compliance tests. The correction displacement, subtracted later from each measured displacement in SSCPOT with corresponding load level, is described in a polynomial function and it is given in Eq. B.1. Where, as "x", the corresponding load level at each measured displacement point was placed.

$$\delta_{0,i}(F_i) = 0.031591 + 0.148051x - 0.03413x^2 + 3.926E^{-3}x^3 - 2.5E^{-4}x^4 + 8.93E^{-6}x^5 - 1.86E^{-7}x^6 + 2.07E^{-9}x^7 - 9.54E^{-12}x^8 \quad \text{(B.1)}$$

Finally, the relative slip between steel and concrete part is evaluated according to Eq. B.2 given below. Where $\delta_{slip,i}$ is the real slip developed in the specimens, $\delta_{md,i}$ is the measured displacement of the travelling part of the test machine and $\delta_{0,i}(F_i)$ is the regression function, which removes an offset of the test machine from the measurement.

$$\delta_{slip,i} = \delta_{md,i} - \delta_{0,i}(F_i) \quad \text{(B.2)}$$

The obtained load-slip curves are shown in Fig. 5.12 of Section 5.3. The extracted data from the aforementioned diagrams is given in Table B.1.

Table B.1.
Small-scale push-out test results summary.

Value	Unit	Untreated surface				Oil-treated surface				Teflon spray-treated surface			
		PS1	PS2	PS3	mean	G1	G2	G3	mean	PTFE1	PTFE2	PTFE3	mean
$\tau_{R,surf}$	[MPa]	2.29	2.57	3.09	2.65	1.14	0.69	0.86	0.90	1.30	1.71	1.40	1.47
F_u	[kN]	18.32	20.58	24.74	21.21	9.12	5.53	6.89	7.18	10.39	13.65	11.18	11.74
F_{adh}	[kN]	9.79	13.10	16.22	13.04	2.24	1.51	1.48	1.74	10.39	13.65	11.18	11.74
δ_u	[mm]	3.20	3.27	2.79	3.09	2.15	1.47	2.19	1.94	0.92	1.00	1.60	1.18
δ_{adh}	[mm]	1.43	1.75	1.66	1.61	0.33	0.12	0.32	0.26	0.92	1.00	1.60	1.18
δ_1	[mm]	2.53	2.79	2.36	2.56	1.64	1.03	1.53	1.40	0.83	0.91	1.48	1.07
δ_2	[mm]	4.22	4.14	3.35	3.90	2.80	2.64	2.79	2.74	0.93	1.02	1.62	1.19
$\frac{\delta_2 - \delta_u}{\delta_u - \delta_1}$	[-]	1.52	1.80	1.29	1.53	1.27	2.64	0.92	1.61	0.13	0.17	0.14	0.15
K_{adh}	[kN/mm]	6.85	7.44	9.76	8.02	6.86	13.42	4.64	8.31	11.31	13.59	6.97	10.62
K_1	[kN/mm]	6.19	7.16	7.42	6.92	5.34	4.89	3.99	4.74	11.31	13.59	5.96	10.29

$\tau_{R,surf}$ shear strength of bond evaluated according to Eq. B.3.
F_u ultimate load
F_{adh} load level at adhesion mechanism failure
δ_u relative slip corresponding to ultimate load level
δ_{adh} relative slip corresponding to adhesion failure load level
δ_1 relative slip at 0.9 F_u, before failure

δ_2 relative slip at 0.9 F_u, after failure
K_{adh} stiffness measured at δ_{adh}
K_1 stiffness measured at relative slip level of 1 mm (for PTFE, one specimen measured at δ_u)

The observed failure pattern in each specimen was identical. The steel bar slid through the concrete block without any visible damage of concrete. A characteristic subtle noise in all specimens was present at the point of adhesion failure.

The resultant shear stresses were evaluated by assuming a uniform distribution over the contact area. Therefore, a fundamental relation between force and area was used as shown in Eq. B.3.

$$\tau_{R,surf} = \frac{F_u}{A_{embd}} \left[\frac{kN}{cm^2}\right] \tag{B.3}$$

The resultant shear stresses are shown in bar diagram in Fig. B.6a. The statistical evaluation of test results is shown in Fig. B.6b.

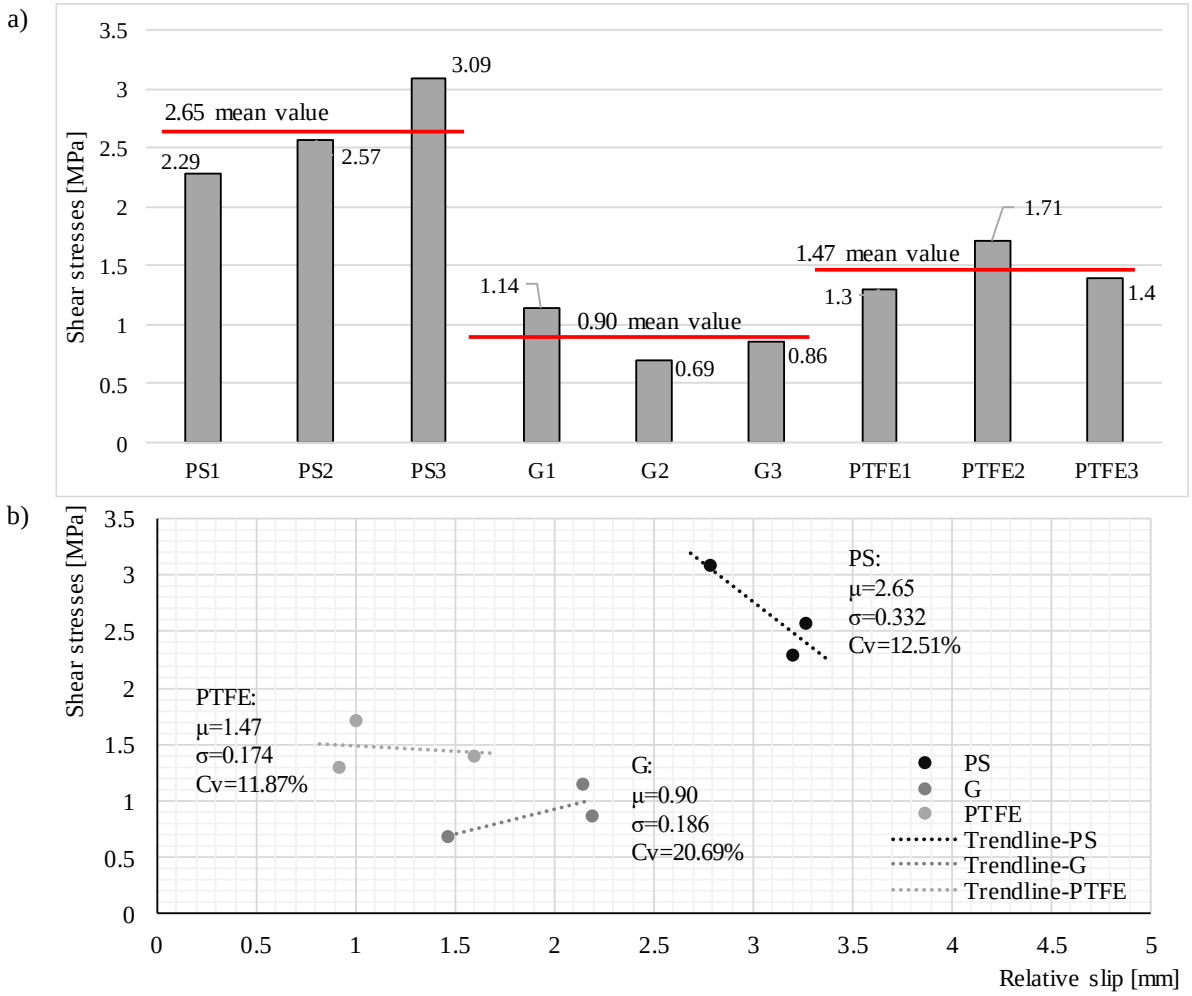


Fig. B.6. Shear stresses obtained from the small-scale push-out tests – a) bar diagram and b) scatter diagram with statistical evaluation.

B.2. Details on the applied demoulding oil

A bond-eliminating product used at the steel-concrete interface for test series G was an anti-adhesive release agent of company HEBAU GmbH, see Fig. B.7. The technical name of the high-performance release agent is WETCAST – FormFluid HP and it has an oil structure. The word 'WETCAST' means that the product is especially foreseen for the fresh concrete mixtures with high slump. That means, it is wash-resistant and it sustains on the covered solid surfaces. The applicability of the release agent covers nearly all types of surfaces, including polyurethane, latex, rubber, silicone, wood or steel and can be used with all types of concrete mixtures. The described product is widely used in the prefabricated decorative concrete industry according to its high demoulding performance. The product manufacturer certifies that FormFluid HP can be used to produce a consistent level of the high-quality film at the interface regardless of the concrete mixtures and mould material. The product is available in different containers, from 1L bottle up to 1000L IBC.

During the application process, it was noticed that the used anti-adhesive agent could be easily applied by a sprayer or by a brush. A high efficiency of the product (approximately 30-100 sqm/l) was confirmed. The product has full demoulding properties directly after application and no drying time has to be respected. Moreover, according to the manufacturer's specification, when coated surface will be sustained for drying, the release agent indicates the same high performance – up to the 72 hours. From the observations, it can be concluded that no chemical aggression against steel or concrete surface occurred and good quality of concrete surface was obtained. The obtained test results indicated that FormFluid HP gave similar values of the shear bond strength at the steel-concrete interface. Moreover, the debonding failure due to shear occurred in the close range of slip.

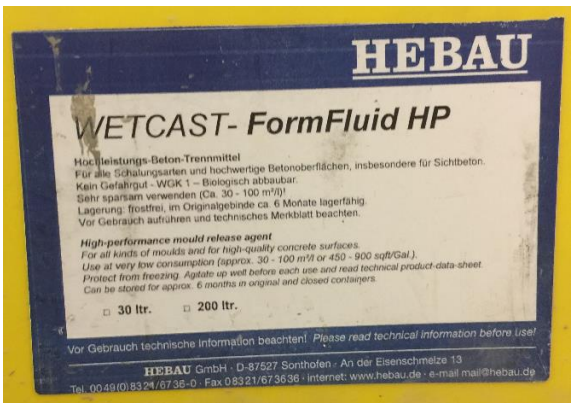


Fig. B.7. Label of the applied demoulding oil and logo of the producer.

B.3. Numerical simulations

B.3.1. Simplified numerical model of the steel-concrete bond

The developed simplified model of bond is based on linear traction separation law, where the elastic traction properties define the behaviour until the failure as given in Eq. B.4-B.5. The damage initiation point is defined by maximum stress criterion and the damage evolution consisted of linear branch converging to zero at the predefined value of total plastic slip [174]. In Eq. B.4, the relation between strains at the interface ε and respective displacement δ is given, where T_0 refers to the initial thickness of the interface. Value of T_0 is by default taken by 1.0 regardless of the actual thickness so the nominal strains and corresponding separations are equal. The indexes "n, s, t" describe respective normal and two shear directions. For uncoupled elastic definition, off-diagonal terms of elastic matrix in Eq. B.5 are set to zero.

$$\varepsilon_n = \frac{\delta_n}{T_0}, \qquad \varepsilon_s = \frac{\delta_s}{T_0}, \qquad \varepsilon_t = \frac{\delta_t}{T_0} \tag{B.4}$$

$$\boldsymbol{t} = \begin{Bmatrix} t_n \\ t_s \\ t_t \end{Bmatrix} = \begin{bmatrix} E_{nn} & E_{ns} & E_{nt} \\ E_{ns} & E_{ss} & E_{st} \\ E_{nt} & E_{st} & E_{tt} \end{bmatrix} \begin{Bmatrix} \varepsilon_n \\ \varepsilon_s \\ \varepsilon_t \end{Bmatrix} = \boldsymbol{E\varepsilon} \tag{B.5}$$

Taking into account that $T_0 = 1.0$, the elastic material law can be described in the form of separation and the traction-separation material law is obtained as shown in Fig. B.8 below.

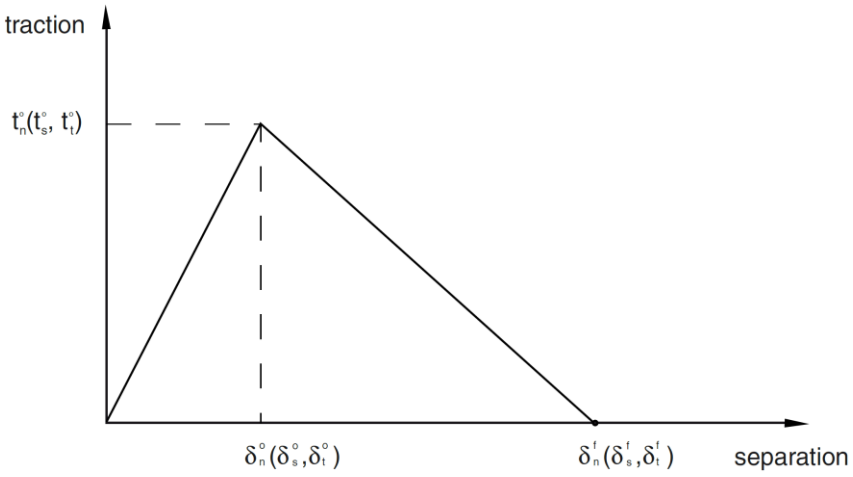


Fig. B.8. Typical linear traction-separation response [174].

The damage initiation point defined as the maximum nominal stress is given in Eq. B.6. The damage will occur when stresses in one of the considered directions will reach the defined strength but they are not considered separately. A more complex model incorporating interaction between different directions is possible and it is described in Section 5.5.3. The Macaulay bracket (‹›) applied to the normal direction specifies that a pure compressive deformation does not initiate damage.

$$max\left\{\frac{\langle t_n\rangle}{t_n^0}, \quad \frac{t_s}{t_s^0}, \quad \frac{t_t}{t_t^0},\right\} = 1 \tag{B.6}$$

When the damage initiation point is reached the stiffness of the cohesive connection is reducing according to the damage variable D. A scalar damage variable D varies from 0 to 1. The variable D, represent overall damage and it includes all the combined effects. The stress components affected by the development of the damage are described in Eq. B.7.

$$\begin{aligned} t_n &= \begin{cases} (1-D)\bar{t_n}, & \bar{t_n} \geq 0 \\ \bar{t_n}, & \bar{t_n} < 0 \end{cases} \\ t_s &= (1-D)\bar{t_s} \\ t_t &= (1-D)\bar{t_t} \end{aligned} \tag{B.7}$$

Applied linear damage evolution in terms of displacement is shown in Fig. B.9 and the damage variable is described by Eq. B.9, where the effective displacement is defined in Eq. B.8. From Fig. B.9, it can be observed that area under the traction-separation diagram is equal to the fracture energy G^c and the damage evolution can be also described in terms of energies. The explanation of variables from Eq. B.9 are shown in Fig. B.9, where δ_m^{max} is the maximum separation from the loading history, therefore, assuming continuously increasing separation, is the considered state of the separation.

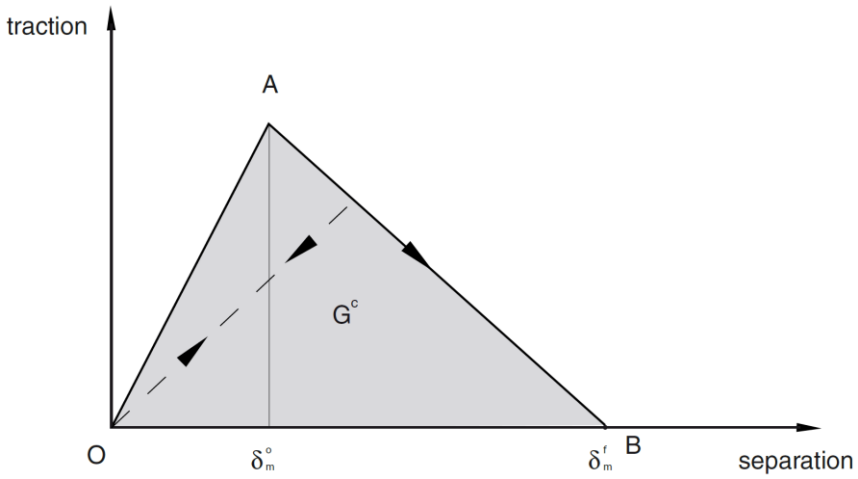


Fig. B.9. Linear damage evolution applied in the simplified numerical model of bond [174].

$$\delta_m = \sqrt{\langle\delta_n\rangle^2 + {\delta_s}^2 + {\delta_t}^2} \tag{B.8}$$

$$D = \frac{\delta_m^f(\delta_m^{max} - \delta_m^0)}{\delta_m^{max}\left(\delta_m^f - \delta_m^0\right)} \tag{B.9}$$

In the development of damage, a viscous regularisation can be defined, which helps to prevent numerical convergence issues and allows defining specific damping behaviour of the cohesive behaviour, which permits stresses to be outside the limits of defined traction-separation law. When

viscous regularization is defined, the variable of damage scalar degradation changes to D_v and it is then defined as given in Eq. B.10-B.11. The viscosity parameter μ represents the relaxation time of the viscous system.

$$\dot{D_v} = \frac{1}{\mu}(D - D_v) \tag{B.10}$$

$$\boldsymbol{t} = (1 - \boldsymbol{D_v})\bar{\boldsymbol{t}} \tag{B.11}$$

The traction separation law can successfully reflect the chemical adhesion and surface roughness of the bond force transferring mechanisms but calibration is required. The above-described traction-separation law can be applied as interaction property or cohesive material at the interface. For the simplified numerical model of bond, the interaction approach was applied. The effects of Coulomb friction are included by applying tangential behaviour interface properties.

B.3.2. Numerical simulation of the small-scale push-out tests

The numerical simulations were performed in 3DS Simulia Abaqus® software [174]. The modelled geometry reflected geometry of the small-scale push-out test specimens shown in Fig. B.1. The applied material laws were based on the fib Model Code 2010 [62] and EN 1993-1-1 [55] for concrete and steel parts, respectively. For the steel part, an elasto-plastic linear material law was implemented, where for the concrete part, the Concrete Damaged Plasticity (CDP) model was employed. In the CDP material law, the compression damage was allowed up to 31%, where for the tension damage it was extended up to 99%. The following plasticity parameters were used to define the plastic behaviour of concrete: Dilation Angle=38°, Eccentricity=0.1, fb0/fc0=1.16, Kc=0.667 and Viscosity Parameter=2.5E-5. For both parts, hexahedral C3D8R finite elements (FE) with reduced integration were used. The mesh size of steel part was approximately 3mm. The concrete part was meshed with 3mm size only in the contact area and, for the outer regions, a 7 mm mesh was used. The size of the mesh in the contact zone required sufficiently small elements [186]. An overview of the numerical model is given in Fig. B.10.

The interaction between steel and concrete was defined as a standard surface-to-surface contact with the finite sliding formulation and node-to-surface discretization method [174]. An important aspect in the contact formulation was the correct assignment of the master and slave surfaces. Cohesive contact properties are applied to the slave surface and the master surface act as the reference points. In this case, the slave surface was defined on the sliding steel part and concrete contact surfaces had the master definition. The contact interaction properties consisted of four groups of mechanical behaviours: Tangential, Normal, Cohesive and Damage. The tangential behaviour defined the Coulomb friction mechanisms and the penalty formulation was implemented with the specified friction coefficients for each series of specimens, see Table B.2. The normal behaviour defined the pressure-overclosure relation and the hard contact formulation was employed, which is characteristic for the solid elements and

prevent the overlapping of solid bodies. The cohesive behaviour defined steel-concrete bond properties at the interface, where the uncoupled stiffness matrix was defined and the input data is given in Table B.2. Damage behaviour defined the damage initiation point and damage evolution of the cohesive interaction. The damage criterion was defined with the maximum nominal stress criterion, as defined in Eq. B.6. The damage evolution option allowed to define the post-failure behaviour of the cohesive interaction. For this option, the linear stiffness degradation in function of maximum plastic displacement was specified. No mix-mode ratios were defined. For the smoother computational process, a small stabilization coefficient was defined for all the specimens with value of 0.001 s, which helps to obtain a convergence with Abaqus/Standard solver and did not affect the brittle behaviour of bond. The defined contact properties are summarised in Table B.2.

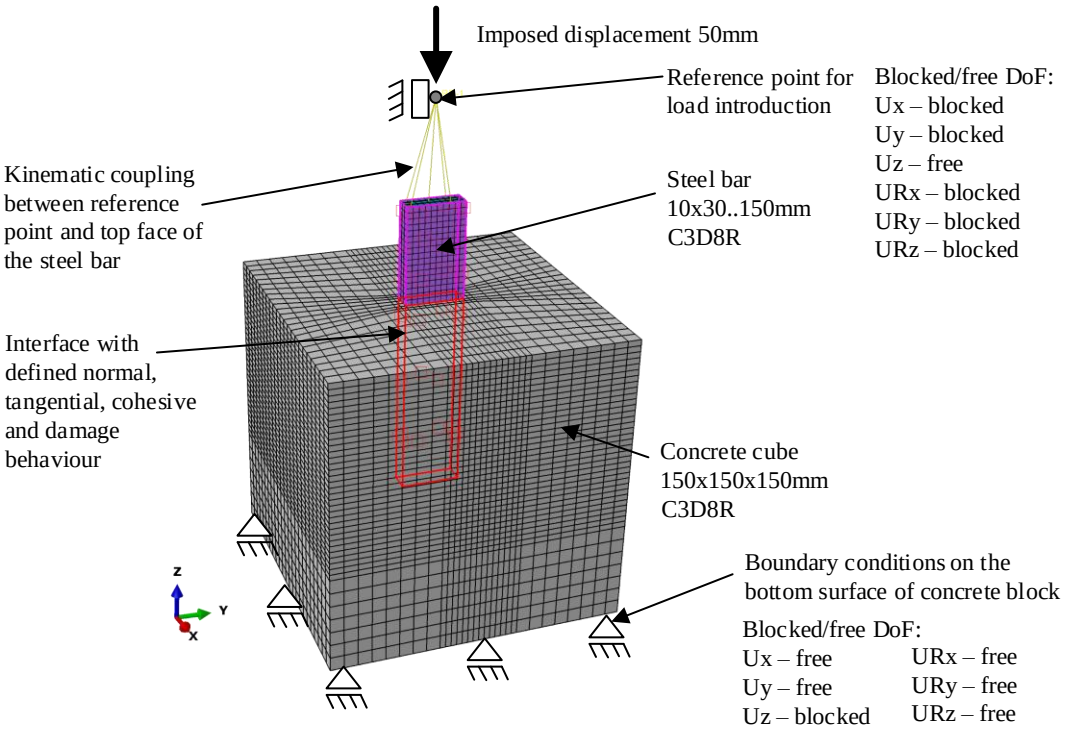


Fig. B.10. Small-scale push-out specimen layout for the FE simulation.

Table B.2.
Contact interaction properties applied in the FE simulations of small-scale push-out tests.

Property	Symbol	Unit	Specimen		
			PS	G	PTFE
Friction coefficient	μ_f	[-]	0.30	0.15	0.08
*Stiffness in normal direction	K_{nn}	[MPa/mm]	0	0	0
Stiffness in tangential shear directions	$K_{ss/tt}$	[MPa/mm]	0.90	0.48	1.25
**Maximum nominal stress in normal direction	t_{nn}	[MPa]	1.00	1.00	1.00
Maximum nominal stress in tangential shear directions	$t_{ss/tt}$	[MPa]	2.62	0.89	1.48
Damage evolution type			Displacement		
Damage character			Linear		
Total plastic displacement	δ_m^f	[mm]	5	5.36	0.05
Viscosity parameter	μ	[s]	0.001	0.001	0.001

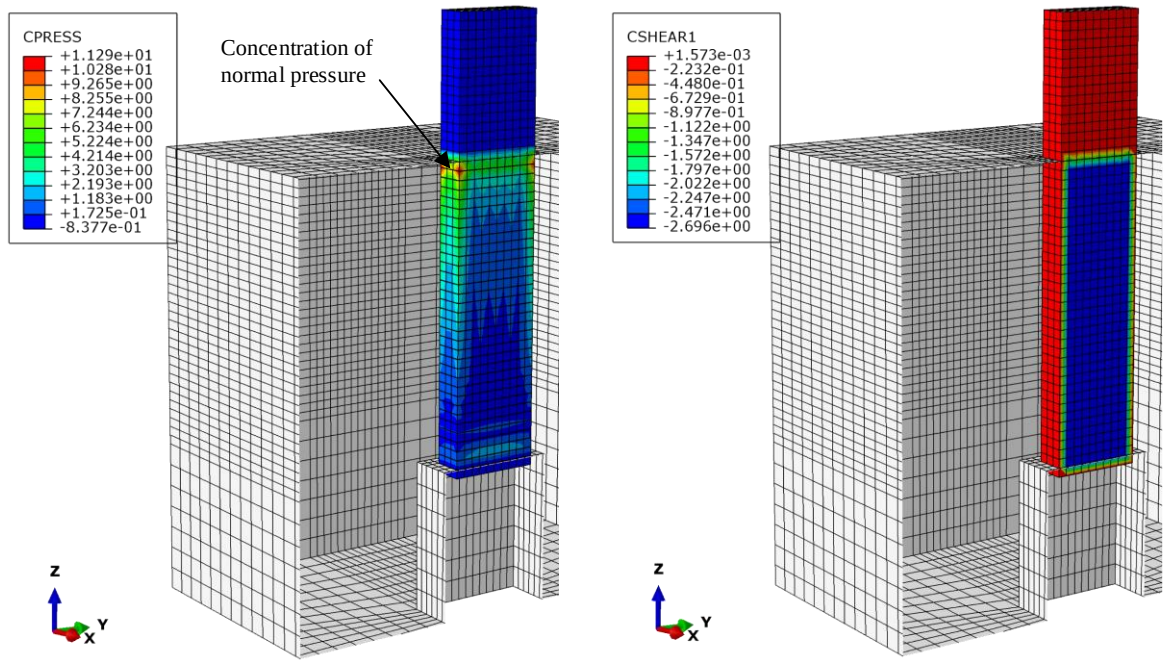
* For stiffness in normal direction value 0 was taken in order to disable the cohesive behaviour in this direction.
** Due to disabled cohesive behaviour in normal direction, a unit value of stress input was taken.

The described numerical models were strongly sensitive to the applied cohesive properties, the damage softening character, the mesh size and the size of the increments used in the analysis step. The steps taken respected sufficiently small increments in order to allow for the accurate analysis of the development of the cohesive stresses and damage evolution. The minimum and maximum increments were defined as 1E-15 and 0.002 respectively.

B.3.3. Results and comparison to the experimental data

The numerical models were calibrated to reach the mean values of shear strength from each series of tests and corresponding mean displacement. The load-slip curves are shown in Fig. 5.13 of Section 5.3.2.

The influence of the Coulomb friction in the force transfer mechanism of plain steel-concrete bond is directly related on the amount of the developed lateral pressure at the interface. From the conducted simulations, it can be observed that even for a small eccentricity between imposed load and reaction forces due to the applied recess, the lateral pressure develops and contributes to the resultant shear strength. In Fig. B.11, a view on the distribution of normal pressure and shear stresses at the steel-concrete interface is given.



a) b)

Fig. B.11. Impact of the normal pressure developed during simulation of PS series on the bond strength – a) contact pressure and b) shear stresses in YZ plane.

From numerical simulations, it can be observed that steel-concrete bond can be numerically reproduced with a high accuracy and with the desired failure behaviour. However, the bond behaviour is very sensitive to the defined parameters.

B.4. Summary and comparison to the literature data

A summary table of the bond strength values with relation to different specimen conditions is given in Table B.3. The aforementioned table is based on literature review and conducted tests.

Table B.3.
Steel-concrete bond – experimental and literature data.

No	Specimen and steel section	Concrete	Surface treatment	Confinement	Embedded length	Effective area	Bond strength
SSCPOT							
1.	3x PS Steel bar 10x30x150 mm	C35/45 cube 150x150x150 mm Age: 21 days	No	Concrete cover: c_x=70 mm c_y=60 mm	100 mm	80 cm^2	2.65 MPa
2.	3x G Steel bar 10x30x150 mm	C35/45 cube 150x150x150 mm Age: 21 days	Anti-adhesive release agent (demoulding oil)	Concrete cover: c_x=70 mm c_y=60 mm	100 mm	80 cm^2	0.90 MPa
3.	3x PTFE Steel bar 10x30x150 mm	C35/45 cube 150x150x150 mm Age: 21 days	Teflon spray cover approx. 25-40 µm	Concrete cover: c_x=70 mm c_y=60 mm	100 mm	80 cm^2	1.47 MPa
CoPOT							
4.	2x 0v2 HEB 120 L=550 mm	C25/30 Block 340x1000x450 mm Age: 28 days	Anti-adhesive release agent (demoulding oil)	Concrete cover: cx=440mm, cy=110mm Stirrups: Ø12/117	350 mm	2401 cm^2	0.87 MPa
Roik et al. [162]							
*5.	29x S1-QR-2D Steel tube rectangular D140 H=280 mm	Tube infill f_c = 72.4 MPa Age: 598 days	No information, Damaged interface, specimens tested before	External tube cover, rectangular	280 mm	1162 cm^2	* 1.01 MPa
*6.	4x S1-QR-D Steel tube rectangular D140 H=140 mm	Tube infill f_c = 72.4 MPa Age: 598 days	No information, Damaged interface, specimens tested before	External tube cover, rectangular	140 mm	581 cm^2	* 0.82 MPa
*7.	20x S1-RR-2D Steel tube circular Ø120 H=240 mm	Tube infill f_c = 72.4 MPa Age: 598 days	No information, Damaged interface, specimens tested before	External tube cover, circular	240 mm	1058 cm^2	* 1.03 MPa
*8.	4x S1-RR-D Steel tube circular Ø120 H=120 mm	Tube infill f_c = 72.4 MPa Age: 598 days	No information, Damaged interface, specimens tested before	External tube cover, circular	120 mm	529 cm^2	* 1.66 MPa
9.	15x S2-RR-2D Steel tube circular Ø140 H=280 mm	Tube infill f_c = 53.4 MPa Age: 34 days	Cleaned with paint thinner (nitrolösung)	External tube cover, circular	280 mm	1170 cm^2	1.12 MPa
10.	3x S2-RR-D Steel tube circular Ø140 H=140 mm	Tube infill f_c = 53.4 MPa Age: 34 days	Cleaned with paint thinner (nitrolösung)	External tube cover, circular	140 mm	586 cm^2	1.65 MPa

11.	3x S2-QR-2D Steel tube rectangular D120 H=240 mm	Tube infill $f_c = 53.4$ MPa Age: 34 days	Cleaned with paint thinner (nitrolösung)	External tube cover, rectangular	240 mm	1062 cm^2	1.32 MPa
12.	6x S2-RS-2D Steel tube circular Ø140 H=280 mm	Tube infill $f_c = 53.4$ MPa Age: 34 days	Cleaned with paint thinner (nitrolösung), greased surface	External tube cover, circular	280 mm	1169 cm^2	0.12 MPa
13.	3x POT-3-A1 HEB 200 L=500 mm	B25/B35 Block 330x330x470 mm Age: 31 days	Cleaned with paint thinner (nitrolösung), coated by rust preventive paint, thickness. 25 µm	Concrete cover: cx=65 mm, cy=65 mm Q131 mesh: Ø5/150	440 mm	5060 cm^2	0.70 MPa
14.	3x POT-4-A2 HEB 200 L=500 mm	B25/B35 Block 330x330x470 mm Age: 31 days	Cleaned with paint thinner (nitrolösung), coated by rust preventive paint, thickness. 60 µm	Concrete cover: cx=65 mm, cy=65 mm Q131 mesh: Ø5/150	440 mm	5060 cm^2	1.40 MPa
15.	3x POT-5-OA HEB 200 L=500 mm	B25/B35 Block 330x330x470 mm Age: 31 days	Cleaned with paint thinner (nitrolösung), no coating	Concrete cover: cx=65 mm, cy=65 mm Q131 mesh: Ø5/150	440 mm	5060 cm^2	0.80 MPa
16.	4x SP-30-1 Steel plate 16x300x300 mm	B25/B35 Encasement 75x400x400 mm Age: 99 days	Mechanically cleaned, Cleaned with paint thinner (nitrolösung), no coating	Concrete cover: cx=50mm, cy=30mm Stirrups: Ø6-8/37-150	300 mm	1896 cm^2	0.45 MPa
17.	4x SP-50-2 Steel plate 16x300x300 mm	B25/B35 Encasement 116x400x400 mm Age: 99 days	Mechanically cleaned, Cleaned with paint thinner (nitrolösung), no coating	Concrete cover: cx=50mm, cy=50mm Stirrups: Ø6-8/37-150	300 mm	1896 cm^2	0.64 MPa
18.	4x SP-80-3 Steel plate 16x300x300 mm	B25/B35 Encasement 176x400x400 mm Age: 99 days	Mechanically cleaned, Cleaned with paint thinner (nitrolösung), no coating	Concrete cover: cx=50mm, cy=80mm Stirrups: Ø6-8/37-150	300 mm	1896 cm^2	0.80 MPa
19.	4x SP-120-4 Steel plate 16x300x300 mm	B25/B35 Encasement 256x400x400 mm Age: 99 days	Mechanically cleaned, Cleaned with paint thinner (nitrolösung), no coating	Concrete cover: cx=50mm, cy=120mm Stirrups: Ø6-8/37-150	300 mm	1896 cm^2	1.06 MPa
Wium [202]							

20.	3x POT6-8 HEB 200 L=500 mm	Block 300x300x470 mm f_c = 36.5 MPa Age: 28 days	Sandblasted Sa2.5	Concrete cover: cx=50mm, cy=50mm Stirrups: Ø8/100	440 mm	5060 cm^2	0.64 MPa
21.	3x POT9-11 HEB 200 L=500 mm	Block 400x400x470 mm f_c = 36.5 MPa Age: 28 days	Sandblasted Sa2.5	Concrete cover: cx=100mm, cy=100mm Stirrups: Ø8/100	440 mm	5060 cm^2	1.20 MPa
22.	3x POT1-3B HEB 200 L=500 mm	Block 300x300x470 mm f_c = 40.2 MPa Age: 28 days	Sandblasted Sa2.5	Concrete cover: cx=50mm, cy=50mm Stirrups: Ø8/100	440 mm	5060 cm^2	0.59 MPa
23.	3x POT4-6B HEB 200 L=500 mm	Block 300x300x470 mm f_c = 44.1 MPa Age: 77 days	Sandblasted Sa2.5	Concrete cover: cx=50mm, cy=50mm Stirrups: Ø8/100	440 mm	5060 cm^2	0.59 MPa
24.	3x POT7-9B HEB 200 L=500 mm	Block 300x300x470 f_c = 42.7 MPa Age: 169 days	Sandblasted Sa2.5	Concrete cover: cx=50mm, cy=50mm Stirrups: Ø8/100	440 mm	5060 cm^2	0.54 MPa
~25.	1x POT-SC-1 HEB 200 L=1120 mm	Block 300x300x1000 f_c = 36.5 MPa Age: 28 days	Sandblasted Sa2.5 (Specimen closed at the base by end-plate – no free relative slip possible)	Concrete cover: cx=50mm, cy=50mm Stirrups: Ø8/50	1000 mm	11500 cm^2	~ 0.90 MPa
~26.	1x POT-SC-2 HEB 200 L=1120 mm	Block 300x300x1000 f_c = 36.5 MPa Age: 28 days	Sandblasted Sa2.5 (Specimen closed at the base by end-plate – no free relative slip possible)	Concrete cover: cx=50mm, cy=50mm Stirrups: Ø8/100	1000 mm	11500 cm^2	~ 0.65 MPa
~27.	1x POT-SC-3 HEB 200 L=1120 mm	Block 350x350x1000 f_c = 36.5 MPa Age: 28 days	Sandblasted Sa2.5 (Specimen closed at the base by end-plate – no free relative slip possible)	Concrete cover: cx=75mm, cy=75mm Stirrups: Ø8/100	1000 mm	11500 cm^2	~ 1.00 MPa
~28.	1x POT-SC-4 HEB 200 L=1120 mm	Block 400x400x1000 f_c = 36.5 MPa Age: 28 days	Sandblasted Sa2.5 (Specimen closed at the base by end-plate – no free relative slip possible)	Concrete cover: cx=100mm, cy=100mm Stirrups: Ø8/100	1000 mm	11500 cm^2	~ 1.40 MPa

~29.	1x POT-SC-5 HEB 200 L=1120 mm	Block 300x300x1000 f_c = 36.5 MPa Age: 28 days	Sandblasted Sa2.5 (Specimen closed at the base by end-plate – no free relative slip possible)	Concrete cover: cx=50mm, cy=50mm Stirrups: Ø8/200	1000 mm	11500 cm^2	~ 0.80 MPa
~30.	3x POT-L1-3 HEB 400 L=1270 mm	Block 500x400x1150 f_c = 36.5 MPa Age: 28 days	Sandblasted Sa2.5 (Specimen closed at the base by end-plate – no free relative slip possible)	Concrete cover: cx=50mm, cy=50mm Stirrups: Ø8/100	1150 mm	22195 cm^2	~ 0.32 MPa
~31.	3x POT-L7-9 HEB 400 L=1270 mm	Block 600x500x1150 f_c = 36.5 MPa Age: 28 days	Sandblasted Sa2.5 (Specimen closed at the base by end-plate – no free relative slip possible)	Concrete cover: cx=100mm, cy=100mm Stirrups: Ø8/100	1150 mm	22195 cm^2	~ 0.53 MPa
~32.	3x POT-L10 HEB 400 L=1270 mm	Block 600x500x1150 f_c = 36.5 MPa Age: 28 days	Sandblasted Sa2.5 (Specimen closed at the base by end-plate – no free relative slip possible)	Concrete cover: cx=100mm, cy=100mm Stirrups: Ø8/100, Ø8/50	1150 mm	22195 cm^2	~ 0.54 MPa
Roeder et al. [157]							
33.	2x POTC1-2 W10x45 L=1220 mm	Circular column Ø 500 mm f_c = 35 MPa Age: 28 days	Blast cleaned to remove mill scale, cleaned with degreaser trisodium phosphate	Concrete cover: cx=122mm, cy=148mm Spiral: Ø3/75	1060 mm	13887 cm^2	Average: 1.32 MPa Local: 2.52 MPa
34.	2x POTC3-4 W10x45 L=750 mm	Encasement 450x450 mm f_c = 35 MPa Age: 28 days	Blast cleaned to remove mill scale, cleaned with degreaser Trisodium Phosphate	Concrete cover: cx=97mm, cy=123mm Double-stirrups: Ø3/75	600 mm	7861 cm^2	Average: 1.08 MPa Local: 2.28 MPa
35.	2x POTC5-6 W10x45 L=1220 mm	Encasement 450x450 mm f_c = 35 MPa Age: 28 days	Blast cleaned to remove mill scale, cleaned with degreaser Trisodium Phosphate	Concrete cover: cx=97mm, cy=123mm Double-stirrups: Ø3/75	1060 mm	13887 cm^2	Average: 1.19 MPa Local: 2.20 MPa
36.	2x POTC7-8 W10x45 L=1675 mm	Encasement 450x450 mm f_c = 35 MPa Age: 28 days	Blast cleaned to remove mill scale, cleaned with degreaser Trisodium Phosphate	Concrete cover: cx=97mm, cy=123mm Double-stirrups: Ø3/75	1525 mm	19978 cm^2	Average: 1.08 MPa Local: 2.75 MPa

37.	2x POTC9-10 W10x22 L=1220 mm	Encasement 450x450 mm f_c = 35 MPa Age: 28 days	Blast cleaned to remove mill scale, cleaned with degreaser Trisodium Phosphate	Concrete cover: cx=96mm, cy=152mm Stirrups: Ø3/200	1060 mm	11554 cm^2	Average: 0.88 MPa Local: 2.52 MPa
38.	2x POTC11-12 W10x45 L=1220 mm	Encasement 450x450 mm f_c = 35 MPa Age: 28 days	Blast cleaned to remove mill scale, cleaned with degreaser Trisodium Phosphate	Concrete cover: cx=97mm, cy=123mm Stirrups: Ø3/200	1060 mm	13887 cm^2	Average: 1.03 MPa Local: 2.41 MPa
39.	2x POTC13-14 W10x77 L=1220 mm	Encasement 450x450 mm f_c = 35 MPa Age: 28 days	Blast cleaned to remove mill scale, cleaned with degreaser Trisodium Phosphate	Concrete cover: cx=90mm, cy=96mm Stirrups: Ø3/200	1060 mm	16430 cm^2	Average: 0.92 MPa Local: 2.34 MPa
Xing et al. [209]							
40.	3x PS14-1 Plain bar Ø 14 mm L=550 mm	Cube 200 mm f_c = 48.5 MPa Age: 28 days	No	Concrete cover c=93 mm	100 mm	44 cm^2	5.10 MPa
41.	3x PS14-2 Plain bar Ø 14 mm L=550 mm	Cube 200 mm f_c = 48.5 MPa Age: 28 days	No	Concrete cover c=93 mm	140 mm	62 cm^2	5.51 MPa
42.	3x PS16-1 Plain bar Ø 16 mm L=550 mm	Cube 200 mm f_c = 40.8 MPa Age: 28 days	No	Concrete cover c=92 mm	115 mm	58 cm^2	2.22 MPa
43.	3x PS16-2 Plain bar Ø 16 mm L=550 mm	Cube 200 mm f_c = 48.5 MPa Age: 28 days	No	Concrete cover c=92 mm	160 mm	80 cm^2	3.22 MPa
44.	3x PS8-1 Plain bar Ø 8 mm L=550 mm	Cube 200 mm f_c = 40.8 MPa Age: 28 days	No	Concrete cover c=96 mm	80 mm	20 cm^2	0.25 MPa
45.	3x PS8-2 Plain bar Ø 8 mm L=550 mm	Cube 200 mm f_c = 40.8 MPa Age: 28 days	No	Concrete cover c=96 mm	120 mm	30 cm^2	2.27 MPa
SmartCoCo [175]							
46.	1x POT-F HEB 120 L=1100 mm	C40/50 Block 340x1000x1000 f_c = 71 MPa Age: 28 days	Rusted profile	Concrete cover: cx=440mm, cy=110mm Stirrups: Ø12/150	900 mm	6174 cm^2	2.91 MPa
47.	1x POT-G HEB 120 L=1100 mm	Encasement 450x450 mm f_c = 35 MPa Age: 28 days	Coated with paint	Concrete cover: cx=440mm, cy=110mm Stirrups: Ø12/150	900 mm	6174 cm^2	1.34 MPa
Tao et al. [181]							
48.	6x concrete-filled tubes, Stainless steel Circular Ø120–400	Tube infill f_c = 42 − 81.8 MPa Age: 31-111 days	Stainless steel, finishing class 2B and 2K (EN10088-4:2009 [49])	External tube cover circular	600–1200 mm	2111-14477 cm^2	0.23-1.44 MPa

49.	5x concrete-filled tubes, Carbon steel Circular Ø120–400	Tube infill $f_c = 42 - 55.8$ MPa Age: 31-1168 days	Untreated surface	External tube cover circular	600–1200 mm	2111-14477 cm^2	0.6-1.85 MPa (one result 0.04 MPa)
50.	4x concrete-filled tubes, Stainless steel Rectangular Ø120–200	Tube infill f_c = 40.4 - 81.8 MPa Age: 35-109 days	Stainless steel, finishing class 2B and 2K (EN10088-4:2009 [49])	External tube cover rectangular	600–850 mm	2111-5036 cm^2	0.12-0.71 MPa
51.	5x concrete-filled tubes, Caron steel Rectangular Ø120–600	Tube infill f_c = 40.4 - 55.8 MPa Age: 35-1176 days	Untreated surface	External tube cover rectangular	600–1800 mm	2111-32798 cm^2	0.13-1.04 MPa (one result 0.03 MPa)
Pecce et al. [142]							
52.	14x partially embedded HEB180, L = 630 mm	Partial embed. $f_c = 22 - 35$ MPa Age: no information	Untreated and oiled	Space between flanges of steel profiles	450 mm	2990 cm^2	0.05-0.45 MPa (flange contact only 0.1-0.75 MPa)
Xu et al. [210]							
53.	7x concrete-filled rectangular tubes, D180 and L=600 mm	Tube infill Expansive mix f_c: no information Age: 33 days	No information	External tube cover	580 mm	3990 cm^2	0.36-0.55 MPa
De Nardin et al. [41]							
54.	1x concrete-filled rectangular tube, D200 and L = 425 mm	Tube infill f_c = 48 MPa Age: no information	No information	External tube cover	375 mm	2811 cm^2	0.22 MPa
Mollazadeh [124]							
55.	5x concrete-filled rectangular tubes, D150 and L = 250–500 mm	Tube infill f_c = 29–32 MPa Age: 28 days	Cleaned with alcohol	External tube cover	200 mm and 450 mm	1120 cm^2 and 2520 cm^2	0.20-0.26 MPa
Hotta [74]							
56.	6 specimens on embedded steel plate section 9x50 mm	Concrete block 130x130x100 mm f_c =28.7-64.4 MPa	No information	External steel box with prestressing bars imposing pressure of: 0.0-7.5 MPa	100 mm	900 cm^2	Approx. values: 2.00-4.10 MPa
Berthet et al. [14]							
57.	Push-out specimens on 5x150x300 mm steel plates (1) bonded on two sides to concrete core and (2) bonded between two concrete blocks	Concrete block 200x150x300 mm f_c =60 MPa	No information	No	285 mm	855 cm^2	0.76-0.8 MPa

Rana et al. [155]							
58.	2 specimens on embedded steel plate section 10x75x350 mm	Concrete block 70x135x350 mm f_c =67 MPa	No information	No	300 mm	4500 cm^2	Ultimate: 1.42 MPa Residual: 0.55 MPa
Wang et al. [197]							
59.	10 specimens on concrete filled rectangular steel tube D150 L=400-800 mm	Tube infill f_c=30-50 MPa	Rust mechanically cleaned with electric device	External tube cover	400-800 mm	2240-4608 cm^2	0.1-0.35 MPa
Qu et al. [152]							
60.	18 specimens on cold formed concrete filled rectangular steel tubes 150x100x4.07 200x150x4.43 300x200x5.73 L=700-1000 mm	Tube infill f_c=29-49 MPa Age: 40 days	Cleaned from dust and degreased. Second series lubricated with butter	External tube cover	600-900 mm	2805-8587 cm^2	Lubricated 0.03-0.15 MPa Not-Lubr. 0.15-0.46 MPa

* Some results disturbed by a plastic deformation of the specimens applied beforehand – reused specimens after creep and shrinkage test of composite columns (see [162]).
~ Author refers to the chemical debonding stress values evaluated (values without friction mechanism) and no raw data available. Moreover, free slip prevented – specimen closed by end-plate. Given values approximated from diagram (see [202]).

Annex C – Details on the production, measurement equipment and opening of the push-out test specimens for flat mechanical shear connectors

Details on the fabrication process of column push-out test specimens (CoPOT) are shown in Fig. C.1-C.15 below.



Fig. C.1. Details on reinforcement cages in CoPOT.

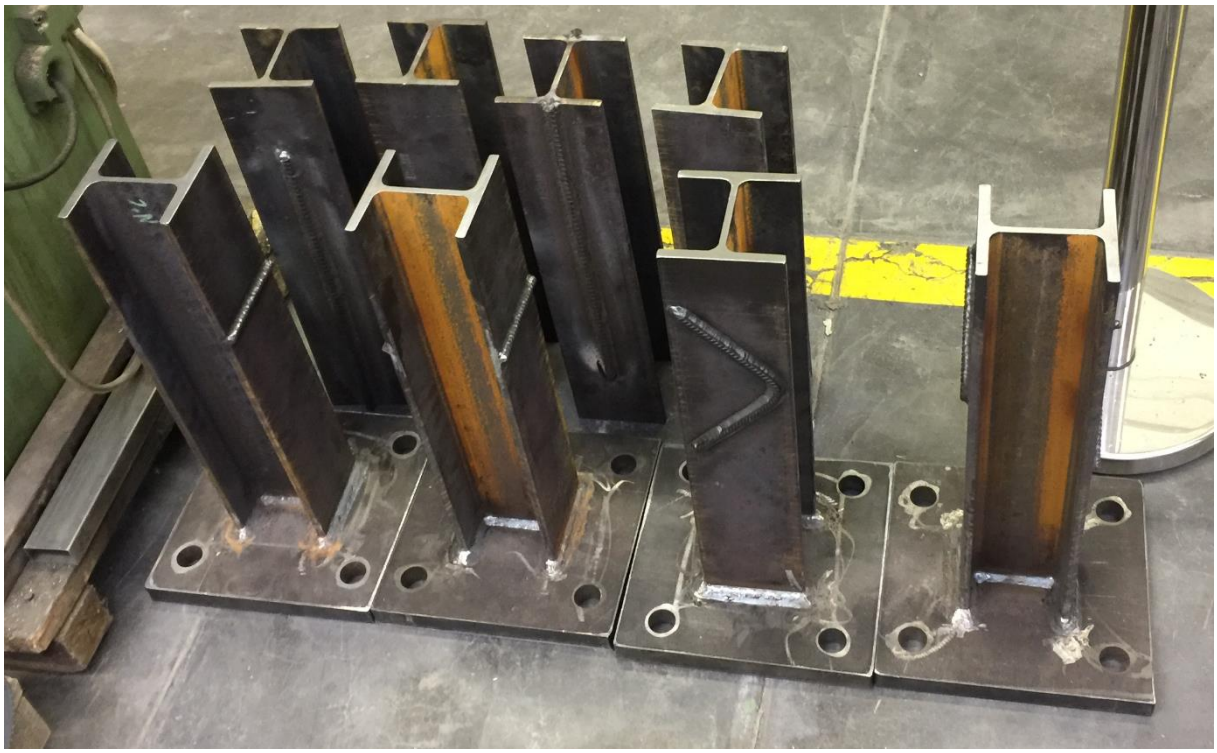


Fig. C.2. Details on steel profiles with flat connectors in CoPOT.

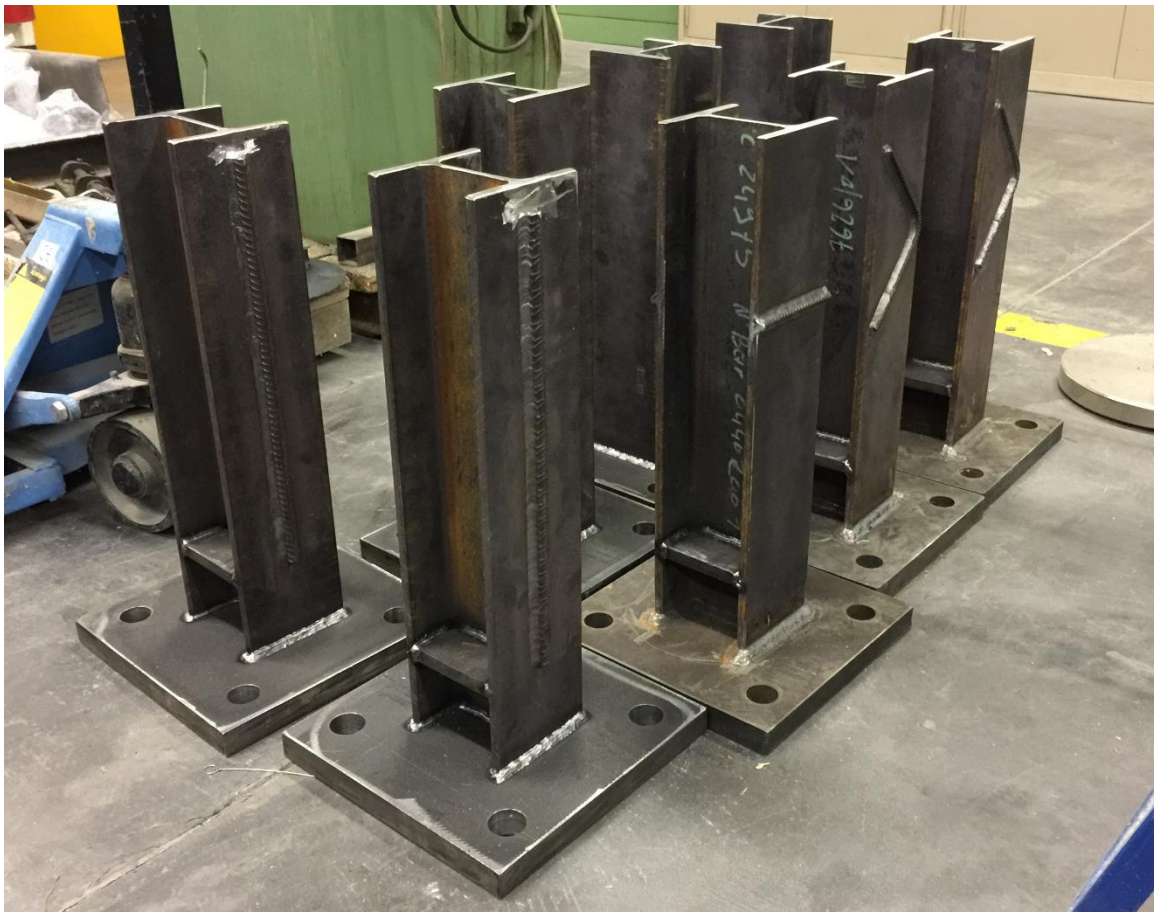
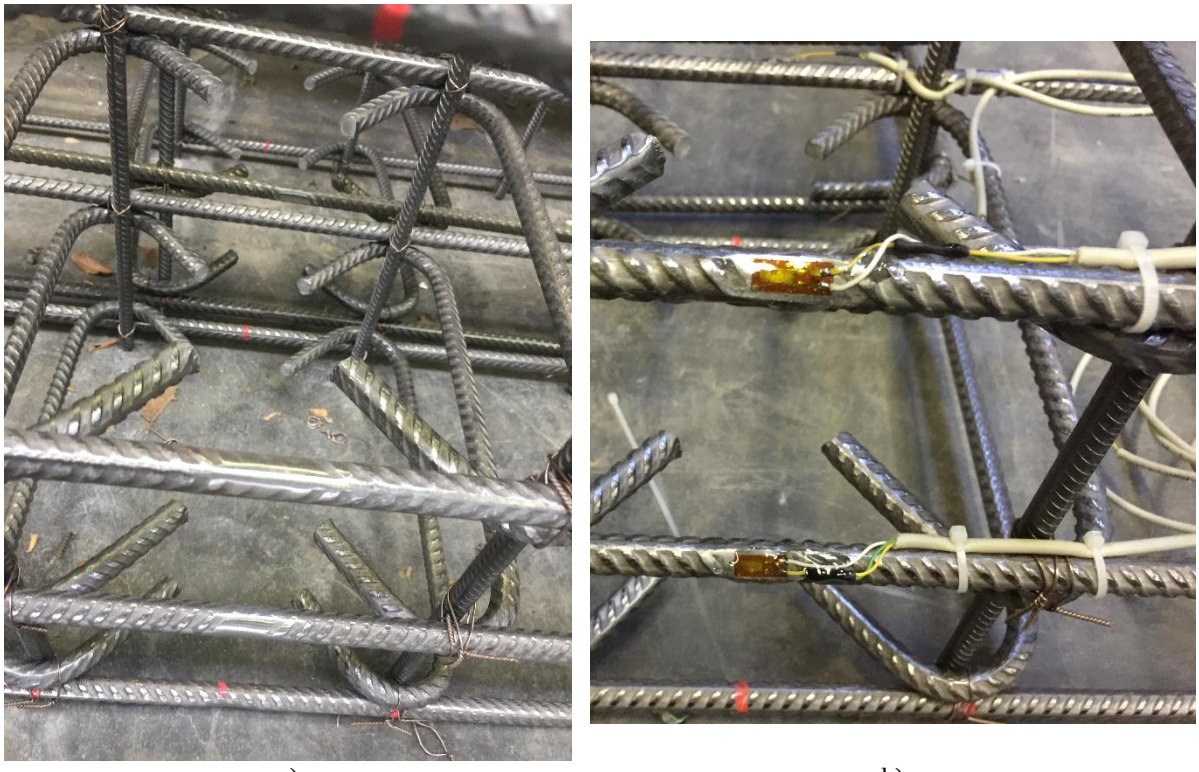


Fig. C.3. Details on steel profiles with flat connectors, stiffeners and top plates in CoPOT.



a) b)

Fig. C.4. Details on gluing of strain gauges to reinforcement bars in CoPOT – a) grinded and polished surfaces and b) glued strain gauges.

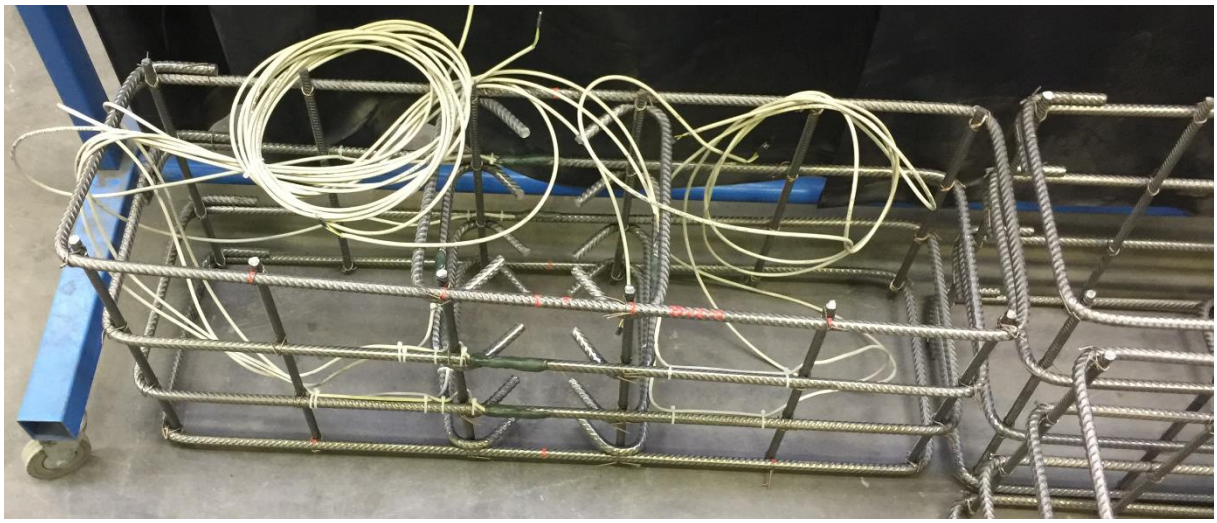
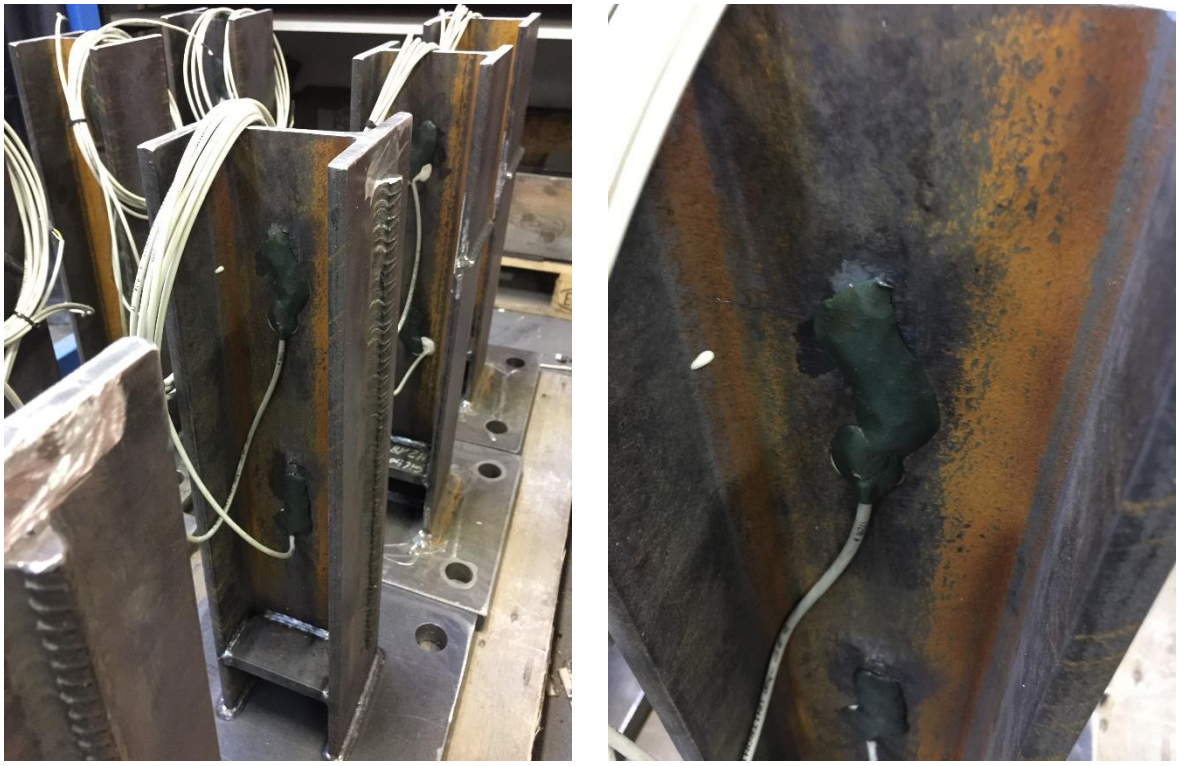


Fig. C.5. Detail of reinforcement cage with glued and secured strain gauges in CoPOT.



a) b)

Fig. C.6. Details of strain gauges glued to steel profiles in CoPOT specimens – a) general view and b) close view on the glued and secured strain gauge.



a) b)

Fig. C.7. Details on fabrication of infill parts placed at the base of CoPOT specimens to create a recess and fix the movement of bottom parts of steel profiles – a) timber core with fixing parts and b) polystyrene collar.

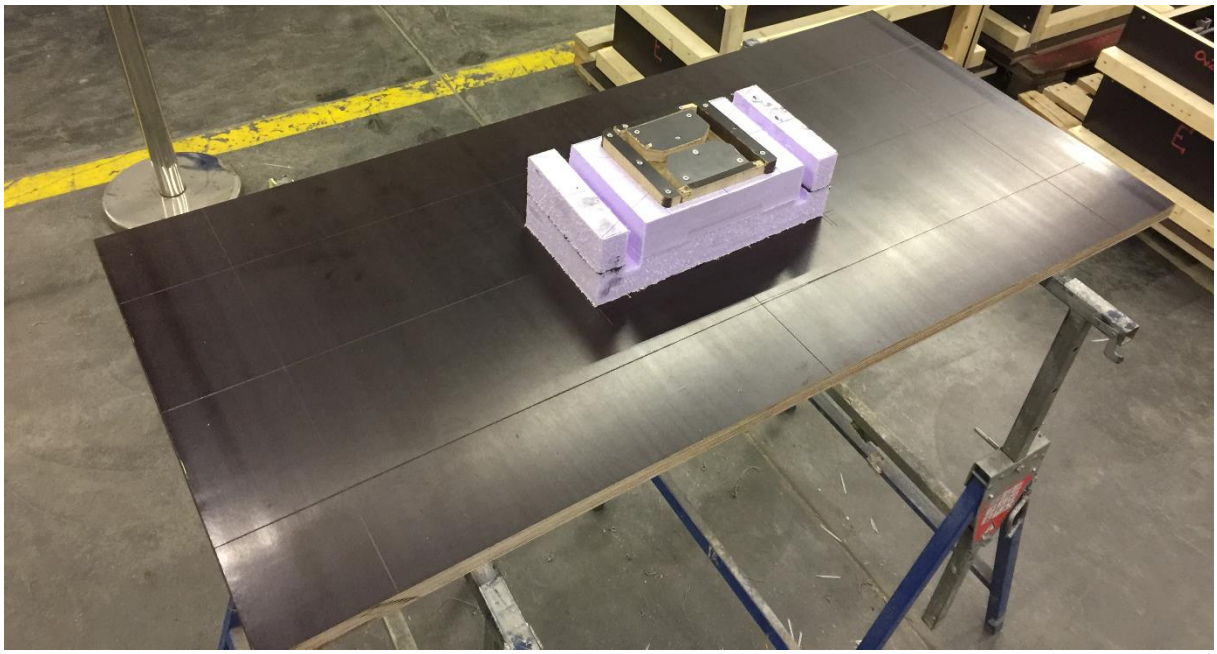


Fig. C.8. Detail on infill part fixed to base plate of formwork to create a recess at the base of CoPOT specimens.



Fig. C.9. Detail on assembly of reinforcement cage into formwork of CoPOT specimens.

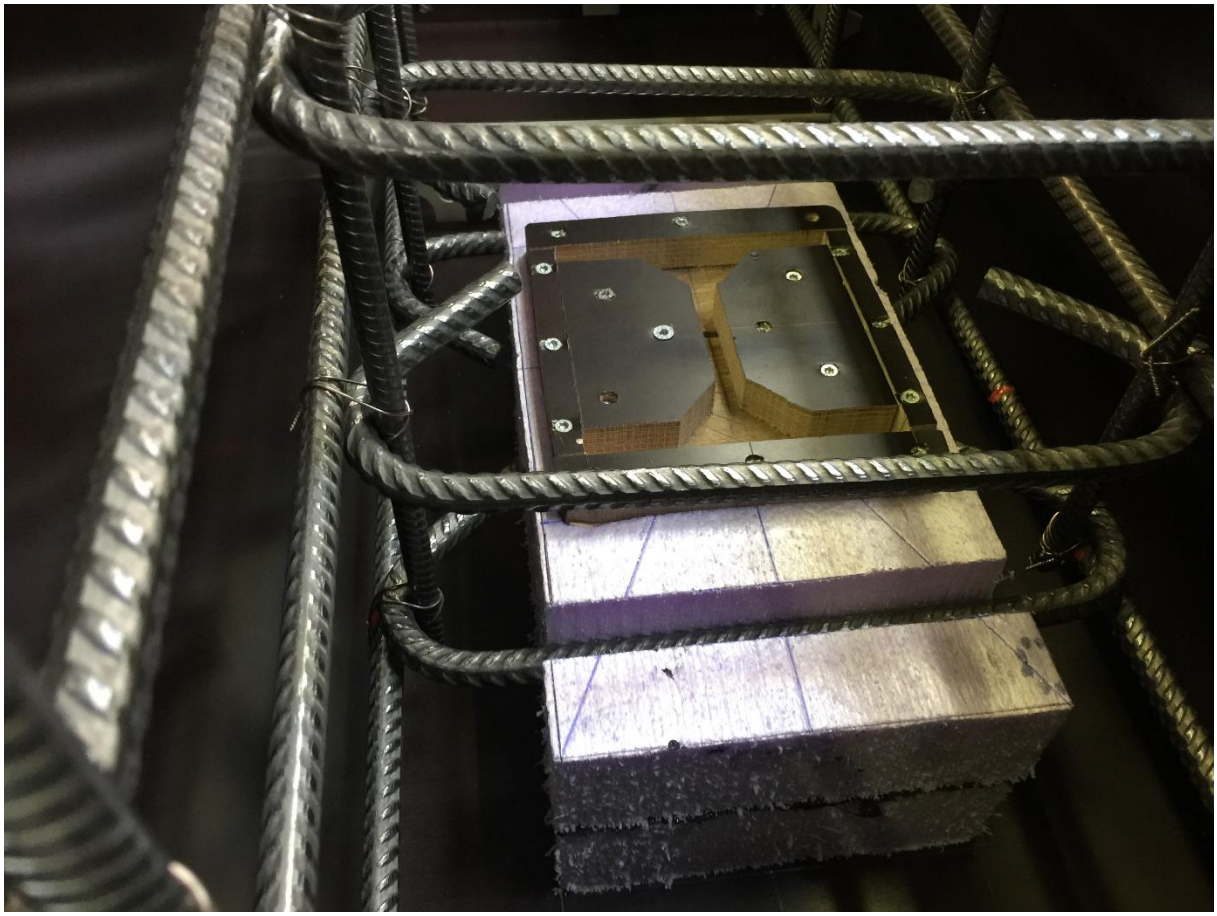


Fig. C.10. Detail on assembly of reinforcement cage and base-infill part of CoPOT specimens.



Fig. C.11. Detail on application of demoulding oil to steel profiles in CoPOT specimens.

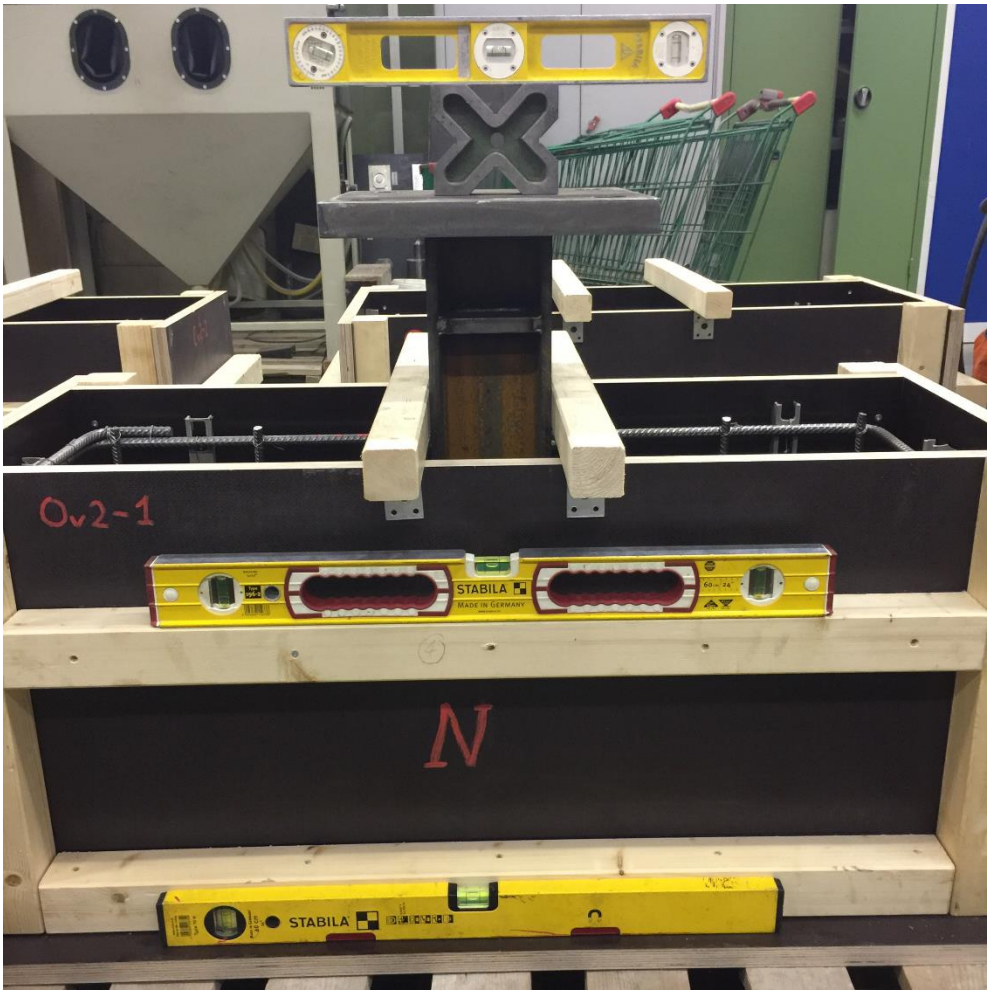


Fig. C.12. Detail on assembly of steel profile into the formwork of CoPOT specimen.



Fig. C.13. Detail on top fixation point of steel profile in the formwork of CoPOT specimen.



a) b)

Fig. C.14. Details on CoPOT specimens after concreting – a) fresh casted concrete and b) foil cover.



Fig. C.15. Detail on recess of the CoPOT specimen after removal of base-infill part.

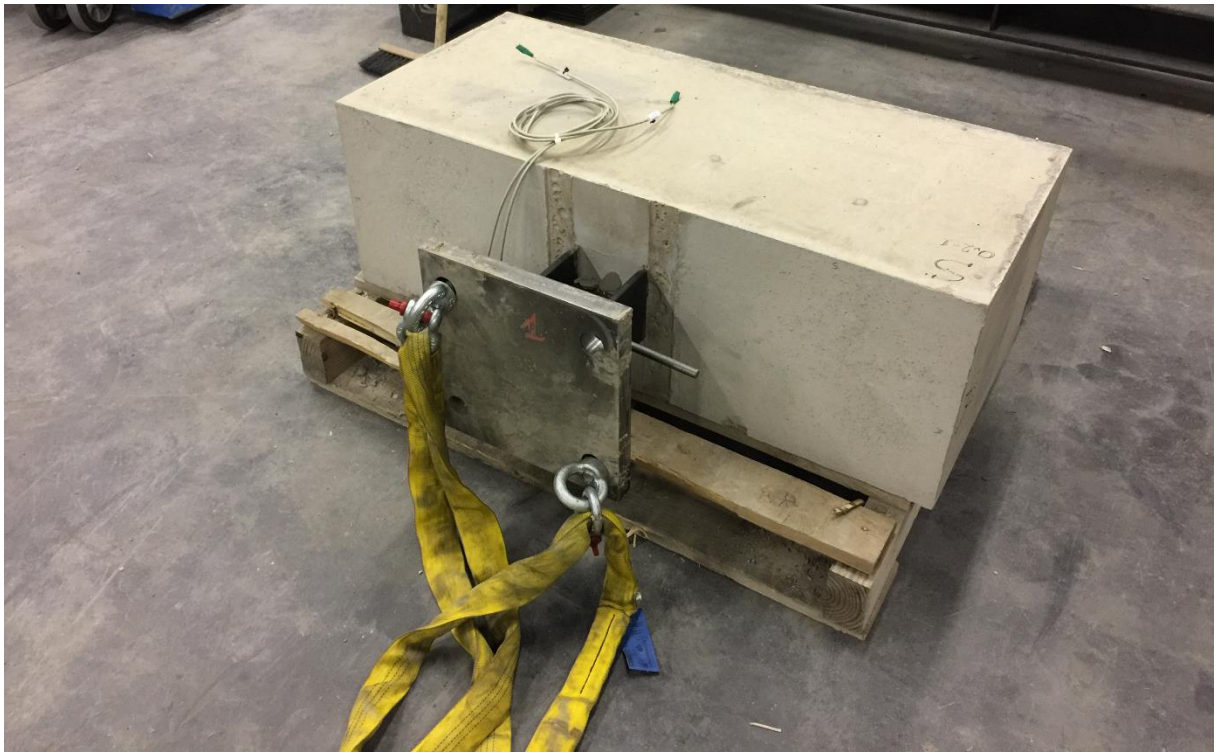
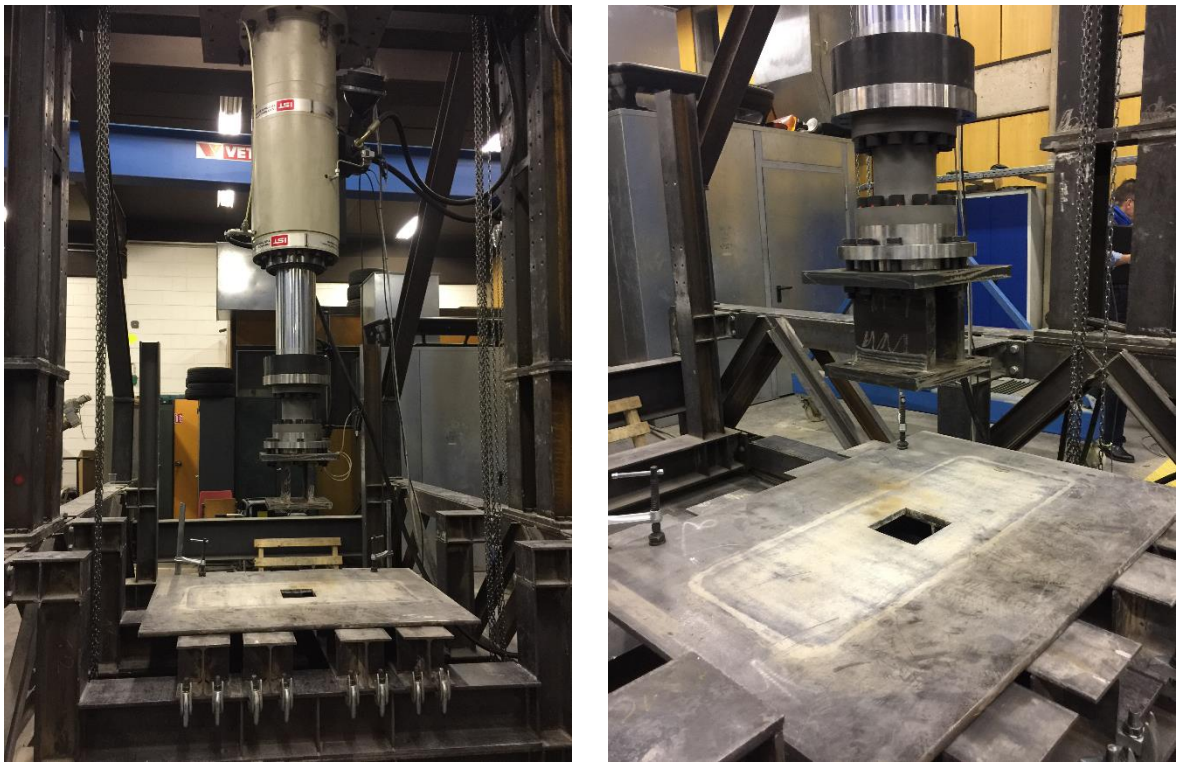


Fig. C.16. CoPOT specimen before its placement in the testing frame.

On Fig. C.16, the CoPOT specimen ready for the placement in the testing frame is shown. In Fig. C.17-C.19, the details on the testing frame and arrangement of displacement transducers are given.



a) b)

Fig. C.17. Detail on testing frame at the University of Luxembourg – a) hydraulic press and b) base plate.



Fig. C.18. CoPOT specimen in the testing frame.



a) b)

Fig. C.19. Details on placement of displacement transducers in CoPOT – a) side and b) top.

Cracking pattern of specimens Cv2, Av2 and Bv2 of CoPOT are shown in Fig. C.20-C.22, respectively.

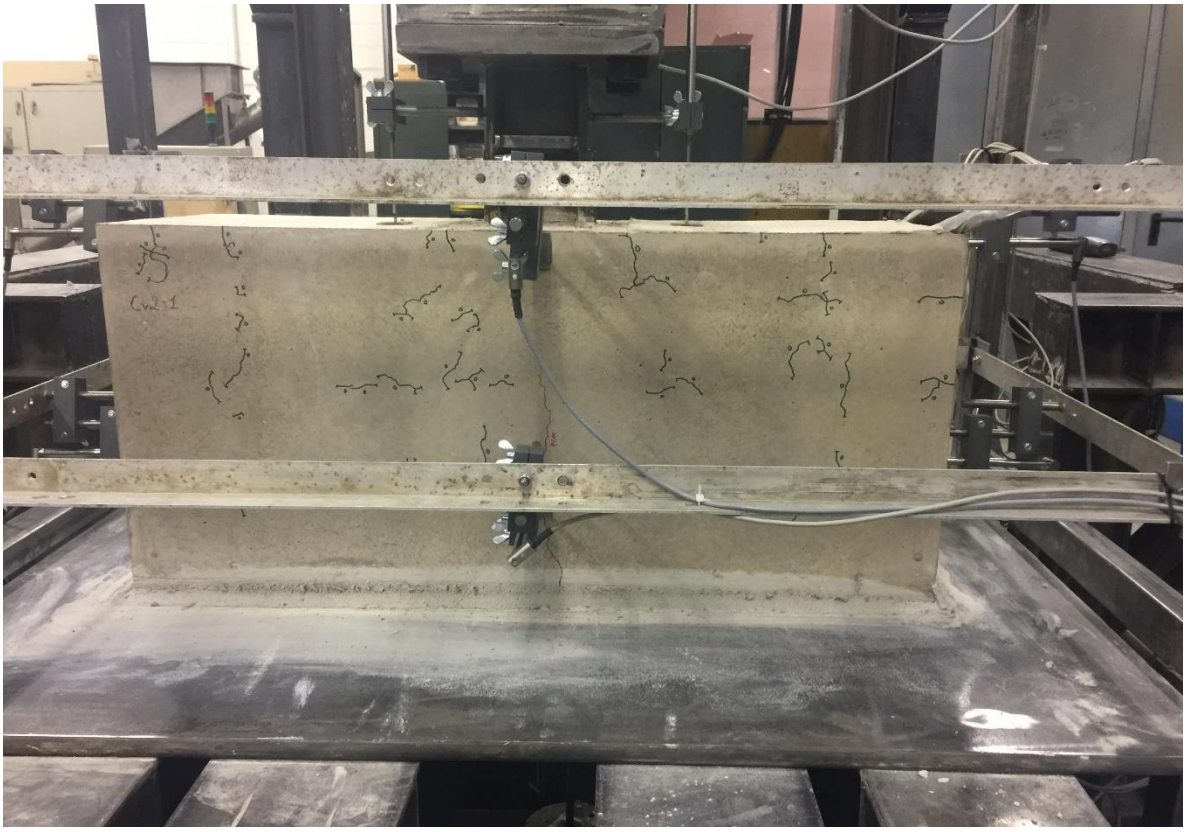


Fig. C.20. Cracking pattern at peak load of specimen Cv2 from CoPOT.

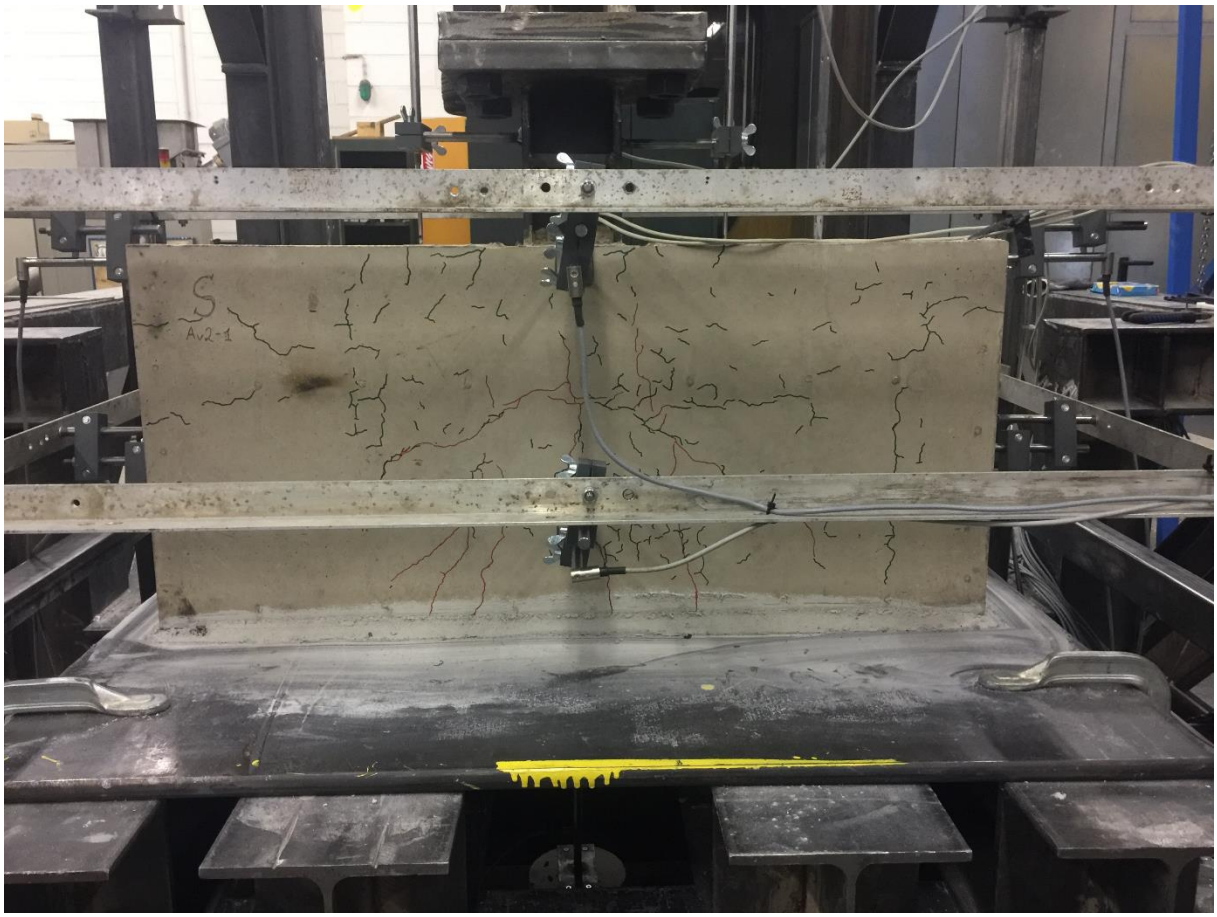


Fig. C.21. Cracking pattern at peak load of specimen Av2 from CoPOT.

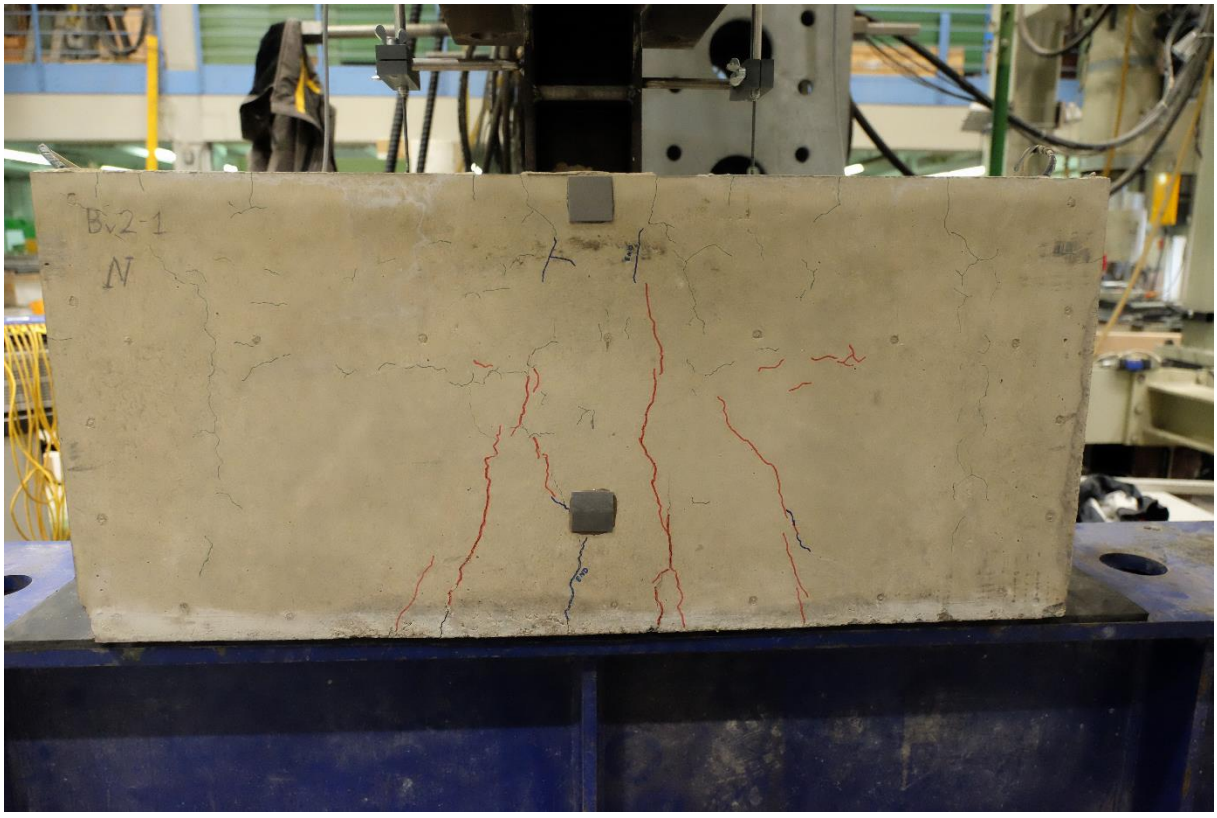


Fig. C.22. Cracking pattern at peak load of specimen Bv2 from CoPOT.

Details on the opening of the specimen Av2 of CoPOT are shown in Fig. C.23-C.27.



Fig. C.23. Opened specimen Av2 of CoPOT.

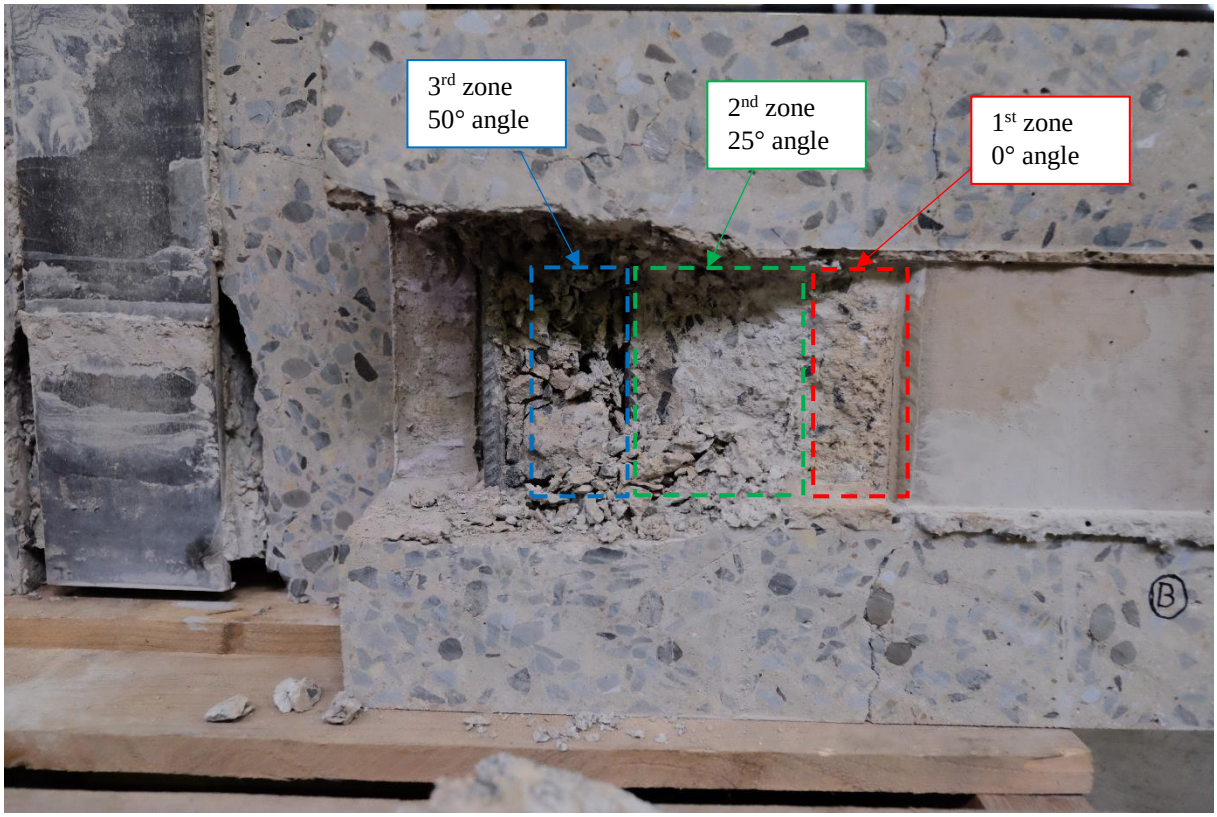


Fig. C.24. Identified failure planes in concrete encasement of specimen Av2 of CoPOT.

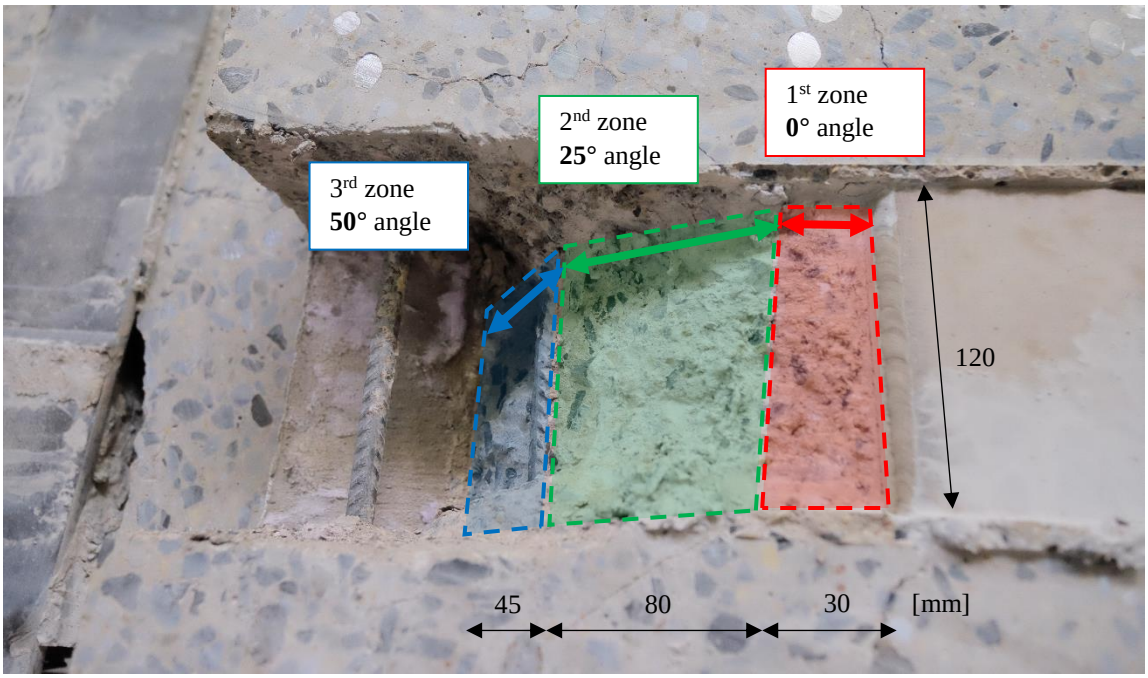


Fig. C.25. Detail on failure planes in concrete ecasement of specimen Av2 of CoPOT.

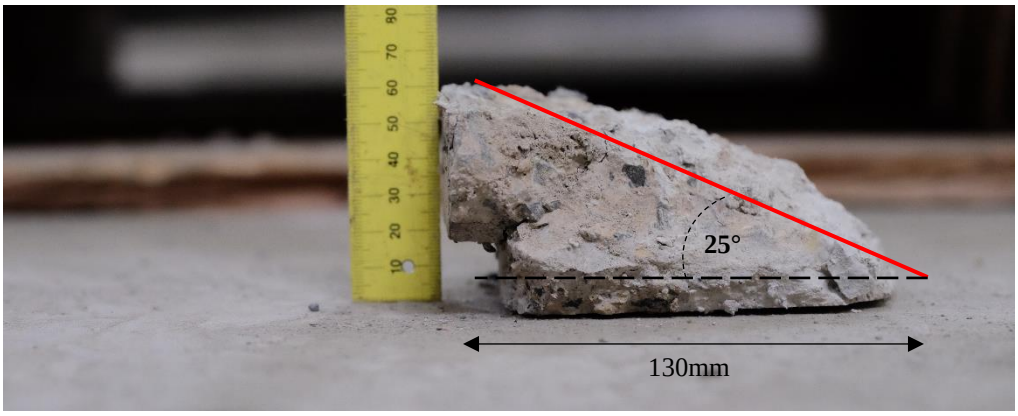
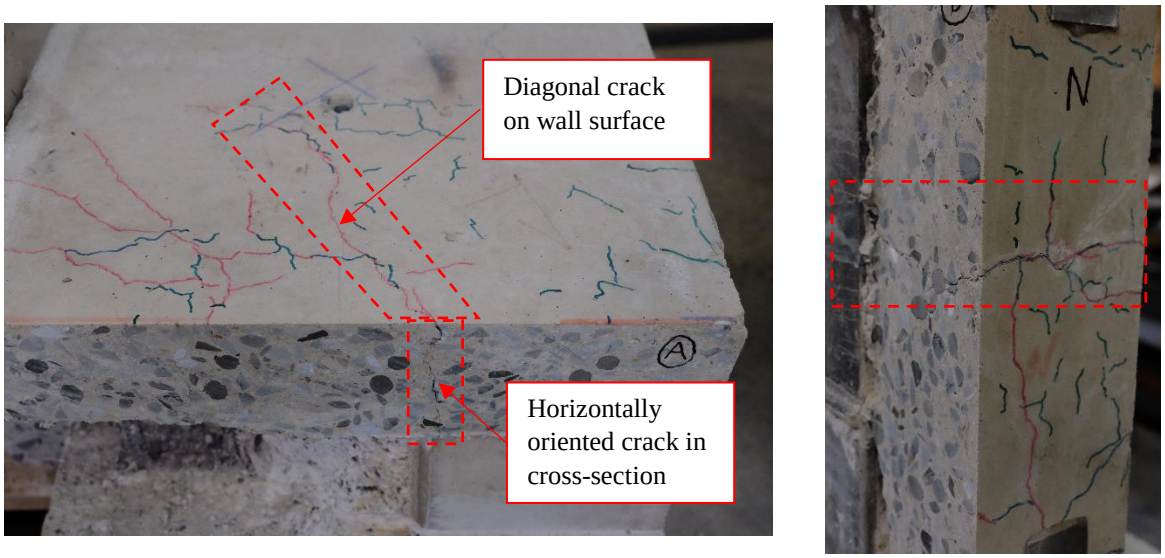


Fig. C.26. Detail on separated concrete cone from concrete encasement in specimen Av2 of CoPOT.



a) b)

Fig. C.27. Details on crack propagation in specimen Av2 of CoPOT – a) side part and b) central part.

Details on the opening of the specimen Bv2 of CoPOT are shown in Fig. C.28-C.31.



Fig. C.28. Opened specimen Bv2 of CoPOT.

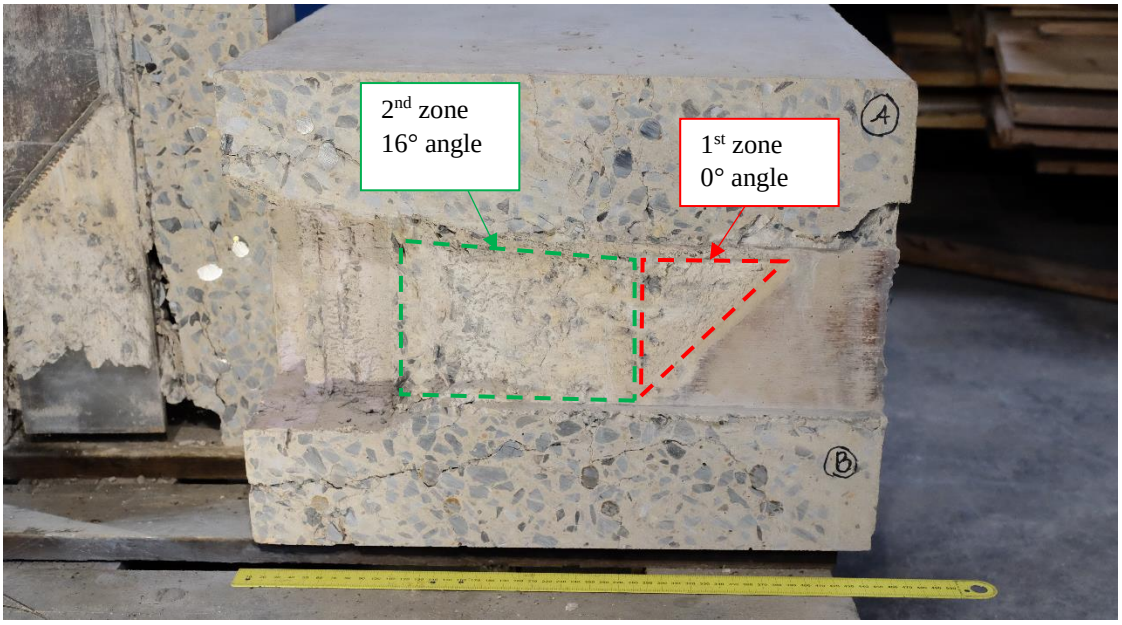


Fig. C.29. Identified failure planes in concrete encasement of specimen Bv2 of CoPOT.

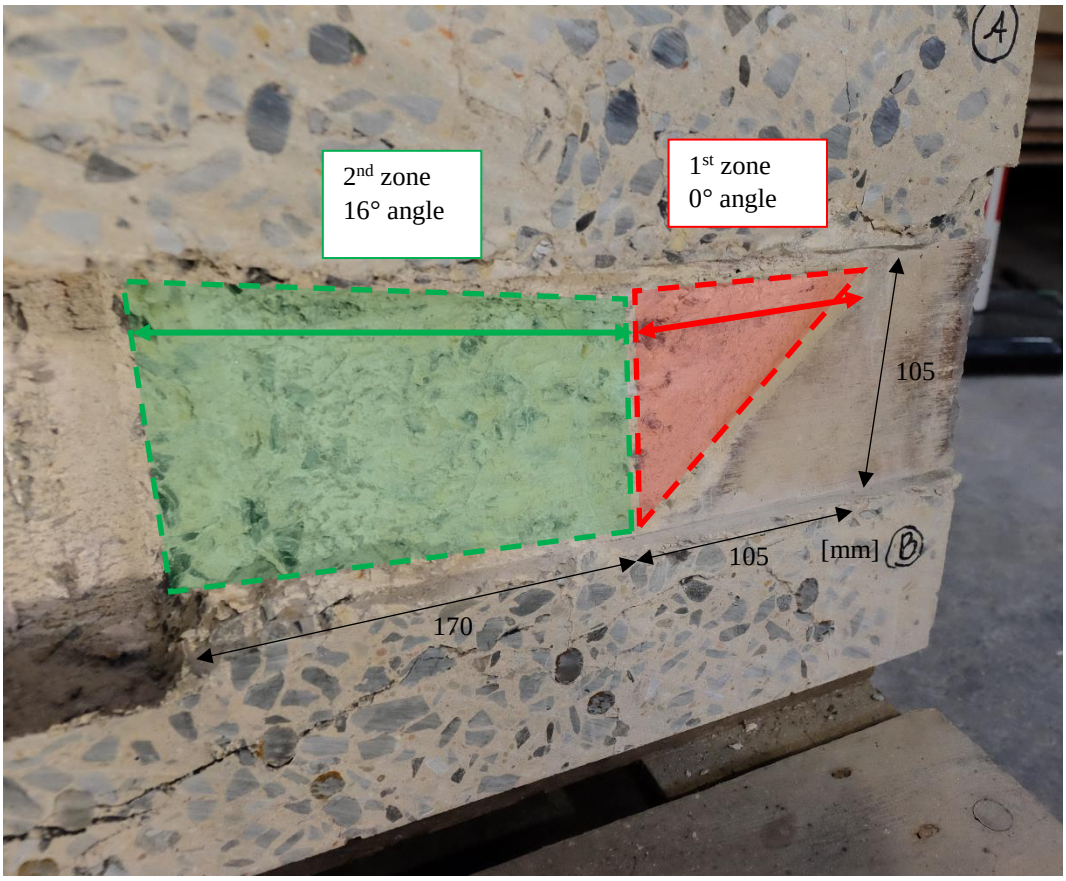
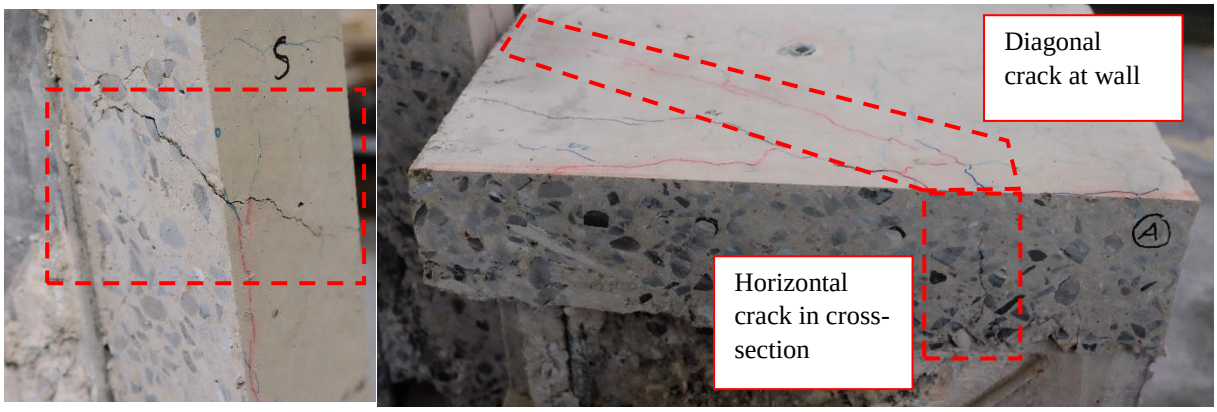


Fig. C.30. Detail on failure planes in concrete ecasement of specimen Bv2 of CoPOT.



a) b)

Fig. C.31. Details on crack propagation in specimen Bv2 of CoPOT – a) central part and b) side part.

Annex D – Solver setup, energy balance and concrete material law in FE simulations of push-out tests for flat mechanical shear connectors

Solver setup for Abaqus/Standard simulation of specimen 0v2 is given in Table D.1.

Table D.1.
Solver setup for Abaqus/Standard simulation of specimen 0v2 of CoPOT.

Specimen	0v2				
Solver	Abaqus/Standard				
Step	Static/General				
Time	1				
Nlgeom	On				
Automatic stabilization	None				
Incrementation	Type	Maximum number of increments	Initial increment size	Minimum increment size	Maximum increment size
	Automatic	10000	0.0001	1E-015	0.002
Method	Direct				
Matrix storage	Solver default				
Solution technique	Full Newton				
Convert severe discontinuity iterations	Propagate from previous step				
Load variation with time	Ramp linearly over step				
Extrapolation of previous state at start of each increment	Linear				

Solver setup for Abaqus/Explicit simulation of specimen 0v2 is given in Table D.2.

Table D.2.
Solver setup for Abaqus/Explicit simulation of specimen 0v2 of CoPOT.

Specimen	0v2					
Solver	Abaqus/Explicit					
Step	Dynamic/Explicit					
Time	380 s					
Speed	0.25 mm/s					
Nlgeom	On					
Amplitude	Smooth step	Time span	Time/Freq.	Amplitude		
		Step time	0	0		
			380	1		
Incrementation	Type	Stable increment estimator	Max. time increment	Time scaling factor		
	Automatic	Global	Unlimited	1		
Mass scaling	Defined scaling definitions	Region	Type	Frequency/ Interval	Factor	Target time increment
	Semi-automatic	Whole model	Factor	Beginning of step	1E+06	None
Other	Linear bulk viscosity parameter	0.06				
	Quadratic bulk viscosity parameter	1.2				

Energy balance for Abaqus/Explicit simulation of specimen 0v2 is shown in Fig. D.1.

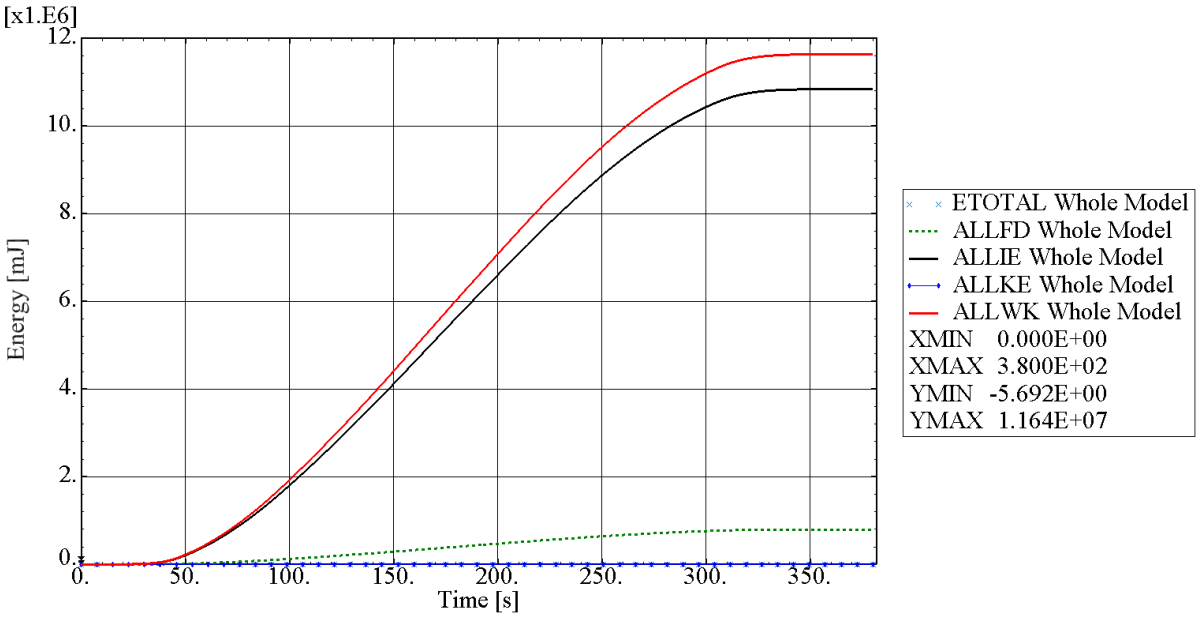


Fig. D.1. Energy balance for quasi-static simulation of specimen 0v2 of CoPOT.

Solver setup for Abaqus/Explicit simulation of specimen Av2 is given in Table D.3.

Table D.3.
Solver setup for Abaqus/Explicit simulation of specimen Av2 of CoPOT.

Specimen	Av2					
Solver	Abaqus/Explicit					
Step	Dynamic/Explicit					
Time	380 s					
Speed	0.25 mm/s					
Nlgeom	On					
Amplitude	Smooth step	Time span	Time/Freq.	Amplitude		
		Step time	0	0		
			380	1		
Incrementation	Type	Stable increment estimator	Max. time increment	Time scaling factor		
	Automatic	Global	Unlimited	1		
Mass scaling	Defined scaling definitions	Region	Type	Frequency/ Interval	Factor	Target time increment
	Semi-automatic	Whole model	Factor	Beginning of step	1E+08	None
Other	Linear bulk viscosity parameter	0.06				
	Quadratic bulk viscosity parameter	1.2				

Energy balance for Abaqus/Explicit simulation of specimen Av2 is shown in Fig. D.2.

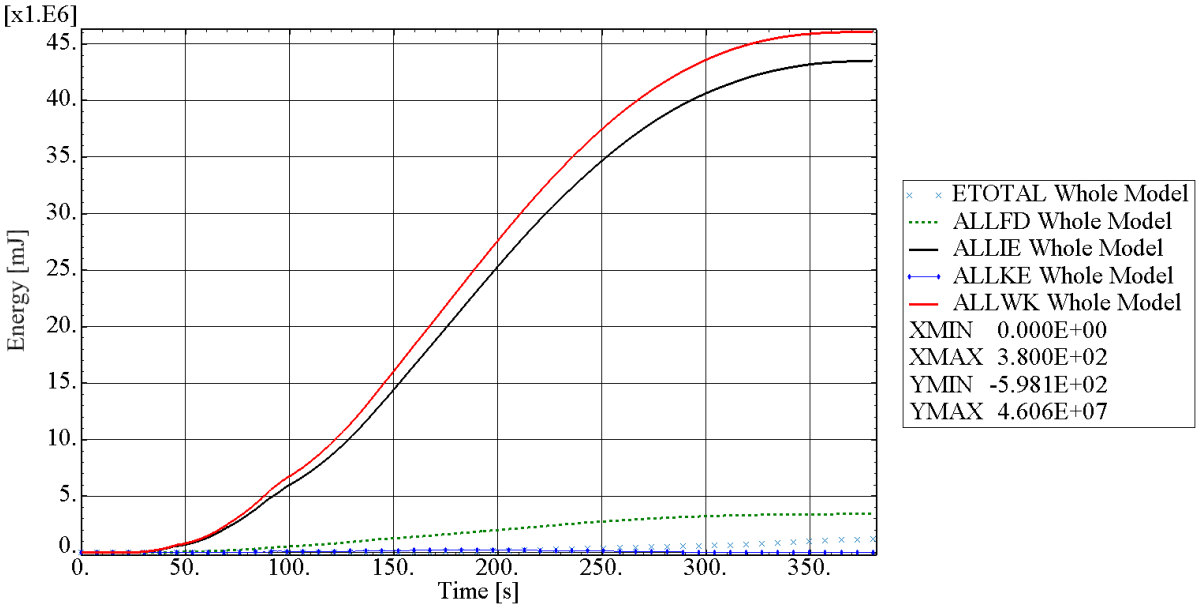


Fig. D.2. Energy balance for quasi-static simulation of specimen Av2 of CoPOT.

Solver setup for Abaqus/Explicit simulation of specimen Bv2 is given in Table D.4.

Table D.4.
Solver setup for Abaqus/Explicit simulation of specimen Bv2 of CoPOT.

Specimen	Bv2					
Solver	Abaqus/Explicit					
Step	Dynamic/Explicit					
Time	380 s					
Speed	0.25 mm/s					
Nlgeom	On					
Amplitude	Smooth step	Time span	Time/Freq.	Amplitude		
		Step time	0	0		
			380	1		
Incrementation	Type	Stable increment estimator	Max. time increment	Time scaling factor		
	Automatic	Global	Unlimited	1		
Mass scaling	Defined scaling definitions	Region	Type	Frequency/ Interval	Factor	Target time increment
	Semi-automatic	Whole model	Factor	Beginning of step	1E+08	None
Other	Linear bulk viscosity parameter	0.06				
	Quadratic bulk viscosity parameter	1.2				

Energy balance for Abaqus/Explicit simulation of specimen Bv2 is shown in Fig. D.3

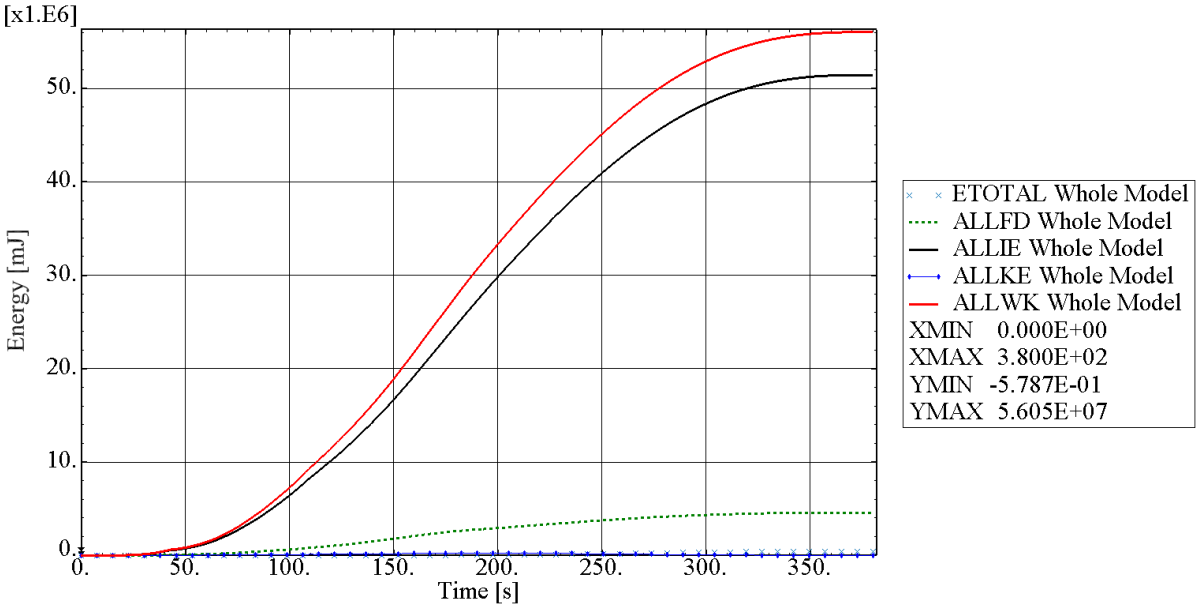


Fig. D.3. Energy balance for quasi-static simulation of specimen Bv2 of CoPOT.

Solver setup for Abaqus/Standard simulation of specimen Cv2 is given in Table D.5.

Table D.5.
Solver setup for Abaqus/Standard simulation of specimen Cv2 of CoPOT.

Specimen	0v2				
Solver	Abaqus/Standard				
Step	Static/General				
Time	1				
Nlgeom	On				
Automatic stabilization	None				
Incrementation	Type	Maximum number of increments	Initial increment size	Minimum increment size	Maximum increment size
	Automatic	10000	0.0001	1E-015	0.002
Method	Direct				
Matrix storage	Solver default				
Solution technique	Full Newton				
Convert severe discontinuity iterations	Propagate from previous step				
Load variation with time	Ramp linearly over step				
Extrapolation of previous state at start of each increment	Linear				

Input data for the concrete damage plasticity material law used in numerical simulations of CoPOT specimens are given in Table D.6-D.9 for the specimens 0v2, Av2, Bv2 and Cv2 respectively.

Table D.6.
Properties used to define concrete material law in the numerical simulations of the CoPOT specimen 0v2.

Properties	Value	Unit	Description	**0v2**
Behaviour: Density				
ρ	2.4E-009	[tonne/mm^3]	Material density	
Behaviour: Elastic				
E_{cm}	34962	[MPa]	Young's Modulus	
ν	0.2	[-]	Poisson's Ratio	
Behaviour: Concrete Damage Plasticity (CDP)				
ψ	25	[°]	Dilation angle at high confining pressure in the p-q plane	
ϵ	0.1	[-]	Eccentricity of hyperbolic function approach (rate)	
fb0/fc0	1.16	[-]	Ratio between uniaxial and biaxial strength	
K_c	0.667	[-]	Ratio between tensile and compressive meridians of effective hydrostatic pressure (shape of yield surface in the deviatoric plane)	
μ_{visc}	0.0001	[s]	Viscosity parameter (relaxation time of the system)	

Uniaxial stress-strain behaviour (CDP)

Properties	Compression			Tension		
	Tension recovery		0.1	Compression recovery		0
	Yield stress	Inelastic strain	Compression damage	Yield stress	Crack opening width	Tension damage
Inp. No.	$\sigma_{c,y}$	$\varepsilon_{c,pl}$	d_c	$\sigma_{t,y}$	$w_{t,pl}$	d_t
Unit	[MPa]	[-]	[-]	[MPa]	[mm]	[-]
1	7.89	0	0	3.09	0	0
2	15.04	0.000040	0	1.85	0.023273050	0
3	21.42	0.000092	0	0.62	0.046546100	0
4	27.01	0.000167	0	0.46	0.093092201	0.25
5	31.81	0.000265	0	0.00	0.232730501	0.99
6	35.78	0.000387	0			
7	38.9	0.000532	0			
8	41.16	0.000703	0			
9	42.54	0.000898	0			
10	43.00	0.001120	0			
11	42.89	0.001238	0.002611177			
12	42.55	0.001363	0.010488931			
13	41.98	0.001494	0.023700447			
14	41.18	0.001632	0.042314055			
15	40.14	0.001777	0.066399258			
16	38.87	0.001928	0.096026756			
17	37.36	0.002087	0.131268475			
18	35.60	0.002252	0.172197587			
19	33.59	0.002424	0.218888543			
20	31.33	0.002604	0.271417100			
21	28.82	0.002791	0.329860348			
22	26.05	0.002985	0.394296740			
23	23.01	0.003187	0.464806122			
24	19.72	0.003396	0.541469768			
25	16.15	0.003613	0.624370405			
26	12.32	0.003838	0.713592251			
27	8.20	0.004070	0.809221047			

Table D.7.
Properties used to define concrete material law in the numerical simulations of the CoPOT specimen Av2.

Properties	Value	Unit	Description	Av2
Behaviour: Density				
ρ	2.4E-009	[tonne/mm^3]	Material density	
Behaviour: Elastic				
E_{cm}	41897	[MPa]	Young's Modulus	
ν	0.2	[-]	Poisson's Ratio	
Behaviour: Concrete Damage Plasticity (CDP)				
ψ	25	[°]	Dilation angle at high confining pressure in the p-q plane	
ϵ	0.1	[-]	Eccentricity of hyperbolic function approach (rate)	
fb0/fc0	1.16	[-]	Ratio between uniaxial and biaxial strength	
K_c	0.667	[-]	Ratio between tensile and compressive meridians of effective hydrostatic pressure (shape of yield surface in the deviatoric plane)	
μ_{visc}	0.0001	[s]	Viscosity parameter (relaxation time of the system)	

Uniaxial stress-strain behaviour (CDP)

Properties	Compression			Tension		
	Tension recovery		0.1	Compression recovery		0
	Yield stress	Inelastic strain	Compression damage	Yield stress	Crack opening width	Tension damage
Inp. No.	$\sigma_{c,y}$	$\varepsilon_{c,pl}$	d_c	$\sigma_{t,y}$	$w_{t,pl}$	d_t
Unit	[MPa]	[-]	[-]	[MPa]	[mm]	[-]
1	10.92	0	0	4.80	0	0
2	21.40	0.001349	0	2.88	0.016501117	0
3	31.37	0.002041	0	0.96	0.033002233	0
4	40.73	0.002748	0	0.72	0.066004467	0.25
5	49.36	0.003472	0	0.00	0.165011167	0.99
6	57.11	0.004217	0			
7	63.77	0.004988	0			
8	69.08	0.005791	0			
9	72.66	0.006636	0			
10	74.00	0.007534	0			
11	73.80	0.007875	0.002703694			
12	73.17	0.008226	0.011233374			
13	72.05	0.008589	0.026292778			
14	70.40	0.008965	0.048703743			
15	68.12	0.009355	0.079432065			
16	65.15	0.009763	0.119620453			
17	61.37	0.010189	0.170630996			
18	56.68	0.010638	0.234100452			
19	50.91	0.011111	0.312013164			
20	43.90	0.011615	0.406798500			
21	35.41	0.012154	0.521463016			
22	25.18	0.012735	0.659772701			
23	12.84	0.013365	0.826508922			
24	6.67	0.013660	0.909908087			
25	1.35	0.013904	0.981791002			

Table D.8.
Properties used to define concrete material law in the numerical simulations of the CoPOT specimen Bv2.

Properties	Value	Unit	Description	Bv2
Behaviour: Density				
ρ	2.4E-009	[tonne/mm^3]	Material density	
Behaviour: Elastic				
E_{cm}	42820	[MPa]	Young's Modulus	
ν	0.2	[-]	Poisson's Ratio	
Behaviour: Concrete Damage Plasticity (CDP)				
ψ	25	[°]	Dilation angle at high confining pressure in the p-q plane	
ϵ	0.1	[-]	Eccentricity of hyperbolic function approach (rate)	
fb0/fc0	1.16	[-]	Ratio between uniaxial and biaxial strength	
K_c	0.667	[-]	Ratio between tensile and compressive meridians of effective hydrostatic pressure (shape of yield surface in the deviatoric plane)	
μ_{visc}	0.0001	[s]	Viscosity parameter (relaxation time of the system)	

Uniaxial stress-strain behaviour (CDP)

Properties	Compression			Tension		
	Tension recovery		0.1	Compression recovery		0
	Yield stress	Inelastic strain	Compression damage	Yield stress	Crack opening width	Tension damage
Inp. No.	$\sigma_{c,y}$	$\varepsilon_{c,pl}$	d_c	$\sigma_{t,y}$	$w_{t,pl}$	d_t
Unit	[MPa]	[-]	[-]	[MPa]	[mm]	[-]
1	11.40	0	0	5.05	0	0
2	22.40	0.001245	0	3.03	0.015879802	0
3	32.91	0.001883	0	1.01	0.031759605	0
4	42.84	0.002536	0	0.76	0.063519209	0.25
5	52.06	0.003204	0	0.00	0.158798023	0.99
6	60.40	0.003893	0			
7	67.65	0.004608	0			
8	73.48	0.005356	0			
9	77.48	0.006147	0			
10	79.00	0.006995	0			
11	78.84	0.007265	0.002019359			
12	78.34	0.007544	0.008376983			
13	77.45	0.007831	0.019574110			
14	76.14	0.008128	0.036192285			
15	74.35	0.008436	0.058910121			
16	72.01	0.008757	0.088524423			
17	69.05	0.009093	0.125977104			
18	65.38	0.009445	0.172389781			
19	60.90	0.009816	0.229108786			
20	55.48	0.010209	0.297764406			
21	48.95	0.010628	0.380349914			
22	41.13	0.011077	0.479328545			
23	31.78	0.011562	0.597780678			
24	20.57	0.012091	0.739610030			
25	7.12	0.012671	0.909838432			
26	1.00	0.012921	0.987288357			

Table D.9.
Properties used to define concrete material law in the numerical simulations of the CoPOT specimen Cv2.

Properties	Value	Unit	Description	Cv2
Behaviour: Density				
ρ	2.4E-009	[tonne/mm^3]	Material density	
Behaviour: Elastic				
E_{cm}	36268	[MPa]	Young's Modulus	
ν	0.2	[-]	Poisson's Ratio	
Behaviour: Concrete Damage Plasticity (CDP)				
ψ	38	[°]	Dilation angle at high confining pressure in the p-q plane	
ϵ	0.1	[-]	Eccentricity of hyperbolic function approach (rate)	
fb0/fc0	1.16	[-]	Ratio between uniaxial and biaxial strength	
K_c	0.667	[-]	Ratio between tensile and compressive meridians of effective hydrostatic pressure (shape of yield surface in the deviatoric plane)	
μ_{visc}	0.000025	[s]	Viscosity parameter (relaxation time of the system)	

Uniaxial stress-strain behaviour (CDP)

Properties	Compression			Tension		
	Tension recovery		0.1	Compression recovery		0
	Yield stress	Inelastic strain	Compression damage	Yield stress	Crack opening width	Tension damage
Inp. No.	$\sigma_{c,y}$	$\varepsilon_{c,pl}$	d_c	$\sigma_{t,y}$	$w_{t,pl}$	d_t
Unit	[MPa]	[-]	[-]	[MPa]	[mm]	[-]
1	8.38	0	0	3.39	0	0
2	16.09	0.000036	0	2.03	0.021607572	0.4
3	23.09	0.000083	0	0.68	0.043215144	0.8
4	29.33	0.000151	0	0.51	0.086430288	0.85
5	34.77	0.000241	0	0.00	0.216075720	0.999
6	39.35	0.000355	0			
7	43.03	0.000494	0			
8	45.74	0.000659	0			
9	47.42	0.000852	0			
10	48	0.001077	0			
11	47.87	0.001190	0.002610120			
12	47.49	0.001310	0.010552629			
13	46.85	0.001438	0.024001231			
14	45.93	0.001574	0.043137258			
15	44.73	0.001717	0.068150093			
16	43.24	0.001868	0.099237620			
17	41.44	0.002027	0.136606709			
18	39.34	0.002195	0.180473732			
19	36.91	0.002372	0.231065111			
20	34.15	0.002558	0.288617916			

Annex E – Details on the production and measurement equipment of big scale beam/column test specimens

Details on the fabrication process of reinforcement cages and placement of strain gauges in beam/column test specimens (VT) are shown in Fig. E.1-E.5 below.



a) b)

Fig. E.1. Details on fabrication of reinforcement cages in beam/column tests – a) initial stage and b) final stage.



a) b)

Fig. E.2. Details on reinforcement cages in beam/column test specimens – a) stirrups and b) internal view.



Fig. E.3. Details on grinded stirrups for gluing strain gauges in beam/column test specimens.



Fig. E.4. Detail of glued strain gauge to stirrup in beam/column test specimen.



Fig. E.5. Detail on closed reinforcement cage and distributed cables from strain gauges in beam/column test specimen.

Details on used steel profiles, application of flat V-shaped mechanical shear connectors and glued strain gauges are shown in Fig. E.6-E.11.



Fig. E.6. Details on welding of flat shear connectors to steel profiles in beam/column test specimens.

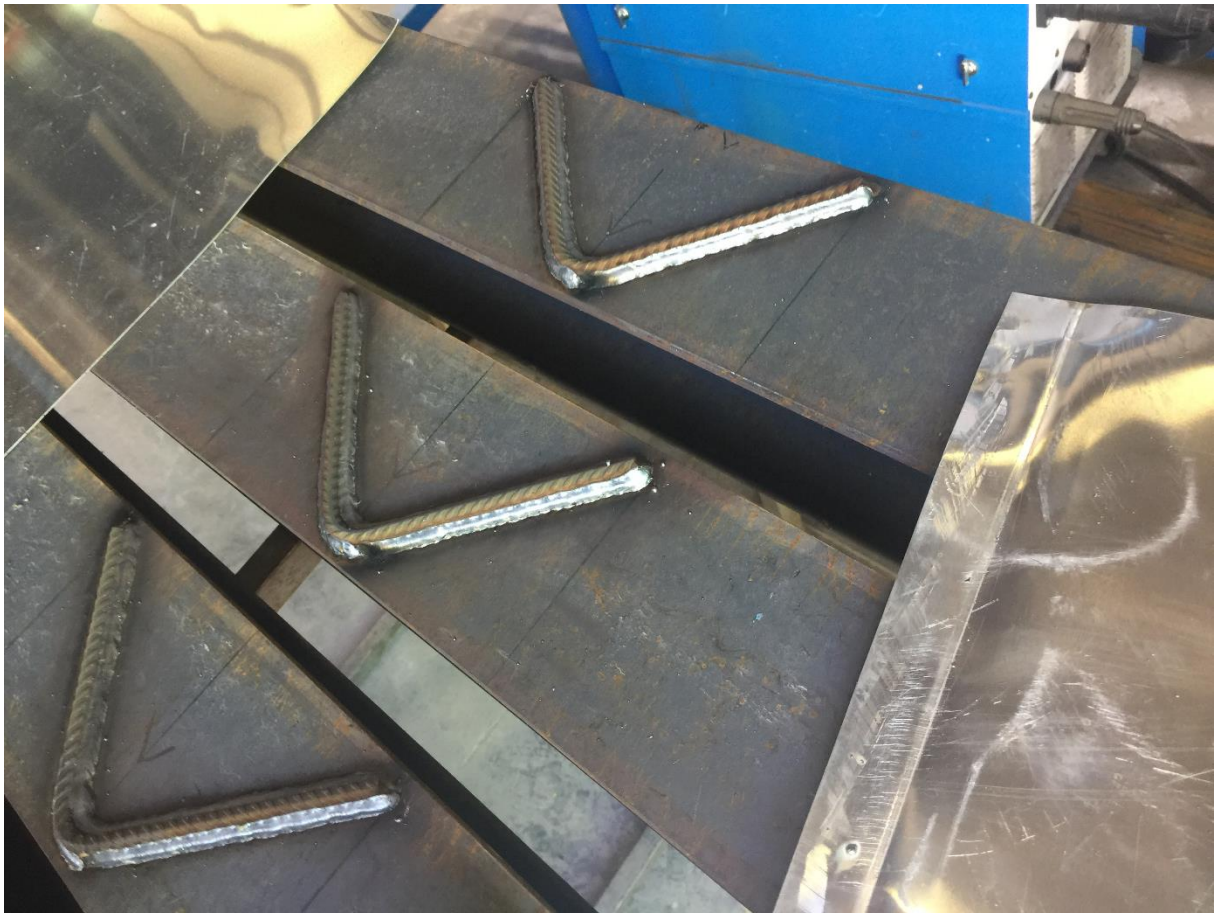


Fig. E.7. Details on welded flat shear connectors in beam/column test specimens.



Fig. E.8. Detail on steel profiles with applied shear connectors from beam/column tests.



a) b)

Fig. E.9. Details on welded slip measuring bars to steel profiles in beam/column test specimens – a) distribution over the length of steel profile and b) close view.



Fig. E.10. Detail on glued strain gauges in the chamber of steel profile in beam/column test specimens.



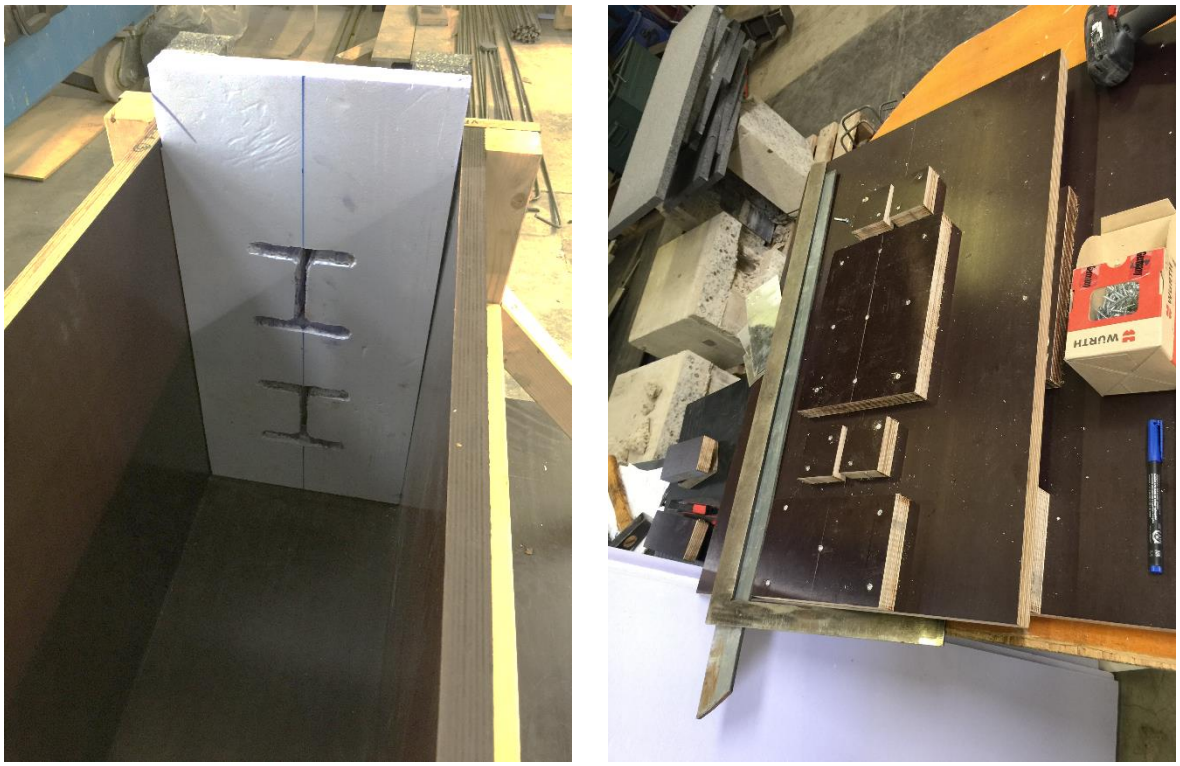
a) b)

Fig. E.11. Details on strain gauges glued to steel profiles in beam/column test specimens – a) general view on steel profiles and b) close view on one set of strain gauges in the chamber of steel profile.

Details on formwork and assembly of the beam/column test specimens is shown in Fig. E.12-E.21.



Fig. E.12. Detail on formwork of beam/column test specimens.



a) b)

Fig. E.13. Details on faceplates of the formwork of beam/column test specimens – a) polystyrene plate next to specimen and b) internal timber plate fixing position of steel profiles in the formwork.



Fig. E.14. Detail on assembly of reinforcement cages in the formwork of beam/column test specimens.



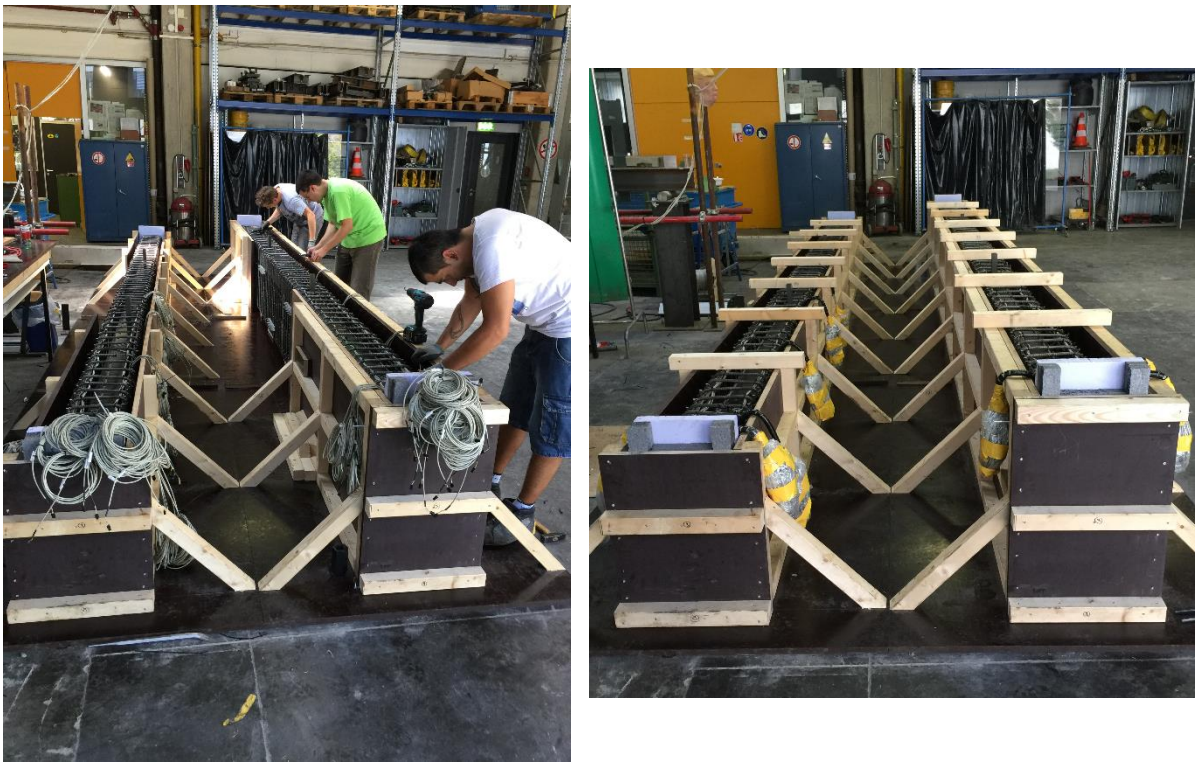
a) b)

Fig. E.15. Details on assembly of steel profiles in the formwork of beam/column test specimens – a) top perspective view and b) face view.



a) b)

Fig. E.16. Details on plastic distance-holders around slip measuring bars of beam/column test specimens – a) side view and b) top view.



a) b)

Fig. E.17. Details on final assembly of beam/column test specimens – a) works to close stirrups and b) finished specimens.



Fig. E.18. Detail on arrangement of parts in beam/column test specimen.



Fig. E.19. Detail on concreted beam/column test specimens.



Fig. E.20. Detail on beam/column test specimens after concrete hardening process.



a) b)

Fig. E.21. Details on beam/column test specimens after removing the formwork – a) slip measuring bar and b) protruding steel profiles.

Details on the measurement equipment and test layout are shown on Fig. E.22-E.32.



Fig. E.22. Detail on drawing of the net pattern on the walls of beam/column test specimens.

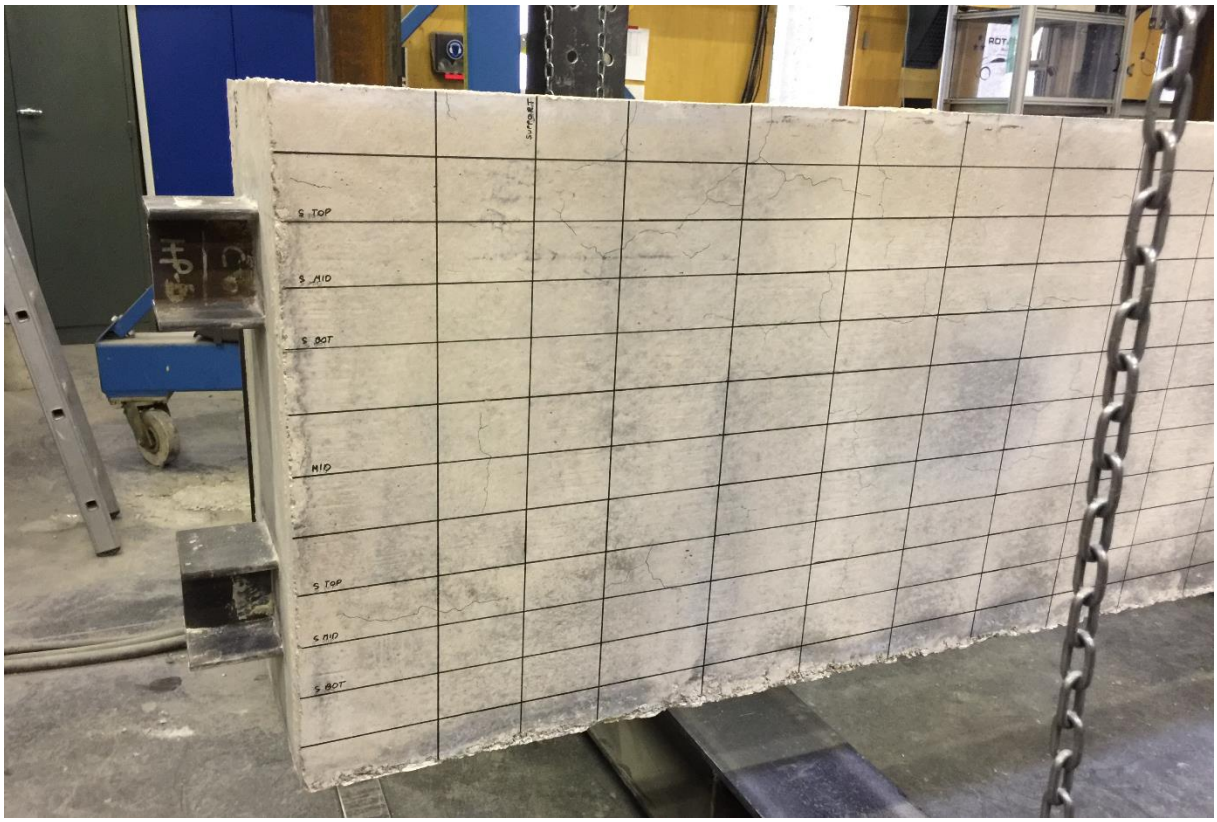


Fig. E.23. Detail on line drawn with reference to the position of steel profiles in beam/column test specimens.



Fig. E.24. Detail on displacement transducer placed to the sidewall of beam/column test specimens.

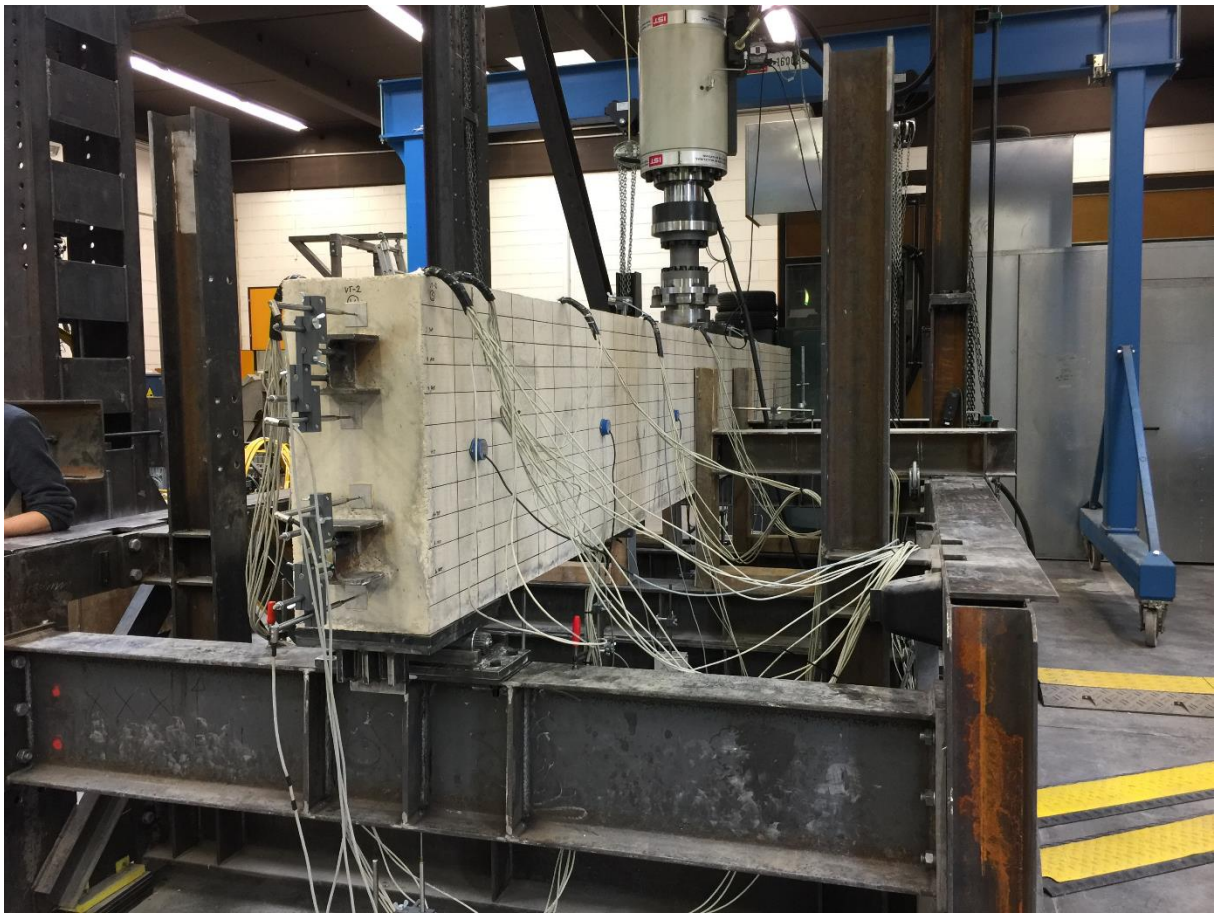
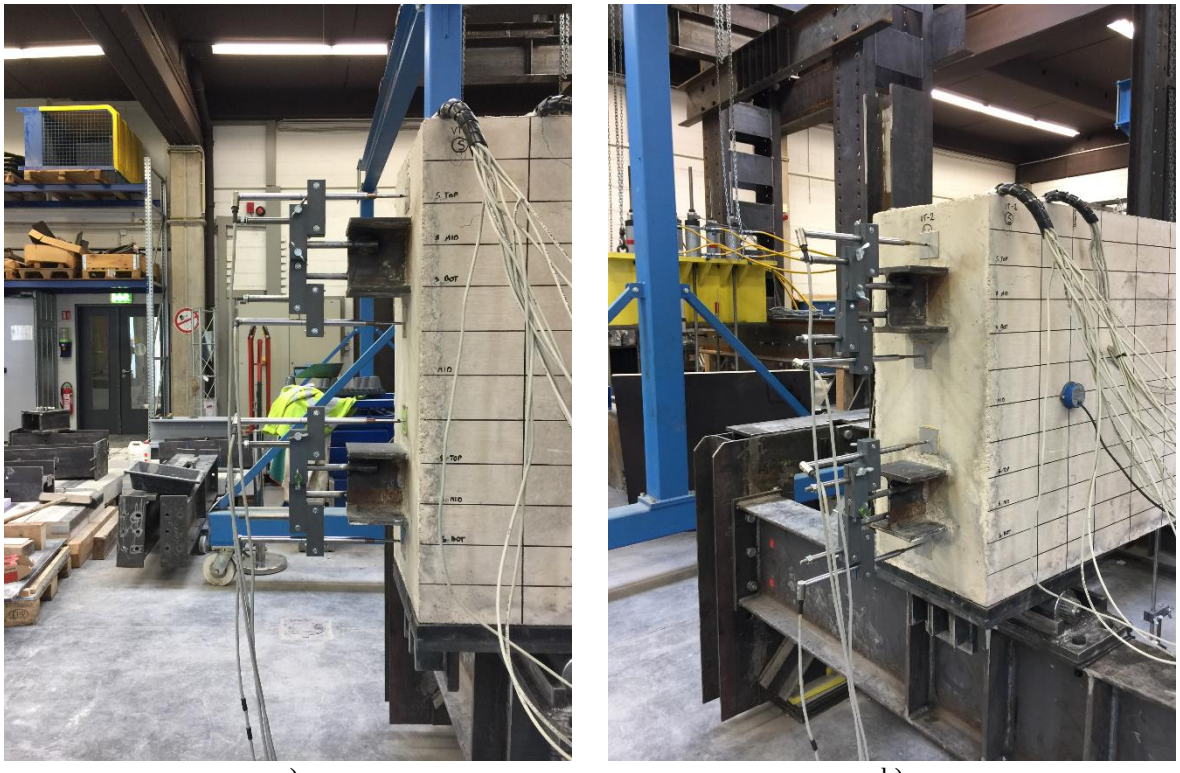


Fig. E.25. Detail on inclinometers and slip-measuring displacement transducers in beam/column test specimens.



a) b)

Fig. E.26. Details on slip-measuring displacement transducers in beam/column test specimens – a) side view and b) perspective view.

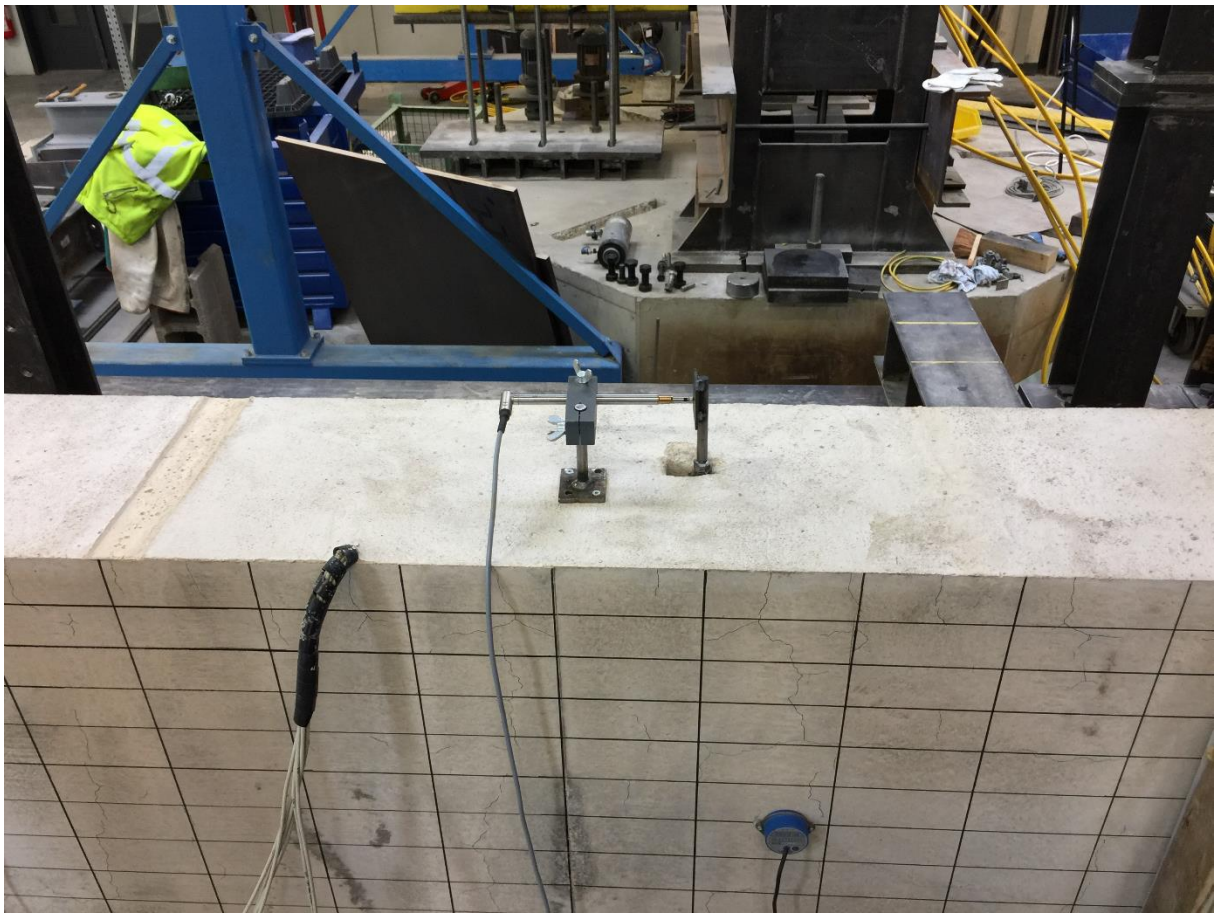


Fig. E.27. Detail on upper mid-slip measuring displacement transducer in beam/column test specimens.



Fig. E.28. Detail on lower mid-slip measuring displacement transducer in beam/column test specimens.



a) b)

Fig. E.29. Details on displacement transducers measuring deflection during beam/column tests – a) on specimen and b) on support beam.



a) b)

Fig. E.30. Details on laser displacement transducers measuring deflection in mid-zone of beam/column test specimens – a) on edge of mid-zone and b) on mid-span point.

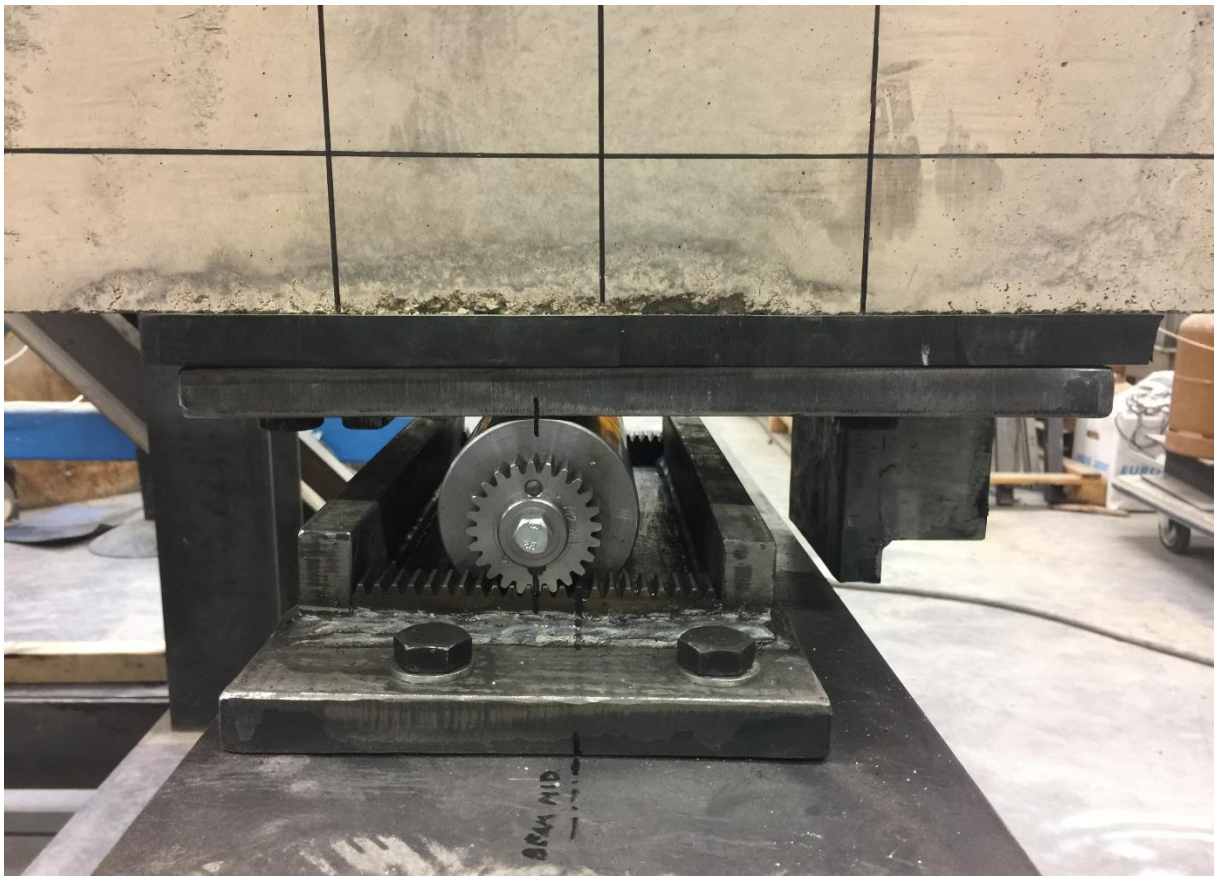


Fig. E.31. Detail on pin-sliding support used during beam/column tests.



Fig. E.32. Detail on test layout and lateral restraint during beam/column tests.

Annex F – Solver setup, energy balance and concrete material law in FE simulations of big scale beam/column tests

Solver setup for Abaqus/Explicit simulation of specimen VT-1 is given in Table F.1.

Table F.1.
Solver setup for Abaqus/Explicit simulation of specimen VT-1 of beam/column tests.

Specimen	VT-1					
Solver	Abaqus/Explicit					
Step	Dynamic/Explicit					
Time	800 s					
Speed	0.25 mm/s					
Nlgeom	On					
Amplitude	Smooth step	Time span	Time/Freq.	Amplitude		
		Step time	0	0		
			800	1		
Incrementation	Type	Stable increment estimator	Max. time increment	Time scaling factor		
	Automatic	Global	Unlimited	1		
Mass scaling	Defined scaling definitions	Region	Type	Frequency/ Interval	Factor	Target time increment
	Semi-automatic	Whole model	Factor	Beginning of step	1E+06	None
Other	Linear bulk viscosity parameter	0.06				
	Quadratic bulk viscosity parameter	1.2				

Energy balance for Abaqus/Explicit simulation of specimen VT-1 is shown in Fig. F.1.

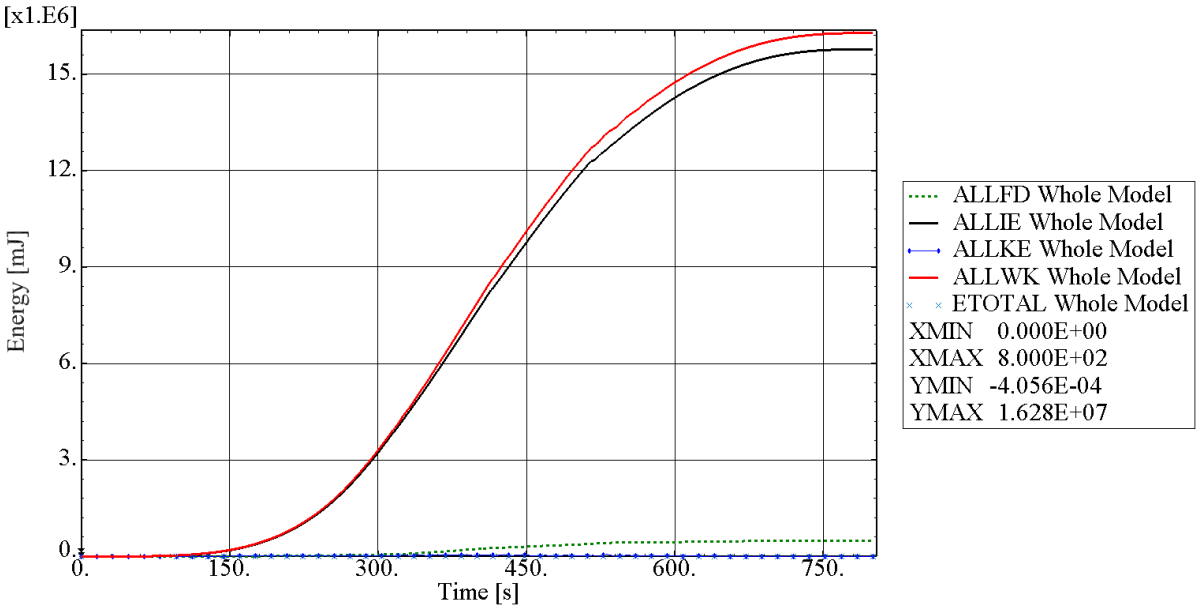


Fig. F.1. Energy balance for quasi-static simulation of specimen VT-1 of beam/column tests.

Solver setup for Abaqus/Explicit simulation of specimen VT-2 is given in Table F.2.

Table F.2.
Solver setup for Abaqus/Explicit simulation of specimen VT-2 of beam/column tests.

Specimen	VT-2					
Solver	Abaqus/Explicit					
Step	Dynamic/Explicit					
Time	800 s					
Speed	0.25 mm/s					
Nlgeom	On					
Amplitude	Smooth step	Time span	Time/Freq.	Amplitude		
		Step time	0	0		
			800	1		
Incrementation	Type	Stable increment estimator	Max. time increment	Time scaling factor		
	Automatic	Global	Unlimited	1		
Mass scaling	Defined scaling definitions	Region	Type	Frequency/ Interval	Factor	Target time increment
	Semi-automatic	Whole model	Factor	Beginning of step	1E+06	None
Other	Linear bulk viscosity parameter	0.06				
	Quadratic bulk viscosity parameter	1.2				

Energy balance for Abaqus/Explicit simulation of specimen VT-2 is shown in Fig. F.2.

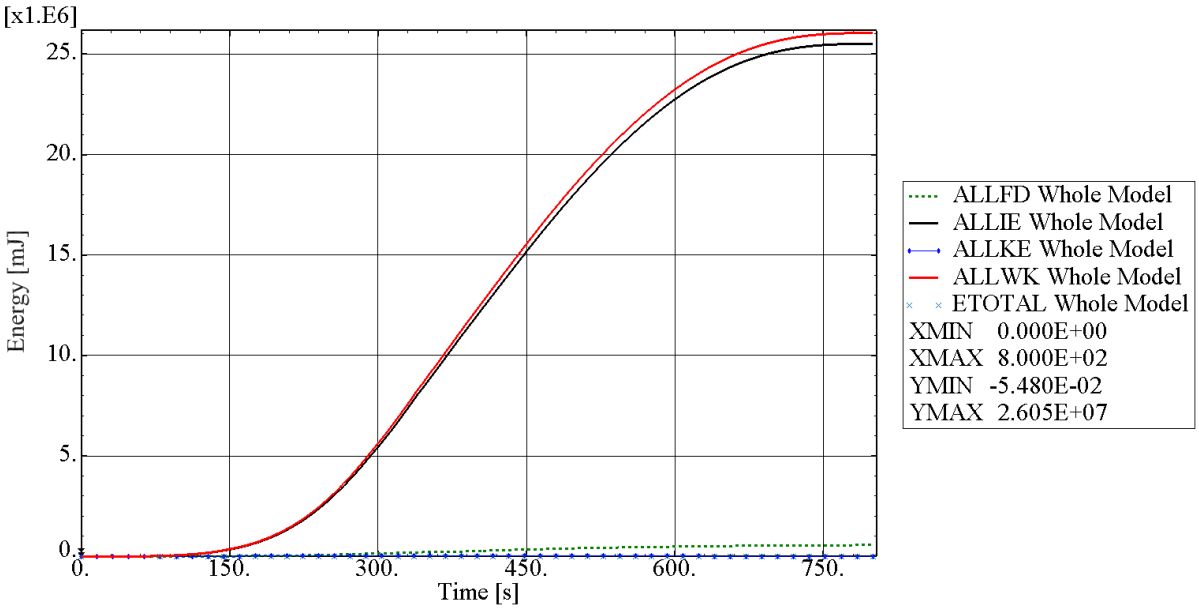


Fig. F.2. Energy balance for quasi-static simulation of specimen VT-2 of beam/column tests.

Input data of concrete material law (CDP) is given in Table F.3 for the specimen VT-1 and in Table F.4 for the specimen VT-2.

Table F.3.
Material properties used to define concrete material law in the FE simulations of beam/column specimen VT-1.

Properties	Value	Unit	Description	VT-1
Behaviour: Density				
ρ	2.4E-009	[tonne/mm^3]	Material density	
Behaviour: Elastic				
0.5 E_{cm}	0.5·39219=19610	[MPa]	Young's Modulus	
ν	0.2	[-]	Poisson's Ratio	

Behaviour: Concrete Damage Plasticity (CDP)			
ψ	25	[°]	Dilation angle at high confining pressure in the p-q plane
ϵ	0.1	[-]	Eccentricity of hyperbolic function approach (rate)
fb0/fc0	1.16	[-]	Ratio between uniaxial and biaxial strength
K_c	0.667	[-]	Ratio between tensile and compressive meridians of effective hydrostatic pressure (shape of yield surface in the deviatoric plane)
μ_{visc}	0.0001	[s]	Viscosity parameter (relaxation time of the system)

Uniaxial stress-strain behaviour (CDP)						
Properties	Compression			Tension		
	Tension recovery		0.1	Compression recovery		0
	Yield stress	Inelastic strain	Compression damage	Yield stress	Crack opening width	Tension damage
Inp. No.	$\sigma_{c,y}$	$\varepsilon_{c,pl}$	d_c	$\sigma_{t,y}$	$w_{t,pl}$	d_t
Unit	[MPa]	[-]	[-]	[MPa]	[mm]	[-]
1	10.36	0	0	3.08	0	0
2	19.95	0.0002	0	1.85	0.0248	0
3	28.72	0.0004	0	0.62	0.0496	0
4	36.60	0.0006	0	0.46	0.0992	0.25
5	43.52	0.0009	0	0	0.2480	0.99
6	49.41	0.0012	0			
7	54.17	0.0016	0			
8	57.71	0.0020	0			
9	59.93	0.0026	0			
10	60.70	0.0031	0			
11	60.62	0.0033	0.0013			
12	60.38	0.0035	0.0053			
13	59.97	0.0038	0.0120			
14	59.39	0.0040	0.0215			
15	58.64	0.0042	0.0340			
16	57.70	0.0045	0.0494			
17	56.57	0.0047	0.0680			
18	55.25	0.0050	0.0897			
19	53.74	0.0053	0.1147			
20	52.01	0.0055	0.1432			
21	50.07	0.0058	0.1751			
22	47.92	0.0061	0.2106			
23	45.53	0.0065	0.2499			
24	42.91	0.0068	0.2930			
25	40.05	0.0071	0.3402			
26	36.94	0.0075	0.3914			
27	33.57	0.0078	0.4469			
28	29.93	0.0082	0.5068			
29	26.02	0.0086	0.5714			
30	21.82	0.0090	0.6406			
31	17.32	0.0095	0.7147			
32	12.51	0.0099	0.7940			
33	7.38	0.0104	0.8784			
34	1.92	0.0108	0.9684			
35	1.01	0.0109	0.9833			

Table F.4.
Material properties used to define concrete material law in the FE simulations of beam/column specimen VT-2.

Properties	Value	Unit	Description	VT-2
Behaviour: Density				
ρ	2.4E-009	[tonne/mm^3]	Material density	
Behaviour: Elastic				
0.5 E_{cm}	0.5·37104=18552	[MPa]	Young's Modulus	
ν	0.2	[-]	Poisson's Ratio	

Behaviour: Concrete Damage Plasticity (CDP)			
ψ	25	[°]	Dilation angle at high confining pressure in the p-q plane
ϵ	0.1	[-]	Eccentricity of hyperbolic function approach (rate)
fb0/fc0	1.16	[-]	Ratio between uniaxial and biaxial strength
K_c	0.667	[-]	Ratio between tensile and compressive meridians of effective hydrostatic pressure (shape of yield surface in the deviatoric plane)
μ_{visc}	0.0001	[s]	Viscosity parameter (relaxation time of the system)

Uniaxial stress-strain behaviour (CDP)						
Properties	Compression			Tension		
	Tension recovery		0.1	Compression recovery		0
	Yield stress	Inelastic strain	Compression damage	Yield stress	Crack opening width	Tension damage
Inp. No.	$\sigma_{c,y}$	$\varepsilon_{c,pl}$	d_c	$\sigma_{t,y}$	$w_{t,pl}$	d_t
Unit	[MPa]	[-]	[-]	[MPa]	[mm]	[-]
1	8.35	0	0	3.59	0	0
2	16.19	0.00003	0	2.15	0.0207	0
3	23.46	0.00008	0	0.72	0.0413	0
4	30.10	0.0002	0	0.54	0.0826	0.25
5	36.02	0.0003	0	0	0.2066	0.99
6	41.16	0.0005	0			
7	45.39	0.0007	0			
8	48.61	0.0010	0			
9	50.67	0.0013	0			
10	51.40	0.0017	0			
11	51.34	0.0019	0.0011			
12	51.17	0.0020	0.0045			
13	50.87	0.0021	0.0103			
14	50.44	0.0023	0.0186			
15	49.88	0.0024	0.0295			
16	49.19	0.0026	0.0431			
17	48.34	0.0028	0.0595			
18	47.35	0.0029	0.0788			
19	46.19	0.0031	0.1013			
20	44.87	0.0033	0.1270			
21	43.38	0.0035	0.1560			
22	41.70	0.0037	0.1886			
23	39.84	0.0039	0.2249			
24	37.77	0.0042	0.2652			
25	35.49	0.0044	0.3094			
26	33.00	0.0047	0.3580			
27	30.27	0.0050	0.4111			
28	27.29	0.0052	0.4690			
29	24.06	0.0055	0.5318			
30	20.56	0.0058	0.6000			
31	16.77	0.0062	0.6737			
32	12.68	0.0065	0.7533			
33	8.27	0.0069	0.8391			
34	5.07	0.0071	0.9014			

Annex G – Calculations made in the evaluation of analytical models for effective stiffnesses of a column member with multiple encased steel profiles

Calculations of the bending stiffnesses given in Section 6.5.4.1 for the pure Euler-Bernoulli beam model and based on the design provisions given in EN 1994-1-1:

$$(EI)_{full} = E_a I_a + E_s I_s + E_{cm} I_c$$

$$(EI)_{eff,EC4} = E_a I_a + E_s I_s + K_c E_{cm} I_c$$

$$(EI)_{eff,II,EC4} = K_0 \left(E_a I_a + E_s I_s + K_{c,II} E_{cm} I_c\right)$$

For the specimen VT-1:

$$(EI)_{full,VT-1} = 2 \cdot E_a \cdot \left(I_{a,0} + A_a \cdot \left(\frac{d_{a,VT-1} + h_a}{2}\right)^2\right) + E_s \cdot I_{s,total,VT-1} + E_{cm,VT-1,EC2} \cdot I_{c,VT-1}$$

$$(EI)_{eff,EC4,VT-1} = 2 \cdot E_a \cdot \left(I_{a,0} + A_a \cdot \left(\frac{d_{a,VT-1} + h_a}{2}\right)^2\right) + E_s \cdot I_{s,total,VT-1} + K_c \cdot E_{cm,VT-1,EC2} \cdot I_{c,VT-1}$$

$$(EI)_{eff,II,EC4,VT-1} = K_0 \cdot \left(2 \cdot E_a \cdot \left(I_{a,0} + A_a \cdot \left(\frac{d_{a,VT-1} + h_a}{2}\right)^2\right) + E_s \cdot I_{s,total,VT-1} + K_{c,II} \cdot E_{cm,VT-1,EC2} \cdot I_{c,VT-1}\right)$$

$E_a = 20770.8\ [kN/cm^2]$ from material tests of structural steel, see Section 6.3.5.1

$I_{a,0} = 864\ [cm^4]$ from steel tables

$A_a = 34\ [cm^2]$ from steel tables

$d_{a,VT-1} = 10\ [cm]$

$h_a = 12\ [cm]$ from steel tables

$E_s = 20616.5\ [kN/cm^2]$ from material tests of reinforcement steel, see Section 6.3.5.1

$I_{s,total,VT-1} = 2314.54\ [cm^4]$

$f_{cm,cube} = 47.75\ [MPa]$ from material tests of concrete, see Section 6.3.5.1

$f_{ck,cube} = f_{cm,cube} - 10\ [MPa] = 37.75\ [MPa]$

$f_{ck} = f_{ck,cube} \cdot \frac{30}{37} = 37.75 \cdot \frac{30}{37} = 30.61\ [MPa]$

$f_{cm} = f_{ck} + 8\ [MPa] = 38.61\ [MPa]$

$E_{cm,VT-1,EC2} = 22 \cdot \left(\frac{f_{cm}}{10}\right)^{0.3} = 32.9933\ [GPa]$ from EN 1992-1-1

$E_{cm,VT-1,EC2} = 3299.33\ [kN/cm^2]$

$$I_{c,VT-1} = I_{g,VT-1} - 2 \cdot \left(I_{a,0} + A_a \cdot \left(\frac{d_{a,VT-1} + h_a}{2} \right)^2 \right) - I_{s,total,VT-1}$$

$$I_{c,VT-1} = \frac{31.5 \cdot 57.5^3}{12} - 2 \cdot \left(864 + 34 \cdot \left(\frac{10 + 12}{2} \right)^2 \right) - 2314.54 = 486766.6 \; [cm^4]$$

$K_c = 0.6$ from EN 1994-1-1

$K_{c,II} = 0.5$ from EN 1994-1-1

$K_0 = 0.9$ from EN 1994-1-1

$$(EI)_{full,VT-1} = 2 \cdot 20770.8 \cdot \left(864 + 34 \cdot \left(\frac{10 + 12}{2} \right)^2 \right) + 20616.5 \cdot 2314.54 + 3299.33 \cdot 486766.6 = 1860517201 \; [kNcm^2]$$

$$(EI)_{eff,EC4,VT-1} = 2 \cdot 20770.8 \cdot \left(864 + 34 \cdot \left(\frac{10 + 12}{2} \right)^2 \right) + 20616.5 \cdot 2314.54 + 0.6 \cdot 3299.33 \cdot 486766.6 = 1218115077 \; [kNcm^2]$$

$$(EI)_{eff,II,EC4,VT-1} = 0.9 \cdot 2 \cdot 20770.8 \cdot \left(864 + 34 \cdot \left(\frac{10 + 12}{2} \right)^2 \right) + 0.9 \cdot 20616.5 \cdot 2314.54 + 0.9 \cdot 0.5 \cdot 3299.33 \cdot 486766.6 = 951763092 \; [kNcm^2]$$

For the specimen VT-2:

$$(EI)_{full,VT-2} = 2 \cdot E_a \cdot \left(I_{a,0} + A_a \cdot \left(\frac{d_{a,VT-2} + h_a}{2} \right)^2 \right) + E_s \cdot I_{s,total,VT-2} + E_{cm,VT-2,EC2} \cdot I_{c,VT-2}$$

$$(EI)_{eff,EC4,VT-2} = 2 \cdot E_a \cdot \left(I_{a,0} + A_a \cdot \left(\frac{d_{a,VT-2} + h_a}{2} \right)^2 \right) + E_s \cdot I_{s,total,VT-2} + K_c \cdot E_{cm,VT-2,EC2} \cdot I_{c,VT-2}$$

$$(EI)_{eff,II,EC4,VT-2} = K_0 \cdot \left(2 \cdot E_a \cdot \left(I_{a,0} + A_a \cdot \left(\frac{d_{a,VT-2} + h_a}{2} \right)^2 \right) + E_s \cdot I_{s,total,VT-2} + K_{c,II} \cdot E_{cm,VT-2,EC2} \cdot I_{c,VT-2} \right)$$

$E_a = 20770.8 \; [kN/cm^2]$ from material tests of structural steel, see Section 6.3.5.1

$I_{a,0} = 864 \; [cm^4]$ from steel tables

$A_a = 34 \; [cm^2]$ from steel tables

$d_{a,VT-2} = 26 \; [cm]$

$h_a = 12 \; [cm]$ from steel tables

$E_s = 20616.5\ [kN/cm^2]$ from material tests of reinforcement steel, see Section 6.3.5.1

$I_{s,total,VT-2} = 4582.56\ [cm^4]$

$f_{cm,cube} = 44.25\ [MPa]$ from material tests of concrete, see Section 6.3.5.1

$f_{ck,cube} = f_{cm,cube} - 10\ [MPa] = 34.25\ [MPa]$

$$f_{ck} = f_{ck,cube} \cdot \frac{30}{37} = 34.25 \cdot \frac{30}{37} = 27.77\ [MPa]$$

$f_{cm} = f_{ck} + 8\ [MPa] = 35.77\ [MPa]$

$$E_{cm,VT-2,EC2} = 22 \cdot \left(\frac{f_{cm}}{10}\right)^{0.3} = 32.2463\ [GPa]$$ from EN 1992-1-1

$E_{cm,VT-2,EC2} = 3224.63\ [kN/cm^2]$

$$I_{c,VT-2} = I_{g,VT-2} - 2 \cdot \left(I_{a,0} + A_a \cdot \left(\frac{d_{a,VT-2} + h_a}{2}\right)^2\right) - I_{s,total,VT-2}$$

$$I_{c,VT-2} = \frac{31.5 \cdot 73.5^3}{12} - 2 \cdot \left(864 + 34 \cdot \left(\frac{26+12}{2}\right)^2\right) - 4582.56 = 1011438\ [cm^4]$$

$K_c = 0.6$ from EN 1994-1-1

$K_{c,II} = 0.5$ from EN 1994-1-1

$K_0 = 0.9$ from EN 1994-1-1

$$(EI)_{full,VT-2} = 2 \cdot 20770.8 \cdot \left(864 + 34 \cdot \left(\frac{26+12}{2}\right)^2\right) + 20616.5 \cdot 4582.56 + 3224.63 \cdot 1011438 = 3901759347\ [kNcm^2]$$

$$(EI)_{eff,EC4,VT-2} = 2 \cdot 20770.8 \cdot \left(864 + 34 \cdot \left(\frac{26+12}{2}\right)^2\right) + 20616.5 \cdot 4582.56 + 0.6 \cdot 3224.63 \cdot 1011438 = 2597155591\ [kNcm^2]$$

$$(EI)_{eff,II,EC4,VT-2} = 0.9 \cdot 2 \cdot 20770.8 \cdot \left(864 + 34 \cdot \left(\frac{26+12}{2}\right)^2\right) + 0.9 \cdot 20616.5 \cdot 4582.56 + 0.9 \cdot 0.5 \cdot 3224.63 \cdot 1011438 = 2043904187\ [kNcm^2]$$

Calculations of the bending and shear stiffnesses given in Section 6.5.4.2 for the Timoshenko beam model are based on the design provisions given in EN 1994-1-1 and theory of elasticity. For the evaluation of bending stiffness, calculations are identical to the described above calculations for pure Euler-Bernoulli beam model. Evaluation of shear stiffness is given below:

$$(A_v G)_{full} = A_{v,full} \cdot G = \frac{I_{v,g,full} \cdot t_{c,\eta a,full}}{S_{v,\eta a,full}} \cdot \frac{E_a}{2 \cdot (1+\nu)}$$

$$(A_v G)_{eff,EC4} = A_{v,eff,EC4} \cdot G = \frac{I_{v,g,eff,EC4} \cdot t_{c,\eta a,eff,EC4}}{S_{v,\eta a,eff,EC4}} \cdot \frac{E_a}{2 \cdot (1+\nu)}$$

$$(A_v G)_{eff,II,EC4} = A_{v,eff,II,EC4} \cdot G = \frac{I_{v,g,eff,II,EC4} \cdot t_{c,\eta a,eff,II,EC4}}{S_{v,\eta a,eff,II,EC4}} \cdot \frac{E_{a,eff,II,EC4}}{2 \cdot (1+\nu)}$$

For the specimen VT-1:

$$(A_v G)_{full,VT-1} = A_{v,full,VT-1} \cdot G = \frac{I_{v,g,full,VT-1} \cdot t_{c,\eta a,full,VT-1}}{S_{v,\eta a,full,VT-1}} \cdot \frac{E_a}{2 \cdot (1+\nu)}$$

$$(A_v G)_{eff,EC4,VT-1} = A_{v,eff,EC4,VT-1} \cdot G = \frac{I_{v,g,eff,EC4,VT-1} \cdot t_{c,\eta a,eff,EC4,VT-1}}{S_{v,\eta a,eff,EC4,VT-1}} \cdot \frac{E_a}{2 \cdot (1+\nu)}$$

$$(A_v G)_{eff,II,EC4,VT-1} = A_{v,eff,II,EC4,VT-1} \cdot G = \frac{I_{v,g,eff,II,EC4,VT-1} \cdot t_{c,\eta a,eff,II,EC4,VT-1}}{S_{v,\eta a,eff,II,EC4,VT-1}} \cdot \frac{E_{a,eff,II,EC4}}{2 \cdot (1+\nu)}$$

$E_a = 20770.8\ [kN/cm^2]$ from material tests of structural steel, see Section 6.3.5.1

$\nu_a = 0.3$ Poisson's ratio for structural steel

$E_{cm,VT-1,EC2} = 3299.33\ [kN/cm^2]$ see calculations for Euler-Bernoulli beam model

$$\eta_{a,full,VT-1} = \frac{E_{cm,VT-1,EC2}}{E_a} = 0.159$$

$t_{w,a} = 0.65\ [cm]$

$t_{f,a} = 1.10\ [cm]$

$b_{f,a} = 12.00\ [cm]$

$t_{c,\eta a,full,VT-1} = B \cdot \eta_{a,full,VT-1} = 5.00\ [cm]$

$t_{w,\eta a,full,VT-1} = t_{w,a} + \eta_{a,full,VT-1} \cdot (B - t_{w,a}) = 5.55\ [cm]$

$b_{f,\eta a,full,VT-1} = b_{f,a} + \eta_{a,full,VT-1} \cdot (B - b_{f,a}) = 15.10\ [cm]$

$I_{v,g,full,VT-1} = 87349.52\ [cm^4]$ according to Fig. G.1a

$A_{S,v,\eta a,full,VT-1} = \frac{A_{total,\eta a,full,VT-1}}{2} = 171.42\ [cm^2]$ according to Fig. G.1a

$z_{S,v,\eta a,full,VT-1} = 14.92\ [cm]$ distance from the centroid of cut half area of the composite section in steel units to the top fibre

$h_{S,v,\eta a,VT-1} = \frac{H_{VT-1}}{2} = 28.75\ [cm]$ according to Fig. G.1a

$S_{v,\eta a,full,VT-1} = A_{S,v,\eta a,full,VT-1} \cdot (h_{S,v,\eta a,VT-1} - z_{S,v,\eta a,full,VT-1}) = 2371.11\ [cm^3]$

$K_c = 0.6$ from EN 1994-1-1

$$\eta_{a,eff,EC4,VT-1} = \frac{K_c \cdot E_{cm,VT-1,EC2}}{E_a} = 0.095$$

$t_{c,\eta a,eff,EC4,VT-1} = B \cdot \eta_{a,eff,EC4,VT-1} = 3.00\ [cm]$

$t_{w,\eta a,eff,EC4,VT-1} = t_{w,a} + \eta_{a,eff,EC4,VT-1} \cdot (B - t_{w,a}) = 3.59\ [cm]$

$b_{f,\eta a,eff,EC4,VT-1} = b_{f,a} + \eta_{a,eff,EC4,VT-1} \cdot (B - b_{f,a}) = 13.86\ [cm]$

$I_{v,g,eff,EC4,VT-1} = 56252.08\ [cm^4]$ according to Fig. G.1a

$A_{S,v,\eta a,eff,EC4,VT-1} = \frac{A_{total,\eta a,eff,EC4,VT-1}}{2} = 115.96\ [cm^2]$ according to Fig. G.1a

$z_{S,v,\eta a,eff,EC4,VT-1} = 15.24\ [cm]$ distance from the centroid of cut half area of the composite section in steel units to the top fibre

$h_{S,v,\eta a,VT-1} = \frac{H_{VT-1}}{2} = 28.75\ [cm]$ according to Fig. G.1a

$S_{v,\eta a,eff,EC4,VT-1} = A_{S,v,\eta a,eff,EC4,VT-1} \cdot \left(h_{S,v,\eta a,VT-1} - z_{S,v,\eta a,eff,EC4,VT-1}\right) = 1566.85\ [cm^3]$

$K_{c,II} = 0.5$ from EN 1994-1-1

$K_0 = 0.9$ from EN 1994-1-1

$\eta_{a,eff,II,EC4,VT-1} = \frac{K_0 \cdot K_c \cdot E_{cm,VT-1,EC2}}{K_0 \cdot E_a} = 0.079$

$t_{c,\eta a,eff,II,EC4,VT-1} = B \cdot \eta_{a,eff,II,EC4,VT-1} = 2.50\ [cm]$

$t_{w,\eta a,eff,II,EC4,VT-1} = t_{w,a} + \eta_{a,eff,II,EC4,VT-1} \cdot \left(B - t_{w,a}\right) = 3.10\ [cm]$

$b_{f,\eta a,eff,II,EC4,VT-1} = b_{f,a} + \eta_{a,eff,II,EC4,VT-1} \cdot \left(B - b_{f,a}\right) = 13.55\ [cm]$

$I_{v,g,eff,II,EC4,VT-1} = 48477.72\ [cm^4]$ according to Fig. G.1a

$A_{S,v,\eta a,eff,II,EC4,VT-1} = \frac{A_{total,\eta a,eff,II,EC4,VT-1}}{2} = 102.09\ [cm^2]$ according to Fig. G.1a

$z_{S,v,\eta a,eff,II,EC4,VT-1} = 15.37\ [cm]$ distance from the centroid of cut half area of the composite section in steel units to the top fibre

$h_{S,v,\eta a,VT-1} = \frac{H_{VT-1}}{2} = 28.75\ [cm]$ according to Fig. G.1a

$S_{v,\eta a,eff,EC4,VT-1} = A_{S,v,\eta a,eff,EC4,VT-1} \cdot \left(h_{S,v,\eta a,VT-1} - z_{S,v,\eta a,eff,EC4,VT-1}\right) = 1365.79\ [cm^3]$

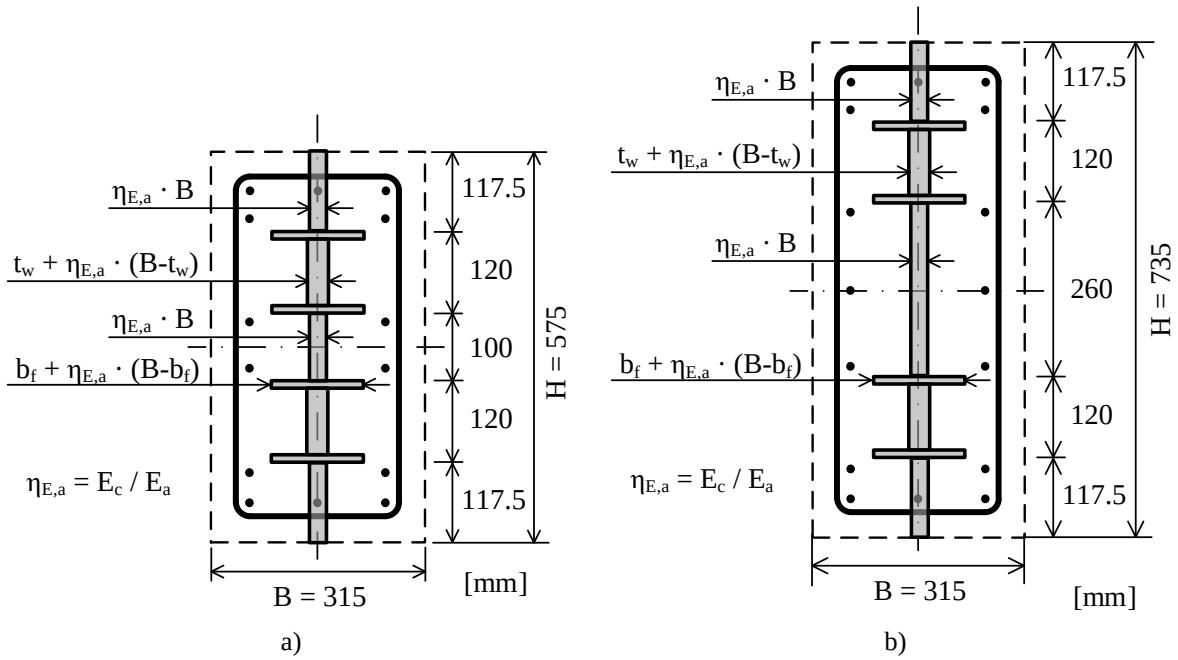


Fig. G.1. Cross-section geometry of the beam/column test specimens in steel units – a) for the specimen VT-1 and b) for the specimen VT-2.

$$(A_v G)_{full,VT-1} = \frac{87349.52 \cdot 5.00}{2371.11} \cdot \frac{20770.8}{2 \cdot (1 + 0.3)} = 1472558\ [kN]$$

$$(A_v G)_{eff,EC4,VT-1} = \frac{56252.08 \cdot 3.00}{1566.85} \cdot \frac{20770.8}{2 \cdot (1 + 0.3)} = 861043\ [kN]$$

$$(A_v G)_{eff,II,EC4,VT-1} = \frac{48477.72 \cdot 2.50}{1365.79} \cdot \frac{0.9 \cdot 20770.8}{2 \cdot (1 + 0.3)} = 638461\ [kN]$$

For the specimen VT-2:

$$(A_v G)_{full,VT-2} = A_{v,full,VT-2} \cdot G = \frac{I_{v,g,full,VT-2} \cdot t_{c,\eta a,full,VT-2}}{S_{v,\eta a,full,VT-2}} \cdot \frac{E_a}{2 \cdot (1 + \nu)}$$

$$(A_v G)_{eff,EC4,VT-2} = A_{v,eff,EC4,VT-2} \cdot G = \frac{I_{v,g,eff,EC4,VT-2} \cdot t_{c,\eta a,eff,EC4,VT-2}}{S_{v,\eta a,eff,EC4,VT-2}} \cdot \frac{E_a}{2 \cdot (1 + \nu)}$$

$$(A_v G)_{eff,II,EC4,VT-2} = A_{v,eff,II,EC4,VT-2} \cdot G = \frac{I_{v,g,eff,II,EC4,VT-2} \cdot t_{c,\eta a,eff,II,EC4,VT-2}}{S_{v,\eta a,eff,II,EC4,VT-2}} \cdot \frac{E_{a,eff,II,EC4}}{2 \cdot (1 + \nu)}$$

$E_a = 20770.8\ [kN/cm^2]$ from material tests of structural steel, see Section 6.3.5.1

$\nu_a = 0.3$ Poisson's ratio for structural steel

$E_{cm,VT-2,EC2} = 3224.63\ [kN/cm^2]$ see calculations for Euler-Bernoulli beam model

$$\eta_{a,full,VT-2} = \frac{E_{cm,VT-2,EC2}}{E_a} = 0.155$$

$t_{w,a} = 0.65\ [cm]$

$t_{f,a} = 1.10\ [cm]$

$b_{f,a} = 12.00\ [cm]$

$t_{c,\eta a,full,VT-2} = B \cdot \eta_{a,full,VT-2} = 4.89\ [cm]$

$t_{w,\eta a,full,VT-2} = t_{w,a} + \eta_{a,full,VT-2} \cdot (B - t_{w,a}) = 5.44\ [cm]$

$b_{f,\eta a,full,VT-2} = b_{f,a} + \eta_{a,full,VT-2} \cdot (B - b_{f,a}) = 15.03\ [cm]$

$I_{v,g,full,VT-2} = 183216.73\ [cm^4]$ according to Fig. G.1b

$A_{S,v,\eta a,full,VT-2} = \frac{A_{total,\eta a,full,VT-2}}{2} = 207.4\ [cm^2]$ according to Fig. G.1b

$z_{S,v,\eta a,full,VT-2} = 18.29\ [cm]$ distance from the centroid of cut half area of the composite section in steel units to the top fibre

$h_{S,v,\eta a,VT-2} = \frac{H_{VT-2}}{2} = 36.75\ [cm]$ according to Fig. G.1b

$S_{v,\eta a,full,VT-2} = A_{S,v,\eta a,full,VT-2} \cdot (h_{S,v,\eta a,VT-2} - z_{S,v,\eta a,full,VT-2}) = 3828.31\ [cm^3]$

$K_c = 0.6$ from EN 1994-1-1

$$\eta_{a,eff,EC4,VT-2} = \frac{K_c \cdot E_{cm,VT-2,EC2}}{E_a} = 0.093$$

$t_{c,\eta a,eff,EC4,VT-2} = B \cdot \eta_{a,eff,EC4,VT-2} = 2.93\ [cm]$

$t_{w,\eta a,eff,EC4,VT-2} = t_{w,a} + \eta_{a,eff,EC4,VT-2} \cdot (B - t_{w,a}) = 3.52\ [cm]$

$b_{f,\eta a,eff,EC4,VT-2} = b_{f,a} + \eta_{a,eff,EC4,VT-2} \cdot (B - b_{f,a}) = 13.82\ [cm]$

$I_{v,g,eff,EC4,VT-2} = 120064.25\ [cm^4]$ according to Fig. G.1b

$A_{S,v,\eta a,eff,EC4,VT-2} = \frac{A_{total,\eta a,eff,EC4,VT-2}}{2} = 137.55\ [cm^2]$ according to Fig. G.1b

$z_{S,v,\eta a,eff,EC4,VT-2} = 18.24\ [cm]$ distance from the centroid of cut half area of the composite section in steel units to the top fibre

$h_{S,v,\eta a,VT-2} = \frac{H_{VT-2}}{2} = 36.75\ [cm]$ according to Fig. G.1b

$S_{v,\eta a,eff,EC4,VT-2} = A_{S,v,\eta a,eff,EC4,VT-2} \cdot (h_{S,v,\eta a,VT-2} - z_{S,v,\eta a,eff,EC4,VT-2}) = 2546.04\ [cm^3]$

$K_{c,II} = 0.5$ from EN 1994-1-1

$K_0 = 0.9$ from EN 1994-1-1

$\eta_{a,eff,II,EC4,VT-2} = \frac{K_0 \cdot K_c \cdot E_{cm,VT-2,EC2}}{K_0 \cdot E_a} = 0.078$

$t_{c,\eta a,eff,II,EC4,VT-2} = B \cdot \eta_{a,eff,II,EC4,VT-2} = 2.44\ [cm]$

$t_{w,\eta a,eff,II,EC4,VT-2} = t_{w,a} + \eta_{a,eff,II,EC4,VT-2} \cdot (B - t_{w,a}) = 3.04\ [cm]$

$b_{f,\eta a,eff,II,EC4,VT-2} = b_{f,a} + \eta_{a,eff,II,EC4,VT-2} \cdot (B - b_{f,a}) = 13.51\ [cm]$

$I_{v,g,eff,II,EC4,VT-2} = 104276.13\ [cm^4]$ according to Fig. G.1b

$A_{S,v,\eta a,eff,II,EC4,VT-2} = \frac{A_{total,\eta a,eff,II,EC4,VT-2}}{2} = 120.09\ [cm^2]$ according to Fig. G.1b

$z_{S,v,\eta a,eff,II,EC4,VT-2} = 18.22\ [cm]$ distance from the centroid of cut half area of the composite section in steel units to the top fibre

$h_{S,v,\eta a,VT-2} = \frac{H_{VT-2}}{2} = 36.75\ [cm]$ according to Fig. G.1b

$S_{v,\eta a,eff,EC4,VT-2} = A_{S,v,\eta a,eff,EC4,VT-2} \cdot (h_{S,v,\eta a,VT-2} - z_{S,v,\eta a,eff,EC4,VT-2}) = 2225.47\ [cm^3]$

$$(A_v G)_{full,VT-2} = \frac{183216.73 \cdot 4.89}{3828.31} \cdot \frac{20770.8}{2 \cdot (1 + 0.3)} = 1869714\ [kN]$$

$$(A_v G)_{eff,EC4,VT-2} = \frac{120064.25 \cdot 2.93}{2546.04} \cdot \frac{20770.8}{2 \cdot (1 + 0.3)} = 1105394\ [kN]$$

$$(A_v G)_{eff,II,EC4,VT-2} = \frac{104276.13 \cdot 2.44}{2225.47} \cdot \frac{0.9 \cdot 20770.8}{2 \cdot (1 + 0.3)} = 823745\ [kN]$$

Calculations of the bending stiffnesses according to the international models as shown in Fig. 6.183 and Fig. 6.184 are given below.

ACI 318

$$w_{ACI318} = \frac{P \cdot L^3}{48 \cdot (EI)_{eff,II}}$$

$\beta_{dns} = 0$ due to the lack of permanent axial load

$\phi_K = 0.875$ stiffness reduction factor for the second-order elastic analysis

$$(EI)_{eff} = 0.2E_cI_g + E_sI_{se}$$

$$(EI)_{eff,II} = \phi_K \cdot (0.2E_cI_g + E_sI_{se})$$

For the specimen VT-1:

$f_c' = f_{cm} = 38.61[MPa] = 5600\ [psi]$

$E_c = 57000 \cdot \sqrt{f_c'} = 4265489\ [psi]$ (in psi) according to ACI 318-14

$E_c = 29388.26\ [MPa] = 2938.83\ [kN/cm^2]$

$I_g = I_{c,VT-1} = 486766.6\ [cm^4]$ see calculations for the pure Euler-Bernoulli beam

$$I_a = 2 \cdot \left(I_{a,0} + A_a \cdot \left(\frac{d_{a,VT-1} + h_a}{2}\right)^2\right) = 2 \cdot \left(864 + 34 \cdot \left(\frac{10 + 12}{2}\right)^2\right) = 9956\ [cm^4]$$

$I_{s,total,VT-1} = 2314.54\ [cm^4]$

$E_a = 20770.8\ [kN/cm^2]$ from material tests of structural steel, see Section 6.3.5.1

$E_s = 20616.5\ [kN/cm^2]$ from material tests of reinforcement steel, see Section 6.3.5.1

$E_sI_{se} = E_aI_a + E_sI_{s,total,VT-1} = 20770.8 \cdot 9956 + 20616.5 \cdot 2314.54 = 254511798.7\ [kNcm^2]$

$$(EI)_{eff,II} = 0.875 \cdot (0.2 \cdot 2938.83 \cdot 486766.6 + 254511798.7) = 473039281\ [kNcm^2]$$

For the specimen VT-2:

$f_c' = f_{cm} = 35.77[MPa] = 5188\ [psi]$

$E_c = 57000 \cdot \sqrt{f_c'} = 4105583\ [psi]$ (in psi) according to ACI 318-14

$E_c = 28287.5\ [MPa] = 2828.75\ [kN/cm^2]$

$I_g = I_{c,VT-2} = 1011438\ [cm^4]$ see calculations for the pure Euler-Bernoulli beam

$$I_a = 2 \cdot \left(I_{a,0} + A_a \cdot \left(\frac{d_{a,VT-2} + h_a}{2}\right)^2\right) = 2 \cdot \left(864 + 34 \cdot \left(\frac{26 + 12}{2}\right)^2\right) = 26276\ [cm^4]$$

$I_{s,total,VT-2} = 4582.56\ [cm^4]$

$E_a = 20770.8\ [kN/cm^2]$ from material tests of structural steel, see Section 6.3.5.1

$E_s = 20616.5\ [kN/cm^2]$ from material tests of reinforcement steel, see Section 6.3.5.1

$E_sI_{se} = E_aI_a + E_sI_{s,total,VT-2} = 20770.8 \cdot 26276 + 20616.5 \cdot 4582.56 = 640249889\ [kNcm^2]$

$$(EI)_{eff,II} = 0.875 \cdot (0.2 \cdot 2828.75 \cdot 1011438 + 640249889) = 1060913456\ [kNcm^2]$$

AISC 360

$$w_{AISC360} = \frac{P \cdot L^3}{48 \cdot (EI)^*}$$

$\tau_b = 0.8$ stiffness reduction factor for slender columns

$$(EI)_{eff} = E_s I_s + E_{sr} I_{sr} + C_1 E_c I_g$$
$$(EI)^* = 0.8 \tau_b (EI)_{eff}$$

For the specimen VT-1:

$f_c' = f_{cm} = 38.61 [MPa]$

$\rho = 2400\ [kg/m^3]$

$E_c = 0.043 \cdot \rho^{1.5} \cdot \sqrt{f_c'}$

$E_c = 0.043 \cdot 2400^{1.5} \cdot \sqrt{38.61} = 3141.41\ [kN/cm^2]$ according to AISC 360-16

$I_g = I_{c,VT-1} = 486766.6\ [cm^4]$ see calculations for the pure Euler-Bernoulli beam

$A_s = A_a = 34\ [cm^2]$

$A_{sr} = A_{s,total} = 7.04\ [cm^2]$

$A_g = A_c = B \cdot H_{VT-1} - 2 \cdot A_a - A_{s,total} = 1743.18\ [cm^2]$ see Fig. G.1a

$$C_1 = 0.25 + 3\left(\frac{A_s + A_{sr}}{A_g}\right) = 0.25 + 3\left(\frac{2 \cdot 34 + 7.04}{1743.18}\right) = 0.38 \leq 0.7$$

$$I_s = I_a = 2 \cdot \left(I_{a,0} + A_a \cdot \left(\frac{d_{a,VT-1} + h_a}{2}\right)^2\right) = 2 \cdot \left(864 + 34 \cdot \left(\frac{10 + 12}{2}\right)^2\right) = 9956\ [cm^4]$$

$I_{sr} = I_{s,total,VT-1} = 2314.54\ [cm^4]$

$E_s = E_a = 20770.8\ [kN/cm^2]$ from material tests of structural steel, see Section 6.3.5.1

$E_{sr} = E_s = 20616.5\ [kN/cm^2]$ from material tests of reinforcement steel, see Section 6.3.5.1

$$(EI)_{eff} = 20770.8 \cdot 9956 + 20616.5 \cdot 2314.54 + 0.38 \cdot 3141.41 \cdot 486766.6 = 834265072.6\ [kNcm^2]$$

$$(EI)^* = 0.8 \cdot 0.8 \cdot 834265072.6 = 533929646.4\ [kNcm^2]$$

For the specimen VT-2:

$f_c' = f_{cm} = 35.77 [MPa]$

$\rho = 2400\ [kg/m^3]$

$E_c = 0.043 \cdot \rho^{1.5} \cdot \sqrt{f_c'}$

$E_c = 0.043 \cdot 2400^{1.5} \cdot \sqrt{35.77} = 3023.75\ [kN/cm^2]$ according to AISC 360-16

$I_g = I_{c,VT-2} = 1011438\ [cm^4]$ see calculations for the pure Euler-Bernoulli beam

$A_s = A_a = 34\ [cm^2]$

$A_{sr} = A_{s,total} = 8.04\ [cm^2]$

$A_g = A_c = B \cdot H_{VT-2} - 2 \cdot A_a - A_{s,total} = 2247.17\ [cm^2]$ see Fig. G.1b

$$C_1 = 0.25 + 3\left(\frac{A_s + A_{sr}}{A_g}\right) = 0.25 + 3\left(\frac{2 \cdot 34 + 8.04}{2247.17}\right) = 0.35 \leq 0.7$$

$$I_s = I_a = 2 \cdot \left(I_{a,0} + A_a \cdot \left(\frac{d_{a,VT-1} + h_a}{2}\right)^2\right) = 2 \cdot \left(864 + 34 \cdot \left(\frac{10 + 12}{2}\right)^2\right) = 26276\ [cm^4]$$

$I_{sr} = I_{s,total,VT-1} = 4582.56\ [cm^4]$

$E_s = E_a = 20770.8\ [kN/cm^2]$ from material tests of structural steel, see Section 6.3.5.1

$E_{sr} = E_s = 20616.5\ [kN/cm^2]$ from material tests of reinforcement steel, see Section 6.3.5.1

$$(EI)_{eff} = 20770.8 \cdot 26276 + 20616.5 \cdot 4582.56 + 0.35 \cdot 3023.75 \cdot 1011438 = 1715310401\ [kNcm^2]$$

$$(EI)^* = 0.8 \cdot 0.8 \cdot 1715310401 = 1097798656\ [kNcm^2]$$

Mirza/Tikka

$$w_{Mirza/Tikka} = \frac{P \cdot L^3}{48 \cdot (EI)_{eff}}$$

$$(EI)_{eff} = \left(0.313 + 0.00334\frac{L}{D} - 0.203\frac{e}{D}\right)E_c(I_g - I_{ss}) + 0.792E_{ss}I_{ss} + 0.788E_{sl}I_{sl}$$

For the specimen VT-1:

$L = 600\ [cm]$ length of the beam/column specimen between supports

$D = 57.5\ [cm]$ depth of the beam/column specimen in the plane of bending

$e = 0\ [cm]$ eccentricity of axial load

$E_c = 2938.83\ [kN/cm^2]$ based on calculations made in ACI 318

$E_{ss} = E_a = 20770.8\ [kN/cm^2]$ from material tests of structural steel, see Section 6.3.5.1

$E_{sl} = E_s = 20616.5\ [kN/cm^2]$ from material tests of reinforcement steel, see Section 6.3.5.1

$(I_g - I_{ss}) = I_{c,VT-1} = 486766.6\ [cm^4]$ see calculations for the pure Euler-Bernoulli beam

$I_{ss} = I_{a,VT-1} = 9956\ [cm^4]$ see calculations made in ACI 318

$I_{sl} = I_{s,total,VT-1} = 2314.54\ [cm^4]$

$$(EI)_{eff} = \left(0.313 + 0.00334\frac{600}{57.5} - 0.203\frac{0}{57.5}\right) \cdot 2938.83 \cdot 486766.6 + 0.792 \cdot 20770.8 \cdot 9956 + 0.788 \cdot 20616.5 \cdot 2314.54 = 698992786.5\ [kNcm^2]$$

For the specimen VT-2:

$L = 600\ [cm]$ length of the beam/column specimen between supports

$D = 73.5\ [cm]$ depth of the beam/column specimen in the plane of bending

$e = 0\ [cm]$ eccentricity of axial load

$E_c = 2828.75\ [kN/cm^2]$ based on calculations made in ACI 318

$E_{ss} = E_a = 20770.8\ [kN/cm^2]$ from material tests of structural steel, see Section 6.3.5.1

$E_{sl} = E_s = 20616.5\ [kN/cm^2]$ from material tests of reinforcement steel, see Section 6.3.5.1

$(I_g - I_{ss}) = I_{c,VT-2} = 1011438\ [cm^4]$ see calculations for the pure Euler-Bernoulli beam

$I_{ss} = I_{a,VT-2} = 26276\ [cm^4]$ see calculations made in ACI 318

$I_{sl} = I_{s,total,VT-2} = 4582.56\ [cm^4]$

$$(EI)_{eff} = \left(0.313 + 0.00334\frac{600}{73.5} - 0.203\frac{0}{73.5}\right) \cdot 2828.75 \cdot 1011438 + 0.792 \cdot 20770.8 \cdot 26276 + 0.788 \cdot 20616.5 \cdot 4582.56 = 1480237490\ [kNcm^2]$$

Lippes/Chanou

$$w_{Lippes/Chanou} = \frac{P \cdot L^3}{48 \cdot (EI)_{eff,mod}}$$

$$(EI)_{eff,mod} = k_B \cdot (EI)_{eff,II,EC4} = k_B K_0 \left(E_a I_a + E_s I_s + K_{c,II} E_{cm} I_c\right)$$

For the specimen VT-1:

$(EI)_{eff,II,EC4,VT-1} = 951763092\ [kNcm^2]$ see calculations for pure Euler-Bernoulli beam

$k_{B,min} = 0.7$

$$(EI)_{eff,mod} = 0.7 \cdot 951763092 = 666234164.2\ [kNcm^2]$$

For the specimen VT-2:

$(EI)_{eff,II,EC4,VT-2} = 2043904187\ [kNcm^2]$ see calculations for pure Euler-Bernoulli beam

$k_{B,min} = 0.7$

$$(EI)_{eff,mod} = 0.7 \cdot 2043904187 = 1430732931\ [kNcm^2]$$

SmartCoCo

$$w_{SmartCoCo} = \frac{P \cdot L^3}{48 \cdot (EI)_{eff}}$$

$$(EI)_{eff} = 0.5\left(1 + \frac{5N_{Ed}}{N_{pl,Rd}}\right)\left(K_0 K_{e,II} E_{cm} I_c + K_0 E_a I_a + K_0 E_s I_s\right)$$

$$(EI)_{eff,II} = K_c E_{c,eff} I_c + K_{sa}(E_s I_s + E_a I_a)$$

For the specimen VT-1:

$N_{Ed} = 0\ [kN]$ lack of normal force in beam/column specimens

$K_0 = 0.9$ calibration factor

$K_{e,II} = 0.5$ stiffness reduction factor

$E_{cm} = E_{cm,VT-1,EC2} = 3299.33\ [kN/cm^2]$ see calculations for pure Euler-Bernoulli beam

$I_c = I_{c,VT-1} = 486766.6\ [cm^4]$ see calculations for pure Euler-Bernoulli beam

$E_a = 20770.8\ [kN/cm^2]$ from material tests of structural steel, see Section 6.3.5.1

$I_a = I_{a,VT-1} = 9956\ [cm^4]$ see calculations made in ACI 318

$E_s = 20616.5\ [kN/cm^2]$ from material tests of reinforcement steel, see Section 6.3.5.1

$I_s = I_{s,total,VT-1} = 2314.54\ [cm^4]$

$K_c = 0.3/(1 + 0.5\varphi_{eff})$ simplified alternative equation, which gives the maximal reduction value

$\varphi_{eff} = 0$ due to the lack of permanent axial load

$K_c = 0.3$

$$E_{c,eff} = E_{cd}/(1 + \varphi_{eff}) = \frac{E_{cm}}{\gamma_{cE}} = \frac{E_{cm}}{1.2} = 2749.4\ [kN/cm^2]$$

$$K_{sa} = \frac{0.450\lambda^{0.147}}{1 + 1.433\varphi_{eff}\exp(-0.027\lambda)}$$

$L = 600\ [cm]$ length of the beam/column specimen between supports

$A_c = 1743.18\ [cm^2]$ see calculations for AISC 360

$A_a = 2 \cdot 34 = 68\ [cm^2]$ see calculations for AISC 360

$A_s = 7.04\ [cm^2]$ see calculations for AISC 360

$$\lambda = \frac{L}{\sqrt{\frac{I_c + I_a + I_s}{A_c + A_a + A_s}}} = \frac{600}{\sqrt{\frac{486766.6 + 9956 + 2314.54}{1743.18 + 68 + 7.04}}} = 36.22$$

$$K_{sa} = \frac{0.450 \cdot 36.22^{0.147}}{1 + 1.433 \cdot 0 \cdot \exp(-0.027 \cdot 36.22)} = 0.76$$

$$(EI)_{eff,VT-1} = 0.5 \cdot (0.9 \cdot 0.5 \cdot 3299.33 \cdot 486766.6 + 0.9 \cdot 20770.8 \cdot 9956 + 0.9 \cdot 20616.5 \cdot 2314.54) = 475881546\ [kNcm^2]$$

$$(EI)_{eff,II,VT-1} = 0.3 \cdot 2749.4 \cdot 486766.6 + 0.76 \cdot (20616.5 \cdot 2314.54 + 20770.8 \cdot 9956) = 595625679\ [kNcm^2]$$

For the specimen VT-2:

$N_{Ed} = 0\ [kN]$ lack of normal force in beam/column specimens

$K_0 = 0.9$ calibration factor

$K_{e,II} = 0.5$ stiffness reduction factor

$E_{cm} = E_{cm,VT-2,EC2} = 3224.63\ [kN/cm^2]$ see calculations for pure Euler-Bernoulli beam

$I_c = I_{c,VT-2} = 1011438\ [cm^4]$ see calculations for pure Euler-Bernoulli beam

$E_a = 20770.8\ [kN/cm^2]$ from material tests of structural steel, see Section 6.3.5.1

$I_a = I_{a,VT-2} = 26276\ [cm^4]$ see calculations made in ACI 318

$E_s = 20616.5\ [kN/cm^2]$ from material tests of reinforcement steel, see Section 6.3.5.1

$I_s = I_{s,total,VT-2} = 4582.56\ [cm^4]$

$K_c = 0.3/(1 + 0.5\varphi_{eff})$ simplified alternative equation, which gives the maximal reduction value

$\varphi_{eff} = 0$ due to the lack of permanent axial load

$K_c = 0.3$

$$E_{c,eff} = E_{cd}/(1 + \varphi_{eff}) = \frac{E_{cm}}{\gamma_{cE}} = \frac{E_{cm}}{1.2} = 2687.19\ [kN/cm^2]$$

$$K_{sa} = \frac{0.450\lambda^{0.147}}{1 + 1.433\varphi_{eff}\exp(-0.027\lambda)}$$

$L = 600\ [cm]$ length of the beam/column specimen between supports

$A_c = 2247.17\ [cm^2]$ see calculations for AISC 360

$A_a = 2 \cdot 34 = 68\ [cm^2]$ see calculations for AISC 360

$A_s = 8.04\ [cm^2]$ see calculations for AISC 360

$$\lambda = \frac{L}{\sqrt{\frac{I_c + I_a + I_s}{A_c + A_a + A_s}}} = \frac{600}{\sqrt{\frac{1011438 + 26276 + 4582.56}{2247.17 + 68 + 8.04}}} = 28.33$$

$K_{sa} = 1.0$ due to $\rho = \frac{A_a + A_s}{A_c} = \frac{68 + 8.04}{2247.17} = 0.034 < 0.04$

$$(EI)_{eff,VT-2} = 0.5 \cdot (0.9 \cdot 0.5 \cdot 3224.63 \cdot 1011438 + 0.9 \cdot 20770.8 \cdot 26276 + 0.9 \cdot 20616.5 \cdot 4582.56) = 1021952093\ [kNcm^2]$$

$$(EI)_{eff,II,VT-2} = 0.3 \cdot 2687.19 \cdot 1011438 + 0.76 \cdot (20616.5 \cdot 4582.56 + 20770.8 \cdot 26276) = 1455627304\ [kNcm^2]$$

Adebar

$$w_{Adebar} = \frac{P \cdot L^3}{48 \cdot (EI)_{eff}}$$

$$(EI)_{eff,up} = (0.6 + n)EI_g \leq EI_g$$

$$(EI)_{eff,low} = (0.2 + 2.5n)EI_g \leq 0.7EI_g$$

For the specimen VT-1:

$n = 0$ due to lack of normal force in beam/column specimens

$EI_g = E_cI_c + E_aI_a + E_sI_s$

$E_c = 2938.83\ [kN/cm^2]$ see calculations made in ACI 318

$I_c = I_{c,VT-1} = 486766.6\ [cm^4]$ see calculations for pure Euler-Bernoulli beam

$E_a = 20770.8\ [kN/cm^2]$ from material tests of structural steel, see Section 6.3.5.1

$I_a = I_{a,VT-1} = 9956\ [cm^4]$ see calculations made in ACI 318

$E_s = 20616.5\ [kN/cm^2]$ from material tests of reinforcement steel, see Section 6.3.5.1

$I_s = I_{s,total,VT-1} = 2314.54\ [cm^4]$

$$EI_{g,VT-1} = 2938.83 \cdot 486766.6 + 20770.8 \cdot 9956 + 20616.5 \cdot 2314.54 = 1685034041\ [kNcm^2]$$

$$(EI)_{eff,up,VT-1} = (0.6 + 0) \cdot 1685034041 = 1011020425\ [kNcm^2]$$

$$\leq 1685034041\ [kNcm^2]$$

$$(EI)_{eff,low,VT-1} = (0.2 + 2.5 \cdot 0) \cdot 1685034041 = 337006808\ [kNcm^2]$$

$$\leq 0.7 \cdot 1685034041 = 1179523829\ [kNcm^2]$$

For the specimen VT-2:

$n = 0$ due to lack of normal force in beam/column specimens

$EI_g = E_c I_c + E_a I_a + E_s I_s$

$E_c = 2828.75\ [kN/cm^2]$ see calculations made in ACI 318

$I_c = I_{c,VT-2} = 1011438\ [cm^4]$ see calculations for pure Euler-Bernoulli beam

$E_a = 20770.8\ [kN/cm^2]$ from material tests of structural steel, see Section 6.3.5.1

$I_a = I_{a,VT-2} = 26276\ [cm^4]$ see calculations made in ACI 318

$E_s = 20616.5\ [kN/cm^2]$ from material tests of reinforcement steel, see Section 6.3.5.1

$I_s = I_{s,total,VT-2} = 4582.56\ [cm^4]$

$$EI_{g,VT-2} = 2828.75 \cdot 1011438 + 20770.8 \cdot 26276 + 20616.5 \cdot 4582.56 = 3501362777\ [kNcm^2]$$

$$(EI)_{eff,up,VT-2} = (0.6 + 0) \cdot 3501362777 = 2356917649\ [kNcm^2]$$

$$\leq 3501362777\ [kNcm^2]$$

$$(EI)_{eff,low,VT-2} = (0.2 + 2.5 \cdot 0) \cdot 3501362777 = 1212472521\ [kNcm^2]$$

$$\leq 0.7 \cdot 3501362777 = 2450953944\ [kNcm^2]$$